Δελτίο της Ελληνικής Γεωλογικής Εταιρίας
Bulletin of the Geological Society of Greece

Τόμος XLVII, No 4

Volume XLVII, No 4

13° Διεθνές Συνέδριο της Ελληνικής Γεωλογικής Εταιρίας
Έρευνα και Εκμετάλλευση Ορυκτών Πόρων

13th International Congress of the Geological Society of Greece
September 5-8 2013, Chania, Crete, Greece

13th International Congress of the Geological Society of Greece
Exploration and Exploitation of Mineral Resources

Χανιά/Chania
2013

ΠΕΡΙΕΧΟΜΕΝΑ/CONTENTS

ΤΟΜΟΣ 1 / VOLUME 1

Εναρκτήριες Ομιλίες
Opening Lectures

Παλαιοντολογία, Στρωματογραφία και Ιζηματολογία
Palaeontology, Stratigraphy and Sedimentology

Γεωμορφολογία

Geomorphology

Πετρολογία και Ορυκτολογία
Petrology and Mineralogy

ΤΟΜΟΣ 2 / VOLUME 2

Tectonics and Geodynamics/Τεκτονική και Γεωδυναμική

Hydrology and Hydrogeology/Υδρολογία και Υδρογεωλογία

Geochemistry and Biogeochemistry/Γεωχημεία και Βιογεωχημεία

Environmental Geology/Περιβαλλοντική Γεωλογία

Geosciences in Education and Geosites/Γεωεπιστήμες στην Εκπαίδευση και Γεώτοποι

Τεκτονική και Γεωδυναμική
Tectonics and Geodynamics

Υδρολογία και Υδρογεωλογία
Hydrology and Hydrogeology

Γεωχημεία και Βιογεωχημεία
Geochemistry and Biogeochemistry

Περιβαλλοντική Γεωλογία
Environmental Geology

Γεωεπιστήμες στην Εκπαίδευση και Γεώτοποι
Geosciences in Education and Geosites

ΤΟΜΟΣ 3 / VOLUME 3

Geophysics and Seismology/Γεωφυσική και Σεισμολογία

Natural Hazards/Φυσικές Καταστροφές

Remote Sensing and GIS/Τηλεπισκόπηση και ΓΣΠ

Marine Geology/Θαλάσσια Γεωλογία

Γεωφυσική και Σεισμολογία
Geophysics and Seismology

Φυσικές Καταστροφές
Natural Hazards

Τηλεπισκόπηση και ΓΣΠ
Remote Sensing and GIS

Θαλάσσια Γεωλογία
Marine Geology

ΤΟΜΟΣ 4 / VOLUME 4

Κοιτασματολογία, Μεταλλευτική Τεχνολογία και Οικονομική Γεωλογία
Ore Geology, Mining Technology and Economic Geology

Τεχνική Γεωλογία και Γεωτεχνική Μηχανική
Engineering Geology and Geotechnical Engineering

Γεωθερμία
Geothermics

Έρευνα και Εκμετάλλευση Ορυκτών Πόρων
Exploration and Exploitation of Mineral Resources

Βιομηχανικά Ορυκτά και Πετρώματα
Industrial Minerals and Rocks

Ενεργειακές Πρώτες Ύλες
Energy Resources

Δελτίο της Ελληνικής Γεωλογικής Εταιρίας, τομ. XLVII , 2013
Πρακτικά 13ου Διεθνούς Συνεδρίου, Χανιά, Σεπτ. 2013

Bulletin of the Geological Society of Greece, vol. XLVII 2013
Proceedings of the 13th International Congress, Chania, Sept. 2013

UTILIZATION TRIALS OF LIGNITE SOLID BYPRODUCTS OF WEST MACEDONIA AND PELOPONNESUS LIGNITE FIRED POWER PLANTS FOR THE PRODUCTION OF LIGHTWEIGHT AGGREGATES

Anagnostopoulos I.[1], Lampropoulou P.[2], Tzevelekou Th.[3], Stivanakis V.[1], Kastanaki A.[4] and Papamantellos D.[3]

[1] *University of Patras, Chemical Engineering Department*

[2]*University of Patras, Geology Department, p.lampropoulou@upatras.gr*

[3]*Helleninc Center of Metals Research S. A., Athens*

[4]*Public Power Corporation S.A., 30 chalkokondyli St., Athens104 32*

Abstract

The production of lightweight aggregates from the utilization of solid byproducts [fly ash (FA) and bottom ash (BA)], of the lignite fired power plants from West Macedonia (Kardia, Ptolemaida) and Peloponnesus (Megalopolis), has been investigated in this study. Sintering of FA and BA with the grate sinter band method was selected because it exploits the energy content of the raw materials for the increase of temperature and completion of the material's sintering. These byproducts contain the necessary carbon content for temperature increase during the sintering process. Detailed XRD analyses show that Megalopoli's FA contains high amounts of amorphous phase (25-54wt%) while fly ashes from Kardia and Ptolemaida power units are more crystalline. Lime and anhydrite are the most abundant crystalline phases in Ptolemaida's and Kardia's fly ashes. The bottom ashes revealed high percentages of amorphous content (58-64wt%) and anorthite and quartz as the major crystalline phases. Mixtures of different BA/FA ratios were prepared for sintering tests. The sintered mixtures from Kardia's and Ptolemaida's regions did not have sufficient mechanical properties for further treatment. The sintercake produced from Megalopolis' ashes exhibited good mechanical properties and was selected for further study for use as light aggregate raw materials to the lightweight concrete production.

Key words: *fly ash; bottom ash, use, grate sintering, mineralogical composition.*

Περίληψη

Στην παρούσα εργασία μελετήθηκε η παραγωγή ελαφροαδρανών από τη χρησιμοποίηση ιπτάμενης τέφρας (ΙΤ) και τέφρας πυθμένα (ΤΠ), που παράγονται από την καύση λιγνίτη στους υποσταθμούς της ΔΕΗ στις περιοχές Καρδιάς, Πτολεμαϊδας (Δ.Μακεδονία), Μεγαλόπολης (Πελοπόννησος). Επιλέχθηκε η μέθοδος πυροσυσσωμάτωσης με σχάρα, διότι εκμεταλλεύεται ως καύσιμο τον άκαυστο άνθρακα που περιέχουν οι τέφρες, για την αύξηση της θερμοκρασίας που απαιτείται κατα την πυροσυσσωμάτωση. Σύμφωνα με τις ορυκτολογικές αναλύσεις περιθλασιμετρίας ακτίνων-Χ, οι ΤΠ περιέχουν υψηλότερο ποσοστό άμορφης μάζας

(58-64wt%) σε σχέση με τις ΙΤ (25-54wt%) και ανορθίτη - χαλαζία ως κύριες κρυσταλλικές φάσεις. Στις ΙΤ Καρδιάς και Πτολεμαϊδας άσβεστος και ανυδρίτης εμφανίζονται συχνά στη μικροδομή τους. Μίγματα διαφορετικών αναλογιών ΤΠ/ΙΤ προετοιμάστηκαν για τις δοκιμές πυροσυσσωμάτωσης. Το πυροσυσσωματωμένο μίγμα από τη Μεγαλόπολη επέδειξε καλές μηχανικές, φυσικές, ιστολογικές ιδιότητες και μπορεί να χαρακτηριστεί ως ελαφροαδρανές και να δοκιμασθεί στην παραγωγή ελαφρομπετόν. Σε αντίθεση με το προϊόν της Μεγαλόπολης, τα μίγματα από Καρδιά και Πτολεμαϊδα επέδειξαν αρνητικές μηχανικές ιδιότητες, είτε άμεσα χρονικά (μίγματα Καρδιάς) είτε σε βάθος χρόνου (μίγματα Πτολεμαϊδας).
Λέξεις κλειδιά: *Ιπτάμενη τέφρα, τέφρα πυθμένα, χρήση, πυροσυσσωμάτωση με σχάρα, ορυκτολογική σύσταση.*

1. Introduction

Nowadays, the utilization of solid fuel combustion byproducts is rapidly increased all over the world, not only because of the lack of land disposal sites but for the global demand of new recycling raw materials, aiming to the combination of environmental and economic profits. The fly ash (FA) and bottom ash (BA) have been mainly found applications to the building construction, road construction or as additives in the cement or concrete (Nishigaki, 2000; Lin, 2006; Vegas et al., 2008; Anagnostopoulos et al., 2010). Many researchers have been aimed to the production of lightweight aggregates by sintering of several municipal solid wastes incineration (Bhatty and Reid, 1989; Cheeseman et al., 2005).

Lignite combustion in West Macedonia and Peloponnesus of Greece results in production of approximately 14Mt/year of FA and BA byproducts. Today, only 10-15% of FA produced in Greece is utilized as raw material mainly in cement production while the BA use is very restricted due to its high carbon content.

This study investigates the utilization of FA and BA from the lignite fired power plants from North Greece (Kardia, Ptolemaida -West Macedonia) and South Greece (Megalopolis-Peloponnesus) as raw materials in the production of lightweight aggregates, using the grate sinter band method. This method has been applied with a lot of advantages to the bottom ash utilization (Anagnostopoulos and Stivanakis, 2009). The later contains a high carbon content which is used as the main fuel for the temperature increase during the sintering process whilst its high humidity could be utilized as the main binder phase for the agglomeration.

2. Experimental Procedure and Analytical Techniques

The developed process for the production of lightweight aggregates from the solid lignite combustion by-products consists of two stages, pelletization and sintering, respectively (Anagnostopoulos and Stivanakis, 2009). The whole pilot-scale sintering installation at ELKEME is shown in Figure 1. Pre -designed ratios of the solid raw materials are first mixed into a mechanical mixer and then introduced into the pelletization disc with the addition of sprayed water, if necessary. The rotating disc is of 0.6m diameter and operates at a slope of 45° with a rotation speed of 40-50 rpm. The formed pellets are introduced into the sinterpot, which is of 0.16m surface. Five thermocouples are set up along the height of the sinterpot for the measuring of temperature inside the formed bed of pellets. A layer with charcoal of 3-4cm is placed at the top of the bed of pellets, in order to assist the ignition of the pellets. The ignition of the pellets occurs the same time with the start-up of the suction blower, connected at the bottom of the pot. The blower creates suction pressure inside the pot and causes movement of the combustion zone downwards. The process of sintering is terminated when the combustion zone reaches the bottom of the pot. The flue gases of sintering are passed through a filter-bag for the removal of the solid particles.

Chemical analyses of the studied samples (raw materials and final sintered products) was carried out in cooperation between UPATRAS (Dep. Chem. Enginnering, METLAB)-ELKEME, using AAS and ICP, while C, S contents have been measured using a Carlo –Erba analyzer. XRD analyses, using a Bruker D8 Advance diffractometer with Ni filter and CuKα radiation, were also performed to identify the phases present in the samples, in the Laboratory of applied Mineralogy (MINTECHLAB), Department of Mineral Resources, Techn. University of Crete, Greece. In addition, quantitative analysis was performed by Rietveld Method using Rayflex Autoquan Software. Microstructures of samples have been studied in ELKEME using a FEI XL40 SFEG scanning electron microscope (SEM). The physical parameters of sintered products have been measured and evaluated according to ASTM 373-88, standards (ASTM C373-88, 2002) in the METLAB.

3. Results and Discussion

The raw materials BA, FA and ML (metallurgical lime) which are used for the sintering production of the final light aggregates materials are characterized below.

3.1. Raw Materials

3.1.1. Chemical Analyses

The %wt of major oxides, carbon and LOI in the raw materials are given in Table 1. Chemical analyses of BA revealed higher percentage of loss of ignition compared with this in FA samples, due to their higher carbon content. In addition, the bottom ashes are significantly poorer in CaO content against to FA samples. In BA samples, the SiO_2 content ranges from 37.46 (in BAP=BA Ptolemaidas) to 41.21wt% (in BAK=BA Kardias), while the Al_2O_3 ranges from 16.27 (in BAK) to 17.39 (in BAP=BA Ptolemaidas). Fly ashes from Kardia and Ptolemaida contain significantly higher amounts of calcium oxide compared with that of Megalopolis. The maximum silicon oxide and aluminium oxide occur in FAM (=FA Megalopolis), while the minimum are contained in FAP (FA Ptolemaidas) and FAK (FA Kardias) samples respectively.

1: Sinterpot, 2: Flue gases' pipe from Sinterpot to Blower, 3: Suction blower, 4: Flue gases' pipe from blower to filter-bag, 5: Filter-bag, 6: Flue gases introduced to the environment.

Figure 1 - Pilot-scale sintering installation.

Table 1 - Chemical analyses (wt%) of major oxides, C and LOI in the raw materials.

Sample	Al_2O_3	CaO	Fe_2O_3	SiO_2	C	LOI
BAK*	16.27	14.32	4.88	41.21	10.13	14.50
BAP	17.39	12.90	3.95	37.46	14.51	23.00
BAM	16.31	12.80	7.78	39.04	9.77	15.30
FAK	14.60	33.15	5.63	29.36	1.64	4.50
FAP	15.03	32.55	6.30	26.36	1.73	4.60
FAM	19.27	14.90	10.68	46.71	1.22	1.10
ML		88.37				11.03

*Abbreviations: BAK=BA Kardias; BAP=BA Ptolemaidas; BAM=BA Megalopolis; FAK=FA Kardias; FAP=FA Ptolemaidas; FAM =FA Megalopolis; ML: metallurgical lime

3.1.2. XRD Analyses

According to the XRD results, the FAM contains the higher amount of amorphous phase (~55%) while in FAK and FAP it ranges to lower percentages (~ 25 to 30 % respectively). In FAK and FAP samples lime and anhydrite appear as the major crystalline phases. Moreover, anorthite, quartz and gehlenite have been detected in all FA samples.

In BA samples the amorphous phase ranges from ~57-64% while anorthite and quartz have been identified as the major crystalline phases. In the metallurgical lime (ML), which has been used as additive, approximately 24% of lime has been hydrated to portlandite.

3.2. Design of Different Raw Materials Mixtures

The ratios of the raw materials (BA, FA, ML) in the different designed mixtures prepared for sintering, are given in Table 2. Taking into account the chemical analyses of all BA samples, the mixtures of Table 2 contain the requisite carbon content used as fuel during the sintering process.

3.3. Characterization of Final Products (pellets)

3.3.1. Macroscopic Characterization

According to macroscopic observations of the sintered products those from Kardia's region did not comprise sound sinter-cake. Formation of sinter-cake (sound bonding of the pellets) is considered to be a characteristic essential visual parameter reflecting the efficiency of the sintering process. Thus, it comprises a criterion for the product's mechanical suitability for further treatment (Figure 2). Ptolemaida's mixtures (Figure 2), although they obtained the base mechanical strength after sintering, autogeneous disintegration occurred after two-three weeks later. The solid sinter cake produced from Megalopolis' ashes (Figure 2) was selected for further study for use as light aggregate raw material to the lightweight concrete production.

3.3.2. Sintering Behaviour of Pellets

A representative temperature-time diagram of sintering process for mixture MMEG is presented in Figure 3. Temperature T1 is recorded at the top of the bed of pellets and the temperature T5 at the bottom of the bed. The temperature T6 corresponds to the flue gases of sintering. The duration of the sintering process is approximately 50min. The temperature of sintering is between 1200 and 1250°C. The temperature increase rate is very fast, from 600°C/min until 1100°C/min.

Table 2 - % of raw materials in the different prepared mixtures for sintering.

Name of mixture	Origin of raw materials	BA (%)	FA(%)	ML(%)
*MMEG	Megalopolis	90	7	3
MP1	Ptolemaidas	55	42	3
MP2	Ptolemaidas	75	22	3
MK1	Kardias	55	42	3
MK2	Kardias	75	22	3
MK3	Kardias	90	7	3

*Abbreviations: M: mixture; MEG:Megalopolis; P:Ptolemaidas; K: Kardias

Figure 2 - Representative macroscopic images of sintered products.

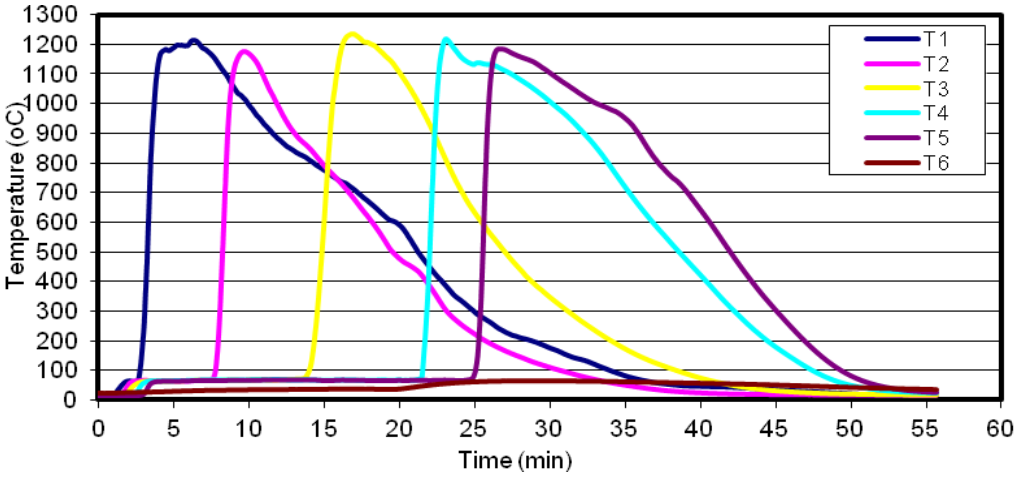

Figure 3 – Representative temperature -time diagram of sintering process (MMEG).

3.3.3. Chemical Analyses and Physical Parameters

The %wt of major oxides in the sintered products are given in Table 3. As expected MMEG mixture is the most poor in CaO and the richer in SiO_2, reflecting the chemistry of the raw materials. The maximum iron oxide has been analysed in MMEG sample. Minor oxides of K_2O (<2.16wt%), MgO (<2.89wt%), Na_2O (<0.51wt%), P_2O_5 (<0.05wt%), TiO_2 (<1.06wt%), Cr_2O_3 (<0.04wt%), CuO (<0.29wt%), MnO (<1.19wt%) and ZnO (<4.29wt%) have been also determined. The low percentage of loss of ignition (max 1.6% in MP2) revealed that the incombustible C

content of raw materials has been utilized as fuel well enough during the sintering process, promoting simultaneously the porous microstructure.

The results of physical parameter's measurements (apparent porosity, apparent specific gravity and water absorption) of products are displayed in Table 4. All samples except of MMEG and MK2, were broken down during the measurement (boiling). MMEG exhibited low apparent specific gravity (0.89g/cm^3) while the MK2 (1.43g/cm^3) higher than a commercial light aggregate one (1g/cm^3). Additionally, MMEG exhibited higher percentage of water absorption and apparent porosity compared to MK2. The same Table contains the weights (kg) of dry mixtures before and after sintering.

Table 3 – Chemical analyses of major oxides in the sintered products (wt%).

Sample	Al_2O_3	CaO	Fe_2O_3	SiO_2
MMEG	20.38	18.41	8.94	44.72
MP1	19.89	29.05	5.90	30.90
MP2	21.14	25.07	5.95	32.25
MP3	22.59	21.39	5.69	38.25
MK1	16.96	30.21	5.71	25.52
MK2	17.41	26.92	5.53	27.04
MK3	15.68	29.96	5.59	33.66

Table 4 – Physical parameters of sintered products.

Physical Parameters	Apparent porosity (%)	Apparent specific gravity (g/cm^3)	Water absorption (%)	Dry weight before sintering (kg)	Weight after sintering (kg)
Sample					
MMEG	59.7	0.89	67.5	33	19.6
MP1	NM*	NM	NM	30	19.4
MP2	NM	NM	NM	27.5	21.25
MP3	NM	NM	NM	25	18
MK1	NM	NM	NM	35	22
MK2	42.8	1.43	30.2	32.5	12.7
MK3	NM	NM	NM	32.5	13.5

*Abbreviation: NM: not efficient for measurement

3.3.4. XRD Analyses

The semiquantitative mineralogical compositions of the sintered products are presented in Table 5. The amorphous phase ranges from ~36 (MK1) to 44 wt% (MP3) while anorthite, gehlenite and diopside (in two of them) are the major detected crystalline phases. It has been previously proved that in such materials, the mechanical strength is increased further by the anorthite appearance than the gehlenite (Anagnostopoulos, 2010). Samples MMEG, MP2 and MP3 contain the higher anorthite percentages (~34-38t%) and the lower gehlenite (~3-9%), whilst the maximum diopside (~15%) is presented in MMEG, thus expected to improve further it's mechanical strength (Bethanis et. al, 2002). Moreover in MMEG most of the hematite has been reducted to the magnetite. Maximum amount of free lime has been detected in the MK3 sintered product. Its

presence is undesired, since its subsequent transformation to portlandite by air humidity is accompanied by volume expansion resulting in disintegration of the solid matrix, making it unsuitable for further utilization. The different ratios of phases in the final products could be attributed to the combination of: 1) different geochemical/mineralogical compositions of BA and FA materials (as well as their lignite raw materials derived from), (Sakorafa et. al., 1996; Filippidis et. al., 1996; Siavalas et. al., 2009), 2) the sintering process, and 3) the different raw material ratios in the prepared mixtures. Moreover the chemically complicated systems of sintered products are reflected to their mineralogical compositions consisting of stable primary phases (eg quartz,) and new formed ones (eg diopside, magnetite) after different reactions mechanisms (decompositions, solid state reactions, reduction reactions, melting), not all in equilibrium conditions during the rapid sintering process (Anagnostopoulos, 2009).

3.3.5. Microstructure by SEM

SEM observations of final products revealed that all of them are characterized by a heterogeneous microstructure. Representative backscattered images are given in Figure 4. The MMEG sample exhibits the most compact structure because of the advanced sintering (via solid state reactions or melting phase bonding). Pores forming from outgassing are very often due to C, S devolatilization, the structural destruction of Ca sulphates/ carbonates and iron oxide reduction. Pore sizes vary not only among the different samples but and in the structure of the same sample, due mainly to the extend grain variation of BA (~2-1000μm). Porosity forming is accompanied with boating effect when the simultaneous mechanisms of melting on the grains surface, trapping gas inner, out gas-sing at high temperature are taking place, leading to the final lightweight products (Anagnostopou-los, 2009).

Table 5 – Semiquantitative (%) analyses of major crystalline phases in the sintered products.

Sample	MMEG	MPI	MP2	MP3	MK1	MK2	MK3
Phases							
amorphous	37	36	37	44	36	32	41
anhydrite	tr	1.5	1	1	1	1.5	1
gehlenite	3	20	9	4	27	17	16
Dicalcium silicate	1	7	7	2.5	5	5	6
diopside	15	5	5	5	6	10.5	5
anorthite	36	26	34	38	22	25	21.5
quartz	4.5	2.5	3.5	3	2.5	6	4
Hematite/	1	-	-	-	tr	-	2
magnetite	2	1	1	1	-	1	1
Brawn millerite	1	1	1	1.5	tr	2	2
Lime/	-	tr	tr	tr	tr	-	1
Portlandite	-	tr	1	-	tr	-	1.5

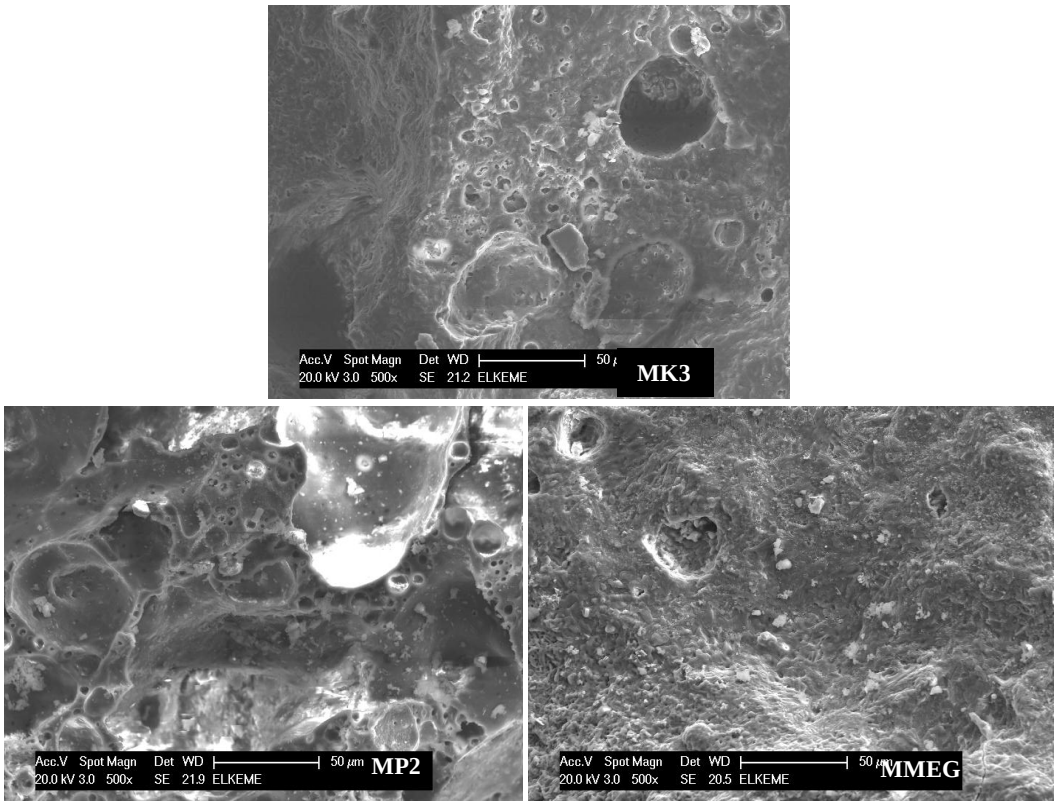

Figure 4 – Representative backscattered images of sintered products.

4. Conclusions

The bottom ashes from Kardia, Ptolemaida and Megalopoli regions contain the demanded incombustible C for its utilization as fuel during the sintering process (till 1200^{o}C) by the sinter band method. The final mineneralogical compositions of sintered products reflecting the complicated mechanisms have taken place during the rapid sintering, leading to the boaming effect and porous structures. The higher SiO_2 content of MMEG is believed to be essential for the evolution of the sintering process by participation in the formation of crystalline phases which enhance bonding and lead to the production of the desired sinter-cake. Presence of free lime in the sintered products is undesired, since its subsequent transformation to portlandite by air humidity is accompanied by volume expansion resulting in disintegration of the solid matrix, making it unsuitable for further utilization. According to the macroscopic characterization, the physical properties as well as the mineral compositions and microstructures, the MMEG sintered mixture could be characterized as a light aggregate material and it is proposed as suitable for further treatment in the lightweight concrete production.

5. Acknowledgments

The authors are grateful for the XRD investigations of fly ashes, bottom ashes and sintered products carried out by Professor Dr. G. Kostakis, Laboratory of Applied Mineralogy, Technical University of Crete, Hania. Professor Dr. Manoutsoglou Emmanuil, Editor; and reviewers, Dr. S. Kalaitzidis and Dr. Koukouzas, are thanked for comments and suggestions which improved the previous version of the manuscript.

6. References

Anagnostopoulos I. M. and Stivanakis V.E. 2009. Utilization of lignite power generation residues for the production of lightweight aggregates, *J. Hazard. Mater.,* 163, 329-336.

Anagnostopoulos I. 2009. Utilization of lignite power generation residues for the production of lightweight aggregates and lightweight concrete, *PhD Thesis*, University of Patras, Greece.

Anagnostopoulos I.M., Stivanakis V.E., Angelopoulos, G.N. and Papamantellos D.C. 2010. Valorization of lignite combustion residues and ferroalumina in the production of aggregates, *J. Hazard. Mater*., 174, 506-511.

ASTM C373-88 2002. *Standard test method for water absorption, bulk density, apparent porosity and apparent specific gravity of fired whiteware products*, Annual Book of ASTM standards, USA.

Bethanis S., Cheeseman C. R. and Sollars C.J. 2002. Properties and microstructure of sintered incinerator bottom ash, *Ceram. Int.*, 28, 881-886.

Bhatty J.J. and Reod K.J. 1989. Lightweight aggregates from incinerated sludge ash, *Waste Manag. Res.*, 7, 363-376

Cheeseman C.R., Makinde A. and Bethamis S. 2005. Properties of lightweight aggregates produced by rapid sintering of incinerator bottom ash, *Resour. Conserv. Recy.*, 45, 147-162.

Filippidis A., Georgakopoulos A. and Kassoli-Fournaraki A. 1996. Mineralogical components of some thermally decomposed lignite and lignite ash from the Ptolemais basin, Greece, *Int. J. Coal Geol.* 30 (4), 303-314.

Lin K.L. 2006. Feasibility study of using brick made from municipal solid waste incinerator fly ash slag, *J Hazard Mater.,* 137(3), 1810–6.

Nishigaki M. 2000. Producing permeable blocks and pavement bricks from molten slag, *Waste Manage,* 20(2–3), 185–92.

Vegas I., Ibañez J.A., San José J.T. and Urzelai A. 2008 Construction demolition wastes, Waelz slag and MSWI bottom ash: a comparative technical analysis as material for road construction, *Waste Manage,* 28(3), 565–74.

Sakorafa V., Michailidis K. and Burragato F. 1996. Mineralogy, geochemistry and physicalproperties of fly ash from the Megalopolis lignite fields, Peloponnese, Southern Greece, *Fuel*, 75(4), 419-423.

Siavalas G., Linou M., Chatziapostolou A., Kalaitzidis S., Papaefthymiou H. and Christanis K. 2009. Palaeoenvironment of Seam I in the Marathousa Lignite Mine, Megalopolis Basin (Southern Greece), *Int. J. Coal Geol.*, 78 (4), 233-248.

Δελτίο της Ελληνικής Γεωλογικής Εταιρίας, τομ. XLVII , 2013
Πρακτικά 13ου Διεθνούς Συνεδρίου, Χανιά, Σεπτ. 2013

Bulletin of the Geological Society of Greece, vol. XLVII 2013
Proceedings of the 13th International Congress, Chania, Sept. 2013

RELATIONSHIP BETWEEN PHOSPHATES MINERALOGY AND MINERAL PROCESSING – THE CASE OF GREECE

Anastassakis G.

National Technical University of Athens (NTUA), School of Mining Engineering and Metallurgy
ganastas@metal.ntua.gr

Abstract

Phosphorus is one of the most important elements for life and growth of plants, animals and humans. Its absence or depletion from the soil necessitates their addition in the form of fertilizers. The only realistic source of elemental phosphorus and phosphoric fertilizers on commercial scale is phosphate rock. The importance of phosphate rocks becomes greater by taking into account that phosphorus can't be obtained by recycling processes as well as that there are no substitutes for it in agriculture.

In most cases, phosphate deposits have to be processed in order to meet the commercial requirements. In the current paper, it is presented the various forms of phosphate deposits, the participating minerals in each case and the effect of mineralogical composition on the beneficiation method applied. Finally, details on the phosphate deposits of Greece are presented, their mineralogy, and the possibility of their beneficiation.

Key words: *Phosphate minerals, phosphate beneficiation methods, Greek phosphate deposits.*

Περίληψη

Ο φωσφόρος είναι ένα από τα σημαντικότερα στοιχεία για τη ζωή και την ανάπτυξη των φυτών, των ζώων και των ανθρώπων. Η απουσία ή η εξάντλησή του από το έδαφος καθιστά αναγκαία την προσθήκη του σε μορφή λιπάσματος. Η μοναδική ρεαλιστική πηγή του στοιχειακού φωσφόρου και των αντιστοίχων λιπασμάτων σε εμπορική κλίμακα είναι τα φωσφορικά κοιτάσματα. Η σημασία αυτών γίνεται μεγαλύτερη, αν ληφθεί υπ' όψη ότι ο φωσφόρος δεν μπορεί να ανακτηθεί από διεργασίες ανακύκλωσης και ότι δεν υπάρχει υποκατάστατό του στη γεωργία.

Στις περισσότερες των περιπτώσεων, τα φωσφορικά κοιτάσματα πρέπει να υποστούν εμπλουτισμό προκειμένου να ικανοποιήσουν τις εμπορικές προδιαγραφές. Στην παρούσα εργασία, παρουσιάζονται οι διάφορες μορφές των φωσφορικών κοιτασμάτων, τα ορυκτά που συμμετέχουν σε κάθε περίπτωση και η επίδραση της ορυκτολσγικής σύστασης των κοιτασμάτων στην μέθοδο εμπλουτισμού. Τέλος, παρουσιάζονται λεπτομέρειες σχετικά με τα ελληνικά φωσφορικά κοιτάσματα, την ορυκτολογία τους και την δυνατότητα εμπλουτισμού τους.

Λέξεις κλειδιά: *Φωσφορικά ορυκτά, μέθοδοι εμπλουτισμού φωσφοριτών, ελληνικά κοιτάσματα φωσφοριτών.*

1. Introduction

Phosphorus, along with potassium and nitrogen, is a very essential element in the agricultural and husbandry sectors as it is the basis for the production of fertilizers and animal stock feed. In case of phosphorus absence or depletion from soil, it must be added in the form of fertilizer. Phosphate rock is the only commercially feasible source for the production of phosphorus fertilizers and elemental phosphorus. The significance of phosphate rock becomes more intensive by taking into account that phosphorus can't be obtained from recycling processes and it can't be substituted in agricultural uses.

The term "phosphate rock" is globally accepted to describe any naturally occurring geological material that contains one or more phosphate minerals suitable for commercial use. This term is a general one as it is referred both to unprocessed rock and phosphate concentrates (Notholt and Highley, 1986). Economic recovery of phosphates is limited to the naturally concentrated mineral deposits. In case of some high-grade phosphate rocks, they are used as mined; in most cases, the deposits are of low-grade and they have to be concentrated in order to be economically utilized. Most of the world phosphate rock annually mined is consumed in phosphate fertilizers production.

Phosphate deposits are distributed worldwide but unevenly. The phosphate-rock producing countries are amounted to more than 30 but only four of them (with descending order China, USA, Morocco, and Russia) produced about 75% of the total production in 2012 (Jasinski, 2013). Studies regarding reserves and resources tonnage are widely varied (Fantel at al, 1984; Cathcart, 1984; Cooper and Manderson, 1984). The global proved reserves vary between 15 and 70 billions metric tons (Mt), the possible are double while the probable reserves are huge. World resources of phosphate rock are more than 300 billion tons (Jasinski, 2013). The market demands during the last 20 years are on average 150 millions Mt per year (UNEP, 2001). Obviously, whatever the tonnage of the proved reserves is, the existing proved reserves are efficient to cover the global demands for a long time under the current rate of production and market conditions. Identified and undiscovered resources worldwide are estimated to be several times greater than the present reserves. The various types of phosphate rock deposits as well as wide variations in P_2O_5 content create difficulties in accurately estimating reserves. The accurate tonnage estimates of reserves can not be made without systematic and extensive prospecting. Hence, the reserve and resource estimates subject to considerable change as exploration work increases the level of knowledge.

2. Phosphate Rocks

2.1. Types

Phosphate rocks appear extensive discrepancies regarding origin, structure, mineralogical composition and quality.

According to their origin, phosphate rocks are classified into sedimentary (or marine), igneous and guano. Most of the world's phosphate rock production (about 75%) is from sedimentary deposits, 23% from igneous origin deposits and the remainder from guano. Sedimentary deposits are classified into autochthonous and heterochthonous while autochthonous are further divided into unaltered and altered.

Slightly different is the division proposed by van Straaten (2002), according which phosphate deposits are classified into the following five major types: marine, igneous, metamorphic, biogenic, and weathered. Metamorphic phosphate rocks derive from sedimentary and igneous phosphate rocks that have been subjected to extremely deep burial, where conditions of high pressure and perhaps shearing forces and/or heat prevail (van Kauwenbergh, 2010).

The most important producing countries of igneous origin phosphate rock are: Russia (in Cola Peninsula), South Africa (Palabora Complex), Zambia, Zimbabwe, Brazil (in Araxa and Jacuperanga), Finland and Sweden (Notholt, 1984). Igneous phosphate ores are often of low grade

(less than 5% P_2O_5), but can be upgraded to high-grade products (from about 35% to over 40% P_2O_5).

Sedimentary deposits (often called phosphorites) are the most important phosphorus raw material sources. Sedimentary phosphate rocks have been formed throughout the geological time scale. Most of them were apparently formed in offshore marine conditions on continental shelves. Sedimentary deposits exhibit a wide range of chemical compositions and great variations in physical form. The most desirable sedimentary phosphate rocks contain distinct phosphate particles that can be separated from the unwanted gangue minerals. They are much more widespread than the igneous ones and usually of higher content. Sedimentary deposits are defined in certain phosphate-bearing regions and countries, such as USA (Florida, North Carolina, Tennessee, Idaho, Montana, Utah, Wyoming etc.), Northern and Western Africa countries (Morocco, Tunisia, Algeria, Western Sahara, Togo etc.), Middle East (Jordan, Israel), China, Vietnam, Australia, Russia etc. Insular deposits, a type of sedimentary deposit associated with oceanic islands (such as Nauru and Christmas Island), have been an important source of phosphate rock for more than 100 years; however, most of these deposits have been totally depleted or have short projected remaining lifetimes (van Kauwenbergh, 2010).

Finally, guano deposits are limited and mainly located on the western Pacific islands of South America.

2.2. Mineralogy

The type of phosphate rock highly influences mineralogy, chemistry, texture and the concomitant gangue minerals. While the known phosphate minerals are amounted to more than two hundreds, the group of apatite is the main mineral found in phosphate deposits (van Straaten, 2002). Several cycles of deposition and reworking may have concentrated the phosphate, and weathering may have removed most of the carbonates from the near-the-surface portions of the deposits. Some igneous phosphate deposits, such as the Kola deposit in Russia, are hard-rock deposits; apatite crystals are found within a hard crystalline fabric of other igneous minerals. With intense weathering, the fabric of igneous phosphate rocks can be destroyed; soft soil-like residual deposits are produced. Sedimentary phosphate rocks can range from loose unconsolidated materials, to weakly cemented materials, to highly indurated rocks (van Kauwenbergh, 2010). Calcium-phosphates of the apatite group are mainly found in primary environments (in sedimentary, metamorphic and igneous rocks) but also in weathering environments. Other phosphates include minerals of the crandallite group, as well as variscite and strengite, which are Fe- and Al-containing phosphates principally found in secondary weathering environments (van Straaten, 2002).

The minerals prevailing in igneous phosphate rocks are mainly those of apatite group, with the general formula $Ca_{10}(PO_4)_6X_2$ (X is F, Cl or OH anion). Due to its structure, apatite is subjected to extended substitutions. More specifically Ca^{2+} can be substituted by a variety of mono- or divalent cations, rare earth elements etc., PO_4^{3-} is substituted by a variety of tri- or divalent radicals, such as BO_3^{3-}, VO_4^{3-}, SiO_4^{3-}, AsO_4^{3-}, CrO_4^{3-}, CO_3^{2-}+ F^- etc., and each one of the anions F^-, Cl^- and OH^- can be substituted by the other two.

Primary igneous deposits owe their origin to the solidification of magma. They are associated with intrusive plutonic rocks, whose distinctive structure (e.g. high crystallinity) and mineral composition result from crystallization under conditions of slow cooling and often at considerable depth. Accordingly, the most common minerals associated with apatite are nepheline-syenites, carbonatite complexes, micas, pyroxenites, amphiboles, magnetite and other iron oxides, titanium minerals, olivine, feldspars, vermiculite etc.

In sedimentary origin deposits, the phosphate minerals prevailing are those of carbonate fluorapatite group or francolite. Some authors use the term “collophane” instead of francolite

although the term “collophane” is referred to the structure of the phosphate rock denoting the micro- and cryptocrystalline apatite occurring in sedimentary rocks.

Francolite group minerals are described by the general formula (Abouzeid et al, 1980)

$$Ca_{10-a-b}Na_aMg_b(PO_4)_{6-x}(CO_3)_xF_yF_2$$

where x is the extension of substitution of PO_4^{3-} by (CO_3^{2-}, F^-). For commercial phosphate rocks x = 0-1.5. Also, for electroneutrality to be maintained the following relationship must be in force a = x-y. Experimentally has been found that y=0.4x and b=0.4a. X-Rays analysis revealed that substitution of PO_4^{3-} by (CO_3^{2-}, F^-) causes changes to the lattice and crystal size with concomitant changes in crystal specific area and reactivity of francolite. The maximum amount of substitution ranges between 6 and 7% CO_2. Sedimentary phosphate rocks containing the most highly carbonate-substituted apatites can only be beneficiated to maximum grades of 33-34% P_2O_5. Depending on the amount of carbonate substitution, the grade can increase to a maximum of about 42% P_2O_5 for sedimentary apatites with essentially no substitution (van Kauwenbergh, 2010).

Gangue minerals in sedimentary phosphate rock mainly include quartz, calcite, dolomite, clays (smectite, palygorskite, kaolinite, sepiolite), shales, iron oxides, pyrite, barite, fluorite and organic material. Some phosphate minerals (wavellite, crandallite, variscite) are also included in gangue.

Marketable phosphate rock is graded according to its content in tricalcium phosphate (64-77%) or P_2O_5 but the content in various impurities is equally important. Deleterious minerals such as calcite, dolomite, iron and aluminum oxides must not exceed a certain percentage.

3. Overview of Beneficiation Methods

Theoretically, processing methods separate efficiently phosphate minerals from gangue for almost all the combinations of minerals. Restrictions are posed as far as it concerns the cost of the processing, given that phosphate rock concentrates are of relatively low value.

Flotation is applied almost exclusively to separate apatite from the other minerals in igneous phosphate rocks using various combinations of reagents (Guimaraes et al, 2005). Commercial grade of the concentrate is achieved through a series of rougher, cleaning and scavenging stages. In addition to flotation, processing of igneous rocks may also include washing, desliming, and magnetic separation depending on the nature of the gangue minerals (Woodrooffe, 1972; Anonymous, 1986).

Various separation methods and flow sheets are applied to separate phosphate from gangue minerals in sedimentary rocks as described in the following paragraphs (Anastassakis, 1989).

- If the gangue minerals is rich in organic material, iron minerals and sulfides, separation of phosphate matter is based on low-temperature roasting (400-600 ^{0}C) combined with dry magnetic separation (Cohen and Hammoud, 1979). In addition, when dolomite and quartz also participate as gangue minerals, then high-intensity electrostatic separation is also applied (Hammoud et al, 1985); in case of ferriferous dolomite high gradient magnetic separation is applied (Blazy and Jdid, 1997).
- The simplest separation is achieved in high grade deposits (content in P2O5 more than 25%) with silica and/ or clays as gangue minerals. Due to the difference in hardness between phosphate and silica, a commercial product is achieved with simple crushing and dry or wet screening (Anonymous, 1986).
- In most commercial applications, gangue is comprised mostly of silica and argillaceous minerals (clays, shale etc.). Argillaceous material usually serves as binding material of phosphate pebbles. Such a typical example is the phosphatic basins of southern United States. The formations of Florida-North Carolina represent more than 80% of the U.S. production. Phosphate ore is slurried in the processing plant and phosphate particles are subse-

quently separated from the waste sand and clays. Beneficiation of the ore is accomplished by washing and flotation (Raden, 1979).

- After removing the coarse particles (+1.5 mm) and the fine ones (-0.1 mm) by washing, the fraction with particles size -1.5+0.1 mm is fed to the flotation plant. This product is mainly composed of phosphate particles and silica sand. The coarse fraction (-1.5+0.5 mm) is separated by agglomerate-skin flotation (Hoppe, 1976; Moudgil and Barnett, 1979). The phosphate material in the finer fraction (-0.5+0.1 mm) is separated from silica sand by rougher and cleaning flotation processing. These circuits operate in parallel while at least two plants in Florida operate flotation without separating circuits for coarse and fine fraction (Custred et al, 1975).
- For phosphate deposits with a higher content, a single flotation stage is required, usually anionic, with fatty acid collectors.
- A serious problem in phosphate processing is the presence of dolomite as gangue mineral. Deposits of low MgO content had been exploited in Florida and western phosphate fields of USA up to now. The depletion of the low MgO content deposits necessitates the phosphate industry to process deposits with dolomitic higher content of impurities. Consequently, efficient processing techniques have to be set to lower the MgO content of the concentrates below 1%, which is the limit for commercial phosphate concentrates. Experimental results show that a noticeable part of dolomite is removed by screening for particle size +6 mm and in the light product of heavy media separation for particle size 1-6 mm (Baumann and Snow, 1980; Lawver et al, 1980; Rule and Daellenbach, 1985). The sink product is processed by double flotation: a) anionic with fatty acid emulsion and H_2SiF_6 as phosphate depressant and b) subsequent cationic flotation of the tailing for silica to be removed, using a mixture of amine with fuel oil or kerosene as collector at slightly acidic pH.
- Approximately, two thirds of the phosphate world deposits have carbonate gangue minerals. Although much effort has been devoted to the separation of carbonates from phosphates, the results are not satisfactory yet because of the similar properties and response to the various physical and physicochemical methods. Unaltered phosphate deposits of low grade (P_2O_5 less than 20%) with calcite as gangue mineral seem to be not amenable to separation on industrial scale despite some encouraging experimental results on lab scale (Woodrooffe, 1972; Anastassakis, 1989).
- Low-grade phosphate rocks (10-12% P_2O_5), rich in carbonates, have been attempted to be beneficiated with dilute organic acids, such as acetic, citric or formic acid. Among them dilute acetic acid seems to be the most promising agent (Economou and Vaimakis, 1997; Sengul, 2006).
- For phosphate deposits with P_2O_5 content higher than 20% and with calcite gangue, calcination followed by slaking with water has been tested successfully (Good, 1976; Özer, 2003). The limited application of this process until now is due to its high energy cost. This process is not applied for relatively increased silica content of the ore.

From the above mentioned overview, it derives that phosphate ores show a wide diversity in the composition of their gangue minerals. Their beneficiation can be achieved by various processes, depending upon the liberation size of phosphate from its associated gangue minerals. Different simple or complex combinations of the following processes may be used: crushing, grinding, screening, washing, heavy media separation, flotation, roasting, acetic acid leaching, and calcination. Given that the value of phosphate concentrates is relatively low, cost and metallurgical results are expected to determine the most proper process.

4. Phosphate Resources of Greece

4.1. Types - Characteristics

Phosphate deposits of Greece are located in Epirus area. They are of sedimentary origin and belong to the Mediterranean province of marine sedimentary deposits along with the deposits of northern Africa, south-eastern Turkey, and Albania. From geo-tectonic point of view, these deposits belong to the central Ionian Zone. In this zone, two types of phosphate deposits are encountered: the compact type (non-weathered) and the weathered.

The weathered deposits are located in the Drymon (Preveza) area; their reserves are limited to approximately 6 Mt, which are considered very limited in comparison to those of the compact type. The average content of these deposits varies between 15% and 23% P_2O_5 with the major gangue mineral being chert (18-40% SiO_2) and, in lesser extend, limestone, iron minerals and clays.

The non-weathered deposits are located within a zone at the eastern part of the Central Ionian Zone, which is extended to a width of about 15km and a length starting from Aitoloakarnania area to the Albanian borders. These phosphate rocks are characterized as phosphate limestone, because their content in P_2O_5 is, generally, less than 19.5% (Skounakis, 1979).

The phosphate limestone of Epirous area is formed as a stratigraphic horizon at the contact between Vigla limestone and limestone of Upper Senonian. It is characterized by a thin-layered structure with alternating layers of phosphate limestone, chert, and limestone. The thickness of the phosphate horizon varies from 2m to 12m. On average, a thickness of 6-8m can be considered that is maintained constant in a relatively extended area. The reserves of these deposits have not been precisely estimated. Based on the data of geological survey, they are estimated to be very large.

The P_2O_5 content of the deposits broadly varies both between the deposits and within each deposit. There have been detected deposits with such high a P_2O_5 content as 28-33% but with limited reserves; also, deposits with very low content such as 7.6% P_2O_5; the great majority of the deposits has a P_2O_5 content from 8 to 16% P_2O_5 while the reserves are more than considerable (Pitsikas, 1981). As regards the content variation in the deposits themselves, it has been confirmed that the high content material is located in the lower part of the phosphate horizon having a thickness of about 2-3m; in the upper part, the content is significantly reduced.

Chert is encountered in the phosphate horizon as layers (thickness 5-20cm) alternating with phosphate and calcitic material; its participation in the phosphate horizon varies from area to area. Sometimes, low-grade phosphate material (1.5-2% P_2O_5) is encountered in the chert layers.

The gangue limestone is encountered in the form of layers or beds (thickness 10-60cm), in white or sub-white colour, with Mn-dendrites encountered on the surface of all the layers.

The phosphate material appears in the phosphate horizon in one of the following types:

- Banded type. In this type the bands are of variable thickness (0.5-4mm) and colour (from white-grey to deep brown). Gangue limestone or sparse phosphate material is intercalated between the phosphate bands. The more banded and the more intensive their colour is, the higher the P2O5 content is.
- Porous type. In this type, phosphate limestone appears compact enough, without intercalations of gangue limestone, with grained structure and high content in P2O5.
- Weathered type. It derives from the compact type after having undergone secondary in situ enrichment due to the dissolution and removal of limestone because of rain water action. In some cases, the upper layers are weathered while the lower maintain their compact form.

4.2. Mineralogy

Extensive geochemical and mineralogical research on the Epirous phosphate rock has been carried out (Tsailas et al., 1980; Perdikatsis, 1991; Leventouri et al., 2000). The phosphate mineral

confirmed for Epirous deposits is francolite with high degree of substitution CO_3^{2-} and F^- for PO_4^{3-} with lattice cell dimensions a_0=9.32 Å and c_0=6.896 Å (Tsailas et al., 1980). According to the statistical standards, francolite mineral with a_0=9.32 Å corresponds to the mineralogical formula

$$Ca_{9.51}Na_{0.35}Mg_{0.14}(PO_4)_{4.74}(CO_3)_{1.26}F_{2.5}$$

Its theoretical content in P_2O_5 is 34.76%.

In the phosphate bands of the rock, francolite aggregates form grains with size of a few micrometers. These very fine grains form compact phosphate concentrations, oolites, spherolites and phosphate nodules. Fine-grained calcite mass, of un-regular shape is encountered between the aforementioned phosphate formations. As regards the phosphate rock texture, it must be pointed out that francolite and calcite are very intimately connected. Liberation study reveals that francolite is liberated from calcite for such a low particle size as -10μm.

The major gangue mineral of the phosphate rock is calcite, and chert in lesser amount; iron oxides and Al-minerals (clays) are also encountered but at a very low percentage. Because of the low P_2O_5 content (12-13%) and the corresponding high in CaO (approximately 50%), the ratio CaO/ P_2O_5 is 4.24, which is considered very high in comparison to those rocks used for industrial purposes and have a corresponding ratio 1.6. The high ratio denotes that the sulfuric acid consumption is high and the process of H_3PO_4 or fertilizers production is not economic. Also, in the current case, the content of the rock in uranium or other rare elements is not significant to increase its value, e.g. 21-22 ppm U, 1270-2300 ppm Sr, 150-225 ppm Ti, 0-200 ppm La, 0-100 ppm Zr, 0-200 ppm Nb, up to 50 ppm W etc. (Tsailas et al., 1980).

4.3. Beneficiation Results

Weathered deposits of Greece have been tested to beneficiation. Tests carried out at pilot-plant scale showed that it is possible to obtain a phosphate concentrate with approximately 29-30% P_2O_5, weight 52% and P_2O_5 recovery 68% through sorting (Tsailas et al., 1978; Tsailas et al., 1981; Kaklamanis, 1983).

Given the texture of the unaltered phosphate rock of Epirus area and the very fine size that the rock has to be ground for complete liberation of phosphate matter from gangue minerals, the beneficiation was targeted either to obtain a preconcentrate or a concentrate, if possible.

Gravity separation methods were employed to examine the possibility to obtain a preconcentrate. Float-sink analysis revealed that it is possible to obtain a sink product with heavy liquid separation at sp. gr. 2.75, for the particle fraction -3.35+0.075 μm. Depending on the size range of the feed, the sink product had 40-55% weight, 20-23% P_2O_5, and 80-90% P_2O_5 recovery. The theoretical results of heavy liquid tests were partially confirmed, when the separation was carried out in dense medium bath, either static or whirling, as it was not possible to obtain a concentrate having both satisfactory P_2O_5 content and recovery. More specifically:

- In static separation, the best results were obtained for the size fraction +6.35 mm at a sp. gr. 2.61. The content of the sink product was 17.15% P2O5 (feed content 14.60% P2O5), its weight 67.18% of the dense medium feed, and the recovery in P2O5 was 79% approximately. Separation at a dense medium density 2.65 increases P2O5 content of the sink to 17.86% but reduces recovery to about 70%. Taking into account the weight of the size fractions in the initial feed, recovery drops to the level of 21-23%, which is very low.
- In cyclone whirling dense medium, the results are increased as regards P2O5 content but decreased as regards recovery. More specifically, for the particle fraction -4+0.6 mm, the content of the sink product was 20% P2O5, its weight 18-30% depending on the size range while the recovery in P2O5 was approximately 40% of the cyclone feed. Taking into account the weight of the size fractions in the initial feed, recovery drops to about 15%, which is very low.

Flotation was extensively investigated as a potential separation method using a great variety of reagents but the results were not satisfactory because of the similar physicochemical properties of phosphate minerals and calcite.

In conclusion, phosphate rock processing of Epirus area doesn't seem easy, because of the similar behavior of phosphate and gangue minerals (especially calcite).

5. Conclusions

Phosphate rock is one of the most important mineral commodities as it is the only source of phosphorous, which is a substantial element for human beings, animal and plants. The mineralogical composition of the phosphate rocks is mainly determined by their origin and conditions of genesis. Separation of phosphate minerals from gangue is primarily achieved through washing and flotation procedures in sedimentary rocks while flotation is the major beneficiation method of igneous deposits.

In respect to the Greek territory, phosphate deposits have been discovered in Epirus area. The weathered type can be beneficiated and produce a commercial concentrate with 30% P_2O_5 but its reserves are relatively limited. On the contrary, the non-weathered type has abundant reserves of low grade (in most cases 12-16% P_2O_5) but the problem is focused on the difficulty to separate phosphate matter from gangue minerals (mostly calcite) due to their similar behaviour both to physical and physicochemical separation methods.

6. References

Abouzeid A.M., El Jallad I.S., and Orphy M.K. 1980. Calcareous phosphates and their calcined products, *Minerals Sci. Engineering*, 12(2), 73-83.

Anastassakis G.N. 1989. Contribution to the beneficiation of unaltered phosphate rock of Epirous area (Greece), *PhD*, National Technical Univ. of Athens, Dept. Mining Eng. and Metallurgy, 223pp.

Anonymous 1986. Phosphates: A review of processing techniques, *World Mining Equipment*, April, 40-43.

Baumann A.N. and Snow R.E. 1980. Processing techniques for separating MgO impurities from phosphate products, *2nd Intern. Congress Phosphorous Compounds*, Boston, April 1980, 269-280.

Blazy P. and Jdid E.A. 1997. Removal of ferriferous dolomite by magnetic separation from the Egyptian Abu Tartur phosphate ore, *Int. J. Miner. Process.*, 49, 49-58.

Cathcart J.B. 1984. Sedimentary Phosphate deposits of the world: Present status and outlook for the future, In *Phosphates: What prospects for growth?*, Metal Bulletin Inc., New York, 9-42.

Cohen E. and Hammoud N.S. 1979. Low temperature roasting in ungrading the non-oxidized phosphorites of Abu-Tartur Plateau (Western Desert, Egypt), *XIII Int. Mineral Process. Congress*, Warsaw, 1979, 1828-1844.

Cooper C.D., and Manderson, M.C., 1984. Phosphate rock: The emerging world and regional supply and demand outlook into the late 1980's, In *Phosphates: What prospects for growth?*, Metal Bulletin Inc., New York, 214-226.

Custred V.K, Degner V.R., and Long E.W. 1975. Recent advance in coarse particle recovery utilizing large capacity flotation machines, *Trans. SME-AIME*, 258, 324-325.

Economou E.D. and Vaimakis T.C. 1997. Beneficiation of Greek calcareous phosphate ore using acetic acid solutions, *Ind. Eng. Chem. Res*., 36, 1491–1497.

Fantel R.J., Anstett T.F., Peterson G.R., Porter K.E. and Sullivan D.E. 1984. Phosphate rock availability: World, *I.C. 8989*, U.S. Bureau of Mines, 4-5, 11.

Good P.C 1976. Beneficiation of unaltered Indian calcareous phosphate rock by calcination and hydration, *RI 8154*, US Bureau of Mines, 1-17.

Guimaraes R.C., Araujo A.C. and Peres A.E.C. 2005. Reagents in igneous phosphate ores flotation, *Minerals Engineering*, 18, 199-204.

Hammoud N.S., Khazback A.A. and El-Gemmizi M.A. 1985. Beneficiation of complex low-grade phosphorites of Abu Shegeila (Red Sea, Egypt), *XV Intern. Miner. Process. Congress*, Cannes, 1985, Vol. 3, 412-423.

Hoppe R. 1976. From matrix of fertilizers. Florida's phosphate industry girds to produce over 50 million t.p.y., *Eng. Min. J.*, 177(9), 81-93.

Jasinski S.M. 2013. Phosphate rock, in *Mineral Commodities Summaries*, USGS, 118-119.

Kaklamanis N. 1983. Results on the operation of phosphate rock pilot-plant in April 1983, *Report* of the Institute of Geology and Mineral Exploration (Greece).

Lawver J.E., Raulerson J.D. and Cook C.C. 1980. New techniques in beneficiation of phosphate rock, *Trans. SME - AIME*, 268, 1787-1802.

Lenentouri Th., Chakoumakos B.C., Moghaddam H.Y. and Perdikatsis V., 2000. Structural studies of a carbonate fluorapatite from powder Neutron Diffraction data, *Materials Science Forum*, Vol. 321-324, 924-930.

Moudgil B.M. and Barnett D.H. 1979. Agglomeration-skin flotation of coarse phosphate rock, *Mining Eng.*, 31(3), 283-289.

Notholt A.J.G. 1984. Igneous phosphate resources: Their growing contribution to world markets, In *Phosphates: What prospects for growth?*, *Metal Bulletin Inc.*, New York, 43-58.

Notholt A.J.G. and Highley D.E. 1986. World phosphate resources, with particular reference to potential low-grade ores, *Trans. Instn. Min. Metall. (Section B: Applied Earth Sci.)*, 95, A125-132.

Özer A.K. 2003. The characteristics of phosphate rock in a fluidized bed for the upgrading, *Adv. Powder Technol.*, 14 (1), 33–42.

Perdikatsis V. 1991. X-Ray power diffraction study of francolite by the Rietveld method, *Mat. Science Forum*, Vol. 79-82, 809-814.

Pitsikas L. 1981. Reserves estimation of the phosphate deposit with compact structure of Kosmiras-Ioannina area with a content 10-14% P_2O_5, *Report of the Institute of Geology and Mineral Exploration (Greece)*.

Raden D.J. 1979. Current problems in beneficiation of phosphate fines, In P. Somasundaran and N. Arbiter (eds), *Beneficiation of Mineral Fines – Problems and Research Needs*, 79-93, AIME, 406 pp.

Rule A.R. and Daellenbach C.B. 1985. Beneficiation of complex phosphate ores containing carbonate and silica gangue, *XV Intern. Mineral Processing Congress*, Cannes, Vol. III, 380-389.

Sengul H., Ozer A.K. and Gulaboglu M.S. 2006. Beneficiation of Mardin-Mazıdagi (Turkey) calcareous phosphate rock using dilute acetic acid solutions, *Chemical Engineering Journal*, 122, 135-140.

Skounakis S. 1979. Contribution to the study of the genesis conditions of the phosphate deposits of western Greece. *Thesis*, University of Athens, Athens, 143 pp.

Tsailas D., Kalantzopoulos G., Kalatzis G. and Grossou-Valta M. 1978. Study on the possibility of amelorization of the altered phosphate rock of Drymon area for phosphoric acid production, *Report* of the Institute of Geology and Mineral Exploration (Greece).

Tsailas D., Grossou-Valta M., and Kalatzis G., 1980. Study on the possibility of amelorization of the unaltered phosphate rock of Epirous area, *Report* of the Institute of Geology and Mineral Exploration (Greece).

Tsailas D., Grossou-Valta M. and Kalatzis G. 1981. Amelorization of the altered phosphate rock of Epirous area, Report of the Institute of Geology and Mineral Exploration (Greece).

UNEP 2001. Environmental aspects of phosphate and potash mining, 61 pp.

Van Straaten P. 2002. *Rocks for Crops: Agrominerals of sub-Saharan Africa*, ICRAF, Nairobi, Kenya, 338pp.

Van Kauwenbergh S.J. 2010. World Phosphate Rock Reserves and Resources, IFDC, 60pp.

Woodrooffe H.M. 1972. Phosphate in the Kola Peninsula, USSR, *Min. Eng.*, 24(12), pp. 54-56.

Δελτίο της Ελληνικής Γεωλογικής Εταιρίας, τομ. XLVII , 2013
Πρακτικά 13ου Διεθνούς Συνεδρίου, Χανιά, Σεπτ. 2013

Bulletin of the Geological Society of Greece, vol. XLVII 2013
Proceedings of the 13th International Congress, Chania, Sept. 2013

PALLADIUM AND PLATINUM IN HYDROTHERMAL SYSTEMS: THE CASE OF PORPHYRY-CU SYSTEMS AND SULFIDES ASSOCIATED WITH OPHIOLITE COMPLEXES

Eliopoulos D.G.[1] and Economou-Eliopoulos M.[2]

[1] *Institute of Geology and Mineral Exploration (IGME), Sp. Loui 1, C Entrance, Olympic Village, GR-13677, Acharnai, Greece, eliopoulos@igme.gr*

[2]*Faculty of Geology and Geoenvironment, University of Athens, Panepistimiopolis, GR-15784 Athens, Greece, econom@geol.uoa.gr*

Abstract

Data on the Pt and Pd contents in sea-floor massive sulfides related to ophiolite complexes indicated elevated Pt contents, up to 1 wt % Pt in sulfides from East Pacific Rise, up to 1000 ppb Pd or Pt in sulfides from mid-Atlantic Ridge and the Pindos ophiolite complex (Greece). Recently, elevated levels of Pd and Pt, have been reported from mineralization associated with alkaline porphyry deposits, such as the Skouries porphyry deposit (Greece), Cordillera of British Columbia, Elatsite (Bulgaria), Santo Tomas II in the Philippines and elsewhere. Current state of knowledge on the solubility of platinum-group elements was applied on hydrothermal systems related to the mineralization in ophiolite complexes and porphyry Cu-Mo-Au±Pd±Pt deposits toward a better understanding of the PGE mineralization in hydrothermal systems and the unknown Pd and Pt potential in porphyry-Cu systems. Ore reserves, mineralogical and geochemical ore data for porphyry-Cu systems are considered to be an encouraging factor for the presence of precious metals. In particular, the occurrence of merenskyite (palladium telluride) associated with chalcopyrite, coupled with the experimental data indicate that porphyry systems are capable to transport significant amounts of Pd and Pt.

Key words: *Platinum, palladium, sulfides, porphyry, Skouries.*

Περίληψη

Η έρευνα σχετικά με την περιεκτικότητα Pt και Pd σε θειούχα μεταλλεύματα που συνδέονται με οφιολιθικά συμπλέγματα έδειξε σημαντική περιεκτικότητα Pt, μέχρι 1% wt στην μεσο-ωκεάνια ράχη του Ειρηνικού Ωκεανού, μέχρι 1000 ppb Pd ή Pt σε θειούχα της μεσο-ωκεάνιας ράχης του Ατλαντικού Ωκεανού και στο οφιολιθικό σύμπλεγμα της Πίνδου. Επί πλέον σημαντικά επίπεδα Pd και Pt, έχουν προσδιοριστεί σε μεταλλοφορίες που συνδέονται με αλκαλικά κοιτάσματα πορφυρικού τύπου όπως στις Σκουριές Χαλκιδικής, Κορδιλιέρες της Βρετανικής Κολομβίας, ΗΠΑ, Elatsite (Βουλγαρία), Santo Tomas II Φιλιππίνες και αλλού. Πρόσφατα δεδομένα που σχετίζονται με την διαλυτότητα των στοιχείων της ομάδας του λευκοχρύσου εφαρμόσθηκαν σε υδροθερμικά συστήματα που συνδέονται με μεταλλοφορίες που φιλοξενούντα σε οφιολιθικά συμπλέγματα και κοιτάσματα πορφυρικού τύπου Cu-Mo-Au ± Pd±Pt, με σκοπό την ερμηνεία της παρουσίας των στοιχείων αυτών σε υδροθερμικά συστήματα και την δυνατότητα προσδιορισμού του δυναμικού του Pd και

Pt σε συστήματα πορφυρικού-Cu. Το αποθεματικό δυναμικό των κοιτασμάτων πορφυρικού-Cu σε συνδυασμό με τα ορυκτολογικά και γεωχημικά τους δεδομένα αποτελούν ενθαρρυντικούς παράγοντες για την φιλοξενία σε αυτά πολυτίμων μετάλλων. Ειδικότερα, η παρουσία παλλαδίου σε πορφυρικά συστήματα χαλκού με την μορφή μερενσκυίτη (τελλουρίδιο του παλλαδίου) και η σχέση του τελευταίου με τον χαλκοπυρίτη, και σε συνδυασμό με πειραματικά δεδομένα υποδηλώνουν δυνατότητα μεταφοράς και απόθεσης Pd και Pt σε κοιτάσματα πορφυρικού χαλκού και άλλα υδροθερμικά συστήματα.
***Λέξεις κλειδιά**: λευκόχρυσος, παλλάδιο, θειούχα, πορφυρικός -Cu, Σκουριές.*

1. Introduction

Recent data on the platinum and palladium contents in sea-floor massive sulfides related to ophiolite complexes indicated that elevated platinum and palladium contents, up to 1 wt % Pt in massive sulfides from East Pacific Rise (Hekinian et al. 1980), up to 1000 ppb Pd in sulfides from mid-Atlantic Ridge (Crocket 1990), up to 1000 ppb Pt in an occurrence of brecciated pipeform diabase, underlying the massive ore from the Pindos ophiolite complex (Economou-Eliopoulos et al., 2008).

In addition, elevated levels of Pd and Pt, have been reported from mineralization associated with several of the alkaline porphyry deposits in the Cordillera of British Columbia (Copper Mountain Galore Creek), Allard Stock, La Plata Mountains and Copper King Mine in USA, Skouries porphyry deposit, Greece, Elatsite, Bulgaria, and from Santo Tomas II in the Philippines (Werle et al. 1984, Mutschler et al. 1985, Eliopoulos & Economou-Eliopoulos 1991, Piestrzynski et al. 1994, Eliopoulos et al. 1995, Tarkian & Koopmann 1995, Tarkian & Stribrny 1999, Economou-Eliopoulos & Eliopoulos 2000, Tarkian et al. 2003). The average Pd and Pt content at the Skouries deposit are about 180 ppb and 26 ppb, respectively (Eliopoulos and Economou-Eliopoulos, 1991). As the ore reserves amount to over 200 million tons, the amounts of Pd and Pt are approximately 15 tons and 3.5 tons, respectively in the Skouries deposit, and 13 tons Pd and 3 tons Pt for the Elatsite deposit (Economou-Eliopoulos, 2005). In addition, the occurrence of these precious metals in porphyry-Cu systems under the form of merenskyite (palladium telluride) and their association with chalcopyrite (Tarkian et al., 1992) were considered to be an encourage factor for the Pd Pt recovery as by products along with gold and copper (Eliopoulos and Economou-Eliopoulos, 1991).

Although the lack of thermodynamic or experimental data preclude a quantitative analysis of Pt and Pd solubility in waters rich in organic material, ammonia, polysulfide, or thiosulfate (Wood 2002, Wilde et al. 2002), experimental data (Gammons et al. 1992) indicated that at about 300ºC, solubilities of Pt and Pd as chloride complexes are restricted to (a) oxidizing conditions over a range of pH < 6, and (b) strongly acidic conditions (pH less than ~3), under reducing conditions (pyrite or pyrrhotite stability fields). Thus, it has been concluded that the highest Pt and Pd concentration will be attained under both oxidized and acidic conditions and that chloride is the most abundant ligand in hydrothermal solutions, forming strong complexes with Pt and Pd, and it is a potentially important ligand for aqueous transport of these metals (Wood 2002).

In the present study the current state of knowledge of solubility of platinum-group elements (Wood, 2002; Hanley, 2005; Simon and Pettke, 2009, and references there in) is applied toward a better understanding of the PGE mineralization in hydrothermal systems and the unknown Pd and Pt potential in porphyry Cu systems.

2. Description of Pt-Pd Enriched Hydrothermal Deposits

2.1. Pt and Pd Contents in Sulfide Mineralization Associated With Ophiolite Complexes

Data compilation of platinum and palladium contents in sea-floor massive sulfides related to ophiolite complexes may indicate that they are quite soluble under a range of hydrothermal conditions. High Pt (up to 1 wt %) contents have been reported in marcasite and chalcopyrite from massive sulfides at 21ºN on the East Pacific Rise (Hekinian et al. 1980). Sulfide deposits at 26ºN on the mid-Atlantic Ridge contain significant palladium, ranging from 3 to 1000 ppb, and gold up to 8 ppb (Crocket 1990). Palladium contents in massive sulphide ores of Cyprus type from the Pindos (Kondro) ophiolite complex, Greece are lower than the detection limit of the method but contain Au up to 3.6 ppm, whilst significant Pt-enrichment, ranging from 160 to 1000 ppb, has been determined in an occurrence of brecciated pipeform diabase, underlying the massive ore of the complex (Economou-Eliopoulos et al., 2008) (Table 1).

Table 1 - Geochemical characteristics of sulfide ores hosted in ophiolite complexes and those from modern seafloor.

	ppb		ppm									wt%		
Main minerals	Pt	Pd	Ag	Au	Se	As	Mo	Sb	Hg	Ni	Co	Zn	Cu	Fe
Pindos														
Kondro: massive ore concisting of pyrite (py), chalcopyrite (cpy), sphalerite (sph), bornite (bn)														
py-cpy	<10	4	45	1.2	750	140	65	8.3	55	90	1300	2.7	8.2	13.2
py-cpy-sph	<10	3.5	35	3.5	1700	80	100	9	425	90	550	6.5	14	24.5
py-bn-cpy	<10	4	37	3.3	970	45	80	1.7	950	90	1500	1.2	22.4	10.8
Aspropotamos (Neropriona): disseminated pyrite (py), chalcopyrite (cpy)														
diabase breccia														
less altered	<10	10		0.011	<5	15	<5	0.3	<1	<100	28	0.007	0.007	6.8
moderatelly altered	400	20		0.018	<5	25	<5	0.3	<1	<100	27	0.007	0.006	7.1
highly altered	1000	27		0.025	<5	25	<5	0.6	<1	<100	15	0.009	0.007	6.9

Abbreviations: py=pyrite; cpy=chalcopyrite; sph=sphalerite; bn=bornite

2.2. Characteristic Features of the Sulfide Ores in the Pindos Ophiolite Complex

Cyprus-type massive sulfide occurrences in the form of small lenses (maximum 4 by 40 m) are found at Kondro Hill on the SE slopes of Smolicas Mountain. The estimated ore potential is ca. 10,000 tonnes with average 6.6 wt. % Cu and 9.4 wt. % Zn (Skounakis et al., 1980). They occur on the top of diabase (massive or pillow lavas) and are directly overlain by Fe-oxide-bearing sediments. Fragments of limestone, entirely enclosed within massive ore, are occasionally present. A salient feature of the Pindos massive ore from Kondro is the significant contents of Au (up to 3.6 ppm), Ag (up to 56 ppm), as well as high contents of Se (up to 1900 ppm), Co (up to 2200 ppm), Mo (up to 310 ppm), Hg (up to 280 ppm) and As up to 150 ppm (average values are presented in the Table 1). The ore comprises mainly pyrite and chalcopyrite. Bornite sphalerite, marcasite, covellite and siegenite are found in lesser amounts. Textural relationships indicate that early pyrite, commonly occurring as fractured large crystals, is extensively replaced by chalcopyrite, and then by bornite in a matrix of quartz. Cu-bearing sphalerite, with up to 3.6 wt. % Fe and 3.2 wt. % Cu, cements minor chalcopyrite and pyrite. Pyrite is extensively replaced by intergrowths between chalcopyrite and Fe-poor sphalerite with an average Cu content of 0.5 wt. %. The latter association, found in cross-cutting veins, hosts selenides (chiefly clausthalite, PbSe), the telluride mineral melonite ($NiTe_2$), gold, galena and barite. Concentrations of 'invisible Au' in coarse-grained pyrite (associated with chalcopyrite and bornite) range from 0.7±0.13 to 1.01±0.27 ppm, whereas concentrations in fine-grained pyrite lie between 7.67±1.6 and 5.3±2.7 ppm, accompanied by significant As content. Disseminated pyrite within diabase breccia in the

brecciated diabase underlying the Kondro massive ore, disseminated pyrite and minor chalcopyrite occur mostly in vesicles filled by quartz, kaolinite, chlorite and epidote. The Pd content in breccia samples (10 to 27 ppb) is low compared to that of Pt (160 to 1000 ppb). The significant enrichment in Pt in kaolinite-rich samples, and the limited range of $\delta^{34}S$ values for pyrite concentrates from the diabase breccia (+1.0 to +1.5‰), are characteristic features (Economou-Eliopoulos et al (2008).

2.3. Genetic Significance of the Platinum and Palladium Contents

Platinum and palladium contents in seafloor massive sulfides related to ophiolite complexes are generally very low. However, in the hydrothermal breccia underlying the massive ore, Pt reaches values of 1000 ppb; 27 ppb Pd was determined (Table 1). The concentration of Au in massive sulfide ore and Pt in the underlying diabase breccia may reflect differences in the relative solubility of the precious metals, and the extent to which they were saturated in a given hydrothermal solution, as well as the specific deposition mechanisms for each metal (Seward and Barnes, 1997; Wood, 2002). Pan and Wood (1994) pointed out that hydrothermal fluids in equilibrium with pyrite or pyrrhotite and alteration minerals such as chlorite, epidote, albite, calcite, etc., would be incapable of transporting significant amounts of PGE as chloride complexes. These authors instead suggested that a typical seafloor hydrothermal vent fluid could contain a significant amount of Pt and Pd as bisulfide complexes and that gold may also be predominantly transported in the form of bi-sulfide complexes. Moreover, they concluded that, under the conditions of their experiments, the solubility of Au as a bisulfide complex was three orders of magnitude higher than that of Pt and Pd. Thus, the elevated Pt contents in the mineralized diabase breccia of Pindos compared to massive sulfide ore seems to confirm the higher solubility, and thus further transport, of Au relative to Pt, causing Au enrichment in the massive ore. The presence of pyrrhotite remnants within pyrite, surrounded by hydroxides or magnetite within vesicles filled by pyrite, quartz, kaolinite and epidote may indicate that the Pt-precipitation was favoured by weakly acidic and oxidizing conditions (Wood, 2002).

Therefore, assuming that Au and Pt/Pd were derived from the same source area and that the transporting complexes of these metals are the same (Wood 2002) the concentration of Au in massive sulfide ore and Pt in the underlying diabase breccia may reflect a difference of the relative solubility (higher solubility of Au that remains more soluble than Pt) and the extent to which these metals are saturated in a given hydrothermal solution.

3. Pd and Pt Contents in Porphyry Cu ± Mo ± Au ± Pd ± Pt Deposits

Porphyry Cu ± Mo ± Au deposits are major sources of these metals and are associated with alkaline and calc-alkaline rocks. Recently, elevated levels of Pd and Pt, have been reported from mineralization associated with several of the alkaline porphyry deposits in the Cordillera of British Columbia (Copper Mountain Galore Creek), Allard Stock, La Plata Mountains and Copper King Mine in USA, Skouries porphyry deposit, Greece, Elatsite, Bulgaria, and from Santo Tomas II in the Philippines (Werle et al. 1984, Mutschler et al. 1985, Eliopoulos & Economou-Eliopoulos 1991, Eliopoulos et al. 1995, Tarkian & Koopmann 1995, Tarkian & Stribrny 1999, Economou-Eliopoulos & Eliopoulos 2000, Tarkian et al. 2003; Table 2).

Late Mesozoic to Tertiaty porphyry Cu-(Mo-Au) porphyry deposits, extending from Romania, through Serbia and Bulgaria to Greece are associated with subduction related magmatism following the change from east-west to north-south converge between Africa and Eurasia, and subsequent continental collision and post-collision magmatism (Kockel et al., 1975; Frei, 1995; Heinrich and Neubauer, 2002).

3.1. Skouries Deposit

The Skouries porphyry Cu-Au deposit, located at the Chalkidiki peninsula, northern Greece belongs to the Serbomacedonian massif consisting of a crystalline basement, which comprise two lithostratigraphic-tectonic units, the lower Kerdylia Formation and the upper Vertiskos Formation. The Vertiskos Formation is consisting of an old basement gneiss, amphibolite, schist and marble (Kockel et al., 1977; Perantonis, 1982; Frei, 1995; Tobey et al., 1998). Isotope data indicated that subvolcanic–porphyritic stocks such as the Skouries are relatively younger, of Miocene age 18 Ma, than the intrusions of the SerboMacedonian massif. The Skouries deposit is related to pipe-like intrusions, of subalkaline-alkaline composition, extending at surface over an area of approximately 200m x 200 m, is developed around two related porphyry centres (Fig. 4a) at depths between 650 and 800 m. The defined reserves in the porphyry Cu-Au deposit of Skouries are approximately 206 Mt at 0, 54 % Cu, and 0.80 ppm Au (Tobey et al., 1998).

Table 2 - Precious metal contents in porphyry Cu-Pd-Pt deposits.

	ppb				wt%
	Au	**Pt**	**Pd**	**Pd/Pt**	**Cu**
Greece					
Skouries (n=24)	3220	34	140	4.4	1.3
Concentrate (composite)	2400	40	60	0.7	22
Bulgaria					
Elatsite (n=11)	840	13	24	2.3	0.64
Concentrates (n=5)	17000	160	1600	19	31.44
British Columbia					
Galore Creek (n=2, cp-py-bn)	5200	17	410	29	7.63
Galore Creek (n=2, mt-py-bn-cp)	34200	49	780	17	16.01
Mt Milligan (n=4)	9500	56	1780	19	2.4
Mt Polley (n=3)	10500	19	140	5.9	7.9
Allard (n=2)	1485	3408	2120	0.7	22.5
Cooper Mountain (n=2)	4500	120	3005	40	34.1
Philippines					
Santo Tomas II	2230	13	48	5	0.31
Russia					
Aksug (=2)	4100	86	73	0.8	14.9
Sora (n=3)	100	88	50	0.6	5.8

Abbreviations: cp = chalcopytite; py = pyrite; bn = bornite; mt = magnetite

3.2. Characteristic Features of Alteration and Mineralization

At least five distinct stages of hydrothermal alteration and mineralization are obvious in the main porphyry. The typical alteration types of the porphyry Cu intrusions described by Lowell and Guibert (1970) are more or less presented in the Skouries intrusion, due to the repeated overprinting and intense silicification, with potassic being the predominant alteration type, whereas the propylitic and surrounding phyllitic alteration are limited. Two mineral assemblages of mineralization, occurring as veinlets/disseminations, can be distinguished: (a) magnetite, reaching up to 10 vol % (average 6 vol %)-bornite-chalcopyrite, linked to pervasive potassic and propylitic alteration type, in the central parts of the deposit, and (b) chalcopyrite-pyrite, dominated at the peripheral parts of the deposit. Molybdenite occurs in small amounts, commonly in late pyrite-sericite-carbonate bearing veinlets. Chalcopyrite, and in a lesser extent bornite, contain exsolutions of galena, which commonly has significant concentrations of Se, while clausthalite is

rare. Minor ore minerals are gold-electrum, clausthalite-galena, hessite and merenskyite-moncheite (Tarkian et al., 1991). A salient feature of the Skouries porphyry is the presence of fine-grained magnetite, which is Cr-bearing, ranging from 0.65 to 0.98 wt% Cr_2O_3 in the matrix in contrast to the Cr-free magnetite of the main porphyry. Also, chalcopytite and pyrite, which contains nickel ranging from 0.45 to 2.4 wt% Ni. And Co ranging from 0.64 to 4.18 wt% Co, as well as the high values of the ratios Ce/Lu (>225), relatively high Th and U contents (up to 63 ppm and 9 ppm, respectively), Ba (up to 2260 ppm) and Sr (up to 1230 ppm) contents, reflecting probably a strong fractionation of parental magmas (Eliopoulos and Economou-Eliopoulos 1991).

3.3. Palladium and its Distribution in the Skouries Deposit

The analysis of representative ore samples showed a significant Pd-enrichment in mineralised samples, up to 490 ppb Pd, in oxidized ore samples (Eliopoulos and Economou-Eliopoulos, 1991). Relatively high Pd content in the major vein-type mineralization of Skouries ranging between 60 and 200 ppb (average 110 ppb Pd), was documented by analysis of a composite drill hole sample (~15 kgs) showing 76 ppb Pd to 5000 ppm Cu (Economou-Eliopoulos and Eliopoulos, 2000). The analysis of mineralized material and highly mineralized portions from deeper parts of the deposit indicated relatively high Pd (average 130 ppb) and Pt (average 46 ppb) contents.

Textural relations between base metal sulphides, PGM and Au–Ag tellurides support the association of precious metals with the Cu-minerals (bornite and chalcopyrite), indicating that the main Pd-bearing mineral merenskyite, has deposited during the major stage of Cu deposition. Thus, assuming that Pd is mainly associated with chalcopyrite, when calculating the measured Pd contents in chalcopyrite (which were normalized to 100 percent chalcopyrite), the Pd values in the mineralized samples from deeper parts of the Skouries deposit is 3000 ppb Pd. These values are comparable to that in the chalcopyrite concentrate (2400 ppb Pd to 21 wt%, Economou-Eliopoulos and Eliopoulos, 2000), while the calculated Pt content is 1230 ppb.

4. Comparison with Other Pd, Pt-Bearing Porphyry-Cu Intrusions

4.1. Elatsite Deposit (Bulgaria)

The Elatsite porphyry Cu-Au-PGE deposit, of Upper Cretaceous (92.3 ± 1.4 Ma) age, extends over an area of approximately 1,300 m long and 200 to 700 m wide. At depth the ore-body was traced more than 550 m. The Elatsite porphyry Cu-Au deposit is found in a spatial association (~10 km distance) with the Chelopech Au-Cu high-sulfidation epithermal type deposit, connected by east-northeast – and north-northwest – trending fault system (Popov and Kovachev, 1996; Popov et al., 2000; Bonev et al., 2002). Ore reserves of the deposit are estimated to be 185 million with 0.4 wt % Cu, 0.3 g/t Au, 0.68–1.9 g/t Ag, 0.07 g/t Pd and 0.02 g/t Pt (Strashimirov et al., 2002; Tarkian et al., 2003; Strashimirov et al., 2003).

Precious metal contents are strongly concentrated in the magnetite (ranging from 2 to 10 vol %, reaching locally up to 30 vol %), -bornite-chalcopyrite assemblage, occurring mainly in the southern part of the ore body. Palladium, Pt and Au concentrations in representative mineralized samples from the Srednogorie metallogenetic zone of Bulgaria, including the Elatsite deposit have been published by Eliopoulos et al. (1995) and noticed Pd and Pt contents up to 20 ppb, while Cr and Co reach values up to 100 and 116 ppm, respectively. The average precious metal contents in flotation concentrates (at 23.5 wt% Cu) are 16200 ppb Au, 1130 ppb Pd and 130 ppb Pt (Tarkian and Stribrny, 1999; Tarkian et al., 2003). Gold and Pd correlate with Te, Bi and Se, while Pt shows a strong correlation (r = 0.93) only with Te (Tarkian et al., 2003).

4.2. Santo Tomas II Philex Philippines

The Santo Tomas II Philex porphyry Cu–Au deposit, of Miocene age (3 Ma), is located at the Luzon Island, Philippines, along the margins of a fault system, extending at surface over an area of approximately 600m x 200 m that represents approximately 800 m of vertical section. It consists

of quartz diorite with calk-alkaline affinities, and is spatially associated with volcanic rocks of dacite composition (Tarkian and Koopmann, 1995).

The predominant wall rock alteration associated with the mineralised zone is potassic and propylitic, with a common overlapping between of these alteration types. Phyllic alteration is of limited extent, overprints earlier potassic and inner propylitic assemblages. Two types of mineral assemblages have been distinguishes: (a) bornite-chalcopyrite-magnetite, which is concentrated in the inner part of the potassic zone (biotite and quartz), and (b) chalcopyrite-pyrite, occurring in the outer part of the potassic zone and in the propylitic zone. The merenskyite occurs exclusively as inclusions in chalcopyrite and bornite (Tarkian and Koopmann, 1995).

4.3. British Columbia Cordillera

Porphyry Cu-Au deposits located in the British Columbia Cordillera are associated with alkaline, subalkaline to calc-alkaline rocks stocks, dikes and sills, which have emplaced into two allochthonous terranes, Quesnellia and Stikinia, North America (McMillan et al., 1995). The majority of these intrusions are Early Jurassic in age (205-195 Ma) although some intrusions in Quesnellia are distinctly younger (~185 Ma; Mortensen et al., 1995). Given that many of those Cu-Au porphyry deposits have formed in areas of long-lived magmatism and subsequent thermal overprinting, age data may reflect cooling rather than actual ages on intrusions.

Apart from Au, elevated levels of platinum group elements (PGE), particularly Pd and Pt, have been reported in high-grade bornite-chalcopyrite and/or flotation concentrates from porphyry Cu-mineralization associated with the alkaline porphyry intrusions at Copper Mountain-Ingerbelle (up to 3.2 ppm Pd and 0.15 ppm Pt), Allard stock, La Plata Mountains (up to 2.3 ppm Pd and 3.9 ppm Pt), Galore Creek, Copper King Mine, Comstock Mine and Sappho in the British Columbia Cordillera (Werle et al., 1984; Mutschler et al., 1985). It has been suggested that the Pd and Pt mineralization in the above porphyry deposits is linked with the genesis of alkaline arc magmas, derived probably from an enriched mantle source. They may reflect partial melting and incorporation into the melt of destabilized precious metal-bearing sulfides, hosted in the mantle source.

5. Critical Factors for the Formation of Porphyry Cu+Au+ Pd ±Pt Deposits

The wide range of physicochemical conditions and the dynamic interplay between magmatic, hydrothermal and tectonic processes during the formation of porphyry Cu deposits in Volcano-plutonic arcs, and the composition of alkaline parent magmas may be major controls of their base/precious metal potential and characteristics. Experimental, thermodynamic, and fluid inclusion studies strongly suggest that Cu and precious metals in potassic alteration zones are transported as an aqueous chloride complex in high temperature (350 to >700°C) and relatively oxidized hydrothermal brines (Burnham & Ohmoto 1980). Given that significant quantities of Au can be transported by hot, saline, magmatic fluids under either reducing or oxidizing conditions, whereas Cu transport is much more favoured in the oxidizing environment. In contrast, “reduced” porphyry Cu–Au deposits that lack primary hematite, magnetite, and sulfate minerals (anhydrite) and contain abundant hypogene pyrrhotite, are relatively Cu-poor, but Au-rich deposits (Hemley et al. 1992, Williams et al. 1995, Rowins 2000).

Experimental studies have constrained the solubilities of As, Au, Cu, Ag and Mo (ore metals in magmatic volatile phases in equilibrium with silicate melts (Candela and Holland, 1984; Williams et al., 1995; Simon et al., 2005) and these data have been used to model quantitatively the behaviour of metals at conditions relevant to shallow-level magma degassing. One important group of ore metals for which there are only very limited solubility data at magmatic conditions is the platinum group elements (PGE). Several experimental studies have been performed to characterize the behaviour of the PGE in low-temperature fluids; however, the mobility of the PGE in fluid-saturated silicate melt assemblages remains almost completely unconstrained.

Recently, experimental data on the solubility and partitioning of Pt in an S-free vapour – brine – rhyolite melt – Pt metal assemblage indicated that the vapour and brine were in equilibrium with the melt at the time of trapping (Simon and Pettke, (2009). Platinum solubilities in vapour, brine and glass (quenched melt) were quantified by using laser ablation – inductively coupled plasma – mass spectrometry (LA-ICP-MS). Based on the major and trace element concentrations of glass-hosted fluid inclusions as well as the silicate melt, they estimated platinum solubility values. Furthermore, they used these data to calculate Nernst-type partition coefficients for Pt between vapour/melt, brine/melt and vapour/brine. The partitioning data were used to model the Pt-scavenging capacity of vapour and brine during the crystallization-driven degassing (i.e., second boiling) of a felsic silicate melt over a depth range of 3–6 km (magmatic-hydrothermal ore deposits). Model calculations suggest that aqueous vapour and brine can scavenge sufficient quantities of Pt, and by analogy Pd to produce economically important PGE-rich magmatic-hydrothermal ore deposits in Earth's upper continental crust.

6. Evaluation of Pd and Pt as an Economic Factor for Porphyry Cu Systems

The palladium telluride, merenskyite, as inclusions in chalcopyrite and bornite, has been described as the main PGE mineral in porphyry Cu–Au–Pd–Pt deposits, such as Skouries, Santo Tomas II, Biga, Elatsite, Mamut (Tarkian et al. 1991; Tarkian et al. 2003; Tarkian & Koopmann 1995, Tarkian & Stribrny 1999). Assuming that Pd in porphyry Cu deposits is mainly associated with chalcopyrite (measured contents are normalized to 100 % chalcopyrite), and using reserves for each deposit, then the Pd and Pt potential in porphyry systems can be estimated (Table 3).

The potential for PGE mineralization associated with such large Au-Cu porphyry deposits is still unknown. Although the analytical data required for the evaluation of the precious metal potential of porphyry deposit are limited, the existence of (Pd+Pt) values (>5 ppm) are considered to be encouraging for Pd and Pt as by-products and porphyry deposits a good target for Pd & Pt exploration.

Table 3 - Palladium and platinum potential in porphyry-Cu-Au-Pd-Pt deposits.

Deposit	Ore tonnage tons x 10^6	**Pd** grade ppm	**Pt** grade ppm	**Pd** tonnage tons	**Pt** tonnage tons
Skouries, Greece	206	0.076	0.017	15	3.5
Elatsite, Bulgaria	185	0.07	0.02	13	3.7
Santo Tommas, Philippines	330	0.032	0.005	10.5	1.6
Afton, B.C.	70	0.13		9	

7. References

Bonev I.K., Kerestedjian T., Atanassova R. and Andrew C. 2002. Morphogenesis and composition of native gold in the Chelopech volcanic-hosted Au-Cu epithermal deposit, Srednogorie zone, Bulgaria, *Mineralium Deposita*, 37, 614-629.

Burnham C. and Ohmoto H. 1980. Late-stage processes in felsic magmatism, *Mining Geology Special Issue*, 8, 1-11.

Candela P.A., Holland H.D. 1984. The partitioning of copper and molybdenum between silicate melts and aqueous fluids, *Geochimica et Cosmochimica Acta*, 48, 373-380.

Economou-Eliopoulos M., Eliopoulos D.G. and Chryssoulis S. 2008. A comparison of high-Au massive sulfide ores hosted in ophiolite complexes of the Balkan Peninsula with modern analogues: Genetic significance, *Ore Geology Reviews*, 33, 81-100.

Economou-Eliopoulos M. and Eliopoulos D.G. 2000. Palladium, platinum and gold concentrations in porphyry copper systems of Greece and their genetic significance, *Ore Geology. Reviews*, 16, 59-70.

Eliopoulos D. G., Economou-Eliopoulos M., Strashimirov St., Kovachev V. and Zhelyaskova-Panayotova M. 1995. Gold, platinum and palladium content in porphyry Cu deposits from Bulgaria: a study in progress, *Bull. Geol. Soc. Greece*, 5, 712–716.

Eliopoulos D.G. and Economou-Eliopoulos M. 1991. Platinum-Group Element and Gold Contents in the Skouries Porphyry-Copper deposit, Chalkidiki Peninsula, N. Greece, *Economic Geology*, 86, 740-749.

Frei R. 1995. Evolution of Mineralizing Fluid in the Porphyry Copper System of the Skouries Deposit, Northern Chalkidiki (Greece): Evidence from combined Pb-Sr and Stable Isotope Data, *Economic Geology*, 90, 746-762.

Gammons C.H., Bloom M.S. and Yu Y. 1992. Experimental investigation of the hydrothermal geochemistry of platinum and palladium: I Solubility of platinum and palladium sulphide minerals in $NaCl/H_2SO_4$ solutions at 300°C, *Ceochemica et Cosmochemica Acta*, 56, 3881-3894.

Hanley J., Pettke T., Mungall J.E. and Spooner E.T.C. 2005. Investigations of the behavior and distribution of platinum and gold in silicate melt – brine mixtures at 1.5 kbar, 600 to 800°C using synthetic fluid inclusions methods: a laser ablation ICPMS pilot study, *Geochimica et Cosmochimica Acta*, 69, 2593-2611.

Heinrich C.A. and Neubauer F. 2002. Cu–Au–Pb–Zn–Ag metallogeny of the Alpine–Balkan–Carpathian–Dinaride geodynamic province, *Mineralium Deposita*, 37, 533–540.

Hekinian R., Fevrier M., Bischoff J.L., Picot P. and Shanks W.C. 1980. Sulfide deposits from the East Pacific Rise near 21 degrees, *Natural Science*, 207(4438), 1433-1444.

Hemley J.J., Cygan G.L., Fein J.B., Robinson G.R. and D'Angelo W.M. 1992.Hydrothermal ore-forming processes in the light of sulfides in rock-buffered systems. I. Iron-copper-zinc-lead sulfide solubility relations, *Economic Geology*, 87, 1–22.

Kockel F., Mollat H. and Gundlach H. 1975. Hydrothermally altered and (copper) mineralized porphyritic intrusions in the Serbo-Macedonian Massif (Greece), *Mineralium Deposita*, 10, 195-204.

Lowell L.D. and Guibert J.M. 1970. Lateral and vertical alteration mineralization zoning in porphyry ore deposits, *Economic Geology*, 65, 535-550.

McMillan W.J., Thompson J.F.H., Hart C.J.R. and Johnston S.T. 1995. Regional geological and tectonic setting of porphyry deposits in British Columbia and Yukon Territory, Porphyry Deposits of the Northwestern Cordillera of North America, In: Schroeter T.G., (ed), *Canadian Institute of Mining and Metallurgy, Special Volume 46*, 40-57.

Mortensen J.K., Ghosh D.K. and Ferri F. 1995. U-Pb geochronology of intrusive rocks associated with copper-gold porphyry deposits in the Canadian Cordillera, Porphyry Deposits of the Northwestern Cordillera of North America, In: Schroeter T.G., (ed), *Canadian Institute of Mining and Metallurgy, Special Volume 46*, 142-158.

Mutschler F.E., Griffin M.E., Scott S.D. and Shannon S.S. 1985. Precious metal deposits related to alkaline rocks in the north American Cordillera - an interpretive review, *Geol. Soc. South Africa Transactions*, 88, 355–377.

Pan P. and Wood S.A. 1994. Solubility of Pt and Pd sulfides and metals in aqueous bisulphide solu- tions. II Results at 200ºC to 350ºC and saturated vapour pressure, *Mineralium Deposita*, 29, 373-390.

Perantonis G. 1982. Genesis of porphyry copper deposits in Chalkidiki peninsula and W. Thrace, Greece, *PhD Thesis*, University of Athens, 150pp.

Piestrzynski A., Schmidt S. and Franco H. 1994. Pd-minerals in the Santo Tomas II porphyry copper deposit, Tuba Benguet, Philippines, *Mineraligia Polonica*, 25 (2), 12-31.

Popov P. and Kovachev V. 1996. Geology, Composition and Genesis of the Mineralizations in the Central and Southern Part of Elatsite-Chelopech Ore Field, In: Popov P. (ed), *Plate Tec-*

tonic Aspects of the Alpine Metallogeny in the Carpato-Balkan Region, UNESKO - IGCP Project No 356, Proceedings of the annual meeting, Sofia, 1996, 1,159–170.

Popov P., Petrunov R., Kovachev V., Strashimirov S. and Kanazirzki M. 2000. Elatsite-Chelopech ore, In: Strashimirov S., Popov P. (eds) *Geology and metallogeny of the Panagyurishte ore region.* Guide to excursion A and C. ABCD-Geode 2000 Workshop, Borovets, May 2000, 8–18.

Rowins S.M. 2000. Reduced porphyry copper-gold deposits: A new variation on an old theme, *Geology*, 28, 491-494.

Seward T.M. and Barnes H.L. 1997. Metal transport by hydrothermal fluids, In: Barnes H. L. (ed) *Geochemistry of Hydrothermal Ore Deposits*, John Wiley, Sons Inc. New York, 435-486.

Simon A.C. and Pettke T. 2009. Platinum solubility and partitioning in a felsic melt – vapor – brine assemblage, *Geochimica et Cosmochimica Acta*, 73(12), 438-454.

Simon A.C., Pettke T., Candela P.A., Piccoli P.M. and Heinrich C.A. 2005. Gold partitioning in melt-vapor-brine systems, *Geochimica et Cosmochimica Acta*, 69, 3321- 3335.

Skounakis S., Economou M. and Sideris C. 1980. The ophiolite complex of Smolicas and the associated Cu-sulfide deposits, Proc. Intern. Symposium *On metallogeny of mafic and ultramafic complexes*, IGCP Pr. No 169 (2), 361-374.

Strashimirov S., Petrunov R. and Kanazirski M. 2002. Mineral associations and evolution of hydrothermal systems in porphyry copper deposits from the Central Srednogorie zone (Bulgaria), *Mineralium Deposita*, 37, 587–598.

Strashimirov S., Bogdanov K., Popov K. and Kehanov R., 2003. Porphyry Systems of the Panagyurishte Ore Region, In: Bogdanov K. and Strashimirov S. (eds), *Cretaceous Porphyry-Epithermal Systems of the Srednogorie Zone, Bulgaria*, SEG Guidebook Series, 132 pp.

Tarkian M., Hunken U., Tokmakchieva M. and Bogdanov K. 2003. Precious-metal distribution and fluid-inclusion petrography of the Elatsite porphyry copper deposit, Bulgaria, *Mineralium Deposita* , 38, 261-281.

Tarkian M. and Stribrny B. 1999. Platinum-group elements in porphyry copper deposits: a reconnaissance study, *Mineralogy and Petrology* ,65, 161-183.

Tarkian M. and Koopmann G. 1995. Platinum-group minerals in the Santo Tomas II Philex porphyry copper–gold deposit, Luzon Island, Philippines, *Mineralium Deposita*, 30, 39–47.

Tarkian M., Economou-Eliopoulos M. and Eliopoulos D. G. 1992. Platinum-group minerals and tetraauricupride in ophiolitic rocks of Skyros island, Greece, *Mineralogy and Petrology*, 47, 55-66.

Tarkian M., Eliopoulos D.G. and Economou-Eliopoulos M. 1991. Mineralogy of precious metals in the Skouries porphyry copper deposit, N. Greece, *Neues Jahrbuch fur Mineralogie Abhandlungen*, 12, 529-537.

Tobey E., Schneider A., Alegria A., Olcay L. Perantonis G. and Quiroga J. 1998. Skouries porphyry copper-gold deposit, Chalkidiki, Greece, In: Porter TM (ed) *Porphyry hydrothermal Cu-Au deposits*. A global perspective of the Australian Mineral Foundation Conference Proceedings, Glenside, South Australia, 159-168.

Werle J.I., Ikramuddin M. and Mutschler F.E. 1984. Allard stock, La Plata Mountains, Colorado — an alkaline rock hosted porphyry copper precious metal deposit, *Canadian Journal of Earth Science*, 21, 630–641.

Wilde A.R., Simpson L. and Hanna S. 2002. Preliminary Study of tertiary hydrothermal alteration and platinum deposition in the Oman ophiolite, *Journal of Virtual Explorer*, 6, 7–19.

Williams T.J., Candela P.A. and Piccoli P.M. 1995. The partitioning of copper between silicate melts and aqueous fluids: An experimental investigation at 1 Kbar, 800°C and 0.5 Kbar, 850°C, *Contributions to Mineralogy and Petrology*, 121, 388-399.

Wood B.W. 2002. The aqueous geochemistry of the platinum-group elements with applications to ore deposits, In: Cabri L.J. (ed.), Geology, Geochemistry, mineralogy, metallurgy and beneficiation of PGE, *Canadian Institute of Mining and Metallurgy Special Paper*, 54, 211–249.

Δελτίο της Ελληνικής Γεωλογικής Εταιρίας, τομ. XLVII , 2013
Πρακτικά 13ου Διεθνούς Συνεδρίου, Χανιά, Σεπτ. 2013

Bulletin of the Geological Society of Greece, vol. XLVII 2013
Proceedings of the 13th International Congress, Chania, Sept. 2013

NATIONAL REPORTING CODES FOR THE MINERAL INDUSTRY: THE CASE OF JORC IN AUSTRALIA

Kalaitzidis S.[1, 2]

[1] *Integral Resource Consulting Pty Ltd, Brisbane, Australia, stavros.kalaitzidis@integralrc.com*

[2] *Department of Geology, University of Patras, Rio-Patras, Greece*

Abstract

A revised version of the Australasian Code for Reporting of Exploration Results, Mineral Resources and Ore Reserves commonly called the JORC Code was released in Australia in December 2012. This paper provides a summary of the principles that guide the Code, and the definitions therein, as well as the rationality behind adopting the Code as a Public Reporting tool. Brief examples of reporting requirements are also discussed. Additionally, references and a general comparison to the Pan-European Reserves & Resources Reporting Code (PERC standard) are presented. Although, in Greece there is no relevant Regulatory Framework in place yet or enforcement of any International Code, the adaptation of PERC is probably ahead, and hence this paper aims to open the discussion among geoscientists and mining engineers for the opportunities and the challenges that they will face.
Key words: *Mineral Resources, Ore Reserves, Competent Person, JORC, PERC.*

Περίληψη

Στην παρούσα εργασία παρουσιάζεται ο Κώδικας για την Ανακοίνωση Κοιτασματολογικών Ερευνών, Γεωλογικών και Οικονομικοτεχνικών Απολήψιμων Αποθεμάτων της Αυστραλίας (JORC), όπως αυτός αναθεωρήθηκε το 2012. Συζητούνται συνοπτικά οι Αρχές που διέπουν τον Κώδικα, οι Ορισμοί που πρέπει να υιοθετούνται στις Δημόσιες Ανακοινώσεις, καθώς και η έννοια του Αρμόδιου Μελετητή (Competent Person), με παράλληλη αναφορά σε παραδείγματα απαιτήσεων του Κανονισμού. Παρουσιάζεται επίσης μια συνοπτική σύγκριση με το αντίστοιχο Παν-Ευρωπαϊκό Πρότυπο Ανακοινώσεων (PERC), όπως αυτό δημοσιεύθηκε στις 15 Μαρτίου 2013. Στην Ελλάδα δεν υπάρχει ακόμα σε εφαρμογή Κανονιστικό Πλαίσιο για τη Δημόσια Ανακοίνωση Κοιτασματολογικών Ερευνών και Αποθεμάτων, αν και το πρότυπο PERC πιθανόν να αποτελέσει το Εθνικό Κανονιστικό Πλαίσιο. Σκοπό της εργασίας αποτελεί η έναρξη συζήτησης ανάμεσα στους γεωλόγους και μηχανικούς για τις ευκαιρίες αλλά και τις προκλήσεις, που θα επιφέρει ένα τέτοιο Κανονιστικό Πλαίσιο.
Λέξεις κλειδιά: *JORC, PERC, Competent Person, Γεωλογικό Απόθεμα, Οικονομοτεχνικά Απολήψιμο Απόθεμα.*

1. Introduction

During the last 20 years there have been significant activities at international level to standardize the reporting and the classification of mineral resources (e.g. UNFC, 2009; CIM, 2011, NI 43-101,

2011; PERC, 2013). Australia was one of the leading countries in implementing standards and guidelines since 1989 with the first edition of the Joint Ore Reserves Committee Code (JORC, www.jorc.org). The Code was adopted the same year by the Australian Securities Exchange (ASX, 2013) and by the New Zealand Market (NZX) in 1992. Other jurisdictions that nowadays accept the Code include, Hong Kong, Papua New Guinea, Singapore, South Africa, UK, UAE and Europe (Goddard, 2013).

In 2012 the Joint Ore Reserves Committee released a new edition of the Code (JORC, 2012), after both national and international cooperation particularly within the framework of the Committee for Mineral Reserves International Reporting Standards (CRIRSCO, 2013), whose members are National Reporting Organizations, from Australia, Canada, Chile, Europe (PERC, 2013), Russia, South Africa, and USA.

The JORC Code has been adopted by the two main Geoscientific Professional bodies in Australia, the Australasian Institute of Mining and Metallurgy (The AusIMM, www.ausimm.com.au) and the Australian Institute of Geoscientists (AIG, www.aig.org.au) and it is binding for their members. The Code sets out minimum standards, recommendations and guidelines for Public Reporting purposes by the listed companies in Stock Markets, who must comply with these standards. It is a Principles based Code for Reporting and does not regulate the means and the methods, which the Competent Persons may use to estimate the Mineral Resources or Ore Reserves.

Greece doesn't have yet a formal framework for Reporting Purposes, neither through the professional bodies of GEOTEE and TEE or the Athens Stock Market (ATHEX). Nor is there any known open discussion on these aspects. The most recent published Pan-European Standard (PERC, 2013) however, in which the Association of Greek Geologists (ΣΕΓ) is a member through the European Federation of Geologists (http://www.eurogeologists.de), might provide a new dynamic for the Code to come into effect. Nevertheless, the current public discussion in Greece is lacking and the legal framework seems also to be out-of-date and needs to be amended for such a Code to be implemented. For example there is no common Professional Organization for the Mining Sector Professionals, mainly Geologists and Mining Engineers, who are the Competent Persons in most cases.

This paper provides a summary of the principles that guide the Australasian JORC Code, and the definitions therein, as well as the rationality behind adopting the Code as a Public Reporting tool. Brief examples of reporting requirements are also discussed. The aim is to open the discussion among the geoscientists and mining engineers for the opportunities and the challenges that the adoption of a Reporting Code will impose.

It should be cautioned however, that for the exact definitions and comprehensive guidelines the reader should refer to the formal JORC Code (2012) website and documentation.

2. Background of JORC

In Australia the necessity for regulated public announcements has its genesis in 1969 when the bubble of the Poseidon NL share prices occurred; Poseidon NL was a mining exploration company that made a major nickel discovery at Windarra in Western Australia (Simon, 2003). The share price of the company rose from $0.80 in September 1969 to $280 in February of 1970, based on drilling results and the high Ni price of that time. Simultaneously, other small exploration companies were announcing or better rumouring exploration results not based on real data; but due to the euphoria in the general public's perception these companies saw their shares skyrocketing, along with the All Mining Index. Finally, the All Mining Index fell rapidly in November 1971, due to lowering Ni prices, as well as due to overrating several deposits, having a significant impact on the perceived reliability of the mining sector and its ability to raise capital. The investigation that followed highlighted that "*the stock market had been poorly regulated and that much of the information relied upon by investors was uncorroborated rumour*".

This gap was meant to be filled by the establishment of the Joint Ore Reserves Committee (JORC), which since published several Reports and Recommendations on the classification and Public Reporting of Ore Reserves, with the 1st edition of the JORC Code in 1989 (JORC, 2012). The latest edition in 2012 aims to significantly increase the level of transparency and disclosure that is required in Public Reports to ensure investors' confidence in the mineral industry.

3. Principles of JORC

The JORC Code is governed by three Principles, those of Transparency, Materiality and Competence (Fig. 1):

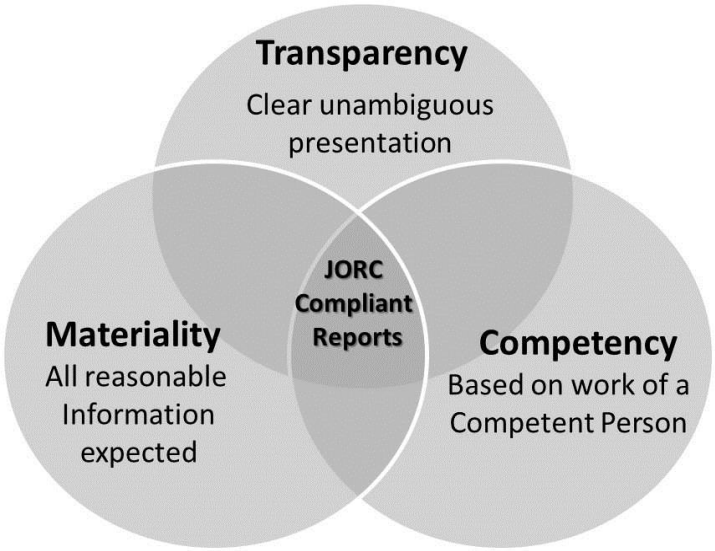

Figure 1 - Principles governing the application of JORC Code (Hunt, 2013).

Transparency (*Διαφάνεια*): the reader of a Public Report is provided with sufficient information, the presentation of which is clear and unambiguous, to understand the report and not be misled by this information or by omission of material information that is known to the Competent Person.

Materiality (***Σχετική Σημασία***): requires that a Public Report contains all the relevant information that investors and their professional advisers would reasonably require, and reasonably expect to find in the report, for the purpose of making a reasoned and balanced judgement regarding the Exploration Results, Mineral Resources or Ore Reserves being reported. Where relevant information is not supplied an explanation must be provided to justify its exclusion.

Competence (***Ικανότητα***): requires that the Public Report be based on work that is the responsibility of suitably qualified and experienced persons who are subject to an enforceable professional code of ethics (the Competent Person).

The wording of these definitions is almost similar within the PERC 2013 Code, with minor differences in the definition of Transparency (Table 1). Additionally, the PERC Code includes additionally in the principles section the Impartiality, according to which the Competent Person's work is not unduly influenced by the Organization commissioning the Report.

4. Competent Person

The JORC 2012 definition for Competent Person (**Αρμόδιος - *με την έννοια του Ικανού* - Μελετητής**) states: "A '**Competent Person**' is a minerals industry professional who is a Member or Fellow of The Australasian Institute of Mining and Metallurgy, or of the Australian Institute of

Geoscientists, or of a 'Recognised Professional Organisation' (RPO), as included in a list available on the JORC and ASX websites. These organisations have enforceable disciplinary processes including the powers to suspend or expel a member. A Competent Person must have a minimum of five years relevant experience in the style of mineralisation or type of deposit under consideration and in the activity which that person is undertaking".

Table 1 - Comparison between JORC (2012) and PERC (2013).

JORC	PERC
Three Principles: Transparency, Materiality, Competence	• Four Principles: Transparency, Materiality, Competence, Impartiality Note: Similar definitions apart for "Transparency", for which the part "…*to understand the report and not be misled by this information or by omission of material information that is known to the Competent Person*" is omitted.
Terminology: Exploration Results, Mineral Resources, Ore Reserves	Terminology: Exploration Results, Mineral Resources, Mineral Reserves
Table of Assessment and Reporting Criteria is enforced to be reported on "if not, why not" basis.	"The authors of reports should both identify and evaluate these important factors in their reports" / it is not necessary… to comment on each item of Table 1"
Prohibited to add financial value to "*in situ*" estimates	

Recognised Professional Organizations (RPO) from Europe include the National Associations which constitute the European Federation of Geologists (EFG, http://www.eurogeologists.de), however not all the members of EFG are recognized. Only members entitled to the professional tittle EurGeol, belonging to member associations of the EFG are recognised as fulfilling the requirements for recognition as members of a RPO (PERC, 2013). At this stage from Greece the member of EFG is the Association of Greek Geologists (www.geologist.gr), but it seems that this membership is not recognised.

The current legislative tool in Greece for reporting of mineral resources and ore reserves, as well as for defining responsibilities between geologists and mining engineers is still the Mining Code 210/1973, with some modifications during the last 30 years. The new Act for Mining and Quarrying Activities (AMQA, 2001) intends to modernize Greek legislation regarding also the studies required to establish mining activities; however there are no provisions for reporting competencies. If Greece is going to adopt a modern reporting code, modification of the legislation might be necessary or even a re-consideration of the Professional Organizations/Chambers of the Mining Professionals, i.e. the establishment of a forum that can host both Geologists, who know are associated in GEOTEE (GeoTechnical Chamber of Greece) and Mining Engineers, who are now associated in TEE (Technical Chamber of Greece), dealing with the Resource and Mining industry.

5. Reporting Terminology

The JORC Code defines the terminology that must be used when reporting Exploration Results (Αποτελέσματα Κοιτασματολογικής Έρευνας), Mineral Resources (Γεωλογικά Αποθέματα) and Ore Reserves (Οικονομοτεχνικά Απολήψιμα Αποθέματα) (JORC, 2012; Fig. 2).

The main objective of the definitions is to distinguish between the different levels of knowledge and confidence in the geological characteristics of the deposits, as well as in the "Modifying Factors", which drive the transition of a Mineral Resource to Ore Reserve.

Exploration Results refer to information commonly reported on early stages of exploration when the available data is not sufficient to allow for reasonable estimates of a Mineral Resource. As the exploration program proceeds and the gathered data, both structural and quality, starts satisfying the requirement for reasonable prospects for eventual economic extraction, the occurrence of the material can be defined as **Mineral Resource** and classified according to the three categories of Inferred (*Υποθετικό*), Indicated (*Ενδεικτικό*) and Measured (*Μετρηθέν*), according to the level of geological confidence. The intention of the Code is that geological confidence should not be a matter of qualitative stochastic approaches but rather an outcome of auditable scientifically-solid geological procedures and methods, suitably reviewed by the Competent Person using their experience in the commodity and style of mineralisation. Tools that are available to the Competent Persons include published guides for a specific commodity, e.g. the Australian Guidelines for Estimating and Reporting of Inventory Coal, Coal Resources and Coal Reserves (2003), geostatistical studies, etc, as well as a quite comprehensive checklist of Assessment and Reporting Criteria, listed within the JORC Code.

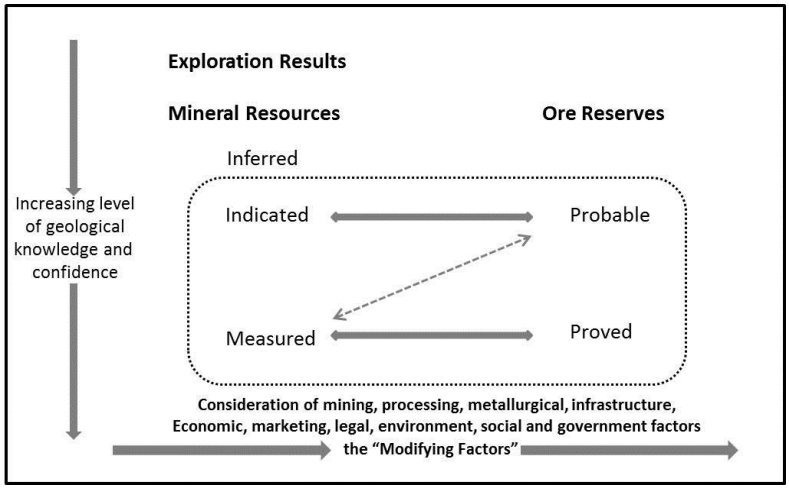

Figure 2 - General relationship between Exploration Results, Mineral Resources and Ore Reserves (according to JORC 2012).

By continuing the exploration program and most significantly by applying the "Modifying Factors" a portion of the Mineral Resource (only the Indicated or Measured) can eventually be assigned as **Ore Reserve** (Mineral Reserve according to the PERC 2013, Table 1), and classified as Probable (*Πιθανό*) or Proved (B*εβαιωμένο*). '**Modifying Factors**' are considerations used to convert Mineral Resources to Ore Reserves. These include, but are not restricted to, mining, processing, metallurgical, infrastructure, economic, marketing, legal, environmental, social and governmental factors (JORC, 2012).

6. Assessment and Reporting Criteria

The JORC Code includes a checklist for use when preparing Public Reports. This checklist is compulsory to be reported on an "*if not why not*" basis for initial or materially changed estimates, which means that the Competent Person must discuss all the aspects described in the JORC Checklist, and if for some of these Sections there are no data, the reason and possible impact should be mentioned. This is in contrast to the PERC Code, according to which it is not necessary to comment on every aspect (Table 1). Sections that are prescribed under the JORC Code include:

- Sampling Techniques and Data: e.g. information on drilling techniques, data spacing and distribution, logging, sub-sampling, quality assays, etc.
- Reporting of Exploration Results: e.g. information on tenements, previous exploration surveys, general geology and further work.
- Estimation and Reporting of Mineral Resources: e.g. information on database integrity, geological interpretations, estimation and modelling techniques, cut-off parameters, metallurgical and environmental factors and assumptions and classifications.
- Estimation and Reporting of Ore Reserves: e.g. information on mineral resource estimate for conversion to ore reserve, site visits of the Competent Person, cut-off parameters, mining factors or assumptions, infrastructure, costs, revenue factors, market, social and economic assessments.

It is noteworthy to mention that the Code emphasizes as best industry practise to have audits or reviews of the Mineral Resources and Ore Reserves estimates.

7. Implementing the revised JORC Code

The implementation of reporting systems like the JORC and PERC imposes reasonable barriers on the language that is used to describe Exploration Results, Resources and Reserves. Some examples are described below (Stoker and Berry, 2013).

Terms like “geological reserve”, “exploration resources”, “mining inventories” etc. are not permitted; Total Mineral Resources or Total Ore Reserves are also not permitted, unless they are also reported under their sub-classification according to Figure 2.

Certain provisions are in place so that the terms “tonnage” and “average grades” cannot be used unless specific cautionary statements are included when reporting Exploration Targets.

It is prohibited to introduce financial values to any “*in situ*” or “in ground” estimations, since no “Modifying Factors” are taken into consideration. Mineral Resources and Ore Reserves must not be reported in terms of “metal/mineral concentration” unless the corresponding “tonnage” and “grades” are also reported.

Additional requirements are imposed for the technical and economic studies that are required, e.g. Scoping Studies for reporting Mineral Resources at an early stage, Pre- and Feasibility Studies for reporting Ore Reserves.

8. Conclusions

During the last 2-3 years there has been an increased interest, both internationally and domestically, for investments in Greek resources. Exploitation opportunities for oil, gas, coal, metals and industrial minerals are in the news daily with comments and estimates from a variety of parties, including Industry Professionals, Academics and Journalists.

Although, it is difficult to regulate the partial information that the Journalists usually communicate in various media, it is important to regulate the information that the Companies, Professional Organizations and Individuals are releasing in order to have an adequately informed investment Community, as well as Public Opinion and Authorities. This regulated framework will allow for reasonable assumptions and cost-effective decisions to be made.

Academics and Industry Professionals, along with the respective Chambers in Geology and Mining Engineering disciplines, should work together towards establishing or adopting best industry practice tools and legislations, like PERC/JORC, which will promote the professional engagement, as well as add value to the domestic resource industry.

9. Acknowledgments

Mark Berry from AMC Consultants, Brisbane, is acknowledged for valuable discussions on the revision of the JORC Code. I would also like to thank Peter Stoker from AMC Consultants, Brisbane, Australia, Professor Kimon Christanis from Department of Geology, University of Patras, Greece, and Adam Steward from Integral Resource Consulting Pty Ltd, Brisbane, Australia, for their critical recommendations, during the preparation of this manuscript.

10. References

Act for Mining and Quarrying Activities, AMQA, 2011. ΚΛΜΕ, Κανονισμός Μεταλλευτικών και Λατομικών Εργασιών), ΦΕΚ 1227-14/06/2011, Available online at: **www.sme.gr** (in greek).

Australian Guidelines for Estimating and Reporting of Inventory Coal, Coal Resources and Coal Reserves, 2003. Coalfields Geology Council of New South Wales and the Queensland Mining Council, 8pp. Available online at: www.resources.nsw.gov.au.

Australian Securities Exchange (ASX), 2013. ASX Listing Rules, Chapter 5: Additional reporting on mining and exploration activities. Available online at: http://www.asxgroup.com.au/media/PDFs/Chapter05.pdf, 6pp.

Canadian Institute of Mining Metallurgy and Petroleum (CIM), 2011. CIM Standing Committee of Reserves Definitions, available online at: http://web.cim.org/standards.

Committee for Mineral Reserves International Reporting Standards (CRIRSCO), 2013. CRIRSCO International reporting template for exploration results, mineral resources and mineral reserves. Available online at: http://www.crirsco.com/template.asp.

Goddard I. 2013. The JORC Code's international reach and cooperation on Resource and Reserve Reporting through CRIRSCO, *The AusIMM Bulletin*, 3, 36-37.

Hunt S. 2013. Changed compliance requirements in the 2012 JORC Code. Available online at: http://www.asxgroup.com.au/media/PDFs/01-asx-resources-reporting-jorc-presentation.pdf.

Joint Ore Reserves Committee Code (JORC), 2012. Australasian Code for reporting of Exploration Results, Mineral Resources and Ore Reserves. Available online at: http://www.jorc.org, (The Joint Ore Reserves Committee of The Australasian Institute of Mining and Metallurgy, Australian Institute of Geoscientists and Minerals Council of Australia).

Mining Code N210/03.05.1973. Μεταλλευτικός Κώδικας, Available online at: www.et.gr (in greek).

National Instrument 43-101, 2011. Standards of disclosure for mineral projects. Available online at: http://web.cim.org/standards/documents/Block484_Doc111.pdf, 44pp.

Pan-European Reserves & Resources Reporting Committee (PERC), 2013. Pan-European standard for reporting of exploration results, mineral resources and reserves. Available online at: http://www.vmine.net/perc., 61pp.

Simon J. 2003. Three Australian asset-price bubbles. Available online at: http://www.rba.gov.au/publications/confs/2003/simon.pdf.

Stoker P. and Berry M. 2013. The JORC Code – Understanding and complying with the CODE. AMC Consultants Pty Ltd, Brisbane, Australia, 82pp.

UNFC 2009. *United Nations Framework Classification for Fossil Energy and Mineral Reserves and Resources 2009,* ECE Energy Series, vol. 39, 20 pp.

Δελτίο της Ελληνικής Γεωλογικής Εταιρίας, τομ. XLVII , 2013
Πρακτικά 13ου Διεθνούς Συνεδρίου, Χανιά, Σεπτ. 2013

Bulletin of the Geological Society of Greece, vol. XLVII 2013
Proceedings of the 13th International Congress, Chania, Sept. 2013

MULTISTAGE ALTERATION, MINERALIZATION AND ORE–FORMING FLUID PROPERTIES AT THE VIPER (SAPPES) AU–CU–AG–TE OREBODY, W. THRACE, GREECE

Kilias S.P.[1], Naden, J.[2], Paktsevanoglou M.[1], Giampouras M.[1], Stavropoulou A.[1], Apeiranthiti D.[1], Mitsis I.[1], Koutles Th.[3], Michael K.[4] and Christidis C.[1]

[1]National and Kapodistrian University of Athens, Faculty of Geology and Geoenvironment, Department of Economic Geology and Geochemistry, Panepistimiopolis, Zographou, 157 84, Athens, Greece

[2]British Geological Survey, Nicker Hill Keyworth, Nottingham NG12 5GG, United Kingdom

[3]Thrace Minerals S.A. 74, Papadima Str., PC 69300, Sappes, Rodopi, Greece

[4]Institute of Geology and Mineral Exploration, Regional Branch of Eastern Macedonia and Thrace, Brokoumi 30, Xanthi 67100, Greece

Abstract

The mineralogy of ore and hydrothermal alteration of the high-sulfidation enargite–Au–Ag–Te Viper (Thrace) orebody, and fluid inclusions, were studied in drillcore samples. The hydrothermal system has evolved through several stages from pre-ore advanced argillic I+vuggy silica alteration, ore-stage advanced argillic II+vuggy silica alteration and silicification that has developed to argillic alteration (sericite)+silicification through pH increase, and a return to acid conditions as crosscutting post-ore advanced argillic alteration III+silicification. Ore is characterized by early barren pyrite I corroded by: (i) enargite–Au± complex Pb–Bi–Cu sulfosalts, tellurides and selenides, coexisting with euhedral quartz, and (ii) zoned pyrite II distinguished by anomalous concentrations of Au, Cu, As, Te, Bi, Pb, Se, within vuggy quartz. High-grade gold ore is also intergrown with late breccia-cementing and vein-type epithermal-like banded quartz+ pyrite. These alteration and mineralization observations are consistent with the changing composition, water fugacity, and density of an expanding column of metal-laden magmatic vapor, combined with changes in structural permeability. Part of the enargite—Au—quartz assemblages have been probably quenched from sulfosalt melt at high—temperatures (>575 ˚ C). End product of the enargite–sulfhide–silica crystallization sequence is the formation of high-grade epithermal quartz-gold colloform-banded ore during cooling and/or dilution/mixing down to ~200 ˚ C.
Key words: *high-sulfidation, sulfosalt melt, epithermal quartz, enargite.*

Περίληψη

Η ορυκτολογική σύσταση του μεταλλεύματος και των υδροθερμικών εξαλλοιώσεων, και ρευστά εγκλείσματα, του κοιτάσματος εναργίτη—Au—Ag—Te της Οχιάς (Viper), μελετήθηκαν σε δείγματα πυρήνων γεωτρήσεων. Το υδροθερμικό σύστημα ακολούθησε μία πορεία σταδιακής εξέλιξης από προγενέστερων του μεταλλεύματος προχω-

ρημένης αργιλικής εξαλλοίωσης(ΠΑΕ) Ι και σκωριώδους πυριτίωσης, ΠΑΕ ΙΙ+σκωριώδους πυριτίωσης, και πυριτίωσης που φιλοξενούν το μετάλλευμα, προς σερικιτική εξαλλοίωση+πυριτίωση μέσω αύξησης του pH, και επιστροφής στις όξινες συνθήκες σαν μεταγενέστερων του μεταλλεύματος ΠΑΕ ΙΙΙ+πυριτίωσης. Το μετάλλευμα χαρακτηρίζεται από σιδηροπυρίτη Ι που αντικαθίσταται από: (1)εναργίτη+Au±πολυσύνθετα θειοάλατα, τελλουρίδια και σεληνήδια των Pb–Bi–Cu, που συνυπάρχει με ιδιόμορφο χαλαζία, και (2) ζωνοειδή σιδηροπυρίτη που διακρίνεται από ανώμαλες συγκεντρώσεις Au, Cu, As, Te, Bi, Pb και Se, που φιλοξενούνται από κοιλότητες σκωριώδους χαλαζία. Υψηλές περιεκτικότητες σε χρυσόχαρακτηρίζουν επίσης τον ύστερο ταινιωτό χαλαζία+σιδηροπυρίτη επιθερμικού τύπου. Αυτές οι παρατηρήσεις συμφωνούν με μεταβολές χημικής σύστασης, πτητικότητας του νερού και πυκνότητας μίας στήλης επεκτεινόμενου μαγματικού ρευστού με υψηλό μεταλλικό δυναμικ, σε συνδυασμό με την περατότητα λόγω τεκτονισμού. Τα συσσωματώματα εναργίτη-Au-χαλαζία πιθανώς αποχωρίστηκαν, τουλάχιστον τμηματικά, από ένα θειούχο τήγμα σε υψηλές θερμοκρασίες (>575°C).Η πορεία κρυστάλλωσης εναργίτη-σουλφιδίων-χαλαζία, κατά τη διάρκεια της επέκτασης του μαγματικού ρευστού, έχει σαν τελικό παράγωγο την απόθεση χρυσοφόρου μεταλλεύματος που συνδέεται με επιθερμικό χαλαζία λόγω ψύξης και/ή αραίω-σης/ανάμειξης έως ~200°C
Λέξεις κλειδιά: *υψηλή σουλφιδίωση, σιδηροπυρίτης, εναργίτης, χημική ζώνωση*.

1. Introduction

The Viper orebody of the Sappes Gold Project (SGP), Sappes, Thrace–NE Greece (Figure 1), is a volcanic-hosted high-grade Au–Cu–Ag deposit that has a measured resource of 710 kt @ 22.2 g/t Au; 11.5 g/t Ag; 0.4 % Cu, and inferred resource of 1,109 kt@17.2 g/t Au; 8.8 g/t Ag; 0.3% Cu (Glory Re-sources, 2012). The economic mineralization at Viper forms a NW-trending, elongated, blind, flat-lying ~60 m thick orebody, and has estimated dimensions of 550 by 1310 m, at a depth of approximately 200–240 m below the current surface. Ore occurs as hydrothermally altered, multi-stage breccias, and disseminations in stockwork quartz-veinlets and vug-fillings. The SGP also comprises outcropping epithermal-style Au- and Te-rich mineralization at St Demetrios (<200 m from Viper) and St Barbara (2.5 km to south of Viper), plus a Cu-rich porphyry-style prospects at Koryfes Hill, (Michael, 2004; Voudouris, 2006; Voudouris et al., 2006). Porphyry and epithermal mineralization in the area has been dated at about 32 Ma (Ortelli et al., 2009). In this paper we present the first data derived from the Viper orebody and utilize hydrothermal alteration patterns, ore mineralization textures and fluid inclusion microthermometry to decipher its genesis.

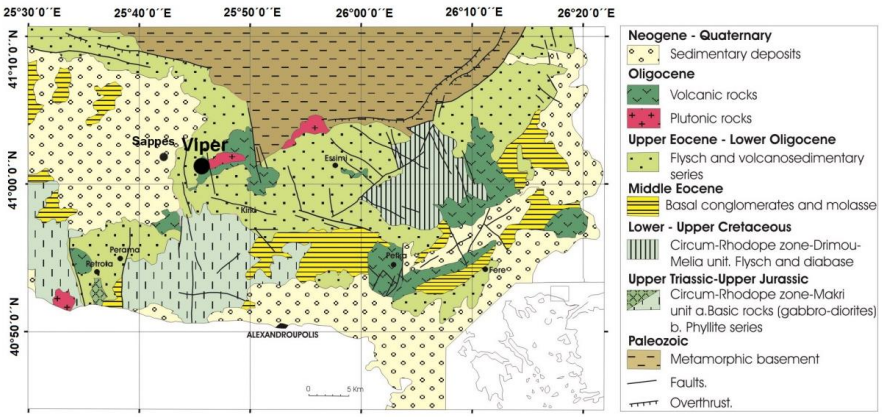

Figure 1 - Simplified geology of Western Thrace showing the location of Viper deposit (modified after Papadopoulos, 1982).

2. Geology and Mineralization

The geological structure of western Thrace consists of three units (Figure 1): a) Palaeozoic or older metamorphic basement (Marchev et al., 2005), b) the Jurassic to early Creataceous age Circum Rhodope Belt (Makri Unit) (Papadopoulos, 1982) and c) Late Eocene to Oligocene sedimentary and volcanosedimentary rocks and Oligocene–Miocene plutonic, subvolcanic and volcanic rocks (Voudouris et al., 2006). In the Sappes area (Figure 1), the Viper deposit is spatially associated with an Oligocene to Lower Miocene composite calc-alkaline to high-K calc-alkaline volcanic rocks (Figure 1), which in turn is linked to Middle to Upper Eocene volcaniclastic sedimentary sequences that discordantly overlying the Mesozoic Circum Rhodope metamorphic basement (Papadopoulos, 1982; Michael et al., 1995; Arikas and Voudouris, 1998; Michael, 2004; Voudouris et al., 2006; Voudouris, 2006). The volcanic rocks comprise a suite of calc-alkaline to high-K calc-alkaline andesites–dacites and dacite and rhyolite porphyries (Voudouris et al., 2006), and hydrothermally altered polymictic and mixed monomictic to polymictic volcanic breccias. Host rocks are dacitic–andesitic polymictic breccia units, and locally mixed monomictic to polymictic volcanic breccias. Bodies of equigranular to porphyritic mineralized microdiorite (Koryfes Hill) and quartz monzodiorite (~32 Ma, Voudouris, 2006) occur as small irregular stocks in the Sappes area. Later (<27 Ma, Voudouris, 2006) dacite and rhyolite porphyry dikes intruded the monzodioritic/dioritic rocks along N to NW regional fault zones. Surface expressions of porphyry-style (Koryfes Hill) and Te-rich epithermal style (St Demetrios, St. Barbara) mineralization have been reported in the Sappes area (Voudouris et al., 2006).

3. Materials and Methods

Samples were collected from drill core. The mineralogy of the ore and alteration assemblages was evaluated in the laboratories of the Department of Economic Geology and Geochemistry, Athens University, by polished thin section transmitted and reflected light petrography, powder X-ray diffraction (PXRD), scanning electron microscopy (SEM), and energy-dispersion spectrometry (EDS). Powder X-ray diffraction [Bruker Model D5005, CuKa radiation at 40kV and 40mA, using a 0.02° step size and 1 or 2 second per step counting time, graphite monochromator], was conducted on randomly oriented samples. The <2 μm fractions were separated by settling, dried on Si-wafers at room temperature and then were solvated with ethylene-glycol vapour at 65°C overnight for maximum saturation. Fluid inclusion microthermometry was undertaken on doubly polished plates (each ~0.15 mm thick), using a LINKAM THSM600 heating-freezing stage, also at Athens University. Calibrations were carried out using commercially available standards. The precision of measured temperatures is ±1.0° and ±0.3°C for heating and freezing, respectively.

4. Results

4.1. Hydrothermal Alteration

The superposition of at least 3 stages of hydrothermal alteration and mineralisation, which are strongly correlated with hydrothermal breccias and veinlets, namely pre-ore, ore and post-ore stages, have been identified.

4.1.1. Pre-Ore Stage I

Vuggy silica alteration: Vuggy silica I contains fine-grained (up to 0.5mm) jigsaw quartz. Vugs, which account for ~10 percent of the rock, have variable size and are commonly lined by chalcedonic quartz. *Advanced argillic alteration I*: Dominates the top of the preserved hydrothermal system above the Viper orebody. The alteration assemblage is quartz, pyrite, diaspore and pyrophyllite. Upward grading leads to alunite±dickite, kaolinite, fine grained pyrite and microcrystalline jigsaw quartz.

4.1.2. Ore-Stage IIa

Vuggy silica alteration: Vuggy silica consists of fine to medium-grained (500µm to 3mm) jigsaw quartz with serrated margins (Figure 2A). Cavities are sometimes filled by cockade quartz, with successive narrow and subparallel bands of crustiform quartz. *Advanced argillic alteration II:* This alteration (Figure 2B) is characterized by vug-filling clusters of coarse-grained minerals comprising assemblages of dickite/kaolinite–quartz–pyrite–aluminium-phosphate-sulfate minerals of the alunite supergroup (APS). Alunite grains are tabular to bladed and overgrown by the APS minerals woodhouseite, svanbergite and hinsdalite (Figure 2C). Dickite occurs as fine-grained masses intergrown with very fine grained quartz and alunite (Figure 2B).

4.1.3. Ore-stage IIb

Argillic (sericitic) alteration: Sericite occurs as rosettes in vugs within colloform quartz veinlets (Figure 2D). In addition, fine-grained flaky clusters of sericite enclose diaspore formed during pre-ore stage I advanced argillic alteration (Figure 2E). Sericite has also been observed by in sharp contact with dickite (Figure 2F). Crosscutting relationships and replacement textures constrain the timing of this alteration to postdate pre-ore advanced argillic alteration I. *Silicification:* This alteration is widespread and its principle feature is the development of colloform-banded quartz, exhibiting combined spherical, botryoidal, reniform and mammillary forms (Figure 2G,H) Silicification occurs along fractures, as vug fills and breccia cements).

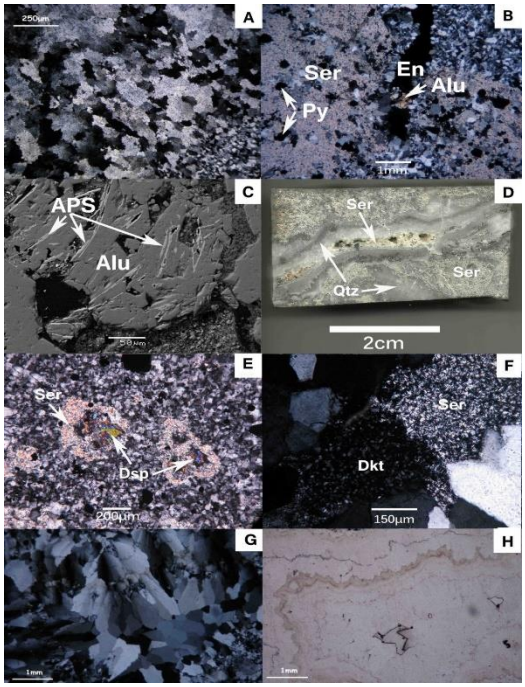

Figure 2 - Photomicrographs and a BSE image of the ore-stage hydrothermal alteration assemblages and textures. A. Vuggy silica consisting of medium-to fine-grained jigsaw quartz with serrated margins. Crossed polars. B. Elongated vug filled with advanced argillic alteration assemblages of tabular alunite crystals, enargite, mantled by microcrystalline jigsaw quartz, pyrite and sericite patches (argillic alteration). Crossed polars. C. 8Tabular alunite grains containing Sr-APS minerals (svanbergite). D. Colloform-banded quartz veinlet with sericite rossetes in vugs crosscutting argillic assemblage of patchy sericite+quartz. E. Diaspore crystals enclosed in flaky sericite patches. F Sericite in sharp contact with dickite. G. Colloform banded jigsaw/plumose quartz. H. Same as G in plain polarized light. Ser:Sericite, Py:Pyrite, Dck:Dickite, Alu:Alunite, Dsp:Diaspore, Qtz:Quartz.

4.1.4. Post-ore stage III

Advanced argillic alteration III: Generally, stage III advanced argillic alteration is restricted to quartz–alunite–pyrite containing veins, veinlets and cavity fillings that crosscut all previous alteration stages. Two varieties of alunite have been recognised: a) euhedral bladed and irregular coarse- to medium-grained needle-like crystals and b) pseudocubic alunite crystals. Dickite/kaolinite occurs as either dark extremely fine-grained masses or medium-grained clusters with recognizable flakes. *Silicification* Vug-filling amethystine quartz and barite represent the final alteration system of the Viper hydrothermal system. Barite crystals are frequently corroded and their size is variable. Amethystine quartz has plumose or jigsaw texture and is distinguished by a gradual increase of the grain size from the margins to the center of cavities.

4.2. Enargite-Gold and Gold Ore Mineralization

Ore mineralogy at Viper is dominated by sulfosalt–sulfide–Au assemblages intimately associated with ore-stage II hydrothermal alteration. It is hosted by vuggy silica and Au-bearing pyrite in colloform-banded quartz II. Ore is characterized by early barren pyrite I followed and replaced by: (i) enargite±chalcopyrite±galena±Au±complex Pb–Bi–Cu sulfosalts, tellurides and selenides (Figure 3A,B,C) and, (ii) zoned pyrite II which is distinguished by anomalous concentrations of Au, Ag, Cu, As, Te, Bi, Pb and Se (Figure 3D). Moreover, high-grade gold ore with pyrite, in which enargite is absent, is intergrown with Stage IIb colloform-banded quartz (Figure 3E). The deepest high-grade samples (~350 m) along discovery drillhole DV36 contain vapor-rich inclusion laden euhedral quartz I crystals within enargite that corrodes earlier pyrite I. Pyrite I is subhedral to anhedral, fractured, infilled, and strongly corroded. It generally has a porous texture, perhaps due to leaching. Enargite textures contain distinct domains of symplectic enargite−chalcopyrite intergrowths similar to those observed in quenched experimental sulfide melts (Figure 3F). Rarely, pyrite II crystals are mantled by pyrite I. Pyrite II contains three types of growth zones: (1) As-rich zones that are enriched in Cu±Bi±Sb±Te±Se±Pb─bearing sulfide/sulfosalt mineral inclusions (Figure 4), (2) As- poor, inclusion-free, zones with significantly lower or absent concentrations of these elements (Figure 4) and, (3) growth zones outlined by micro-vugs that locally host native gold grains (Figure 3D). Micron-sized gold at Viper occurs as: (i) inclusions of native gold in pyrite I, (ii) native gold intergrown with enargite, alunite and APS minerals (Figure 3B), or as vug infillings associated with complex Pb–Bi–Cu sulfosalts, tellurides and selenides, and rarely sphalerite, (iii) native gold decorating "vuggy" growth zones in pyrite II (Figure 3D), and (iv) intergrown with epithermal (*sensu stricto*, Bodnar et al., 1985) colloform-banded quartz II (Figure 3E), and (v) sub-micron to micron-sized inclusions or chemically held gold within, pyrite II and enargite (*unpublished data*). Native gold may contain up to 9 wt% Ag.

4.2. Fluid Inclusion Data

4.2.1. Samples and Methodology

Analyses of primary fluid inclusions focused on ore-stage IIb and post-ore stage III euhedral epithermal quartz II (*sensu stricto*; Bodnar et al., 1985). Twenty-five (25) doubly polished thick sections (~150 μm thick) and chips sampled with the use of a microcorer sampler, were prepared from eighty-five (85) drillcore high-grade (11–63.4 g/t) intersection samples; the samples are from the discovery boreholes DV36A, DV42 and SD8, and cover about 90 m, 10 m and 3 m of drillcore, respectively. Salinities have not been corrected for the potential of dissolved CO_2 on freezing point depression.

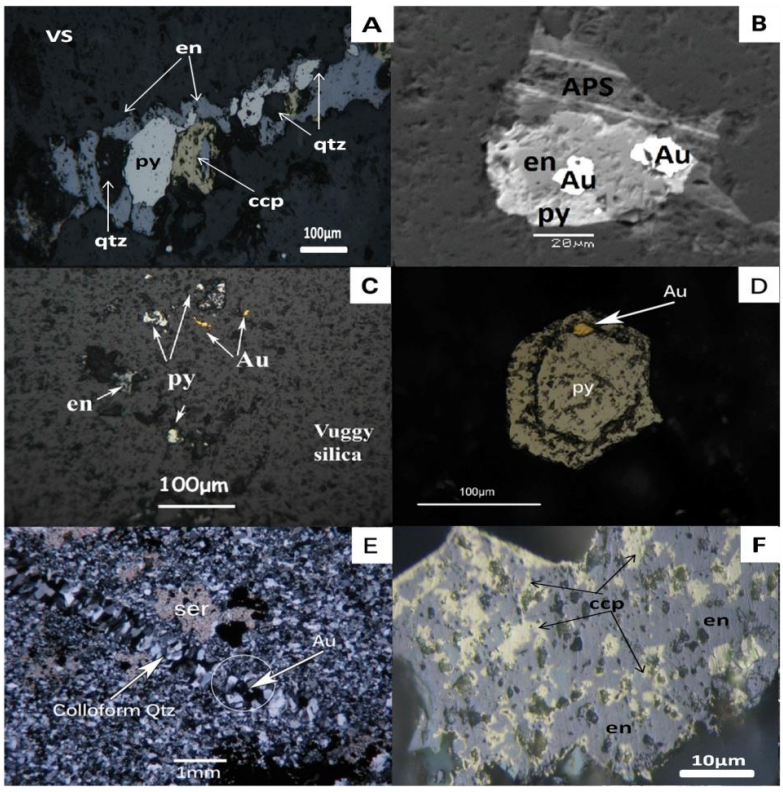

Figure 3 - A. Dissolution of early pyrite I by enargite (En) and chalcopyrite (Ccp) with euhedral quartz (Qz) infilling void spaces within "vuggy" silica. B. BSE image of native gold intergrown with enargite,alunite and APS minerals, showing Ca-Sr-Pb-rich bands, in vug. C. Vuggy quartz infilling by native gold, enargite and pyrite I. D. Native gold on a pyrite II growth zone E. Native gold intergrown with colloform-banded quartz crosscutting argillic alteration. F. Symplectic enargite-chalcopyrite intergrowths resembling quenched experimental sulfide melts (en: enargite, py: pyrite, ccp: chalcopyrite, qtz: quartz, VS: vuggy silica, Au: gold, APS: aluminum-phosphate-sulfate minerals, ser: sericite).

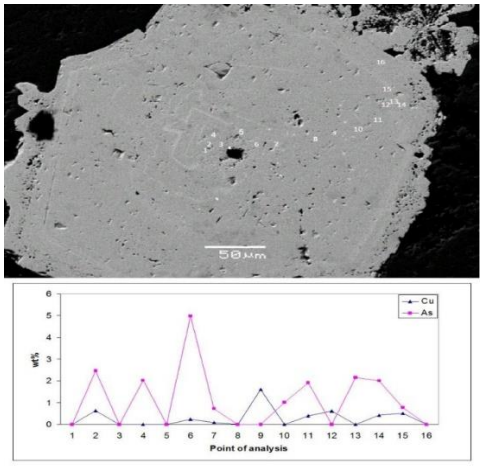

Figure 4 - Top: BSE image of a coarse-grained, trace element-rich ore-stage zoned pyrite II, showing oscillatory zoning: 'bright' zones in BSE are enriched with As and/or Cu. Bottom: Element profile across the pyrite grain in "top". Points of analysis refer to numbers in "top".

4.2.2. Fluid Inclusion Types

Two types of primary fluid inclusions were identified: Type 1 includes two-phase, liquid-rich (10−45% vapor) fluid inclusions, and Type 2 fluid inclusions are vapor-rich (>80% vapor), two phase inclusions. Primary inclusions occur as isolated, randomly distributed inclusions, or in crystal growth zones. The majority of measured inclusions ranged between 20μm and 30μm. Inclusion shapes are variable including rounded, angular and equant or negative crystal shapes. Fluid inclusion assemblages (FIA's) defined by coexisting, type 1 and 2 inclusions were observed in quartz throughout the drillcore depth range studied. Type 1 inclusions with consistent liquid-to-vapor ratios decorate growth zones of post-ore stage III quartz. We did observe single-phase, liquid-filled inclusions coexisting with vapor-filled inclusions in ore-stage IIb samples, which suggest that vapor-rich inclusions were formed by vapor-phase trapping rather than necking (Bodnar et al., 1985). Liquid CO_2 or CH_4 were not observed or detected during freezing runs.

4.2.3. Microthermometry

Data were obtained only from type 1 inclusions, because phase changes in type 2 inclusions proved difficult to observe and accurately record. Microthermometric measurements of Type 1 inclusions show liquid Th that range from 140°C to 270°C and $T_{m\text{-}ice}$ between –0.9 and –3.3°C, corresponding to salinities between 1 and 6 wt% NaCl equiv, which fall within typical ranges for this variety of epithermal gold deposit (e.g. Simmons et al., 2005) (Figure 7). First melting temperatures range from –20.4 to –34.1°C and are consistent with H_2O–NaCl (±KCl±$MgCl_2$) salt solutions (Bodnar et al., 1985). Microthermometric data show trends of decreasing T_h and salinity from the ore-stage IIb quartz to the post-ore stage III quartz.

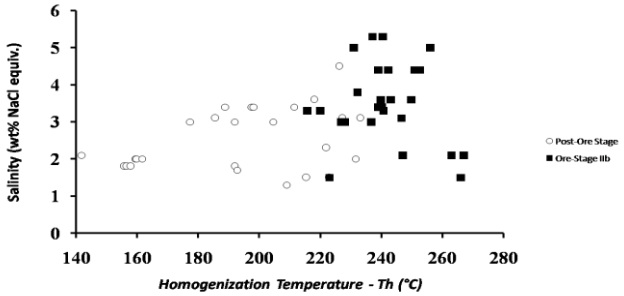

Figure 5 - Th-salinity diagram showing the evolution of hydrothermal fluids at Viper deposit. The trend is consistent with mixing and/or boiling.

5. Discussion – Concluding Remarks

The Viper Au–Ag–Cu–Te orebody is one of several Tertiary volcanic-hosted precious and base metal Te-rich deposits on the margins of the eastern Greek Rhodope, which are considered to reflect formation in a porphyry−epithermal environment (Voudouris 2006; 2010, Voudouris et al., 2011). While alike in many features to typical high-sulfidation epithermal deposits (e.g. Hedenquist et al., 2000; Simmons et al., 2005), Viper differs from other deposits of this type most notably because it is characterized by multistage evolution involving early magmatic and later epitherma" (*sensu stricto*; Bodnar et al., 1985) ore stages.

5.1. Multistage Hydrothermal System

High-sulfidation gold deposits are commonly characterized by a pre-sulfide vuggy residual quartz−alunite±pyrophyllite advanced alteration envelope, and a subsequent contrasting sequence of ore-stage sulfide assemblages typically including pyrite, that progresses through a range of

sulfosalt minerals (i.e. enargite and tennantite), to later sulfosalt, sulfide and telluride minerals, Au, nd Ag; this progression is tightly constrained by syn-hydrothermal brittle faulting and/or brecciation (Berger and Henley, 2011; Henley and Berger 2011). The mineral relationships shown in Figures 2 and 3 illustrate a complex rapidly evolving sulfate–sulfide–sulfosalt–silica depositional setting at Viper, and the apparent superposition of recurring events of advanced argillic alteration. The earliest stage (Stage I), which is unrelated to the ore, involved pervasive quartz+alunite+pyrite±dickite/kaolinite that graded downwards to pyrophyllite–quartz–pyrite±diaspore. This, when combined with associated sulfosalt-sulfide free vuggy quartz textures, is strongly indicative of early extremely acid (pH<2) fluids (Stoffregen, 1987). A second stage of advanced argillic alteration (dickite−quartz−pyrite−APS minerals−alunite) (Stage IIa), followed by a stage of argillic alteration (quartz−sericite) (Stage IIb) which in turn was suceeded by colloform-banded quartz, indicate that pH temporarily evolved to higher values (~ 6), as a result of dilution, **or** the interaction of the fluid with the rock at progressively lower fluid/rock ratios and decreasing temperature (Chouinard et al., 2005; Scher et al., 2013). A third stage of vein-type crosscutting advanced argillic alteration (quartz–alunite–pyrite) (Stage III) indicates a return to acidic conditions. Late-stage silicification (quartz–barite) (Stage III) characterized by amethystine quartz and barite mark the waning stages of the hydrothermal activity.

5.2. Ore Forming Processes A: the Magmatic Connection

In the light of: (i) euhedral quartz crystals wholly enclosed within veinlets and cavities with enargite that dissolves early pyrite I (Figure 3A,B), (ii) asymmetrical zonation of arsenic (±Cu, Te, Sb) in pyrite II around earlier leached pyrite±quartz (Figure 4), and, (iii) symplectic enargite−chalcopyrite textures that resemble quenched melts (e.g. Tomkins, 2010) (Figure 3F), (iv) vapor-rich fluid inclusions in quartz within enargite, we suggest that sulfosalt crystallization within vugs and veinlets from a composite vapor−saturated Fe-Cu-As-Sb-S (±Si, P, Pb, Ca, Te, Au, Ag, Se, Bi) sulfosalt melt at high temperatures; the perfect hexagonal morphology of quartz crystals in our samples suggests, but does not prove deposition temperatures in the β-quartz field (>575°C) (Mavrogenes et al., 2010; Henley and Berger, 2011; Henley et al., 2012). Furthermore, the pyrite to enargite reaction characterizes high-sulfidation lode copper–gold deposits worldwide (i.e. El Indio [Chile], Lepanto [Philippines], Summitville [USA], Red Mountain [USA]; Berger and Henley 2011), and may suggest sulfide-sulfate deposition via solidification of a sulfosalt melt that condensed from an expanding magmatic vapor phase at high-temperatures (>600°C) and near lithostatic pressures, in a non-equilibrium chemical environment, following higher temperature deposition of crystalline pyrite. Our data support such a model for the formation of least part of the enargite and pyrite II–gold (±Ag±Sb±Pb±Te±Se) mineralization at Viper. A vapor rich environment at Viper is also supported by the abundance of vapor-rich inclusions in lower-temperature auriferous "epithermal" quartz (*sensu stricto*; Bodnar et al., 1985), and confirms a wide range of temperatures and temperature gradients during development of the ore. The involvement of magmatic vapor is further supported by oscillatory zonation patterns in pyrite II adjacent to pyrite I and quartz I contacts (Deditius, 2009; Mavrogenes et al., 2010).

5.3. Ore-forming Processes B: the Epithermal Connection

Temperature–pressure profiling for HS gold deposits is burdened with problems (Berger & Henley 2011; Henley& Berger 2011). This is because, the characteristic silica−alunite assemblages of HS environments preserve local domains developed during cooling and recrystallization in the presence of acid condensate and groundwater, so that fluid inclusion data from crystalline quartz record only cooling history rather than primary events (Henley and Berger, 2012). Unlike most HS gold deposits, auriferous colloform−banded jigsaw, plumose, and crustiform quartz is ubiquitous throughout the Viper orebody (Figure 3E). Our fluid inclusion data stemming from this epithermal quartz indicate boiling of a low-salinity fluid during ore-stage IIb breccia formation because: (i) vapor- and liquid-rich inclusions coexist in boiling fluid inclusion assemblages (ii) decreasing T_h and salinity trends possibly the result of boiling (e.g. Bodnar et al., 1985) (Figure 5); boiling in

this case would result in competing effects of increased salinity, and decreased apparent salinity due to CO_2 degassing in the residual fluid (Hedenquist and Henley, 1985), (iii) gangue silica textural evidence for colloform-banded quartz (Figure 2G,H) indicating rapid temperature/pressure drop that leads to oversaturation and rapid deposition, such as might occur during boiling (Bodnar et al., 1985). Conversely, the trend shown in figure 5 could be the result of mixing of low (~0–2 wt % NaCl equiv) and moderate-salinity (~10 wt% NaCl equiv) fluids (Hedenquist and Henley, 1985). At Viper, fluid inclusion data (Figure 5) indicate that formation temperature was higher in the epithermal ore-stage IIb quartz (270–220°C), and decreased through the post-ore stage III quartz from ~230–160°C.

5.4. Environment and Conditions of Ore Deposition

We interpret enargite–Au–Ag–Te ore deposition at Viper to have occurred by two main processes that contributed to the high-grade and complex nature of the deposit. First, solidification of a Fe–Cu–As–Sb–S (±Pb, Zn, Si, P, Ca, Sr, Te, Se, Au, Ag, Bi) sulfosalt melt condensed from an expanding magmatic vapor phase at high temperatures (>575°C) and near lithostatic pressures (Mavrogenes et al., 2010; Henley and Berger, 2011). Second, boiling and/or mixing, and mixing-induced cooling, which is most effective at depositing quartz (Simmons et al., 2005), produced the ubiquitous auriferous silica phase at Viper. This epithermal quartz-flooding may represent the end-product of the sulfosalt−sulfide crystallization sequence within an expanding plume of magmatic vapor, the spatial control of which has been effected by active fracturing and brecciation (Henley and Berger, 2011). The epithermal silica at Viper is highly probably recrystallized and homogenization temperatures data record trapping and gold–quartz II deposition during cooling from >500°C the primary deposition temperature of the quartz I and enargite−gold assemblage (Mavrogenes et al., 2010; Henley and Berger, 2011), through stage II temperatures of 270–220°C, to the waning stages of post-ore assemblages at 230–160°C. Thus, the Viper orebody was formed by evolving magmatic to hydrothermal−epithermal processes that took place in multistage sequences of advanced argillic, vuggy silica, and argillic alteration and silicification, either earlier than, contemporaneous with or later than ore. The complexity of the Viper system is a cumulative consequence of the chemical evolution within an expanding column of ore-forming magmatic vapor, in combination with changes in structural permeability (i.e. multistage hydrothermal brecciation) due to the coupling of alteration and fracture dynamics (Henley and Berger, 2011; Berger and Henley, 2011).

6. Acknowledgments

Funding by the Special Account for Research Grants of the National and Kapodistrian University of Athens to SPK is gratefully acknowledged. JN publishes with the permission of the Director of the British Geological Survey.

7. References

Arikas K. and Voudouris P. 1998. Hydrothermal alterations and mineralizations of magmatic rocks in the southern Rhodope Massif, *Acta Vulcanol*, 10, 353–365.

Berger B.R. and Henley R.W. 2011. Magmatic-vapor expansion and the formation of high-sulfidation gold deposits: Structural controls on hydrothermal alteration and ore mineralization, *Ore Geology Reviews*, 39(1), 75-90.

Bodnar R.J., Reynolds T.J. and Kuehn C.A. 1985. Fluid-inclusion systematics in epithermal systems, *Reviews in Economic Geology*, 2, 73−97.

Chouinard A., Williams-Jones A. E., Leonardson R.W., Hodgson C.J., Silva P., Téllez C. and Rojas F. 2005. Geology and genesis of the multistage high-sulfidation epithermal Pascua Au-Ag-Cu deposit, Chile and Argentina, *Economic Geology*, 100(3), 463-490.

Deditius A., Utsunomiya S., Ewing R., Chryssoulis S., Venter D. and Kesler S. 2009. Decoupled geochemical behavior of As and Cu in hydrothermal systems, *Geological Society of America*, 37, 707-710.

Glory Resources 2012 website (http://www.gloryresources.com.au/projects/sapes-gold-project/)

Hedenquist J. W. and Henley R. W. 1985. The importance of CO 2 on freezing point measurements of fluid inclusions; evidence from active geothermal systems and implications for epithermal ore deposition, *Economic geology*, 80(5), 1379-1406.

Henley R. W. and Berger B.R. 2011. Magmatic-vapor expansion and the formation of high-sulfidation gold deposits: Chemical controls on alteration and mineralization, *Ore Geology Reviews*, *39*(1), 63-74.

Henley R. W. and Berger B.R. 2012. Pyrite–sulfosalt reactions and semimetal fractionation in the Chinkuashih, Taiwan, copper–gold deposit: a 1 Ma paleo-fumarole, *Geofluids*, *12*(3), 245-260.

Henley R. W., Mavrogenes J. and Tanner D. (2012). Sulfosalt melts and heavy metal (As-Sb-Bi-Sn-Pb-Tl) fractionation during volcanic gas expansion: the El Indio (Chile) paleo-fumarole, *Geofluids*, *12*(3), 199-215.

Marchev P., Kaiser-Rohrmeier M., Heinrich C., Ovtcharova M., von Quadt A. and Raicheva R. 2005. Hydrothermal ore deposits related to post-orogenic extensional magmatism and core complex formation: The Rhodope Massif of Bulgaria and Greece, *Ore Geology Reviews*, 27, 53-89

Mavrogenes J., Henley R. W., Reyes A. G. and Berger B. 2010. Sulfosalt melts: Evidence of high-temperature vapor transport of metals in the formation of high-sulfidation lode gold deposits, *Economic Geology*, 105(2), 257-262.

Michael C., Perdikatsis V., Dimou E. and Marantos I. 1995. Hydrothermal alteration and ore deposition in epithermal precious metal deposit of Agios Demetrios, Konos area, Northern Greece, *Bull. Geol. Soc. Greece*, sp. Publ., 4/2, 778-782.

Michael C. 2004. Epithermal systems and gold mineralization in western Thrace (North Greece), *Bull. Geol. Soc. Greece*, 36, 416-423.

Ortelli M., Moritz R., Voudouris P. and Spangenberg J. 2009. Tertiary porphyry and epithermal association of the Sapes-Kassiteres district, Eastern Rhodopes, Greece, In*: Proceedings of the 10th biennial SGA meeting*, Townsville, Australia, August 2009, Williams, P. et al (eds), 536-538.

Papadopoulos P. 1982. Geological Map of Greece, *Maronia sheet*, scale 1:50000, I.G.M.E., Athens.

Ring U., Glodny J., Will T. and Thomson S., 2010. The Hellenic Subduction System: High-Pressure Metamorphism, Exhumation, Normal Faulting, and Large-Scale Extension, *Annual Review of Earth and Planetary Sciences*, 38, 45-76.

Scher S., Williams-Jones A. E. and Williams-Jones G. 2013. Fumarolic Activity, Acid-Sulfate Alteration, and High Sulfidation Epithermal Precious Metal Mineralization in the Crater of Kawah Ijen Volcano, Java, Indonesia, *Economic Geology*, 108(5), 1099-1118.

Simmons S. F., White N. C. and John D. A. 2005. Geological characteristics of epithermal precious and base metal deposits, *Economic Geology*, 100th Anniversary Volume, 485-522.

Tomkins A. G. 2010. Wetting facilitates late-stage segregation of precious metal–enriched sulfosalt melt in magmatic sulfide systems, *Geology*, 38(10), 951-954.

Voudouris P. 2006. A comparative mineralogical study of Te-rich magmatic-hydrothermal systems in northeastern Greece, *Mineralogy and Petrology*, 87, 241-275.

Voudouris P., Tarkian M. and Arikas K. 2006. Mineralogy of telluride-bearing epithermal ores in the Kassiteres-Sappes area, western Thrace, Greece, *Mineralogy and Petrology*, *87*(1-2), 31-52.

Voudouris P. C. 2011. Conditions of formation of the Mavrokoryfi high-sulfidation epithermal Cu–Ag–Au–Te mineralization (Petrota Graben, NE Greece), *Mineralogy and Petrology*, *101*(1-2), 97-113.

Δελτίο της Ελληνικής Γεωλογικής Εταιρίας, τομ. XLVII , 2013
Πρακτικά 13ου Διεθνούς Συνεδρίου, Χανιά, Σεπτ. 2013

Bulletin of the Geological Society of Greece, vol. XLVII 2013
Proceedings of the 13th International Congress, Chania, Sept. 2013

QUANTITATIVE DETERMINATION OF MINERAL MATTER IN LIGNITE BY X-RAY SPECTROMETRY, USING THE COMPTON EFFECT

Perdikatsis V.

Technical University of Crete, Department of Mineral Resources Engineering, Chania, Greece, vperdikatsis@isc.tuc.gr

Abstract

For the evaluation of lignite quality, apart from the calorific value, it is necessary to determine the mineral phases, which are deposited simultaneously with the organic matter during the formation of peat or formed epigenetically during the coalification stages.
The mineral matter content is usually expressed as ash, after the combustion of lignite, and its determination is a quite time consuming process.
In this paper an attempt is made for a fast and easy quantitative determination of mineral matter in lignite samples with unknown concentrations, with the use of an X-ray spectrometer and in particular the Compton effect of the X-ray tube.
The intensity of the Compton peak is a function of the mass absorption coefficient of the lignite sample, which in turn depends on the type and amount of the mineral matter contained.
Using this property of the Compton Effect, the percentage of mineral matter of lignite was determined. The method was verified by analyzing lignites with known concentrations of inorganic mater.
The results of this study showed, that the mineral matter content can be determined, by the proposed method, fast and accurately without lignite combustion.
Key words: *Lignite, mineral matter, XRF, Compton Scattering.*

Περίληψη

Κατά την αξιολόγηση της ποιότητας των λιγνιτών εκτός από την θερμογόνο δύναμή τους γίνεται προσδιορισμός της ανόργανης ύλης, η οποία έχει εναποτεθεί συγγενετικά με την οργανική ύλη κατά τον σχηματισμό τους, αλλά και κατά το στάδιο της ενανθράκωσης. Ο προσδιορισμός της ανόργανης ύλης γίνεται συνήθως ως τέφρα μετά από καύση του λιγνίτη, διαδικασία η οποία είναι αρκετά χρονοβόρα.
Στην παρούσα εργασία γίνεται προσπάθεια για εύκολο και γρήγορο προσδιορισμό του ποσοστού της ανόργανης ύλης ή της τέφρας σε δείγματα λιγνιτών με άγνωστες συγκεντρώσεις, με φασματόμετρο ακτίνων-Χ. Ειδικότερα γίνεται χρήση του Φαινομένου Compton της λυχνίας ακτίνων-Χ του φασματόμετρου.
Η ένταση του Φαινομένου Compton είναι συνάρτηση του συντελεστή απορρόφησης μάζας, ο οποίος με τη σειρά του εξαρτάται από το είδος και το ποσοστό της ανόργανης ύλης που περιέχεται στον λιγνίτη.
Εκμεταλλευόμενοι την ιδιότητα αυτή του φαινομένου Compton, προσδιορίστηκε το ποσοστό της ανόργανης ύλης των λιγνιτών. Η ακρίβεια της μεθόδου που

χρησιμοποιήθηκε πιστοποιήθηκε με αναλύσεις δειγμάτων Ελληνικών λιγνιτών, με γνωστές περιεκτικότητες ανόργανου υλικού ή τέφρας.
Τα αποτελέσματα της εργασίας δείχνουν ότι, με την προτεινόμενη μέθοδο, μπορεί να προσδιοριστεί το ποσοστό του ανόργανου υλικού γρήγορα χωρίς την χρονοβόρα διαδικασία της καύσης του λιγνίτη.
Λέξεις κλειδιά: *Λιγνίτης, ανόργανη ύλη, XRF, σκέδαση Compton .*

1. Introduction

The quality of lignite, apart from the calorific value, depends strongly on the mineral matter, which is deposited simultaneously with the organic matter during the peat forming stage, but also epigenetically during the coalification stages. The mineral matter content is fundamental for the evaluation of coal quality for a variety of applications. The content of the mineral matter can also be used to evaluate the behavior of particular coals in utilization processes, including the processes that control the characteristics of fly ashes, slags and other combustion by-products.

"Mineral matter" is defined by Gary et al. (1972) as "the inorganic material in coal". More specifically is defined by Australian Standards (2000) as "the sum of the minerals and inorganic matter in and associated with coal". Similar definitions are provided by Harvey and Ruch (1986) and by Finkelman (1994).

The most common method for the determination of mineral matter content is the combustion of lignite, expressed as ash (ASTM 3174), a process which is quite time consuming. In Low Temperature Ashing (LTA) the organic matter is destroyed by an electronically-excited oxygen plasma at temperature of around 120^{o}C (Gluskoter, 1965). The oxygen is excited to ozone, which is passed around the sample and removes completely the organic matter. By LTA all the minerals of the inorganic matter are preserved more or less in their original state, which is very important, especially for the clay minerals, gypsum, sulfides, etc.

A comparative study of the different methods for the determination of mineral matter is given by Colin R. Ward (2002). Ritz and Klika (2010) determined mineral matter by recalculation of the bulk chemical analysis of lignite. Tickner and Roach (2004) determined the mineral matter content by a Compton profile analysis via XRF (X-ray Fluorescence). The apparatus used for the coal measurements comprised a 300 mCi (11.1 GBq) ^{241}Am source (producing 59.54 keV gamma-rays, with a weaker component at 26.34 keV) and a 36 · 10 mm germanium detector.

In the present paper the mineral matter content was determined using the Compton Peak by a commercial energy dispersive X-ray fluorescence spectrometer (EDXRS). Compton scattering is an inelastic scattering of a photon by an electron. It results in a decrease of the X-ray energy, called the Compton Effect. The amount of energy change is called the Compton shift which is expressed as the Compton peak, near the main peak of the X-ray tube.

The intensity of the Compton peak is inversely proportional to the mass absorption coefficient (μ, cm^2/gr), Reynolds (1963). Taking into account that the mass absorption coefficient increases with the Atomic Number of a chemical element, it is clear that it is mainly defined by the mineral mater and therefore a relationship between the Compton Intensity and the amount of mineral mater is expected. In Figure 1 the peaks of PdKα_1 and its Compton peak of a Pd X-ray tube are given. Due to higher mass absorption coefficient of the mixed sulfide sample, the Compton intensity is lower than the PdKα_1 intensity.

On the contrary in lignite, because of the low mass absorption coefficient, the Compton intensity is higher than the PdKα_1 intensity.

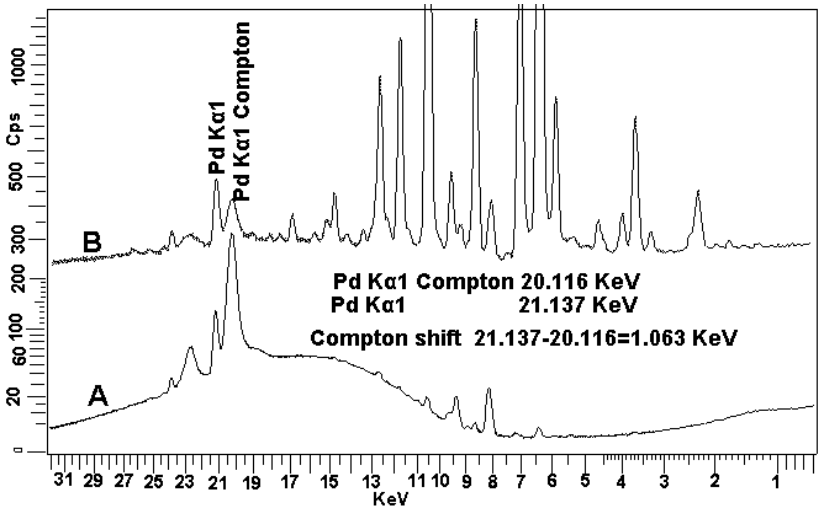

Figure 1 - X-spectra of a lignite (A) and a mixed sulfide ore (B) from a Pd X-ray tube.

2. Sampling and Experimental Methods

Five lignite samples with different content of mineral matter were selected from the Ptolemais basin, which is the main source of lignite fly ash produced in Greece. Each year approximately l0 millions tons of lignite fly ash are produced. Ptolemais lignite is of low quality, characterized by low calorific value and high mineral matter content (Koukouzas et al., 2006). The mineral matter and the calorific value of the analyzed samples are given in Table 1 and in Figure 2.

Table 1 - Mineral matter represented as ash wt-%, and the calorific value of the analyzed samples (air-dried).

Sample	Ash%	Cal. Value (kJ/Kg
Sector 6_1	17.28	4491
Sector 6_4	42.65	1547
Bunker 2	32.27	2947
Bunker 3	24.95	3775
Bunker 4	35.76	2584

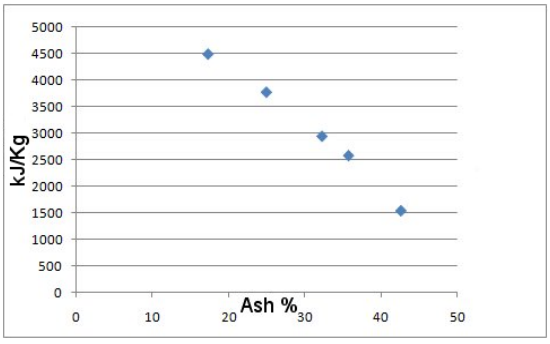

Figure 2 - Ash versus calorific value of the analyzed samples.

LTA was applied to isolate the mineral matter of the lignite samples. An energy dispersive X-ray fluorescence spectrometer (EDXRS), type S2 RANGER, BRUKER Company (Germany) was used with Pd X-ray tube. The operating conditions, for the X-ray tube, were 40 KV, high voltage and 250 μA.

The lignite samples were air dried and grinded to -60 μm and pressed to tablets of 40 mm diameter. The crystalline phase analysis of the crystalline matter, after the LTA, was carried out on a Bruker D8 Advance Diffractometer, using Ni-filtered Cu Kα radiation (35 kV, 35mA) with a Lynx Eye strip silicon detector. Data were collected from 3° to 70° 2θ with a step size of 0.019° and a count time of 1 sec per strip step. The diffractograms were qualitatively interpreted using the software Diffrac Plus from Bruker and the Powder Diffraction File (PDF). The quantitative analysis was performed by the Rietveld method, using the TOPAS software from BRUKER. In Table 2 the mineralogical composition of the mineral matter of the analyzed samples is given. A typical X-ray diffractogram is given in Figure 3.

Table 2 - Mineralogical composition of the analyzed samples after Low Temperature Ashing.

Sample	Aragonite %	Calcite %	Illite %	Pyrite %	Quartz %
Lignite 1 LTA	5.8	91.1	1	0.4	1.7
Bunker 3 LTA	8.3	84.9	3	0.2	3.6
Bunker 4 LTA	7.6	87	2.5	0.3	2.5
Bunker 2 LTA	7.6	88.8	2.5	0.2	0.9
Lignite 4 LTA	2.4	96.6	0.5	0	0.5

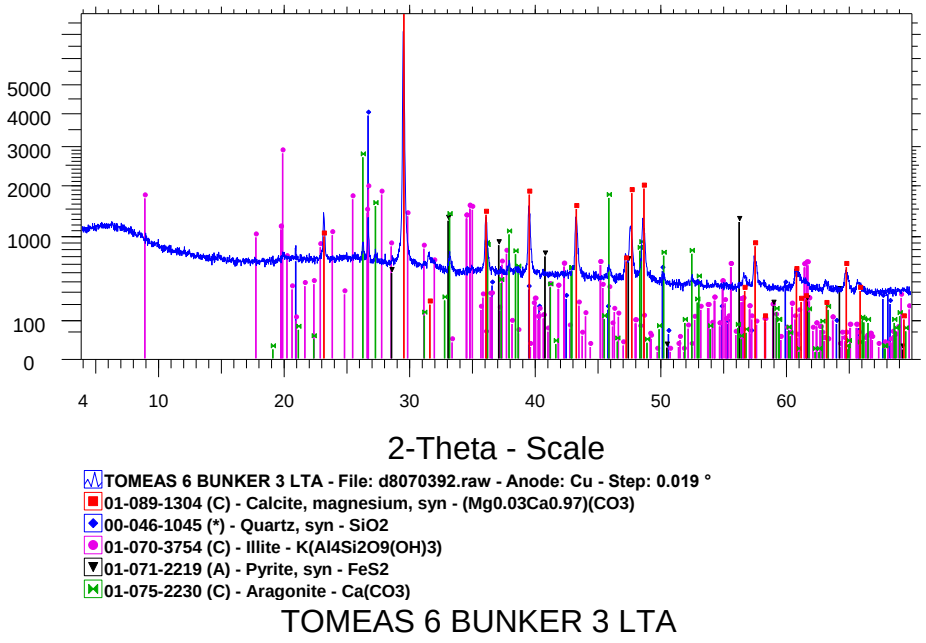

Figure 3 - X-Ray diffractogram after Low Temperature Ashing (LTA).

As mentioned before, the Compton peak intensity is reversely proportional to the mass absorption coefficient. To test this, synthetic standards were prepared with a xylite free of mineral matter (woody remnants) as matrix (Table 3).

The mass absorption coefficient was calculated for the energy of the Pd Kα Peak (21.137KeV→ λ = 0.5854 Å) according to the formula :

$\mu_\lambda = \sum_{i=1}^{n} \mu_{\lambda i} \text{ x } C_i$, where $\mu_{\lambda i}$ is the μ_λ for the compound i and C_i its concentration.

In Figure 4 the relation between concentration of mineral matter and μ of the standard samples is presented. It is expected, that the amount of $CaCO_3$ in the analyzed lignite samples determines the value of μ, since calcite is the main mineral. Figure 5 presents the relation between mineral matter of the synthetic samples and the Compton intensity. To avoid intensity shifts and instrumental recalibration, in Figure 6 the Ratio Compton Intensity to PdKα intensity is given, since this ratio is a constant number and independent from instrumental recalibration. According to these diagrams a clear relation is recognized between Compton intensity and mineral matter.

Table 3 - Bulk composition of synthetic standards using xylite as matrix.

Compound / Standard	K	L	M	N
SiO_2 %	20.96	15.72	10.48	5.24
Al_2O_3%	1.61	1.21	0.81	0.40
$CaCO_3$%	11.52	8.64	5.76	2.88
$CaSO_4$%	1.1	0.82	0.55	0.27
Fe_2O_3%	1.61	1.21	0.81	0.40
MgO%	0.64	0.48	0.32	0.16
KCl%	2.55	1.91	1.27	0.64
Xylite%	60	70	80	90
Sum	100	100	100	100
μ(cm^2/gr)	1.588	1.243	0.898	0.554
1/μ(gr/cm^2)	0.629	0.804	1.113	1.806

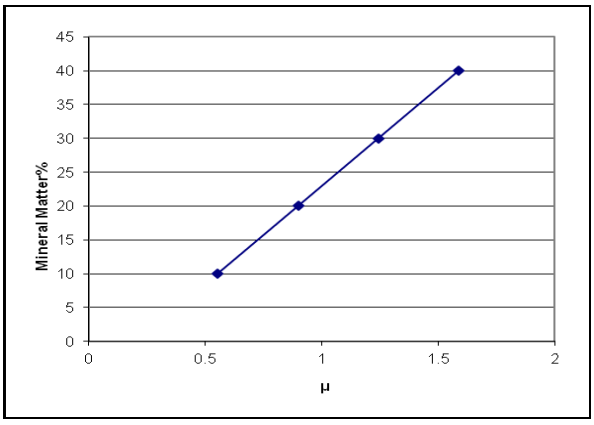

Figure 4 - Relation between mass absorption coefficient and mineral matter of the synthetic standards.

The same measurements were performed on the lignite samples. Again we observe a clear relation between Compton intensity and mineral matter content, expressed as ash % (from table 1)

(Figures 7 and 8). Therefore the lignite ash content can be determined easily by the measurement of the Compton Peak intensity by X-ray fluorescence.

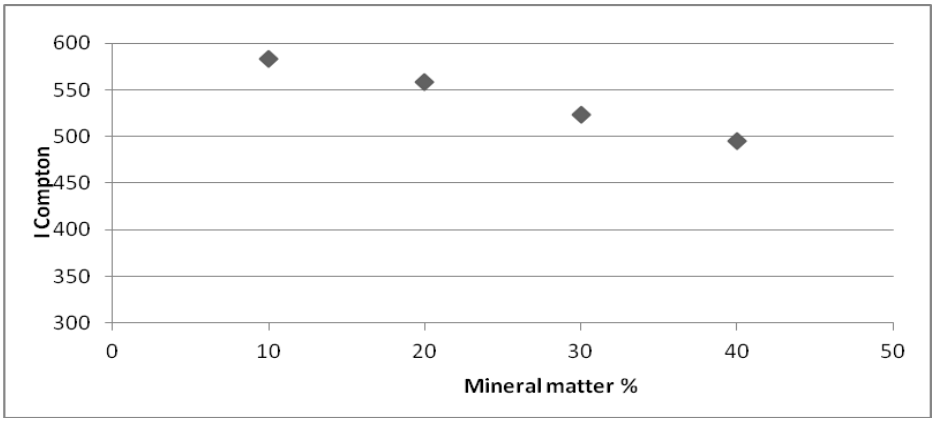

Figure 5 - Relation of mineral matter content and Compton Peak Intensity in synthetic samples.

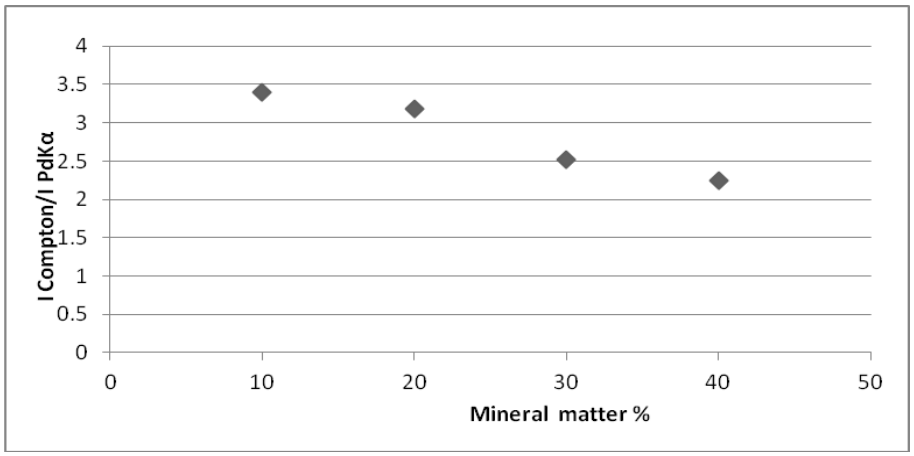

Figure 6 - Relation of mineral matter content and Ratio of the Compton Peak/PdK*α* Intensity in synthetic samples.

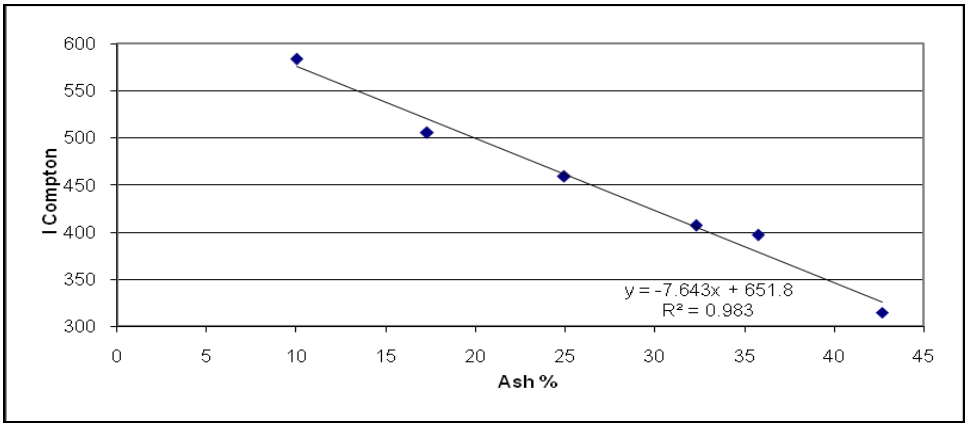

Figure 7 - Relation of ash content in lignite and the Compton Peak Intensity.

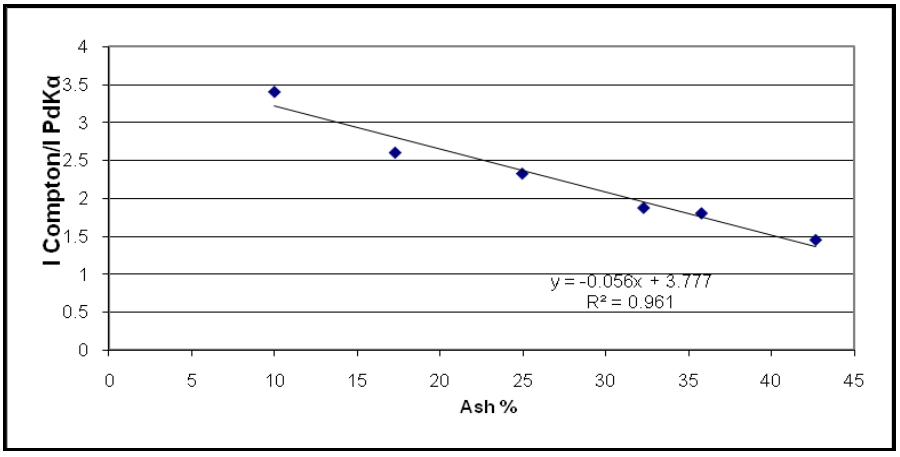

Figure 8 - Relation of ash content in lignite and Ratio of the Compton Peak/PdKα Intensity.

3. Discussion and Conclusion

The mineral matter content in lignite can be easily determined by the use of X-ray fluorescence spectroscopy and the Compton peak intensity of the X-ray tube. This can be done by a calibration curve with mineral matter % or ash%, of known lignite samples versus Compton peak intensity. Calibrated samples and unknown lignite samples must have, qualitatively, the same mineralogical composition, regarding mineral matter. This is in most cases given for a certain lignite layer, as in the analyzed lignite samples, with calcite as the main mineral. This is important because the total value of mass absorption coefficient of a lignite sample can have the same value, theoretically, by different quantitative combination of the minerals in mineral matter.

4. References

ASTM D3174-12 Standard Test Method for Ash in the Analysis Sample of Coal.

Australian Standards 2000. Higher rank coal mineral matter and water of constitution. Australian Standard 1038, Part 22, 20pp.

Colin R. 2002. Analysis and significance of mineral matter in coal seams, *International Journal of Coal Geology*, 50, 135-168.

Finkelman R.B. 1994. Abundance, source and mode of occurrence of inorganic constituents in coal, in: Kural, O. (ed.) Coal. Istanbul Technical University, Istanbul, pp. 115-125.

Gary M., McAfee R. and Wolf C.L. (Eds) 1972. Glossary of Geology, *American Geological Institute*, Washington, DC, 805 pp.

Gluskoter H.J. 1965. Electronic low temperature ashing of bituminous coal. *Fuel*, 44, 285-291.

Harvey R.D., Ruch R.R. 1986. Mineral matter in Illinois and other US coals, in. Vores, K.S. (ed.) Mineral Matter in coal Ash and coal. American Chemical Society Symposium Series 301, pp 10-40.

Koukouzas N., Zeng R., Perdikatsis V., Xu W. and Kakaras E. 2006. Mineralogy and geochemistry of Greek and Chinese coal fly ash, *Fuel*, 85, 2301-2309.

Ritz M. and Klika Z. 2010. Determination of minerals in coal by methods based on the recalculation of the bulk chemical analyses, Acta Geodyn. Geomater., Vol. 7, No. 4 (160), 453–460.

Reynolds R.C. 1963. Matrix corrections in trace element analysis by X-ray Fluorescence: Estimation of mass absorption coefficient by Compton scattering, *American Mineralogist*, 48, 1133-1143.

Tickner J. and Roach G. 2004. Characterization of coal and minerals using Compton profile analysis, *Nuclear Instruments and Methods in Physics Research B* 213, 507-510.

Δελτίο της Ελληνικής Γεωλογικής Εταιρίας, τομ. XLVII , 2013
Πρακτικά 13ου Διεθνούς Συνεδρίου, Χανιά, Σεπτ. 2013

Bulletin of the Geological Society of Greece, vol. XLVII 2013
Proceedings of the 13th International Congress, Chania, Sept. 2013

MINERALOGICAL INVESTIGATION AND MINERAL PROCESSING OF IRON ORE FROM THE SKINES AREA (CHANIA – WEST CRETE)

Trichos D.[1], Alevizos G.[1], Stratakis A.[1], Petrakis E.[1] and Galetakis M. [1]

[1] *Technical University of Crete, Department of Mineral Resources Engineering, Chania, Greece, alevizos@mred.tuc.gr, astratak@mred.tuc.gr, vpetraki@mred.tuc.gr, galetaki@mred.tuc.gr*

Abstract

Several iron ore occurrences are placed in the island of Crete and especially in the prefectures of Chania and Rethymno (Western Crete), some of which have been occasionally exploited. The aim of the present study is the mineralogical examination and the investigation of mineral processing potential of an iron ore occurrence located in the area of Skines village near to the city of Chania. The investigated iron ore occurrence form lenses which are placed within the contact of the phyllite-quartzite of Phyllite-Quarzite-Series (PQS) of Crete and the overlaid limestones. The major minerals of the iron ore are goethite, hematite and quartz, while the less common are muscovite, lepidocrocite, gibbsite, talc and pyrite. The ore microscopy exanimation indicated that an extended epigenetic ferruginisation process has taken place. In general, mineral processing by using heavy liquid and magnetic separation did not give satisfactory results, except for the size fraction -1+0,250 mm of the heavy liquid and the magnetic products of size ftactions -8+4 mm, -4+1 mm and -1+0,250 mm. Ore microscopy examination of the different size fractions indicated that the difficulties in mineral processing are closely related to the ore liberation.
Key words: *Ore microscopy, epigenetic ferruginisation, Phyllite-Quartzite Series.*

Περίληψη

Σε περιοχές της Κρήτης και ιδιαίτερα στους Νομούς Χανίων και Ρεθύμνου (Δυτική Κρήτη) απαντώνται αξιόλογα κοιτάσματα σιδηρομεταλλευμάτων, μερικά από τα οποία υπήρξαν κατά καιρούς αντικείμενο εκμετάλλευσης. Σκοπός της παρούσας μελέτης είναι η ορυκτολογική εξέταση και οι δυνατότητες εμπλουτισμού δειγμάτων σιδηρομεταλλεύματος από την περιοχή Σκινέ Χανίων, Δυτικής Κρήτης. Το υπό διερεύνηση σιδηρομετάλλευμα εντοπίζεται πλησίον του χωριού Σκινέ και απαντάται με φακοειδή μορφή στην επαφή μεταξύ των φυλλιτών-χαλαζιτών της Φυλλιτικής-Χαλαζιτικής σειράς της Κρήτης και των υπερκείμενων ασβεστολιθικών πετρωμάτων. Τα κύρια ορυκτολογικά συστατικά του μεταλλεύματος είναι γκαιτίτης, αιματίτης, χαλαζίας και δευτερευόντως μοσχοβίτης, λεπιδοκροκίτης, γκιπσίτης, τάλκης και σιδηροπυρίτης. Σύμφωνα με τη μικροσκοπική διερεύνηση του μεταλλεύματος, πρόκειται για μία ευρείας έκτασης μεταλλοφορία σιδήρου επιγενετικής προέλευσης. Οι δοκιμές εμπλουτισμού δεν έδωσαν γενικά ικανοποιητικά αποτελέσματα με εξαίρεση το βαρυτομετρικό κλάσμα -1+0,250 mm καθώς και τα μαγνητικά προϊόντα των κοκκομετρικών κλασμάτων -8+4 mm, -4+1 mm και -1+0,250 mm, όπου παρατηρείται οριακά ένας εμπλουτισμός του μεταλλεύματος. Η μικροσκοπική εξέταση

των διαφόρων κοκκομετρικών κλασμάτων έδειξε, ότι η δυσκολία εμπλουτισμού του μεταλλεύματος συνδέεται στενά με τα ιστολογικά χαρακτηριστικά του.
Λέξεις κλειδιά: *Μικροσκοπική εξέταση, επιγενετική σιδηρούχος μεταλλοφορία, Φυλλιτική-Χαλαζιτική σειρά.*

1. Introduction

Considerable iron ore deposits are placed in several regions of Greece, some of which were occasionally investigated for exploitation. Iron ore deposits which consist mainly of magnetite, hematite and limonite, have been mined up to 1964 (S.M.E., 1979). These iron ores are usually located into marbles or in contact with schists. The major deposits are those of Thassos, Kavala, Grammatico in Attica and Serifos. Occurrences of iron ore are located also in some islands of Cyclades and Eastern Aegean as well as in Peloponnese, Crete, Chalkidiki, Serres, etc. (Tsirampidis, 2005).

The quality of Greek iron ores is generally poor so they require mineral processing. The chemical composition of ores and particularly their content in iron, the character of the hosted minerals, as well as, the content of harmful elements are the main factors affecting their exploitability. Iron ores with content in iron above 52% are commercial as exploited, while poor ones with iron concentration between 20-52%, must be enriched (Foufris, 1980). The content of harmful elements in iron ores should be under specific limits. According to Pohl (2005) the concentration of phosphorous in the ore should be under 0,045%, the Mn under 2%, the Cr under 1%, the Ni under 0,5%, the S under 0,2% and the As, Cu, Zn and Pb under 0,1%.

Several iron ore occurrences are placed in Western Crete. The most important of these are found in the regions of Skines, Ravdoucha, Kakopetros, Drakona, Sklavopoula in the Prefecture of Chania, as well as, in the regions of Arolithi, Ano Valsamonero in the Prefecture of Rethymno. Iron ores of the regions Skines and Ravdoucha have been partially exploited. The aim of the present study is the mineralogical examination and the investigation of mineral processing of iron ore samples from the region of Skines. For the mineral processing tests of the iron ore samples, the heavy liquid and the magnetic separation methods were used.

2. Geological and Deposit Setting

The Phyllite-Quartzite Series (PQS) of Crete hosts several iron ore occurrences mainly in the western part of the island. The PQS contains mainly phyllites and quartzites as well as metaconglomerates, marbles, calcareous phyllites and metabasalts (Figure 1). The PQS and the Gypsum-Rauhwacke formation represent the lower unit of Phyllite Nappe of Crete. The Phyllite Nappe is a structural unit of external Hellenides, which is composed by the metamorphosed rocks lying between the Plattenkalk series underneath and Tripolitza series above (Dornsiepen and Manutsoglu, 1994).

According to Seidel et al. (2005), the iron ore deposits of Western Crete are hosted by an extensional detachment zone that is found in the upper parts of high pressure/low temperatures metamorphic Phyllite-Quartzite series. $\delta^{18}O$ values of goethite from the iron deposits at Kakopetros and Ravdouxa in Western Crete indicate crystallization of iron ores at low temperatures between 31o and 40 oC and at a depth of 1 to 1,5 km, approximately.

Considerable iron ore occurrences are located near the Skines village about 17 km south-west of Chania. The investigated occurrence is placed around 1 km south of the village in the place named Chliaro. The largest part of the deposit lays in the slope of a hill in the form of lenses between phyllites underneath and limestones above. Except this deposit, there are other such occurrences in the region nearby but in a smaller extension (Papastamatiou, 1952). According to the researcher, the iron ore is composed of cellular limonite, which encloses grains of schists. In some places

phyllite is impregnated by limonite. Limonite has penetrated into the brecciated phyllite and in a way it constitutes the matrix between grains of pre-existing minerals. The origin of iron ores can be associated to the presence of chalcopyrite, pyrite mineralization in the near village Fourne. The researcher considers that the appearances of iron ores in Western Crete come from the oxidation of Fe-sulfide deposits.

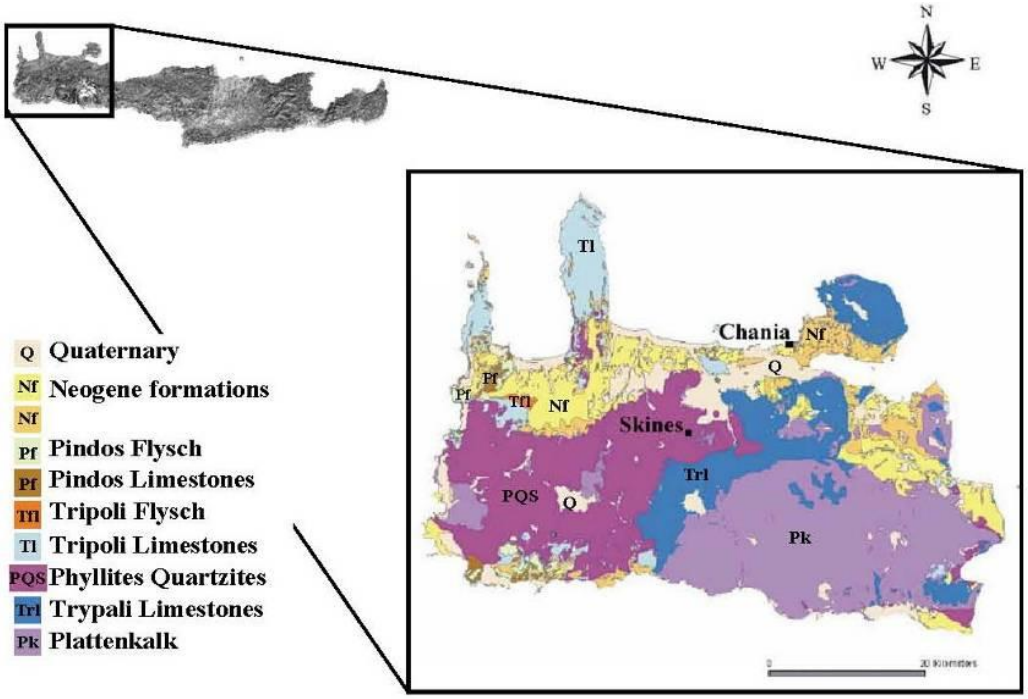

Figure 1 - Geological map of Skines area in western Crete (Electronic form of Geological Map of Greece, I.G.M.E. 1983, 2nd edition).

According to Mineral Resources Map (1965), six iron ore deposits occur in the south-east part of the Skines village. They consist mainly of limonite and hematite with low concentration in pyrolusite. They are placed in the contact of dolomites and phyllites and are considered of hydrothermal origin. The iron ore deposit has been partially mined in the past by the Mediterranean Group company (approximately 200 thousand tonnes have been extracted) while the remaining reserves of the deposit are estimated to 1 million tonnes.

3. Experimental

The mineralogical examination of the iron ore was carried out using the X-ray diffraction method. The automated X-ray diffractometer, D8 Advance of Bruker AXS company was used. The identification of the ore minerals and the description of the fabric, as well as, the examination of the intergrowth in the different products were performed via ore microscopy. A JENA ore microscope equipped with an OLYMPUS digital camera was used. The chemical analysis of iron ore was carried out using the automated X-ray fluorescence spectrometer, Bruker S2 Ranger. For the gravimetric separation of iron ore samples the heavy liquid Tetrabromoethane with density d=2,96 g/cm3 was used. The magnetic separation was performed with the Perm Roll magnetic separator of IMPROSYS, as well as, with the high intensity Induced Roll Magnetic Separator MIH 111-5 of Carpco.

4. Mineralogy

The iron ore deposit under investigation is located south of the village Skines and it forms lenses placed in the contact between the phyllite-quartzite and limestones. Several successive spot samples, from the top to the base of the exposed face, were taken. The collected samples were carefully selected to represent the alteration of the mineralization. The iron ore samples near the contact of phyllite-quartzites (base) are relatively rotten and are characterized by their reddish-brown colour. Samples collected from the middle and the upper part of the exposed iron ore face, are more compact and cohesive.

The microscopic examination and x-ray diffraction analysis of ore samples from the base of occurrence showed wide extent of ferruginisation mainly in the form of goethite, hematite and rarely lepidocrocite. The ferruginisation is developed between the grains of parent rocks of phyllite-quartzite replacing progressively the matrix (Figure 2). The major mineralogical component of these rocks is quartz and the minor ones are muscovite, talc and rarely gibbsite. The quartz is found in the form of allotriomorphic crystals that are fragmented to a large degree, as a result of tectonism of the parent rocks. A partial penetration of ferruginous solutions in capillary form was observed inside the quartzite grains. The iron ore is developed between the quartzite grains with the form of goethite and partially with the form of lepidocrocite. Goethite is formed in concentric shells along the gaps and fault zone, alternating gradually to hematite, because of dehydration. Crystals of pyrite in relatively small sizes were also observed occasionally scattered inside the iron ore. The presence of pyrite, as well as, lepidocrocite is also referred in iron rich breccien from Karanou area in Western Crete (Markopoulos et al., 2005).

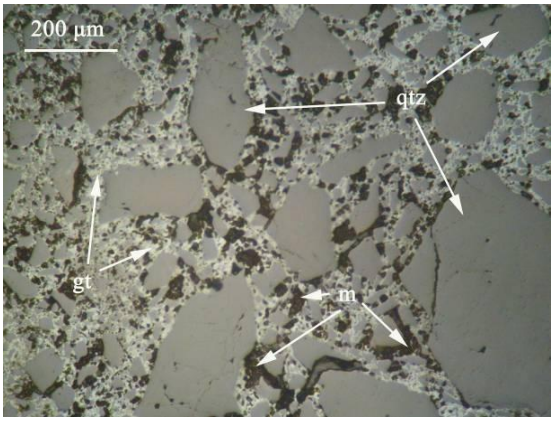

Figure 2 - Goethite replacing progressively the matrix between the grains of phyllite-quartzite. (gt:goethite, qtz: quartz, m: matrix). Reflected light, // Nicols.

In the samples collected from the middle of the exposed face extensive ferruginisation was observed, which has been placed in the form of goethite replacing the binder between the grains. Goethite forms occasionally concentric shells along the cracks and gaps returning progressively into hematite (Figure 3). The quartz crystals are inequigranular, allotriomorphic and generally fragmented. The clay minerals, muscovite and talc, have a scale-like and an acicular form respectively, forming lenses that are developed between the quartzite grains. The x-ray diffraction analysis of a representative sample verified the presence of quartz 43%, goethite 39%, muscovite 11%, gibbsite 3%, hematite 2% and talc 2% wt equivalent.

In the upper parts of the exposed face of the iron ore occurrence, the microscopic examination showed an appreciable ferruginisation. The quartz is found mainly in the form of rough, inequigranular crystals. The ferruginisation developed in the form of goethite between the grains of parent rocks, as well as, along the cracks and gaps, providing cement shaped textures. Other mineralogical components are hematite, muscovite and gibbsite.

According to the microscopic investigation of the samples collected from the ore face, an extended ferruginisation of epigenetic origin is evident. It is developed mainly in the form of goethite inside phyllite-quartzite, replacing gradually the binder between the grains. The fabric of the iron ore is generally characterized as cement shaped.

The chemical analyses of representative samples collected from the various parts of occurrence are presented in Table 1. The content of Fe2O3 in samples from the base of the face is 63.96%, from the middle 63% and from the top 55.76% wt.

Concentrations of harmful elements in the initial sample show relatively small variations. The content of SO3 ranges between 0.12 and 0.18 wt%, P2O5 between 0.19 and 0.48 wt%, ZnO between 0.02 and 0.03 wt% and MnO between 0.34 and 0.41 wt% respectively. The Cr2O3 content in the ore is up to 0.08 wt% (Table 1).

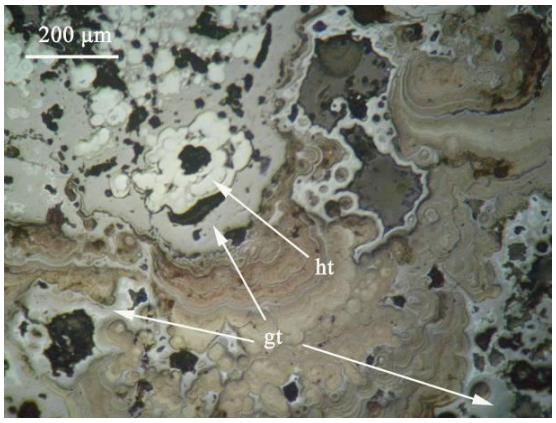

Figure 3 - Concentric shells of goethite alters progressively to hematite. (gt:goethite, ht:hematite) Reflecterd light, // Nicols.

Table 1 - Chemical composition (wt%) of samples collected from different point of the exposed face of the iron ore occurrence.

Location of sample	SiO_2	Fe_2O_3	Al_2O_3	MgO	K_2O	TiO_2	SO_3	CaO	MnO	P_2O_5	ZnO	Cr_2O_3	LOI	Sum
Base of the face	16.96	63.96	4.29	-	0.12	0.07	0.12	0.19	0.35	0.19	0.03	-	13.86	100.14
Middle of the face	14.43	63.00	5.55	1.57	0.72	0.33	0.13	0.37	0.41	0.48	0.02	0.08	13.15	100.24
Top of the face	24.69	55.76	5.69	-	0.18	0.12	0.18	0.22	0.34	0.21	0.02	-	12.67	100.08

5. Mineral Processing Tests

5.1. Experimental Procedure

The collected bulk sample was crushed in size -8 mm using a jaw crusher. The product of the jaw crusher was sieved into fractions of -8+4 mm, -4+1 mm, -1+0,250 mm and -0,250+0,063 mm. These size fractions were divided into two equal parts for the magnetic and gravity separation tests. The fine fraction of -0,063 mm is not suitable for these mineral processing tests and therefore it was not used.

The gravimetric separation of the ore was carried out using the heavy liquid Tetrabromoethane with density 2.96 g/ml.

For the magnetic separation of fractions -8+4 mm and -4+1 mm the Perm Roll separator (equipped with permanent magnets) was used. Each fraction was separated with decreasing rotation speed starting with a rotation speed of 180 rpm, afterwards decreasing to 150 rpm and finally to 100 rpm. With the above rotation speeds three successive passes of the material were carried out. In each pass the magnetic product is collected and weighed, while the non-magnetic is used to feed the next pass. In each pass the magnetic material is collected and at the final pass, at 100 rpm, the last magnetic and the final non-magnetic product were collected.

For the fractions -1+0,250 mm and -0,250+0,063 mm the Induced Roll magnetic separator was used. These fractions were separated initially with a rotation frequency 180 rpm and electric current I = 1.6 A. From this process two products (a magnetic and a non-magnetic) were collected. The non-magnetic product was passed again from the separator at electric current I = 3.2 A and the same frequency. At this pass the final magnetic and the final non-magnetic products were collected.

5.2. Mineral Processing Results

The chemical analyses of selected elements of the initial sample's size fractions are presented in Table 2. From the evaluation of chemical analyses in the different size fractions it is obvious that the content of the Fe2O3 is reduced by reducing the size of the particles. The highest value is observed in fraction -8+4 mm, while there are small variations in the content of the intermediate size fractions. In contrast, the content of SiO2 increases gradually with the decrease of the grain size, indicating the smallest value in fraction -8+4 mm.

Table 2 - Chemical analysis of size fractions from initial sample.

Size fractions	Weight (%)	SiO_2 (%)	Fe_2O_3 (%)	Al_2O_3 (%)	CaO (%)	LOI (%)
-8+4 mm	55.72	16.61	61.87	5.01	0.30	9.01
-4+1 mm	25.87	30.28	51.51	6.61	0.31	8.68
-1+0.250 mm	10.19	32.92	40.23	6.59	0.49	8.01
-0.250+0.063 mm	5.45	36.15	41.63	7.86	1.12	8.98
-0.063 mm	2.77	37.98	44.24	6.22	0.33	9.06
Total	100.00	23.47	56.42	5.77	0.37	9.38

5.2.1. Gravimetric Separation

The results of the gravimetric separation of the fractions -8+4 mm, -4+1 mm, -1+0,250 mm and -0,250+0,063 mm are shown in Table 3.

According to the results of Table 3, it is clear that the weight percentages of the sinks are generally higher compared to those of the floats for all size fractions. The content of Fe2O3 in the sinks is clearly higher (42-71 wt %), while higher percentages are observed in coarser size fractions (Figure 4a). Similar conclusions emerge for the distribution of Fe2O3. In the sinks the distribution of this component ranges between 87-95 wt%. The SiO2 shows, as expected, higher concentration compared to Fe2O3 in the floats in all size fractions, except in the fraction -4+1 mm. The highest percentages of SiO2 are observed in the fractions -1+0,250 mm and -0,250+0,063 mm, 67% and 58 wt% respectively (Figure 4b). Of course, its distribution in the sinks is lower than that of Fe2O3, while in the floats it has a higher value than that of Fe2O3. However, a significant percentage of SiO2 remains in the concentrate of several size fractions except the -1+0,250 mm, where the greater amount of SiO2 is moved to the floats (53% versus 47 wt% in sinks).

The above results are shown by the microscopic examination of size fractions. Figure 5a shows the sink product and Figure 5b shows the float one of the fine size fraction -0,250 +0,063 mm. It must be observed that even in the fine size fraction there are partially liberated ferrous mineral grains, matrix and quartz, which are driven in the sinks at the stage of mineral processing.

The chemical analyses of the size fractions showed that the Fe2O3 has higher concentration in the sinks, while the SiO2 in the floats. Hence the corresponding mineralogical phases goethite, and hematite are mainly concentrated in the sinks while the quartz in the floats. The Al2O3 presents the greatest concentrations mainly in the floats and therefore the minerals gibbsite, muscovite are concentrated in the tailing. The concentration of LOI that corresponds mainly to the presence of goethite is greater in the sink than the floats.

Table 3 - Results of gravimetric separation.

		Weight (%)		Chemical analysis (%)				Distribution of the fraction (%)			
Size fraction	**Products**	**of the fraction**	**of the initial**	**Fe_2O_3**	**SiO_2**	**Al_2O_3**	**LOI**	**Fe_2O_3**	**SiO_2**	**Al_2O_3**	**LOI**
-8 + 4 mm	Float	8.36	4.66	41.82	43.32	5.14	8.12	5.08	29.73	9.59	5.25
	Sink	91.64	51.06	71.24	9.34	4.42	13.37	94.92	70.27	90.41	94.75
	Total	100	55.72	68.78	12.18	4.48	12.93	100	100	100	100
-4 + 1 mm	Float	16.69	4.32	43.93	39.46	5.62	9.06	12.90	26.80	15.63	13.64
	Sink	83.31	21.55	59.43	21.60	6.08	11.50	87.10	73.20	84.37	86.36
	Total	100	25.87	56.84	24.58	6.00	11.10	100	100	100	100
-1 + 0.250 mm	Float	24.56	2.50	15.97	66.51	8.10	6.58	10.94	52.71	34.89	6.43
	Sink	75.44	7.69	42.34	19.43	4.92	31.18	89.06	47.29	65.11	93.57
	Total	100	10.19	35.86	30.99	5.70	25.14	100	100	100	100
-0.250 + 0.063 mm	Float	12.21	0.67	22.41	57.66	13.64	3.75	6.25	20.97	22.57	3.93
	Sink	87.79	4.78	46.77	30.23	6.51	12.76	93.75	79.03	77.43	96.07
	Total	100	5.45	43.79	33.58	7.38	11.66	100	100	100	100
-0.063 mm	Total	100	2.77	44.24	37.98	6.22	9.06				
Grand Total		100	100	60.30	19.19	5.20	4.10				

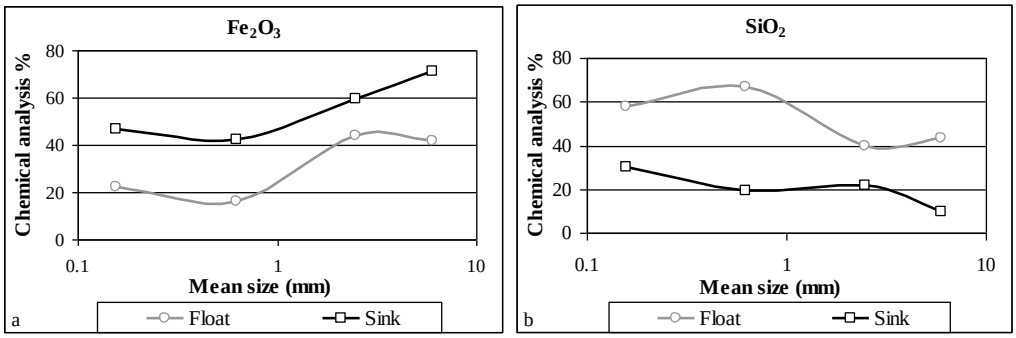

Figure 4 - Fe2O3 (%wt) (a) and SiO2 (%wt) (b) contents of the products obtained from the gravimetric separation.

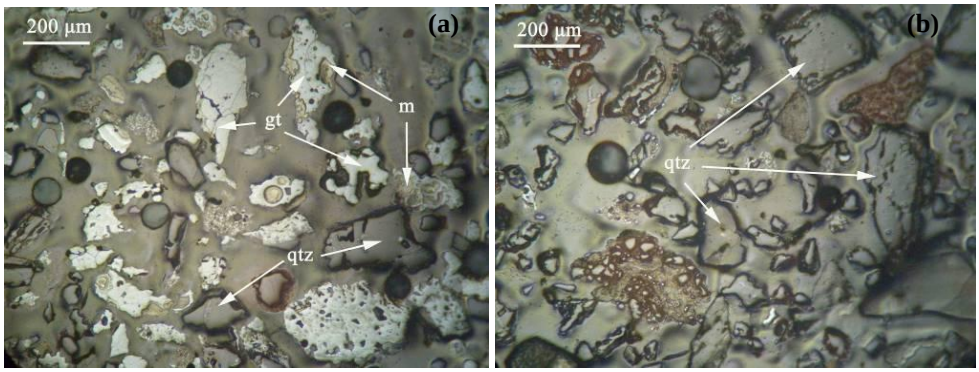

Figure 5 - Goethite grains and matrix partially liberated. Quartz is also present. (size fraction -0.250+0.063 mm). a. Sink b. Float (gt: goethite, qtz: quartz, m: matrix). Reflected light, // Nicols.

5.2.2. Magnetic Separation

The results of magnetic separation in fractions -8+4 mm, -4+1 mm, -1+0,250 mm and -0.250 +0.063 mm are shown in table 4. The main components in the various size fractions are Fe_2O_3 and SiO_2. The Fe_2O_3 occurs in the ferrous minerals such as goethite and hematite, while the SiO_2 is mainly found in quartz and in smaller quantities in the muscovite and talc. The Al_2O_3 occurs in gibbsite and muscovite. The data of table 4 show that the percentages of magnetic products are higher than those of non-magnetic in both the coarser and fine size fractions. The content of Fe_2O_3 is significantly greater in the magnetic products (44-63 wt%) compared to those of non-magnetic (8-34 wt%). The Fe_2O_3 content of all magnetic products decreases with the reduction of grain size (Figure 6a). On the contrary, the content of SiO_2 is higher in non-magnetic products (50-71 wt%) compared to magnetic ones (Figure 6b). Nevertheless, the content of SiO_2 in the magnetic products is significant (16-35 wt%) which indicates that the liberation of the minerals is not satisfactory. This was also confirmed by the microscopic examination of various size fractions (Figure 7a, b). Figure 7a shows a considerable amount of quartz, goes into the magnetic products due to the poor liberation of the specific size fraction.

The chemical analyses of size fractions shows that the Fe_2O_3 is concentrated in the magnetic products and consequently the corresponding mineralogical phases goethite and hematite. Instead, the SiO_2 is present in the non-magnetic products of all size fractions and therefore the mineral quartz. The concentration of Al_2O_3 shows higher values in the non-magnetic products in all size fractions and consequently the minerals muscovite and gibbsite are mainly concentrated in the tailing. The LOI have greater values in the magnetic than in the non-magnetic products due to the concentration of goethite in these products.

6. Discussion and Conclusions

The ore deposit of Skines area Chania (West Crete) found in the form of lenses in the contact of phyllite-quartzite of Phyllite-Quartzite series of Crete and the overlaid limestones. The phyllite-quartzite is strongly brecciated and is impregnated by limonite. Microscopic examination of the ore showed a widespread epigenetic ferruginisation.

The major minerals of the ore are goethite, hematite and quartz, while minor are muscovite, lepidocrocite, gibbsite, talc and pyrite. The ferruginisation is developed mainly in the form of goethite, hematite and rarely lepidocrocite within the brecciated phyllite-quartzite replacing gradually the matrix between the grains. The main mineralogical component of the parent rock is quartz with smaller percentage of muscovite, talc and the rarely gibbsite.

Table 4 - Results of magnetic separation.

		Weight (%)		Chemical analysis (%)				Distribution of the fraction (%)			
Size fraction	**Products**	**of the fraction**	**of the initial**	**Fe_2O_3**	**SiO_2**	**Al_2O_3**	**LOI**	**Fe_2O_3**	**SiO_2**	**Al_2O_3**	**LOI**
-8 + 4 mm	Magnetic 1	2.07	1.15	52.13	24.45	4.80	16.26	1.83	2.41	1.79	2.80
	Magnetic 2	64.24	35.79	63.79	15.44	5.62	12.79	69.49	47.15	65.17	68.32
	Magnetic 3	20.23	11.27	60.96	18.95	4.52	12.98	20.91	18.22	16.50	21.83
	Magnetic(Total)	86.54	48.22	62.85	16.48	5.34	12.92	92.23	67.77	83.47	92.94
	Non magnetic	13.46	7.50	34.04	50.35	6.80	6.30	7.77	32.23	16.53	7.06
	Total	100	55.72	58.97	21.04	5.54	12.03	100	100	100	100
-4 + 1 mm	Magnetic 1	18.19	4.70	64.35	16.28	5.44	12.12	25.72	8.23	13.70	25.03
	Magnetic 2	42.36	10.96	54.76	25.35	6.36	10.80	50.98	29.84	37.30	51.93
	Magnetic 3	21.44	5.55	38.11	44.71	8.06	7.10	17.96	26.64	23.92	17.30
	Magnetic(Total)	81.99	21.21	52.53	28.40	6.60	10.12	94.66	64.70	74.92	94.25
	Non magnetic	18.01	4.66	13.50	70.52	10.06	2.81	5.34	35.30	25.08	5.75
	Total	100	25.87	45.50	35.99	7.22	8.81	100	100	100	100
-1 + 0.250 mm	Magnetic 1	24.21	2.47	57.48	19.56	6.34	14.20	31.19	13.59	20.52	33.79
	Magnetic 2	42.92	4.37	54.76	23.98	6.79	11.22	52.69	29.53	38.96	47.35
	Magnetic(Total)	67.13	6.84	55.74	22.39	6.63	12.30	83.88	43.12	59.48	81.14
	Non magnetic	32.87	3.35	21.87	60.30	9.22	5.84	16.12	56.88	40.52	18.86
	Total	100	10.19	44.61	34.85	7.48	10.17	100	100	100	100
-0.250 + 0.063 mm	Magnetic 1	69.48	3.79	46.83	31.57	7.40	9.69	82.57	56.64	61.67	78.25
	Magnetic 2	19.06	1.04	31.43	46.53	10.36	7.51	15.20	22.89	23.68	16.64
	Magnetic(Total)	88.54	4.83	43.51	34.79	8.04	9.22	97.77	79.53	85.35	94.89
	Non magnetic	11.46	0.62	7.68	69.15	10.65	3.83	2.23	20.47	14.65	5.11
	Total	100	5.45	39.41	38.73	8.34	8.60	100	100	100	100
-0.063 mm	Total	100	2.77	44.24	37.98	6.22	9.06				
	Grand Total	100	100	52.55	27.75	6.34	10.74				

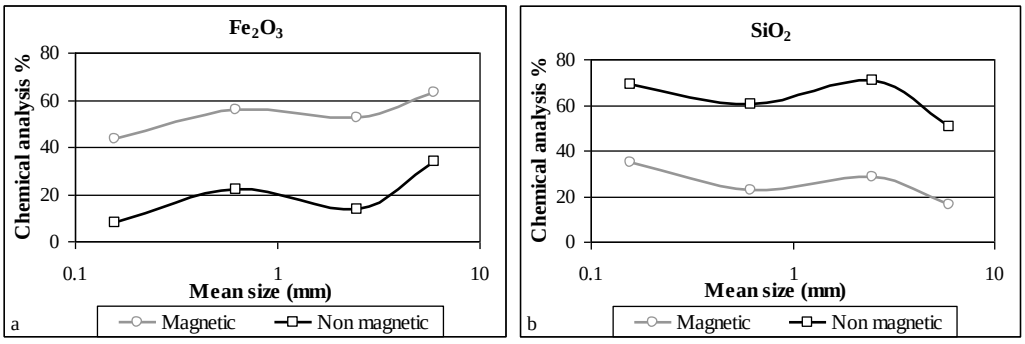

Figure 6 - Fe2O3 (%wt) (a) and SiO2 (%wt) (b) content of magnetic separation products.

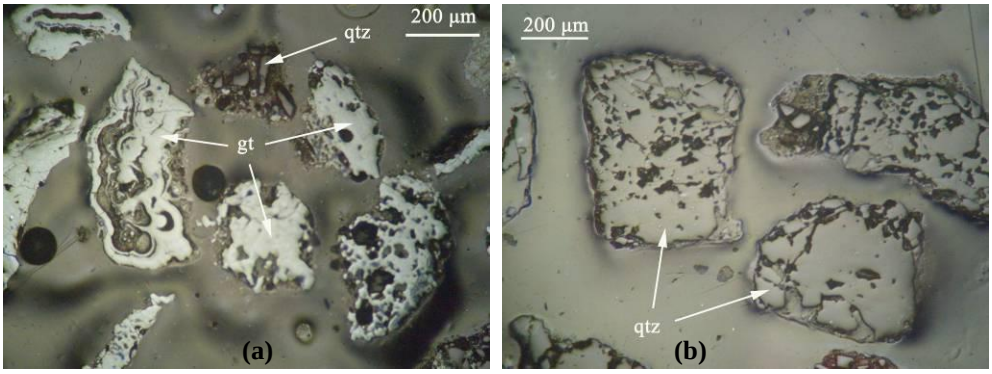

Figure 7 - Goethite grains with traces of quartz of size fraction -1+0.250 mm. a. Magnetic product 1 b. Non magnetic product. (gt: goethite, qtz: quartz). Reflected light, //Nicols.

Goethite often forms concentric shells along fault zone and gaps that gradually alters to hematite due to dehydration. Scattered pyrite crystals are occasionally observed in the ore. The fabric of the ore is generally characterized as cement shaped textures. The presence of pyrite in the ore residues reinforces the view that the formation of ore in Skines area can be related genetically to the existing Fe-sulfide mineralization near to Fournes village.

The gravimetric separation of the ore was moderately satisfactory. The weight percentages of the sinks is increased compared to those of the floats for all size fractions (75-92 wt%). The content of Fe2O3 is clearly greater in the sinks (42-71 wt%). The SiO2 shows, as expected, slightly higher content related to Fe2O3 in the floats in all size fractions except size fraction -4 +1 mm, due to the poor liberation of the material in this fraction. The highest concentration (67 wt%) is observed in the fraction of -1+0,250 mm. However a significant percentage of SiO2 remains in the concentrate of most size fractions except the size fraction -1 +0,250 mm, where the greater part of SiO2 is driven to the floats (53% versus 47 wt% in heavy).

The magnetic separation of the ore, generally, showed better results than those of the gravimetric separation. The weight percentages of magnetic products are much higher than those of non-magnetic in both the coarser and fine size fractions. The concentration of Fe2O3 is higher in the magnetic products (44-63 wt%) compared to the non-magnetic (8-34 wt%), while the recovery varies between 84 and 98 wt% in all size fractions. On the other hand, the SiO2 shows a higher concentration in the non-magnetic products (50-71 wt%) compared to the magnetic ones. However a significant percentage, between 16 and 35 wt%, remains in the magnetic products.

The mineral processing tests were moderately satisfactory, except for the fraction -1 +0,250 mm of the gravimetric separation and the magnetic products 2 of size fractions -8 +4 mm, -4 +1 mm, -1 +0,250 mm of the magnetic separation, as shown by the distribution of these fractions. According to the Fe2O3 content in all size fractions of mineral processing tests, it is obvious that the ore cannot be considered to be commercially exploitable (74.3% Fe_2O_3 or 52% Fe), except for the size fraction -8+4 mm of the gravimetric separation (71%).

Microscopic examination of the different size fractions showed that the liberation of ferrous minerals from waste rock was not satisfactory. This is due to the fact that the goethite replacing the matrix between the granules of the parent rock and often penetrates by capillary-needle form in the quartz grains thus makes difficult their separation. The tests of the ore processing confirmed the results of microscopic investigation of the different size fractions which had shown that the mineral processing of the examined ore could be difficult due to its formation and its fabric characteristics.

7. References

Dornsiepen U. F. und Manutsoglu E. 1994. Zur Gliederung der Phyllit-Decke Kretas und des Peloponnes, *Z. dt. geol. Ges.*, 145, 286-304.

Greek Mining Enterprises association (S.M.E) 1979. *The Greek Mineral Wealth*, Athens 696 pp. (in Greek)

Markopoulos Th., Alevizos G., Manutsoglu E. and Repouskou E. 2005. Mineralogische und erzmikroskopische Untersuchung eisenvererzter Breccien aus der Karanouregion, West-Kreta, Griechenland., *Ber. Deutsch. Mineral. Ges., Beih. z. Eur. J. Mineral*., v.17, 86.

Mineral Resources Map 1965. *Explanatory issue of Metallogenetic Map of Greece*, 1:1.000.000, P ublished by Institute for Geology and Subsurface Research, 1973, Athens, 254 p. (in Greek)

Papastamatiou J. 1952. The mineral wealth of Crete, *Institute of Geological and Mining Research, Report No 256*, Athens, 38 pp. (in Greek).

Pohl W. L. 2005. *Mineralische und Energie-Rohstoffe*. 5 Auflage, E. Schweizerbart'sche Verlagsbuchhandlung (Naegele u. Obermiller), S.527.

Seidel M., Pack A., Sharp Z. and Seidel E. 2005. The Kakopetros and Ravdoucha iron-oxide deposits, Western Crete, Greece: Fluid transport and mineralization within a detachment zone, *Economic Geology*, v.100, 165-174.

Tsirampidis A. 2005. *The mineral wealth of Greece*, Editors Jachoudi, Thessaloniki, 391 pp. (in Greek).

Fufris A. 1980. Study on possibility of enrichment poor iron ores of Serifos Island, *Report*, No 23, I.G.M.R., Athens, 40 pp. (in Greek).

Δελτίο της Ελληνικής Γεωλογικής Εταιρίας, τομ. XLVII , 2013
Πρακτικά 13ου Διεθνούς Συνεδρίου, Χανιά, Σεπτ. 2013

Bulletin of the Geological Society of Greece, vol. XLVII 2013
Proceedings of the 13th International Congress, Chania, Sept. 2013

ROCKFALL HAZARD AND RISK ASSESSMENT OF ROAD SLOPES

Andrianopoulos A.[1], Saroglou H.[1] and Tsiambaos G.[1]

[1] National Technical University of Athens, School of Civil Engineering, Dept. of Geotechnics, aandrian@tee.gr, saroglou@central.ntua.gr, gktsiamb@ central.ntua.gr

Abstract

This paper presents and compares the main methods of hazard and risk assessment for road slopes. Hazard assessment is achieved by rating several parameters such as the slope's geometry, traffic conditions, the geology and the rockmass properties, weather conditions, historical rockfall data etc. A hazard assessment can also be executed using 2D or 3D trajectory models, by combining the frequency of a rockfall and the kinetic energy of a falling rock. Several methodologies have been developed for risk assessment, varying from simplistic approaches to comprehensive probabilistic or quantitative risk assessment methods. Finally, the most suitable methods were used in order to assess the level of hazard and risk as an example (the data from two sections of the national road at Tempi Gorge, Greece) where many rockfall events occurred in the past few years.
Key words: *RHRS, rating, Tempi, Geotechnical conditions.*

Περίληψη

Οι καταπτώσεις βράχων σε οδικές αρτηρίες, οδηγούν σε σημαντικές επιπτώσεις και συνεπώς είναι ιδιαίτερα σημαντική η εκτίμηση του επιπέδου της επικινδυνότητας σε πρανή οδοποιίας και η λήψη μέτρων προστασίας.

Στην παρούσα εργασία συγκρίνονται οι σημαντικότερες μέθοδοι εκτίμησης της επικινδυνότητας και της διακινδύνευσης καταπτώσεων βράχων. Όσον αφορά την επικινδυνότητα, λαμβάνονται υπόψη παράμετροι όπως η γεωμετρία του πρανούς, οι κυκλοφοριακές συνθήκες, η γεωλογία και τα χαρακτηριστικά της βραχόμαζας, οι καιρικές συνθήκες, τα ιστορικά δεδομένα, κ.α. Εκτίμηση της επικινδυνότητας μπορεί επίσης να προκύψει μέσω δισδιάστατων ή τρισδιάστατων μοντέλων προσομοίωσης τροχιάς, όπου συνδυάζονται τα δεδομένα της συχνότητας βραχοπτώσεων με την κινητική ενέργεια του καταπίπτοντος τεμάχους βράχου. Όσον αφορά την εκτίμηση της διακινδύνευσης, έχουν αναπτυχθεί διάφορες μέθοδοι, που ποικίλουν από απλοϊκές προσεγγίσεις, έως ολοκληρωμένες πιθανολογικές ή ποσοτικές μέθοδοι. Τέλος, ως παράδειγμα, χρησιμοποιήθηκαν οι καταλληλότερες μέθοδοι εξ αυτών για την εκτίμηση της επικινδυνότητας και διακινδύνευσης από καταπτώσεις βράχων, σε δύο τυπικές διατομές της Εθνικής Οδού Αθηνών – Θεσσαλονίκης, στο τμήμα των Τεμπών, όπου έχουν καταγραφεί αρκετά συμβάντα καταπτώσεων βράχων τα τελευταία χρόνια.
Λέξεις κλειδιά: *Καταπτώσεις, διακινδύνευση, γεωτεχνικές συνθήκες, Τέμπη.*

1. Introduction

Rockfall phenomena often occur at highway road cuts in mountainous terrain. Until the mid 90's, the common practice for managing an unstable slope was to stabilize it after its failure (WSDOT, 2010). By recognizing the importance and the severity of rock falls and taking into account the difficulties arising from them, several researchers have developed both hazard and risk classification systems of unstable road cut slopes, based on visual observation, simple calculations and by estimating the rock mass properties through rock mass classification systems (Pantelidis, 2009). The purpose of these ratings is to identify the slopes with the highest level of hazard or risk and thus determine priorities for immediate mitigation measures or further detailed investigation. The most efficient and widely applied hazard and risk assessment methods are presented in this paper.

The principal landslide type in Greece is rockfall and usually occurs after heavy rainfalls or earthquake events. Rockfalls are more common in Western Greece, due to a combination of factors related to topography, geological and tectonic conditions, climate and human activities (Koukis et al., 1994). Indicatively, recent rockfall incidents occurred at Monemvasia historical site (Saroglou et al., 2008), at the archaeological site of Delphi (Marinos et al., 2005) and the severe rockfall at Tempi Gorge on the 17th of December 2009, which led to one human life loss and caused major problems on the national road network between Athens and Thessaloniki (Gazetas et al., 2010).

2. Hazard Assessment Methods

In terms of hazard rockfall analysis, one of the most widely used methods is the Rockfall Hazard Rating System, also known as RHRS (Pierson, 1991). RHRS is a standardized methodology, which sets rockfall project priorities.

The following should be executed in order to assess the hazard level (Pierson, 1991):

- Slope Survey. Accurate determination of the number and location of the rockfall sites. According to RHRS, a rockfall section is defined as "any uninterrupted slope along a highway where the level and occurring mode of rockfall are the same"
- Preliminary rating. The rockfall sections are categorized into three broad categories, shown in Table 1.

Table 1 – Preliminary Rating System – RHRS methodology (Pierson, 1991).

Class / Criteria	A	B	C
Estimated potential for rock on roadway	High	Moderate	Low
Historical rockfall activity	High	Moderate	Low

- Detailed rating. 10 categories are evaluated, scored and summed. Slopes with higher scores present higher risk. These categories are presented in Table 2 and represent their contribution to the overall hazard. Each category is associated to a score of 3, 9, 27 or 81 depending on the severity of each category, which is representative of a continuum of points between 0 to 100. This exponential scoring system aims to a rapid and user-friendly way of distinguishing the hazardous sites.

Table 2 – Rating Categories of RHRS.

Rating Categories			
Slope Height*	Ditch effectiveness	Average Vehicle Risk*	Percent of Decision Sight Distance*
Roadway width including paved shoulders*	Block size / Volume of rockfall-event*	Climate and presence of water on slope	Rockfall History
Geological Characters			
Case 1		Case 2	
Structural condition	Rock friction	Structural condition	Difference in erosion rates

*Scored with values between 0 and 100, according to the NHI-RHRS

Based on the rating, suitable rockfall remedial measures are recommended and preliminary a cost estimate can be determined. It is noted that no recommendations on remedial action, depending on the hazard rating, are included in the RHRS system, since decisions on remedial action for a specific slope depend upon many factors such as the budget allocation for highway work, which cannot be taken into account in the ratings. However, literature data indicate that slopes with a rating of less than 300 can be considered as of very low priority while slopes with a rating greater than 500 are identified for urgent remedial action.

Pierson et al. (1993) proposed a slight modification of the initial RHRS known as the improved RHRS method (in this paper denoted as NHI-RHRS). This system allows scoring of parameters with values between 1 and 100, those marked with an asterisk (*) in Table 2. Using the full range of points instead of the set points, it allows greater flexibility in evaluating the relative impact of conditions that are extremely variable.

The NHI-RHRS was adapted to the requirements of the region of Tennessee and a new system was developed (in this paper denoted as TRHRS). The system focuses mainly on the geological characterization; by considering failure modes based on the standard failure mechanisms of rock slopes (Vanderwater et al., 2005).

Russell et al. (2008) proposed a modified RHRS method for Colorado region (in this paper denoted as CRHRS). This version of RHRS includes the categories shown in Table 3.

Moreover, equations were proposed from which the total hazard scores can be estimated from four of the RHRS parameters, depending on the slope type (Santi et al., 2009). Based on the total score and the geological character of the studied slope, the hazard level can be characterized as Low, Medium or High.

Singh (2004) developed a different approach in order to determine an index, known as Falling Rock Hazard Index (in this paper denoted as FRHI). The parameters taken into account and scored are the following: slope height, slope inclination, slope irregularities, rock condition, spacing of discontinuity, block size, volume of rockfall, excavation method and duration without remedy and rockfall frequency. The hazard level estimation is followed by the proposal of proper mitigation systems.

Saroglou et al. (2012) proposed a rating system, which is slightly based on the RHRS system, but it is not limited on roadway and railway slopes. It refers also to the effect of rockfalls on inhabited areas and estimates the hazard and the risk levels of a potential rockfall. This system involves 20,

appropriately weighted, parameters, grouped in categories according to the geometry of the slope, the geological conditions, the potential triggering mechanisms of the rock fall and the consequences of the hazard. Suggestions for support measures associated with the proposed risk rating assessment are also proposed in this system.

Table 3 – Rating Categories of the CRHRS.

Rating Categories				
Slope				
Slope Height	Rockfall Frequency	Average slope height	Launching features	Ditch Catchment
Climate				
Annual Precipitation	Annual freeze thaw cycles	Seepage/water	Slope aspect	
Geology				
Sedimentary Rock: (degree of undercutting, jar slake, degree of interbedding)	Crystalline Rock: (rock character, degree of overhang, weathering grade)	Discontinuities: (block size/volume, persistence/orientation, aperture, weathering condition, friction.	Block in matrix: (block size, block type, vegetation)	
Traffic*				
Sight Distance	Average vehicle Risk	Number of accidents		

*For rating the risk level

Abbruzzese et al. (2009) developed a methodology using 2D or 3D trajectory models based on Swiss case studies, in order to assess the hazard level. The hazard analysis is assessed by taking into account rock fall intensity, expressed by the total kinetic energy (translational and rotational) of the falling blocks, which is obtained by rock fall trajectory simulations and the return period, defined as the mean reference time within which a rock fall may occur (inverse of the mean rock fall frequency). According to a matrix diagram combining intensity and return period (shown in Figure 1), the rock fall hazard was classified into three levels: low, moderate, and high.

The methods described above are an indicative selection of the most important and widely applied hazard assessment methods. Depending on the special conditions of the rock slope that is analyzed, the user may find in the literature many different approaches that in some cases may be more appropriate and suitable for a particular case study.

3. Risk Assessment Methods

Many methods have been developed for the assessment of the level of risk of a rockfall.

A risk assessment method has been developed by the Washington State department of Transportation (WSDOT, 2010), (in this paper denoted as WSDOT system) in order to provide a methodology to rationally evaluate known unstable slopes. Following the same scoring principle of RHRS, 11 risk categories are scored with 3, 9, 27 or 81 (Huang et al., 2009). These categories include: the type of the problem that is evaluated (for Soil: cut or fill slope, erosion / settlement or piping / slow-moving landslides / rapid landslides or debris flows and for Rock: minor rockfall, good catchment / moderate rockfall, fair catchment / major rockfall, limited catchment, major

rockfall, no catchment), the average daily traffic, the decision site distance, the impact of failure on roadway, the average vehicle risk, the pavement damage, the failure frequency, the annual maintenance costs, the economic factor (detours distance) and the number of accidents in the last 10 years.

The Swiss Federal Roads Office – FEDRO, 2009, has developed another methodology for risk-based assessment, prevention and response to gravitational natural hazards on national roads. The methodology comprises of three parts:

1. Risk analysis – what could happen? This is made up of the hazard, exposure and consequence analysis.
2. Risk evaluation – what is allowed to happen?
3. Planning of measures – what needs to be done?

The risk analysis is broken down into the following steps:

1. Goals, system boundaries and preparatory work.
2. Hazard analysis: risk identification and impact analysis.
3. Exposure analysis.
4. Consequence analysis.
5. Risk calculation and representation.

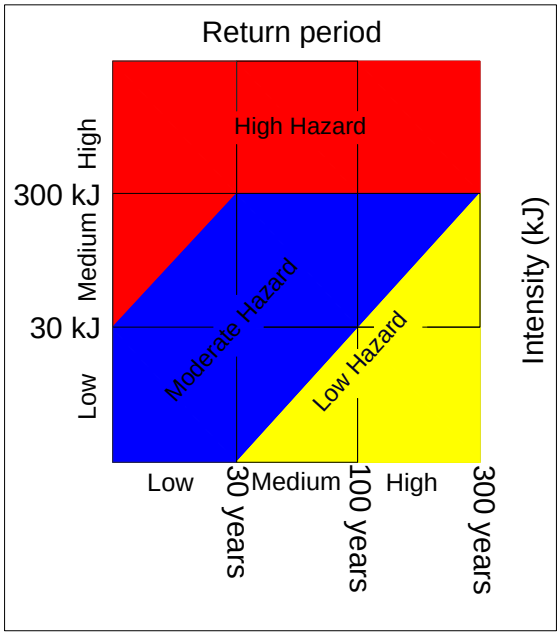

Figure 1 – Hazard level based on intensity – frequency diagram (Abbruzzese et al., 2009).

In FEDRO methodology, several different damage profiles can be assessed. These profiles are divided into direct and indirect damage. Direct damage refers to people that can be killed or injured as a result of a natural event and to endangered objects (e.g. buildings, infrastructure such as roads or railway tracks, power lines, pipes, green areas, etc.) that are buried, damaged or even destroyed by natural events. Indirect damage refers to the consequential damage, the costs resulting from interrupted operations or losses in earnings, damage to nature and the environment and objects to which an economic value cannot easily be assigned can also be affected, such as cultural objects that cannot be replaced either in full or in part when damaged.

Corominas et al. (2008) proposed a quantitative risk assessment method (in this paper denoted as QRA) in which the probability of occurrence of a rockfall is obtained by means of a statistical analysis of past events. While estimating risk in a quantitative manner, integration of the frequency analysis and the consequences is involved. The hazard frequency-magnitude relation has to be determined for the examined type of rockfall. The temporal spatial probability of vehicles and the vulnerability of the persons in the vehicles are calculated in order to estimate the risk. Therefore, the annual probability of the person at risk, which may lose his life by a rockfall event while driving on the road, can be determined.

4. Evaluating Hazard Assessment Methods

The RHRS method is the basis of the most hazard assessment methods. It is an approach that leads to an immediate and relatively user-friendly way of scoring the hazard level of the examined rock slope. In the scoring procedure, several critical parameters concerning the geological and the geometrical features are evaluated. The scoring system divides the influence of each parameter into four scoring areas (3, 9, 27, 81), following an exponential increase in the form of $y=3^x$. This results in an easier discrimination between slopes of low and high hazard level. However, the above separation impairs sensitivity analyzes, because if this analysis is performed over the whole scoring range of a parameter (3 to 81), it will lead to concrete results, the same as for any other parameter examined in the same scoring range. Finally, the scoring result is not interpreted and the hazard level is not categorized e.g. as high, medium or low.

The NHI-RHRS method is a slight variation of the initial RHRS method. A more detailed scoring system (range 1-100) is suggested on five main parameters, thus providing greater flexibility and greater accuracy to the rater, especially when performing sensitivity tests. However, if the level of uncertainty, when estimating a parameter, is high, the sensitivity test results will lead to a broader range between the minimum and the maximum level of hazard. Therefore, it is necessary that the user is trained and experienced enough, to avoid misjudgment.

The TRHRS method is also based on the initial RHRS, but the parameters' influence is differently weighted. The geological character is examined thoroughly by taking into account different kinds of failure modes, thus revealing the effect of the geology on the outbreak of a rockfall. However, in order to accurately rate a slope using this method, a thorough knowledge of the area is needed, which is translated to a sufficient amount of field data and monitoring systems.

The CRHRS method is a reliable and widely accepted method. As mentioned above, it is based on RHRS as well, but it is enriched with more parameters, concerning the slope's geometry, the climatic and the geological conditions. It also includes the four scoring areas (3, 9, 27, 81) with their respective advantages and disadvantages mentioned above. As for the geology, a distinction is made, depending on the rock type (sedimentary, crystalline structure, chaotic), thus enabling more targeted assessment on their characteristics. It requires a very good knowledge of the area to be rated, as it includes 19 scoring parameters. However, statistical analyses of large samples can lead to different weighting of each parameter and eventually some of them can be omitted. A main advantage of this method is that, depending on the geological character the final level of hazard can be divided to low, moderate or high, which helps the user to easily realize the level of hazard. The level of risk is also estimated using this method, however it is not as precise as that calculated from risk assessment methods but it is an indicative and convenient approach.

The Falling Rock Hazard Index (FRHI) was developed to determine the danger to workers and installations in the immediate vicinity of an excavated rock slope as a consequence of rock falls and therefore is not directly related to the hazard assessment of a rockfall at a road cut. Nevertheless, it is easily applicable and therefore can be used for a rapid forecast against rockfalls. The main feature that differentiates this method is that it includes the influence of the excavation method and therefore the disturbance of the rock mass, which leads to fragmentation and activation of rock falls.

The rockfall hazard and risk assessment method proposed by Saroglou et al. (2012) is based on morphological and structural criteria of rock mass and on vulnerability and consequences. It can be applied in any case and is not limited to road cuts. As it is not applicable only for road cuts, it is unable to estimate parameters such as the average daily traffic, the vehicle speed, the number of the passengers, etc. It includes many geological parameters that are to be evaluated, providing a fairly detailed assessment of the geological condition of the examined rock slope. This requires a thorough investigation of the area's geological conditions. The method introduces the influence of seismicity, since an earthquake is a triggering factor for a rockfall and needs to be taken into account when assessing the hazard and risk level in a seismic territory, like the Greek one. The method interprets its results in a qualitative way, providing direct information on the risk level.

The Swiss methodology that is based on 2D or 3D trajectory models is considered as a reliable tool when assessing the rockfall hazard level. It requires detailed topographic data as an input to the trajectory models and historical data in order to determine the return period. The method has set very low limits at the intensity of a rockfall, expressed as kinetic energy of falling rocks. Therefore, it could be concluded that it is not directly applicable, in its original form, for slopes with a significant height.

5. Evaluating Risk Assessment Methods

The WSDOT system is a risk assessment method that is based, as a concept, on the corresponding hazard assessment method of RHRS. The system evaluates four areas of scoring parameters, using the 3^x scoring system, with its respective advantages and disadvantages described earlier. A key element of this method is that it can be applied to both soil and rock slopes, thus providing a broad area of application. On the other hand, the method requires financial input data e.g. annual maintenance cost, which is a value that must be continuously adapted to the constantly changing financial environment, both considering the applied time period and the economic status of each country.

FEDRO methodology is considered in this paper as the most efficient method of probabilistic risk assessment. It is a highly detailed method and examines in detail the traffic conditions of the area, providing great adaptability on the special conditions of area under consideration. It is based on scenarios, such as the direct hit, collision, burial and availability scenario, thus allowing for almost all consequences of a rockfall incident. It enables risk assessment not only for people and vehicles, but for secondary facilities as well. Finally, the method takes into account the existence (or non-existence) of bypass roads and the traffic diversion through them, as it is a crucial parameter when calculating the consequences of a road been closed for remediation or restoration.

6. The Case of Tempi Gorge

The valley of Tempi is formed along a fault zone at a NE – SW direction, along Pinios River. The geological formations in the area are mainly crystalline limestones and locally phyllites. The natural terrain is developed at heights of 10 to 350m, with morphological gradients ranging from 20^o to 75^o. The national highway that connects Athens and Thessaloniki passes at an altitude of 13 to 50m, at the east steep road slopes, where unstable rock blocks with unfavourable orientation exist (Gazetas et al., 2010). During the period between 1997 and 2009, 31 rockfall incidents have been recorded approximately.

Two road sections have been studied in this area, assessing their level of hazard and risk, as an example: a) Section 1, at chainage 386+200 – 386+300 and b) Section 2, at chainage 387+060 – 387+160. The parameters used for the ratings are shown in Table 4.

For both sections, the hazard has been rated using methods RHRS, NHI-RHRS, CRHRS and the risk level has been assessed using QRA and FEDRO methodologies. In order to compare the hazard assessment methods, all hazard ratings were converted to % values.

It is noted, that, when using the FEDRO methodology, only the scenario of direct hit was calculated. For every method used, suitable sensitivity tests were performed in those parameters that considered as more critical, or of greater uncertainty.

The scoring results for hazard are presented in Figure 2 while the risk rating is presented in Table 5.

Table 4 – Parameters for risk rating in Tempi area.

Geology: thin bedded crystalline limestone, slightly weathered, with discontinuities of unfavorable orientation			
Annual Rainfall: 1800-2000mm			
Average daily traffic: 21500 vehicles, average speed: 70km/h			
Section 1		Section 2	
Slope height	90m	Slope height	55m
Average slope angle	60^o	Average slope angle	70^o
Road width	8.2m – no trench	Road width	10.4m – no trench
5 rockfall events in the past 13 years (maximum volume: $40m^3$)		6 rockfall events in the past 13 years (blocks of 1-$3m^{3)}$)	

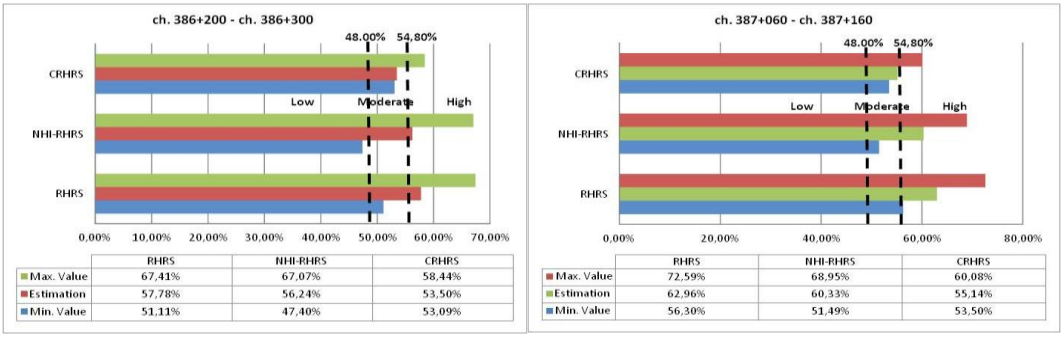

Figure 2 - Hazard rating results. The hazard level limits were set according to CRHRS method for crystalline rock type.

According to the rating results, the hazard level of Section 1 is determined as moderate (to high). Concerning the risk level, it is estimated that the possibility of a car hitting directly to a falling rock is 1.50×10^{-6} for a return period of 300 years and 1.60×10^{-7} for a return period of 10 years.

Respectively, the hazard level of Section 2 is estimated as high (to moderate). The possibility of a car hitting directly to a falling rock is estimated equal to 5.00×10^{-6} for a return period 300 years and 2.5×10^{-6} for a return period of 10 years.

In conclusion, the hazard level of both sections is high and a rock fall is possible to occur. On the other hand, the level of risk, when assuming that only the scenario of direct hit of a car on a falling rock might occur, is lower than the FEDRO's acceptable limits. Nevertheless, if more scenarios (collision, burial, availability) and the possibility of combined incidents are taken into account and calculated, then the level of risk will increase significantly.

Therefore, the appropriate mitigation measures should be applied in order to decrease both the hazard and the risk level of the studied area.

Table 5 – Risk rating results.

Method	Min. Value	Estimation	Max Value	Risk Level
Risk Assessment at Chainage 386+200 – 386+300				
FEDRO (Individual Risk)	Without 500 years scenario			High
	$1{,}04 \times 10^{-6}$	$1{,}49 \times 10^{-6}$	$2{,}09 \times 10^{-6}$	
	For 10 years			-
	$1{,}15 \times 10^{-7}$	$1{,}66 \times 10^{-7}$	$2{,}18 \times 10^{-7}$	
QRA	$4{,}00 \times 10^{-7}$	$5{,}71 \times 10^{-7}$	$8{,}00 \times 10^{-7}$	-
Risk Assessment at Chainage 387+060 – 387+160				
FEDRO (Individual Risk)	Without 500 years scenario			High
	$3{,}39 \times 10^{-6}$	$4{,}84 \times 10^{-6}$	$6{,}78 \times 10^{-6}$	
	For 10 years			-
	$1{,}68 \times 10^{-6}$	$2{,}40 \times 10^{-6}$	$3{,}36 \times 10^{-6}$	
QRA	$1{,}38 \times 10^{-7}$	$1{,}99 \times 10^{-7}$	$2{,}61 \times 10^{-7}$	-

Comparing the aforementioned hazard assessment methods, it is concluded that their results generally converge. According to the CRHRS method, hazard is underestimated in relation to the other two methods, but the difference between the minimum and maximum values is smaller, revealing the lower sensitivity of the method.

Concerning risk calculation, the risk level differentiates between methods at the two studied sections. The QRA method depends on the rockfall history, thus if insufficient rockfall data exist the result could be significantly different. In contrary, FEDRO's analytical risk rating overcomes the lack of precise rockfall records.

7. Conclusions

The significance of preventing rock falls, by taking proactive actions has led many researchers in developing methods to rate the hazard and the risk level of a rock slope.

The hazard assessment methods are mainly based on the RHRS system. Since its publication, many alternative methods have been developed, redefining the rated parameters in order to adjust in the special conditions of the area for which they were developed. The CRHRS method is considered as one of the most efficient methods, as it allows characterization of the hazard level and additionally results in a preliminary risk assessment. The hazard and risk assessment method proposed by Saroglou et. al. (2012), introduces the significance of the earthquake triggering effect on a rockfall, thus this method is more applicable when refering in seismic areas.

The risk assessment method that was developed by FEDRO Swiss authorities is considered as the most efficient when rating risk, due to the range of options available to approach the case study and the flexibility in adapting to the case study's conditions.

The main methods of assessing hazard and risk were used for two cross sections of the Tempi Gorge. The hazard level was determined as moderate and high respectively and the risk between 1.50 and 5.00×10^{-6} for a return period of 300 years and 1.60×10^{-7} and 2.5×10^{-6} for a return period of 10 years. The calculated levels of hazard and risk for the studied Sections denote the need for application of proper mitigation measures.

8. References

Abbruzzese J.M., Sauthier C. and Labiouse V. 2009. Considerations on Swiss methodologies for rock fall hazard mapping based on trajectory modeling, *Natural Hazards and Earth System Sciences (NHESS)*, 9, 1095-1109.

Corominas J. and Moya J. 2008. A review of assessing landslide frequency for hazard zoning purposes, *Engineering Geology*, 102, 193–213.

Federal Road Office (FEDRO) 2009. "Risk concept for natural hazards on national roads. Methodology for risk-based assessment, prevention and response to gravitative natural hazard on national roads", version 2009 V1.30, Confédération Suisse, ASTRA 89 001.

Gazetas G., Kavounidis S., Rozos D. and Tsiambaos G. 2010. Corollary Expert Committee for forfeitures in Tempi, *Technical Chamber of Greece*, (*in greek).*

Huang S., Darrow M. and Calvin P. 2009. Unstable Slope Management Program, Background Research and Program Inception, *Phase I Final Report*, Alaska Department of Transportation and Public Facilities, INE, Alaska.

Koukis G., Tsiambaos G. and Sabatakakis N. 1994. Slope movements in the Greek territory: A statistical approach, *Proc. of the 7th International Congress of the International Association of Engineering Geology*, Lisboa, Portugal, 7, 4621 – 4628.

Marinos P. and Rondoyanni Th. 2005. The archaeological Site of Delphi, Greece: a Site Vulnerable to Earthquakes, Rockfalls and Landslides, *Landslides*, 241-249.

Pantelidis L. 2009. Rock slope stability assessment through rock mass classification systems, *International Journal of Rock Mechanics & Mining Sciences*, 46, 315–325.

Pierson L. 1991. *The rockfall hazard rating system*. Oregon Department of Transportation.

Pierson L. and Vickle R. 1993. The rockfall hazard rating system. Participant's Manual. National Highway Institute, *NHI course No.130220*, FHWA SA-93-057.

Russell C., Santi P. and Higgins J. 2008. Modification and statistical analysis of the Colorado Rockfall hazard rating system, Colorado Department of Transportation, DTD applied research and innovation branch, *Report No. CDOT-2008-7*.

Santi M., Russell C., Higgins J. and Spriet J. 2009. Modification and statistical analysis of the Colorado Rockfall Hazard Rating System, *Engineering Geology*, 104, 55–65.

Saroglou H., Marinos V., Marinos P. and Tsiambaos G. 2012. Rockfall hazard and risk assessment: an example from a high promontory at the historical site of Monemvasia, Greece, *Natural Hazards and Earth System Sciences*, 12, 1823–1836.

Singh A. 2004. FRHI. A system to evaluate and mitigate Rockfall hazard in stable rock excavations, *IE (I) Journal.CV*, vol. 85.

Vanderwater C., Dunne W., Mauldon M., Drumm E. and Bateman V. 2005. Classifying and assessing the geologic contribution to Rockfall hazard, *Environmental & Engineering Geoscience*, XI, (2), 141-154.

Washington State department of Transportation (WSDOT) 2010. WSDOT's unstable slope management program.

Δελτίο της Ελληνικής Γεωλογικής Εταιρίας, τομ. XLVII , 2013
Πρακτικά 13ου Διεθνούς Συνεδρίου, Χανιά, Σεπτ. 2013

Bulletin of the Geological Society of Greece, vol. XLVII 2013
Proceedings of the 13th International Congress, Chania, Sept. 2013

THE INFLUENCE OF ROCKMASS PROPERTIES AT THE PLASTIC ZONE AROUND A CIRCULAR TUNNEL

Antoniou A.[1] and Spyropoulos I.[2]

[1] *National Technical University of Athens, School of Civil Engineering, Department of Geotechnics, andreasan19@yahoo.com,*

[2] *DOMI S.A.,14 Korgialeniou St.r., 115 21, Athens*

Abstract

Tunneling in weak rock has to be carefully designed since the overestimation of weak rock mass properties or the underestimated design and behaviour of the support system can lead to increased cost or even to failure. Based on the generalized Hoek-Brown failure criterion this paper presents relation between geometrical parameters (tunnel's radius, depth, etc) and rock's mass parameters (GSI, mi, etc) with the extension of plastic zone around a circular tunnel, as well as the wall displacement of an unsupported circular tunnel. All the analyses were executed considering hydrostatic stress field and isotropic behaviour of the surrounding rock mass.
Key words: *weak rock, unsupported tunnel, shallow tunnel.*

Περίληψη

Η μελέτη διάνοιξης σηράγγων σε ασθενείς βραχόμαζες χρειάζεται ιδιαίτερη προσοχή, αφενός γιατί μπορεί να γίνει υπερεκτίμηση των ιδιοτήτων της ασθενούς βραχόμαζας και αφετέρου μπορεί να γίνει υποεκτίμηση της συμπεριφοράς και του σχεδιασμού του συστήματος υποστήριξης οδηγώντας σε κάθε περίπτωση είτε σε αυξημένο κόστος κατασκευής είτε ακόμη και σε αστοχία. Βασιζόμενοι στο γενικευμένο κριτήριο αστοχίας των Hoek and Brown το άρθρο αυτό παρουσιάζει συσχετίσεις μεταξύ γεωμετρικών παραμέτρων όπως ακτίνα σήραγγας, βάθος σήραγγας κλπ, παραμέτρων βραχόμαζας, όπως GSI, m_i κλπ με την έκταση της πλαστικής ζώνης γύρω από μία κυκλική σήραγγα, όπως επίσης με τη μετακίνηση των τοιχωμάτων μίας ανεπένδυτης σήραγγας. Όλες οι αναλύσεις έγιναν λαμβάνοντας υπόψη υδροστατικό τασικό πεδίο και ισοτροπική συμπεριφορά της περιβάλλουσας βραχόμαζας.
Λέξεις κλειδιά: *Ασθενής βραχόμαζα, ανυποστήρικτη σήραγγα, αβαθής σήραγγα.*

1. Introduction

Understanding the failure mechanism of a rock mass surrounding an underground opening is necessary for the design of support systems for the openings. In any case this mechanism depends on the in situ stress level and the characteristics of the rock mass. Usually at shallow depths, where rock mass strength is controlled from weathering processes and is presented jointed the stability problems are related with wedge free falls or slides from the roof or side walls of the opening. As the depth below ground surface is increased, the in situ stresses increased and may reach a level at

which the failure of the rock mass is induced. In that case the failure can include spalling, slabing and rock burst.

An ideal condition could be excavation of an underground opening in unweathered massive rock mass paired together with low in situ stress, where the deformation is relatively low and the necessity of support is limited. Unfortunately this condition is not very common, especially in Greece due to the complexity of the geological environment, leading to a complex in situ stress field. On the other hand many tunnels have been constructed successfully in Greece the last two decades and their design for the temporary lining was based to finite element analysis.

Due to the size of tunnel openings in most infrastructures, the rock around the tunnel behaves more like a discontinuum. Behavior of a tunnel in a continuous material depends on the intrinsic strength and deformation properties of that material, leading to analytical modeling whereas behavior of a tunnel in a discontinuous material depends on the character and spacing of the discontinuities, leading to consider possible wedge movement or failure. Thus the behavior of the tunnel is a combination of a blocky medium and a continuum and only to soft rock or to a small tunnel in a massive rock, where the distance between joints is greater than tunnel's diameter the assumption of a continuous material can be used.

As the depth of a tunnel becomes greater or the ground conditions become unfavorable, the stress within the surrounding mass increases and failure occurs when the stress exceeds the strength of the rock mass. The failure type can be spalling, or slabbing or even a rock burst leading to significant rock volume's failure.

The analyses present herein through RocSupport computer program of RocScience, assume that the rock mass exhibits elastic-perfectly plastic failure, presents isotropic behavior and the in situ stress field constitutes from equal principle stresses. In case of non hydrostatic stress field, more complex rock masses, or other than circular tunnel, RocSupport can not predict the convergence and more sophisticated computer programs should be used, for example finite element analysis, since these simplifying assumptions mean that important bending moments and shear forces can be induced in the lining and these may result in premature failure of the support systems (Hoek, 2012).

2. Deformation Around an Advancing Tunnel, Definition of Failure Criterion and Tunnel Behaviour

The state of stress due to tunnel excavation can be calculated from analytical elastic closed form solutions. Kirsch's elastic closed form solution is one of the most commonly used analytical solutions, but can be applied to simple geometry tunnel and to limited stress field; thus its practical use is limited. However it is considered as a very practical tool to check results from numerical analysis. Figure 1 presents deformations ahead, on and behind tunnel face (Hoek, 1998a). Elastic deformation of the rock mass starts about two tunnel diameters ahead of the advancing face and reaches its maximum value at about two diameters behind the face, while at the tunnel's face position about one third of the total radial inward deformation of the tunnel has already occurred. The assumption that these deformations affect the stability of the tunnel depends on the ratio between the rock mass strength and the in situ applied stress.

Hoek (1998b) presented a very simple analytical model based on Mohr-Coulomb failure criterion, where a circular tunnel is subjected to a hydrostatic stress filed and is driven in a homogeneous rock mass which behaves as an elastic – perfectly plastic material, in which failure involving slip along intersecting discontinuities is assumed to occur with zero plastic volume change (Dancan-Fama, 1993).

According to this the plastic failure is defined by Mohr-Coulomb criterion and is expressed as:

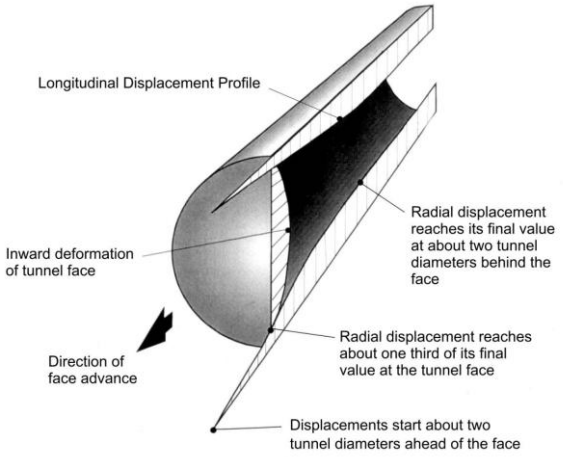

Figure 1 - Radial and longitudinal deformations ahead, on and behind tunnel's face (after Hoek, 1998a).

Equation 1 - Plastic failure defined by Mohr-Coulomb criterion

$$\sigma_1^{'} = \sigma_{cm} + k\sigma_3^{'}$$

where the uniaxial compressive strength of the rock mass σ_{cm} is calculated as:

Equation 2 - Uniaxial compressive strength of the rock mass

$$\sigma_{cm} = \frac{2c^{'} * \cos\phi}{1 - \sin\phi}$$

and k is expressed as

Equation 3 - Calculation formulae of parameter k

$$k = \frac{1 + \sin\phi}{1 - \sin\phi}$$

where σ_1' is the axial stress where failure occurs
σ_3' is the confining stress
c' is the cohesion
φ' is the friction angle of rock mass

According to Hoek (1998b) the surrounding rock mass of a circular tunnel of radius r_0 which is subjected to hydrostatic pressure p_0 and to uniform support pressure p_i will fail when the internal pressure p_i is less than the critical support p_{cr} defined by:

Equation 4 - Calculation of the critical support p_{cr}

$$p_{cr} = \frac{2 * p_0 - \sigma_{cm}}{1 + k}$$

If the internal support pressure p_i is greater than the critical support pressure $p_{cr,}$ no failure occurs, the behavior of the rock mass surrounding the tunnel is elastic and the inward radial elastic

displacement u_i of the tunnel wall is given by:

Equation 5 - Calculation of the inward radial elastic displacement u_i of the tunnel wall

$$u_i = \frac{r_0 * (1+v) * (p_0 - p_i)}{E_m}$$

where *Em* is the deformation modulus and
v is the Poisson's ratio.

In case where the internal support pressure p_i is less than the critical support pressure $p_{cr,}$ then failure occurs and the radius r_p of the plastic zone around the tunnel is given by:

Equation 6 - Calculation of the radius r_p of the plastic zone around the tunnel

$$r_p = r_0 \left[\frac{2 * \left(p_0 * (k-1) + \sigma_{cm} \right)}{(1+k) * (k-1) * p_i + \sigma_{cm}} \right]^{\frac{1}{k-1}}$$

and the inward radial plastic displacement u_i of the tunnel wall is given by:

Equation 7 - Calculation of the inward radial plastic displacement ui of the tunnel wall

$$u_i = \frac{r_0 * (1+v)}{E} \left[2 * (1-v) * (p_0 - p_{cr}) * \left(\frac{r_p}{r_0} \right)^2 - (1-2v) * (p_0 - p_i) \right]$$

3. Tunnel Deformation Analysis

3.1. Introduction

One of the major problems in rock is that of estimating the strength of the rock mass which usually comprises of an interlocking matrix of discrete but uneven blocks with various degrees of weathering, while the contact surfaces between the blocks may vary from clean and fresh to clay covered and slickensided. Determination of the strength of an in situ rock mass by laboratory testing is generally not practical; therefore this strength must be estimated from geological observations and from test results on individual rock pieces or rock surfaces which have been removed from the rock mass. The answer to this problem was given through the empirical failure criterion of Hoek and Brown (1980).

The most important component of the Hoek- Brown criterion is the process of reducing the material constants σ_{ci}, m_i and modulus of elasticity E, determined as “laboratory” values to appropriate in situ values. This is accomplished through the Geological Strength Index (GSI), which is a chart combined structural and surface conditions in order to detail the geological conditions existing in nature. Note that although Hoek and Brown criterion assume that the rock mass behaves isotropically, the behavior of the rock mass is usually controlled by movement and rotation of rock blocks separated by intersecting structural features such as discontinuities and joints. Hoek (1998a) used the - presented in the previous paragraph analytical model where a circular tunnel is subjected to a hydrostatic stress filed and is driven in a homogeneous rock mass which behaves as an elastic and perfectly plastic material - criterion and examined through a Monte Carlo analysis 2000 iterations for uniform distributions of a rock mass properties, tunnel

radius and in situ stress level in order to explore the concepts of rock support interaction. In his analyses the rock mass properties were varied from fair (*GSI* = 35) to extremely poor (*GSI* = 5), corresponding to the properties of weak sandstones and mudstones down to material that can almost be classified as soil, while Hoek and Kazurlovic (2000) in their analyses denote that the value of GSI equal to 25 refers to rock masses of good to reasonable quality. The in situ stresses ($p_{0)}$ were varied from 2 to 20 MPa, corresponding to depths below surface from 75 to 750 m, and the tunnel diameters were varied from 4 to 16 meters. The results of this analysis are presented through equations 8 and 9 which estimate the diameter of the zone of plastic failure (d_p) and the closure of the tunnel (δ_i) as ratios of in situ uniaxial rock mass strength to in situ stress and support pressures. Note that in these equations the in situ uniaxial rock mass strength is calculated by using equation 10.

Equation 8 - Tunnel deformation versus support pressure

$$\frac{\delta_i}{d_0} = \left(0.002 - 0.0025\frac{p_i}{p_0}\right)\frac{\sigma_{cm}}{p_0}^{(2.4\frac{p_i}{p_0}-2)}$$

Equation 9 - Size of plastic zone versus support pressure

$$\frac{d_p}{d_0} = \left(1.25 - 0.625\frac{p_i}{p_0}\right)\frac{\sigma_{cm}}{p_0}^{(\frac{p_i}{p_0}-0.57)}$$

δi = Tunnel sidewall deformation
do = Original tunnel radius in meters
pi = Internal support pressure
po = In situ stress = depth · unit weight of rock mass
σcm= Rock mass strength = $2c\cos\phi/(1-\sin\phi)$
dp = Plastic zone radius

Equation 10 - Calculation of the insitu uniaxial rock mass strength

$$\sigma_{cm} = \sigma_{ci} * 0.019 * e^{(0,05*GSI)}$$

In a later version of Hoek Brown failure criterion (Hoek et al, 2002) the in situ uniaxial rock mass strength is calculated by the following equation:

Equation 11 - Calculation of the in situ uniaxial rock mass strength

$$\sigma_c = \sigma_{ci} * s^{\alpha}$$

where:

Equation 12 - Calculation of the parameter s

$$s = e^{(\frac{GSI-100}{9-3D})}$$

Equation 13 - Calculation of the parameter α

$$\alpha = \frac{1}{2} + \frac{1}{6}(e^{-\frac{GSI}{15}} - e^{\frac{-20}{3}})$$

while D is a factor which depends upon the degree of disturbance to which the rock mass has been subjected by blast damage and stress relaxation.

3.2. Evaluation of the Parameters Used in the Analyses

Table 1 presents the values of parameters that were used in the presented hereinafter analyses. Wherever necessary the later version of Hoek Brown failure criterion was applied.

Table 1 - Parameters and their values that have been used in the analyses.

Parameter	Value	
Geological Strength Index (GSI)	5 - 45	
Strength of intact rock σ_{ci}(MPa)	5 - 20	
Material constant m_i	9 - 25	
Thickness of overburden (m) – In situ stress (MPa)	15 -135	0.405 – 3.605
Tunnel radius	3 - 10	

3.2.1 GSI

Marinos and Hoek (2000) denote that the petrographic characteristics of each rock do not allow all the possible combinations derived from the following chart to exist in a geological environment. For instance a limestone mass can not present less than "fair" conditions in its discontinuities and the same time a thin bedded rock can not present better structural conditions than "seamy". Having this remark in mind, Figure 2 presents the variation of GSI values used in our analyses (hatched area).

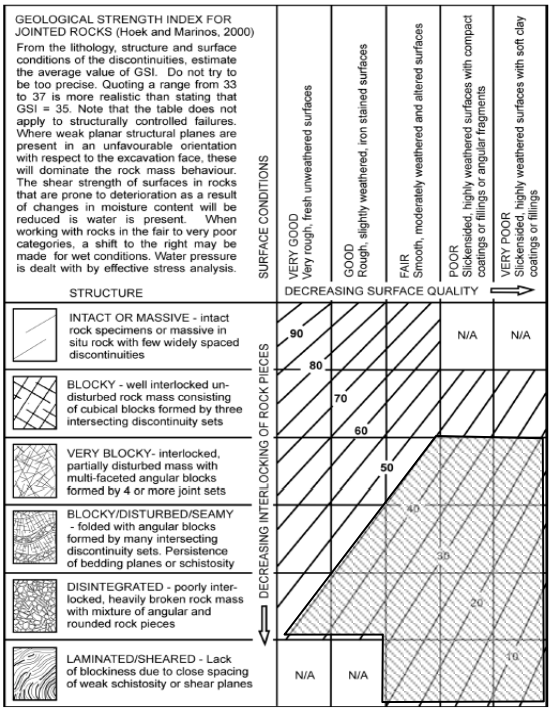

Figure 2 - Variation of GSI values' according to rock mass structure's and surface conditions of joints.

3.2.2 Strength of Intact Rock

Brown (1981) titled “very weak” and “weak” rock masses where their uniaxial compression strength varied from 5 to 25 MPa, while Hoek (2002) denoted that a rock mass is considered to be weak when its in situ uniaxial compressive strength is less than about one third of the in situ stress acting upon the rock mass through which the tunnel is being excavated. In the analyses presented hereinafter values between 5 and 20 MPa were used for the uniaxial compressive strength.

3.2.3 Strength of Intact Rock

Rocks such as shales, mudstones, siltstones, phyllites and tuffs are typical weak rocks in which even moderate in situ stresses are likely to induce failure in the rock surrounding underground excavations. Usually the uniaxial compressive strength and the material constant m_i are determined by laboratory testing or are estimated from published tables; the extraction of their values by statistical analysis of the results of a set of triaxial tests on carefully prepared core samples is highly preferred. Additionally, the m_i parameter depends upon the frictional characteristics of the component minerals in the intact rock sample and it has a significant influence on the strength characteristics of rock. The values for mi parameter were varied from 9 to 25, trying to refer to as many rock materials as possible.

3.3. Results - Conclusions

Taking into account the abovementioned remarks, the following figures present the results of the analyses. Table 2 present the calculated equation for convergence of an unsupported tunnel and radius of plastic zone for specific values of m_i, while Figures 3 and 4 show a remarkable change in the radius of the plastic zone and the closure of the tunnel when the ratio of in situ uniaxial rock mass strength to in situ stress falls below a critical level, while. As it can be seen from the diagrams for tunnels at great depths, the displacements and the plastic zone are significantly large. The demands on the support system may be such that it may be very difficult to support a large tunnel in poor ground at considerable depth below surface (Hoek, 1998a).

Table 2 - Convergence of an unsupported tunnel and radius of plastic zone for specific values of m_i.

m_i	Equation	R^2	Equation	R^2
9-25	$\frac{\delta_t}{D} = 0.007 * \frac{\sigma_{cm}}{p_0}^{-1.329}$	0.94	$\frac{r_p}{D} = 0.76 * \frac{\sigma_{cm}}{p_0}^{-0.38}$	0.75
9	$\frac{\delta_t}{D} = 0.007 * \frac{\sigma_{cm}}{p_0}^{-1.474}$	0.95	$\frac{r_p}{D} = 0.70 * \frac{\sigma_{cm}}{p_0}^{-0.53}$	0.86
13	$\frac{\delta_t}{D} = 0.007 * \frac{\sigma_{cm}}{p_0}^{-1.369}$	0.96	$\frac{r_p}{D} = 0.75 * \frac{\sigma_{cm}}{p_0}^{-0.41}$	0.86
17	$\frac{\delta_t}{D} = 0.007 * \frac{\sigma_{cm}}{p_0}^{-1.288}$	0.96	$\frac{r_p}{D} = 0.78 * \frac{\sigma_{cm}}{p_0}^{-0.34}$	0.85
25	$\frac{\delta_t}{D} = 0.007 * \frac{\sigma_{cm}}{p_0}^{-1.184}$	0.95	$\frac{r_p}{D} = 0.82 * \frac{\sigma_{cm}}{p_0}^{-0.26}$	0.85

Figures 5 to 7 present the closure of an unsupported tunnel related to uniaxial compressive strength σ_{ci}, tunnel's depth, GSI and m_i of the surrounded rock mass. The diagrams clearly depict that for tunnel's depth greater than 40m, GSI values less than 30 and low value of uniaxial compressive strength (σci = 5MPa), the convergence of the tunnel is significantly large, while the deformations present low values for all examined depths and especially for GSI values greater than

15 and values of uniaxial compressive strength greater than 10MPa.

Finally Figure 8 presents the radius of plastic zone of an unsupported tunnel related to tunnel's depth, GSI and m_i of the surrounded rock mass while uniaxial compressive strength σ_{ci}, is equal to 5 MPa. From the diagram is clearly depicted that for GSI values less than 15 and depths greater than 40m the radius of plastic zone is more than ten times tunnel's radius.

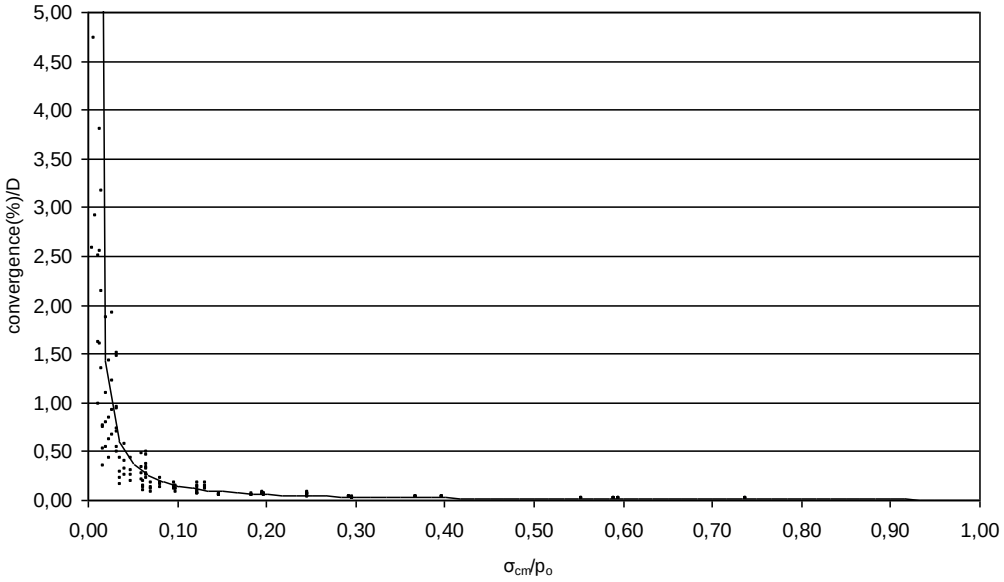

Figure 3 - Convergence of a tunnel versus ratio of in situ uniaxial rock mass strength to in situ stress.

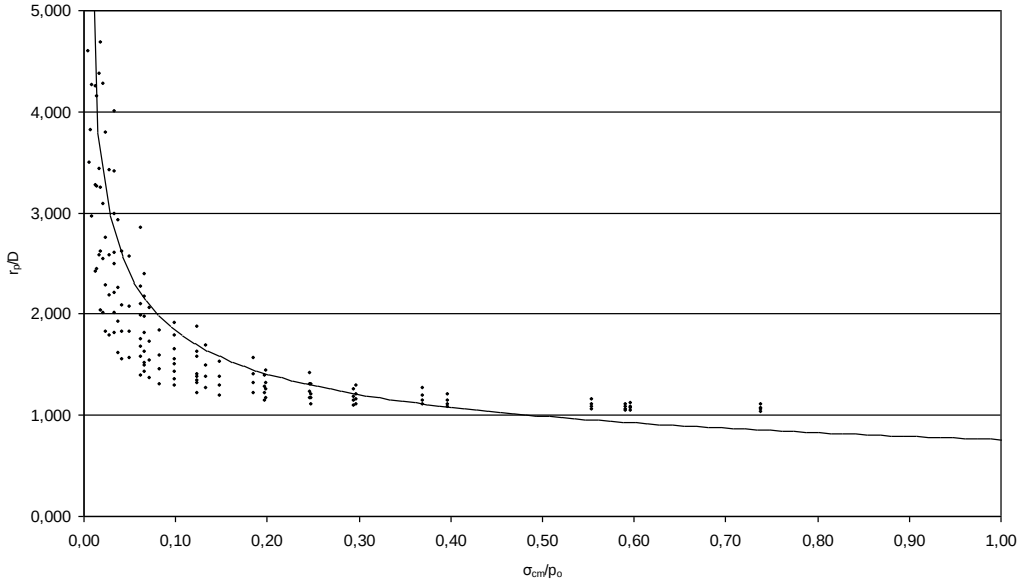

Figure 4 - Tunnel's radius versus ratio of in situ uniaxial rock mass strength to in situ stress.

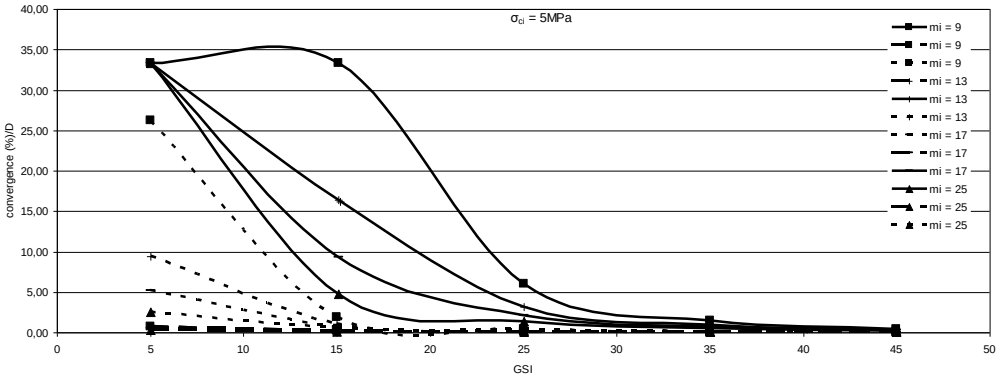

Figure 5 - Convergence of a tunnel versus GSI for various depths and m_i Uniaxial compressive strength equal to 5MPa.

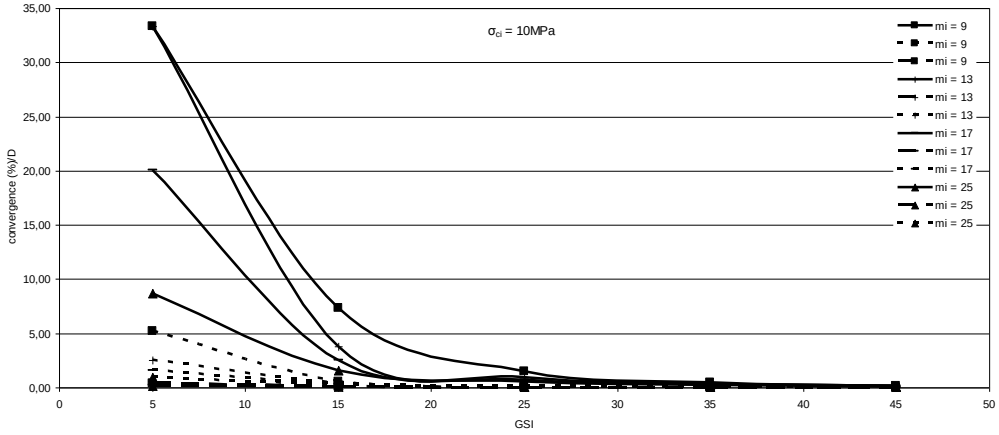

Figure 6 - Convergence of a tunnel versus GSI for various depths and m_i Uniaxial compressive strength equal to 10MPa.

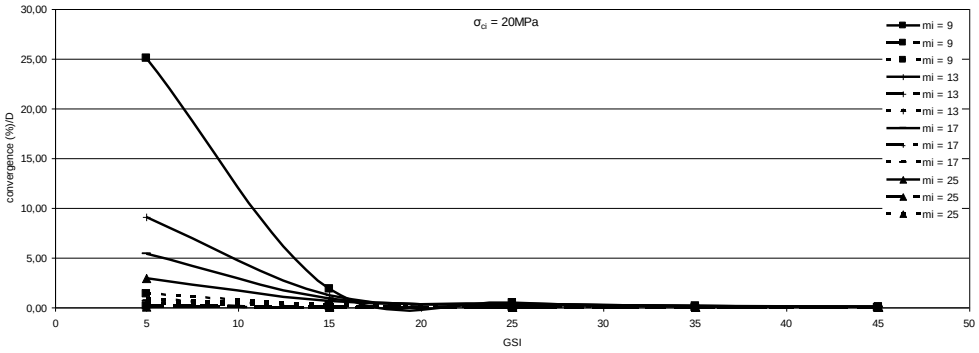

Figure 7 - Convergence of a tunnel versus GSI for various depths and m_i Uniaxial compressive strength equal to 20MPa.

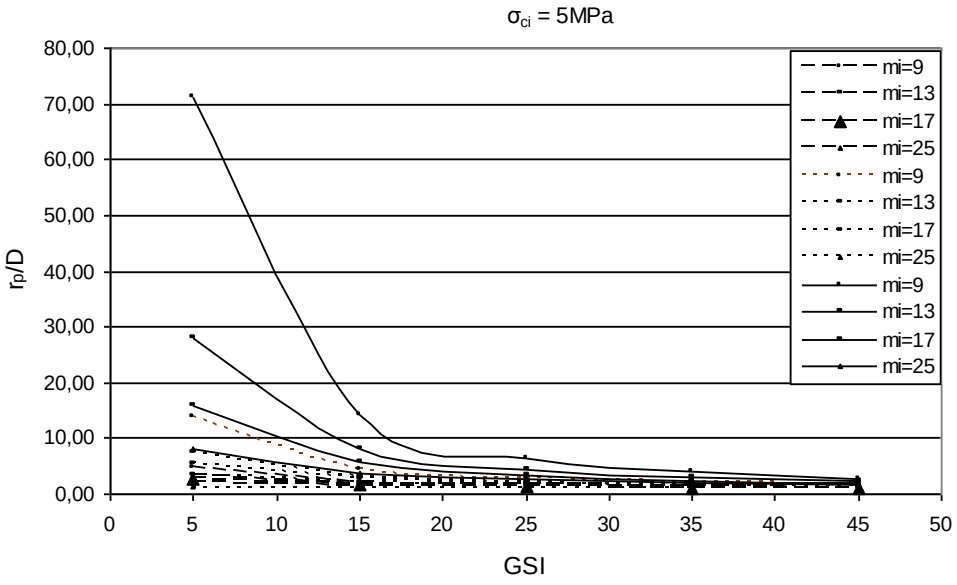

Figure 8 - Radius of plastic zone of an unsupported tunnel versus GSI for various depths and m_i Uniaxial compressive strength equal to 5MPa.

4. References

Brown E. T. 1981. *Rock characterization, testing and monitoring – ISRM suggested methods*. Pergamon, Oxford, pp 171–183.

Duncan-Fama M. E. 1993. Numerical modeling of yield zones in weak rocks. In Hudson, J. A., ed., *Comprehensive rock engineering*, 2, 49-75. Oxford: Pergamon Press.

Hoek E. 2012. Rock-Support Interaction analysis for tunnels in weak rock masses. Available online at: www.rocscience.com.

Hoek E. 1998a. Tunnel support in weak rock. Keynote address, *Symposium of Sedimentary Rock Engineering*, Taipei, Taiwan, November 20-22.

Hoek E. 1998b. Reliability of Hoek-Brown estimates of rock mass properties and their impact on design. Technical note, *Int. J. Rock Mech. Min. Sc*, 35(I), 63-68.

Hoek E. and Brown E. T. 1980. Empirical strength criterion for rock masses, *J. Geotech. Eng Div.*, ASCE 106 (GT9), 1013-1035.

Hoek E. Carranza-Torres C.T. and Corkum B. 2002. Hoek-Brown failure criterion – 2002 edition, *Proc. North American Rock Mechanics Society. M*eeting in Toronto in July.

Hoek E. and Karzulovic A. 2000. Rock mass properties for surface mines. In Hustralid, W., A., McCarter, M. K., and van Zyl, D. J. A. (eds). *Slope Stability in Surface Mining*, Colorado: Society for Mining, Metallurgical and Exploration (SME), Littleton, pp. 59-70.

Marinos P. and Hoek E. 2000 GSI—a geologically friendly tool for rock mass strength estimation, *Proc. of GeoEng2000 conference*, Melbourne, Australia.

Δελτίο της Ελληνικής Γεωλογικής Εταιρίας, τομ. XLVII , 2013
Πρακτικά 13ου Διεθνούς Συνεδρίου, Χανιά, Σεπτ. 2013

Bulletin of the Geological Society of Greece, vol. XLVII 2013
Proceedings of the 13th International Congress, Chania, Sept. 2013

ROCKFALLS: INFLUENCE OF ROCK HARDNESS ON THE TRAJECTORY OF FALLING ROCK BLOCKS

Asteriou P.[1], Saroglou H.[1] and Tsiambaos G.[1]

[1] *National Technical University of Athens, School of Civil Engineering, Geotechnical Department, paster@central.ntua.gr, saroglou@central.ntua.gr, gktsiamb@central.ntua.gr*

Abstract

Rockfalls pose significant hazard on human activities and infrastructure. The assessment of rockfall risk along roads and on other human activities is of great importance. Geological assessment can predict the outbreak of such events; explain the mechanism of occurrence and assist in the effective design of protection measures. The trajectory of a falling block is significantly affected by its response to the impact with the slope, since block kinematics properties mainly depend on the coefficient of restitution values. In this research a laboratory procedure based on the free fall of small blocks of different rock types and artificial materials was implemented in order to address the effect of their mechanical properties on the coefficient of restitution values. From the evaluation of testing results a correlation between kinematic coefficient of restitution and Schmidt rock hardness is proposed.
Key words: *Rockfalls, Coefficient of restitution, Laboratory testing.*

Περίληψη

Οι καταπτώσεις βράχων θέτουν σε σημαντικό κίνδυνο τις ανθρώπινες δραστηριότητες και τις υποδομές. Η εκτίμηση του κινδύνου αυτού κατά μήκος οδών και άλλων ανθρώπινων δραστηριοτήτων έχει ιδιαίτερη σημασία. Με κατάλληλη γεωλογική αξιολόγηση είναι δυνατόν να προβλεφθούν οι επισφαλείς θέσεις έναντι καταπτώσεων, να εξηγηθεί ο μηχανισμός ενεργοποίησης του φαινόμενου και να καταστεί αποτελεσματικότερος ο σχεδιασμός των μέτρων προστασίας. Η τροχιά ενός τεμάχους επηρεάζεται σημαντικά από την αλληλεπίδρασή του με το πρανές κατά την κρούση, όπου οι κινηματικές συνθήκες του τεμάχους μεταβάλλονται ανάλογα με τους συντελεστές αναπήδησης. Για την διερεύνηση των ιδιοτήτων των πετρωμάτων που επηρεάζουν τους συντελεστές αναπήδησης πραγματοποιήθηκε εργαστηριακή έρευνα που βασίζεται στην ελεύθερη πτώση τεμαχών διαφορετικών βραχωδών και τεχνητών υλικών. Από την εργαστηριακή διερεύνηση προτείνεται μια συσχέτιση του συντελεστή αναπήδησης με την σκληρότητα που προσδιορίζεται με τη σφύρα Schmidt.
Λέξεις κλειδιά: *Καταπτώσεις, Συντελεστής αναπήδησης, Εργαστηριακές δοκιμές.*

1. Introduction

Rockfalls pose a significant hazard on human activities and infrastructure. The geological structure of Greece favors such events; the mountainous terrain – steep topography in combination with the frequent occurrences of rock formations and the overall high seismicity create a significant

rockfall risk, as shown from recent events. Slope movements, which occur in the form of rockfalls, are the most frequent type in Greece, with a frequency of about 55% (Koukis et al., 1994).

A number of rockfalls have occurred in Greece in the recent years, i.e. Achaia, Lefkada, Skyros and others. The major rockfall event at Tempi in 2009 resulted in human loss and temporary closure of the Athens – Thessaloniki National road. Additionally, recent events with casualties occurred in Argos and Santorini, which all outline the significance of rockfall assessment and mitigation.

Two distinct stages constitute the rockfall phenomenon; the initial stage and the post-failure stage. The first describes the circumstances under which a block is detached from a slope. Rockfall intensity increases radically during periods of low temperature and high rainfall (Attewell et al., 1976). The post-failure stage describes the motion of the block along the rock slope. The study of the resulting block trajectory raises many uncertainties due to the number of parameters involved.

The outbreak of rockfalls can be predicted by geological hazard assessment. However, in order to quantify the risk, the exposure to the hazard must be determined. In a rockfall event the exposure is estimated based on the trajectory of the block. Additionally, the kinematic characteristics of the trajectory are the main parameters used for the design of remedial measures. Thus, the importance of a reliable trajectory analysis is crucial in order to address rockfall phenomena.

This paper presents part of the experimental research concerning rockfall trajectory modeling, currently held in the Engineering Geology – Rock Mechanics Laboratory of the School of Civil Engineering at the National Technical University of Athens. The response of a rock block impacting a rock slope is considered as the most important aspect. In relevant literature, this is connected to a qualitative characterization of the rock material, whereas in this research study a quantified approach is attempted.

2. Literature Review

2.1. Rockfall Trajectory Modeling

The trajectory of a block can be modelled as a combination of four movement types: free flight (or preferably aerial phase), rolling, sliding and bouncing (Descoeudres et al., 1987). The aerial phase is relatively easy to study; the general equations of motion for the block projectile describe adequately this part of the motion. Rolling and sliding are mainly controlled by the interaction of the block with the slope and they are affected from many parameters, among which are the friction angle, slope roughness, block shape. Bouncing is the most difficult part of the motion to predict, due to its complexity and its very limited understanding (Labiouse et al., 2009). The parameters, which influence the bouncing phenomenon, are summarized in Table 1.

Table 1 - Parameters assumed to influence the bouncing phenomena (Labiouse et al., 2009).

Slope characteristics	Block characteristics	Kinematics
Strength	Strength	Translational velocity
Stiffness	Stiffness	Rotational velocity
Roughness	Weight - Size	Collision angle
Inclination	Shape	Configuration of block at impact

Trajectory analysis is performed via computer simulation software, most commonly based on lumped mass model approach, in which the block is considered to be a point with a concentrated

mass. The most important input parameters, regarding block's trajectory, are the so-called coefficients of restitution, which describe the response of the block to an impact.

2.2. Coefficients of Restitution

In general, the coefficient of restitution (COR) is defined as the value representing the ratio of velocities (or impulses or energies; depending on the definition used) before and after an impact of two colliding entities. Theoretically, a COR that equals one corresponds to a perfect elastic collision, a COR value less than 1 defines an inelastic collision and a COR that equals zero is obtained when the object instantaneously stops at the surface area without bouncing, hence a perfectly plastic behavior (Goldsmith, 1960).

Various definitions on the coefficients of restitution have been proposed, such as the kinematic, kinetic or energy coefficients of restitution, but it seems that there is no consensus on which of them is more appropriate for rockfall trajectory prediction (Chau et al., 2002). The kinematic approach, which is derived from the inelastic collision of particles in the Newtonian mechanics, is the most commonly used due to its overall simplicity.

When the block comes in contact with the slope, its velocity changes according to the COR value. Hence, COR is assumed to be an overall value that takes into account all the characteristics of the impact; including deformation, sliding upon contact point, transformation of rotational moments into translational and vice versa, etc (Giani, 1992).

For an object impacting a steadfast surface the COR definition, known as kinematic coefficient of restitution (v_{COR}), is simplified as:

Equation 1 – Kinematic Coefficient of Restitution, v_{COR}

$$v_{COR} = \frac{v_r}{v_i}$$

where v_r and v_i are the magnitudes of the rebound and impact velocities of block, respectively. For an initial free-fall motion of the block, which impacts on a horizontal surface, equation 1 yields to:

Equation 2 – Kinematic Coefficient of Restitution, v_{COR}

$$v_{COR} = \sqrt{\frac{h_r}{h_d}}$$

where h_r is the maximum height gained after impact and h_d the block release height.

The most common definition is derived from the normal and tangential to the impact surface projections of the velocity vector. Hence, the normal (n_{COR} or Rn) and the tangential (t_{COR} or Rt) coefficients of restitution are defined as:

Equation 3 – Normal Coefficient of Restitution, n_{COR}

$$n_{COR} = \frac{v_{nr}}{v_{ni}}$$

Equation 4 – Tangential Coefficient of Restitution, t_{COR}

$$t_{COR} = \frac{v_{tr}}{v_{ti}}$$

where the first subscript, n or t denotes the normal or the tangential components of the velocity, and the second subscript i and r denote the impacting or the rebounding velocities respectively.

Typical values of these coefficients can be found in the literature, e.g. (Heidenreich, 2004) and (Richards et al., 2001), but these values depend on the slope and block material type and in some cases on the vegetation cover. This is considered an oversimplification, which can lead to miscalculations, since the response of a colliding block is controlled by many other parameters, as previously mentioned. A more accurate method for the estimation of the coefficient values is by performing back analysis on known rockfall trajectories and comparing with those determined in the laboratory (Saroglou et al., 2010).

2.3. Relevant Experimental Studies

Coefficients of restitution can be determined either by experimental studies or by back-analysis with computer simulations of the field evidences induced from natural rockfall events, such as the impact marks and run-out distances (Paronuzzi, 2009). Experimental studies are made either with the aid of physical models or with in situ testing (i.e. Spadari et al., 2012). In literature, little evidence from experimental research with physical models exists. Due to the randomness caused by the shape of the falling rock block, most researchers have used artificial materials, which could be easily formatted into spheres (Chau et al., 2002). Experimental research studies with natural rock materials and angular boulders are therefore limited.

A relevant study (Richards et al., 2001) was conducted with free fall drop tests on different rock types (basalt, diorite, gneiss, granite, limestone, marble, rhyolite, sandstone and schist), and also on debris and soil materials. The following correlation between the normal COR and the Schmidt hammer rebound hardness values (R) of both the block and the impacting surface, as well as the impact surface's angle (θ) was proposed.

Equation 5 – Correlation of Normal Coefficient of Restitution (n_{COR}) with Schmidt Hammer Rebound Hardness and slope inclination

$$n_{COR} = \frac{-110 + 9R_{slab} + 4R_{ball} + 4\theta}{1000}$$

where R_{slab} and R_{ball} are the Schmidt hammer rebound hardness values for the impact surface and the block respectively, and θ the angle of impact surface in degrees. The aforementioned correlation indicates that the hardness of the falling block affects less the normal COR value than the hardness of the impact surface. Furthermore, from Equation 5 it is observed that normal COR increases with the impact surface's angle

Asteriou et al. (2012), carried out an experimental physical model research study with cubical boulders from various rock types of the Greek territory (i.e. marble, schist, limestone, sandstone and marl), seeking the effect of Schmidt hardness coefficient on COR values. The following correlation was proposed:

Equation 6 – Correlation of Kinematic Coefficient of Restitution (v_{COR}) with Schmidt Hammer Rebound Hardness

$$v_{COR} = 0.235\exp(0.022R)$$

The experimental study presented hereafter is an extension of the previously mentioned study, concerning three more rock types and three artificial materials. Additionally, all materials were tested according to ISRM (2007), in order to examine the effect of the mechanical properties on COR values.

3. Laboratory Investigation

3.1. Experimental Setup

Almost cubic shaped rock specimens with smooth edges were used as colliding blocks (Figure 1a). The surface area, upon which the impact of the blocks occurred, was a smooth and planar plate with 5 cm thickness formed by the same material as the impacting block. The plate was embedded in plaster in order to obtain a square shape with 15 cm sides (Figure 1b), able to adjust in a massive dead weight base, ensuring the preservation of the momentum caused by the impact.

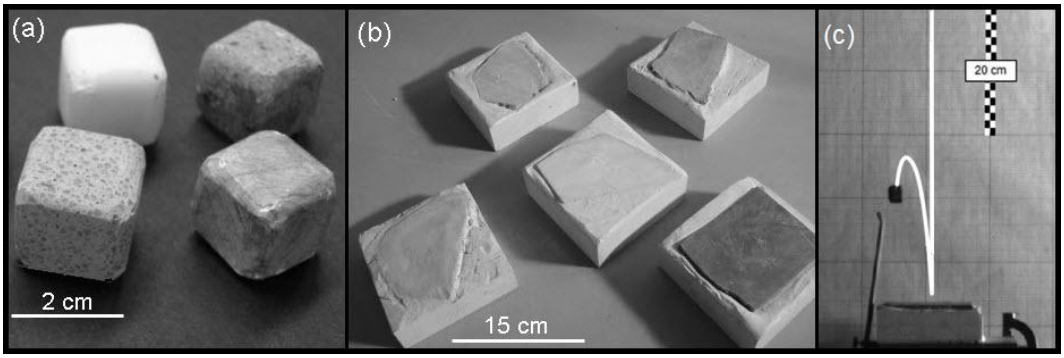

Figure 1 – Colliding blocks (a); impact surfaces (b); and recorded trajectory (c).

The release mechanism used for the tests constituted of an arm where the block was attached and held with suction produced by a vacuum pump. By switching the vacuum pump off, suction force reduces letting the block to a free fall drop from a height of 80 cm, developing only vertical translational velocity prior to impact.

The trajectory of the blocks (Figure 1c) was recorded with a digital high-speed video camera, at a capture speed of 250 fps and resolution of 640 x 480 pixels. The camera was fixed with its axis perpendicular to the trajectory plane XY, in order for the capture plan to be parallel to the trajectory plane leading to a two dimensional projection. The recorded video was then analyzed with an image analysis software, providing the coordinates x, y and the time of each frame. These data were processed by an Excel routine in order to determine the coefficients of restitution.

3.2. Materials

The rock types of blocks and impact surfaces tested were: marble, schist, green schist, crystalline limestone, limestone, quartz sandstone and marl. Two types of marble were tested; type I exhibiting a micro-sparitic, calcitic and granular texture and type II of a similar composition but with a micritic texture, both with an origin from the ancient quarries of Penteli Mountain. Schist is a calcitic mica-schist with well-developed schistosity, sampled from Hymettus Mountain. The green Schist has a pronounced schistosity and originates from Tempi area in central Greece. Crystalline limestone has a fine texture, sampled from Lavrion area, Attica. Limestone is a sparitic limestone, obtained from Tourkovounia hill in Athens. Sandstone is quartzitic, medium to coarse grained, grey-colored from Kalydona tunnel in western Greece. Marl is a limey one, obtained from Derveni area in the Northern Peloponnesian coast.

Three artificial materials were also tested: an epoxy resin grout, a high strength cement-based grout and a mixture of polyester with quartzitic sand. The use of artificial materials has two main advantages: first that different shapes can be easily achieved which allows the investigation of shape effect and second that their mechanical properties can be chosen in order to fulfill the requirement of similarity between laboratory and field tests. The purpose of using these artificial materials in the current study was to compare the properties between natural and artificial

materials, in order to be used in the aforementioned tasks which are part of the ongoing research currently held by the authors.

The physical and mechanical properties of the tested materials, which are summarized in Table 2, were determined according to ISRM suggested methods (ISRM, 2007). The following tests were performed: a) Ultrasonic test, B) Schmidt rebound hardness test (L-type), c) Uniaxial compression strength test with measurement of elastic properties, d) Indirect tensile strength test (Brazilian test). Diametrical and axial displacements, during the UCS tests, were measured by circumferential and dual axial extensometers.

Table 2 – Physical and Mechanical Properties of Tested Materials.

Material Type	ρ kN/m^3	$\sigma_{c(50)}$ MPa	E_t GPa	v	σ_t MPa	Vp m/s	Vs m/s	SHV
Marble I	25.2	66.1	40.2	0.261	6.2	4954	2861	38.2
Marble II	27.6	143.0	83.7	0.217	13.7	4130	2822	50.8
Schist	23.6	17.5	2.4	0.157	4.7	2208	1348	22.3
Green Schist	26.1	23.1	15.1	0.109	4.6	4439	2914	30.7
Crystalline limestone	25.6	52.9	40.8	0.124	6.6	6013	3322	36.7
Limestone	26.2	67.0	44.2	0.221	5.0	5828	3240	36.1
Sandstone	25.2	107.5	35.4	0.252	11.3	4606	2981	44.7
Marl	22.1	2.6	1.8	0.123	0.5	1733	1188	18.2
Epoxy Resin	20.4	86.5	11.0	0.377	15.6	4125	2429	42.3
Cement Grout	21.9	37.4	15.7	0.113	7.5	4335	2574	33.4
Polyester	16.9	90.2	5.2	0.451	20.5	3295	1675	41.8

3.3. Experimental Assumptions

According to the lumped-mass model, the angular velocity of falling rock block is not taken into account for the determination of COR values (Equations 1-4). Therefore, angular velocity was not measured in the performed tests. Additionally, the geometry of the falling block and its orientation during impact were not considered, even though both affect the trajectory. These parameters result in deviations from real rockfall conditions and they are not considered in the lumped-mass model, therefore COR values for blocks with random shapes are unreliable. However, modeling with the lumped-mass theory using those values is a common in rockfall engineering practice.

Theoretically, the rebound angle of a spherical object impacting on horizontal surface should be 90^o. However, due to the cubical shape of the blocks and their orientation at impact, the values of rebound angles have a wide range. When rebound deviates from the vertical direction, normal COR is underestimated since the energy dissipating in the horizontal direction becomes more significant. Hence, a number of tests were executed for each material but only the 25% of the impact tests with the least deviation from vertical direction were furthermore analyzed. Additionally, tangential COR, which could describe the horizontal energy dissipation, cannot be defined for a free fall motion (Equation 4), because the tangential velocity before impact is zero. However, normal and tangential COR of cubic blocks can be estimated from kinematic COR according to the proposed methodology by Asteriou et al. (2012).

4. Evaluation of Results

4.1. Comparison of Normal COR with Kinematic COR

The normal and kinematic COR were determined based on equations 1 and 3 using the data results from the performed tests. The relation between the ratio of normal to kinematic COR and the rebound angle is presented in Figure 2. As previously mentioned, when the block's rebound trajectory deviates from vertical direction, therefore when the rebound angle receives low values, the normal COR is underestimated. The data points (n=110) plotted represent the 25% of the tests for each material which show the least deviation.

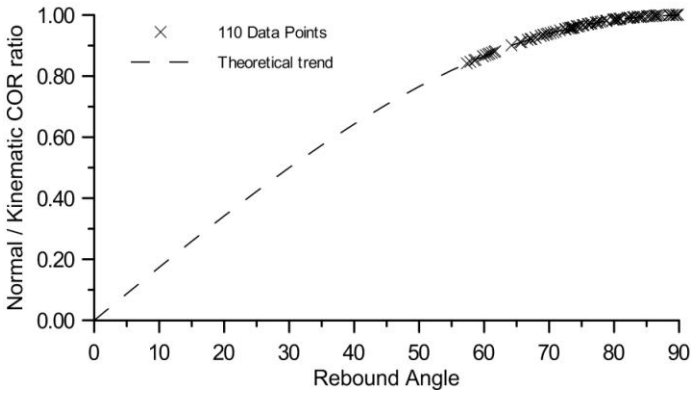

Figure 2 – Effect of rebound angle on the Normal/Kinematic COR ratio.

4.2. Applicability of COR Value Correlations with Physical-Mechanical Properties

Normal and kinematic COR values versus the Schmidt Hammer (SH) rebound hardness values are presented in Figure 3. It is observed that both coefficients values increase as the material hardness increases; which has been stated as a general rule in rockfall studies. From the present research data it is observed that the kinematic COR is more consistent compared to normal COR and thus its use is preferable when correlating with material properties. In Figure 3b, the probability boundaries at 75% and 100% are shown. The mathematical expressions defining these boundaries and their regression coefficients are also shown, denoting strong correlations.

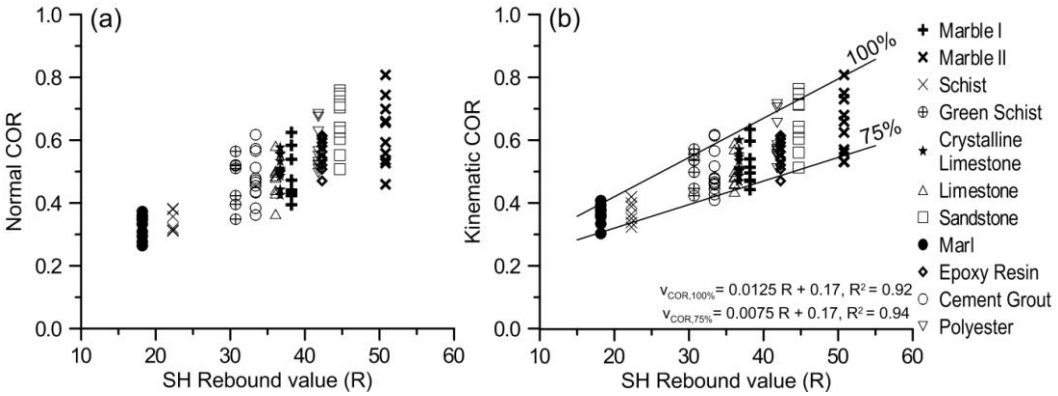

Figure 3 – Normal (a) and Kinematic (b) COR against Schmidt Hammer rebound hardness.

Kinematic COR values increase with increasing compressive and tensile strength as shown in Figure 4. Additionally, the probability boundaries for kinematic COR are also presented. However, in Figure 4b, these boundaries have been calculated without considering the tests held with polyester and epoxy resin samples (encircled values). These are not taken into account due to their

bulging behaviour, which results in high tensile strength, greater than the expected for rock materials.

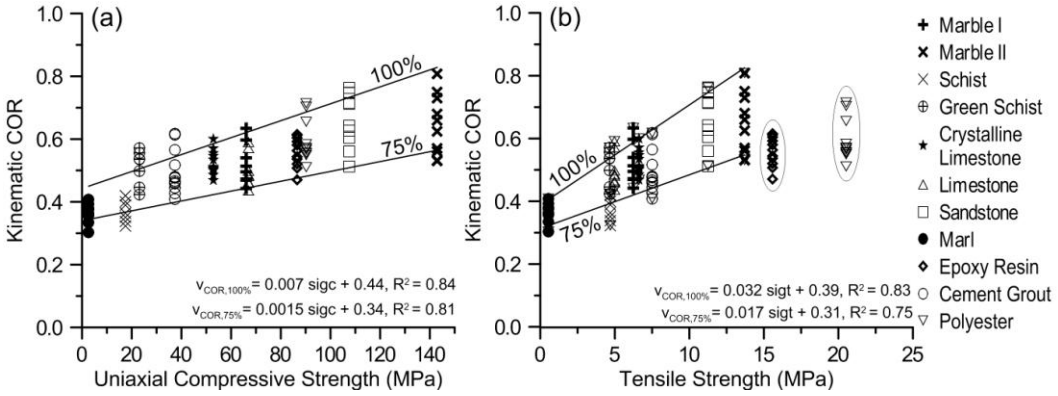

Figure 4 – Kinematic COR against compressive (a) and tensile (b) strength.

Tangent Young's modulus and Poisson's ratio were determined during uniaxial compression tests for all materials. Kinematic COR values against tangent Young's modulus are presented in Figure 5a. Although rebound is affected by the elastic properties of the colliding entities, which control the extent of plastic deformation during impact, a trend between Young's modulus and kinematic COR is not clearly expressed from the analysis of the testing data. Similarly, no trend was found with the Poisson's ratio.

Compression and shear wave velocities were also determined for all tested materials. As shown in Figure 5b quantitative correlation between Kinematic COR values and P-wave velocity is not applicable. This is also valid for the relation between kinematic COR and S-wave velocity.

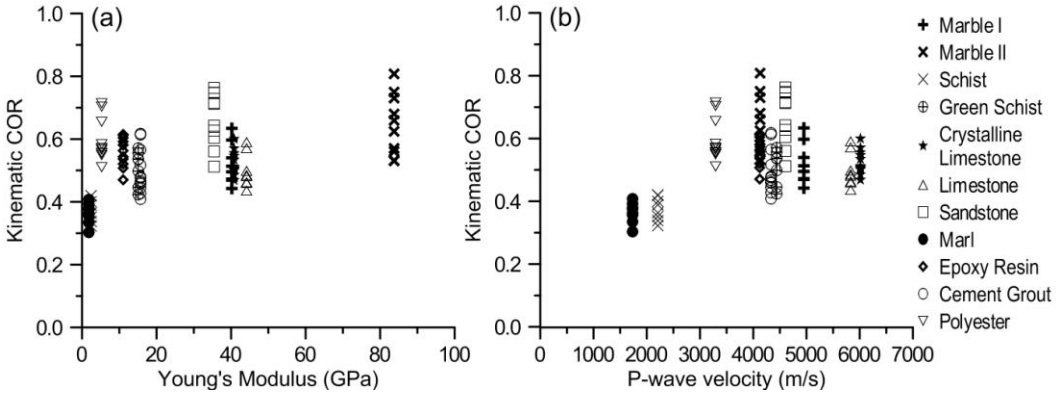

Figure 5 – Kinematic COR against tangent Young Modulus (a) and P-wave velocity (b).

5. Schmidt Hammer Correlation

As presented in section 4, the best correlation of kinematic COR is achieved with the Schmidt hammer rebound hardness value. This is anticipated since the operational principle of Schmidt hammer test is quite similar to the drop tests performed; Schmidt hammer measures the percentage of the energy which is recovered after an impact of a spring-loaded piston against a surface (Aydin, 2009).

The boundary lines shown in figure 3b allow a correlation of kinematic COR with rebound hardness for a chosen probability. The boundary corresponding to any chosen probability, in the range of 75% to 100%, can be calculated from the following equation.

Equation 7 – Probabilistic correlation of v_{COR} with Schmidt Hammer Rebound Hardness

$$v_{COR} = \left[0.0075 + \left(p - 75\right)0.0002\right]R + 0.17$$

Where p (%) is the probability of kinematic COR value to be less than the calculated value. This correlation is applicable for materials with Schmidt hardness greater than 15.

The additional data of v_{COR} values from present study are plotted in the same area defined in Asteriou et al. (2012). Furthermore, the testing results of this research present significantly higher values of kinematic COR compared to those acquired by the correlation proposed by Richards et al. (2001). This could be attributed to many reasons, the most important of which is that the impact energy level used in the aforementioned study was approximately 20 times higher than the one imposed in the present experiments. It is obvious that any increase of the impact energy results in less rebound due to the larger extent of plastic deformations within the colliding entities. Additionally, Richards et al. (2001) used normal COR which results in lower values than those of kinematic COR, as previously shown. However, even though the test conditions between these studies are different, the trend and rate of change of COR values against SH rebound hardness is quite similar. An indirect method to account the effect of the imposed energy level on COR values is presented in literature (Pfeiffer et al., 1989). According to this method, COR value is scaled by an empirical factor which depends on impact velocity and represents the transition from elastic to inelastic conditions as impact velocity increases.

6. Discussion and Conclusions

Rockfall phenomena pose a significant hazard on human activities, which are more pronounced in the Greek territory due to the high seismicity. Accurate rockfall modeling relies amongst other parameters on the determination of restitution coefficients of the geological formations involved. The aims of the present paper were to quantify the increase of the coefficient of restitution (COR) values with increasing hardness of different rock materials and to establish correlations between their physical and mechanical properties and COR values. For this purpose a number of rock materials (marble, schist, green schist, crystalline limestone, limestone, sandstone and marl) as well as artificial materials (epoxy resin, high strength cement grout and a polyester mixture) were selected and tested in the laboratory by performing mechanical properties tests and free fall tests.

Based on the results of the present study it was concluded that kinematic COR is more concise for use in correlations compared to the normal COR. Furthermore, the kinematic COR increases with increasing hardness and shows also an increasing trend with the uniaxial compressive strength and the tensile strength. It is evident according to the experimental results, that compressive and tensile strength can be used for the prediction of kinematic COR. However, the correlation between rock hardness and kinematic COR is preferable due to the simplicity of Schmidt hammer test and the better correlation achieved.

An equation for the probabilistic determination of kinematic COR relevant to Schmidt hammer rebound hardness is proposed. The portable, quick and inexpensive measurement of Schmidt hammer renders the proposed equation as a useful tool for the acquisition of rockfall analysis parameters.

7. References

Asteriou P., Saroglou H. and Tsiambaos G. 2012. Geotechnical and kinematic parameters affecting the coefficients of restitution for rock fall analysis, *Int. J. Rock Mech. Min. Sci.* 54, 103-113.

Attewell P. and Farmer I. 1976. *Principles of engineering geology*. London.

Aydin A. 2009. ISRM Suggested method for determination of the Schmidt hammer rebound hardness: Revised version, *Int. J. Rock Mech. Min. Sci.*, 46(3), 627-634.

Chau K.T., Wong R.H.C. and Wu J.J. 2002. Coefficient of restitution and rotational motions of rockfall impacts, *Int. J. Rock Mech. Min. Sci.*, 39(1), 69-77.

Descoeudres F. and Zimmermann T. 1987. Three-dimensional dynamic calculation of rockfalls, *Proc. 6th Congress Int. Soc. Rock Mech. Montreal*, Vol. 1, 337-342.

Giani G.P. 1992. *Rock Slope Stability Analysis*, Balkema.

Goldsmith W. 1960. *Impact: The theory and physical behavior of colliding solids*. Edward Alrnold, London.

Heidenreich B. 2004. Small- and half-scale experimental studies of rockfall impacts on sandy slopes, *PhD Thesis*, Lausanne.

ISRM 2007. The complete ISRM suggested methods for Rock characterization, testing and monitoring: 1974-2006. Ulusay R, Hudson JA (eds), Ankara.

Koukis G., Tsiambaos G. and Sabatakakis N. 1994. Slope movements in the Greek territory: A statistical approach, *Proc. of the 7th Int. Con. of IAEG*, Lisboa, 4621-4628.

Labiouse V. and Heidenreich B. 2009. Half-scale experimental study of rockfall impacts on sandy slopes, *Nat. Hazards Earth Syst. Sci.*, 9(6), 1981-1993.

Richards L.R., Peng B. and Bell D.H. 2001. Laboratory and field evaluation of the normal Coefficient of Restitution for rocks, *Proc. of ISRM Reg. Symp. EUROCK2001*, 149-155.

Paronuzzi P. 2009. Field evidence and kinematical back-analysis of block rebounds: The lavone rockfall, Northern Italy, *Rock Mech. Rock Eng.*, 42(5), 783-813.

Pfeiffer T.J. and Bowen T.D. 1989. Computer simulation of rockfalls, *Bull. of Assoc. of Eng. Geol*., 26(1), 135-146.

Saroglou H., Mpekri E. and Tsiambaos G. 2010. Determination of critical geotechnical parameters of geological formations for the modeling of rockfalls in slopes, *6th Hellenic Conf. of Geotech. & Geoenv. Eng.*, Volos. Vol. 2, 43-50.

Spadari M., Giacomini A., Buzzi O., Fityus S. and Giani, G. P. 2012. In situ rockfall testing in New South Wales, Australia, *Int. J. Rock Mech. Min. Sci.*, 49, 84-93.

Δελτίο της Ελληνικής Γεωλογικής Εταιρίας, τομ. XLVII , 2013
Πρακτικά 13ου Διεθνούς Συνεδρίου, Χανιά, Σεπτ. 2013

Bulletin of the Geological Society of Greece, vol. XLVII 2013
Proceedings of the 13th International Congress, Chania, Sept. 2013

ROCK MASS BLASTABILITY DEPENDENCE ON ROCK MASS QUALITY

Chatziangelou M.[1] and Christaras B.[2]

[1] *Department of Civil Infrastructure Engineering, School of Technological Applications of Thessaloniki, Greece, mcha@geo.auth.gr*

[2]*Department of Geology, Aristotle University of Thessaloniki, Greece, christar@geo.auth.gr, tel./fax. +3023198506, mobile: +306944332554*

Abstract

The present paper tries to investigate the influence of rock mass quality characteristics on blasting results. In order to come to some conclusions, blastability and quality of rock mass were put together using the already known classification systems. Taking into account the quantity of blastability index (BI) for every possible structural appearance of the poor rock mass, the relation of discontinuities characteristics and blastability index are investigated. The estimations of the above trial gave arise on a new classification system being called "Blastability Quality System (BQS)", which can be an easily and wide use tool as it is a quickly calculator for blastability index (BI) and rock mass quality.
Key words: *Blastability, rock mass, quality, classification.*

Περίληψη

Η παρούσα εργασία προσπαθεί να εκτιμήσει την επίδραση των χαρακτηριστικών της ποιότητας της βραχομάζας στα αποτελέσματα ανατίναξης για την εκσκαφή βραχωδών σχηματισμών. Με σκοπό την εκτίμηση αυτή, η δυνατότητα ανατίναξης και η ποιότητα βραχομάζας συνδέονται αξιοποιώντας τα ήδη γνωστά συστήματα ταξινόμησης. Λαμβάνοντας υπόψη την τιμή του Δείκτη Δυνατότητας ανατίναξης (BI) για κάθε περίπτωση φτωχής ποιότητας βραχομάζας, μπορεί να εκτιμηθεί η σχέση των χαρακτηριστικών των ασυνεχειών και του Δείκτη Δυνατότητας Ανατίναξης (BI). Με αυτά τα στοιχεία δημιουργούμε ένα νέο σύστημα ταξινόμησης που ονομάζεται «Σύστημα Δείκτη Ανατίναξης και Ποιότητας βραχομάζας (BQS)», το οποίο μπορεί να χρησιμοποιηθεί εύκολα και να αποτελέσει εργαλείο για τον συνδυασμό του Δείκτη Δυνατότητας Ανατίναξης (BI) και της ποιότητας της βραχομάζας.
Λέξεις κλειδιά: *Σήραγγες, εκσκαφής, ανατίναξη, συστήματα ταξινόμησης.*

1. Introduction

Many rock mass quality classification systems –RQD (Deere, 1989), Q (Barton et al, 1980), RMR (Bieniawski, 1989), GSI - have been developed for drilling and excavation ability estimation, but not for blasting calculations (Jimeno et al, 1995). The several rock types of rock mass, which are affected by numerous stages of alteration in varying stress conditions, may be explored in a

different manner under specified blast design, explosive characteristics and specified legislative constraints depending on structural characteristics.

The present paper investigates the influence of rock mass quality characteristics on blasting results. Rock blastability (Kaushik & Phalguni, 2003, Murthy et al, 2003) is quantified using the blastability index, which is calculated based on geotechnical characteristics. Rock mass quality can also be estimated using the already known classification systems. The relation between discontinuity characteristics and blastability index for every possible structural appearance of the poor rock mass is estimated. The above estimations can be used in a new classification system called "Blastability Quality System (BQS)".

The rock mass in this study is poor and friable, shared with lack of blockiness due to close spacing of weak schistosity or sheer planes and disintegrated with poorly interlocked, heavily broken rock mass with mixture of angular and rounded rock pieces (Hoek et al, 1998). Although the quality is very poor, a light blast may be needed as the small rock pieces are tightly connected.

2. Connecting Blast Ability and Quality Ability

The laminated and sheared rock mass, with lack of blockiness due to the close spacing of weak schistosity or sheer planes and disintegrated rock mass, with poorly interlocked, heavily broken rock with mixture of angular and rounded rock pieces, which are described by the lower part of the GSI diagram (Hoek, 1983, Hoek & Brown, 1997, Marinos and Hoek, 2000) , is divided into eight parts (Fig.1); A - GSI about 0-12, B – GSI about 12-23, C – GSI about 22-23, D – GSI 7-17, E – GSI about 18-28, F – GSI about 16-36, G – GSI 35-43, H - GSI 42-50.

Table 1 – Specific gravity influence (SGI).

SGI	**specific gravity of rock (t/m^3)**
25*specific gravity of rock (t/m^3)-50	
-22,5	1,1
-20	1,2
-17,5	1,3
-15	1,4
-12,5	1,5
-10	1,6
-7,5	1,7
-5	1,8
-2,5	1,9
0	2
2,5	2,1
5	2,2
7,5	2,3
10	2,4
12,5	2,5
15	2,6
17,5	2,7
20	2,8
22,5	2,9
25	3

Taking into account the parameters of the Blastability Index (Scott, 1996) (BI = 0.5 x (RMD+JPS+JPO+SGI+H) (Lilly, 1986), the Blastability Index (BI) is calculated for every possible combination of the above parameters, which refers to powdery/friable rock mass. That means RMD (rock mass description) is equal to 10 (powdery / friable rock mass). JPS (joint plan spacing) is used equal to 10 for closely spacing, 20 for intermediate spacing and 50 for widely spacing. JPO (joint plane orientation) is used equal to 10 for horizontal discontinuities, 20 for inclined discontinuities where the excavation drives against dip direction, 30 for inclined discontinuities with strike parallel to face, 40 for declined discontinuities where the excavation drives with dip direction. SGI (specific gravity influence) is calculated using specific gravity of rocks (t/m^3) (table 1). 2400 different rock mass combinations are estimated (tables 2, 3, 4).

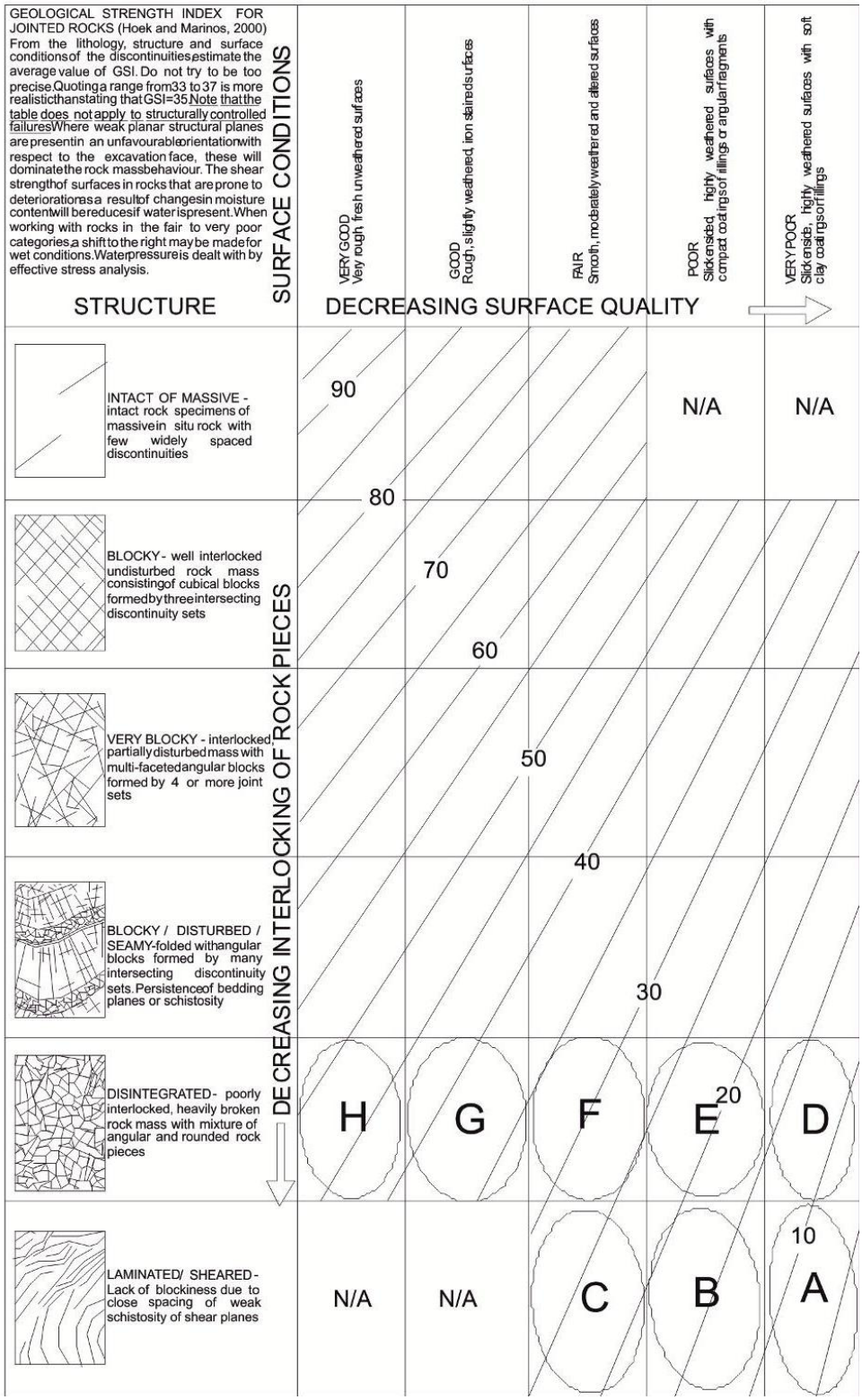

Figure 1 – Eight part division of GSI diagram.

The blastability index, of a rock mass with closely spaced discontinuities is calculated as shown in table 2. The blastability index, of a rock mass with intermediate spaced discontinuities, is calculated in table 3. The blastability index, of a rock mass with widely spaced discontinuities, is calculated in table 4. The parameters of BI calculation are also presented in the above tables, where the different rock mass types are numbered from 1 to 2400.

Subsequently, the above rock structures are grouped according to RMR range and GSI parts, taking into account rock mass hardness a well as discontinuities' spacing and orientation. Additionally, the calculation of the range of BI is presented in tables 5, 6, 7, 8, 9, 10, 11, 12. GSI range is calculated, in tables 5,6,7,8, for every rock mass type with a specific RMR. The different types of rock mass are also numbered from 1 to 2400 and they are grouped together according to RMR range. In the same tables, GSI parts are equivalent to RMR range. Actually, 90000 rock mass types are investigated. In tables 9, 10, 11, 12 the blastability index is appeared for the above grouped rock masses in addition to the GSI parts. In the same tables the RMR range is equivalent to the GSI parts.

Table 2 – BI calculations for closely spacing discontinuities.

A/A	RMD	JPS	JPO	SGI	H	BI	A/A	RMD	JPS	JPO	SGI	H	BI
001-20	10	10	10	from -22,5 to 25	1	4,25-28	401-420	10	10	30	from -22,5 to 25	1	14,25-38
21-40	10	10	10	from -22,5 to 25	2	4,75-28,5	421-440	10	10	30	from -22,5 to 25	2	14,75-38,5
41-60	10	10	10	from -22,5 to 25	3	5,25-29	441-460	10	10	30	from -22,5 to 25	3	15,25-39
61-80	10	10	10	from -22,5 to 25	4	5,75-29,5	461-480	10	10	30	from -22,5 to 25	4	15,75-39,5
81-100	10	10	10	from -22,5 to 25	5	6,25-30	481-500	10	10	30	from -22,5 to 25	5	16,25-40
101-120	10	10	10	from -22,5 to 25	6	6,75-30,5	501-520	10	10	30	from -22,5 to 25	6	16,75-40,5
121-140	10	10	10	from -22,5 to 25	7	7,25-31	521-540	10	10	30	from -22,5 to 25	7	17,25-41
141-160	10	10	10	from -22,5 to 25	8	7,75-31,5	541-560	10	10	30	from -22,5 to 25	8	17,75-41,5
161-180	10	10	10	from -22,5 to 25	9	8,25-32	561-580	10	10	30	from -22,5 to 25	9	18,25-42
181-200	10	10	10	from -22,5 to 25	10	8,75-32,5	581-600	10	10	30	from -22,5 to 25	10	18,75-42,5
201-220	10	10	20	from -22,5 to 25	1	9,25-33	601-620	10	10	40	from -22,5 to 25	1	19,25-43
221-240	10	10	20	from -22,5 to 25	2	9,75-33,5	621-640	10	10	40	from -22,5 to 25	2	19,75-43,5
241-260	10	10	20	from -22,5 to 25	3	10,25-34	641-660	10	10	40	from -22,5 to 25	3	20,25-44
261-280	10	10	20	from -22,5 to 25	4	10,75-34,5	661-680	10	10	40	from -22,5 to 25	4	20,75-44,5
281-300	10	10	20	from -22,5 to 25	5	11,25-35	681-700	10	10	40	from -22,5 to 25	5	21,25-45
301-320	10	10	20	from -22,5 to 25	6	11,75-35,5	701-720	10	10	40	from -22,5 to 25	6	21,75-45,5
321-340	10	10	20	from -22,5 to 25	7	12,25-36	721-740	10	10	40	from -22,5 to 25	7	22,25-46
341-360	10	10	20	from -22,5 to 25	8	12,75-36,5	741-760	10	10	40	from -22,5 to 25	8	22,75-46,5
361-380	10	10	20	from -22,5 to 25	9	13,25-37	761-780	10	10	40	from -22,5 to 25	9	23,25-47
381-400	10	10	20	from -22,5 to 25	10	13,75-37,5	781-800	10	10	40	from -22,5 to 25	10	23,75-47,5

Finally, three useful diagrams, of composite rock mass quality and range of Blastability Index (BI), derive from the above estimations (Fig. 2-4). Figure 2 refers to rock mass with close spaced discontinuities. The above rock planes may strike parallel or perpendicular to tunnel axis. The underlying rock, which strike parallel to tunnel axis, may be extremely soft of medium hard or hard and very hard. The blastability index is calculated to be between 14 and 41 for the first case and between 17 and 42 for the second case. Taking into account the surface conditions and the structure of the rock mass, we can estimate the GSI and RMR range. Furthermore, the underlying rock, which strikes perpendicular to tunnel axis, may consist only of gradient discontinuities, when the tunnel drives with dip direction, or consist of gradient and perpendicular discontinuities, when the tunnel drives against dip direction. The blastability index is calculated to be between 19 and 47 for the first case and between 4 and 37 for the second case. Taking into account the surface conditions and the structure of the rock mass, we can estimate the GSI (Hoek., 1994) and RMR range.

Figure 3 refers to rock mass with intermediate spaced discontinuities (Deere and Deere, 1988). The rock mass may consist of horizontal or gradient discontinuities. In case there are only horizontal discontinuities, the rock mass may be extremely soft to soft or medium hard to very hard. The blastability index is calculated between 9 and 34 for the first case and between 11 and 37 for the second case. In case of gradient discontinuities, the rock mass may strike perpendicular to tunnel axis when excavation drives against dip direction, the rock mass may strike perpendicular to tunnel axis when excavation drives with dip direction, and the rock mass may strike parallel to tunnel axis. Where the rock mass strikes perpendicular to tunnel axis, when

excavation drives against dip direction, the rock mass may be extremely soft to medium hard or hard and very hard. The blastability index is calculated between 14 and 46 for the first case and between 17 and 47 for the second case. Where the rock mass strikes perpendicular to tunnel axis, and excavation drives with dip direction, the blastability index is calculated to be between 24 and 52. Where the underling rock strikes parallel to tunnel axis, the rock mass may be medium hard, or extremely soft to soft. The blastability index is calculated to be between 14 and 46 for the first case and between 19 and 44 for the second case. Taking into account the surface conditions and the structure of the rock mass, we can estimate the GSI and RMR range.

Table 3 – BI calculations for intermediating spacing discontinuities.

A/A	RMD	JPS	JPO	SGI	H	BI	A/A	RMD	JPS	JPO	SGI	H	BI
801-820	10	20	10	from -22,5 to 25	1	9,25-33	1201-1220	10	20	30	from -22,5 to 25	1	19,25-43
821-839	10	20	10	from -22,5 to 25	2	9,75-33,5	1221-1239	10	20	30	from -22,5 to 25	2	19,75-43,5
841-860	10	20	10	from -22,5 to 25	3	10,25-34	1241-1260	10	20	30	from -22,5 to 25	3	20,25-44
861-880	10	20	10	from -22,5 to 25	4	10,75-34,5	1261-1280	10	20	30	from -22,5 to 25	4	20,75-44,5
881-900	10	20	10	from -22,5 to 25	5	11,25-35	1281-1300	10	20	30	from -22,5 to 25	5	21,25-45
901-920	10	20	10	from -22,5 to 25	6	11,75-35,5	1301-1320	10	20	30	from -22,5 to 25	6	21,75-45,5
921-940	10	20	10	from -22,5 to 25	7	12,25-36	1321-1340	10	20	30	from -22,5 to 25	7	22,25-46
941-960	10	20	10	from -22,5 to 25	8	12,75-36,5	1341-1360	10	20	30	from -22,5 to 25	8	22,75-46,5
961-980	10	20	10	from -22,5 to 25	9	13,25-37	1361-1380	10	20	30	from -22,5 to 25	9	23,25-47
981-1000	10	20	10	from -22,5 to 25	10	13,75-37,5	1381-1400	10	20	30	from -22,5 to 25	10	23,75-47,5
1001-1020	10	20	20	from -22,5 to 25	1	14,25-38	1401-1420	10	20	40	from -22,5 to 25	1	24,25-48
1021-1039	10	20	20	from -22,5 to 25	2	14,75-38,5	1421-1439	10	20	40	from -22,5 to 25	2	24,75-48,5
1041-1060	10	20	20	from -22,5 to 25	3	15,25-39	1441-1460	10	20	40	from -22,5 to 25	3	25,25-49
1061-1080	10	20	20	from -22,5 to 25	4	15,75-39,5	1461-1480	10	20	40	from -22,5 to 25	4	25,75-49,5
1081-1100	10	20	20	from -22,5 to 25	5	16,25-40	1481-1500	10	20	40	from -22,5 to 25	5	26,25-50
1101-1120	10	20	20	from -22,5 to 25	6	16,75-40,5	1501-1520	10	20	40	from -22,5 to 25	6	26,75-50,5
1121-1140	10	20	20	from -22,5 to 25	7	17,25-41	1521-1540	10	20	40	from -22,5 to 25	7	27,25-51
1141-1160	10	20	20	from -22,5 to 25	8	17,75-41,5	1541-1560	10	20	40	from -22,5 to 25	8	27,75-51,5
1161-1180	10	20	20	from -22,5 to 25	9	18,25-42	1561-1580	10	20	40	from -22,5 to 25	9	28,25-52
1181-1200	10	20	20	from -22,5 to 25	10	18,75-42,5	1581-1600	10	20	40	from -22,5 to 25	10	28,75-52,5

Figure 4 refers to rock mass with widely spaced discontinuities. The rock mass may be extremely soft to soft, medium hard to hard, or hard and very hard. In case the rock mass is extremely soft to soft the discontinuities may be horizontal or gradient with strike perpendicular to tunnel axis, when excavation drives against dip direction, gradient discontinuities with strike perpendicular to tunnel axis, when excavation drives with dip direction, or strike parallel to tunnel axis. The blastability index is calculated to be between 24 and 54 when the discontinuities are horizontal or gradient with strike perpendicular to tunnel axis, when excavation drives against dip direction. The blastability index is calculated to be between 39 and 64 when strike is perpendicular to tunnel axis, when excavation drives with dip direction. The blastability index is calculated to be between 34 and 59 when the strike is parallel to tunnel axis. Concerning medium hard to hard rock mass, the blastability index is calculated to be between 26 and 51 where the discontinuities are horizontal.

Table 4 – BI calculations for widely spacing discontinuities.

A/A	RMD	JPS	JPO	SGI	H	BI	A/A	RMD	JPS	JPO	SGI	H	BI
1601-1620	10	50	10	from -22,5 to 25	1	24,25-48	2001-2020	10	50	30	from -22,5 to 25	1	34,25-58
1621-1640	10	50	10	from -22,5 to 25	2	24,75-48,5	2021-2040	10	50	30	from -22,5 to 25	2	34,75-58,5
1641-1660	10	50	10	from -22,5 to 25	3	25,25-49	2041-2060	10	50	30	from -22,5 to 25	3	35,25-59
1661-1680	10	50	10	from -22,5 to 25	4	25,75-49,5	2061-2080	10	50	30	from -22,5 to 25	4	35,75-59,5
1681-1700	10	50	10	from -22,5 to 25	5	26,25-50	2081-2100	10	50	30	from -22,5 to 25	5	36,25-60
1701-1720	10	50	10	from -22,5 to 25	6	26,75-50,5	2101-2120	10	50	30	from -22,5 to 25	6	36,75-60,5
1721-1740	10	50	10	from -22,5 to 25	7	27,25-51	2121-2140	10	50	30	from -22,5 to 25	7	37,25-61
1741-1760	10	50	10	from -22,5 to 25	8	27,75-51,5	2141-2160	10	50	30	from -22,5 to 25	8	37,75-61,5
1761-1780	10	50	10	from -22,5 to 25	9	28,25-52	2161-2180	10	50	30	from -22,5 to 25	9	38,25-62
1781-1800	10	50	10	from -22,5 to 25	10	28,75-52,5	2181-2200	10	50	30	from -22,5 to 25	10	38,75-62,5
1801-1820	10	50	20	from -22,5 to 25	1	29,25-53	2201-2220	10	50	40	from -22,5 to 25	1	39,25-63
1821-1840	10	50	20	from -22,5 to 25	2	29,75-53,5	2221-2240	10	50	40	from -22,5 to 25	2	39,75-63,5
1841-1860	10	50	20	from -22,5 to 25	3	30,25-54	2241-2260	10	50	40	from -22,5 to 25	3	40,25-64
1861-1880	10	50	20	from -22,5 to 25	4	30,75-54,5	2261-2280	10	50	40	from -22,5 to 25	4	40,75-64,5
1881-1900	10	50	20	from -22,5 to 25	5	31,25-55	2281-2300	10	50	40	from -22,5 to 25	5	41,25-65
1901-1920	10	50	20	from -22,5 to 25	6	31,75-55,5	2301-2320	10	50	40	from -22,5 to 25	6	41,75-65,5
1921-1940	10	50	20	from -22,5 to 25	7	32,25-56	2321-2340	10	50	40	from -22,5 to 25	7	42,25-66
1941-1960	10	50	20	from -22,5 to 25	8	32,75-56,5	2341-2360	10	50	40	from -22,5 to 25	8	42,75-66,5
1961-1980	10	50	20	from -22,5 to 25	9	33,25-57	2361-2380	10	50	40	from -22,5 to 25	9	43,25-67
1981-2000	10	50	20	from -22,5 to 25	10	33,75-57,5	2381-2400	10	50	40	from -22,5 to 25	10	43,75-67,5

The blastability index is calculated to be between 31 and 61 where the strike is perpendicular to tunnel axis, when excavation drives against dip direction. The blastability index is calculated to be between 41 and 66 where the strike is perpendicular to tunnel axis, when excavation drives with dip direction. Concerning hard and very hard rock mass, the blastability index is calculated to be between 27 and 52 where the discontinuities are horizontal. The blastability index is calculated to be between 32 and 57 where strike is perpendicular to tunnel axis, when excavation drives against dip direction. The blastability index is calculated to be between 42 and 67 where strike is perpendicular to tunnel axis, when excavation drives with dip direction. The blastability index is calculated to be between 32 and 62 where strike is parallel to tunnel axis. Taking into account the surface conditions and the structure of the rock mass, we can estimate GSI and RMR range.

3. Blastability Index (BI) Related to Structural Geology

Taking into account the calculations of BI for every possible quality of the rock mass, a diagram which connects the structural description, the hardness of rock mass and BI (Fig.5) can be easily developed, where; rock mass quality 1 refers to closely spaced discontinuities (Priest &Hudson, 1976), horizontal formations, and gradient formations where the excavation drives against dip direction. Rock mass quality 2 refers to intermediate spaced discontinuities and horizontal formations. Rock mass quality 3 refers to closely spaced discontinuities and gradient formations, where excavation drives with dip direction. Rock mass quality 4 refers to intermediate spaced discontinuities and gradient formations. Rock mass quality 5 refers to widely spaced discontinuities, horizontal formations, and soft gradient rock mass, where excavation drives against dip direction. Rock mass quality 6 refers to widely spaced discontinuities and gradient formations (except soft gradient rock mass where excavation drives against dip direction).

Table 5 – RMR estimations for different types of rock mass with specific GSI range.

GSI (PART)	A/A: 001-80	A/A: 81-140	A/A: 141-200	A/A: 201-280	A/A: 281-340	A/A: 341-400	A/A: 401-480	A/A: 481-540	A/A: 541-600	A/A: 601-680	A/A: 681-740	A/A: 741-800
	RMR	RMR	RMR	RMR	RMR	RMR	RMR	RMR	RMR	RMR	RMR	RMR
0-12 (A)	008-28	009-29	010-30	003-28	004-29	005-30	001-28	002-29	003-30	011-33	0012-34	13-35
012-23 (B)	012-32	13-33	14-34	007-32	008-33	009-34	005-32	006-33	007-34	15-37	16-38	17-39
22-32 (C)	21-40	22-41	23-42	16-40	17-41	18-42	14-40	15-41	16-42	24-45	25-46	26-47
007-17 (D)	14-33	15-34	16-35	009-33	010-34	011-35	007-33	008-34	009-35	17-38	18-39	19-40
018-28 (E)	18-37	19-38	20-39	13-37	14-38	15-39	011-37	012-38	13-39	21-42	22-43	23-44
16-36 (F)	27-45	28-46	29-47	22-45	23-46	24-47	20-45	21-46	22-47	30-50	31-51	32-52
35-43 (G)	26-44	27-45	28-46	21-44	22-45	23-46	19-44	20-45	21-46	29-49	30-50	31-51
42-50 (H)	29-47	30-48	31-39	24-47	25-48	26-49	22-47	23-48	24-49	32-52	33-53	34-54

Table 6- RMR estimations for every GSI classification part.

GSI (PART)	A/A: 801-880	A/A: 881-940	A/A: 941-1000	A/A: 1001-1080	A/A: 1081-1140	A/A: 1141-1200	A/A: 1201-1280	A/A: 1281-1340	A/A: 1341-1400	A/A: 1401-1480
	RMR	RMR	RMR	RMR	RMR	RMR	RMR	RMR	RMR	RMR
0-12 (A)	011-36	012-38	013-37	006-36	007-38	008-39	004-36	005-38	006-39	14-41
012-23 (B)	015-39	16-41	17-42	010-40	011-40	012-41	008-39	009-40	010-41	18-44
22-32 (C)	22-47	23-48	24-49	17-47	18-48	019-49	015-60	16-48	17-49	25-52
007-17 (D)	012-41	13-42	14-43	007-40	008-41	009-43	006-36	006-41	007-42	15-45
018-28 (E)	16-44	17-45	18-46	011-44	012-45	13-46	010-40	010-45	011-46	19-49
16-36 (F)	23-52	24-53	25-54	18-52	019-53	20-54	16-48	017-53	018-54	26-57
35-43 (G)	29-56	30-57	31-58	24-56	25-57	26-58	22-52	23-57	24-58	32-61
42-50 (H)	34-58	32-59	33-60	26-58	26-59	28-60	24-54	24-59	25-60	34-63

Table 7 – RMR estimations for different types of rock mass with specific GSI range.

GSI (PART)	A/A: 1481-1540	A/A: 1541-1600	A/A: 1601-1680	A/A: 1681-1740	A/A: 1741-1800	A/A: 1801-1880	A/A: 1881-1940	A/A: 1941-2000	A/A: 2001-2080
	RMR	RMR	RMR	RMR	RMR	RMR	RMR	RMR	RMR
0-12 (A)	15-42	16-43	13-43	20-58	28-58	008-43	15-58	23-58	006-43
012-23 (B)	17-45	20-46	15-45	22-60	30-60	011-45	17-60	25-60	008-45
22-32 (C)	26-53	27-54	29-30, 33-42, 44-45,49-50	36-37, 40-57, 59-62,64-65	42-43, 46-55, 57-58,62-63	24-25, 28-42,44-45	31-32, 35-57, 59-62,64-65	39-40, 43-57, 59-60,64-65	22-23, 26-45,49-50
007-17 (D)	16-46	18-47	13-45	20-58	28-58	008-45	15-58	23-58	006-45
018-28 (E)	20-50	21-51	16-60	23-60	31-60	011-60	18-60	26-60	009-60
16-36 (F)	27-58	28-59	29-57, 59-62,64-65	36-37, 40-57, 59-62,64-65	44-45, 48-57, 59-60,64-65	30-69, 65-68,70-71	31-32, 35-57, 59-62,64-65	34-40, 43-57, 59-60,64-65	22-62,64-65
35-43 (G)	33-62	34-63	33-71	40-71	48-66,68-71	28-71	35-57	43-66,68-71	26-71
42-50 (H)	35-64	36-65	37-65, 67-70,72-73	44-45, 48-65, 67-70,72-73	52-53, 56-65, 67-68,72-73	32-45, 67-70,72-73	39-40, 43-65, 67-70,72-73	47-48, 51-65, 67-68,72-73	30-70,72-73

Table 8 – RMR estimations for different types of rock mass with specific GSI range.

GSI (PART)	A/A: 2081-2140	A/A: 2141-2200	A/A: 2201-2280	A/A: 2281-2340	A/A: 2341-2400
	RMR	RMR	RMR	RMR	RMR
0-12 (A)	13-58	45-46,49-68,72-73	16-33	23-61	31-63
012-23 (B)	15-60	23-60	20-50	25-65	33-65
22-32 (C)	29-30,33-62,64-65	37-38,41-60,64-65	32-50,52-55	39-70	47-65,67-70
007-17 (D)	13-58	21-58	16-50	23-63	31-63
018-28 (E)	16-60	24-60	19-65	26-65	34-65
16-36 (F)	29-33,34-62,64-65	37-38,41-60,64-65	32-70	39-70	47-65,67-70
35-43 (G)	33-71	41-66,68-71	36-76	43-76	51-76
42-50 (H)	37-38,41-70,72-73	42-46,49-68,72-73	40-78	47-78	55,-73,75-78

Looking at the above diagram, we can easily conclude that

- The wider the spacing of discontinuities is, the bigger the BI is.
- The BI is lower in horizontal formations than in gradient formations.
- The BI is higher where the excavation drives with dip direction than where it drives against dip direction.

Table 9 – GSI estimations for different types of rock mass with specific RMR range.

RMR	A/A: 001-80	A/A: 81-140	A/A: 141-200	A/A: 201-280	A/A: 281-340	A/A: 341-400	A/A: 401-480	A/A: 481-540	A/A: 541-600	A/A: 601-680	A/A: 681-740	A/A: 741-800
	BI: 4-29	BI: 6-31	BI: 7-32	BI: 9-34	BI: 11-36	BI: 12-37	BI: 14-39	BI: 16-41	BI: 17-42	BI: 19-44	BI: 21-46	BI: 22-47
	GSI (PART)	GSI (PART)	GSI (PART)	GSI (PART)	GSI (PART)	GSI (PART)	GSI (PART)	GSI (PART)	GSI (PART)	GSI (PART)	GSI (PART)	GSI (PART)
0-20	ABDE	ABDE	ABDE	ABCDE	ABCDE	ABCDE	ABCDE FG	ABCDE FG	ABCDE	ABD	ABD	ABD
21-40	ABCDEF GH	ABCDEF GH	ABCDEF GH	ABCDEF GH	ABCDE FGH	ABCDE FGH	ABCDE FGH	ABCDE FGH	ABCDE FGH	ABCDE FGH	ABCDE FGH	ABCDE FGH
41-60	FGH	CFGH	CFGH	FGH	FGH	CFGH	FGH	FGH	CFGH	CEFGH	CEFGH	CEFGH
61-80												
81-100												

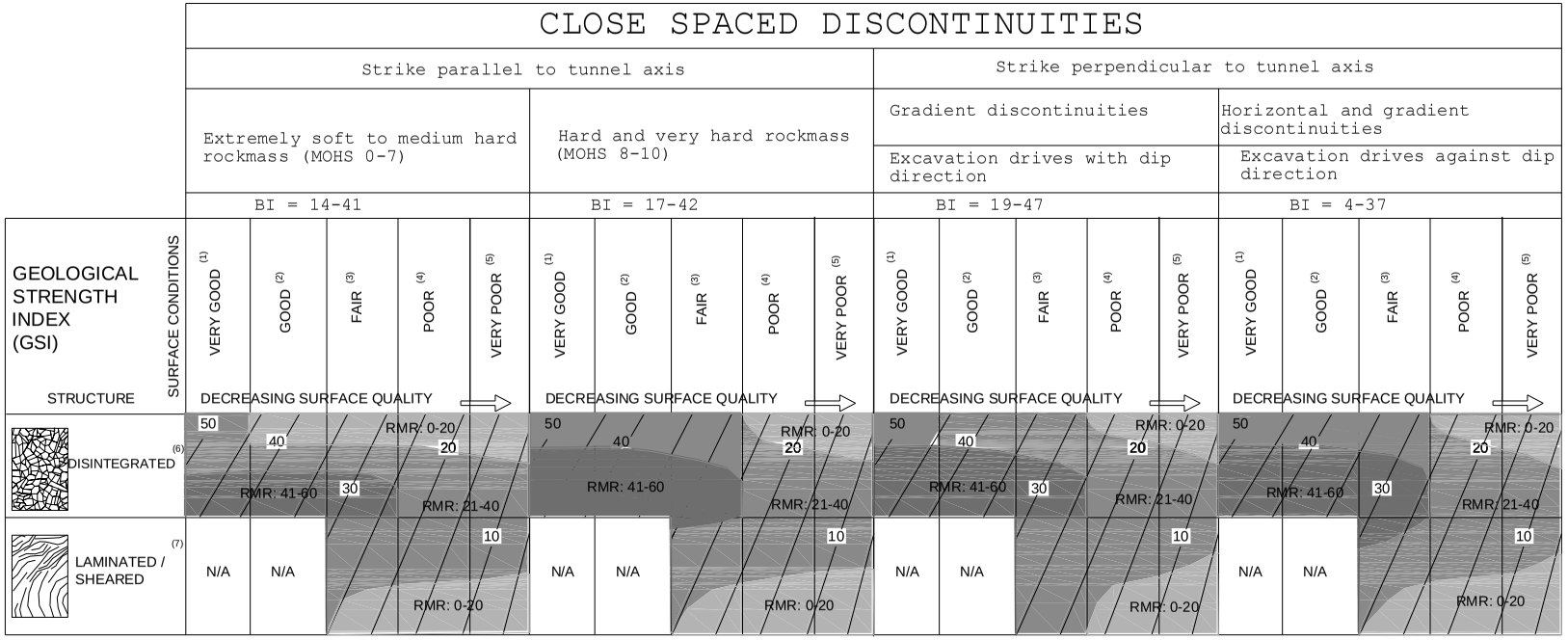

(1) Very rough, fresh unweathered surfaces

(2) Rough, slightly weathered, iron stained surfaces

(3) Smooth, moderately weathered and altered surfaces

(4) Slickensided, highly weathered surfaces with compact coatings of rillings or angular fragments

(5) Slickenside, highly weathered surfaces with soft clay coatings or fillings

(6) Poorly interlocked, heavily broken rock mass with mixture of angular and rounded rock pieces

(7) Lack of blockiness due to close spacing of weak schistosity of shear planes

Figure 2 – BQS for close spaced discontinuities.

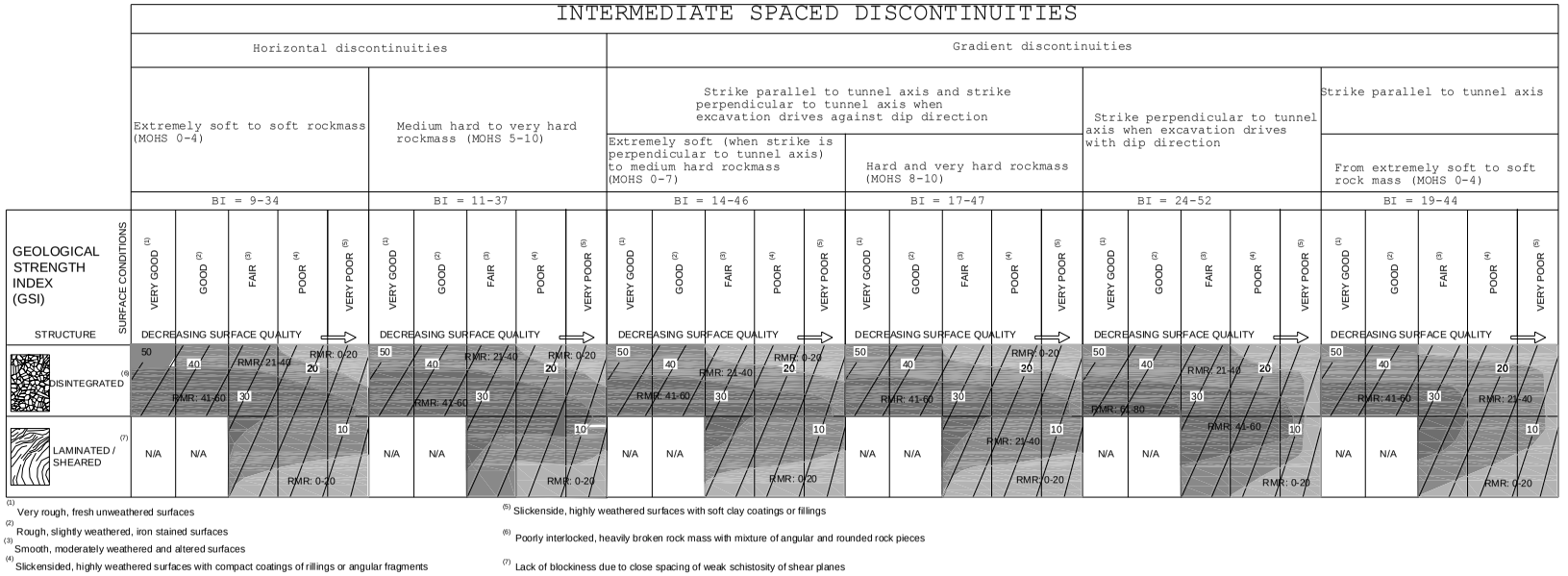

(1) Very rough, fresh unweathered surfaces

(2) Rough, slightly weathered, iron stained surfaces

(3) Smooth, moderately weathered and altered surfaces

(4) Slickensided, highly weathered surfaces with compact coatings of rillings or angular fragments

(5) Slickenside, highly weathered surfaces with soft clay coatings or fillings

(6) Poorly interlocked, heavily broken rock mass with mixture of angular and rounded rock pieces

(7) Lack of blockiness due to close spacing of weak schistosity of shear planes

Figure 3 – BQS for intermediate spaced discontinuities.

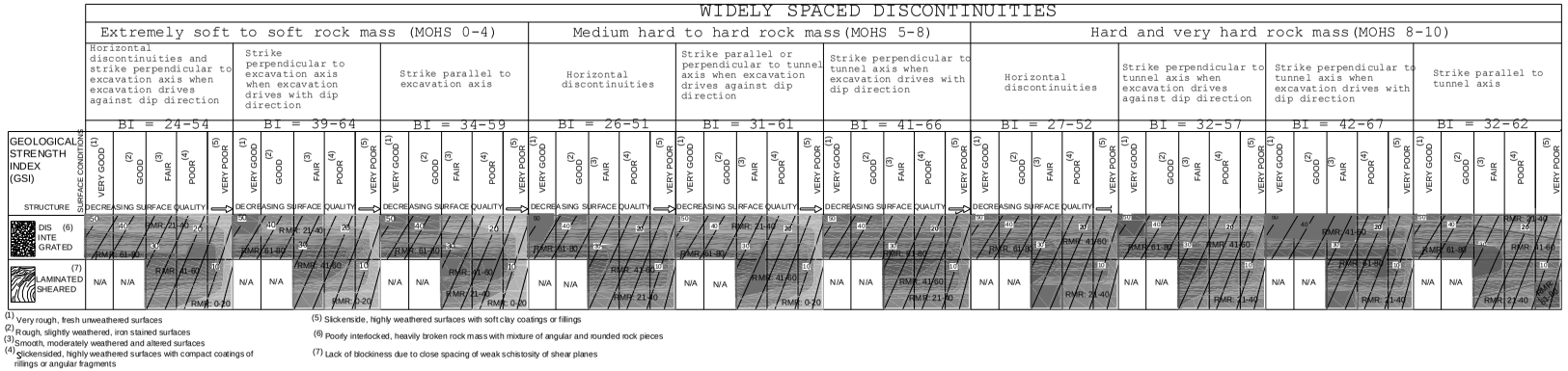

(1) Very rough, fresh unweathered surfaces
(2) Rough, slightly weathered, iron stained surfaces
(3) Smooth, moderately weathered and altered surfaces
(4) Slickensided, highly weathered surfaces with compact coatings of fillings or angular fragments
(5) Slickenside, highly weathered surfaces with soft clay coatings or fillings
(6) Poorly interlocked, heavily broken rock mass with mixture of angular and rounded rock pieces
(7) Lack of blockiness due to close spacing of weak schistosity of shear planes

Figure 4 – BQS for widely spaced discontinuities.

Table 10 – GSI estimations for different types of rock mass with specific RMR range.

RMR	A/A: 801-880 BI:9-34 GSI (PART)	A/A: 881-940 BI:11-36 GSI (PART)	A/A: 941-1000 BI:12-37 GSI (PART)	A/A: 1001-1080 BI:14-39 GSI (PART)	A/A: 1081-1140 BI:16-41 GSI (PART)	A/A: 1141-1200 BI:17-42 GSI (PART)	A/A: 1201-1280 BI:19-44 GSI (PART)	A/A: 1281-1340 BI:21-46 GSI (PART)
0-20	ABCDE	ABDE	ABDE	ABCDEF	ABCDEF	ABCDE(F)	ABCDEF	ABCDEF
21-40	ABCDEFGH	ABCDEFGH	ABCDEFGH	ABCDEFGH	ABCDEFGH	ABCDEFGH	ABCDEFGH	ABCDEFGH
41-60	C(D)EFGH	(B)CDEFGH	BCDEFGH	CEFGH	C(D)EFGH	(B)CDEFGH	CGH	C(D)EFGH
61-80								
81-100								

Table 11 – GSI estimations for different types of rock mass with specific RMR range.

Table 11. GSI classification part for RMR range

RMR	A/A: 1341-1400 BI:22-47 GSI (PART)	A/A: 1401-1480 BI:24-49 GSI (PART)	A/A: 1481-1540 BI:26-51 GSI (PART)	A/A: 1541-1600 BI:27-52 GSI (PART)	A/A: 1601-1680 BI:24-49 GSI (PART)	A/A: 1681-1740 BI:26-51 GSI (PART)	A/A: 1741-1800 BI:27-52 GSI (PART)	A/A: 1801-1880 BI:29-54 GSI (PART)
0-20	ABCDEF	ABDE	ABD(E)	A(B)D	ABDE			ABDE
21-40	ABCDEFGH	ABCDEFGH	ABCDEFGH	ABCDEFGH	ABCDEFGH	ABCDEF	ABDE	ABCDEFGH
41-60	CDEFGH	(A)BCDEFGH	ABCDEFGH	ABCDEFGH	BCDEFGH	ABCDEFGH	ABCDEFGH	ABCDEFGH
61-80		(G)H	GH	GH	FGH	CFGH	CFGH	FGH
81-100								

Table 12 – GSI estimations for different types of rock mass with specific RMR range.

Table 12. GSI classification part for RMR range

RMR	A/A: 1881-1940 BI:31-56 GSI (PART)	A/A: 1941-2000 BI:32-57 GSI (PART)	A/A: 2001-2080 BI:34-59 GSI (PART)	A/A: 2081-2140 BI:36-61 GSI (PART)	A/A: 2141-2200 BI:37-62 GSI (PART)	A/A: 2201-2280 BI:39-64 GSI (PART)	A/A: 2281-2340 BI:41-66 GSI (PART)	A/A: 2341-2400 BI:42-67 GSI (PART)
0-20	ABDE		ABDE	ABDE		A(B)DE		
21-40	ABCDEFGH	AB(C)DEF	ABCDEFG	ABCDEFGH	BCDEF	ABCDEFG	ABCDEF	ABD
41-60	ABCDEFGH	ABCDEFG	ABCDEFGH	ABCDEFGH	ABCDEFGH	BCDEFGH	ABCDEFGH	ABCDEFGH
61-80	CFGH	(CF)GH	FGH	CFGH	ACFGH	EFGH	BCDEFGH	ABCDEFGH
81-100								

4. Blastability Quality System (BQS)

The Blastability Quality System (BQS) is a very useful approach as it includes the most useful characteristics of rock mass, which are easily estimated and used in situ. In addition to its easy and wide use, it is a quick calculator for BI and rock mass quality, which make our choice of excavation, blast (Hino, 1959) and support measures quicker.

The BQ system (Fig. 2-4) connects the rock mass classification systems RMR and GSI, structural data, hardness of rock mass, and BI.

Initially, the discontinuities spacing is characterized. Secondly, the orientation of discontinuities in addition to the hardness of the rock mass is described. Having completed the above classification, the BI range can easily be determined. By visually inspecting the rock mass, we can easily distinguish discontinuity spacing and orientation. Also, we can estimate rock mass hardness using a Schmidt Hammer.

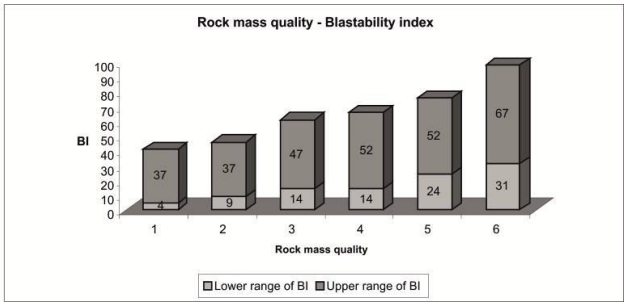

Figure 5 – Rock mass quality versus BI.

Finally we can combine structure and surface conditions in order to estimate Geological Strength Index (GSI) (Hoek & Brown, 1980) and Rock Mass Rating (RMR).

5. Conclusions

Taking into account the calculations of BI for every possible poor rock mass quality, the wider the spacing of discontinuities is, the bigger the BI is. The BI is, also, lower in horizontal formations than in gradient formations. Finally, the BI is higher, in cases where the excavation drives with dip direction than where it drives against it.

Evaluating the rock mass quality estimated by the RMR and GSI classification systems together with the calculated blastability index, a useful system, called Blastability Quality System (BQS), is created.

This "blastability quality system" can be a useful "in-situ tool", for estimating poor and friable rock masses, shared with lack of blockiness due to close spacing of weak schistosity or sheer planes and disintegrated, with poorly interlocked, heavily broken, with mixture of angular and rounded rock pieces. It connects rock mass quality, discontinuity orientation, rock mass hardness and BI. It can be easily applied during the excavations, in order to estimate rock mass quality and the range of BI very quickly. This is a viable tool for estimating the quantity of explosions and support measures to be decided using the already known methodology.

6. References

Barton N.R., Lien R. and Lunde J. 1980. Application of the Q-system in design decisions, in Subsurface space, (eds. M. Bergman) 2, 553-561. New York: *Pergamon*.

Bieniawski Z.T. 1989. Engineering rock mass classifications. New York: *Wiley*.

Deere D.U. and Deere D.W. 1988. The rock quality designation (RQD) index in practice, in Rock classification systems for engineering purposes, (eds. L. Dirkaldie), *ASTM Special Publication 984, 91-101. Philadelphia: Am. Soc. Test. Mat.*

Deere D.U. 1989. Rock puality designation (RQD) after 20 years. U.S. Army Corps Engrs Contract Report GL-89-1, Vicksburg, *MS: Waterways Experimental Station*.

Hino K. 1959. Theory and Practice of Blasting, *Noppon Kayaku Co, Ltd, Japan*

Hoek E. 1983. Strength of jointed rock masss, 23rd Rankine Lecture. *Geotechnique* 33(3), 187-223

Hoek E. 1994. Strength of rock and rock masses, *ISRM News Journal*, 2(2). 4-16.

Hoek E. and Brown E.T. 1980. Empircal strength criterion of rock masses, *J. Geotech Engng. Div., ASCE*, 106 (gt9), 1013-1035.

Hoek E. and Brown, ET. 1997. Practical estimates of rock mass strength *Int. J. Rock Mech Min Sci* 1997; 34(8):1165-86.

Hoek E., Marinos P. and Benissi M. 1998. Applicability of the Geological Strength Index (GSI) classification for very weak and sheared rock masses. The case of the Athens Schist Formation, *Bull. Engg. Geol. Env*. 57(2), 151-160.

Jimeno C.L., Jinemo E.L. and Carcedo F.J.A. 1995. Drilling & Blasting of Rocks, *A.A.Bulkema*, Rotterdum, Brookfield Publication, pp160-180.

Kaushik D. and Phalguni S. 2003. Concept of Blastability – An Update, *The Indian Mining & Engineering Journal*, Vol-42, No.-8&9, pp24-31.

Lilly P. 1986. An Empirical Method of Assessing Rockmass blastability, *Large Open Pit Mine Conference, Newman*, Australia, October, pp89-92.

Marinos P. and Hoek E. 2000. GSI – A geologically friendly tool for rock mass strength estimation, *Proc. GeoEng2000 Conference, Melbourne*. 1422-1442.

Murthy, V., Day, K. and Raitani R., 2003. Prediction of overbreak in underground tunnel blasting, A case study, *Journal of Canadian Tunneling Canadien*, P109-115.

Priest S.D. and Hudson J.A. 1976. Discontinuity spacings in rock. *Int. Jour. Rock. Mech. Min. Sci. & Gomech*, v.13, p.135-148.

Scott A. 1996. Blastability and Blast Design, Rock Gragmentation by Bloastin, (ed) Mohanty, *Balkema*, Rotterdam, pp27-36.

Δελτίο της Ελληνικής Γεωλογικής Εταιρίας, τομ. XLVII , 2013
Πρακτικά 13ου Διεθνούς Συνεδρίου, Χανιά, Σεπτ. 2013

Bulletin of the Geological Society of Greece, vol. XLVII 2013
Proceedings of the 13th International Congress, Chania, Sept. 2013

STABILITY ANALYSIS OF CONSTRUCTION AND DEMOLITION WASTE (CDW) DEPOSITS IN THE ABANDONED QUARRY OF PROFITIS ILIAS, KOZANI, GREECE

Konstantopoulou G.[1] and Spanou N.[1]

[1] National Centre for Viable Development (NCVD), Institute of Geology and Mineral Exploration (IGME), 1, Sp. Louis Str., Olympic Village, Acharnae, Greece, 13677, kongar@igme.gr, spanou@igme.gr

Abstract

Abandoned quarries become favourable sites for uncontrolled waste dumps, causing major safety hazards because of potential mass movements. An old quarry, near the town of Kozani, is filled with 772.000 m^3 Construction and Demolition Wastes (CDW), containing a variety of materials (aggregates, wood, metals, plastics, bricks, soil etc.), in a wide range of fragment sizes, from clay to boulders. The size of particles and voids influence the behaviour of the filled slope, affecting both shear strength and drainage characteristics. Major factors that should be considered in a stability analysis for CDW, include waste material and soil cover composition, overall degree of compaction, moisture contented, permeability, pore pressure and shear strength parameters.

Shear strength parameters were chosen by bibliographic references based on specialized field tests of similar materials. The analyzed profiles computed slip zones of low thickness and range. Therefore, successive back analysis was conducted to the sites of mapped cracks, aimed to determinate the mechanical properties of the slope during the failure. Since, friction angle and bulk density were retained for back analysis, the cohesion was examined. Although deposits are composed of loose heterogeneous materials, which have not been condensed, cohesion exists owing to the "interlocking" of the varying particle size of materials.

Key words: *uncontrolled waste dumps, mass movements, successive back analysis, "interlocking", protection measures.*

Περίληψη

Τα εγκαταλειμμένα λατομεία αποτελούν συχνά χώρους ανεξέλεγκτης διάθεσης απορριμμάτων, δημιουργώντας κινδύνους λόγω πιθανών μετακινήσεων μαζών. Ένα παλιό λατομείο, κοντά στην πόλη της Κοζάνης, έχει πληρωθεί με 772.000 m^3 υλικών κατεδαφίσεων ποικίλης σύστασης (αδρανή, ξύλα, μέταλλα, πλαστικά, τούβλα, υλικά εκσκαφών κλπ) σε ένα ευρύ φάσμα μεγεθών, από άργιλο έως ογκόλιθους. Το μέγεθος των τεμαχών, καθώς και η ύπαρξη κενών επηρεάζουν τη συμπεριφορά των πρανών των αποθέσεων, την αντοχή και την αποστράγγιση τους. Η ανάλυση ευστάθειας τέτοιων υλικών πρέπει να λαμβάνει υπόψη παράγοντες όπως η σύσταση, ο βαθμός συμπύκνωσης, το υλικό κάλυψης, η υγρασία, η διαπερατότητα, η αντοχή και η πίεση των πόρων.

Οι παράμετροι διατμητικής αντοχής επιλέχθηκαν βάσει της βιβλιογραφίας από εξειδικευμένες δοκιμές πεδίου σε παρόμοια υλικά. Οι αναλύσεις ευστάθειας που πραγματοποιήθηκαν υπολόγισαν πολλές ασταθείς ζώνες μικρού πάχους και εύρους. Για αυτό το λόγο, ακολούθησε ανάστροφη ανάλυση στις θέσεις των χαρτογραφημένων ρωγμών, με σκοπό τον υπολογισμό των μηχανικών παραμέτρων κατά την αστοχία. Δεδομένου ότι, η γωνία τριβής και η πυκνότητα βασίστηκαν σε βιβλιογραφικά δεδομένα, εξετάστηκε η τιμή της συνοχής των υλικών. Παρόλο που οι αποθέσεις αποτελούνται από χαλαρά ετερογενή υλικά, τα οποία δεν έχουν συμπυκνωθεί, παρατηρείται κάποια συνοχή των υλικών λόγω της "αλληλεμπλοκής" των ποικίλου μεγέθους συστατικών των αποθέσεων.
Λέξεις κλειδιά: *χώροι ανεξέλεγκτης ταφής απορριμμάτων, μετακινήσεις μαζών, διαδοχικές ανάστροφες αναλύσεις, αλληλεμπλοκή τεμαχών, μέτρα προστασίας.*

1. Introduction

Construction and Demolition Waste (CDW) describes material that is produced in the process of construction, renovation, or demolition of structures. Structures include buildings of all types (both residential and non-residential) as well as roads and bridges. Components of CDW debris typically include concrete, asphalt, wood, metals, gypsum wallboard and roofing. Land clearing debris, such as stumps, rocks and dirt, are also included in some definitions of CDW (Franklin Associates, 1999).

In the hilly area of Profitis Elias, situated northwest of Kozani town (Figure 1), four open pit limestone quarries had been in function during the decade 1971-1981 for the extraction of construction aggregates. After that, quarries were abandoned and the site remained unused creating environmental impact and safety issues.

The 6.5R magnitude earthquake's major macro seismic effect, manifested on the 13th May 1995 in Kozani area, was the destruction of many buildings and infrastructures. In the following years, the reconstruction and large expansion of Kozani town due to the rapid urbanization and population growth resulted in the production of a great volume of C&D waste. Municipal authorities tried to combine the rehabilitation of the abandoned quarries with the need of finding adequate disposal sites for CDW. Besides, it is a common practice in Greece to restore abandoned quarries by land filling.

The three lower and easiest accessed quarries have been partly filled and properly shaped to be used as a parking facility for the municipal vehicles and a local waste transfer station. The examined largest quarry was used exclusively for the deposition of the CDW materials, that has reduced environmental and safety risks and has provided significant cost and time savings for landfill disposal, due to its proximity to Kozani town. However, both the deposition method and the composition of CDW materials are not quite clear.

Recently, some failures have been occurred on the top debris/soil cover of the deposits, creating concern to the local authorities for a serious landslide. The aim of this study is the slope stability analysis of the CDW deposits and the investigation of failure mechanism, in order to propose the appropriate protection measures.

2. Site Characteristics and Geometry of CDW

The examined quarry is located in the south-eastern slope of Profitis Elias hill, between the altitudes of 805-875 m (Figure 2). Since the main body of CDW had been deposited soon after 1995, it is assumed that the residual relief of the pit prior to deposition is roughly represented on the topographic map of HMGS (Hellenic Military Geographical Service), at 1:5.000 scale, version 1984 (Figure 3a), which is the only available for the quarry site. The pit had been developed along NE-SW direction with maximum length of 315 m and 100 m width. The quarry faces, steeply

dipping to the East, had an average height of 45 m. The above considerations approximately result to a total volume of about 1.500.000 m^3 of limestone that was exploited during the decade 1971-1981.

The CDW materials have been deposited in a stepped arrangement. Slope inclination among terraces is ranging between 33º and 45º. The old pit has been completely filled, except some areas close to the western, northern and north-eastern boundary, where the residual rock quarry faces form slopes from 1 to 30 m high. The waste has been covered by a 50 cm thick top soil layer used for planting. Positive outcomes of this procedure have been the partial recovery of the natural relief and the reduction of the aesthetic distraction of the site, while slope stability conditions and potential pollution are questionable.

To calculate the thickness and hence the volume of CDW deposits, a detailed topographic map at 1:1.000 scale (Liakos, 2012), showing the current status of the quarry (Figure 3b), was contrasted to the one before the deposition (Figure 3a). The superimposition of the two digital elevation models reveals both the spatial distribution and the overall thickness of the deposits. Thus, the average thickness of CDW is estimated to 25 m, reaching 42 m locally, while the total volume of the deposits is calculated to 772.000 m^3 (Figure 3c). Apart from the above considerations, the thickness of the CDW deposits was estimated by a representative sampling borehole located around to the centre of the old quarry and found to be 25 m.

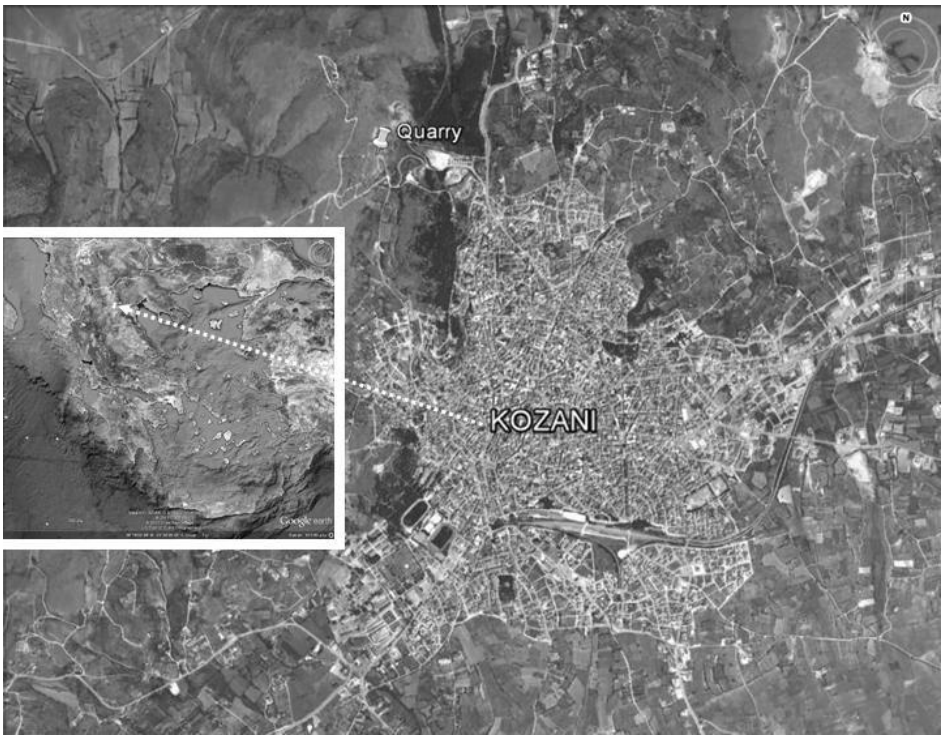

Figure 1 – The examined quarry is located in the vicinity of Kozani Town, in Profitis Elias area.

3. Engineering Properties of CDW Deposits

3.1. Composition and Structure of CDW

A detailed engineering geological map at 1:1.000 scale (Figure 4) was compiled for the study area using the topographic map provided by the Municipality of Kozani (Liakos, 2012). The

composition of CDW materials can not be defined in detail, but can be estimated by the uncovered waste remnants as well as by the borehole survey. Typically, CDW appears to be a mixture of concrete, asphalt, wood, metals, plastics, rubber, textiles and soils (both waste products and soil cover). A wide range of particle sizes is encountered sorted from soil particles to large objects from the demolition procedure (reinforced concrete and masonry). The proportion of these materials varies within the site. These variations produce fundamental and significant differences in waste engineering behaviour. Supposed that the waste dumps are inert, they have been deposited directly on the native basement of the quarry without any geosynthetic liner system or drainage system installed before the waste deposition.

Figure 2 – Plan view (A) and panoramic photo (B) of the CDW deposits.

3.2. Classification and Mechanical Properties of CDW

The existing engineering classification systems for soils can not be directly applicable in the case of CDW materials. They may describe an individual but not well defined material class, since they exhibit an extreme diversity changing shape and proportion of their natural or synthetic components. Some classification systems have been proposed for Municipal Solid Wastes (MSW) (Siegel et al., 1990; Langer and Dixon, 2004) on the base of particular physical or mechanical parameters, but the current understanding of C&D waste behaviour is far from being complete due to the lack of both agreed classification system and test standards, making it difficult to compare published results.

As a part of site data collection, one borehole was drilled on about the central of the CDW body to the depth of 29 m below ground surface, giving information about: i) waste material type and soil stratification, ii) permeability of CDW in specific depths, iii) strength and compressibility parameters, iv) depth to bedrock. Standard Penetration Tests (SPT) were performed to investigate the penetration resistance, compressibility and settlement of CDW. Although the materials of the

studied quarry can not be classified as soils, SPT N values may be indicative of the relative density (D_r %) variation with depth (Terzaghi and Peck, 1967). These indicative values corresponding from very loose to medium density materials due to the low compaction and existing voids within CDW body. Additionally, all in situ permeability tests considered very high permeable materials by calculating values for the coefficient k greater than $1x10^{-2}$ cm/sec.

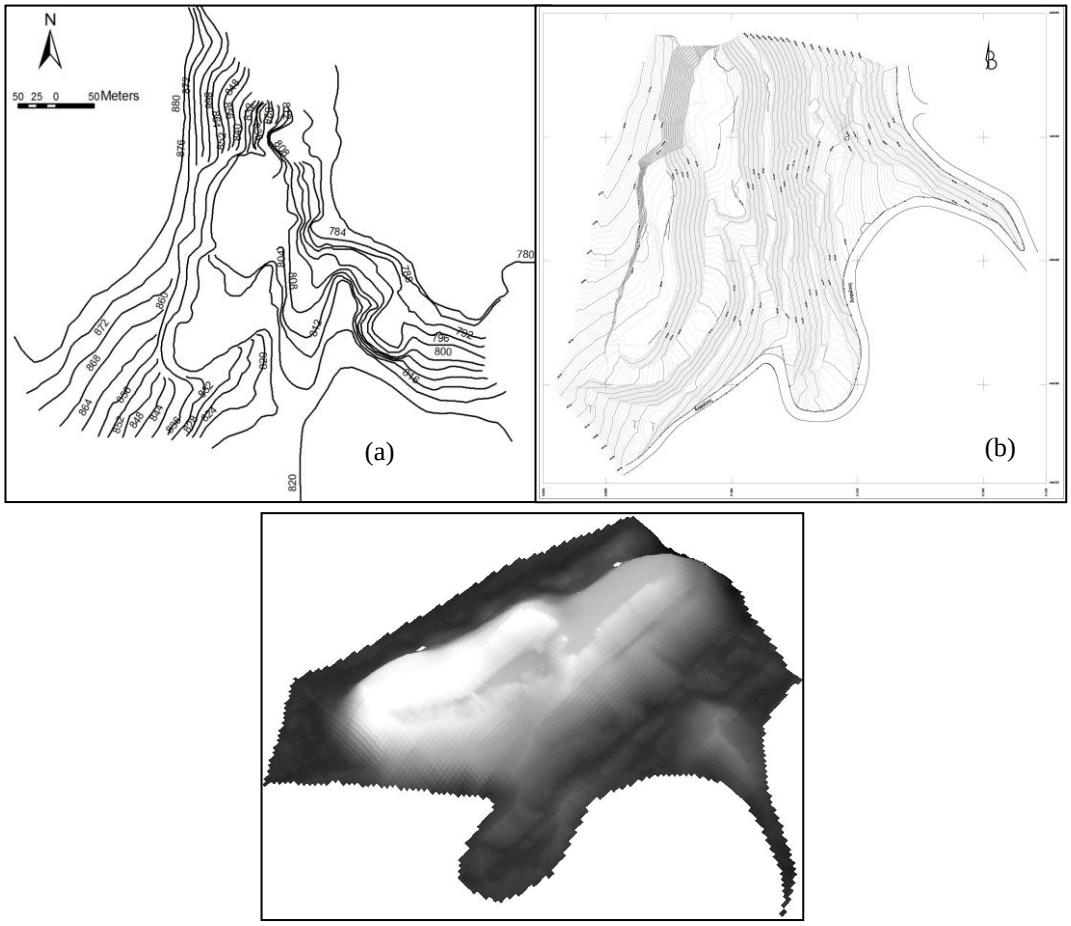

Figure 3 – (a) Topographic map (scale 1:5.000) of the abandoned quarry site (HMGS, 1984), (b) topographic map (scale 1:1.000) of the same area (Liakos, 2012) and (c) digital model interpreting the current thickness of the CDW deposits (-10 – 42 m), exported by the superimposition of the above base maps.

Regarding the engineering properties of CDW, there are no internationally accepted standard sampling and testing procedures for the waste materials at the moment. Thus, evaluating the engineering properties and hence the mechanical behaviour of CDW bodies is problematic, because it is difficult to quantify the contribution of the different waste components to the behaviour of the whole deposit. A review paper by Langer and Dixon (2004) concentrates on unit weight, compressibility, shear strength, lateral stiffness, in situ horizontal stress and hydraulic conductivity as the key parameters for the mechanical behaviour of the MSW materials.

Unit weight is mainly dependent on the waste composition, moisture content and the degree of compaction during deposition. Compressibility is related to the total settlement of the waste body. Apart from the mechanical compaction during waste deposition, secondary compression may also occur by self compaction from the weight of subsequent layers including soil cover. Due to the heterogeneous nature of waste constituents and their varied rates of decomposition, differential

settlements may occur. Concerning the shear strength parameters, it is hard to obtain representative and reliable estimations for CDW due to the large particle size, heterogeneity, particular structure etc. The majority of the published studies for MSW give a large scatter of strength values taken mainly from direct shear box tests and back-analyses of failures (Jones et al., 1997; Stark et al., 2008).

3.3. Characteristics of the Failures

Ground failures are evident on the soil cover of the upper three terraces of the CDW body. The mode of failures includes profound, almost vertical extensional fractures, 10-60 m long and 5-40 cm wide with local expansions. They are wavy in form, usually running parallel and close to the edge of the terraces (Figure 4).

Slope failures on soil cover may be started by ravelling and collapse due to the movement of fines into larger voids or sudden collapse of hollow structures within the buried CDW deposits, which may cause significant settlement. When current tension cracks fill with water, the hydrostatic pressure exerted on their walls can lead to failure. At the same time, tension cracks may facilitate rainwater infiltration increasing seepage forces acting to cause slope movement.

4. Stability Analysis

In order to propose the appropriate prevention or protection measures, a stability analysis of the CDW deposits was performed using the computer package LARIX 5. The stability analysis is aiming both to the theoretical determination and interpretation of fractures appearance and development as well as the estimation of the critical mechanical parameters values of the deposited materials.

Stability analysis for CDW is considerably different from stability calculations in soil mechanics, due to the fact that they typically have an extreme variety of material types, sizes, and characteristics. Many factors should be considered in a proper stability assessment of the slope including waste type and composition, degree of compaction, cover material, density, moisture content, permeability, shear strength and pore pressure.

According to the above, shear strength parameters were chosen by bibliographic references based on specialized field testing in large samples of similar materials (Table 1). The used values were selected by evaluating the general description of CDW and estimating geotechnical properties for them using published correlations or assigning typical properties for similar materials (Stark et al., 2009). These values are: $\varphi=32^{o}$, c=0 kN/m^2 and $\gamma=15$ kN/m^3.

Table 1 - Representative physical and mechanical parameters of the CDW from the available bibliographic sources.

Material	In-Place Unit Weight (lb/ft^3)	Saturated Unit Weight (lb/ft^3)	Angle of Internal Friction (degrees)	Cohesion (lb/ft^2)
Mixed Construction Debris and Soil	96.0	116.0	32	0

Four geotechnical sections, designed from a detailed topographic background, were used for the calculations and two series of analysis were conducted (Figure 4, A-A□, B-B□□, C-C□ and D-D□). Janbu method was selected, since the slip surfaces constituted by linear segments and the failure mechanism is corresponded by a translational movement.

Very low safety factors lower than 1, and slip zones of low thickness and range were computed. For this reason successive back analysis was conducted to the places of mapped cracks, aimed to determinate the mechanical parameters of the slope during the failure. Since it has been assumed that the values of friction angle and bulk density taken by the bibliography feet to the current CDW materials, they were kept unchanged during the back analysis in order to estimate the cohesion (c) value. Despite the fact that the deposits are composed of heterogeneous materials, which have not been condensed, the overall cohesion of the slope is not zero, on account of the "interlocking" of varying size particles of the material. Geotechnical parameters outcome from the back analysis are: $\varphi=32^{o}$, $c=5$ kN/m^2 and $\gamma=15$ kN/m^3. Matching the instability phenomena observed on the slope, safety factor varies close to the limit equilibrium confirming the values of the shear strength parameters chosen for the analysis (Figure 6).

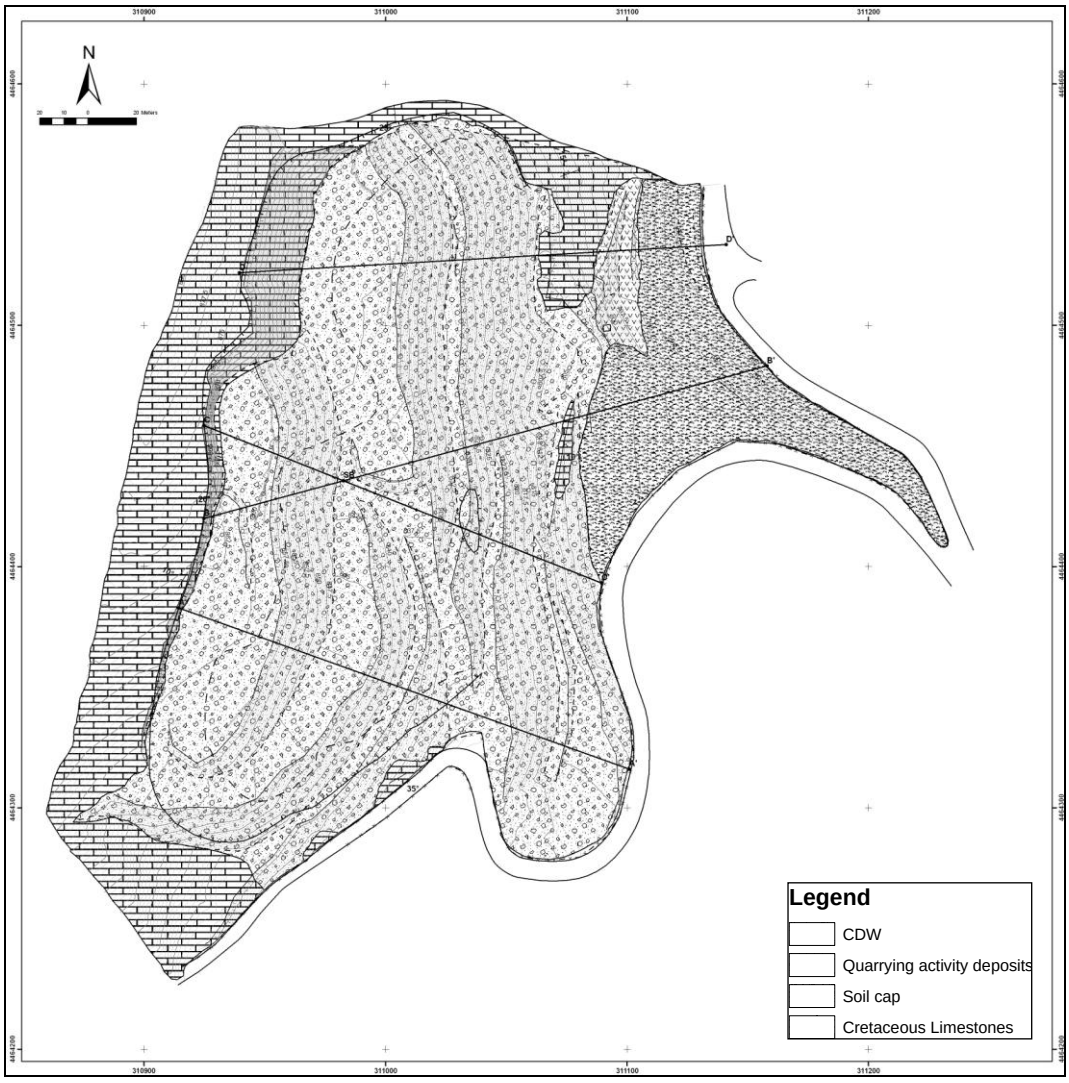

Figure 4 – Engineering geological map of the studied area.

5. Discussion – Mechanism of Failure Development – Protection Measures

The main reason for the occurrence of top soil tension cracks in the studied area is the settlement of underlying CDW deposits. Mechanisms resulting in settlement may be: a) Physical compression

and creep (mechanical distortion, bending, crushing and re-orientation of particles), b) Raveling settlement (migration of small particles into voids between large particles), c) Collapse of containers and bridging components due to physical/chemical changes such as corrosion and oxidation. The magnitude of settlement may be controlled by the following factors: a) Initial composition of waste (grading, particle shape, material properties of components, e.g. metal, paper), b) Initial density and voids ratio, c) Layer type and thickness, d) Leachate levels and fluctuations, e) Environmental controlled factors (moisture content, temperature) (Manassero et al., 1996).

Apart the settlement mechanism, rain water plays an important role in the evolution of observed cracks. The high permeability of CDW materials reduce the surface flow of rainwater resulted in high rate water infiltration into the waste body. The leachate water increases pore water pressure within the fine grain layers of deposits, decreasing the shear strength of material.

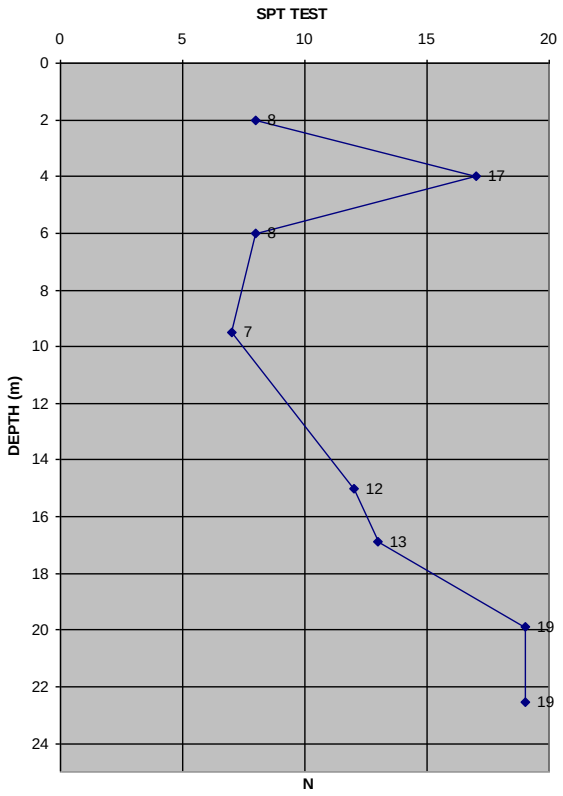

Figure 5 – Standard Penetration Test's results.

The protection measures aim on reduction of water infiltration, improving the leachate drainage and minimizing the settlements. Vegetation also could improve the stability conditions, as well as the filling of the open cracks.

The above examination of the dynamic evolution of cracks showed that the probability of failure of a large CDW volume is limited. However, to increase slope stability the following measures are proposed herein: 1) Closure of the existing cracks with clay material in order to reduce the water infiltration within the CDW body, 2) Improvement of the runoff system by configuration of the slope for the free removal of surface waters, 3) Vegetation thickening, 4) Installation of a flexible metal ring net barrier at the south-eastern boundary of the old quarry, following the superelevation of the residual rock quarry faces which operates as a natural barrier.

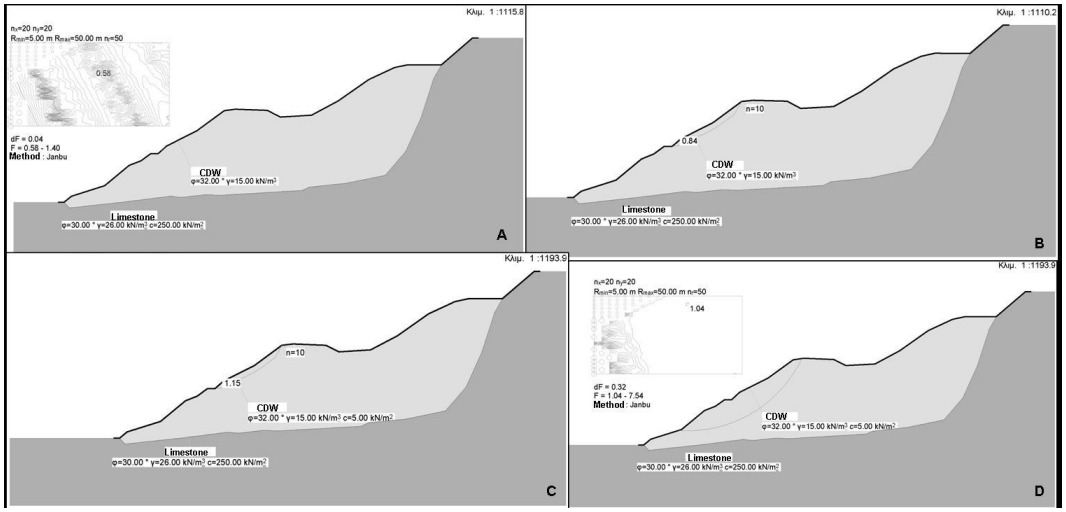

Figure 6 – Slope stability analysis performed in cross section BB□ (A: Stability analysis without a predefined rupture surface, B: Stability analysis considering existing tension cracks, C: Back analysis considering existing tension cracks, D: back analysis without a predefined rupture surface).

6. Acknowledgments

The current paper presents the results of the study titled: "Geological – Geotechnical Study at Prophet Elias area for the restoration of the old quarry", conducted by the Institute of Geology and Mineral Exploration of Greece (IGME) and assigned by Municipality of Kozani.

7. References

Franklin Associates, 1999. Characterization of Building-Related Construction and Demolition Debris in the United States, *U.S. Environmental Protection Agency*, Washington DC, June 1999.

Jones D.R.V. Taylor D.P. and Dixon N. 1997. Shear strength of waste and its use in landfill stability analysis. In: Yong R.N., Thomas H.R. (Eds), *Proceedings Geoenvironmental Engineering Conference*, Thomas Telford, pp. 343–350.

Langer U. and Dixon N. 2004. Mechanical properties of MSW: development of a classification system. In: Yong, R.N., Thomas, H.R. (Eds.), *Proceedings Fourth British Geotechnical Association Geoenvironmental Engineering Conference*, Integrate d Management of Groundwater and Contaminated Land, pp. 267–274.

Liakos C.V. 2012. *Topographic map in 1:1.000 scale* (in Greek).

Manassero M., Van Impe W.F. and Bouazza, A. 1996. Waste disposal and containment. *Proc. 2nd Intl. congress on environmental geotechnics*, Osaka, Japan, Rotterdam: Balkema 3: 1425-1474.

Siegel R.A., Robertson R.J. and Anderson D.G. 1990. *Slope Stability Investigations at a Landfill in Southern California*, Geotechnics of Waste Fill—Theory and Practice; ASTM STP 1070.

Stark T.D., Huvaj-Sarihan N. and Li G. 2009. Shear strength of municipal solid waste for stability analyses, *Environ Geol* (2009) 57: 1911–1923.

Terzaghi K. and Peck R. 1968. Soil mechanics in Engineering Practice, J. Wiley, INC. New York, 2nd edition, 729 pp.

Δελτίο της Ελληνικής Γεωλογικής Εταιρίας, τομ. XLVII , 2013
Πρακτικά 13ου Διεθνούς Συνεδρίου, Χανιά, Σεπτ. 2013

Bulletin of the Geological Society of Greece, vol. XLVII 2013
Proceedings of the 13th International Congress, Chania, Sept. 2013

ENGINEERING GEOLOGICAL MAPPING OF THE PALLINI URBAN AREA

Kotsanis D.[1], Panagiotopoulos P.[1], Rozos D.[1] and Loupasakis C.[1]

[1] National Technical University of Athens, School of Mining and Metallurgical Engineering, Section of Geological Sciences, dkotsanis@metal.ntua.gr , p_panagio@hotmail.com, rozos@metal.ntua.gr , cloupasakis@metal.ntua.gr

Abstract

Engineering geological thematic maps can provide substantial information for the development of cities, the land planning of future infrastructures and even more for the planning of the natural hazards prevention and/or mitigation.
To this direction the engineering geological map of the Municipality of Pallini, at the Eastern Attica prefecture, at a scale of 1:20.000, was compiled. For that purpose, the following workflow was adopted: Firstly, a desk study helped in selecting the relevant topographic and geologic maps, which were digitized and introduced in a GIS environment. Secondly, the data coming from detailed geological mapping were elaborated to the same GIS environment. Thirdly, geotechnical data collected from borehole logs, such as lithostromatographic sequence, in situ tests and laboratory tests were introduced in geotechnical database. The statistical evaluation of this data provided estimates for numerous geotechnical parameters. Finally, the engineering geological map was compiled by merging the geological formations into lithologic units according to their origin, age, natural condition, and geotechnical characteristics.
Key words: *lithologic units, physical characteristics, mechanical properties.*

Περίληψη

Οι τεχνικογεωλογικοί θεματικοί χάρτες δύναται να παρέχουν σημαντικές πληροφορίες για την ανάπτυξη των πόλεων, τον χωροταξικό σχεδιασμό των μελλοντικών υποδομών και ακόμη περισσότερο για τον σχεδιασμό της πρόληψης ή/ και της ανάσχεσης των φυσικών καταστροφών.
Προς την κατεύθυνση αυτή συντάχθηκε τεχνικογεωλογικός χάρτης του Δήμου της Παλλήνης, της Νομαρχίας Ανατολικής Αττικής, σε κλίμακα 1:20.000. Για τον σκοπό αυτό η ακόλουθη ροή εργασίας υιοθετήθηκε: Πρώτον, στα πλαίσια των εργασιών γραφείου συλλέχθηκαν οι σχετικοί τοπογραφικοί και γεωλογικοί χάρτες οι οποίοι ψηφιοποιήθηκαν και εισήχθησαν σε περιβάλλον ΓΣΠ. Δεύτερον, δεδομένα που συλλέχτηκαν στα πλαίσια των εργασιών πεδίου από λεπτομερή γεωλογική χαρτογράφηση εισήχθησαν στο ίδιο περιβάλλον ΓΣΠ. Τρίτον, στοιχεία που συγκεντρώθηκαν από γεωτεχνικές γεωτρήσεις, όπως, λιθοστρωματογραφικές ακολουθίες, αποτελέσματα επί τόπου και εργαστηριακών δοκιμών, εισήχθησαν σε αντίστοιχη γεωτεχνική βάση. Η στατιστική επεξεργασία των δεδομένων αυτών παρέχει εκτιμήσεις για πολλές γεωτεχνικές παραμέτρους. Τέλος, ο τεχνικογεωλογικός χάρτης συντάχθηκε ενοποιώντας τους σχηματισμούς σε λιθολογικές ενότητες με βάση

τη φυσική κατάσταση, την προέλευση, τη σχετική ηλικία, τα λιθολογικά χαρακτηριστικά, και τη γεωτεχνική συμπεριφορά.
Λέξεις κλειδιά: *λιθολογικές ενότητες, φυσικά χαρακτηριστικά, μηχανικές ιδιότητες.*

1. Introduction

The study area occupies 18,93 km^2 in Eastern Attica prefecture and is located 18km E-NE of Athens (Figure 1). The terrain is gentle in the major part, where the Mesogia Basin is developed, and becomes hilly at the piedmont of Penteli Mountain, with a maximum elevation of about 400m.

Pallini is currently undergoing a rapid urban development with many new constructions developed and the population is expected to grow in the forthcoming years. Under these circumstances engineering geological mapping can support land use planning by providing substantial information. Therefore, the examination of the engineering geological conditions and finally the compilation of the engineering geological map of this area, which is the main purpose of this study, give a valuable tool to local authorities and engineers for its correct planning and development.

Figure 1 - Location map of the Municipality of Pallini.

2. Geological Aspects

The alpine bedrock of the study area belongs to the Attico–Cucladic Massif (Katsikatsos, 1992). The formations of the autochthonous system occur at the northern part, consisting of marbles (Figue 2d). The crystalline limestones and schists with bodies of ophiolitic rocks, outcropping at the hilly area of Kantza, belong to the Neo – Hellenic Nappe.

Post alpine formations mainly Upper Miocene in age and of lacustrine and fluviolacustrine origin occupy the major part of the study area. According to Mettos, 1992, they cover a part of the Mesogia Basin and consist of marls (Figure 2b) with sandstones, brecciоconglomerates and travertine intercalations (Figure 2c). Loose fluviolacustrine formations including fans, talus cones, occur at the piedmont of Penteli Mountain (Figure 2a).

Generally, the Neogene formations and in some places the schists of the Neo – Hellenic Nappe are covered by younger unconsolidated materials such as Pleistocene deposits.

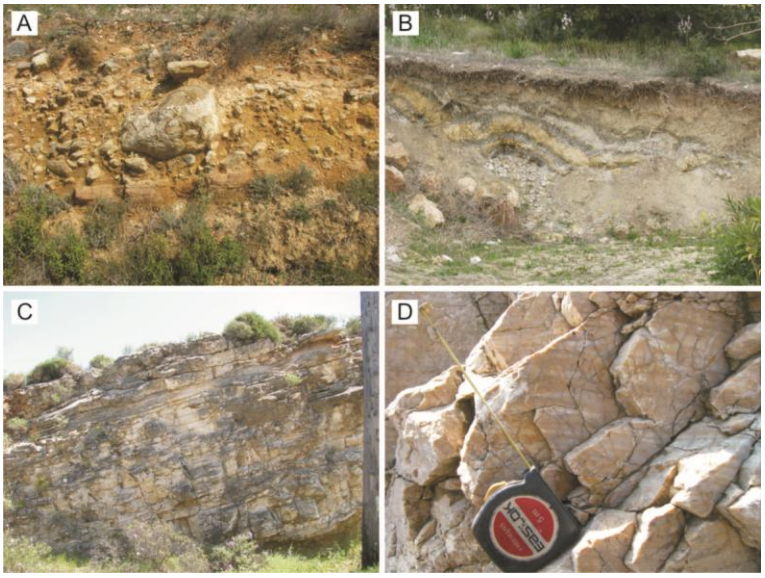

Figure 2 – (a) Mixed phase formations of fluviolacustrine origin, (b) Marls` slubbings, (c) intensively fractured travertine, (d) intensively fractured marbles.

3. Engineering Geological Behaviour of the Formations in the Study Area – Compilation of the Engineering Geological Map

The need of compilation of engineering geological maps was completely understandable the last 40 years. At the beginning of that period the international community were started to recognize the value of those maps regarding every kind of civil works (dams, tunnes, etc), infrastructures as well as urban and land planning.

In Greek territory the compilation of engineering geological maps of wider areas such as urban or industrial sites started to be published the last 3 decades. Characteristic examples are the map of Xanthi, *1:25.000* in scale (Marinos and Xidakis, 1991), map of Achaia county, *1:100.000* in scale (Rozos, 1989), map of Athens, *1:25.000* in scale (Sabatakakis, 1991), geotechnical map of Greece, *1:500.000* in scale, (IGME, 1993), map of Trikala town, *1:10.000* in scale (Koukis, et al., 1997), map of Athens prefecture, *1:10.000* in scale (IGME – University of Patras, 2009), map of wider Thessaloniki area, *1:10.000* in scale (Rozos et al., 2004), map of Patras town, *1: 5.000* in scale (Rozos, et al., 2006), land suitability maps of Trikala Prefecture (Bathrellos, et al., 2012).

The engineering geological map of the study area, proper for urban planning and development, was compiled at a scale of 1:20.000. For its compilation a large number of data obtained by field work, laboratory tests as well as by bibliographic sources were systematically collected and evaluated. This distinction was made according to guide of UNESCO (UNESCO/I.A.E.G, 1976).

Based on this guide, the geological formations in the examined area were grouped into 7 lithological units according to the scale of the map. However, the analysis of the behavior of every unit includes much more information and data than those which the guide indicates. This is because of the abundance of available data and the uniformity of the lithological types included in every lithological unit. Therefore, the min, max, mean, and standard deviation for every geomechanical parameter examined are given. These geomechanical parameters (physical and mechanical properties) that were used to characterize the lithological units, according to available data and new lab tests, are: Liquid limit (w_L), Plasticity index (PI), Bulk unit weight (γ_b), moisture content (w) initial void ratio (e_o), unconfined compressive strength (q_u), total cohesion (c) total angle of friction (φ), effective cohesion (c´), effective angle of friction (φ´), compression index

(C_c), standard penetration test (N_{SPT}) for soils, and porosity (n) dry density (ρ_d), unconfined compressive strength (σ_c), Young modulus (E), diametrical point load index (I_{s50d}), axial point load index (I_{s50a}), indirect tensile strength from Brazilian test(σ_t) and slake durability index (I_{d1}) for rocks.

Unit 1: Streambed deposits

The lithological unit of those deposits consist of brownish red, grayish and brownish yellow clayey to silty gravels (GC - GM), with intercalations of brownish red clayey sands (SC) of low to medium plasticity. Sandy clays of medium to high plasticity (CL) and silty sands are also occurred as intercalations. This unit occupies the bed and banks of torrents in the study area with maximum thickness ranging from 0.5-8m. It is high permeable but does not develops a significant aquifer. Table 1 presents the descriptive statistics of the physical and mechanical properties of this unit.

Table 1 – Descriptive statistics for the physical and mechanical properties of Unit 1.

Clayey to silty gravels (GC – GM)						
	w_L (%)	**PI (%)**	**γ_b (kN/m^3)**	**w (%)**	**c (kPa)**	**φ (°)**
min	23	9	20,5	5,8	7,8	30
max	39	20	23,2	21,8	35,3	40
mean	29	12	21,9	14,1	21,5	35
std	4	3	1,3	5,6	13,7	5
Clayey sands (SC)						
min	18	5	19,9	11,3	19,6	5
max	42	22	21,5	19,6	23,5	33
mean	29	13	20,6	16,7	20,0	21
std	8	4	0,6	3,8	9,2	11
Lean clays (CL)						
min	30	13	17,8	4,8	0,7	21
max	44	19	20,5	21,0	19,0	31
mean	35	16	18,8	11,7	9,8	26
std	5	2	1,2	6,3	9,1	5

Unit 2: Mixed phase Pleistocene deposits

Brownish red, medium to very dense, clayey sands (SC) and medium dense to dense clayey gravels (GC) are the main lithological types of this unit. Very stiff clays of moderate to high plasticity and medium degree of compressibility also occur. These formations cover a large part of the study area and its thickness varies reaching up to 20m. The coarse-grained layers are high permeable and can develop local aquifers. Table 2 presents the descriptive statistics of each physical and mechanical property of this unit.

Unit 3: Coarse grained Neogene deposits

This unit consists of fluviolacustrine loose brecciated materials with intercalations of marly soils and thin layers of sandstones (Figure 2a). These formations occupy a large part the area adjacent to Penteli Mountain. The mainly coarse nature of this unit does not allow the sampling of proper specimens for lab tests.

Unit 4: Travertinoid limestones

These limestones are yellow – brown, weak to moderate weak, thin to thick bedded, very porous and frequently fractured (Figure 2c).

Table 2 – Descriptive statistics for the physical and mechanical properties of Unit 2.

Clayey sands (SC)												
	w_L (%)	**PI (%)**	**γ_b (kN/m^3)**	**W (%)**	**c (kPa)**	**φ (°)**	**c´ (kPa)**	**φ´ (°)**	**C_c**	**e_o**	**q_u (kPa)**	**N_{SPT}**
min	20	4	18,7	4,9	9,8	29	17,2	10	0,070	0,370	46,0	12
max	33	19	22,4	20,6	106,0	43	62,7	32	0,145	0,531	59,0	>50
mean	27	11	20,6	10.0	37,2	35	46,9	21	0,108	0,451	52,5	
std	3	4	1,2	5,7	39,7	5	21,0	8	0,040	0,080	6,5	
Clayey gravels (GC)												
min	20	5	21	7,7	0,0	38	8,0	38	----	----	----	12
max	30	19	21	15,4	24,0	46	8,0	46	----	----	----	>50
mean	26	11	21	11,7	12,0	42	8,0	42				
std	4	4	0	3,1	12,0	4	0,0	4				
Lean clays (CL)												
min	26	7	19,0	7,7	0,0	9	0,0	26	0,080	0,412	189,0	25
max	43	29	21,6	24,7	194,0	30	18,4	34	0,260	0,860	635,0	>50
mean	33	16	2,3	15,6	82,8	23	6,4	30	0,147	0,647	481,6	
std	5	5	5,1	5,1	58,2	8	7,0	2	0,070	0,180	173,6	

The rock mass quality according to RQD measurements can be characterized as very poor to fair. They are permeable due to their secondary porosity and the dense joint sets, but the developed aquifers are poorer than those of the unit 2 (Lekkas, 1992). The main mechanical properties of the intact rock are listed in Table 3.

Table 3 – Descriptive statistics for the main mechanical properties of Unit 4.

	σ_c (MPa)	**E (MPa)**	**I_{s50d} (MPa)**	**I_{s50a} (MPa)**
min	10,71	6781,54	0,39	0,64
max	25,15	11306,25	1,98	2,05
mean	18,64	9043,90	1,03	1,52
std	5,50	2262,35	0,69	0,51

Unit 5: Neogene deposits mainly fine-grained

This unit consists of Upper Miocene deposits, mainly marls, with intercalations of sandstones and brecciоconglomerates. The thickness of this unit may exceed 150m and occupies the largest part of

the study area. Local aquifers developed in the weathering zone of the marls and when the sandstones and brecciоconglomerates occur. The marls (Figure 2b) are stiff to hard and white, yellow and green in color. According to USCS, they can be classified as clays of low to high plasticity (CL, CH) and silts of low to high compressibility (ML, MH) (Figure 3). A distinctive property of these soils, according to oedometer tests results, is the high swelling pressure (up to 294kPa). Moreover, grey organic marls locally occur with compression index (C_c) up to 0,547.

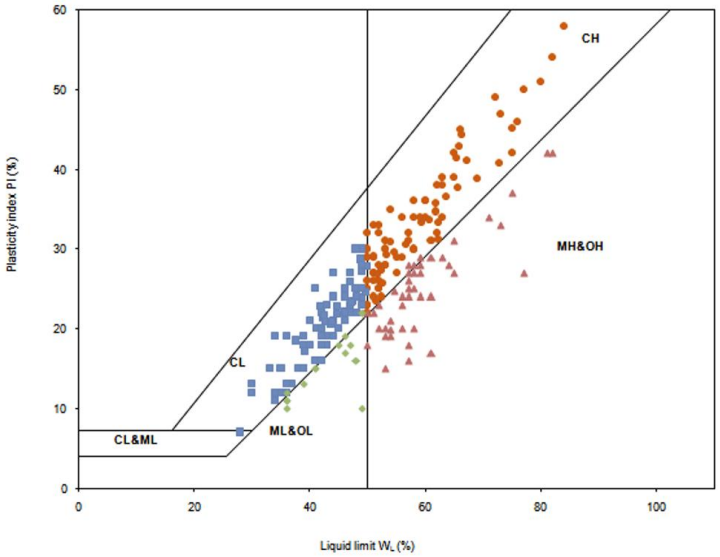

Figure 3 – Projection of the samples studied in the Casagrande plasticity chart.

Table 4 presents the descriptive statistics of each physical and mechanical property of the marly formations.

Table 4 – Descriptive statistics for the physical and mechanical properties of inorganic marls of Unit 5.

Fat clays (CH)												
	w_L (%)	**PI (%)**	**γ_b (kN/m^3)**	**W (%)**	**c (kPa)**	**φ (°)**	**c´ (kPa)**	**φ´ (°)**	**C_c**	**e_o**	**q_u (kPa)**	**N_{SPT}**
min	50	18	16.9	12,2	0,0	9	0,0	24	0,060	0,540	100,0	20
max	86	61	25,0	42,7	196,6	28	98,0	36	0,289	1,110	687,8	>50
mean	59	33	19,4	27,2	88,4	19	35,1	30	0,140	0,779	366,9	
std	8	8	1,2	5,6	64,4	5	41,3	3	0,040	0,131	160,6	
Lean clays (CL)												
min	28	7	17	12	0,0	4	8,2	13	0,060	0,362	109,0	28
max	48	30	23	44	421,6	49	421,6	47	0,280	1,040	824,2	>50
mean	42	20	19	22	95,0	23	114,1	26	0,124	0,714	354,0	
std	5	4	1	5	93,3	12	125,5	9	0,050	0,160	206,9	

Silts of high compressibility (MH)												
min	50	15	17,4	14,7	7,0	15	2,1	4	0,030	0,469	69,0	11
max	82	42	24,2	42,1	80,0	30	45,0	33	0,222	1,296	2595,0	>50
mean	60	25	19,9	26,0	30,0	21	19,7	16	0,107	0,741	424,3	
std	7	6	1,5	8,3	20,5	5	13,5	9	0,050	0,220	483,5	
Silts of low compressibility (ML)												
min	25	10	17,1	10,1	0,0	11	19,0	18	0,037	0,413	57,0	11
max	49	22	21,6	30,3	225,0	50	59,6	25	0,126	1,827	2186,0	>50
mean	41	15	19,8	21,9	35,6	27	33,7	22	0,078	0,652	395,1	
std	6	3	1,0	5,3	67,2	11	15,4	3	0,020	0,14	514,9	

Due to the various degrees of diagenesis, the marls locally behaves like rock material and can be characterized as weak to moderate weak, of very low durability, moderate weathered and fractured. The rock mass quality according to RQD measurements is very poor to fair. The main physical and mechanical properties of the intact rock are listed in Table 5.

Table 5 – Descriptive statistics for the main physical and mechanical properties of rocky marls.

	n (%)	**ρ_d (kN/m^3)**	**Id_1 (%)**	**σ_c (MPa)**	**E (MPa)**	**I_{s50d} (MPa)**	**I_{s50a} (MPa)**
min	10,39	18,52	4,20	0,57	357,60	0,21	0,16
max	24,72	23,82	15,50	38,10	1019,58	1,78	1,31
mean	16,71	19,79	9,80	6,71	659,65	0,69	0,52
std	5,90	1,63	5,65	8,46	242,30	0,45	0,30

The sandstones intercalations are red, yellow or grey, weak to moderate weak, thin to medium bedded, fine to coarse grained, slightly to moderate altered and frequently fractured. The rock mass quality according to RQD measurements is very poor to fair. The main physical and mechanical properties of the intact rock are listed in Table 6.

Table 6 – Descriptive statistics for the main physical and mechanical properties of the sandstones of Unit 5.

	n (%)	**ρ_d (kN/m^3)**	**σ_c (MPa)**	**E (MPa)**	**I_{s50d} (MPa)**	**I_{s50a} (MPa)**
min	5,69	20,88	2,35	193,05	0,32	0,27
max	16,23	24,80	23,61	6325,63	4,33	1,94
mean	9,585	22,94	9,30	1715,71	1,21	0,68
std	4,06	1,52	6,34	2061,40	1,24	0,53

The brecciоconglomerates are loose to well cemented with yellowish brown clayey-sandy matrix, weak to moderate weak, slightly to moderate weathered and moderate to high fractured. The rock mass quality according to RQD measurements can be characterized as very poor to poor. The main physical and mechanical properties of the intact rock are listed in Table 7.

Table 7 – Descriptive statistics for the main physical and mechanical properties of breccio-conglomerates of Unit 5.

	n (%)	**ρ_d (kN/m^3)**	**σ_c (MPa)**	**E (MPa)**	**I_{s50d} (MPa)**	**I_{s50a} (MPa)**
min	0,28	22,84	3,81	471,16	0,31	0,30
max	17,22	26,07	19,09	4367,72	5,69	3,91
mean	8,05	24,81	7,58	1870,70	1,29	0,99
std	6,28	1,20	5,35	1303,16	1,52	1,08

Unit 6: Marbles and crystalline limestones

Marbles and crystalline limestones of the autochthonous system and the Neo – Hellenic Nappe, respectively, of the Attico - Cycladic massif, constitute this unit. These formations outcrop in a small part at the northern and at the hilly region of Kantza. They are mainly white in colour, thick bedded to massive, moderate to high strong and highly fractured (Figure 2d). The main mechanical properties of the intact rock are listed in Table 8.

Table 8 – Descriptive statistics for the main mechanical properties of carbonated rocks of Unit 6.

	σ_c (MPa)	**I_{s50d} (MPa)**	**σ_t (MPa)**
min	31,97	1,22	5,25
max	71,69	3,13	7,23
mean	55,222	2,08	6,24
std	13,22	0,65	0,99

Unit 7: Schists

This unit includes mica schists, with tectonized ophiolitic bodies, highly fractured, moderate to high weathered, and weak to moderate strong. They create a weathering zone which can reach up a thickness of about 7m. The main mechanical properties of the intact rock are listed in Table 9.

Table 9 – Descriptive statistics for the main mechanical properties of schists of Unit 7.

	σ_c (MPa)	**E (MPa)**	**I_{s50d} (MPa)**	**I_{s50a} (MPa)**
min	10,60	779,50	0,40	0,90
max	34,10	3219,20	3,75	5,01
mean	22,35	1999,35	2,07	2,95
std	11,75	1219,85	1,67	2,05

Based on the above lithological units, the engineering geological map of the study area was compiled at a scale 1:20.000 and is presented in Figure 4.

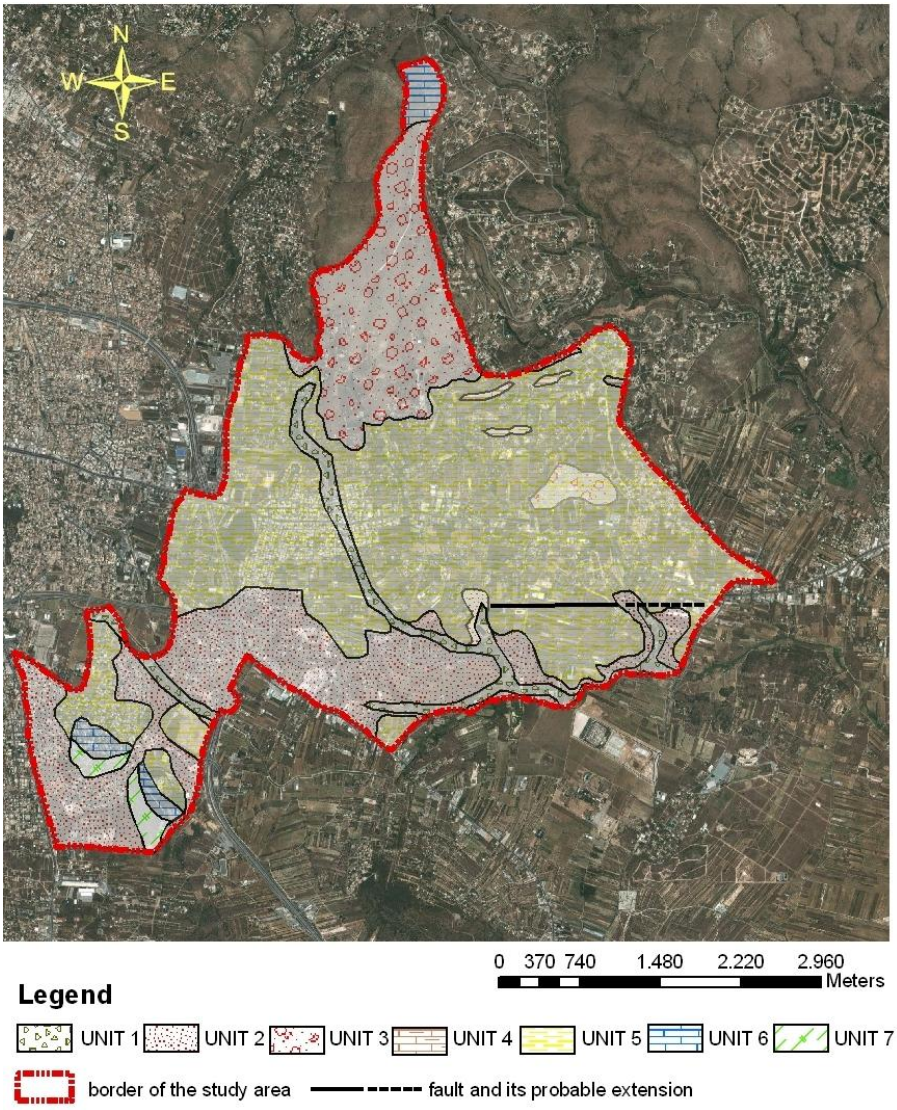

Figure 4 – Engineering geological map of Pallini prefecture.

4. Correlation of Compression Index (C_c) with Physical Parameters

In the last six decades, various single and multiple variables empirical equations have been developed by researchers (Carter and Bentley, 1991; Holtz and Kovacs, 1981; Murthy, 1993) for the estimation of the compression index (C_c) by correlating it with other physical parameters.

In the current study an attempt has been made to estimate the compression index (C_c) of fat clays (CH) from other physical and index properties. For this reason a multiple regression analysis was performed using the liquid limit (w_L) and the initial void ratio (e_o) as independent variables.

Subsequently, the estimated empirical equation is:

$$C_c = 0{,}317 e_o + 0{,}00168 w_L - 0{,}123 \quad (1)$$

It has a fairly good R^2 (0,703) and both independent variables are involved to the above equation. The equation (1) is plotted three dimensionally together with the data set in Figure 5.

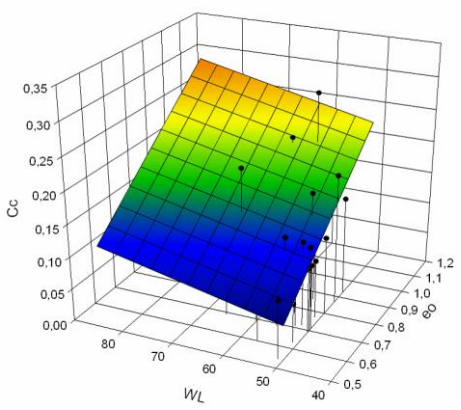

Figure 5 – 3D – plot of the best – fit multiple regression plane relating compression index (C_c) to both liquid limit (w_L) and initial void ratio (e_o), as described by equation (1) in the text.

5. Results

A large number of geotechnical data were collected and evaluated. From the combination of the geotechnical database and geological information, a multipurpose engineering geological map compiled at a scale 1:20.000. The map and the geotechnical values quoted in this paper can be used as a general guide for site investigation and design calculations. Moreover, in the frame of the examination of the various physical and mechanical properties of fat clays, a correlation between compression index (C_c), with both liquid limit (w_L) and initial void ratio (e_o), was thought to be valuable for engineers, who work in the wider study area.

6. Acknowledgments

The authors wish to thank the private consultants (EDAFOMICHANIKI SA, SOTIROPOULOS & ASSOCIATES SA) and the public agencies (KEDE, EYDAP), for their support and yield of geotechnical data.

7. References

Bathrellos G.D., Gaki – Papanastassiou K., Skilodimou H.D., Papanastassiou D., Chousianitis K.G. 2012. Potential suitability for urban planning and industry development using natural hazard maps and geological – geomorphological parameters, *Environmental Earth Sciences*, (66 (2)), 537 – 548.

Carter M. and Bentley S.P. 1991. Correlation of soil properties, London, Pentech Press, 130pp.

Holtz R.D. and Kovacs W.D. 1981. An introduction to geotechnical engineering, New Jersey, Prentice Hall, 733pp.

IGME 1993. Geotechnical map of Greece, 1:500.000 in scale.

IGME – Univesrity of Patras, 2009. Engineering geological map of Athens prefecture, 1:10.000 in scale.

Katsikatsos G. 1992. Geology of Greece, Athens, Patras University Publications, 451pp.

Koukis, G., Rozos, D., Apostolidis, E., 1997. Engineering Geological Conditions of the Formations in the Wider Area of the City of Trikala (Thessaly), *Proc. of 3rd Hellenic Conference on Geotechnical Engineering, 1*, Patra, 113 – 120.

Lekkas S. 1992. Hydrogeological observations in the region of Mesogia (Attica, Greece), *Bull. Geol. Soc. Greece*, XXXVIII/3, 309 – 322.

Marinos P.G. and Xidakis G.S. 1991. Engineering geology and mapping of the Quaternary deposits of the city of Xanthi, N. Greece, *Geological Society, London, Engineering Geology Special Publications , v. 7*, 541-547.

Mettos A. 1992. Geological and paleogeographical study of the terrestrial Neogene and Quaternary rocks of NE Attica and of NE Beotia, *Phd Thesis*, Department of Geology, University of Athens, 259pp.

Murthy V.N.S. 1993. Text book of Soil Mechanics and Foundation Engineering : Geotechnical Engineering Series, Bangalore, SAITECH, 936pp.

Rozos D., 1989. Engineering Geological conditions in Achaia Country. Geomechanical characteristics of Plio – Pleistocene sediments. *Phd Thesis*, Department of Geology, University of Patras, 453pp.

Rozos D., Koukis G. and Sabatakakis N. 2006. Large scale engineering geological map of the Patras city wider area, Greece. *The Geological Society of London, IAEG 2006*, paper No 241.

Rozos D., Apostolidis E. and Xatzinakos I. 2004. Engineering – Geological map of the wider Thessaloniki area, Greece, *Bulletin of Engineering Geology and the Environment*, (63), 103 – 108.

Sabatakakis N. 1991. Engineering geological reaserch of Athens basin, *Phd Thesis*, Department of Geology, University of Patras, 277pp.

UNESCO/IAEG, 1976. Engineering geological maps. A guide to their preparation, Paris, The Unesco Press, 79pp.

Δελτίο της Ελληνικής Γεωλογικής Εταιρίας, τομ. XLVII , 2013
Πρακτικά 13ου Διεθνούς Συνεδρίου, Χανιά, Σεπτ. 2013

Bulletin of the Geological Society of Greece, vol. XLVII 2013
Proceedings of the 13th International Congress, Chania, Sept. 2013

CORRELATION BETWEEN MECHANICAL AND PETROGRAPHIC PARAMETERS OF SANDSTONES

Ktena St. and Sabatakakis N.

University of Patras, Department of Geology, Section of Applied Geology and Geophysics, Laboratory of Engineering Geology, 26500 Patras, Greece

Abstract

Sandstone intact rock specimens are tested to study their point loading strength, while the microscopic properties of the tested specimens are analyzed in thin sections to determine the mineral composition, grain size, cement and contact modes between grains. The intrinsic influence of petrographic characteristics on measured strength is evaluated using regression analysis among the obtained laboratory data.
Key words: *microscopic characteristics, rock strength, packing density.*

Περίληψη

Σε βραχώδες υλικό από ψαμμίτες έγιναν δοκιμές προσδιορισμού της αντοχής σε σημειακή φόρτιση, ενώ στα ίδια δείγματα έγιναν πετρογραφικές αναλύσεις με λεπτές τομές, για τον προσδιορισμό της σύστασης, του μεγέθους των κόκκων, του υλικού συγκόλλησης καθώς και του τρόπου επαφής των κόκκων. Εκτιμήθηκε η επίδραση των πετρογραφικών χαρακτηριστικών στην αντοχή του πετρώματος με την εφαρμογή στατιστικών μεθόδων συσχετισμού μεταξύ των αποτελεσμάτων της εργαστηριακής έρευνας.
Λέξεις κλειδιά: *ορυκτολογικά χαρακτηριστικά, αντοχή πετρώματος.*

1. Introduction

The strength of intact rock is one of the main mechanical characteristics of rock material. Test results obtained from point loading test are indirectly applicable to the estimation of rock mass classification and behavior, while conversion factors relating point load strength and uniaxial compressive strength have been at times proposed (Bieniawski, 1974; 1975; Hawkins and Oliver, 1986; Norbury, 1986; Romana, 1999; Kahraman, 2001; Tsiambaos and Sabatakakis, 2004; Sabatakakis et al, 2008).

The petrographic characteristics of rocks have a constructive effect on the macro-mechanical properties and especially on rock strength. Mineral composition, grain size and microstructure as described by the means of petrographic indices (microscopic factors), are the most important parameters that influence the rock strength.

The influence of microscopic factors on the macroscopic strength of rock is studied with regard to the following aspects: (a) Mineralogical composition and especially the quartz content (q_z), (b) Matrix – cement content (mtx) that is often referred to the fine particles between the grains and (c) Grain particle packing that can be described by parameters such as packing density (PD) and grain

area ratio (GAR) which is defined as the ratio between the grain area and the total area in the selected range of the specimen image (Ersoy and Waller, 1995).

This study aims at investigating the influence of petrography on point load values of intact sandstone rocks tested. The examined sandstone samples have been obtained from different sites and belong to the flysch formation of Olonos – Pindos, Gavrovo and Ionia geotectonic zones which occupies a large area of western Greece. In general, the studied sandstones have a variable composition and are composed of quartz (up to 50%), while they have a large of feldspar (up to 50%) and up to 30% rock fragments. They can be classified as "very fine to fine sands" according to (Wentworth, 1922) grain size scale, "well to poor shorting" and "angular to rounded" based on (Pettijohn et al., 1987) classification scheme.

2. Test Procedure

Twenty one block samples were obtained from different outcrops of sandstones formations. Laboratory core drill and saw machines were used to cut the samples and end faces in order to provide cylindrical specimens in size, shape and ends geometries according to testing requirements. The specimen size was 54 mm (NX) in diameter. Diametrical point loading tests were carried out with the loading axis perpendicular to any visible discontinuity surface, otherwise the test was unacceptable.

The execution of point load tests on intact rock material was in accordance with I.S.R.M. suggested methods (1985).

A quantitative analysis of rock specimen petrographic characteristics was carried out on thin sections using standard polarizing microscope. The main rock – forming minerals, the percentage composition, the cement and contact modes between grains in thin sections were examined.

3. Test Results

In Table 1 the test results are summarized including for each parameter the range of values, the mean value and the number of specimens tested. The scattering of data is mainly due to the different degree of diagenesis (compaction or/and cementation) for the various horizons of the sandstone sediments.

Table 1 – Results of intact rock strength and microscopic factors.

Results and statistical parameters	**$I_{s(50)}$ (MPa)**	**q_z (%)**	**mtx (%)**	**GAR (%)**	**PD (%)**
Minimum value (Min)	0.42	10.00	3.00	11.00	29.70
Maximum value (Max)	10.31	50.00	30.00	70.00	62.04
Mean value (Mean)	5.05	29.18	16.66	41.88	50.39
Standard deviation (Std dev)	3.05	13.18	8.48	14.46	8.78
Number of samples (N)	21	17	19	17	16

4. Correlations Between Rock Properties

Regression analysis was applied to define the relations among the testing data. The procedure is to fit a line through the points, which is computed so that the squared deviations of the measured points from the line are minimized. The line is defined by the relevant equation, whereas the value of coefficient of determination or R-square value is determined. The number of samples (n) used for regression analysis is also shown.

- Quartz content , q_z (%) and point loading index $I_{s(50)}$ (MPa)
  As shown in Figure 1 the quartz content contributes positively to the point load strength of the tested sandstones and the trend relating these parameters is an approximately linear function. Positive relations with uniaxial compressive strength of sandstones have been also described by (Smart et al., 1982), (Shakoor and Bonelli, 1991), (Zorlu et al., 2004). Nevertheless, there are situations that the quartz content of sandstones has no effect on their strength (Bell, 1978; Dobereiner and De Freitas, 1986; Ulusey et al., 1994).

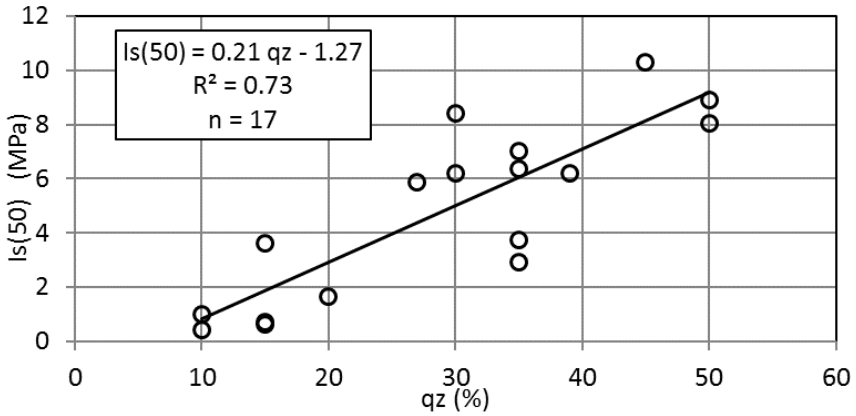

Figure 1 – Correlation between point loading strength ($I_{s(50)}$) and quartz content (q_z).

- Matrix content , mtx (%) and point loading index $I_{s(50)}$ (MPa)
  The correlations between strength and cement or matrix percent were investigated by limited number of researchers. Generally, sandstones with higher matrix content tend to have higher strength than those of lower matrix content (Clough et al. 1981; David et al. 1998). In this study, these parameters are related conversely (Figure 2) and a linear decrease of strength with increasing matrix content is shown. The term "matrix" is often referred to the fine particles between the grains. These fine particles in fact include "matrix" deposited during sediment processes and "matrix" formed during diagenetic processes (cement). The bonding strength of the matrix depends on the cement content within it. In practice, it is difficult to distinguish the cement content within the fine particles especially when observing thin sections. So, the estimated inverse correlation may be due to the low cement content of the mixture of "matrix" that gives lower bonding strength to the total "matrix".
- Packing Density, PD (%) and point loading index $I_{s(50)}$ (MPa)
  The packing density is a measure of grain packing arrangements and can be determined by thin section studies considering the descriptions proposed by(Kahn, 1956). In this study, the estimated values of PD are generally low (<60%) due to high amount of matrix. A positive relation between PD and point loading strength is shown with an approximately linear function (Figure 3). (Ulusay et al. 1994) and (Zorlu et al., 2004) have also determined some moderate positive relationships.
- Grain Area Ratio (GAR) (%) and point loading index $I_{s(50)}$ (MPa)
  The majority of the tested sandstones have a rather small grain ratio (GAR<50%), which indicates that more than a half of the area is filled with matrix material and porosity. In this study, these parameters are related proportional (Figure 4) and a linear increase of strength with increasing grain area ratio is shown.

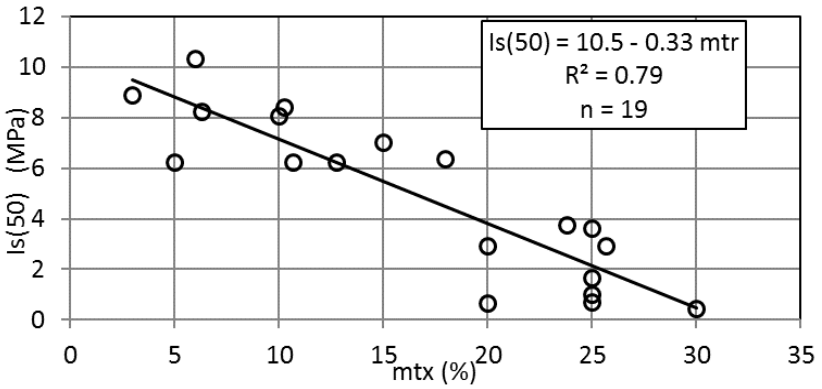

Figure 2 – Correlation between point loading strength ($I_{s(50)}$) and matrix content (mtx).

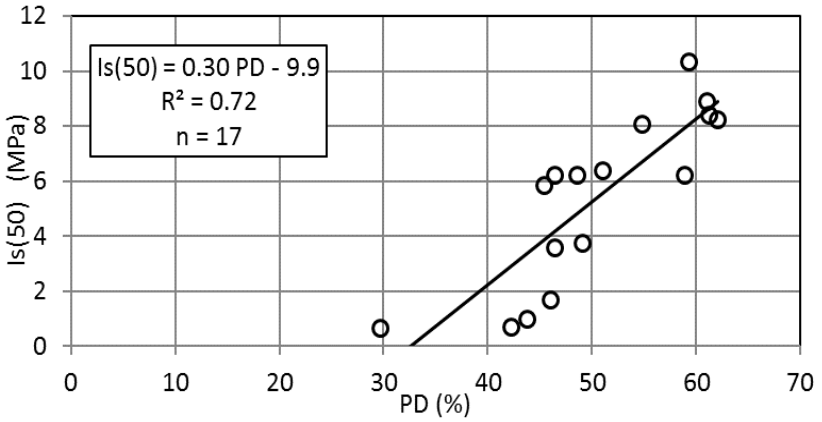

Figure 3 – Correlation between point loading strength ($I_{s(50)}$) and packing density (PD).

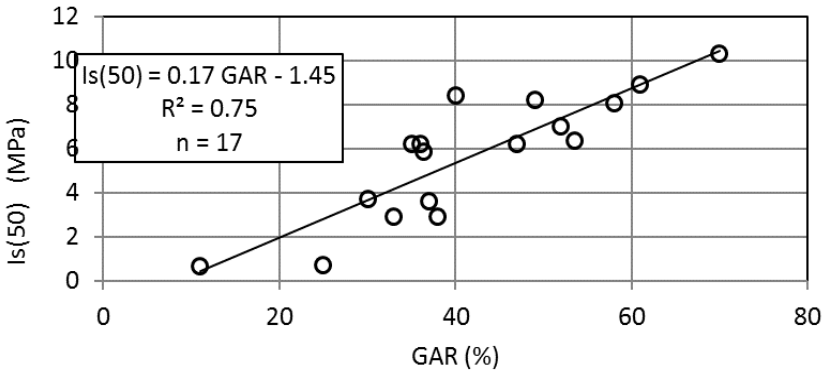

Figure 4 – Correlation between point loading strength ($I_{s(50)}$) and grain area ratio (GAR).

5. Conclusions

Being the inherent attributes of rock, the petrographic characteristics are the constructive parameters which influence its strength. With the increasing percentage composition of quartz grains in sandstones the point loading strength is gradually increased having a linear variation. Contrary, increasing percentage of matrix content resulted to strength decrease.

The textural characteristics (packing density and grain area ratio) also appear to be very important to the mechanical behavior of sandstone. They have a positive influence on the strength measures with a linear trend.

6. References

Bell F.G. 1978. The physical and mechanical properties of the Fell sandstones, Northumberland, England, *Engineering Geology*, 12, 11 – 29

Bieniawski Z.T., 1974a. Estimating the strength of rock materials. Jl. S., *Afr. Inst. Min. Metall*., 74, No 8, 312 – 320.

Bieniawski Z.T. 1975. The point load test in geotechnical practice, *Engng. Geology*, 9, 1 – 11.

Clough G.W., Sitar N. and Bachus R.C. 1981. Cemented sands under static loading, *Journal of Geotechnical Engineering Division*, 107(6), 700 – 817.

David C., Menendez B. and Bernabe Y. 1998. The mechanical behaviour of synthetic sandstones with varying brittle cement content, *International Journal of Rock Mechanics and Mining Sciences*, 35(6), 759 – 770.

Dobereiner L. and De Freitas M.H. 1986. Geotechnical properties of weak sandsones, *Geotechnique*, 36, 79 – 94.

Ersoy and Waller 1995. Textural characterization of rock *Engineering Geology*, 39, 123 – 136.

Hawkins A.B. and Olver J.A.G. 1986. Point load tests: correlation factor and contractual use. An example from the Corralian at Weymouth. In: Hawkins, A.B. (Ed), Site Investigation Practice: Accessing BS 5930, *Geological Society*, London, 269-271.

ISRM Suggested Methods 1985. Suggested method for determining point load strength, *Int. J. Rock Mech. Min. Sci. and Geomech*. Abstr., 22, 51 – 62.

Kahn J.S. 1956. The analysis and distribution of the properties of packing in sand size sediments, *Journal of Geology*, 64, 385 – 395

Kahraman S. 2001. Evaluation of simple methods for assessing the uniaxial compressive strength of rock, *International Journal of Rock Mechanics and Mining Sciences and Geomechanics*, Abstracts 38, 981 – 994.

Norbury D.R. 1986. The point load test. In: Hawkins, A.B. (Ed.), Site Investigation Practice: Accessing BS 5930, *Geological Society*, London, 325-329.

Pettijohn F.J., Potter P.E. and Siever R. 1987. Sand and sandstones, *Springer* Verlag, Berlin, 533p.

Romana M. 1999. Correlation between uniaxial compressive and point load (Franklin test) strengths for different rock classes, *9th ISRM Congress*, Vol1, Balkema, Paris, 673 – 676.

Smart B.D., Rowlands N. and Isaak A.K. 1982. Progress towards establishing relationships between the mineralogy and physical properties of coal measures rocks, *International Journal of Rock Mechanics and Mining Sciences and Geomechanics*, Abstracts 19, 81 – 89.

Sabatakakis N., Koukis G., Tsiambaos G. and Papanakli S. 2008. Index properties and strength variation controlled by microstructure for sedimentary rocks, *Engineering Geology*, 97, 80 – 90.

Shakoor A. and Bonelli R.E. 1991. Relationships between petrographic characteristics, engineering index properties and mechanical properties of selected sandstone, *Bulletin of the Association of Engineering Geologist*, 28, 55 – 71.

Tsiambaos G. and Sabatakakis N. 2004. Considerations on strength of intact sedimentary rocks, *Engineering Geology*, 72, 261 – 273.

Ulusay R., Tureli K. and Ider M.H. 1994. Prediction of engineering properties of selected litharenite sandstone from its petrographic characteristics using correlation and multivariate statistical techniques, *Engineering Geology*, 37, 135 – 157.

Wentworth C.K. 1922. A scale of grade and class terms for clastic sediments, *The Journal of Geology*, vol. 30, No 5, 377 – 392.

Zorlu K., Ulusay R., Ocakoglu F., Gokceoglu C. and Sohmez H. 2004. Predicting intact rock properties of selected sandstones using petrographic thin – sections data, *International Journal of Rock Mechanics and Mining Sciences*, 41(1), 93 – 98.

Δελτίο της Ελληνικής Γεωλογικής Εταιρίας, τομ. XLVII , 2013
Πρακτικά 13ου Διεθνούς Συνεδρίου, Χανιά, Σεπτ. 2013

Bulletin of the Geological Society of Greece, vol. XLVII 2013
Proceedings of the 13th International Congress, Chania, Sept. 2013

REDUCTION OF ROCKFALL RISK OF THE TELEFERIK AREA OF SANTORINI - GREECE

Lekkas E.[1], Alexoudi V.[1] and Lialiaris I.[1]

[1] National and Kapodistrian University of Athens, Faculty of Geology and Geoenvironment, Department of Dynamic, Tectonic and Applied Geology, elekkas@geol.uoa.gr, valexoudi@geol.uoa.gr, lialiarisj@gmail.com

Abstract

The Teleferik area of Santorini Volcanic Complex, is characterized by rockfall risk due to existing morphological, geological, geotechnical and geodynamic conditions. It is therefore considered a high risk area because of the huge number, in annual base, of its visitors. The objects of the research are: (i) To identify areas with increased risk of boulders' detachment, ii) The mapping of rockmasses for direct intervention projects,(iii)To suggest scenarios of rockfall events, (iv) To recommend the urgent works required upslope of the lower lift station of the Teleferik in order to reduce the existing risks to an utmost minimum. The calculations for the above assessments were mostly based on back analysis method, processing data of the recent rockfall events. The proposed interventions belong to the general context of large-scale projects, while top priority is given to works upslope of the lower lift station, which will work as an extra last line of defense in case of large-scale geodynamic events in the future.
Key words: *Rockfalls, Hazard, Santorini, Hellas.*

Περίληψη

Η περιοχή της καλδέρας της Σαντορίνης, ανάντη του τελεφερίκ και του Παλαιού λιμένα Φηρών, χαρακτηρίζεται από υψηλό κατολισθητικό κίνδυνο λόγω των υφιστάμενων μορφολογικών, γεωλογικών, γεωτεχνικών και γεωδυναμικών συνθηκών. Δεδομένης της διέλευσης εκατοντάδων χιλιάδων τουριστών σε ετήσια βάση, γίνεται εύκολα αντιληπτή η αναγκαιότητα λήψης συγκεκριμένων μέτρων μείωσης του κινδύνου. Η έρευνα έχει ως στόχους: i)Την υπόδειξη περιοχών με αυξημένη πιθανότητα εκδήλωσης αποκολλήσεων βραχοτεμαχών ii) Την υπόδειξη των όγκων στους οποίους θα πρέπει να γίνει άμεση παρέμβαση, iii) Την παρουσίαση σεναρίων κατολισθήσεων – καταπτώσεων, iv) Την υπόδειξη επειγόντων έργων ανάντη του κάτω Σταθμού του Τελεφερίκ προκειμένου να μειωθεί στο ελάχιστο δυνατό η επικινδυνότητα. Χρησιμοποιήθηκε γνωστό λογισμικό ανάλυσης καταπτώσεων, με το οποίο έγιναν ανάδρομες επιλύσεις και προσομοιώσεις σύμφωνα με τα στοιχεία από πρόσφατα φαινόμενα. Οι παρεμβάσεις εντάσσονται στο γενικότερο πλαίσιο των έργων μεγάλης κλίμακας, ενώ δίνεται ιδιαίτερη έμφαση στα προτεινόμενα επείγοντα έργα ανάντη του κάτω Σταθμού Τελεφερίκ, τα οποία θα λειτουργήσουν ως πρόσθετη δικλείδα ασφαλείας σε περίπτωση εκδήλωσης έντονων κατολισθητικών γεγονότων.
Λέξεις κλειδιά: *Καταπτώσεις, Κίνδυνος, Σαντορίνη, Ελλάδα.*

1. Introduction – Background - Scope

The area of Teleferik - Old Port of the island of Thera presents an increased rockfall risk which is expressed by numerous events, occurring on the slopes of the caldera (Figure 1).

The high rockfall risk is due to a combination of factors and in particular: (i) the steep slopes and existing morphological discontinuities, (ii) the vertical primary and secondary discontinuities, that intersect the volcanic formations, (iii) the combination of geological and geotechnical conditions and particularly the succession of the rocky and loose formations, (iv) the earthquake and volcanic activity, (v) the severe weathering and (vi) the human interventions (Lekkas, E., 2009a).

Since, during the last decades, the area is attracting more than one million visitors per year, a number of effective projects has been implemented, in order to address rockfall events (technical report Damala, et al., 1994).

Over the last few years due to: (i) the intense geodynamic processes and the subsequent weathering of rockmass, (ii) the increasing number of visitors and (iii) the occurrence of severe events, extensive research has taken place (Lekkas, E. 2009b), in order to propose the required works, construction of which, is expected to begin in November 2013.

However at the end of February 2012, there has been a rockfall event of a volume of 0.5 m^3 from the North slope which broke into the building of the Lower Station of the Teleferik, fortunately causing damage only in the waiting room and other facilities of the building. From the fieldwork it was found that there are more blocks in various parts of the slopes, prone to wedge – planar or toppling failure. Based on this fact, there has been an in-situ research project in order to determine the appropriate, urgent measures against rockfall hazard in the area, until the construction of the aforementioned large scale works starts.

Figure 1 - General view of the study area. The Teleferik line is marked with a dotted line, Fira appears on the upper part of the slope and the Old Port appear at the Lower part of the slope.

This research aims to:

- Identify the boulders with increased rockfall risk.
- Present rockfall simulations in areas of increased probability of failure.
- Designate the necessary rockfall protection measures over the Lower Station which are required in order to reduce the existing risk.

2. Design Criteria

Based on data from previous surveys (Druitt, Th, et al., 1999, Lekkas, E., 2009b, Antoniou, A. & Lekkas, E., 2010, Rathmayr, B., et al., 2012), fieldwork and consideration of all the evidence, nine areas have been identified where a rockfall could possibly start (Figure 2, 3). The design data are presented in Tables 1, 2. Five of these areas are located on the northern slope (N-A to N-E) and four in the southern slope (S-A to S-D). The parameters and design criteria are described below.

2.1. Parameters for Calculating Size of Unsafe Boulders

The size of unsafe boulders varies, as it primarily depends on the geological - geotechnical characteristics of the rockmass. It should be noted that detailed geological – geotechnical mapping of the area exist at a scale of 1:500 (Lekkas E., 2009b). The parameters (Table 1, 2) that were taken under consideration are:

- The unsafe boulders of Rhyodacitic Lava of Thirasia (TL) are large in volume, which can reach up to 30 m^3, since the average distance between vertical discontinuities, as well as the distance between horizontal discontinuities are 5 and 6 m respectively, where the undermining of the slope takes place.
- For the formation of Basaltic Andesitic Lava of Scaros (SL) the boulders volume is smaller and can reach up to 15m^3, since the average distance between vertical discontinuities, as well as between horizontal discontinuities, are 3 and 5 m respectively.
- For the formation of bedded and breccia Tuffs (T) as well as for the formations of Black Pumice and Ignimbrite (BP and IGN) the boulders volume is less than 5 m^3.

Consequently, the maximum weight of blocks which might be detached from the formation of Rhyodacitic Lava of Thirasia (TL) was estimated at 77 tn, while the blocks weight of Basaltic Andesitic Lava of Scaros (SL) formation was estimated at 33 tn. The blocks weight for the formation of bedded and breccia Tuffs (T) was considered to be 5 tn. As an input parameter for the analysis, it was considered only the 1/3 of the values above, because of the "cracking" of the boulders due to impacts along their route.

2.2. Terrain Parameters

The following parameters were taken under consideration (Table 2):

- The altitude at which the volume is located, the horizontal distance that the block will traverse, while additional importance is given to the topographic profile from the starting to the "impact" point (i.e. building of the Lower Station).
- The friction angle φ of the geological formation, the vertical and tangential coefficient of the material Rn and Rt respectively (natural and geomorphological feature) as well as the standard deviation of these values.

2.3. Capacity of Absorbing Energy of the Intermediate Area

The intermediate area, from the starting point of the rockfall to the Lower Station has a variable capacity to absorb the total kinetic energy of the falling blocks, depending on the nature of the formation on the slope surface. The absorbing capacity is divided into high, medium and low (Table 1).

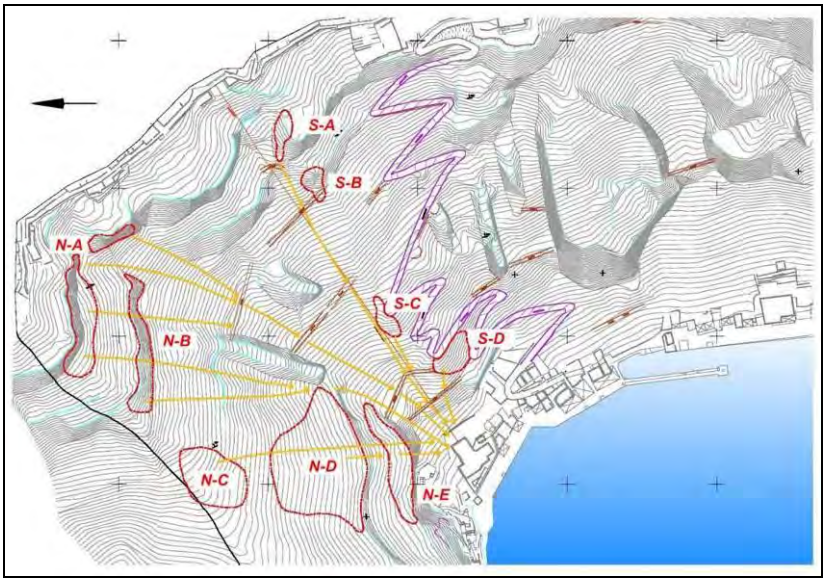

Figure 2 - Map with the locations –areas at the North (N-A to N-E) and South (S-A to S-D) slopes where it is highly likely that landslide phenomena may occur.

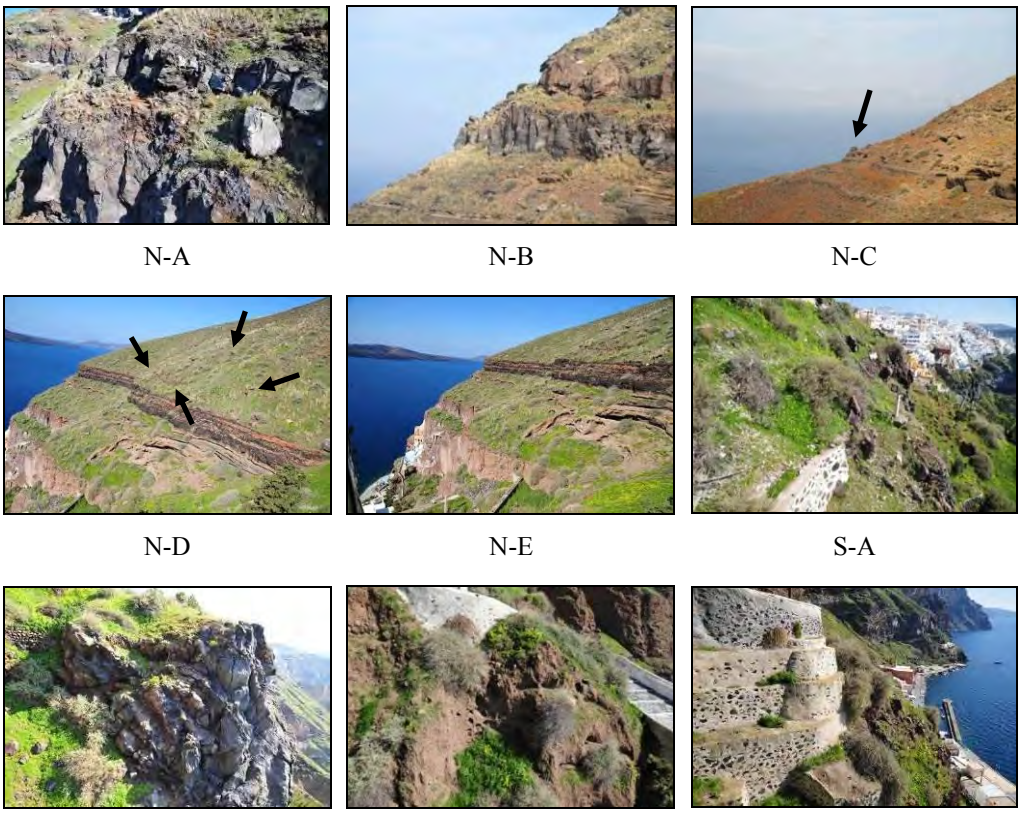

N-A N-B N-C

N-D N-E S-A

S-B S-C S-D

Figure 3 - Hanging boulders corresponding to the areas N-A to N-E and S- A to S-D.

Table 1 – Parameters for calculating size of unsafe boulders.

Area	Formation Type	Max Volume (m^3)	Height (m)	Horizontal Distance (m)	Hazard Estim.	Damping	Risk for the Lower Station
N-A	TL	30	220-240	300	High	High on scree	Mean
N-B	SL	20	170-180	250	High	High on scree	Mean
N-C	T	5	120-150	150	High	Low	High
N-D	SL	5	80-100	100	High	Low	High
N-E	BP, IGN	5	40-80	50	High	Low	High
S-A	TL	30	200-240	300	High	High on scree	Mean
S-B	SL	8	130-150	250	High	High on scree	Mean
S-C	SL	2	70-90	70	High	High	Mean
S-D	IGN	2	40-50	30	High	Low	High

Table 2 – Terrain parameters.

Description	Unit	Friction Angle φ	Vertical Coefficient Rn		Tangential Coefficient Rt	
			Mean Value	Standard Deviation	Mean Value	Standard Deviation
Tuffs	T	24	0.20	0.04	0.70	0.04
Lava	SL	30	0.30	0.04	0.75	0.04
Lava	TL					
Ignimbrite	IGN					
Black Pumice	BP					
Scree	TSC	30	0.32	0.04	0.82	0.04
Asphalt	B	30	0.40	0.04	0.90	0.04

3. Risk of Lower Station

The risk of Lower Station derives from the combination of existing risk per specific risk areas (N-N-A to N-E and A to S-D) and the 'absorbing energy' capacity along the boulder's travelling downwards, until they reach the lower morphological section. In particular, the risk derives from the equation:

$$Risk = Hazard \times 1 / Absorbing\ Capasity$$

Based on the above, it is possible to estimate the risk of Lower Station for any rockfall starting point (Table 1).

4. Rock Fall Event of February 2012

As it has been previously stated, in February 2012 a boulder was detached from the North Slope and finally crashed inside the building of the Lower Station causing material damage to the facilities. The volume of the boulder, which was detached from the Black Pumice formation over the Lower Station, was estimated at about 0.5m^3 and after it bounced on various parts of the slope, it landed inside the Lower Station (Figure. 4).

Analyses of the observed rock fall event were executed, based on the data of the original volume, the morphological profiles and its route on the slope, using the software Rocfall by Rocscience Ltd, version 4.0 (Figure 5a, 5b, 5c, 5d).

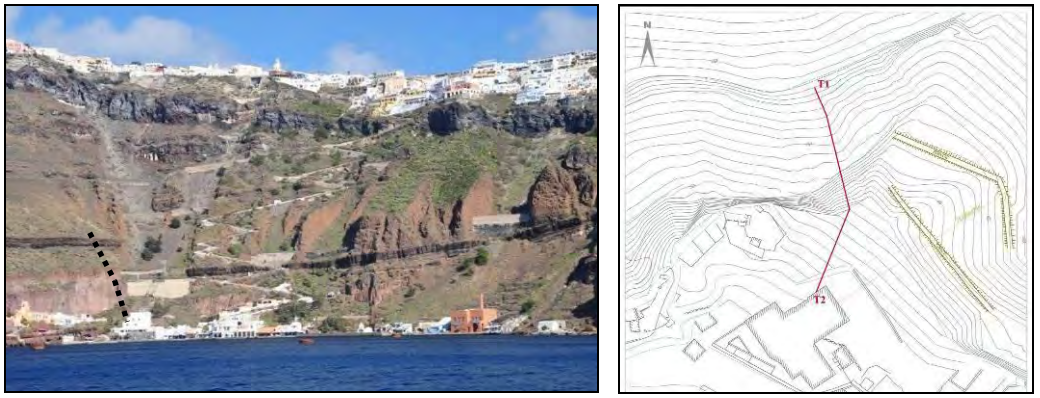

a b

c d e f g

Figure 4 - The route of the Black Pumice rock boulder that was detached (a,b) and landed at the Lower Station of the Teleferik (c-g).

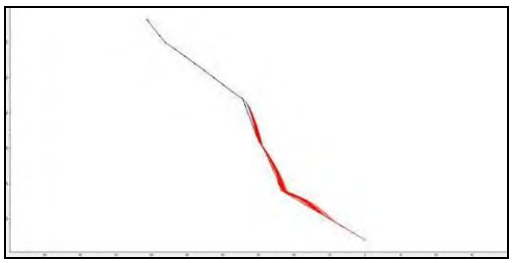

Figure 5a - Trajectory of the Black Pumice rock boulder at section T1-T2.

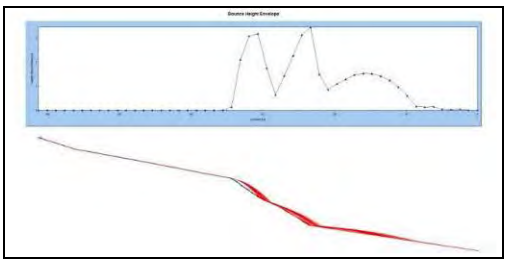

Figure 5b - Variation of bounce height of Black Pumice boulder at section T1-T2.

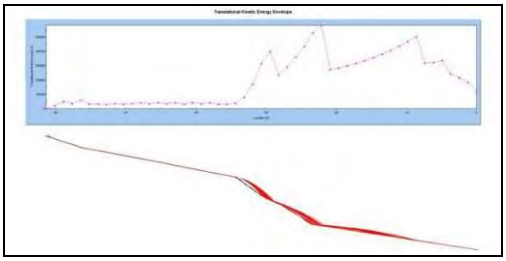

Figure 5c - Kinetic Energy Envelope for falling boulders at section T1-T2.

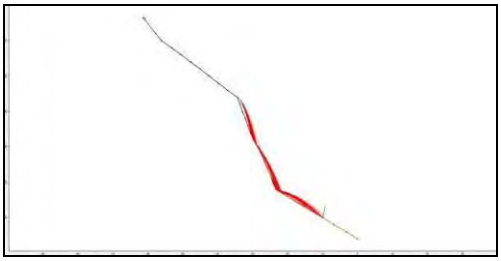

Figure 5d - Trajectory of Black Pumice rock boulder with rock fall barrier system at section T1-T2.

The vertical and tangential coefficients, Rn and Rt respectively (natural and geomorphological characteristics), as well as the standard deviation of these values which are presented in Table 2 and concern each geotechnical section have been assessed, by using the backup analysis method.

5. Rock fall analysis – Suggested Protection Measures

Based on the collected data, simulations have been made for the three high risk areas of the north slope, (N-C, N-D, N-E) and one high risk area of the south slope (S-D). It should be noted that there are not many incidents of rockfall events of volcanic formations, available in international bibliography. For this reason, coefficients Rn and Rt have been used based on the data of the backup analysis. The input data are:

- The geometry of the terrain has been assessed from the representative cross sections which were selected in relation to the areas designated as potentially unstable.
- The geotechnical characteristics of the geological formations which appear on the surface of the slope. The geological formations encountered in the area are divided into sub-sections (Table 1, 2), with different design input values.
- Parameters which characterize the terrain, such as the friction angle of the material φ, the vertical and tangential coefficients Rn and Rt respectively (natural and geomorphological features) and the standard deviation of these values (Table 1, 2).
- The characteristics of the boulders, such as the Weight W (kg) =Volume V (m^3) * Specific Weight γ (kN/m^3), the initial speeds at the time of detachment (horizontal and vertical) and the standard deviations of these values.

Rockfall simulations were conducted at each location (Tracks of Falling Blocks, Kinetic Energy and Bounching Height Diagrams). Based on the simulation data, the maximum capacity of the required Rock Fall Barrier from the North side of the Lower Station is estimated at 1000kJ at 4 meters height. From the South side of the Lower Station the maximum capacity of the Rock Fall Barriers is estimated at 500kJ at 3 meters height. For safety reasons the values above, have been doubled.

The layout of the Rock Fall Barriers, after on site investigation of the application areas of the selected systems is shown in Figures 6a, 6b.
In total, three Rock Fall Barriers are suggested as follows:

- Between the Lower Station and pillar No 1, crosswise to the route of Teleferik with the following features: Length: 20m, Height: 3m, Capacity: 1000kJ.
- On the side of the Lower Station, upwards at a 60 degrees angle relative to the direction of the Teleferik lines with the following features: Length: 10m, Height: 4m, Capacity : 2000kJ.
- On the side of the Lower Station, downwards at 60 degrees angle, relative to the direction of the Teleferik lines with the following features: Length: 10m, Height: 4m, Capacity : 2000kJ.

a b c

Figure 6a - Views of the area showing the rock fall barriers systems a, b and c.

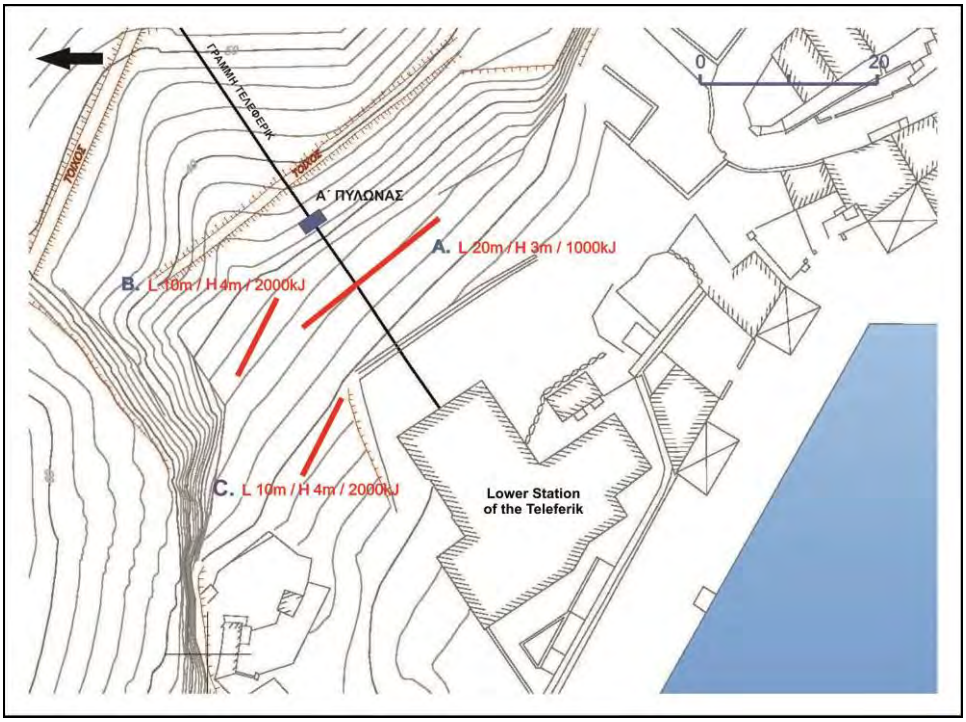

Figure 6b - Topographic diagram showing the layout of the proposed rock fall barriers (a, b, c) above the installations of the Lower Station of the Teleferik.

6. References

Antoniou A. and Lekkas E. 2010. Rockfall susceptibility map for Athinios port, Santorini Island, Greece. Elsevier, *Geomorphology*, 118 (2010) 152–166.

Druitt T.H., Edwards L., Mellors R.M., Pyle D.M., Sparks. R.S.J., Lanphere M., Davies M. and Barriero B. 1999. Santorini volcano. *Memoir* No 19, p. 165, Geological Society of London.

Lekkas E. 2009a. Landslide hazard and risk in geologically active areas. The case of the caldera of Santorini (Thera) volcano island complex (Greece). International Association for Engineering Geology (IAEG), *7th Asian Regional Conference* for IAEG, p. 417-423, Chengdu.

Lekkas E. 2009b. Reduction of landslide risk in the Santorini Caldera slopes in the area of the Teleferik and Old Port of Fira (in Greek), *Research Project*, Department of Dynamic, Tectonic and Applied Geology, National and Kapodistrian University of Athens, Athens.

Rathmayr B., Kunzli B., and Graf K. 2012. Island of Santorini, Greece – Rock Fall Mitigation Measures for Thira area. *GEOTEST Report* No 14111050.3, Zollikofen.

Δελτίο της Ελληνικής Γεωλογικής Εταιρίας, τομ. XLVII , 2013
Πρακτικά 13ου Διεθνούς Συνεδρίου, Χανιά, Σεπτ. 2013

Bulletin of the Geological Society of Greece, vol. XLVII 2013
Proceedings of the 13th International Congress, Chania, Sept. 2013

SAFETY ASSESSMENT AND REMEDIAL MEASURES DESIGN FOR AN EXTENSIVE ROCKFALL ALONG THE MAIN ROAD TO KIMI, EAST EUBOEA, GREECE

Loupasakis C.[1], Lalos G.[1] and Rozos D.[1]

[1] Laboratory of Engineering Geology and Hydrogeology, School of Mining and Metallurgical Engineering, National Technical University of Athens, 9 Iroon Polytechneiou, Athens, Greece
cloupasakis@metal.ntua.gr, rozos@metal.ntua.gr

Abstract

The steep morphology and the intense tectonic fragmentation of the mountainous areas of Greece combined with the dense road network create conditions favorable for the manifestation of rockfalls. Numerous events are recorded through the years, some of them causing injuries or even worse loss of lifes.
The rockfall that took place along the Kimi – Platana – Paralia provincial road on August 2008, was studied in detail and is presented in the current paper. The rock detachment area was defined 200m away and at an altitude of 140m (130m higher from the road), while the rock pieces detached had a maximum volume of 4m^3. The final consequences were two crashed cars and a heavily injured civilian.
The causual factors as well as the proposed remedial measures, estimated by the use of RocFall by Rockscience Ltd., are described in detail. Furthermore, the temporary remedial measures applied by contractors are evaluated, pointing their defects.
Key words: *Marl formations, RocFall Software, statistical analysis, risk assessment.*

Περίληψη

Το απότομο μορφολογικό ανάγλυφο και η έντονη τεκτονική καταπόνηση των γεωλογικών σχηματισμών του Ελλαδικού χώρου σε συνδυασμό με την ύπαρξη πυκνού οδικού δικτύου δημιουργεί συνθήκες ευνοϊκές για την εκδήλωση καταπτώσεων. Τα περιστατικά που έχουν κατά καιρούς σημειωθεί είναι πολυάριθμα, προκαλώντας σε κάποιες από τις περιπτώσεις τραυματισμούς ή ακόμα και απόλυα ζωών .
Στην παρούσα εργασία παρουσιάζονται αναλυτικά τα αποτελέσματα της έρευνας του μηχανισμού εκδήλωσης καταπτώσεων κατά μήκος του οδικού δικτύου Κύμη – Πλατάνα – Παραλία τον Αύγουστο του 2008. Η αποκόλληση των βραχοτεμαχίων έλαβε χώρα σε θέση που απέχει 200m από το οδικό δίκτυο και 130m ανάντι. Το μέγιστο μέγεθος των βραχοτεμαχίων που κατέληξαν τελικά στο δρόμο ανέρχεται στα 4 m^3 και το αποτέλεσμα της κατάπτωσης ήταν η συντριβή δύο διερχόμενων αυτοκινήτων και ο σοβαρός τραυματισμός πολιτών.
Τα αίτια πρόκλησης των καταπτώσεων καθώς και τα προτεινόμενα μέτρα για την μελλοντική ανάσχεσή τους αναλύονται με λεπτομέρεια. Επίσης τα μέτρα ανάσχεσης που έχουν ήδη εφαρμοστεί από εμπειροτέχνες, αξιολογούνται αναδεικνύοντας τις πιθανές αστοχίες τους.
Λέξεις κλειδιά: *Μαργαϊκοί σχηματισμοί, ανάσχεση καταπτώσεων, εκτίμηση κινδύνου καταπτώσεων, στατιστική ανάλυση.*

1. Introduction

The continuous urbanization and development in landslide-prone areas led to the manifestation of an increasingly high landslide activity during the last decades in Greece. Among the failures, rockfalls hold a leading role acting rapidly, without any former notification, causing serious socio-economic consequences (Loupasakis et al, 2010; Antoniou & Lekkas, 2010; Christaras et al, 2010). Unfortunately, sometimes beside the significant economic losses, they cause serious injuries or even worse loss of lives.

The case study presented through this paper refers to a failure that took place on August 13, 2008, at the provincial road connecting Paralia village with Kimi seaport. Kymi is a town at the eastern central part of Euboea Island and the above mentioned road is highly important as it is the main artery leading to the harbour.

The currently examined failure along this road causes up to now serious socio-economic consequences as the remedial measures applied are temporary and incomplete. The unobstructed road connection with the harbour cannot be accomplished, as the slope still presents serious stability problems. Besides the abovementioned long lasting problems, the failure left behind a civilian with permanent disability, as the rocks crashed two cars passing through at the time (Figure 1).

This paper focuses on the description of failure as well as on the design of the appropriate remedial measures. Furthermore, the temporary remedial measures applied up to now by contractors are evaluated, pointing at their defects. All abovementioned Rockfall simulations were conducted by using RocFall by Rockscience Ltd. This is a statistical analysis program designed for rockfalls` risk assessment (Rocscience, 2002).

Figure 1 – View of the road, right after the Rockfall took place. The oversize blocks as well as the crashed cars are presented.

2. Historical Background of the Failure

As mentioned above, the examined failure took place on August 13, 2008, at 20:30 approximately, at the provincial road connecting Paralia village with Kimi seaport, 900m from Paralia village. The rock seeder (rock detachment area) was defined 200m away and at an altitude of 140m (130m higher from the road) (Figures 2 & 3). The marly limestone rock pieces were detached from the upper parts of the slope. The majority of the limestones` rectangular rock pieces slid a few tens of meters from the seeders and stopped without causing any damages. Unfortunately a few oversized pieces, reaching to a maximum volume of $4m^3$, rolled down the slope and finally reached the road. The rock pieces reached the road with an enormous kinetic energy causing the aforementioned results.

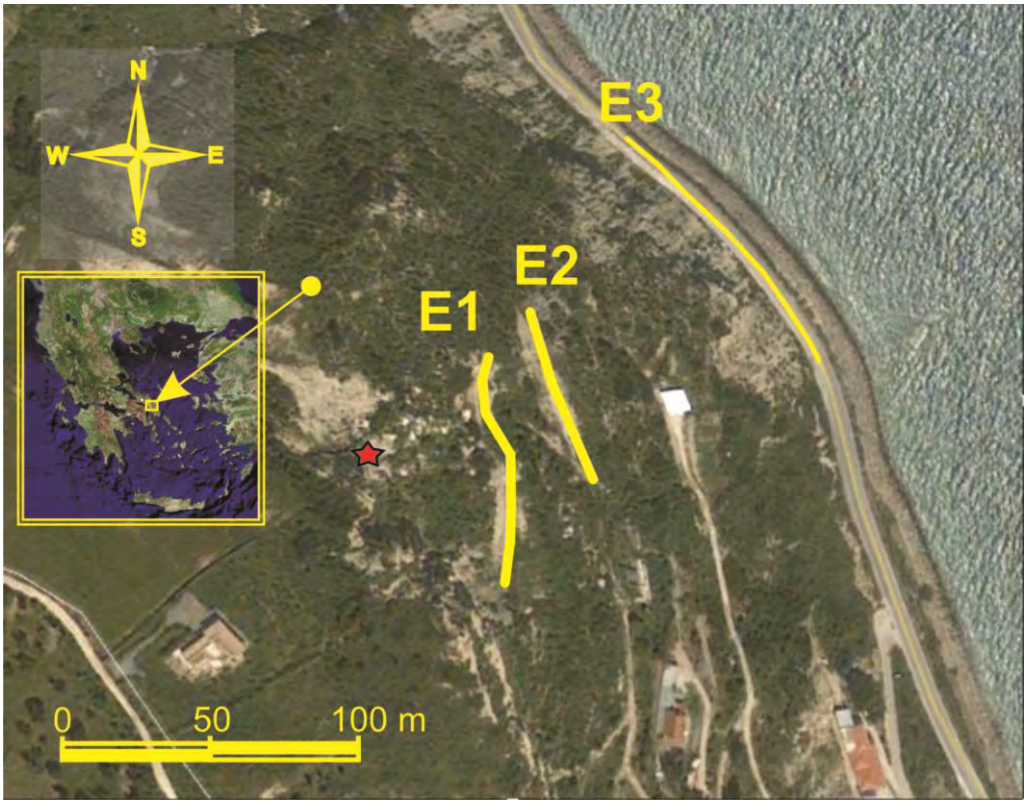

Figure 2 – Location map of the study area. The star indicates the rock detachment area of the August 13, 2008 failure. The lines E1 and E2 indicate the position of the soil embankments constructed over the slope and line E3 the position of a temporary embankment installed in the middle of the road, with gravel filled big bags.

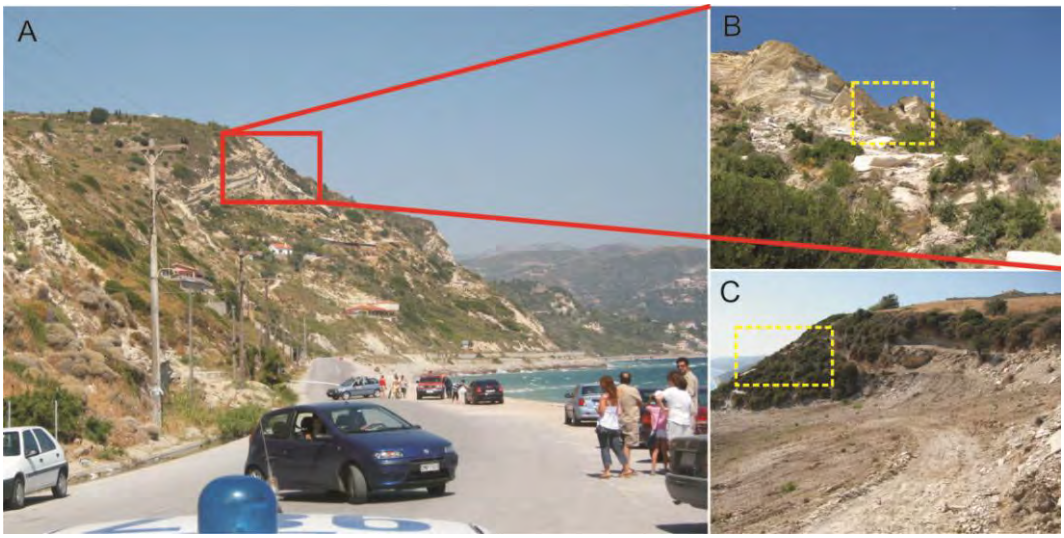

Figure 3 – View of the examined slope. The rock detachment area is indicated on picture A. Picture B provides a closer view of the detachment area. Picture C presents the earth moving works that took place before the failure at the crest of the slope.

The following days, and before conducting a complete geotechnical study, a temporary embankment was installed in the middle of the road (Figures 2 & 4A,B). This 2m high embankment (E3 at Figure 2) was constructed by two series of big bags filled with gravels, aiming to provide a safety at the external lane of the road, preventing the complete blocking of the traffic. This temporary embankment still remains there as none ever decided to remove it. Figure 4A, B proves that although it was installed based on empirical estimations, it operated perfectly during the years, trapping several rock block and protecting the external lane of the road.

Besides the above mentioned embankment, extensive earth moving works took place on the slope aiming to modify its morphology, forming a complex of ditches and embankments, E1 & E2, as remediation measures (Figures 2 & 4C,D). This works took place after the installation of the E3 temporary embankment by contractors appointed by the municipality. Despite all these works the temporary embankment E3 was not removed at the end.

At the same period, extensive emendatory earth moving works took place around the rock detachment area. The detachment area was located right next to an extensive excavation (Figure 3C) that was under construction at the period of the failure. So in order to prevent farther failures from the same location several rock blocks were moved from the site.

Figure 4 – A & B Photos present the embankment, E3, constructed in the middle of the road. The numerous trapped rock blocks prove the effectiveness of the embankment, initially constructed as a temporary protection measure. C & D photos present the embankments, E1 and E2.

3. Geological Setting

The study area has a steep relief and the road connecting Paralia village with Kimi seaport is constructed along the coast line. The neighbouring slopes present numerous failures and several

studies concerning their stability have been conducted the last years (Apostolidis & Pogiatzi, 1996; Koutsouveli & Milonaki, 1996, Koumantakis et. al, 2007).

The wider study area consists of pre-alpine rocks, alpine formations, of the Pelagonian geotectonic zone, and post alpine Neogene and Quaternary deposits (Katsikatsos et al. 1986; Mettos et al. 1991; Serelis et al. 2004). The geological formations occupying the wider study area are: (a) Quaternary deposits (coastal, alluvial, terra rossa, fans ech), (b) Neocene sediments (marls- clayey marls, marly limestones and cohesive clastic formations), (c) Volcanic rocks, (d) flysch formations, (e) limestones, (f) shist-cherts, (g) bauxite bodies and (h) metamorphic rocks.

The examined slope consists of Neogene formations, clayey marls and calcitic marls to marly limestones. The clay marls occupy the lower parts of the slope and the marly limestones the upper. The morphology of the slope is highly affected by its geological structure. As presented at figure 3A, the lower parts, occupied by the relatively soft and erodible clayey marls, appear gentler inclination and the upper, occupied by the hard calcitic marls to marly limestones, much steeper, forming vertical slopes. Furthermore, the differences on the erodibility of the two formations lead to the underexcavation of the marly limestones, forming sections with overhanging blocks.

4. Rockfall Risk Assessment

The evaluation of the stability conditions was established by analysing six cross sections along the slope (figure 5). The selected cross sections cover the entire unstable slope section, including all possible rock detachment areas. By using Rockfall Software each cross section was analysed by considering two different profiles, the natural slope profile as well as the new profile formed after the construction of the embankments (Figure 5). Two rock detachment areas (seeders) have been defined on each cross section, the upper seeder, located along the crest of the slope and the lower seeder, located at the steep slope section attached on the side of the road. Defining the initial conditions, the starting velocity of the rock blocks was set 0m/s and their mass was set to range from 20 to 2500kgr, covering the majority of the blocks located on site.

Altering the friction angle value of the slope surface – rock block interface (Phi), two different project scenarios were defined. According to the first scenario the friction angle gets zero value, signifying that the rock blocks roll down the slope. At the second scenario, the friction angle gets values reflecting the properties of the formation occupying the slope surface. The assignment of friction angle values indicates that the rock blocks slide on the slope surface, decelerating due to the friction.

Considering the slope surface material properties four different types of materials were defined, as follows:

a) Marly limestones (calcitic marls to marly limestones): occupying the crest of the slope, the upper seeder.
b) Marls: occupying the lower section of the slope right next to the road, the lower seeder.
c) Talus cover: extending at the feet of the seeders, formed by the detached rock blocks.
d) Soil with vegetation: occupying the gentle sections of the slope. Practically this material is the vegetated weathering mantle of the marls.
e) Asphalt: occupying the road

The properties assigned to the abovementioned materials were estimated by in situ tests or selected from bibliographic sources (Giani, 1992; Rocscience, 2002; Asteriou, 2012) (Table 1).

The numerous rockfall simulations conducted according to the above described scenarios have been evaluated by examining the kinetic energy (Total, Translational, and Rotational) envelopes as well as the velocity and bounce height envelopes.

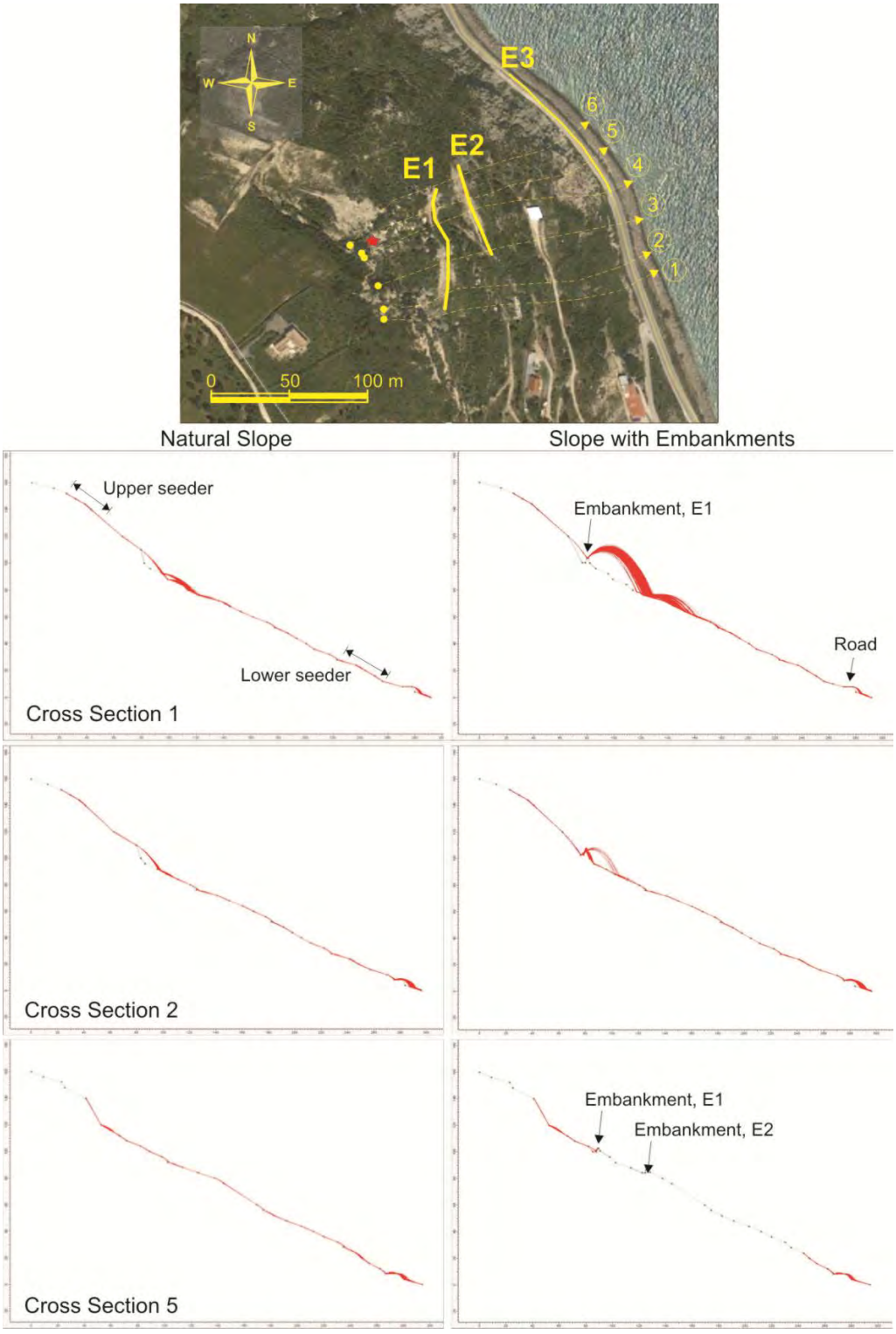

Figure 5 – The Satellite pictures, taken from Google Earth, points the six cross sections selected along the slope for the simulation of the rockfalls. Characteristic examples of simulation results are presented in selected cross sections.

Table 1 – Material properties (Giani, 1992; Rocscience, 2002).

Material Name	Rn* (mean / sd)	Rt** (mean / sd)	Phi (°) (mean / sd)	Roughness (°) (sd)
Marly limestone	0.40/0.02	0.85/0.02	30°/2°	2°
Marl	0.35/0.02	0.80/0.02	30°/2°	2°
Talus cover	0.32/0.04	0.82/0.04	30°/2°	1°
Soil with vegetation	0.30/0.04	0.80/0.06	30°/2°	1°
Asphalt	0.40/0.04	0.92/0.04	30°/2°	0°

*Rn: Normal coefficient of restitution, the ratio of the outgoing velocity (normal to the surface) to the incoming velocity (normal to the surface).
**Rt: Tangential coefficient of restitution, the ratio of the outgoing velocity (tangential to the surface) to the incoming velocity (tangential to the surface)

.

The simulations proved that the embankments E1 and E2 improved the safety conditions of the slope but unfortunately they did not eliminate the risk. The outcomes of the simulations can be listed as follows:

Considering the natural slope

a) The majority of the rock blocks rolling from the upper seeder reach the road. The kinetic energy values at the level of the road are presented in Table 2.
b) All the rock blocks sliding from the upper seeder stop covering a maximum distance of 100m, depending on the morphology. They never reach the road.
c) All the rock pieces rolling from the lower seeder reach the road. The fact that the lower seeder does not bear large pieces reduces the risk and makes the necessary remedial measures simpler.
d) Due to the gentle morphology of the lower southeastern part of the slope, the rock blocks sliding from the lower seeder never reach the road (cross sections 1 - 3). On the contrary the pieces sliding from the rest of the lower seeder (cross sections 4 - 6) reach the road with a small kinetic energy (Table 2).

Considering the slope with the embankments

e) All the rock block sliding or rolling from the northwestern part of the upper seeder (cross sections 3 – 6), get blocked by the embankments. The results are the same with the pieces sliding from the rest of the upper seeder (cross sections 1 & 2).
f) The results are completely different with the blocks rolling form the southeastern part of the upper seeder (cross sections 1 & 2). This particular section is protected only by the embankment E1. As presented in Figure 5, embankment E2 does not extent so far south. The simulations saw that the rocks hit the embankment, pass over it and continue their course to the road. Furthermore, as presented in table 2, the blocks bouncing on the embankment accelerate, hitting the road with a little higher kinetic energy.

Concluding, the embankments, E1 and E2, protect the road from the rock blocks detached from the northwestern part of the upper seeder (cross sections 3-6). On the contrary, they make the safety conditions at the rest of the seeder (cross sections 1&2) worse, accelerating the rolling blocks. Furthermore, the road stays completely unprotected from the lower seeder.

Table 2 – Prominent kinetic energy values

Cross section no.	Natural slope – rock blocks rolling from the upper seeder – kinetic energy at the level of the road (Kj) (max / min)	Slope with embankments – rock blocks rolling from the upper seeder		Natural slope – rock blocks sliding from the lower seeder – kinetic energy at the level of the road (Kj) (max / min)
		kinetic energy at the level of the road (Kj) (max / min)	kinetic energy at the level of the em-bankments (Kj) (max / min)	
1	175 / 2	185 / 1	pass over	no rock blocks
2	300 / 2.8	330 / 2.5	250 / 2.1	no rock blocks
3	300 / 2.4	no rock blocks	220 / 1.8	no rock blocks
4	350 / 2.8	no rock blocks	310 / 2.4	40 / 0.3
5	310 / 2.5	no rock blocks	280 / 2.2	50 / 0.4
6	600 / 4.7	no rock blocks	156 / 1.5	223 / 1.8

5. Remediation Measures Design

In order to secure the road and safely remove the ``temporary`` embankment E3, a few additional remedial measures have to be constructed. The new remedial measures must block the boulders passing over E1 embankment, at the cross sections 1 and 2, and also secure the lower seeder.

The rockfall simulations indicated that the rock blocks bouncing over the embankment can be stopped by installing a new embankment, EN, at the location indicated in Figure 6. At this particular location the rock pieces move with a reduced kinetic energy and their bouncing height is decreased (Table 3). The current embankment can be constructed, as the previous embankments, by compacted soil materials or even better by reinforced soil materials. The reinforcement of the soil material can be accomplished by the use of geotextiles. The impact catchment face of the embankment can be protected by installing gabion blocks, gabion like wall face or impact catchment bags (Figure 7). Considering the bounce height (max 1.4m) and the radius (0.5m) of the boulders, an embankment 3m high is sufficient for the current position. Furthermore considering that reinforced embankments can stand an impact force up to several thousand Kj, this, low-price, solution can be sufficient even in the case of a bigger block rockfall. Most sophisticated and at the same time most expensive, pathetic remedial measures, suitable for the current location, are the rockfall fences.

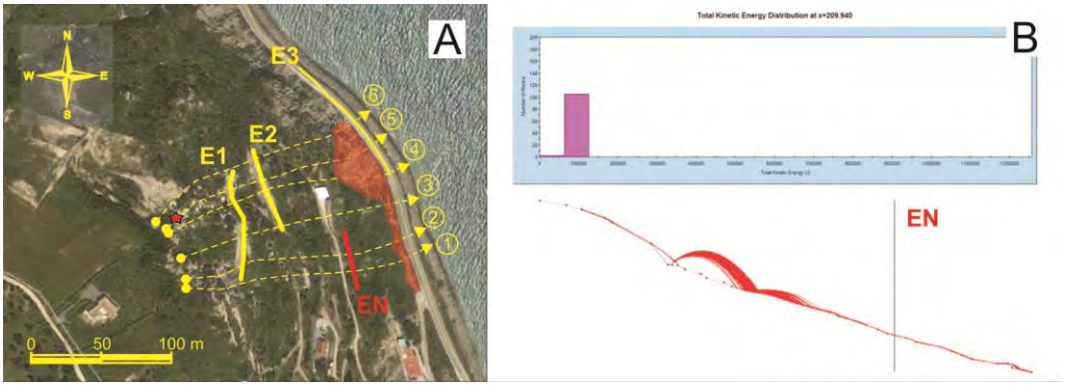

Figure 6 – A) Arrangement of the proposed extra remediation measures. B) The kinetic energy envelope at the location of the EN embankment.

Table 3 – Maximum kinetic energy and bouncing height at the location proposed for the installation of the new embankment, EN.

Cross section no.	Kinetic energy (Kj)	Bounce height (m)
1	130	1.4
2	210	1.3

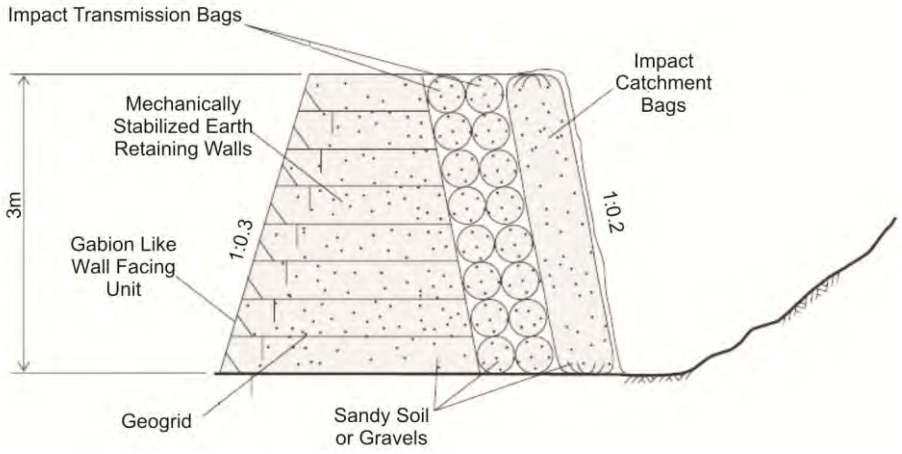

Figure 7 – A typical cross section of a reinforced soil embankment, containing all possible combinations of geomaterials (geogrids, gabion like wall face and impact catchment bags) (modified from Yoshida, 1999).

The lower seeder can be secured by installing a uniaxial double-twist wire mesh covering the entire lower seeder. Double-twist mesh is the ideal solution due both to its flexibility in every direction and the fact that gaps in the mesh are avoided in the event of accidental breakage of some wires. The wire mesh must be suspended by using fixed anchorage at the top and removable anchorage at the bottom, to facilitate during the maintenance. The mesh must be kept free along the slope, letting the rock masses fall to the base of the slope but always keeping them between the rock slope and the barrier mesh. Before the installation of the mesh all individual hanging rock blocks must be removed. The installation of the wire mesh besides the obvious support, forces detached rock pieces to slide instead of rolling. So it does not allow them to obtain substantial kinetic energy.

At this point it should be noted that, the exact location or the extension of the proposed remedial measures, presented in Figure 6, can be slightly modified or corrected by using a new custom-made detailed topographic map. The current simulations as well as the proposed measures were designed by taking under consideration the topographic maps of the Hellenic Military Geographical Service, at a scale of 1:5000.

6. Conclusions

The current case study provides a combination of new additional remediation measures able to secure this particular slope at the provincial road connecting Paralia village with Kimi seaport. These measures incorporate the existing embankments decreasing the cost of the additional constructions.

Besides its practical value, this study indicates the necessity of taking under consideration the stability conditions of natural rock slopes when constructions are planned. At this particular case study the stability conditions were ignored both during the pre failure period, when the extensive excavation took place at the crest of the slope, as well as during the construction of the remedial measures, after the rockfall. Unfortunately these actions have already caused and will farther generate unacceptable economic loss.

7. References

Antoniou A. and Lekkas E. 2010. Rockfall susceptibility map for Athinios port, Santorini Island, Greece, *Geomorphology*, 118, pp. 152–166.

Apostolidis E. and Pogiatzi E. 1996. Geological study and mapping along the national road network of Paralia Kimis – Platana – Stomio. *Unpublished technical report*, *IGME*, Athens.

Asteriou P., Saroglou H. and Tsiambaos G. 2012. Geotechnical and kinematic parameters affecting the coefficients of restitution for rock fall analysis, *International Journal of Rock Mechanics & Mining Sciences*, Vol. 54, pp. 103-113.

Christaras B., Papathanassiou G., Vouvalidis K. and Pavlides S. 2010. Preliminary results regarding the rock falls of december 17, 2009 at Tempi, Greece, *Proceedings of the 12th International Congress of the Geological Society of Greece*, Patras.

Giani G.P. 1992. Rock slope stability Analysis. *Balkema*, Roterdam.

Katsikatsos G., Migiros G., Triantaphyllis M. and Mettos A. 1986 Geological structure of Internal Hellenides (E. Thessaly-SW Macedonia-Euboea-Attica-Northern Cyclades Islands and Lesvos), *IGME*, Geol. & Geoph. Res., Special Issue, pp. 191-212).

Koutsouveli A. and Milonaki J. 1996. Geotechnical study of the road network ``Paralia Kimis – Platana – Stomio`` S. Euboea, *Unpublished technical report*, *IGME*, Athens.

Koumantakis J., Rozos D., Markantonis K., Ilia J. and Tsagaratos P. 2007. Landslide phenomena at Kimi municipality area, *Unpublished work* 121 pp. Athens.

Loupasakis C., Galanakis D. and Rozos D. 2010. Rock Slope Stability Problems in Natural Sightseeing Areas - An Example From Arvanitia, Nafplio, Greece, *Proceedings of the 12th International Congress of the Geological Society of Greece, Bulletin of the Geological Society of Greece vol. XLIII*, No 3, pp. 1465-1473.

Mettos A., Rondogianni Th., Papadakis I., Paschos P. and Georgiou C. 1991. New data on the geology of the Neogene deposits of N. Euboea, *Bulletin of the Geological Society of Greece XXV (3)*, pp. 71–83 (in Greek).

Serelis K., Gartzos E. and Tsaousidou P. 2004. Study of the wall rock alteration occurring in ultramafic rocks hosting magnesite deposits, Euboea, Greece. *Bulletin of the Geological Society of Greece vol. XXXVI*, 377 – 386.

Yoshida H. 1999. Recent experimental studies on rockfall control, in: Masuya P, Labiouse V (eds) *Proceedings of Joint Japan–Swiss Scientific Seminar on impact load by falling rocks and design of protection structures*, Kanazawa (Japan), pp 69–78

Δελτίο της Ελληνικής Γεωλογικής Εταιρίας, τομ. XLVII , 2013
Πρακτικά 13ου Διεθνούς Συνεδρίου, Χανιά, Σεπτ. 2013

Bulletin of the Geological Society of Greece, vol. XLVII 2013
Proceedings of the 13th International Congress, Chania, Sept. 2013

THE ENGINEERING GEOLOGICAL BEHAVIOUR OF DISTURBED AND WEATHERD GNEISS IN SLOPES. THE CASE OF THE "VERTICAL AXIS" OF EGNATIA MOTORWAY, KOMOTINI – NYMFEA, NORTHERN GREECE

Marinos V.[1] and Goricki A.[2]

[1] *Aristotle University of Thessaloniki, Faculty of Sciences, School of Geology, Division of. Geology, marinosv@geol.auth.gr,*

[2] *3G Gruppe Geotechnik Graz ZT GmbH, goricki@3-g.at*

Abstract

Sound gneiss forms evidently very competent rock masses with minor problems in geotechnical works. However, poor rock masses and problematic behaviour can be encountered in engineering projects in a geological environment characterized by intensive and sequent tectonic disturbance, where, weathering may be strongly favoured. Case studies with slope instability problems are analysed from the Egnatia Motorway along the vertical axis from Komotini to Nymfea, in Northern Greece.

The basic engineering geological consideration focuses on the weathering degree, the tectonic disturbance, the foliated structure and the presence of shear zones. In the paper the gneissic rock masses are categorized in a number of specific rock mass types according to key engineering geological characteristics that define the rock mass behaviour in slopes. Subsequently, the slope behaviour of each rock mass type is discussed. The geotechnical properties of such failure surfaces are very difficult to be estimated due to the heterogeneous nature of these planes and back analysis is the best method to obtain reliable parameters. Back analysis results from two case studies showed significant differences to the laboratory test results. Finally, the concepts of the appropriate support measures based on the mechanism of failure of two case studies are presented in the paper.

Key words: *slope stability, weathered gneiss, rock mass types, slope behaviour, back analysis.*

Περίληψη

Ο υγιής γνεύσιος διαμορφώνει πολύ ικανές βραχόμαζες με περιορισμένα προβλήματα στα γεωτεχνικά έργα. Ασθενείς όμως βραχόμαζες και προβληματικές συμπεριφορές μπορεί να προκύψουν στα τεχνικά έργα μέσα σε ένα γεωλογικό περιβάλλον που χαρακτηρίζεται από έντονη, πολλαπλών φάσεων, τεκτονική διαταραχή όπου ευνοείται η αποσάθρωση. Στην παρούσα εργασία παρουσιάζεται η συμπεριφορά των γνευσιακών βραχομαζών στην διαμόρφωση ορυγμάτων κατά μήκος της Εγνατίας Οδού στον κάθετο άξονα Κομοτηνή-Νυμφαία.

Τα κύρια τεχνικογεωλογικά χαρακτηριστικά εντοπίζονται στον βαθμό αποσάθρωσης, στη τεκτονική διαταραχή, στην ένταση της σχιστότητας και στην παρουσία διατμημένων ζωνών. Στο άρθρο αυτό οι βραχόμαζες κατηγοριοποιούνται σε τύπους

ανάλογα με τα τεχνικογεωλογικά χαρακτηριστικά – «κλειδιά»- που ορίζουν τη συμπεριφορά τους στα πρανή. Έτσι, εξετάζεται ο πιθανότερος μηχανισμός αστοχίας στην διαμόρφωση πρανών για κάθε τύπο βραχόμαζας. Οι γεωτεχνικές ιδιότητες των επιφανειών αυτών είναι αρκετά δύσκολο να εκτιμηθούν λόγω της φύσης των γεωυλικών που αναπτύσσονται σε αυτές ενώ οι ανάστροφες αναλύσεις είναι η καλύτερη μέθοδος για να προσδωθούν αξιόπιστες παράμετροι σχεδιασμού. Εδώ παρουσιάζονται τα αποτελέσματα δύο ανάστροφων αναλύσεων, μία για πλήρως αποσαθρωμένο γνεύσιο και μία για διατημένες επιφάνειες. Τα αποτελέσματα αυτά παρουσιάζουν σημαντικές διαφορές με τις εργαστηριακές δοκιμές. Τέλος, συζητούνται πιθανά μέτρα σταθεροποίησής ανάλογα με τον μηχανισμό αστοχίας για τις δύο περιπτώσεις.
Λέξεις κλειδιά: *ευστάθεια πρανών, αποσαθρωμένος γνεύσιος, τύποι βραχομάζας, συμπεριφορά πρανούς, ανάστροφες αναλύσεις.*

1. Introduction

Fresh gneiss forms evidently very competent rock masses with minor problems in geotechnical works. However, under certain geological conditions gneiss can produce poor to very poor rock masses. This environment is produced by intensive and sequent tectonic disturbance and thus weathering and alteration is favoured in various degrees and depths. In such conditions, the intact rock and rock mass strength present a wide range in values and the behaviour concerning slope stability can be from simple to extremely complex and problematic.

The rock mass characteristics and their properties against slope instabilities are described in the paper along the so-called vertical axis of Egnatia Motorway, Komotini-Nymfea, in Northern Greece. More specifically, the slide phenomena of a tunnel portal cut and a road cut are presented. The vertical axis "Komotini – Nymfania – Hellenic-Bulgarian borders (75.0)" is of 22.5km length, links the Egnatia Highway with the Hellenic-Bulgarian borders and is a part of the European road network. The construction works involve several road cuts and five tunnels.

The area of study mainly consists of the metamorphic rocks of the Rhodope massif and more specifically of the Sidironero Unit. In general, crystalline – schistosed rocks like gneisses, gneissic schists, amphivolites and marble layers are met. The area of study is built-in in the Rhodope massif, which consists of two large units: the tectonically lower Unit of the Pangaio and the tectonically overlaid Unit of Sidironero. The area belongs in the Sidironero Unit, which thrusts over the Pangaio Unit from the North to the South, along a great tectonic line of NW-SE direction that ends to E-W (Mountrakis, 1985). The tectonical analysis of this metamorphic mass shows three folding phases (Mountrakis, 1985). The first phase, of Paleozoic age, consists the main metamorphic event of the crystallic-shistosed mass with a general N-S direction. The second folding phase has axis direction NE-SW to ENE-WSW, while the third has a tectonic deformation with folds of NW-SE axis, which folds again the previous folding phases. The third folding phase, of Oligocene age, is believed that is connected with the thrust of the Sidironero Unit upon to the Pangaio Unit (Mountrakis, 1985). This tectonic deformation had strongly affected the fracturation and quality of the rock mass formations in the studied area.

The evaluation of the geological conditions of the area and the differentiation of the geological units are of major importance. Here, the geological model is based on discontinuities, the orientation of schistosity, the material properties but also on the weathering profile and on the frequent participation of shear zones The definition of the geotechnical characteristics and the critical mechanisms of failure are based on the site investigation data and the results of back analysis after the slide phenomena in two case studies. Thus, geotechnical properties of completely weathered geomaterials and sheared gneisses are developed from back analysis here and compared to the laboratory test results. These engineering geological characteristics are distinguished in rock

mass types according to their behaviour in slopes. The assessment of the possible solutions to prevent or control the slope stability problems is also discussed in certain examples.

2. Engineering Geological Characteristics - "keys" for the Stability of Slopes

2.1. General

In general, weathering is a very important factor in slope stability of gneissic rock masses. Gneissic rock masses can vary from massive and very well interlocked to highly or completely weathered because of the feldspar alteration to clayey minerals. Fresh gneiss is a very competent geomaterial with high mechanical properties showing very good slope stability, presenting only some structural instabilities like planar and wedge sliding and toppling failures. In its weathered form (above grade III in ISRM characterisation, Anonymous 1981) the behaviour is dramatically different, presenting circular or multi-planar landslides. Weathering intensity is generally dictated by the climate conditions and the fracturing degree, formed by the tectonic disturbance and the foliation or schistosity of the rock mass. In this study weathering has resulted mainly by fracturing. It is noted that cases of residual soils are not examined here.

Weathering starts from the surface and continues in depth through the fracturing system. If there are no significant weak zones, like faults or aplitic-quartzitic veins, which helps weathering penetration, weathering is limited close to the surface (e.g. few meters to few tens of meters depth) along the discontinuities. In highly disturbed areas, where shear surfaces and satellite fractures create a dense tectonic fabric, weathering may extend to greater depths. Moreover, if the parent rock is schistosed and already deformed, shearing is enhanced. Shearing thickness may be extended in zones from few to several meters. These shear zones are crucial for the slope instabilities, since sliding is favoured along these surfaces, especially if they are highly laminated and weathered and contain sandy-clayey materials.

The geotechnical characteristics of the ground types were estimated from a site investigation program, including laboratory and in situ tests. Gneiss, schistosed gneiss and gneissic schists are the fundamental rocks in the studied area. Gneisses are fractured by several joint systems and are slightly to completely weathered. The principal engineering geological considerations here are: a) the thick weathered cover that can give some circular slides, b) the weak nature of the jointed rock mass that can behave isotropically presenting greater, but again circular, slides and c) the presence of certain shear zones that can guide to an anisotropical behaviour with one or combined multi-surfaces envelops. The general engineering geological characteristics of the gneissic rock mass towards slope stability are presented in Table 1.

2.2. Hydrogeological Conditions

Gneiss formations are generally classified as of low permeability. Groundwater percolates along the fresh discontinuities but is blocked when these are filled or composed of clayey impermeable gauge, imposing a higher hydrostatic level. No significant aquifer has been identified in the investigated boreholes, while only minor seapages close to the surface has been observed. Some small quantities of water can percolate in certain fractured zones. Weathering cover may present some permeability due to the loosening of the mass and the high presence of sandy materials resulted from weathering. This permeability though is not high due to the existence of clays. This is adverse for the stability of the slopes in weathered rock masses since water cannot be drained easily and pore pressures are developed.

2.3. Rock Mass Types

The general characteristics of the gneissic rocks towards the engineering geological evaluation are based upon their fracturing, the intense of schistosity and the weathering degree. In the next paragraphs these general characteristics are grouped in rock mass types and presented in relation to

the slope stability. The case, where rock mass behaviour is strongly affected by the frequent presence of sheared and fault zones, is also discussed in the paper.

Rock mass type I is fresh, massive with minor to medium fractures. The intact rock strength of gneiss here is very high, ranging from 70MPa to 120MPa. The rock mass quality is governed by the fracturing degree. The structure is very tight and the discontinuities are generally very closed with rough surfaces but with considerable persistence. The gneissic texture consist a "sewed" surface and due to the fresh conditions, there are no clear detachable blocks. When this type is met in some depth (~5-10m) it confines and stops any potential circular or multi-surface slide. The rock mass type can be stable or show structural control instabilities (planar and wedge slides, toppling failures) according to the discontinuity and slope geometry.

Table 1 - General engineering geological characteristics of the gneissic rock mass concerning slope stability.

	Engineering geological characteristics	Influence on slope stability
Complex rock mass	Irregular geological contacts of the lithological and engineering geological types	Due to the irregular weathering and fracturing degree and the alternations of gneissic rocks of different schistosity with or without aplitic veins, the mechanical properties can be modified within few meters. The behaviour can change from isotropical to anisotropical and vice versa, according to the in situ engineering geological conditions: • rock anisotropy (schistosity and joint geometry in relation to the slope geometry) • as the weathering and fracturing degree increases the behaviour tends to isotropical • shear or fault zones with very low properties may guide to anisotropical or multi-surface failure
Weak rock mass	Weathering of intact rock and rock mass	The nature of intact rock is altered. Intact rock and overall rock mass strength characteristics can be dramatically reduced.
	High presence of secondary clayey materials	Shear strength along the discontinuities, especially of the foliation or schistosity, is reduced. Rock block interlocking is loosened.
	Tectonic disturbance	High degree of fracturing and weathering Presence of shear zones

Rock mass type II is slightly weathered and medium to highly fractured. The intact rock strength remains very high. The rock mass quality is mainly defined from the fracturing degree and less from the weathering one, which is only confined along the discontinuities. The structure is not very tight and the joints are generally open with fair to poor surface characteristics. The gneissic foliation band is the basic discontinuity surface, since weathering is favoured along the foliation planes and easier separates the - great size - rock blocks. Clay minerals from weathering have minimum presence along the discontinuities. The behaviour of this rock mass type is not very different comparing with the type I that is controlled by the presence and direction of the discontinuities according to the slope geometry and the joint characteristics. In this type, however, the probability of the occurrence of these slides increases significantly due to the reduced shear strength.

Rock mass type III has similarities with the type II but its difference lays to the frequent foliation planes and the weathering extent, since alteration is favoured here. The intact rock strength remains high and only slightly decreased due to weathering. Weathering is mainly produced along the gneissic bands producing a sandy-clayey "coating". Although clay minerals have minimum presence along the discontinuities, they are more frequent and separate the rock mass in smaller size blocks. Rock blocks have medium size and decreased friction along the joints. In this case, rock blocks that will fall or slide are smaller in size and the weathering cover is thicker. Hence there may be some minor circular slides and/or a number of falls of small blocks.

The rock mass quality in type IV is moderately weathered with new clayey surface zones. The intact rock strength is significantly reduced and becoming friable but it remains medium to fairly high. The structure of the rock mass is loosened with open discontinuities and poor to very poor surface conditions. The joints have low persistence, since the clayey weathering products interrupt them. Gneissic bands are still the principle joint surfaces, while clayey zones (~5-10cm) further disintegrate the rock mass. These zones can also extend along other joints, with an angle to the foliation planes, creating smaller blocks, which have poor interlocking and friction. A characteristic of the behaviour of this rock mass type and its poor quality is the presence of several circular slides. Only few planar or wedge slides in small blocks can be now possible.

The rock mass type V is moderately weathered, highly schistosed and highly fractured. Weathering easily extends through the frequent foliation planes, which are consequently divided every 5 to 10cm by the clayey zones. Fracturing is very intensive not only due to tectonic disturbance, but also to the frequent gneissic bands. Weathering extends to the whole mass without though the pieces becoming friable and the structure is loosened with open discontinuities and poor to very poor surface conditions. These surfaces-thin zones extend parallel and normal to the fissility, present low friction and produce even poorer interlocking. Rock blocks or slabs are sized around 5-15cm and have poor assemblance. The intact rock strength is significantly reduced. The principal behaviour of the rock mass is isotropic, due to the very close separation by the schistosity and the dense sandy-clayey zones along them. This results in mainly circular failure mode.

Highly weathered and fractured rock mass quality (type VI) is mainly defined from the weathering and the clayey products. Weathering extends to the whole mass dividing in small – partially friable - blocks the non-weathered pieces. The microtectonic structure and gneissic band have been however almost preserved. The structure is very loose and the discontinuities are open with poor surfaces, since they separate with clayey - sandy fillings the less weathered gneissic slabs. The foliation planes have great persistence, while soil materials interject the vertical joints. These zones (~10-30cm) are more frequent than in the rock types IV and V and disintegrate the mass in very small pieces. Hence, the less weathered blocks cannot come in immediate contact and thus can rotate easier along the soil zones. The intact rock strength has been significantly decreased, since weathering has penetrated into the rock itself. Groundwater presence decreases not only the mechanical properties of the clayey surfaces but the rock mass in total. Circular slides or multi-surface (polygonal) slides are the typical mode of failure due to the high presence of the sandy-clayey weathered zones that separates the blocks.

In its completely weathered form (type VII) the rock mass has faintly retained its structure. It is highly fractured, and it is classified as very disturbed or disintegrated. The few rock blocks are decomposed and friable. The discontinuities are not clearly defined with certain geometrical characteristics, while the gneissic foliation is highly altered and separated by clayey-sandy zones of significant thickness. The small rock blocks have very poor interlocking and can easily rotate along the low friction soil zones. The intact rock strength has been dramatically decreased (σ_{ci}~5-10MPa). Any kinematic analysis of planar or wedge instability has no point in such case. The principal mechanism of failure is circular or multi-surface failure if combined with other weak elements. Several minor slides and some more significant have been noted in the area. Such failure mechanism is further analysed in case study 1 below.

The final type, type VIII, does not follow the same concept of weathering. This type consist a tectonically sheared and foliated rock mass, where the intact rock strength is generally low to very low. If the parent rock is schistosed then tectonically deformed shearing is enhanced. Shear zones may be extended from few to several meters usually parallel to the gneissic texture. They are often met inside a symmetrical model, where a brecciated cohesionless gneissic material is centered (Laws et. al. 2003). The shear strength of the rock mass is almost similar to the strength along the foliation surfaces. This strength can be further decreased because of the intensive schistosity or the thin particle increased presence or low cohesion between the foliation planes or the increased content in the mica minerals due to weathering. This rock mass type is often formed in specific fault zones and is very important to slope stability since they may consist the failure surface. When more than one shear surface is present in a slope, these may be combined forming a multi-planar slide. An example is presented in case study 2 below.

2.3 Case Studies

Case study 1

The first case study discusses a slide that occurred close to the entrance portal of Nymfea tunnel (Figure 1). The rock mass in the area is comprised of gneissic schists in the surface and schistosed gneiss in depth. The rock mass is highly to completely weathered at the surface (type V and VII) and becomes moderately weathered (type III) in depth. Six boreholes with inclinometers and piezometers were drilled to investigate the slide. The identification of weak zones, the thickness of the weathered cover in the specific area and the evaluation of inclinometer and piezometer measurements were of primary importance. Taking into consideration the above parameters, it was evaluated that the slide was driven within the weathered zone, occurred after the excavations of the tunnel portal. It started several meters above the cut and ended in the second bench of the excavated cut, developing several cracks in the already applied shotcrete. The weathered zone, other geological features and the tensile cracks are highlighted in the Figure 2. It is highlighted here that sliding could have been also assisted by the weathered schistosity that is favourable dipping with 30^{o} towards the slope.

Figure 1 - View of the entrance portal of Nymfea tunnel. The gabion wall is used here for the stabilization of the whole slope. The slide occurred above the gabion wall.

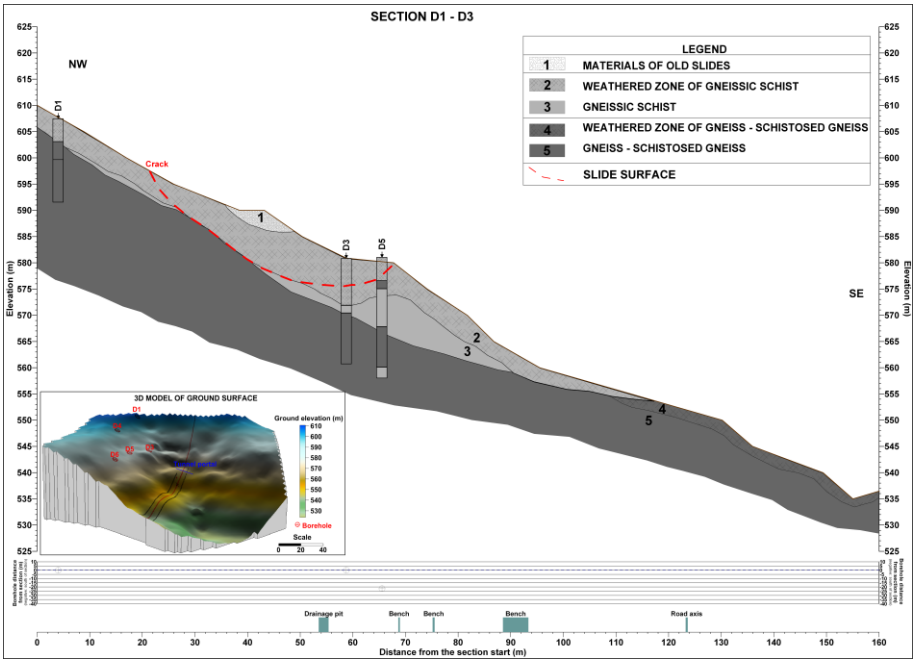

Figure 2 - Geological section along the slide of the Nymfea entrance tunnel portal cut (Case Study 1).

Case study 2

The slope stability problems along the road cut numbered O28 started on summer 2009. The road cut has a height of 30m with 4m wide benches every 10m and consists of schistosed gneiss. After the excavation of the second bench, the first cracks on the slope surface were observed and then a greater slide of a significant part of the slope followed (Figure 3). This failure triggered a greater landslide that developed tension cracks in the natural ground, in a distance 70m behind the scarp of the road cut. The shotcrete along the benches failed and a significant part of the slope has been displaced. After that, the excavation works stopped and the slope was backfilled with a temporary buttress. These temporary actions stabilised the slope since no movement had been observed for two wet periods. In order to face these instabilities permanently, slight modification of the road axis with a horizontal offset of about 15m was decided and a new geotechnical design was implemented.

1. Two shear zones have been recognised in cut O28, one sub-vertical and one sub-horizontal. The first was evident after the slide of the slope and the second was recognised in one of additionally drilled investigation boreholes (Γ19Α). The mechanical characteristics of these zones are very poor, since they are consisted of foliated particles of clayey-sandy nature with small rock fragments. The shear zones, other geological features and the tensile cracks are highlighted in the Figure 4. These features can be combined geometrically and it can be presumed that the failure occurred along this surface. It is multi-planar but can be conceptualized in significant degree as circular. It is evident that the excavations of the cut, the design of the slope angles and the presence of shear zones created adverse conditions for the stability of the road cut. Although there are no detailed information about the groundwater conditions at the time of the failure, the fact that sliding occurred during the dry season (summer period), led to the conclusion that the shear zones were the crucial elements triggering the slope failure.

Figure 3 - The slide of the road cut O28. Drain trenches and benches have cracked.

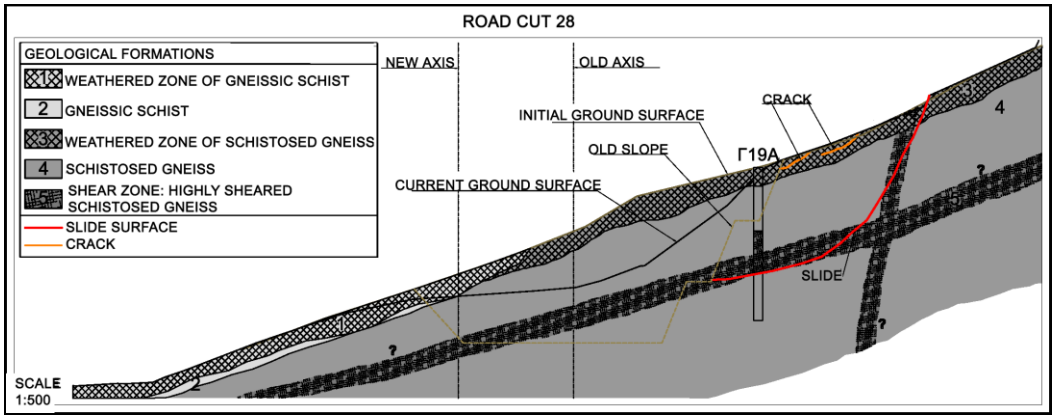

Figure 4 - Geological section along the slide of the road cut O28 (Case Study 2).

3. Geotechnical Properties

3.1. General - Geotechnical Classification

To classify gneissic rock masses, the well-known systems of RMR, Q and GSI can be used. In case of weathered to completely weathered rock mass, a more specific classification might be required. A modified GSI chart has been proposed for gneissic rock masses (Marinos, 2007) with GSI values for every gneissic rock mass type as described above. If the rock mass is not isotropic and the failure mechanism is controlled by several weak elements (shear or fault zones, weak and/or weathered rock mass, foliation planes) the use of geotechnical classification systems is questionable and must be carefully applied. For the back analyses presented in the case studies geotechnical classification systems were generally not applied.

3.2. Geotechnical Properties in the Case Studies

The purpose of the back analysis was to identify the properties of the slided material in the two case studies. In the first case of Nymfea tunnel portal cut the properties of the completely

weathered cover (type VII) and in the second case the properties of the sheared gneiss (type VIII) are back analysed. The analyses were based on field observations, borehole logs, geotechnical classification and data from inclinometers. For the analysis process the software Slide v.5.0 of Rocscience corp. was used.

Case study 1

The scope of the back analysis is to estimate the geotechnical properties of the completely weathered gneiss (type VII). The slide was driven within the weathered cover, starting several meters above the cut and ending in the second bench of the excavated cut, developing several cracks in the already applied shotcrete after the excavations of the tunnel portal. From the grain size distribution analysis of the completely weathered soil-like geomaterials it is found that the percentage of sand is around 50-70% and of silt and clay around 20-30%. Plasticity index is around 5-7. The shear strength properties that resulted from laboratory tests (cohesion c=31kPa and angle of friction φ=37º) are considered high and not representative for the material within the failure plane. An important parameter that influences the analysis results is the status of the pore water pressure at the time of the failure. The piezometric surface was assumed along the contact of the weathering cover and the more fresh bedrock. Moreover, due to intense raining before the slide and some infiltration within the weathering cover, a r_u coefficient of 0.25 was considered. It is noted that the weathered cover has some small cohesion since clayey-silty material are present in the mass. The concluded values from the analysis are c = 5 kPa, φ = 28º. It is highlighted that the analyses were done for circular and non-circular surfaces. The results from both the analyses were almost similar (0.998 for the non-circular and 1.029 for the circular surface with the Janbu-corrected method). The actual sliding surface seemed to be the non-circular one as it resulted from the tension cracks, the depth of the bedrock and the cracks in the shotcrete above the portal cut.

Case study 2

In this case study, the sliding occurred along two shear zones, consisting of foliated gneiss that resembles almost to sandy-clayey soil material after its tectonic disturbance. The first shear zone forms the scarp of the slide, and the second - the main sliding surface – is almost parallel to the slope surface. Although the geotechnical parameters of the surrounded gneissic rock mass (type III, $\gamma = 25$ kN/m^3, σ_{ci}=35MPa, GSI= 25-35, c= 100 kPa and φ= 30°) were incorporated in the analyses, the critical parameters are the ones of the shear zones. The piezometric surface has been found in a depth of 13m due to the fracturing of the rock mass. The concluded values from the analysis are c = 50 kPa, φ = 23º. Similarly to case study 1, the analyses were done for circular and non-circular surfaces. Although the sliding surface fits better (geometry of shear zones, location of surface cracks on the cut and the natural slope, depth of movement) to a non-circular surface, the results were similar (0.999 for the non-circular and 1.015 for the circular surface).

4. Support Principles

Case study 1

The solutions to stabilize the entrance portal cut of Nymfea tunnel can be categorised in two alternative solutions.

- Measures within the area of the failed rock mass by supporting with a pattern of pre-stressed anchors or removing the failed material.
- Measures at the bottom of the failed rock mass by retaining measures. Support the failed material at the lower to those focused to secure the road from further slides with the construction of passive measures.

Due to the large area and the great depth of the slide it was found, that retaining measures are the economic way to stabilise the slope. Reinforced concrete walls with pre-stressed anchors were combined with the Cut&Cover structure of the tunnel portal and constructed from the road level.

Case study 2

The slide has a length of 150m and a width of 80m. To avoid intensive, costly and time consuming retaining structures the road axis was slightly modified by moving it approx. 15m horizontally away from the side. Due to this the extension and height of the cut slope decreased significantly and it was only necessary to stabilise a small part of the failed rock mass. This was done by cement grouting of the jointed gneiss. Additionally drainage holes were drilled in the rock mass to drain the surface water saturating into the ground and to avoid the development of any water pressure.

5. Conclusions

The paper focuses on the engineering geological characterization and behaviour of disturbed and weathered gneiss in slopes. The case of the vertical axis "Komotini-Nymfea" of Egnatia Motorway in Northern Greece is presented. The area is dominated by intensive and sequent tectonic disturbance, where weathering was favoured. Thence, poor to very poor rock masses have been generated, where the intact rock and rock mass strength present a wide range of values. The behaviour in slope stability of these rock masses can vary from stable to highly unstable causing extremely complex and problematic conditions. The general characteristics of fracturing and weathering degree, the intense of schistosity and the presence of shear and fault zones are grouped in 8 rock mass types (I to VIII) and presented with respect to the slope stability.

Moreover, the behaviour of certain gneissic rock mass types in slopes is presented with two different case studies. Cases of circular or multi-planar failure surfaces on highly weathered and fractured rock masses and sheared zones are studied. As the geotechnical properties of such failure surfaces can hardly be tested in the laboratory, back analysis was used to obtain reliable parameters. The results of the back analysis showed significant differences to the laboratory test results. The concluded values from the analysis are $c = 5$ kPa, $\varphi = 28^{o}$ for the completely weathered type and $c = 50$ kPa, $\varphi = 23^{o}$ for the multi-planar surface, consisted of sheared gneiss. Finally, the support principles according to the mechanism of failure of two case studies are presented.

6. Acknowledgments

We would like to thank Egnatia Odos S.A. for their support and permission to publish the paper.

7. References

Anonymous 1981. ISRM Commission on Classification of rocks and rock masses. *International Journal of Rock Mechanics and Mining Sciences and Geomechanical*, abstracts 18, pp. 85-110.

Laws S., Eberhardt E., Loew S. and Descoeudres F., 2003. Geomechanical Properties of Shear Zones in the Eastern Aar Massif, Switzerland and their Implication on Tunnelling, *Rock Mechanics and Rock Engineering*, 36(4), pp. 271-303.

Marinos V. 2007. Geotechnical classification and engineering geological behavior of weak and complex rock masses in tunneling, *Doctoral thesis,* School of Civil Engineering, Geotechnical Engineering Department, National Technical University of Athens (NTUA), Athens, July (in greek).

Mountrakis D. 1985. Geology and Geotectonic evolution of Greece. University studio press, Thessaloniki (in Greek).

Δελτίο της Ελληνικής Γεωλογικής Εταιρίας, τομ. XLVII , 2013
Πρακτικά 13ου Διεθνούς Συνεδρίου, Χανιά, Σεπτ. 2013

Bulletin of the Geological Society of Greece, vol. XLVII 2013
Proceedings of the 13th International Congress, Chania, Sept. 2013

ENGINEERING GEOLOGICAL BEHAVIOUR OF RECENT CONGLOMERATE DEPOSITS IN DAM FOUNDATION. THE CASE OF AGIOKAMPOS DAM IN THESSALY, CENTRAL GREECE

Marinos V.[1], Lazaridou S.[2], Perleros V.[3] and Sotiropoulou K.[4]

[1] *Aristotle University of Thessaloniki, Faculty of Sciences, School of Geology, Division of. Geology, marinosv@geol.auth.gr,*

[2] *Hydroexigiantiki Cons.Engineers, Evias 3, 15125 Athens, Greece*

[3] *Perleros V., Geologist, Dionysou 56, 152 34, Halandri, Greece*

[4] *Sotiropoulou K., Geologist, Miaouli 18 Kifisia, 145 61, Kifissia, Greece*

Abstract

A typical example of dam foundation on Neogenic conglomerate deposits is presented in this paper. The case of Agiokampos dam in east Thessaly in central Greece. The level of natural compactness and the nature of the cementing material are crucial elements for the strength, the bearing capacity and the permeability of these formations. These conglomerates of medium consistency, do not allow relying on traditional sampling and tests in the boreholes. Lugeon tests are meaningless and falling head tests are recommended. Back analysis on slopes is certainly a useful tool for approaching the strength parameters of the global rock mass. Thus it is understood that the engineering geological assessment before any testing and analysis is of prime importance.

Due to the fine nature of the cement, permeability is generally low and no leakages are expected. However, an impermeable grout curtain must be created due to some higher values. Conglomerates are not easily groutable and a combination of a diaphragm wall is suggested. Finally, a carpet grouting is designed since the surficial zone is susceptible to internal erosion.

Key words: *conglomerates, earthfill dam, foundation, permeability, water tightness.*

Περίληψη

Πρόσφατες ιζηματογενείς αποθέσεις, όπως τα κροκαλοπαγή, είναι σε γενικές γραμμές υλικά με πτωχές γεωτεχνικές ιδιότητες, αλλά πιθανώς δεν εγείρουν σοβαρούς προβληματισμούς για τη θεμελίωση ενός χωμάτινου φράγματος. Η τεχνικογεωλογική αξιολόγηση, σε τέτοια υλικά, πρέπει να είναι ιδιαίτερα προσεκτική. Ο βαθμός συνεκτικότητας και η φύση του υλικού σιμέντωσης είναι κρίσιμα στοιχεία για την αντοχή, τη φέρουσα ικανότητα και τη διαπερατότητα των σχηματισμών αυτών.

Ένα τυπικό παράδειγμα θεμελίωσης φράγματος σε πρόσφατους κροκαλοπαγείς σχηματισμούς παρουσιάζεται στην εργασία αυτή. Η περίπτωση του φράγματος Αγιοκάμπου στην ανατολική Θεσσαλία. Λόγω της λεπτόκοκκης φύσης του υλικού σιμέντωσης, η περατότητα είναι γενικά χαμηλή και δεν αναμένονται διαφυγές. Ωστόσο, μία κουρτίνα τσιμεντενέσεων πρέπει να κατασκευαστεί εξαιτίας ορισμένων

υψηλότερων τιμών. Τα κροκαλοπαγή αυτά δεν είναι εύκολα ενεματώσιμα και για αυτό το λόγο προτείνεται και η κατασκευή ενός διαφραγματικού τοίχου. Τέλος, έχουν σχεδιαστεί και τσιμεντενέσεις τάπητα, δεδομένου ότι η επιφανειακή ζώνη είναι ευαίσθητη στην εσωτερική διάβρωση. .

Τα κροκαλοπαγή μέσης συνεκτικότητας, δεν μπορούν να χαρακτηριστούν, τεχνικογεωλογικά και γεωτεχνικά, με παραδοσιακές τεχνικές δειγματοληψίας και δοκιμές στις γεωτρήσεις. Ειδικές τεχνικές δειγματοληψίας θα μπορούσαν να βοηθήσουν προς την κατεύθυνση αυτή. Οι ανάστροφες αναλύσεις στα πρανή της στενής περιοχής αποτελούν ασφαλώς ένα χρήσιμο εργαλείο για την εκτίμηση των παραμέτρων αντοχής. Οι δοκιμές Lugeon εδώ είναι χωρίς νόημα. Συνίστανται οι δοκιμές μεταβλητού φορτίου (Maag). Είναι κατανοητό λοιπόν ότι η τεχνικογεωλογική αξιολόγηση πριν από κάθε δοκιμή και ανάλυση είναι ιδιαίτερα πρωταρχικής σημασίας.

Λέξεις κλειδιά: *κροκαλοπαγή, χωμάτινο φράγμα, θεμελίωση, περατότητα, στεγανή κουρτίνα.*

1. Introduction

The Agiokampos dam is studied to be constructed in the eastern part of the prefecture of Larissa on Pouri stream about 3,7 km from its mouth. In Pouri stream 2 branches are met, where their runoff is enhanced by the discharges of several springs from the southern edge of Ossa and Mavrovouni mountains. The area belongs to both municipalities of Agia and Larissa. The project, supervised by Hellenic Ministry of Rural Development and Food and funded by the NSRF, is under the final study, since the technical preliminary design has been recently submitted.

The catchment area is 75 km^2, while the inundation area is 0,61 km^2. The dam is constructed for irrigation purposes. It will have a maximum height of 37,5m with a reservoir net capacity of 4.4 km^2. The elevation of the river at the central cross-section of the dam is at +32,5 m, while the maximum altitude of the basin is 1182m. The dam foundation is placed around 250m downstream of the junction of the two main branches of the stream. The width of the riverbed at the site of the dam is approximately 100m.

In the wider zone of the riverbed a fluvial terrace is developed with a difference in height up to 7m from the present riverbed, an indication of upward tectonic movements in the region. The riverbed is confined by steep slopes, which in the area of the dam reach the heights of 30m in the left abutment and about 12m in the right. At the higher parts of the basin, mild slope surfaces are developed (flattening planes) of varying size, on which red clays and sands are present. The basis of these deposits consists a characteristic palaeorelief. These surfaces are believed to be associated with tectonic terraces.

The geological context of the broader region of the Agiokampos dam is of the Pelagonian series, consisting of metamorphic rocks, covered by recent Neogene and alluvial deposits. These Pelagonian series, encountered in the wider region of Eastern Thessaly, are represented here with crystalline schists, phyllites, gneisses, amphibolites, and marbles often in alternating units, while ophiolites are present (Geological map of Greece, 1:50000, Sheet Ayia-Panayia Ayias, see also Stamatis and Miggiros, 2004). At the base of the whole area schists are encountered with frequent intercalations of ankeritic marbles, as isolated lenses though. The formations that are specifically met in the inundation area are the medium-thick-bedded marbles (Cretaceous), which are intensely karstified and fractured with intercalations of crystalline dolomite. They are found in the Monastery of Sts. Anargiron at the tail of the inundation area. Schists are outcropping just downstream of the dam foundation on the right abutment. These formations have been also met in the borehole drillings below the dam foundation as the bedrock over which the Neogene formations were deposited. A simplified geological map of the inundation area (a) and the dam

axis (b) is presented in Figure 1. The geological formations of the foundation zone are described in more detail in the next paragraph.

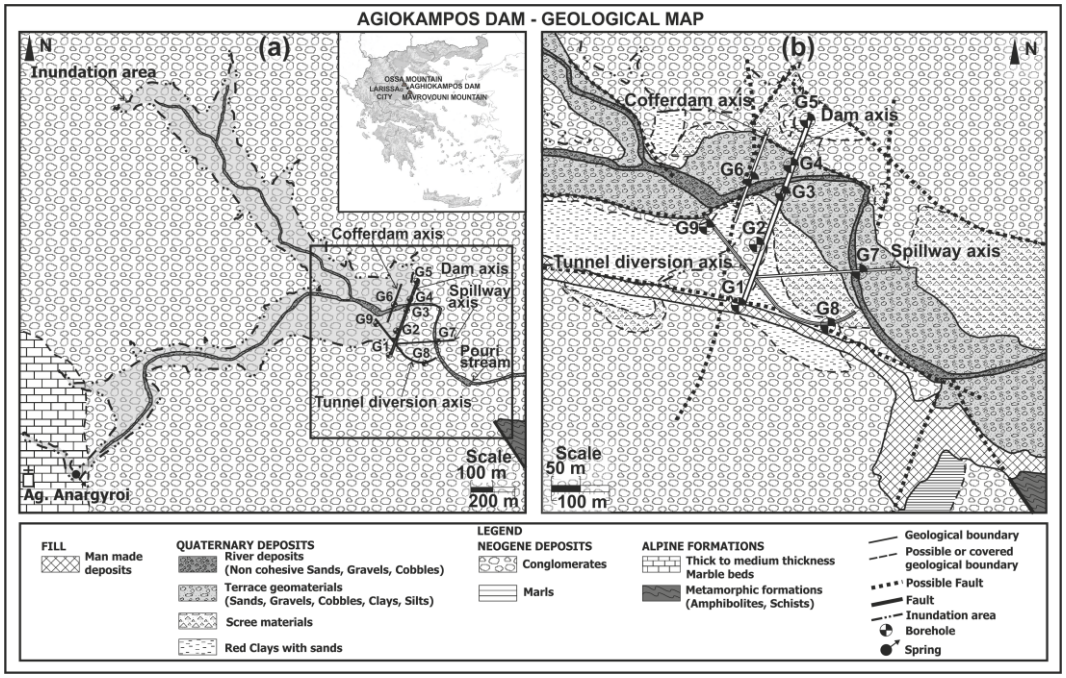

Figure 1 – (a) Geological map along the inundation area of Agiokampos Dam, (b) Geological map along the Agiokampos Dam axis.

2. Geological Conditions Along the Dam Axis

2.1. Lithological Conditions

Neogene formations, possibly extending to the Pleistocene, cover almost the whole studied area. The formations consist of conglomerates (containing also angular fragments of rocks) with irregular torrential structure, although bedding is frequently developed. Siltstones, sandstones and marls are also encountered in places, as lenses or irregular beds, in the conglomeratic environment. Their thickness is exceeding 300m. The cementation material is mostly silty-sandy and only in places can be characterized as clayey. The conglomerates are medium to fairly strong cemented. The deposits have experienced significant tectonic uplift and have a monoclinic structure.

Terrace deposits are also encountered and they are developed 15-20m higher than the present riverbed. They mainly include sands, pebbles, gravel with some silty clays. Their thickness reaches 7-8m. Scree materials and the elluvial weathered zone of conglomerates cover the slopes. They involve loose materials of clays, sands and pebbles and their thickness can reach 5m. The recent river deposits involve loose materials, which include pebbles, cobles mainly from marbles and ultramafic rocks and sands. Finally, man made deposit are only found in borehole G1 with thickness 1-2m.

2.2. Tectonic Conditions

The development of basins or troughs in the area of Thessaly started on Miocene with faults of NNE-SSW and E-W direction (Stamatis and Migkiros, 2004, Caputo and Pavlides, 1991). The primary deformation NNE-SSW is connected with structures, thrusts and faults and the secondary E-W with direction faults. Characteristic of the tectonics in the studied area is the presence of troughs of E-W direction transversal of the directions of the Tempi valley and the Anavra - Agia

basin forming the basins of lacustrine and continental sediments. The E – W fault system, despite being a secondary one in the region, is greatly expressed forming well-distinguished morphological reliefs. In the foundation zone of the dam it is estimated that the riverbed zone is defined by two faults that have allowed the formation of the steep slopes of the area. The action of these two faults has contributed to a local fracturing of the conglomerates, met in the exploratory drilling. This neotectonic setting is also the reason of the inclination of the Neogene strata.

In the left abutment, immediately upstream of the dam axis, the possible position two faults are noted along the local streams. Few collapses and landslides occur on slopes along the streams that may be linked to the fault activity and deep erosion. From the seismotectonic study of the dam design (by and Prof. E. Papadimitriou and Ass. Prof V. Karakostas of the University of Thessaloniki), it was revealed that there is no further evidence of activity of these faults. It is recommended however to provide those features in the design of the dam, such as thick filters, in order to face a potential displacement along the faults in earthquake. This potential should be nevertheless low in the area.

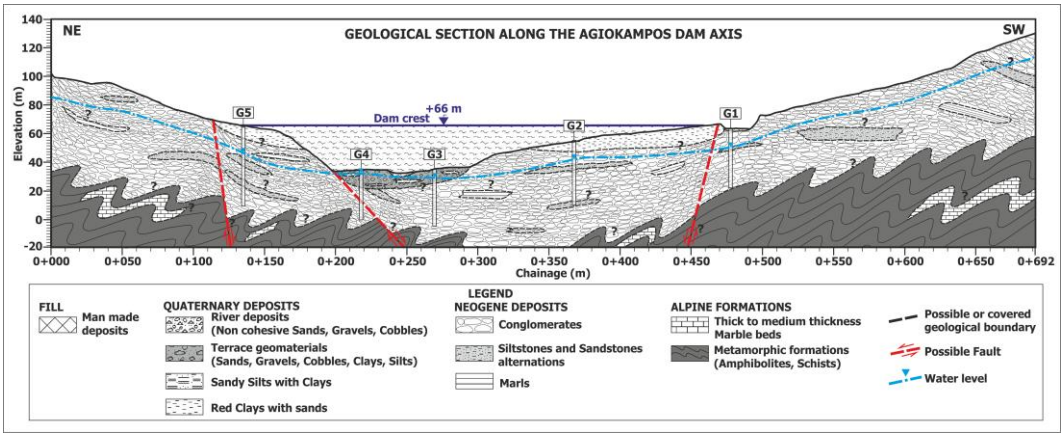

Figure 2 – Geological section along the axis of Agiokampos Dam.

3. Engineering Geological Conditions

3.1. General

The engineering geological assessment for a proper geotechnical design of a dam, on such materials, must be very careful since the usual tools of geotechnical characterization cannot be easily applied here. This is due to the nature of the materials, that either they fall on the hard soil or the weak rock margin. The level of natural compactness and the nature of the cementing material are crucial elements for the strength, the bearing capacity and the permeability of these formations.

In order to investigate the engineering geological and geotechnical conditions of the dam and the appurtenant structures (spillway, diversion tunnel, cofferdam), a site investigation program was performed. The evaluated data were provided from field observations and geological mapping, from the results of boreholes (9 boreholes) and from in situ and laboratory tests. Specifically, the data used were surface observations of bedrock exposures, slope stability features depending on the nature of the ground, permeability values, rock quality designation index (RQD), standard penetration test values (SPT), and physical characteristics. These parameters were to be evaluated for the geotechnical description of the formations and subsequently, the assessment and proposal of geotechnical parameters of the geomaterials.

3.2. Engineering Geological Conditions of the Dam Axis

The conglomerates in the left abutment of the dam are found with higher presence of finer silty-sandy materials while more systematic presence of pebbles exists in the right one. A typical stratigraphic image of the left and right abutment is shown in Figures 3a and 3b respectively. The layers present a moderate inclination to the N-NS, without forming however practicable sliding planes. The slopes are generally homogeneous and they do not show clear variations in strength. Although the conglomerates are globally homogeneous, alternations of fine-grained and coarse layers are present. Note that the left abutment, though steeper in slope, presents several phenomena of erosion. On the other hand, at the base of the slope, near the riverbed, the conglomerates occur with increased consistency due to calcitic presence. Conglomerates are not very cohesive close to the surface but soon, in small depth, they become more compact, at an acceptable level for bearing an earth structure of the size of this dam.

Recent deposits, on terraces and of clay nature, are overlying these materials. Terrace deposits are generally soft, of low consistency and they must be removed for the foundation of the dam, while they can be used for the core of the dam.

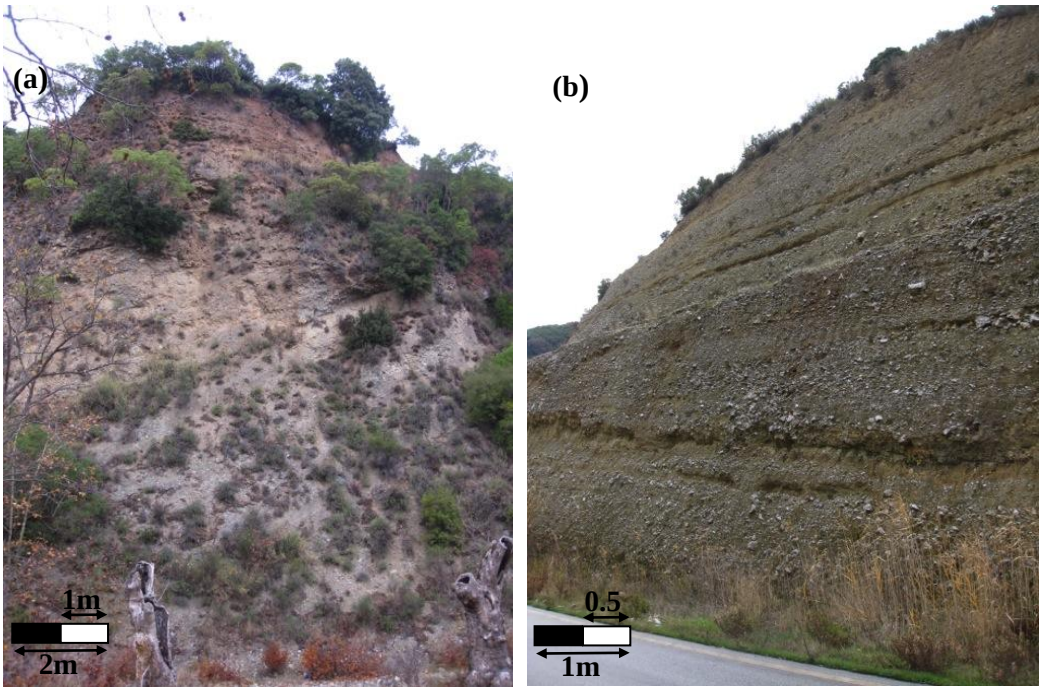

Figure 3 - Typical series of the formation at the left (a) and right (b) abutment of the dam. Conglomerates are met here with a high presence of fine, silty-sandy, materials in the left a butment, while in the right one there is more systematic presence of pebbles. The formatio ns show moderate consistency but good friction angle, due to the interlocking of the granul ar materials, since they form steep and high slopes.

The nature of soil formations, along the axis of the dam, based on the description of drilled cores as classified by the USCS classification, is sandy-gravelly. However, the recorded permeability values (Figure 6, 7) are quite low for such formations. The presence of fine material in the matrix is the reason for the low permeability measured. This fine material, seen at the outcrops was probably wash out during drilling and thus a misleading on interpretation in such material is possible. On the other hand, such a loss of fine material during drilling in the conglomerates probably indicates a moderate consistency of this geomaterial. Improvement of sampling procedure in bore-

holes is difficult in such ground, thus the engineering geological judgement from the appearance in outcrops is essential.
Regarding the assessment of rock mass quality with the RQD index, the following notes must be highlighted. The RQD should be marginally only used for post-alpine formations and for weak rocks which have not been fractured due to tectonism, stress relief or weathering. The RQD values here range from zero up to about 75%, if strictly considered (Figure 4). The "disorganized structure" as shown in the cores is certainly due to the disturbance and washing out of fine material during drilling and sampling, provoking a collapse of the rock mass. Larger values of RQD were recorded mainly in sandstone and mudstone layers within the formation of conglomerates, but these zones are only sporadic. Furthermore, there is no significant change of values with depth. This is normal, as RQD rating does not represent here the logic of reducing the fragmentation due to tectonism or weathering by the increased confinement in depth.
Regarding the distribution of standard penetration test (N_{SPT}) values along the axis of the dam (Figure 4), most of these tests have moderate (N_{SPT} = 16-30) to high values (N_{SPT} = 31-50) or even refusals (Figure 4). These values are typical of the consistency of the formations present, while refusals may be due to the systematic presence of pebbles, gravels and boulders in the conglomeratic mass.
Thus RQD or SPT tests are useless to apply since the recovered cores have very poor structure easily disintegrated (RQD's=0) or coarse fractions providing refusals on penetration values. The series of these weak formations are not expected however to be liable to significant compression and subsidence, provided the upper loose zone is defined and removed.
The sampling in these materials must be carefully executed so to allow the maintenance of the sample undisturbed in the form of a core. A double or even triple split core barrel is required for this reason. Exploratory trenches or wells and, in case of major need of information; adits offer a better source in the site investigation procedure.

4. Type of Dam and Construction Materials

The appropriate type of dam to be constructed in these geological conditions with formations of moderate consistency and (although not important) heterogeneity is an earthfill one. The solution of a hard embankment is not considered feasible because of the moderate strength of the conglomeratic formation, lied in the foundation zone.

For the construction of this type of dam no major excavation for the foundation is required while it can accommodate deformations and displacements in case of an earthquake activity. Based on the material needs, a geological survey was conducted in the inundation area and the broader basin to find the necessary quantities of suitable construction materials.
Materials for the core were found in locations within the Neogene deposits including marly materials and in clays in the terrace deposits. In case of insufficient quantities of clay, the solution of an impermeable membrane could be considered, either on the upstream face or inside the mass of the dam (Schleiss and Pougatssch, 2010).
For the shells of the embankment the granular materials from both the riverbed and the conglomerates are most suitable (Figure 5). Materials for the filters – drains may easily be derived from the riverbed, and the terraces, after appropriate screening to remove the fine clay fraction. As far as the riprap and paving materials is concerned, sizeable boulders of high strength may be obtained from the outcrops of marbles or fresh gneisses and amphibolites. No suitable material was found though within the inundation area and areas beyond it were examined.
Materials suitable for concrete aggregates within the area of the dam can be derived from the outcrops of marbles. These outcrops though are part of the Natura area located near the Monastery of Agion. Anargyron. Positions outside this area were studied, while there is also the possibility to use riverbed boulders or the conglomerates after the appropriate check that harmful materials, as cherts, are not contained.

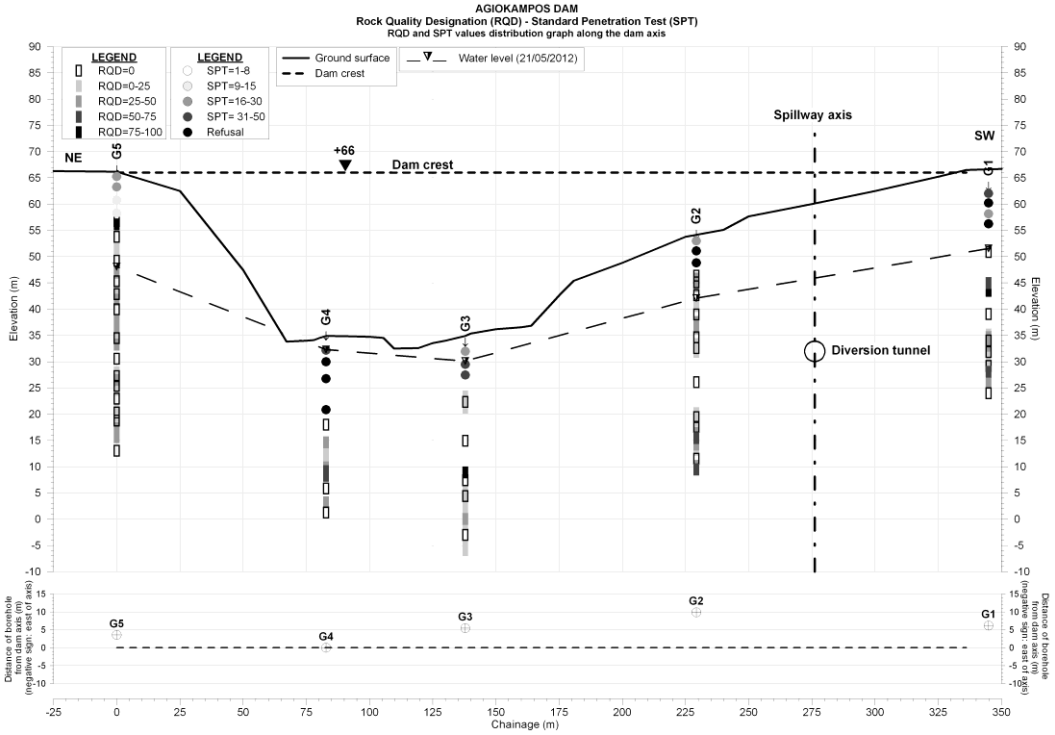

Figure 4 – RQD and N_{SPT} values along the Agiokampos Dam axis. The RQD can be marginally used for post-alpine, formations and weak rocks which have not been fractured due to tectonism, stress relief or weathering. The RQD values here range from zero up to about 75%. The "disorganized structure" as shown in the cores is certainly due to the disturbance and washing out of fine material during drilling and sampling provoking a collapse of the rock mass.

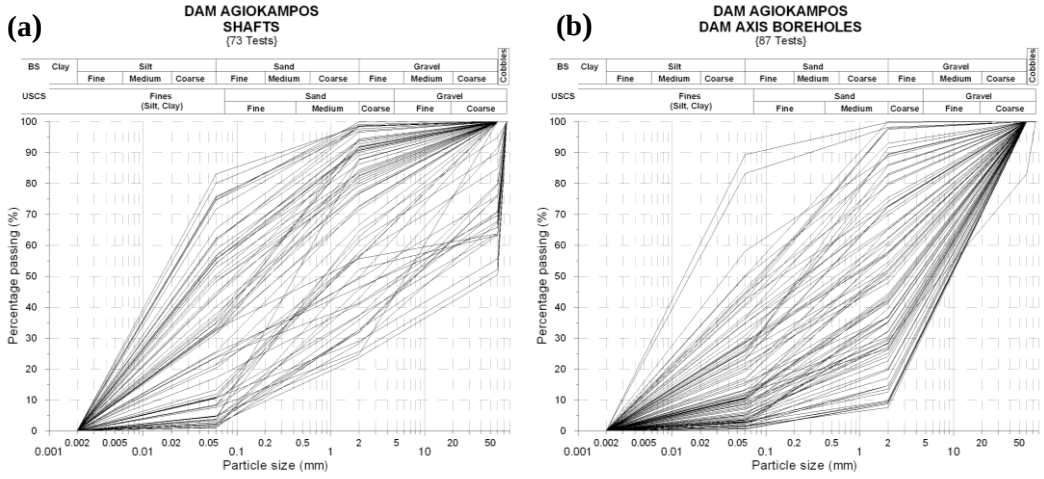

Figure 5 – a: Particle size distribution of the investigated shafts for the shells and filters-drains of the embankment of Agiokampos dam, b: Particle size distribution of the borehole samples along the dam axis

5. Hydrogeological Conditions. Water Tightness and Risk of Erosion

The dam axis and the inundated basin are covered by the conglomerate formations, which are impermeable in the big scale, excluding their surficial part. In the inundation area there are also limestones, in a short extent; they are permeable but their lowest outcropping point is inside the inundation area, in the stream of Agion Anargiron monastery. Springs are discharged at this point.

The hydrogeological conditions, water tightness and risk of erosion for the dam axis are presented in detail in this study. In situ permeability tests, mainly of falling head (commonly called Maag test), were performed in 5 boreholes. We do not recommend Lugeon tests, as usually applied (Houlsby, 1976), since even moderate pressures disintegrate this kind of rock. The distribution of the permeability (K) values along the axis of the dam is presented in Figure 6. Due to the fine nature of the cement material of the conglomerates, permeability at the abutments is low to very low (K about 10^{-7} m/sec) and no leakages are expected under the dam foundation zone or from the future reservoir. It is highlighted that the ground water level in the boreholes is always higher than the riverbed, meaning that the water table in the abutments is drained towards it. Thus no lateral deep drainage exists. This piezometric surface has a trend to reach elevations higher than the future reservoir level (Figure 6). This situation will not necessitate a significant extension of the grout curtain. The presence of some local small springs or permanent moisture higher than the elevation of the riverbed indicates the existence of local horizons with higher individual permeability forming weak perched aquifers.

The distribution of permeability values (K) with depth is shown in Figure 7. The higher values (~10^{-3} m/sec) are found in the riverbed materials to about 10-12m depth, while high values appear in a zone at the left abutment at around 25m of depth. Hence, there is an apparent need to address the high permeability of the bed material by removal. However, locally below the dam axis, there are variations in K values, with the higher ones being in the order of 10^{-3}m/sec (in a depth of 10-

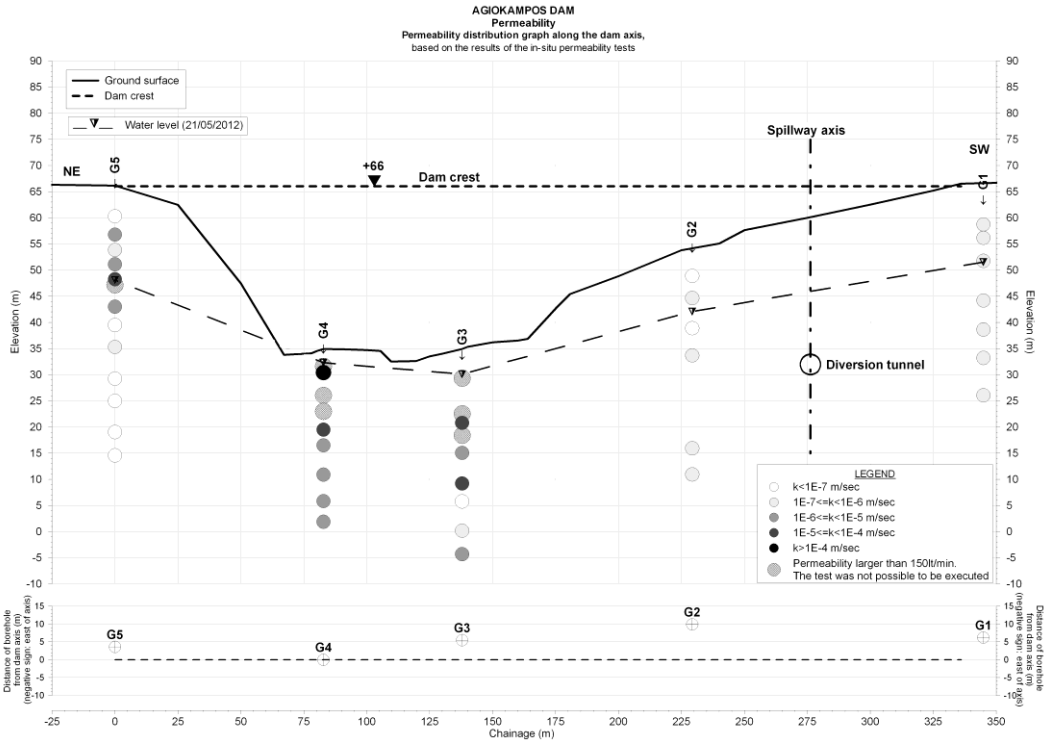

Figure 6 - Distribution of the permeability (K) values along the axis of the dam.

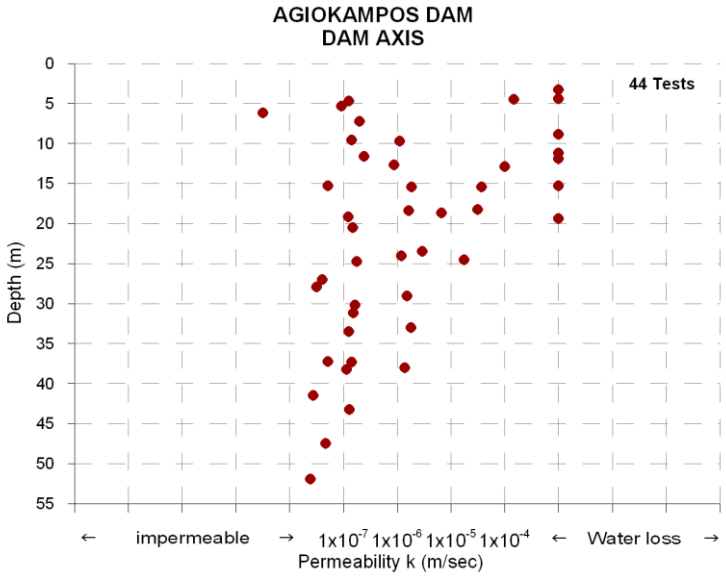

Figure 7 - Distribution of permeability values (K) with depth.

20m depth in borehole G5 and of 18-25m in borehole G3). These high values are possibly associated with weak cementation of the rock mass. Thus, based on the results of the in situ permeability tests it is necessary to construct a grout curtain, having although a moderate depth.

Given the variation of consistency and compactness of the conglomerates, the possibility achieving an effective penetration and sealing in all parts under the dam foundation, if grout injections holes are to be used, should be of concern. Thus a combination with a diaphragm wall could be the solution. Finally given the medium cementation, erosion mechanism can develop, under the hydraulic gradient that will develop with the creation of the reservoir. The implementation of a carpet grouting is thus essential.

6. Conclusions

The engineering geological assessment and behaviour of recent conglomerates in dam foundation is presented in the paper. The case of the design of Agiokampos dam, where the conglomerates persist, is studied here. The particular issue in the case of a dam in such rock mass, of conglomerate of medium consistency, is that this material does not allow relying on traditional sampling and tests in the boreholes. Lugeon tests are meaningless and falling head tests are recommended. In order to get the geotechnical parameters, special sampling procedures are required. Deep trenches and adits allow more reliable observation and certainly representative sampling. Back analysis on slopes is without doubt a useful tool for approaching the strength parameters of the global rock mass. Thus it is understood that the engineering geological assessment before any testing and analysis is of prime importance.

The conglomerates in the area of study have clayey or sandy-silty matrix and generally show medium consistency with generally good interlocking between the pebbles. The material, geotechnically speaking, is weak but it does not raise serious concerns for the foundation of an earthfill dam. It has low strength but low compressibility against settlement. The bedrock of the conglomerate formation is crystalline limestones and metamorphic schist-ophiolithe tectonic complex but does not interfere in the project, since the conglomerates are sufficiently thick, several tens of meters.

The material in the foundation zone is however erodible even under moderate hydraulic gradient of groundwater flow. For this reason, the foundation of the core must be done in deeper excavation levels, where conglomerates are tighter. A grout carpet will nevertheless be needed for this pur-

pose, while the main impermeable grout curtain under the dam will complement protection against erosion.

Based on the in-situ permeability tests it is necessary to construct a grouting curtain, not deep though. Since it is not certain that the material will be easily injected the case of a diaphragm wall is considered in the design. The morphology in the area off the dam, in the abutments, together with the low permeability is adverse to favour groundwater seepage from detours. Only a small extension of the grout curtain is estimated to be sufficient. Drainage relief holes, downstream of the dam slope abutments are needed due to the low permeability of the material and the high water level that will be established downstream of the dam.

7. Acknowledgments

We would like to acknowledge the Hellenic Ministry of Rural Development and Food that supervised the geological design of Agiokampos dam, which is funded by the NSRF (National Strategic Reference Framework). Thanks are also given to "Sotiropoulos and Associates L.T.D." for the data provided.

8. References

Caputo R. and Pavlidis S. 1991. Neotectonics and structural evolution of Thessaly, Central Greece, *Bull. Geol. Soc, of Greece*, XXV/3, 119-133, Athens

Houlsby AC. 1976. Routine interpretation of the Lugeon Water test, *Quarterly Journal of Engineering Geology*, 9,303-313.

Migiros G. Vidakis M. Papazeti E. and Skourtsi-Koronaiou V. 1984. Geological Map of Agia Sheet, 1:50 000, IGME, Athens.

Schleiss J.and Pougatsch H. 2010. Les barrages. Du projet à la mise en service, Presses Polytechniques et Universitaires Romandes. EPFL, vol. 17.

Stamatis G. and Migiros G. 2004. The relationship between fractured tectonics and groundwater reservoir of massive formations of Ossa mountain (East Thessaly, Greece), *Proceedings of the 10th International Congress of Geological Society of Greece*, Thessaloniki, 2077-2086 (in Greek).

Δελτίο της Ελληνικής Γεωλογικής Εταιρίας, τομ. XLVII , 2013
Πρακτικά 13ου Διεθνούς Συνεδρίου, Χανιά, Σεπτ. 2013

Bulletin of the Geological Society of Greece, vol. XLVII 2013
Proceedings of the 13th International Congress, Chania, Sept. 2013

PRELIMINARY RESULTS OF INVESTIGATIONS OF POSSIBLE GROUND DEFORMATION STRUCTURES IN THE EARLY CHRISTIAN BASILICA, ANCIENT LECHAION HARBOUR, CORINTH, GREECE

Minos-Minopoulos D.[1], Pavlopoulos K.[1], Apostolopoulos G.[2], Dominey-Howes D.[3], and Lekkas E.[4]

[1] *Harokopio University, Department of Geography, 70 El. Venizelou Str., Kallithea, 176 71, Athens, Greece, dminou@hua.gr, kpavlop@hua.gr*

[2] *National Technical University of Athens, School of Mining and Metallurgical Engineering, Applied Geophysics Laboratory, 9 Iroon Polytechniou Str., Zografou, 157 80, Athens, Greece, gapo@metal.ntua.gr*

[3] *University of New South Wales, School of Biological, Earth and Environmental Sciences, Sydney 2052 NSW, Australia, dale.dh@unsw.edu.au*

[4] *National and Kapodistrian University of Athens, Faculty of Geology and Geoenvironment, Department of Dynamic, Tectonic and Applied Geology, Panepistimioupolis Zografou, 157 84, Athens, Greece, elekkas@geol.uoa.gr*

Abstract

The Early Christian Basilica of Lechaion, Corinth, located on the western jetty of the ancient Lechaion harbour, was constructed during the late 5th century AD and archaeological excavations suggest that it was destroyed by seismic activity during 551-552 AD. Numerous depressions and buckling structures observed on the Basilica floor are indicative of ground deformation structures, likely associated with liquefaction. In an attempt to investigate the subsurface soil structure, and stratigraphy, a GPR survey and horizontal distribution of ground conductivity along ten selected transects was carried out, supplemented by stratigraphic data as described by archaeological trenches. The results of the study revealed subsurface deformation features providing sufficient indications that allow us to suggest that the surface structures observed on the Basilica floor are the surface expression of earthquake-induced ground liquefaction.
Key words: *ground liquefaction, GPR survey, ground conductivity*.

Περίληψη

Η Παλαιοχριστιανική Βασιλική Λεχαίου, Κόρινθος, κατασκευάστηκε στα τέλη του 5ου αι. μ.Χ. στον δυτικό βραχίονα του αρχαίου λιμανιού του Λεχαίου, και σύμφωνα με αρχαιολογικές ανασκαφές καταστράφηκε από την σεισμική δραστηριότητα του 551-552 μ.Χ.. Διάσπαρτα βυθίσματα και υβώματα που παρατηρήθηκαν στο δάπεδο της Βασιλικής αποτελούν ενδεικτικές δομές εδαφικής παραμόρφωσης η οποία πιθανόν να σχετίζεται με ρευστοποίηση εδάφους. Με στόχο την διερεύνηση της στρωματογραφίας και της δομής του υπεδάφους πραγματοποιήθηκαν γεωφυσικές διασκοπήσεις GPR και

μετρήσεις αγωγιμότητας του εδάφους κατά μήκος δέκα επιλεγμένων τομών και συσχέτιση τους με τη στρωματογραφία όπως αυτή περιγράφεται από αρχαιολογικά σκάμματα. Τα αποτελέσματα της μελέτης είναι ενδεικτικά δομών παραμόρφωσης των υποκείμενων εδαφικών σχηματισμών με χαρακτηριστικά που επιτρέπουν την συσχέτιση των επιφανειακών δομών που παρατηρήθηκαν στο δάπεδο της Βασιλικής με το φαινόμενο της ρευστοποίησης εδάφους.
Λέξεις κλειδιά: *ρευστοποίηση εδάφους, διασκόπηση GPR, αγωγιμότητα εδάφους.*

1. Introduction

The archaeological site of the ancient harbour of Lechaion is located on the southeastern coast of the Corinthian Gulf, 3km to the west of the modern city of Corinth, Greece. It is the western harbour of the ancient city of Corinth. Its construction dates to the 6th-7th century BC, and archaeological evidence suggest that its use continued throughout the Roman period (Pallas 1959, 1965, Rothaus 1995, Stiros et al., 1996). The harbour was located in a marshy area and is composed of an outer harbour edged by moles and an inner artificially excavated harbour (cothon) connected to the Corinthian Gulf by a stone-lined channel surrounded by two dredging mounds (Figure 1).

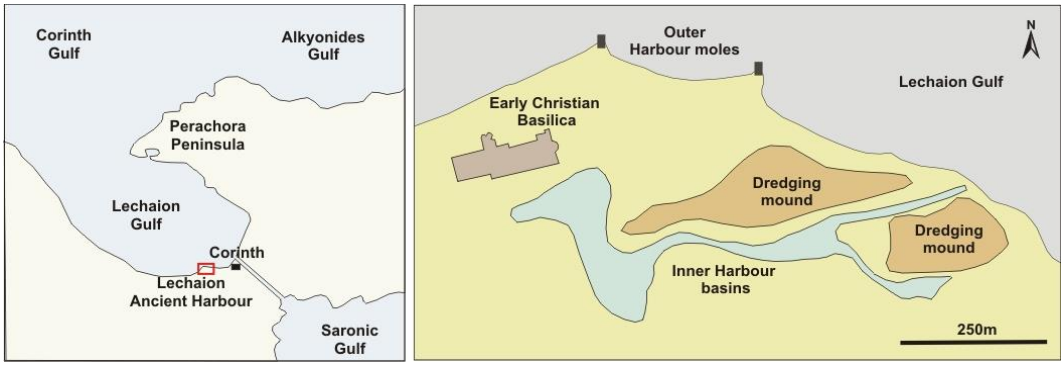

Figure 1 – Left: Location map of the study area, Right: The ancient harbour of Lechaion.

During the late 5th to early 6th century AD, an Early Christian Basilica was built in the western jetty of the harbour. The Basilica is thought to have only been in use for a short period of time since it is believed that it was destroyed by seismic activity in the mid 6th century (Pallas 1956, 1959, 1960, 1965, Rothaus 1995). This destruction is commensurate with the extensive damage sustained in ancient Corinth (Pallas 1956, Scranton 1957), and is thought to have been associated with the earthquake of 551 AD (Pallas 1956, 1959, 1960, 1961, 1965). The aim of this paper is to investigate the origin and triggering mechanism of deformation structures observed on the floor of the Early Christian Basilica. These surface structures are indicative of earthquake-induced liquefaction and an effort is made to examine their relationship with the subsurface soil stratigraphy and structure.

2. Background

2.1. Geodynamic Setting

The Corinth Gulf is an active continental rift system in a subduction zone setting, with extensional tectonics expressed through intense seismicity and marginal uplift. The Lechaion Gulf (Figure 1), the southeastern sub-basin of the Corinth Gulf is an asymmetric basin representing an inactive relict of early rifting (Sakellariou et al., 2004, Leeder et al., 2005, Turner et al., 2010). Spatial uplift rates of raised shorelines suggest a fault slip related uplift for the Perachora peninsula of the

order of 0.31±0.04 mm/yr since Marine Isotope Stage MIS 7 (Leeder 2005, Turner et al., 2010) while the southern margin is considered to be exhumed independent of fault slip and uplift of basin sediments is attributed to non spatially uniform isostatic uplift with rates from 0.19±0.05 mm/yr to 0.31±0.05 mm/yr (Leeder et al., 2003, Turner et al., 2010).

2.2. Previous Work

For the Lechaion ancient harbour, geomorphological, and sedimentological studies suggest an episodic uplift of the order of ~1.1m that according to radiometric dating of marine organisms (*Lithophaga*) bored in raised walls of the ancient port is dated to circa 340 BC, (Stiros et al., 1996). Supplementary radiometric data for this event comes from Morhange et al., (2012) from studies carried in the inner harbour basin, suggesting uplift of the order of ~1.2m around 375±120 cal. B.C. This uplift event is suggested to have been followed by coastal submergence of the outer harbour moles as recorded by Flemming (1978), (Turner et al., 2010). Koster et al., (2011), performed drill core sampling and GPR/ERT survey suggesting possible tsunamigenic layers and abrasion scours at the west part of the harbour at a depth of 2.00m. In addition, Hadler et al., (2011) based on geomorphological, sedimentological, geoarchaeological and geophysical data suggest a multiple tsunamigenic impact at the Lechaion harbour site and surrounding coastal area by at least three distinct event layers that according to radiocarbon dating occurred around 760 cal BC, 50 cal AD., with the youngest and obviously most destructive event dating to the 6th century AD triggered during the 521 or 551 AD earthquake series, related to the destruction of the Early Christian Basilica.

2.2.1. Stratigraphy

The subsurface lithostratigraphy of the Basilica presented in Figure 2, represents a synthesis of the stratigraphic data described by Pallas during original site excavations (1956 to 1965). Trial trenching (Pallas 1959, 1960, 1965) was carried out at various sites in the Basilica floor (trenches 1 and 2) and surrounding locations (3, 4, 5 and 6). The ground on which the temple was founded can be observed at ~1m below the floor of the Basilica (trenches 1, 2, 3, 4). It is composed of sand that at locations (trench 2) contains clay intercalations and fragments of calcareous sandstone (trench 1), representing the preparation ground for the Basilica construction works (Pallas 1960, 1965). This foundation horizon, having a minimum thickness of ~0.5m is dated to the 3rd century BC according to coins found on trial trench 3. The stratigraphy that overlies the foundation horizon represents the artificial fill used during the works of levelling the floor of the Basilica (Pallas 1960, 1965). This levelling horizon is composed of sand and pebbles as observed in trial trenches 1, 2 and 3. In trench 1 the upper parts include lithic fragments, while in trench 2 it contains fragments of ceramics and mortar. Contrasting dates from coins dating from 408-450 AD (trench1) to 518-527 AD (trench 2) and 425-475 AD (trench 3) are also indicative of the artificial nature of this levelling horizon. Finally, a layer of angular calcareous sandstone boulders mixed with sand was recorded in trenches 5 and 6 located to the SW of the Basilica extending from 1.45m below the ground surface. It represents an artificial layer possibly related to early harbour installations (Pallas 1959). Although the continuation of this layer under the Basilica is unknown, its existence is indicative of artificial fills extending to a depth of 3m.

Summarising, the subsurface stratigraphy of the Basilica could be characterised as an artificial fill composed mainly of sand and pebbles with occasional intercalations of clay, lithic and ceramic fragments and mortar. This fill extends to a depth of a least 1.50m below the Basilica floor. As suggested by the existence of a layer of boulders at 3m depth located to the SW of the Basilica, the artificial nature of the subsurface stratigraphy possibly extends to a depth of 3m.

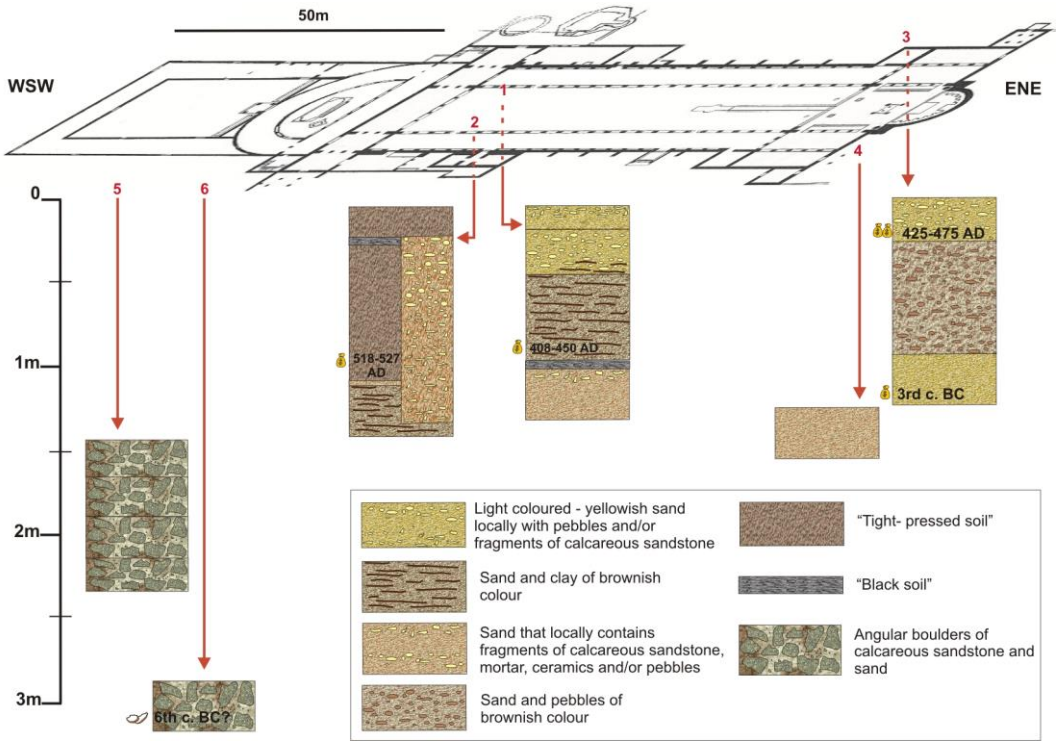

Figure 2 – Trial trenches stratigraphy within the Basilica (1, 2) and in surrounding locations (3, 4, 5 and 6) according to Pallas (1959, 1960 and 1965).

2.3. Ground Deformation Structures

Recent restoration works carried out on the Early Christian Basilica brought to the surface the decorated floor of the temple. Numerous depressions were recorded in the southern aisle, of circular and linear geometry, concentrated mainly at the northern end of the aisle striking in a general E-W direction (Figure 3a), with dimensions varying from 0.45x0.33m and 0.12m depth to 1.80x1.33m and 0.4m depth for the circular depressions (Figure 3b) while the linear depressions (Figure 3d) have a variable depth ranging from 0.05 to 0.12m. It has to be noted that some of these linear structures are in contact with the depressions (Figure 3c). In the central aisle, where the floor is not preserved in a good condition, scattered linear and circular depressions were recorded along with linear and circular buckling structures. Their distribution does not suggest any general trend besides clustering recorded in the central part and near the limit with the southern aisle. The northern aisle remained covered with gravel and soil and was not possible to identify surface ground deformation structures.

Liquefaction is the transformation of cohesionless loosely packed sediments from a solid to a liquid state as a result of increased pore pressure and reduced shear stress leading to ground failures due to hydraulic fracturing (Obermeier & Pond 1999). During earthquake shaking, liquefaction occurs in sediments such as silt, sand and gravel, originating at a depth ranging from a few meters to about 10m below the ground surface (Obermeier 1996). The phenomenon leads to surface failures such as cracking and formation of localised depressions due to densification and settlement of liquefied sediment that can reach 0.25 - 0.5m where thick sands liquefy severely (Obermeier 1996). In addition, circular depressions (craters) form along the length of cracks induced by seismic shaking in a clay rich cap (Obermeier 1996). Such depressions according to Takahama et al., (2000), represent the final “draw-in” process in liquefaction that occurs just after an earthquake.

Figure 3 – Depressions recorded on the southern aisle of the Early Christian Basilica.

3. Methodology

Since the study area is an archaeological site and special laws apply for its protection, a non-invasive approach with respect to the monument was applied (Wolf et al., 2006). After authorisation by the 25th Ephorate of Byzantine Antiquities in Corinth, a geophysical survey was carried out in the Basilica. GPR profiling along with electromagnetic measurements giving the apparent conductivity of the ground in two depths was performed in an attempt to examine the subsurface structure, its possible relation to the surface structures observed and to identify the triggering mechanism (Wolf et al., 2006, Maurya et al., 2006). All geophysical measurements were positioned with Differential GPS system (LEICA GPS 1200). The survey included 10 profiles of GPR using MALA system with shielded antenna 250MHz, and electromagnetic measurements using GF Instruments "CMD2" conductivity meter (compatible with Geonics EM-31) with two setups, "low" for 1.5m depth and "high" for 3.0m depth of detection, positioned by differential global positioning system (Figure 4). Both geophysical methods are affected by the conductivity of underground formations that is dependent upon the compaction, grain size, permeability and saline water intrusion of the sediments and have been used successfully in the past for imaging liquefaction features (Liu and Li., 2001, Al-Shukri et al., 2006, Maurya et al., 2006, Wolf et al., 2006).

Figure 4 – Location of profiles (lines) and major deformation structures (dots) based on Google Earth Imagery.

4. Results

4.1. Ground Conductivity Survey

The cumulative apparent conductivity distribution to the two depth levels (1.5m and 3.0m) is presented in Figure 5. Generally the apparent conductivity is increasing gradually from east to west suggesting at the western part higher permeability and/or higher percentages of fine-grained deposits in comparison to the eastern part where lower permeability and/or higher percentages of coarse-grained deposits are expected.

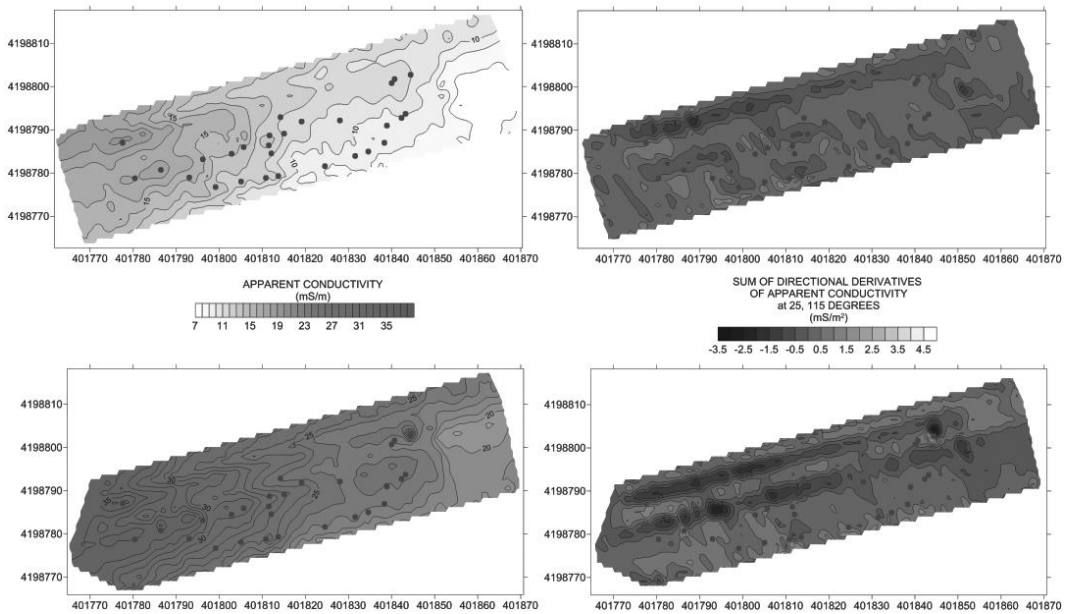

Figure 5 – Left: Apparent conductivity distribution, Right: Sum of directional derivatives of apparent conductivity distribution, in two depth levels, (1.5m top maps and 3.0m bottom maps). Blue dots indicate major ground deformation structures.

Tight circular contours indicate areas of possible liquefaction vent locations (Wolf et al., 2006). These are better discernible on the 3m depth level but only a few correlate well with the surface deformation structures. The contours at the eastern part of the temple and more specifically under the sanctuary of the Basilica are indicative of a potential anthropogenic structure. In addition to the general apparent conductivity distribution, "linear" like and continuous disturbances of the contours are observed under the northern aisle and the northern part of the central aisle of the temple, striking in a direction parallel to the Basilica. In order to enhance the effect of this latter observation the directional derivatives of the apparent conductivity in two directions, 25° and 115°, parallel/vertical to the walls of Basilica was calculated, and the sum for the two depth levels was produced (Figure 5). It seems that two linear structures-zones exist under the northern aisle and the northern part of the central aisle of the temple, striking in a direction parallel to the Basilica. Both resistive structures are clearly documented on the 3m depth map and although the structure-zone under the northern aisle also appears in all of its length in the 1.5m depth map, the structure-zone under the central aisle appears fragmented in two parts. Since the northern aisle structure has been detected by both setups it is suggested that it is located near the surface, while the central aisle structure is possibly located at a depth under but near 1.5m.

4.2. GPR Survey

The GPR profiles provided the opportunity to investigate the lithology/stratigraphy, geometry and deformation of the Basilica sandy substratum to a depth of 6m (suggested velocity 0.12m/ns). The GPR processing steps were a) subtract mean, b) move start time (statics), c) manual gain, d)band-pass frequency filtering, e) background removal and f) deconvolution. In Figure 6, two indicative GPR profiles are presented with interpretation depicting interfaces between different formations (solid and dashed lines) or local features being related either to coarse material (dashed line circles) or fine material (solid line circles). Distinct surface depressions observed along the GPR profiles are indicated by arrows.

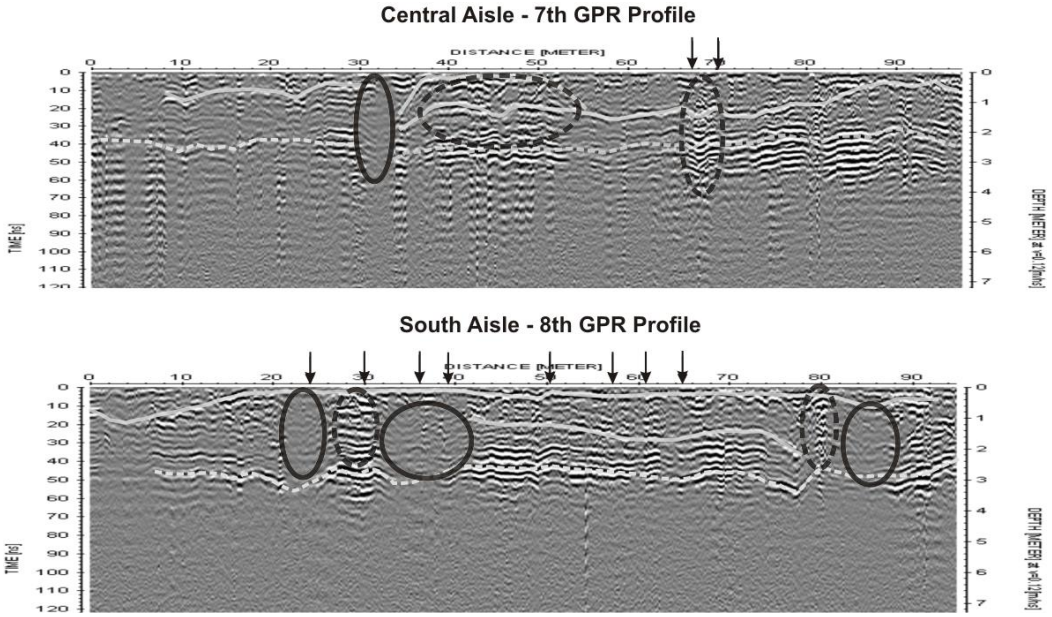

Figure 6 - GPR profiles with interpretation (interfaces with lines, local features with circles). The arrows show positions of observed depressions.

The stratigraphy presents a complex reflection profile with heterogeneities involving coarse grained laminated stratum that dominates the upper 3m of the profile and an underlying fine grained structureless stratum that could correspond to the saline water table (Figure 6). In the

upper 2m of the profile two interfaces have been recognised (solid lines) and another interface has been identified at approximately 3m depth representing a strong reflection signal horizon (dashed line). The profiles are considered to be in agreement with the conductivity contour maps indicating, coarser stratum at the eastern parts of the substratum up to a depth of 3m indicated by strong reflection signals that gradually fade westward.

The GPR profiles are indicative of substratum ground deformation that at locations could relate to liquefaction processes, (Maurya et al., 2006). The upper stratum presents convolutions especially in the upper horizons, indicative of plastic deformation. Sharp vertical discontinuities of weak signal have been identified across the coarse grained laminated stratum (host sediment), indicative of conductive areas permeable to saline water probably related to sand vents (solid line circles), Dimensions vary from 0.5m to 5m and extend clearly down to a depth of 3m suggesting liquefied sediment source below 3m depth. In addition, laminations of the coarse grained material dip towards the centre of these sharp vertical discontinuities exhibiting a concave up geometry. This concave up geometry is in conformity to surface depressions, indicative of the downward settlement of the sediments after release of pressure, (Takahama et al., 2000). For profile 8 in the south aisle and profile 7 for the central aisle the correlation of the surface depressions with the substratum discontinuities has been possible, indicative of their direct association. For the profiles of the north aisle correlation has not been possible since the floor remains artificially covered by gravel and soil and surface depressions have not been recorded.

5. Discussion and Conclusions

Correlation between the stratigraphy described by Pallas (1959, 1960, and 1965) and the geophysical survey provides a better understanding of the subsurface lithostratigraphy on which the Early Christian Basilica was founded. The foundation ground horizon of the construction according to the trial trenches is located approximately 1m below the Basilica floor and is composed mainly of sand with local intercalations of clay. This horizon relates well with the horizon identified at the western part of the central aisle GPR profile (profile 7) extending at ~1m depth. The conductivity contour maps appear to be in agreement with the stratigraphy described by Pallas (1965) in trial trenches 1 and 2 - that is sand with local clay intercalations.

It could also be suggested that the clay intercalations have a dominant character in the western part of the foundation ground in contrast to the eastern part that appears to be coarser grained. The stratigraphy that overlies the foundation surface (<1m) in trial trenches 1, 2 and 3, is dominated by an artificial fill composed of sand and pebbles containing fragments of ceramics, mortar and lithic fragments representing the works of levelling the ground for the construction of the temple. This horizon has been identified in the GPR profiles with strong signal reflections. However it is difficult to identify its continuity since the horizon presents intense convolution and is frequently interrupted by vertical discontinuities possibly associated with sand vents. The angular boulders and sand horizon that according to archaeological trenches extends from ~1.45 to at least 3m depth at locations to the SW of the Basilica, is suggested that could correspond to the strong reflection signal horizon that appears in all the GPR profiles at an approximate depth of ~2-3m. The thickness of this horizon varies from ~1 to 1.5m and it is not continuous.

The GPR profiles have provided indications that could support ground liquefaction and information on its characteristics (Maurya et al., 2006). The existence of numerous sharp vertical discontinuities in the upper 3m of the profiles with dimensions that range from 0.5m to 5m characterised by weak reflection signals are indicative of sand vents. This indication is further supported by the geometry observed in the lateral margins of the vents, where the host sediment presents laminations dipping towards the centre of the vents that in combination with concave-up geometry observed in the upper parts of the vents, is indicative of the sediment settlement (draw – in process) (Takahama et al., 2000). The sand vents and observed geometry have been successfully correlated with the surface linear and circular depressions. Since the sand vents discontinuities

appear to fade out below ~3m, a liquefaction sediment source below ~3m depth is suggested. Special care has to be taken for the two linear structures-zones under the northern aisle and the northern part of the central aisle of the temple, striking in a direction parallel to the Basilica that have been detected by electromagnetic measurements. These zones in depths between 1.0 - 2.5m consisted of coarse material have to be interpreted and be considered if they relate to the liquefaction phenomenon.

We further suggest that the liquefaction is earthquake-induced. The geomorphology of the area can be characterised as a coastal lagoon with the Christian Basilica founded on a coastal dune separating the coast from the inner basin. According to the classification of geomorphological units to their earthquake-induced susceptibility (Kotoda et al., 1988), the location is characterised as highly susceptible. The dimensions of the vents and surface depressions are indicative of violent venting due to rapid hydraulic pressure increase in the liquefied sediment (Obermeier 1996). Since the Early Christian Basilica is considered to have been destroyed by the earthquake of 551-552 AD (Pallas 1960, Papazachos & Papazachou 1989 and references therein), it is possible that its destruction could relate to earthquake-induced ground liquefaction.

In summary, preliminary correlation of the stratigraphy with GPR profiles and conductivity contour maps has provided sufficient indications that allow us to suggest that the surface structures observed on the Basilica floor are the surface expression of earthquake-induced ground liquefaction. However, further research is required for a better understanding of the factors controlling the ground failure mechanism and its relation to the post 5th century AD seismicity of the region.

6. Acknowledgments

We would like to thank D. Athanasoulis, Director of the 25th Ephorate of Byzantine Antiquities for allowing us to carry out the study at the site and the Ephorate's personnel for their warm support. Additionally, many thanks to G. Amolochitis Geophysicist of NTUA Applied Geophysics Laboratory, A. Papadopoulos and A. Stylianou NTUA students for their assistance during the geophysical survey and to the two Anonymous reviewers for their constructive comments which helped us to improve the manuscript. The research was conducted as part of D. Minos-Minopoulos PhD thesis.

7. References

Al-Shukri H.J. and Mahdi H.H. 2006. Three-Dimensional Imaging of Earthquake-induced Liquefaction Features with Ground Penetrating Radar Near Marianna, Arkansas, *Seismological Research Letters*, 77(4), 505-513.

Flemming N.C., 1978. Holocene Eustatic changes and Coastal Tectonics in the Northeast Mediterranean: Implications for Models of Crustal Consumption, *Phil. Trans. R. Soc. Lond.* A 289, 405-458.

Hadler H., Vött. A., Koster B., Mathes-Schmidt M., Mattern T., Ntageretzis K., Reicherter K., Sakellariou D. and Willershäuser T. 2011. Lechaion, the ancient harbour of Corinth (Peloponnese, Greece) destroyed by tsunamigenic impact, in *Proceedings of the 2nd INQUA-IGCP-467 International Workshop on Active Tectonics, Earthquake Geology, Archaeology and Engineeering*, Corinth Greece 2011.

Koster B., Reicherter K., Vött A. and Grützner C. 2011. The evidence of tsunami deposits in the gulf of Corinth (Greece) with geophysical methods for spatial distribution, in *Proceedings of the 2nd INQUA-IGCP-467 International Workshop on Active Tectonics, Earthquake Geology, Archaeology and Engineeering*, Corinth Greece 2011.

Kotoda K., Wakamatsu K., and Masahiko O. 1988. Mapping Liquefaction Potential based on Geomorphological Land Classification, Proceedings of Ninth World Conference on Earthquake Engineering, August 2-9, 1988, Tokyo, Japan, III, 195-200.

Leeder M.R., McNeill L.C., Collier R.E.LL., Portman C., Rowe P.J. Andrews J.E. and Gawthorpe R.L., 2003. Corinth rift margin uplift: New evidence from Late Quaternary marine shorelines, *Geophysical Research Letters*, 30(12), 13.1-13.4.

Leeder M.R., Portman C., Andrews J.E., Collier R.E.LL., Finch E., Gawthorpe L.C., McNeill L.C., Perez-Arlucea M. and Rowe P. 2005. Normal faulting and crustal deformation, Alkyonides Gulf and Perachora peninsula, eastern Gulf of Corinth rift, Greece, *Journal of the Geological Society of London*, 162, 549-561.

Liu L., and Li Y. 2001. Identification of liquefaction and deformation features using ground penetrating radar in the New Madrid seismic zone, USA, *Journal of Applied Geophysics*, 47, 199-215.

Maurya D.M., Goyal B., Patidar A.K., Mulchandani N., Thakkar M.G. and Chamyal L.S. 2006. Ground Penetrating Radar imaging of two large sand blow craters related to the 2001 Bhuj earthquake, Kachchh, Western India, *Journal of Applied Geophysics*, 60, 142-152.

Morhange C., Pirazzoli P.A., Evelpidou N. and Marriner N. 2012. Late Holocene Tectonic Uplift and the Silting up of Lechaion, the Western Harbor of Ancient Corinth, Greece, *Geoarchaeology: An International Journal, Short Communication*, 27, 278-283

Obermeier S.F. 1996. Use of liquefaction-induced features for paleoseismic analysis – An overview of how seismic liquefaction features can be distinguished from other features and how their regional distribution and properties of source sediment can be used to infer the location and strength of Holocene paleo-earthquakes *Engineering Geology*, 44, 1-76.

Obermeier S.F. and Pond E.C. 1999. Issues in using liquefaction features for paleoseismic analysis, *Seismological Research Letters*, 70(1), pp. 34-58.

Pallas D.I., 1956. Lechaion Basilica Excavation, *Proceedings of the Archaeological Society at Athens, (1961)*, 164-178 (in Greek).

Pallas D.I., 1959. Lechaion Basilica Excavation, *Proceedings of the Archaeological Society at Athens, (1965)*, 126-140 (in Greek).

Pallas D.I., 1960. Lechaion Basilica Excavation, *Proceedings of the Archaeological Society at Athens, (1966)*, 144-170 (in Greek).

Pallas D.I., 1961. Lechaion Basilica Excavation, *Proceedings of the Archaeological Society at Athens, (1964)*, 137-154 (in Greek).

Pallas D.I., 1965. Lechaion Basilica Excavation, *Proceedings of the Archaeological Society at Athens, (1967)*, 137-166 (in Greek).

Papazachos B. and Papazachou K. 1989 (eds). The Earthquakes of Greece, Ziti Publications, Thessaloniki 1999, p. 356. (in Greek).

Rothaus R. 1995. Lechaion, western port of Corinth: A preliminary archaeology and history, *Oxford Journal of Archaeology*, 14(3), 293-306.

Sakellariou D., Fountoulis I. and Lykousis V. 2004. Lechaion Gulf: The last descendant of the Proto-Gulf-of-Corinth basin, In *Proceedings of the 5th International Symposium on Eastern Mediterranean Geology*, Thessaloniki, Greece, 14-20 April 2004, 2, 881-884.

Scranton, R.L., 1957, (eds). Mediaeval Architecture: In the Cental Area of Corinth, vol. 16, *The American School of Classical Studies at Athens*, Princeton N.J., 1957, p.147.

Stiros S., Pirazzoli P., Rothaus R., Papageorgiou S., Laborel J. and Arnold, M. 1996. On the Date of Construction of Lechaion, Western Harbour of Ancient Corinth, Greece, *Geoarchaeology: An International Journal*, 11(3), 251-263.

Takahama N., Otsuka T., and Brahmantyo B., 2000. A new phenomenon in ancient liquefaction – the draw-in process, its final stage, *Sedimentary Geology* 135, 157-165.

Turner J.A., Leeder M.R., Andrews J.E., Rowe P.J., Van Calsteren P. and Thomas L. 2010. Testing rival tectonic uplift models for the Lechaion Gulf in the Gulf of Corinth rift, *Journal of the Geological Society of London*, 167, 1237-1250.

Wolf L.W., Tuttle M.P., Browning S., and Park S. 2006. Geophysical surveys of earthquake-induced liquefaction deposits in the New Madrid seismic zone, *Geophysics,* 71(1), B223-B230

Δελτίο της Ελληνικής Γεωλογικής Εταιρίας, τομ. XLVII , 2013
Πρακτικά 13ου Διεθνούς Συνεδρίου, Χανιά, Σεπτ. 2013

Bulletin of the Geological Society of Greece, vol. XLVII 2013
Proceedings of the 13th International Congress, Chania, Sept. 2013

STABILIZATION OF THE LIMESTONE ESCARPMENT OF THE SKETE OF OSIOS NIKANORAS UNDER WET CONDITIONS DUE TO FUTURE FILLING OF THE ILARION DAM'S RESERVOIR

Mourtzas N.D. [1], Gkiolas A. [2] and Kolaiti E. [1]

[1]GAIAERGON Ltd, Kefallinias Str. 16-18, 152 31 Chalandri, Athens, gaiaergon@gmail.com

[2] Civil Engineer, 15 Hydras Str, 104 34, Athens, agkiolas@gmail.com

Abstract

The Skete of Osios Nikanoras is located in a cavern of a vertical limestone escarpment 80m high, over Aliakmon River in West Macedonia. The vertical slope is structured predominantly of thick-bedded limestone, dipping moderately towards NW and only locally of thin-bedded limestone. It is crossed by three transverse and four normal faults. Rock mass was divided in sections, demarcated by bedding planes and major discontinuities. Each section was subdivided into rock blocks. Rock mass description was carried out in areas below the entrance level and the surrounding areas of the Skete as well.

The future water level rise, due to the filling of the Ilarion Dam's reservoir, followed by water level fluctuations, will impose an initial increase and a subsequent variation of water pressures in the rock mass discontinuities. The evaluation of the rock mass stability, due to water induced loads, was therefore required. Stability analysis has been performed in order to determine potential wedge, plane and toppling failure modes.

The measures that were adopted for the conservation of the monument were designed taking into account the restrictions regarding the monuments preservation. The proposed solution comprised three stages of installation of support measures, namely, installation of temporary rock bolts for the pre-strengthening of the rock mass, followed by the execution of grouting and finally installation of permanent rock anchors, thus ensuring adequate factors of safety.

Key words: *engineering geology; rock mass description;stability analysis;support measures.*

Περίληψη

Ο ασβεστολιθικός κρημνός, σε σπηλαίωση του οποίου έχει κατασκευαστεί η σκήτη του Αγ. Νικάνορα, έχει ύψος 80m και κατακόρυφη μορφολογία στον ποταμό Αλιάκμονα, Δυτική Μακεδονία. Η κρημνώδης κλιτύς δομείται κυρίως από παχυστρωματώδεις ασβεστόλιθους με μέτριες ΒΔ κλίσεις και παρεμβολές λεπτοστρωματωδών ασβεστόλιθων. Διασχίζεται, δε, σε όλο το ύψος της από τρία ανάστροφης δομής ρήγματα και τέσσερα κανονικά ρήγματα. Η ευρύτερη βραχομάζα αποτυπώθηκε λεπτομερώς, διαχωρίστηκε σε επιμέρους τομείς και σε επιμέρους υποτμήματα και έγινε μικροτεκτονική ανάλυση της κυρίως στα τμήματα που εδράζεται και στηρίζεται η σκήτη.

Η μελλοντική άνοδος της στάθμης των υδάτων και εν συνεχεία η διακύμανσή της, θα έχει σαν αποτέλεσμα τη μεταβολή των πιέσεων στις ασυνέχειες της βραχομάζας. Κατά συνέπεια απαιτείται έλεγχος των φυσικών πρανών με το νέο καθεστώς φορτίσεων. Η ευστάθεια του πρανούς της ασβεστολιθικής βραχομάζας ελέγχθηκε έναντι δυνητικής αστοχίας τύπου σφήνας, επιπέδου και ανατροπής.
Λαμβάνοντας υπόψη τους περιορισμούς για τη διατήρηση του μνημείου, επιλέχθηκε η εφαρμογή μέτρων αντιστήριξης σε τρία στάδια και συγκεκριμένα να προηγηθεί η τοποθέτηση προσωρινών ράβδων αγκύρωσης ακολουθούμενη από διάτρηση οπών για εκτέλεση τσιμεντενέσεων και στη συνέχεια η εφαρμογή μονίμων αγκυρίων από ανοξείδωτο χάλυβα, σημειακής πάκτωσης, τα οποία εξασφαλίζουν ικανοποιητικούς συντελεστές ασφαλείας.
***Λέξεις κλειδιά**: τεχνική γεωλογία; βραχόμαζα; μικροτεκτονική ανάλυση; μέτρα αντιστήριξης; Σκήτη Οσίου Νικάνορα (Φράγμα Ιλαρίωνα).*

1. Introduction

The scattered archaeological and historical monuments throughout the Greek territory are, usually, exposed to physical processes, in different climatic, topographical and geological conditions. Therefore, they are subject to weathering of their structural features, modification of the initial bearing capacity of foundation, erosion mainly due to uncontrolled discharge of surface water drainage, groundwater activity, earthquake loading in an active geotectonic environment, and human interventions.

The Skete of Osios Nikanoras is located on the sheer northern slope of Aliakmonas River, at the southern foothills of Mt. Kallistrato (Figure 1). The construction of the Skete begun in 964 AD by Monk Georgios and was completed by Osios Nikanoras, who followed an ascetic life on the sacred rock for 15 years.

Due to the construction of Ilarion hydroelectric project at the Aliakmonas River in Kozani prefecture, and the future filling of the Ilarion dam's reservoir, the base of the Skete will be located near the uppermost water level of the artificial lake. The ensuring of the surrounding rock mass stability and the support of the monument's slopes were therefore required, as the Skete will be directly affected by the operation of the dam, taking into account the restrictions regarding the monuments preservation as specified by the Greek Ministry of Culture. The project was financed and supervised by the Public Power Corporation SA.Due to the steep relief of the project area and the difficulty to access parts of the Skete's slope in order to acquire a detailed documentation of the rock mass fracturing and the engineering geological conditions of the vertical limestone escarpment, a 3D surface model of the rock mass deriving from 3D laser Scanning, was produced. The rock mass has been recorded using a Trimple GX200Plus terrestrial laser scanner at a resolution of 1cm.

2. Geological Outlines

2.1. Geomorphological Context

Mt. Kallistrato forms a conical steep foothill at the SW edge of the Vourinos Mountain. A deep, semicircular gorge, at a curve of Aliakmon River just before it follows a NE direction towards Serbia area, separates Vourino Mountain from Vounasa Mountain which develops to the South (Figure 1).

The Aliakmon's river bed develops along the gorge formed between Mt Kallistarto to the North and Petrota area to the South, bypassing Mt Kallistrato with a semicircular clockwise curve. The right bank is 124m high and the left one 100m, with steep morphological inclinations of 70° approx. The Skete of Osios Nikanoras has been built in a cavern of the limestone escarpment which

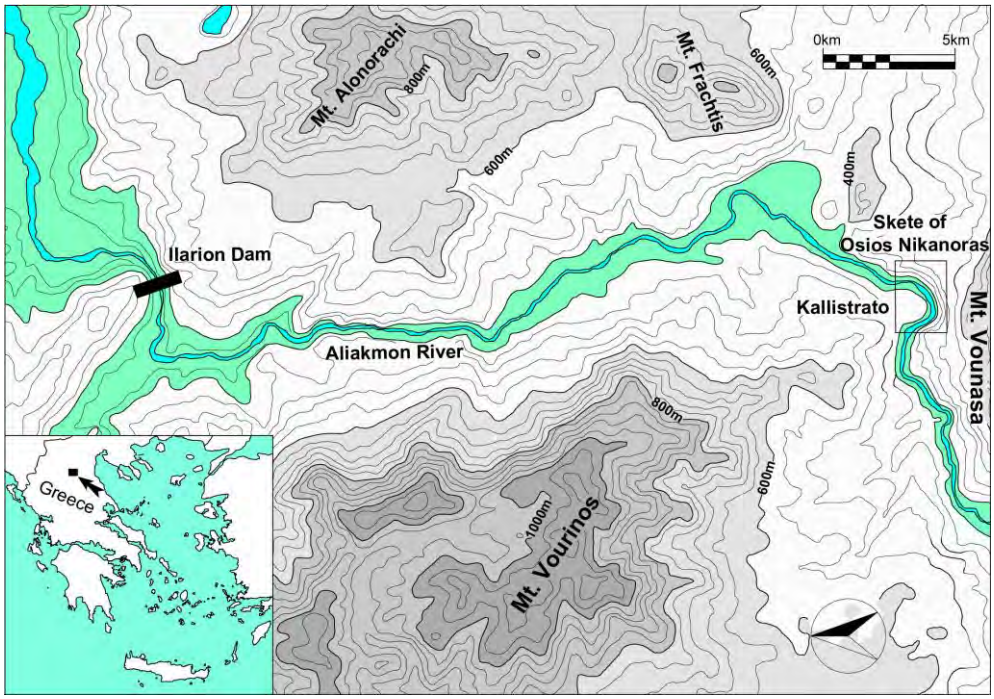

Figure 1 – Location map of the wider area of the Skete of Osios Nikanoras and Ilarion Dam.

develops in WNW-ESE direction and inclines towards SE, at elevation that ranges from 450m to 360m asl, forming the western section of the southern slope of Mt. Kallistrato. It has a length of 274m, a height of 80m and very steep gradients (inclinations ca 80°). Its surface is almost planar with caverns and cavities, mainly along the tectonic zones and major discontinuities of the rock mass. The relief becomes smoother at the base of the escarpment, where the semi-metamorphic schist bedrock appears, beneath the elevation of 360m asl and up to the river bed, with reduction of morphological gradients to 35°, dipping to the SW (Figure 2).

The cavern of the Skete is formed by a fault surface with NW-SE direction and almost vertical inclination to the SW in its eastern side, a major discontinuity with NW-SE direction dipping almost vertically to the NE in the northern side and the limestone layer on the roof, which inclines to the NW at angle of 40°. The cavern with almost vertical side walls has dimensions of 25m by 7m, a height of 21m and an area of 450m^2 (Figure 2).

2.2. Geological Structure

The pre-alpine metamorphic bedrock of the Pelagonian zone consists of Paleozoic gneiss-schists and mica schists, the Triassic marbles of Vounasa-Tranovaltos, phyllites of the Early Jurassic, ophiolithes of the Middle and Late Jurassic, and limestones of the Late Jurassic-Cretaceous (Vérgely, 1984; Katsikatsos, 1992; Karapantelakis, 2008).

Mt. Kallistrato is formed by partially crystallized, thickly bedded, light coloured limestones of the Middle Triassic – Jurassic with interpolations of thinly-bedded strata. They are, actually, the normal upward evolution of the Palaeozoic – Early Triassic semi-metamorphic rocks of the Pelagonian zone. The Middle Triassic – Jurassic schists are the bedrock of the calcareous mass and appear at the base of the escarpment, with bedding and schistosity planes dipping smoothly towards NW.

The sheer slope is structured mainly by thickly bedded limestones, with thickness of bedding that ranges from 1.60m to 3.0m, and dip direction to the NW, at angles between 30° and 40°. Two horizontal layers, 7.0m thick, of thinly-bedded limestones with thickness of bedding that ranges from

0.02m to 0.10m come between; with their continuity and thickness interrupted and transformed among the faults which cross the limestone mass (Figure 2).

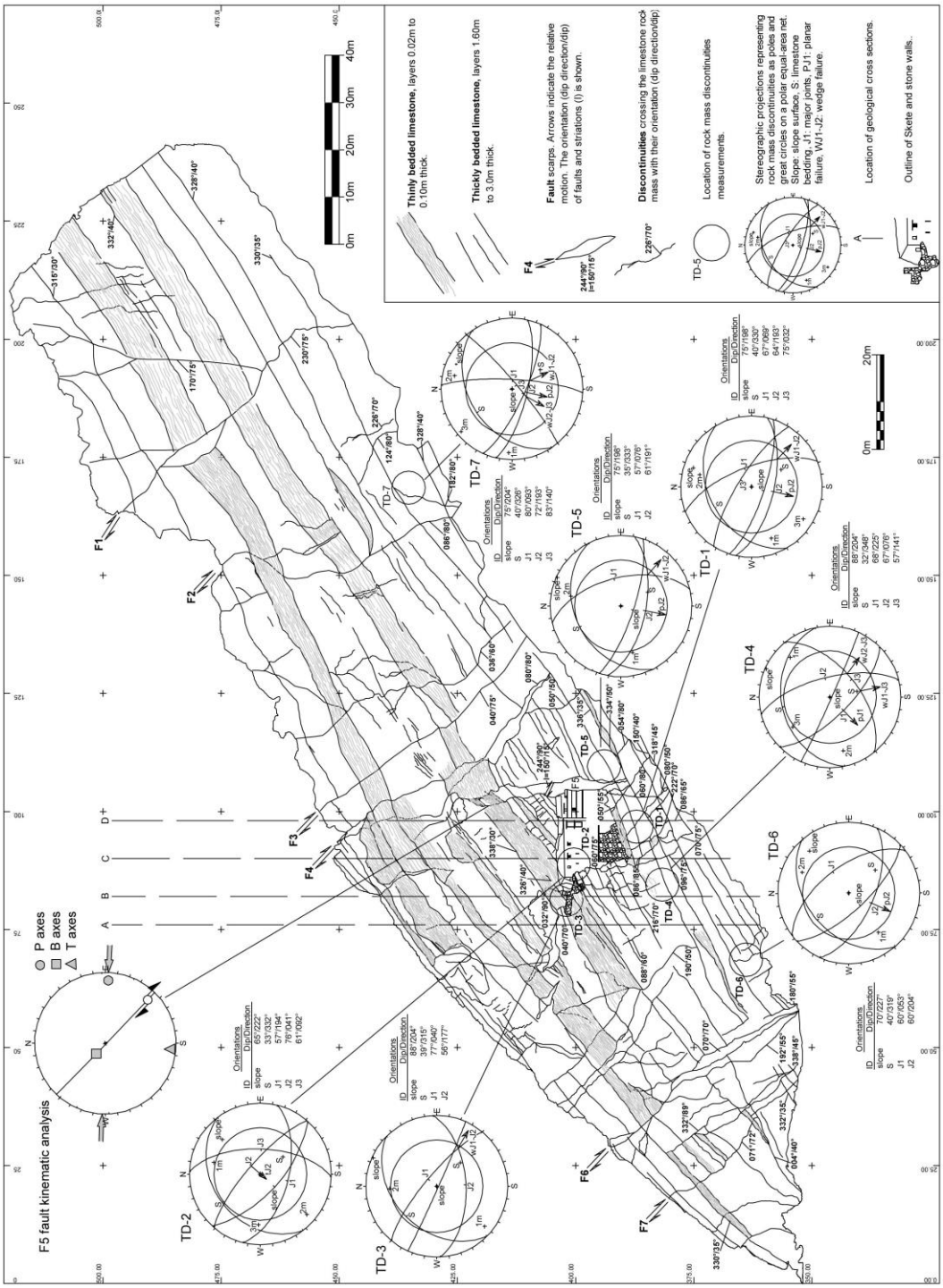

Figure 2 – Geological and tectonic map of the slope face.

2.3. Tectonic Setting

Three reverse faults (F1, F5 and F6) and four normal faults (F2, F3, F4 and F7) which have caused the interruption in continuity and the displacement of the limestone layers cross the entire, calcareous, sheer slope (Figure 2). The westernmost fault F1, with its trace at the upper and lower part of the slope at elevations 496m and 447m, respectively, dips to the SW at angle of 75° and it has caused a small upward displacement of its western block by ca. 1m. The next downward fault F2, with its trace 475m and 426m in elevation, dips to the ENE at an angle of 80° and it has, also, caused a small downward movement of its eastern block. Fault F3, with its trace 454m and 410m in elevation, dips to the NE at an angle of 75° and has given rise to a downward displacement along the eastern block by 2m. The following fault F4, with its trace at elevations 450m and 405m, dips to the ENE at an angle of 80° and it has caused downward movement of its eastern block by 5.50m approx. The F5 fault, with its trace 450m and 389m in elevation, dips almost vertically to the SW and it has given rise to an upward displacement of its western block by 2m. The striations on the fault slip surface dip to the SE at an angle of 15° referring to a compressive event of a WNW-ESE direction (Figure 2). Finally, faults F6 and F7, at the eastern end of the sheer slope, with their traces at elevations 450m, 389m and 380m, 350m, respectively, dip to the NE at an angle of 70° and they have caused the interruption in the continuity and the displacement of the layers (Figure 2, Figure 3).

2.4. Seismicity and Seismic Hazard

The wider area of Ilarion dam is characterized by medium seismic hazard. The most important historical earthquakes, which hit the greater area of the Skete of Osios Nikanoras the period between 375AD and 1646AD, were three events with estimated magnitudes of 6.0 up to 7.3 (Papazachos and Papazachou, 1989). There are not records for earthquakes of magnitude greater than or equal to 7.0 in the study area for the same time period. The area belongs to the seismic zone II of the revised Seismic Hazard Map, provided by the modified Greek Antiseismic Regulations (EAK, 2000). In this zone the value of ground acceleration is A=0.24g (g: gravity acceleration), with a ten percent (10%) probability of exceedance in fifty years. According to the aforementioned Regulations (EAK, 2000), the limestone rock mass is classified as soil category A.

3. Quantitative Description of Discontinuities in the Rock Mass

In order to evaluate the engineering geological conditions and to determine the rock mass properties, discontinuities were investigated and data was collected at seven (7) areas throughout the Skete's slope. The data were selected on the basis of support requirements mainly in the rock mass sections where the Skete is founded (Figure 2) (Hoek and Brown, 1981; ISRM Suggested Methods, 1981). It was concluded that the rock mass fragmentation is, mainly, due to four discontinuity sets, with dominant discontinuity the limestone bedding with a NE-SW direction and a smooth dip towards NW. Three major joint sets of NW-SE, WNW-ESE and NE-SW directions dipping to the NE, SSW and SE, respectively, are also developed in the rock mass. The quantitative description of discontinuities according to ISRM (1981) is presented in Table 1. Stereographic projections for each selected area representing discontinuities as poles and great circles on a polar equal-area net were plotted and are presented in Figure 2.

4. Potential Slope Failure Modes

Kinematic analysis has been performed to determine potential failure modes utilizing stereographic projection technique and data for each selected area, based on the methods designated to evaluate the possibility of wedge, plane and toppling failure modes (Markland, 1972; Hocking, 1976; Goodman, 1976; Hoek and Bray, 1981; Matherson, 1988). Rocky blocks kinematically feasible in relation to the geometry (dip direction/dip) of the slope face, were

identified, assuming that the mean value of the friction angle of all discontinuities in the limestone rock mass is 35°. The sliding potential and modes of failure are presented in Table 2.

Table 1 – Classification of discontinuity sets according to ISRM (1981).

STEREOPLOT OF DISCONTINUITIES	GEOLOGICAL FORMATION	ELEVATION (m)	DISCONTINUITY SETS			SPACING [2]	PERSISTENCE [3]	APERTURE [4]	FILLING [5]	WEATHERING [6]	ROUGHNESS [7]	SEEPAGE [8]	BLOCK SIZE [9]
			Discontinuity type [1] Set number	Dip direction (°)	Dip (°)								
TD-1	thick and thin bedded limestone	+387	**S**	330	40	d,f	e	a	O	I	VIII	III	a
			J1	69	67	e,f,g	d,e	b,c	O	I	V	III	
			J2	193	64	e,f,g	d,e	b,c	O	I	V	III	
			J3	32	75	e,f,g	d,e	b,c	O	I	V	III	b
TD-2	thick and thin bedded limestone	+400	**S**	332	33	d,f,g	e	a	O	I	VIII	III	a
			J1	194	57	e,f,g	d,e	b,c	O	I	V	III	
			J2	41	76	e,f,g	d	b,c	O	I	V	III	b
			J3	92	61	e,f,g	d	b,c	O	I	V	III	
TD-3	thin bedded limestone	+400	**S**	315	39	d	e	a	O	I	VIII	III	d
			J1	40	77	e,f,g	d,e	b,c	O	I	V	III	a
			J2	177	56	e,f,g	d,e	b,c	O	I	V	III	
TD-4	thick and thin bedded limestone	+382	**S**	348	32	d,f	e	a	O	I	VIII	III	a,d
			J1	225	68	e,f,g	d,e	b,c	O	I	V	III	a
			J2	76	67	e,f,g	d,e	b,c	O	I	V	III	
			J3	141	57	e,f,g	d	b,c	O	I	V	III	b
TD-5	thick and thin bedded limestone	+394	**S**	333	35	d,f	e	a	O	I	VIII	III	a
			J1	76	57	e,f,g	d	b,c	O	I	V	III	b
			J2	191	61	e,f,g	d,e	b,c	O	I	V	III	a
TD-6	thick bedded limestone	+362	**S**	319	40	f	e	a	O	I	VIII	III	a
			J1	53	60	e,f,g	d,e	b,c	O	I	V	III	
			J2	204	60	e,f,g	d,e	b,c	O	I	V	III	
TD-7	thick bedded limestone	+431	**S**	326	40	e,f,g	d,e	a	O	I	VIII	III	a
			J1	93	80	e,f,g	d,e	b,c	O	I	V	III	
			J2	193	72	e,f,g	d,e	b,c	O	I	V	III	
			J3	140	83	e,f,g	d,e	b,c	O	I	V	III	

[1] **S**: bedding, **J**: major joint, J: minor joint
[2] extremely close spacing (<20mm): a, very close (20-60mm): b, close (60-200mm): c, moderate (200-600mm): d, wide (600-2000mm): e, very wide (2000-6000mm): f, extremely wide (>6000mm): g
[3] very low persistence (<1m): a, low (1-3m): b, medium (3-10m): c, high (10-20m): d, very high (>20m): e
[4] very tight (<0.1mm): a, tight (0.1-0.25mm): b, partly open (0.25-0.50mm): c, open (0.50-2.50mm): d, moderately wide (2.50-10mm): e, wide (>10mm): wide, very wide (1-10cm): f, extremely wide (10-100cm): g, cavernous (>1m): h
[5] filling material: a, no filling material: b
[6] fresh: I, slightly weathered: II, moderately weathered: III, highly weathered: IV, completely weathered: V, residual soil: VI
[7] I: rough, stepped, II: smooth, stepped, III: slickensided, stepped, IV: rough, undulating, V: smooth, undulating, VI: slickensided, undulating, VII: rough, planar, VIII: smooth, planar, IX: slickensided, planar
[8] tight, dry, water flow no possible: I, dry, no evidence of water flow: II, dry, evidence of water flow: III, damp, no free water present: IV, seepage, drops of water, no continuous flow: V, continuous water flow: VI
[9] very large blocks (Jr, joints/m^3<1,0): a, large blocks (1<Jr<3): b, medium-sized blocks (3<Jr<10): c, small blocks (10<Jr<30): d, very small blocks (Jr>30): e

Table 2 – Sliding potential and failure modes utilizing stereographic projections for each selected area.

Stereoplot	Discontinuity Sets			Slope orientation (dip direction/dip)	Sliding Potential - Failure modes		
	system **S**: bedding **J**: major joint **j**: minor joint	dip direction (°)	dip (°)		wedge	planar	toppling
TD-1	**S**	330	40	WNW-ESE dipping towards SSW at angle 75° (198°/75°)	J1-J2	J2	
	J1	69	67				
	J2	193	64				
	J3	32	75				
TD-2	**S**	332	33	NW-SE dipping towards SW at angle 65° (222°/65°)			J2
	J1	194	57				
	J2	41	76				
	J3	92	61				
TD-3	**S**	315	40	NW-SE dipping towards SW at angle 88° (204°/88°)	J1-J2		
	J1	40	70				
	J2	177	56				
TD-4	**S**	348	32	NW-SE dipping towards SW at angle 88° (204°/88°)	J1-J3 J2-J3	J1	
	J1	225	68				
	J2	76	67				
	J3	141	57				
TD-5	**S**	333	35	WNW-ESE dipping towards SSW at angle 75° (198°/75°)	J1-J2	J1	
	J1	76	57				
	J2	191	61				
TD-6	**S**	319	40	NW-SE dipping towards SW at angle 70° (227°/70°)		J2	
	J1	53	60				
	J2	204	60				
TD-7	**S**	326	40	NW-SE dipping towards SW at angle 75° (204°/75°)	J1-J2 J2-J3	J1	
	J1	93	80				
	J2	193	72				
	J3	140	83				

5. Description of the Rock Mass Surrounding the Skete

The cavern of the Skete is formed to the west by a rupture surface with dip direction/dip 240°/90°, to the northwest by a major joint with dip direction/dip 326°/40°, and its roof follows the limestone bedding with dip direction/dip 320°/35°. The limestone rock mass that surrounds the Skete has been divided into seven sections (1-7). Each section includes a 2.50m to 3.50m thick rock mass segment, which is separated by its underlying one with a nearly vertical joint of high to very high persistence and NW-SE direction, dipping to the NE up to SW (dip direction/dip: 032°-212°/85°-90°). Each of the seven rock mass sections, according to its sequence number, superimposes parts of the previous section and partially covers them. Also, each section is subdivided into rock blocks (with codes: a,b,c,d,e…) which are demarcated by the limestone bedding and rock mass major joints (Figure 3).

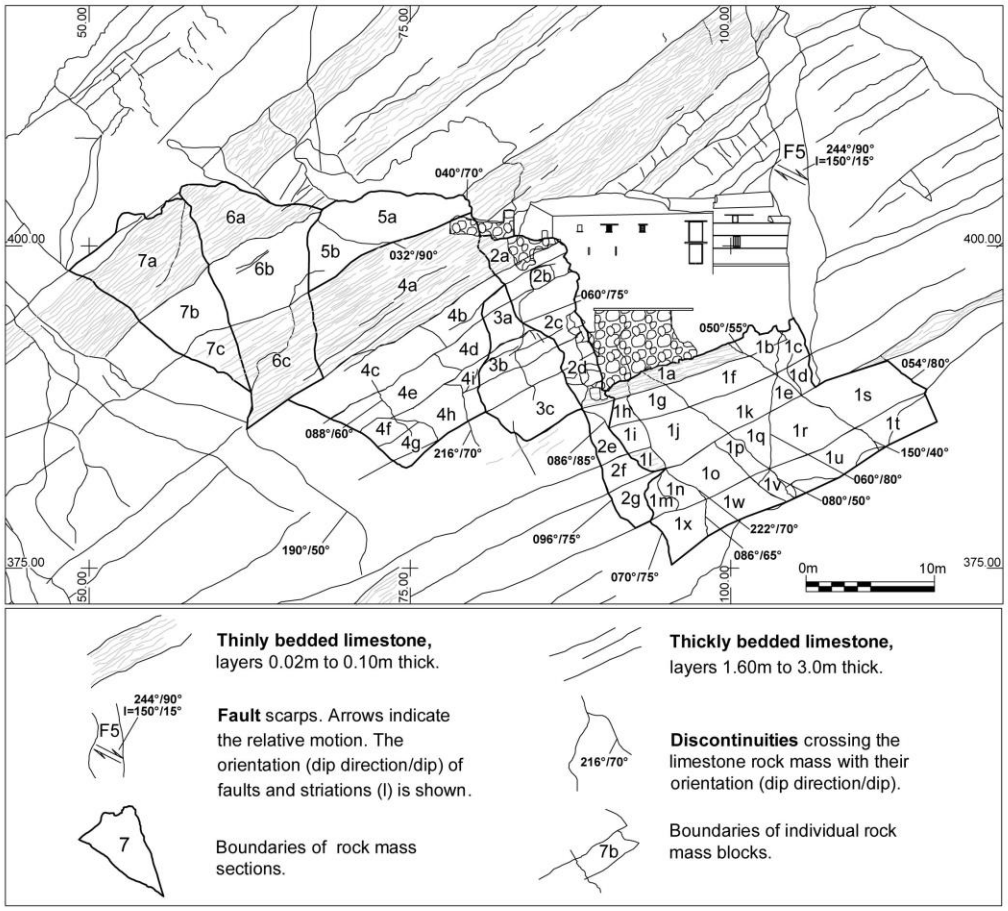

Figure 3 – Geological and tectonic map of the Skete's surrounding area.

Section 1 has dimensions (width x height) of 22.0m by 13.0m, is located at the base of the sheer slope under the Skete, at elevation that ranges from 375m to 391m, and its upper part is embedded in the Skete's foundations. It consists of four limestone layers, of thickness that ranges from 2.30m to 3.80m and orientation (dip direction/dip) 316°-333°/35°-45°. At its upper part a 1.30m thick layer of thinly-bedded limestone is intercalated, having the same bedding dip. Three major joints are developed, which together with the bedding demarcate the rock blocks. Their orientations are 225°/68°, 067°/76°, and 140°/57°. Section 1 is divided into 23 rock blocks, with dimensions that range from 3.40m x 2.50m x 1.80m to 6.0m x 4.0m x 3.0m.

Section 2 has dimensions of 5.0m (w) by 24.5m (h), is an elongate rock block that retains the western side of the Skete. It develops between elevations 378m and 401m and its upper part is embedded in the wall of the Skete's small courtyard. It comprises twelve limestone layers with orientation 326°-332°/35°-40° and thickness of 1.10m to 3.30m. At its upper part a 2.50m thick layer of thinly-bedded limestone is intercalated, which maintains the same bedding dip. The eastern and western boundaries of this section are defined by two major joint sets with orientations 070°/75° and 074°/70°, respectively. Apart from bedding, rock blocks are demarcated also by two major joint sets with orientations 077°/40° and 177°/56°. Section 2 is divided into seven rock blocks with dimensions that range from 2.0m x 2.50m x 1.50m to 5.0m x 4.50m x 2.50m.

Section 3 has dimensions of 12.0m (w) by 7.0m (h) and is developed at the west side of the Skete, between 385m and 397m in elevation. It consists of six limestone layers, of thickness ranging from

1.0m to 3.50m and orientation 348°/35°. The major joints, which demarcate the section from the east and west, have orientations 216°/70° and 060°/75°, respectively. Together with bedding, three major joint sets with orientations 225°/68°, 076°/67° and 141°/57° divide this section into three rock blocks, with dimensions ranging from 3.80m x 2.50m x 2.50m to 6.0m x 3.50m x 2.50m.

Section 4 has dimensions of 13.50m (w) by 19.0m (h) and is located to the west of the Skete, between 383m and 402m in elevation. Its upper part is embedded in the wall of the Skete's courtyard. It comprises seven limestone layers of thickness ranging from 1.50m to 2.50m and orientation 315°/40°. At its upper part a 7.0m thick layer of thinly-bedded limestone is intercalated, having the same bedding dip. The two major joint sets which together with the bedding define the rock blocks have orientations 040°/77° and 177°/56°. Section 4 is divided into nine rock blocks with dimensions between 2.60m x 2.20m x 2.0m and 11.0m x 3.50m x 2.50m.

Section 5 has dimensions of 12.0m (w) by 8.0m (h) and also develops to the west of the Skete at elevation ranging from 396m to 404m. Two major joint sets with orientations 040°/77° and 177°/56° define the rock blocks. This rock mass section is divided into two sizeable rock blocks with dimensions ranging from 6.0m x 5.0m x 3.0m to 12.0m x 4.0m x 3.0m.

Section 6 has dimensions of 11.0m (w) by 19.0m (h) and is located to the west of the Skete at elevation ranging from 386m to 405m. It consists of one limestone layer 7.50m thick and with orientation 315°/40°, lying between two layers of thinly-bedded limestone 6.0m and 7.0m thick, respectively, having the same dip of bedding. The two major joints that demarcate the rock block boundaries have orientations 040°/77° and 177°/56°. The rock mass section is divided into three rock blocks of dimensions 7.0m x 6.0m x 3.0m.

Finally, **section 7** has dimensions 15.0m (w) by 11.0m (h) and is developed to the west of the Skete, between 389m and 404m in elevation. It comprises a 3.50m thick limestone layer, with an orientation 315°/40°, lying between two layers of thinly-bedded limestone, 6.0m and 7.0m thick, respectively, that maintain the same bedding dip. The main joints, which define the boundaries of the rock blocks, are classified into two major joint sets with orientations 040°/77° and 177°/56°. The section is divided into three rock blocks with dimensions ranging from 5.50m x 4.0m x 3.0m to 8.50m x 6.0m x 3.0m.

6. Evaluation of Rock Mass Stability

Under the conditions hitherto prevailing, both major sections and sub-sections of the limestone escarpment, have demonstrated a stable behavior. The future water level rise, up to the entrance level of the Skete, due to the filling of the Ilarion Dam's reservoir (estimated max. water level: +398.50m), will impose an initial increase, and subsequent variations of water pressures in the rock mass discontinuities. The evaluation of the rock mass stability, due to water induced loads, was therefore required.

Stability of the limestone slope was checked against potential wedge and plane failure, utilizing Swedge (v. 5.010) and RocPlane (v. 2.029) programs (Rocscience), respectively, with assumed shear strength of discontinuities: c=0, φ=35°. The following cases were examined:

- **a.** Static loads, with required factor of safety (F.O.S. A1) >1.50
- **b.** The worst-case scenario for water-induced loads assumed a sudden drop of water level, without any dissipation of water pressures in rock fissures, resulting in the development of pressures corresponding to 100% water filled fissures, with required F.O.S. A2 >1.30
- **c.** Furthermore, the extreme case of seismic loading with simultaneous full hydrostatic pressures in rock fissures was also examined, with required F.O.S. A3 >1.00

All sections and subsections were checked, based on the results of the microtectonic analyses. The results of unsupported sections are presented in Table 3.

Table 3 - Stability analysis of unsupported sections.

No.	Wedge	Plane	Factors of Safety			Wedge weight (tn)	Weight per m (tn)
			A1	A2	A3		
Section 1: Subsections 1a to 1x							
1	J1-J2	-	0.34	0.00	0.00	243.75	-
2	S-J2	-	2.33	1.27	0.98	1733.25	-
3	-	J2	0.34	0.22	0.14	-	34.11
Section 2: Subsections 2a to 2g							
1	J1-J2	-	0.47	0.00	0.00	0.7	-
2	S-J2	-	2.46	1.88	1.28	6.5	-
Section 3: Subsections 3a to 3c							
1	J1-J2	-	2.38	1.70	1.22	17.4	-
2	J1-J3	-	0.62	0.26	0.18	27.3	-
3	J2-J3	-	0.45	0.00	0.00	6.7	-
Section 4: Subsections 4a, 4b, 4d, 4h and 4i							
1	J1-J2	-	0.47	0.00	0.00	2.0	-
2	S-J2	-	2.56	1.95	1.33	17.8	-

The above-presented results of the stability analyses of unsupported sections demonstrate the necessity of adopting appropriate support measures to increase stability. In order to achieve the adequate factors of safety, appropriate numbers of 6m long rock anchors, of 16tn working load each, are adopted. The results of supported sections are presented in Table 4.

Table 4 - Stability analysis of supported sections.

No.	Wedge	Plane	Factors of Safety			Wedge weight (tn)	Weight per m (tn)
			A1	A2	A3		
Section 1: Subsections 1a to 1x with 33 anchors							
1	J1-J2	-	6.48	2.50	1.70	243.75	-
2	S-J2	-	3.24	1.85	1.22	1733.25	-
3	-	J2	1.50	1.32	1.04	-	34.11
Section 2: Subsections 2a to 2g with 13 anchors							
1	J1-J2	-	25.64	8.27	7.84	0.7	-
Section 3: Subsections 3a to 3c with 8 anchors							
2	J1-J3	-	3.75	2.83	2.10	27.3	-
3	J2-J3	-	4.72	1.49	1.23	6.7	-
Section 4: Subsections 4a, 4b, 4d, 4h and 4i with 7 anchors							
1	J1-J2	-	9.64	3.01	2.86	2.0	-

The above-presented results of the stability analyses of supported sections demonstrate the adequacy of the proposed number of anchors for each corresponding section.

7. Support Measures

Based on restrictions on monument preservation, the adoption of measures such as the application of shotcrete or concrete or wire mesh installation is excluded. The proposed solution comprises three stages of installation of support measures, namely, installation of temporary rock bolts for the pre-strengthening of the rock mass, followed by the execution of grouting and finally

installation of permanent active rock anchors (Figure 4, Figure 5). The proposed measures intend to increase the cohesion of the rock mass by means of grouting rock discontinuities and to support potentially unstable rock blocks by means of active permanent rock anchors.

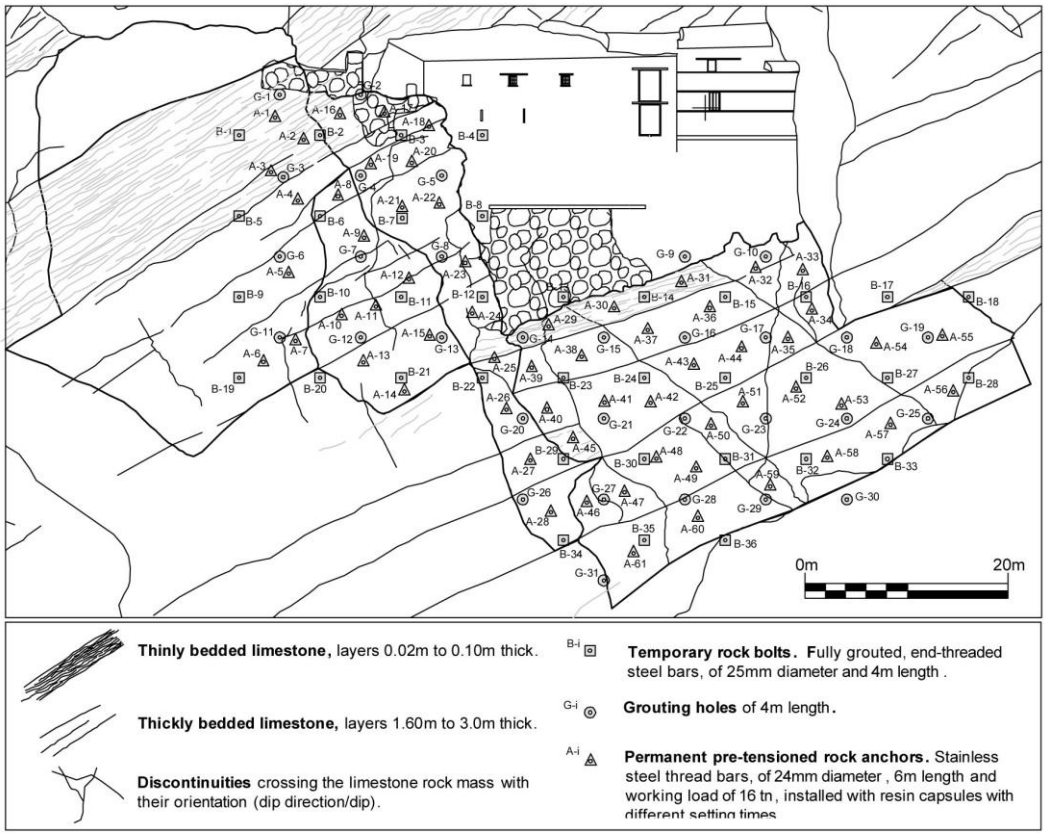

Figure 4 – Slope face of the Skete's surrounding area, indicating the position of the support measures.

Temporary rock bolts, will be installed for the pre-strengthening of the rock mass, in order to avoid any failures in weaker parts of the slope as a result of the applied pressures during subsequent grouting works. The temporary rock bolts are fully grouted, end-threaded steel bars, of 25mm diameter and 4m length, applied in an indicative 4m x 4m pattern (Figure 4, Figure 5). Grouting holes of 4m length will be drilled in a 4m x 4m pattern on the entire slope area, in order to increase the cohesion of the rock mass, combined with targeted grouting in open discontinuities. Cement grout of a water to cement ratio of 1:1 will be initially injected and according to observed absorptions it may vary up to 0.5:1 (w:c). The grout mix will also include 1% bentonite (Figures 4, Figure 5).

Permanent rock anchors of appropriate length and of adequate capacity will be used for the stabilization of all potentially unstable blocks. Selection of location and length of permanent rock anchors was made in order to ensure stability of all sections and subsections. Therefore, the application of at least one anchor per section and subsection was considered necessary. The number, the location, the length and the angle of installation of the permanent rock anchors were selected in order to ensure adequate factors of safety, against plane and wedge failures along discontinuities, for various combinations of static, water and earthquake loading combinations, of both subsections and major sections of the rock mass.

The permanent rock anchors are end-anchored, stainless steel thread bars, of 24mm diameter and 4m to 6m lengths, with working loads of 16 tn. The anchors are installed with resin capsules with different setting times, thus enabling quick installation and anchor pre-tensioning. The anchors will be pre-tensioned in the working load of 16 tn (Figure 6).

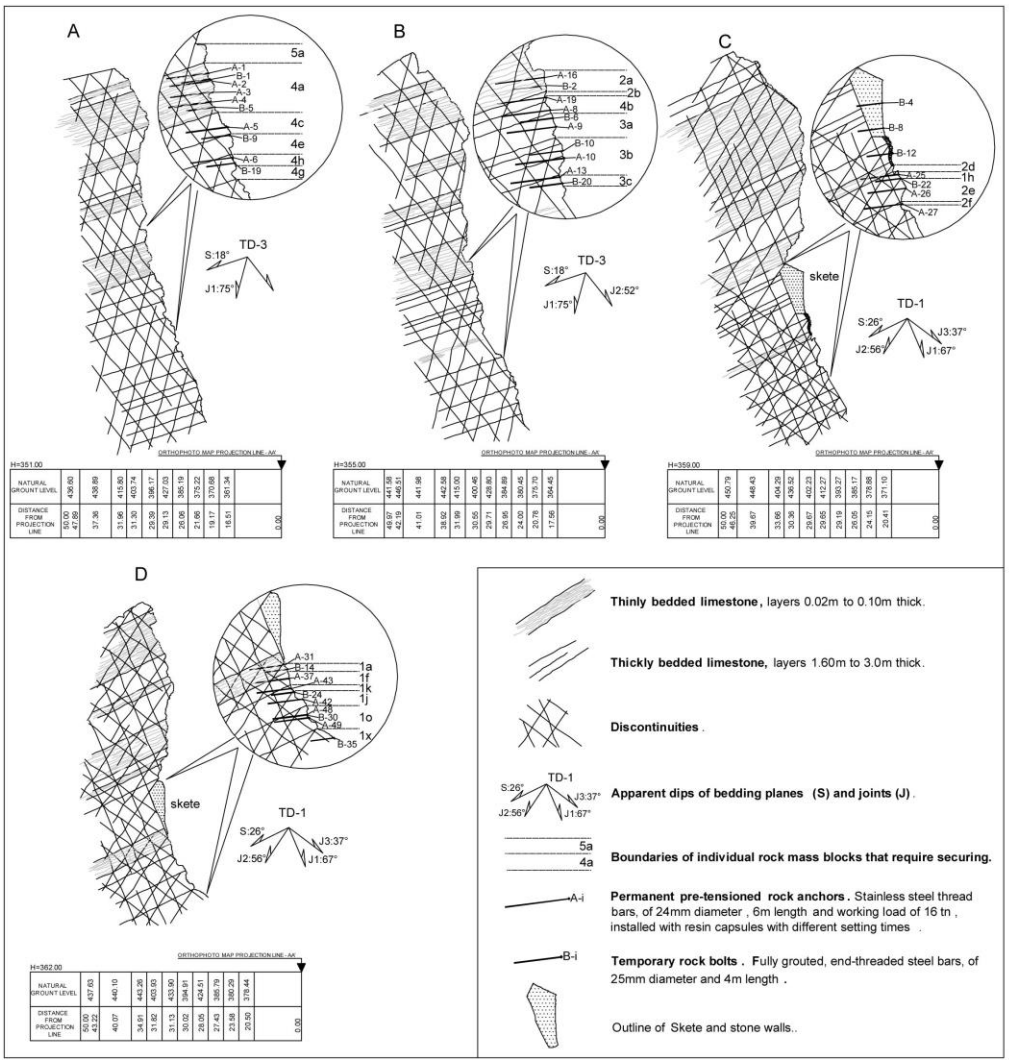

Figure 5 – Geological cross sections indicating the position of the support measures.

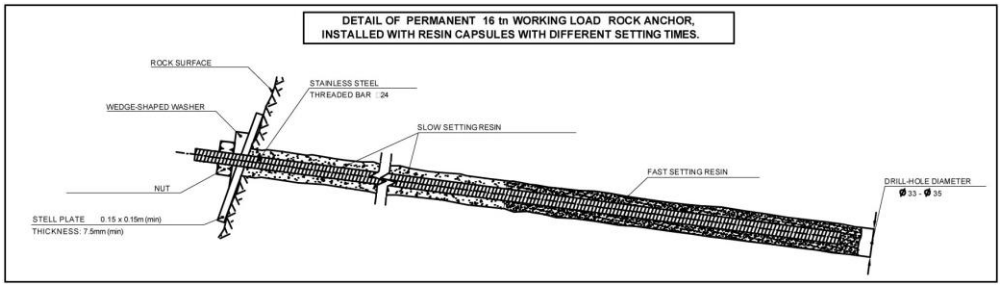

Figure 6 – Drawing of a Permanent rock anchor system.

8. Conclusions

Filling of the Ilarion Dam's reservoir will result in the water level rise up to the entrance level of the Skete of Osios Nikanoras and water level fluctuations. Therefore, the behavior of the surrounding rock mass before and after the rise of water level was investigated. Due to the difficulty of accessing the Christian monument, besides the conventional geological and geotechnical techniques, the terrestrial laser scanning method was employed, so that a complete engineering geological rock mass evaluation and analysis of the instability mechanisms to be achieved.

The limestone rock mass was divided into discrete sections and these were subdivided into individual rock blocks, as defined by the rock mass discontinuities. The geomechanical analysis of rock mass has demonstrated a stable behavior under dry conditions that seems to change in a wet environment and it is burdened with seismic loading.

The adoption of support measures in three stages of installation, namely, installation of temporary rock bolts for the pre-strengthening of the rock mass, followed by the execution of grouting and finally installation of permanent active rock anchors. Selection of the above measures is in accordance to the restrictions regarding the monument and historic landscape preservation and aims at the ensuring of the rock mass stability against unfavorable future conditions.

9. References

EAK 2000. Greek Antiseismic Code: Ministry of Public Works of Greece, FEK 2184 B'/20-12-1999.

Eurocode 7 1995. European standards for design of geotechnical projects.

Eurocode 8 1998. European standards for earthquake design.

Goodman R.E. 1976. *Methods of Geological Engineering in Discontinuous Rocks*. West Publishing, San Francisco.

Hocking G. 1976. A method for distinguishing between single and double plane sliding of tetrahedral wedges, *Int. J. Rock Mech. Min. Sci. Geomech*. Abstr. 13, 225–226.

Hoek E., Bray J.W. 1981. *Rock Slope Engineering Institution of Mining and Metallurgy*, London.

ISRM Suggested Methods, 1981., in Brown, E.T. (ed), *Rock Characterization Testing & Monitoring*, Pergamon Press, 211pp.

Karapantelakis K., Emmanoyhlidis G., Karagiannaki V. and Minopetros Ch. 2008. Ilarion Dam: The most important geological and geotechnical problems that have been faced during the designs as well as the construction. *Proc. of the 1st Hellenic Congress on Big Dams,* Larisa, 13-18 November 2008, 1-13.

Katsikatsos G.X. 1992. *Geology of Greece*. Athens: Katsikatsos, 451pp. (in Greek).

Markland J.T. 1972. A useful technique for estimating the stability of rock slopes when the rigid wedge sliding type of failure is expected. Imp. Coll. Rock Mech. Res. Rep. 19, 10.

Matherson G.D., 1988. The collection and use of field discontinuity data in rock slope design. Q. J. Eng. Geol. 22, 19–30.

Papazachos, B.C. and Papazachou, K., 1989. *The Earthquakes of Greece*. Ziti Editions, Thessaloniki, 356pp. (in Greek).

Rockscience Inc., 2005. Phase2 6.0, A 2-D FE elastoplastic Code for geotechnical applications. Toronto, Ontario, Canada.

Stamatis A., 1987. Geological map of Greece: Deskati sheet (scale 1:50.000), IGME Publications, Athens.

Vérgely P., 1984. Tectonique des ophiolites dans les Hellénides internes (déformations, métamorphismes et phénomènes sédimentaires). Conséquences sur l'évolution des régions téthysiennes occidentales, *Thèse, sciences*, Univ. Paris Sud, Orsay, pp. 649.

Δελτίο της Ελληνικής Γεωλογικής Εταιρίας, τομ. XLVII , 2013
Πρακτικά 13ου Διεθνούς Συνεδρίου, Χανιά, Σεπτ. 2013

Bulletin of the Geological Society of Greece, vol. XLVII 2013
Proceedings of the 13th International Congress, Chania, Sept. 2013

INVESTIGATION AND MITIGATION OF A FAILURE AT THE TAXIARCHES CANAL OF MORNOS AQUEDUCT

Mourtzas N.D.[1], Gkiolas A.[2], Vakiris D.[2] and Soulis V.[3]

[1]*GAIAERGON Ltd, 16-18 Kefallinias Str., 152 31 Chalandri, Athens, gaiaergon@gmail.com*

[2] *GEOMECHANIKI S.A., 91 Eth. Antistaseos Str., 15351 Pallini, Athens, geomsot@gmail.com*

[3] *EYDAP S.A., Directory of Water Intake,16 Galatsiou Str., 1114, Athens, vsoulis@eydap.gr*

Abstract

The sudden soil fracture and failure at the Taxiarches canal of Mornos Aqueduct of the Athens Water Supply and Sewerage Company (EYDAP SA), took place approximately 540m after the exit of Elikonas tunnel and resulted in failure and displacement of the canal segments along an 80m long section. Due to the failure the water supply was interrupted and two extensive gullies, spaced 75m apart, were created by the water outflow. The water discharge resulted in subsoil erosion and transportation of vast masses of geomaterial and two of the canal segments downhill. The debris flow destroyed part of Prodromos-Saranti Road, swapping along olive cultivations and causing extensive damage to Saranti settlement. The failure of the canal occurred in an area of steep morphology, at the front of an overthrust, within tectonic breccia and calcareous-clayey material of chaotic structure and reduced mechanical properties, vulnerable to erosion. The boundaries of the main fracture were defined by the thrust geometry.

The study of permanent remedial measures included excavation of a cut in the natural slope on the uphill side of the failure, construction of a bypass pipe founded on bedrock and of an anchored pile wall with pre-stressed anchors on the downhill side of the new pipe, excavation and removal of the temporary fill and finally construction of a reinforced fill for rehabilitation of the slide area.

Key words: *debris flow, soil fracture, overthrust, reinforced fill, rehabilitation.*

Περίληψη

Η αιφνίδια αστοχία του υπεδάφους έδρασης της Διώρυγας Ταξιαρχών του Υδαταγωγού του Μόρνου (Ε.ΥΔ.ΑΠ. Α.Ε.), σε απόσταση 540m μετά την έξοδό της από τη σήραγγα Ελικώνα, προκάλεσε τη θραύση και μετακίνηση των φατνωμάτων της, σε μήκος 80 m. Αποτέλεσμα της αστοχίας ήταν η προσωρινή διακοπή της υδροδότησης και η δημιουργία δύο εκτεταμένων μισγαγγειών, σε απόσταση 75 m μεταξύ τους, που διαμορφώθηκαν από την ορμή του διαφυγόντος νερού. Ο όγκος του νερού που διέφυγε μετέφερε τεράστιες μάζες γεωυλικών (λασπορροή) και δύο εκ των φατνωμάτων της διώρυγας. Από την αστοχία καταστράφηκε τμήμα του επαρχιακού δρόμου Πρόδρομου-Σαράντι, αποξηλώθηκαν ελαιοκαλλιέργειες και κατακλύστηκε σημαντικό τμήμα του οικισμού Σαράντι. Η αστοχία της διώρυγας εκδηλώθηκε σε περιοχή απότομου μορφολογικά ανάγλυφου, στην κεφαλή του μετώπου επώθησης και σε θέση όπου επικρατούν τεκτονικά λατυποπαγή, χαοτικής δομής ασβεσταργιλικά υλικά, τεκτονικά καταπονημένα, ευκολοδιάβρωτα και με μειωμένα μηχανικά χαρακτηριστικά. Τα όρια

της κύριας ολίσθησης καθορίζονται από τη γεωμετρία της επώθησης. Η μελέτη μόνιμης αποκατάστασης της υδροδότησης, περιελάμβανε την εκσκαφή ορύγματος στο φυσικό πρανές ανάντη της ολίσθησης, την κατασκευή νέου αγωγού εδραζομένου επί του βραχώδους υποβάθρου και πασσαλότοιχου με προεντεταμένα αγκύρια κατάντη του νέου αγωγού και τέλος εκσκαφή και απομάκρυνση της προσωρινής επίχωσης και κατασκευή οπλισμένου επιχώματος αποκατάστασης.
Λέξεις κλειδιά: *εδαφική θραύση, λασπορροή, επώθηση, οπλισμένο επίχωμα, Αποκατάσταση.*

1. Introduction

Debris flows are fast moving, liquefied landslides of unconsolidated mixtures of water and debris. They are common in sparsely vegetated steeplands throughout the world (Berti et al., 1999; Cannon et al., 2001a; Cannon et al., 2001b; Cannon et al., 2003; Godt and Coe, 2007; McArdell et al., 2007; Coe et al., 2008; Santi et al., 2008). Flows can carry material ranging in size from clay to boulders, and may contain a large amount of woody debris such as logs and tree stumps. Debris flows and landslides may lead to large-scale natural hazards, and may contribute to a large fraction of long-term sediment yields from mountain areas (Dadson et al., 2004). It is widely recognized that hillslope instability can be caused by increased subsurface pore pressures during periods of intense rainfall (Anderson and Sitar, 1995; Iverson et al., 1997), which reduce the shear strength of hillslope materials (Keefer, 1984). Relative to flows that initiate from a discrete landslide source, the mechanisms that contribute to the initiation and propagation of debris flows produced during runoff events are less understood (Cannon et al., 2003; Berti and Simoni, 2005; Coe et al., 2008; McCoy et al., 2010). Although hillslopes provide an important source of material, it has been recognized that a significant portion of the debris-flow volume is generated by erosion of channel fill (Cenderelli and Kite, 1998; Bovis and Jakob, 1999; Jakob et al., 2005; Santi et al., 2008). Mobilization of material stored in the channel can be considered to be the product of shear forces applied on the bed by the flow, impulsive loading, liquefaction of channel fill, bank failure, and headward migration of knickpoints (Bovis and Dagg, 1992; Egashira et al., 2001; Hungr et al., 2005). Channel deposition will occur when friction increases along flow margins and internal pore-fluid pressures diminish (Major, 2000).

The soil failure at the Taxiarches Canal, on the southern outskirts of the mountainous mass of Elikonas, around 3 km West and North of the settlements of Prodromos and Saranti in Thiva region 540m after the exit of Elikonas tunnel, caused fracture and movement of its segments (Figure 1). Due to the canal segments failure, Athens' water supply was temporary interrupted and large amounts of water flowed out, causing sudden erosion and massive displacement of soil material. Two extended gullies formed throughout the steep slope and downhill to the Spartia streams's riverbed, flooding it with debris. Part of the Road connecting Saranti and Prodromos settlements were destroyed. Olive cultivations swept along and a significant part of Saranti settlement, mainly houses near the sea, flooded. In the greater area of the landslide, a significant number of soil movements and canal failures have been recorded in the past, during the earthquake of 1981 but also within the following years (Leonards et al., 1993).

2. Description of the Failure

In the afternoon of 29/03/2011 a significant soil fracture and failure at the Taxiarches canal of Mornos Aqueduct took place, extending to a section of approximately 7 canal segments, with an 11.50 m to 12 m length each (total length 80 m).

The reinforced concrete canal cross-section is U-shaped with a width of 5 m and 4.50 m height. The canal is constructed in cut and its hillside wall was backfilled up to a 4m height, where a surveillance road is allocated. Due to the failure, two of the canal segments (No 6 and 7) slid

downhill and four segments upstream (2, 3, 4 and 5) and another one downstream (8) tilted and were damaged (Figures 1 and 2). During the final phase of the failure, water discharge dropped from 100 m^3/sec to 10 m^3/sec, within a two to three minutes time period, resulting in an estimated outflow volume in the order of 300 to 400 thousand cubic meters. This sudden outflow resulted in erosion of 45.000 m^3 soil material, consisting of fine and coarse grained material of the overthrust zone.

Figure 1 - Aerial view of the slide area.

At the area of the slid segments, the subsoil, the surveillance road and part of the cut slope have also slid downhill forming a gully (eastern) with steep high sides, with a length of 150 m, a maximum width of 45 m and depth ranging between 10 m to18 m. Upstream the main failure area, four canal segments have undergone significant displacements, mainly horizontal towards lower elevations. At the area of the most distant segment a secondary gully (western gully) with steep sides was formed, with a length of 250 m, a maximum width of 18 m and depth ranging from 2 m to3 m (Figures 1 and 2).

Figure 2 - Canal segment failure (left), Main slide shortly after occurrence (right).

Immediate remedial measures were taken, including temporary filling of part of the failed and eroded soil mass and construction of temporary twin bypass pipes, of 2 m diameter each. Backfilling for the pipes foundation was implemented by means of a steep temporary embankment, using material from a nearby quarry, without proper compaction.

3. Morphological Features of the Landslide Area

The landslide area is located at the SW outskirts of an extended morphological range, with an axis of NW-SE direction, and defined by the two main hydrographic features of the greater area, the streams of Taxiarchis at the East and Spartia at the West, which converge at its lower end, downhill the slide, forming the Saranti stream (Figure 1).

The sudden discharge of a great water volume, after the canal failure, created two gullies spaced 75 m apart. The eastern major gully, of a length of 150 m, has a direction of NNW-SSE, maximum width of 45 m and it is 18 m deep (Figures 1 and 3). Its slopes are steep with gradients reaching 80% in the western slope, where friable and vulnerable to erosion calcareous-clayey materials are predominant and 100% in the eastern, where sandstones and conglomerates are developed.

The morphological gradients of the relatively steep riverbed can be divided into three sections, which are separated by two scarps, with heights of 9m and 5m, respectively. The first scarp is located in a distance of 70 m from the canal level and the second in a distance of 103 m. The gradients reach 70% in the first section, 37% in the second and 57% in the lower one (Figures 1, 3 and 4).

The western and smaller size gully has a direction of NE-SW, a length of 110 m, a maximum width of 17 m and it is 8 m deep, due to less volume of discharge. The inclinations of its eroded sides are in the order of 100% at the western and 65% at the eastern side slope, while the mean longitudinal gradient of the gully is 65% (Figures 1, 3 and 4).

4. Geology of the Landslide Area

The greater landslide area is characterized by geological formations of the Parnassos – Giona unit and by sediments of the Subpelagonic zone (Papastamatiou et al., 1971; Papanikolaou, 1986). The boundaries of the unstable mass coincide with the overthrust zone of Cenomanian and Upper Triassic flysch formations of the Subpelagonic unit, overlying the Palaeogene flysch of the Parnassos-Giona unit. The intense tectonic deformation of flysch materials, has favoured the formation of a zone with poor mechanical properties, which coincides with the slid section of the unstable mass.

The flysch formations of the Parnassos-Giona unit comprise the massive bedrock of the landslide area (Figures 3 and 4). The conglomerates of this unit show a high degree of diagenesis and consist of schist, quartz, chert and limestone gravels and cobbles, with a particle size ranging from 0.01 m to 0.10 m, within a quartz, siliceous or carbonic matrix. Sandstone layers consisting of coarse-grained, ash-green coloured, massive sandstone crossed by quartz veins as well as lenticular intercalations of limestones, are interpolated. The green to ash-green coloured schists, with white quartz veins, present an intense microfolding as well as fragmentation and detachment along the schistosity planes.

Due to its intense tectonic deformation the Cenomanian overthrusted flysch system is a mélange without a specific stratigraphic meaning in the wider area. It is comprised of sandstones, purple coloured clayey schists and mudstones and coarse fragments and limestone blocks. It has been eroded and removed from the failure area. Calcareous relics of the Subpelagonic unit are also located uphill and downhill of the failure area. Tectonic materials lie above the overthrust surface and have a total thickness of ca. 15 m. They consist of intensively fragmented sandstones and conglomerates, clays with cobbles and gravels and calcareous-clayey foliaceous soils. Finally, scree and eluvial flysch deposits are the youngest formations of the landslide area.

According to the geological mapping of the failure area (Figures 3 and 4), schists with intercalations of thinly and thickly bedded sandstones are located at the base of the stratigraphic sequence. At their southern boundary show a general dip towards the south (ranging from SE to SW) at angles 50° to 80°. At their northern appearances are dipping towards NNE and NNW at

angles 35° to 40°. The extended limestone body, massive to thickly bedded, with a general dip to NE at angle 20°, follows. The next formation uphill are alternations of thinly to thickly bedded sandstones with a limited schist intercalation, dipping 25° to 35° NE, with thickness of ca.35 m. They are followed by cohesive and massive conglomerates. Tectonic breccia covers the tectonic surfaces. The ash-green coloured schists with limestone intercalations are located at the foot of the western gully, dipping 10° WNW. Thickly and thinly bedded, intensively tectonized sandstones follow, dipping 70° to 75° SW (Figures 3 and 4).

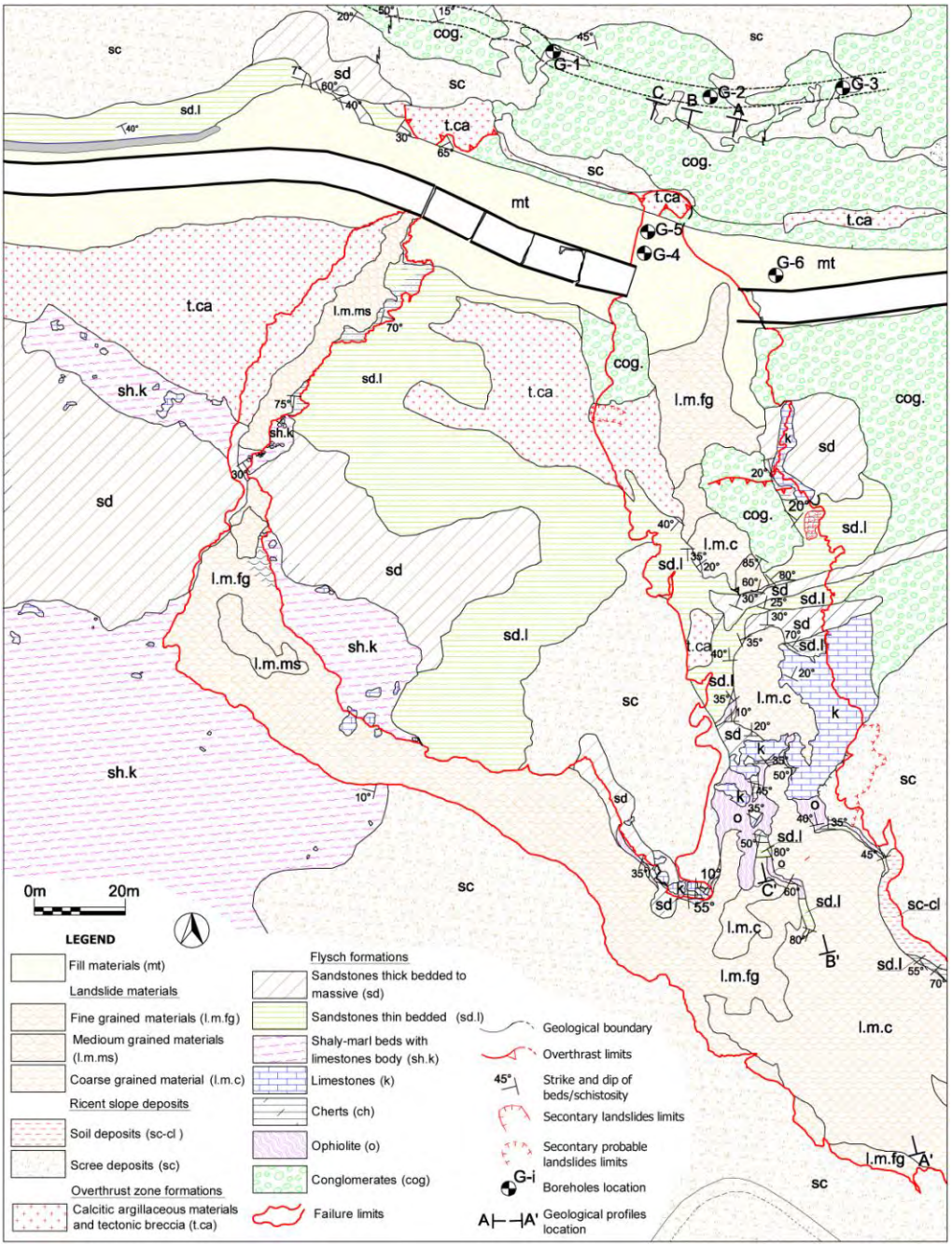

Figure 3 - Geological map of the landslide area.

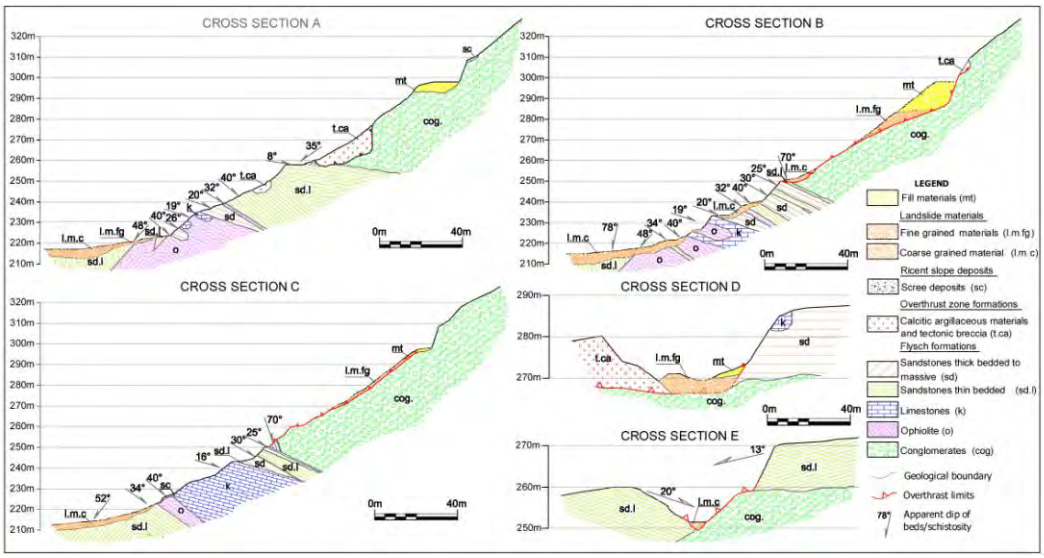

Figure 4 - Geological cross-sections of the landslide area.

5. Tectonic Structure of the Landslide Area

The north edge of the overthrust face is located along the excavated slope of the surveillance road for a length of 67m (Figures 3, 4 and 8). The overthrust surface in its western part dips 50° to 70° SW and the striations dip 55° to 70° WSW. In its eastern part, namely in the area of the main failure, the overthrust surface dips towards the SW at angles of 75° changing gradually into 35°. The soil tectonic material, which covers it, has a thickness of ca. 12 m, as determined by geotechnical borehole drillings and geophysical survey. In a distance of 50 m south of the overthrust northern edge, the surface dips 35° SSE. The striations in the overthrust plane, on the conglomerate bedrock, are dipping 50° SW. Southernmost, in a distance of 83 m from its northern edge, the last trace of the overthrust surface is located on the sandstone bedrock. The overthrust plane dips 55° SW and the striations dip 55° WSW.

The kinematic analysis of the overthrust, based on the orientation data (dip direction/dip) of the overthrust plane and the orientation of striations, revealed that this large-scale compressive event took place under a compressive stress regime of WNW-ESE direction (Figure 5).

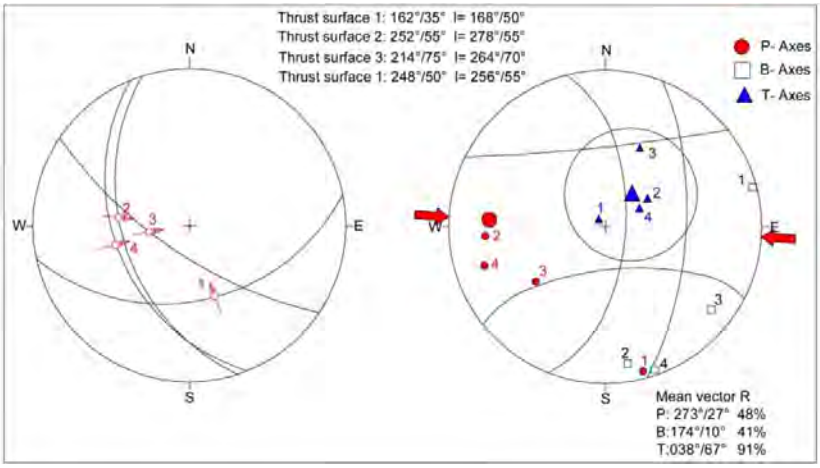

Figure 5 - Kinematic analysis of overthrust.

The tectonic depression formed in the overthrust zone was filled with calcareous-clayey, friable, light-yellow material of a thickness of 10m to 12m, as seen on the eastern slope of the eastern gully. Small-scale thrusts, with surfaces dipping mainly to the SE and ESE and secondarily to the NE at angles ranging from 30° to 35°, were mapped along the excavated slopes uphill the failure area, crossing the sandstone and conglomerate bedrock. Their length reaches 50 m, their aperture does not exceed 0.30 m and have been filled with friable calcareous-clayey material. An extended tectonic zone filled with light-yellow calcareous-clayey material, is usually formed at thrusts' ends or at their intersection (Figures 3, 4 and 8).

The rock mass is crossed by three major and one minor discontinuity sets dipping towards the SSE, NE, SW, and SE at angles ranging from 60° to 70°. According to ISRM (1981), their spacing is characterized as close to very wide (0.10 m up to 2.0 m), their persistence low (greater than 1m up to 1.50m), their surfaces are smooth to slightly rough, planar (VII–VIII), fresh with evidence of oxidation at positions, very tight to open (aperture up to 1mm), without filling material (Figure 8).

6. Investigation of the Slide Mechanism

The study of the causes of failure was based on geological mapping, evaluation of the engineering geological conditions, soil fracture characteristics, scarp geometry, the damages of the independent canal segments and their displacement, tilting and interaction, as well as the findings of the performed investigation, including geotechnical borehole drilling, inclinometers installation and geophysical survey. The evaluation outcomes regarding the causes of failure and the timeline of the failure events are presented below:

- The soil fracture and the following canal failure is not considered limited in the area of the two slid canal segments (No 6 and 7), but extended throughout the area of all the tilted canal segments (No 2 to 8). Furthermore it is delimited by the overthrust geometry. The western limit of the failure is located in the contact area of segments No 1 and 2, where a soil subsidence on the uphill side of the left canal wall is evident (Figure 6), causing tilting of segment No 2, thus enabling the canal water outflow at the right (downhill) canal wall, resulting in soil erosion and formation of the western (smaller) gully. The northern limit of the failure is related to the geometry of the overthrust.

Figure 6 - Soil subsidence on the uphill side of the left canal wall between segments 1 and 2 and along the surveillance road.

- Based on a detailed recording of the canal segments displacements (Figure 7) and their associated structural damages, it is concluded that the main displacement was perpendicular to the canal (N to S), but also along the canal with direction from segment No 2 towards segment No 5 and 6, along with rotation. The above displacement is considered to occur instantly, resulting in increase of the curvature of the canal with downhill (N to S) direction. The above

kinematics is also confirmed by the fact that all joints between hillside (northern) wall canal segments demonstrate compression failures, while all downhill (southern) wall canal segments are detached (extension).

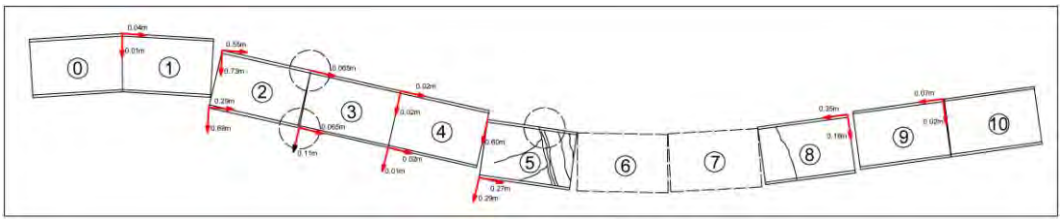

Figure 7 - Displacement of canal segments.

- With respect to the factors inducing the aforementioned displacements, groundwater hydrostatic pressure below the surveillance road, acting on the hillside (northern) canal wall, is considered critical. Based on morphology and geology of the area and the time of failure (spring time associated with high water level), it is reasonable to assume that the backfilled soil behind the hillside (northern) wall was saturated and therefore the hydrostatic pressure built up on the hillside wall and the buoyancy of the canal bottom plate, are considered as major destabilizing factors.
- The displacement of canal segments No 2 to 5 induced a void at the hillside canal wall. It is considered that this void was filled with the saturated subsoil of the surveillance road. This is demonstrated by the approximately 0.5 m vertical displacement (sinking) of the subsoil of the surveillance road in contact with the canal wall (Figure 6) and furthermore by the longitudinal cracks (parallel to the canal) on the surveillance road.
- The displacement of canal segments resulted in canal water outflow from the detached joints, which in turn caused soil erosion. The relatively large size of detachment at the joint area between canal segments No 1 and 2 resulted in severe soil erosion thus forming the western gully (Figures 1, 2). It is considered that a similar or even larger size detachment occurred at the joint area between canal segments No 6 and 7. Due to the opening of the joint between canal segments No 6 and 7, large amounts of water flowed out, causing sudden erosion and massive displacement of soil material, which finally led to the formation of the eastern gully (main slide).
- The hypothesis of a large size detachment between canal segments No 6 and 7 is considered reasonable, taking into account that the canal curvature is maximized there and furthermore due to the displacement of adjacent canal segments. Furthermore at the area of segments No 6 and 7 the thickness of erodible material (mainly tectonic breccias) is increased, thus explaining the larger size of the main slide area (eastern gully).
- With respect to the timeline of events it is considered that the canal segments displacements were practically instantaneous. The detachment of the joint between canal segments No 1 and 2, resulting in the western gully, most probably preceded the main slide, or, with less probability, both events occurred simultaneously.

7. Water-supply Remedial Works

The remedial works aimed at the restoration of the full discharge capacity of the canal, by structures founded on stable ground, delimiting any potential future hazards to the existing risk probability level of the whole canal. The decided remedial scheme included the excavation of a cut on the uphill side of the failure, where there was evidence of massive rock existence, the construction of a circular, 3.2 m diameter, bypass pipe, founded on stable rocky ground at the cut base, fully substituting the temporary, twin pipes of 2 m diameter each. Moreover, the time

margins for construction were very strict, since there was evidence that the temporary fill, where the twin bypass pipes of 2 m diameter were founded, being an immediate remedial measure, was in limit equilibrium and potentially unstable. This was suggested by its fast construction, with steep, higher that 2:3 (h:b), slope inclination, without proper compaction of the fill material of unknown grading, the creep deformations observed at the fill crown, and the readings of the inclinometer installed through the fill, which gave clear evidence of deformation.

The decided remedial works solution was based on the hypothesis of the existence of massive rock at the new cut base, suggested by the evaluation of the geological conditions and the assessment of the overthrust geometry, combined with the findings of the geotechnical investigation. These factors gave confidence on the proposed solution, which exhibits significant advantages in terms of simplicity and construction cost and time, compared to alternatives, like bypassing the failure area by a tunnel.

Based on the geological mapping of the slope faces, the quantitative description of discontinuities of the rock mass, their stereographic projection in individual rock mass parts and sliding potential failure modes, the geological structure and the engineering geological conditions along the new cut slopes, designed parallel and 5 to 6 m uphill of the existing cut, were estimated (Figures 8 and 9).

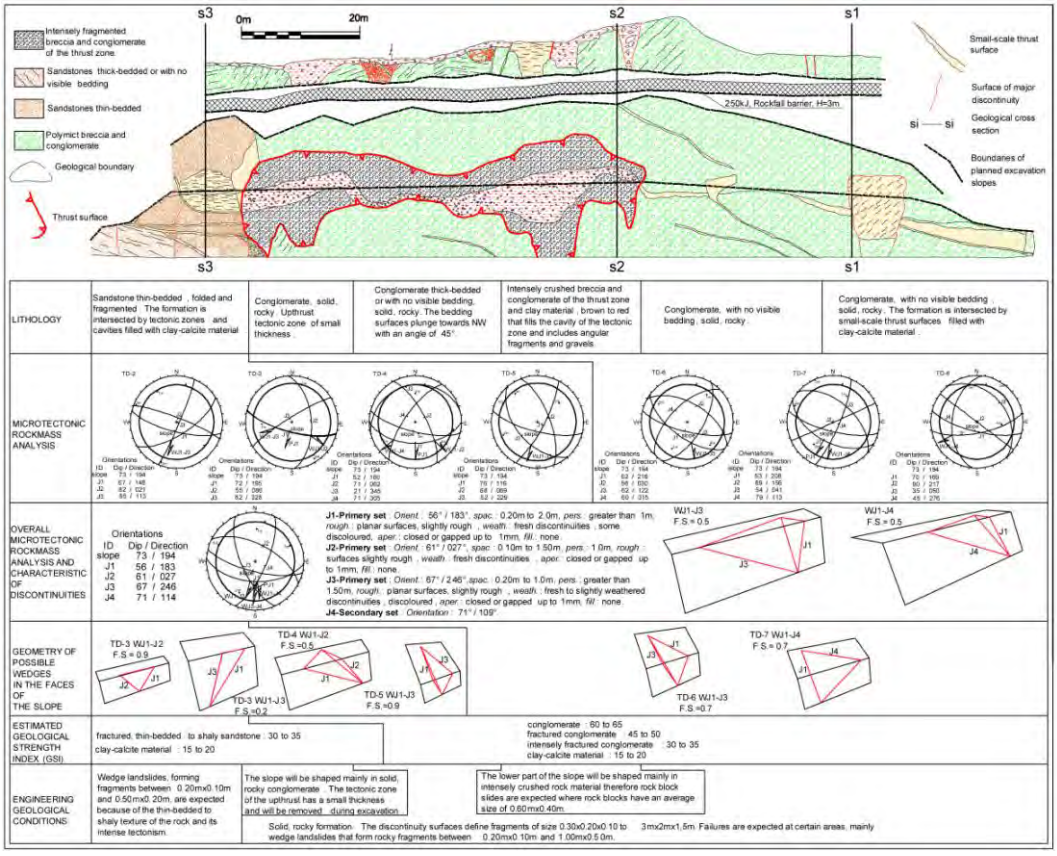

Figure 8 – Engineering geological mapping of existing slope face.

The new slope at its western end was expected to be excavated in sandstones, mainly thinly bedded and fragmented, crossed by three major discontinuity sets. Wedge failures of rock blocks of estimated sizes ranging from 0.20 m x 0.10 m to 0.50 m x 0.20 m were expected, due to the thinly bedded to foliaceous structure and intense fragmentation of the rock mass. Subsequently, the slope was anticipated to be excavated in massive to thickly bedded conglomerates, crossed by

three major and one minor discontinuity sets. Wedge failures of rock blocks of estimated size ranging from 0.20 m x 0.10 m to 1.0 m x 0.50 m, were expected. Rock quality was considered downgraded, mainly in the overthrust area and also in places where the rock mass was crossed by small-scale thrusts and major joints. The development of small-scale cavities filled with clayey and calcareous-clayey material was considered possible (Figures 8 and 9).

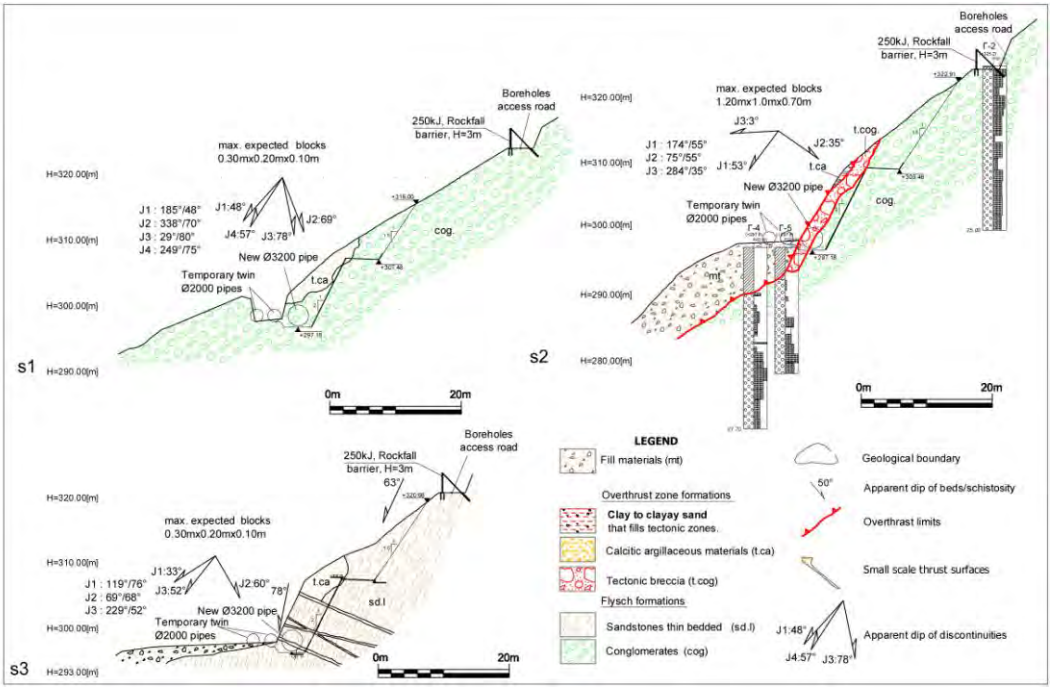

Figure 9 – Engineering geological cross-sections along the new slope.

The average cut height was 25 m. The cut was excavated mostly within fresh and massive rock, as expected. A 5 m wide berm was constructed at intermediate height of the cut, for stability and protection reasons. The cut inclination was selected 2:1 (h:b) below the berm and 3:2 (h:b) above it. Stability measures included installation of 6 m long rockbolts of 200 kN capacity in 3 m x 3 m pattern, and application of wire mesh on the upper part of the slope and wire mesh combined with 10 cm shotcrete on the lower part of the slope. To ensure protection against rockfalls commencing on the natural slope above the cut, the construction of a 3m high rockfall barrier, of 250 kJ capacity at the cut crown, in front of a rock trap, was constructed. Finally to avoid water pressures behind the shotcrete, installation of a row of drainage holes of 3" diameter was also implemented (Figure 10).

8. Rehabilitation of the Slide Area

The safe restoration of the canal water supply, being urgent and critical, has been achieved, though the completion of the remediation should include also rehabilitation of the slide area. The proposed solution for the rehabilitation comprises the removal of the southern temporary pipe of 2 m diameter, in order to provide space at the crest of the temporary fill, for the construction of a pile wall, of 80 cm diameter concrete piles. The pile wall will secure the stability of the remaining northern temporary pipe of 2 m diameter and will be used as temporary support for the suggested excavation in order to remove the loose temporary fill. Excavation of the loose fill will be executed in stages and the pile wall will be supported by two rows of pre-stressed anchors (Figure 11).

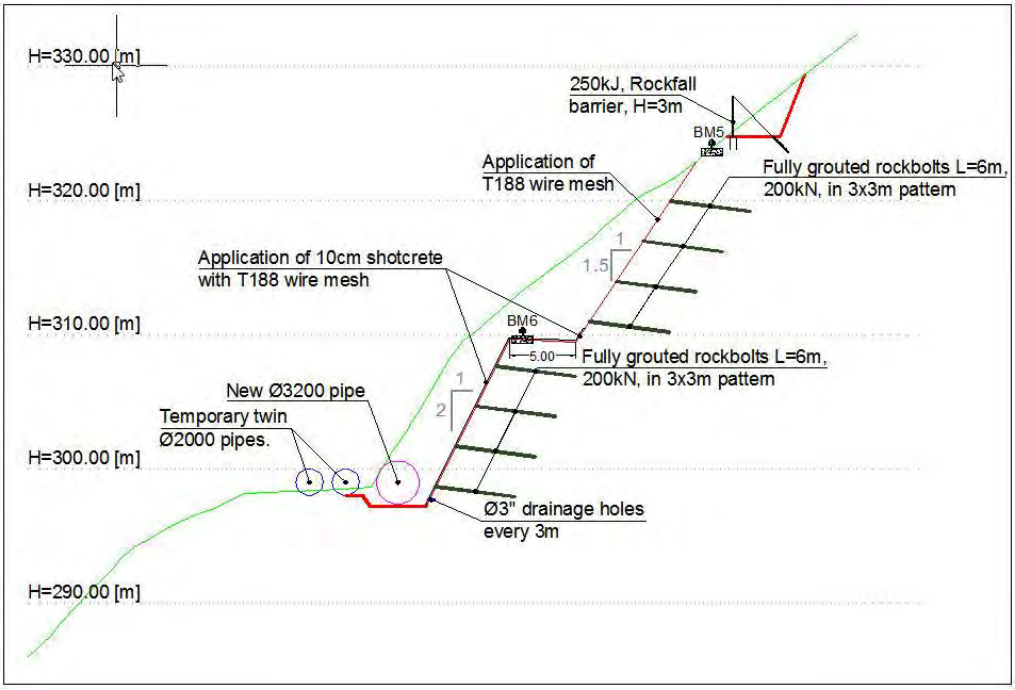

Figure 10 – Excavation geometry - support and protection measures.

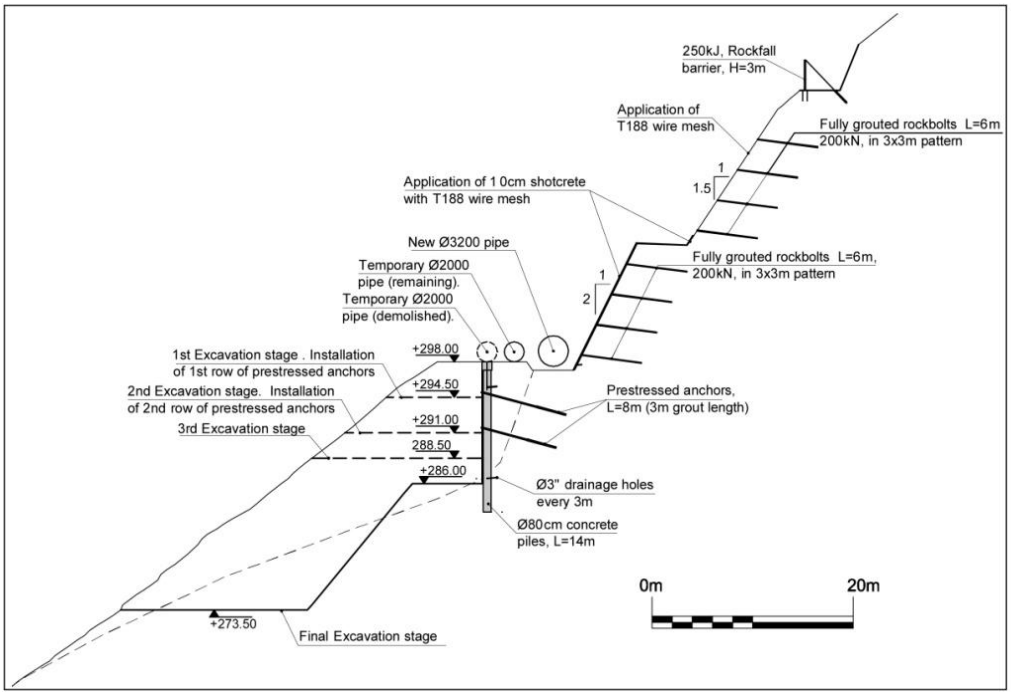

Figure 11 - Support measures and excavation stages for removal of temporary fill.

Following the above construction methodology, full removal of the uncompacted temporary fill or any other loose superficial material is feasible. Rehabilitation will be achieved by the construction of a reinforced embankment under fully controlled conditions, founded on sound rock (Figure 12).

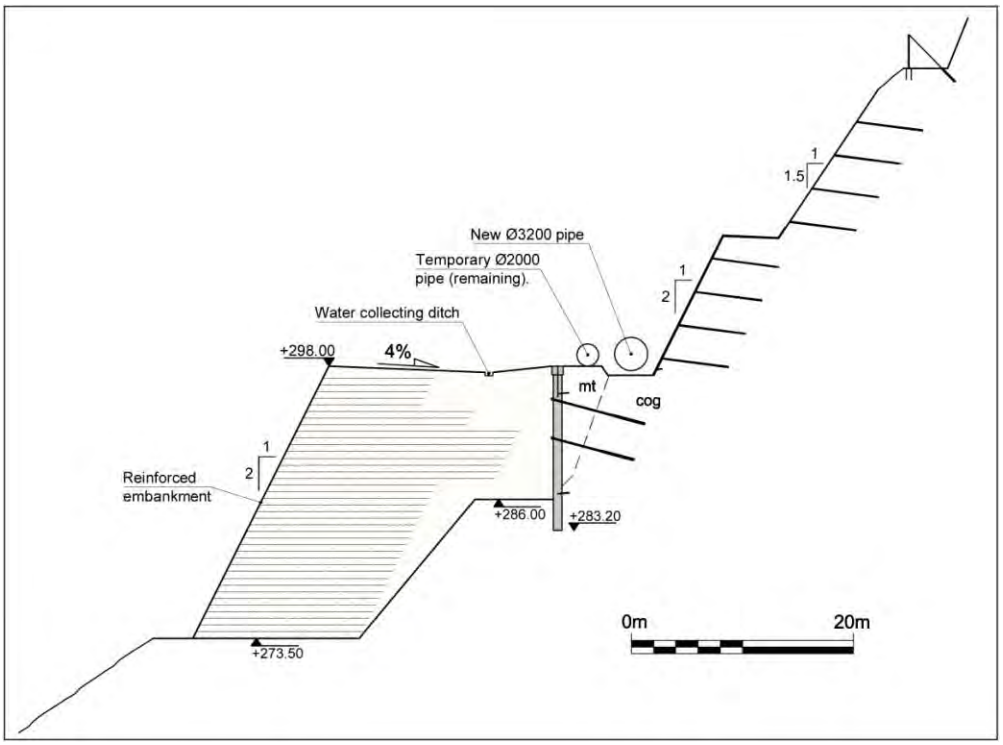

Figure 12 - Rehabilitation by reinforced embankment construction.

9. Design Implementation

The proposed cut was excavated from February to August 2012. The encountered geological conditions fully complied with the expected ones and the application of the proposed stability and protection measures ensured long term stability. Furthermore, construction of the new by-pass pipe of 3.2m diameter, founded on sound rock, was completed by September 2012 and its operation commenced in November 2012. Pile wall construction is expected to commence in spring 2013 and will be followed by the slide rehabilitation by means of the proposed reinforced embankment.

10. Acknowledgements

The Authors wish to acknowledge the contribution, regarding collection of necessary data required for the failure study, by Mr. S. Geogriadis, Executive Director Networks & Operations of EYDAP S.A., Mr. A. Avgerinos, former Assistant Executive Director Networks & Operations EYDAP S.A., and the staff of EYDAP S.A. Finally, thanks are due to Mrs. E. Kolaiti, Mining Engineer, for her contribution to improve this paper.

11. References

Anderson S.A. and Sitar N. 1995. Analysis of rainfall-induced debris flows, *J. Geotech. Eng.,* 121, 544-552.

Berti M., Genevoi R., Simoni A. and Tecca P.R. 1999. Field observations of a debris flow event in the Dolomites, *Geomorphology*, 29, 265-214.

Berti M. and Simoni A. 2005. Experimental evidences and numerical modeling of debris flow initiated by channel runoff, *Landslides,* 2, 111-182.

Bovis M.J. and Dagg B.R. 1992. Debris flow triggering by impulsive loading: mechanical modeling and case studies, *Canadian Geotechnical Journal*, 29, 345-352.

Bovis M.J. and Jakob M. 1999. The role of debris supply conditions in predicting debris flow activity *Earth Surface Processes and Landforms*, 24, 1039-1054.

Cannon S.H., Bigio E.R. and Mine E. 2001a. A process for fire-related debris flow initiation, Cerro Grande fire, New Mexico, *Hydrological Processes*, 15, 3011-3023.

Cannon S.H., Kirkham R.M. and Parise M. 2001b. Wildfire-related debris flow initiation processes, Storm King Mountain, Colorado, *Geomorphology*, 39, 111-188.

Cannon S.H., Gartner J.E., Parrett C. and Parise M. 2003. Wildfire related debris-flow generation through episodic progressive sediment-bulking processes, western USA. In: Rickemann, D., Chen, C.L. (eds), Debris-Flow Hazards Mitigation - Mechanics, Prediction and Assessment, *Proc. of the 3rd International Conference on Debris-Flow Hazards Mitigation*, 10-12 September 2003, I, 71-82.

Cenderelli, D.A. and Kite, J.S. 1998. Geomorphic effects of large debris flows on channel morphology at North Fork Mountain, eastern West Virginia, USA, *Earth Surface Processes and Landforms*, 23, 1-19.

Coe J.A., Kinner D.A. and Godt J.W. 2008. Initiation conditions for debris flows generated by runoff at Chalk Cliffs, central Colorado, *Geomorphology*, 96, 210-297.

Dadson S.J., Hovius N., Chen H., Dade B.W., Lin J.C., Hsu M.L., Lin C.W., Horng M.J., Chen, T.C., Milliman J. and Stark C.P. 2004. Earthquake-triggered increase in sediment delivery from an active mountain belt, *Geology*, 32, 733-736.

Egashira S., Honda N. and Itoh T. 2001. Experimental study on the entrainment of bed material into debris flow, *Physics and Chemistry of the Earth (C),* 26, 9, 645-650.

Godt J.W. and Coe J.A. 2007. Alpine debris flows triggered by a 28 July 1999 thunderstorm in the central Front Range, Colorado, *Geomorphology*, 84, 1-2, 80-97.

Hungr O., McDougall S. and Bovis M. 2005. Entrainment of material by debris flows. ln Jakob, M., Hungr, O. (eds) *Debris-flow hazards and related phenomena*, Springer Berlin, Heidelberg, 135-158.

ISRM Suggested Methods 1981. In Brown, E.T. (ed), *Rock Characterization Testing & Monitoring*, Pergamon Press, 211pp.

Iverson R.M., Reid M.E. and LaHusen R.G. 1997. Debris flow mobilization from landslides, *Annu. Rev. Earth Planet. Sci.,* 25, 85-138.

Jakob M., Bovis M. and Oden M., 2005. The significance of channel recharge rates for estimating debris-flow magnitude and frequency, *Earth Surface Processes and Landforms*, 30, 155-166.

Keefer D.K. 1984. Landslides caused by earthquakes, *Geological Society of America Bulletin*, 95, 4, 406-421.

Leonards A.G. Sotiropoulos, E.S. Mourtzas N.D., Marinos P.G. and Kountouris P.J. 1993. Two case studies of slope instability in soft rock, in Anagnostopoulos et al. (eds), *Geotechnical Engineering of Hard Soils-Soft Rocks*, Balkema, Rottetdam, 1125-1136.

Major J. 2000. Gravity driven consolidation of granular slurries: implications for debris-flow deposition and deposit characteristics, *Journal of Sedimentary Research*, 70, 1, 64-83.

McCardell B.W., Bartelt P. and Kowalski J. 2007. Field observations of basal forces and fluid pore pressure in a debris flow, *Geophysical Research Letters*, 34*,* L07406, doi: 10.1029/2006GL029183.

McCoy S.W., Kean J.W., Coe J.A., Staley D.M., Wasklewicz T.A. and Tucker G.E. 2010. Evolution of a natural debris flow: In situ measurements of flow dynamics, video imagery and terrestrial laser scanning, *Geology*, 38, 8, 735-738.

Papanikolaou D. 1986. Geology of Greece, Eptalofos Publications, Athens, 240pp.

Papastamatiou I., Tataris A.A., Maragoudakis N. and Monopolis D. 1971. Geological map of Greece: Levadia sheet (scale 1:50.000), IGME Publications, Athens.

Santi P.M., deWolfe V.G., Higgins J.D., Cannon S.H. and Gartner J.E. 2008. Sources of debris flow material in burned areas, *Geomorphology*, 96, 310-321.

Δελτίο της Ελληνικής Γεωλογικής Εταιρίας, τομ. XLVII , 2013
Πρακτικά 13ου Διεθνούς Συνεδρίου, Χανιά, Σεπτ. 2013

Bulletin of the Geological Society of Greece, vol. XLVII 2013
Proceedings of the 13th International Congress, Chania, Sept. 2013

PALAEOTECTONIC ENVIRONMENT AND LANDSLIDE PHENOMENA IN THE AREA OF MALAKASA, GREECE

Mourtzas N.D.[1] and Sotiropoulos E.[2]

[1]GAIAERGON Ltd, Kefallinias Str. 16-18, 152 31 Chalandri, Athens, gaiaergon@gmail.com, nikosmourtzas@gmail.com

[2] GEOMECHANIKI S.A., Ethnikis Antistaseos Str. 91, 153 44 Pallini, Athens, geomsot@gmail.com

Abstract

The extended landslide of Malakasa area, located 35km to the North of Athens, occurred in a neopalaeozoic schist-sandstone klippe, a complex Palaeotectonic environment in the northern roots of Parnitha Mt. Due to this failure, railway line and highway connection between Athens and central and North Greece were cut off. In this paper, it is attempted to approach the landslide mechanism based on: (i) the kinematic data on the failure surface, (ii) the morphological features of the surface, (iii) the movement vectors, and (iv) the lithostratigraphy and hydro-geological features of the sliding mass. According to the above criteria, three soil blocks can be identified in the landslide mass, which are differentiated by their lithological structure, kinematic features, type of deformation and hydro-geological behavior. The causal factor of the extended landslide was the gradual loss of support of these three blocks and their slide on a pre-sheared surface of low strength that has been caused by the extended excavation in the slope toe. The palaeotectonic structure and the development and geometry of the geological formations in the landslide area were not taken into account during the construction of the drainage works, for slope stabilization and the increasing of safety factor, something which led to the over-designing of the remedial measures.

***Key words**: lithostratigraphy, upthrust, kinematic, groundwater, slope stabilization.*

Περίληψη

Η εκτεταμένη κατολίσθηση στην περιοχή της Μαλακάσας, 35km βόρεια της Αθήνας, εκδηλώθηκε σε σχιστοψαμμιτικό ράκος των νεοπαλαιοζωικών σχηματισμών, σε ένα πολύπλοκο παλαιοτεκτονικό περιβάλλον, στις βόρειες υπώρειες του όρους Πάρνηθας, διακόπτοντας τη σιδηροδρομική και οδική σύνδεση της πρωτεύουσας με την κεντρική και βόρεια Ελλάδα. Στην εργασία αυτή, ο μηχανισμός της κατολίσθησης προσεγγίζεται αφενός με βάση τα κινηματικά στοιχεία στην επιφάνεια ολίσθησης, τα μορφολογικά επιφανειακά στοιχεία και τα ανυσματικά στοιχεία της κίνησης και αφετέρου με βάση τη λιθοστρωματογραφία της μάζας που αστόχησε και τα υδρογεωλογικά της χαρακτηριστικά. Με βάση τα ανωτέρω κριτήρια διαχωρίζονται σαφώς στη μάζα της κατολίσθησης τρία διαφορετικά εδαφικά τεμάχη που διαφοροποιούνται ως προς την λιθολογική τους δομή, τα κινηματικά τους χαρακτηριστικά, την παραμόρφωσή τους και την υδρογεωλογική τους συμπεριφορά. Γενεσιουργό αίτιο της εκτεταμένης αστοχίας αποτελεί η διαδοχική απώλεια στήριξης των τριών ανεξάρτητων τεμαχών

που την συνθέτουν και η ολίσθησή τους επί μίας προδιατετμημένης επιφάνειας μειωμένων αντοχών, λόγω των εκτεταμένων εκσκαφών στον πόδα της. Τα μόνιμα έργα αποστράγγισης που στόχευαν στην αύξηση του συντελεστή ασφαλείας της κατολισθαίνουσας μάζας και στη σταθεροποίηση της κλιτύος, δεν έλαβαν υπόψη τους την παλαιοτεκτονική δομή, την ανάπτυξη και τη γεωμετρία των γεωλογικών σχηματισμών του στενού και ευρύτερου χώρου της αστοχίας και οδήγησαν σε υπερδιαστασιολόγηση των έργων αποκατάστασης.
Λέξεις κλειδιά: *λιθοστρωματογραφία, επώθηση, κινηματική, υπόγεια νερά, σταθεροποίηση κλιτύος.*

1. Introduction

The early hours of February the 18th, 1995, an extended landslide occurred in the north roots of Parnitha Mt., at CH. 35+000 of the Athens-Thessaloniki Highway which caused damages to the railway line and the road connection between Athens and northern Greece (Figure 1a). The displaced soil mass swept the Athens-Thessaloniki railway line away, for about 7m downwards, deforming and destroying the gravel ballast in a length of 240m. This movement ended at the deck of the National Highway which leads to Athens, causing serious damages in a length of 80m.

The complex palaeotectonic evolution of the wider area with repeated fold systems, the synclinal and anticlinal structures, and the overthrusts and small-scaled up-thrusts have intensely deformed and altered the schist-sandstone neopalaeozoic formations causing large-scale landslides to the mountainous areas of Parnitha, Kithaironas and Pateras Mountains (Dounas, 1971; Mourtzas et al., 1993).

Cavounidis et al. (1997) describe the general features of the landslide and the proposed remedial measures. Marinos et al. (1997) refer, in general, to the geological features of the landslide and to its hydro-geological regime, while Sotiropoulos et al. (1998) present the results of a 3D groundwater flow study in the vicinity of the rapture surface and examine several draining options at the toe of the slide. Pantelidis and Cavounidis (1997) perform a series of 2D and "pseudo-three dimensional" forward and back slope stability analyses, before and during the occurrence of the failure, as well as after the construction of the proposed remedial measures. Georgopoulos and Vardoulakis (2001) models the sliding mass with a four-rigid body failure mechanism, highlighting the need of draining the soil mass, as the estimated factors of safety, with the consideration of high water table, reveal a slope with limited equilibrium. At the same time the possibility of an extended landslide is examined.

Although it is a geological phenomenon par excellence, in the aforementioned studies it is treated strictly as a geotechnical problem, ignoring important geological features concerning the geology and tectonic environment of the landslide wider area as well as the morphologic and kinematic components which are directly connected with the occurrence and rational remedy of the failure mass.

2. History of the Landslide

2.1. Precursory Phenomena

Enough time before the main landslide occurred, there were clear evidences that the soil mass movements at the level of the Railway line and the Highway had already begun. In May 1993, a small scaled failure occurred at the western end of the Athens-Thessaloniki Highway slope, immediately after its excavation and construction with an inclination of 1:1. In order to confront the failure, slope was reconstructed with an inclination of 1:1.2 and a retaining wall was built at the foot.

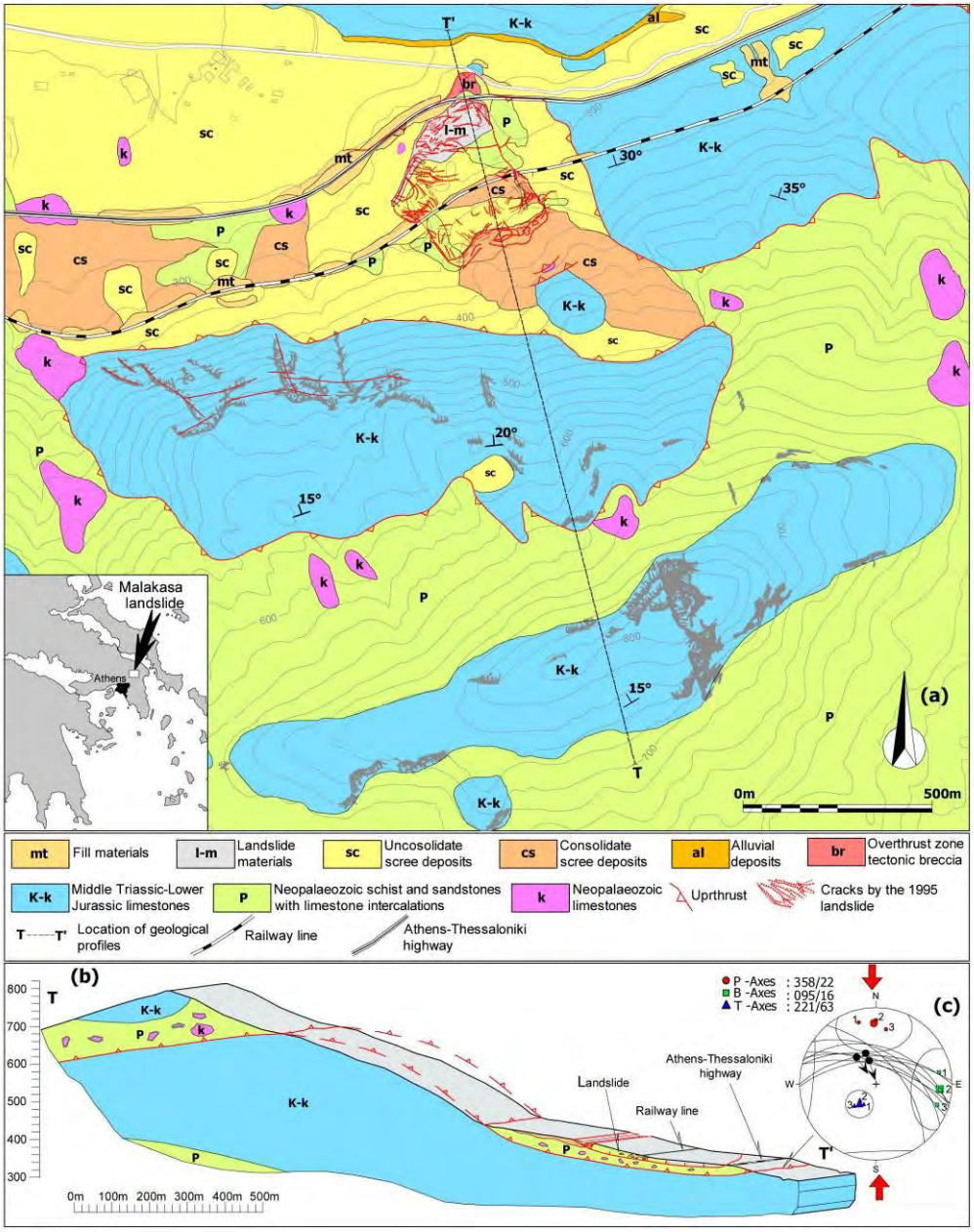

Figure 1 - (a) Location map of Malakasa landslide (b) Detailed geological map of the NE slope of Mt Parnitha in the wider area of Malakasa landslide (c) Geological cross-section along the longitudinal axes of the north-east slope of Mt Parnitha (d) Up-thrust surface data and palaeostress mechanism analysis.

The aforementioned circular failure, being almost 40m wide, which appeared in the western slope of the Highway and the following landslide, which occurred in January 1994, it turned into extended instabilities, with secondary fragmentations downwards of the loose soil mass and spreading of the cracks to the East and upwards, in a 90m long and 20m wide zone, up to the crown of the artificial slope (Figure 2). The landslide caused the detachment of the retaining wall at the joint and its rotation, with maximum vertical and horizontal displacement of 0.1m. It also

caused the failure of two wells. The failure was thought to be small-scaled and it was treated as a local phenomenon. It was assumed that its occurrence was due to the heterogeneity of the lithology, the degradation of the physical and mechanical properties of the materials, and their long-term watering from the spring which was located upwards. Remedial works for the gathering and removal of the spring water took place and the slope angle was reduced to 1:1.5 up to 1:2, with a 4m wide bench in the middle. Also, an embankment, as a foundation for the adjacent road, was constructed and series of piles of 1m in diameter and 12m-14m in length were installed in the slope toe in order to improve the soil (technical report - OMETE S.A., 1994).

From January 1995 up to February 1995, continuous anomalies on the general plan of the railway line, failure of monitoring points which were located in the masonry retaining wall for the protection of the railway, and development and gradual expansion of cracks on the wall were reported. A small local failure occurred after an initial remedial measure which included the excavation of the upwards slope. During the reclamation actions, moisture appeared in a 15m wide zone in the slope and water was gushing from it.

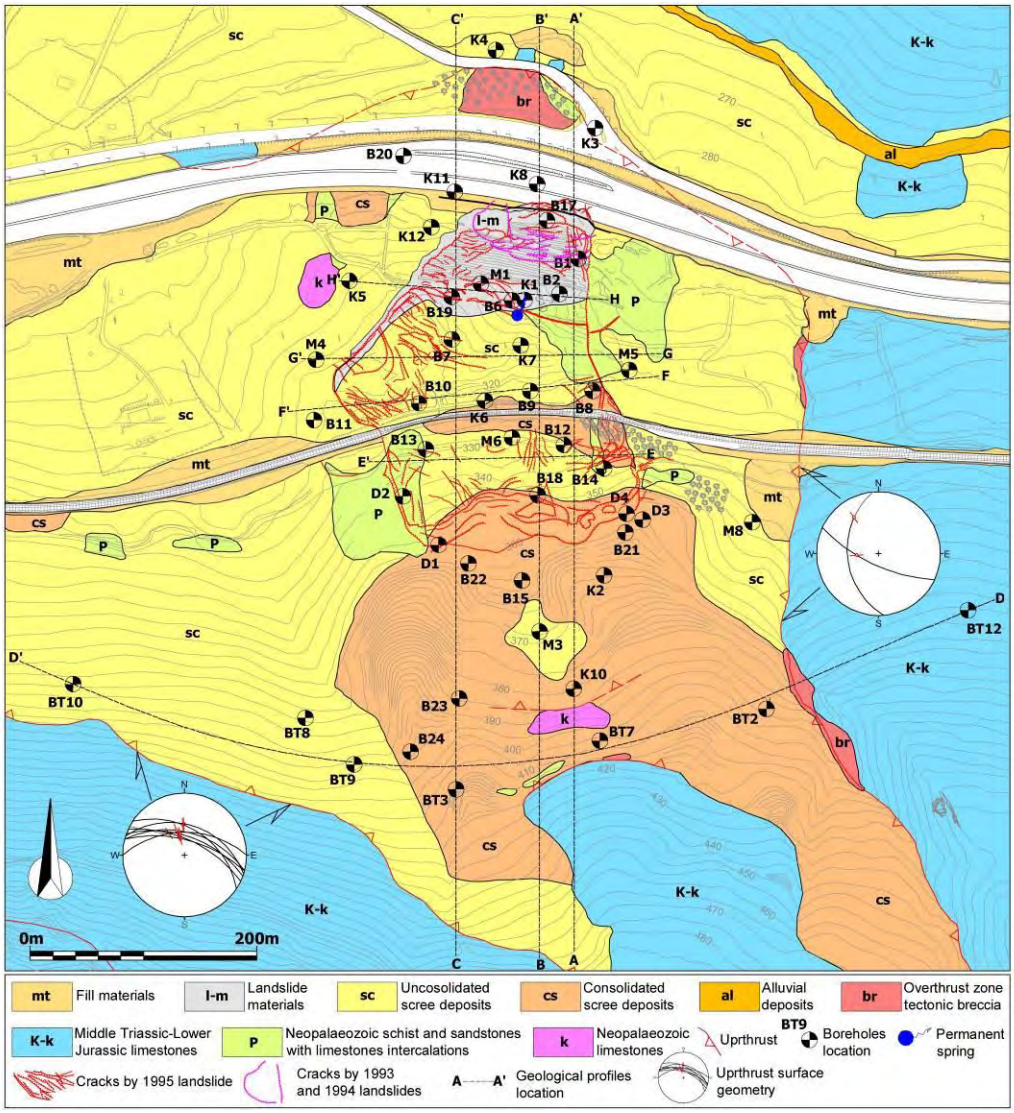

Figure 2 - Detailed geological map of Malakasa landslide.

2.2. Main Landslide Event

In the afternoon of February 16th, 1995, the emergency lane of the highway was lifted by 0.1m, in a 5m wide zone, and within the next few hours the lift was 0.2m and it was spread in all its width. The landslide was activated during the night of February the 18th, 1995. The upwards slope of the highway was cut off by the failure in an altitude of 360m and the 310m long and 240m wide soil mass slid downwards, lifting the main highway lane by 3m up to the position of the New Jersey barrier which was displaced by 3m in plan and finally overturned.

3. Tectonic Structure and Evolution of the Landslide Area

The thrust of the neopalaeozoic formations to the Triassic limestones constitutes the main palaeotectonic structure of the landslide area. This large-scale tectonic movement took place during the first orogenetic phase and affected the wider area. It caused strong foliation of the geological formations, with the strike of the main fold axis being NNW-SSE, and the generation of tangential forces that pushed the schist-sandstones towards a SE direction over the carbonate formations of the Sub-Pelagonian geotectonic unit. The following erosion removed significant parts of the tectonically overlying schist-sandstone formations and revealed the younger underlying carbonate bedrock in the form of a “tectonic window”. Also, the erosion caused the fragmentation of the nappes into klippes which lay on the Triassic substratum. The Malakasa landslide occurred in one of these klippes (Figures 1 and 2).

The result of the intense tectonic deformation of the neopalaeozoic sediments is their weathering, alteration, and total loss of their initial structure in some positions, as well as the fragmentation of the inflexible gray sandstone and contained limestone bodies. The slickenside of the thrust has an inclination of 50° – 65° to the NE, while the tectonic glide lines on its surface reveal a compressive movement with orientation of the slide to the SE (Figures 1d and 2). At least another two of the small-scaled thrusts, in the schist-sandstone mass, have similar geometrical features on their slickenside with those of the main thrust. These determine two clearly identified pre-sheared surfaces in the material (Figure 3). The mylonites and fault breccias of the main and secondary thrusts are the result of the mechanical stress on the rocks. The most recent tectonic structure of the area, which has orientation WNW – ESE and forms the steep landscape of the north borders of Mt Parnitha, is the rupture zone “Malakasa – Avlona” and it passes through the south side of the landslide upwards area.

4. Lithostratigraphy of the Landslide Area

The lithostratigraphy of the landslide area was determined based on the results from the geological investigation and geological mapping, made on a scale of 1:5000 and 1:1000, as well as on the data coming from the drillings and testing of the cores (Figures 2 and 3).

The Triassic limestones and the up-thrusted neopalaeozoic formations constitute the Alpine substratum of the wider landslide area, while the oldest and youngest phases of the colluvial deposits, covering the bedrock, constitute the most recent formations. The remainders of the neopalaeozoic nappe, which cover the Triassic limestones in the landslide area, consist of alternation of highly eroded schist-sandstones, shales, and mica schists, which have lost their initial structure and are present in the form of gravels, medium plastic clays, clayey sands, and clayey gravels. They are soft to very soft materials with olive-green, green and gray-green colours. They have been transformed into graphitic schists with intense abrasion and dark or dark-grey colours in deeper layers, and they are presented as clayey sands and sandy clays with medium plasticity, very soft and of medium cohesiveness, as well as silty sands and clayey sands and gravels with sandstone fragments. The former are arkoses of grey to dark colours which are crossed by light-coloured calcite veins (Figures 2 and 3).

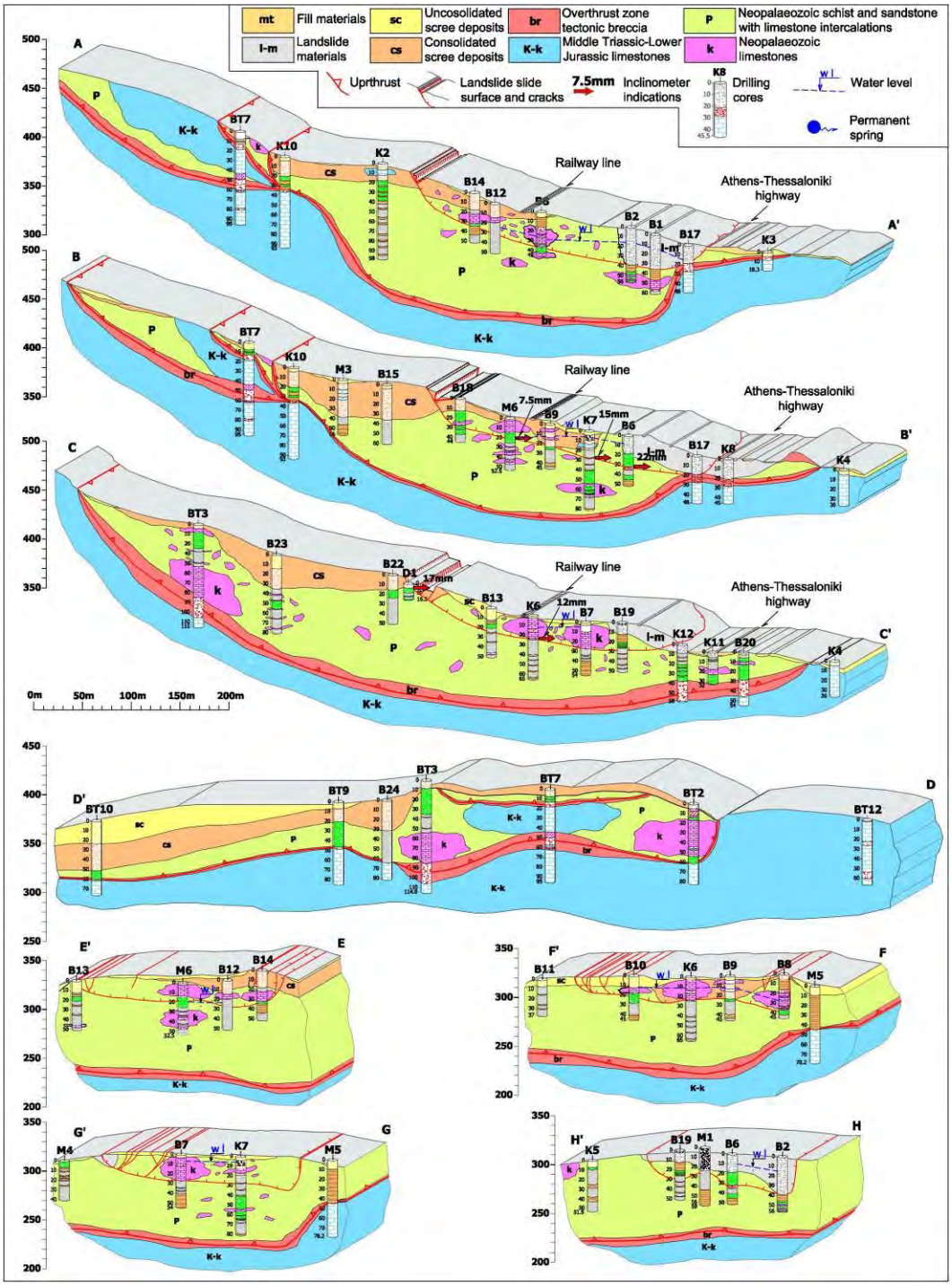

Figure 3 - Geological cross-section of Malakasa landslide.

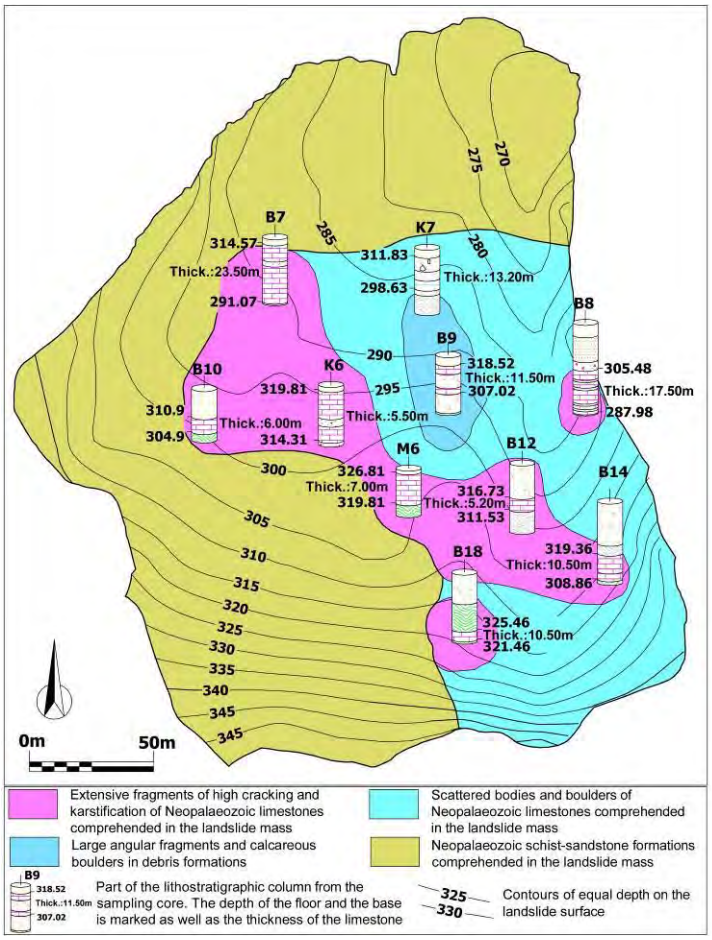

Figure 4 - Dispersion map of the limestone bodies in the mass of the landslide.

The limestone bodies are thinly bedded with intense folding and medium to high fragmentation and karstification. The discontinuities and karstic voids of the rock mass are filled by green clays and clayey sands. The largest proportion of RQD index values is between 0% and 20%. At least three large limestone bodies are contained in the schist-sandstone mass. The first one is about 40m thick and can be found in the western section of the up-thrusted mass, 170m upwards and NE of the landslide head. The second is about 35m thick and it is located 200m upwards and to the north of the landslide head. Finally, the third is located in the central section of the landslide, having NW-SE direction, extends up to a depth of 3m, and has a length of 195m and maximum width of 70m. Its thickness reaches 24m in its NW end, 5 to 7m in the most extended central section, and 10m in its SE end, while its volume is estimated at 216,000 m^3. The two smaller limestone bodies, in the north-eastern and southern sides of the main section, are about 25 to 30m long and are having a thickness of 10 and 17m respectively, while their total volume is estimated at 33,000 m^3 (Figure 4).

The Upper Triassic limestones are white, grey-white, grey and locally brown in colour. They are unsorted and present high and extremely high strength. At positions they are highly fractured and significantly karstified, in the form of rillenkarren and karstic voids of 4m to 6m in diameter. The filling material contains calcareous fragments and gravels, while it consists of clayey to clayey sandy material and calcareous clay with, locally, high degree of cementation. Two main joint systems cross the calcareous formation in NNE-SSW and NW-SE orientation and dips from 70° to 90°, while the largest proportion of RQD index values is between 20% and 50%. The fault breccia

of the thrust zone consists of calcareous clays, red, pale yellow, off-white, brown-red and dark red in colour, which contain calcareous and shaly fragments and gravels with size 0.02 to 0.15m in varying proportions. It is a highly cemented formation of significant strength which is crossed by sequential surfaces of tectonic slip and its thickness is 20m. It is presented as clayey-silty sand, clayey sand, clayey sand-gravel or clayey-silty gravel of medium plasticity, where it is strongly tectonized and weathered.

The schist-sandstone bedrock is covered by cemented colluvial deposits which consist of calcareous fragments, gravels and angular rock pieces with size 0.02m-0.4m. These are strongly cemented in a matrix which is composed by calcitic-sandstoned, sandy-marly, and clayish-marly material in red to maroon colour and it presents great strength, high degree of fragmentation, and joints with great length and openings with calcareous material on their walls. The erosion along the discontinuities and the gaps from the erosion and from the joints, have induced a great secondary permeability and the fluctuation of the water level, which infiltrates and is stored into the underlying limestones. Finally, the loose colluvial deposits are slope deposits of low strength, consisting of gravels, granular fragments, and boulders of limestones in fine grained material with significant thickness in some places. They are characterized as sandy clays, clayey sands or clayey sands and gravels of medium plasticity.

5. Morphological Features of the Landslide

The mountainous, bold to rugged morphological relief dominates the NNE ending of Parnitha Mt., near the landslide area. As a result of the karstification, vertical dissection, and following erosion, there are steep slopes and vertical stream walls. The relief becomes smooth where the neopalaeozoic schist-sandstones dominate, due to their uniform erosion and the ease of weathering (Figures 1b and 1c). A small “horseshoe” order of the contour lines and a rapid normalization of the relief, in accordance to the mean upwards slope angle of 25°, for a 65m wide zone with sub-horizontal morphology and small inclination of 10° to the North, discerns in the upwards area and in all the width of the landslide head, in altitudes between +360 and +345 meters above principal datum. A small hill is formed at the north side of the landslide toe, downwards the diversion of the NR, by a reflective smooth and concave surface which dips 35° to the S or SSW and has glide lines on it. The inclination of the soil mass, in the intermediate morphology, is 20° to the N at the upwards section of the railway line and 10° at the downwards one. A small morphological crest, which is developed on a NE-SW axis, is formed at the western side of the central section of the landslide, downwards the railway line. The morphology refers to an old landslide, which was developed in the flat between the altitudes of +360 and +345 meters, and its toe ended up to the rising ground, downwards the NR, which stopped its progress and acted as a buttress.

The landslide presents classic tensile cracks at the head, with almost vertical walls and vertical displacement of few meters. These cracks turned into trench gaps, after the mass movement, being 15m to 30m wide and 15m deep. At its sides, the landslide is clearly defined by continual cracks which revealed the failure surface with characteristic glide lines to the direction of the movement. There is, also, intense ground elevation at the landslide toe and multiple failure surfaces, extremely smooth and with glide lines, in different levels (Figure 3).

6. Inclinometer Measurements – Determination of the Failure Surface

Fifteen (15) sampling boreholes, supplied with inclinometer tubes, carried out in the area for the observation of the soil mass movements, six (6) of them within failure zone limits and nine (9) out of it. After seven repeated measurements, which took place within nine months, the movement vectors from the inclinometers showed that only some of them presented systematic movement, although within the limits of the instrument error. Movements were located by the inclination tubes in borehole GK1, in the depth of 30.50m (21.50mm), in GK6, in the depth of 22.30m (13.00mm), in GK7, in a depth of 28.20m (15.00mm) and in GM1, in the depth of 26.50m

(11.50mm). Finally, the inclinometer which was installed in borehole D1, in the west end of the landslide head, showed maximum movement of 17mm in the depth of 3.50m, in a time period of 104 days (Figures 3 and 4).

Older sequential failure surfaces, with similar geometric and kinematic features with the recent one, are located on calcareous crusts of core drillings, as well as at the edge and toe of the south slope of the outcrop, downwards the new highway. These surfaces reveal the secondary nature of the landslide because of the pre-existence of a zone of low shear strength with continual activations in the past.

7. Data from the Surface Deformation

The total number of cracks recorded on the sliding mass surface was 114 and the sequential measurements of their position and size did not give clear results for the direction and magnitude of the movement. The variations of their size did not seem to come from factors related to the soil mass movement but they can be attributed to conditions that affect the soil surface. However, the presence, density, and orientation of the cracks on the landslide surface provide significant evidence about the movement of the soil mass (Figures 2 and 5).

By the dispersion of the cracks at the failure surface, the following conclusions are reached:

- The absence of cracks in the central and eastern section of the landslide reveals the solid nature of the block and its movement into one block.
- The large number of cracks, which are located at the west side of the central section and at the toe of the landslide, reveals that they are developed in an area of compression which has, almost, transverse orientation in regard to the landslide boundaries and the direction of movement, as it appears from the glide lines, due to the blocks movement halt.
- The tensile cracks in the area between the head of the landslide and the railway line are parallel or almost parallel to the lateral boundaries of the landslides.

8. Data from the Kinematic Analysis of the Landslide

According to the geometric data of the movement, the tension and compression zones of the landslide, the orientation of the tensile and compressive axes, and the direction of the movement, in every location, are determined (Figure 5). An extended tension zone was determined at the SE side and the central section of the landslide mass, upwards and downwards the railway line. At its north section, failure surface dips to the NW and glide lines have NNE direction and NW-SE orientation of the tension axis (Tension area II). At the NE side of the landslide, movement took place on a surface dipping to the ESE, glide lines with NNE and NE direction, determining a zone of compressive events with orientation of the compressive axis to the NE-SW (Compressive area II). At least two older slip planes, with striations that have the same orientation as the recent ones, were determined at the sequential planes of the calc-crust, at the SE end of the compressive area II. At the SW section of the landslide, upwards the railway line, a tension zone was determined with tension axis orientation N-S and mass movement to the NNW at the most southern part, to the North at the middle part, and to the NNE when approaching the railway line (Tension area III). A compression zone by sequential compressive cracks was determined immediately downwards the morphological crest, which has planes with SW inclination and glide lines to the ENE (Compressive area III).

A limited extended tension area is formed at the NW end of the landslide toe, exactly where tension cracks occurred by the 1993 and 1994 failures. Slip planes, in this area, incline to NNE, N and NNW, while one inclines to the NW, by dispensation, with glide lines oriented to the N and direction of the tension axis to the NNW-SSE (Tension area I).

The NW end of the landslide toe is been dominated by compressive events, with sequential planes that incline to the SW, glide lines with NE direction and compressive axis with NE-SW orientation (Compressive area I).

The calcareous surface at the north slope of the morphological outcrop downwards the National Road inclines to the SSW with glide lines which are headed to the NNE and compressive axis of NNE-SSW orientation. So, it is confirmed that the geometrical features of older soil mass activations in the area of the landslide toe are barely different from the recent one.

In conclusion, tension area (I) with compressive area (I), tension area (II) with compressive area (II), and tension area (II) with compressive area (III) define three different soil blocks of the unstable mass (Figure 5).

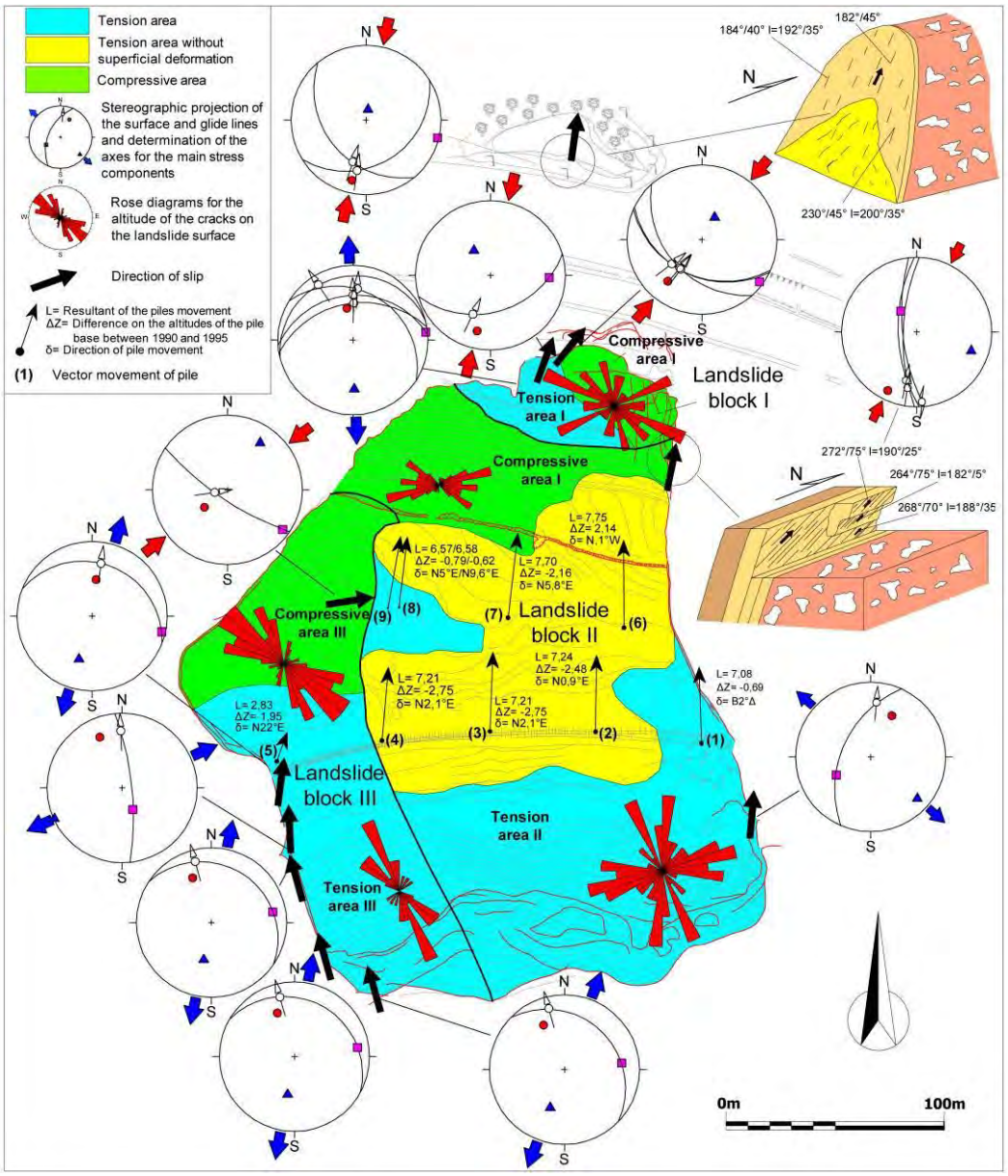

Figure 5 - Kinematic analysis of the landslide.

9. Kinematics of the Landslide

Based on the aerial photographs taken before (9/21/1987) and after (2/21/1995) the occurrence of the landslide, the photogrammetric impression of the greatest landslide area was drawn up, with the determination of 12 ground control points through satellite Global Positioning System (GPS) (Figure 5).

The comparison of the two maps gives significant information about the morphology of the area before the widening of the National Road and after the occurrence of the landslide. The dense forest cover at some parts of the area does not allow the determination of the exact movement vectors with desirable accuracy. However, due to the existence of ten telegraph poles along and in a distance 50m downwards the railway line, the accurate measurement of the vectorial movement was possible.

Two areas with distinct kinematic can be clearly defined by the movement vectors. The area which includes the western section of the landslide is defined by the poles 14 (5) and 5 (8) and the western boundary of the sliding mass (Figure 5). This section has been moved by 2.83m to the NE. The eastern section of the landslide shows its maximum movement at the central part, from 7.21m up to 7.75m, reducing at 6.57m up to 7.08m in its western and eastern margin. On the other hand, the eastern section of the landslide is divided, considering the direction of movement, into the western part, to the west of the poles 12 (3) and 6 (7) with a movement direction to the NNE, and the eastern part with a movement direction to the NNW (Figure 5).

10. Hydro-geological Conditions of the Landslide Mass

The spread of the Triassic and Neopalaeozoic limestone phases of the Parnitha Mt. favors the development of a rich karstic underground water potential. The spring at the landslide mass, in the altitude of +313 and with constant flow of 1.5m^3/h to 2m^3/h, is an overflow spring and gushes out at the contact between the entrapped, highly cracked, karstic, Palaeozoic, calcareous blocks and the impermeable schist-sandstone bedrock. Also, the discharge of high quantities of water during the winter, at the wider spring area and the slope upwards the railway line, shows the existence of a significant, unsteady, hydraulic load in the landslide mass, whose volume depends on the rainfall (Figure 2). The underground karstic aquifer is developed in the central section of the landslide, between the elevation contour lines of +335, at the railway line area, and +310, at the drainage cemented trench. From the piezometer measurements in 42 vertical drillings, distributed in three parallel to the motorway axis branches and a conjunctive vertical branch, arises that the groundwater table varies between 2.00 and 35.11 meters from the surface (Figure 6a). In the central and most extended section of the aquiferous zone, the piezometric level ranges between +305 and +310 and reduces sharp to the NW in +282 and smoothly to the South in +304, displaying a small mean hydraulic gradient of 5° to the North (Figure 6b).

The groundwater in the central section of the landslide mass forms a significant hydraulic head above the failure surface with a volume of 500.000m^3. The distribution of the hydraulic head is not uniform, so there are four distinct areas which are recognized. At the northern section of the aquiferous zone, the hydraulic head is over 20m, at the central section is between 10m and 20m, at the southern and the eastern sections is between 0m and 10m, while at the southern and eastern margins the piezometric surface is lower than the failure surface (Figure 6c).

The pumping tests, which carried out at the vertical drillings for the degradation of the piezometric level, revealed high drainage volumes and recharge rates at the section with the highest piezometric level and hydraulic head (KG5 to KG9), in relation to the rest of the drillings which had low drainage volumes and slower recharge. The drainage at the west side drillings, downwards the railway line (EY11 and EY12), was achieved by 50% of the desirable, at those of the east side (B2, EY1 and EY8) by 40%, while at the central section drainage did not exceed 15%. Also, the

discontinuity of the impermeable beddings does not allow the hydraulic contact even between neighbouring drillings.

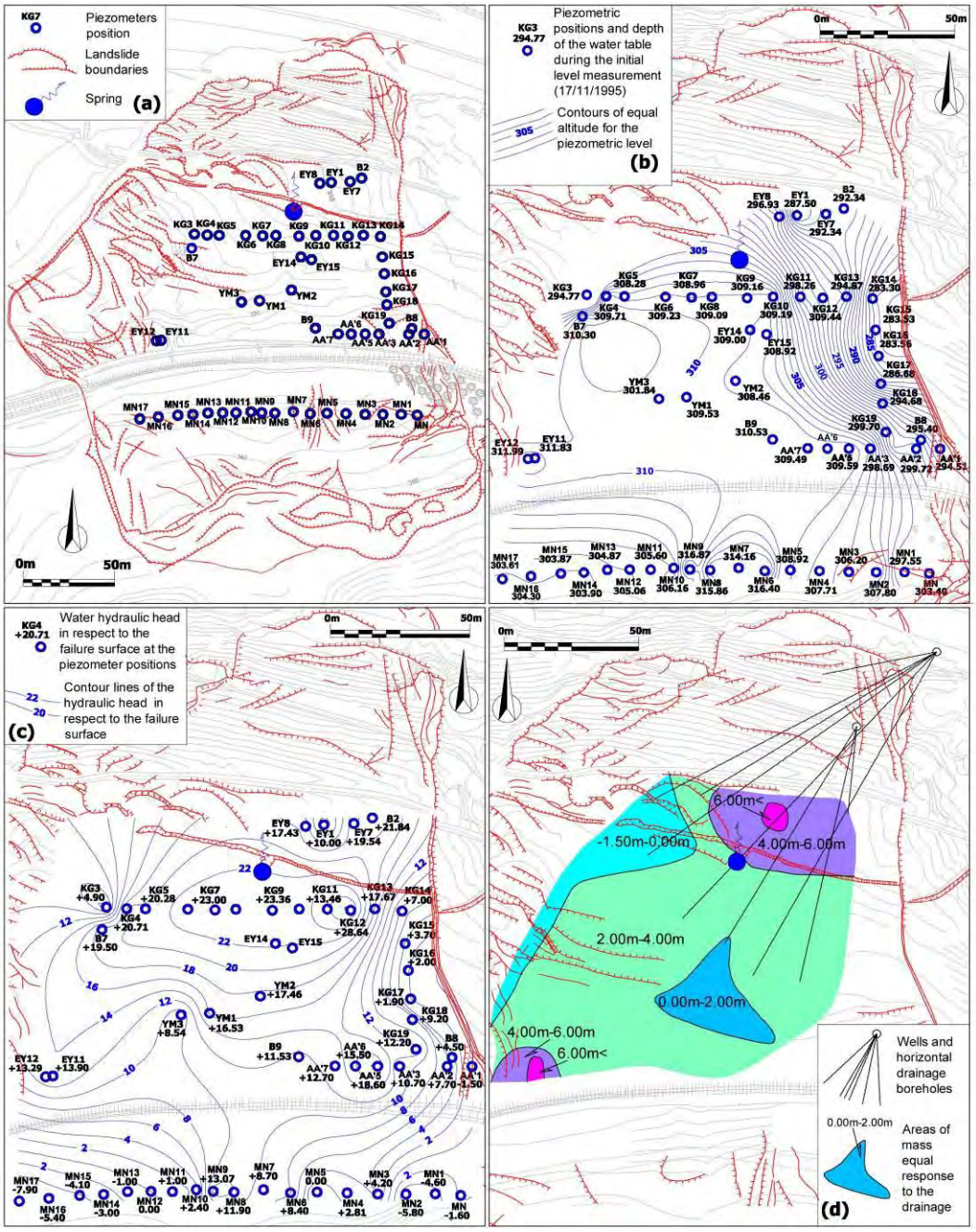

Figure 6 - Maps of groundwater conditions in the Malakasa landslide. (a) Distribution of Casagrande type piezometers in the landslide mass. (b) Piezometric map of Malakasa landslide. (c) Potentially groundwater pressures on the slide rupture surface. (d) Response in the draining at the different locations in the slide mass by placing horizontal drains

Twelve horizontal drillings were executed in two positions through equal number of shafts, 3 and8 meters deep, and they extended from 10 to 150 meters. Discharge, in both shafts, varied between 1 and 8m^3/h.

The response to the drainage was different from place to place. The western side of the central section of the landslide showed degradation of the piezometric level between 0m and 9m, while at the rest of the western side the piezometric level increased up to 1.5m. Consequently, there is a clear discrimination into two areas, one of increased ground water capacity, high hydraulic head, increased discharge volumes and quick recharge, at the central section of the aquifer zone, and one area of decreased respective hydraulic parameters at the eastern and northern borders (Figure 6d).

11. Data Evaluation

The landslide mechanism been approached, on the one hand based on the kinematic features, morphological superficial data and vectorial features of the movement, and on the other hand on the lithostratigraphy of the failure mass and its hydro-geological features. Based on these criteria, there is clear discrimination of the landslide mass into two different blocks, which are differentiated by their lithological structure, kinematic features, deformation and hydro-geological behaviour (Figure 7). The sudden detachment and downwards movement of the extended soil mass of 1,300,000m^3 volume, in the 18th of February 1995, at the Kilometer Post (KP) 35+000 of the new National Highway Athens – Thessaloniki, occurred in an area of intensive palaeotectonic processes. The Neopalaeozoic schist-sandstone formations with extended limestone bodies in their mass and in the greater landslide area are up-thrusted to the Triassic limestones, are highly cracked, eroded, and have been turned into clay with total loss of their initial structure at positions.

The main front of the thrust has surfaces which incline to the NE, with angles between 60° and 65° and lines which refer to a compressive movement with direction of sliding to the SE. This front, actually, defines the schist-sandstone klippe in which the failure occurred from the North. At its western boundaries, it is developed in NW-SE up to NNW-SSE direction, with surfaces which incline to the SW up to WSW and with angles between 50° and 75°, respectively. Another two up-thrusted events, in the schist-sandstone mass, present similar geometrical features with the main fronts of the thrust and have caused extra fatigue to the neopalaeozoic formations.

The landslide mass was separated into two distinct blocks: (i) to the eastern, and most extended block, with estimated volume of 993,000m^3, where the significantly folded and fractured, permeable calcareous mass of estimated volume 250,000m^3 develops on the tectonically stressed and impermeable schist-sandstone mass and (ii) to the longitudinal western block of limited extend, with estimated volume 225,000m^3, where there are, exclusively, soil layers with increased permeability (Figure 7). The eastern block moved totally and independently, in respect to the western one, at NNE up to NE direction, with total horizontal movement of 7m and vertical movement of 2.50m. The tension and compressive cracks at the head and toe of the slope, respectively, accumulated at the periphery of the sliding mass and were totally absent from the central section due to its rigid nature. The western part of the sliding mass made up a distinct soil mass with independent spatial and temporal resultant movement to the North, total horizontal movement of 3m and vertical movement of 2m. The differential movement of 4m between the two fragments was covered through the numerous and dispersed cracks of the western section. The southern part of the eastern block seems to be an independent block which has boundaries that coincides with the failure of 1994. This soil block, with estimated volume of 63,000m^3, moved in NW up to NNW direction with clockwise sliding component, pushed by the upward section of the landslide (Figure 7).

From the discharge of the horizontal drainage drillings, which perforate the sliding mass radically in order to unload it, the great potential of the calcareous aquifer was determined, with the discharge flows being over 100 times than the one of the western section (Figure 7). The sequential older failure surfaces, which were determined to the NE end of the landslide and in

drilling cores, as well as to the calcite surface, which covers the southern slopes of the morphological outcrop, downwards the NR, with geometric and kinematic features in respect to these of the recent one, show the presence of a zone with low shear strength (residual strength) and the secondary nature of the sliding.

The gradual loss of support, caused by the sequential excavations in the slope toe made in a length of 110m, 155m in width and varied depth between 5m and 16m, in combination with the increased hydraulic head of the upward mass, was one of the most important factors for the landslide occurrence (Figure 8).

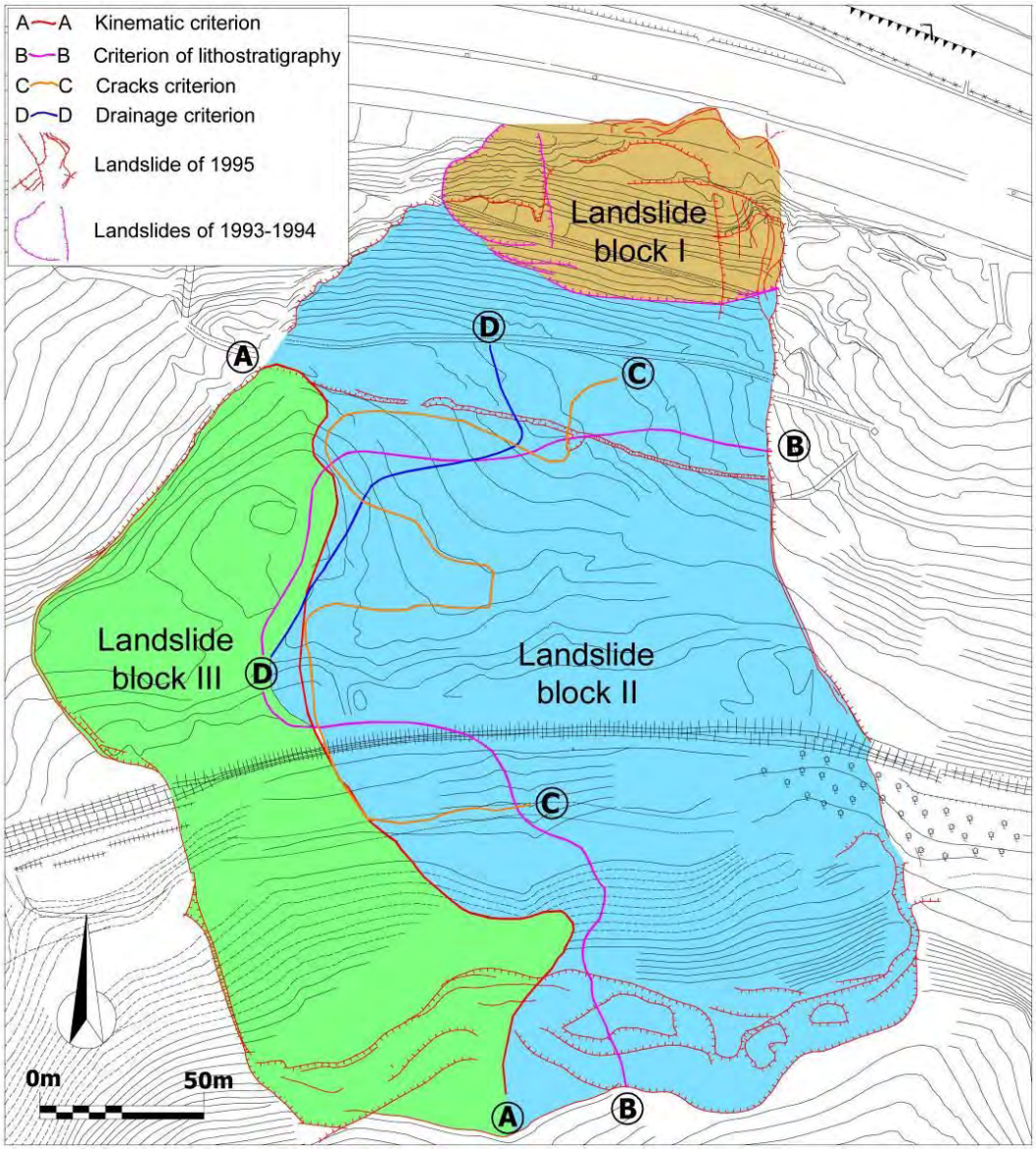

Figure 7 - Delineation criteria of the soil blocks which form the landslide mass.

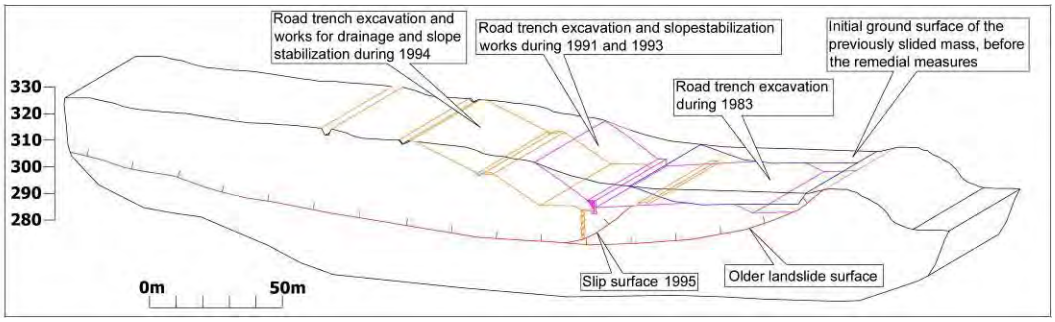

Figure 8 - Representation of the different excavation stages for the figuration of the National Highway at the landslide toe.

12. Conclusions

The evaluation of all data mentioned above lead to a different outlook for the failure mechanism of the landslide. The main causal factor was the gradual loss of support of three independent blocks which form the sliding mass and their slip upon a pre-sheared surface of limited strength.

The extended works for the drainage of the sliding mass included, among others, the construction of an expensive drainage system of tunnels, with one longitudinal and six transverse branches of 1,400m in length. During these works, the Palaeotectonic structure and the development and geometry of the geological formations of the narrow and wider area were not taken into account. The construction of a vertical drainage drilling network in the area of the aquifer zone to a maximum depth of 150m, ending at the Triassic limestones of increased secondary permeability, would ensure the full drainage of the Neopalaeozoic limestone bodies being at the central section of the landslide, with significantly low cost.

13. References

Cavounidis S., Sotiropoulos E., Vettas P., Avgeropoulos P. and Marinos P. 1997. The Malakasa Landslide. A general review, *Proc. of the 3rd Greek Congress of Geotechnical Engineering*, Patras, Greece, 227-236.

Dounas A.G. 1971. Geology of the area between Megara and Erithraia village (Attica), *PhD Thesis*, University of Athens, 141pp.

Georgopoulos I.O. and Vardoulakis I. 2001. Study of the Malakasa Landslide of 18-2-1995 by using Combined Block Failure Mechanisms, *Proc. of the 4th National Congress of Geotechnical Engineering*, Athens, Greece, 403-410.

Marinos P., Yannatos M., Sotiropoulos E. and Cavounidis S., 1997. Increasing the stability of a failed slope by pumping, Malakasa Landslide, Athens, Greece, in Marinos et al. (eds), *Engineering Geology and the Environment*, Balkema, Rotterdam, 853-857.

Mourtzas N.D, Kolaiti E. and Papanikolaou P. 1993. Geological Features of the Landslide at Aspropyrgos Area (Attica, Greece), in Anagnostopoulos et al. (eds), *Geotechnical Engineering of Hard Soils-Soft Rocks*, Balkema, Rotterdam, 1137-1146.

Pantelidis P. and Cavounidis S. 1997. Slope Stability Analyses for Malakasa Landslide. *Proc. of the 3rd Greek Congress of Geotechnical Engineering*, Patras, Greece, 261-268.

Sotiropoulos E., Dendrou B. and Papanikolaou P. 1998. Groundwater Conditions and Drainage of a Large Slide. *Proc. of the 4th Int. Conf. on Case Histories in Geotechnical Engineering*, 8-15/3/1998, St Louis Missouri, USA, paper No 2.44.

Δελτίο της Ελληνικής Γεωλογικής Εταιρίας, τομ. XLVII , 2013
Πρακτικά 13ου Διεθνούς Συνεδρίου, Χανιά, Σεπτ. 2013

Bulletin of the Geological Society of Greece, vol. XLVII 2013
Proceedings of the 13th International Congress, Chania, Sept. 2013

APPLICABILITY OF THE "LEFKA ORI" WESTERN CRETE REGION GEOFACTORS' INTERACTION MATRIX (GFIM) AS A KEY TO UNDERSTANDING THE ENGINEERING GEOLOGICAL CONDITIONS

Pavlaki A.[1], Meladiotis I.[2] and Pavlakis P.[3]

[1] *Geologist, PhD-Civil Engineering Department AUTH. "Consulting Engineering Bureau of Geological Researches & Studies", 56 Tzanakaki Str, Chania, Greece, catrpaul@otenet.gr, ppavlakis@tellas.gr*

[2] *Professor, Aristotle University of Thessaloniki, Department of Civil Engineering, Laboratory of Engineering Geology, 54 124 Thessaloniki, Greece, imeladiotis@yahoo.gr*

[3] *Civil Engineer, PhD-Civil Engineering Department AUTh. "Consulting Engineering Bureau", 56 Tzanakaki Str, Chania, Greece, ppavlakis@tellas.gr*

Abstract

The results of extensive and long-lasting investigations on various geofactors in the "Lefka Ori - Chania" W.Crete region revealed the major role of their interaction in the engineering geological conditions' formation. The investigated region has a specific scientific interest due to its admirable geoenvironment which is governed by an active geodynamic regime and affects the active development of all the geofactors. It also shows a rapid growth, which evolves into a fragile balance with the valuable geoenvironment thus the vision of its aeiforos development in the future, needs, among others, the wide recognition of its engineering geological conditions. The methodology was based on multidisciplinary and thorough research studies utilizing qualitative & quantitative analysis of various geofactors. The results, which are depicted on new geothematic maps, prove that these geofactors are the product of parallel progressive and interactive evolutions in an environment dominated by an active geodynamic regime, where the corresponding stress field affects in a catalytic way to many geo-developments. Besides this, a great number of striking geo-structures have been revealed, characterizing the investigated area of "Lefka Ori - Chania", as a globally unique Natural Geological Laboratory. The GeoFactors' Interaction is represented graphically on a Matrix form creation, called then "Lefka Ori Western Crete GFIM". This matrix can serve us, as a useful scientific tool, for the investigated area's engineering geological conditions' recognition and we propose its application to relevant research studies.
Key words: *Lefka Ori -Chania, aeiforos development, geofactors' interaction, active regime.*

Περίληψη

Από την επεξεργασία και συναξιολόγηση των αποτελεσμάτων εκτεταμένων ερευνών στην ευρύτερη περιοχή Λευκών Ορέων-Χανίων Δυτικής Κρήτης, αναδείχτηκε και παρουσιάζεται ο καθοριστικός ρόλος της αλληλοεπίδρασης των επί μέρους γεωπαραγόντων στη διαμόρφωση των τεχνικογεωλογικών της συνθηκών. Η περιοχή έρευνας έχει ένα ιδιαίτερο επιστημονικό ενδιαφέρον δεδομένου ότι διέπεται από ένα

ενεργό γεωδυναμικό καθεστώς το οποίο επιδρά στην ενεργή εξέλιξη όλων των γεωπαραγόντων. Επίσης, παρουσιάζει μία ραγδαία ανάπτυξη η οποία εξελίσσεται μέσα σε μια εύθραυστη ισορροπία με ένα πολύτιμο γεωπεριβάλλον και το όραμα για την αειφόρο ανάπτυξή της στο μέλλον, απαιτεί, μεταξύ των άλλων, την ευρεία γνώση των τεχνικογεωλογικών της συνθηκών.

Η μεθοδολογία βασίστηκε στην πολυδιάστατη και ενδελεχή διερεύνηση με ποιοτική & ποσοτική ανάλυση των επί μέρους γεωλογικών, τεκτονικών, μορφολογικών, κλιματολογικών, υδρογεωλογικών γεωσυνθηκών και γεωμηχανικών χαρακτηριστικών των σχηματισμών, τα αποτελέσματα της οποίας αποτυπώθηκαν σε γεωθεματικούς χάρτες. Διαπιστώθηκε δε, ότι ο καθένας γεωπαράγοντας διαμορφώνεται μέσα από μία προοδευτική εξέλιξη η οποία βρίσκεται σε στενή επήρεια με εκείνης των άλλων γεωπαραγόντων, σε ένα περιβάλλον όπου κυριαρχεί το ενεργό γεωδυναμικό καθεστώς το οποίο μέσω του αντίστοιχου πεδίου τάσεων, επιδρά καταλυτικά σε πολλούς γεωπαράγοντες. Παράλληλα διαπιστώθηκε μία εντυπωσιακή ποικιλότητα γεωλογικών διεργασιών και γεωδομών, που καθιστούν την περιοχή έρευνας ως ένα μοναδικό Γεωλογικό Εργαστήριο της Φύσης. Για την ευχερή απεικόνιση της σχέσης αλληλοεπίδρασης, δημιουργήθηκε και παρουσιάζεται, το "Μητρώο Αλληλοεπίδρασης Γεωπαραγόντων περιοχής Λευκών Ορέων - Χανίων Δυτικής Κρήτης" το οποίο αποτελεί ένα επιστημονικό εργαλείο "κλειδί", που συμβάλλει στην εποπτική αναγνώριση των τεχνικογεωλογικών της συνθηκών και εκτιμάται ότι θα μπορούσε να εφαρμοσθεί σε ανάλογες έρευνες.

Λέξεις κλειδιά: *Λευκά Όρη-Χανιά, αειφόρος ανάπτυξη, αλληλοεπίδραση γεωπαραγόντων, ενεργό καθεστώς.*

1. Introduction

Engineering Geology is a relatively new field of earth sciences and very important as well, especially in today's era of rapid urban growth and development planning associated with major infrastructure projects. **The engineering geologic conditions** of a region formed by the interacting geofactors relative to geology, tectonic, seismotectonic, climate, morphology, hydrogeology and geomechanical properties of materials, which predetermine the engineering geological response which may arise from influences derived from endogenous & exogenous natural processes and human activities (Pavlaki, 2006). Based on this consideration and in the context of an integrated & efficient investigation of the engineering geologic conditions of the region under study, we investigated all the above geofactors, with emphasis on their interaction. **The investigated region** lies in the west part of Crete (Figure 1); the largest and the most southern Hellenic island which as it is located on the Eastern Mediterranean Sea's centre, holds a key-position **with great geoscientist and geopolitical importance**.

Figure 1 – The investigated region of "Lefka Ori" (+2,452 m) – "Chania" in western Crete.

The surrounding area has always drawn **international geoscientific interest** due to its **rich geological history** characterized, as mentioned in numerous published works, by strong geodynamic processes & changes, including oceanic creations, continental collisions, orogenesis

(Figure 2). The geological structure of Crete is represented by an accumulated nappes' pile which was developed during Jurassic to Miocene, within the Alpine Orogenesis, under a general compression regime closely connected to plates' convergence (Kilias et al. 1994). From Tertiary until recently, the geodynamic regime is represented by the Eurasian and African plates' convergence, which evolves through a roll-back mechanism causing the southward migration of the convergence's limit until the present position which lies along the middle zone of Eastern Mediterranean (Papazachos & Papazachou 2003, Ten Veen & Kleinspehn 2003). **The migration of the convergence's limit** is evolving through complex operations which have impacted the geologic & tectonic setting of the surrounding region. Moreover these processes especially the **corresponding stress field, affect in a direct or an indirect way, the individual geofactors' formation** (Pavlaki, 2006), resulting in the region's geoenvironment which is characterized by **an unprecedented diversity of geomorphological features** which make it unique.

In the central and southern part of the study area, the spectacular **"Lefka Ori" Mountains** (+2,452 m) dominates, which represents a great tectonic window created under strong uplifting processes, associated by the extensional exhumation of the lower tectonic nappes. The mountains are constructed from carbonated and fractured rocks, the lithology of which in combination with the tectonic processes (especially the uplift) and the high rainfall as well, have contributed to the wide karstic development. The karstification of the mountains results in an impressive variety of karstic geostructures, including caves, potholes, gorges, plateaus and **major aquifers.** The latter transports large quantities of groundwater which flows to the surface through springs and into the sea via submarine groundwater discharge (Pavlakis, 1989, Meladiotis et al., 1993, Pavlaki, 2006).

In the central-northern part of the study region, a different landscape is formed, represented by the **Chania - Souda tectonic basin**. This is bound by neotectonic normal faults, which were generated progressively from Miocene to present under a general extensional regime (Mountrakis, Kilias, et al., 2012, Pavlaki, 2006). That period, the Neocene sediments were progressively deposited in the basin as well. This area is now covered by bountiful vegetation and cultivated land. The northern and western parts of the study's region, including the gulfs of Chania and Kissamos and the capes of Spatha and Gramboussa (Figure 1), are very famous for their beautiful shores and constitute a major attraction for the residents and visitors alike. Furthermore, these coasts are known for their endless sandy beaches and picturesque rocky bays which record the neotectonic evolution. These are shown on the coastlines' lifting and on the well preserved faults' coastal surfaces.

The residential development is linked to the expansion of settlements in the northern zone (149,100 inhabitants), clustering in the city of Chania, which is comprised of the old and new town, reflecting a diverse architectural influence & cultural history (e.g. Venetian, Muslim, neoclassic, modern). **The tourism development** is significant with a capacity of 55,300 beds. Moreover, in the northern part of the Regional Unit of Chania most of the main **infrastructure projects** have been planned and constructed, such as, the National Road along the northern coastline which connects the city of Chania to the rest of Crete, the Chania Airport, the Port of Souda, the large Project of the Water Resources' Management for Irrigations and Water Supplies of the W. Crete Region, the Waste Water Treatment Plants etc.

The valuable geoenvironment, the precious natural environment which involves a huge amount of valuable endemic species, the favourable climatic conditions and the significant cultural heritage, make up **the comparative advantages of the Lefka Ori – Chania region** (Regional Unit of Chania, Prefecture of Crete). It is noted that this area, like the rest of the island of Crete, freed recently (in the early 20th century) by **Eleftherios Venizelos,** after centuries of enslavement and many revolutions. Today, in the framework of its development, is trying to exploit its comparative advantage, as it aspires to become an important cultural and tourist Eastern Mediterranean's hub. Nevertheless, **the rapid growth at an undoubtedly active and complex geoenvironment,** led, in some cases, to **uncontrolled interventions** on the environment, which caused adverse effects such as degradation, significant alterations and failures' events. Considering all the foregoing we

appreciated **the necessity for engineering geological knowledge** and we proceeded to the preparation of this survey without any financial support, but having the deep belief that **it can contributes** to **the vision of an "aeiforos development**" for **the region's future.**

*[We propose using the Hellenic word **"AEIFOROS",** which begins with the first & most powerful letter of the Hellenic alphabet: A and in contrast to the word "sustainable" where the concept has been defined, the Hellenic word has itself the original & comprehensive meaning (AEI=always, Foros=who has and brings, produces). It also includes the sense of upgrading. Beside this, it is noted that in the Hellenic alphabet, the letters' symbolism and the words' formation are not random but they include the conceptual meaning & blessing, thus the Hellenic language is considered ideal, the great feeder of all languages..Ex: the letter A means the beginning under the initial sunlight's force].*

The purposes & scopes of this work's preparation were: **1. Contributing to the science**, due to the scientific interest which arises from the individual geofactors' investigation in a rapidly developing area, governed by an active regime. **2. Contributing** to the study's region development projects' & human activities' **rational planning**, by providing support through; the engineering geologic knowledge, the identification of geological hazards and the determination of the uncontrolled human interventions that cause alterations and failures' events. **3. Contributing to** the protection, enhancement & rational use of the study's area **geoenvironment** which represents a valuable Geological Laboratory of Nature, thus to give it unharmed to future generations.

2. Methodology

This paper focuses on **evaluating the results** derived from qualitative & quantitative analysis of individual geofactors relative to geology, tectonic, geomorphology, hydrogeology, climate, hydrogeology and geomechanical properties of materials, with emphasis on their interaction in the engineering geological conditions which formed in the survey's region. The course of the investigations was extensive and required a multidisciplinary scientific research which included:

- **The collection, processing and evaluation** of primary data, of the various research data (geophysical, boreholes), of the existing geothematic maps & bibliographic data relevant to the object and the area of research, but also relevant to the methods' applied in other analogous regions (more than 1,000 works were collected). In addition, the surveys included the concentration and using of scientific data, which refer to colour aerial photos, orthophotos, thermal images, satellite images (Landsat 5, Spot 2).
- **The realization of extensive field research** which lasted 18 years and had as main subject: **1**. **The investigation & registration** of many geological characteristics in the framework of the geothematic maps' preparation (contacts, beddings, faults, discontinuities etc). Moreover, the definition, analysis and interpretation of various geomorphological processes and structures which make the investigated area a complete Natural Geological Laboratory (karstic formations, gorges, uplifting coastlines etc). **2. The quantification** of the coefficient K of the geological formations' permeability, by performing pumping tests in water drillings and by measuring the geometric features of the discontinuities in many locations in the context of the "Killary's" method. **3. The investigation regarding the rockmass qualitative condition**, by utilizing the macroscopic observation and recording the features relevant to the structure, the discontinuities' surfaces and the weathering degree. **4. The quantitative analysis** of the geological formations' **geomechanical properties** based on the results of extensive works (field & laboratory). **5. The determination of the intentional and unintentional human impacts** that cause adverse effects on the geoenvironment.

In order to create a graphical representation of the geofactors' interaction, we used "Hudson's first Matrix" (1992) as a framework and in addition we expanded its implementation to the engineering geological conditions existing in an extensive region. This led to the creation of the "Lefka Ori" Western Crete **GFIM** (**G**eo**F**actors **I**nteraction **M**atrix).

3. Geofactors

3.1. Geodynamic Processes

The geological history of the surrounding **Mediterranean Region** is characterized by **strong geodynamic processes.** Some of them influenced the study's area geologic creation, which is closely connected with the old basins' evolution, the Alpine orogenesis and the modern geodynamic regime represented by the Eurasian and African plates' convergence. The Mediterranean's geodynamic evolution is reflected in its corresponding **paleogeographic evolution**, highlights of which are attributed to the paleogeographic maps of Figure 2-a (Scotesse et al, 1998). The progressive location of Crete's geoenvironment is relatively determined (indicating by red symbols), based on the multi-geological criteria's evaluation (Pavlaki, 2006).

From Oligocene until now, the dominant process is the African and Eurasian plates' **convergence**, evolving via the subduction of the African lithosphere under the Aegean plate. **The subduction** is characterised by a **southwards** progressive **retreating** (Figure 2b), through a roll–back mechanism, accompanied by the southward **Aegean plate's expansion** as well (Mountrakis, 2001, Papazachos & Papazachou, 2003, Ten Veen & Kleinspehn 2003). This geodynamic retreat has affected the corresponding **migration of a "double system" stress field**, characterised by the development of compression regime in every convergence's boundary and of the corresponding extension in the relative inner (Kilias 2001). This represents the **controlling factor** which influenced the **geologic & tectonic evolution of the study area.** Particularly, the southward migration of the convergence's limit from the earlier Crete's position to its recent position in the middle of E. Mediterranean (**M**editerranean **R**idge), was associated by the corresponding southward compression's migration, which dominates today in the M.R. Zone (Figure 3). In the internal region (back-arc basin, Crete), the initial compression was followed, from Miocene until now, by an extensional regime which induced the extensional exhumation of the lower tectonic nappes of Crete, resulting in the tectonic windows' generation.

Today, **the convergence is characterized by strong active processes,** represented on the map of Figure 3 (from Pavlaki, 2006. The map, as mentioned in that work, was prepared according to the evaluation of geodetic, tectonic and seismotectonic data, obtained from many published papers). As it is clearly shown on Figure 3, the recent geodynamic regime can be described as **a counter-clockwise continuously compounded plates system shift**, including **Arabian**, **Anatolian** and **Aegean** plates, which under successively pushing movements, through progressively increasing speeds, reached the maximum velocity of ~3.9cm/yr in the SW part of the Aegean plate (the location of the study area), which **thrusts on the African plate**. The latter is moving northwards at a velocity of ~1cm/yr and is subducting amphitheatrically beneath the Aegean plate in Crete region, as it was initially detected from Papazachos & Comninakis 1970, via the Benioff zone's definition. At present, the movements that have been recorded in the investigated area, show SW direction and velocities up to ~3,9cm/y, which are of the highest ever been registered in the Hellenic arc (Pavlaki, 2006). The crust under west Crete consists of a continental top layer of 15-20km thickness above a 20-30km thick subducting fossil accretionary wedge with a characteristic an echelon fault sequence, while the downgoing Moho lies at a depth of 40-60 km (Knapmeyer & Harjes, 2000). The pushing of the subducting African plate in combination with the accretionary wedge's formation beneath west Crete is considered to have contributed **to the strong uplift** which is observed on the study area (Pavlaki, 2006).

The plates' convergence, especially the subduction of the African lithosphere beneath the Aegean has affected the strong active deformation of the surrounding area and the Hellenic arc formation. Moreover, the strong compression in the recent convergence's zone has resulted in the generation of the **"Mediterranean Ridge",** a great Accretionary Prism which extends **south of Crete** (Figure 3). This is the fastest outward growing wedge in most recent Earth history. The rate of accretion is mirrored by enormous average outward growth rates of the M.R. up to 17.7km/my which makes it the fastest growing wedge known on earth (Kopf et al, 2003).

The intense geodynamic evolution and the corresponding stress field development have had the decisive impact on the study's area geological creation and on its active deformation associated with the faults' activation and the strong seismic activity.

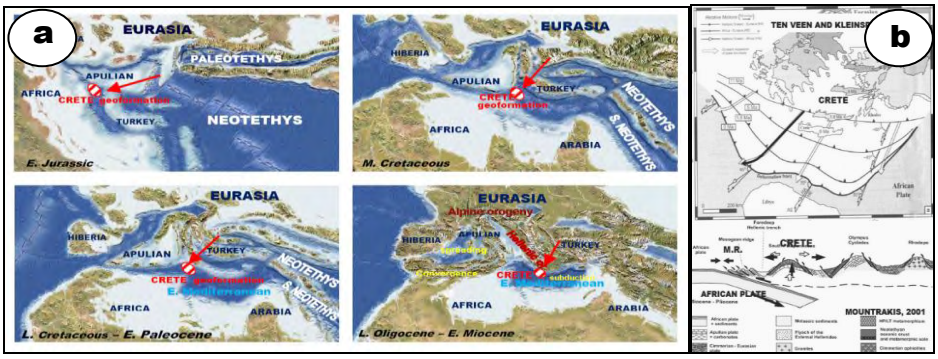

Figure 2 –a) The Mediterranean's paleogeographic evolution (Scotesse et al, 1998), whereas is depicted the progressive position of Crete's geoenvironment (Pavlaki, 2006). b) The southward migration of the convergence's limit since Miocene (Ten Veen & Kleinspehn, 2003), which gave rise to the corresponding orogenesis (Mountrakis, 2001).

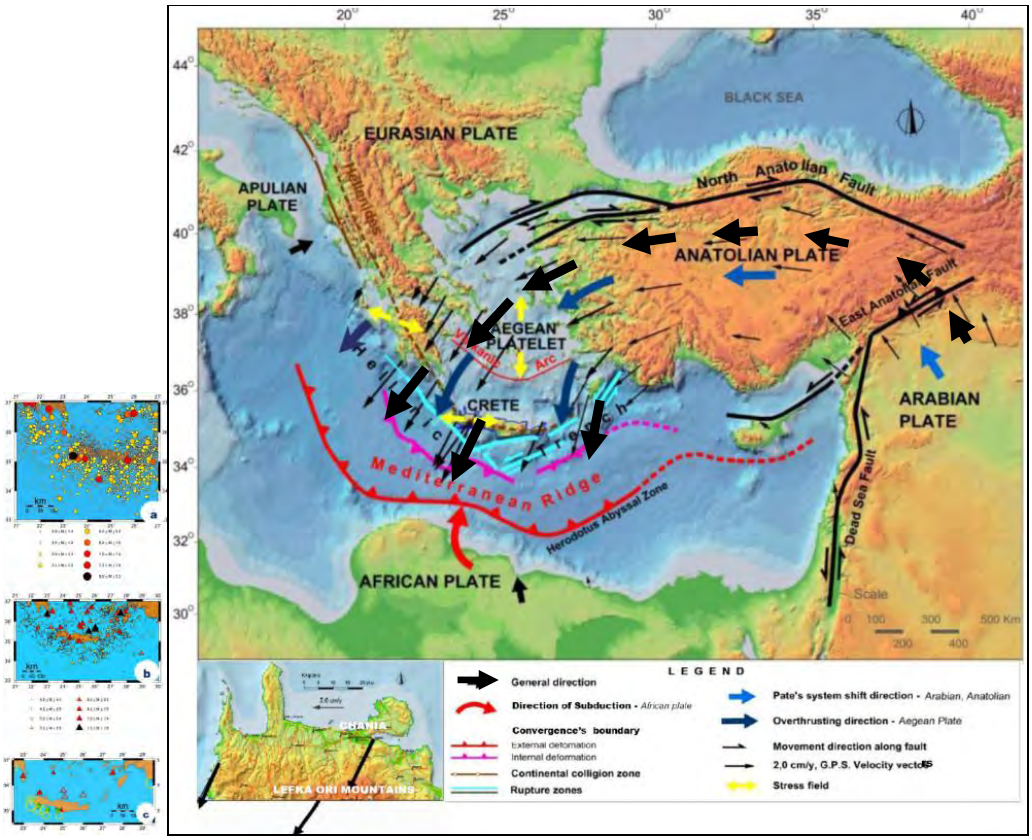

Figure 3 – The Geodynamic Regime of the surrounding Region of Crete (Pavlaki, 2006). The spatial distributions of the earthquakes' epicentres are depicted in maps: (a) shallow earthquakes (b) intermediate-depth earthquakes (c) earthquakes that caused damage (see explanations in § 3.2)

3. 2. Seismicity

The strong active geodynamic processes, especially the subduction of the eastern Mediterranean lithosphere under the Aegean plate, contributes to the study's area active tectonic deformation, associated with **intense seismic activity and strong earthquakes' incurrence** (M > 7.5). The strongest earthquake known to have been in Mediterranean, had occurred on 365 AD, M 8.3, with an estimated epicentre in the undersea area which lies SW of Crete. The earthquake which was followed by a large tsunami caused widespread damage and intensely natural disasters in the island of Crete and throughout Eastern Mediterranean (Papazachos & Papazachou 2003).

The qualitative assessment of the surrounding area's seismicity is represented on the maps of Fing.3, in which, the spatial distribution of the earthquakes' epicentres are depicted; shallow earthquakes (3-a), intermediate-depth earthquakes (3-b) (Pavlaki, 2006). The data cover the period 550BC – 2003AD and have been obtained from the list of Geophysics, Aristotle University (http:// lemnos.geo.auth.gr). As it is shown the seismic activity the relevant to the shallow earthquakes is important in the sea region which extends SW of west Crete and is closely connected (among others) with three significant undersea faults (Pavlaki 2006). The seismic activity the relevant to the intermediate-depth earthquakes is important in the NE Crete's marine area and is closely connected with the Benioff zone (part of 70-100km depths, Papazachos & Papazachou 2003).

Moreover, the spatial **epicentres'** distribution of the **AD strong earthquakes that have caused damage** in west Crete (Figure 3-c, shallow: circles, intermediate-depth: triangles), indicates that the shallow earthquakes' epicentres present the largest concentration in the marine area which is extended S-SW of west Crete, while the intermediate depths earthquakes' epicentres, concentrate in the N-NE Cretan's sea area. Furthermore, important information about the earthquakes which caused damage in the area are given in the works of Papazachos & Papazachou, 2003 and of Pavlaki, 2006 as well, in which, data from all historical records of Crete have been concentrated.

The quantitative assessment of seismic hazard in the region is presented in a recently published, specific and detailed research of Mountrakis, Kilias et al., 2012, based on an integrated approach of geological, seismological & seismotectonic data. This work provides the respective technical design values which are essential to be applied in the survey's region.

3. 3. Genesis of the Natural Geological Laboratory "Lefka Ori - Chania", within the Interactive Evolutions of the Individual Geofactors

The geological structure of west Crete is very complicated and always attracts the interest of many scientists, who in many cases have reconsidered and revised their views, as it is indicatively shown in many published works and on the geological maps of IGME as well (sheets, Chania, Alikianos, Brusses), which do not fit together. This led to the need of a new geological map's preparation, scale.1:50.000, which was based on the results of extensive and long lasting research. This map is presented in reduced in Figure 4, with the stratigraphic sequence - corresponding photos of all the geological formations. Moreover, indicative results of qualitative & quantitative analysis of the geofactors relevant to geology, tectonic and geomorphology are represented in reduced as well in the same figure. The order of the representation corresponds to the evolution's order, from bottom upwards (the yellow arrow helps by indicating the sense of the evolution or the sense of influence) and can be described as the following:

The **stress fields** which were evolved through the progressive geodynamic processes have affected the creation of the study's area **geological structure.** This is represented as a tectonic pile, which is consisting of different units' tectonic nappes, which were emplaced successively within the Alpine Orogenesis, under a generally compression regime, closely connected with the plates' convergence. During the period of **L. Oligocene - E. Miocene**, the configuration of the convergence's boundary in Crete area, had caused **the culmination of an N-S compression's regime.** This affected the extensive thrusts' evolution which was completed with the immersion of the lower nappes as a slab (Kilias et al., 1994), that included the Plattenkalk unit (Pk), the

Tripalion unit (Trip) and the Phyllites - Quartzites unit (Ph), beneath the upper plate with the upper nappes of Tripolis, Pindos etc (Figure 4, bot). We consider that during this period, in the framework of **N-S compression regime,** the origin structures of **the major F1, F2, F3, F4** zones (and other similar) were **generated** (Figure 4, geologic map), **as frontal, oblique and lateral zones of footwall ramps**, in order to enable the extensive thrusting (Pavlaki, 2006). The geometry of their topography is completely compatible with those of the thrust model according to Price & Cosgrove, 1992 (Figure 4, bot.-cent).

Within the Miocene, **the southward migration of the convergence's boundary** from the region of Crete to the Eastern Mediterranean's middle zone, led to the development of an N-S **extension regime** (in Crete region) (Figure2,3,4-bot-right), while at Pliocene-Pleistocene the direction changed to E-W extension (Mountrakis, Kilias et al., 2012). The wide extension, in combination with the pushing of the subducting African plate beneath Crete and the existence of an accretionary wedge beneath west Crete, have contributed to the **strong tectonic uplifting** (Pavlaki, 2006) and to the uncover of the lower nappes in form of **tectonic windows**. The largest of these, is the **Lefka Ori Mountains**, while we have identified a lot of smaller throughout the study area. The most striking of them is the **Malaxa** tectonic window (Figure 4) which, according to the results of our research, can be represented as an **impressive geological & tectonic miniature** of "Lefka Ori' tectonic window.

During all this evolution, the **F1, F2, F3, F4** and other similar zones have acted in a catalytic way as precious "articulated levers" that **have enabled the huge scale's uplift,** resulting in the creation of successive **normal faults series (**Figure 4**)**, the kinematic of which are the corresponding to the successively evolving stress fields. Such fault zones constitute today the borders of **the "Lefka Ori" Mountains** and **the tectonic basins.** The largest of these is the **Agia-Chania-Souda basin**, where the Neocene & Quaternary sediments have deposited from Miocene until now.

The faults and all the **tectonic discontinuities** which have been developed throughout the study area, **contribute in a catalytic way to the engineering geological conditions' formation**. Thus we proceeded to a detailed investigation regarding the discontinuities, which, according to their evolution and characteristics, can be distinguished, **as normal-oblique faults**, **thrusts-reverse faults and fracture zones** represented by long cataclasis. These discontinuities are depicted on a tectonic map sc.1:50.000, presented in miniaturization in Figure 4 (middle).

Moreover, the evaluation of the results derived from the investigations relative to the geological formations, tectonic, morphology and hydrogeology, have revealed the diversification of the geological conditions existing in the study area, that led us to divide it into **four sub-geo regions,** which are (Tec.map, Figure 4):

1. The Surrounding "Lefka Ori" Mountains Region

The mountains are **bounded** by the **F1, F4,** E-W trending **and F2, F3,** N-S trending normal faults (Figure 4, maps, photos). As we have analyzed, their geometry and morphotectonic development indicates that they had been created as deformation structures, during the thrusting events of U.Oligocene -E.Miocene. They have been reactivated in all the subsequent phases, to enable the mountains' uplift, in compatible operating way with the current stress field, acting as normal, oblique normal or tears faults. This consideration is in tune with the results of a detailed study relative to their neotectonic action of Mountrakis, Kilias et al., 2013.

The main **mountain** constitutes a **huge tectonic window** of the uncovered lower tectonic nappes, of (Pk) and (Trip), which are the dominant geological formations of the investigated area. According to the results of our extensive field research, **Plattenkalk unit** (Pk, Triassic-Eocene), appears being formed, such as in the typical published descriptions, by the development of well bedded, grey-blue, recrystallized limestones (marbles), including thin cherts' intercalations-bulbs. In the upper horizons they have being progressively evolved to thick-bedded marbles with ash-greenish calcisiltites intercalations, culminated at the top in a flysch horizon.

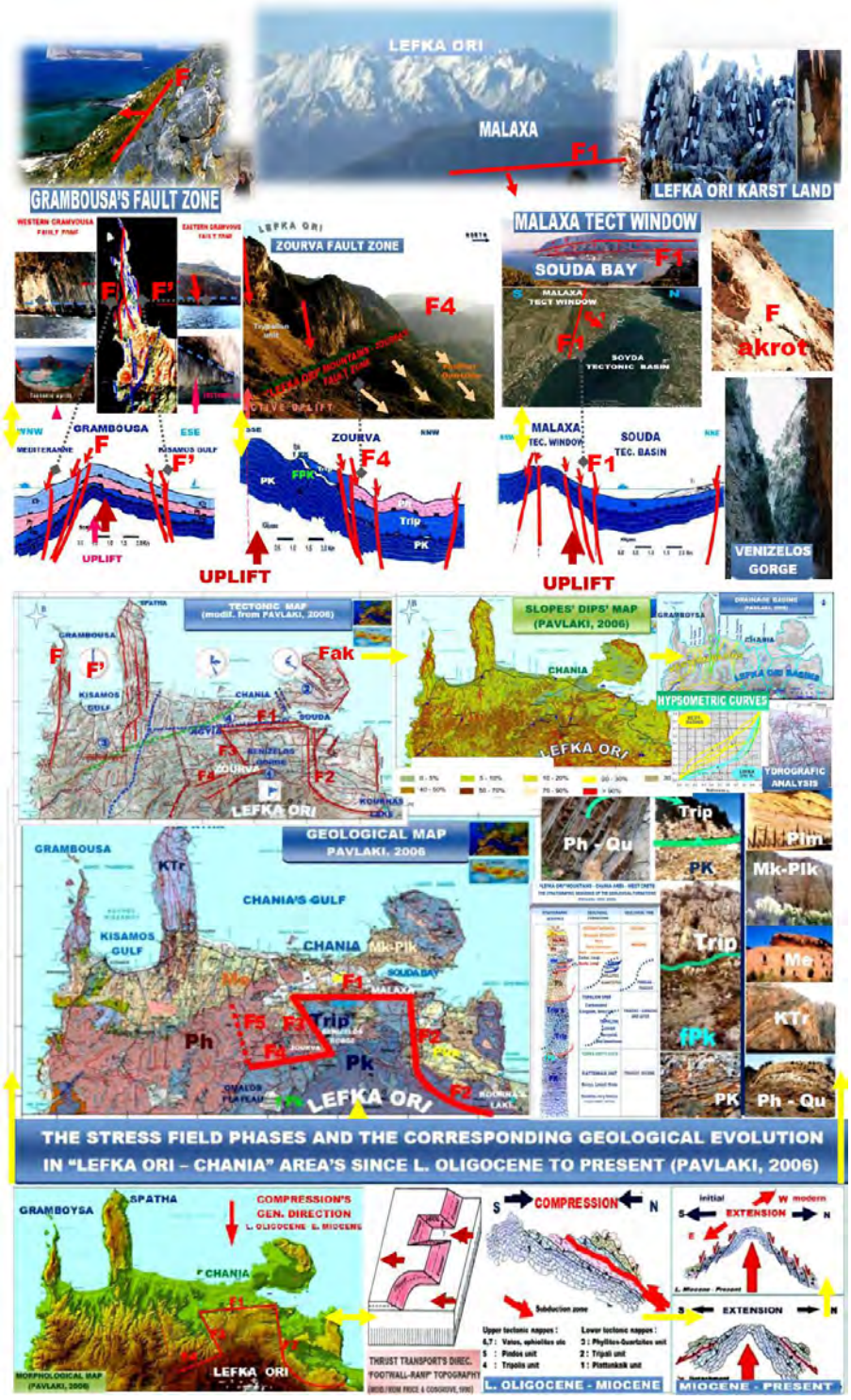

Figure 4 –"Lefka Ori - Chania" West Crete Region: Geological evolution & recent geology imprinted in: geological simulations, geothematic maps, geological structures - corresponding profiles, which represent the geologic generation (*From the bottom up wards. The yellow arrow indicates the order of the evolution or influence*).

Flysch, which was identified by Pavlaki, 2006, as the "**Lefka Ori -Plattenkalk metaflysch"(fPk),** consists of slight metamorphism's calcitic - chloritic fhyllites. It is characterized by thin developments (~2cm - 55m) and rare appearances (Lefka Ori - Gourgouthes, Omalos, Theriso). We consider that the intense tectonic thinning of flysch and its observed disintegrating behaviour have contributed to its disappearance. In some cases (in the SE area), we have observed intense effects of a strong tectonic compression, reflected in internal thrust slices, shown preferably operate on the thin calcisiltites' surfaces and which bring into contact different Pk horizons.

As we have found, **Tripalion unit** (**Trip,** Triassic - later) is clearly thrusting on the PK unit (Figure 4, photos) and includes two different and distinct lithophases (Pavlaki et al 1990, Manoutsoglou, et al., 2001); **The lower horizons** which resemble those of Pk and which are consisting of well bedded gleaming white -grey marbles, by the difference being, that they have not included cherts. These horizons evolve through lateral lithophases' transitions to **the medium-upper** and strong tectonised **horizons**. These consist of thick to unbedded and micro-medium crystalline's carbonate rocks, including white limestones, black dolomites, black cellular dolomites (dol. powder in cells) and carbonated breccia-conglomerate, the pebbles' and breccias' of which, **originate from the Pk and lower Trip** rocks. **Regarding the origin of Tripalion unit**, we estimate that it is closely connected with that of Pk unit and probably represents Pk stratigraphic sections, which during early compressive tectonic stages, have detached from their position and have moved over their own unit (preferably on the plastic behaviour's metaflysch surfaces). These operations, have given rise to intense tectonic development, which led to their fragmentation and reagglutination within various phases. A second possibility is that Trip unit has been formed in an adjacent environment to that of Pk and within a subsequent compression, was thrusted on it.

The interaction of all these developments resulted in the Lefka Ori formation as huge carbonated massif - tectonic window, which has only a few local interferences of schist or flysch.

The evaluation of the results that derived from our multi factorial survey (field research, geophysical logs, drillings, cores, pumping tests, etc) showed **the significant influence of the F1, F2, F3, F4 faults in the engineering geological conditions' formation.** The most impressive of them is the spectacular **Zourva's fault**, which dominates in the northern part of the Lefka Ori Mountains, as part of the **F4 fault zone** (Figure 4). Its particular characteristics are: **a.** The spectacular fault's slickenside formation, associated with the huge displacement of >200m. It constitutes the tectonic contact between Trip unit -limestones and Phyllites - Quartzites overthrusting unit (Ph). **b.** The strong dip faulted slopes and the corresponding steeply inclined strata, associated with the intense failure's events, such as landslides & rockslides. **c.** The impressive southern fault-block upthrown, expressed by the huge displacement which contributes to the northern Lefka Ori uplifting and at the same time to the northern fault-block downthrown. This condition has caused the corresponding lowering and northern extension of the carbonated rocks which extend underground beneath the overthrusting Ph unit, resulting in a catalytic way to the formation of significant **underground aquifers.**

In the northern part, the **significant F1 -Agyia - Malaxa - Souda- fault zone** dominates (Figure 4), which is developed by a sequence of normal faults as en echelon trending E-W to ENE–WSW. As we have determine, these faults have contributed to the **Malaxa tectonic window** formation, especially to the southern fault-block upthrown and to the **uncover of the Pk and Trip tectonic nappes** and not of Tripolis as it is shown on Igme maps and many published papers as well. Furthermore, these faults have caused the northern fault-block downthrown, resulting in the formation of the **Agyia - Souda tectonic basin.** They also have affected the Trip-carbonate rocks' underground northern extension, beneath the neocene & quaternary sediments at depth 20 - 90m, as shown the geophysical logo and drilling data. Along parts of this fault zone, a **cataclacite formation** has been developed up to 50m thickness, which, like the rest of the F1 zone contributes to the **hydrogeological & engineering geological conditions' formation.** The most impressive of

all is that the F1 zone, due to its cataclacite, which according to our research is characterized by the average permeability K of 10^{-9}m/sec, acts as a valuable natural diaphragm to the underground flows, resulting this way to the discharge of the aquifers and to the Agyia springs' formation.

According to the results of our investigations in Lefka Ori region, **the interaction of the geofactors** relative to the **geological formations**, represented by the carbonate rocks' growth, the **tectonic**, characterised by the significant discontinuities development, the strong **tectonic uplift**, (>5mm/yr, Pavlaki, 2006) and the **climate** as well, have **affected the intense Karst development,** characterized by extending exokarst and endokarst formations, including a famous variety of karst structures such as pinnacles, dolines, poljes, caves, sinkholes, underground aquifers etc.

2. The Western part of the study region, includes the entire western area and it is characterized by the creation of significant B-N and NE-SW trending normal fault zones, which are considered to be active (in the aforementioned neotectonic study). According to our morphological quantitative analysis, these active fault zones contribute to the regeneration of the western drainage basins and to the western coasts formation as well (photo Grambousa, profile, Figure 4).

3. The Chania's Akrotirion (NE part of the study region) is dominated by long NW - SE trending normal faults, which are characterized by a sequential action. In the centre of this area an extensive surface leveling has been developed.

4. The northern – central part of the study area, includes the Chania - Agia- Souda tectonic basin, in which, the sediments of Neocene and Quaternary have been deposited. In this area, as we have determined, normal faults, which are characterized by small displacements and NNE-SSW & NW-SE directions, have been developed. The major tectonic structure is the **Venizelos** NW-SE trending normal **fault zone**, which contributes to the Chania's eastern tectonic slopes' formation.

Finally, the results of quantitative analysis of all the geofactors throughout the region under survey are given in the geothematic maps & the representative shapes of Figures 4 & 5.The main points which indicate **the contribution of the interaction of these geofactors** in the individual geological and engineering geologic conditions' formation can be summarized in the following:

1. Following the assessment of the qualitative and quantitative analysis of the morphological relief, drainage basins, hydrographic network and the one of the active faults, a tectonic uplift /erosion mechanism has been identified as the major controlling factor of the geomorphological evolution of the area. The interpretation of the previous data-analysis indicated that the drainage basins are characterized by distinct differentiations relevant to their evolution, according to which they were classified in **two main units**, the Eastern and the Western one (Figure 4). **The Eastern Drainage-Basins "Lefka Ori Mountains (2.454m)"** are characterized by a long uplifting history and continuous erosional process at the limestone Mountains which were upfaulted as tectonic horst through successive tectonic uplift episodes. On the other hand, **the Western Drainage-Basins** are younger than the Eastern as the data analysis results have shown and they have been uplifted later. What is impressive is that their formation is linked to the west-ward migration of fault activity towards the active faulting coasts of western-Crete. As the tectonic and hydrographic analyses have shown, the drainage system development reflects the active tectonic deformation.

2. The modern E-W trending stress field contributes to the configuration of many processes & geostructures, especially to the reactivation of the neotectonic faults, to the N-S trending gorges' formation and to the underground water flows along the N-S compatible faults.

3. Large fault zones influence the formation of strong slope slips associated with failures events, the degradation of rockmass quality and the underground water flows.

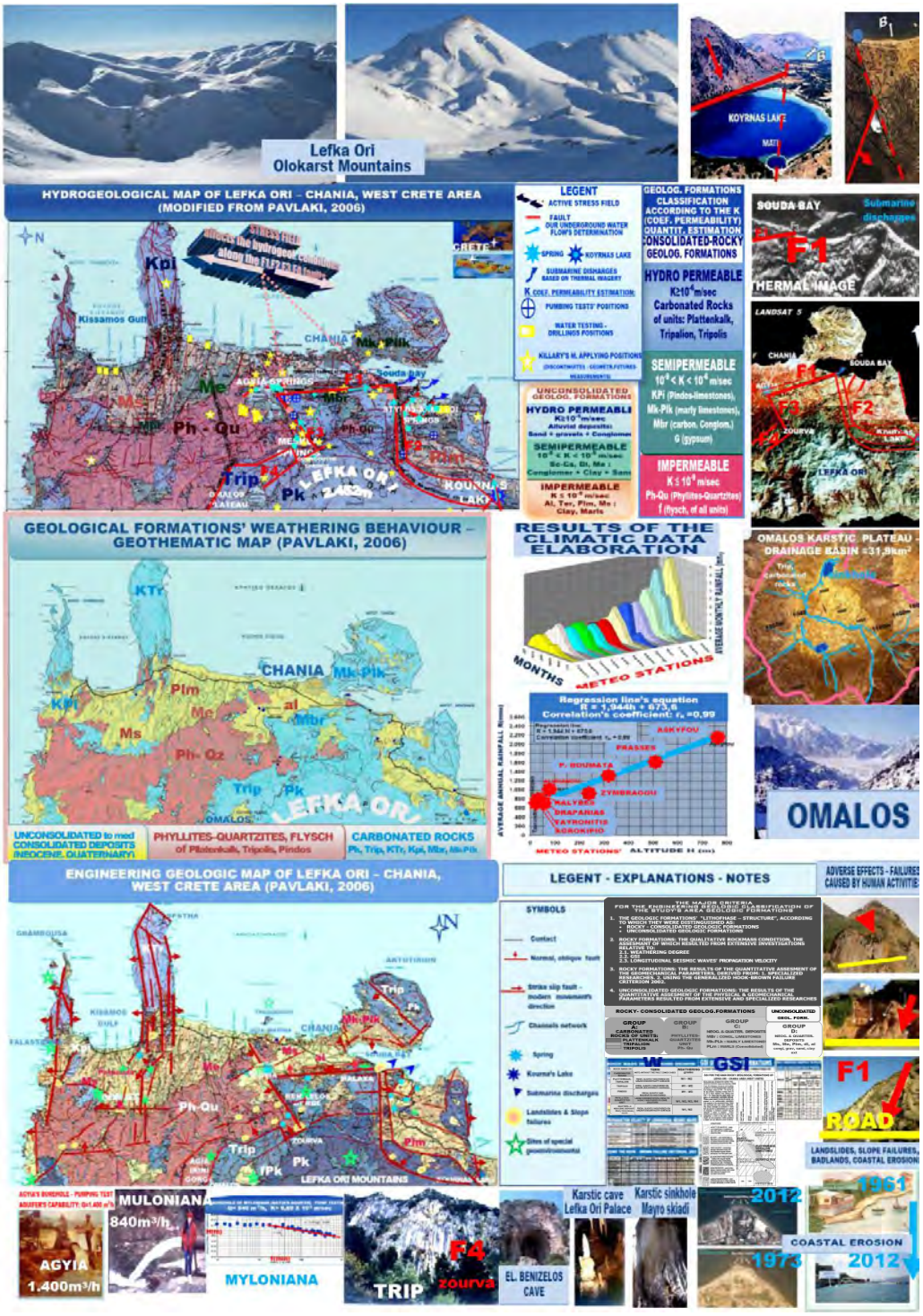

Figure 5 –"Lefka Ori - Chania" Western Crete Region: The results of the qualitative & quantitative analysis of the individual geofactors relative to hydrogeology, climate, erosion, and geomechanical properties of all the geological formations, depicted in geothematic maps, diagrams and photos. The significant adverse effects by human activities are shown as well.

4. Geofactors Interaction Matrix

In order to create a graphical representation of the geofactors' interaction, we used "Hudson's first Matrix" (1992) as a framework and in addition we expanded its implementation to the engineering geological conditions existing in an extensive region. This led to the creation of the "Lefka Ori" Western Crete **GFIM** (**G**eo**F**actors **I**nteraction **M**atrix), which is presented in Figure 6. In this matrix where the main geofactors have been defined (1-8), the impacts & the corresponding effects of each geofactor are described.

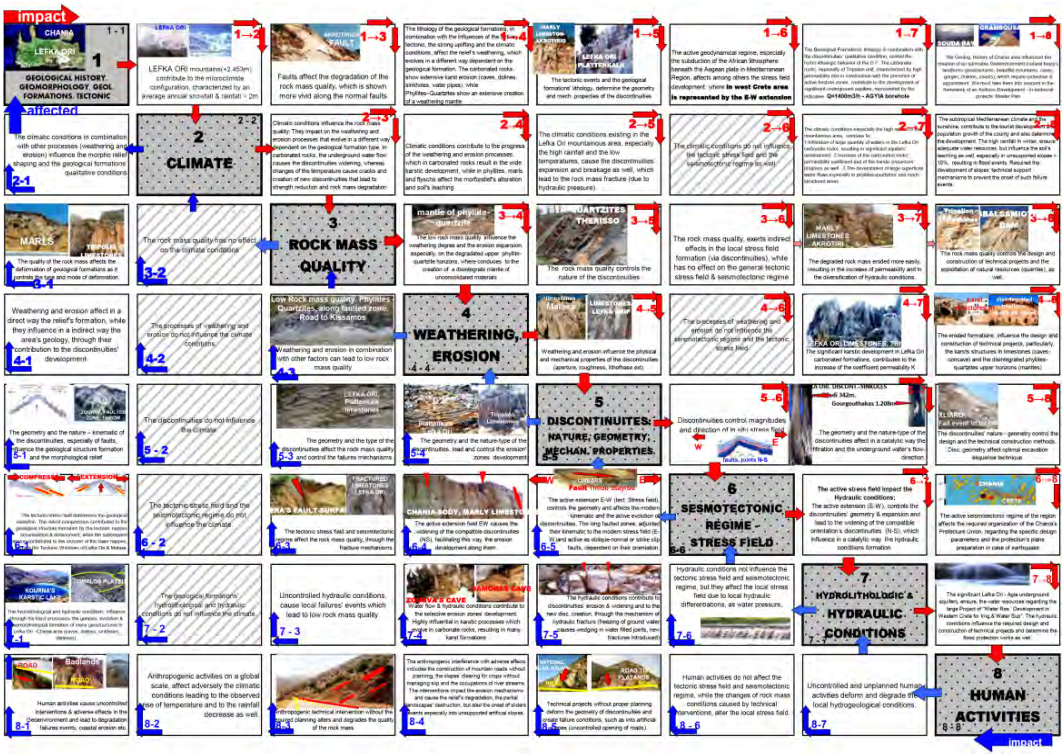

Figure 6– The Geofactors Interaction Matrix of the Lefka Ori – Chania Geoenvironment, based on the "the Hudson's first Matrix" (1992), by expanded and adapted its implementation to the engineering geological conditions existing in the investigated area.

5. Conclusions

The results of extensive and long-lasting investigations on various geofactors in the "Lefka Ori - Chania" W.Crete region revealed the major role of their interaction in the engineering geological conditions' formation. They also prove that these geofactors are the product of parallel progressive and interactive evolutions in an environment dominated by an active geodynamic regime, where the corresponding stress field affects in a catalytic way to many geo-developments.

Besides this, a great number of striking geo-structures have been revealed, characterizing the investigated area of "Lefka Ori - Chania", as a globally unique Natural Geological Laboratory.

The GeoFactors' Interaction is represented graphically on a Matrix form creation, called then "Lefka Ori Western Crete GFIM", which can serve us, as a useful scientific tool, for the investigated area's engineering geological conditions' recognition.

6. Acknowledgments

The work described in this paper is the product of a long series of investigations that have been self-funded. We thank Prof. **A. Kilias and D. Mountrakis** for their reviews as well as for their ongoing mentorship both professionally & scientifically throughout the years.
We heartfelt thank **Rebecca Pavlaki** for her relentless support throughout the years, because without her precious assistance this work would have never been realized. Moreover we want to heartfelt thank **Pauline Goumenaki** for her valuable support and **Gina Pavlaki** for her significant assistance. We would like to thank **Mr. Manoutsoglou** for his significant support & enduring patience. Also we would like to thank **Terry Stratoudakis** for his precious support. We thank **Ch. Riziotis** and **J. Antonopoulos** for their helpful scientific discussion throughout the years.

7. References

Hudson J.A., 1992. Rock engineering systems. Theory & Practice. *E. Horwood, Great Britain* p185.

Kilias A., Fassoulas Ch. and Mountrakis D. 1994. Tertiary extension of continental crust and uplift of Psiloritis metamorphic core complex, in the central part of the Hellenic arc (Crete, Greece*, Geol. Rdsch,* 83*,* 417-430.

Κίλιας Α. 2001. Βραδυ-ορογενετική έκταση στις Ελληνίδες οροσειρές, *Πρακτ. 9ου Διεθν. Συνεδρ. Ελλην. Γεωλ. Εταιρ.,* Αθήνα, Δελτ., Τομ. XXXIV/1, 149-156.

Knapmeyer M. and Harjes H-P. 2000. Imaging crystal discontinuities and the down going slab beneath western Crete, *Geophys. J. Int.,* 143, 1-21.

Kopf A., Mascle J. and Klaeschen D. 2003. The Mediterranean Ridge: A mass balance across the fastest growing accretionary complex on Earth, *Journal of Geophys. Research,* Vol. 108, No B8, 2372, doi:10.1029/2001JB000473.

Μανούτσογλου Ε., Σπυρίδωνος Ε., Soujon A. and Jacobshagen V. 2001. Αναθεώρηση του Γεωλογικού χάρτη και τρισδιάστατη προσομοίωση της γεωλογικής δομής της ευρύτερης περιοχής του φαραγγιού της Σαμαριάς, Δ. Κρήτη, *Πρακτ. 9ου Διεθν. Συνεδρ. Ελλην. Γεωλ. Εταιρ.,* Αθήνα, Δελτ., Τομ. XXXIV/1, 29-36.

Μελαδιώτης Ι., Παυλάκης Π., Δεμίρης Κ., και Δερμίσης Β. 1993. Εντοπισμός υποθαλάσσιων εκφορτίσεων γλυκών νερών στο βόρειο τμήμα της Δυτικής Κρήτης με τη βοήθεια τηλεκαταγραφών, *Μεταλ. Χρονικά, Τομ. 3(4), 75 -87.*

Μουντράκης Δ. 2001. Τεκτονική εξέλιξη του Ελληνικού Ορογενούς. Γεωμετρία και κινηματική της παραμόρφωσης, *Πρακτ. 9ου Διεθν. Συνεδρ. Ελλην. Γεωλ. Εταιρ.,* Αθήνα. Δελτ., Τομ. XXXIV/6, 2113-2126.

Mountrakis D., Kilias A., Pavlaki Aik., Fassoulas Ch., Thomaidou E., Papazachos C., Papaioannou Ch. and Roumelioti Z. 2012. Neotectonic study of Western Crete and implications for seismic hazard assessment, *Journal of the Virtual Explorer*, Electronic Edition, ISSN 1441-8142, volume 42, paper 2.

Παπαζάχος Β.Κ. και Παπαζάχου Κ.Β. 2003. Οι σεισμοί της Ελλάδας, *Εκδόσεις Ζήτη*, *γ΄ έκδοση,* Θεσσαλονίκη, σελ. 286.

Παυλάκη Αικ. 2006. Τεχνικές Γεωλογικές Συνθήκες στο Νομό Χανίων, *Διδακτορική Διατριβή, Πολυτεχνική Σχολή Αριστοτελείου Πανεπιστημίου Θεσσαλονίκης,* σελ. 540.

Παυλάκης, Π., 1989. Συμβολή στην υδρογεωλογική διερεύνηση του ασβεστολιθικού υδροφόρου συστήματος των πηγών Αγυιάς Δυτικής Κρήτης. *Διδακτορική Διατριβή, Πολυτεχνική Σχολή Αριστοτελείου Πανεπιστημίου Θεσσαλονίκης*, σελ 130.

Price N.J. and Gosgrove J.W. 1991. Analysis of Geological Structures, *University of Cambridge.* Prnt. In Great Britain, Univ. Press, pp 502.

Scotesse C.R. et al. 1998. Sedimentation, Tectonics and Paleogeography of Southern Europe and the Mediterranean Region, availiable at: http://jan.ucc.nau.edu/~rcb7/globaltext.html

Ten Veen J.H. and Kleispehn K.L. 2003. Incipient continental collision and plate-boundary curvature: Late Pliocene -Holocene transtensional Hellenic forearc, Crete, Greece, *Journal of the Geological Society,* London, Vol. 160, 161-181.

Δελτίο της Ελληνικής Γεωλογικής Εταιρίας, τομ. XLVII , 2013
Πρακτικά 13ου Διεθνούς Συνεδρίου, Χανιά, Σεπτ. 2013

Bulletin of the Geological Society of Greece, vol. XLVII 2013
Proceedings of the 13th International Congress, Chania, Sept. 2013

DIGITAL METHODS FOR MEASURING GRAIN SIZE PARAMETERS OF AGGREGATE–BINDER MIXTURES

Profitis E.[1], Kapatos D.[1], Chatzitheodoridis E.[1], Xirouchakis D.[2] and Loupasakis C.[1]

[1]N.T.U.A., School of Mining and Metallurgical Engineering, Athens, Greece

[2]GeoTerra Ltd, 12 Anthrakorichon Str, Nea Ionia 142 35

Abstract

Geometrical parameters of natural and crushed aggregates such as grain length, perimeter, area, etc., underline the shape and flakiness indices definition. The latter indices have a measurable effect on the mechanical properties of aggregates–binder mixtures, e.g. concrete, mortar, bituminous mixtures. In this work, digital methods were developed with the mathematical software Matlab, by applying a statistical method called k-means clustering for the exact separation between background and aggregates to compute the aforementioned properties. The overall code can be applied in real time by analysing quickly a large volume of data with accuracy and significant cost reduction. Currently, only the two dimensions of the grains could be measured. Future work will focus on full three-dimensional measurements by comparing paired images taken from different angles but also aggregate segmentation in case of touching particles.
Key words: *aggregates, shape, flakiness, Matlab.*

Περίληψη

Οι γεωμετρικές παράμετροι χαλικιών, όπως μήκος, περίμετρος, εμβαδόν κλπ., υποδεικνύουν τους δείκτες πλακοειδούς και σχήματος. Αυτοί οι δείκτες έχουν μια σημαντική επίδραση στις μηχανικές ιδιότητες αυτών ως αδρανή υλικά π.χ. στο σκυρόδεμα, το ασβεστοκονίαμα, την άσφαλτο. Στην παρούσα εργασία παρουσιάζονται ψηφιακές μέθοδοι βασισμένες στο μαθηματικό πακέτο Matlab. Εφαρμόστηκε η στατιστική μέθοδος k-means clustering, για τον ακριβή διαχωρισμό φόντου και χαλικιών και με στόχο τον υπολογισμό των προαναφερθέντων ιδιοτήτων. Ο συνολικός κώδικας μπορεί να εφαρμοστεί σε πραγματικό χρόνο αναλύοντας γρήγορα έναν μεγάλο όγκο δεδομένων με μεγάλη ακρίβεια και με σημαντική μείωση του κόστους. Επί του παρόντος μπορούν να μετρηθούν μόνο οι δύο διαστάσεις των κόκκων. Μελλοντική εργασία θα εστιάσει σε τρισδιάστατες μετρήσεις συγκρίνοντας ζεύγη εικόνων που θα παρθούν από διαφορετικές γωνίες αλλά επίσης και διαχωρισμός κόκκων που ακουμπούν μεταξύ τους.
Λέξεις κλειδιά: *χαλίκια, σχήμα, πλακοειδές, Matlab.*

1. Introduction

Limestone aggregates are the major component of hydraulic and asphalt concrete. Aggregate industry requires a precise and reproducible method for measuring their most significant

geometrical properties, such as maximum and minimum length, area, and perimeter, as well as other composite properties, such as degree of compaction, circularity, flakiness and elongation index. These parameters affect the packing density of mixtures and consequently the mechanical properties of them as aggregates.

The geometrical properties of aggregates are key parameters for concrete quality, because mechanical properties depend on aggregates and cement paste. Particularity, when the proportion of flat particles is increased, the compressive strength, and workability decrease (Frazao et all, 984). In addition, the use of rounded and smoothed particles increases the workability of concrete. Size distribution of aggregates is also important because it determines the paste's requirements for a workable concrete. Furthermore, the above-mentioned requirements control the construction cost, because cement is the most expensive component and its optimal volume, or mass should be reduced by increasing the mixture packing density. The required amount of cement is dependent upon the amount of void space that must be filled and the total surface area that must be covered. When particles are of uniform size the spacing is the greatest, but when a range of sizes is used, the void spaces are reduced and the paste requirement is lowered.

It is evident that methods for characterising the size and the shape of aggregates are necessary. Currently, the assessment of aggregate geometrical properties is carried out by manual methods, such as sieving, including bar sieving for defining their elongation and Danish-box or callipers. Sieving methods are very time consuming and may involve larger statistical errors because of the small sampling volume or because of untrained personnel. In addition various digital methods for 2D (Profitis et al, 2011) but also for 3D (Kim et al, 2003, Fernlund, 2004, Tafesse et al, 2012) aggregate characterization have been used, by using either a digital camera or a laser or even both. Digital methods are expected to be faster, more accurate, also providing more geometrical information while minimizing statistical errors. When automated, they do not require any trained personnel and can be performed in real time.

The performance of digital methods has been investigated by using image processing and by comparing the results with conventional laboratory techniques, such as sieving. For the demonstration of the method limestone aggregates taken from an active limestone quarry in Greece were used.

2. Materials and Methods

2.1. Materials

A representative sample of limestone aggregates was acquired and dried at 110 ± 5 °C. The sample was sieved into different fractions with square sieves according to the EN 933-3:1997/A1:2003 standard test method. Aggregate grains below 4 mm were discarded. Bar sieves were also used to separate the resulting fractions according to their flakiness ($d < {}^1/_2D$, where d and D are the smallest and largest dimension of the grains) in order to define the flakiness index. The bar sieves have the following Di/2 openings in mm: 40, 31.5, 25, 20, 16, 12.5, 10, 8, 6.3, 5, 4, 3.15 and 2.5. Elongation was finally measured with a calliper by measuring the maximum length of the grain and comparing to the minimum. If the minimum dimension (d) was less than 1/3 of the maximum dimension of the grain (D), then grains were characterised as non-cubic, whereas the rest were characterised as cubic. The original total mass of the aggregate sample was 19 kg. The laboratory measurements using sieves and calliper are shown in Table 1.
Pictures were acquired with a rock photography table, stabilising a 6 Mpixel colour camera on a vertical post at a distance of 30 cm. The table is ruled to allow scaling of the images. Ambient diffuse light was used for photography. Images were processed using the Matlab mathematical package, using a custom-made image-processing routines.The algorithm consists of two parts, the first one implements segmentation between the background and the foreground by applying k-means clustering and the second part automatically calculates their most important geometrical properties

measured in pixels. This results to the derivation of a series of important parameters, such as circularity, compactness, elongation and sphericity, shape and form definition. The results are from binary images.

Table 1 - Results of laboratory measurements with sieves and flakiness index calculation.

SQUARE SIEVES				BAR SIEVES			FLAKI NESS
Di (mm)	**di (mm)**	**Fraction di/Di**	**Fraction di/Di**	**Di/2 (mm)**	**Mass of passing fraction mi (g)**	**Mass of passing fraction mi (%)**	**Fli 100*(mi/ Ri) %**
		Ri (g)	**Ri (%)**				
80	63	0.00	*0.00*	40	0.00	*0.00*	0
63	50	227.13	*1.20*	31.5	0.00	*0.00*	0
50	40	566.86	*2.98*	25	0.00	*0.00*	0
40	31.5	1388.70	*7.31*	20	158.30	*11.19*	11.40
31.5	25	1697.50	*8.93*	16	200.80	*14.19*	11.83
25	20	1650.20	*8.69*	12.5	166.00	*11.73*	10.06
20	16	1738.50	*9.15*	10	105.20	*7.44*	6.05
16	12.5	1852.10	*9.75*	8	195.85	*13.84*	10.57
12.5	10	1067.00	*5.62*	6.3	116.90	*8.26*	10.96
10	8	1149.60	*6.05*	5	112.90	*7.98*	9.82
8	6.3	1059.20	*5.57*	4	111.00	*7.85*	10.48
6.3	5	781.10	*4.11*	3.15	68.76	*4.86*	8.80
5	4	1191.40	*6.27*	2.5	179.03	*12.65*	15.03
Original Total (g):		19000.00	75.63			100.00	
M1 (Σri) =		**14369.29**		**M2 (Σmi) = 1414.74**			
Fl = (M2/M1)*100= 9.84							

2.2. Methods

2.2.1. Aggregate Size

Aggregate size is often a matter of debate. Because aggregates are shown as two-dimensional images, the length and width represent their size. There are various ways of defining these two axes; the most common are the following:

1. The maximum distance between two points on the perimeter of the grain represents the length, whereas the width is the maximum distance perpendicular to the length (Figure 1a).
2. The dimensions of the smallest rectangle that can be fitted around the grain (Figure 1b). This method is applied when the Danish-box is used.
3. The dimensions of the best-fitted ellipse of the grain. The ellipse should have the same area with the grain.

Sometimes the length and the width are not related to each other. For example, one could take the length as in the first case and the width as in the second case, or just the first case for both (Fernlund et al., 2007). The third case is often used to define the orientation of the grain rather than its dimensions.

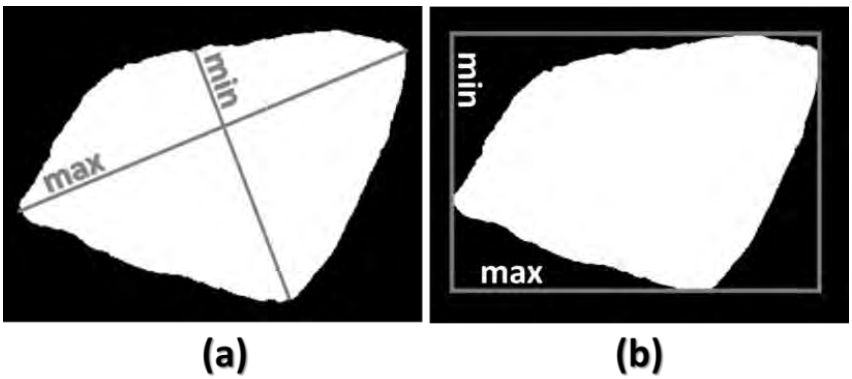

Figure 1 - Maximum (length) and minimum (width) distances as defined in the first two cases.

2.2.2. Shape Characterization

Objects can be categorised in a variety of shapes, or how close to a shape they may look like. Shape is determined by calculating the ratios between various primary dimensions and comparing them to standard shapes (Dunlop,H., 2006). Simple geometrical shapes, such as circle and square, have standard values given in Table 2.

Shape can be divided in three categories: form, roundness, and texture. Here, the first category was examined. Form describes the overall shape, for example, how close to a sphere it is. The following formula scan is used in this task:

- Riley sphericity is defined as: $\text{Riley sphericity} = \sqrt{\frac{d_i}{d_c}}$

where d_i is the diameter of the largest inscribed circle and d_c is the diameter of the smallest circumscribed circle (Figure 3).

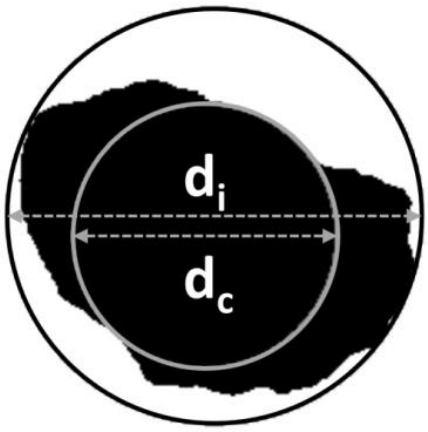

Figure 3 - Circumscribed (black) and inscribed (grey) circle of an object used to define Riley sphericity.

- Elongation is defined as the ratio of the major (M) and the minor (m) length of the object. It is important to mention which of the three cases defined above for maximum length are chosen: $\text{Elongation} = \frac{m}{M}$
- Compactness is defined as $\frac{\sqrt{\text{Area}}}{\text{Perimeter}}$
- Circularity is defined as $\frac{\text{Perimeter}^2}{4\pi * \text{Area}}$

Table 2 - Standard values of different specific shapes.

	Circle	Square	Rectangle
Riley sphericity	1	$\sqrt{2}/2$	$<\sqrt{2}/2$
Elongation	1	1	<1
Compactness	$\sqrt{\pi}/2\pi$	0.25	<0.25
Circularity	1	$4/\pi$	$>4/\pi$

2.2.3. Aggregate measurements via conventional laboratory methods

Conventional laboratory methods for measuring the geometrical properties of aggregates include sieving. In addition, bar sieving is applied to evaluate the elongation of coarse aggregates (gravel). The major disadvantage of this method is that it does not measure the axial dimensions of particles and the results are dependent on the particle's shape (Fernlund et al., 2007). Finally, each particle is measured by hand, with the use of Danish-box or calliper. These methods are time-consuming and the particles that have to be measured are quite small, generally over 200 particles per sample. To distinguish the sieving methods from the digital methods, from now on the notation "analogue sieves" for the conventional laboratory sieves and "digital sieves" for the filters made by using the computer algorithms is introduced.

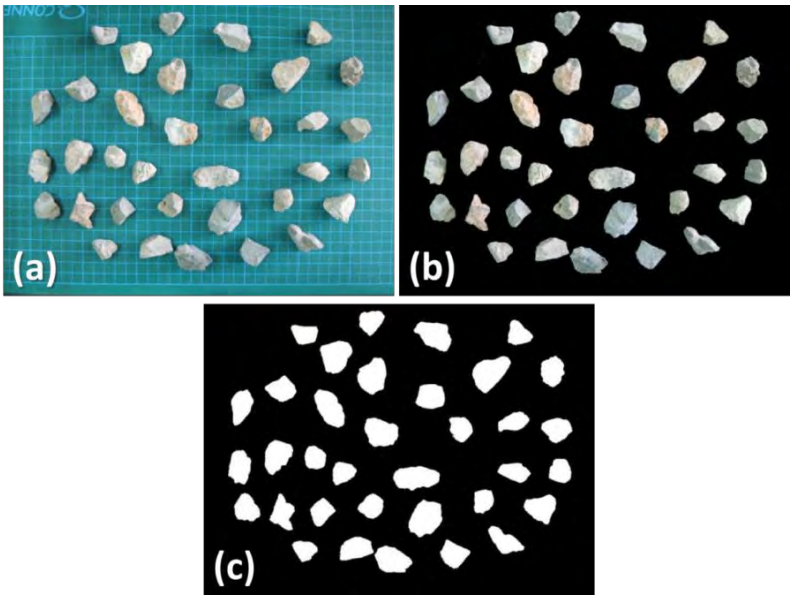

Figure 4 - (a) Original image of aggregates; (b) segmentation between the background and the aggregates; (c) binary image.

2.2.4. Aggregate Measurements via Digital Methods

Digital methods provide measurement of a particle's properties in two dimensions through image processing. The methodology generally depends on the quality and the type of the image and the final purpose of the study. The algorithm must be produced so that any statistical errors minimize and maximize the precision of the results. The whole algorithm consists of two parts. The first one implements segmentation between background and foreground by applying k-means clustering. The segmentation depends on the colour of the object and thus regions with the same colour and/or brightness are plotted separately compared to regions with different colour and/or brightness (Figure 4a-b). The second part consists of the automated calculation of their most important geometrical properties, such as maximum–minimum length, the area and the perimeter, leading to a series of important parameters, such as circularity, compactness, elongation and sphericity, shape and form definition. Finally, the results are derived from binary images (Figure 4c).

3. Results and Discussion

3.1. Reproducibility of Digital Measurements

The assumption that a grain thrown on a flat surface will lay on its flattest surface was tested by performing ten repetitive random throws of certain aggregate clusters. The variances were calculated and compared with analysis of variance (ANOVA). Consequently, the null hypothesis is that the ten throws are similar. When the alpha value is 0.05, the possibility for the null hypothesis to be true is very high, while the F-values stay very low compared to the F-critical value. The test is performed for two different fractions of cubic aggregates and one for non-cubic aggregates (Table 3). Consequently, when either cubic or non-cubic aggregates are thrown and digitally processed for calculating their sizes, the standard error remains low; therefore measurements resulting from image processing are reproducible within approximately 5%. For comparison, the studied aggregates are also separated with analogue sieves.

A second test involved the investigation of the significance of overlapping grains in estimating the geometrical parameters of interest. To perform this test, an aggregate was randomly thrown and photographed and then rearranged so that there is no overlap between grains, photographed again and compared to the first throw. Overlapping results in decreasing the size of a number of grains, or the wrong estimation of the margins of overlapping grains. It is therefore expected that overestimations of one grain against another can occur, increasing the error. For this purpose, three aggregates were used and tested for cubic grains of different sizes and grains of the same size, but one is cubic and the other is non-cubic. As in all tests, the fractions used are made of aggregates separated with analogue sieves.

Table 3 - Results of the reproducibility test of digital measurement.

		45–31,5 Cubic	**22,4–16 Cubic**	**16-11,2 non-Cubic**
Length (max dimension)	P-value	0.9994	0.9999	0.9999
	Mean ± SE (*% SE*)	54.51 ± 3.00 (*5.50%*)	27.49 ± 0.78 (*2.85%*)	24.45 ± 0.74 (*3.01%*)
Width (min dimension)	P-value of width	0.9983	0.9787	0.8866
	Mean ± SE (*% SE*)	44.96 ±1.97 (*4.38%*)	21.83 ± 0.50 (*2.28%*)	18.33 ± 0.51 (*2.76%*)

SE=Standard Error, P-Value =Probability Value

Table 4 - Results of grain overlapping tests.

	31.5–22.4 Cubic	16–11.2 Cubic	16–11.2 non-Cubic
Length			
Oriented Mean ±Variance (cm)	4.1377 ± 0.6963	2.0179 ± 0.1650	2.2989 ± 0.2275
Random Mean ±Variance (cm)	4.1616 ± 0.7593	2.1222 ± 0.1964	2.3854 ± 0.1992
t	−0.1359	−2.7696	−0.8054
P(T<=t)	0.8922	0.0058	0.4232
t critical, two-sided	1.9861	1.9646	1.9935
Width			
Oriented Mean ±Variance (cm)	3.3342 ± 0.3159	1.6437 ± 0.0563	1.8298 ± 0.0774
Random Mean ± Variance (cm)	3.3036 ± 0.3174	1.7576 ± 0.0751	1.9578 ± 0.1027
t	0.2637	−5.0150	−1.8353
P(T≤t)	0.7926	0.000001	0.0706
t critical, two-sided	1.9861	1.9646	1.9935

To compare between the oriented and random cases, the t-Students statistical test was used and the results are shown in Table 4. From the results, it is made clear that cubic aggregates of large size (31.5–22.4 mm) are less prone to errors due to overlapping and an acceptable separation is performed by using digital methods (e.g., it is highly probable that the two cases, oriented and random, have the same mean and variance). However, this similarity is lost in aggregates of smaller fractions (16–11.2 mm), which show probabilities much less than the alpha value (0.05), therefore the null hypothesis is rejected. It is interesting though to mention that the small-size, non-cubic aggregates show slightly higher possibilities of being similar, possibly because since they are flaky they tend to lay on a preferred orientation and with distinct distribution. It is possible that the problem can be overcome by photographing aggregates with smaller number of grains that are additionally separated by vibrating the photography board, while also using higher resolution photo cameras.

3.2. Digital Sieving

Digital methods can be used to readily estimate the geometrical and shape parameters of aggregate grains. However, because these are measured from two-dimensional images, the third dimension is lost, which in a way it is sensed by the analogue sieves. Here, it is investigated how digital sieves compare with the analogue sieves. This is performed by counting the number of grains that are retained in each sieve, either analogue in the lab, or digital when filtering is performed through computer algorithms. The results are shown in Table 5 and graphically in Figure 5. Digital sieving seems to retain more grains in the consecutive larger in opening sieves, compared to the analogue sieves. In addition, it is observed that the digital histograms present a more structured distribution, with positive anomalies in the middle size sieves, compared to the smoother distributions of the analogue sieves. This observation is more pronounced in the cubic aggregates but less in the non-cubic ones. There is no easy explanation why this occurs; except maybe that, the analogue sieves

allow the grains to rotate as they go through them compared to the static grains of the digital sieves. The third dimension that is missing from the digital sieves should not be a reason for that, because only one dimension is responsible for retaining a grain to a certain sieve. It is suggested that for quality control during industrial applications the information provided by the digital processing is more useful, because it describes the general shape of the grain.

Table 5 - Comparison between analogue and digital sieving.

Sieves		Analogue sieves			Digital sieves		
Di	**di**	**Number of cubic grains (M1)**	**Number of non-cubic grains (M2)**	**TOTAL (M1+M2)**	**Number of cubic grains (M1)**	**Number of non-cubic grains (M2)**	**TOTAL (M1+M2)**
63	**45**	0	0	**0**	10	1	**11**
45	**31.5**	18	0	**18**	42	11	**53**
31.5	**22.4**	47	9	**56**	77	14	**91**
22.4	**16**	121	15	**136**	242	38	**280**
16	**11.2**	255	37	**292**	453	93	**546**
11.2	**8**	438	96	**534**	408	122	**530**
8	**5.6**	1231	226	**1457**	1716	304	**2020**
5.6	**4**	2605	325	**2930**	1680	120	**1800**
4	**0**	0	0	**0**	87	5	**92**
Sum		**4715**	**708**	**5423**	**4715**	**708**	**5423**

Using the measurements, an effort was made to surpass the lack of the third dimension of each grain with statistical methods. A t-Students test between cubic and non-cubic grains of at least two sizes that we tested resulted in significantly different distributions. Despite this, it was difficult at this stage to precisely estimate the parameters of these two distributions from the distribution of the total sample, in order to predict the number of grains contributing to cubic and non-cubic grain fractions.

3.3. Shape Parameters Acquired with Digital Methods

Shape parameters such as sphericity, elongation, compactness and circularity, as defined in the previous paragraph of this paper, are easily acquired using digital methods. Table 6 demonstrates this, while it also demonstrates that between different size fractions the shapes remain quite similar. Different fractions were tested for similarity with the t-Students test using different combinations if the measured geometrical parameters, such as sphericity; the results seem to vary. However, it is easy to conclude that sphericity values are generally very close to 0.707, which characterises all fractions as cubic, which is true since the fractions belong to the cubic laboratory separate. Similarly, elongation is close to unity as expected for circular cubic grains. Compactness seems to be between cubic and rectangular, whereas circularity values indicate rectangular shapes but not far from cubic.

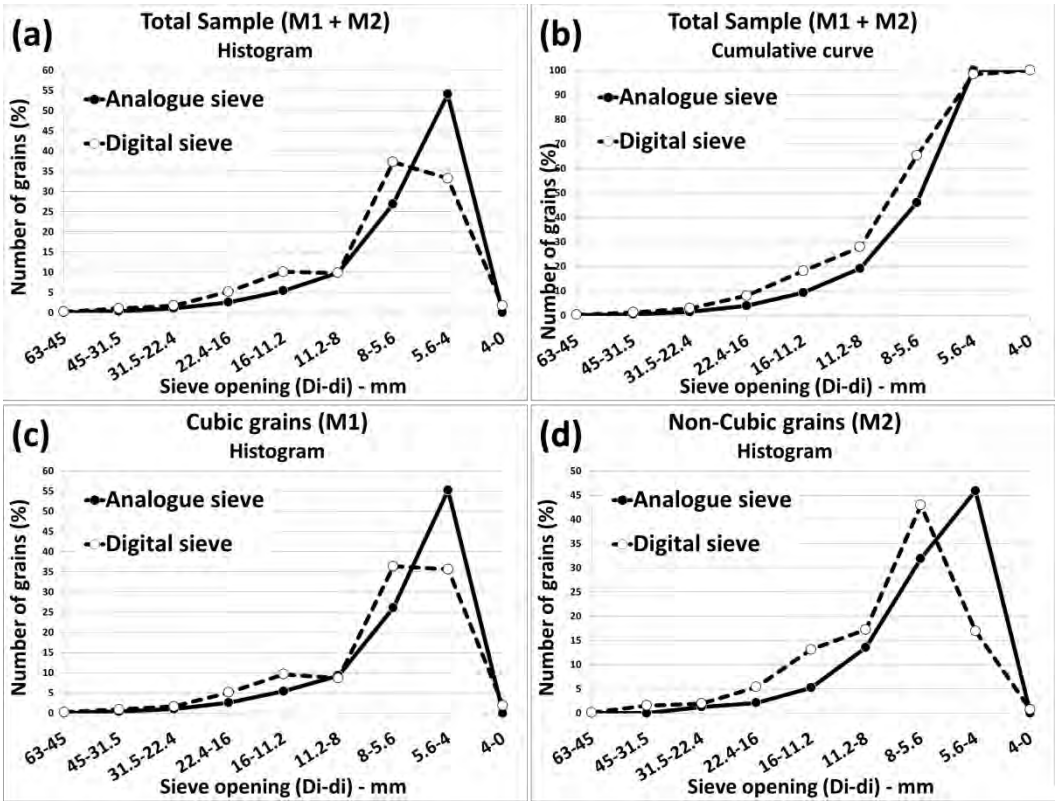

Figure 5 - Allocation of the retained grains (% of number of grains) for analogue (continuous line) and for digital (broken line) sieves, histogram (a) and cumulative (b) plots. Similar histogram plots for cubic (c) and non-cubic grains (d).

Table 6 - Shape parameters measured with digital methods (cubic grains).

Fraction (mm)	Riley Sphericity	Elongation	Compactness	Circularity
45–31.5	0.77 ± 0.067	0.860 ± 0.108	0.218 ± 0.013	1.692 ± 0.217
31.5–22.4	0.77 ± 0.070	0.823 ± 0.128	0.225 ± 0.012	1.575 ± 0.191
22.4–16	0.79 ± 0.047	0.854 ± 0.145	0.288 ± 0.050	1.422 ± 0.109
16–11,2	0.77 ± 0.064	0.814 ± 0.128	0.235 ± 0.009	1.396 ± 0.120
11.2–8	0.77 ± 0.061	0.822 ± 0.119	0.234 ± 0.125	1.460 ± 0.161
8–5.6	0.78 ± 0.076	0.815 ± 0.128	0.229 ± 0.018	1.536 ± 0.261
5.6–4	0.77 ± 0.075	0.811 ± 0.122	0.236 ± 0.017	1.547 ± 0.291

4. Conclusions

An effort was made to replace conventional sieves with digital sieves using image processing. It is expected that construction and mining industry would profit from automated equipment, which would improve quality control, as well as it would enable measuring more geometrical characteristics of aggregate grains. Methods were applied to aggregates of certain flakiness, measured with conventional methods.

In the two dimensions, a variety of geometrical parameters can be acquired only with digital methods in high precision. Assuming that aggregates would most often lay with their maximum

area, their two maximum dimensions can be computed, while the third dimension, thickness, should be equal or almost equal with the minimum of the two first dimensions when cubic aggregates are considered, or much smaller if flacky aggregates are considered. A statistical check was applied using ANOVA in ten different throws of different size fractions, which shows that indeed different events result to statistically the same distributions. Therefore, digital methods are reliable for shape parameter measurements of aggregates. A second test has shown that digital methods can have the appropriate precision in measuring sizes of aggregates, even during different rearrangements.

Digital sieves are also capable of replacing conventional analogue sieves, performing better in capturing the overall shape of aggregate grains rather than perforations that allow each grain to go through the sieve due to rotational movements. Therefore, digital sieving results in capturing more grains of the larger size fractions compared to analogue sieves. Finally, digital measurements can provide a variety of geometrical information, such as sphericity, elongation, compactness and circularity. However, to fully replace the conventional sieves, the third dimension is required to estimate flakiness and shape indices.

5. References

Dunlop H. 2006. Automatic Rock Detection and Classification in Natural Scenes, *MSc Thesis*, Carnegie Mellon University.

Fernlund J.M.R. 2004. Image analysis method for determining 3-D shape of coarse aggregate. *Cement and Concrete Research* 35 (2005) 1629– 1637

Fernlund J.M.R., Zimmerman R.W. and Kragic D. 2007. Influence of volume/mass on grain-size curves and conversion of image-analysis size to sieve size, *Engineering Geology* 90 (2007) 124–137

Frazao E.B. and Sbrighi Neto C. 1984. The influence of the shape of the coarse aggregate on some hydraulic concrete properties, *Bulletin of the International Association of Engineering Geology*, No 30.

Kim H., Haas C.T. and Rauch A.F. 2003. 3D image segmentation of aggregates from laser profiling, Computer-Aided Civil and Infrastructure Engineering 18 (2003) 254–263.

Profitis E., Chatzitheodoridis E. and Xirouchakis D. 2011. Digital methods for flakiness and shape definition. in ETNDT5, *Proceedings of the fifth International Conference on Emerging Technologies in Non-Destructive Testing*, Ioannina Greece, 19-21 September 20122, p. 437-440.

Tafesse S., Fernlund J.M.R. and Bergholm F. 2012. Digital sieving-Matlab based 3-D image analysis, *Engineering Geology* 137–138 (2012) 74–84.

Δελτίο της Ελληνικής Γεωλογικής Εταιρίας, τομ. XLVII , 2013
Πρακτικά 13ου Διεθνούς Συνεδρίου, Χανιά, Σεπτ. 2013

Bulletin of the Geological Society of Greece, vol. XLVII 2013
Proceedings of the 13th International Congress, Chania, Sept. 2013

ASSESSING AREAS OF SLOPE INSTABILITY THROUGH A SPATIAL DECISION SUPPORT SYSTEM

Rozos D.[1], Tsangaratos P.[1], Loupasakis C.[1], Koumantakis I.[1] and Markantonis K.[1]

[1] National Technical University of Athens, School of Mining and Metallurgical Engineering, Department of Geological Studies, rozos@metal.ntua.gr, ptsag@metal.ntua.gr, cloupasakis@metal.ntua.gr, koumantakisioannis@gmail.com, markantonis@ metal.ntua.gr

Abstract

The purpose of this study was to highlight the analytic power of a Spatial Decision Support System (SDSS) in slope stability problems and to present the process followed during the systematic study of the landslide phenomena manifested in the Chalki village, Korinthos Prefecture, Greece. The mass movements affected the residential area of Chalki village making urgent the need of immediate mitigation measures. The two main objectives of the developed Spatial Decision Support System (SDSS) were to evaluate the landslide susceptibility of the research area and to locate the most suitable areas for addressing investigation schemes and installing landslide monitoring systems.
Key words: *Landslide susceptibility, Ranking Method, Landslide monitoring system.*

Περίληψη

Ο σκοπός της παρούσας εργασίας ήταν να τονίσει την αναλυτική δύναμη των Συστημάτων Χωρικής Υποστήριξης Αποφάσεων σε προβλήματα ευστάθειας πρανών και να παρουσιάσει τη διαδικασία που ακολουθήθηκε κατά τη διάρκεια της συστηματικής μελέτης των κατολισθητικών φαινομένων που εκδηλώνονται στον οικισμό Χαλκίου, του Νομού Κορινθίας, Ελλάδα. Οι εδαφικές μετακινήσεις επηρέασαν την περιοχή του οικισμού κάνοντας επιτακτική την ανάγκη της εφαρμογής μέτρων θεραπείας. Δυο ήταν οι κύριοι στόχοι του Συστήματος Υποστήριξης Χωρικών Αποφάσεων, (α) η δημιουργία ενός μοντέλου κατολισθητικής επιδεκτικότητας, και (β) η χωροθέτηση των συστημάτων παρακολούθησης των εδαφικών μετακινήσεων.
Λέξεις κλειδιά: *Κατολισθητική επιδεκτικότητα, συστήματα παρακολούθησης εδαφικών μετακινήσεων.*

1. Introduction

The Village of Chalki, Korinthos Prefecture, Greece, is being affected by severe mass movements that have disrupted large portions of the urban settlement, since 1950. These phenomena have been occasionally reactivated either as a consequence of human activities or as a consequence of extreme natural events, such as heavy rainfall and seismic activity (Rozos et al., 2012). A number of serious damages on existing buildings, fencing walls, water supply networks as well as on the road infrastructure were recorded in 2003, after a three years period of increased rainfall. The

observed mass movements had the form of shallow slope movements (creep) characterized by slow deterioration of the ground that caused serious problems in the region that surrounded the village of Chalki. As reported widely through the literature, landslide phenomena can be managed using a variety of analytic methods depending on the objective and the scale of the study, but also on the available data (Cruden & Varnes, 1996, Dai et al., 2002, Fell et al., 2008). The deterministic limit equilibrium methods are used for the study of local site conditions, while geomoprhological or multivariate statistical methods are implemented over larger areas (Glade et al., 2005). Regardless the method initialized, the outcomes of a landslide assessment provide useful knowledge about the probability of failure and also serve as guidance in making land use decisions and planning procedures. An appropriate tool that could assist in identifying effective decision calls is a computer model that comprises a decision support system and a geographic information system, referred to as Spatial Decision Support System (SDSS). A Spatial Decision Support System is an interactive, computer-based system designed to assist in decision making while solving a semi-structured spatial problem (Sprague & Carlson, 1982). Several SDSS for managing slope stability and soil erosion problems have been developed by researchers (Lawrence et al., 1997, Dragan et al., 2003, Barac et al., 2004, De la Rosa et al., 2004, Mickovski et al., 2005). There can also been found several projects that initialize Geographic Information System (GIS) modelling for landslide susceptibility and hazard (Lazzari & Salvaneschi, 1999, Carrara et al., 1999, Cavallo & Norese, 2000, Donati & Turrini, 2002, Rozos et al., 2011), erosion vulnerability (Huang et al., 2003) and environmental vulnerability (Li et al., 2006). Based on recent studies of GIS applications, which model landslide susceptibility, it is established that models need to improve their ability to predict landslides and be more helpful for engineers, policy – makers and developers. They need to be more helpful in the direction of providing the ability to locate appropriate areas to carry out investigation schemes, or to locate areas to install landslide monitoring systems and to implement effective landslide hazard mitigation measures. The present study focused on developing a SDSS within a GIS platform that had two main objectives: (a) the development of a landslide susceptibility model and (b) locating areas for installing landslide monitoring systems. The developed SDSS was evaluated at Chalki village, in the prefecture of Korinthos, Greece.

2. Materials and Methods

2.1. Framework for Producing a Susceptibility Map Through SDSS

The developed SDSS module consisted of three components: (a) a spatial database management system (SDMS), (b) a set of techniques and methods for enabling specific spatial functions for landslide assessment and (c) a graphical user interface (GUI) to assist users' interaction with the system. The first component, the spatial database management system is the main core of the system. In the ArcGIS platform, the GIS software that is used in this study, the SDMS is a well designed geodatabase. The second component consists of a set of techniques and methods to assess slope stability and landslide hazards, in particular techniques that assist in producing landslide susceptibility models and conduct spatial analysis for locating areas to address landslide monitoring systems. The third component of the developed SDSS module is the GUI that allows interaction between the user's and the system in a graphical and friendly way. The present study focuses on the techniques and methods that are embodied in the SDSS, a brief description of which is given in the following section.

2.2. Calculating Landslide Susceptibility Index

Landslide susceptibility is a quantitative or qualitative assessment of classification, volume, and spatial distribution of landslides, which exist or potentially occur in an area. In a landslide susceptibility analysis, time - frame is explicitly not taken into consideration (Corominas et al., 2000, Glade et al., 2005). In the present study the landslide susceptibility index is calculated by applying the weighted linear combination (WLC) method, which is one of the best know and

commonly used methodology in spatial analysis (Malczewski, 1999, Ayalew et al., 2004). The main objective is to estimate the total score an area achieves and thus compiling the landslide susceptibility map. The linear correlation is given by the formula showed in equation 1.

Equation 1 – Landslide susceptibility index

$$Lsi = \frac{1}{n}\sum_{i=1}^{n} f_i w_i * w_{cij}$$

where, L_{si} is the overall score that represents the landslide susceptibility index, n the number of factors, fw_i the weight coefficient of the i^{th} factor and w_{ci} the weight coefficient of the j^{th} class of the i^{th} factor .

The Ranking Method was utilized to estimate both the weight of importance that each landslide related factor has, and also the weight of susceptibility that each class of each factor has. The Ranking Method is one of the simplest methods for estimating importance weights in a set of criterion, while the most popular procedure for generating numerical weights is the Rank Sum method (Stillwell et al., 1981, Malczewski, 1999). The weights from the Rank Sum method, which also engaged in this study, are calculated according to equation 2.

Equation 2 – weight coefficient using the Rank Sum method

$$w_i = \frac{n - r_i + 1}{\sum (n - r_k + 1)}$$

where, w_i is the normalized weight for the i^{th} criterion, n is the number of criteria (k=1,2…n), r_i is the rank position of the criterion.

Following the above concept, the landslide susceptibility index is categorized into three classes utilizing natural breaks classification based on accumulative weight and score (Jenks, 1967). The method seeks to minimize each class's average deviation from the class mean, in other words reducing the variance within the class, while maximizing each class's deviation from the means of the other groups, leads to maximizing of the variance between classes (De Smith et al., 2007). To complete the analysis the L_{SI} map must be validated. For this purpose, depending on the technique of analysis, a portion or the complete landslide database is overlaid in the form of a layer, known as landslide inventory map. A landslide inventory map indicates the location and, if available, additional information about past and present mass movements characteristics (e.g., type of movements, depth, date, age, degree of activity, magnitude, direction and velocity) that left discrete features in an area (Hansen, 1984, Guzzetti et al., 2000). Statistical directives are then estimated taking account the spatial distribution of the landslide incidence and the zones of susceptibility that have been produced by the model. The approach that this study follows depends on expert knowledge, thus the landslide inventory map is mainly used in the procedure of locating the areas for establishing landslide monitoring systems than for validation reasons.

2.3. Indentifying Areas to Address Geotechnical Investigation Schemes and to Install Landslide Monitoring Systems

Landslide hazard mitigation strategies comprise a range of activities including hazard mapping and assessment, real time monitoring and warning systems, protective engineering measures, and also development of public awareness and emergency planning (Savvaidis et al., 2001). It also must be reported that for accurate landslide inventory mapping and analysis of landslide characteristics, aerial photos, geotechnical data and monitoring results should be integrated with field surveys and any other available information. All the above activities have a spatial dimension in which location play a very important role. After contacting a landslide susceptibility analysis, the next phase is to locate the areas for installing landslide monitoring systems. Both of these actions are very

significant in a landslide assessment and could be thought as a spatial decision analysis problem, defined as how to maximize the information and data that one can get by choosing among several spatial alternative schemes. The developed SDSS allows inputting layers of information, e.g. infrastructure network, urban areas and land use cover, etc. and also utilizing specific spatial functions the output of which could be useful during the decision analysis phase. It also allows manipulating data that concern damages reported on structures and infrastructure or the agriculture facilities, within a spatial framework. By this procedure the SDSS provide a metric function with which the user assigns priority values to the entire area. Another important aspect that the SDSS provides is the ability to map the land use characteristics of the surrounding area and assign to the different types, values of significance according to expert judgment. As an example, it is obvious that in a landslide hazard assessment urban areas are more significant than areas located in a forest, in the sense that if a landslide incidence evolve in an urban area, the casualties and disruption would be much more important. In the same way, areas that had previously reported as been affected have priority against non-affected areas, since reactivation of the mass movement may be possible. As for the landslide monitoring systems they can be classified as remote sensing or satellite techniques, photogrammetric techniques, geodetic or observational techniques, and geotechnical or instrumentation or physical techniques (Gili et al., 2000, Corominas et al., 2000, Savvaidis et al., 2001). For the purpose of the study, geotechnical techniques were under consideration. Specifically, geotechnical techniques involve the installation and monitoring of inclinometers, extensometers, piezometers, geophones, tiltmeters and crack meters. The type of instrument also defines the location of installation. As for example, inclinometers are installed in boreholes drilled within the landslide mass. In the case where the available instruments are few and a decision should be made of where to be installed, the proximity to urban settlements plays a role in choosing an alternative. The closer the urban settlements, the more critical the information extracted are. Within this framework, distance functions are applied to each layer of information and each zone is assigned a value of significance. The final process is to combine the landslide susceptibility map with the findings of the above analysis and provide a decision upon the most suitable area for installing landslide monitoring systems.

3. The Case Study

3.1. Geological Settings

The urban settlement of Chalki village (37° 52 40, 22° 43 40) is part of the municipality of Vochas located approximately 3 km southwest of the village of Soulinari. The village is located on gentle slopes northwest of Mount Foukas which forms the eastern slopes of the basin of Zapantis having altitude values ranging from 240 to 320 meters, Figure 1.

The geological formations that cover the wider research area consist of neogene sediments, plio-pleistocene deposits (conglomerates, clayey marls, calcite marls) and diluvial conglomerates. These formations are covered in places by a thin weathering mantle that has been created by erosion and alteration process (Figure 1). The most dominant formations that cover the research area are the clayey marls and the calcite marls. The clayey marls are characterized as easily weathered, semi-coherent and with varying permeability. Their water content increases significant upon wetting, decreasing its geomechanical characteristics. The calcite marls appear to be more resistance to weathering process and characterized as hard to stiff marl formation with very low permeability. The field survey and the study of aerial photos, revealed the presence of two main set of tectonic lineaments with directions SW - NE and NNW – SSE respectively that have altered the geomorphologic characteristics of the area. As for the seismic activity, the seismicity of the area is indirectly influenced by the seismic epicentres of the Corinth Gulf and therefore the values of the peak ground acceleration are expected to be high (Koumantakis et al., 2005). Finally, the mean annual precipitation reaches 538mm with 72.5% falling between the months of November and March.

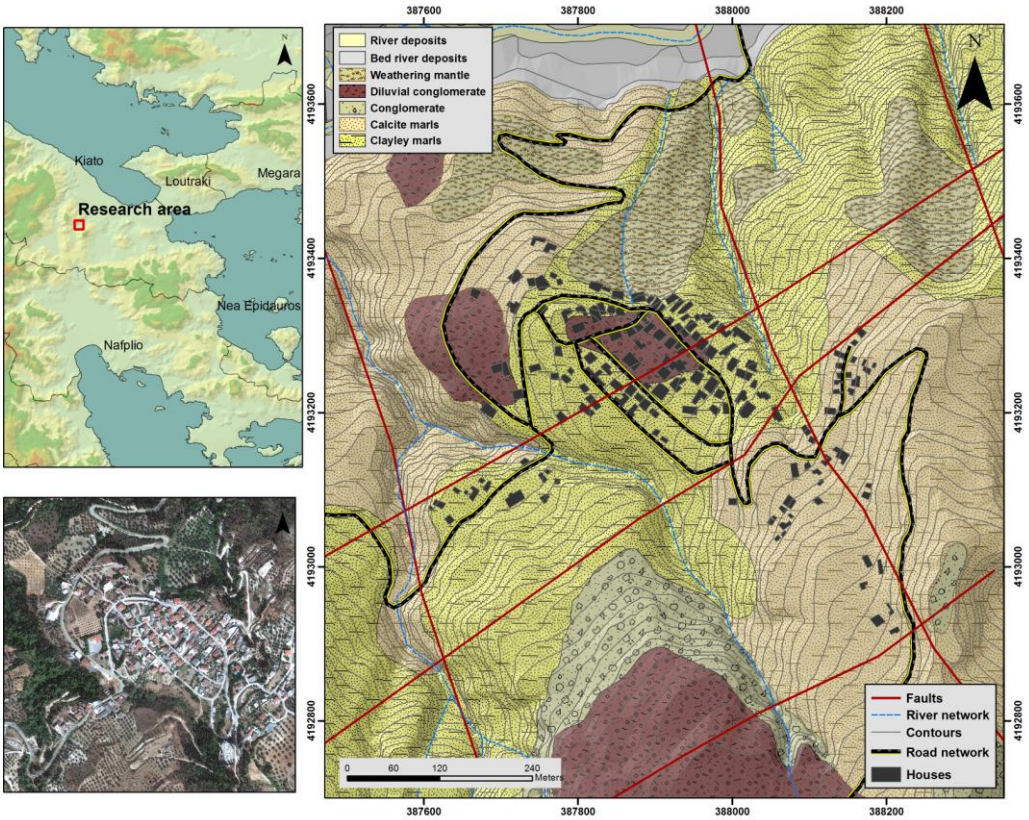

Figure 1 – The geological setting of the study area.

3.2. Selecting the Appropriate Factors and Assessing the Weight Coefficients

The factors that appear to influence the manifestation of a landslide in a site could be distinguished into causative and triggering factors. Causative factors actually determine the favourable settings that may cause a landslide, while triggering factors determine the temporal characteristics of a landslide incidence. Seismic activity, intensive rainfall and human activities are thought to be the most common triggering factors. However, the usage of these types of data that appear to be unpredictable and vary in time is limited in landslide assessments (Guzzetti et al., 2000). On the other hand the causative factors are easily defined and used extensively in landslide assessments (Glade et al., 2005). It is well know that lithology plays a crucial role in controlling instability. The reclassified map had three classes based on different susceptibilities to landslide and accordingly are assigned a higher or lower ranking value (Table 1). The river deposits, bed river deposits and the weathering mantle are classified into the most susceptible class, eguA. The diluvial conglomerate, conglomerate and clayey marl formations have been classified into class eguB, that represent medium susceptible formations, while the calcite marls are classified as the less susceptible class, eguC.

As reported in the literature, geo-morphological settings can affect the landslide occurrence. Specifically, the dynamic behaviour of a landslide event has close affinity to the slope values (Carrara, 1983, Maharaj, 1993). Slope controls the subsurface flow velocity after rainfalls, the runoff rate and the soil water content. As slope value increases shear stress in unconsolidated soil cover increases as well. The raster format file was obtained from the DEM file. In the reclassified map, slope values were subdivided into three classes: (a) Gentle slopes (< 13^o), Moderate steep slopes (13^o – 27^o), Steep slopes (> 27^o).

Table 1 – Assessing weights to each class of each factor.

Factors	Classes	Straight rank	Normalized weight
A. Eng. Geol. Units		**1**	**0.3334**
River deposits	eguA	1	0.50
Bed River deposits	eguA	1	0.50
Weathering mantle	eguA	1	0.50
Diluvial conglomerates	eguB	2	0.3334
Conglomerate	eguB	2	0.3334
Calcite marls	eguC	3	0.1667
Clayey marls	eguB	2	0.3334
B. Slope		**4**	**0.1334**
(0^o-13^o)	slpA	1	0.50
(13^o-27^o)	slpB	2	0.3334
>27^o	slpC	3	0.1667
C. Aspect		**2**	**0.2667**
N-NE	aspA	1	0.50
E-W	aspB	2	0.3334
S-SW	aspC	3	0.1667
D. Proximity to river network		**3**	**0.20**
< 50m	rvrA	1	0.6667
> 50m	rvrB	2	0.3334
E. Proximity to tectonic lineaments		**5**	**0.0667**
< 50m	tectA	1	0.6667
> 50m	tectB	2	0.3334

Also, the aspect of the surface contributes to the overall slope instability in the same way the slope factor does. It's known that certain orientations are associated with increased snow concentration or intense erosion and weathering processes. It also affects indirectly other factors such as the flora distribution, the degree of saturation and evaportranspiration of the slopes and also the soil thickness. It is general considered that N and NW – facing slopes are the most favourable to landslide due to their shadier and colder conditions that favour the accumulation and preservation of soil moisture (Guzzetti et al., 1999). The frequency of landslides is expected to be higher on N and NW facing slopes, due to water accumulation and lower on east – facing and SE facing slopes as a result of decreased wetness. The aspect raster file has been divided into three classes, namely aspA, aspB and aspC. In the research area those orientations are the N-NE, E-W and S - SW. Another factor of great importance is the proximity to the stream network. An area closer to the river path has higher water content and hence may exhibit higher susceptibility to landslide phenomena. The thematic layer of proximity to river network was generated using a buffer around the streams. It was classified into two distance classes, (a) < 50m from streams, (b) greater than 50 m. As the distance from the network increases the landslide susceptibility decreases. Hence, the classes of the buffered proximity to river network map have been assigned rating values in decreasing order based on the distance from the streams. Proximity of landslide incidence to thrust and fault zones is consequence of the contacts between overlaying more permeable rocks and underlying less permeable or impermeable formations resulting in abundance of springs and also sheared zones of weakened and fracture rocks. On the vectorized layer a distance function was applied to define two buffer zones along the structural discontinuities, a zone less than 50m from

tectonic features and a zone greater than 50m. As the distance from the tectonic lineaments increased landslide susceptibility decreases. Hence, the classes of the buffered proximity to tectonic features were rated in a decreasing order according to their distance to thrust and fault zones. Table 1 shows both the weight of importance that each factor has, and also the weight of susceptibility that each class of each factor has as they were calculated by the Rank Sum method.

3.3. Producing the Landslide Susceptibility Index Map

The landslide susceptibility index values are varying within the range of 0 and 1. The higher the value the more susceptible the area is. However, the L_{SI} map was reclassified into three categories namely, "low", "moderate" and "high", as shown in Figure 2. Applying ArcMap Field Calculator and the Calculate Geometry dialog box, it was found that about 43 % of the research area is characterized as low susceptible, 35% as medium susceptible and 22% as high susceptible. The L_{SI} map shows that the high susceptible zones were found mainly in areas where clayey marl outcrop, on moderate to steep slopes and near streams and fault zones. It also shows that only a small portion of the urban area is appreciated as high susceptible. It must be noted that these location have been reported of having the most serious damages on buildings, fencing walls, water supply networks as well as on the road infrastructure.

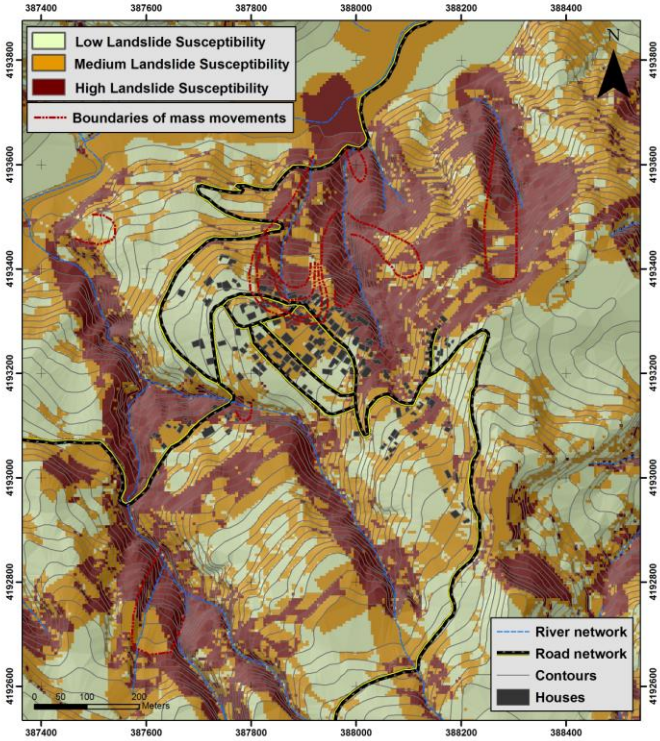

Figure 2 – The landslide susceptibility map and the overlaid landslide inventory map.

3.4. Locating Areas to Apply Systems and Techniques for Monitoring Mass Movements

Three different geotechnical techniques for landslide monitoring where selected: (a) inclinometers, (b) piezometers, and (c) tile-tale crack meters. According to the methodology, on the vectorized landslide inventory map, a distance function was applied to define a buffer zone, 50m from each landslide features, assigning to those zones high value of significance (Figure 3). Within those zones inclinometers should be more appropriate to install.

As already mentioned the exact location is a decision-making problem and other considerations should be taken into account in order to evaluate the alternatives. The most critical consideration is the proximity to urban settlements. To obtain the proximity value, the Calculate Geometry dialog box was enabled in order to find the centroid of the polygon that represents the urban settlements. Then, the distance between the centroid and each landslide buffer zone is calculated (Figure 3).

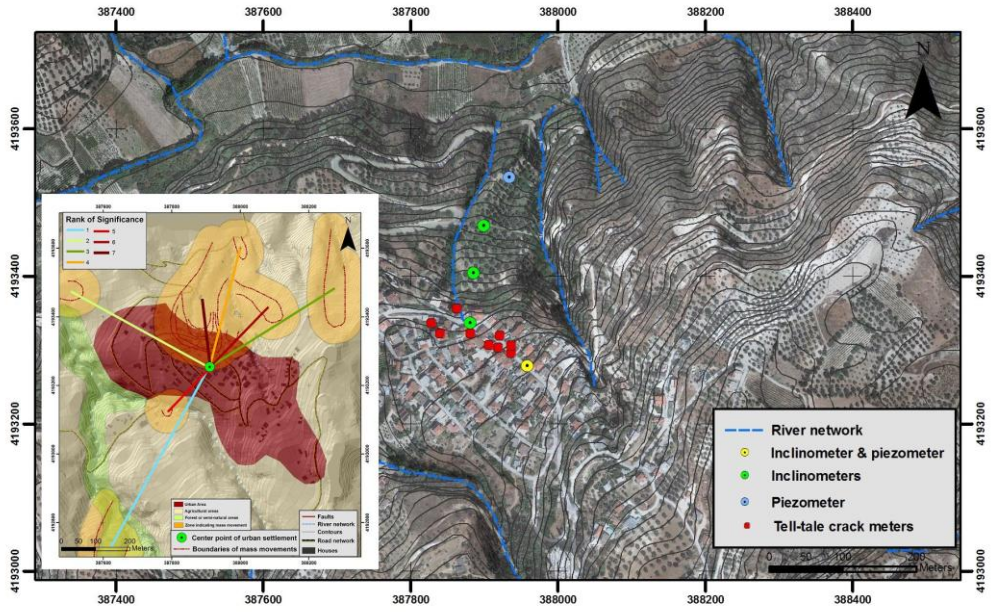

Figure 3 – The locations of the proposed landslide monitoring system.

The piezometers measure the fluctuations of the ground water table and eventually the pore water pressure within a geological structure. So, they give an indication of the build up of stresses and strains within a ground mass. As previously referred, the landslide zones are the most suitable for installing the piezometers and the exact location is found applying the same procedure. Finally, the installation of the tell–tale crack meters in areas where damages on building and wall fences are reported is the most common approach.

4. Discussion and Conclusions

The shape and size of mass movements vary because of the complex interrelationship that arises among several preparatory and triggering factors (Coates, 1977). Mass movements may be controlled by the topographic factor, such as considering the inclination, orientation and shape of the slope, the lithologic ones such as physical characteristics and mechanical properties, the geological structure, considering the tectonic features, the hillslope hydrologic factors such as pore pressure, or a combination of all these factors. The study indicated that the last serious reactivation of the observed mass movements had as a triggering factor the intensive rainfall that have been recorded in the year 2003. It also concluded that the type of the lithological units found in the area, specifically the Plio-Pleistocene clayey marl horizons and the underlying calcite marls were responsible for the evolution of mass movements. In addition, the weathering action of the surface water and the raising of the water table could alter the physical and mechanical properties of the formations. Failure occurs, when the driving forces that create movement exceed the resisting forces of the material, while triggering factors may increase the shear stress or decrease the shearing resistance of the material or enable both of these mechanisms. The main objective of the developed SDSS was to be a useful tool in manipulating data and information that are collected

from the analytic observation and study of the area susceptible to landslide manifestation. Applying the Rank Sum method the weight values of the landslide related factors were obtained and by implementing WLC method the landslide susceptibility index was estimated for each cell of the entire research area. The produced landslide susceptibility map was reclassified into three landslide susceptibility zones that indicated that small portions of the urban settlement are in the high landslide susceptibly zone. The main landslide monitoring systems that were proposed for installation in the area included (a) a number of inclinometers for measuring deep displacements, (b) a number of tell-tale crack meters, to measure the surface movements and (c) piezometers, to monitor the fluctuation of groundwater level. There exact placement location was found within the developed SDSS by applying spatial functions and assigning in the entire area values of significance. The outcomes of the study maximized the information that was provided and helped in the direction of defining the surface of displacement.

5. References

Ayalew L., Yamagishi H. and Ugawa N. 2004. Landslide susceptibility mapping using GIS-based weighted linear combination, the case in Tsugawa area of Agano River, Niigata Prefecture, Japan, *Landslides* 1, 73–81.

Barac A., Kellner K. and De Klerk N. 2004. Land user participation in developing a computerized decision support system for combating desertification, *Environmental Monitor and Assessment*, 99, 223–231.

Carrara A. 1983. Multivariate models for landslide hazard evaluation, *Mathematical Geology*, 15 (3), 403–426. doi:10.1007/BF01031290.

Carrara A., Guzzetti F., Cardinali M. and Reichenbach P. 1999. Use of GIS technology in the prediction and monitoring of landslide hazard, *Natural Hazards* 20, 117-135.

Cavallo A. and Norese M. F. 2000. GIS and multi-criteria analysis to evaluate and map erosion and landslide hazards, *Informatica*, 12, 25-44.

Coates D. R. 1977. Landslide Perspectives, in Coates, D. R. (ed.), Landslides, *Reviews in Engineering Geology*, Vol. III, Geological Society of America, Boulder, Colorado, 3-28.

Corominas J., Moya J., Lloret A., Gili J.A., Angeli M.G., Pasuto A. and Silvano S. 2000. Measurement of Landslide Displacements using a Wire Extensometer, *Engineering Geology*, 55, 149-166.

Cruden D. M. and Varnes D. J. 1996. Landslide types and processes, in: Turner A.K.; Shuster R.L. (eds) Landslides: Investigation and Mitigation. Transp Res Board, Spec Rep, 247, 36–75.

Dai F.C., Lee C.F. and Ngai Y.Y. 2002. Landslide risk assessment and management: an overview, *Engineering Geology*, 64 (1), 65–87.

De la Rosa D., Mayol F., Diaz-Pereira E., Fernandez M. and de la Rosa D., 2004. A land evaluation decision support system (MicroLEIS DSS) for agricultural soil protection, *Environmental Modelling & Software*, 19, 929–942.

De Smith M. J., Goodchild M. F. and Longley P.A. 2007. *Geospatial Analysis: A comprehensive guide to principles, techniques, and software tools* (2nd Edition) Leicester, UK. Matador Publishing Ltd.

Dragan M., Feoli E., Fernetti M. and Zerihun W. 2003. Application of a spatial decision support system (SDSS) to reduce soil erosion in northern Ethiopia, *Environmental Modelling & Software*, 18, 861–868.

Donati L. and Turrini M.C. 2002. An objective method to rank, the importance of the factors predisposing to landslides with the GIS methodology: application to an area of the Apennines (Valnerina; Perugia, Italy), *Engineering Geology*, 63, 277-289.

Fell R., Corominas J., Bonnard C., Cascini L., Leroi E. and Savage W.Z. 2008. Guidelines for landslide susceptibility, hazard and risk zoning for land use planning, *Engineering Geology*, 102 (3–4), 85–98.

Gili J.A., Corominas J. and Rius J. 2000. Using Global Positioning System Techniques in Landslide Monitoring, *Engineering Geology*, 55, 167-192.

Glade T., Anderson M. and Crozier M.J. 2005. *Landslide Hazard and Risk*, John Wiley & Sons, Ltd., Chichester, England, 802pp.

Guzzetti, F. Cardinali M., Reichenbach P. and Carrara A. 2000. Comparing landslide maps: a case study in the upper Tiber River Basin, Central Italy, *Environmental Management*, 25(3), 247–363.

Guzzetti F., Carrara A., Cardinali M. and Reichenbach P. 1999. Landslide hazard evaluation: a review of current techniques and their application in a multi-scale study, Central Italy, *Geomorphology*, 31, 181–216.

Hansen A. 1984. Strategies for classification of landslides, in: Brunsden, D., Prior, D.B. (Eds.), Slope Instability. Wiley, New York, 1–26.

Huang Y.F., Chen X., Huang G.H., Chen B., Zeng G.M., Li J.B. and Xia J. 2003. GIS-based distributed model for simulating runoff and sediment load in the Malian River Basin, *Hydrobiologia*, 494, 127–134.

Jenks F. G. 1967. The Data Model Concept in Statistical Mapping, *International Yearbook of Cartography*, 7, 186-190.

Koumantakis I., Rozos D., Markantonis K., Tsangaratos P., 2005. Final technical survey "Study of Landslide phenomena in Chalki, Korinthos. School of Mining and Metallurgical Engineering, Laboratory of Engineering Geology and Hydrogeology, pp 62.

Lawrence P.A., Stone J.J., Heilman P. and Lane L.J., 1997. Using measured data and expert opinion in a multiple objective decision support system for semiarid rangelands, *Transactions of the ASABE,* 40(6), 1589-1597.

Lazzari M. and Salvaneschi P., 1999. Embedding a geeographic information system in a decision support system for landslide hazard monitoring, *Natural Hazards*, 20, 185–195.

Li A.N., Wang A.S., Liang S.L. and Zhou W.C. 2006. Eco-environmental vulnerability evaluation in mountainous region using remote sensing and GIS - A case study in the upper reaches of Minjiang River, China, *Ecological Modelling*, 192, 175–187.

Maharaj R.J. 1993. Landslide processes and landslide susceptibility analysis from an upland watershed: a case study from St. Andrew, Jamaica, West Indies. Eng Geol, 34, 53–79.

Malczewski J. 1999. *GIS and Multicriteria Decision Analysis*, (John Wiley and Sons, New York, 1999).

Mickovski S.B., Stokes A. and van Beek L.P.H. 2005. A decision support tool for windthrow hazard assessment and prevention, *Forest Ecology and Management*, 216, 64–76.

Rozos D. Bathrellos D. G. and Skilodimou D. H. 2011. Comparison of the implementation of Rock Engineering System (RES) and Analytic Hierarchy Process (AHP) methods, based on landslide susceptibility maps, compiled in GIS environment. A case study from the Eastern Achaia County of Peloponnesus, Greece, *Environmental Earth Sciences*, 63(1), 49–63.

Rozos D., Loupasakis, C., Koumantakis, J., Tsangaratos, P. and Markantonis, K., 2012. Remediating Mass Movements induced by Water, in Urban Environments - an example from Chalki Village, Peloponnese, Greece. *EGU General Assembly 2012*, Austria, pp.6492.

Savvaidis P., Lakakis, K. and Zeimpekis A. 2001. Monitoring Ground Displacements at a National Highway Project: The Case of "Egnatia Odos" in Greece. *Proceedings of IAG Workshop "Monitoring of Constructions and Local Geodynamic Process*", Wuhan University, China.

Sprague R. H. and Carlson E. D. 1982. *Building effective decision support systems*, Englewood Cliffs N.J., Prentice-Hall., pp.329.

Stillwell W.G., Seaver D.A. and Edwards W. 1981. A comparison of weight approximation techniques in multi-attribute utility decision making. *Organizational Behavior and Human Performance*, 28, 62-77.

Δελτίο της Ελληνικής Γεωλογικής Εταιρίας, τομ. XLVII , 2013
Πρακτικά 13ου Διεθνούς Συνεδρίου, Χανιά, Σεπτ. 2013

Bulletin of the Geological Society of Greece, vol. XLVII 2013
Proceedings of the 13th International Congress, Chania, Sept. 2013

CSD CORRECTION AS A TOOL FOR ESTIMATING 3D BLOCK SIZE DISTRIBUTION

Rusi M.[1] and Hoxha P.[2]

[1] *Jacobs Consulting Geologists, baugeologie.at, Leobendorf, Austria, megirusi@yahoo.com.*

[2] *Polytechnic University of Tirana, Albania, Faculty of Geology and Mining, Department of Applied Geology, Environment and Geoinformatics, p_hoxha@yahoo.com.*

Abstract

For the headrace Moglicë-Grabovë, part of Devoll Hydropower Project in Albania, two different techniques of tunnelling are planned: DS TBM for the Flysch series starting in Moglicë and Drill & Blast for the Ophiolite section, starting in Grabovë. A major question concerning the tunnelling seems to find the point where DS-TBM excavation from the Moglicë side should stop to "wait" for the Drill&Blast excavation from the Shemsit access tunnel side. Assumed that the so called "block in matrix" rock mass is very unfavourable, respectively disqualifying for TBM excavation. These mixtures of hard blocks embedded in weaker and finer matrix that are very difficult to characterize, frequently challenge the engineering geologists with the characterization, design and construction problems associated with them. Evaluating Block Size Distribution in the BiM rock zone of this project area has been only the first step in characterizing all the geological and geotechnical parameters of the rock mass which will influence a decision that has major economic consequences. CSDCorrections 1.39 is the program used to convert the two dimensional data gathered from thin sections, outcrops, photographs etc. to true three dimensional crystal size distributions (CSD).

Key words: *Block& Matrix, tunnelling, geotechnical parameters.*

Περίληψη

Η σήραγγα του αγωγού μεταφοράς νερού Moglicë-Grabovë, που αποτελεί τμήμα του Υδροηλεκτρικού έργου Devoll στην Albania, θα διανοιχθεί με δυο διαφορετικές τεχνικές, με χρήση TBM διπλής ασπίδας στην περιοχή του φλύσχη στην περιοχή Moglicë και με χρήση εκρηκτικών στην περιοχή οφιολίθων στην περιοχή Grabovë. Βασικό ερώτημα για τον σχεδιασμό κατασκευής των σηράγγων αποτελεί ο προσδιορισμός του σημείου που θα σταματήσει η διάνοιξη με χρήση TBM για να συναντηθεί με την εκασκαφή με εκρηκτικά από τη σήραγγα πρόσβασης Shemsit. Η παρουσία των πετρωμάτων "block in matrix"είναι δυσμενής για τη διάνοιξη με χρήση TBM. Τα συγκεκριμένα μίγματα σκληρών τεμαχών εντός ασθενούς συνδετικού υλικού είναι δύσκολο να χαρακτηριστούν και σχετίζονται με προβλήματα σχεδιασμού και κατασκευής των σηράγγων. Η εκτίμηση της κατανομής του μεγέθους τεμαχών στα ετερογενή πετρώματα bimrock της περιοχής του έργου αποτελούν το πρώτο στάδιο χαρακτηρισμού των γεωλογικών και γεωτεχνικών παραμέτρων της βραχομάζας και επηρεάζουν την απόφαση σχεδιασμού. Για την μετατροπή των δυσδιάστατων δεδομένων από λεπτές τομές, εμ-

φανίσεις πετρωμάτων σε τρισδιάστατες κατανομές μεγέθους των τεμαχών (CSD) έγιναν με χρήση του προγράμματος CSDCorrections 1.39.
Λέξεις κλειδιά: *Ετερογενείς βραχόμαζες, σήραγγες, γεωτεχνικές παράμετροι.*

1. Introduction

Block-in-matrix rocks (BiM rocks) are mixtures of hard blocks embedded in weaker and finer matrix that are very difficult to characterize. Engineering geologists and the geotechnical engineers are frequently challenged by the characterization, design and construction problems associated with these heterogeneous geological mixtures. The Moglicë - Grabovë headrace tunnel in the Devoll Hydropower Project will go throw this type of Rock. Evaluating Block Size Distribution in the BiM rock zone of this project area is only the first step in characterizing all the geological and geotechnical parameters of the rock mass which will influence a decision that has major economic consequences.

1D Borings and 2D outcrop and maps of melanges and BiM rocks produce distributions that differ considerably from the 3D block size distributions, but there is promise that rules may yet be devised to estimate reliable block size distributions of melanges from chord length and surface distributions. Estimation of 3D particle size distributions from measurements in 1D and 2D are considered by stereology, a discipline blended from geometrical statistics, mathematics, microscopy, image analysis and empirical research. The paper at hand is an attempt to show why there is currently little reliable procedures for evaluating spatial distribution of block size, which are these methods and how can they be applied in the engineering practice.

2. Material and Method

2.1. Description of the Project

Devoll Hydropower Project consists of developing, planning, constructing and operating three hydropower plants along the Devoll River with an installed capacity of approx. 280 MW. DHP has the right to harness the hydrological potential of the Devoll River between 95 and 810 m above sea level, between Banjë Village in Elbasan District and Maliq Municipality in Korçë District. Through the three hydropower plants, Banjë HPP, Kokël HPP and Moglicë HPP the project will yearly generate approx. 800 GWh of renewable, environmental-friendly energy, increasing the current electricity production in Albania by approx. 20%. Based on average electricity consumption for Albanian household of 200 kWh/month, the energy generated by the Devoll Hydropower Project can supply more than 300.000 Albanian households. Devoll Hydropower Project is one of the largest hydropower investments in the Balkans and the first large scale Public-Private-Partnership investment in Albania. The Moglicë Hydroelectric Project will utilise a head of 300 m along an about 22 km long stretch of Devoll River between 650 m a.s.l. and 350 m a.s.l.. The intake is situated upstream the 140 m high rock fill dam planned at Moglicë. The powerhouse is located in an underground cavern on the east bank of Devoll River and has two Francis units with total capacity of 165 MW. Transmission voltage is 220 kV and estimated average annual energy production is 452 GWh. The tailrace outlet is at the upper end of the reservoir created by a 50 m high dam planned at Kokël. Approximately 11.7 km of tunnels with a diameter of 5.4m will be excavated in different rock masses and 700m of which will go throw BiM rocks and mélanges.

2.1.1. Geological and Tectonic Features

Moglicë hydropower project is part of two major tectonic zones. The eastern most part lies within the Mirdita zone which consists of alloctone Jurasic Ophiolithic massifs of Vallamara, Voskopoja and Devoll. The last one is placed isolated in the west and it is separated from the other ophiolithic massifs throw a corridor which belongs to the Krasta tectonic zone. The Grabove-Moglice tunnel system will be excavated throw the Devoll ophiolithic massif of Mirdita zone as well as throw the

flysch series of sandstones, clays, siltstones, conglomerates and limestone rocks of ages Crete-Eocene which belong to the Krasta zone. The lithological unit that will be studied in this paper represents the transitional area between the flysch series and ophiolitic body which consists of reprocessed material originating from the ophioliths as well as the flysch. The part of the Mélange which covers the ophiolithic complex is also part of Mirdita tectonic zone. We can distinguish four rock types within the area of the Mirdita heterogeneous melange. According to the principle used in this paper regarding their mechanical behaviour during excavation, all these rocks nevertheless the type, strength, the cementation degree etc. belong to the Block in Matrix rock type. But according to a genetic and lithological characterization, the encountered rock types in this area are more than one. After the competition of the detailed mapping campaign in 2011 it was concluded that the rock types are lhercolites / serpentinites, ophiolitic tectonic breccias, vulcanites, radiolarites and limestones. One of the results of this geological mapping phase was the preparation of the detailed longitudinal profiles and cross sections over the tunnel axis. The main rock lithologies that are found along the tunnel axes in the melange zone include sheared serpentinites, ophiolithic breccias, flysch formations of folded limestone, radiolarites, vulcanites.

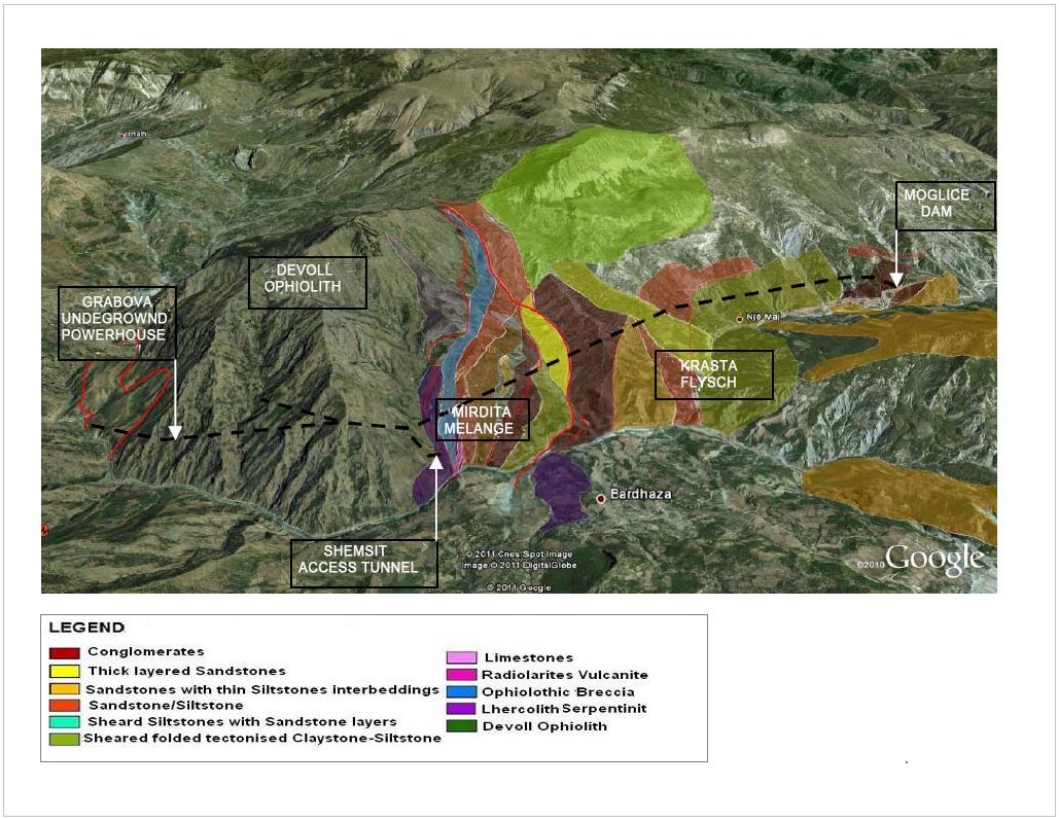

Figure 1 – The main lithologies mapped in the Mirdita melange zone.

2.1.2. Tunnel Sections

The alignment of the headrace tunnel was divided in sections referring to the present lithology and rock conditions. In total 28 tunnel-sections were defined along the overall length of 11.775 meters. Five of these sections which consist of approximately 700m of tunnel alignment run throw the mélange zone.

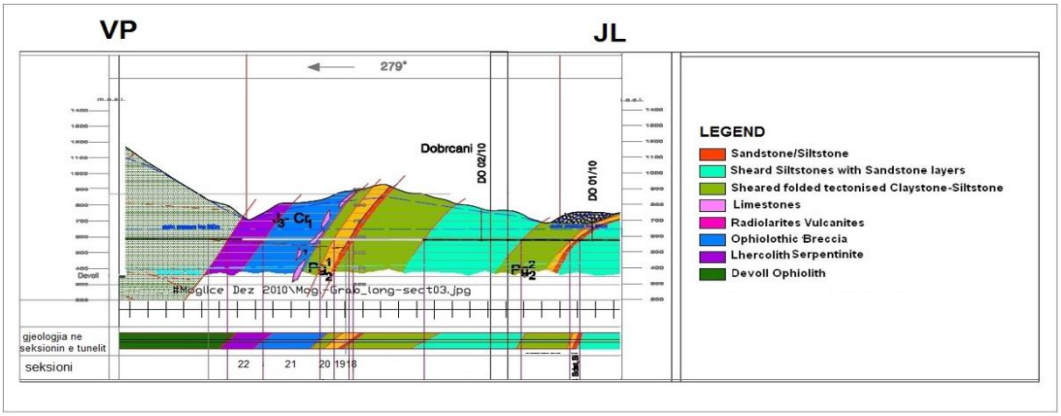

Figure 2 - Geological longitudinal section along tunnel axis in the Melange zone.

- From station 7450 m to approx. station 7550 m the tunnel alignment crosses section 18 and 19 and is expected to run through medium to thick bedded inter beddings of sandstone and siltstone layers with intercalations of silty shale layers over a length of approx. 100 m. The strata dip moderately steep between 45 and 65° to the NW to NNW. The borders of this section are not known very well.
- From station 7.550 m to approx. station 7.630 m, section 20, the tunnel alignment is expected to run through thin to medium bedded inter beddings of clayey shale and siltstone layers with intercalations of sandstone layers and randomly occurring lenticular lenses of conglomerates over a length of approx. 80 m. The strata dips moderately steep between 45 and 65° to NW to NNW.
- In section 21 from station 7.630 m to approx. station 7.950 m the tunnel alignment is expected to run through the rim related ophiolitic fault conglobreccia of the Devoll ophiolith over a length of approx. 320 m. This rock can be named a real tectonic mélange. The strata dips 35 and 50° NNW.
- From station 7.950 m until station 8.150 m the tunnel alignment passes section 22 and it is expected to run through intensely tectonized and highly alterated lherzolites that are already part of the Devoll ophiolith massif along a distance of approx. 200 m.

2.2. The Method

The transition zone affected by the ophiolithic thrusting is the project area to which a special attention has been given during all the stages. Ophiolithic breccias and different melange zones, BIM rocks, together with intensively folded flysch formations and complex tectonic history were the object of the detailed mapping for this study. More than 100 outcrops have been documented in this area which is 700 m along the tunnel axes. The outcrops have been randomly selected throw scanlines. These outcrops have been photographed with high resolution cameras, and the pictures have been reworked afterwards.

2.2.1. Guide to Digitalisation

Before using the photograph for CSD it needs to be properly digitalised with image treatment programs and graphic programs (Adobe Photoshop, Adobe Illustrator, ImageJ etc.). Every block has to be outlined and layered separately. After outlining all the blocks, and turning off the picture layer it is needed to export the black and white image as an uncompressed tif. file to the ImageJ .This program makes possible the scale, measurement, particle analyses.

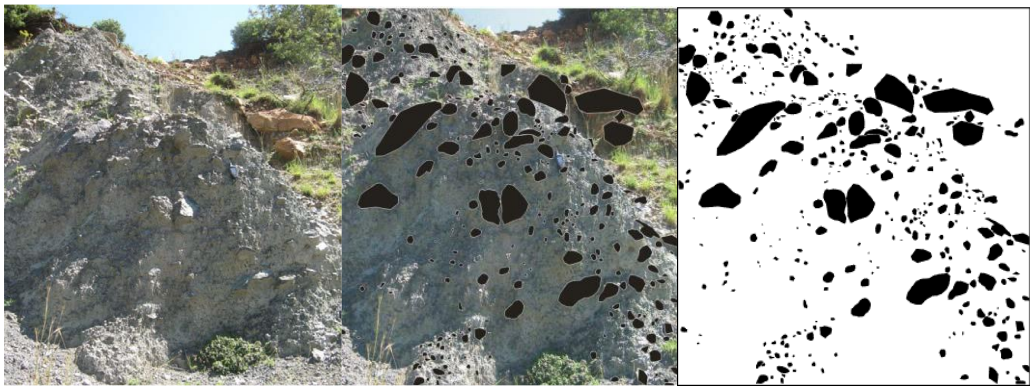

Figure 3- BiM rock outcrop and Digitalising Method.

2.2.2. CSD Correction Utilisation

CSD Corrections 1.39 is a program for converting two dimensional intersection data gathered from thin sections, outcrops, photographs etc. to true three dimensional crystal size distributions (CSD).The program constructs a solid of the dimensions indicated by the Short, Intermediate and Long dimensions. The orientation of the solid is constrained by the nature of the fabric (massive or foliated or lineated), the quality of the foliation (weak to strong) and the orientation of the desired section (parallel or normal to the fabric). This is sectioned by a plane placed a random distance from the centre of the solid. The outline of the intersection of the solid with the plane is determined and the length and width calculated. The distribution of these lengths and widths is used to correct the two dimensional for the cut section effect. The most likely intersection length (or width) is used to correct for tailing to smaller intersections. There is no tailing correction for intersections larger than the most likely intersection. This is rarely a problem if wide bins are used for the frequency distribution. After these tailing corrections have been made then corrections for the intersection probability effect are applied.

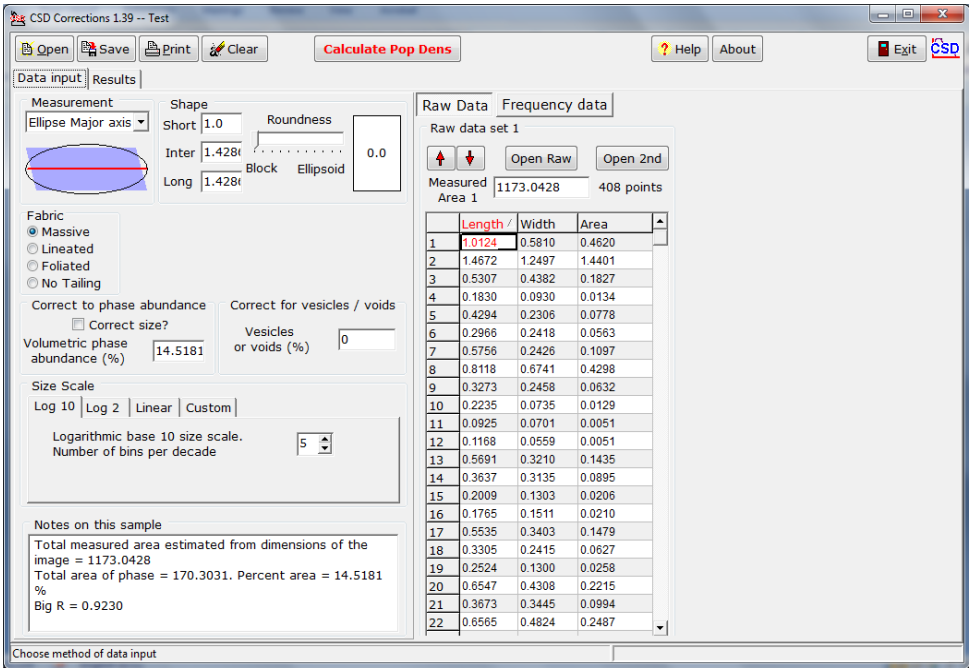

Figure 4 - CSD Correction Program Preview.

2.2.3. Data Entry

Data can be entered as a list of Lengths, Widths and/or Areas. They can be typed directly into the grid or loaded from a simple file of data, with one measurement on each line. They can also be pasted from the clipboard if the cell has a dotted line around it (push the up and down arrows to get this). A maximum of ten thousand points can be measured. Rows can be deleted (with Del) or inserted (with Ins) if the cell has a dotted line around it. Data can be transferred directly from the ImageJ image processing program. It is possible to load two separate data sets. These will be summed. This may arise if data is measured at two different scales on the same rock. Data can also be loaded as a series of bins (size intervals) and number of measurements in each bin. The upper limit of the bin is put in the left column, with the number opposite in the right column. The last line must be the lower limit of smallest bin size and the number zero in the adjacent column. Bin sizes must decrease downwards. Rows, and hence bins, can be deleted (with Del) or inserted (with Ins) if the cell has a dotted line around it.

3. Results and Discussion

Results are shown in tables and diagrams. The table columns show the following data. Column 1: Corrected Size of the middle of the interval. The size is long dimension of parallelepipeds, the major axis of ellipsoids, or the diameter of spheres. Errors are calculated using only the counting statistics. No error has been accorded to the tailing corrections, because it is not clear how to do this. Hence the error bars should be regarded as minimum values. Column 2: The natural logarithm of the population density. Column 3, 4: The error limits of the population density. They are calculated from the square root of the number of intersections in each bin. This is propagated to the other bins. The error calculations do not take into account any error in the correction factors, and hence should be viewed as minimum errors. Column 5: Numbers of crystals per unit volume in the interval. This can be used to make other kinds of CSD diagram. Column 6: Per cent volume of crystals in each interval. The error in the larger size intervals can be significant.

The diagrams in show the crystal size distributions through the a) CSD in semi logarithmic diagram, b) Cumulative Distribution Function diagram, c) Fractal Dimension diagram and d) Population Density diagram.

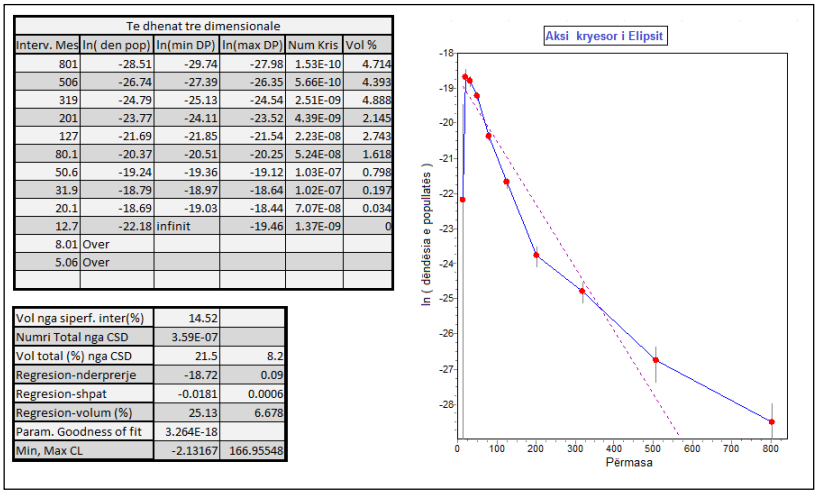

Te dhenat tre dimensionale

Interv. Mes	ln(den pop)	ln(min DP)	ln(max DP)	Num Kris	Vol %
801	-28.51	-29.74	-27.98	1.53E-10	4.714
506	-26.74	-27.39	-26.35	5.66E-10	4.393
319	-24.79	-25.13	-24.54	2.51E-09	4.888
201	-23.77	-24.11	-23.52	4.39E-09	2.145
127	-21.69	-21.85	-21.54	2.23E-08	2.743
80.1	-20.37	-20.51	-20.25	5.24E-08	1.618
50.6	-19.24	-19.36	-19.12	1.03E-07	0.798
31.9	-18.79	-18.97	-18.64	1.02E-07	0.197
20.1	-18.69	-19.03	-18.44	7.07E-08	0.034
12.7	-22.18	infinit	-19.46	1.37E-09	0
8.01	Over				
5.06	Over				

Vol nga siperf. inter(%)	14.52	
Numri Total nga CSD	3.59E-07	
Vol total (%) nga CSD	21.5	8.2
Regresion-nderprerje	-18.72	0.09
Regresion-shpat	-0.0181	0.0006
Regresion-volum (%)	25.13	6.678
Param. Goodness of fit	3.264E-18	
Min, Max CL	-2.13167	166.95548

ln (Limimiti i permas. siperm)	% Kumulative	CDF
6.45	100	3.33
5.99	99.8	2.88
5.53	99.1	2.37
5.07	97.9	2.03
4.61	91.7	1.38
4.14	77.1	0.741
3.68	48.4	-0.041
3.22	20.1	-0.839
2.76	0.381	-2.67
2.3		
1.84		
1.38		

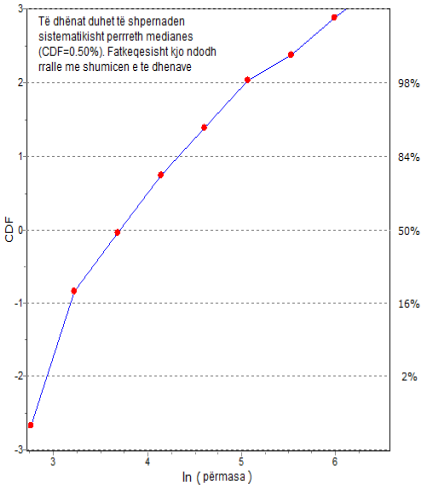

Figure 5 - CSD in semi logarithmic diagram and Cumulative Distribution Function diagram.

ln (Limimiti i permas. siperm)	ln (n < permas)	Min	Max
6.91	-22.6	-22.1	-23.8
6.45	-21.1	-20.7	-21.5
5.99	-19.6	-19.4	-19.8
5.53	-18.7	-18.5	-18.9
5.07	-17.3	-17.2	-17.4
4.61	-16.3	-16.2	-16.4
4.14	-15.5	-15.4	-15.6
3.68	-15.1	-15	-15.1
3.22	-14.8	-14.8	-14.9
2.76	-14.8	-14.8	
2.3			
1.84			
1.38			

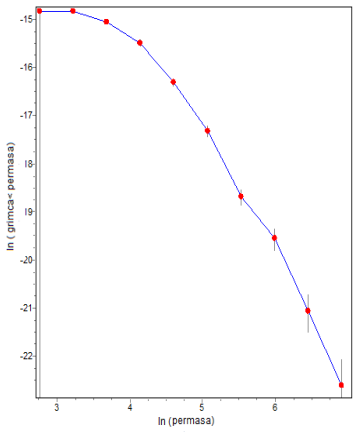

Limiti permases se siperme	Dendesia popullates	Min PD	Max PD
1.00E+03	4.14E-13	1.21E-13	7.06E-13
631	2.43E-12	1.27E-12	3.59E-12
398	1.71E-11	1.22E-11	2.20E-11
251	4.73E-11	3.38E-11	6.08E-11
158	3.82E-10	3.23E-10	4.40E-10
100	1.42E-09	1.24E-09	1.60E-09
63.1	4.42E-09	3.90E-09	4.94E-09
39.8	6.91E-09	5.78E-09	8.04E-09
25.1	7.63E-09	5.45E-09	9.80E-09
15.8	2.34E-10	0.00E+00	3.53E-09
10	0.00E+00		
6.31	0.00E+00		
3.98	0		

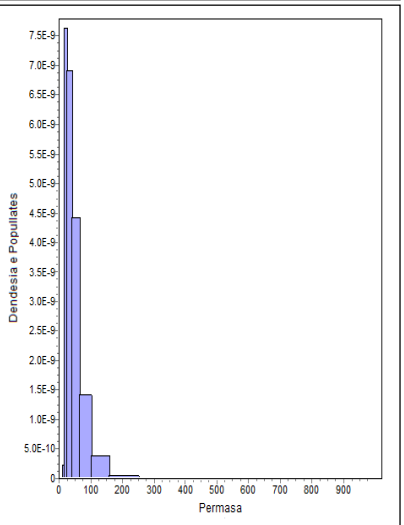

Figure 6- Fractal Dimension diagram and Population Density diagram.

3.1. Result Interpretation

The semi-log graph or semi-log plot shows the visualizing data that are changing with an exponential relationship. If CSD is linear in this diagram it matches with the regression line and slope angle can be defined. It is obvious that the size distribution in this case at some point does not align very well with the law and the log shape makes the match impossible. Possible errors correspond to the statistical counting. The refraction of CSD-curve comes from mixed population (blocks of various proportions), but the proportions of the blocks are reasonable. It is noted that the overall low is that by increasing the size of the blocks their density decreases. But there is also a decrease in population density for blocks of smaller size, which is actually normal for natural samples. Such a reversal in small sizes in natural rocks may come as a result of many reasons, one of which may be inadequate spatial resolution. Log-normal distribution is a continuous probability distribution of a random variable whose logarithm is normally distributed. Cumulative data are transferred by using the normal standard cumulative distribution function inverse. In this diagram the log normal distribution appears as a straight line. Mixtures of log normal distributions are identified as two or more straight segments of the graphic. In our case, we can see four such distributions. In the third plot, the steepness of the line can be used to determine the Fractal dimension distribution. In the cases where the line has more than one visible slope, the distribution can be described as multi Fractal. In our chart although the curve does not match 100% the straight line, it can be determined only one Fractal dimension with a value of approximately 1.45.The histogram is a graphical representation showing a visual impression of the distribution of data. It is an estimate of the probability distribution of a continuous variable. It proves the first statement that the overall low is that by increasing the size of the blocks their density decreases.

3.2. Discussion

Mélanges and BiM rocks are very common in nature and a lot of engineering projects are obligated to be constructed in these chaotic rocks. Excavating tunnels in BiM rocks can result highly problematic for a number of different reasons, one of which is the fact that in these types of rocks the blocks vary in size. Knowledge of the size distribution of blocks is a key parameter that should be evaluated in these studies. Between the maximum and minimum block size, in the scale range, it is important that the blocks are characterized by their respective volumes. The methods presentet in this paper intend to help geologists and engineers in the characterization of melange blocks. CSD Correction is a useful tool in the field of mineralogy and petrology, but there are still doubts about its use in big ‘sample’ size. With a more detailed research and study it can be helpful for the engineering geologist and for further developing the BiM rock study. The CSD produced by the program for small size sections have reasonable errors from 10%, but for complex shapes the application of CSD Correction seems to make just a first aproxximation, so care should be taken for the interpretations.

4. Acknowledgments

We are very grateful to PhD Sven Jacobs, who encouraged with the persuasion of this topic and spent extra time helping to achieve better results.

This paper would not have been possible without the support of DHP who gave us the permit to access their reports. Besides, we would like to thank the Faculty of Geology and Mining in Tirana for providing us with a good environment and facilities to complete this work.

5. References

Adam D., Markiewicz R., Brunner M. 2011. Block –in-Matrix structure- tunnelling in hard soil and/or weak rock, *Proceedings of the 15th European Conference on soil Mechanics and Geotechnical Engineering*, A. Anagnostopoulou et al. IOS Press, pp 607-1614.

American Geological Institute 1987. Glossary of Geology, Bates R.L. and Jackson J.A. (eds.), 3rd Edition; American Geological Institute, Alexandria.

Brugger C.R. and Hammer J.E. 2010. Crystal size distribution analysis of plagioclase in experimentally decompressed hydrous rhyodacite magma, *Earth and Planetary Science Letters*, pp 246-254.

Button E., Riedmuller G., Schuber W., Klima K. and Medley E. 2003. Tunneling in tectonic mélanges- accommodating the impacts of Geomechanical complexities and anisotropic rock mass fabrics, *Bulleting of engineering geology and Environment*, pp 1-24.

Fasching F. and Vanek R. 2011. Engineering geological characterization of fault rocks and fault zones, *Geomecanics and tunneling*, Volume 4, No 3, pp 181-194.

Ferreira T., Rasband W., Image J. 2012. User Guide, ImageJ/Fiju1.46.

Haneberg C.W. 2004. Simulation of 3D Block Populations to characterize Outcrop Sampling Bias in BiM rocks, FELSBAU 22 No 5, pp 9- 26.

Higgins M. D. 2002. Closure in crystal size distributions (CSD), verifications of CSD calculations, and the significance of CSD fans, *American Mineralogist*, January, v. 87, pp 171-175

Higgins M. D. 2006. Quantitative textural measurements in igneous and metamorphic petrology. Cambridge University Press – August, 265p.

Jacobs S., Jacobs S., Rusi M. and Bartl N. Devoll 2011. _20110408_Moglice-Headrace-Geol-Longsection-A0_10000. *Geological Report*. HPP Moglica.

Jacobs S., Rusi M., Bartl N. and Jacobs S. 2011. Harnessing of Hydropower Potential of Devoll River, *Geological Report*, Part III-HPP Moglica, Chapter 7, Waterway Moglicë-Grabovë. 7.4 Headrace tunnel Dobercan-Shemsit: Mirdita Melange.

Jagnow R., Dorsey J. and Rushmeier H. 2004. Stereological Techniques for solid textures, p 7.

Laznicka P. 1998. Breccias and Coarse Fragmentites: *Petrology, Environments, Associations, Ores 25 of Developments in Economic Geology:* Elseveir, New York, 1988, p 823.

Lindquist E.S. 1994. The strength and deformation properties of Melange, *PhD Dissertation*, 1994.

Lindquist E. S. and Goodman R.E. 1994. The Strength and Deformation Properties of a Physical Model Melange, *Proceedings of First North American Rock Mechanics Symposium*, Austin, Texas (June 13,1994): Rotterdam, Netherlands, AT. Balkema.

Marinos P. and Hoek E. 2001. Estimating the geotechnical properties of the heterogeneous rock masses such as flysch, *Bulletin of Engineering Geology and environment*, 60, p 85-92.

Marsh B.D. 1988. Crystal size distribution (CSD) in rocks and the kinetics and dynamics of crystallization I. Theory. *Contributions to Mineralogy and Petrology*, *Springer-Verlag* 99, pp 277-291.

Meco S., Aliaj S. and Turku I. 2000. Geology of Albania, contribution to the regional geology of the Earth, Volume 28, Borntraeger brothers, Berlin, Stuttgart, 205 p.

Medley E.W. and Zekkos D. 2011. Geopractitioner approaches to working with antisocial mélanges, *The Geological Socirty of America*, Special paper 480, pp 261- 277.

Medley E.W. 2002. Estimating Block Size Distributions of Melanges and Similar Block- in-Matrix Rocks (Bimrocks), *Proceedings of 5th North American Rock Mechanics Symposium (NARMS)*,Toronto, Canada, pp 509-606.

Medley E.W. 2002. Some guidelines to characterization of Franchescan mélanges and other BiM rocks. Appendix B to Melange and fault rocks exposed in and around abandoned quarry at the Schmidt lane recycling center, El Cerrito, California.

Medley E.W. 1994. The engineering characterization of Melanges and similar Block in Matrix Rocks, *PhD Dissertation* 1994.

Mock A. and Jerram D.A. 2005. Cristal Size Distributions in three dimentions. Insights from the 3D reconstruction of a highly porphyritic rhyolite, *Journal of Petrology*, Volume 46, Number 8.

Perfect E. 1997. Fractal models for the fragmentation of rocks and soils: a review, pp 1525-1541

Raymond L.A. 1984. Classification of Melanges, in Melanges: Their nature, origin and significance; 228 of special paper, Boulder, Colorado, *Geological society of America*, pp 7-10.

Robertson A. and Shallo M. 2000. Mesozoic-Tertiary tectonic evolution of Albania in its regional Eastern Meditettanean context, *Tectonophysics* 316, pp 197-254.

Russ, J.C. and Dehoff R.T. 2000. Practical Stereology. *Plenum Press, Second Edition*. New York, 381 p.

Sahagian D.L. and Proussevitch A.A. 1998. 3D particle size distributions from 2D observations: stereology for natural applications, *J. Volcanology and Geothermal Research*, pp 173-196

Shallo M. 1990. Ophiolithic melange and flyschoidal sediments of the Tithonian-Lower Cretaceous in Albania, *Terra Nova, Wiley –Blackwell*, Oxford, 2, pp 470-488.

Tremblay A., Meshi A., Bedard J. H. 2009. Oceanic core complex and ancient oceanic lithosphere: In sights from Iapetan and Tethyan ophiolithes (Canada and Albania.2009), *Tectonophysics*, (473), pp 36-52.

Turcotte D. L. 1992. Fractals and Chaos in Geology and Geophysics. Cambridge, 221 p.

Wakabayashi J. and Dilek Y. 2011. Characteristics and tectonic settings of mélanges, and their significance for societal and engineering problems, *Geological Society of America*, Special papers, 480, pp v-x

Wakabayashi J. and Medley E. 2004. Geological characterization of Mélanges for practitioners FELSBAU 22 (2004) Nr5, pp 10-18.

http://depcom.uqac.ca/~mhiggins/

http://depcom.uqac.ca/~mhiggins//csdcorrections.html

http://bimrocks.com/

http://www.rocscience.com/education/hoeks_corner

Δελτίο της Ελληνικής Γεωλογικής Εταιρίας, τομ. XLVII , 2013
Πρακτικά 13ου Διεθνούς Συνεδρίου, Χανιά, Σεπτ. 2013

Bulletin of the Geological Society of Greece, vol. XLVII 2013
Proceedings of the 13th International Congress, Chania, Sept. 2013

SÃO PAULO CAVERN-SHAFT COLLAPSE VIEWED AS A TRAP-DOOR PROBLEM

Saratsis G.[1] and Stavropoulou M.[2]

[1] *Mine Design Lab, Mineral Resources Engineering Department, Technical University of Crete (gsaratsi@gmail.com)*

[2] *National and Kapodistrian University of Athens, Faculty of Geology and Geoenvironment, Department of Dynamic, Tectonic and Applied Geology, , GR-15784, Greece (mstavrop@geol.uoa.gr)*

Abstract

This paper refers to the numerical simulation of the conditions that have lead to the collapse of the shaft-cavern collapse in São Paulo, Brazil (2007) constructed with the Conventional Tunnelling Method (CTM) or the New Austrian Tunneling Technique (NATM). The Pinheiros station where the incident has occurred, is located in an area known as the Caucaia Shear Zone, resulting in a highly fractured medium (four main families of discontinuities, i.e. two subvertical and two dipping towards the tunnel walls).The main observed lithologies were biotite gneiss and granite gneiss. According to the Bieniawski classification, the following rock mass classes were observed: II,III,IV (partially corresponding to saprolite), and V (partially corresponding to residual soils). The shaft-tunnel construction is simulated by virtue of the 3D finite differences code FLAC3D™. Special emphasis is given on the appropriate quantitative description of the geological conditions. A kinematic cohesion-friction softening model of the discontinuous rock mass is used. It was found that failure is manifested with the evolution of shear bands starting from the corners of the cavern periphery as this approaches the shaft while retreating. Before this, another cylindrical shear band initiates from the bottom of the shaft and also propagates upwards to connect with the former and hence producing the final collapse.

Key words: *shear band, strain softening, strain localization, jointed rock.*

Περίληψη

Στο παρόν άρθρο εξετάζονται με τη βοήθεια αριθμητικού μοντέλου οι συνθήκες που οδήγησαν στην κατάρρευση του συνδεδεμένου συστήματος φρέατος-θαλάμου στην μεγαλούπολη Sao Paulo της Βραζιλίας το 2007. Οι δύο θάλαμοι αντιδιαμετρικά του φρέατος εξορύχθηκαν με τη Νέα Αυστριακή ή Τμηματική Μέθοδο. Ο σταθμός Pinheiros όπου εκδηλώθηκε το περιστατικό αυτό βρίσκεται εντός γεωλογικής ζώνης γνωστής ως Caucaia Shear Zone. Εντός της ζώνης αυτής ο βιοτιτικός και γρανιτικός γνεύσιος είναι έντονα κατακερματισμένος που διασχίζεται από τέσσερεις οικογένειες ασυνεχειών (οι δύο εξ αυτών είναι παρακατακόρυφες και οι άλλες δύο με κλίσεις προς τις αντίθετες παρυφές των θαλάμων). Σύμφωνα με το σύστημα ταξινόμησης RMR του Bieniawski οι θάλαμοι εξορύχθηκαν σε βραχόμαζα κλάσης II,III,IV (η τελευταία αναφέρεται σε σαπρόλιθο), με υπερκείμενα σαπρόλιθο και εδάφη αποσάρθρωσης

κλάσης V. Η προσομοίωση της κατασκευής του συστήματος φρέατος-θαλάμου έγινε με τον τρι-διάστατο κώδικα πεπερασμένων διαφορών FLAC3D™. Δόθηκε ιδιαίτερη προσοχή στην ποσοτική περιγραφή των επί τόπου γεωλογικών συνθηκών. Λόγω του έντονου κατακερματισμού της βραχομάζας αυτή προσομοιώθηκε με ένα κινηματικό μοντέλο χαλάρωσης της συνοχής και της γωνίας τριβής. Από τις προσομοιώσεις βρέθηκε ότι σε κάοια στιγμή της εκσκαφής του θαλάμου σχηματίζεται συζυγές σύστημα ζωνών διατμήσεως που εκκινούν από τις γωνίες της προπορευόμενης σήραγγας το οποίο ενώνεται με μια κυλινδρική ζώνη διάτμησης που σχηματίζεται γύρω από το φρέαρ. Καταυτόν τον τρόπο σχηματίζεται σφήνα βραχομάζας η οποία και καταρρέει ως μηχανισμός θυροπαγίδας.
Λέξεις κλειδιά: *ζώνη διάτμησης, παραμορφωσιακή χαλάρωση, εντοπισμός παραμόρφωσης, ασυνεχής βραχόμαζα.*

1. Introduction

This paper refers to the numerical simulation of the conditions that have lead to the collapse of the shaft-cavern collapse in Sao Paulo, Brazil (2007) constructed with the Conventional Tunnelling Method (CTM) or the New Austrian Tunneling Technique (NATM). These constructions (shaft and caverns) are close to the Pinheiros river, in the SW sector of the city, and are part of the new Line 4 (Yellow Line) of the presently expanding São Paulo Metro. This line is 12.5 km long, linking city center with western suburbs with four interchange stations. An artistic isometric view of the access shaft the two antidiametrical stations (caverns) and the associated running tunnels are shown in Figure 1a.

On the afternoon of Friday 12th January 2007, a dramatic metro construction accident occurred in São Paulo. Nearly the whole of one of the station caverns of 40 m length suddenly collapsed, immediately followed by collapse of nearly half of the adjacent 40 m diameter and 35 m deep station shaft. The multiple accident shown in Figure 1b occurred so fast that there was no time for warning to be given. The seven unfortunate victims died after falling from the surface and becoming deeply buried under the collapsed rock and soil.

Referring to Figure 1a the design parameters of the Pinheiros Metro Station design were one shaft with a diameter of 40m, depth of 36m, two platforms of running length of 46m, height of 14.2m and width of 18.6m, and two rail double track tunnels with a diameter of 9.6 m. The height of overburden above cavern's crown is more or less 20 m.

The shaft-tunnel construction is simulated by virtue of the 3D finite differences code FLAC3D™ (Itasca, 2009). Special emphasis is given on the appropriate quantitative description of the geological conditions. This collapse incident is viewed in this work as a trap-door problem (Terzaghi, 1936) due to localization of strain along pre-existing joints of the rock mass above the cavern. The elastic and strength properties of the rock identified in lab are upscaled by using a special upscaling theory (Exadaktylos and Stavropoulou, 2008). A kinematic cohesion-friction softening Mohr-Coulomb model of the discontinuous rock mass is employed. This model is supported from fundamental rock mechanics considerations of heavily jointed rocks, namely the activation of pre-existing joints and subsequent sliding along their surfaces as the excavation advances and the rock adjacent to the openings is further loaded. From the simulations it was found that the failure is manifested with the evolution of shear bands starting from the corners of the top-heading of the cavern as this approaches the shaft, while retreating. Before this, another shear band initiates from the bottom of the shaft and also propagates upwards. The failure surface from the cavern extends upwards and forwards to connect with the shear band propagating from the shaft forming a rigid block of rock mass of weight of 20,000 t that finally caves in the tunnel and shaft; hence, the system behaves as a trap-door mechanism.

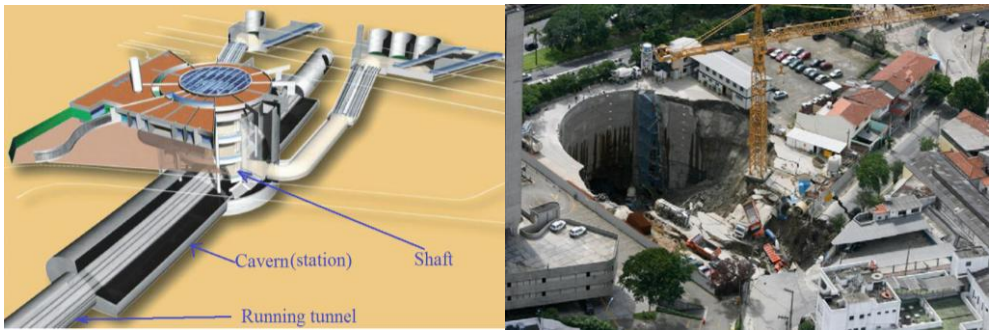

(a) *(b)*

Figure 1 - *(*a) Artistic isometric view of the Pinheiros Station (after Barros et al. 2008), (b) collapse incident occurred on 12/Jan./2007, producing more than 20,000 t of failed mtl. During the bench excavation, very close of arriving to the shaft. The antidiametrical failure surfaces extending around the shaft as is indicated by the arrow may be observed.

2. Rock Mass Structure

The Pinheiros station where the incident has occured, is located in an area known as the Caucaia Shear Zone, resulting in a highly fractured medium (four main families of discontinuities, i.e. two subvertical and two dipping towards the tunnel walls as is illustrated in the lower hemisphere stereographic projection of Figure 2a. The main observed lithologies were biotitic gneiss and granitic gneiss of the Pre-Cambrian age. According to the Bieniawski classification, the following rock mass classes were observed: II,III,IV (partially corresponding to saprolite), and V (partially corresponding to residual soils). The appearance of the rock core from the borehole 8704 that was drilled near the centre of the station cavern is shown in Figure 2b. The eighteen plastic containers contain the (minimal) recovery of 18 m of overlying above the rock materials such as saprolite, soil and sand. The rock head, encountered first at the depth of 18 m, that is at the elevation of 706m, was weathered gneiss. The near-vertical foliation is not appearing in the rock core.

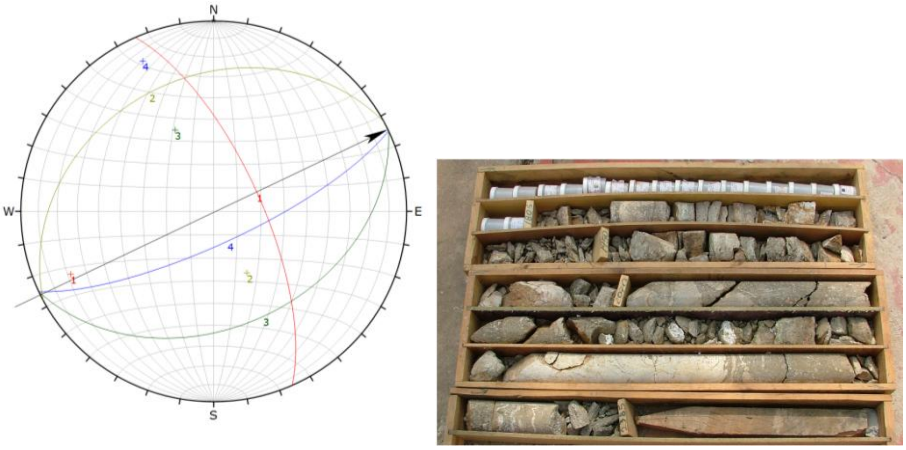

(a) *(b)*

Figure 2 – (a) Stereographic projection of the four rock joint sets and the tunnel advance direction with the arrow (right), and (b) the appearance of the rock core from the borehole 8704 that was drilled near the centre of the station cavern. The eighteen plastic containers contain the (minimal) recovery of 18 m of overlying sand, soil and saprolite. The rock head, encountered first at 18 m depth, at elevation 706m, was weathered gneiss. The near-vertical foliation is not shown (Barton 2009).

3. Rock Mass Mechanical Behavior

In this work the rock mass is assumed to be both isotropic and continuous. Both simplifying assumptions are reasonable due to the large number of joint sets transecting the gneiss and their dense network. Furthermore it is assumed that the rock mass behaves like a Mohr-Coulombic material with a linear elastic behavior up to the peak (p) strength, that is followed by a softening part and finally a residual (r) part as is illustrated in Figure 3a. Thus it is implicitly assumed that the discontinuous rock mass follows after it reaches its peak strength a kinematic cohesion-friction softening model as is illustrated in Figure 3b. For simplification it a constant and small value of the dilatancy angle of the rock mass is assumed. Further, the assumption of constant elasticity rock mass is justified by the fact that we do not expect damage (i.e. formation of new cracks) up to the peak load of the already heavily jointed rock mass.

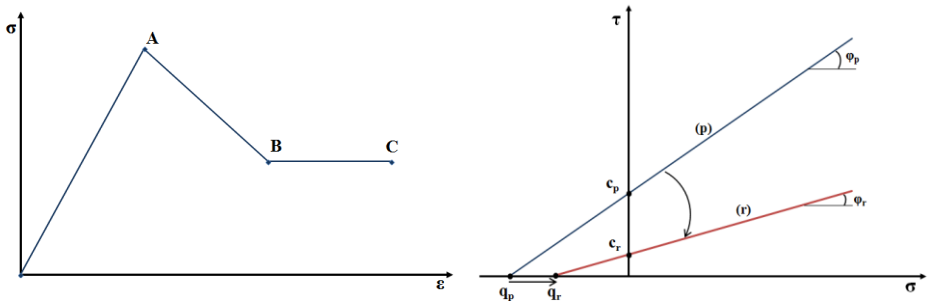

(a) **(b)**

Figure 3 – (a) The continuous strain softening model illustrated by a simple stress-strain diagramm, and (b) the kinematic cohesion-friction softening model in the plane (σ,τ) for a heavily jointed rock.

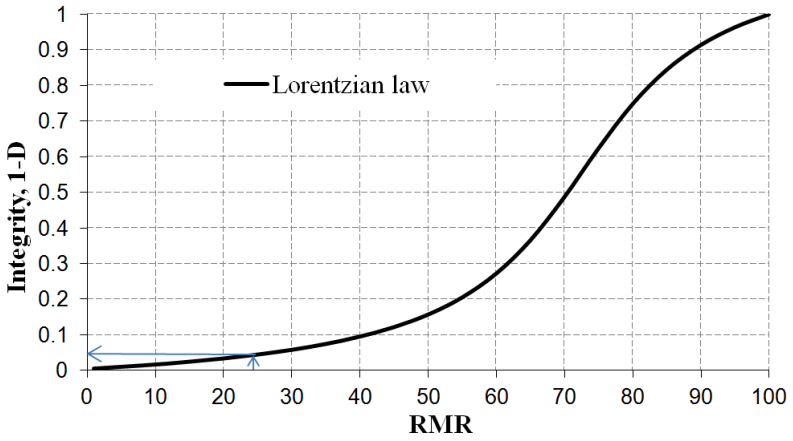

Figure 4 - Relation of rock mass integrity with RMR. Gneiss rock mass has properties that are found by multiplying the integrity of 5 % with the intact rock parameters identified in the lab.

The elastic and strength properties of the intact rock identified in lab were upscaled by using a special upscaling theory suited for discontinuous rocks (Exadaktylos and Stavropoulou, 2008). From this paper we have taken the diagram shown in Figure 4. Based on a mean RMR of the order of 25 of the rock mass above the cavern it is found that the remaining integrity (1-D) - with D referring to damage of the rock ranging from 0 (completely disintegrated rock) to 1 (intact rock) – is of the order of 0.05 or 5 %. Hence all the elastic (apart from Poisson's ratio) and strength parameters (apart from the friction and dilatancy angles) necessary for the model have been

derived by multiplying the values of parameters found from lab tests by the constant factor of 0.03 (Table 1).

Table 1 – Mechanical parameters of the model of the rock mass and intact rock parameters.

Rock Parameter [units]	Intact gneiss	Damaged gneiss
Elastic modulus [GPa]	100	5.1
Poisson's ratio	0.16	0.16
Peak Cohesion [kPa]	8000	400
Peak Internal friction angle [deg]	34	34
Residual Cohesion [kPa]	-	30
Residual Internal friction angle [deg]	20	20
Dilatancy angle [deg]	10	10
Tensile strength [MPa]	12	0.6

For this rock mass model one should prescribe the two decreasing curves of cohesion and friction angle with the accumulation of plastic shear strain in the rock mass and feed them as an input into the FLAC3D code like those shown in Figure 5. Hence, the plastic shear strain is chosen as the softening (aging) parameter of the rock adjacent to the shaft – cavern construction as it is loaded during excavation.

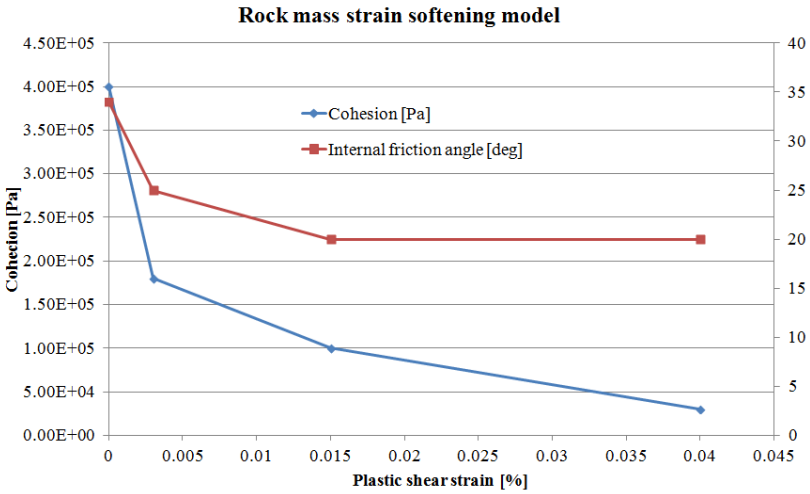

Figure 5 – Both c and φ strain softening models.

4. Numerical Simulations and Results

The shaft-tunnel construction is simulated by virtue of the 3D finite differences code FLAC3D™ as is shown in Figure 6. It should be noted that 3D modeling is indispensable in order to consider the interaction of both shaft and cavern constructions. Special attention was given to the appropriate creation of the nodes grid around the junction of the shaft with the cavern. Due to symmetry of the problem only one-quarter of the problem, i.e. the one quarter of the shaft and the cavern, have been simulated as is shown in Figure 6. The current model includes all station components such as the shaft and platform tunnel (cavern), apart from and running tunnel. The simulated excavation sequence follows that which have been applied in reality as is illustrated in

Figure 6. The support (i.e. shotcrete lining, lattice girders, and forepoling) was not considered in this first attempt. The effect of the support to resist the loads applied to the rock was considered indirectly by slightly increasing the properties of the rock mass. This is justified by the fact that here we are only interested to investigate the rock mass failure mechanism around the shaft and the cavern. In a next publication we are going to consider the support and its installation sequence and its effect on ground deformations. The construction sequence was (i) excavation of the shaft down to the first working level (invert of the platform top headings); (ii) simultaneous excavation of the headings of the two platform tunnels in opposite directions; (iii) excavation of the bench (second working level), and then (iv) the excavation of the invert of the platform tunnels. During excavation of the platform tunnels, the top heading advanced in steps of 1.60 m from the shaft towards the running tunnel. The bench was excavated in advances of 2.0 m from the running tunnel towards the shaft. It is noted that the invert was not excavated due to the collapse at the end of the bench excavation. The model has been subjected only to gravitational loading and the lateral stress to vertical stress ratio is depicted by the known Poisson's ratio $\nu/(1-\nu)$. The low value of the ratio 0.18 (class of rocks with low Poisson's ratio between 0 and 1/6) means in turn a small dilatancy of the rock mass due to joint activation and formation. This assumption rests upon the fact that there not new formed fractures but simply frictional sliding along pre-existing joints with states more or less close to residual friction angle.

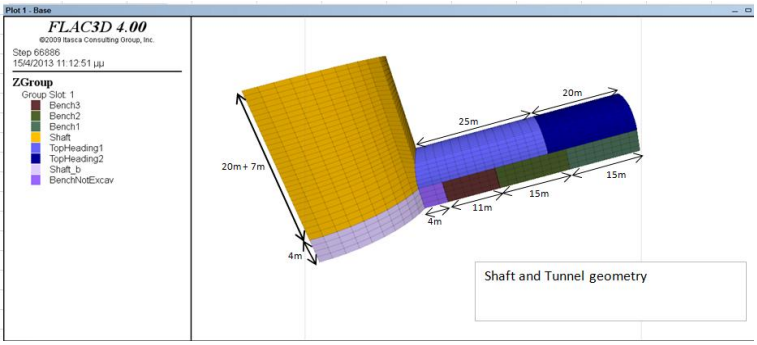

Figure 6 – Simulation of the cavern-tunnel construction steps by virtue of FLAC3D.

The localization of plastic shear strain along shear bands after the excavation of the third bench (only one bench remaining to reach the shaft) is clearly illustrated in Figure 7a. At the same more or less excavation step, that was actually just before the collapse, the formation of the symmetrical shear bands around the cavern are shown in Figure 7b. These shear bands, as was expected, have started from regions with high stress concentrations (top – heading and shaft corners). The displacement distribution after final excavation and the isosurface of vertical displacement greater than 0.15 m is shown in Figure 8 a and b, respectively. It is worth noticing that inside the rock mass a polyhedral block enclosed by this isosurface of 0.15 m vertical displacement is formed that could collapse as a rigid body.

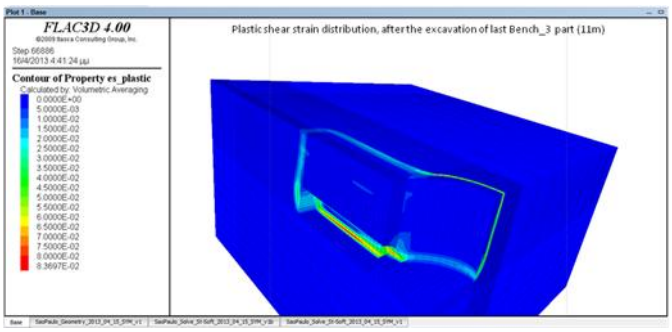

(a)

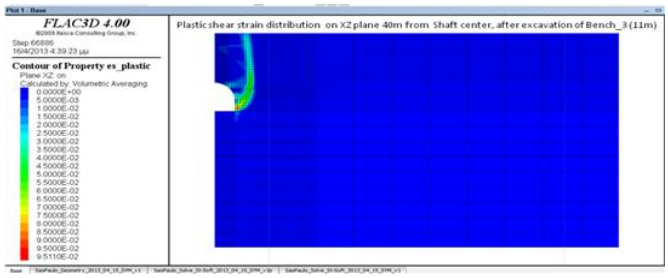

(b)

Figure 7 – (a) Final configuration of the shear band (localization of plastic shear) around the shaft and the cavern that finally collapses as a rigid body (one-quarter of the model). (b) Vertical section perpendicular to the cavern's longitudinal axis of the plastic showing the shear strain distribution.

One may also notice: (a) the similarity of the predicted trace of shear band around the shaft at the surface that is shown in Figure 7a with the actual failure at the collar of the shaft as is shown in Figure 1b; (b) the similarity of the predicted transversal to the cavern's axis vertical shear band at the far-end of the cavern at a distance of 45 m from the shaft's wall that may be seen in Figure 7a, with the activated fault at the same location captured by the aerial photo of Figure 8c; and finally, the time of collapse occurrence predicted by the model (i.e. just before the excavation of the last bench) which is in agreement with the actual timing of the collapse incident.

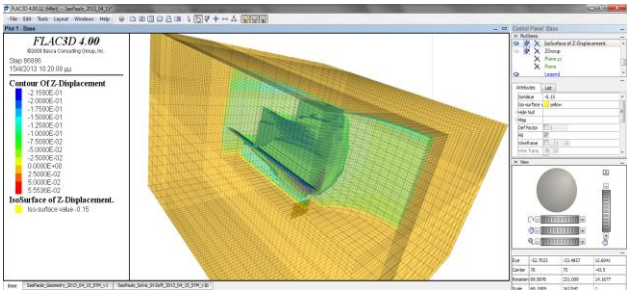

(a)

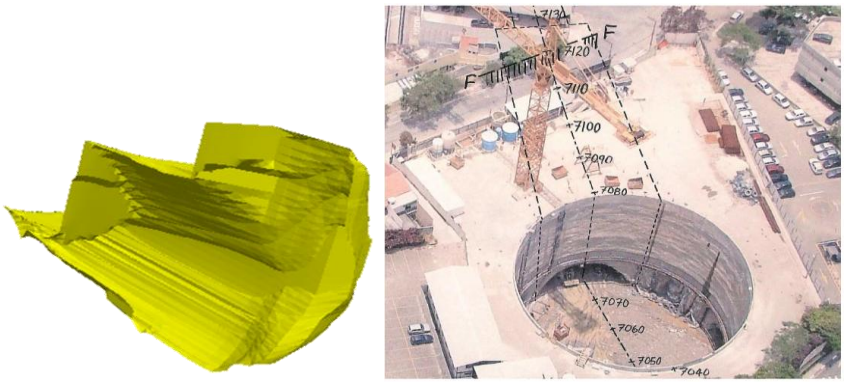

(b) *(c)*

Figure 8 – (a) Displacement distribution after final excavation (b) IsoSurface of vertical displacement greater than 0.15 m (c) Aerial view of the Pinheiros Station shaft. The black curved arch at 20m depth down the shaft wall is the topheading of the station platform cavern. The shaft wall chainage at 7080 m and the rear discontinuity (FF) at chainage 7120 m, mark the approximate limits of the 40 m long station cavern collapse (Barton, 2009).

Finally, in Figure 9a we have plotted the vertical displacements predicted by the model from the onset until the collapse at the two history points TN – G2 and TN – G3 which are shown in Figure 9b.

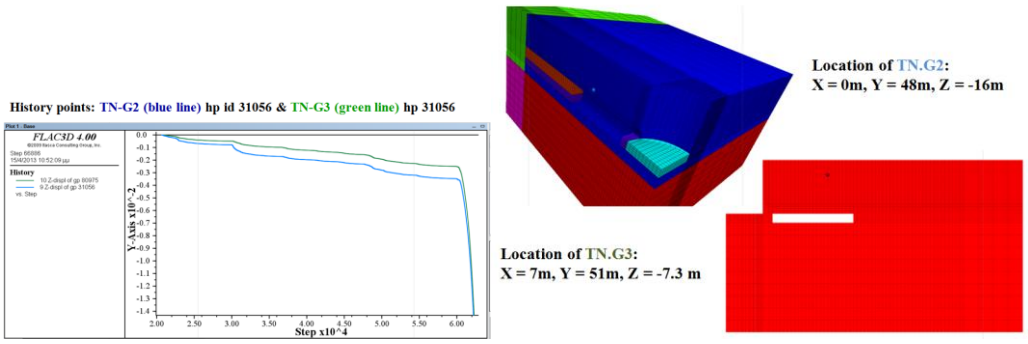

(b) *(c)*

Figure 9 – (a) Vertical displacements during the excavation process measured on two history points above the tunnel (b) location of history points.

5. Acknowledgments

The authors would like to thank the financial support from the EC 7th Framework Project (FP7-SEC-2010-1) DESURBS (Designing Safer Urban Spaces).

6. References

Barros J.M., Iyomasa W., Azevedo A.A., Eisenstein Z. and Assis A.P. 2008. Lessons from Brazil: pinheiros examined, *Tunnels Tunnelling Int*., 16–20.

Barton N. 2009. Differential weathering and adverse discontinuities were the apparent causes of a tragic metro accident in Brazil, *Proceedings of the International Conference on Rock Joints and Jointed Rock Masses*, Tucson, Arizona, USA, Special Paper.

Exadaktylos G. and Stavropoulou M. 2008. A Specific Upscaling Theory of Rock Mass Parameters Exhibiting Spatial Variability: Analytical relations and computational scheme, *International Journal of Rock Mechanics and Mining Sciences*, 45, 1102–1125.

Itasca Consulting Group, Inc. 2009. FLAC3D, Fast Lagrangian Analysis of Continua in 3 Dimensions, *Ver. 4.0, User's Manual*, Minneapolis: Itasca

Terzaghi K. 1936. Stress distribution in dry and saturated sand above a yielding trap-door, *Proc. Int. Conf. Soil. Mech.., Cambridge, Mass.*, I, 307-311.

Δελτίο της Ελληνικής Γεωλογικής Εταιρίας, τομ. XLVII , 2013
Πρακτικά 13ου Διεθνούς Συνεδρίου, Χανιά, Σεπτ. 2013

Bulletin of the Geological Society of Greece, vol. XLVII 2013
Proceedings of the 13th International Congress, Chania, Sept. 2013

ENGINEERING GEOLOGICAL CONDITIONS OF KLOKOVA MOUNTAIN, GREECE

Saroglou H.[1] and Kazilis N.[2]

[1] National Technical University of Athens, School of Civil Engineering, Department of Geotechnics, saroglou@central.ntua.gr

[2] Geodata Greece, Theodorou Litsa Str. 9, 115 27, Thessaloniki

Abstract

The paper presents the engineering geological conditions of Klokova Mountain and discusses the problems, which relate with the presence of fault structures, karst features and steep rock slopes in relation to the existing and planned motorway. The engineering geological setting of the limestone formations is characterized by the development of karst and the fault presence.

The karst pattern and an interpretation of the fault geometry of the area are presented based on geological mapping. Additionally, rockmass conditions are presented based on field data and borehole findings. The geotechnical conditions have been assessed by geotechnical investigations, which were executed for the design of the new highway.

Finally, a risk assessment of the area due to rockfalls is presented, considering that the risk level is very high due to the presence of very steep and fractured slopes, formed partially parallel to fault surfaces, and the high seismicity of the broader area. Rockfall episodes are prone to occur under seismic loading during a strong earthquake in the area but also due to high rainfall incidents.

Key words: *Karst, Limestone, Fault, Rockfall.*

Περίληψη

Στην παρούσα εργασία παρουσιάζονται οι τεχνικογεωλογικές συνθήκες της περιοχής της Κλόκοβας, οι οποίες χαρακτηρίζονται από την ύπαρξη ρηξιγενών ζωνών, την ανάπτυξη καρστικού συστήματος και την παρουσία απότομων βραχωδών πρανών. Η ανάπτυξη του κάρστ καθώς και η γεωμετρία των ρηξιγενών ζωνών διερευνήθηκαν από την γεωλογική χαρτογράφηση. Επίσης, γίνεται αναφορά στα χαρακτηριστικά της ασβεστολιθικής βραχομάζας με βάση τα αποτελέσματα των γεωτεχνικών ερευνών που έχουν εκτελεστεί για το σχεδιασμό του νέου αυτοκινητόδρομου.

Τέλος, εξετάζεται η επικινδυνότητα έναντι καταπτώσεων κατά μήκος του υφιστάμενου δρόμου σε συγκεκριμένες θέσεις, από όπου προκύπτει ότι είναι σημαντική δεδομένου ότι το ύψος των πρανών είναι μεγάλο και η συνθήκες εκδήλωσης του φαινομένου είναι εν γένει ευνοϊκές λόγω του κερματισμού της βραχομάζας και της σεισμικής δραστηριότητας της περιοχής.

Λέξεις κλειδιά: *Κάρστ, Ασβεστόλιθος, Ρήγμα, Καταπτώσεις βράχων.*

1. Introduction

The mountain range of Klokova has a NNW direction, with maximum altitude of 1050 m and is surrounded by zones of milder morphology. The mountain in the south ends in the north coastline of Patraikos gulf, which is characterized by steep slopes (mean angle of 50^0 and at some places up to 75^0), while their slope foot is covered by lateral slope scree material with varying degree of cementation. The steep morphology of Klokova slopes is formed due to fault surfaces, which intersect or align parallel to the National roadway. The new highway in the area of Klokova mountain is planned to be constructed either with bridges or twin tunnels. The alignment of the civil engineering works is not shown in the present paper since it has not been finalized.

2. Geological Setting

2.1. Geological Formations

The geological formations encountered in Klokova area are: a) loose slope talus, b) limestone scree with varying degree of cementation and c) limestones. Klokova mountain is forms an anticline (Aubouin et. al., 1958).

Loose slope talus

The formation of the talus is recent slope scree, which due to their placement on the steep limestone slopes has an extremely loose and metastable nature. It is in a state of periodical downward movement on the slopes. Due to their meta-stable condition, these periodical movements may trigger with only small scale mechanisms, such as a temporary wetting (or maybe saturation) of the material during a heavy rainfall, a relatively weak seismic loading or foot erosion of the talus slope due to natural or man made causes (excavation of slopes). Concerning the thickness of the talus formation the maximum thickness encountered in the boreholes performed in the area was 16 m.

Limestone scree slightly to moderately cemented.

They are characterized by a varying degree of cementation, while their bedding is well developed. At some places clay layers are encountered in the formation. They consist of gravel, pebbles and limestone fragments, with dimensions up to 10 cm, cemented with silty-sandy but also calcitic materials. In some places, the cementing material is clayey. Generally, the cementation degree depends on the nature of the cementing material and the age of the individual layers in the formation.

Limestone scree moderately to highly cemented.

The moderately to highly cemented scree is characterized by high cohesion, which originates from the secondary high degree of their cementation. The degree of cohesion depends highly on the type of cementing material. Additionally, they have rock-like behaviour thus a high friction angle since they are found stable in the existing highway slopes. It was formed by the cementation of the limestone scree, following chemical procedures with cementing matrix that is mainly of calcareous origin. The formation is karstified and the karst is developed along the bedding planes with dimensions between a few centimeters up to 1-2 meters and in the form of gullies when related to faults.

Eocene limestones, encountered in the east part of Klokova mountain.

It is characterized as moderately bedded with very good interlocking of the rock blocks. The rock blocks are cubic, formed by three main joint sets. The discontinuity surfaces are moderately rough to rough, slightly to moderately weathered, with clay or travertine infillings or empty. The bedding planes of the limestone are pervasive. The limestone is slightly karstified. The development of karst is only along bedding planes leading to their widening up to 30-40 cm.

Cretaceous limestones, encountered in the central and west part of Klokova mountain.

The mountain is primarily formed by the Cretaceous limestones. They are usually slightly to moderately fractured, with cubical blocks formed by three orthogonal discontinuity sets, which result to a blocky rockmass with good behaviour. In some locations, they are moderately to heavily fractured due to the presence of more than three discontinuity sets, which form a very blocky rockmass with generally small blocks. In this case the interlocking of rock pieces remains very good. In both rock types encountered, the discontinuity surfaces are rough, slightly to moderately weathered, generally open, with or without hard calcitic infilling material.

Additionally, broken zones exist in some places due to the presence of faults, which generally have a width of a few meters. In these zones, the rockmass is characterized by a tight structure and thus the interlocking of the rock particles is good. The limestone is characterized as moderately karstified with fracture karst (developed along faults with opening of a few centimeters up to 2-3 m) and sometimes along discontinuity planes.

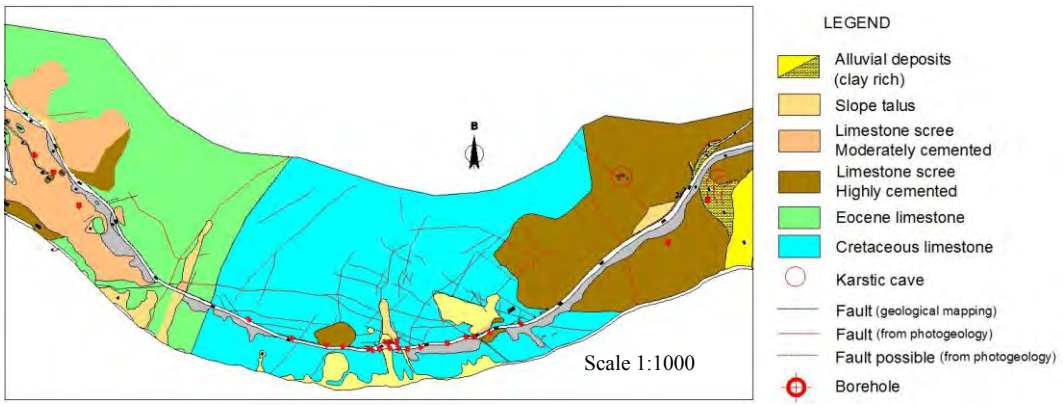

Figure 1 – Geological map of Klokova area.

2.2. Tectonic Setting

The most important tectonic structures of the broader area are interconnected with tectonic lines with ENE-WSW direction, parallel to which major discontinuities are developed that sometimes are very wide with openings in the range of tenths of centimeters up to a meter.

Furthermore, fault surfaces are encountered, with a general NE-SW and WNW-ESE trend, parallel to which some sets of minor discontinuities form.

3. Karst Development – Fault structure

3.1. Karst

The importance of determining the karstic network pattern and the anticipated groundwater flow in such carbonate rocks when tunneling is very crucial in order to forecast and confront related problems (Marinos P., 2005). The geological formations that are characterized by karstic voids in Klokova area were: a) the highly cemented limestone scree, b) The Cretaceous limestones and c) the Eocene limestones. The karst types were evaluated based primarily on geological mapping (Geodata, 2009) and compared with the borehole findings (from Nama S.A. – Kastor Ltd, 2005 and General Consulting Ltd – Istria, 2007).

Two types of karstic voids were found in the formation of the highly cemented limestone scree:

- Those developed along the bedding planes, with generally small dimensions up to 1 m

- Gullies developed along faults with dimensions up to 5 m (Figure 2 a and b). The location of such a karstic void is shown in Figure 1, coinciding with a fault line.

Two types of karstic features were encountered in the Cretaceous limestones:

- Fracture karst, which is developed along fault planes with dimensions ranging from a few centimeters up to 2-3 meters.
- More rarely, fracture karst, developed along discontinuity planes, is encountered, which has dimensions less than one meter.

The development of karst in the Eocene limestone is encountered only along bedding planes, thus the width of the voids is up to 0.5 m.

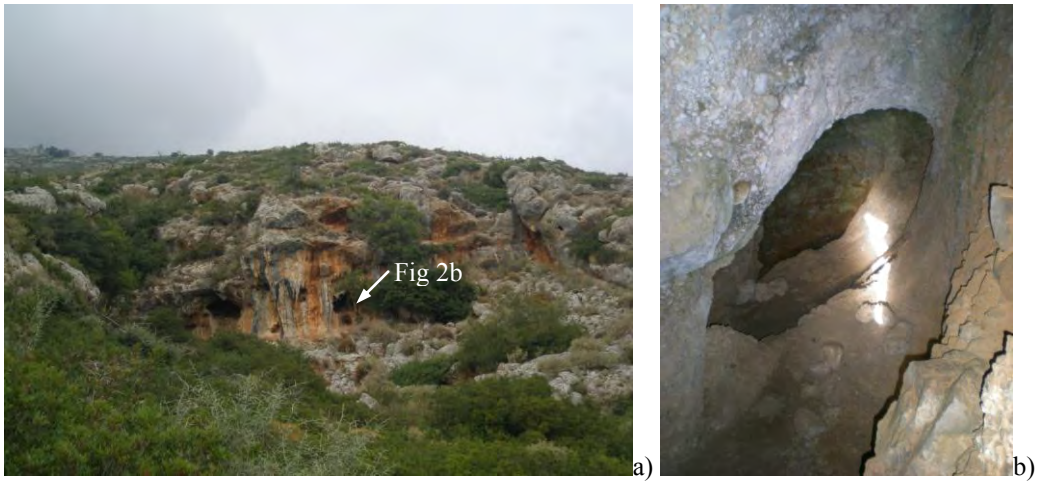

Figure 2 - Karstic voids related to faults in cemented scree a) general view, b) detail of void.

The dimensions of the voids in the cemented scree formation, as encountered in boreholes, range between 0 and 1.0 m mainly depicting karst developed along bedding planes (Figure 3a). Both karst types of the limestone formation were found in the boreholes. More specifically, karst developed along discontinuities with dimensions less than 1.0 m was commonly encountered (Figure 3b) as well as one case of an empty void with dimensions equal to 3.2 m reflecting the connection with fault structure.

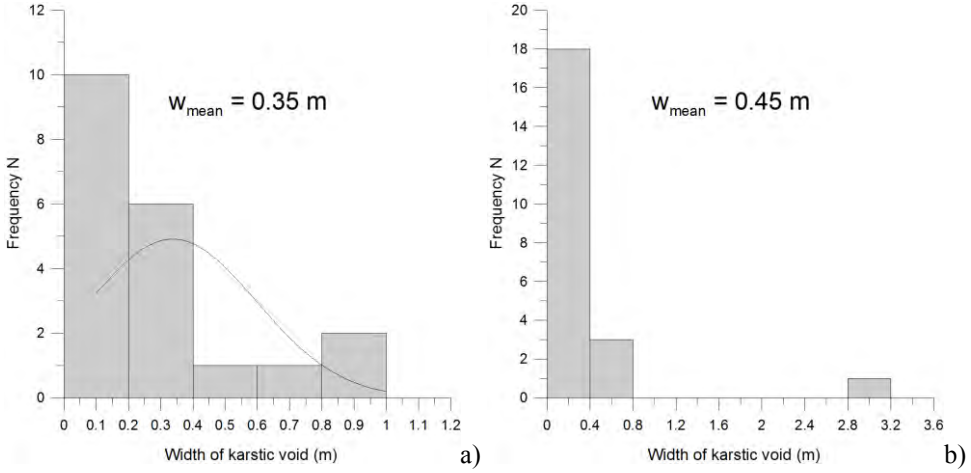

Figure 3 - Histogram of width of karstic voids encountered in a) highly cemented scree and b) Cretaceous limestone.

3.2. Fault Zone Geometry

The geometry of the major fault lines was determined by photogeological interpretation of the aerial photographs of the area. The major fault zones intersecting the existing highway are presented in Figure 4a. In order to determine the predominant directions of the major faults that intersect the area of Klokova, a rose diagram was prepared based on the data collected during the geological mapping, as shown in Figure 4b.

The following major fault systems were determined:

- 1st system B060^0 (angle 86^0)
- 2nd system B120^0 (angle 83^0)
- 3rd system B90-100^0 (angle 77^0)
- 4th system B170^0 (angle 72^0)

Figure 4 a) Major fault structures of Klokova area b) Orientation diagram.

3.3. Fault zone characteristics

The fault zones, which were recorded in the limestone rockmass along the existing road, were distinguished in two types:

- Tectonised zones in which the degree of fracturing of the limestone is high. The tectonised zones have a width in the range of a few meters (between 1 and 5 m). In few locations these are found with greater width up to 15 m resulting in highly broken rockmass with relatively good interlocking of rock pieces.
- Zones, which are, delineated as tectonic lines and characterised by the presence of a single fault plane. In this case, the rockmass conditions adjacent to the fault plane are not influenced. These fault zones are generally open and empty.

The fault zones are characterized by the presence of secondary filling material in few cases, highly cemented which consists of gravels and irregular limestone fragments with small sizes. Generally, few of these zones were found on the surface while these were encountered in the boreholes. Their width was in the range between 2 and 5 m.

The fault zones encountered in the boreholes were distinguished in three categories, confirming the findings of the geological mapping:

- Zones of highly broken limestone, which have a width between 1 and 5 m. The resulting rockmass has good interlocking.
- Major fault lines, which are seen as voids in the boreholes (due to core loss) reflecting the opening along the fault plane. On either side of the zone, either mylonite material with small thickness or an abrupt transition to the fresh or slightly fractured limestone mass was recorded.

4. Rockmass Conditions

4.1. Mechanical Properties of Geological Formations

The mechanical properties of the scree and limestone formations were evaluated based on the uniaxial compressive strength tests.

The compressive strength of the scree varies significantly in relation to the degree of cementation. The range of the uniaxial compressive strength of the cemented scree and the limestone formation is presented in Figure 5. The mean uniaxial compressive strength, σ_{ci}, of loose to moderate and high cemented scree is equal to 13.2 MPa and 22.2 MPa respectively. The uniaxial compressive strength of limestone is equal to 55.1 MPa.

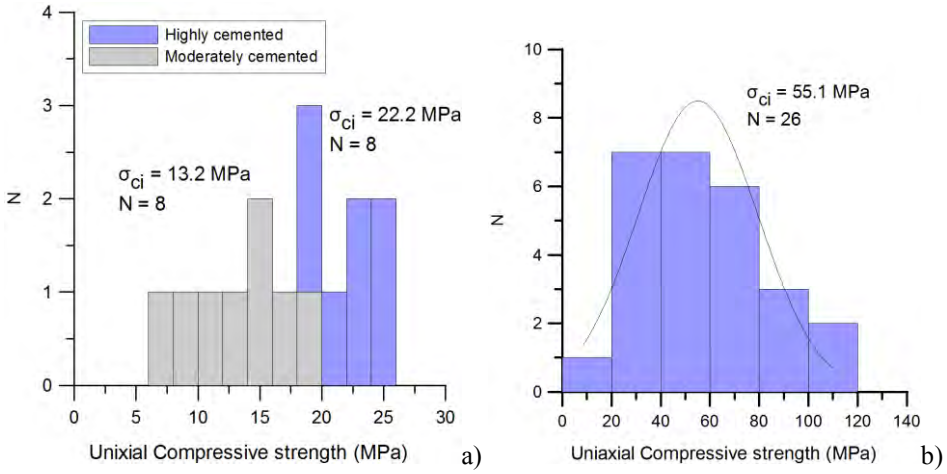

Figure 5 - Histogram of uniaxial compressive strength of a) loose to moderately and highly cemented scree and b) Cretaceous limestone.

4.2. Rock Mass Classification

In order determine the rockmass conditions of the limestones encountered at the surface and in the boreholes, a classification according to RMR (Bieniawski, 1976) and GSI (Marinos & Hoek, 2000) was performed for the total length of the borehole cores (392 m approximately). A typical view of these rockmass types in boreholes as well as the range of GSI values is shown in Figure 6. Three main rock types were distinguished:

- Blocky rockmass type, which locally presents parts of practically intact rock (in which the distance of discontinuities is greater than 2 m), with good to fair joint surface conditions (Figure 6a and b). This rockmass type is rated in the range RMR=70-85 and GSI=65-80.
- Very blocky rockmass type, which generally entails parts of better quality rockmass (blocky) with fair to good joint surface conditions (Figure 6c). This rockmass type is rated in the range RMR=50-65 and GSI=40-60. It can be seen, that the very blocky rockmass type includes sections with lower degree of fracturing resulting in a blocky rockmass.
- Disintegrated rockmass type due to the tectonic disturbance in fault zones. The width of these zones is generally small, up to 2-5 m (Figure 6d). This rockmass type is rated in the range RMR=35-45 and GSI=25-35.

The rockmass categories, as encountered in the boreholes in Klokova area, were the following: Category 1: RMR> 65 and GSI > 65 (presence at a percentage of 43.9%), Category 2: 45 < RMR < 65 and 35 < GSI < 65 (presence at a percentage of 52.8%), Category 3: RMR < 45 and GSI < 35 (presence at a percentage of 3.3%). The range of GSI of each rockmass category in respect to the borehole core length is presented in Figure 6e.

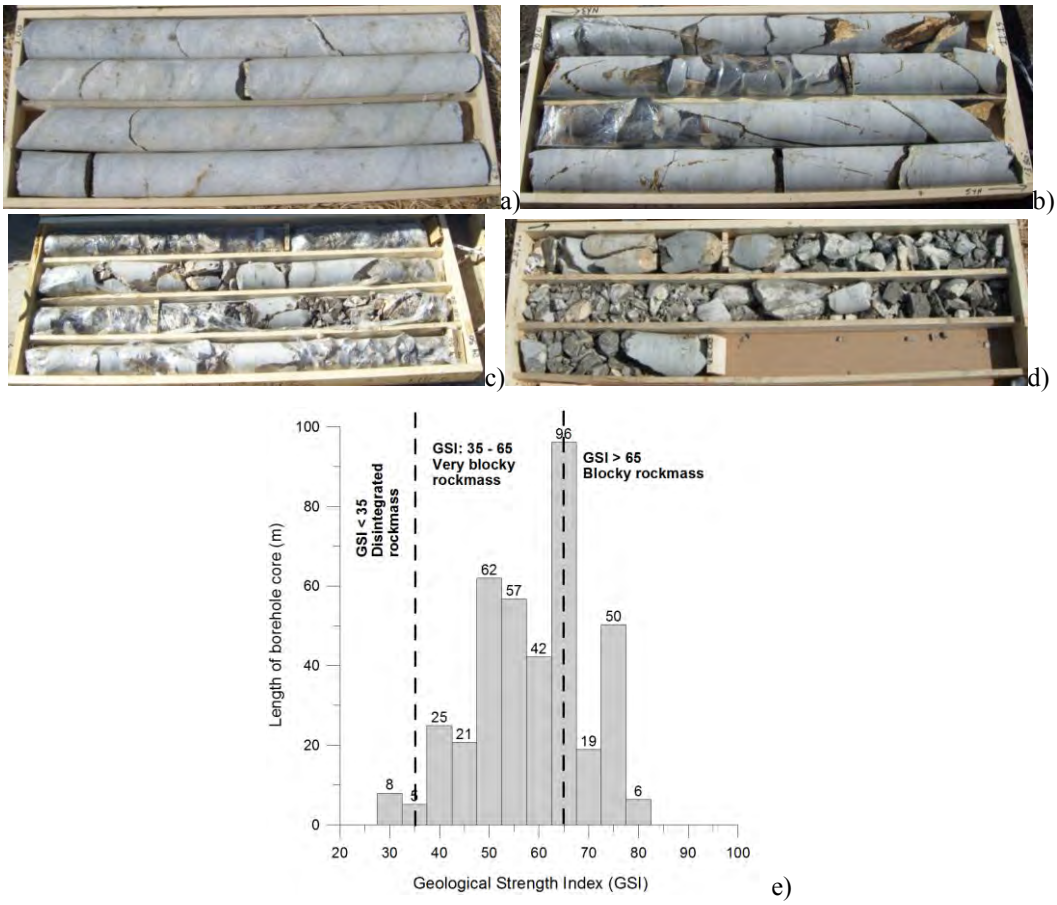

Figure 6 – a) to d) Rockmass types e) range of GSI for each rockmass category of limestones

5. Rockfall Risk

5.1. General

The rockfall risk of Klokova area is very high due to the overhanging steep rocks slopes adjacent to the existing roadway and the high seismic activity of the broader area. The areas with high rockfall hazard are the following:

- Sections where fault surfaces form very steep (almost vertical) or overhanging rock slopes adjacent to the roadway as shown in Figure 7a. Single rock blocks can be found at the crest or on distinct locations on these slopes.
- Sections where the rock cliffs at higher elevations create potential conditions for detachments of large rock quantities, which although part of the rockfall trajectory may be on slope talus the falling blocks may eventually reach the roadway with substantial impact energies.
- Sections where the rockmass is highly fractured and the slopes are adjacent to the roadway, usually found at moderate slope heights. The risk becomes higher if the slope height is higher (Figure 7b). Such cases are encountered in tectonised zones in which the degree of fracturing of the limestone is high.

The detachment of rocks may occur due to seismic loading or by the action of water percolating through the limestone rockmass. The phenomenon may be triggered also due to the loss of support

of blocks where open discontinuities and karstic voids exist. Low or medium risk areas are those in sections with relatively small heights of slopes. Considering the proximity of the high rock slopes (height up to 100 m) to the roadway and the magnitude of impact of a potential rockfall episode, it could be considered that the existing retaining structures offer little protection. The existing mitigation measures include two retaining walls with low energy barriers on their crest, located in the middle section of Klokova area (Figure 7a and b) as well as wire rope nets installed on rock slopes with relatively small height and in restricted length.

5.2. Rockfall Analysis

A rockfall analysis was performed in two sections of the roadway, at Chainage 7+730 and 7+850, which have different characteristics both in slope geometry and geological materials on the slope. In Section 7+730, scree is found in the lower part of the slope with an inclination of 35^0 and limestone in the upper part of the slope. In Section 7+850, the limestone slope has an inclination of 85^0 overhanging the road.

The height of the potential rockfall source is 115 and 85 metres respectively above the road level. Their locations were defined during geological mapping. The size of the unstable blocks, which are more probable to fall, is between 1 m^3 and 4 m^3. The size of the falling block in the analysis was considered equal to 2 m^3. In order to model the trajectory of the falling rocks and calculate the impacting kinetic energy, it is necessary to estimate accurately the normal and tangential coefficients of restitution (R_n and R_t) of the scree and limestone. The coefficients of normal and tangential restitution for the scree and limestone were considered equal to R_n=0.35 and 0.45 and R_t=0.55 and 0.80 respectively (Saroglou et. al, 2010). The initial velocity of the falls was taken equal to 0.48 m/s due to seismic triggering (based on the acceleration coefficient of the area according to the Greek Earthquake Resistant Regulations, 2004). The analysis was performed using the software RocFall of Rocscience Inc (1998).

a) b)

Figure 7 - Very steep slope morphology (overhanging slopes) posing a very high rock fall risk.

The maximum kinetic energy on the roadway in Chainage 7+730 was 1100 kJ while in Chainage 7+850 it reached 3500 kJ. The presence of scree on the slope and its lower inclination in section 7+730 resulted in lower total kinetic energy and bounce height.

An example of the analysis in Chainage 7+850 is shown in Figure 8, depicting the trajectories of rocks and the total kinetic energy distribution at the road level. Based on the results of the analyses, it can be concluded that the nature of the geological formation on the slope as well as the slope geometry, is decisive on the magnitude of the total kinetic energy at impact on the road. It can also

be concluded that rockfall barriers should be installed on the slope face in order to restrain the falling rock before the falling rock reaches the road. The installation of barriers in locations with adequate catchment area can be effective, while in locations with no or very limited catchment area, the construction of rockfall galleries may be necessary.

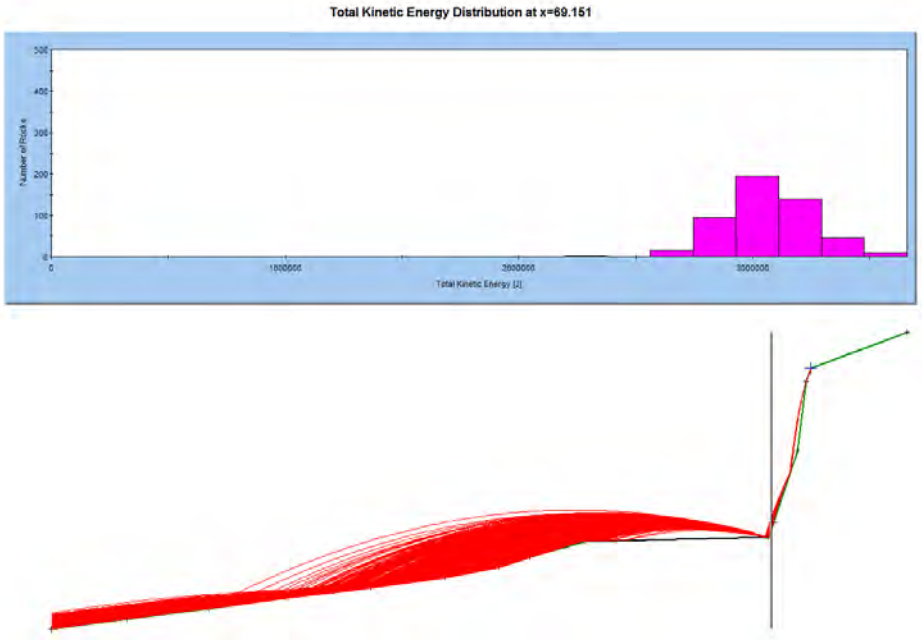

Figure 8 - Rockfall analysis at chainage 7+850.

6. Conclusions

In the present paper, the engineering geological conditions of Klokova area were determined and analyzed based on geological mapping and evaluation of geotechnical investigations. These are characterized by the existence of a unique tectonic regime due to the neo-tectonic activity of the broader area, the development of a karstic network in the carbonate rocks (cemented scree and limestone) as well as the formation of very high steep rock slopes parallel to fault surfaces. The karstic network was described taking into account the conditions of fracturing due to faults. The network is developed in the cemented scree formation and limestones mainly parallel to bedding surfaces and along faults in the form of fracture karst and gullies.

The quality of the limestone rockmass is determined by the frequency of fracturing and the possible presence of karstic voids. Three main rockmass types were evaluated in the limestone formation according to GSI classification defined by distinct degree of fracturing and discontinuity surface conditions, ranging between disintegrated, very blocky and blocky to massive categories.

Finally, the rockfall conditions were analyzed for the study area by selecting two different sections with similar total slope height but with different slope geometry and geological materials on the slopes. It was concluded that the nature of the geological formation on the slope, either scree or limestone, as well as the slope geometry, was very decisive on the magnitude of the total kinetic energy at impact on the road.

7. References

Aubouin J., Brunn J.H. and Celet P., 1958. Les massifs du Klokova et Varassova (Akarnanie), *Annales Geologiques de Pays Helleniques*, Geological Society of Greece, 9, 256-59.

Bieniawski Z.T., 1976. Rock mass classification in rock engineering, in: Bieniawski ZT (eds) Exploration for rock engineering, vol 1. Balkema, Cape Town, 97–106.

Nama S.A., – Kastor Ltd., 2005. Geotechnical investigation for the project of Klokova from Chainage 7+379 – 8+622.84 in the frame of studies for the section Antirio – Kefalovriso of the West Highway Axis N-S – Ionia Highway.

General Consulting Ltd – Istria, 2007. Geotechnical report and evaluation from chainage 9+300 to 10+200.

Greek Earthquake Resistant Regulations 2004. Earthquake Planning and Protection Organisation.

Geodata Greece, 2009. Geological – geotechnical evaluation report of Klokova Tunnel.

Marinos P. 2005. Experiences in tunneling through karstic rocks. Water resources & environmental problems in Karst, KARST 2005, *IAH Inter. Conf. Proceedings*, Belgrade, 617-644.

Marinos P., Hoek E. 2000. GSI: a geologically friendly tool for rock mass strength estimation. Proceedings of the GeoEng2000, *International conference on geotechnical and geological engineering*, Australia, Melbourne, Technomic Publishers, Lancaster, 1422–1446.

Saroglou H., Mpekri E., Tsiambaos G. 2010. Determination of critical geotechnical parameters of geological formations for the modeling of rockfalls in slopes. *Proc. 6th Hellenic Conf. of Geotechnical and Geoenvironmental Engineering*, Volos, 2, 43-50.

Δελτίο της Ελληνικής Γεωλογικής Εταιρίας, τομ. XLVII , 2013
Πρακτικά 13ου Διεθνούς Συνεδρίου, Χανιά, Σεπτ. 2013

Bulletin of the Geological Society of Greece, vol. XLVII 2013
Proceedings of the 13th International Congress, Chania, Sept. 2013

APPLICATION OF GEOSTATISTICAL SIMULATION MODELS IN THE CHARACTERIZATION OF COMPLEX GEOLOGICAL STRUCTURES

Sideri D.[1], Modis K.[1] and Rozos D.[1]

[1] National Technical University of Athens, School of Mining and Metallurgical Engineering, 9 Heroon Polytechniou St, 15780 Athens, Greece, dsideri@metal.ntua.gr, kmodis@mail.ntua.gr, rozos@metal.ntua.gr

Abstract

Geostatistical simulation methods are able to generate numerical models or relations of the spatial distribution of a continuous geologic variable (grade, thickness, density, etc.) or a categorical variable (geological units and lithofacies or rock types). In this work, a review of traditional simulation techniques, as the Sequential Indicator Simulation (SIS), reveals a major pitfall that comes from theoretical difficulties in the development of a valid cross covariance model. On the contrary, a valid indicator cross covariance model is automatically defined in the framework of the Truncated Gaussian Simulation Method (TGS). This method is based on the concept that the categorical variables are obtained by truncating one standard multigaussian random variable at different thresholds. Plurigaussian Simulation Method (PGS) is an extension of the TGS Method but based on the simultaneous truncation of several multigaussian variables. An application of Plurigaussian method to simulate the lithofacies in the alluvial formations of the West Thessaly Basin is finally presented. This method was shown to be effective in reproducing the spatial characteristics of the different lithofacies and their distribution across the studied area.

Key words: *Plurigaussian, Lithofacies modelling, Categorical variables.*

Περίληψη

Η χρήση μεθόδων προσομοίωσης στη γεωστατιστική μπορεί να οδηγήσει στην ανάπτυξη αριθμητικών μοντέλων χωρικής κατανομής συνεχών γεωλογικών μεταβλητών (περιεκτικότητα, πάχος, πυκνότητα, κλπ) ή κατηγορικών μεταβλητών (γεωλογικοί σχηματισμοί και λιθολογικές φάσεις ή τύποι πετρωμάτων). Στην παρούσα εργασία, η ανασκόπηση των κλασικών μεθόδων προσομοίωσης, όπως η Sequential Indicator Simulation (SIS), αναδεικνύει ένα σημαντικό μειονέκτημα που προκύπτει από τις θεωρητικές δυσκολίες στην ανάπτυξη ενός έγκυρου μοντέλου συνδιασποράς. Αντιθέτως, ένα παρόμοιο μοντέλο μπορεί να οριστεί αυτόματα στο πλαίσιο της Truncated Gaussian Method (TGS). Η μέθοδος αυτή βασίζεται στη δημιουργία κατηγορικών μεταβλητών μέσω της αποκοπής μίας πολλαπλά κανονικής τυχαίας μεταβλητής σε διάφορα όρια. Η Plurigaussian Simulation Method (PGS) αποτελεί επέκταση της προηγούμενης με τη διαφορά στην ταυτόχρονη αποκοπή περισσότερων της μίας τυχαίων μεταβλητών. Στη συνέχεια της εργασίας παρουσιάζεται μία

εφαρμογή αυτής της μεθόδου στην πεδιάδα της Δυτικής Θεσσαλίας. Τα αποτελέσματα δείχνουν ότι η μέθοδος είναι αποτελεσματική στην αναπαραγωγή των χωρικών χαρακτηριστικών των διαφόρων λιθολογικών σχηματισμών και της κατανομής τους στο χώρο.
Λέξεις κλειδιά: *Plurigaussian, Λιθολογικές φάσεις, Κατηγορικές μεταβλητές.*

1. Introduction

To model the geology and patterns of compressible structures in heterogeneous alluvial deposits and other complex geological formations, conceptual and deterministic models are not in general as flexible and realistic to adequately represent the internal geometry (Falivene et al., 2007a). Although a possible exception is the Inverse Distance Weighting (IDW) interpolation method, geostatistics is preferable (Modis et al., 2008). For this reason, stochastic models such as geostatistical estimation and simulation are most commonly used (Bierkens and Burrough, 1993; Deutsch, 2006; Mariethoz et al., 2009; Stafleu et al., 2011) particularly for the characterization of hydrofacies distribution within the alluvial deposits.

Geostatistical estimation is used to interpolate the value of a given attribute at a given location, by minimizing the error and bias of the estimate. It facilitates quantification of the spatial features of geological parameters and enables spatial interpolation (Komnitsas and Modis, 2006).

The use of estimation methods for obtaining facies reconstruction has not been as widespread in the literature as the use of simulation methods for obtaining facies models (see next paragraph). Johnson and Dreiss (1989) and Ritzi et al. (1995) applied a categorical estimation method (Indicator Kriging: IK) to obtain facies reconstructions in clastic aquifers, in both cases with only two different facies categories, making the results of this method very similar to those obtained with a continuous method. Falivene et al. (2007b) used a categorical method (IK) to reconstruct facies distribution in a fine-grain alluvial fan. Moreover, Falivene et al. (2007a) compared visually and statistically several facies reconstruction methods (Truncated Inverse Distance Weighting: TIDW, Truncated Kriging: TK, Indicator Inverse Distance Weighting: IIDW, and Indicator Kriging, among others) applied to a heterogeneous coal seam, this work was based on the same dataset as here. Other studies have focused on estimation of continuous parameters that can directly be related to facies (mud fraction in Flach et al., 1998; grain-size compositions in Koike et al., 1998; or results of geotechnical cone penetration tests in Lafuerza et al., 2005). This approach is conceptually similar to continuous methods for facies reconstruction (TK and TIDW). In all cases, published facies reconstructions achieved by estimation methods have been derived from extensively sampled sites. The scarcity of facies estimation in the literature (compared to simulation facies models, see below) is due to: a) the lack of digital high-density (with respect to facies heterogeneity) detailed facies descriptions; and b) the smoothing effect of estimation methods (Isaaks and Srivastava, 1989; Olea and Pawlowsky, 1996; Journel et al., 2000; Yamamoto, 2005), which results in facies reconstructions yielding usually optimistic results compared to the real heterogeneity distribution (i.e. more homogeneous distributions), limiting their predictive use. Moreover, as the density of the dataset with respect to facies heterogeneity decreases, the smoothing effect of facies reconstructions increases.

Geostatistical simulations on the other hand, consist of a set of methods being able to generate numerical models or relations of the spatial distribution of a continuous rock variable (grade, thickness, density, etc.) or a categorical variable (geological units and lithofacies or rock types). The aim is to generate equiprobable images of the real situation showing the characteristics of the phenomena, such as variability of the dataset and probability distribution function (Deutsch and Journel, 1997; Chiles and Delfiner, 1999). Simulated images exhibit the complexity of the dispersion as equally probable scenarios of the internal structure of the alluvial deposits.

The objective of this study is to review and explain the application of geostatistical simulation methods for the characterization of complex geological structures. As an example, the powerful and flexible PGS method (Le Loc'h et al., 1994) is applied to investigate the spatial variability of compressible units in the West Thessaly basin, where extensive land subsidence has been observed the last decades (Kallergis, 1973; Marinos et al., 1995; Rozos and Tzitziras, 2002).

2. Materials and Methods

2.1. Related Concepts from Geostatistics

In geostatistics, the variable under study is considered as a Random Function (RF) in space- time. A RF can be viewed as a collection of correlated random variables, say, $\boldsymbol{x}_{map}=(x_1, \ldots, x_m, x_k)$ at the points $\boldsymbol{p}_{map}=(\boldsymbol{p}_1, \ldots, \boldsymbol{p}_m, \boldsymbol{p}_k)$, where the symbol $\boldsymbol{x}_{map}$ is adopted because the goal is to obtain maps displaying estimates at points $\boldsymbol{p}_k$ of the unknown values χ_k of the natural variable from its observed values $\chi_1, \ldots, \chi_m$. A realization of the RF at these points is denoted by the vector $\boldsymbol{\chi}_{map}=(\chi_1, \ldots, \chi_m, \chi_k)$. If available, the complete characterization of a RF is provided by the multivariate probability density function (pdf) f_G defined as

$$\text{Prob}[\chi_1 \leq x_1 \leq \chi_1 + d\chi_1, \ldots, \chi_m \leq x_m \leq \chi_m + d\chi_m, \chi_k \leq x_k \leq \chi_k + d\chi_k] = f_G(\boldsymbol{\chi}_{map})\, d\boldsymbol{\chi}_{map}$$

where the subscript *G* denotes the general knowledge base (Christakos, 2000) used to derive the pdf.

A generally incomplete but in many practical applications satisfactory characterization of this RF is provided by a limited set of statistical moments, generally calculated from the experimental data.

In most practical applications, the underlying pdf is considered as Gaussian, and as a result, first and second order moments are sufficient to characterize. Since the first moment (mean) function is not generally known, a special form of the second moment, namely the variogram function (Journel and Huijbregts, 1978), is most widely used.

In the case of categorical attributes (e.g. geological facies) indicator variables are used to define whether a given point lies within a certain facies (Deutsch, 2006). The indicator variable takes the value 1 if the point belongs to the facies in question or 0 otherwise. Hydrofacies in our example (see section 2.3) is a categorical variable. The spatial average of the indicators is the average probability representing the proportion of that type of facies in the study field.

2.2. Geostatistical Simulation Methods

The traditional simulation techniques for several facies, as the Sequential Indicator Simulation (SIS), for indicators are based on the use of a random path through the field to sequentially simulate each node of the simulation grid (Gomez-Hernandez and Srivastava, 1990; Goovaerts, 1994; 1997). For the current node the indicator is firstly cokriged from those points already simulated and the conditioning data. The resulting estimate is assumed to represent an estimate of the probability that the node belongs to the different facies. The major pitfall in applying this technique comes from the cross covariance model required for the cokriging step. Direct and cross indicator covariances must satisfy the positive definiteness conditions for a valid cross covariance model to be defined (Emery, 2004). To avoid this very difficult step, an intrinsic correlation model is often assumed (Journel and Huijbregts, 1978). All direct and cross covariances are assumed to be proportional to one underlying covariance model, which reduces the cokriging to kriging.

On the other hand a valid indicator cross covariance model is automatically defined in the framework of the Truncated Gaussian Method (Galli et al., 1994). In this method (see end of this section), the lithofacies are not simulated directly: a stationary gaussian random function is simulated first, and then, it is transformed into the lithofacies variable by truncation (Armstrong et al., 2011). It is based on the notion that the indicators are obtained by truncating one standard

multigaussian random variable at different thresholds that are calculated from the known means of the various indicators.

Plurigaussian Simulation Method (Le Loc'h et al., 1994; Armstrong et al., 2011) is an extension of the Truncated Gaussian Method but based on the simultaneous truncation of several multigaussian variables thus allowing the simulation of different facies displaying different spatial anisotropies. The Plurigaussian technique provides a valid indicator cross covariance model because the indicator covariances are directly deduced from the covariance model of the Gaussian variables. Assigning a standard covariance model (for example spherical, exponential or Gaussian) to Y1 and Y2 ensures that the indicator covariances are valid covariance functions. The two Gaussian variables will be assumed to have stationary covariances.

2.3. Geology and Dataset

Thessaly basin is a lowland area in Central Greece, of about 4,520 km^2, mainly drained by Pinios River. The basin is subdivided by a group of hills in two sub-basins, the Western and the Eastern one. They are two main individual hydro-geological units, developing high potential aquifers.

The alluvial deposits of the Western one, which is the examined area of this study, constitute a system of unconfined shallow aquifers, extending in the upper layers, and successive confined - artesian aquifers developing in the dipper permeable layers (Marinos et al., 1995; 1997). This system besides the percolated surface water is also supplied by water through the lateral infiltration from the karstic aquifers of the alpine carbonate formations, outcropping in the margins of the basin. In general, the richest aquifers are developed in the western sub-basin of Thessaly plain, due to their rich supply both from the big infiltrating part of the surface runoff and the lateral infiltration. The overexploitation of these aquifers during the last decades led to the manifestation of land subsidence phenomena (Marinos et al., 1995; 1997), with extended damages in certain sites (Rozos et al., 2010).

According to geological studies of Western Thessaly basin (Mariolakos et al., 2001; Rozos and Tzitziras, 2002), Mesozoic Alpine formations outcrop in the margins of the study area, while, post alpine deposits are presented in the lowland of the basin. The Mesozoic Alpine formations consist of Schist-chert formation, Ophioliths, Limestones and Flysch sediments. They belong to the Pelagonian (Subpelagonian) geotectonic zone and they constitute the bedrock of post Alpine deposits of the West Thessaly basin.

The post-alpine deposits consist of: (a) Fluvial and lacustrine Neogene or molasse deposits, including various phases such as clayey silts, clayey sands with scattered gravels and pebbles of various origin and semi coherent conglomerates, (b) Terrestrial Pleistocene deposits consisting of clayey silts, sandy silts & clays and sands, with grits and gravels and (c) Alluvial deposits consisting of clays to sandy clays of variant thickness.

Throughout the Western Thessaly basin, several hundreds of sampling boreholes were drilled, in order to provide data for various geotechnical and hydro geological studies. Based on the above data, but also on some extra laboratory tests in samples collected from various soil horizons from the study area, all geotechnical parameters were analyzed and interpreted. Following to this action, a dataset was created, including soil characterization of distinguished horizons and their range of main physical characteristics and mechanical properties.

This dataset includes lithological information of 8029 samples taken from 1039 boreholes (Figure 1).

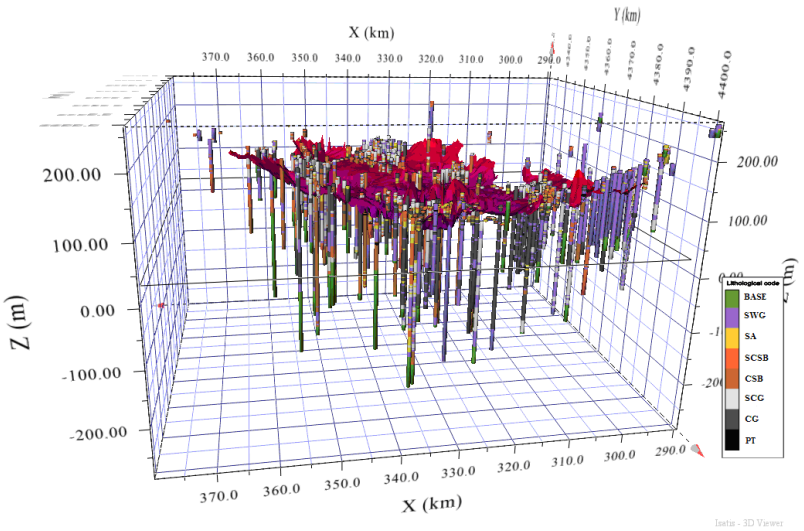

Figure 1 - 3D plot of the available boreholes with the location of the examined samples and the boundary surface between upper and lower aquifer systems.

After the examination of the well logs, 8 geologic types were identified and coded as following: Peat (PT), Clay gray (CG), Sandy clay gray (SCG), Clayey silt brown (CSB), Sandy clayey silt brown (SCSB), Sand (SA), Sand with gravels (SWG) and Basement formations (BASE). These lithotypes were further simplified for the modelling purposes into five lithofacies. The different lithofacies identified in the region are described in terms of categorical variables, or indicators, and represent the following categories: fine materials, fine materials with organic matter, sand, gravels and basement formations (Figure 2). The differentiation between the first two classes is based on the variation in compressibility, a characteristic that mainly depends on the presence of the organic matter in the soil.

PT	Clay and silt gray - peat
CG	
SCG	
SCSB	Clay and silt brown
CSB	
SA	Sand
SWG	Sand with gravels
BASE	Basement

Figure 2 - Correspondence between geological type and simplified lithotype sets.

3. Results and Discussion

3.1. Application of the Plurigaussian Method in the West Thessaly Basin

According to the available information (SOGREAH SA, 1974; Marinos et al., 1995; 1997) the two alluvial aquifer systems existing in the West Thessaly basin, can be approximately defined by three boundary surfaces, as shown on Figure 3. A thin impermeable layer separates the two aquifer systems, while the lower surface is the limit between the alluvial deposits and the bedrock.

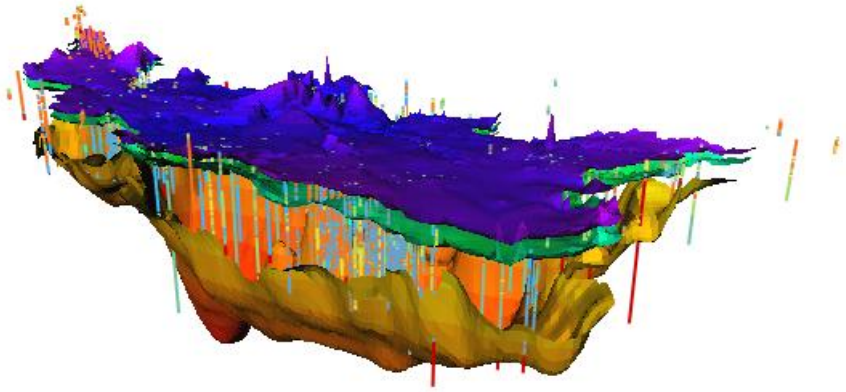

Figure 3 - Boundary surfaces of the two aquifer systems and exploratory boreholes. Z scale is magnified x50.

The upper aquifer lies between elevations 70 m and 170 m, while the bottom surface of the lower aquifer extends up to -450 m. The total working area is discretized into 180 x 140 x 71 (1,789,200) blocks of 500 x 500 x 10 m. The coordinates of the center of the lower left block are x = 290,000 m, y = 4,330,000 m, z = -450 m. Discretization of the working domains and further application of Plurigaussian simulations were performed using ISATIS® software from Geovariances.

The lithofacies proportions at each domain must be modeled as a function of the point considered in the field. This modeling procedure is guided mainly by the experimental data. Vertical Proportion Curves (VPCs), first proposed by Matheron et al. (1987), are a simple tool for quantifying the evolution in the amount of each facies or lithotype present as a function of depth. They are computed along lines vertical to the chosen reference level. The results are presented as a graph showing the proportion of each facies at each level.

The global VPCs in the case of Western Thessaly basin are shown in Figure 4 for the two working domains. The differentiation between these hydrogeological units is apparent. A higher proportion of clays and silts with organic matter (black color) are observable in the second VPC. This is an indication of increased compressibility of the lower aquifer related to the upper one. Also, sand with gravels proportions (blue color) are grater in the lower aquifer and this suggests a more permeable structure.

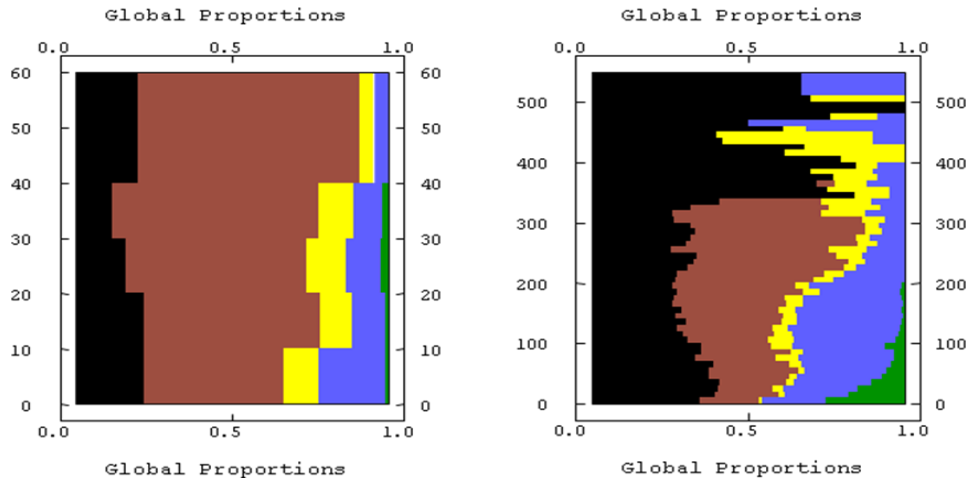

Figure 4 - Global VPCs for the upper (left) and the lower (right) aquifer.

In our case (Figure 5) we used two Gaussian functions G1 and G2. G1 represents the transition between greyish clays & silts with organic matters and sand with gravels, sand with gravels and sand, sand and basement formations. G2 represents the transition between brownish clays and silts and all the other lithofacies. This rule reflects the fact that the clay & silt brown facies is in contact with all other facies as seen from the histograms on the right column of Figure 5, which are calculated from the borehole data. Experimentation with alternative lithotype rules showed that the above rule leads to improved variogram fitting, as can be seen in the next paragraphs of this section.

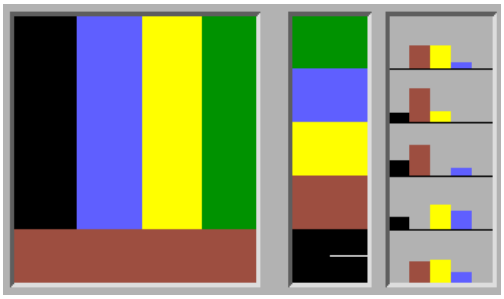

Figure 5 - Lithotype rule with facies transition proportions on the right column. The correspondence between colors and lithofacies is shown in Figure 2.

The next step of the Plurigaussian technique is the inference of the variogram models for the underlying multi-Gaussian functions. Direct adjustment to the experimental variograms is not possible since the only available experimental variograms are the variograms of the indicator functions describing the lithofacies (one per lithofacies, plus all the bivariate combinations), while the two variograms needed for the model are the variograms of the underlying and continuous multi-Gaussian functions. The variogram inference was based on an inverse procedure in which the ranges of the variograms of the multi-Gaussian fields were adjusted iteratively through an inverse procedure, until an acceptable match was obtained between the experimental and the computed variogram (Figure 6).

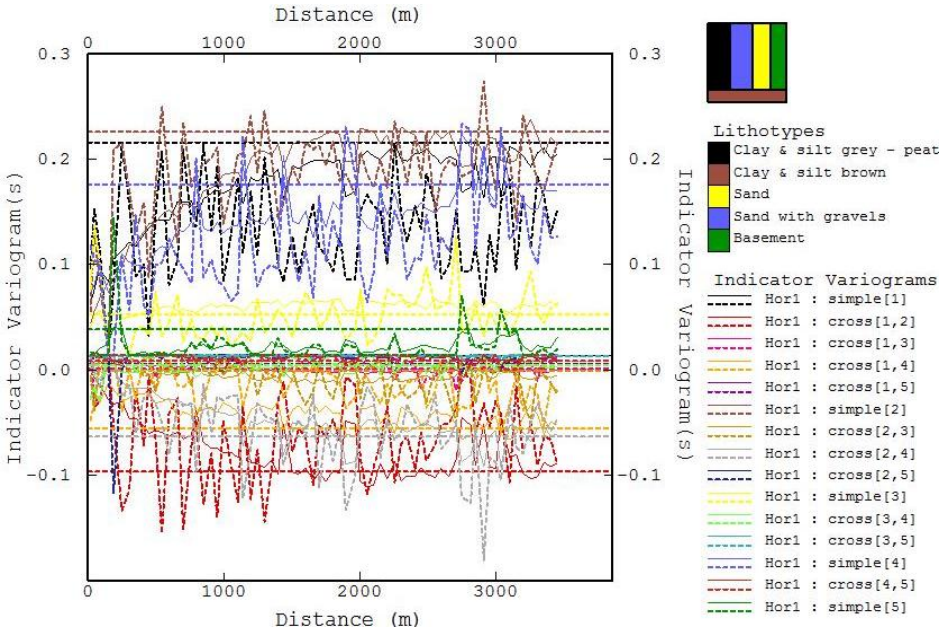

Figure 6 - Horizontal indicator simple and cross variograms of the lower aquifer.

3.2. Simulation Results and Discussion

The resulting model of the Plurigaussian simulation is shown in Figure 7. A spatial differentiation concerning facies proportions is clear in this model, as for example the gravel percentage in the NW part, which is in agreement with observations concerning water recharge variations, as verified in relative studies (Kallergis, 1973; Bathrellos, 2005). The amount of grayish clays & silts with organic matters is clearly grater in the lower aquifer of the Plurigaussian model compared to the upper one, being in accordance to the proportion curves (Figure 4). Also, the existence of basement formations in the lower edges of the model is justified by the definition of the model boundaries. In general, the distribution of spatial characteristics of the basin is acceptably represented by the Plurigaussian model (Figure 7).

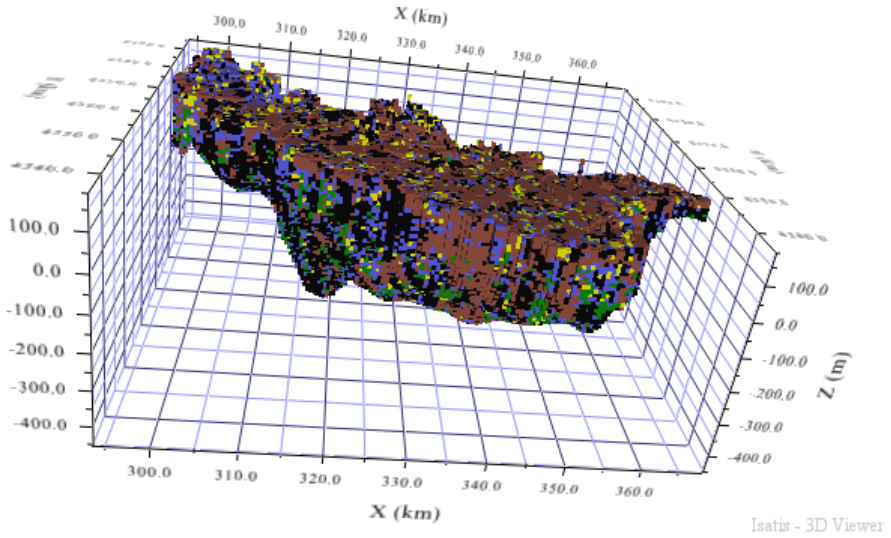

Figure 7 - 3D Plurigaussian model of the West Thessaly aquifer systems.

4. Conclusions

A theoretical drawback in applying the traditional simulation techniques for several facies comes from the cross covariance model required for the cokriging step. Direct and cross indicator covariances must satisfy the positive definiteness conditions for a valid cross covariance model to be defined. On the contrary, the Plurigaussian technique provides a valid indicator cross covariance model because the indicator covariances are directly deduced from the covariance model of the Gaussian variables.

The main characteristic of the Plurigaussian technique is that it allows incorporating a simple geological concept in the stochastic simulations. This is an important feature as in most applications, a detailed geological model is difficult to establish. The geological rule is not derived only from a statistical analysis of the borehole data but also from a geological analysis of all the available information.

In the case of western Thessaly basin, the Plurigaussian technique was shown to be effective in reproducing the spatial characteristics of the different lithofacies and their distribution across the studied area, as determined by the proportions of the borehole samples and other sources of empirical knowledge concerning water recharge variations.

5. Acknowledgements

The authors acknowledge Edafos S.A., Ferrovial Agroman S.A. and HellasLab for the supply of all necessary borehole data for the analysis.

6. References

Armstrong M., Galli A., Beucher H., Le Loc'h G., Renard D., Doligez B., Eschard R. and Geffroy F. 2011. Plurigaussian Simulations in Geosciences. Berlin, *Springer-Verlag.*

Bathrellos G. 2005. Geological, geomorphological and geographical study of urban areas in Western Thessaly (Trikala prefecture). *Ph.D. Thesis,* National & Kapodistrian University of Athens.

Bierkens M.F.P and Burrough P.A. 1993. The indicator approach to categorical soil data. I. Theory, *Journal of Soil Sciences*, Vol. 44, pp. 361-368.

Chiles J.P. and Delfiner P. 1999. Geostatistics: Modelling spatial uncertainty, New York: *Wiley*.

Christakos G. 2000. Modern Spatiotemporal Geostatistics, *Oxford Univ. Press*: New York, 288 p.

Deutsch C.V. and Journel A.G. 1997. GSLIB: Geostatistical software library and user_s guide (Applied Geostatistics Series) (2nd edition.). New York: *Oxford University Press.*

Deutsch C.V. 2006. A sequential indicator simulation program for categorical variables with point and block data: BlockSIS. *Computers & Geosciences,* Vol. 32, pp. 1669-1681.

Emery X. 2004. Properties and limitations of sequential indicator simulation, *Stochastic Environmental Research and Risk Assessment*, Vol. 18 (6): pp. 414-424.

Falivene O., Cabrera L., Muñoz J.A., Arbués P., Fernández O. and Sáez A. 2007. Statistical grid-based facies reconstruction and modelling for sedimentary bodies. Alluvial-palustrine and turbiditic examples, *Geologica Acta*, Vol.5, Nº 3, pp. 199-230 (a)

Falivene O., Cabrera L. and Sáez A. 2007. Large to intermediate- scale aquifer heterogeneity in fine-grain dominated alluvial fans (Cenozoic As Pontes basin, NW Spain): Insight based on 3D reconstruction, *Hydrogeology Journal*, 15: 861–876 (b)

Flach G.P., Hamm L.L., Harris M.K., Thayer P.A., Haselow J.S. and Smits A.D. 1998. A method for characterizing hydro-geologic heterogeneity using lithologic data. In: Fraser, G.S., Davis, J.M. (eds.). Hydrogeologic models of sedimentary aquifers, *SEPM Special Publication, Concepts in Hydrogeology and Environmental Geology,* 119-136.

Galli A., Beucher H., Le Loc'h G., Doligez, B. and the Heresim Group 1994. The pros and cons of the truncated gaussian method, *Geostatistical Simulations: Proceedings of the Geostatistical Workshop, Fontainebleau*, France, M. Armstrong & P. Dowd, eds, Kluwer Academic Publishers, Dordrecht, pp. 217–233.

Goovaerts P. 1994. Comparative performance of indicator algorithms for modeling conditional probability distribution functions, *Mathematical Geology*, 26 (3), pp. 385–410.

Goovaerts P. 1997. Geostatistics for Natural Resources Evaluation, *Oxford University Press*, New York, pp. 496.

Gomez-Hernandez J.J. and Srivastava R.M. 1990. ISIM3D: An ANSI-C three dimensional multiple indicator conditional simulation program, *Computers & Geosciences,* 16 (4), pp. 395–410.

Isaaks E.J. and Srivastava R.M. 1989. An introduction to Applied Geostatistics. New York, *Oxford University Press*, 561 pp.

Johnson N.M. and Dreiss S.J. 1989. Hydrostratigraphic interpretation using indicator geostatistics, *Water Resources Research*, 25, 2501-2510.

Journel A.G. and Huijbregts Ch.J. 1978. Mining Geostatistics, *Academic Press*, London.

Journel A.G., Kyriakidis P.C. and Mao S. 2000. Correcting the Smoothing Effect of Estimators: A Spectral Postprocessor. *Mathematical Geology*, 32, 787-813.

Kallergis G. 1973. Hydrogeological study in sub-basin of Kalampaka (Western Thessaly). *Institute of Geology and Mineral Exploration (IGME)*, unpublished report (in Greek), vol. XIV, No 1, Athens.

Koike K., Shiraishi Y., Verdeja E. and Fujimura K. 1998. Three- Dimensionsal Interpolation and Lithofacies Analysis of Granular Composition Data for Eathquake-Engineering Characterization of Shallow Soil, *Mathematical Geology*, 30, 733-759.

Komnitsas K. and Modis K. 2006. Soil risk assessment of As and Zn contamination in a coal mining region using geostatistics, *Science of the Total Environment*, Vol. 371, pp. 190–196.

Lafuerza S., Canals M., Casamor J.L. and Devincenzi J.M. 2005. Characterization of deltaic sediment bodies based on in situ CPT/CPTU profiles: A case study on the Llobregat delta plain, Barcelona, Spain, *Marine Geology*, 222-223, 497-510.

Le Loc'h G., Beucher H., Galli A., Doligez B. and the Heresim Group. 1994. Improvement in the truncated gaussian method: combining several gaussian functions, ECMOR IV: *4th European Conference on the Mathematics of Oil Recovery*, Roros, Norway, Conference Proceedings, 13 pp.

Mariethoz G., Renard P., Cornaton F. and Jaquet O. 2009. Truncated Plurigaussian Simulations to Characterize Aquifer Heterogeneity, *Ground Water*, Vol. 47(1), pp. 13–24.

Marinos P., Thanos M., Perleros V. and Kavadas M. 1995. Water dynamic of Thessaly basin and the consequences from its overexploitation, *Proceedings of the 3rd Hydrogeological Congress* (in Greek), Heraklion Crete.

Marinos P., Perleros V. and Kavadas M. 1997. Deposited and karsic aquifers of Thessaly plain. New data for the status of their overexploitation, *Proceedings of the 4th Hydrogeological Congress* (in Greek), Athens.

Mariolakos H., Lekkas S., Papadopoulos T., Alexopoulos A., Spyridonos E., Mandekas I. and Andreadakis E. 2001. Underground tectonic structure in Farsala plain (Thessaly) as a determinative factor of the formation of the hydrogeological conditions of the area, *Proceedings of the 9th Congress of Greek Geological Society* (in Greek).

Matheron G., Beucher H., de Fouquet C., Galli A., Guerillot D. and Ravenne C. 1987. Conditional simulation of the geometry of fluvio-deltaic reservoirs, SPE 1987 *Annual technical conference and exhibition*, Dallas, Texas, pp 591–599. SPE 16753.

Modis K., Stavrou S., Terezopoulos N. and Vattis D. 2008. Geostatistics versus inverse distance squares in ore reserves estimation: comparative case study in copper ore body in Cyprus, *Mining Technology*, vol. 117, no 1, pp. 48-52.

Olea R. and Pawlowsky V. 1996. Compensating for estimation smoothing in kriging. *Mathematical Geology*, 28, 407-417.

Ritzi R.W., Dominic D.F., Brown N.R., Kausch K.W., McAlenney P.J. and Basial M.J. 1995. Hydrofacies distribution and correlation in the Miami Valley aquifer system, *Water Resources Research*, 31, 3271-3281.

Rozos D. and Tzitziras A. 2002. Report of the Engineering geological examination of ground water in Farsala area, *Institute of Geology and Mineral Exploration (IGME)*, unpublished report (in Greek).

Rozos D., Sideri D., Loupasakis C. and Aposolidis E. 2010. Land Subsidence due to Excessive Ground Water Withdrawal. A Case Study from Stavros - Farsala Site, West Thessaly Greece, *Proceedings of the 12th International Congress*, Patras, Greece.

SOGREAH SA 1974. Groundwater development project of the plain of Thessaly. Republic of Greece, Ministry of Agriculture, Directorate General of Agricultural Development and Research Land Reclamation Service, Athens.

Stafleu J., Maljers D., Gunnink J.L., Menkovic A. and Busschers F.S. 2011. 3D modelling of the shallow subsurface of Zealand, The Netherlands. *Netherlands Journal of Geosciences*, Vol. 90(4), pp. 293-310.

Yamamoto J.K. 2005. Correcting the Smoothing Effect of Ordinary Kriging Estimates, *Mathematical Geology*, 37, 69-94.

Δελτίο της Ελληνικής Γεωλογικής Εταιρίας, τομ. XLVII 2013
Πρακτικά 13ου Διεθνούς Συνεδρίου, Χανιά, Σεπτ. 2013

Bulletin of the Geological Society of Greece, vol. XLVII 2013
Proceedings of the 13th International Congress, Chania, Sept. 2013

INFLUENCE OF GEOLOGICAL AND GEOTECHNICAL CONDITIONS TO DESIGN A WATER RESERVOIR IN KARST AREA

Steiakakis E.[1], Vafidis A.[1], Manoutsoglou E.[1] and Vavadakis D.[1]

[1] Technical University of Crete, Department of Mineral Resources Engineering, stiakaki@mred.tuc.gr, vafidi@mred.tuc.gr, emanout@mred.tuc.gr, vavadaki@mred.tuc.gr

Abstract

The design of a water reservoir in a site underlain by karstified carbonate rocks, encounters many difficulties mainly due to unpredictable location, dimensions and geometry of the karst structure and voids.
The objective of this work is to present part of the investigation work that was carried out in Omalos plateau (W. Crete) where a water reservoir is going to be constructed.
The survey was based on geological mapping, geophysical exploration, boreholes drilling, sampling and laboratory testing for the geotechnical parameters determination.
The soil thickness that is required to provide stability against soil collapse into voids and the subsequent formation of sinkholes was estimated.
The evaluations represent a useful decision-support tool in the management of the investigation results for the design purposes of the water reservoir in Omalos plateau.
Key words: *Karst, sinkholes, geotechnical investigation.*

Περίληψη

Ο σχεδιασμός και η κατασκευή μιας λιμνοδεξαμενής σε καρστικό περιβάλλον , αντιμετωπίζει πολλά προβλήματα λόγω της απρόβλεπτης θέσης, των διαστάσεων και της γεωμετρίας της καρστικής δομής και των πιθανών εγκοίλων.
Στόχος αυτής της εργασίας είναι να παρουσιάσει μέρος των αποτελεσμάτων έρευνας που διεξήχθη στο οροπέδιο του Ομαλού (Δ. Κρήτη), όπου μια λιμνοδεξαμενή πρόκειται να κατασκευαστεί. Η έρευνα βασίστηκε σε γεωλογική χαρτογράφηση, γεωφυσική διασκόπηση, γεωτρητική έρευνα, δειγματοληψία και εργαστηριακές δοκιμές για τον προσδιορισμό γεωτεχνικών παραμέτρων των σχηματισμών. Εκτιμήθηκε το πάχος του εδάφους που απαιτείται για να εξασφαλισθεί η ευστάθεια εδαφικού σχηματισμού πάνω από έγκοιλα διαφόρου μεγέθους που ενδεχομένως υπάρχουν.
Τα αποτελέσματα αποτελούν ένα χρήσιμο εργαλείο για τη διαχείριση των αποτελεσμάτων της έρευνας και το σχεδιασμό της λιμνοδεξαμενής στο οροπέδιο του Ομαλού.
Λέξεις κλειδιά: *Καρστ, γεωτεχνική έρευνα, εδαφική υποχώρηση.*

1. Introduction

Omalos plateau encompasses an area of approximately 6 km^2. It lies in a distance of 45 km S-SW of Chania city (Figure 1), at an altitude of about 1,050 m asl.

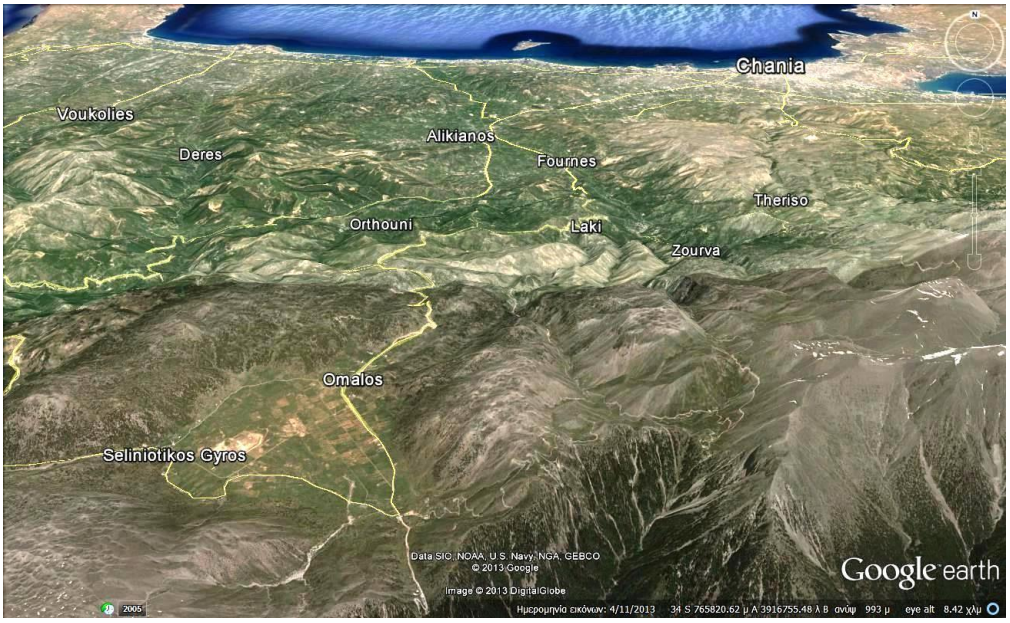

Figure 1 - Omalos Plateau.

The surface profile in Omalos plateau appears to be smooth, with elevation differences not higher than 15 m.

An embankment pond is under construction in the SW part of the Plateau, North of "Seliniotikos Gyros", within the administrative boundaries of Kantanos-Selino municipality. The impounded water will be used for irrigation purposes.

The water reservoir is created partly by the construction of an embankment of maximum height of 10 m, and partly by excavation.

According to the initial design, the inundation area is 1.97 km^2 and the reservoir net capacity is estimated to 750,000 m^3.

The area was investigated and evaluated in 1993 as a potential site for the water reservoir. Original approval of this site was based mainly upon its favourable topography and water-impoundment capabilities of the area. However, this decision did not adequately consider the geology in depth.

In 2012, a second exploration was conducted. The stability of the soil formations that overlie the solution cavities was a concern during the latter research. Based on the investigation results, the soil thickness that is required to provide stability against soil collapse into possible underlying cavities was estimated.

The results can be used to evaluate the stability of the candidate site for a range of anticipated sizes of voids.

2. Evolution of Sinkholes

Two types of mechanisms are responsible for the development of sinkholes in a site underlain by carbonate rocks.

The first, and by far the most common, is an upward ravelling of soil over a cavity in the bedrock (Sowers, 1978 as stated by Adams and Lovell, 1984).

Figure 2 shows the development of a sinkhole over an opening in the rock, which may be a small cave, an enlarged joint or fracture, or a narrow vertical pipe. As has been ascertained, in sandy

soils surface subsides slowly. On the other hand, in clay soils cavity forms first at rockhead, then grows in size until cohesive soil bridge fails, to cause sudden dropout collapse of surface (Waltham, 2002).

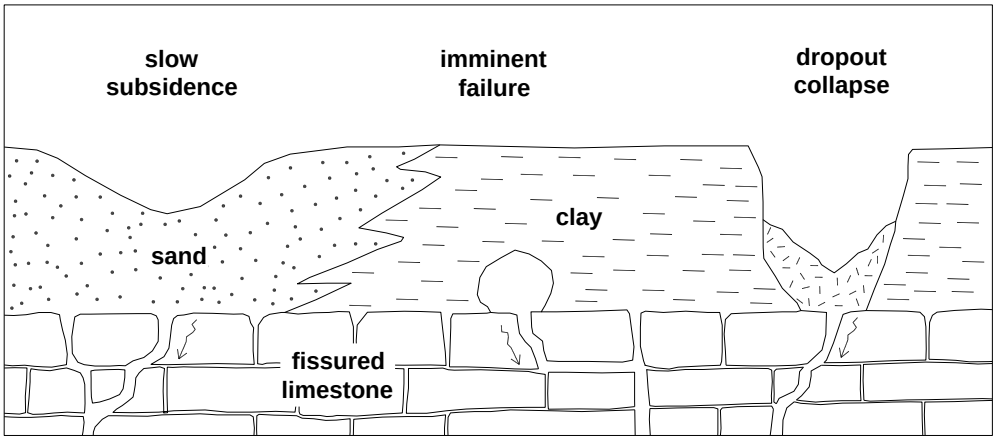

Figure 2 - Schematic of sinkhole development (Waltham, 2002, modified).

It is worth noting that groundwater fluctuations may enlarge the void over time. Particularly, the shear strength of the soil is weakened as it becomes saturated. When the water level drops again, the effective stress increases, and soil ravelling occurs as the stresses are redistributed. If the thickness of the stronger soil above the void is insufficient for arching to develop, the soil above the dome will fail, resulting in a depression at the surface in the form of a doline.

The second mechanism responsible for sinkhole development is collapse of the soil and rock roof above a cavity. Such a phenomenon is rare, however (Adams, and Lovell, 1984).

As has been documented by the literature, ravelling failures are the most widespread and probably the most dangerous of all the subsidence phenomena associated with karstic carbonate rocks.

Furthermore, thicker soil covers develop fewer subsidence sinkholes. As stated by Waltham (2005), China has many thousands of recorded subsidence sinkholes, and data from different areas within the karst indicate that over 60% of sinkholes occur in cover soils less than 5 m thick and over 85% in cover less than 10 m thick. A similar picture appears in East Tennessee, where about 70% of the sinkholes surveyed had overburden thickness less than 10 m (Newton and Tanner, 1986).

Moreover, a similar trend has occurred in Florida, where most sinkholes occur in cover less than 20m – 30m thick. Only where soil cover is more than 60 m thick sinkholes are described as very rare (Waltham, 2005).

3. Geological Layout

The geological section defined in Figure 3, present the geological structure in the study area. It was constructed with base the published geological maps (Tataris and Christodoulou 1969) and the geological survey realized in the area.

The Omalos Plateau is underlain by karstic carbonate rocks of Trypali unit. Trypali unit overlies the system of Plattenkalk limestone, and it forms a separate hydrogeological entity in the area with intensive karstification.

The overlying Quaternary alluvium is considered to be the result of several depositional events of the wide alluvial fans. It covers an extensive area of Omalos plateau and it constitutes the subsurface of the embankment pond. The field investigation showed that karstic features such as

dolines are prominent in the wider region, mainly in the northern portion of the Plateau, outside the reservoir perimeter.

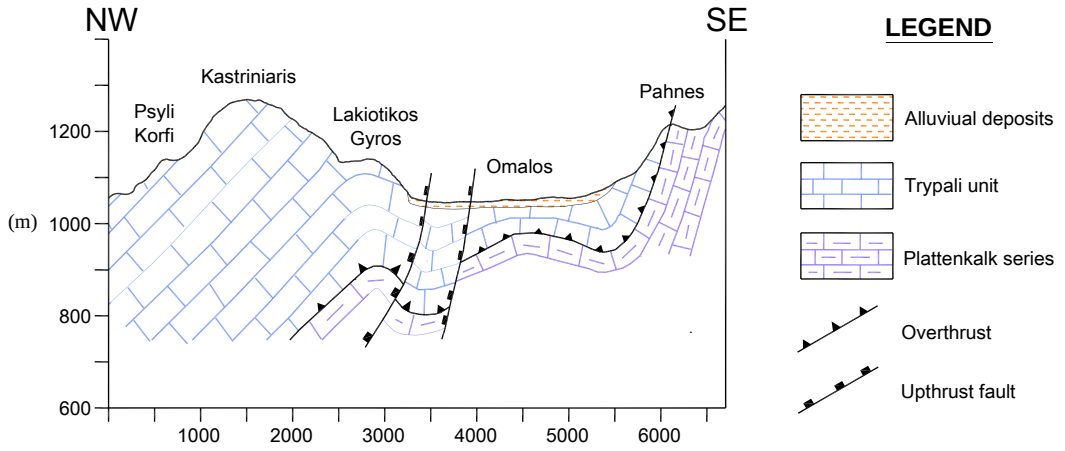

Figure 3 - Schematic geological section (Steiakakis et al., 2011, modified).

The plateau is dissected by a number of north-south trending normal faults.

These faults play an important role in the formation of sinkholes, but mainly they contribute to the enlargement of the voids over the groundwater water table, and their evolution towards higher elevations (ground surface). This is because the surface runoff water easily infiltrates fault zones, increasing the unit weight of dry soil and inducing seepage forces. Furthermore, the increase in saturation reduces suction in the unsaturated soil voids, which decreases the effective stress and the strength of the soil above the cavity (Zhiqiang Yang M., Drumm E., 2002).

From the hydrogeological point of view, perched water table lies within the gravely sands (bordered by the underlying silty - clayey layers) of the alluvial formation.

4. Geotechnical Investigation

The geotechnical investigation included drilling and sampling of four (4) boreholes (BH1, BH2, BH2 and BH4) to a maximum depth of 35 m below existing ground surface, at the locations shown in Figure 4.

The groundwater conditions were observed in the boreholes during augering and sampling, and after completion.

In addition, a laboratory testing program consisting of moisture content, Atterberg limits, grain size analyses and shear strength determination, were carried out on selected samples.

Based on drilling exploration, the succession of the layers founded in the first 35 m below the ground surface, is as follows.

Topsoil

The boreholes encountered approximately 0.7 m to 1.0 m of topsoil. It should be noted that its thickness could vary considerably in between and beyond borehole locations. Thicker topsoil is normally expected in low-lying areas and water courses while topsoil is absent in the area that has been excavated for the reservoir construction purposes.

Brownish-yellow sandy silty clay

Underlying the topsoil, all boreholes except BH4 encountered a sandy silty clay formation.

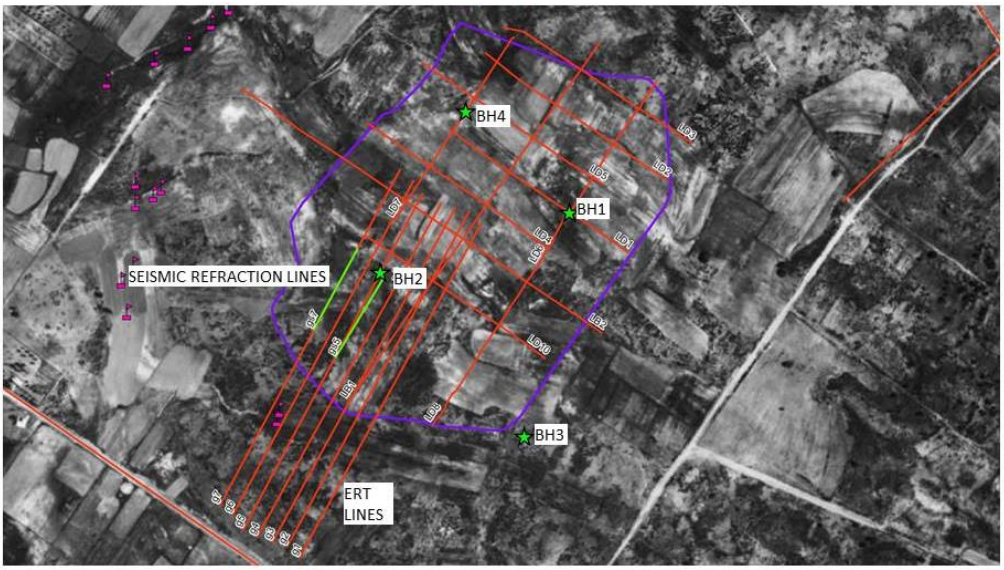

Figure 4 - Electric tomography grid (gX), Seismic refractions lines (gsX) and locations of Boreholes (BSX) in Omalos plateau.

In BH1 the layer was found to extend to the depth 13.8 m in BH2 up to 14.4 m, in BH3 up to 8.5 m and in BH4 up to final depth of the borehole (15 m).

This layer is ascribed to the alluvial fan that is composed of a heterogeneous mixture of clay and silt with some sand and gravel size particles. Due to the nature of the formation, the presence of cobbles and boulders were met during drilling (BH3 5.40-8.50m depth).

It should be noted that BH1 showed signs of minor cavities in depth 6.4 m, when the drilling was advancing just by the self-weight of the rods for several centimetres. At the same depth perched water table was detected, that lies within gravely sand layer bordered by the underlying clayey layer of the alluvial formation.

This layer is generally moist with measured moisture contents ranging between 18 and 23%, and its dry unit weight estimated equal to 22 kN/m^3.

The results of grain size analyses of samples taken from this layer showed that they contain gravel (3-11%), sand (4–21%), silt (68–86%) and clay (1–9%).

Moreover, the liquid limit estimated equal to LL=24%, the plastic limit PL=20% and the plasticity index PI=4%.

Based on these results the samples are classified, according to the Unified Soil Classification System (USCS), as sandy silty clay.

For the samples taken, the direct shear testing program yielded cohesion that ranges from c'=19.7 kN/m^2 to 33.3 kN/m^2 and friction angle between φ'=22 and 32°.

Brown Sandy - Clayey Silt layer

Underneath the brownish-yellow sandy silty clay, encountered a brown sandy - clayey silt layer with lower moisture content. In BH1 and BH2 this layer was found to extend at depths between 14.0 and 35.0 m below existing ground surface, while in BH3 this deposit extends to depths between 8.5 to 23.3 m below existing ground surface where the carbonate formation is found.

The measured moisture content ranges between 16 and 21%.

The results of grain size analyses in the samples taken from this layer showed that they contain gravel (1-3%), sand (9–11%), silt (83%) and clay (4–6%).

Moreover, the liquid limit estimated equal to LL=20%, the plastic limit PL=18% and the plasticity index PI=2%.

Based on these results the samples are classified, according to the Unified Soil Classification System (USCS), as sandy - clayey silt.

For the samples taken, the testing program yielded cohesion ranges from c'=15.7 kN/m^2 and friction angle $\varphi' = 33.8°$.

Carbonate rock formation

Cores, from Borehole 3 showed that the karst carbonate formation founded 23 m below the surface; it is highly fissured and unstable. The TCR ranges between 44 and 100% and the RQD varies between 0% (in core lengths 0.2-0.7m) and 100% (in core lengths 0.2-0.5m).

Groundwater Conditions

No groundwater was encountered in boreholes on completion of all the boreholes except BH1 where groundwater was encountered at depth of about 6.5 m below existing ground surface.

However, it should be noted that the groundwater table could fluctuate seasonally and in response to severe weather events.

5. Geophysical Investigation

The geophysical survey in Omalos Plateau was conducted by employing the VES, ERT and seismic refraction methods. The former (VES method) estimates the average thickness of the alluvial deposits, while the ERT and seismic refraction methods map the relief of the underlying karstic carbonate formations.

Further interpretation of the data obtained by ERT and seismic refraction methods offered a further indication regarding the detection of subsurface cavities.

The results of the geophysical campaign fixed the variations of alluvium thickness and the depth of the carbonate rocks formation at between 25 and 40 m. This depth also being supported by the exploratory drilling, extend down to 35 m.

The produced map, based on the detected geophysical anomalies up to a depth of 40m, was subsequently used to outline areas of high risk regarding the presence of subsurface cavities inside the reservoir area.

Based on data collected on a grid in the south west portion of Omalos plateau, none subsurface cavity with width greater than 20 m was detected up to 40 m depth.

However, a more comprehensive geophysical exploration is necessary in order to cover the rest of the study area in detail and to detect potential smaller subsurface cavities.

6. Stability Evaluation of a Potential Site

The stability evaluation against soil collapse into voids was performed on the basis of the expected soil thickness and the anticipated range of soil voids.

Seven model tests were conducted to examine sinkhole development in the soil formation over cavities with different sizes.

Based on Adams and Lovell (1984) suggestion, a simplified analysis of soil stability above a developing cavity in carbonate rocks was adopted.

The analysis is based on Terzaghi's equations for soil arching over an infinitely long void, assuming that the lateral load transfer is achieved through shear stresses along vertical planes located at the edges of the void (Figure 5).

The real surfaces of sliding, as observed by Terzaghi in 1936, are curved and at the soil surface their spacing is greater than the width of the yielding strip. However, vertical sides were assumed for simplicity. In addition, the horizontal stresses were assumed to be of the active mode, since erosion of the arch has resulted in a release of lateral pressure.

The soil layer was assumed to be horizontal and to have a uniform thickness, while the groundwater table was considered to be lower than the bottom of alluvial formation. The stress applied on the ground surface was assumed to be normal, uniformly distributed and equal to the imposed load from the reservoir project construction.

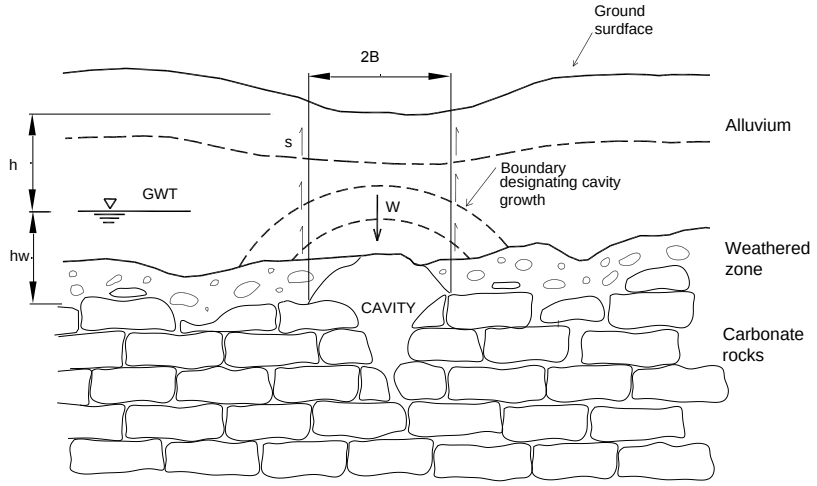

Figure 5 - Subsurface profile of a void developing in the soil formation above a solution-enlarged cavity in the bedrock (Adams and Lovell, 1984, modified).

Based on Mohr-Coulomb strength criterion, the strength (s) along vertical planes (Fig. 5), is equal to $s = c' + \sigma'_h \cdot \tan\varphi'$ and assuming fully mobilized active earth pressure along the sides of the soil block, the shearing strength is equal to:

$$s = 2[c'(h + h_w) + (\frac{1}{2}k_a\gamma h^2 + k_a\gamma h h_w + \frac{1}{2}k_a(\gamma - \gamma_w)h_w^2)]\tan\phi'$$

where

s = soil shear strength in terms of effective stress

c' = cohesion intercept of soil in terms of effective stress

σ'_h = effective horizontal stress

φ' = effective angle of internal friction of soil

γ = unit weight of the soil

γ_w = unit weight of the water

h = depth to ground water-table

h_w = depth of water

k_α = coefficient of lateral earth pressure

The weight (W) of the block (Fig. 5) is equal to $W = 2B\cdot[h\cdot\gamma + h_w\cdot(\gamma-\gamma_w)]$, where 2B = width of the yielding strip.

Equating s and W (equilibrium conditions), and rearranging to solve for B yields:

$$B = \frac{c'(h+h_w) + (\frac{1}{2}k_a\gamma\ h^2 + k_a\gamma_m h h_w + \frac{1}{2}k_a(\gamma\ -\gamma_w)h_w^2)\tan\phi'}{h\gamma\ + h_w(\gamma\ -\gamma_w)}$$

The required thickness of the soil to assure the stability of the soil formation over openings of different sizes was estimated and the results are presented in Table 1.

Table 1 - Relationship between void size and overburden thickness of the soil formation sufficient to assure stability with respect to failure under the imposed loadings.

Overburden thickness of the soil formation h (m)	5	10	15	20	25	30	40
Void size 2B (m)	1.15	2.20	3.22	4.21	5.20	6.18	8.12

It was concluded that for the measured friction angle φ´ = 28° and cohesion c´ = 25 kN/m^2, a soil thickness of 25 m over a void of 5.2 m width is sufficient to assure the stability. In any case, using the results of Table 1 may facilitate the dome detection by geophysical methods and define the problem sites.

However, it should be noted that the above method may lead to poor predictions because of the true, three dimensional nature of the sinkholes and because of the simplifying assumptions.

Therefore, only if the assumptions and limitations are kept in mind, this approach can be a useful tool for planning the location and the size of the reservoir out of the problem areas.
The risk assessment can be determined more accurately taking further geotechnical and geophysical survey and simulating local conditions through finite element software. This simulation will help in predicting the potential movement of the subsoil in various positions of the project.

7. Conclusions and Discussion

The geological model of the study area shows that the Quaternary alluvial mainly constitute the subsurface of the water reservoir site with a thickness variable from more than 25 m in the western portion, to 40 m in the eastern sector of the site where is placed the water reservoir.

Karstic features such as dolines are prominent in the region, mainly in the northern portion of Omalos Plateau, outside the reservoir perimeter.

Sudden occurrence of sinkholes can be resulted from collapse of the roof of a cavity to its progressive enlargement in size until cohesive soil bridge fails. The evaluation of the soil thickness that is required to provide stability against soil collapse into underlying openings and the subsequent formation of sinkholes represents a useful decision-support tool in the management of the investigation results for the design of the water reservoir.

It should be noted that in any case, the position and variability of the water table is a key aspect in sinkhole development since it affects the stresses acting on the soil and rock. For this reason, it is required an increased protection from leaks of the reservoir. It is necessary to ensure the proper construction of an extensive network of drains (if possible impervious to their base) in order to prevent any infiltration into the subsoil.

It is advisable to execute additional drilling - geotechnical investigation particularly in sites where geophysical survey indicates that the underground void has an opening that does not assure stability according to the estimations.

8. References

Adams F.T. and Lovell C.W. 1984. Geotechnical Engineering Problems in the Karst Region of SouthernIndiana. Publication FHWA/IN/JHRP-84/12, Joint Highway Research Project, Indiana Department of Transportation and Purdue University, West Lafayette, Indiana, 1984. doi: 10.5703/ 1288284314078.

Newton J. G.1976. Early detection and correction of sinkhole problems in Alabama, with a preliminary evaluation of remote sensing applications: Alabama Highway Department, Bureau Research and Development, *Research Report* no. HPR-76, 83 p.

Newton J. G. 1984. Natural and induced sinkhole development in the Eastern United States. U.S. Geological Survey, Tuscaloosa, Alabama. Available online at: http://iahs.info/redbooks/a151/iahs_151_0549.pdf.

Newton J. G. and Tanner J. M. 1986. Regional inventory of karst activity in the Valley and Ridge Province, Eastern Tennessee, Phase 1. Oak Ridge National Laboratory ORNL/Sub/11-79811/1.

Sowers G.F. 1978. Mechanisms of Subsidence Due to Underground Openings, Subsidence Over Mines and Caverns, Moisture and Frost Actions, and Classification, TRB, Transportation Research Record , 612, 2-8 pp.

Steiakakis E. Monopolis D. Vavadakis D. and Manutsoglu E. 2011. Hydrogeological research in Trypali carbonate Unit (NW Crete). *9th International Hydrogeological Congress*. 5-8 October 2011. N. Lambrakis et al. (Eds.), Advances in the Research of Aquatic Environment, Vol. 1. DOI 10.1007/978-3-642-19902-8, Springer-Verlag Berlin Heidelberg 2011. pp. 561-567.

Tataris A. and A. Christodoulou G. E. 1969. Geological map of Greece, sheet Alikianou, scale 1:50,000, Institute for Geology and Subsurface Research.

Waltham T. 2002. Foundations of Engineering Geology, 2nd Edition. Spon press. Taylor and Francis Group.

Waltham T. Bell and F. G., Culshaw M. G. 2005. Sinkholes and Subsidence: Karst and Cavernous Rocks in Engineering and Construction. Praxis Publishing Ltd, Chichester, UK.

Zhiqiang Yang and M., Drumm Eric C. 2002. Stability evaluation for the siting of municipal landfills in karst. Engineering Geology 65, pp.185–195.

Δελτίο της Ελληνικής Γεωλογικής Εταιρίας, τομ. XLVII , 2013
Πρακτικά 13ου Διεθνούς Συνεδρίου, Χανιά, Σεπτ. 2013

Bulletin of the Geological Society of Greece, vol. XLVII 2013
Proceedings of the 13th International Congress, Chania, Sept. 2013

APPLYING ARTIFICIAL NEURAL NETWORKS IN SLOPE STABILITY RELATED PHENOMENA

Tsangaratos P.[1] and Benardos A.[2]

[1] *National Technical University of Athens, School of Mining and Metallurgical Engineering, Department of Geological Studies, ptsag@metal.ntua.gr,*

[2] *National Technical University of Athens, School of Mining and Metallurgical Engineering, Department of Mining Engineering, abenardos@metal.ntua.gr*

Abstract

Over the past years, Artificial Neural Networks (ANN) have been successfully used for the modelling in a great number of geoscience applications. In this paper we discuss the architecture and the way ANN work, presenting a specific learning algorithm which has been applied in the estimation of landslide susceptibility within a GIS environment.
Key words: *Landslide Susceptibility, Data Mining, Artificial Neural Networks, Geographic Information System.*

Περίληψη

Τα τελευταία χρόνια, τα Τεχνητά Νευρωνικά Δίκτυα (ΤΝΔ) έχουν επιτυχώς χρησιμοποιηθεί για την μοντελοποίηση και προσομοίωση γεωλογικών διεργασιών από ένα μεγάλο πλήθος γεω-επιστημόνων. Σε αυτή την εργασία γίνεται μια συνοπτική περιγραφή της αρχιτεκτονικής και του τρόπου λειτουργίας των ΤΝΔ, παρουσιάζοντας με περισσότερη λεπτομέρεια τον αλγόριθμο οπισθόδρομης μετάδοσης σφάλματος για την εκτίμηση της κατολίσθησης επιδεκτικότητας μέσω ενός συστήματος ΓΣΠ (Γεωγραφικού Συστήματος Πληροφοριών)
Λέξεις κλειδιά: *Κατολισθητική Επιδεκτικότητα, Εξόρυξη Δεδομένων, Τεχνητά Νευρωνικά Δίκτυα, Γεωγραφικά Συστήματα Πληροφοριών.*

1. Introduction

The use of artificial neural networks (ANN) in problem solving has received considerable attention in recent years in various geo - engineering applications. This is mainly due to the capability of these networks to solve problems, in which the involved parameters are either large in number or are not fully understood. In the case of landslide hazard and susceptibility analysis, ANNs have been widely used for landslide susceptibility zonation (Lee et al., 2003, Lu & Rosenbaum, 2003, Lee et al., 2004, Ermini et al., 2005, Gomez & Kavzoglu, 2005). Different reasons of applying such methods are reported by many researchers; however their reports share a common belief that the prediction of future landslide events is based on complex, unknown, and non-linear relationships between mass movement distribution and conditioning factors (Aleotti & Chowdhury, 1999, Lee et al., 2003, Neaupane & Achet, 2004, Ferentinou & Sakellariou, 2007, Pradhan & Lee, 2010). Current research has proven that ANNs, especially multilayer perceptrons

(MLP), have several advantages when applied for landslide susceptibility mapping. A MLP can model non-linear relationships, extract useful relationships from imprecise data, and generate reasonable results even when some of the training inputs are flawed (Ermini et al., 2005, Kanungo et al., 2006). As many researchers have noted such abilities are not perfectly provided by multivariate statistical methods (Gomez & Kavzoglu, 2005, Vahidnia et al., 2010). The most widely used learning method in ANN is the back-propagation neural network, an abbreviation for "backward propagation of errors" (Rumelhart et al., 1986) and is the algorithm that will be described in this paper. The objective of the present paper is to discuss the main architecture features and the way ANN works and to present in more detail the back-propagation algorithm and how it is implemented in a landslide susceptibility analysis within a GIS environment.

2. Artificial Neural Networks

Artificial Neural Network (ANN) is considered as information – processing system capable of learning and generalizing from the "experience". Haykin (1999), described ANN as machines that are designed to model the way the human mind works when it performs a specific task. The operation of ANN is based on the following assumptions: The processing of the stimulus is carried out by a set of processing units, the neurons. Each neuron has the ability to receive and transmit a signal - the stimulus. Each signal - stimulus received or transmitted from one neuron to another in the neural network associated with a weight (synaptic weight) which indicates the strength of the connection between the respective neurons. The higher the value of the weighting factor, the more important is the contribution of the node. The sum of the received signals - stimuli, is aggregated through a function, the activation function to emit the final signal (Fausett, 1994). The most distinguished characteristic of an Artificial Neural Network is the ability to generalize (make prognosis) once trained. Thus, they are capable of "learning" from a set of data whose characteristics are known, even if the form of their relationships are unknown or their physical interpretation is difficult to be explained and after that, they can make predictions on a set of new input data. This property makes the ANNs to be more advanced against empirical and statistical methods, which require prior knowledge of the data distribution and also the nature of the relationship (linear, non – linear, etc.).

2.1. The Learning Process Method

The neural networks receive stimuli (information and knowledge) through an iterative learning process, as people do, and knowledge is stored in the network connections (Haykin, 1999). The ANN models tries to combine the thinking of the human brain with the abstract mathematical thinking, following parallel distributed processing (McClelland & Rumelhart, 1986). There are typically three types of learning, supervised, unsupervised and reinforcement learning. In supervised learning, learning is accomplished by presenting a set of training patterns each with an associated target output vector, while in unsupervised learning type, learning is accomplished by grouping a similar set of input patterns together without the use of training data to specify what a typical member of each group looks like or to which group each pattern belongs to (Fausett, 1994). Reinforcement learning is learning by interacting with an environment. A reinforcement learning model learns from the consequences of its actions, rather than from being explicitly taught. It selects its actions on the basis of its past experiences (exploitation) and also by new choices (exploration), which is essentially a trial and error learning process. The most typical ANN setting is the one that enables supervised training. During the training phase, the hidden and output layer neurons process their inputs by multiplying each input by a corresponding weight, summing the product, and then processing the sum using a non-linear transfer function to produce a result. An ANN learns by adjusting the weights between the neurons in response to the errors between the actual output values and the target output values. At the end of this training phase, the neural network provides a model that should be able to predict a target value from a given input value. In general the method used to estimate the values of the synaptic weights, trains the multilayered until some targeted minimal error is achieved between the desired and actual output values of the

network. Once the training is complete, the classification phase follows, where the network is used as a feed-forward structure to produce a classification for the entire data.

2.2. The Basic Features of ANN Models

As it is evident, each neural network is characterized by three basic features (Fausett, 1994, Benardos & Benardos, 2005):

- The way in which the neurons are connected to each other, which is called the network architecture.
- The method used to establish the values of the weights on the connections, called training or learning algorithm.
- The type of activation function used.

Defining the architecture of ANN is a critical process and requires on the part of the researcher, the fullest possible knowledge of the problem application (Benardos & Kaliampakos, 2004). Neural networks are often classified as single layer or multilayer, which are examples of feed-forward networks in which the signals flow from the input units to the output units in a forward direction. In MLP networks, such as the one that is presented in this study, there is always an input layer, a hidden layer and an output layer (Figure 1). The first layer of the network, or input layer, contains a node for each of the input variables. The input variables are analogous to the independent variables in multiple regression techniques. The second layer, the hidden layer, consists of nodes that allow complexities to develop among input nodes. The last layer of the network, or output layer, contains *t* nodes, one for each output type.

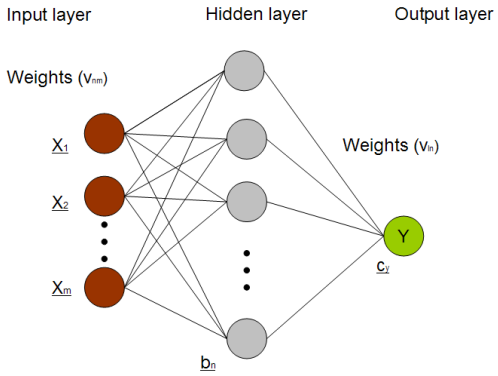

Figure 1 – The feed – forward multi-layer artificial neural network.

2.3. The Back – Propagation Algorithm

The training of an ANN by back-propagation learning algorithm involves three stages: the feed-forward of the input training pattern, the calculation and back-propagation of the associated error and the adjustment of the weights. After the training phase, application of the model involves only the computations of feed-forward phase. In the first stage, each input unit receives an input signal and transmits this signal to each of the hidden units. Each hidden unit then calculates its activation and transmits its signal to each output unit, by applying a function:

Equation 1 – the output signal of the net

$net_j^{(l)}(t) = \sum_{i=0}^{p} \left(y_i^{(l-1)}(t) w_{ji}^{l}(t) \right)$, the net input of j[th] neuron of layer l and t iteration

Each output unit computes its activation to form the response of the net for the given input pattern by applying the following formula:

Equation 2 – the response of the net

$$y_j^{(l)}(t) = f\left(net_j^{(l)}(t)\right)$$

Each neuron in the network may employ a nonlinear activation function at the output end, producing smooth signals to other neurons. One of most commonly used activation functions is the binary sigmoid transfer function which has range of (0, 1) and is defined as (Hagan et al., 1996):

Equation 3 – the sigmoid function

$$f(net) = \frac{1}{1+e^{(-net)}}$$

Each output unit compares it's activation with its target value to determine the associated error for that pattern with that unit.

Equation 4 – the associated error

$$e_j(t) = c_j(t) - a_j(t)$$

Based on this error, a δ factor, is computed which is used to distribute the error at output unit back to all units in the hidden and input layer.

Equation 5 – the δ factor for the output layer

$\delta_j^{(l)}(t) = e_j^{(l)}(t)a_j(t)\left[1 - a_j x(t)\right]$, δ factor or neuron jth in the output layer ith

Equation 6 - the δ factor for the hidden layer

$\delta_j^{(l)}(t) = y_j^{(l)}(t)\left[1 - y_j(t)\right]\sum_k \delta_j^{(l+1)}(t)w_{kj}^{(l+1)}(t)$, δ factor for neuron jth in hidden layer ith

After the entire δ factors have been calculated, the weights for all layers are adjusted simultaneously, according to the generalized Least – Square - Mean rue (Hagan et al., 1996):

Equation 7 – the formula for the weight estimation

$$w_{ji}^{(l)}(t+1) = w_{ji}^{(l)}(t) + \alpha\left[w_{ji}^{(l)}(t) - w_{ji}^{(l)}(t-1)\right] + \eta\delta_j^{(l)}(t)y_i^{(l-1)}(t)$$

where η is the learning rate, and α is the momentum rate for speeding up learning without running into the risk of oscillation.

There are several aspects that need to be taken into account during the construction and implementation of the back-propagation algorithm that are related to the non - deterministic nature of this method. Specifically there are several learning performance indices or cost functions that should be selected according to the related problem and they are mainly based on distance functions. Furthermore, the initial weight of the multilayer feed-forward neural network strongly

influences the convergence of the back - propagation learning algorithm and so does the learning rate η. A large learning rate value speeds up the convergence but the weights may then oscillate, while a low learning rate results in slow learning. An alternative way in coping with this problem is by introducing a momentum term to the gradient – descent method, giving to each weight some inertia (momentum) is such a way that it tends to maintain its direction. Some other issues that are not always clear are firstly, the choice on the number of the hidden layers and nodes required solving a learning problem and secondly the choice on the number of the training samples required (Grima, 2000).

3. Artificial Neural Network and Landslide Susceptibility Analysis

In the literature there are numerous studies that present various kinds of physical (process-based), statistical, or combined approaches for dealing with the landslide hazard and susceptibility zonation mapping (Glade et al., 2005). Landslide susceptibility is the likelihood of a landslide occurring in an area on the basis of local terrain conditions (Brabb, 1984). It is the degree to which a terrain can be affected by slope movements, an estimate of "where" landslides are likely to occur. As reviewed through the literature, there is no agreement on the methods for susceptibility maps production as several qualitative and quantitative methods have been proposed for landslide susceptibility evaluation (Carrara et al., 1995, Aleotti & Chodwdhury, 1999, Guzzetti et al., 1999, Dai et al., 2002, Glade et al., 2005).

Most of these methods share a common limitation that has to do with the difficultly to objectively handle the non-linear multivariate characteristics of the landslide phenomena that is assumed to be due to the spatial and temporal variability, scale dependency, and complicated interrelationship of the factors affecting landslide manifestation. Statistical models, such as multiple regression and discriminate function techniques, are primarily designed to deal with linear problems and therefore, may be inappropriate for assessing complex non-linear problems. The physical models require detailed spatial information about the geomechanical features of the geological and hydrological materials that are involved in a landslide susceptibility or hazard assessment. These parameters show high spatial variability and in fact are very difficult to be presented in a large scale (van Westen et al., 2006).

During the last two decades, Artificial intelligence and Data Mining techniques have been introduced as efficient tools in susceptibility and hazard analysis (Flentje et al., 2007, Kawabata et al., 2009, Tsangaratos et al., 2011). These techniques can deal with non-linear problems and, at the same time, minimizing subjectivity. One of the most promising methods is the one that use the artificial neural networks techniques. Elias & Bandis (2000) proposed a neuro-fuzzy approach for Landslide Susceptibility Zonation mapping. The authors used Fuzzy linguistic rules to assign fuzzy membership values to different classes of thematic data layers. The fuzzy membership values were used to provide data to the input neurons of a Back Propagation neural network model. A single output neuron with values from 0 to 1 was considered to represent the degree of landslide susceptibility based on actual landslide data. Lee et al. (2001) applied ANN in the Yongin in Korea to obtain a landslide hazard zonation map. The authors introduced a back-propagation algorithm twice, firstly to produce a landslide inventory map and secondly to determine the weight coefficients of each input landslide related parameter. The verification results between the calculated landslide susceptibility index and the existing landslide location data showed a good agreement and satisfactory output results. Ermini et al. (2005) applied Probabilistic Neural Network (PNN) and Multi Layered Preception (MLP) to create a landslide hazard map in Riomaggiore Italy. The researches converted the input factors to binary variables and used these variables as input data of the developed ANN model. Ferentinou & Sakellariou (2007) applied several computational intelligence tools in slope performance prediction both in static and dynamic conditions. Specifically, the used the back-propagation algorithm, the theory of Bayesian neural networks and the Kohonen self-organizing maps, for estimating the slope stability controlling variables by combining these computational intelligence tools with generic interaction

matrix theory. Their study, focused on the prediction and estimation of slope stability, coefficient of critical acceleration, earthquake induced displacements, unsaturated soil classification, and the classification according to the status of stability and failure mechanism for dry and wet slopes. Caniani et al. (2008) applied the back-propagation learning algorithm within a three layered model, input, hidden and output layer, in a research area at Potenza, Italy. The authors concluded that the neural networks model that they used constituted a relatively simple solution to complex problems, such as those concerning the estimation of landslide susceptibility. However, they also reported that the knowledge acquired by the network is expressed through a set of weights and hence not in an immediately comprehensible format. They finally noted that a neural network can be progressively improved with the availability of additional information by refining the details of the input maps that are found to be the most important, according to the assessed ANN weights. Melchiorre et al. (2008) introduced an integrated use of supervised and unsupervised techniques to improve the results of neural classifiers during a landslide susceptibility analysis. The use of Cluster analysis methods and the possibility of choosing the distance measure make it possible to introduce expert knowledge to the process of landslide susceptibility analysis. Marjanovic et al. (2009) used support vector machine (SVM), neighbor k-NN algorithms and Analytical Hierarchy Process (AHP) for weighting influences of different landslide related input parameters. Authors combined multi-criteria analysis and machine learning techniques to capture the different importance of several inputs parameters and give a single outcome of the modeled landslide phenomenon. Oh & Pradhan (2011) applied the Adaptive Neuron – Fuzzy Inference System (ANFIS) for landslide susceptibility mapping in Penang Island, which is based on both expert knowledge using fuzzy inference system (FIS) and supervised learning (ANN). Landslide-susceptible areas were analyzed by the ANFIS approach and mapped using landslide-conditioning factors. The applied ANFIS model learns the "if–then" rules between landslide-related conditioning factors and landslide location, for generalization and prediction. The authors used various membership functions (MFs) for the landslide-susceptibility mapping and their results were compared with the field-verified landslide locations.

3.1. The Process of Landslide Susceptibility Analysis Through ANN Models in a GIS Environment

In recent years, GIS has become a very important tool for landslide susceptibility and hazard assessment (Carrara et al., 1995, David & Douglas 1998, Guzzetti et al., 1999, Dhakal et al., 2000, Lee et al., 2003, Glade et al., 2005). GIS is a computer-based technology designed to capture, store, manipulate, analyze, and display diverse sets of spatial data. In general there are four phases involved in the process of manipulating landslide related data through ANN in a GIS environment: the data preparation phase, the training phase, the classification phase and landslide susceptibility mapping phase, and the validation phase. The first phase consists in constructing the GIS spatial database that will be used during the landslide susceptibility and hazard analysis. The advance of GIS is that it may accept different types of variables (e.g., class, ordinal, continuous, and categorical) as input values and that it can also handle imperfect or incomplete data. The thematic data layer that refers to each factor depicts the categories of each factor (Figure 2). Each category is assigned an attribute value subjectively (expert knowledge), depending upon its relative significance in causing landslides. These attribute values must be normalized with regard to the highest attribute within the corresponding causative factor and form the input data for the ANN model. During the data preparation phase the GIS spatial database must be converted to the format of input for the artificial neural, in most cases in ASCII data format. Also, in the preparation phase the spatial data are partitioned into two subsets, the training and testing dataset. The first subset, subset of the training data, includes all the data belonging to the problem domain and is used in the phase of training that follows.

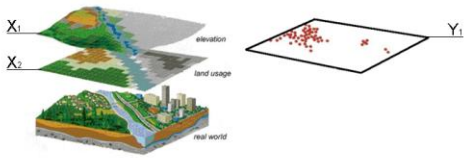

elevation		land usage	
classes	Normalized attribute	classes	Normalized attribute
1. 0 -100m	0.1	1. Class a	0.1
2. 100 - 300m	0.3	2. Class b	0.3
3. 300 - 500m	0.5	3. Class c	0.5
4. 500 - 700m	0.7	4. Class d	0.6
5. > 700m	0.9	5. Class e	0.7
		6. Class f	0.8
		7. Class g	0.9

Figure 2 – Applying ANN in a GIS environment.

The training process begins by assigning randomly initial connection weights to the input nodes which are constantly updated until an acceptable training accuracy is reached. The adjusted weights obtained from the trained network have been subsequently used to process the testing data in order to evaluate the generalization capability and accuracy of the network. The output layer of ANN contains a single neuron that represents the presence or absence of existing landslide locations (i.e., a target output of 0.9 denotes presence and 0.1 denotes absence). The next phase involves the production of the landslide susceptibility map. The artificial neural network output data must be converted to the appropriate format for the GIS spatial database. The categorization of a terrain into ordinal zones of landslide susceptibility has been regarded as a pure classification problem. The outputs of any model that adopts the ANN technique could be considered as the degree of the membership of each terrain unit with regard to the occurrence of landslide (Ermini et al., 2005). The higher the membership value, the more susceptible is the terrain unit to the occurrence of landslide and vice versa (Equation 8).

Equation 8 – Landslide susceptibility Index

$$Ls_i = f\left(\sum_{r=1}^{n} w_{ir} f\left(\sum_{j=1}^{m} v_{rj} u_j + b_r\right) + c_y\right)$$

where, u is the m x 1 input vector layer, y the output vector layer, n the number of neurons in the hidden layer, v and w are the weight factors, and b_r and c_y the bias values of the neurons in the hidden and output layer, respectively.

The final phase is the validation phase. In general, models for landslide susceptibility are predictions of the spatial occurrence of landslides, and their performance should be evaluated (Guzzetti et al., 2005). A landslide susceptibility assessment should be evaluated against the information used to prepare the prediction, in a way evaluate the "goodness of fit" of the produced model. Measures of goodness of fit are obtained by preparing contingency tables showing the number of incidence correctly classified and by comparing them against the cases that were misclassified by the model. To visualize the results of the verification a graph showing the model success rates is considered as appropriate (Chung & Fabbri, 1999, Guzzetti et al., 2005). The graph is formed by taking account the percentage of the study area against the cumulative distribution function of landslide area in each predicted susceptibility class. A rapid deviation of the success rate curve from the diagonal line indicates a model with high performance.

An example of the landslide susceptibility map that can be produced from the feed forward back propagation learning algorithm is seen in Figure 3 (Tsangaratos, 2012). The model had eight neurons in the input layer one hidden layer, with seven hidden neurons and one output layer. The eight neurons in the input layer correspond to the landslide related factors (geology, geological boundaries, elevation, slope inclination, slope orientation, tectonic features, hydrographic features, road network) that had been identified as causative factors in an area of high landslide manifestation in Xanthi prefecture, Greece. The model was trained using the training database that included 260 locations of landslide and non-landslide sites. A number of trials were performed using different learning rate ranging from 0.6 to 0.9. From these trials, the learning rate of 0.88 was found to be stable. When a momentum rate of 0.05 was added to the network, the convergence of the model took longer, it reached 18000 epochs, but the error was minimized. The weight for each factor that has been calculated during the training phase is then assigned to the each factor in order to estimate the landslide susceptibility index according to equation 8. The final product of which is the landslide susceptibility map, with five classes of susceptibility, namely: Very Low Susceptibility, Low Susceptibility, Medium Susceptibility, High Susceptibility and Very High Susceptibility.

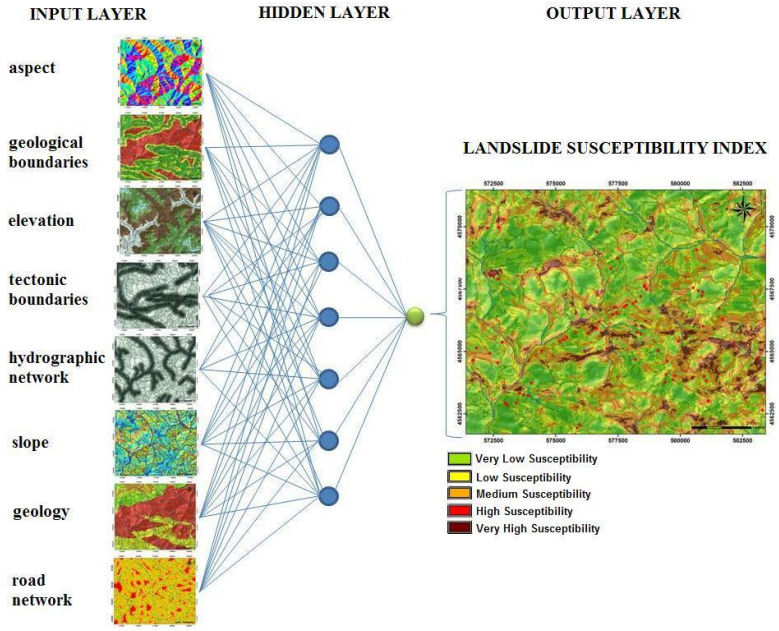

Figure 3 – The landslide susceptibility map from the feed forward back propagation neural network.

According to the methodology to validate the model, data that are not used during the training phase should be introduced to the model. By superimposing the data that formed the testing database over the landslide susceptibility map a simple validation measure of accuracy was obtained. The accuracy index, an index that corresponds to the degree of closeness of measurements of a quantity to that quantity's actual (true) value, reached 95.45%.

4. Discussion and Conclusion

In problem solving process the lack of understanding for complicated physical behaviour is easily supplemented by either over-simplifying the problem or incorporating several assumptions into the model. Consequently, many mathematical models may fail to simulate the complex behaviour of geotechnical problems. One a most promising alternatives in problem solution techniques are the

non-parametric techniques that artificial intelligence and data mining domain. ANNs use learning algorithms to model knowledge and save this knowledge in weighted connections, mimicking the function of a human brain (Pradhan & Lee, 2010). They are considered as heuristic algorithms in the sense that they can learn from experience via samples and are subsequently applied to recognize new unseen data (Kavzoglu & Mather, 2000). The parallel distribution of information within the ANNs provides the capacity to model complicated, non-linear and interrelated processes. This ultimately allows ANNs to model environmental systems without prior specification of the algebraic relationships between variables (Lek et al., 1999). The most important advantage of the ANN method is that it is independent from the statistical distribution of the spatial data and there is no need for use of specific statistical variables (Lee et al., 2004). Compared with statistical methods, the ANN methods allow the target classes to be defined, taking into account their distribution in the corresponding domain of each data source (Lee et al., 2003, 2004, Zhou, 1999). Another major advantage for developing ANN process models is that they do not depend on simplified assumptions such as linear behavior or production heuristics. Neural networks possess a number of attractive properties for modeling a complex mechanical behavior or a system: universal function approximation capability, resistance to noisy or missing data, accommodation of multiple nonlinear variables for unknown interactions, and good generalization capability. Despite its simplicity and popularity, back – propagation algorithm present several problematic aspects. It may be slow and may need a considerable number of iterations to train the network. It may also be trapped easily in a local minimum and thus the learning algorithm may fail to solve the problem, independent on the network configuration. The initial weights cannot be large, otherwise the activation function becomes saturated from the very beginning and the solution will be trapped in a local minimum or a very flat plateau close to the starting point. However several researchers have proposed efficient methods that deal in an efficient way with the above mentioned aspects (Neguyen & Widrow, 1990, Nefeslioglu et al., 2010). Combining ANN techniques with GIS in a landslide analysis system can further extend the functionality of the ANN models and, at the same time, increase the set of possible applications of GIS. The major advantages of using an ANN system within a GIS environment for landslide susceptibility and hazard analysis are as follows: The collection, manipulation, and analysis of the landslide related data can be accomplished much more efficiently and cost effectively. The outcomes of the overlay functions and spatial analysis performed by a GIS can be used as the input and training conditions of a neural network and, while the results of the neural network may be manipulated by a GIS to produce a geospatial product. Each spatial input data and outcome of the neural network can be easily compiled, normalized, rescaled, re-projected and overlaid. It may accept different types of parameters (e.g., class, ordinal, continuous, and categorical) as input or output values and can handle imperfect or incomplete data. The system is extremely flexible and self-adaptive, capable of incorporating any improved new data set.

5. References

Aleotti P. and Chowdhury R. 1999. Landslide hazard assessment: Summary review and new perspectives, *Bulletin of Engineering Geology and the Environment*, 58(1), 21-44.

Benardos A.G. and Kaliampakos D.C. 2004. A methodology for assessing geotechnical hazards for TBM tunnelling—illustrated by Athens Metro, Greece, *International Journal of Rock Mechanics and Mining Science*, 41(4), 987–999.

Benardos A. G. and Benardos A. P. 2005. Applications of Artificial Neural Networks in Geotechnology, *Chronicles of Mining and Metallurgical*, 15(1), 65-81, (in Greek).

Brabb E.E. 1984. Innovative approaches to landslide hazard mapping, *Proceedings of IV International Symposium of Landslides*, Toronto, 1, 307-324.

Caniani D., Pascale S., Sdao F. and Sole A. 2008. Neural networks and landslide susceptibility: a case study of the urban area of Potenza, *Natural Hazards*, 45, 55-72.

Carrara A., Cardinali M., Guzzetti F. and Reichenbach P. 1995. GIS technology in mapping landslide hazard. In: Carrara A, Guzzetti F (eds), *Geographical information systems in assessing natural hazards*, Kluwer, Dordrecht, 135–175 pp.

Chung C-J. F. and Fabbri A. G.1999. Probabilistic Prediction Models, *Photogrammetric Engineering & Remote Sensing*, 65(12), 1389-1399.

Dai F.C., Lee C.F. and Ngai Y.Y., 2002. Landslide risk assessment and management: an overview, *Engineering Geology*, 64(1), 65–87.

David N.R., and Douglas D. 1998. GIS modeling of slope stability in Phewa Tal watershed, Nepal, *Geomorphology*, 26,151–170, doi:10.1016/S0169-555X(98)00056-7.

Dhakal A.S. Amada T. and Aniya M. 2000. Landslide hazard mapping and its evaluation using GIS: an investigation of sampling schemes for a grid-cell based quantitative method, *Photogrammetric Engineering & Remote Sensing*, 66, 981–989.

Elias P.B. and Bandis, S.C., 2000. Neurofuzzy Systems in Landslide Hazard Assessment, in: *Proceedings of 4th International Symposium on Spatial Accuracy Assessment in Natural Resources and Environmental Sciences*, July 2000, 199-202.

Ermini L., Catani F. and Casagli N. 2005: Artificial neural networks applied to landslide susceptibility assessment, *Geomorphology*, 66, 327–343.

Fausett L. 1994. Fundamentals of neural networks architectures, Algorithms and applications, Prentice Hall, USA, pp 461.

Fell R., Corominas J., Bonnard C., Cascini L., Leroi E. and Savage W. 2008. Guidelines for landslide susceptibility, hazard and risk zoning for land-use planning, *Engineering Geology*, 102, 99-111.

Ferentinou M. and Sakellariou G. 2007. Computational intelligence tools for the prediction of slope performance, *Computers and Geotechnics*, 34, 362-384.

Flentje P. Stirling D. and Chowdhury R. 2007. Landslide susceptibility and hazard derived from a landslide inventory using data mining — an Australian case study, *Proceedings of the First North American Landslide Conference*, Vail, Colorado, June 2007.

Glade T., Anderson M. and Crozier M.J. 2005. *Landslide Hazard and Risk*. John Wiley & Sons, Ltd., Chichester, England, 802 pp.

Gomez H. and Kavzoglu T. 2005. Assessment of Shallow Landslide Susceptibility using Artificial Neural Networks in Jabonosa River Basin, Venezuela, *Engineering Geology*, 78(1-2), 11-27.

Grima M. A. 2000. *Neuro-Fuzzy Modelling in Engineering Geology*, Balkema, Rotterdam, pp 244,

Guzzetti F., Carrara A., Cardinali M., and Reichenbach P., 1999. Landslide evaluation: a review of current techniques and their application in a multi-scale study, Central Italy, *Geomorphology*, 31, 181–216.

Guzzetti F., Reichenbach P., Cardinali M., Galli M. and Ardizzone F. 2005. Probabilistic landslide hazard assessment at the basin scale, *Geomorphology* 72, 272–299.

Hagan T.M., Demuth B.H. and Beale H.M. 1996. *Neural network design*, Electrical Engineering Series, Brooks / Cole, pp730.

Haykin S. 1999. *Neural Networks. A Comprehensive Foundation*, 2nd Edition. Prentice Hall, Englewood Cliffs, New Jersey, USA, pp 696.

Kanungo D.P., Arora M.K., Sarkar S. and Gupta R.P. 2006. A comparative study of conventional, ANN black box, fuzzy and combined neural and fuzzy weighting procedures for landslide susceptibility zonation in Darjeeling Himalayas, *Engineering Geology*, 85, 347-366.

Kavzoglu T. and Mather P.M. 2000. Using feature selection techniques to produce smaller neural networks with better generalization capabilities, *Proc IEEE 2000 International Geoscience Rem Sens Symposium*, Hawaii 3:3069–3071.

Kawabata D. and Bandibas J. 2009. Landslide susceptibility mapping using geological data, a DEM from ASTER images and an Artificial Neural Network (ANN), *Geomorphology*, 113(1-2), 97-109.

Lee, S. Ryu J. Min, K. and Won, J. 2003. Landslide susceptibility analysis using G.I.S. and artificial neural network, *Earth Surface Processes and Landforms*, 28, 1361–1376.

Lee S. and Min K. D. 2001. Statistical Analysis of Landslide Susceptibility at Yongin, Korea, *Environmental Geology*, 40(9), 1095-1113.

Lee S., Ryu J., Won J. and Park H. 2004. Determination and application of the weights for landslide susceptibility mapping using an artificial neural network, *Engineering Geology*, 71, 289-302.

Lek S., Guiresse M. and Giraudel J.L. 1999. Predicting stream nitrogen concentration from watershed features using neural network, *Water Research*, 33(16):3469–3478.

Lu P. and Rosenbaum M.S. 2003. Artificial neural network and grey system for the prediction of slope stability, *Natural Hazards*, 30, 383–398.

Marjanovic M., B. Bajat. and M. Kovaevi. 2009. Landslide susceptibility assessment with machine learning algorithms, *Proceedings of the International Conference on Intelligent Networking and Collaborative Systems*, November 4-6, 2009, IEEE, Barcelona, pp: 273-278.

McClelland J. L. Rumelhart D. E. and the PDP research group, 1986. *Parallel distributed processing: Explorations in the microstructure of cognition. Volume II.* Cambridge, MA: MIT Press.

Melchiore C., Matteucci A., Azzoni A. and Zanchi A. 2008. Artificial neural networks and cluster analysis in landslide susceptibility zonation, *Geomorphology*, 94, 379–400.

Neaupane K.M. and Achet S.H. 2004. Use of back propagation neural network for landslide monitoring: a case study in the higher Himalaya, *Engineering Geology*, 74(3–4), 213–226.

Nefeslioglu H.A., Sezer E., Gokceoglu C., Bozkir A.S. and Duman T.Y. 2010. Assessment of landslide susceptibility by decision trees in the metropolitan area of Istanbul, Turkey, *Mathematical Problems in Engineering*, doi:10.1155/2010/901095, Article ID 901095

Nguyen D. and Widrow B. 1990. Improving the learning speed of two-layer neural networks by choosing initial values of the adaptive weights, *Proceedings of IJCNN'90*, 3, 21-26.

Oh H.J. and Pradhan B., 2011. Application of a neuro-fuzzy model to landslide-susceptibility mapping for shallow landslides in a tropical hilly area, *Computer & Geosciences*, 37:1264–1276.

Pradhan B. and Lee S., 2010. Landslide susceptibility assessment and factor effect analysis: backpropagation artificial neural networks and their comparison with frequency ratio and bivariate logistic regression modelling, *Environmental Modelling Software*, 25(6), 747–759.

Rumelhart D.E. Hinton G.E. and Williams R.J. 1986. Learning representations by back-propagating errors, *Nature*, 323, 533–536.

Tsangaratos P. 2012. Research on the engineering geological behaviour of the geological formations by the use of information systems, *PhD Thesis*, School of Mining Engineering Geology, Department of Geological Section, NTUA, Athens, pp. 363.

Tsangaratos P., Ilia I. and Rozos D. 2013. Case Event System for landslide susceptibility analysis, *Proceedings of the Second World Landslide Forum Abstracts*, WLF2 - 2011– 0389, Rome, pp. 10.

Vahidnia M.H., Alesheikh A.A., Alimohammadi A. and Hosseinali F. 2010. A GIS-based neuro-fuzzy procedure for integrating knowledge and data in landslide susceptibility mapping, *Computers & Geosciences*, 36, pp1101–1114.

VanWesten J. Van Asch J. and Soeters, R., 2006. Landslide hazard and risk zonation — why is still so difficult?, *Bulletin of Engineering Geology and the Environment*, 65, 167–184.

Zhou W. 1999. Verification of the nonparametric characteristics of backpropagation neural networks for image classifications, *IEEE Transactions on Geosciences and Remote Sensing*, 37(2), 771–779.

Δελτίο της Ελληνικής Γεωλογικής Εταιρίας, τομ. XLVII , 2013
Πρακτικά 13ου Διεθνούς Συνεδρίου, Χανιά, Σεπτ. 2013

Bulletin of the Geological Society of Greece, vol. XLVII 2013
Proceedings of the 13th International Congress, Chania, Sept. 2013

THE GEOTHERMAL OCCURRENCE OF KAPISTRI, IERAPETRA AREA, CRETE

Chatzigiannis G.[1] and Kavouridis Th.[1]

[1] *I.G.M.E., Spyrou Loui Str. 1, 13677, Acharnes, Athens*

Abstract

The geothermal occurence is located close to the Kapistri village, Ierapetra town, prefecture of Lassithi. In some water wells temperature of about 25°C in a depth of 100 - 150 m below surface, were measured. The calculated geothermal gradient is thus double in size compared to normal gradient.
The geological environment is composed of platy limestones of the autochthonous series of Crete on which units of phyllite – quartzite series as well as Pindos and Tripoli zones are overthrusted. Granite intrusion occurs in the carbonates with distinct contact metamorphism, in the Kapistri area. Intense tectonic activity is observed in the wider area of the Ierapetra graben with main fault direction N – S, E – W, NW – SE, and NE – SW.
The elevated geothermal gradient, the intense faulting of the area and the existence of deep circulated water indicates the development of a deeper geothermal field.
Key words: *Geothermal Energy and gradient, heat flow.*

Περίληψη

Η γεωθερμική εμφάνιση εντοπίζεται κοντά στο χωριό Καπίστρι,στην ευρύτερη περιοχή της πόλης της Ιεράπετρας στο νομό Λασηθίου της Κρήτης. Σε μερικές υδρογεωτρήσεις μετρήθηκαν θερμοκρασίες περί τους 25°C σε βάθος 100 – 150 μ.από την επιφάνεια. Η γεωθερμική βαθμίδα που υπολογίστηκε είναι διπλάσια της κανονικής.
Η Περιοχή καλύπτεται από πλακώδεις ασβεστολίθους της αυτόχθονης σειράς της Κρήτης πάνω στην οποία είναι επωθημένες μονάδες της φυλλιτικής – χαλαζιτικής σειράς και των ζωνών Πίνδου και Τριπόλεως. Εντός των ασβεστολίθων έχουν διεισδύσει μαγματικά πετρώματα (γρανιτοειδή) που έχουν προκαλέσει μεταμόρφωση επαφής και ρηγμάτωση κοντά στο Καπίστρι. Έντονη τεκτονική δραστηριότητα παρατηρείται στην ευρύτερη λεκάνη Ιεράπετρας με κύριες διευθύνσεις των ρηγμάτων Β – Ν, Α – Δ, ΒΔ – ΝΑ και ΒΑ – ΝΔ.
Η αυξημένη γεωθερμική βαθμίδα, η έντονη ρηγμάτωση της περιοχής και η γεωχημική ένδειξη για την παρουσία νερού που κυκλοφορεί σε μεγάλο βάθος δείχνουν την πιθανή ανάπτυξη ενός βαθύτερου γεωθρμικού πεδίου.
Λέξεις κλειδιά: *Γεωθερμική ενέργεια και βαθμίδα, θερμική ροή.*

1. Introduction

The Kapistri village is located in the wider area of Ierapetra, Lassithi prefecture in east Crete Island (Figure 1). Its distance from Ierapetra town is 5.5 to 6 km. The geothermal occurrence was located during reconnaissance prospecting in the frame of a relative research program of IGME

(general geothermal reconnaissance in Greece). The relief of the area is hilly to plain with olive trees and greenhouses cultivations.

The location and development of geothermal field will contribute to the further development of greenhouses decreasing the heating cost which is necessary for the winter months. Moreover it will contribute to the mitigation of CO_2 emissions.

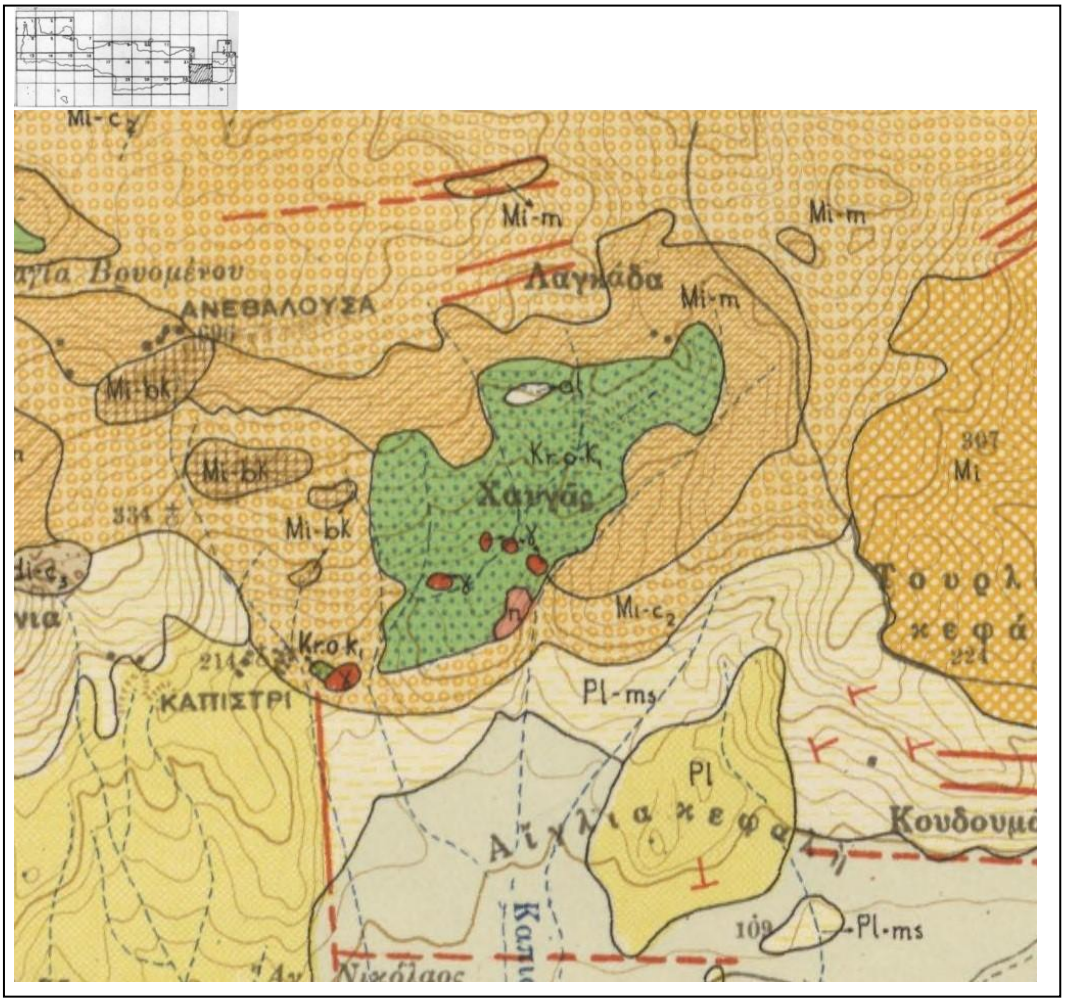

Figure 1 - Geology of the Kapistri area (al= recent alluvial deposits, di-c3= fluviatile terrace, Pl= Pliocene formations undivided, Pl-ms= marls, Mi= undivided Miocene formations, Mi-c2=basal conglomerate, Mi-m= marls, Mi-bk=limestones, kr o k1= Cretaceous coarse grained limestones, π=peridotites, γ=granitoids), from Papastamatiou J., 1959.

2. Geological Setting

According to the geological map of the area (map sheet Ierapetra, scale 1:50.000, Papastamatiou J., 1959) it is located in the west part of Ierapetra graben (Figure 1).

The geological basement consists of platy limestones of the autochthonous series of Crete on which the following series have been overthrusted:

- The nappe of phyllitic – quartzitic series
- The nappe of Tripoli geotectonic zone, and

- The nappe of the internal Hellenides zones (Pindos zone).

The Upper Cretaceous platy limestones have been intruded by acid magmatic rocks (mainly granitoids), which caused recrystallization of carbonates by contact metamorphism. The magmatic rocks outcrop more to the north close to the sea coast.

During the middle Miocene time the deposition of younger sediments started and continued to Pliocene and Holocene. The Tertiary sediments consist of clastic rocks, marls and marly limestones. The Quaternary sediments consist of sand and conglomerates. During the Holocene alluvial sediments were deposited (Lambrakis, N., 1987).

The structural geology of the area is marked by the Ierapetra graben with NE – SW direction and by four faults directions, i.e. N – S, E – W, NE – SW and NW – SE. Although there is a reactivation of the faults during different periods, it is observed that the N – S and E- W faults are older than the other two directions. The big fault of Kavoussi – Vainia has very large throw and determines the east margin of Ierapetra graben.

3. Geothermal Data

The intrusion and solidification of the magma into the limestones caused contact metamorphism as well as zones of intense faulting which constitute as channels of secondary water circulation. The Kapistri narrow area has been suffered of intense tectonic movements resulted in remarkable faults observed both in the limestones and in their contact with the younger sediments.

In the following figure (Figure 2) the main faults close to Kapistri and the sampled water boreholes are shown. Five boreholes were located, two of which do not yield any water. The temperature of all of the boreholes was measured and from two of them water samples were taken.

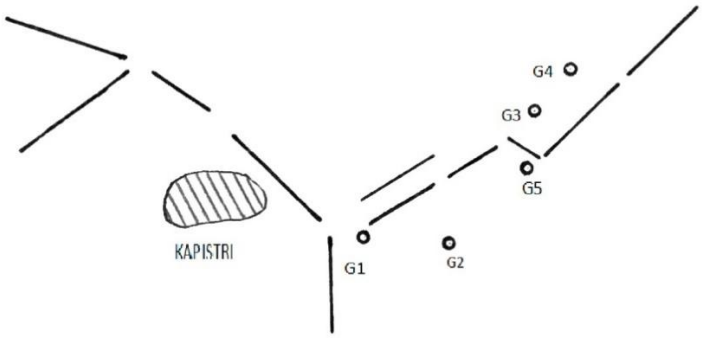

Figure 2 - Sketch map of observed faults and the measured boreholes (approx. scale 1:25000).

In the following Table1 the temperature recorded in each borehole is presented. The temperature in dry boreholes was measured down the hole and in the remaining the water temperature was measured in the outflow.

The mean annual temperature of Ierapetra area is 19.8^{o}C. Considering that the Kapistri is located in an altitude of 150 – 200 m.a.s.l. and that the atmospheric temperature gradient is 0.006^{o}C/m the mean annual temperature is 1^{o}C less than that of Ierapetra, namely 18.8^{o}C. Taking into account that the mean normal terrestrial geothermal gradient is 3.3^{o}C per 100 m. we can estimate that the expected temperature, in a depth of 100 m., will be about 22^{o}C. This value, compared to the meas ured temperatures of 22 – 25^{o}C it is evident that a thermal anomaly exists in the area. This local

geothermal gradient is almost double of the normal gradient and gives enough geothermal interest in the area.

Table 1 – Measurements of temperature in boreholes.

Borehole	Depth in m	Temperature in ^{o}C	Comments
G1	110	25	
G2	100	23	No water
G3	142	23.2	
G4	170	22	6pt
G5	100	20	No water

Another important observation is that the highest temperature was measured in the borehole G1 which lies in the intersection of two main fault directions (Figure 2). It shows an upwards circulation of warm water. It is well known that faults can operate as surfaces of flow of rain water to depth where it is heated, becomes lighter and rises towards the surface again through faults.

In the wider area there are main faults reaching big depth and assisting the water circulation too deep in the earth where they are heated, by geothermal gradient, and they rise up to the surface creating thermal anomalies. During its up rise the warm water mixes with near surface cold aquifers and loses some heat. Water mixing and heat loss is evident from the chemical composition of analyzed water samples.

3.1 Water Geochemistry

Two samples of water were collected in the outflow of the boreholes G1 and G3. The samples were analyzed for the 17 elements and the physical parameters as shown in the Table 2.

Table 2 – Results of chemical analyses of water.

Element	Borehole G1 (mg/l)	Borehole G3 (mg/l)
pH	7.85	7.6
Conduct.	1022	705
Ca	73.74	76.15
Mg	32.1	27.72
Na	131.1	55.20
K	3.91	2.35
HCO3	305.7	334.30
Cl	212.7	88.62
SO4	45.62	24.01
NO3	<3	18.60
Trace	**(In ppm)**	**(In ppm)**
SiO2	17.14	13.40
Fe	0.04	0.03
B	0.11	0.05
F	0.01	<0.01
Li	0.01	<0.01

Element	Borehole G1 (mg/l)	Borehole G3 (mg/l)
Sr	0.59	0.35
As	0	0

Observing and comparing the analyses of the two samples one can see that the water of borehole G1, which presents the higher temperature and is located closer to the fault intersection than the borehole G3, contains more salts (as shown by the conductivities) and has higher concentration of the elements characterizing the geothermal water (Na, K, Cl, SO_4, SiO_2, B, Li, Sr). The position of the water samples in the diagram Langelier – Ludwig (1942), (Figure 3) indicates that the sample of borehole G1 has a deeper origin compared to the sample of borehole G3. This sample contains more alkali elements and Cl ions and less alkali earths and carbonic acidic elements compared to their concentration in surface aquifers.

From the correlation diagrams of the elements Na with Cl and Na with Ca (Figures 5, 6) it is clear this differentiation of the two water samples as regards their origin. The enrichment of the water sample G1 in Na and Cl and in Ca and HCO_3 of the sample G3 determines the different circulation of these waters. Namely the water from borehole G1 seems that it has circulated for longer time and has come to contact with no carbonate rocks, in deeper level containing low Ca. In contrast the water of borehole G3 seems to circulate in carbonate rocks containing mainly Ca and sited close to the or on the surface. This conclusion is supported also from the diagram of Ca – Mg (Figure 4) on which it is observed the higher content in Mg and lower in Ca of the sample from the borehole G1compared with the water from borehole G3.

4. Conclusions

The geological setting of the Kapistri area (limestones with granite intrusions) as well as the intense faulting are favorable geothermal factors that can cause deep water circulation and result in heat transfer. The temperature measurements indicate a computed geothermal gradient twice the size of normal gradient. It is a fact which shows a significant geothermal interest for the area.

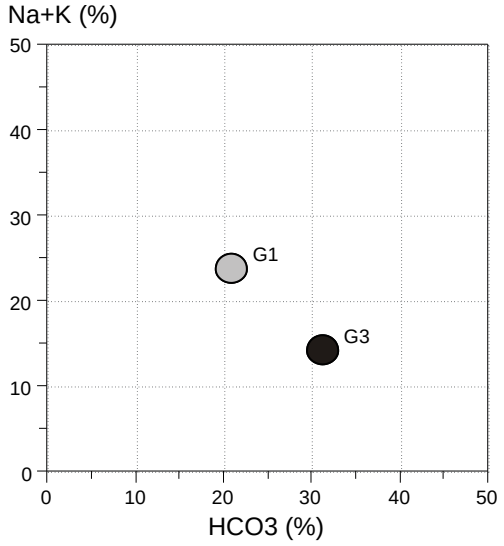

Figure 3 - Diagram Langelier – Ludwig.

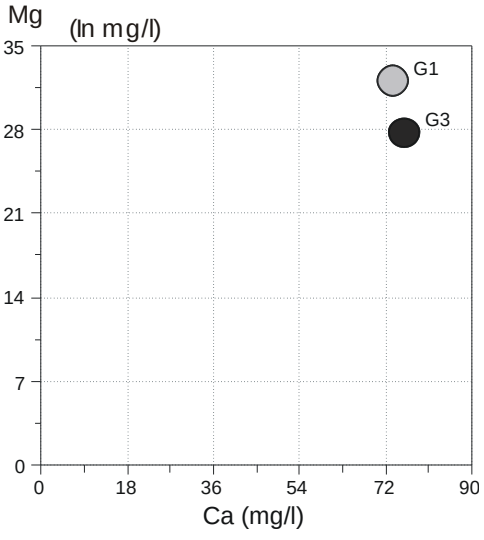

Figure 4 - Diagram Mg – Ca.

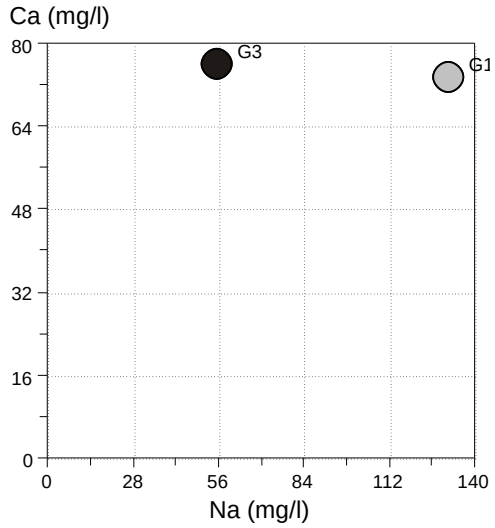

Figure 5 - Diagram Ca – Na.

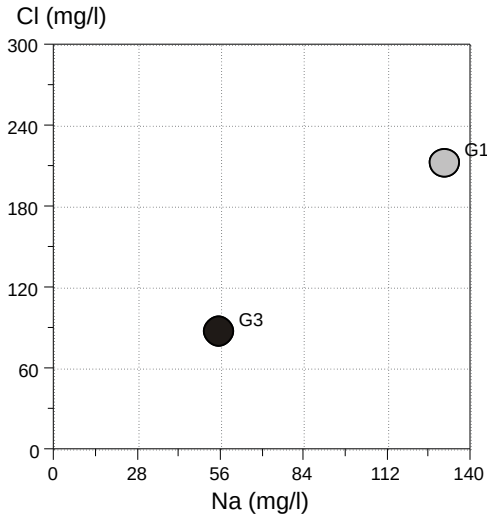

Figure 6 - Diagram Na – Cl.

The chemical composition of the warm water sample leads to the conclusion that, in addition to the near surface aquifer, there is another one occurring in deeper level with different geochemistry and higher content in soluble salts. This aquifer, as it is evident from its chemical composition, has come in contact with no carbonate rocks for a long time while its dissolving capability (in which the high salt content is due) may be the result of a higher than measured temperature, too.

From the above mentioned we conclude that in the area there are the necessary conditions to support the geothermal interest for exploring for geothermal fluids with higher temperature than the known 25^{o}C. Therefore it is proposed that a systematic geothermal exploration program must be applied. In a first phase this program should have as a target the detailed identification of the thermal anomaly with the collection of geological, geochemical and temperature data. An indicative phased exploration program must contain the following works:

- Geological reconnaissance in the wider area with the aim to find the distribution and separation of the formations with geothermal criteria, such as permeable formations, storage formations and cap rock.
- Search for altered rocks and their relation with geothermal manifestation.
- Temperature measurements in the wider area in order to determine the extent of thermal anomaly and its relation with faults.
- Water sampling for determining the chemical composition and the study of circulation mechanism.
- Processing and evaluating of the resulted data in order to continue for deep exploration.

5. References

Lambrakis N. 1987. Hydrogeological conditions in the wide area of Ierapetra, *Ph.D.,* University of Patras.

Langelier W.F. and Ludwig H.F. 1942. Graphical method for indicating the mineral character of natural waters, *J. Am. Water Works Assoc.*, 34, 335 – 352.

Papastamatiou J. 1959. Geological map of Ierapetra, I.G.S.R., (Geological map of Greece, 1:50,000).

Δελτίο της Ελληνικής Γεωλογικής Εταιρίας, τομ. XLVII , 2013
Πρακτικά 13ου Διεθνούς Συνεδρίου, Χανιά, Σεπτ. 2013

Bulletin of the Geological Society of Greece, vol. XLVII 2013
Proceedings of the 13th International Congress, Chania, Sept. 2013

HYDROTHERMAL METHANE FLUXES FROM THE SOIL AT LAKKI PLAIN (NISYROS ISLAND, GREECE)

D'Alessandro W.[1], Gagliano A.L.[2], Kyriakopoulos K.[3] and Parello F.[2]

[1] *Istituto Nazionale di Geofisica e Vulcanologia – Sezione di Palermo, Via U. La Malfa 153, 90146 Palermo, Italy, w.dalessandro@pa.ingv.it*

[2] *University of Palermo, Dept. DiSTeM, via Archirafi 36, 90123 Palermo, Italy*

[3] *National and Kapodistrian University of Athens, Faculty of Geology and Geoenvironment, Panepistimioupolis, 157 84 Ano Ilissia, Greece*

Abstract

Methane and CO_2 flux measurements from the soils were made with the accumulation chamber method in Lakki plain covering an area of about 0.06 km^2 including the main fumarolic areas of Kaminakia, Stefanos and Phlegeton. Flux values measured at 77 sites range from –3.4 to 1420 mg m^{-2} d^{-1} for CH_4 and from 0.1 to 383 g m^{-2} d^{-1} for CO_2. The three fumarolic areas show very different methane degassing patterns, Kaminakia showing the highest flux values. Methane output can be estimated in about 0.01 t a^{-1} from an area of about 2500 m^2 at Phlegeton, about 0.1 t a^{-1} from an area of about 20,000 m^2 at Stefanos and about 0.25 t a^{-1} from an area of about 30,000 m^2 at Kaminakia. The total output from the entire geothermal system of Nisyros should not exceed 1 t a^{-1}. Previous estimates of the CH_4 output at Nisyros, based on soil CO_2 output and CH_4/CO_2 ratios in fumarolic gases, were more than one order of magnitude higher. The present work further underscores the utmost importance of direct CH_4 flux data.

Key words: *accumulation chamber, soil degassing, hydrothermal systems, methane output.*

Περίληψη

Μετρήσεις φυσικής ροής μεθανίου και διοξειδίου του άνθρακα από το έδαφος πραγματοποιήθηκαν με τη μέθοδο συγκέντρωσης θαλάμου στην περιοχή Λακκί της Καλδέρας της Νισύρου, καλύπτοντας έκταση περίπου 0.06 km^2 συμπεριλαμβάνοντας τις περιοχές Καμινάκια, Στέφανος και Αλέξανδρο όπου παρατηρείται έντονη ατμιδική δραστηριότητας. Οι τιμές ροής που μετρήθηκαν σε 77 σημεία κυμαίνονται από –3.4 μέχρι 1420 mg m^{-2} d^{-1} για το CH_4 και από 0.1, μέχρι 383 g m^{-2} d^{-1} για το CO_2. Στις τρεις ατμιδικές περιοχές παρουσιάζονται διαφορετικοί ρυθμοί διαφυγής μεθανίου, ιδίως στα Καμινάκια όπου προέκυψαν οι μεγαλύτερες τιμές ροής. Η εξερχόμενη ποσότητα μεθανίου εκτιμάται σε 0.01 t a^{-1} από μια έκταση περίπου 2500 m^2 στον Αλέξανδρο, περίπου 1 t a^{-1} από μια έκταση περίπου 20,000 m^2 στον Στέφανο και περίπου 0.25 t a^{-1} από μια έκταση περίπου 30,000 m^2 στα Καμινάκια. Η συνολική εξερχόμενη ποσότητα από ολόκληρο το γεωθερμικό σύστημα της Νισύρου δεν πρέπει να υπερβαίνει το 1 t a^{-1}. Οι προηγούμενες εκτιμήσεις για την ποσότητα του εξερχόμενου μεθανίου από τη Νίσυρο, βασιζόμενες στην ποσότητα του CO_2 που διαφεύγει από το έδαφος και του λόγου CH_4/CO_2 των αερίων από τις φουμαρόλες,

ήταν περισσότερο από μία τάξη υψηλότερες. Στην παρούσα εργασία υπογραμμίζεται κυρίως η μεγάλη σημασία που παρουσιάζουν τα δεδομένα της απευθείας ροής του Μεθανίου.
Λέξεις κλειδιά: *Θάλαμος συγκέντρωσης, απαέρωση εδάφους, υδροθερμικά συστήματα, διαφυγή μεθανίου.*

1. Introduction

Methane plays an important role in the Earth's atmospheric chemistry and radiative balance being the second most important greenhouse gas after carbon dioxide (IPCC 2001). Methane is released to the atmosphere by a wide number of sources, both natural and anthropogenic, with the latter being twice as large as the former (IPCC 2001).

It has recently been established that geogenic gases contribute significantly to the natural CH_4 flux to the atmosphere (Etiope et al. 2008). Volcanic/geothermal areas contribute to this flux, being the site of widespread diffuse degassing of endogenous gases (Chiodini et al. 2005). In such an environment soils are a source rather than a sink for atmospheric CH_4 (Cardellini et al. 2003; Castaldi & Tedesco 2005; D'Alessandro et al. 2009; 2011). Preliminary studies (Etiope et al. 2007) estimated a total CH_4 emission from European geothermal and volcanic systems in the range 4-16 kt a^{-1}. This estimate was obtained indirectly from CO_2 or H_2O output data and from CO_2/CH_4 or H_2O/CH_4 values measured in the main gaseous manifestations. Such methods, although acceptable to obtain order-of-magnitude estimates, completely disregard possible methanotrophic activity within the soil. Furthermore at hydrothermal systems which display a rather large range in fumarolic CO_2/CH_4 values, like that of Nisyros (from 25 to 1600 in volume – Marini and Fiebig, 2005; Fiebig et al, 2009), the use of an average value could introduce a large uncertainty in the indirect estimation of the total CH_4 output to the atmosphere.

The Greek territory is geodynamically very active and has many volcanic and geothermal areas (Fytikas et al. 1995) which potentially contribute to the atmospheric CH_4 burden. Here we report on soil gas flux measurements made at Nisyros a currently quiescent active volcanic system with strong fumarolic activity due to the presence of a high enthalpy geothermal system. Measurements were used to estimate the total CH_4 output of this hydrothermal system.

2. Study Area and Methods

2.1. The Nisyros Volcanic and Geothermal System

The island of Nisyros belongs to the easternmost volcanic group of the South Aegean active volcanic arc. It was built up during the last 200 ka and is considered still active though at present in quiescent status (Vougioukalakis and Fytikas, 2005). Its volcanic activity has been characterized by (i) an early submarine stage, (ii) a subaerial cone-building stage, culminating in the formation of a central caldera, and (iii) a post-caldera stage, when several dacitic-rhyolitic domes were extruded (Keller, 1982). No historical magmatic activity is known on Nisyros and the most recent activity was of hydrothermal character (Marini et al. 1993). Such activity concentrated in the southern Lakki plain and on the southeastern flank of the Lofos dome both within the caldera. This hydrothermal activity formed a series of hydrothermal whose age decreases from southeast to northwest. The last events took place in 1871–1873 and 1887 partially destroying the small Lofos dome. A large fumarolic field is now present in this area mainly within the hydrothermal craters and being affected by fracturing along the main NW- and NE-trending active fault systems (Papadopoulos et al. 1998). Two deep explorative geothermal wells drilled in the Lakki plain revealed the existence of two distinct hydrothermal aquifers. The shallowest at about 500 m depth has temperatures around 150 °C while the deeper one (> 1500 m) reaches temperatures up to 340 °C (Brombach et al., 2003).

2.2. Sampling and Analytical Methods

Previous studies assessed a widespread CO_2 degassing in the whole fumarolic area and in the nearby areas (Caliro et al., 2005). The highest CO_2 fluxes (> 300 g m^2 day) were measured within the above described hydrothermal craters. Basing on these results we decided to concentrate our CH_4 flux measurements in the most representative craters (Kaminakia, Stefanos and Phlegeton) with some additional measurements in the fumarolic field of Lofos (outside any crater) and a few points in the low flux areas (Fig. 1a).

Measurements were made at 77 sites during two field campaigns (3-6 September 2009 and 24 August – 4 September 2010). At each sampling site the soil temperature was also measured at 20 and 50 cm depth and the soil CH_4 and CO_2 concentrations were determined at 50 cm depth.

Flux measurements were made with the accumulation chamber method (Livingstone & Hutchinson 1995; Baciu et al. 2008; D'Alessandro et al. 2009). The flux chamber has a cross-sectional area of 0.07 m^2 and height of 10 cm. The chamber top has two fixed capillary tubes, one used to collect chamber gas samples and the other used to balance the pressure between inside and outside. Three gas samples were drawn from the headspace in the chamber at fixed intervals after deployment (5, 10 and 15 min). The 20 mL samples are collected using a syringe and injected through a three-way valve and a needle into a 10 mL pre-evacuated sampling vial (Exetainer®, Labco Ltd.). The overpressured vials were sent to the laboratory for CH_4 and CO_2 analysis.

The flux of CO_2 and CH_4 from the soil can be calculated as the rate of concentration increases in the chamber:

Equation 1

$$\Phi = dC/dt \times V/A$$

where Φ is the flux of a gas, V is the volume of air in the chamber (m^3), A is the area covered by the chamber (m^2), C is the chamber concentration of a gas and dC/dt is the rate of concentration change in the chamber air for each gas. Volumetric concentrations are converted to mass concentrations accounting for atmospheric pressure and temperature. Flux values are expressed as g m^{-2} d^{-1} for CO_2 and as mg m^{-2} d^{-1} for CH_4. Positive values indicate fluxes directed from the soil to the atmosphere and negative values indicate flow from the atmosphere into the soil.

Ground temperature measurements were taken at 10 and 50 cm depth using thermal probes and a digital thermometer.

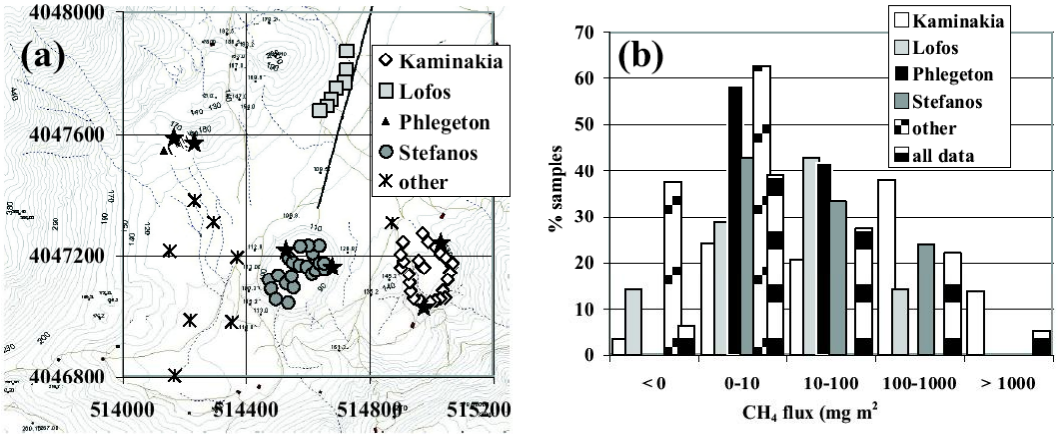

Figure 1 - (a) study area with CH_4 flux measurements points and sampled gas manifestations (stars). (b) Percent frequency distribution of CH_4 flux values.

Samples of soil gas were collected at each site at a depth of 50 cm through a Teflon tube of 5 mm ID using a syringe. During the 2009 campaign CH_4 and CO_2 concentrations were determined in the field with an IR gas analyser (LFG 20 - ADC Co Ltd). During the 2010 campaign soil gas samples were collected and stored for subsequent laboratory analyses in the same way as gases from the flux chamber.

Samples of the many fumarolic manifestations were collected during both campaigns with soda filled bottles (Giggenbach and Goguel, 1989) and analysed in the laboratory for H_2O, H_2S, He, H_2, O_2, N_2, CH_4 and CO_2. Two fumaroles for each of the craters investigated for soil CH4 fluxes were sampled both in 2009 and 2010.

Gas concentrations were measured using the GC Perkin Elmer Clarus 500 equipped with Carboxen 1000 columns, Hot Wire and Flame Ionisation detectors with methanizer. The gas samples were injected through an automated injection valve with a 1000 μL loop. Calibration was made with certified gas mixtures. Analytical precision ($\pm 1\sigma$) was always better than ±5%. The detection limit for CH_4 was about 0.1 μmol mol^{-1}.

Geographical distribution of the CH_4 flux values and the estimation of the total output have been made by using a GIS software (ArcMap™ 9.3, ESRI®).

3. Results

3.1. Geochemistry of the Fumarolic Gases

Results of the chemical composition of the fumarolic gases are shown in Table 1. All samples are dominated by water vapour that accounts for 91 to 99% of their composition. For the remaining gases the composition generally follows the order $CO_2 > H_2S > H_2 \approx N_2 \approx CH_4 \gg He > O_2 \approx CO$. Methane displays a wider range in composition with respect to the other gases which is reflected in the wide range in CO_2/CH_4 ratios (Table 1). The main difference between the three fumarolic areas can be summarised in a lower content in H_2O and H_2S and a higher CO_2 and CH_4 content in the fumaroles of Kaminakia (K6 and K7). This has been explained by previous authors (Marini and Fiebig, 2005) with condensation of water vapour close to the surface. Dissolution in the liquid phase changes the relative concentrations of the remaining gases depending on their solubility. This results in a depletion of the more soluble species (H_2S) and a relative increase of CO_2 and especially of CH_4.

3.2. Soil Flux Measurements

Results of the flux measurements are summarized in Table 2. Values range from –3.4 to 1419 mg m^{-2} d^{-1} for CH_4 and from 0.1 to 383 g m^{-2} d^{-1} for CO_2. To get insight in the methane output of the Lakki plain we focalised our measurements in restricted exhaling areas: Kaminakia, Stefanos and Phlegeton craters and the southeastern flank of the Lofos dome. Some measurements were also made in areas of lower hydrothermal output and indicated in the figures as other. The latter sites display the lowest CH_4 flux values (Fig. 2b) never exceeding 2.6 mg m^{-2} d^{-1} and frequent negative values. Of the investigated exhaling areas those where the most recent activity occurred show the lowest CH_4 flux values (Lofos and Phlegeton ~ 0-100 mg m^{-2} d^{-1}) while to the older craters reach progressively higher values (Stefanos up to 714 mg m^{-2} d^{-1} and Kaminakia up to 1419 mg m^{-2} d^{-1}).

4. Discussion

The CH_4 flux distribution maps have been used to estimate the CH_4 output of the three investigated craters. The three areas according to the very different flux values show also very different CH_4 outputs. Phlegeton shows an output of about 0.01 t a^{-1} from an area of approximately 2500 m^2, that of Stefanos is about 0.1 t a^{-1} from an area of some 20,000 m^2 and that of Kaminakia about 0.3 t a^{-1} from an area of approximately 30,000 m^2. Our flux measurements did not cover the whole exhalative area but likely the remaining areas would not add significant amounts of CH_4 to

the entire output of the geothermal system. In fact, of the remaining area the highest hydrothermal flux areas (Micro Polyvotis, Megalos Polyvotis, Logothetis), with strong fumarole emissions, have characteristics that are very similar to Phlegeton and their contribution will be of the same order of magnitude and thus probably negligible. A more substantial contribution could probably derive form the area northeast and southwest of Kaminakia along the caldera border where soil gases could be enriched in CH_4 in the same way as at Kaminakia. Previous studies on CO_2 soil degassing (Caliro et al., 2005) indicate that in these areas the fluxes tend to decrease rapidly away from the Kaminakia area especially in the southwest direction lowering their possible contribution to the total output.

Table 1 - Chemical composition of some selected fumaroles at Nisyros.

sample	date	H_2O	CO_2	H_2S	He	H_2	O_2	N_2	CO	CH_4	CO_2/CH_4
	dd-mm-yyyy	%				µmol mol^{-1}					
K6	03-09-2009	95.6	874811	96343	18	12572	0	3979	6	12272	71
K6	31-08-2010	91.2	890317	90278	28	7914	7	8006	2	3448	258
K7	03-09-2009	92.2	890682	73796	22	5217	8	7045	5	23226	38
K7	31-08-2010	94.7	890636	78563	51	10974	18	13386	1	6370	140
S15	31-08-2009	98.3	774458	211925	29	6640	8	4213	3	2723	284
S15	31-08-2010	99.0	740627	217953	22	7515	27	30830	1	3026	245
S4	31-08-2009	98.3	794665	190003	28	5372	13	6910	3	3006	264
S4	31-08-2010	99.1	736916	223931	24	6169	41	29539	1	3380	218
A13	04-09-2009	98.0	753938	227194	24	10830	0	7186	2	826	912
A13	30-08-2010	98.6	738197	245342	28	10303	3	5543	1	582	1268
AM	04-09-2009	97.9	755731	225266	25	11190	0	6968	2	818	924
AM	31-08-2010	97.9	739933	204683	25	8751	3	46073	47	485	1525

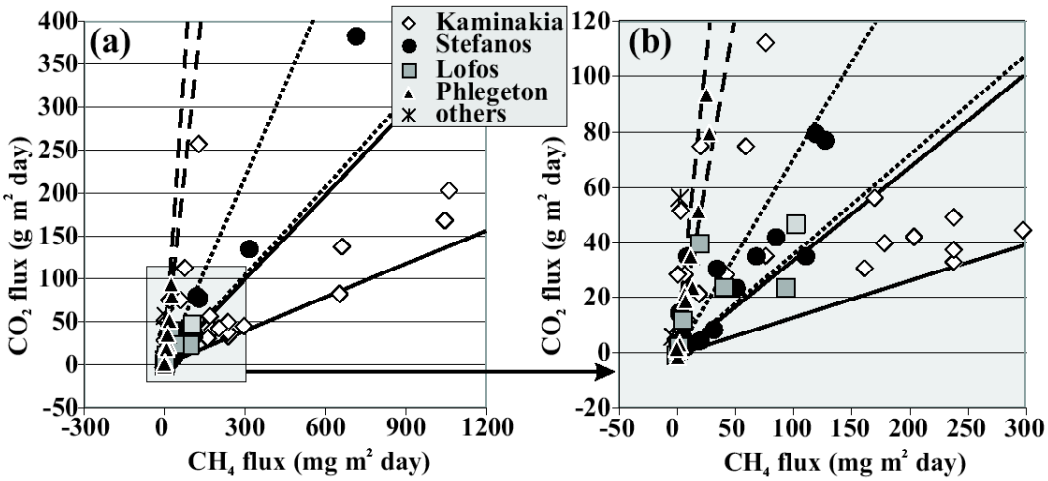

Figure 2 - CH_4 vs. CO_2 fluxes. The right graph is the enlargement of the left one. The black lines represent the range of CO_2/CH_4 concentration ratios in the Kaminakia fumaroles, the stippled line that of the Stefanos fumaroles and the dashed lines that of the Phlegeton fumaroles.

Table 2 - Soil gas and temperature measurements in the Lakki plain area.

Site	area	date	UTM coordinates		concentration		T°C	T°C	flux	
		d-mm-yy	easting	northing	CO_2	CH_4	@20cm	@50cm	CH_4	CO_2
			m	m	µmol mol^{-1}				mg m^2 day	g m^2 day
1	K	3-09-09	515021	4047221	447000	6500	44.2	64.4	238	32.7
2	K	3-09-09	515065	4047167	226000	3300	35.6	53.2	1062	203
3	K	3-09-09	515014	4047051	269000	5100	44.9	77.7	76.5	35.0
4	K	3-09-09	514946	4047060	197000	3400	37.2	54.2	238	37.2
5	K	3-09-09	514966	4047167	51300	800	41.5	45.7	3.4	51.3
6	K	3-09-09	514907	4047243	132000	2900	42.9	74.8	663	138
7	O	3-09-09	514871	4047306	23400	500	39.6	48.4	-3.4	5.5
8	S	3-09-09	514472	4047121	992000	5800	99.3	99.3	127	77.0
9	S	3-09-09	514479	4047093	992000	5400	92.5	100.4	314	135
10	S	3-09-09	514494	4047059	410000	1800	74.5	99.6	51.0	23.3
11	S	3-09-09	514534	4047047	615000	1000	54.0	86.8	110	35.0
12	O	4-09-09	514371	4047194	199000	3300	45.8	35.3	2.6	56.0
13	O	4-09-09	514295	4047308	13600	100	32.8	31.5	-0.9	1.5
14	O	4-09-09	514233	4047380	30500	100	43.2	34.7	-0.9	4.5
15	O	4-09-09	514153	4047215	1600	50	42.2	35.8	0.0	1.2
16	O	4-09-09	514219	4046989	1600	30	44.2	31.0	0.9	1.3
17	O	4-09-09	514169	4046795	2000	50	30.6	30.2	0.9	1.4
18	O	4-09-09	514353	4046983	25300	100	33.8	35.3	2.6	2.8
19	S	4-09-09	514502	4047137	992000	6500	74.2	99.0	1.7	0.5
20	S	4-09-09	514527	4047111	630000	3700	56.4	92.7	68.0	35.0
21	S	4-09-09	514551	4047097	992000	7100	70.7	98.8	6.0	4.7
22	S	4-09-09	514544	4047134	362000	3200	63.4	99.7	85.0	42.0
23	S	5-09-09	514537	4047192	662000	3500	63.2	97.2	34.0	30.3
24	S	5-09-09	514549	4047179	39000	300	32.7	41.5	2.6	14.0
25	S	5-09-09	514571	4047170	47000	300	30.4	36.0	1.7	14.3
26	S	5-09-09	514594	4047165	214000	1800	39.9	50.4	714	383
27	S	5-09-09	514611	4047141	12000	20	42.4	63.4	5.1	4.2
28	S	5-09-09	514624	4047151	63500	1000	52.2	91.0	68.0	35.0
29	S	5-09-09	514636	4047176	285000	1500	48.4	74.6	6.7	1.8
30	S	5-09-09	514654	4047155	784000	4000	99.0	100.9	20.0	4.3
31	S	5-09-09	514650	4047176	610000	3000	69.2	100.8	31.7	8.3
32	S	6-09-09	514613	4047209	152000	300	34.8	43.9	0.3	2.2
33	S	6-09-09	514635	4047233	212000	800	69.0	95.0	119	79.3
34	S	6-09-09	514599	4047233	85500	200	46.7	64.8	8.5	35.0
35	S	6-09-09	514573	4047231	24300	30	37.8	48.2	5.1	10.7
36	K	24-08-10	514971	4047271	52600	22	40.3	47.3	2.6	14.0
37	K	24-08-10	514988	4047244	56500	18	40.3	46.7	0.9	7.0
38	K	24-08-10	515012	4047226	32600	16	40.6	48.4	5.1	7.8

39	K	24-08-10	515029	4047205	167400	50	42.1	49.4	6.8	28.0
40	K	25-08-10	515046	4047191	271000	3841	41.4	51.5	1045	168
41	K	25-08-10	515068	4047174	536200	9215	57.4	69.6	297	44.3
42	K	25-08-10	515059	4047143	157000	1015	43.3	55.0	76.5	112
43	K	25-08-10	515052	4047120	155300	651	37.5	44.3	20.4	74.7
44	K	25-08-10	515037	4047084	253600	1368	53.5	62.7	59.5	74.7
45	K	25-08-10	515043	4047061	248800	5271	58.3	74.0	1419	154
46	K	25-08-10	515027	4047058	60600	847	60.2	66.0	654	81.7
47	K	27-08-10	515010	4047051	143500	1624	56.3	69.5	1419	261
48	K	27-08-10	514995	4047047	488900	7117	65.9	82.4	127	257
49	K	27-08-10	514965	4047050	22200	58	46.6	58.7	8.5	11.7
50	K	27-08-10	514942	4047060	257100	2750	44.4	57.6	170	56.0
51	K	27-08-10	514932	4047082	300400	3735	64.9	77.7	178	39.7
52	K	27-08-10	514929	4047111	660500	9890	63.5	87.0	238	49.0
53	K	27-08-10	514925	4047138	840000	13900	65.0	95.0	161	30.3
54	Ph	2-09-10	514219	4047572	749100	531	77.3	99.9	1.7	0.8
55	Ph	2-09-10	514206	4047584	739900	535	80.7	99.9	1.7	1.3
56	Ph	2-09-10	514199	4047572	17500	12	99.9	n.m.	13.6	23.3
57	Ph	2-09-10	514177	4047590	743500	515	63.2	87.5	6.8	21.0
58	Ph	2-09-10	514188	4047586	221600	156	51.0	70.3	7.7	18.7
59	Ph	2-09-10	514183	4047571	533	3	71.3	89.0	18.7	51.3
60	Ph	2-09-10	514175	4047566	496700	387	61.2	89.4	28.1	79.3
61	Ph	2-09-10	514165	4047573	661300	478	75.4	99.5	25.5	93.3
62	Ph	2-09-10	514155	4047570	n.m.	n.m.	62.2	n.m.	11.9	35.0
63	Ph	2-09-10	514157	4047552	21400	23	52.8	75.0	2.6	3.0
64	Ph	2-09-10	514148	4047551	1700	4	44.8	54.0	0.9	0.1
65	Ph	2-09-10	514134	4047552	3600	5	38.1	43.1	0.0	1.4
66	L	3-09-10	514724	4047872	121000	49	41.5	52.8	5.1	11.7
67	L	3-09-10	514723	4047809	535	3	33.9	41.6	-0.9	0.1
68	L	3-09-10	514717	4047770	33500	12	37.5	49.0	1.7	2.0
69	L	3-09-10	514690	4047753	74400	229	47.3	65.0	19.5	39.7
70	L	3-09-10	514674	4047717	82900	584	49.2	82.2	93.5	23.3
71	L	4-09-10	514661	4047692	414900	2892	48.6	76.4	40.4	23.5
72	L	4-09-10	514637	4047679	734600	5033	97.5	99.9	102	46.7
73	K	4-09-10	514901	4047159	112500	784	46.2	80.0	42.5	28.0
74	K	4-09-10	514908	4047180	142600	1376	47.0	77.0	19.1	21.0
75	K	4-09-10	514900	4047202	873800	14700	66.0	98.4	204	42.0
76	K	4-09-10	514958	4047183	1300	3	36.0	43.5	-0.9	4.7
77	K	4-09-10	514976	4047159	63800	4	36.0	43.8	0.9	28.0

Area: K=Kaminakia, S=Stefanos, Ph=Phlegeton, L=Lofos, O=other; UTM coordinates: reference system WGS84; n.m.=not measured.

Consequently our best estimation of the total CH_4 output of the geothermal system of Nisyros is about 1 t a^{-1}, which is more than one order of magnitude lower than the previous estimation (54 t a^1 - Etiope et al., 2007). The latter was made simply multiplying an estimated average CH_4/CO_2 ratio of the fumarolic emissions by the total CO_2 output obtained by Chiodini et al. (2005). As previously evidenced (D'Alessandro et al., 2009; 2011), part of the difference could be attributed to the disregarding of methanotrophic activity within the soils. Microbial activity has the potential to oxidize great quantities of CH_4 also within the soils of geothermal areas (Castaldi and Tedesco, 2005; Pol et al., 2007). Clues for methanotrophic activity in the soils of the study area can be evidenced in Figure 2 where, especially in the area of Kaminakia and Stefanos some of the sites show much higher CO_2/CH_4 ratios with respect to the relative fumarole gases.

Another source of error in the estimation of Etiope et al. (2007) derives from the great variability both in time and space of the CO_2/CH_4 ratios of the fumarole emissions at Nisyros (Table 1) as also evidenced by Marini and Fiebig (2005). Such great variability could introduce a great error in the CO_2/CH_4 ratio used to obtain the total CH_4 output. The CO_2/CH_4 ratio used by Etiope et al. (2007) is indeed low (167 by volume), close to the mean value of the Kaminakia crater, which is by no means representative of the whole area. Other strongly degassing areas show all considerably higher mean values accounting for a significant part of the difference in output estimation.

5. Conclusions

Flux measurements at Nisyros confirm that this geothermal system is diffusively degassing significant amounts of CH_4 (~1 t a^{-1}) through the soils. This study further confirms that volcanic/geothermal areas are significant sources of CH_4 to the atmosphere but also that probably their contribution has been overestimated. The present study indicates that the previous estimate (54 t a^{-1}) at Nisyros, made by cross-correlating CO_2 output data with the CO_2/CH_4 ratios of its gaseous manifestations, has been excessively large. This great difference derives from both disregarding methanotrophic activity within the soils and from an incorrect mean CO_2/CH_4 ratio of the fumarolic emissions used in the calculation of the total output.

6. Acknowledgments

We acknowledge the help of Jens Fiebig and Mika Gousgouni in the field and of Mauro Martelli and Francesco Salerno in the laboratory.

7. References

Baciu C., Etiope G., Cuna S. and Spulber L. 2008. Methane seepage in an urban development area (Bacau, Romania): origin, extent, and hazard, *Geofluids*, 8, 311–320.

Brombach T., Caliro S., Chiodini G., Fiebig J., Hunziker J.C. and Raco B. 2003. Geochemical evidence for mixing of magmatic fluids with seawater, Nisyros hydrothermal system, Greece, *Bull. Volcanol.*, 65, 505–516.

Caliro S., Chiodini G., Galluzzo D., Granieri D., La Rocca M., Saccorotti G. and Ventura G. 2005. Recent activity of Nisyros volcano (Greece) inferred from structural, geochemical and seismological data, *Bull. Volcanol*., 67, 358–369.

Cardellini C., Chiodini G., Frondini F., Granieri D., Lewicki J., Peruzzi L. 2003. Accumulation chamber measurements of methane fluxes: application to volcanic–geothermal areas and landfills, *Appl. Geochem.*, 18, 45–54.

Castaldi S., Tedesco D. 2005. Methane production and consumption in an active volcanic environment of Southern Italy, *Chemosphere*, 58, 131-139.

Chiodini G., Granieri D., Avino R., Caliro S. and Costa A. 2005. Carbon dioxide diffuse degassing and estimation of heat release from volcanic and hydrothermal systems, *J. Geophys. Res.*, 110, B08204.

D'Alessandro W., Bellomo S., Brusca L., Fiebig J., Longo M., Martelli M., Pecoraino G. and Salerno F. 2009. Hydrothermal methane fluxes from the soil at Pantelleria island (Italy), *J. Volcanol. Geotherm. Res.*, 187, 147-157.

D'Alessandro W., Brusca L., Kyriakopoulos K., Martelli M., Michas G., Papadakis G. and Salerno F. 2011. Diffuse hydrothermal methane output and evidence of methanotrophic activity within the soils at Sousaki (Greece), *Geofluids*, 11, 97–107.

Etiope G., Fridriksson T., Italiano F., Winiwarter W. and Theloke J. 2007. Natural emissions of methane from geothermal and volcanic sources in Europe, *J. Volcanol. Geotherm. Res.*, 165, 76 – 86.

Etiope G., Lassey K.R., Klusman,R.W. and Boschi E. 2008. Reappraisal of the fossil methane budget and related emission from geologic sources, *Geophys. Res. Lett.*, 35, L09307.

Fiebig J., Woodland A.B., D'Alessandro W. and Püttmann W. 2009. Excess methane in hydrothermal emissions is abiogenic, *Geology*, 37/6, 495–498.

Giggenbach W.F. and Goguel R.L. 1989. Collection and Analysis of Geothermal and Volcanic Water and Gas Discharges. *Report of the Dep. of Sci. and Ind. Res., Chem. Div.*, Petone, New Zealand, 81 pp.

Hanson R.S., Hanson T.E. 1996. Methanotrophic bacteria, *Microbiol. Rev.*, 60, 439– 471.

Intergovernmental Panel on Climate Change 2001. Climate change 2001, In: Houghton, J.T., Ding Y., Griggs D.J., Noguer M., van der Linden P.J., Dai X., Maskell K. and Johnson C.A., (Eds.), *The Scientific Basis*. Cambridge University press, UK.

Keller J. 1982. Mediterranean island arcs, In: Thorpe, R.S. (ed.) *Andesites*. Wiley, New York, pp 307–325.

Koschorreck M. and Conrad R. 1993. Oxidation of atmospheric methane in soil: Measurements in the field, in soil cores, and in soil samples, *Glob. Biogeochem. Cycles*, 7, 109– 121.

Livingston G.P. and Hutchinson G.L. 1995. Enclosure-based measurement of trace gas exchange: applications and sources of error, in: *Biogenic Trace Gases: Measuring Emissions from Soil and Water*. Methods in Ecology (Matson, P.A. and Harriss, R.C. eds.), pp. 14–51. Blackwell Science Cambridge University Press, London.

Marini L. and Fiebig J. 2005. Fluid geochemistry of the magmatic-hydrothermal system of Nisyros (Greece), *Mém. Géol*., 44, 192.

Marini L., Principe C., Chiodini G., Cioni R., Frytikas M. and Marinelli G. 1993. Hydrothermal eruptions of Nisyros (Dodecanese, Greece). Past events and present hazard, *J. Volcanol,Geotherm*. Res., 56, 71–95.

Papadopoulos, G.A., Sachpazi M., Panopoulou G. and Stavrakakis G. 1998. The volcanoseismic crisis of the 1996–97 in Nisyros, SE Aegean Sea, Greece, *Terra Nova*, 10, 151–154.

Pol A., Heijmans K., Harhangi H.R., Tedesco D., Jetten M.S.M. and Op den Camp H.J.M. 2007. Methanotrophy below pH 1 by a new Verrucomicrobia species, *Nature*, 450, 874-878.

Vougioukalakis G.E. and Fytikas M. 2005. Volcanic hazards in the Aegean area, relative risk evaluation, monitoring and present state of the active volcanic centers. In: Fytikas M., Vougioukalakis G.E. (Eds.), *The South Aegean Active Volcanic Arc*. Developments in Volcanology, vol. 7, 161–183.

Δελτίο της Ελληνικής Γεωλογικής Εταιρίας, τομ. XLVII , 2013
Πρακτικά 13ου Διεθνούς Συνεδρίου, Χανιά, Σεπτ. 2013

Bulletin of the Geological Society of Greece, vol. XLVII 2013
Proceedings of the 13th International Congress, Chania, Sept. 2013

VARIOUS MORPHOLOGICAL TYPES OF THERMOGENIC TRAVERTINES IN NORTHERN EUBOEA AND EASTERN CENTRAL GREECE

Kanellopoulos C.[1]

[1]*Doctor in Geological Sciences, 15 Pindou str., Vrilissia, Athens, 15235, Greece, ckanellopoulos@gmail.com*

Abstract

In the northern part of Euboea Island and the neighbouring part of the mainland in eastern central Greece, many hot springs exist and some of them create travertine deposits. The objectives of the study were to identify and describe the various morphological types of the thermogenic travertine deposits. The samples were studied at the lab with optical microscopy, X-Ray Diffraction, Scanning Electron Microscopy (SEM) and Energy Dispersive Spectroscopy (EDS), in order to verify their main mineralogical composition and their mineral chemistry. The studied travertine deposits consist mainly of aragonite and calcite, but in some cases, as main mineral phase, an amorphous hydrous ferric oxyhydroxide (ferrihydrite), was also identified. The morphological types that were identified were of great variety (mounds, travertine caves etc) and some of them were quite rare (cascades, remora etc). Morphological data and field observations suggest possible inorganic and organic controls on carbonate precipitation. Similar morphological types have been recorded at large travertine systems like Mammoth hot springs, Yellowstone National Park in USA and at Rapolano Terme, Italy.

Key words: *hot spring deposits, travertine, Edipsos, Ilia, Thermopylae.*

Περίληψη

Στο Βόρειο τμήμα της Εύβοιας και στην Ανατολική Στερεά Ελλάδα, υπάρχουν πολλές θερμές πηγές και σε κάποιες από αυτές αποτίθεται τραβερτίνης. Σκοπός της παρούσας μελέτης είναι να αναγνωριστούν και να περιγραφούν οι μορφολογικοί τύποι των θερμογενών τραβερτινικών αποθέσεων. Για να διαπιστωθεί η σύσταση των κύριων ορυκτών φάσεων και η χημική τους σύσταση, δείγματα μελετήθηκαν με οπτικό μικροσκόπιο, περιθλασιμετρία ακτίνων Χ (XRD), ηλεκτρονικό μικροσκόπιο και διεξήχθησαν μικροαναλύσεις (EDS). Όλες οι αποθέσεις διαπιστώθηκε ότι είναι θερμογενής τραβερτίνης και αποτελούνται κυρίως από αραγωνίτη και ασβεστίτη, σε μερικές περιπτώσεις σαν κύρια ορυκτή φάση διαπιστώθηκε και ένα άμορφο ένυδρο υδροξείδιο του σιδήρου (φειϋδρίτης). Οι μορφολογικοί τύποι που αναγνωρίστηκαν και περιγράφηκαν, παρουσιάζουν μεγάλη ποικιλία και μερικοί από αυτούς είναι σπάνιοι. Μορφολογικές παρατηρήσεις μαζί με παρατηρήσεις υπαίθρου υποδηλώνουν και πιθανή συμμετοχή οργανικών παραγόντων κατά τον σχηματισμό των υπό μελέτη τραβερτινών. Παρόμοιοι μορφολογικοί τύποι, σε τόσο μεγάλη ποικιλία απαντώνται σε μεγάλα ενεργά υδροθερμικά-τραβερτινικά συστήματα όπως π.χ. Yellowstone, Rapolano Terme.

Λέξεις κλειδιά: *Αποθέσεις θερμών πηγών, τραβερτίνης, Αιδηψός, Ήλια, Θερμοπύλες.*

1. Introduction

The word travertine is thought to originate from the lapis tiburtinus, a Roman building stone mentioned by several Latin authors (e.g. Plinius, Statius, Vitruvius). The stone was quarried near the town of Tibur (Tivoli). Various researchers (Whitten and Brooks, 1972; Mitchell, 1985; Bates and Jackson, 1987; Riding, 1991; Koban and Schweigert, 1993; Glover and Roberston, 2003) have proposed many definitions for the term travertine. Perhaps the most comprehensive and clear definition was proposed by Pentecost (2005), who defined travertine as a chemically-precipitated continental limestone formed around seepages, springs and along streams and rivers, occasionally in lakes and consisting of calcite or aragonite, of low to moderate intercrystalline porosity and often high mouldic or framework porosity within a vadose or occasionally shallow phreatic environment. Precipitation results primarily through the transfer (evasion or invasion) of carbon dioxide from or to a groundwater source leading to calcium carbonate supersaturation, with nucleation/crystal growth occurring upon a submerged surface and can take many forms.

Three main criteria have been used for travertine classification: i) geochemical, ii) fabric and iii) morphology. Classification schemes based on these criteria are not mutually exclusive, but it is convenient to consider them separately (Penecost and Viles, 1994). Based on geochemistry two classes of travertines are recognized: a) the meteogene and b) the thermogenic travertines. The second group consists of travertines of hot springs and the carrier CO_2 results primarily from the interaction between hot rock and CO_2-rich fluids. The term fabric refers to the architecture of the deposit (i.e. the arrangement, density and size of the building units). Density is related to deposit porosity and the nature of the porosity provides valuable clues to the mode of deposition. Bacteria and plants in particular can influence the travertine fabric. Also important is the rate of deposition, the mineralogy, and the extent of diagenesis (Viles and Goudie, 1990).

For the characterization of travertines based on morphological criteria, many classifications have been suggested (Ordonez et al., 1986; Chafetz and Folk, 1984; Scheuer and Schweitzer, 1989). The most recent and probably the most comprehensive classification is proposed by Penecost and Viles (1994). Based on that morphological classification, travertines can be grouped into nine main categories, divided into two sub-groups. The first sub-group contains all of the autochthonous deposits associated with springs, streams, rivers, lakes and marshes and concludes with the allochthonous (clastic) travertines.

In Northern Euboea and Eastern Central Greece many hot springs exists and in some of them thermogenic travertines are depositing (Edipsos, Ilia, Thermopylae; Figure 1). Thermogenic travertine deposits near to the hot springs, where the hot water cools, degasses and rapidly precipitates calcium carbonate, creating different depositional facies-lithotypes having different crystal forms (Kanellopoulos, 2011; 2012) and many different morphological types.

The aim of this paper is to identify and describe the various morphological types of thermogenic travertine deposits in Northern Euboea and Eastern Central Greece. A further aim of this paper is to study their main mineralogical phases and to identify indications of possible organic controls on carbonate precipitation, in addition to the inorganic ones.

2. Geological Setting

North-western part of Euboea Island and Eastern Central Greece belongs geologically to the western part of the geotectonic units of the internal units of Greece, more specifically the Pelagonian and Sub-Pelagonian units (Aubouin, 1959; Mountrakis, 1986). The study area consists of various rock formations non-metamorphic rocks, ophiolitic rocks and metamorphic rocks. Large parts of NW Euboea and eastern central Greece are covered by Post Alpine Formations, Quaternary and Neogene age sediments (Figure 1). In the center of northern Euboea gulf the volcanogenic islands of Lichades are located (Georgalas, 1938). They are made mainly of trachyandesite lava flows, dated at 0.5 Ma (Pe-Piper and Piper, 2002). The whole area is highly faulted due to extensional tectonics (McKenzie, 1970; 1972; Le Pichon and Angelier, 1979; Vavassis, 2001). Also, in the studied area many hot springs exist (Gioni-Stavropoulou, 1983), as a

part of an active hydrothermal system, which present high concentrations to a large group of major and trace elements (Kanellopoulos, 2006; 2011).

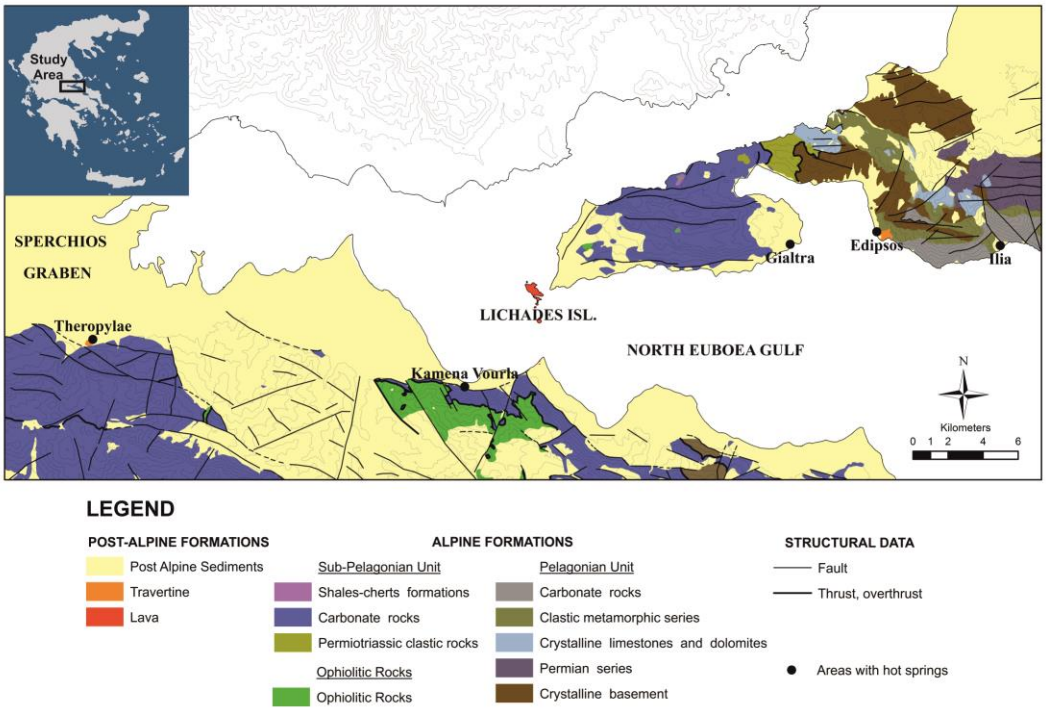

Figure 1 - Geological map of the study area (from Kanellopoulos, 2012).

3. Materials and Methods

All samples were studied at the laboratories of the Department of Geology and Geoenvironment, University of Athens. The mineralogical composition was investigated mainly by optical microscopy and X-Ray Diffraction. XRD analyses were carried out using a Siemens Model 5005 X-ray Diffractometer, Cu Ka radiation at 40 kV, 40 nA, 0.020° step size and 1.0 s step time. The XRD patterns were evaluated using the EVA v.10.0 program of the Siemens DIFFRACplus and the D5005 software package. Scanning Electron Microscopy (SEM) and Energy Dispersive Spectroscopy (EDS) analyses were carried out using a Jeol JSM 5600 SEM instrument, equipped with an Oxford ISIS 300 OXFORD, with the following operating conditions: accelerating voltage 20 kV, beam current 0.5 nA, time of measurement 50 sec and beam diameter 1–2 μm. The spectra were processed using the ZAF program (3interaction). The microprobe analyses were conducted on polished sections of the samples after carbon coating.

4. Location and Lithotype Description of Studied Travertine Deposits

In the studied area, newly and older formed thermogenic travertine deposits occur in three different areas: Edipsos, Ilia and Thermopylae (Figure 1). In these areas the travertine deposits are thermogenic, created by the local hot springs. By the term older travertines, we mean all the travertines that have been created in the past; and the precipitation process has ended. In Edipsos, large deposits of thermogenic travertine occur, presenting great variety of morphological types and lithotypes. The most common active lithotypes in Loutra of Edipsos are crystalline crusts, rafts, foam type, lamination and spicular types (Kanellopoulos, 2012). Their color varies from white-yellow to red, with orange prevailing. The hot springs in Edipsos exist from historical times and for that reason many ancient structures, such as Roman baths can be found. The deposition rate is

high and in this area hot springs are self-settled in a short time with the depositing material and new springs arising nearby. The high rate of deposition creates problems for the exploitation of hot springs for spa therapy, as in a short period of time it results in the clogging of pipes used for the transfer of the hot water. Ilia area is located 7 km east of Edipsos. The travertine deposit in Ilia covers a small area (~2 m^2) and is created at the point where the pipe from the borehole vents out the hot water. At that position a reddish brown cascade has been created which consists of newly formed Fe-rich laminated travertine (Kanellopoulos, 2011). This travertine has Fe-rich parts, which sometimes appear as metallic zone layers creating botryoid structures. In Thermopylae, extensive deposits of thermogenic travertine occur. Their color varies from white to grey. During the field survey, we discovered newly formed travertine deposits and old ones, since the hot springs in the area exist from historical times. Works for the construction of a new National highway road as well as other supporting works were carried out in this area and many of these works have destroyed travertine deposits by digging and mixed them (Figure 2A).

5. Results

5.1. Mineralogical Study and Chemical Composition of Main Mineral Phases

The main mineral phases identified by XRD and SEM micro-probe analysis are aragonite and calcite, which in many cases coexist. In the Edipsos samples the predominant phase is aragonite. Its crystals tend to create hexagonal prisms, which at many times appear as radial spheres, while calcite usually creates rhombohedral crystals. In Ilia iron-rich travertine deposit, in addition to calcium carbonate mineral phases, an amorphous hydrous ferric oxyhydroxide phase was found (Table 1, anal. 9-10), identified as amorphous ferrihydrite (Kanellopoulos, 2011; 2012). In Thermopylae samples, only calcite was identified as the main mineral phase.

The chemical composition of calcium carbonate minerals varies (Table 1). The calcium carbonate mineral phases from Edipsos (Table 1, anal. 1-3) in addition to Ca, C, and O, contain S and/or Si and/or Na and/or Cl and/or Fe, the travertines from Ilia (Table 1, anal. 4-6) in addition to Ca, C, and O, contain Fe and/or As and/or Si and/or S and/or Sr and/or Na and/or Cl and the travertines from Thermopylae (Table 1, anal. 7-8) in addition to Ca, C, and O, contain Mg and/or S.

Table 1 - Microanalysis of Aragonite - Calcite and Ferrihydrite (in compound %).

	Aragonite and Calcite							
	1	**2**	**3**	**4**	**5**	**6**	**7**	**8**
SiO_2	-	-	0.34	3.66	1.75	0.58	-	-
FeO	-	-	0.35	12.99	7.98	0.60	-	-
CaO	47.57	49.45	48.17	38.35	44.35	47.71	47.80	47.53
Na_2O	-	-	0.73	-	-	0.55	-	-
As_2O_3	-	-	-	0.53	0.54	-	-	-
MgO	-	-	-	-	-	-	1.43	1.75
SO_3	-	0.40	3.70	0.82	-	-	-	0.87
SrO	-	-	-	-	-	1.05	-	-
Cl	-	0.18	-	-	0.10	-	-	-
Total	47.57	50.03	53.29	56.36	54.73	50.50	49.23	50.15
Atoms	**2**	**2**	**2**	**2**	**2**	**2**	**2**	**2**
Si	-	-	0.0064	0.0649	0.0321	0.0114	-	-
Fe	-	-	0.013	0.4611	0.2915	0.0239	-	-
Ca	2	1.9768	1.8081	1.3611	1.6210	1.8896	1.9201	1.8955
Na	-	-	0.0546	-	-	0.0438	-	-
As	-	-	-	0.0125	0.0132	-	-	-
Mg	-	-	-	-	-	-	0.0799	0.0698
S	-	0.0053	0.0462	0.0097	-	-	-	0.0116
Sr	-	-	-	-	-	0.0417	-	-
Cl	-	0.0072	-	-	0.0037	-	-	-

	Ferrihydrite	
	9	**10**
Si	6.37	4.67
Fe	38.34	39.49
Ca	3.12	1.6
As	2.92	5.19
Total	50.75	50.95
Atoms	**2**	**2**
Si	0.1915	0.1429
Fe	1.3861	1.4539
Ca	0.1227	0.0641
As	0.0722	0.1307

5.2. Morphological Types

In the studied areas, eleven morphological types of travertine were identified. All of them were thermogenic, mostly autochthonous created by the local hot springs. Some types are quite common, while some others are rare, (e.g. cascades, remoras). The main morphological types of the studied travertines are:

I) Spring mounds are domes of travertine, in surrounding of a spring orifice. Most mounds require hydrostatic head and the orifice shape determine their solid geometry. In the studied area two mound types were identified: **mounds with wide orifices and smooth walls containing pools of water** (Figure 2B) and some **low mounds**, usually their height is less than 15 cm. The low mounds are of low relief with a dip of just a few degrees. In these cases, the mound outlines become irregular, presumably in response to minor differences in ground level surrounding the springs (Figure 2K). In Edipsos, the orifices of mounds frequently self-seal due to the rapid deposition and maybe the short operating time is one of the major reasons for not having high mounds types. The formation of mounds is not understood in detail but it is clear that most of them require water under pressure, like Edipsos (Figure 2C). The hydrostatic pressure needed to form the largest mounds is considerable, approaching 7 kg/cm at ground level (Pentecost, 2005). These pressures exist in artesian systems and most mounds probably develop in this way, but geyser-like activity may be responsible on mound height must be limited by the hydrostatic head and the rate of flow presumably falls as the mound builds. Kerr and Turner (1996) have shown that the overflow of water at a mound orifice is controlled by surface-tension effects. The orifice necks of old mounds in Edipsos are often smooth and symmetrical. The high degree of supersaturation lead to rapid deposition around the vent giving a steep mound, while waters closer to saturation are likely to deposit at increasing distances, providing a more modest profile under conditions of equal discharge.

II) At active travertine sites two types of **cascade** can be distinguished: the erosively-shaped deposits, approximately parabolic in section and frequently with fluted channels, with morphology which is largely controlled by stream direction, and the accretionary deposits, irregular and regular deposition in which the deposition rate is bigger than the erosion rate over long periods (Pentecost, 2005). Accretionary types are typical of high-discharge streams with vertical falls formed along resistant rock layers (Dennen et al., 1990). Thermogene travertines forming on hillsides and cliffs often develop this type. In these cases, lateral extension is restricted only by the mechanical strength of the travertine. In Edipsos **accretionary**, mainly **keeled cascade** and **remora types** were identified. Throughout the city of Edipsos, near the hot springs, narrow channels have been constructed. Their purpose is to collect the hot water from the residential area and drive it away. Usually the end of these channels is a slot at the top of a cliff. Water overtops the slot and seeps down slope, depositing travertine in the process, building up the sides of the keel, slowly raising the height (Figure 2D). Deposition ceases soon after the water flows down the wall, otherwise, the walls extend outwards and lose their almost vertical form. In Edipsos, many active and non-active cascades were identified. Usually, active cascades have rich flora (boggy hollows, cyanobacteria, Figure 2E). Cascades which were formed near the sea level have cave forms at their bases. Probably the erosion at the base of these cascades is significantly higher due to sea waves, which are reaching the cascade base. These morphological types were also identified in Ilia and Thermopylae. In Ilia at the point where the pipe from the borehole vents out the hot water, a small cascade has been created. In Thermopylae, cascade type was identified at the point where the channel of hot water ends, creating a hot water waterfall (Figure 2F). **Remora types** develop in slow or intermittent water flow over steep slopes (older cascades or cement walls) and consist of stalactite-like masses often of gravity-defying forms (Figure 2G).

III) Dams (barrage) distinguished from cascades by their localized vertical accretion leading to water impoundment as pools (terraces, Figures 2H, I). Dams usually occur in series along watercourses. In Edipsos their height ranges from millimeters to few centimeters and the distance between them ranges from few centimeters to few meters, probably depending on the gradient of

the stream bed and the discharge. Each dam is separated by a pool and their depth usually is up to few cm (<5 cm). The dams themselves are composed of travertine formed in situ. In Thermopylae dams' height ranges from millimeters to 1 centimeter.

IV) Fluvial crusts include a range of superficial deposits formed in the running water of small and large streams (Figure 2J). They develop on a variety of structures which are either smooth, or nodular and coralloid. Detached crusts, called oncoids develop around stones and plant nuclei. In Edipsos and Ilia many laminated oncoids develop around bedrock stones, old compact travertine fragments and plant nuclei (Figure 2J). Also, in Edipsos travertine crusts usually grade into low-relief mounds around spring orifices, forming sheets over the bedrock. In Thermopylae usually laminated smooth surfaces were developed around bedrock.

V) Lake deposits (Terraces) are pools with small depth and low flow velocity. They are part of the fluvial system, the slow passage of water through lakes means that CO_2 evasion is reduced, while photosynthesis and evaporation become increasingly important as progenitors of carbonate precipitation. They are very common in Edipsos (Figure 2K). Over the rim and on the steep outside wall of the terrace (dam), water flows in a thin sheet and flow velocity increases. Morphological classification schemes for travertine terrace have been proposed by several authors (Bargar, 1978; Bates and Jackson, 1987; Pentecost and Viles, 1994; Fouke et al., 2000;). Using the classification suggested by Bargar (1978) and Fouke et al. (2000) in Edipsos "terracettes" i.e. areas of a few square meters and "microterracettes" of a few square centimeters or less, were identified. Hammer et al. (2010) suggested the term "terrace" as a general term regardless of size. In Edipsos the height of terracettes (dam) and microterracettes is up to few centimeters, regardless of slope, thus producing pools of much larger area in regions of small slope. It is commonly observed at terrace systems which are partly dry. This is not always due to primarily reduction in overall flux. As a result of travertine build-up, water continuously finds new routes. Old pathways may be abandoned and dry up, but become active again at a later date (Chafetz and Folk , 1984; Hammer et al., 2010). Inside Edipsos pools of many different lithotypes are being created, like rafts, foam, shrubs etc (Kanellopoulos, 2012).

VI) Reefs are small morphological types (millimeters to few centimeters in size) found attached to sediments or rock walls at terraces and stream margins (Figure 2L). In Edipsos, reefs at stream margins usually create spicular lithotypes. Their origin is unclear, probably they are some form of agglutination process, possibly related with microbial mediated occur (Thompson and Ferris, 1990). These deposits although resembling travertine, may not be primarily the result of degassing and need further investigation (Pentecost, 2005).

VII) Paludal deposits are low-relief accumulations often including much carbonate mud. They are found in marsh environments with slow-flowing water and much vegetation. Edipsos` paludal deposits are probably associated with sulfur- and cyano-bacteria based on field observations. At these sites grass and moss cushions can be found (Figure 2M).

VIII) Cemented clasts consist of cemented scree, alluvium, breccia, and gravel formed as a result of ground and surface water degassing to the epigean atmosphere, but it is not always possible to distinguish between near-surface and hypogeal cementation, the latter resulting from precipitation from calcite supersaturated ground waters. In Edipsos grains are from fine sand and silt (10-120 μm) (Figure 2N) to large clasts (few centimeters). They are cemented by $CaCO_3$ and they are usually highly resistant to erosion and very hard. In Ilia, travertine deposits on a beach. It is usual inside the travertine to be found cemented grain (up to few centimeters) from the beach.

IX) Allochthonous (Clastic) travertines are forming in turbulent environments. Travertines soon after formation they often undergo erosion, so many deposits contain a significant proportion of clastic material (Garcia del Cura et al., 2000). Travertine-marls forming in paludal environments are especially prone to re-deposition and a range of predominantly clastic deposits have been distinguished in the studied area, especially in natural streams at the outskirts of Loutra of Edipsos city and in Thermopylae.

X) In Edipsos, travertine caves are frequently exist beneath cascades near seashore. These develop either as the travertine builds a protuberance over a steep cliff which eventually meets the ground

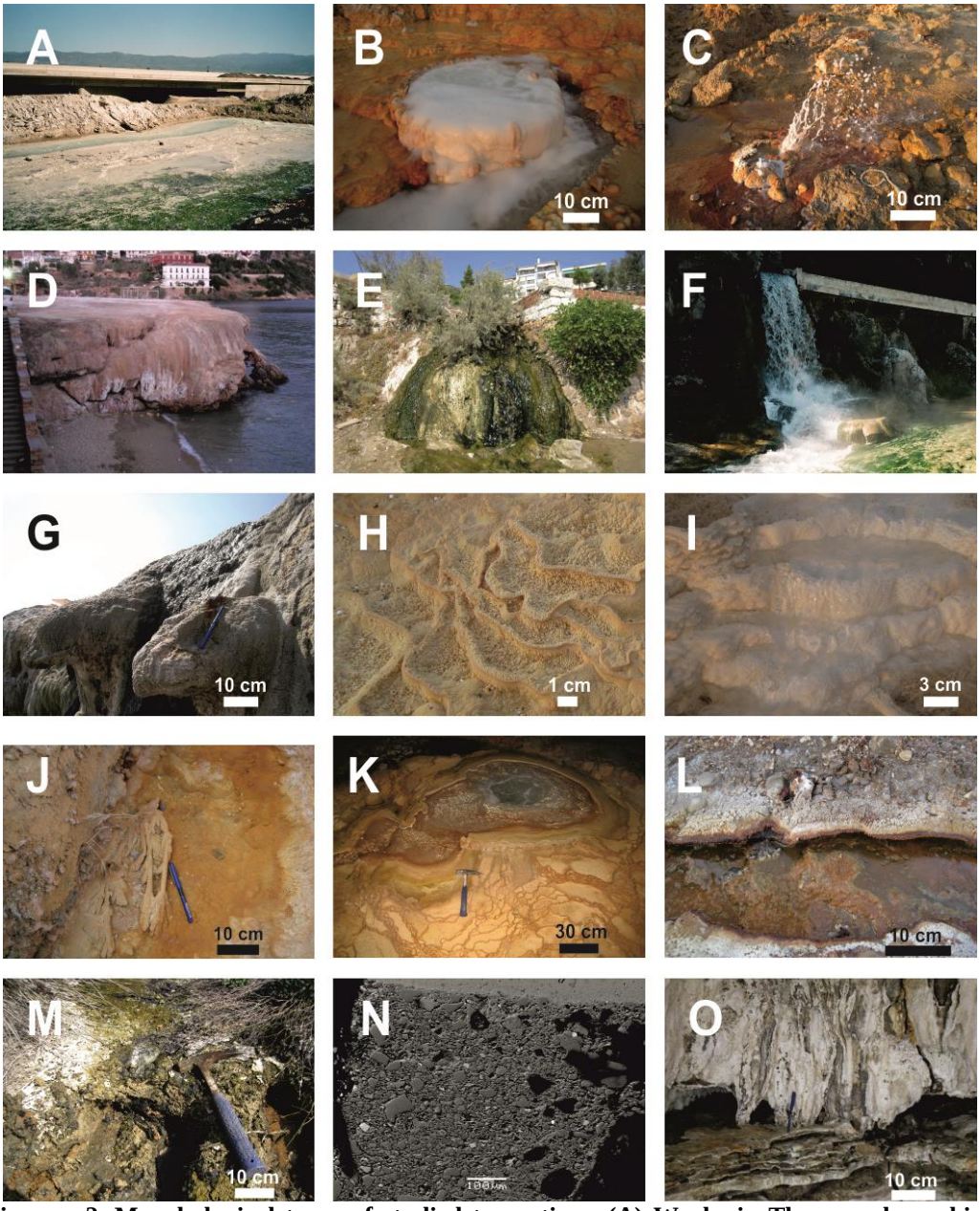

Figure - 2. Morphological types of studied travertines. (A) Works in Thermopylae, which have destroyed the travertine morphological types. (B) Steep-smooth spring mound in Edipsos. (C) Hot spring with high hydrostatic pressure, proving that Edipsos hot springs are artesian systems. (D) Active cascades with rich flora (boggy hollows, cyanobacteria) in Edipsos seashore. (E) Hot water waterfall in Thermopylae creating cascade (existence of cyanobacteria). (F) Large non-active now cascade formation in Edipsos, at the base of the cascade travertine caves can be distinguished. (G) Remora type, in Edipsos, developed on a large cascade, at the seashore, only few meters (2 m) above sea level. (H) Dams (barrage) part of a dry terrace system in Edipsos. (I) Dams (barrage) part of an active terrace system in Edipsos. (J) Fluvial crusts in a dry stream (Edipsos). The crusts covered the old travertines (bedrock) and in the left side can be distinguish fluvial crust developed using plants as nuclei. (K) Spring mound with pools (terraces system) creating low mounds in Edipsos. (L)

Reefs with spicular lithotypes attached to stream margins, in Edipsos. (M) Paludal deposits in marsh environment (associated with sulfur- and cyano-bacteria, in Edipsos). (N) Cemented clasts in Edipsos (Fe oxides, Ti oxides, quartz and apatite). (O) Speleothems from an Edipsos travertine cave on the base of a cascade.

leaving a cavity behind it or as a result of the significantly higher erosion at the base of these cascades due to sea waves, which are reaching the cascade base (Figure 2D). Usually they are located near the sea level at the base of cascades and they have small dimensions e.g. height usually less than 1 m.

XI) Speleothems are morphological types formed in caves. Hill and Forti (1997) provide a good overview of these forms and recognize five hydrological mechanisms responsible for most of the variation: dripping, flowing, seeping, pooled and splashing water. Other processes such as evaporation, airflow, and joint geometry account for much of the remaining variation. In Edipsos straws, stalactites, stalagmites (some joined into columns) and flowstones with lamination forms were identified (Figure 2O). Based on field observations (e.g. cyanobacteria growths), possible inorganic and organic controls on carbonate precipitation in these sites are suggested.

6. Discussion-Conclousions

In this study, Northern Euboea and Eastern Central Greece travertines (Edipsos, Ilia and Thermopylae), were examined and a large variety of morphological types were identified and described. Edipsos and Thermopylae are probably the biggest active travertine-forming systems in Greece, while Ilia is a smaller one. Also some of the data recorded during this study suggest possible organic controls on carbonate precipitation in the studied hot springs. The studied travertine deposits are composed of two calcium carbonate polymorphs (i.e. aragonite and calcite), which, in many cases were found to coexist. Aragonite tends to create hexagonal prisms, which many times appear as radial spheres or fan-shaped radiating needles, while calcite usually creates rhombohedral crystals.

From the mineralogical study it was found that the predominant phase of the travertines in Euboea was aragonite, while Thermopylae travertines have only calcite. The exact conditions that favor aragonite precipitation at one time and calcite at another are unclear. Kanellopoulos (2012) suggests that most important factors favoring the dominant creation of aragonite in Euboea travertines and calcite in Thermopylae travertines are temperature and Sr content of the hot springs. In Thermopylae hot springs the temperatures (33-40 ^{o}C) are lower compared to Euboea hot springs (43-82 ^{o}C). The formation of aragonite from high-temperature waters is suggested by many studies (Sturchio, 1990; Folk, 1994; Fouke et al., 2000). Folk (1994) observed that if the water temperature is above 40 ^{o}C, aragonite would precipitate, regardless of the fluid composition and calcite would form if the water is rich in Ca and cooler than 40 ^{o}C. Fouke et al. (2000) also showed that if the water temperature is above 44 ^{o}C, aragonite forms. The Sr content in Thermopylae hydrothermal fluid (11900 μg/L) and travertines (2160 mg/kg) is lower compared to Edipsos hydrothermal fluid (up to 17400 μg/L) and travertines (up to 3960 mg/kg) and to Ilia hydrothermal fluid (up to 29900 μg/L) and travertines (up to 4260 mg/kg) (Kanellopoulos, 2011). Similar cases (i.e. low content of Sr-creation of calcite) have been presented by many studies. Ishigami and Suzuki (1977) point out a strong positive correlation between Sr content and the proportion of aragonite in Japanese travertines. Malesani and Vannucchi (1975) suggest that a high level of Sr in hydrothermal fluid favors the deposition of aragonite. The travertine deposits developed in hot springs with a high concentration of iron (e.g. Ilia), containing an amorphous hydrous ferric oxyhydroxide mineral phase ($5Fe_2O_3*9H_2O$; Kanellopoulos, 2012), which, along with aragonite, are the main mineral phases.

The chemical composition of calcium carbonate mineral phases varies from area to area, depending on the chemical composition of the hydrothermal fluid (Kanellopoulos, 2011). So, the calcium carbonate mineral phases from Edipsos in addition to Ca, C, and O, contain S and/or Si and/or Na and/or Cl and/or Fe, the travertines from Ilia, in addition to Ca, C, and O, contain Fe

and/or As and/or Si and/or S and/or Sr and/or Na and/or Cl and the travertines from Thermopylae, in addition to Ca, C, and O, contain Mg and/or S (Table 1). Previous studies at the same travertines (Kanellopoulos, 2011) prove that except from the calcium carbonate minerals other mineral phases were present, usually in the form of very small crystals, which are located within the pores of the travertine deposits.

In the present study the major morphological types of Northern Euboea and Eastern central Greece thermogenic travertine deposits were identified, characterized and described. Almost all the morphological types of thermogenic travertines, that the classification of Pentecost and Viles (1994) propose, were identified. More specifically, in the studied areas, eleven main morphological types of thermogenic travertine were found. Some of them are common (i.e. fluvial crust), while some others are rare ones (i.e. cascades, remoras, caves). The co-existence of all these morphological types in one area is not usual. Also, in the same area Kanellopoulos (2012) identified and described a great variety of lithotypes. Signs of biological processes were detected (growths of cyanobacteria and/or algae in the travertines), suggesting possible inorganic and organic controls on carbonate precipitation in the studied systems. All these make the Northern Euboea and Eastern central Greece active travertine systems of quite important and create questions for further research, in order to determine the controlling factors that favor the deposition of each type.

7. Acknowledgments

The author would like to thank Prof. P. Mitropoulos for his encourage and support in this research.

8. References

Aubouin J. 1959. Contribution a l'étude géologique `de la Grèce septentrionale: Les confins de l'Epire et de la Thessalie, *Ann. Géol. Pays Hellen*, 10, 1-483.

Bargar K.E. 1978. Geology and thermal history of Mammoth Hot Springs, Yellowstone National Park, Wyoming, *U.S. Geol. Surv. Bull.*, 1444, 1–55.

Bates R.L. and Jackson J.A. 1987. *Glossary of Geology*, 3rd Ed., Alexandria, Va. (American Geological Institute).

Chafetz H.S. and Folk R.L. 1984. Travertines: depositional morphology and the bacterially constructed constituents, *J. Sed. Petrol*., 54, 289–316.

Dennen K.O., Diecchio R.J. and Stephenson M.A. 1990. The geology of the Falling Spring travertine deposit, Alleghany Co., Virginia, 79–92, in: J.S. Herman, D.A. Hubbard (eds), *Travertine-marl: Stream Deposits in Virginia*. Virginia Division of Mineral Resources Publication 101, Charlottesville, Va (Virginia Division of Mineral Resources).

Folk R.L. 1994. Interaction between bacteria, nannobacteria and mineral precipitation in hot springs of Central Italy, *Geogr. Phys. Quaternaire*, 1994, 48, 233–246.

Fouke B.W., Farmer J.D., Des Marais D.D., Pratt L., Sturchio N.C., Burns P.C. and Discipulo M.K. 2000. Depositional facies and aqueous-solid geochemistry of travertine-depositing hot springs (Angel Terrace, Mammoth Hot Springs, Yellowstone National Park, U.S.A.), *Journal of Sedimentary Research*, 70, 565–585.

Garcia del Cura M.A., Pedley H.M., Ordoρez S. and Gonzalez Martin J.A. 2000. Petrology of a barrage tufa system (Pleistocene to Recent) in the Ruidera Lakes Natural Park (Central Spain), *Geotemas*, 1, 359–363.

Georgalas G.C. 1938. Le volcans des ıˆles Likhades et de Hagios Ioannis (Kammena Vourla), *Praktika Academia Athinion*, 13, 86–98.

Gioni-Stavropoulou G. 1983. Inventory of hot and mineral springs of Greece, I, Aegean sea, *Hydrological and Hydrogeological Investigation Report*, No. 39, IGME, Athens (in Greek).

Glover C. and Roberston A.F.H. 2003. Origin of tufa (cool water carbonate) and related terraces in the Antalya area, SW Turkey, *Geol. J.*, 38, 329–358.

Hammer Ø, Dysthe D. K. and Jamtveit B. 2010. Travertine terracing: patterns and mechanisms, *Geological Society Special Publication*, 336, 345- 355.
Hill C.A. and Forti P. 1997. *Cave Minerals of the World*. 2nd Edn., 463 pp., Alabama (National Speleological Society).
Ishigami T. and Suzuki R. 1977. Factors affecting the crystalline form of calcareous sinters, Geochemistry, Tokyo.
Kanellopoulos C. 2006. Geochemical research on the distribution of metallic and other elements to the groundwater in Fthiotida Prefecture and Northern Euboea, *Master Thesis*, University of Athens, Greece (in Greek).
Kanellopoulos C. 2011. Geochemical research on the distribution of metallic and other elements to the cold and thermal grondwater, soils and plants in Fthiotida Prefecture and N. Euboea. Environmental impact, *Ph.D. Thesis*, University of Athens, Greece (in Greek).
Kanellopoulos C. 2012. Distribution, lithotypes and mineralogical study of newly formed thermogenic travertines in Northern Euboea and Eastern Central Greece, *Central European Geosciences*, 4(4), 545-560.
Kerr R.C. and Turner J.S. 1996. Crystallization and gravitationally controlled ponding during the formation of mound springs, terraces, and "black smoker" flanges, *J. Geophys. Res.*, 101, 25125–25137.
Koban C.G. and Schweigert G. 1993. Microbial origin of travertine fabrics- two examples from Southern Germany, *Facies*, 29, 251–264.
Le Pichon X. and Angelier J. 1979. The Hellenic Arc and Trench system: A key to the neotectonic evolution of the Eastern Mediterranean area, *Tectonophysics*, 60, 1-42.
Malesani P. and Vanucchi S. 1975. Precipitazione di calcite di aragonite dalle acque termominerali in relazione alla genesi e all'evoluzione dei travertine, *Accademia Lincell, Rendiconti Scienze fisica, matematica e natural*, 58, 761–776.
McKenzie D. 1970. Plate Tectonics of the Mediterranean Region, *Nature*, 226, 239-242.
McKenzie D. 1972. Active tectonics of the Alpide – Himalayan belt: the Aegean Sea and surrounding regions (Tectonics of the Aegean Region), *Geophys. J.Roy. Astr. Soc.*, 55, 217-254.
Mitchell R.S. 1985. *Dictionary of Rocks*, New York (Van Nostrand).
Mountrakis D. 1986. The Pelagonian zone in Greece: A polyphase deformed fragment of the Cimmerian continent and its role in the geotectonic evolution of the Eastern Mediterranean, *Journal of Geology*, 94, 335 - 347.
Ordoρez S., Gonzalez J.A. and Garcia del Cura M.A. 1986. Pıtrographie et morphologie des ıdifices tuffeux quaternaires du centre de l'Espagne, *Mediterranıe*, 1–2, 52–60.
Pentecost A. and Viles H. 1994. A review and reassessment of travertine classification, *Geographie physique et Quatemaire*, 48, 3, p. 305-314.
Pentecost A. 2005. Travertine, *Springer-Verlag*.
Pe-Piper G.and Piper D. 2002. *The igneous rocks of Greece, the anatomy of an orogen*, (Gebruder Borntraeger), Berlin.
Riding R. 1991. Classification of microbial carbonates, In: R. Riding (Ed.), *Calcareous Algae and Stromatolites*, Berlin (Springer-Verlag), 21–51.
Scheuer G. and Schweitzer F. 1989. Genetics and occurrence of Holocene travertines in Hungary. *Studies in Geography in Hungary, Akademici Kiado*, 25, 39–48, Budapest.
Sturchio N.C. 1990. Radium isotopes, alkaline earth diagenesis, and age determination of travertine of Mammoth Hot Springs, Wyoming, U.S.A., *Appl. Geochem.*, 5, 631–640.
Thompson J.B. and Ferris F.G. 1990. Cyanobacterial precipitation of gypsum, calcite and magnesite from natural alkaline lake water, *Geology*, 18, 995–998.
Vavassis I. 2001. Geology of the Pelagonian zone in Northern Evia Island (Greece): Implications for the geodynamic evolution of the Hellenides, *These de doctorat*, Univ. de Lausanne.
Viles H.A. and Goudie A.S. 1990. Reconnaisance studies of the tufa deposits of the Napier Range, N.W. Australia, *Earth Surf. Proc. Landf.*, 15, 425–443.
Whitten D.A. and Brooks J.V.R. 1972. *The Penguin Dictionary of Geology*, London (Penguin).

Δελτίο της Ελληνικής Γεωλογικής Εταιρίας, τομ. XLVII , 2013
Πρακτικά 13ου Διεθνούς Συνεδρίου, Χανιά, Σεπτ. 2013

Bulletin of the Geological Society of Greece, vol. XLVII 2013
Proceedings of the 13th International Congress, Chania, Sept. 2013

GEOTHERMAL RESOURCE MANAGEMENT-A RESERVOIR SIMULATION APPROACH-THE PARIS BASIN CASE

Papachristou M.[1], Ungemach P.[2] and Fytikas M.[1]

[1] *Aristotle University of Thessalonki, Faculty of Sciences, Department of Geology, 54124, Thessaloniki, mariap@geo.auth.gr, fytikas@geo.auth.gr*

[2] *GPC Instrumentation Process, PARIS NORD II - Immeuble Business Park - Bâtiment 4A, 165, rue de la Belle Etoile - B.P. 55030, 95946 ROISSY CDG CEDEX, France, pierre.ungemach@geoproduction.fr*

Abstract

Numerical modeling has become an indispensable part of geothermal resource management, especially when long-term production is involved, offering the ability to forecast the reservoir behavior under various exploitation scenarios. This paper illustrates the simulation results of the "Dogger" reservoir in Val de Marne region (south of Paris), where 16 doublets (production-injection wells) are still in operation today. The "Dogger" low enthalpy geothermal reservoir in Paris Basin is being under intensive and systematic exploitation since the early 1980's. Almost 40 years after the initiation of the heat mining project, the longevity of the reservoir and applications have become critical issues for achieving the exploitation system's sustainability. The simulation covers a period of 52 years (1984-2035), attempting to recreate the exploitation history and to provide an early estimation of the time-space variation of pressure and temperature inside the reservoir under future production/injection schemes and schedules. For the majority of the wells, the calculated production temperatures match quite well the field data up to the year 2011. The prediction models indicate that certain modifications in the development scheme could result in the stabilization of the fluids temperature, or at least in slower depletion rates.

Key words: *geothermal exploitation, Dogger, sustainability.*

Περίληψη

Οι αριθμητικές προσομοιώσεις αποτελούν ένα χρήσιμο εργαλείο διαχείρισης των γεωθερμικών ταμιευτήρων, ιδιαίτερα αυτών που βρίσκονται υπό μακροχρόνια εκμετάλλευση, παρέχοντας μεταξύ άλλων τη δυνατότητα πρόβλεψης της μελλοντικής συμπεριφοράς τους υπό διάφορα σενάρια αξιοποίησης. Η εργασία αυτή πραγματεύεται τα αποτελέσματα των προσομοιώσεων στο τμήμα του γεωθερμικού ταμιευτήρα Δογγέριου ηλικίας, που εκτείνεται στην περιοχή Val de Marne (νότια του Παρισιού), όπου λειτουργεί πυκνό δίκτυο γεωτρήσεων. Η εντατική εκμετάλλευση του γεωθερμικού δυναμικού στη λεκάνη του Παρισιού ξεκίνησε τη δεκαετία του 1980, με τη διάνοιξη πολλών γεωτρήσεων παραγωγής και επανεισαγωγής για την παροχή θέρμανσης και ζεστού νερού χρήσης. Αναπόφευκτα, περίπου τέσσερις δεκαετίες μετά, η βιωσιμότητα του συστήματος εκμετάλλευσης εξαρτάται άμεσα από την παράταση του χρόνου ζωής του ταμιευτήρα και των εφαρμογών. Η προσομοίωση καλύπτει περίοδο 52 ετών

(1984-2035), αναπαριστώντας το ιστορικό εκμετάλλευσης και παρέχοντας εκτιμήσεις για τη μελλοντική χωροχρονική μεταβολή της θερμοκρασίας και του υδραυλικού φορτίου μέσα στον ταμιευτήρα. Για την πλειονότητα των γεωτρήσεων, οι θερμοκρασίες που υπολογίστηκαν για το έτος 2011 είναι συγκρίσιμες με τα πραγματικά δεδομένα, ενώ τα μοντέλα πρόγνωσης έδειξαν ότι η τροποποίηση του σχήματος εκμετάλλευσης, μπορεί, υπό προϋποθέσεις, να οδηγήσει σε σταθεροποίηση της θερμοκρασίας των παραγόμενων ρευστών ή τουλάχιστον σε πιο αργούς ρυθμούς μείωσής της.
Λέξεις κλειδιά: *γεωθερμική εκμετάλλευση, Δογγέριος ταμιευτήρας, βιωσιμότητα.*

1. Introduction

Geothermal energy is an environmentally friendly energy source, which can be regarded as renewable, yet not inexhaustible at human time scale and under intensive exploitation. This is simply attributed to the fact that heat is abstracted faster from a geothermal system (via convection) that is naturally replaced by the terrestrial heat flow (via conduction) (Ungemach et al., 2005). Therefore, the crucial issue of achieving sustainability largely depends on creating a balance between the longevity of the resource and the demands of the heat mining project. An important factor for accomplishing sustainability is, among others, the effective geothermal field management, which in turn is based principally on the rational reservoir management. Ungemach and Antics (2003) have suggested an intergraded approach to sustainable reservoir management strategies as a combination of the exploitation system economics, the reservoir/well life, the offer/demand heat amounts, the reservoir engineering, certain externalities, etc.

Numerical simulations constitute a very useful tool for reservoir engineering purposes by providing an early estimation of the temperature and pressure (or hydraulic head) space-time variations inside the reservoir, thus contributing to the better understanding of its response under long-term exploitation.

The aforementioned will be discussed for the well-documented low enthalpy reservoir of Dogger (Middle Jurassic) age in Paris basin. The geothermal exploitation of the Dogger reservoir started in the early 1970's and boosted in the 1980's with the construction of 55 doublets (110 production and injection wells) for district heating purposes. As for the year 2012, 71 geothermal wells have been in operation, supplying 27 district heating networks.

The area of Val de Marne is located south of Paris and includes a dense network of 32 geothermal wells, following the doublet (production-injection) concept (Figure 1). The simulations regard the past and future exploitation strategies over an entire period of 52 years and aim at investigating the behaviour of a relatively large part of the Dogger reservoir under a complex production scheme that was designed according to the anticipated well and reservoir lifetimes.

2. Geological-Geothermal Setting of the Study Area

Paris Basin is a stable intra-cratonic sedimentary basin that occupies the largest part of northern France, covering an area of 110.000 km^2 (Perodon and Zabek, 1990). Its basement consists of Palaeozoic igneous and metamorphic rocks (Pomerol, 1978), overlaid by a thick sequence of Mesozoic and Tertiary sedimentary rocks that gradually filled the basin. Their thickness reaches its maximum (3000 m) in the central part of the basin. The geothermal fluids are hosted by the Middle Jurassic (Dogger) marine carbonate sediments that lay between marls of Low Jurassic and Callovian age (Rojas et al., 1989; Perrodon and Zabek, 1990). The most productive layers are white oolithic limestones, typical of a warm-sea sedimentary environment. The salinity of the hot fluids is very high (5.8-35g/l), varying significantly from the southwest to the northeast of the basin (Rojas et al., 1989). The high salinity and the CO_2/H_2S gas phase of the fluids have made injec-

tion of the heat-depleted brine into the reservoir an environmental prerequisite, alongside pressure maintenance (Ungemach et al., 2005).

The detailed geothermal exploration in Paris basin (Rojas et al., 1987; 1989) revealed the high vertical and lateral heterogeneity of the reservoir, regarding both its structure and major features. The reservoir depths and formation temperatures range from 1400-2000 m and 56-80°C, respectively. The mean geothermal gradient is 35°C/km and increases to the east. The overall reservoir consists of several successive productive and interbedded impervious layers.

The reservoir top in Val de Marne region deepens from the west (1550 m below sea level) to the east (1720 m b.s.l.) and the fluids temperatures range from 70°C to 79-80°C accordingly. The first geothermal doublet was drilled in 1984; today 16 doublets are still in operation.

3. Simulation

3.1. Techniques and Methods

The transient processes that have been simulated are groundwater flow and heat transfer. The numerical simulator used is SHEMAT® (Clauser et al., 2003), which solves the 3-D coupled problem of flow and transport in fluid-saturated porous media, on a 3-D grid with x, y, z coordinates. It uses a finite difference method to approximate the partial differential equations that describe the internal processes. The spatial discretization of the advection term in the transport equation was made by the Il'in flux blending system (Il'in, 1969) and the resulting system of equations was solved implicitly by the strongly implicit procedure (SIP, Weinstein et al., 1969).

3.2. Simulation Features

The simulated part of the reservoir covers an area of 256 km^2 (Figure 1a), which exhibits significant vertical and lateral heterogeneities. The model grid consists of 25600 cells (160 rows and 160 columns) with cell dimensions of 100 m x 100 m x z (z: the thickness -in m- of each layer).

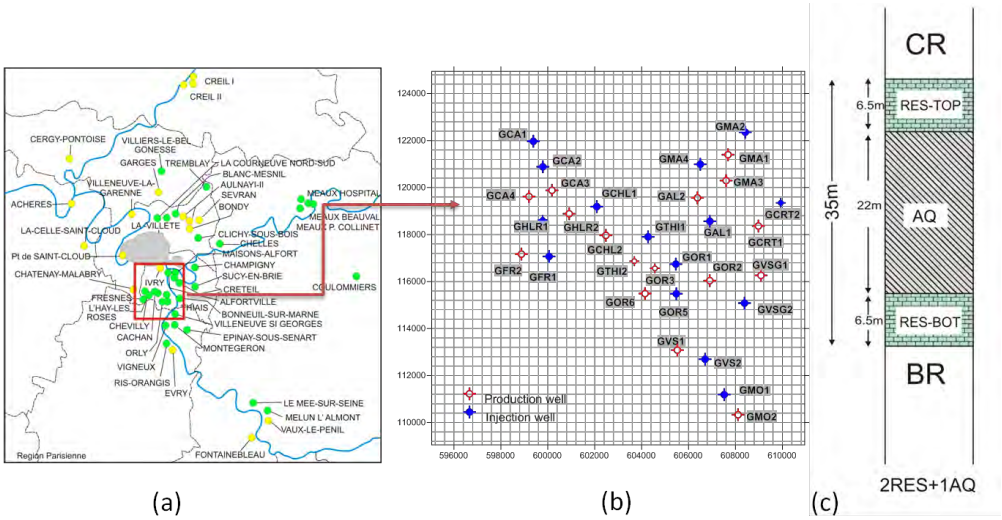

Figure 1 - (a) Sketch map of the Val de Marne simulation domain, (b) doublets configuration (b) reservoir structure (RES: productive layers, AQ: aquitard, CR: cap rock, BR: bed rock).

The geometry of the multilayered reservoir is depicted by the so called "sandwich" configuration (Antics et al., 2005) (Figure 1b), which includes two symmetric (geometrically and hydraulically) productive units and an intermediate single aquitard (hydraulically impervious but thermally conductive layer). The reservoir is bounded by two confining layers, the cap (CR) and the bedrock

(BR). The simplified "sandwich" structure is used to meet the software constrains, regarding the thickness and depth variation of each layer in the model domain and the total amount of monitoring points (i.e. operating wells) taken into account.

Nevertheless, it should be mentioned that the sandwich configuration is regarded as a satisfactory substitute for the real, more complex geometry, especially for large simulation time scales, according to the sensitivity analysis of the cooling kinetics to various reservoir structure and settings for Paris Basin (Antics et al., 2005; Ungemach et al., 2007; Papachristou, 2011; Ungemach et al., 2011). The production temperature declines more rapidly for the first few years in the sandwich model than to a multi-layered model that corresponds the real stratigraphy of the reservoir. However, the depletion rate becomes slower and finally matches the multi-layer case for long simulation times.

The thickness of the reservoir layers (Figure 1b) has been calculated by averaging the correspondent thicknesses identified from flowmeter loggings in each well. The thickness of the cap and bedrock in the model are set to 200 m and 100 m respectively. The vertical boundary conditions consist of constant temperature, assigned for each cell midpoint according to the temperature gradient for the caprock, and constant heat flow (0.09 W/m^2) for the bedrock. The lateral boundary conditions are set as constant head and temperature.

The lateral reservoir heterogeneities have been assigned in the model by extrapolating, via Kriging, the available field data. The overall initial conditions regarding head, temperature, permeability and porosity are displayed in Figure 2. It is assumed that the three reservoir layers were in thermal equilibrium prior to exploitation.

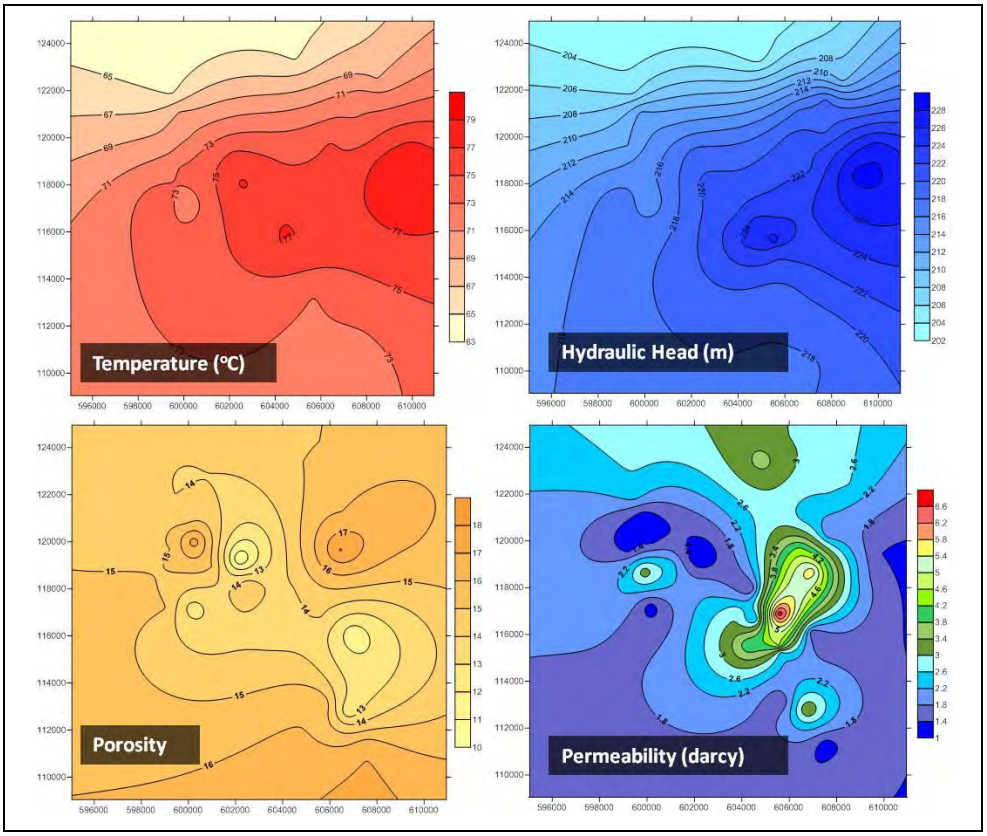

Figure 2 - Permeability and porosity distribution and initial head/temperature conditions in the Dogger reservoir of Val de Marne region.

Table 1: Production/Injection Schedule.

Doublet/Triplet	Operation Period	Prod/Inj rate (m^3/h)	T_{in} (°C)	$T_{inj.}$ (°C)
GFR1(i)+GFR2(p)	1987-2010	137	74.30	48.0
	2011	145		48.0
	2012-2013	177		48.0
	2014-2015	100		50.0
	2016-2020	116		50.0
	2021-2035	149		50.0
GFR4(i)+GFR3(p)	2014-2015	118	73.90*	50.0
	2016-2020	136		50.0
	2021-2035	210		50.0
GTHI1(i)+GTHI2(p)	1987-2015	160	76.60	50.0
GTHI1(i)+GTHI2(i)+GTHI3(p)	2016-2035	125	76.72*	46.0
GCA1(i)+GCA3 (p)	1986-2015	110	71.00	48.0
GCA1(i)+GCA3(i)+GCA5(p)	2016-2035	110	71.37*	46.0
GCA2(i)+GCA4 (p)	1986-2015	125	70.00	48.0
GCA2(i)+GCA4(i)+GCA6(p)	2016-2035	125	69.00*	46.0
GCHL1(i)+GCHL2(p)	1986-2015	170	77.20	48.0
GCHL1(i)+GCHL2(i)+GCHL3(p)	2016-2035	180	75.73*	45.0
GHLR1(i)+GHLR2(p)	1986-2015	165	74.10	47.0
GHLR1(i)+GHLR2(i)+GHLR3(p)	2016-2035	175	73.30	45.0
GMA2(i)+GMA1(p)	1986-2010	160	73.30	52.0
	2011-2016	185		53.0
GMA2(i)+GMA1(i)+GMA5(p)	2021-2035	200	75.72	52.0
GMA4(i)+GMA3 (p)	1986-2010	180	75.2	58.0
	2011-2020	140		57.0
GMA4(i)+GMA3(i)+GMA6(p)	2016-2035	200	73.56*	52.0
GAL1 (i)+GAL2 (p)	1988-2015	180	75.20	45.0
GAL1(i)+GAL2(i)+GAL3(p)	2016-2035	200	75.89*	40.0
GVS2(i) +GVS1(p)	1988-2015	137 (1986-1995)	72.9	44.0
		147 (1996-2005)		46.0
		117 (2006-2015)		47.0
GVS2(i)+GVS1(i)+GVS3(p)	2016-2035	150	75.02*	44.0
GOR1(i)+GOR2(p)	1984-2015	75	76.0	45.0
	2016-2035	125		42.0
GOR4(i)+GOR3(p)	1987-2005	177	76.9	45.0
GOR5(i)+GOR6(p)	2009-2010	190	77.0	42.0
	2011-2035	200		42.0
GMO1(i)+GMO2(p)	1986-2010	100	72.5	50.0
GVSG2(i)+GVSG1(p)	1988-2015	170 (1988-2005)	77.9	45.0
		135 (2005-2015)		47.0
GVSG2(i)+GVSG1(i)+GVSG3(p)	2016-2035	150	77.16*	43.0
GCRT2(i)+GCRT1(p)	1986-2010	180	78.9	45.0
	2011-2015	190		42.0
GCRT2(i)+GCRT1(i)+GCRT3(p)	2016-2035	200	78.15*	45.0
IADP(i)+PADP(p)	2011-2015	180	75.0	42.0
IADP(i)+PADP(p)	2016-2035	190	75.05*	42.0

*T_{in}=initial production temperature, T_{inj}=injection temperature, * =simulation result.*

The total simulation time is 52 years, divided into three periods: 1984-2010, 2011-2015 and 2016-2035 (Table 1). The first represents the exploitation history and the others the future production/injection schemes and schedules, with the construction of new wells and the triplet array sub-

stituting, in many cases, for the former doublet configuration (Figure 3). The head and temperature time-space distribution at the end of the first simulation period provide the necessary information for planning the future exploitation scenarios and new well locations.

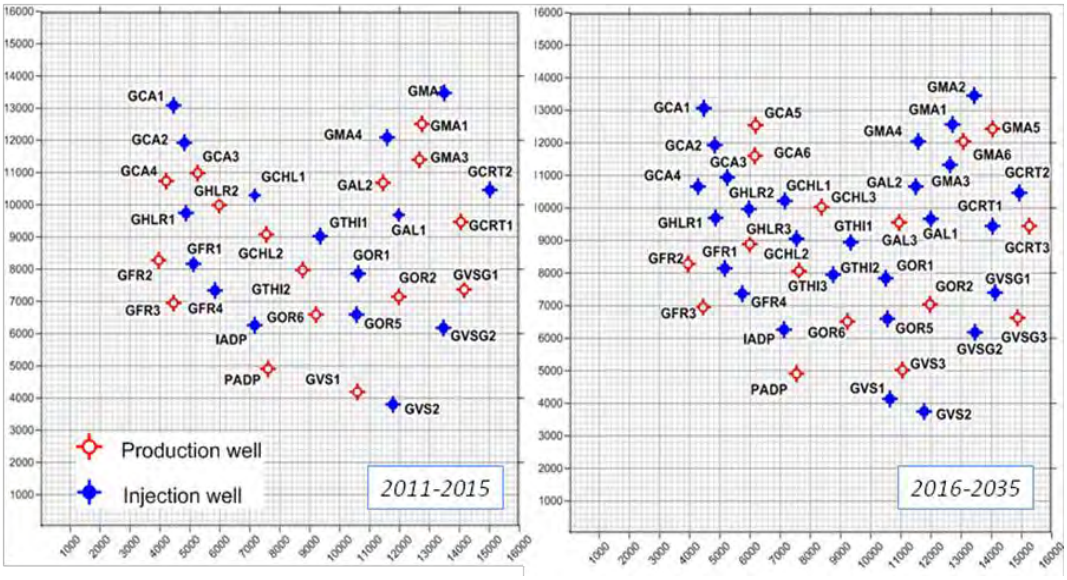

Figure 3 - Well network in 2011-2015 and 2016-2035 periods.

4. Results-Discussion

The temperature depletion results ($T_{initial}$-T_{final}) for each simulation period are as follows:

- 1984-2010: **GFR2** (-1.09), **GCA3** (-1.03), **GCA4** (-0.30), **GCHL2** (-1.33), **GHLR2** (-2.58), **GVS1** (-1.12), **GOR2** (+0.54), **GOR3** (-2.57), **GTHI2** (-1.45), **GVGS1** (-1.00), **GAL2** (-2.68), **GMA1** (-2.78), **GMO2** (-0.75), **GMA3** (+0.76), **GCRT1** (-1.44)
- 2011-2015: **GFR2** (-0.36), **GCA3** (-0.28), **GCA4** (-0.33), **GCHL2** (-0.47), **GHLR2** (-0.69), **GVS1** (-0.43), **GOR2** (+0.00), **GTHI2** (-0.88), **GVGS1** (-0.18), **GAL2** (-0.60), **GMA1**(-0.52), **GMA3** (-0.10), **GOR6** (-1.48), **GCRT1** (-0.46), **PADP** (0.00), **GFR3** (+0.06)
- 2016-2035: **GFR2** (-1.99), **GCA5** (-0.74), **GCA6** (-0.63), **GCHL3** (-2.10), **GHLR3** (-3.50), **GVS3** (-2.21), **GOR2** (-0.65), **GTHI3** (-2.13), **GVGS1** (-1.89), **GAL2** (-6.16), **GMA3**(-0.07), **GMA5** (-1.89), **GMA6** (-7.73), **GOR6** (-2.79), **GCRT3** (-4.11), **PADP** (-1.97), **GFR3** (-3.54)

4.1. Simulation Period 1984-2010

Between the years 1984 and 2010, 16 doublets were gradually set in operation. After the year 2005, the GOR3-GOR4 doublet was abandoned due to serious technical problems. For the majority of the wells, the calculated temperature and the thermal breakthrough time (t_b), which is assumed equal to a 1°C temperature drop, match well or slightly differ from the actual data (year 2011), given the inevitable simplifications of the reservoir geometry previously discussed.

The most important temperature decrease occurs in the GAL2, GMA1, GHLR2 and GOR3 wells. An average drop of 2-3°C has been indeed recorded for the GAL2 well (Lopez et al., 2010; Le Brun et al., 2011); therefore the simulation result is considered reliable. On the contrary, there are not any available recorded temperature data for the problematic GOR3 well. The difference between calculated and actual data for the GHLR2 and GMA1 wells could be explained by the simplified reservoir structure in the model, which affects more the wells that are located at sites with

much more complicated layering. However, the case of the GMA doublet should be further commented. According to the drilling data, the depth of the reservoir top between the production (GMA3) and the injection (GMA4) wells is notably different (-1628 and -1531 m, respectively). This important lateral depth variation has not been accounted for in the simulation due to software limitations, according to which it is assumed that all wells operate in the same depth inside the reservoir. Therefore, neither the time delay of the thermal/hydraulic front arrival nor the thermal exchanges for this depth interval are calculated.

4.2. Simulation Period 2011-2015

During this period, 15 doublets are in operation according to the exploitation schedule. In 2011, the PADP-IADP wells have been completed and set in operation in the ORLY Airport of Paris.

The significant temperature decrease of the GOR6 fluids is mostly attributed to the intensification of heat production (high production/injection rates in combination to low injection temperatures). Additional simulation runs show that the final production temperature is not affected by the increase of injection temperature by 2°C. In contrast, lower production/injection rates (by 30m^3/h) result in a significantly lower temperature depletion (0.5°C).

4.3. Simulation Period 2016-2035

Many of the existing production and injection wells are recompleted and converted into injectors between the years 2016 and 2035. New, large diameter, production wells are constructed at selected sites, changing the array from doublet to triplet. The heat generation is maximized to meet higher future demands.

The simulation results show fast temperature depletion rates in five wells: GFR3, GHLR3, GAL3, GMA6 and GCRT3. In all cases, these results are related to the wells' location. Clearly, as it can been seen at the temperature and head pattern maps of Figure 4, these wells are affected by the neighboring injectors and the development of a high pressure (head) zone that cause faster flow of the (colder) fluids towards the lower pressure areas.

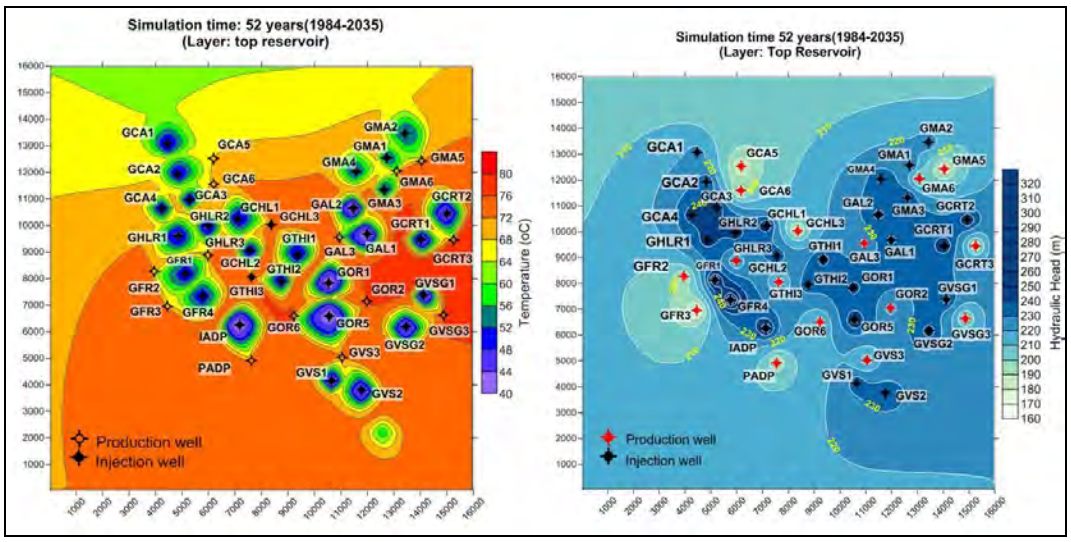

Figure 4 - Temperature and head distribution (31.12.2035).

Certainly, the significantly lower temperature is more or less expected for the GHLR3 case, given that in this specific area the effect of the simplified stratigraphy is more obvious, as discussed in Chapter 4.1. Nevertheless, modifying the GHLR3 well location (at reservoir depth) by 200 m, the temperature drops by 2.45°C (opposite to 3.50°C), with no changes in pressure.

The case of GAL3 and GMA6 wells, which show the most important temperature drop (-6.16 and -7.73°C respectively), need further investigation in order to find the proper combination of tolerable temperature depletion and reasonable head decrease.

By re-locating the GAL3 well around 400m to the northwest (Figure 5a), the temperature reduction becomes significantly smaller (-3°C). Similarly, by moving GMA6 800 m towards the east-southeast (Figure 5a), the temperature drops by 1.5°C only. However, in this new GMA6 location the pressure becomes an issue as a result of the long distance between the production well and its injectors (GMA3-GMA4) on one hand, and the operation of the nearby GMA5 production well that causes an additional head drop on the other. To avoid this, GMA6 is placed 200 m further to the south, whereas GMA3 operates as the only injector, in order to maintain adequate pressure levels (Figure 5b). In this case, the temperature reduces 2.5°C and the hydraulic head are higher. The system operates a doublet instead of a triplet.

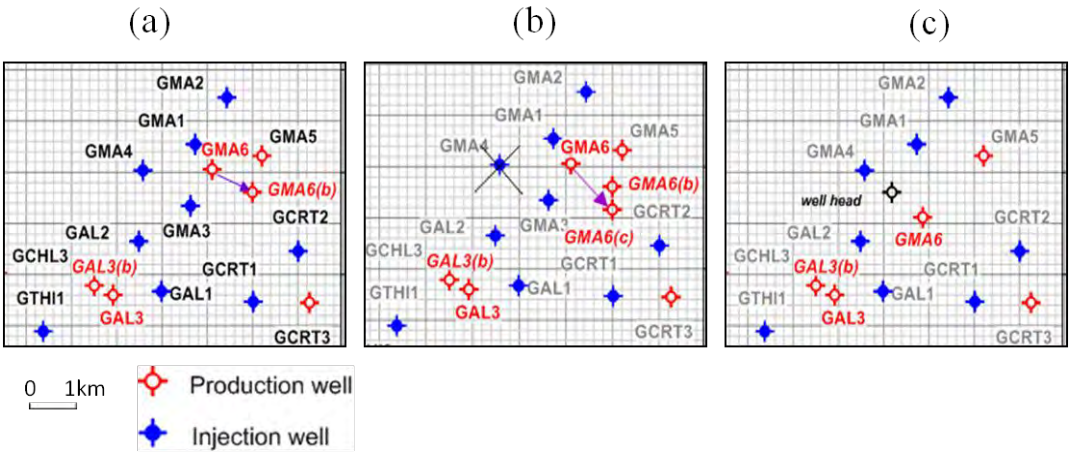

Figure 5 - GAL3 and GMA6 various well locations.

Nonetheless, when dealing with well placement, the well architecture should not be ignored. Especially for Paris basin, the production and injection wells are routinely drilled from the same platform on surface, with an average 30-35°C angle securing a well spacing in top reservoir depth varying from 900-1200 m (Ungemach et al., 2011). This condition is not satisfied by the last tested scenario, due to the platform position in surface ("well head" in Figure 5c). Subsequently, the optimal setting for the GMA wells that takes into consideration both technical and thermodynamic issues, regard as most "realistic" the case of the new production well (GMA6) encountering the top reservoir very close to the former production well GMA3. The latter is abandoned and the new well system remains as a doublet, with only one injector, the GMA4 well (Figure 5c). This simulation results in lower temperature decrease (-1.76°C) and significantly smaller head drop. Such scenarios were not examined for GCRT3 well, since its vicinity to the model domain boundary would cause boundary effect and distort the simulation results.

One more observation that should be mentioned is the progressive reservoir temperature built-up at the abandoned injection well sites, which indicates the gradual reservoir thermal replenishment (due to the natural head flow) and confirms the renewability of the source. The top reservoir head and temperature spatial variation at the end of simulation time, after defining the final well locations is presented in Figure 6.

5. Conclusions

The detailed sensitivity analysis described in Antics et al. (2005) and Papachristou (2011), provi-

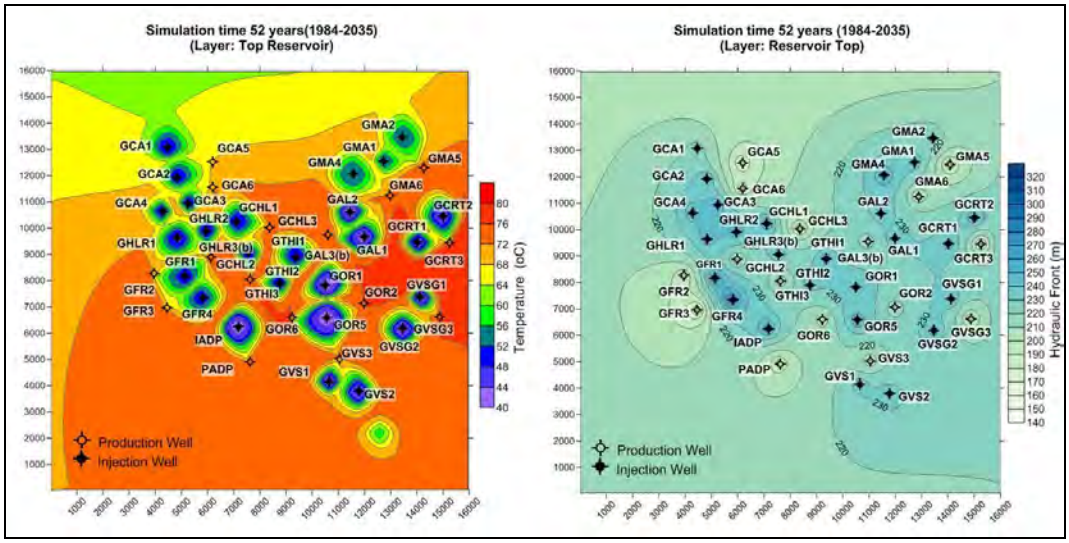

Figure 6 - Final temperature and head distribution (31.12.2035).

ded useful clues on the reservoir structure applied in the model, as well as on the assignment of the bedrock/caprock thermal boundary conditions. The geostatistical interpolation of the available data, regarding initial reservoir parameters, contributed to the more realistic representation of the lateral heterogeneities.

The simulation of the Val de Marne region addressed the 1984-2010 period, in order to calibrate the model by reconciling the simulation outputs with factual evidence. It also accounted for a 25 year (2011-2035) well and reservoir life sequence, an assumption that is considered reasonable, based on the particularities of the geothermal conditions and exploitation in the Paris Basin.

In most cases (10 out of 15 production wells), the simulation results match well the recorded data, given that no temperature drop more than 1°C has been yet observed, except for the GAL2 case. Despite the more "pessimistic" figures, the overall results are consistent and reliable. As expected, the simplification of the reservoir layering affected more the sites of complicated structure and resulted in higher temperature depletion rates. The latter should not be overlooked.

The reservoir temperature and head distribution at the end of 2010 offered important information on positioning the new wells for the period 2011-2035. It was clearly shown that, whereas temperature is the most decisive factor in selecting well locations, pressure (or head) should not be ignored either, because it may affect significantly the cooling kinetics.

All things considered, the validity of the simulation results should not merely rely on absolute figures, but mainly on the general observed trends. From this perspective, it is reasonable to regard the simulations as an interesting and reliable tool for establishing the characteristics of a long-term sustainable geothermal development, as in the case of Paris basin. Specifically for the Dogger reservoir, it was proven that sustainable exploitation can significantly extend the reservoir life, even if the mined heat is maximized.

6. References

Antics M., Papachristou M. and Ungemach P. 2005. Sustainable heat mining. A reservoir engineering approach, *Proceedings 30th Workshop on Geothermal Reservoir Engineering*, Stanford University, Stanford, California, USA, January 2005.

Bartels J., Cheng L.Z., Ranalli G., Pape, H., Hurter S., Kuhn M., Schneider W., Stofen H., Meyen V. and Pribnow D. 2003. Numerical Simulation of Reactive Flow in Hot Aquifers-SHEMAT and Processing SHEMAT, Ed. Clauser CH., Springer, New York. 332 pp.

Il'in, V.P. 1969. On an integral inequality, Mat. Zametki, 6(2), 139–148.

Lopez S., Hamm V., Le Brun M., Schaper L., Boissier F., Cotiche C. and Giouglaris, E. 2010. 40 years of Dogger aquifer management in Ile-de-France, Paris Basin, France, *Geothermics*, 39, 339-356.

Le Brun M., Hamn V., Lopez S., Ungemach P., Antics M., Ausseur J.Y., Cordier E., Giuglaris E., Goblet P. and Lalos, P. 2011. Hydraulic and thermal impact modelling at the scale of the ge othermal heating doublet in the Paris basin, France, *Proceedings 36th Workshop on Geother mal Reservoir Engineering,* Stanford University, Stanford, California, Jan. 31-Febr. 2.

Papachristou M. 2011. Contribution to the low enthalpy geothermal reservoir management by using numerical simulations-The Paris basin case, *PhD Thesis*, Aristotle University of Thessaloniki, Dept. of Geology, 282 pp.

Perrodon A. and Zabeck J. 1990. Paris Basin, In: Leighton M.W., Kolata D.R., Oltz D.F. Eidel J.J., (eds), *Interior Cratonic Basins,* American Association of Petroleum Geologists*,* 51*,* 633 679

Pomerol Ch. 1978. Paleogeographic and structural evolution of the Paris Basin, from the Precambr ian to the present day, in relation to neighbouring regions*, Geologie En Mijnbouw,* 57(4), 5 33-543.

Rojas J. Menjoz A., Martin J., Criaud A. and Fouillac C. 1987. Development and exploitation of low enthalpy geothermal systems: example of the "Dogger" in the Paris basin, France, *Proceedings 12th Workshop on Geothermal Reservoir Engineering*, Stanford University, Stanford, January 20-22 1987.

Rojas J., Giot D., Le Nindre Y.M., Criaud A., Fouillac C., Brach M., Menjoz A., Martin J.C. and Lambert M. 1989. Caractérisation et modélisation du réservoir géothermique du Dogger, Bassin Parisien, France*, Final Report,* EUR 12636 FR, European Community Commission-DG XII, 240 pp.

Ungemach P. and Antics M. 2003. Inside into Modern Geothermal Reservoir Management Practice, *Text Book, International Geothermal Days*, Turkey, 2003.

Ungemach P., Papachristou M. and Antics M. 2005. Sustainable geothermal reservoir management. *Proceedings World Geothermal Congress*, Antalya, Turkey, 24-29 April 2005.

Ungemach P., Papachristou M. and Antics M. 2007. Renewability versus sustainability. A rerervoir management approach, *Proceedings European Geothermal Congress 2007*, Unterhaching, Germany, 30 May-1 June 2007, paper 216.

Ungemach P., Antics M., Lalos P., Borozdina O., Foulquier L. and Papachristou M. 2011. Geomodelling and well architecture, key issues to sustainable reservoir development, *Proceedings 36th Workshop on Geothermal Reservoir Engineering*, Stanford University, Stanford, California, January 31-February 2, 2011.

Weinstein H.G., Stone H.L. and Kwan T.V. 1969. Iterative procedure for solution of systems of parabolic and elliptic equations in three dimensions*, Industrial and Engineering Chemistry Fundamentals* 8(2**)**, 281-287.

Δελτίο της Ελληνικής Γεωλογικής Εταιρίας, τομ. XLVII , 2013
Πρακτικά 13ου Διεθνούς Συνεδρίου, Χανιά, Σεπτ. 2013

Bulletin of the Geological Society of Greece, vol. XLVII 2013
Proceedings of the 13th International Congress, Chania, Sept. 2013

MAPPING HYDROTHERMAL ALTERATION ZONES FROM SPECTRAL BAND RATIOS: A GEOSTATISTICAL APPROACH BASED ON THE STABLE SEMIVARIOGRAM MODEL

Skianis G. Aim[1] and Vaiopoulos A. D.[2]

[1] National and Kapodistrian University of Athens, Faculty of Geology and Geoenvironment, Department of Geography-Climatology, Remote Sensing Laboratory, skianis@geol.uoa.gr

[2] National and Kapodistrian University of Athens, Faculty of Geology and Geoenvironment, Remote Sensing Laboratory

Abstract

An alteration zone may be clearly expressed in an image of a spectral band ratio, as long as the spatial variation of its tonality is strong enough. A measure of the spatial variation of the target of interest (in our case the alteration zone) can be the semivariogram of the band ratio.

In the present paper, the spatial variation of the band ratio, in terms of the statistical behavior of the individual bands, is studied. The semivariograms of the individual bands is simulated by the stable semivariogram model, which is quite flexible in describing the spatial variation of the tonality. The correlation between the spectral bands is also taken into account. Using proper distributions for the reflectance of individual bands and taking into account theorems of statistics, a mathematical expression for the semivariogram of the spectral band is derived. This expression provides information about how the spatial variation of the band ratio is affected by the statistical parameters of the individual bands. Experimentation with satellite images shows that theoretical predictions agree with real data.

The results and conclusions of this paper may help in assessing the efficiency of the images of spectral band ratios over potential mineralization zones.

Key words: *Spectral band, band ratio, semivariogram, stable model, alteration zone.*

Περίληψη

Μια ζώνη υδροθερμικής εξαλλοίωσης μπορεί να αποτυπωθεί ευκρινώς σε εικόνα λόγου φασματικών ζωνών, στο βαθμό που η χωρική διαφοροποίηση της τονικότητας είναι έντονη. Ένα μέτρο της χωρικής διαφοροποίησης των αποτυπωνόμενων στην εικόνα σχηματισμών είναι το ημιβαριόγραμμα του λόγου φασματικών ζωνών.

Στην παρούσα εργασία μελετάται η χωρική διαφοροποίηση του λόγου φασματικών ζωνών, σε συνάρτηση με τις στατιστικές παραμέτρους των επιμέρους ζωνών. Η χωρική διαφοροποίηση της κάθε ξεχωριστής ζώνης προσεγγίζεται με το σταθερό μοντέλο ημιβαριογράμματος, που είναι αρκετά ευέλικτο στο να περιγράφει τις διακυμάνσεις της τονικότητας των εικονοστοιχείων στο χώρο. Αξιοποιώντας κατάλληλες κατανομές και θεωρήματα της στατιστικής, και λαμβάνοντας ακόμα υπόψη τη συσχέτιση μεταξύ των φασματικών ζωνών, συνάγεται μια μαθηματική

έκφραση για το ημιβαριόγραμμα του λόγου φασματικών ζωνών. Με βάση αυτήν την έκφραση μελετάται το πώς διαμορφώνεται η χωρική διαφοροποίηση του λόγου φασματικών ζωνών από τις στατιστικές παραμέτρους της κάθε ξεχωριστής ζώνης. Στη συνέχεια, ο πειραματισμός με δορυφορικές εικόνες δείχνει συμφωνία μεταξύ θεωρητικών προβλέψεων και πραγματικών δεδομένων.
Τα πορίσματα αυτής της εργασίας μπορούν να αξιοποιηθούν στην παραγωγή ψηφιακών εικόνων βελτιωμένης αξιοπιστίας, με σκοπό των εντοπισμό πιθανών μεταλλοφόρων ζωνών.
Λέξεις κλειδιά: *Φασματική ζώνη, λόγος φασματικών ζωνών, ημιβαριόγραμμα, σταθερό μοντέλο, ζώνη εξαλλοίωσης.*

1. Introduction

It is well known (Parcharidis et al. 1999; Gupta 2000; Skianis et al. 2012) that the image of the simple spectral band ratio u between two bands with reflectances x and y may be useful in detecting alteration zones, which are potentially associated with hydrothermal mineralization. The ratio u is defined by:

Equation 1 - definition of the band ratio

$$u = \frac{x}{y}$$

x and y may be, for example, the reflectance of band 5 (SWIR 1) and band 7 (SWIR 2) of the Landsat Thematic Mapper, respectively. They can also be reflectances at SWIR band and blue or red band. A reliable measure of the clarity by which the target of interest appears in the band ratio image, can be the intensity of its spatial variation, which may be represented by the semivariogram of the image (Woodcock et al. 1988a, 1988b; Curran 1988; Lacaze et al. 1994; Atkinson 2001; Garrigues et al. 2007).

The semivariogram $\gamma_x(h)$ of band x is defined by (Liang 2004):

Equation 2 - definition of the semivariogram

$$\gamma_x(h) = \frac{1}{2N}\sum_{i=1}^{N}[x(p_i) - x(p_i + h)]^2$$

p_i is the position of a pixel with a certain reflectance value at band x. $p_i + h$ is the position of a pixel at distance h from that at position p_i. N is the number of pairs of pixels at distance h each other. In a similar way, the semivariograms $\gamma_y(h)$ and $\gamma_u(h)$, of band y and ratio u, respectively, may be defined.

The definition of the semivariogram, according to equation 2, does not provide much insight about how the spatial variation of the individual bands controls that of the band ratio. This is the subject of the present paper. First, a mathematical expression for the semivariogram $\gamma_u(h)$ of the simple band ratio, in terms of the semivariograms of x and y, is derived. For such a purpose, proper positively skewed distributions are used in order to model the histograms of bands x and y (Vaiopoulos et. al. 2004) and small variances of x and y are assumed, in order to neglect terms of order higher than one in the Taylor expansion of $u(x, y)$ (Skianis 2012; Skianis & Vaiopoulos 2012). The semivariograms of x and y are simulated by the stable semivariogram model, the parameters of which may produce a wide variety of spatial variation patterns. Then, the behavior of the expression for $\gamma_u(h)$ is studied in order to see how the spatial variation of u is controlled by the parameters of the semivariograms $\gamma_x(h)$ and $\gamma_y(h)$, as well as by the correlation coefficient

between x and y. Finally, the validity of this mathematical formula is tested by experimentation with satellite images over areas of hydrothermal activity.

2. The Semivariogram of the Spectral Band Ratio

The first step to derive a mathematical expression for the semivariogram of the spectral band ratio $\gamma_u(h)$ is introduce a semivariogram model to describe the spatial variation of x and y bands. In this paper, the stable model is introduced, which is defined by (Liang 2004):

Equation 3 - the stable semivariogram model

$$\gamma_x(h) = a\left[1 - \exp\left(-\frac{h^c}{b^c}\right)\right]$$

a is the sill of the semivariogram and b is the range. Parameter c takes values between 0 and 2. The same expression can be used to describe $\gamma_y(h)$.

In Figure 1 the stable semivariogram model for various values of c is presented. It can be observed that for c = 0, $\gamma_x(h)$ (or $\gamma_y(h)$) is a straight horizontal line, which presents a nugget effect at h = 0 (the semivariogram takes a value which is other than zero). As long as c increases, the convexity of the semivariogram at low h values changes. For c less than unity, the spatial variation of x is relatively strong at small h values, compared to that of c values between 1 and 2.

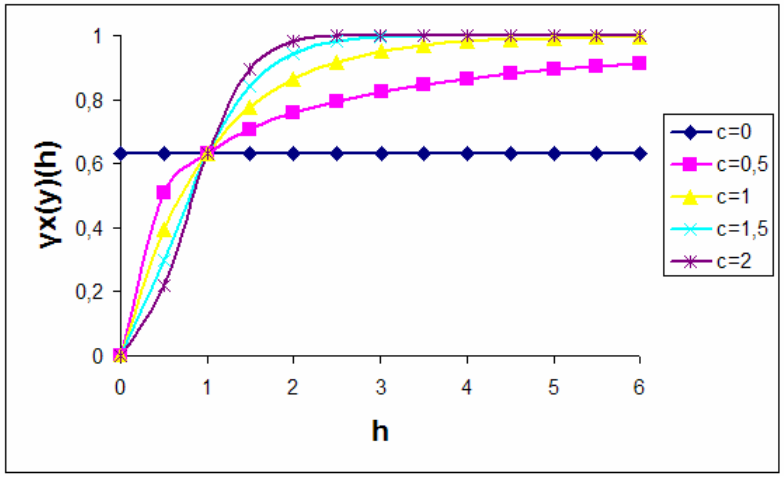

Figure 1 - The stable semivariogram model of *x* and *y* bands for various *c* values. *a*=*b*=1.

Parameter c provides the semivariogram model with a certain flexibility, in order to describe various types of spatial variation.

Assuming that the variances of x and y are small enough in order to linearize the expression of u in terms of x and y, and taking into account a well known theorem of statistics, it can be proved (Skianis 2012, Skianis and Vaiopoulos 2012) that the semivariogram $\gamma_u(h)$ of the simple band ratio u is related to $\gamma_x(h)$ and $\gamma_y(h)$ by:

Equation 4 - the semivariogram $\gamma_u(h)$

$$\gamma_u(h) \cong \left\langle \frac{\partial u}{\partial x} \right\rangle^2 \gamma_x(h) + \left\langle \frac{\partial u}{\partial y} \right\rangle^2 \gamma_y(h) + 2\rho \left\langle \frac{\partial u}{\partial x} \right\rangle \left\langle \frac{\partial u}{\partial y} \right\rangle \sqrt{\gamma_x(h) \cdot \gamma_y(h)}$$

ρ is the correlation coefficient between bands x and y.

The mean values <…> can be found, assuming that the histograms of bands x and y may be modeled by simple positively skewed distributions and that mean values $\langle x \rangle$ and $\langle y \rangle$ are constant along the whole images of the spectral bands (Vaiopoulos et. al. 2004, Skianis 2012). Making these necessary calculations and recalling equation (3) for $\gamma_x(h)$ and $\gamma_y(h)$, equation (4) becomes:

Equation 5 - the final expression for $\gamma_u(h)$

$$\gamma_u(h) \cong \frac{Var(x)}{Var(y)} \left\{ \begin{array}{l} 0{,}273 \cdot \left[1 - \exp\{-[h/b_1]^{c_1}\} + \frac{\pi^2}{4} \cdot \left(1 - \exp\{-[h/b_2]^{c_2}\}\right) \right] - \\ 0{,}858\rho\sqrt{\left(1 - \exp\{-[h/b_1]^{c_1}\}\right) \cdot \left(1 - \exp\{-[h/b_2]^{c_2}\}\right)} \end{array} \right\}$$

$Var(x)$ and $Var(y)$ are the variances of spectral bands x and y, respectively. b_1 and b_2 are the ranges of the semivariograms of x and y, respectively. c_1 and c_2 are the values of c for the semivariograms of x and y, respectively.

Equation (5) provides the theoretical background to study the spatial variation of the simple band ratio u, in terms of the spatial variation of the spectral bands x and y. It is obvious that the sill of the semivariogram $\gamma_u(h)$ depends on the ratio $Var(x)/Var(y)$, as well as on the correlation coefficient ρ between the spectral bands x and y.

In Figure 2, it can be seen how the form of the semivariograms x and y, which is controlled by the parameter c, influences the behavior of $\gamma_u(h)$. For c = 0, a horizontal semivariogram curve is produced. For c = 2, the curve $\gamma_u(h)$ is convex for small values of h. For c = 1, the curve $\gamma_u(h)$ is concave.

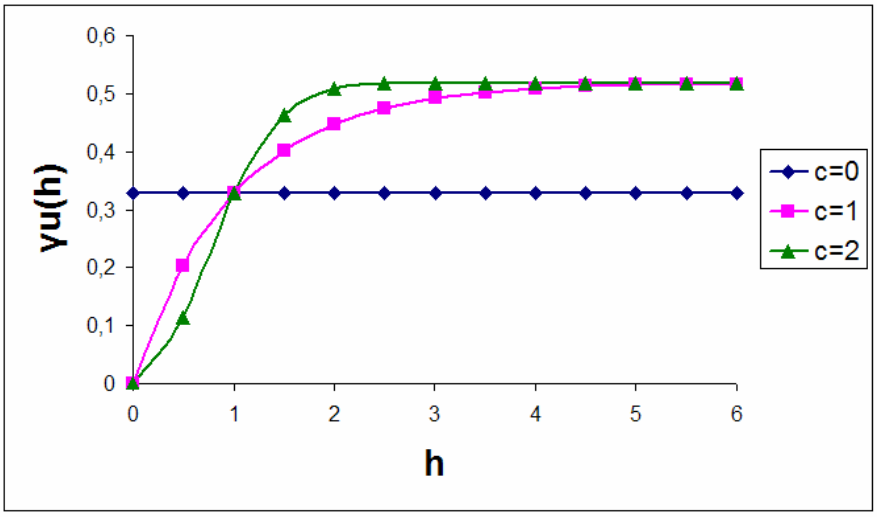

Figure 2 - The semivariogram of *u* for various values of *c*, which is common for the semivariograms of *x* and *y*. *Var*(*x*)=*Var*(*y*), ρ=0,5, b_1=b_2=1.

In Figure 3 and Figure 4, it can be seen how the parameters c_1 and c_2 influence the shape of $\gamma_u(h)$, for various values of the correlation coefficient ρ. For c_1 =1 and c_2 = 2 and small h values, the curve $\gamma_u(h)$ is convex. On the other hand, the curve is concave for c_1 =2 and c_2 = 1. The sill of the semivariogram of u decreases, as long as ρ increases.

In Figure 5 it can be seen how different c_1 and c_2 values produce semivariograms $\gamma_u(h)$ with different characteristics. When c_1 or c_2 is equal to zero, a nugget effect is produced at h = 0. For c_1 and c_2 different from zero, the curve $\gamma_u(h)$ starts from the origin of the axes. $\gamma_u(h)$ is convex at small h values, for c_2 = 2 and c_1 equal to zero or unity. In such a case the semivariogram $\gamma_u(h)$

reaches the sill at lower h values than a concave semivariogram, like that of $c_1 = 2$ and $c_2 = 1$ does.

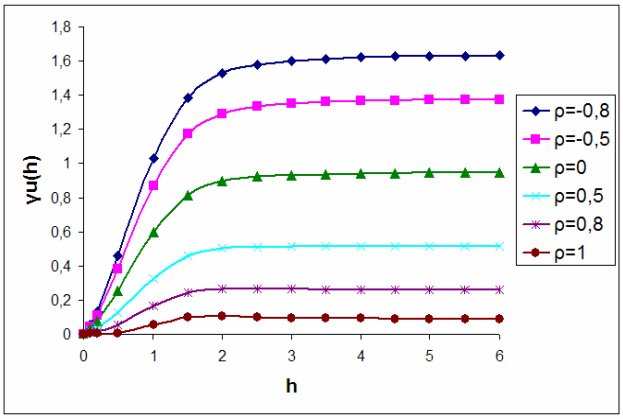

Figure 3 - The semivariogram of u for c_1=1 and c_2=2. $Var(x)=Var(y)$, $b_1=b_2=1$.

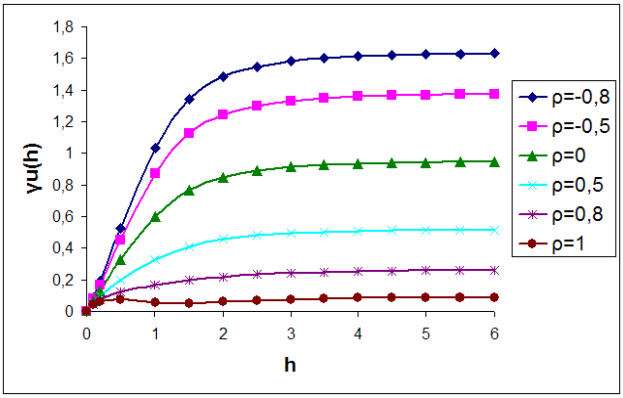

Figure 4 - The semivariogram of u for c_1=2 and c_2=1. $Var(x)=Var(y)$, $b_1=b_2=1$.

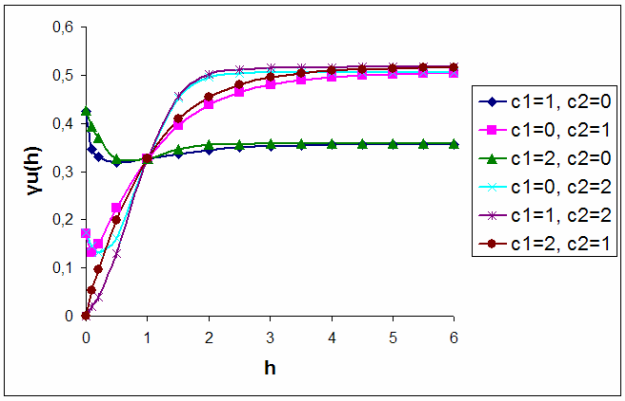

Figure 5 - Semivariograms $\gamma_u(h)$ for various c_1 and c_2 values. $Var(x)=Var(y)$, ρ=0,5, $b_1=b_2=1$.

3. Methodology of Experimentation with a Multispectral Image

One of the main objectives of the present study is to examine and compare the actual semivariograms of satellite imagery (depicting hydrothermal activity and/or mineralization), with the theoretical semivariograms, which can be calculated from equations 3 and 5. The scope of the above objective is to observe and measure how well the theoretical models can fit and predict the real data.

As stated in the introduction, the semivariograms of interest are those of band 5 and band 7 of the Landsat 7 satellite image, as well as the spectral band ratio band5/band7, which can provide valuable information for tracking and mapping hydroxyl-bearing minerals which are related with hydrothermal activity (Parcharidis et. al. 2001, Bodruddoza and Fujimitsu 2012).

Specifically, the methodology in order to obtain the theoretical semivariogram of the band ratio, is described below:

1. First of all, Landsat-7 ETM+ imagery over Milos Island, Aegean Sea, is acquired. It is well known that hydrothermal activity and mineralization is developed in this area (Naden et al. 2003).
2. Secondly, the actual semivariograms of bands 5 and 7 are calculated, using equation (2).
3. Then, the actual semivariogram of band ratio 5/7 is calculated, using the same equation. The calculations of step 1 and step 2, as well as the calculation of the correlation coefficient between the spectral bands, were performed with a Matlab program, which was developed for the purpose of the present study.
4. Afterwards, the theoretical semivariograms of bands 5 and 7 are estimated, assuming that the actual semivariogram can be approximated with proper calibration of the stable semivariogram model. This model is expressed in equation 3. Parameters a and b (sill and range respectively), are now known, since they can be obtained from the previously calculated actual semivariograms of step 2. Parameter c needs manual adjustment and experimentation for fine tuning. The value of c, which yields the best approximation of the actual semivariance curve, is kept.
5. Calculation of the correlation coefficient (ρ) between the two bands (5, 7) is carried out.
6. Finally, the theoretical semivariogram of the band ratio 5/7 can be calculated, by applying the equation 5.

At this point every parameter is known. $Var(x)$ and $Var(y)$ are the sills of the actual semivariograms of band 5 and 7 respectively, calculated in step 2. Parameters b_1 and b_2 are also known from step 2 (range of band 5 and 7 respectively). Parameters c_1 and c_2 are determined in step 4, by a trial and error procedure. The correlation coefficient (ρ) is known from step 5.

4. Area of Interest – Milos Island

In Figure 6, the satellite image of Milos Island is presented. At the eastern part of the island, hydrothermal activity is developed (Fontaine et al. 2003), therefore it is interesting to map the band ratio 5/7, over this area. In Figures 7 and 8, the channels 5 and 7, respectively, over the eastern part of the island, are presented. In Figure 9, the band ratio 5/7 is mapped.

Figure 6 – A Landsat-7 natural color composite (321) of Milos island. Hydrothermal manifestations are present in the studied red framed area, among other sites in the island.

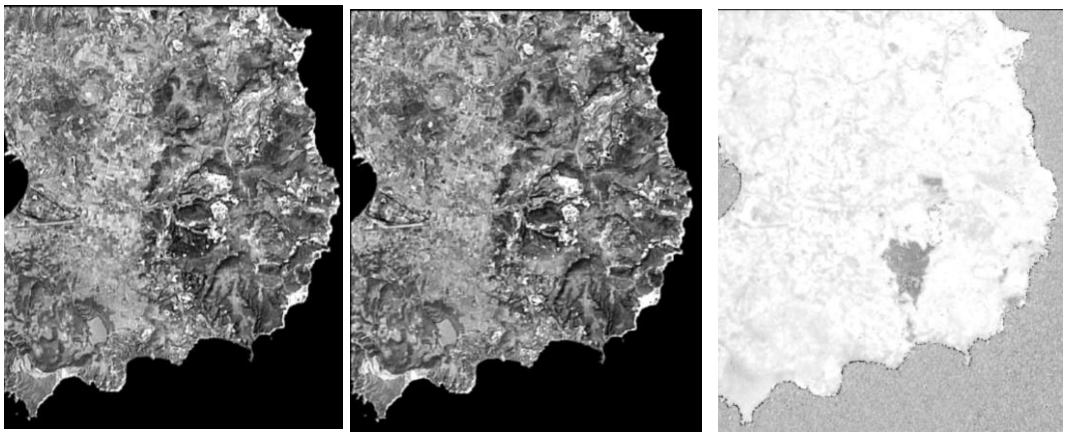

Figure 7, 8 and 9 (Left to right) – Visualization of band 5, band 7 and ratio 5/7 respectively. The images above are depicting the red framed area of figure 6.

5. Results

In Figures 10, 11 and 12 the semivariograms of bands 5 and 7, as well as those of the ratio 5/7 are presented. It must be noted that in the above graphs, y-axis measures semivariance in square brightness values of the image, while x-axis measures distance (h) in pixels. Since the imagery has been pan sharpened from Landsat-7 panchromatic band with the HPF method (Nikolakopoulos et al. 2010, Vaiopoulos 2011), distances must be multiplied by 15, in order to be converted to meters.

Bands 5 and 7 have a very high correlation coefficient, equal to 0.9843.

The horizontal semivariogram of band 5 has been fitted by a stable semivariogram model with a_1 = 3200, b_1 = 80, c_1 = 0.8. The vertical semivariogram of band 5 has been fitted by a_1 = 4000, b_1 = 80, c_1 = 1.0. The parameters of the stable model which fits the horizontal semivariogram of band 7 are a_2 = 2500, b_2 = 250, c_2 = 0.8. Finally, the parameters of the stable model for the vertical semivariogram of band 7 are a_2 = 2500, b_2 = 300, c_2 = 0.6.

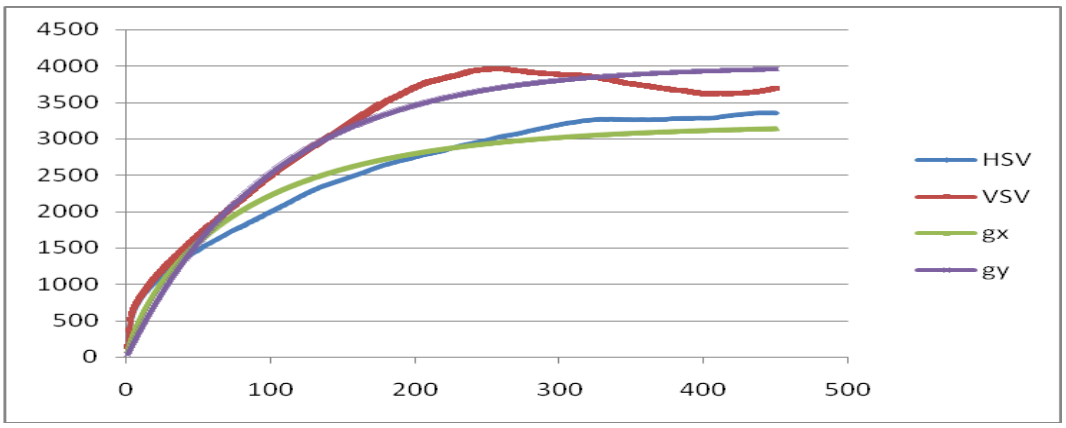

Figure 10 – Actual Horizontal and Vertical semivariograms (HSV, VSV) and theoretical horizontal and vertical semivariograms (gx, gy) of band 5.

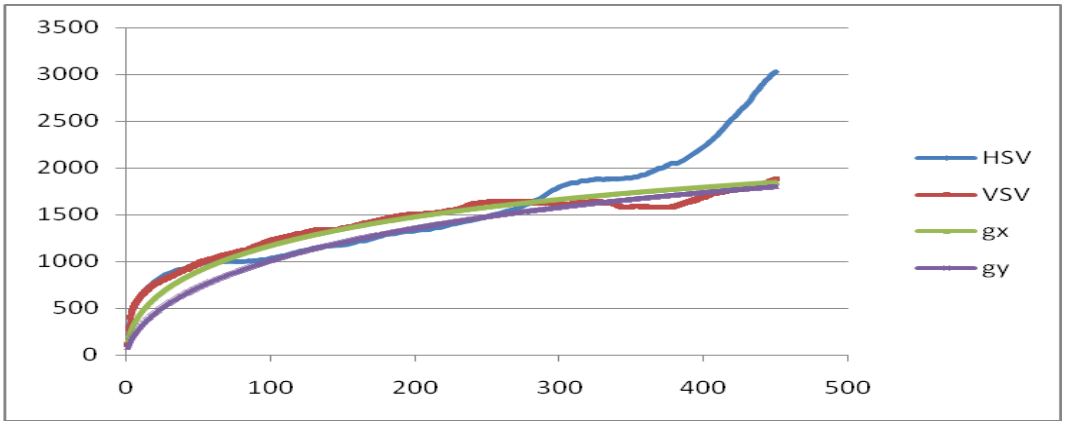

Figure 11 – Actual Horizontal and Vertical semivariograms (HSV, VSV) and theoretical horizontal and vertical semivariograms (gx, gy) of band 7.

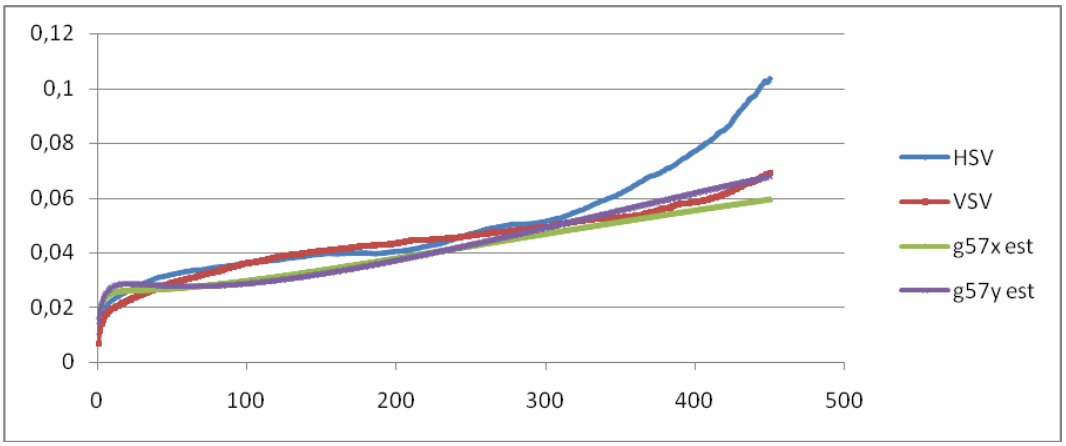

Figure 12 – Actual Horizontal and Vertical semivariograms (HSV, VSV) and theoretical horizontal and vertical semivariograms (g57x est, g57y est) of band ratio 5/7.

From the diagrams of Figures 10 and 11, it can be observed that the stable semivariogram model (equation 3) provides satisfactory approximation of the actual semivariograms for distance ~ 400 pixels (or 6 km). A notable exception is the actual horizontal semivariogram of band 7 (see Figure 11), which presents a strong ascending tendency for h more than 300 pixels (or 4.5 km). This curve should be fitted by a more complex semivariogram model, or by a combination of standard semivariogram models. However, fitting of complex semivariograms is beyond the scope of the present paper. Anyway, with the exception of the actual horizontal semivariogram of band 7, the theoretical models seem to approximate well the actual semivariograms.

In addition, as it can be observed in Figure 12, the theoretically calculated vertical semivariogram according to equation 5, is in good agreement with the actual semivariogram. Considerable deviations between theory and actual data are observed in the case of the horizontal semivariogram 5/7, since the stable model could not fit adequately the horizontal semivariogram of band 7.

6. Discussion and Conclusions

Equation (5) gives an insight on how the spatial variation of the individual spectral bands controls the semivariogram of the band ratio. The ratio $Var(x)/Var(y)$ of the variances (sills) of bands x and y and the correlation coefficient ρ between the two bands control the sill of the semivariogram

$\gamma_u(h)$ of *x/y*. A high $Var(x)/Var(y)$ value favors the production of a semivariogram $\gamma_u(h)$ with a high sill. On the contrary, a high correlation coefficient ρ produces a $\gamma_u(h)$ with a low sill.

The parameter c controls the convexity of the semivariogram $\gamma_u(h)$ at low h values. More specifically, when the parameter c_2 of the semivariogram of y is equal or tends to 2, the curve $\gamma_u(h)$ is convex at low h values, which means that the spatial variation of the spectral ratio *x/y* is relatively smooth for small distances h between pixels. On the other hand, for c_2 more than zero and not exceeding unity, the curve $\gamma_u(h)$ is concave, therefore a relatively strong spatial variation between pixels at small distances h is developed.

The physical meaning of these comments is that in order to produce an image of a spectral band ratio with clearly expressed targets of interest, such as hydrothermal zones, a high ratio $Var(x)/Var(y)$ and a low correlation coefficient between x and y is needed. A low c_2 value of the semivariogram of y (which actually means a concave semivariogram), also favors the production of a *x/y* image with a good spatial variation.

The bands 5 and 7 of the multispectral Landsat ETM+ image of Milos island are very strongly correlated. This is an important reason why the band ratio of Figure 6 has a diffuse bright tonality, which does not help in discriminating different targets of interest. On the other hand, as long as the individual bands 5 and 7 are adequately fitted by the stable semivariogram model, the theoretically calculated semivariogram of the ratio 5/7 is in a good agreement with the actual one.

The results and conclusions of this paper may be useful in mapping hydrothermal zones with the aid of multispectral imagery, in the context of a mineral exploration project.

7. References

Atkinson P.M. 2001. Geostatistical regularization in remote sensing. In Atkinson, N. J. and Atkinson, P. M. (eds), *Modelling Scale in Geographic Information Science*, 237-260, Wiley, New York.

Bodruddoza M. and Fujimitsu Y. 2012. Mapping hydrothermal altered mineral deposits using Landsat 7 ETM+ image in and around Kuju volcano, Kyushu, Japan, *Journal of Earth System Science*, 121(4), 1049-1057.

Curran P.J. 1988. The semivariogram in remote sensing: An introduction, *Remote Sens. Environ.*, 24(3), 493-507.

Fontaine F.Jh., Rabinowicz M. and Boulegue J. 2003. Hydrothermal processes at Milos Island (Greek Cyclades) and the mechanisms of compaction-induced phreatic eruptions, *Earth and Planetary Science Letters*, 210 (1-2), 17-33.

Garrigues S., Allard D. and Baret F. 2007. Using First- and Second –Order Variograms for Characterizing Landscape Spatial Structures From Remote Sensing Imagery, *IEEE Transactions on Geoscience and Remote Sensing*, 45(6), 1823-1834.

Gupta R.P. 2003. *Remote Sensing Geology*, second edition, Berlin, Heidelberg. Springer-Verlag, 655 pp.

Lacaze B., Rambal S. and Winkel T. 1994. Identifying spatial patterns of Mediterranean landscapes from geostatistical analysis of remotely sensed data, *Int. J. Remote Sens*, 15(12), 2437-2450.

Liang S. 2004. *Quantitative Remote Sensing of Land Surfaces*, Wiley-Interscience, New York, 534 pp.

Naden J., Kilias S.P., Leng M.J., Cheliotis I. and Shepherd T.J. 2003. Do fluid inclusions preserve δ18O values of hydrothermal fluids inepithermal systems over geological time? Evidence from paleo- and modern geothermal systems, Milos island, Aegean Sea, *Chemical Geology* 197, 143-159.

Nikolakopoulos K.G., Vaiopoulos A.D. and Tsobos P.I. 2010. Ameliorating the spatial resolution of GeoEye data, *Proc. SPIE 7831, Earth Resources and Environmental Remote Sensing/GIS Applications*, 783104, doi:10.1117/12.864442.

Parcharidis I., Gartzos E. and Psomiadis E. 1999. Alteration zones detection in Lesbos island (Greece), through the application of Landsat 5 TM band ratio images, *Journal of Mineral Wealth* 112, 37-46.

Parcharidis I., Gartzos E. and Psomiadis E. 2001. Evaluation of different remote sensing methods for the detection of hydrothermal alteration zones in Milos island (Greece). *Proceedings of the 9th International Congress of the Geological Society of Greece*, Vol. 5, 2047-2054.

Skianis G. Aim. and Vaiopoulos A. D. 2012. The spatial variation of a spectral band ratio with a considerable correlation between the bands, *Proceedings of the 4th EARSel Workshop on Remote Sensing and Geology*, Mykonos, Greece, 24th-25th May 2012, 28-43.

Skianis G. Aim. 2012. The problem of the spatial variation of a spectral band ratio: a first order approach based on probability theory, *Earth Science Informatics*, 5(1), 13-21.

Skianis G. Aim., Nikolakopoulos K. G. and Vaiopoulos D. A. 2012. *Remote Sensing*, Athens, Ion publications, 336 pp.

Vaiopoulos A.D. 2011. Developing Matlab scripts for image analysis and quality assessment, *Proc. SPIE 8181, Earth Resources and Environmental Remote Sensing/GIS Applications II*, 81810B, doi:10.1117/12.897806.

Vaiopoulos D. A., Skianis G. Aim. and Nikolakopoulos K. 2004. The contribution of probability theory in assessing the efficiency of two frequently used vegetation indices, *International Journal of Remote Sensing*, 25(20), 4219-4236.

Woodcock C.E., Strahler A. and Jupp D.L.B, 1988a. The use of variograms in remote sensing: A/scene models and simulated images, *Remote Sens. Environ*, 25(3), 323-348.

Woodcock C.E, Strahler A.H. and Jupp D.L.B. 1988b. The use of variograms in remote sensing: B/Real digital images, *Remote Sens. Environ*, 25(3), 349-379.

Δελτίο της Ελληνικής Γεωλογικής Εταιρίας, τομ. XLVII , 2013
Πρακτικά 13ου Διεθνούς Συνεδρίου, Χανιά, Σεπτ. 2013

Bulletin of the Geological Society of Greece, vol. XLVII 2013
Proceedings of the 13th International Congress, Chania, Sept. 2013

AGGREGATE TRANSPORT AND UTILIZATION: ECOLOGICAL FOOTPRINT AND ENVIRONMENTAL IMPACTS

Agioutantis Z.[1], Komnitsas K.[1] and Athousaki A.[2]

[1] Department of Mineral Resources Engineering, Technical University of Crete, 73100 Hania, Greece zach@mred.tuc.gr, komni@mred.tuc.gr

[2] Civil Engineer, Hania

Abstract

The Ecological Footprint (EF) measures how much of the biosphere's annual regenerative capacity is required to renew the natural resources used by a defined population in a given year. In essence, the EF is a resource accounting tool that measures how much biologically productive land and sea is used by a given population or activity, and compares this with the available land and sea.
Productive land and sea support population demands for food, fiber, timber, energy, and space for infrastructure. These areas also absorb gaseous emissions (i.e. CO_2) generated from human activities.
The present paper discusses a methodology that allows the parametric estimation of the EF due to the transport of aggregates to urban areas as a function of tonnage and distance.
Key words: *quarry, emissions, sustainable aggregate management.*

Περίληψη

Το οικολογικό αποτύπωμα (ΟΑ) μιας διεργασίας προσδιορίζει την ετήσια ικανότητα της βιόσφαιρας να ανανεώνει τις φυσικές πρώτες ύλες που χρησιμοποιήθηκαν από συγκεκριμένο πληθυσμό ένα συγκεκριμένο έτος. Βασικά, το ΟΑ είναι ένα λογιστικό εργαλείο που μετατρέπει τις χρησιμοποιηθείσες, από συγκεκριμένο πληθυσμό ή δραστηριότητα, πρώτες ύλες σε παραγωγική γη και θάλασσα και τις συγκρίνει με τα αντίστοιχα διαθέσιμα μεγέθη.
Η παραγωγική γη και θάλασσα υποστηρίζει τις ανάγκες του πληθυσμού σε τρόφιμα, ίνες, ξυλεία, ενέργεια και χώρο για υποδομές, ενώ λαμβάνεται υπόψη η δυνατότητα της βιόσφαιρας να απορροφήσει τις αέριες εκπομπές, π.χ. CO_2, οι οποίες παράγονται από ανθρώπινες δραστηριότητες.
Στην εργασία αυτή παρουσιάζεται μια μεθοδολογία παραμετρικής εκτίμησης του ΟΑ της διαδικασίας μεταφοράς αδρανών υλικών (για χρήσεις στο αστικό περιβάλλον) ως συνάρτηση της ποσότητας και της απόστασης μεταφοράς.
Λέξεις κλειδιά: *λατομείο, εκπομπές ρύπων, βιώσιμη διαχείριση αδρανών.*

1. Introduction

Economic development is closely linked to the extraction and use of natural resources. Over the recent decades, however, the demand for natural resources has increased dramatically and has created huge environmental problems including biodiversity loss, ecosystem degradation and climate change, and, thus, it is now considered as a serious threat to the economic and social equilibrium of the planet. One of the key sustainability challenges for the following decades is to improve the management of natural resources in order to reduce current levels of anthropogenic environmental pressure.

The extensive use of natural aggregates in construction projects has been gradually depleting this resource near the areas where aggregates are in high demand. The need for resource conservation and longer transportation distances highlights the need to quantify the environmental impacts associated to aggregates production, transport and utilization as well as to assess potential and demand for substitute materials (Henry et al., 2011). Aggregates consist of natural, artificial or recycled materials. In essence, natural aggregates can be considered as non-renewable, non-metallic and non-fossil mineral resources that are vital for modern societies. Natural aggregates are produced in surface or underground quarries, while artificial or recycled materials used for aggregates (i.e. broken glass, slag, etc) are processed in industrial plants.

The production of aggregates is the fastest growing activity worldwide since huge quantities (about 15 billion t/y) are required by the construction industry; the total direct value of this production is estimated to be in the order of €20 billion (UEPG, 2013). The U.S. Geological Survey (USGS) in its 2013 Mineral Commodity Summaries estimates that the U.S. aggregates production of 2.08 billion tons in 2012 increased by about 7.6 percent over 2011 numbers (USGS, 2013). The value of primary aggregates produced in the U.K was £1.425bn in 2009, representing nearly a 30 percent drop from values shown in 2006 through to 2008 of around 1.8bn. The total aggregates sales in Great Britain in 2009 were 198 million tons. This is down from a peak in the late 1980s of 330 million tons of which 300 million were primary aggregates. Sales of recycled and secondary aggregates have grown steadily accounting for just over 50 million tones (UK Office of Fair Trading, 2011).

Construction aggregates are essential and valuable resources for the economic and social development. Recycled aggregates (RA) and natural aggregates (NA) are not therefore in competition, but their joint utilization is considered as strategic for the construction industry. Transportation contributes heavily to the life cycle impacts of aggregates. Under different assumptions relevant to transportation distances, and considering the type and grade of RA, as well as local availability of NA, it is possible to define the geographical coverage of market demand in order to identify and quantify energy consumption and environmental impacts (Blengini and Garbarino, 2010).

The quantity of aggregates used in construction applications varies from country to country and depends on the type, size and quality of applications. Table 1 presents estimates of aggregate consumption for two activities associated with urban areas: housing and road construction.

Table 1 - Estimates of aggregate consumption for two activities associated with housing and road construction.

Country	Housing	Highways	Reference
UK	60 tons / average house	7,500 tons/km (single motorway lane)	Brown et al., 2008
US	400 tons / average house	20,000 tons/km (4 lane highway)	USGS, 2006
Greece	3.22 / m^2 of a house	36,400 tons/km (6 lane road)	Kaliampakos and Benardos, 2000

It is thus estimated that in the U.K 60 tons of aggregates are required for the construction of an average house (assuming that no construction of roads or other infrastructure is required); for the construction of 1 km of a single motorway lane 7,500 tons of aggregates are required. In the USA these figures amount to 400 and 5,000 tons respectively. In Greece, earlier studies estimate that 3.22 tons of aggregates are required for every m^2 of a house, while for the construction of 1 km of a 6 lane highway 36,400 tons are required. Even if the number of large construction projects will decrease in the near future in this recession period, demand for aggregates is expected to continue at reasonable levels due to projected population growth and demand for infrastructure improvements and maintenance.

2. Ecological Footprint

2.1. General Issues

Sustainable development has become a primary objective for almost all countries since the late 1980s. A major difficulty associated with sustainable development objectives, however, is the absence of reliable indicators to measure progress towards the goal of sustainability. An accurate indicator to do so is the Ecological Footprint (EF) which measures how much of the biosphere's annual regenerative capacity is required to renew the natural resources used by a defined population in a given year. On an aggregate basis, the EF may be compared with the area of ecologically productive land available to provide an indication of whether consumption patterns are likely to be sustainable (Venetoulis and Talberth, 2006).

EFs can be calculated for individuals, groups of people (such as a nation), and activities (such as manufacturing a product). The EF is the leading biophysical accounting tool for comparing present aggregate human demand on the biosphere with the ecological capacity to sustain life (Niccolucci et al., 2012).

Recently, a number of organizations and governments have begun using the term Carbon Footprint (CF) to refer to the quantities of CO_2 emissions associated with a specific activity, process, or product. This carbon footprint, typically measured in tons of CO_2, is an initial step towards calculating a full CF, which in turn is a percentage of the total EF. CF translates as tons of CO_2 released and is measured as the total area, in global hectares, required to sequester these carbon emissions (GFN, 2008). A full CF systematically covers the complete supply chain and, therefore, all the stages of the lifecycle of a process or product in a systematic way. The footprint is strongly correlated with the per capita consumption expenditure. In Greece for example, the per capita GHG Footprint for 2001 was 13.7 tCO_2e per person per year (py), while the construction sector accounted for 14% (Hertwich and Peters, 2009).

Non-renewable fossil fuels are treated differently from other minerals since they actually represent ancient materials of biological origin, and their combustion releases CO_2, which is part of the biosphere's material cycles. The footprint of carbon released from the combustion of fossil fuels is, therefore, defined as the productive area required to sequester the generated CO_2 and prevent its accumulation. An alternative method would be to calculate the consumption of fossil fuels according to the productive area required to regenerate them, which would result in a CF much higher than the current calculation (GFN, 2008).

Non-renewable mineral resources, excluding fossil fuels, i.e., copper, iron, etc., do not have an EF in the same way as one ton of timber, which requires bio-productive area for its production. There is, however, an EF associated with the energy and other materials used in extracting, refining, processing, and shipping these mineral resources; all of these factors are often reported as the EF or CF of the specific mineral resource. At the same time, it should be emphasized that when mined materials such as mercury or arsenic enter the environment, they may cause damage and loss of productivity; all these impacts can be properly addressed in an appropriate Life Cycle Analysis (LCA) study, which is a method of accounting for the environmental impacts associated with a

product, a process or a service (Chowdhury et al., 2010). Since aggregates are an abiotic resource, several other indicators can be used to assess environmental impacts in LCA studies. These can be based on a thermodynamic approach (use of energy or exergy indicators), on a mass flow approach (use of a total mass requirement indicator), on a surplus of energy that will be needed for future extractions (eco-indicator approach, Goedkoop and Spriensma, 2001) or on a scarcity approach.

Transportation includes emissions associated to the production of fuels, focusing on well-to-wheel analysis. Well-to-wheel is the specific LCA that is carried out for transport of fuels and vehicles, and is commonly used among others to assess total energy consumption, or the energy conversion efficiency and emissions impact of motor vehicles including their CF and the fuels used in this transport means. However, it does not take into account the production of the vehicles, which, alone, emitted some 1000 million metric tons of CO_2 equivalent ($MtCO_2e$); this figure is comparable to aviation emissions. Life-cycle assessments indicate that about half of the GHG emissions of the car manufacturing sector are related to materials, and since car manufacturing involves complex international supply chains, a detailed analysis of the emissions from the production of imported products is essential (Hertwich and Peters, 2009).

2.2. Definitions

The EF is usually measured in 'global hectares'. A global hectare is defined as a hectare with world-average productivity for all biologically productive land and water in a given year. Biologically productive land includes areas such as cropland, forest, and fishing grounds, and excludes deserts, glaciers, and the open ocean (GFN, 2008).

Some researchers and organizations measure the EF in productive hectares, land hectares or forest hectares, while others in tons of carbon instead of carbon dioxide or in hectares/year. Table 2 presents a comparison of a number of definitions. It is immediately evident that there is a wide range of values for the EF. The evaluation of the assumptions and results for each study is beyond the scope of the present paper.

It is known that oceans cover 72% of the earth's surface, while forests cover around 29% of continents. Based on this data, extreme values shown in Table 2 and representing only specific systems were disregarded and values involving global hectares were considered; the more representative value of 3.75 tons CO_2/year/hectare was used in this study.

Construction aggregates are usually transported in bulk in large trucks or containers in order to achieve economy of scale. A typical unit used for freight calculations is expressed as the product of [Payload x Distance]; this is commonly expressed as a ton-km. The transportation cost decreases as the cost per ton-km decreases. Figure 1 presents a conceptual diagram of how supply locations A and B may service demand locations 1, 2, and 3. The products A1, A2, A3 and B1, B2, B3 correspond to the resulting ton-km for each route. The issue becomes more complicated when two or more sources of aggregates are available in a given area. Large trucks will achieve a lower unit transportation cost, but appropriate road infrastructure should be available.

3. Estimating the EF of Aggregate Transport

In this study, emphasis was given to the utilization of conventional transport vehicles and principally the consumption of fuel, which is the dominating component of this operation. The production chain of fuel including crude oil extraction, refining and distribution as well as the manufacturing of production plants and the manufacturing of vehicles was not taken into account. The average fuel consumption per ton-km is based on the work by Erkkila (2005) (Figure 2).

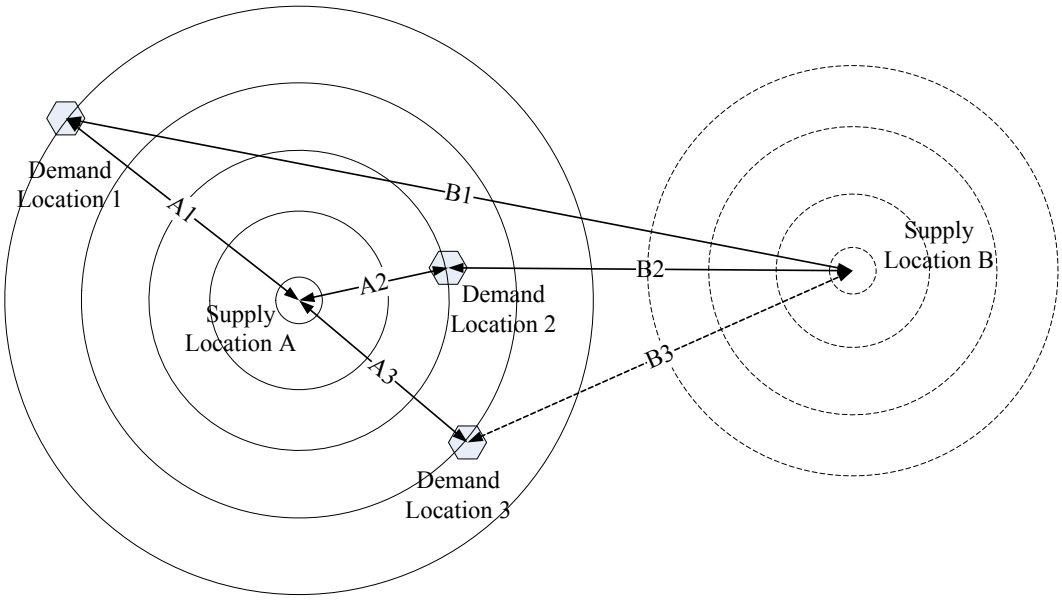

Figure 1 - Conceptual diagram of transportation options between two supply and three demand locations.

Table 2 - Definitions of Ecological Footprint.

Hectare description	**EF** $t\ CO_2\ y^{-1}\ ha^{-1}$	**Reference**
Productive hectare (unproductive land and water surface areas were excluded)	0.059	Zhang (2005)
Global hectare (EFs have been calculated for six land use categories)	3.73	EPA Victoria (2005); Wackernagel et at. (2004)
Global hectare (includes the entire surface of the Earth in biocapacity)	0.22	Venetoulis and Talberth (2006)
Forest hectare (Natural eucalypt forest systems of NSW Australia)	0.15	Livesley (2007)
Forest hectare (environmental trees at age 10)	5-10	Carruthers (2008)
Forest hectare in high rainfall regions	20	Carruthers (2008)
Forest of growing trees	6	UNEP (2008)
Global hectare of year 2003, fossil fuel	3.77	WWF (2006)

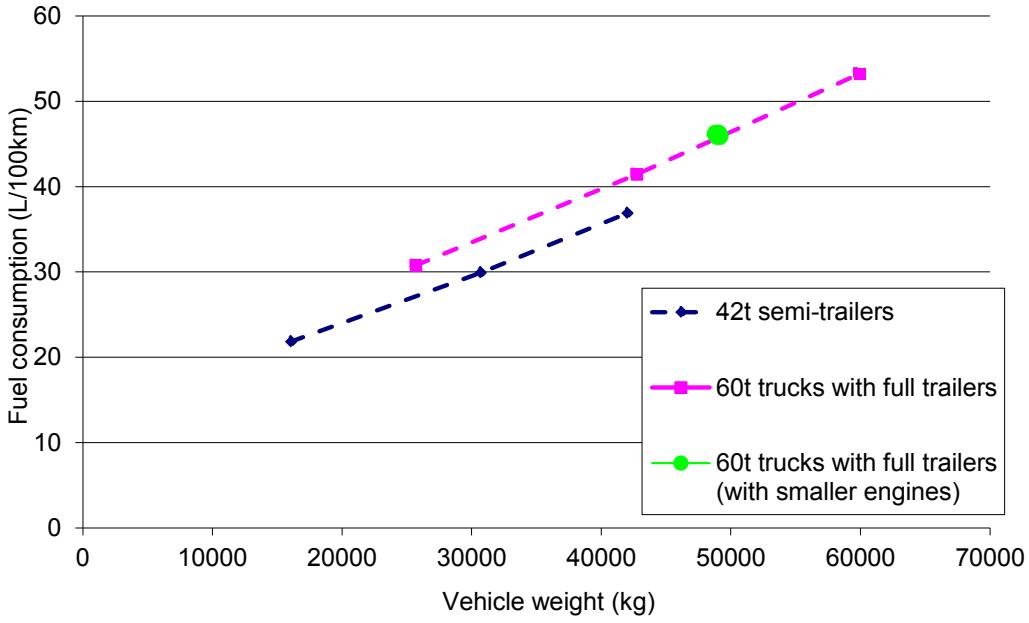

Figure 2 - Estimation of fuel consumption on highway cycle (Erkkila, 2005).

In order to estimate the EF of aggregate transport the following assumptions/simplifications are considered:

- Only large trucks are used.
- Highway cycle is applied.
- Fuel consumption is converted to fuel emissions assuming the use of diesel fuel.
- Only CO_2 emissions are taken into account (i.e. equivalent NO_x or SO_x emissions are ignored).
- Using data for 60ton trucks (which corresponds to a payload of about 35 tons), it is calculated that the consumption on a highway cycle is about 55L/100km. This value is quite similar to the value suggested by EPA for truck mileage which is in the order of 5mpg (miles per US gallon; US 2007), or about 47L/100km. Hence the consumption per ton-km was taken as 0.0148L/ton-km. Similar data compiled for the British Department of Transport can be summarized in Table 3 (UK Department of Transport, 2007).

Figure 3 presents the steps utilized in order to perform the parametric analysis. For each step the following data/assumptions were used:

- Based on Table 3, a higher fuel consumption, in terms of L/ton-km, was considered for smaller trucks under the assumption that for every 5 tonne reduction of payload, the specific fuel consumption increases by 0.001 L/ton-km.
- The CO_2 emitted per liter of diesel was taken as 2.6kg CO_2 per liter (UNEP, 2008). Thus CO_2e was calculated.
- To convert the CO_2e to the area required to absorb the emitted CO_2 the value of 3.7 tons CO_2/year/hectare was used. It should be noted that similar graphs can be generated for any value of tons CO_2/year/hectare.

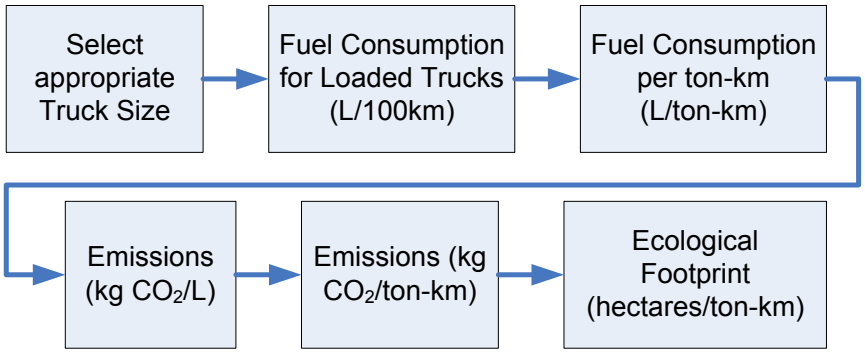

Figure 3 – Steps in parametric analysis.

Table 3 - Specific fuel consumption for truck transport (UK Dept. of Transport, 2007).

Condition	Miles per gallon	Liters per ton-km
44 tonne truck empty (16 tonnes)	10.27	0.017
10 tonnes cargo	7.44	0.015
16 tonnes cargo	6.53	0.014
28 tonnes cargo	5.51	0.012

The results derived are presented in the form of parametric graphs. Figure 4 shows a chart for consumption (L/100km) versus distance (km) for different truck payloads. It is evident that the absolute consumption increases with the heavier trucks, while the specific consumption ranges from 0.012L/ton-km for the 35tonne payload to 0.017L/ton-km for the 10tonne payload.

Figure 5 shows the CO_2e for a 10 tonne payload trucked under different conditions. In this case, the CO_2 decreases when the specific fuel consumption decreases for higher payloads. As an example, 10 tonnes of aggregates trucked for a distance of 50km using a 10tonne payload truck will generate about 22kg of CO_2e, while if the same material is trucked in a 35tonne payload truck it will generate about 15kg of CO_2e.

4. Other Issues for Consideration

4.1. Transport Cost

Aggregate transport cost cannot be easily compared between countries. It is known that diesel prices differ substantially among USA, EU Member States, South East Europe (SEE countries) and Eastern Europe, Caucasus and Central Asia (EECCA countries) (EEA, 2012), making thus difficult to compare costs for the transport of aggregates in different regions. Usually fuel prices increase by 3 cents per litre for each USD increase in the oil price per barrel, but this is not the case in several countries. By taking into account different custom costs and increased taxation, imposed on fuels in this recession period in many parts of the world, it is difficult to predict diesel prices in the future and thus calculate and compare cost of transport. A very good example is the evolution of diesel price in Luxembourg and Italy as a result of the increase of oil price in 2007. When the start of the year one barrel oil cost 50.77 USD, 1 L diesel was sold for 0.85€ in Luxembourg and for 1.16€ in Italy. The barrel price increased about 72.58% until the end of year 2007 and was sold 87.62 USD in December. For the same period the increase in the price of one litter of diesel was 14.11% in Luxembourg and 17.24% in Italy.

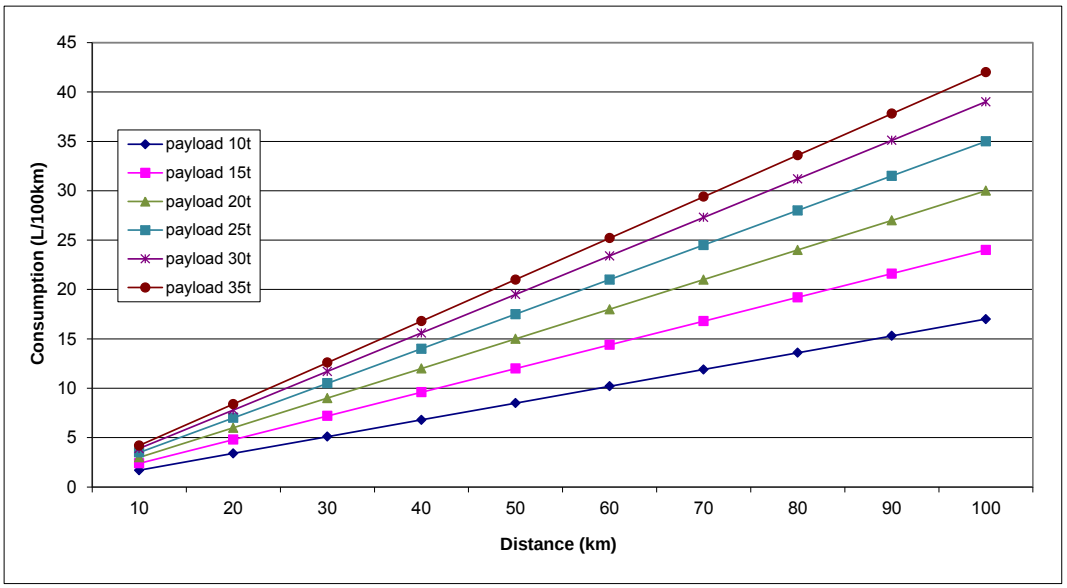

Figure 4 – Consumption vs Distance.

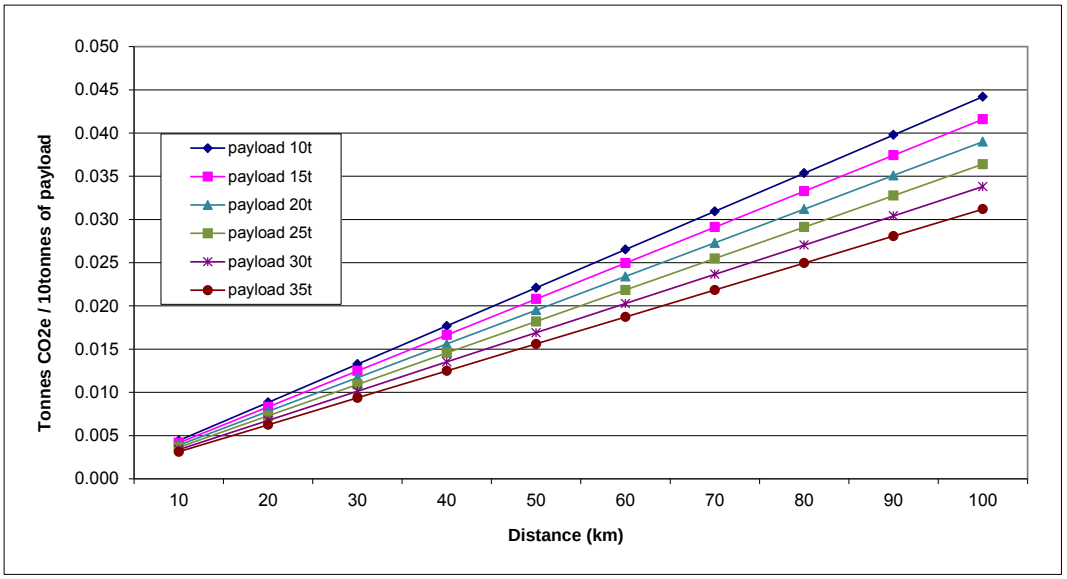

Figure 5 – Equivalent tonnes of CO_2 as a function of specific payload.

4.2. Intermediate Transport Stations

As quarries are pushed away from the urban and suburban environment, transfer of aggregates to the urban consumers becomes more expensive and more challenging. In addition, the EF of such operations is definitely becoming higher, especially if smaller vehicles are used to transport aggregates for longer distances.

A sustainable solution proposed in this paper is to use transport stations close to urban environments. Thus, bulk material can be transported in large vehicles, trains or boats if possible to intermediate stations, and then distributed to the consumer using smaller vehicles. The EF of

such an operation should be calculated by taking into account the EF for unloading, reloading and maintaining aggregate stockpiles in transport stations. The wide utilization of ready mix stations, except for the quality advantage, contributes to the reduction of the EF footprint of aggregate transport, since only the necessary materials will be transported to the end user and in the requested quantity.

5. Conclusions

The need for resource conservation and longer transportation distances highlights the importance to quantify the environmental impacts associated to aggregates production, transport and utilization as well as to assess potential and demand for substitute materials. In this paper a methodology followed for a parametric estimation of the Environmental Footprint (EF) for the transport of aggregates for urban applications as a function of tonnage and distance is presented.

Fuel consumption, in terms of L/ton-km, was calculated for different truck payloads. It was assumed that for every 5 tonne reduction of payload, the specific fuel consumption increases by 0.001 L/ton-km. The CO_2e was calculated using the estimated CO_2 emissions per liter of diesel. In order to convert the CO_2e to the area required to absorb the emitted CO_2 the value of 3.7 tons CO_2/year/hectare was used. It was calculated that 10 tonnes of aggregates trucked for a distance of 50km using a 10tonne payload truck will generate about 22kg of CO_2e, while when the same material is trucked in a 35tonne payload truck it will generate about 15kg of CO_2e.

Finally, by considering the probability that in the near future a number of quarries will be relocated and new quarries will be sited far away from urban centres, the establishment of intermediate transport stations close to urban environments seems to be a feasible and sustainable option.

6. Acknowledgements

The authors would like to acknowledge the financial support of the European Commission for the projects SARMa (Sustainable Aggregates Resource Management), Contract No SEE AF/A/151/2.4/X (www.sarmaproject.eu), and SNAP-SEE (Sustainable Aggregates Planning in South East Europe), Contract No SEE/D/0167/2.4/X (http://www.snapsee.eu).

7. References

Blengini G.A. and Garbarino E. 2010. Resources and waste management in Turin (Italy): the role of recycled aggregates in the sustainable supply mix, *J. Clean Prod.*, 18, 1021-1030.

Brown T.J., McEnvoy F., Mankelow J., Ward J., Bloomfield S., Goussarova T., Shah N. and Souron L. 2008. The need for indigenous aggregates production in England, *British Geological Survay Open Report*, OR/08/026, 74 pp.

Carruthers I. 2008. International, Land and Analysis Division, Australian Greenhouse Office, URL:http://www.abc.net.au/science/expert/realexpert/energy/05.htm (accessed January 18, 2013)

Chowdhury R., Apul D. and Fry T. 2010. A life cycle based environmental impacts assessment of construction materials used in road construction, *Resour. Conserv. Recycl.,* 54, 250-255.

EEA (European Environment Agency), http://www.eea.europa.eu/data-and-maps/figures/petrol-and-diesel-fuel-prices-in-europe-by-region (accessed January 25, 2013)

EPA Victoria 2005. EPA Ecological Footprint Calculators: Technical Background Paper, http://epanote2.epa.vic.gov.au/EPA/Publications.nsf/2f1c2625731746aa4a256ce90001cbb5/f4750e35750290ecca256fbd000b030c/$FILE/972.pdf (accessed January 11, 2013)

Erkkila K. 2005. Heavy-duty truck emissions and fuel consumption simulating real-world driving in laboratory conditions, 2005 DEER Conference, 21-25 August, Chicago, Illinois, USA.

GFN (Global Footprint Network) 2008. http://www.footprintnetwork.org/, (accessed January 18, 2013).

Goedkoop M. and Spriensma R. 2001. The Eco-indicator 99, a damage oriented method for Life Cycle Impact Assessment, methodology report. PRé Consultants B.V., 132 pp. http://www.pre.nl (accessed March 1, 2013)

Henry M., Pardo G., Nishimura T. and Kato Y. 2011. Balancing durability and environmental impact in concrete combining low-grade recycled aggregates and mineral admixtures, *Resour. Conserv. Recycl.,* 55, 1060-1069.

Hertwich E. and Peters A. 2009. Carbon Footprint of Nations: A Global, Trade-Linked Analysis, *Environ. Sci. Technol.*, 43, 6414-6420.

Kaliampakos D. and Benardos A. 2000. Quarrying and sustainable development in large urban centres: A contradiction in terms?, *CIM Bull.*, 93, 86-89.

Livesley S. 2007. Mitigating greenhouse gases, http://www.onlineopinion.com.au/view.asp?article=6257 (accessed March 11, 2013)

Niccolucci V., Tiezzi E., Pulselli F.M. and Capineri C. 2012. Biocapacity vs Ecological Footprint of world regions: A geopolitical interpretation, *Ecol. Indic.*, 16, 23-30.

UEPG (European Aggregates Association) 2013. http://www.uepg.eu/statistics/current-trends (accessed Feb. 28, 2013)

UNEP 2008. Tool 18 (excel inventory option), sheet 'Impacts-Climate Change', United Nations Environment Programme, www.unep.org/tut-unep/tolkit/index.htm (accessed 19 March 2013

UK Department of Transport 2007. Effects of payload on the fuel consumption of trucks, http://www.freightbestpractice.org.uk/effects-of-payload-on-fuel-consumption-of-trucks/ (accessed March 15, 2013).

UK Office of Fair Trading 2011. Aggregates. Report on the market study and proposed decision to make a market investigation reference, August 2011, Fleetbank House, 2-6 Salisbury Square, London EC4Y 8JX

US 2007. Combination Truck Fuel Consumption and Travel, table 4-14, http://www.bts.gov/publications/ national_transportation_statistics/2007/index.html

USGS (U.S. Geological Survey) 2006. Materials in use in U.S. interstate highways, Fact Sheet 2006–3127, October 2006, http://pubs.usgs.gov/fs/2006/3127/2006-3127.pdf (accessed March 5, 2013).

USGS (U.S. Geological Survey) 2013. Mineral commodity summaries 2013: U.S. *Geological Survey*, 198 p., Reston, Virginia, January 24, 2013.

Venetoulis J. and Talberth J. 2006. Refining the ecological footprint, *Environ. Dev. Sustain.*, 10, 441-469.

Zhang T. 2005. Ecological footprint budgeting: Environmental analysis of the generic American car. Green Manufacturing Group, Laboratory for Manufacturing and Sustainability, UC Berkeley, http://www.escholarship.org/uc/item/55z9v0f2, (accessed March 7, 2013)

Wackernagel M., White K.S. and Moran D. 2004. Using Ecological Footprint accounts: from analysis to applications, *Int. J. Environ. Sust. Dev.*, 3, 293-315.

WWF 2006. Living Planet Report 2006, http://wwf.panda.org/about_our_earth/all_publications/living_planet_report/living_planet_report_timeline/lp_2006/, (accessed January 9, 2013)

Δελτίο της Ελληνικής Γεωλογικής Εταιρίας, τομ. XLVII , 2013
Πρακτικά 13ου Διεθνούς Συνεδρίου, Χανιά, Σεπτ. 2013

Bulletin of the Geological Society of Greece, vol. XLVII 2013
Proceedings of the 13th International Congress, Chania, Sept. 2013

THE TECTONO – STRATIGRAPHIC EVOLUTION OF EASTERN MEDITERRANEAN WITH EMPHASIS ON HERODOTUS BASIN PROSPECTIVITY FOR THE DEVELOPMENT OF HYDROCARBON FIELDS

Elia C.[1], Konstantopoulos P.[1], Maravelis A.[2] and Zelilidis A.[1]

[1]University of Patras, Department of Geology, Laboratory of Sedimentology, 26504 Patras, Greece, A.Zelilidis@upatras.gr
[2]School of Environmental and Life Sciences, University of Newcastle, Callaghan 2308 NSW, Australia, Angelos.Maravelis@newcastle.edu.au

Abstract

The eastern part of the Mediterranean Sea is of great geological interest. One of the main interesting topics is the genesis and the development of hydrocarbon fields in the area. The analysis of the palaeogeographic evolution of two major basins in eastern Mediterranean Sea, such as Levantine basin and Herodotus basin, shows the same evolution and accommodate the same sediment types. Also, the presence of the Eratosthenes Continental Block (E.C.B.) and the Nile cone, have their own role in the development of the basins and the wider Eastern Mediterranean region. With the help of seismic data, petroleum geology, the evolution of both basins and other geological structures of the region, we can compare the two basins. From the comparison we concluded that Herodotus basin hosts at least the same amount of gas and oil as the Levantine basin.
Key words: Levantine basin, Herodotus abyssal plain, hydrocarbons, eastern *Mediterranean*.

Περίληψη

Το Ανατολικό τμήμα της Μεσογείου παρουσιάζει έντονο γεωλογικό ενδιαφέρον. Μεγάλο ενδιαφέρον παρουσιάζει το θέμα γένεσης και ανάπτυξης πεδίων υδρογονανθράκων στην περιοχή. Η ανάλυση της παλαιογεωγραφικής εξέλιξης των δυο κύριων λεκανών της ανατολικής Μεσογείου, της λεκάνης Λεβαντίνης και Λεκάνης Ηροδότου, δείχνουν ίδια εξέλιξη, φιλοξενώντας ίδιους τύπους ιζημάτων. Επίσης η παρουσία του ηπειρωτικού μπλοκ του Ερατοσθένη και του κώνου του Νείλου διαδραματίζουν το δικό τους ρόλο στην ανάπτυξη των λεκανών αλλά και της ευρύτερης περιοχής της Ανατολικής Μεσογείου. Με τη βοήθεια σεισμικών δεδομένων, της γεωλογίας πετρελαίων, την ιστορία εξέλιξης των δυο λεκανών και των υπόλοιπων γεωλογικών δομών της περιοχής, γίνεται μια σύγκριση μεταξύ τους. Από τη σύγκριση των λεκανών συμπεραίνεται ότι η λεκάνη Ηροδότου φιλοξενεί τουλάχιστον τις ίδιες ποσότητες σε φυσικό αέριο και πετρέλαιο με την λεκάνη της Λεβαντίνης.
Λέξεις κλειδιά: *Λεκάνη Λεβαντίνης, Αβυσσικό πεδίο Ηροδότου, Υδρογονάνθρακες, Ανατολική Μεσόγειος.*

1. Introduction

The hydrocarbons in order to produced in high concentrations and can be regarded as economically exploitable, should be kept the following requirements: existence of source rock, migration conditions, existence of reservoir, seal, and trap. The source rocks are fine sediments rich in organic material and which contain the precursors to hydrocarbons, such that the type and quality of expelled hydrocarbon can be assessed. The organic material in order to generate hydrocarbons must be buried in such depths as far as the temperature is between 90^{o} - 120^{0}C. The reservoir is a porous and permeable rock that hosts the hydrocarbon reserves. Analysis of reservoir at the simplest level requires an assessment of their porosity, in order to calculate the volume of hydrocarbons and their permeability in order to calculate how easily the hydrocarbons will flow out of them. The seal rock is a unit with low permeability that impedes the escape of hydrocarbons from the reservoir rock. Common seals include evaporates, chalks and shales. Analysis of seals involves assessment of their thickness and extent; such their effectiveness can be quantified. The trap is the stratigraphic or structural feature that ensures the juxtaposition of reservoir and seal such that hydrocarbons remain trapped in the subsurface, rather than escaping and being lost. Finally, careful studies of migration on how hydrocarbons move from source to reservoir and help quantify the source of hydrocarbons in a particular area.

In this paper we analyse the above requirements in the Levantine basin and compare them with Herodotus basin.

2. Geological Setting

The Levantine basin is located SE of Cyprus in eastern Mediterranean Sea (Figure 1). It is a fore-land basin at the southern end of the front of the Alpine deformation zone, in the zone of interaction between the tectonic plates of Africa, Arabia and Anatolia (Vidal et al., 2000). The basin formed in Middle Miocene as a result of subduction of African tectonic plate under Eurasia. It has an average length ~ 325km, an average width ~ 155km and water depth over 2km. It covers an area of ~50.375km^2. It is bounded to the north from Larnaca thrust zone, to the northwest from Eratosthenes continental block. The Nile cone and the eastern margin of Mediterranean are the southwest and east margins respectively. The basin contains Mesozoic and Cenozoic sequences with thickness up to 14km. The basin has a complex structure due to compression and extension regime that produced movement of tectonic plates and tectonic gravity processes (Roberts & Peace, 2007).

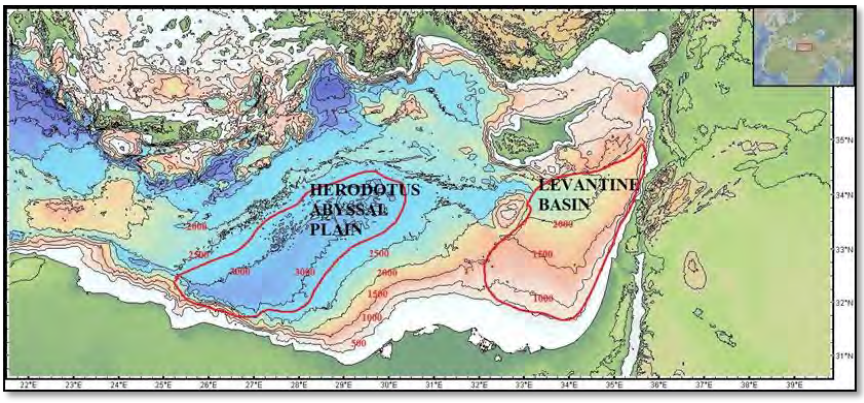

Figure 1 - Bathymetrical map which shows the two basins. NE of Cyprus is the Levantine basin and NW of Cyprus the Herodotus abyssal plain. (Geomap).

Te Herodotus abyssal plain is located SW of Cyprus (Figure 1). The abyssal plain also formed in Middle Miocene as a result of subduction of African tectonic plate under Eurasia. It is a deep basin

with water depth over 3km. It has an average length ~450km and an average width ~255km. It covers an area of ~113,000km^2, which is two times bigger than the Levantine basin. On the north is bounded from the Mediterranean ridge, from the African (Libyan/Egyptian) continental slope on the SW and from the Anatolian rise on the NE. The Herodotus basin also contains Mesozoic and Cenozoic sediments up to 15km in thickness (Montadert et al., 2009). The size of the basin is reduced during time as the Nile cone proceeds and progrades into the basin. As a result the sediments accreted to the Mediterranean ridge.

3. Stratigraphy

3.1. Herodotus Basin

The Herodotus basin as mentioned above is composed of clastic sediments with a thickness up to 15km (Figure 2). The bedrock of the basin is oceanic crust of Triassic age. The sediments from bottom to top are divided into: a) Mesozoic and Paleogene sediments, b) pre-Messinian sediments (Miocene), c) Messinian evaporites and d) Plio - Quaternary sediments.

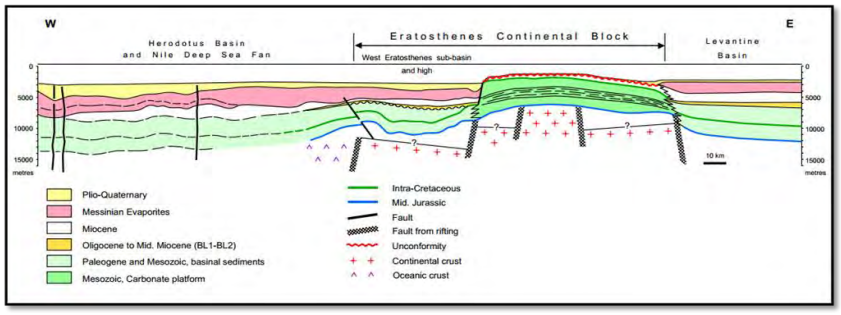

Figure 2 - Stratigraphic cross section of the Herodotus basin and Eratosthenes continental block (Montadert & Nicolaides, 2010).

3.1.1. Pre-Messinian Sediments

These sediments have a thickness greater than 7.5km and are divided into seven lithotypes (Figure 2). Calcarenites (Aquitanian) siltstones (Burdigalian), calcareous siltstones (Burdigalian-Langhian), fossiliferous micrites (Serravallian), sapropels (Tortonian), grated biomicrites (Tortonian-Messinian), bio-arenites (Tortonian-Messinian).

3.1.2. Messinian Evaporites

The Messinian evaporites have thickness many times more than 2.5km (Figure 2). They were deposited by the closure of Gibraltar so that no water enters from the Atlantic Ocean to the Mediterranean, resulting intense evaporation, and the deposition of halite, gypsum and anydrite in the Mediterranean. The water level fell 3-5km in Mediterranean. The structure of the basin is characterized from domes which can form either by syn-depositional folding or diapirism. From magnetic measurements made in the region appear to not be magmatic origin as there are no magnetic anomalies related to the domes. In contrast, sedimentary diapirism indicated by the concentration of domes in a small area of the deepest parts of the basin. The sedimentary diapirs caused by mud or evaporites movement. In gravity measurements made in similar blocks close to this area, show steep negative anomalies Bouguer and show that under these there is a low density material. This material shows evaporitic composition despite mud.

3.1.3. Plio - Quaternary Sediments

The Plio - Quaternary deposits consist of sediments rich in carbonate material deposited in the open sea, with plenty of pelagic organisms and benthic fauna. These deposits are brown to black, laminated, rich in organic material sapropels and sand turbidites. The turbidites were divided into

three types, type A and type B and C also debris flow (Figure 3 and 4) according to their source. The types differ in composition and thickness. Finally, they were detected 12 layers of sapropel (Figure 5) rich in organic material, laminated, deposited in anaerobic, deep waters in Quaternary. (Hilgen, 1991; Kempler et al., 1996).

The Type A turbitides (Figures 3 and 4) are rich in smectite which means that the source of this type is the Nile cone because the sediments of the Nile are rich in smectite. They are also rich in organic material. Their thickness range from 15cm to 750cm (Reeder et al., 2000) and their age range from Middle Pleistocene to Holocene. The transportation from the Nile cone in the basin, made by channels that favor the transport by turbititic mud flows. The Type B turbitides (Figure 3 and 4) are richer in carbonates, ranging from 36% to 84,5%, and that shows that the source of these turbitides is the African continental slope. The transport is done through submarine canyons. Their age is Upper Pleistocene. The most noticeable layer of this type turbidite is called ''beta'' by the Greek letter (β). The turbidite sequence ''β'' reaches 7m. in thickness. Finally, their thickness range from 6-1.570cm (Reeder et al., 2000). The Type C turbitides (Figure 4) derived from the Anatolian rise and are directed towards the east and northeast parts of the basin. Finally, the debris flows (Figure 3 and 4) derived from the Mediterranean ridge and they are limited in the northern part of the basin (e.g. Stow & Piper, 1984; Stow et al., 1996; Cita et al., 1984a; Lucchi & Camerlenghi, 1993).

3.2. Levantine Basin

The Levantine basin is composed of clastic sediments with a thickness of 14km (Figure 5). The bedrock of the basin of Triassic age is not clear whether it is oceanic or continental crust. The sediments from bottom to top are divided into: a) Triassic section, composed by ten depositional cycles, b) Jurassic section, composed by seven depositional cycles, c) Cretaceous section, composed by eight depositional cycles, d) Tertiary section, composed by eleven depositional cycles. The types of the sediments are referring in figure 5.

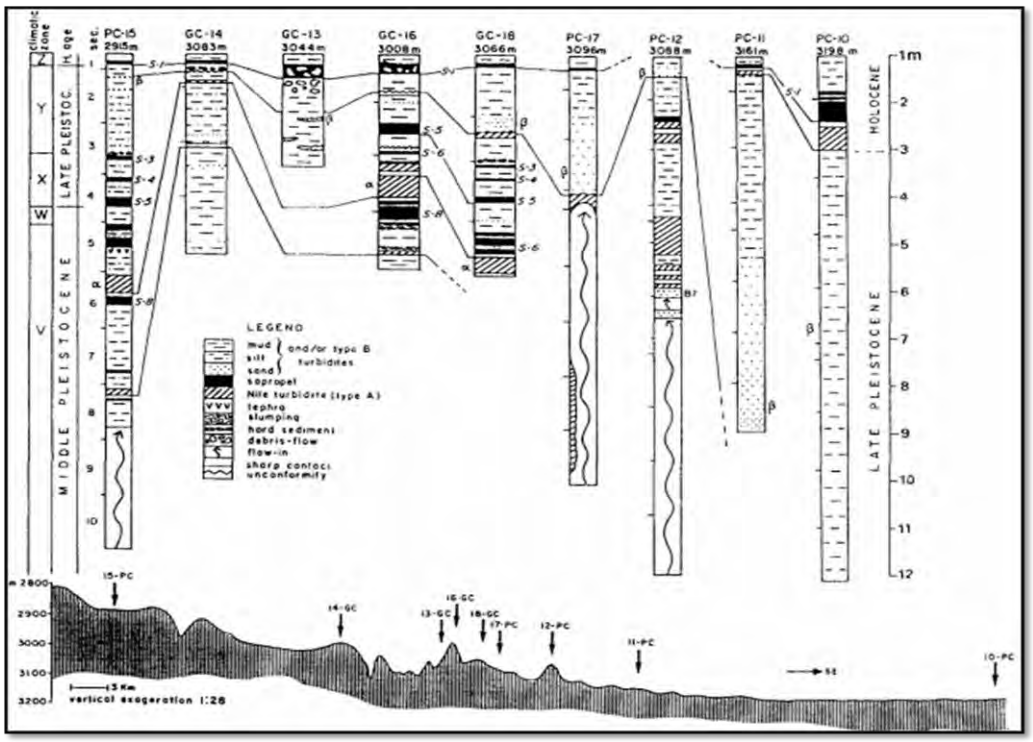

Figure 3 - Stratigraphic columns of type A and B turbitides of 9 cores that were taken in the Herodotus basin. Also in black colour are shown the layers of sapropel (Cita et al., 1984).

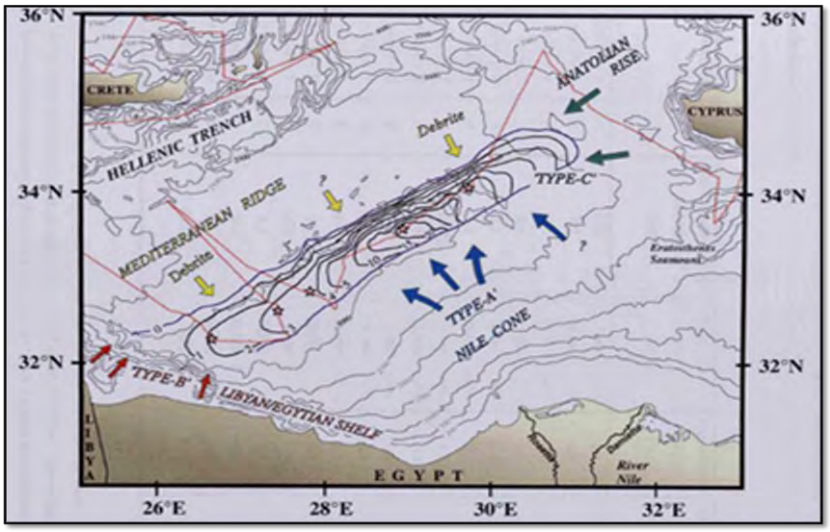

Figure 4 - Bathymetric map that shows the four turbitides sources in the Herodotus basin (Reeder et al., 2000).

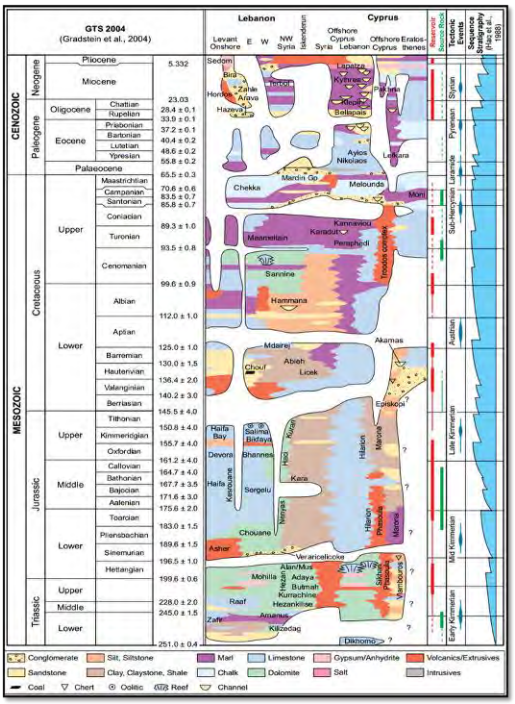

Figure 5 - Levantine basin stratigraphy (Roberts & Peace 2007).

4. Hydrocarbon Plays in Levantine Basin

The source rocks (Figure 6) in the Levantine basin are Pliocene clays and are the source of dry biogenic gas. The source rocks that have the potential to give natural gas are the fine coarse

sediments of Triassic and Jurassic age (Nader & Swennen, 2004). In contrast, the source rocks that have the potential to give oil are sediments of Upper Cretaceous age

Potential reservoirs (Figure 6) are sandstones of Plio - Pleistocene, endo - Messinian, Oligocene, Eocene and Paleocene age. Sandstones and limestones of Cretaceous, including carbonate reefs. Sandstones, limestones, dolomites and oolitics limestones are the reservoirs of the Jurassic. Finally the oldest reservoirs are the Triassic sandstones.

The cap rocks (Figure 6) are the Messinian evaporites, Paleogene, Neogene and Cretaceous clays and marls and finally Triassic and Jurassic evaporates.

The migrations is through faults that exist in the basin (Figure 6). The traps are stratigraphic and structural such as anticline and pinch outs.

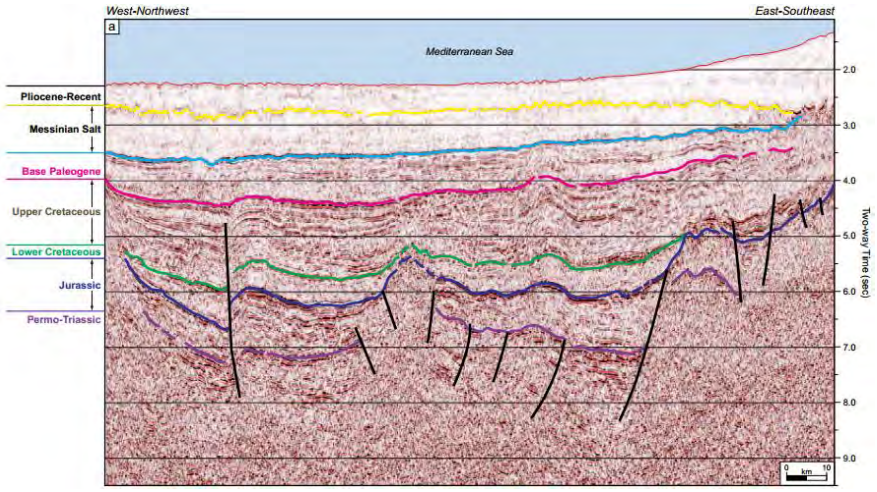

Figure 6 - WNW-ESE seismic line over the southern part of the Levantine Basin showing a Triassic-Jurassic rifted terrain and the age of the sequences. Section width approximately 160 km (Roberts & Peace 2007).

5. Direct Hydrocarbons Indicators (DHIs)

5.1. Seismic Flat Spot

A seismic flat spot (Figure 7) may be a reflection from a well-defined fluid contact, commonly the gas/oil or gas/water contacts. The acoustic impedance contrast between the two phases may be sufficiently large to produce a strong reflection. In a section with dipping reflections, it stands-out because of its flat attitude. This is usually taken to be the most definitive and inJormative of all the Direct Hydrocarbon Indicators (Sheriff, 1995).

5.2. Seismic Bright Spot

A seismic bright spot (Figure 7) is a strong-amplitude reflection caused by large changes in acoustic impedance and tuning effects. In general, bright spots are mostly caused by lateral changes in lithotogy rather than DHIs. Nevertheless bright spot DHIs can also be due to a gas-saturated sandstone reservoir underlying a shale interval. When seismic bright spots are on top of a structural high they are often associated with gas accumulation. Gas-induced bright spots usually have negative polarity for the reflection from the top of the reservoir (Semb 2009).

5.3. Seismic Gas Chimneys and Velocity Pushdown

A gas chimney (Figure 7) describes the effects of escaped gas that is dispersed upwards in the sediments as imaged in the seismic data. The presence of the gas causes the seismic reflections to abruptly become dim or altogether disappear in the zone. The reduction of velocity through a hydrocarbon accumulation will also affect reflections from deeper intervals by increasing the two-way times. This is because the accumulation has a lower seismic velocity that causes the reflections to sag (Sheriff, 1995, Semb 2009).

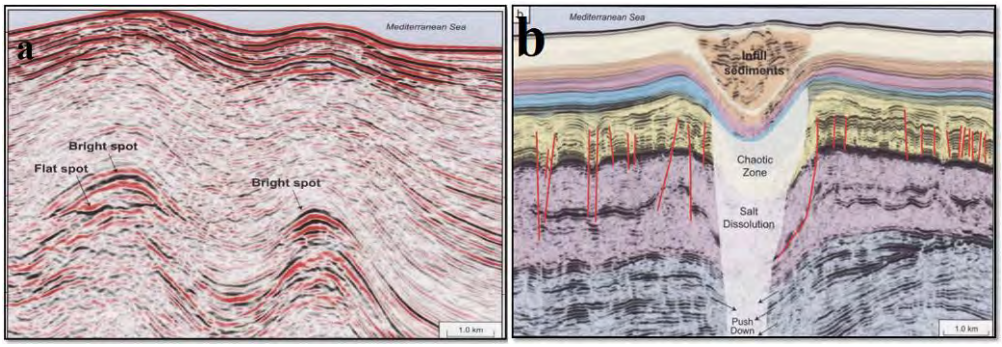

Figure 7 - Seismic sections showing a)flat spot, bright spot, b)recent sediments filling zone, dissolution of the salt and the deepest portion may represent gas chimney and pushdown zone (Semb 2009).

5.4. Seismic Dim Spot

By contrast to a bright spot, a seismic dim spot shows weak rather than strong amplitudes. The weak amplitude can correlate to the presence of hydrocarbons that reduce the contrast in acoustic impedance (AI) beiween the reservoir and the overlying rock. Such dim spots are often associated with the occurrence of oil or gas (Semb 2009).

5.5. Seismic Shadow Zones

A lowering of the seismic instantaneous frequency is often observed immediately beneath hydrocarbon accumulations. Such low-frequency seismic shadows (Figure 8) seem to be confined to a couple of cycles below accumulations. One anonymous reviewer invoked attenuation of the higher frequencies through the hydrocarbon zone as an explanation for this phenomenon; in particular for gas this effect can be quite large. The second anonymous reviewer further suggested that the removal of higher frequencies may be due in part to improper stacking with erroneous velocity assumptions or ray-path distortions (Semb 2009).

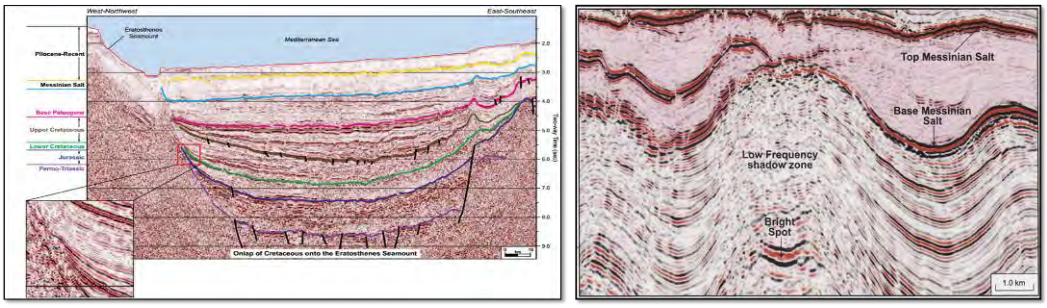

Figure 8 - WNW-ESE seismic line over the central part of the Levantine Basin shows pinch-outs on the east Eratosthenes slopes (right image) (Roberts & Peace 2007). Seismic section showing a shadow zone (Semb 2009).

5.6. Pinch-outs

The pinch - outs (Figure 8) is when a porous reservoir rock lies between two layers of impermeable rock, such as clay layer or evaporites and the thickness is reduced to form a wedge which can be trap hydrocarbons.

6. Genesis Conditions and Hydrocarbon Fields in Herodotus Basin Compared with Levantine Basin

The source rocks in Herodotus basin for natural gas, are Pleistocene siltstones and sapropels, sapropel of Upper Miocene, Lower-Middle Miocene calcareous siltstones and fine coarse sediments of Upper Jurassic and Lower Cretaceous. For oil the source rocks are fine coarse sediments of Upper Cretaceous-Lower Cenozoic (Table 1).

Table 1: Comparative table of the two basins.

CHARACTERISTICS	*LEVANTINE BASIN*	*HERODOTUS BASIN*
AGE OF SEPARATION	CRETACEOUS	CRETACEOUS
AGE OF DEVELOPMENT	MIDDLE MIOCENE	MIDDLE MIOCENE
LENGTH	~325 KM AVERAGE	~450 KM AVERAGE
WIDTH	~155 KM AVERAGE	~255 KM AVERAGE
WATER DEPTH	>2 KM	>3 KM
EXTEND	~50.375 KM^2	~113.000.KM^2
SEDIMENT THIKNESS	10-14 KM	12-15 KM
SOURCE ROCKS	PLIOCENE CLAYS, CRETACEOUS CLAYS, FINE CARBONATES AND MARLS, JURASSIC AND TRIASSIC CLAYS AND SILTSTONES	PLEISTOCENE SILTSTONES AND SAPROPELS, MIOCENE SAPROPELS AND CALCAREOUS SILTSTONES, U.JURASSIC-L.CRETACEOUS FINE SEDIMENTS
POTENTIAL RESERVOIRS	PLIO-PLEISTOCENE, MESSINIAN, TERTIARY SANDSTONES, CRETACEOUS SANDSTONES, LIMESTONES AND CARBONATE REEFS, JURASSIC SANDSTONES, LIMESTONES, DOLOMITES AND OOLITIC LIMESTONES, TRIASSIC SANDSTONES	TURBITIDE SANDS AND SAND FORMATIONS RICH IN CARBONATE MATERIAL OF PLEISTOCENE, BIOMICRITES, BIOARENITES, FOSSILIFEROUS MICRITES AND CALCARENITES OF MIOCENE, POROUS SEDIMENTS OF JURASSIC AND CRETACEOUS
SEAL ROCKS	MESSINIAN EVAPORITES, TRIASSIC, JURASSIC AND CRETACEOUS CLAYS AND MARLS, TRIASSIC AND JURASSIC EVAPORITES	MESSINIAN EVAPORITES, CALCAREOUS SILTSTONES LOWER-MIDDLE MIOCENE AND SILTSTONES OF PLEISTOCENE
TRAPS	STRUCTURAL AND STRATIGRAPHIC (ANTICLINES, PINCH-OUTS, UNCONFORMITIES)	STRUCTURAL AND STRATIGRAPHIC (ANTICLINES, PINCH-OUTS, UNCONFORMITIES)
MIGRATION	FAULTS	FAULTS
OIL (BBL)	1.68	≥1.68
NATURAL GAS (TCF)	122	≥122

Potential reservoirs are turbitide sands and sand formations rich in carbonate material of Pleistocene age, biomicrites, bioarenites, fossiliferous micrites and calcarenites of Miocene age, and finally porous sediments of Jurassic and Cretaceous age.

The cap rocks are the Messinian evaporites, Lower-Middle Miocene calcareous siltstones and siltstones of Pleistocene age.

The migrations are through faults that exist in the basin. The traps are stratigraphic and structural such as anticline and pinch outs.

7. Conclusions

In conclusion, as shown in Table 1, the two basins formed at the same age (Upper Cretaceous), and developed as foreland basins during middle Miocene. They have the same evolution story and host the same types of sediments with approximately the same thickness. However the Herodotus basin seems to have twice the area of Levantine basin. The Levantine basin has certified reserves of natural gas (122 tcf) and oil (1.68 bbl). So, we can say that Herodotus basin contains at least the same amount of natural gas and oil as in the Levantine basin.

8. References

Bruneton A., Konofagos E. and Foscolos E. A. 2012. Cretan Gas Fields–A New Perspective For Greece's Hydrocarbon Resources.

Bruneton A., Konofagos E. and Foscolos E. A. 2012. The importance of Eastern Mediterranean gas fields for Greece and the EU.

Camerlenghi A. 1990. Anoxic Basins of the Eastern Mediterranean. *Marine Chemistry*, 31 1-19 1, Elsevier Science Publishers B,V., Amsterdam Geological Framework.

Cita M.B., Beghi C., Camerlenghi A., Kastens K.A., McCoy F.W., Nosetto A., Parisi E., Scolarp F. and Tomadin L. 1984. Turbidites And Megaturbidites From The Herodotus Abyssal Plain (Eastern Mediterranean) Unrelated To Seismic Events, *Marine Geology,* 55: 79-101.

Foscolos A. 2011.Geological and geochemical evidences indicating the existence of large hydrocarbon deposits in the Libyan sea within the Greek exclusive economic zone (EEZ).

Gardosh M., Druckman Y., Buchbinder B. and Rybakov M. 2006. The Levant Basin Offshore Israel: Stratigraphy, Structure, Tectonic Evolution and Implications for Hydrocarbon Exploration.

Gardosh M. and Druckman Y. 2006. Seismic Stratigraphy, Structure and Tectonic Evolution of the Levantine Basin, Offshore Israel. *Geological Society, London, Special Publications,* 260: 201-227.

Harrison W.R. 2008. A Model For The Plate Tectonic Evolution Of The Eastern Mediterranean Region That Emphasizes The Role Of Transform (Strike-Slip) Structures, *1st WSEAS International Conference on ENVIRONMENTAL and GEOLOGICAL SCIENCE and ENGINEERING (EG'08)* Malta, September 11-13.

Kempler D. 1998. Eratosthenes Seamount: The Possible Spearhead of Incipient Continental Collision in the Eastern Mediterranean, *Proceedings of the Ocean Drilling Program, Scientific Results, Vol. 160.*

Loncke L., Gaullier V., Mascle J., Vendeville B. and Camera L. 2006. The Nile Deep Sea Fan: An Example of Interacting Sedimentation, Salt Tectonics, and Inherited Subsalt Paleotopographic Features, *Marine and Petroleum Geology,* 23: 297-315.

Maldonado A. and Stanley J.D. 1976. The Nile Cone: Submarine Fan Development By Cyclic Sedimentation, *Marine Geology*, 20: 27-40.

Maravelis A., Manutsoglu E., Konstantopoulos P., Makrodimitras G., Zoumpouli E. and Zelilidis A. 2013. Hydrocarbon Plays and Prospectivity of the Mediterranean Ridge, *Energy Sources, Part A: Recovery, Utilization, and Environmental Effects (in press).*

Mascle J., Zitter T., Bellaiche G., Droz L., Gaullier V. and Loncke L. Prismed Scientific Party, 2001. The Nile Deep Sea Fan: Preliminary Results From a Swath Bathymetry Survey, *Marine and Petroleum Geology,* 18: 471-477.

Montadert L., Nicolaides S., Semb H.P. and Lie O. 2009. Petroleum Systems Offshore Cyprus.

Netzeband L.G. Gohl K., Hubscher P. C., Ben-Avraham Z., Dehghani A. G., Gajewski D. and Liersch P., 2006. The Levantine Basin – Crustal Structure and Origin, *Tectonophysics,* 418: 167-188.

Netzeband L.G., Hubscher P.C. and Gajewski D. 2006. The Structural Evolution of the Messinian Evaporites in the Levantine Basin, *Marine Geology,* 230: 249-273.

Reeder S.M., Rothwell G.R. and Stow A.V.D. 2000. Influence Of Sea Level And Basin Physiography On Emplacement Of The Late Pleistocene Herodotus Basin Megaturbidite, SE Mediterranean Sea, *Marine and Petroleum Geology,* 17: 199-218.

Reeder S.M., Rothwell G.R., Stow A.V.D., Kahler G. and Kenyon H. N., 1998. Turbidite Flux, Architecture And Chemostratigraphy Of The Herodotus Basin, Levantine Sea, SE Mediterranean, *Geological Society, London, Special Publications* 129: 19-41.

Reeder S.M. 2000. Megaturbidites And The Late Quaternary Regional Sedimentology Of The Eastern And Central Mediterranean Sea, University of Southampton, Faculty of Science, School of Ocean and Earth Science, *Doctoral Thesis, 381pp.*

Roberts G. and Peace D. 2007. Hydrocarbon Plays and Prospectivity of the Levantine Basin, Offshore Lebanon and Syria From Modern Seismic Data*, GeoArabia Vol. 12, No 3.*

Robertson H.F.A., Kidd B.R., Ivanov K.M., Limonov F.A., Woodside M.J., Galindo-Zaldivar J., Nieto L. and the Scientific Party of the 1993 TTR-3 Cruise. Eratosthenes Seamount: Collisional Processes in the Easternmost Mediterranean in Relation to the Plio – Quaternary Uplift of Southern Cyprus. *Terra Nova,* 7: 255-264.

Rothwell R.G., Reeder M.S., Anastasakis G., Stow D.A.V., Thomson J. and Khaler G. 2000. Low Sea-Level Stand Emplacement Of Megaturbidites In The Western And Eastern Mediterranean Sea, *Sedimentary Geology,*135,(1/4):75-88.

Scalera G. 2006. The Mediterranean as a slowly nascent ocean.

Semb H.P. 2009. Possible Seismic Hydrocarbon Indicators in Offshore Cyprus and Lebanon, *GeoArabia* 14: 49-66.

Semb H.P. 2010. Offshore Cyprus and Lebanon, a Feature Hydrocarbon Player, *8th Biennial International Conference & Exposition on Petroleum Geophysics.*

Smith G.S. 1976. Diapiric Structures In The Eastern Mediterranean Herodotus Basin, *Earth and Planetary Science Letters,* 32: 62-68.

Stanley J.D. 1973. Basin Plains In The Eastern Mediterranean: Significance In Interpreting Ancient Marine Deposits, *Marine Geology,* 15: 295-307 *Herodotus Basin area Bullard Laboratories, Department of Earth Sciences.*

Tanner J. S. 1983. A Detailed Survey In The Mediterranean Rise And Herodotus Basin Area, *Geophjx. J. R. astr.* SOC. 13: 173-195.

Tari G., Hussein H. and Novotny B. 2010. Play Types and Hydrocarbon Potential of Deep-Water NW Egypt.

Vidal N., Alvarez-Marron J. and Klaeschen D. 2000. Internal Configuration of the Levantine Basin From Seismic Reflection Data (Eastern Mediterranean), *Earth and Planetary Science Letters* 180: 77-89.

Voogd D. B., Truffert C., Chamot-Rooke N., Huchon P., Lallemant S. and Le Pichon X. 1992. Two-Ship Deep Seismic Soundings In The Basins Of The Eastern Mediterranean Sea (Pasiphae cruise), *Geophys. J. Int.,* 109: 536-552.

Δελτίο της Ελληνικής Γεωλογικής Εταιρίας, τομ. XLVII , 2013
Πρακτικά 13ου Διεθνούς Συνεδρίου, Χανιά, Σεπτ. 2013

Bulletin of the Geological Society of Greece, vol. XLVII 2013
Proceedings of the 13th International Congress, Chania, Sept. 2013

USE OF MINE PLANNING SOFTWARE FOR THE EVALUATION OF RESOURCES AND RESERVES OF A SEDIMENTARY NICKEL DEPOSIT

Kapageridis I.[1], Apostolikas A.[2], Pappas S.[2] and Zevgolis I.[2]

[1] Department of Geotechnology and Environmental Engineering, Technological Educational Institute of Western Macedonia, Koila, 50100, Kozani, Greece, ikapa@teikoz.gr

[2] LARCO GMMSA, 81-83 Kifisias Avenue, Athens, Greece

Abstract

The use of mine planning software in the evaluation of deposits and estimation of mineral resources and reserves has become widespread and is considered a prerequisite for the reporting of reserves according to international reporting standards and codes. The main principles of operation and application of these codes are transparency of reported material, the relevance of reported information (materiality) and the competence of people involved in producing the reports. The application of specialised mine planning software described in this paper currently takes place at operational mines of sedimentary nickel deposits in Central Evia, Greece. It involves all stages of processing of exploration data including entry, analysis, processing and modelling of data, geostatistical estimation of quantities and qualities of mineral resources and mineral reserves, and the design, optimisation and scheduling of mining operations.
Key words: *geostatistics, pit optimisation, reporting standards.*

Περίληψη

Η χρήση λογισμικού μεταλλευτικού σχεδιασμού για την αξιολόγηση κοιτασμάτων και την εκτίμηση ορυκτών πόρων και αποθεμάτων είναι διαδεδομένη και θεωρείται προϋπόθεση για την αναφορά αποθεμάτων με βάση διεθνή πρότυπα και κώδικες αναφοράς. Οι βασικές αρχές λειτουργίας και εφαρμογής αυτών των κωδικών είναι η διαφάνεια του αναφερόμενου υλικού, η σχετικότητα των αναφερόμενων πληροφοριών (ουσιαστικότητα) και η επάρκεια των ατόμων που εμπλέκονται στην παραγωγή των αναφορών. Η εφαρμογή ειδικού λογισμικού μεταλλευτικού σχεδιασμού που περιγράφεται στην εργασία αυτή λαμβάνει χώρα στα λειτουργικά μεταλλεία ιζηματογενών κοιτασμάτων νικελίου στην Κεντρική Εύβοια. Περιλαμβάνει όλα τα στάδια της επεξεργασίας ερευνητικών δεδομένων συμπεριλαμβανομένης της εισαγωγής, ανάλυσης, επεξεργασίας και μοντελοποίησης των δεδομένων, της γεωστατιστικής εκτίμησης των ποσοτήτων και ποιοτήτων των ορυκτών πόρων και αποθεμάτων, και το σχεδιασμό, βελτιστοποίηση και προγραμματισμό των μεταλλευτικών δραστηριοτήτων.
Λέξεις κλειδιά: *γεωστατιστική, βελτιστοποίηση εκσκαφής, πρότυπα αναφοράς.*

1. Introduction

1.1. Geological Setting

The nickeliferous mineralization in Greece is related to the geotectonic zones of Almopia, Pelagonian and Sub-Pelagonian, - the main metalliferous regions are situated in Locris, Euboea and Kastoria. In Central Euboea, iron and nickel ores of Cretaceous age occur, which are of sedimentary type and consist of stratified lenses and layers, overlain by Upper Cretaceous limestones and underlain by ophiolites (and in exceptional cases by Jurassic limestones). The mineralization is either pissolitic or compact with silcretes developed within the ore, the development of lenticular intercalations or siliceous layers is also common, while silcretes are also found in the bedrock. A large number of significant deposits exist in the Psachnon area, the Akres, Katsikiza, Isomata and the Katavolo-Fterada in the Kimi's area. The deposit used in the study presented in this paper is from the Akres area (Figure 1).

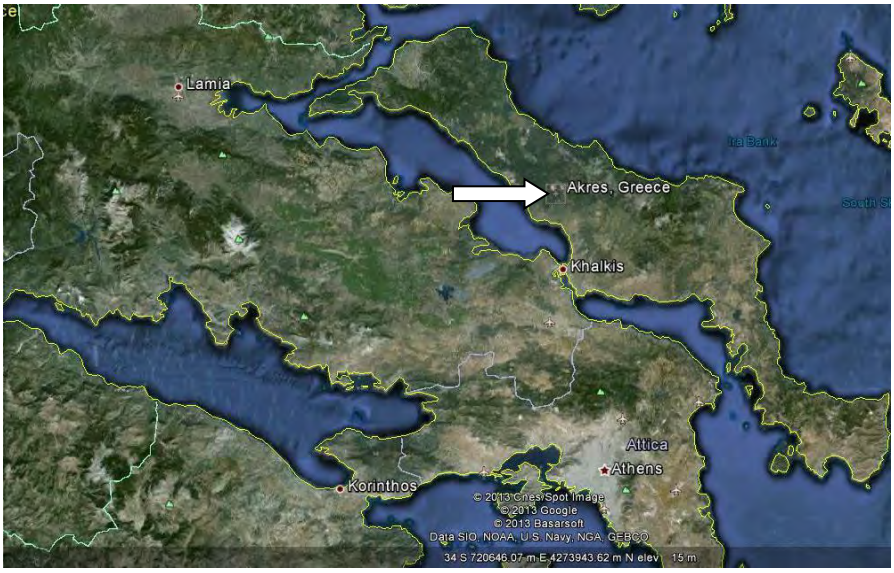

Figure 1 – Location of Akres deposits in Euboea.

1.2. Available Data

Drilling information from 126 surface drillholes from the NE Akres deposit was provided for the purposes of this study in the form of CSV files. This data was imported to a drillhole database in Vulcan. The database has four tables to hold collar, survey, lithology and assay information. The database was validated using a number of checks for overlapping intervals, numerical field ranges (coordinates and grade fields), and numeric order (lithology and assay interval fields). The drillhole lithological information was used to model the boundaries of the orebody in three dimensions. The assay information was used to perform structural analysis (variography) of the nickel spatial distribution and grade estimation on the basis of a block model. Financial and technical information concerning the mining and processing methods used were also available and were used in the pit optimisation and design stages of the study.

1.3. Procedure

The modelling and resource/reserve estimation study presented in this paper was performed in a number of steps using Maptek's Vulcan 3D software – one of the major commercial mine planning packages implemented by LARCO SA since 2007. The implementation of industry standard software based mine planning techniques aimed at meeting the requirements set by international

reporting codes (SAMREC, 2009, JORC, 2012, NI 43-101, 2011, and PERC, 2013). These techniques regarded database generation and validation, statistical analysis and compositing of samples, geological modelling of the orebody, structural analysis (variography), grade estimation on a block model basis, pit optimisation and design, and reporting of resources and reserves. All steps were supervised by qualified personnel as required by reporting codes. The implementation of reporting code guidelines to resources and reserves estimation and reporting using mine planning software has been examined in the past by Snowden (1996), Duke *et al.* (1999), and Kapageridis (2007).

2. Geological Modelling

2.1. Orebody Boundaries Modelling

The structural roof and floor of the main orebody area and of an internal low grade envelope were modelled using grid model interpolation based on drillhole lithological intervals. The highest points of a particular lithology code (20) which corresponds to the main orebody area were derived from the database and were used to generate a grid model of the roof. The same procedure was used to model the floor from the lowest points of the same lithology code. The triangulation algorithm with trending was used to interpolate grid points between drillholes in all cases. Figure 2 shows a section through all four structural surfaces.

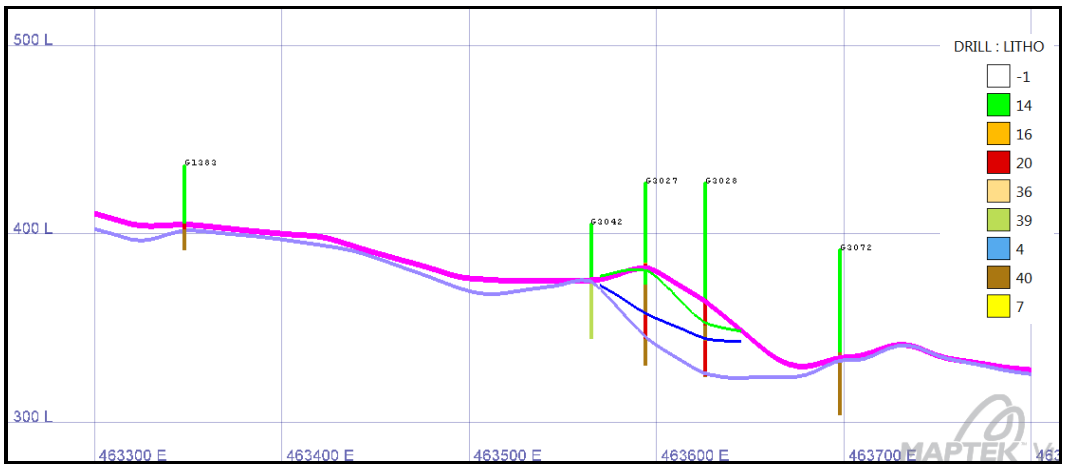

Figure 2 – West-East section looking North showing roof and floor models of main orebody area and internal low grade envelope derived from drillhole lithological intervals.

2.2. Unfolding Orebody Deformities

A number of methods for modelling deformations produced by various folding mechanisms have been developed. Earlier methods of unfolding deposits were based on various geometrical, mathematical or even manual techniques such as least squares, cylindrical unfolding or the fitting of splines (Royle 1979, Dagbert et al. 1983, Dowd 1986). Other more recent methods were based on the use of an unfolded coordinate system for the transformation of every sample and every estimation point for variography and grade estimation (Newton 1995). Tetrahedral modelling for variography and grade estimation was developed by Trevor Coulsen in 1995 (Maptek Pty Ltd) and implemented in Maptek's VULCAN 3D software package. Further improvements to the original algorithm were made by Peter Borovina (Maptek Pty Ltd) in 2002. Tetrahedral modelling is a method of adjusting the search ellipse used in variography and grade estimation to follow the geometrical structure of the deposit by forming a 3D tetrahedral model of the deposit volume. For this model to be generated, the structural surfaces of the deposit need to be modelled as surface triangulations. In tetrahedral modelling the search ellipse is distorted to follow nominated

structural surfaces leading to improved estimation accuracy (Kapageridis, 2006) and improved classification of resources.

A tetrahedral model was generated in this study using the structural roof and floor models of the main orebody area. This model (Figure 3) captured the orientation and shape of all deformities as represented by the structural models and was used to bring samples to an unfolded location relative to blocks during grade estimation.

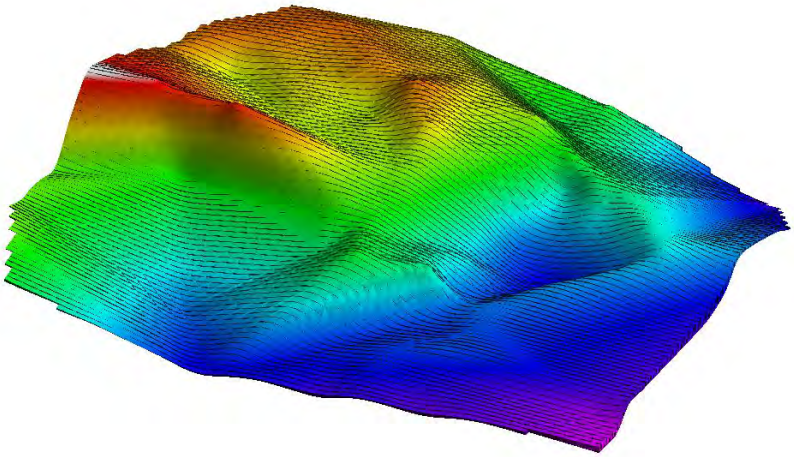

Figure 3 – 3D representation of tetrahedral model used in unfolding.

3. Variography - Grade Estimation

3.1. Statistics and Sample Compositing

General statistics and histograms of nickel grade were calculated to gain a better understanding of its distribution characteristics. Original assay intervals were then composited to standard length composites (1m) to derive a set of equal support values to use for variography and grade estimation. The choice of composite length was based on the selectivity of the mining method used in this deposit and also on the effect of the compositing to the statistical characteristics of the composited values.

3.2. Variography – Structural Analysis

In order to model the structure underlying the Ni grade distribution represented by the available composites, fix the search region to be used during sample selection, and provide a model to ordinary kriging for weights calculation, structural analysis was performed using only the composites from the main orebody area. The procedure applied to derive the final variogram model is discussed in the following paragraphs.

3.2.1. Downhole Variography – Nugget Effect Approximation

Downhole variography was performed in order to set the nugget effect presented by the composites used in this study. The standard semivariogram was used in this study as the mode for experimental variography. The downhole variogram was calculated using nickel composited values, a lag of 1m to match the composite length, 30 lags, and a lag tolerance of 0.3m. Figure 4 below displays the experimental downhole semivariogram and the fitted model. The range and sill displayed was also used for the final variogram model as the drillholes are all vertical, hence correspond to a particular direction in space. The fitted value for the nugget effect was 0.002. This value was used in the final variogram model fitted in different directions.

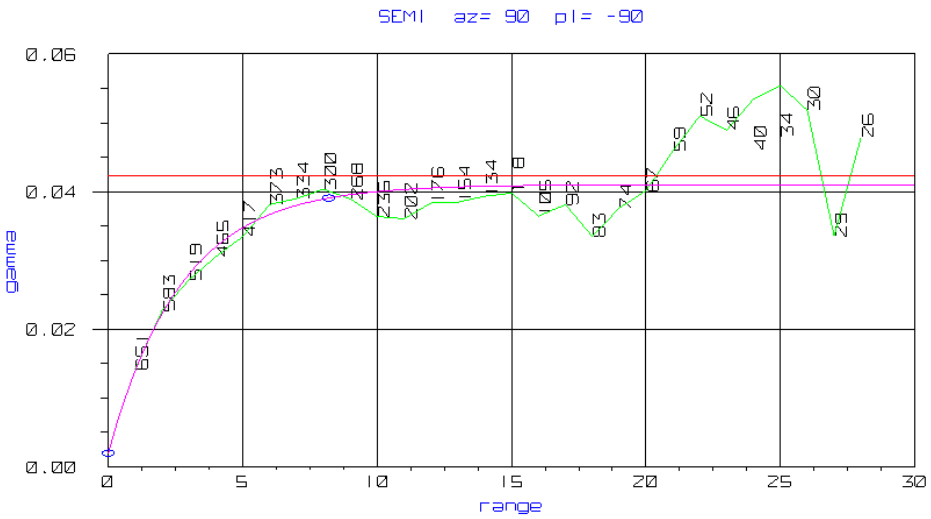

Figure 4 – Downhole experimental semivariogram and fitted exponential model.

3.2.2. Directional Variography

Directional experimental variograms of the Ni composited values were calculated in various directions and were used to fit a model. A lag size of 10 was used in all directions and a total number of 15 lags were calculated, i.e. a semivariogram value was calculated every 10m and up to 150m. A lag tolerance of 2m was used to allow for irregularities of the drilling pattern. Azimuth and plunge tolerances were set to 20º and a horizontal and vertical bandwidth of 20m was applied. Figure 5 explains in graphical form the way these parameters are applied when searching for pairs of samples to calculate experimental variogram points.

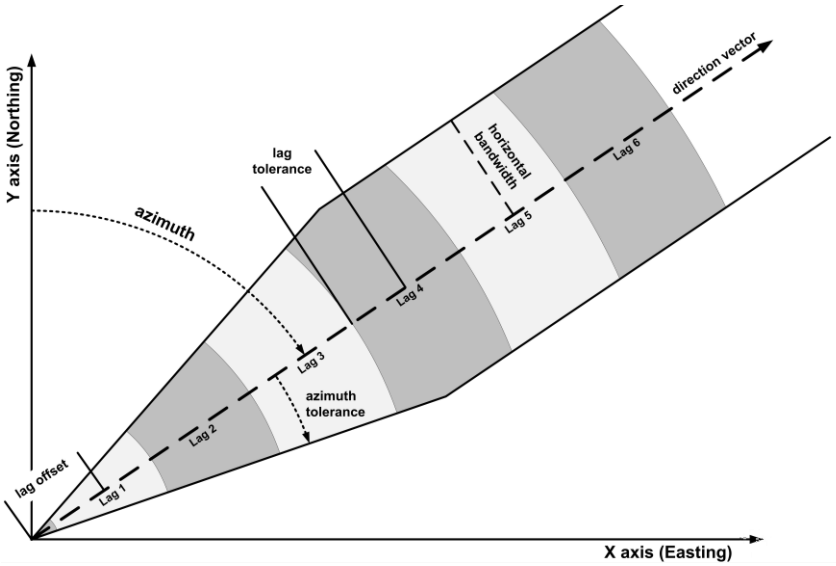

Figure 5 - Explanation of lag and direction setup parameters for directional variography.

3.2.3. Variogram Model

A variogram model consisting of a single exponential structure was fitted to the experimental variogram as shown in the two indicative directions in Figure 6. The exponential model was

chosen as it seemed to match better the curvy shape of the experimental variogram at distances between 0 and 50 meters. The spherical model which is the most common choice in similar studies, has an almost linear beginning that did not fit well in this case. Table 1 gives the parameters of the final variogram model used for grade estimation.

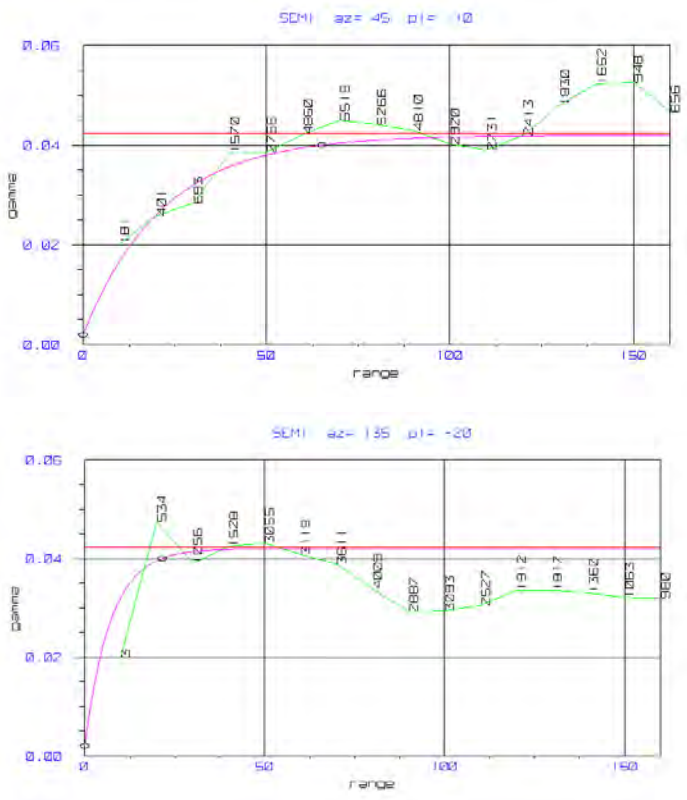

Figure 6 – Experimental semivariograms and fitted exponential model (point labels are pair counts).

Table 1 – Fitted Variogram Model Parameters.

Experimental Variogram Type	Standard Semivariogram
Fitted Model Type	Exponential
Nugget Effect	0.002
Sill Differential	0.04
Bearing	45
Plunge	-15
Dip	0
Major range	65
Semimajor range	42.85
Minor range	8.2

3.3 Grade Estimation and Resource Classification

A block model with 10x10x12m main blocks and a minimum sub-block size of 1x1x1m was generated covering the entire area of the deposit. The main and sub-block sizes were set to reflect pit geometry and mine method selectivity. The model was not rotated around any axis in order to be used for pit optimisation. Ordinary Kriging (OK) was used as the method for interpolating Ni values to the blocks coded as part of the main orebody. OK used the fitted variogram model consisting of a single exponential structure as described in Section 3.2. Three separate estimation runs were performed, each with different sample selection strategies and varying search ellipsoid dimensions, corresponding to three different resource classifications. In each run the blocks estimated received a flag in the class variable of the block model according to the classification: 1 for measured, 2 for indicated, and 3 for inferred. Blocks estimated with the 1st run (measured) were excluded from the 2nd run (indicated), and blocks estimated with the 1st and 2nd run were excluded from the 3rd run (inferred). Table 2 summarises the parameters used in each run and then number of blocks estimated.

Table 2 - Summary of Grade Estimation Parameters.

	Measured	**Indicated**	**Inferred**
Bearing	45	45	45
Plunge	-10	-10	-10
Dip	-25	-25	-25
Major	32.5	65	65
Semi	21.4	42.8	42.8
Minor	8.2	8.2	8.2
Minimum Samples	8	4	4
Maximum Samples	16	16	16
Octant Based Search	Yes	Yes	No
Maximum Samples per Octant	2	2	-
Minimum Octants	4	-	-
Minimum Samples per Octant	2	-	-
Blocks Estimated	9958	27528	1

4. Pit Optimisation and Design

4.1. Estimation and Application of Technical and Financial Parameters

Technical and financial parameters related to the mine geometry and location, mining method, haulage and ore processing were calculated for each block individually using a script written in Perl and utilising Vulcan's Lava extensions to this popular scripting language. The parameters set by the script and the values used for the purposes of this study are shown as entered in the panel in Figure 7. The calculated values for the various parameters were used to estimate a total block value that was used for pit optimisation using the following equation:

$$block\_value = revenue - mining\_cost - haulage\_cost - crushing\_cost - metallurgy\_cost - sea\_transport\_cost - other\_block\_cost$$

The values for the each of the parameters were also stored in separate block model variables for validation purposes. Through this process, all the applicable resources to reserves conversion

parameters according to reporting standards were applied to the resource block model before using it for pit optimisation.

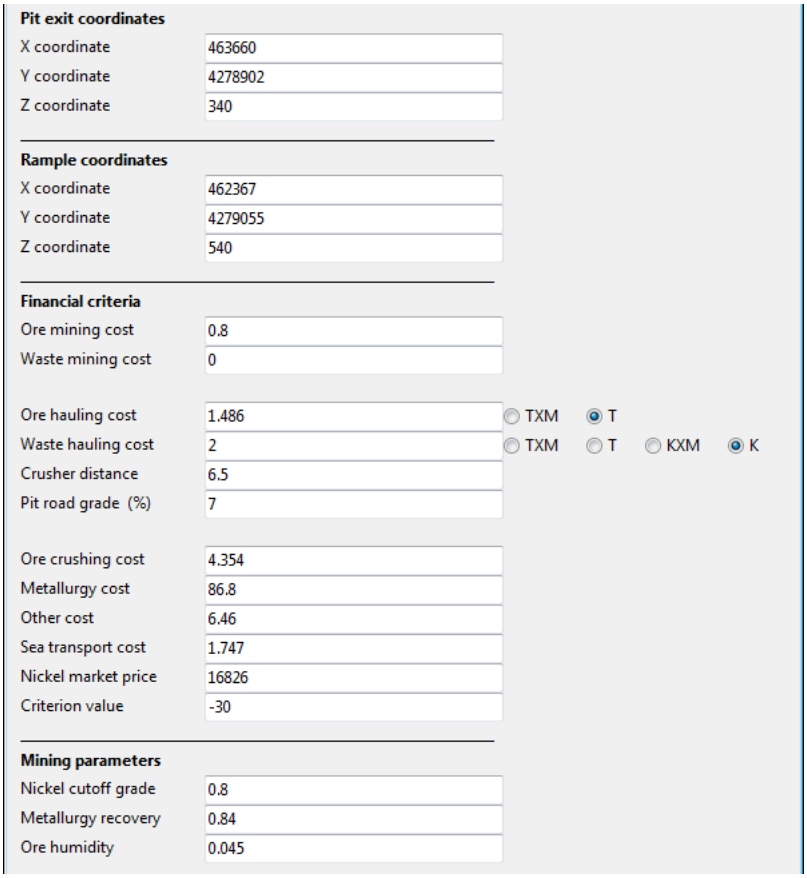

Figure 7 – Configuration panel for pit optimisation mining and financial criteria generated by the script.

4.2. Pit Optimisation

The block value calculated in the previous step was passed to Vulcan's Pit Optimiser module – an implementation of the Lerchs-Grossman algorithm. Two different angles were used to control the slope of the final pit limits, matching the bench angle and height, and berm width configuration and also allowing for the presence of haul road on one side of the pit. A 45º pit slope was used in the East side of the pit and a 25º slope in the west side (the side of the haul road). The pit slope was also controlled by a lithology block model variable. The result of pit optimisation was stored as a code in a block model variable. Blocks that belong to the optimum pit (including ore and waste blocks) receive a different value from those that do not. This way, a subset of the resource blocks were converted to potential reserve blocks. However, the optimum pit as presented by the contours shown in Figure 8 is not a complete pit design and can only be used as a guide for the next important step of designing a feasible pit.

4.3. Pit Design

Pit design was performed using the optimum pit limits as a guide (Figure 8). The top part of the pit from the lowest open bench, i.e. the lowest bench that could be accessed from the surface, was

designed with projections upwards and outwards of the corresponding optimum pit limit to generate the toe and crest polygons without a haul road. The bottom part of the pit from the highest closed bench, was designed using a more complex function in Vulcan that inserts the haul road and then projects the toe and crest polygons for each bench. Two switchbacks were introduced to maintain the haul road only on the west side of the pit as this was the side with the lower pit slope set in pit optimisation. The benches were 12m high with 8m berms and a 70° batter angle. The haul road was 12m wide with a 10% grade applied to the shortest side. The haul road polygons were adjusted to provide bench access both inside and outside of the road. The complete pit design was intersected and cropped with current topography.

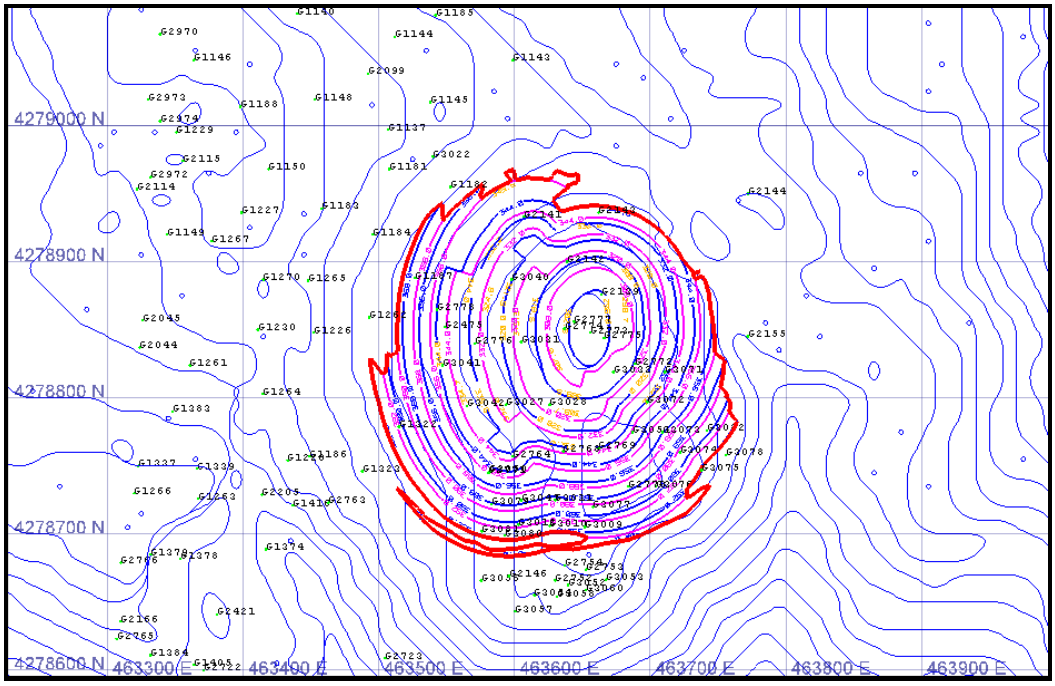

Figure 8 – Optimum pit contours and final pit design.

5. Resources / Reserves Reporting

In order to compare the estimated reserves with the production figures for the period up to the end of 2012, a solid triangulation model was generated representing the volume of the actual excavation at the end of this period. Table 3 gives a summary of the total estimated resources for the NA Akres deposit, the estimated reserves inside the solid model and the actual reserves mined from the same volume. There is some over-estimation of tonnage combined with an under-estimation of grade which translates to very similar nickel content in both cases (6,005t actual versus 6,344t estimated).

6. Conclusions

This paper discussed most aspects of the application of mine planning software to the evaluation of mineral resources and mineral reserves of the sedimentary nickel deposits in Euboea. The implementation of commercial mine planning software produced results that increased confidence as to the available resources, aided the configuration of the mining methods applied, and helped in planning future mining operations by developing different mining scenarios with speed and clarity. The adoption of a geostatistical approach to grade/reserves estimation increased confidence in the produced results and reduced the risks associated with the estimates. The use of a pit optimisation

tool helped convert resources to reserves with more confidence and in a more standardised fashion that is widely accepted by the mining industry. The procedures described in this paper have been adopted with minor adjustments to other nickel deposits exploited by LARCO SA in other areas of Greece.

Table 3 – Summary of ore resources and reserves from NA Akres deposit.

	Total Estimated Resources		**Estimated Reserves (2011- 2012)**			**Actual Reserves (2011-2012)**
	Measured	**Indicated**	**Measured**	**Indicated**	**Total**	**Total**
Ore Tonnage	587,812	1,108,906	96,851	479,925	**576,777**	**508,926**
Ore Ni Grade %	1.07	1.08	1.15	1.09	**1.10**	**1.18**

7. References

Dagbert M., David M., Crozel D. and Desbarats A. 1983. Computing variograms in folded, strata-controlled deposits, Geostatistics for Natural Resource Characterisation, NATO A.S.I. Series C, Volume 122, Part 1: 71-90.

Dowd P.A. 1986. Geometrical and geological controls in geostatistical estimation and orebody modelling, *19th International Symposium on the Application of Computers and Operations Research in the Minerals Industries (APCOM),* Colorado, Chapter 8: 81-94.

Duke J. and Hanna P. 1999. Computer-based Resource Estimation in Accordance with the 1999 JORC Code, White paper, ECS International Pty Ltd.

Joint Ore Reserves Committee. The Australasian Code for Reporting of Exploration Results, Mineral Resources and Ore Reserves (JORC 2012).

Kapageridis I. 2006. Use of Tetrahedral Modelling for Variography and Grade Estimation of a Structurally Deformed Phosphate Deposit. *11th International Congress for Mathematical Geology (IAMG'06 – Quantitative Geology from Multiple Sources), International Association for Mathematical Geology,* Liege.

Kapageridis I. Implementation of Reporting Code Guidelines for Mineral Resources and Mineral Reserves Using a General Mine Planning Package, in: *3rd International Conference on Sustainable Development Indicators in the Minerals Industry (SDIMI) - Entering the 'International Year of Planet Earth', Milos Conference Series,* Milos 2007.

National Instrument 43-101, Standards of Disclosure for Mineral Projects, Canadian Securities Administrators, 2011.

Newton M.J. 1995. Structural analysis for folded deposits. *Mining Magazine*, August 1995.

Pan-European Reserves and Resources Reporting Committee, Pan-European Standard for Reporting of Exploration Results, Mineral Resources and Reserves (PERC Standard 2013).

Royle A.G. 1979. Plane projections of tabular orebodies for evaluation purposes, *Transactions IMM*, Volume 88: A87-A91.

Snowden D.V. 1996. Practical Interpretation of Resource Classification Guidelines*, AusIMM Annual Conference "Diversity, the Key to Prosperity",* Perth.

SAMREC/SAMVAL Committee. South African Code for Reporting of Exploration Results, Mineral Resources and Mineral Reserves (SAMREC 2009).

Δελτίο της Ελληνικής Γεωλογικής Εταιρίας, τομ. XLVII , 2013
Πρακτικά 13ου Διεθνούς Συνεδρίου, Χανιά, Σεπτ. 2013

Bulletin of the Geological Society of Greece, vol. XLVII 2013
Proceedings of the 13th International Congress, Chania, Sept. 2013

EVALUATION OF CRETACEOUS LIMESTONES FROM THE AITOLOAKARNANIA PROVINCE (WESTERN GREECE) FOR THEIR USE AS ROAD AGGREGATES IN TERMS OF THEIR CONTENT IN SWELLING CLAY MINERALS

Mpalatsas I. [1], Rigopoulos I. [1], Tsikouras B. [1, 2] and Hatzipanagiotou K. [1]

[1] University of Patras, Department of Geology, Section of Earth Materials, 265 00, Patras
mpalatsas@upatras.gr, rigopoul@upatras.gr, v.tsikouras@upatras.gr, k.hatzipanagiotou@upatras.gr

[2] University of Brunei Darussalam, Department of Petroleum Geoscience, Jalan Tungku Link, Gadong BE1410, Bandar Seri Begawan, Brunei Darussalam

Abstract

The aim of this paper is to assess the suitability of a significant number of carbonate rocks from the Aitoloakarnania province (Western Greece) for their use as road construction aggregates, in terms of their content in swelling clay minerals. The study focuses on Cretaceous limestones from the Olonos-Pindos zone. Detailed petrographic analysis and the sand equivalent and methylene blue tests are carried out, in order to estimate the quantity of swelling clay minerals in aggregate particles. Special emphasis is given on correlating the results of the sand equivalent and methylene blue tests, as well as on the relationships between these engineering parameters and the petrographic data. The results are evaluated in accordance with the Greek and International suitability Standards for road construction aggregates. Although the results of the sand equivalent test indicate the suitability of the studied samples, the results of the methylene blue test imply that they are not suitable for use in all applications of road construction. Hence, it is proved that the methylene blue test is of fundamental importance for the determination of the lithotypes which are suitable for use as road aggregates in various applications.

Key words: *Carbonate rocks, Olonos-Pindos zone, aggregates, sand equivalent, methylene blue.*

Περίληψη

Σκοπός της εργασίας αυτής είναι η εκτίμηση της καταλληλότητας ενός σημαντικού αριθμού ανθρακικών πετρωμάτων από το Νομό Αιτ/νίας (Δυτική Ελλάδα) για χρήση τους ως αδρανή υλικά σε έργα οδοποιίας, ως προς την περιεκτικότητά τους σε διογκούμενα αργιλικά ορυκτά. Η μελέτη επικεντρώνεται σε Κρητιδικούς ασβεστόλιθους από τη ζώνη Ωλονού–Πίνδου. Πραγματοποιήθηκε λεπτομερής πετρογραφική εξέταση και επιπλέον προσδιορίστηκαν οι δοκιμές ισοδύναμου άμμου και μπλε του μεθυλενίου, έτσι ώστε να εκτιμηθεί η περιεκτικότητα των υπό μελέτη αδρανών σε αργιλικά ορυκτά. Ιδιαίτερη έμφαση δόθηκε στον προσδιορισμό των συσχετίσεων μεταξύ των δοκιμών ισοδύναμου άμμου και μπλε του μεθυλενίου, καθώς και στη σύνδεση των αποτελεσμάτων των δοκιμών αυτών με τις πετρογραφικές παραμέτρους. Οι τιμές των υπό μελέτη ασβεστόλιθων αξιολογήθηκαν με βάση τις ελληνικές και διεθνείς προδιαγραφές, στις

οποίες αναφέρονται οι τυπικές αποδεκτές τιμές όσον αφορά στην καταλληλότητά τους για χρήση ως αδρανή υλικά οδοποιίας. Παρότι τα αποτελέσματα της δοκιμής ισοδύναμου άμμου υποδεικνύουν την καταλληλότητα των υπό μελέτη δειγμάτων, από τη δοκιμή μπλε του μεθυλενίου προκύπτει ότι αυτά δεν είναι κατάλληλα για χρήση τους σε όλες τις εφαρμογές οδοποιίας. Συνεπώς, προκύπτει ότι η δοκιμή μπλε του μεθυλενίου είναι εξαιρετικής σημασίας για τον προσδιορισμό εκείνων των πετρωμάτων που είναι κατάλληλα για χρήση τους στις διάφορες εφαρμογές οδοποιίας.
Λέξεις κλειδιά: *Ανθρακικά πετρώματα, ζώνη Ωλονού–Πίνδου, αδρανή υλικά, ισοδύναμο άμμου, μπλε του μεθυλενίου.*

1. Introduction

The increasing demand for crushed rock aggregates in various applications and especially the requirement for hard aggregates in numerous infrastructure works of Greece, have increased the necessity for the detection of carbonate rocks which are suitable for the production of aggregates used for: bases and sub-bases, improvement layers, bituminous mixtures, concrete and embankments. The suitability of aggregate materials depends on their various physicomechanical properties, as well as on their content in clay minerals. In terms of grain size, clay refers to particles less than 2 μm in diameter, while clay minerals are hydrous aluminium phyllosilicates. Swelling clay minerals are considered to be the minerals of the smectite group. The latter absorb water and tend to swell, causing significant problems in the unbound road layers. Clay minerals also reduce the cohesion of bituminous mixtures, due to the fact that they destroy the adhesion between asphalt and aggregate particles (Smith and Collis, 2001; Nikolaides *et al*., 2007).

The sand equivalent test is used for the determination of clay-like fines in aggregates; however the methylene blue test is applied to obtain an assessment of the quantity of swelling clay minerals of the smectite type in a sample of aggregate. These tests are carried out in aggregates used in both unbound and bound road layers. This paper investigates the suitability of 51 carbonate rock samples from the Aitoloakarnania province (Western Greece) for their use as road construction aggregates, based on their mineralogical-textural features and on the results of the sand equivalent and methylene blue tests.

2. Geological Setting

The carbonate rocks of the Olonos-Pindos zone (Aitoloakarnania province, Western Greece) (Fig. 1), cover a total area of 417 km^2. They comprise part of the lower unit (thickness more than 1000 m) of the Olonos-Pindos zone, which includes pelagic limestones of Triassic to Upper Cretaceous age. These limestones are intercalated with radiolarites of Middle Jurassic to Lower Cretaceous, while their thickness varies from 200 to 400 m (Katsikatsos, 1992; Mountrakis, 1985). The Upper Cretaceous limestones, which comprise the upper part of this lower unit, are whitish limestones, gray micritic limestones with veins filled with secondary calcite and red limestones.

The studied area (Fig. 1) and especially the Upper Cretaceous carbonate rocks cover an area of 301 km^2, which corresponds to the 72.35 % of the overall carbonate formations of the Olonos-Pindos zone. The rock slopes of the area exhibit layers up to 35 cm thick and are cut by joints with opening up to 3-4 cm. These lithologies are characterized by intense fracturing and folding.

3. Petrography

The petrographic study of the Upper Cretaceous carbonate rocks of the Olonos-Pindos zone (Aitoloakarnania province) includes the macroscopic and microscopic examination of 51 samples. These samples were collected from representative localities of quarry faces or natural slopes, with a view to be fresh and to represent the full variability of the quarry products.

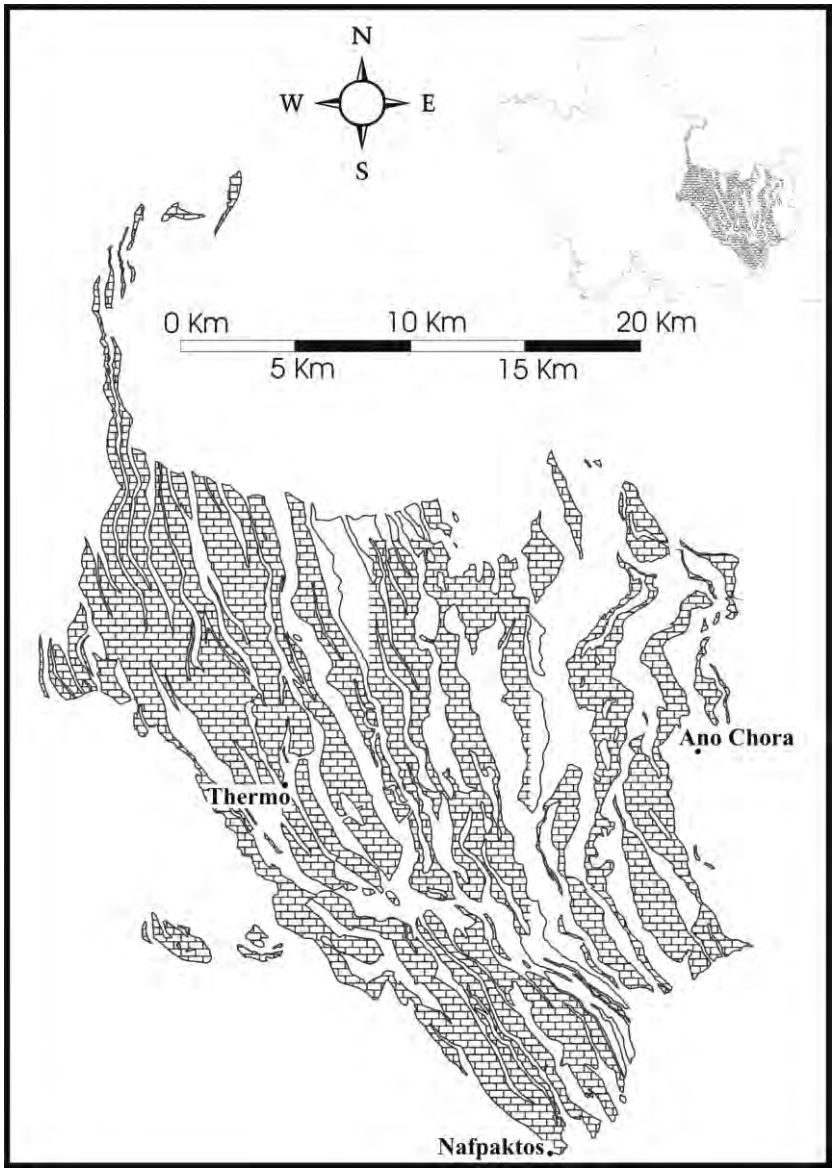

Figure 1 - Simplified geological map of the studied Upper Cretaceous limestones of the Olonos-Pindos zone (Aitoloakarnania province).

Macroscopically, the studied rock types show a dense network of sparitic veins and their colour is whitish to gray, except for samples AT2B, AT6C, AT8C, AT9B, AT17C, AT19B, AT22B and AT42B, which have a red colour. The samples were collected based on petrographic criteria, which significantly determine their quality as aggregate material (Zarif and Tuğrul, 2003; Tsikouras *et al*., 2005; Pomonis *et al*., 2007).

The microscopic examination, which was carried out using polarized microscopy at the Research Laboratory of Minerals and Rocks, Department of Geology, University of Patras, indicated that the samples are micritic or sparitic microcrystalline limestones with veins filled with secondary calcite. Quartz crystals, as well as the phyllosilicate minerals muscovite and/or biotite are also present. The dominance of bioclasts is obvious, however many samples also contain lithoclasts, endoclasts or opaque minerals. The Upper Cretaceous limestones can be classified according to the grains/matrix ratio and their content in endoclasts, lithoclasts or bioclasts, as follows:

(a) Fossiliferous-micrites according to Folk (1962) or mudstones according to Dunham (1962) with a joint system which cuts a micritic matrix. The joints have been filled with sparitic calcite (Fig. 2a). Additionally, there is a low content of fossils in a uniform, dark coloured micritic matrix. Joints with a thickness up to 0.3 mm, which are filled with secondary, microcrystalline calcite, are also present. Moreover, areas with channel or fracture porosity are observed (Fig. 2b).

(b) Sparse biomicrites according to Folk (1962) and wackestones/packstones according to Dunham (1962). They are biomicritic limestones, which contain pieces of broken fossils, as well as sizeable and well preserved bioclasts (skeletal remains of planktonic foraminifera). In addition, the characteristic fossils of Upper Cretaceous *Calpionella* (Fig. 2c) and *Globotruncana* (Fig. 2d) occur in a micritic matrix. The joints of this lithology are filled with microcrystalline calcite, while the stylolithes are filled with Fe-oxides and clay minerals (Fig. 2d).

(c) Packed biomicrites according to the classification scheme of Folk (1962) and packstones according to the classification scheme of Dunham (1962). These rocks contain bioclasts in a proportion of more than 50 % (Fig. 2e, f), as well as carbonate grains which are surrounded by a micritic matrix.

(d) Sorted-unsorted intrabiosparites according to Folk (1962) and grainstones according to Dunham (1962). They comprise lithoclasts, endoclasts, bioclasts (Fig. 2g, h) and opaque minerals in a sparite cement, while the micritic matrix is absent. These rocks are characterized by the presence of isometric, coarse grains of calcite, which contain abundant lithoclasts, endoclasts and fossils (Fig. 2h). The porosity is primarily channel-type, filled with sparite material. Stylolithic or fenestral porosity filled with Fe-oxides and/or clay minerals can also be observed.

4. Geometrical Properties

The suitability of the studied limestones for their use as aggregate material in highway engineering was assessed based on the results of the sand equivalent and methylene blue tests. Subsequently, the results were evaluated in accordance with the Greek and International suitability Standards for road construction aggregates (Tables 1, 2).

The sand equivalent test (SE) defines the relative proportions of clay-like fines in aggregates passing ASTM Sieve No 4 (4.75 mm), since an excess of clays is usually detrimental to the performance of any aggregate (Hveem, 1953). This test was carried out in accordance with ASTM D2419. As can be seen in Table 3, the SE values of the studied rocks are $\geq 60\%$; hence they are suitable for use in base and sub-base layers, bituminous mixtures for wearing courses and cold bituminous mixtures. Specifically, the SE values range as follows:

- Fossiliferous micrites: 60 – 77 %
- Biomicrites: 60 – 79 %
- Sparites: 68 – 81 %

The methylene blue test (MB), which is applied to obtain an assessment of the quantity of swelling clay minerals of the smectite type in a sample of aggregate, was determined according to the procedure described in EN 933-9. This test was determined in the fine aggregate fraction of 0-0.125 mm (MBf), taking into account that it gives results with better repeatability (Nikolaides *et al*., 2007). The MBf values of the studied rocks range as follows:

- Fossiliferous micrites: 8.6 – 26.6 g/kg
- Biomicrites: 6.6 – 20.0 g/kg
- Sparites: 4.3 – 9.3 g/kg

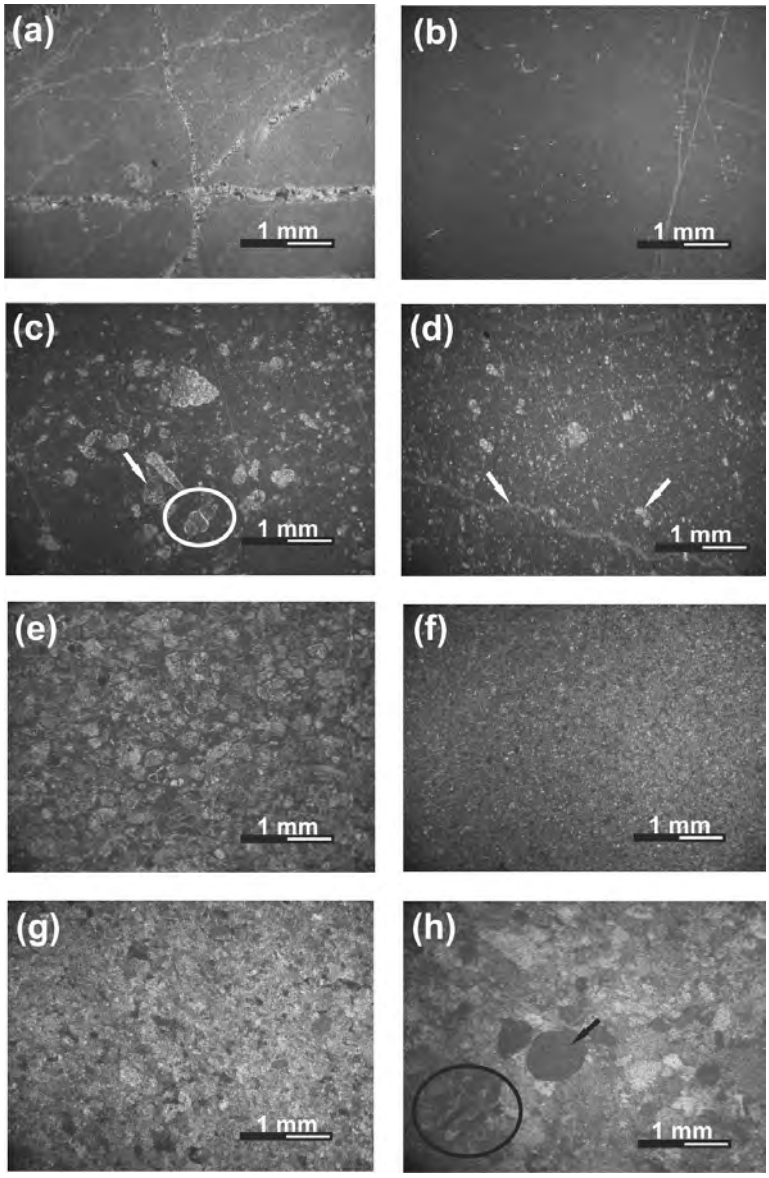

Figure 2 – (a) Fossiliferous micrite: joints filled with sparry calcite in a micritic matrix (Nicols+); (b) Fossiliferous micrite: sparsely scattered fossils in a micritic matrix with fracture porosity (Nicols+); (c) Sparse biomicrite/wackestone: pieces of broken calpionellids (arrow) and foraminifera (ellipse) (Nicols+); (d) Sparse biomicrite/wackestone: moderate participation of fossils in a rock type with fracture porosity. Fe-oxides and clay minerals fill the stylolith at the lower part of the field of view (left arrow). The right arrow shows a Globotruncana (Nicols+); (e) Packed biomicrite/packstone: abundant bioclasts (>50%) in a micritic matrix (Nicols+); (f) Packed biomicrite/packstone: bioclasts and opaque minerals (Nicols+); (g) Sorted intrabiosparite/ grainstone: participation of lithoclasts-bioclasts (Nicols+); (h) Unsorted intrabiosparite/grainstone: participation of endoclasts (arrow) and fossils (ellipse) (Nicols+).

Table 1 - Permissible sand equivalent (SE) values.

Aggregates for:	SE (%) Greek Specifications
Bituminous mixtures for wearing courses	> 55
Bituminous base courses	> 50
Unbound base courses	> 50
Unbound sub-base courses	> 40
Cold bituminous mixtures for wearing courses	> 50
Cold bituminous mixtures for base layers	> 45

Table 2 - Permissible methylene blue (MBf) values.

Aggregates for:	Specifications (MBf) NF XP P 18-540	Greek Specifications (MBf)
Base and sub-base layers	≤ 10(3)	≤10(1)
Bituminous bases	≤ 10(3)	≤10
Bituminous bound layers	≤ 10(3)	≤10
Wearing courses	≤ 10(3)	≤10
Concrete	≤ 10(3)	
Cold bituminous mixtures Micro-surfacing layers	≤ 7 or ≤ 8 MBf (2) ≤ 10 MBf (2)	

(1) Egnatia Odos S.A.
(2) Specifications of other countries
(3) French specifications

(e.g. linear, logarithmic) and it was observed that the logarithmic model gives the higher R^2 values. As can be seen in Figure 3, different trends were calculated for fossiliferous micrites, biomicrites and sparites, which are described by the following equations:

$$SE = -12.962 \times \ln MBf + 105.79, \quad R2 = 0.5666 \quad \textit{(Fossiliferous micrites)}$$

$$SE = -9.0277 \times \ln MBf + 94.156, \quad R2 = 0.3255 \quad \textit{(Biomicrites)}$$

$$SE = -10.157 \times \ln MBf + 91.664, \quad R^2 = 0.3853 \quad \textit{(Sparites)}$$

The calculated R^2 values indicate weak to moderate negative correlations between SE and MBf. The insignificant correlations between these geometrical parameters can be attributed to the different nature of the sand equivalent and methylene blue tests.

Based on the petrographic classification according to Folk (1962) and Dunham (1962) and the dispersion of the results of the geometrical properties (Fig. 3), the studied carbonate rocks can be further grouped into:

A) Fossiliferous micrites

1st Group: Samples AT7A, AT10A and AT11A with MBf values varying between 8.6 and 9.6 g/kg and SE values ranging from 76 to 77 %.

2nd Group: Samples AT6D, AT8A, AT13A, AT13B, AT17B, AT17C, AT20B and AT42B with MBf values from 13.0 to 26.6 g/kg and SE values from 60 to 76 %. The substantially higher MBf values of the samples of this group, compared to those of the first group, are due to the clay minerals which fill the styloliths of the samples of the second group.

Table 3 - Results of the Methylene Blue and Sand Equivalent of the studied rock samples from the Olonos-Pindos zone (Aitoloakarnania province).

Sample	Rock Type	Methylene Blue (g/kg)	Sand Equivalent (%)
AT6D	Fossiliferous micrite	21.0	64
AT7A	Fossiliferous micrite	9.6	76
AT8A	Fossiliferous micrite	26.6	68
AT9B	Fossiliferous micrite	19.6	63
AT10A	Fossiliferous micrite	8.6	76
AT11A	Fossiliferous micrite	9.0	77
AT13A	Fossiliferous micrite	13.0	76
AT13B	Fossiliferous micrite	16.6	70
AT17B	Fossiliferous micrite	16.0	77
AT17C	Fossiliferous micrite	17.6	65
AT20B	Fossiliferous micrite	16.6	73
AT42B	Fossiliferous micrite	20.3	60
AT2A	Biomicrite	13.3	71
AT2B	Biomicrite	16.3	68
AT4A	Biomicrite	10.7	70
AT6A	Biomicrite	8.0	77
AT6C	Biomicrite	10.6	67
AT7B	Biomicrite	8.0	76
AT8C	Biomicrite	16.6	68
AT11C	Biomicrite	8.3	72
AT12A	Biomicrite	6.6	77
AT12B	Biomicrite	10.0	78
AT14A	Biomicrite	10.0	69
AT15A	Biomicrite	11.6	71
AT16A	Biomicrite	16.6	60
AT18B	Biomicrite	11.0	73
AT18C	Biomicrite	15.0	75
AT19A	Biomicrite	12.3	77
AT19B	Biomicrite	14.0	68
AT22A	Biomicrite	9.0	73
AT22B	Biomicrite	20.0	72
AT22C	Biomicrite	10.0	71
AT48	Biomicrite	8.3	77
AT49A	Biomicrite	10.0	79
AT49B	Biomicrite	15.0	70
AT54	Biomicrite	10.0	76
AT2C	Sparite	8.6	77
AT4B	Sparite	5.6	76
AT6B	Sparite	7.6	68
AT8B	Sparite	9.3	67
AT9A	Sparite	5.6	68
AT10B	Sparite	8.6	70
AT11B	Sparite	8.3	68
AT14B	Sparite	9.0	72
AT15B	Sparite	6.6	70
AT16B	Sparite	9.3	71
AT17A	Sparite	4.3	81
AT18A	Sparite	5.0	77
AT19C	Sparite	6.3	69
AT20A	Sparite	5.0	76
AT42A	Sparite	9.3	68

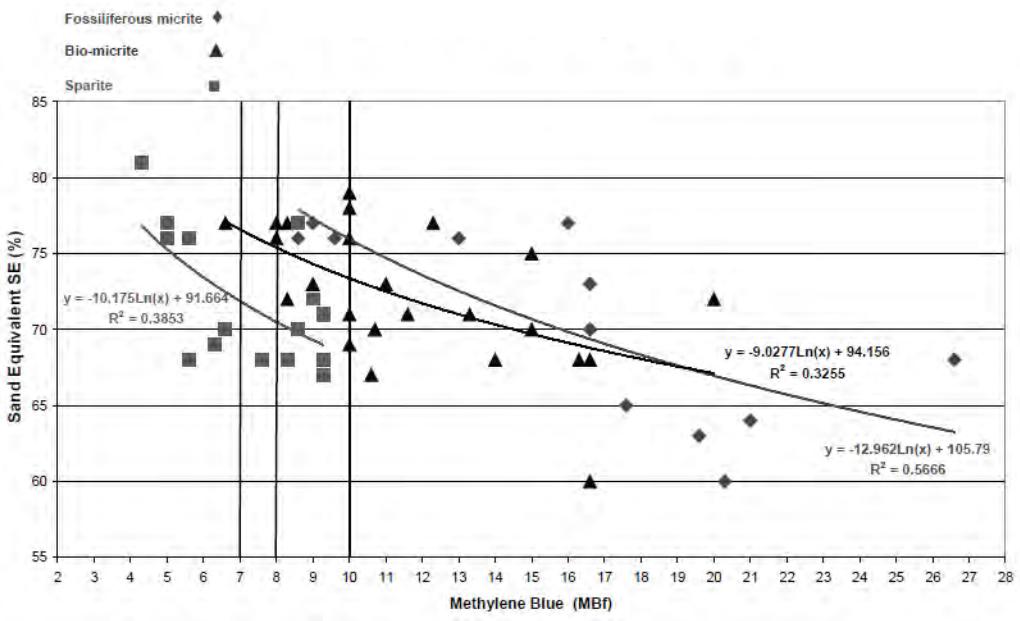

Figure 3 - Correlation between methylene blue (MBf) and sand equivalent (SE) of the studied limestones.

B) Biomicrites

1st Group: Samples AT12A, AT6A, AT11C, AT22A and AT7B whose MBf values range from 6.6 to 9.0 g/kg and SE values from 72 to 77 %.

2nd Group: Samples AT2A, AT2B, AT4A, AT6C, AT8C, AT12B, AT14A, AT14B, AT15A, AT16A, AT18B, AT18C, AT19A, AT19B, AT22B, AT48, AT49A, AT49B, AT54 and AT22C with MBf values ranging from 8.3 to 16.6 g/kg and SE values ranging from 60 to 79 %. The stylolith or channel porosity of these samples has been filled with clay material and this is considered to be the reason for their higher MBf values.

C) Sparites

1st Group: Samples AT2C, AT4B, AT17A, AT18A and AT20A with MBf varying from 4.3 to 8.6 g/kg and SE ranging from 72 and 81 %. The higher MBf value of sample AT2C compared to the other samples is attributed to its stylolithic porosity, which is filled with Fe-oxides and clay minerals.

2nd Group: Samples AT6B, AT8B, AT6C, AT9A, AT12B, AT11B, AT14B, AT15B, AT16B, AT19C and AT42A with MBf ranging between 5.6 and 9.3 g/kg and SE varying from 67 to 73 %. The higher MBf and lower SE values of these samples, compared to those of the first group, are assigned to the fact that the samples of the second group have higher percentage of stylolythic and channel porosity, filled with clay material.

5. Discussion

The petrographic features, as well as the degree of tectonic deformation and porosity of rocks are determinative parameters for their quality as aggregate material (Hartley, 1974; Kazi and Al-Mansour, 1980; Al-Jassar and Hawkins, 1991; Smith and Collis, 2001; Jensen *et al*., 2010). Additionally, the geometrical properties of aggregates play an important role in the estimation of aggregate performance in-service (Nikolaides *et al*., 2007; Rigopoulos *et al*., 2013). The results of this study bring new details to the understanding of the interrelations between the sand equivalent test,

the methylene blue test and the petrographic characteristics of carbonate rocks. The suitability of the studied samples for their use as aggregates in road construction is also assessed.

The petrographic examination indicated that the carbonate rocks of this study can be grouped into: (a) fossiliferous micrites, (b) biomicrites, and (c) sparites. The geometrical properties of these lithotypes seem to be highly controlled by their microscopic features. Those samples which have stylolithic and/or channel porosity, filled with clay material, tend to have lower sand equivalent and higher methylene blue values, implying the interdependence among petrography and engineering parameters. Similar relationships have been referred by various researchers (e.g. Miskovsky *et al*., 2004; Kondelchuk and Miskovsky, 2008; Rigopoulos *et al*., 2013).

Regarding the correlation between sand equivalent and methylene blue, regression analysis indicated that there is no significant relationship between these geometrical parameters due to the different nature of the two tests. Similar results have also been referred by Nikolaides *et al*. (2007).

The values of the sand equivalent test for the studied Upper Cretaceous limestones are ≥60%; hence they are all considered suitable for use in base and sub-base layers, bituminous mixtures for wearing courses and cold bituminous mixtures. However, the sand equivalent test defines the relative proportions of clay-like fines in aggregates; thus the results of the methylene blue test, which determines the quantity of swelling clay minerals, should also be taken into consideration. Samples AT2C, AT14B, AT16B, AT10B, AT42A, AT8B, AT11B, AT11C, AT14B, AT7A, AT14B, AT10A, AT22A, AT7A and AT11A have MBf values ≤10 g/kg and ≥8 g/kg, so they are suitable for use in base and sub-base road layers and bituminous mixtures for wearing courses. Samples AT4B, AT6A, AT6B, AT7B, AT9A, AT12A, AT15B, AT17A, AT18A, AT19C and AT20A, which show MBf values ≤8 g/kg, can also be used as aggregates in cold bituminous mixtures. On the other hand, samples AT12B, AT14A, AT22C, AT49A and AT54 are near the MBf limit of 10 g/kg and exhibit relatively high sand equivalent values (SE: 69-79%). The rest of the samples (AT2A, AT2B, AT4A, AT6C, AT6D, AT8A, AT8C, AT9B, AT13A, AT13B, AT15A, AT16A, AT17B, AT17C, AT18B, AT18C, AT19A, AT19B, AT22B, ATA22B, AT42B and AT49B), whose MBf values range from 10.6 to 26.6 g/kg, are unsuitable for use in road construction due to the high proportion of swelling clay minerals in their porosity.

6. Conclusions

The carbonate lithotypes of this study can be grouped into: (a) fossiliferous micrites, (b) biomicrites, and (c) sparites. Their geometrical parameters seem to be significantly controlled by their mineralogical and textural characteristics. The samples which have stylolithic and/or channel porosity, filled with clay material, tend to have lower sand equivalent and higher methylene blue values. This indicates that the knowledge of the petrographic features of rocks is of great importance for the estimation of their engineering behaviour.

There is insignificant relationship between the results of the sand equivalent and methylene blue tests, which is assigned to the different nature of these two geometrical properties.

The results of the sand equivalent test indicate that the studied samples are suitable for use as aggregates in base and sub-base layers, bituminous mixtures for wearing courses and cold bituminous mixtures; however the results of the methylene blue test imply that a number of the studied limestones are not suitable for use in road construction. Thus, it is proved that the methylene blue test is of fundamental significance for the determination of the lithotypes which are suitable for use as road aggregates in various applications.

7. Acknowledgements

Critical reviews by Professor Dr. Georgia Pe-Piper and an anonymous reviewer are gratefully appreciated.

8. References

Al-Jassar S. and Hawkins A.B. 1991. The Carboniferous Limestone of the Bristol area: a review of the influence of the lithology and chemistry on its use as a geomaterial, *Q. J. Eng. Geol. Hydrogeol.*, 24, 143-158.

Dunham R.J. 1962. Classification of carbonate rocks according to depositional texture, in Ham, W.E. (ed), Classification of carbonate rocks: *Am. Assoc. Petroleum Geologists Memoir*, 108-121.

Folk R.L. 1962. Spectral subdivision of limestone types. In Ham, W.E., ed., Classification of carbonate rocks: *Am. Assoc. Petroleum Geologists, Memoir* 1, 62-84.

Hartley A. 1974. A review of the geological factors influencing the mechanical properties of road surface aggregates, *Q. J. Eng. Geol.*, 7, 69-100.

Hveem F.N. 1953. Sand Equivalent test for control of materials during construction, *Highway Research Board Proceedings*, 32, Washington.

Jensen L.R.D., Friis H., Fundal E., Møller P. and Jespersen M. 2010. Analysis of limestone micromechanical properties by optical microscopy, *Eng. Geol.*, 110, 43-50.

Katsikatsos G. 1992. *Geology of Greece*, University of Patras, 451 pp.

Kazi A. and Al-Mansour, Z.R. 1980. Influence of geological factors on abrasion and soundness characteristics of aggregates, *Eng. Geol.*, 15, 195-203.

Kondelchuk D. and Miskovsky K. 2008. Determination of the test methods sensitive to free mica content in aggregate fine fractions, *J. Mater. Eng. Perform.*, 18, 282-286.

Miskovsky K., Taborda Duarte M., Kou S.Q. and Lindqvist, P.-A., 2004. Influence of the mineralogical composition and textural properties on the quality of coarse aggregates, *J. Mater. Eng. Perform.*, 13, 144-150.

Mountrakis D. 1985. *Geology of Greece, University Studio Press, Thessaloniki*, 207 pp.

Nikolaides A., Manthos E. and Sarafidou M. 2007. Sand equivalent and methylene blue value of aggregates for highway engineering, *Foundations of Civil and Environmental Engineering*, 10, 111-121.

Pomonis P., Rigopoulos I., Tsikouras B., and Hatzipanagiotou, K. 2007. Relationships between petrographic and physicomechanical properties of basic igneous rocks from the Pindos ophiolitic complex, NW Greece, *Bull. Geol. Soc. Greece*, XXXVII, 947-958.

Rigopoulos I., Tsikouras B., Pomonis P. and Hatzipanagiotou K. 2013. Correlations between petrographic and geometrical properties of ophiolitic aggregates from Greece, *Bull. Eng. Geol. Env.* (in press).

Smith M.R. and Collis L. 2001. Aggregates: Sand Gravel and Crushed Rock aggregates for Construction Purposes, *Geological Society, London Eng. Geol., Sp. Publ. 17*, 339 p.

Tsikouras B., Pomonis P., Rigopoulos, I., and Hatzipanagiotou, K., 2005. Investigation for the suitability of basic ophiolitic rocks from Mikrokleisoura, Grevena, for their use as antiskid aggregates and railway ballast, *Proc. 2nd Congress of the Committee of Economic Geology, Mineralogy, and Geochemistry of the Geological Society of Greece*, 347-356.

Zarif I.H. and Tuğrul A., 2003. Aggregate properties of Devonian limestones for use in concrete in Istanbul, Turkey, *Bull. Eng. Geol. Env.*, 62, 379-388.

Δελτίο της Ελληνικής Γεωλογικής Εταιρίας, τομ. XLVII , 2013
Πρακτικά 13ου Διεθνούς Συνεδρίου, Χανιά, Σεπτ. 2013

Bulletin of the Geological Society of Greece, vol. XLVII 2013
Proceedings of the 13th International Congress, Chania, Sept. 2013

THE UPGRADING AMENABILITY OF THE PHOSPHATE DEPOSITS OF WESTERN GREECE

Pantelaki O.[1], Bellis G.[1] and Stamboliadis E.[1*]

[1]Technical University of Crete, [*]Corresponding author elistach@mred.tuc.gr

Abstract

In Epirus, Western Greece, there exist extensive low quality phosphate rock deposits. Although phosphate fertilizers are extensively used in agriculture and Greece imports about 200.000 ton/y, of phosphate ore in addition to ready to use phosphate fertilizers, these deposits are not yet exploited.

This work examines the possibility to upgrade this type of ore using different methods of mineral processing. The results obtained are poor and unsatisfactory for commercial exploitation. The main reasons are the type of P_2O_5 bearing mineral and mainly it's intergrowth with the associated gangue ones.

The present work examines the mineralogy and chemistry of the ore, the energy size relationship in crushing using a centrifugal crusher, its behavior in grinding, its behavior to heavy liquid treatment and its floatability using oleic acid as well as dialkyl-orthophosphate collectors. The later were specially prepared for this purpose. Finally the ore was calcined at 950 ^oC in order to dissociate the existing calcite to CaO, which is subsequently selectively hydrolyzed to give $Ca(OH)_2$ that is finely disseminated in the pulp and can be separated from the coarser phosphate grain.

Key words: *Energy size relationship, Flotation, calcination and hydrolysis*.

Περίληψη

Στη Δυτική Ελλάδα, στην περιοχή της Ηπείρου, υπάρχουν κοιτάσματα φωσφοριτών μεγάλης έκτασης αλλά χαμηλής ποιότητας. Τα κοιτάσματα αυτά δεν υφίστανται εκμετάλλευση μέχρι και σήμερα, παρόλο που η Ελλάδα εισάγει πάνω από 200,000 τόνους φωσφορίτη ετησίως για την παραγωγή φωσφορικών λιπασμάτων που χρησιμοποιούνται στη γεωργία.

Η εργασία αυτή εξετάζει την πιθανότητα αναβάθμισης ενός τέτοιου τύπου κοιτάσματος χρησιμοποιώντας διαφορετικές μεθόδους του εμπλουτισμού μεταλλευμάτων. Τα αποτελέσματα που εξήχθησαν δεν κρίνονται ικανοποιητικά για οικονομική εκμετάλλευση. Κύρια αιτία είναι ο τύπος των ορυκτών του P_2O_5 και κυρίως η σύμφυσή τους με τα στείρα ορυκτά.

Στη μελέτη αυτή αρχικά εξετάστηκε η ορυκτολογία και η χημεία του πετρώματος, η σχέση ενέργειας και μεγέθους κατά τη θραύση τους χρησιμοποιώντας ένα φυγοκεντρικό μύλο και η συμπεριφορά του πετρώματος κατά τη λειοτρίβηση. Στη συνέχεια μελετήθηκε η συμπεριφορά του σε δοκιμές με βαρέα υγρά καθώς και σε δοκιμές επίπλευσης τόσο με ελαϊκό οξύ όσο και με διαλκυλι-ορθοφωσφορικους συλλέκτες. Οι τελευταίοι παρασκευάστηκαν ειδικά για το σκοπό αυτό. Τέλος, το πέτρωμα καυστικοποιήθηκε στους 950 ^oC, με σκοπό την μετατροπή του περιεχόμενου ασβεστίτη σε CaO, που στη συνέχεια υποβάλλεται σε υδρόλυση εκλεκτικά και

σχηματίζει $Ca(OH)_2$ το οποίο κατανέμεται λεπτόκοκκα στον πολφό και μπορεί να διαχωριστεί από τα χονδρύτερα τεμαχίδια του φωσφορίτη.
Λέξεις κλειδιά: *Σχέση ενέργειας μεγέθους, Επίπλευση, καυστικοποίηση και υδρόλυση.*

1. Introduction

The need for the development of the Greek mineral resources is very urgent, especially in times of economic recession and negative foreign commercial balance. The imports of phosphate ores, to cover the needs of the fertilizers plant in Kavala are of the order of 200.000 ton/year not including the imports of ready to use phosphate fertilizers products.

In Epirus, Western Greece, there are millions of tons of low grade phosphate ore deposits that remain unexploitable, mainly due to their low grade. The P_2O_5 % content varies between 10-30% with an average of 20% (Tsailas et al., 1980). The present work is an effort; to investigate the properties of the above material and at the same time reveal the reasons of the existing difficulty to obtain a commercial grade concentrate. The ore sample under investigation was collected by IGME, the Institution of Geological and Metallurgical Research in Preveza and forwarded to the Technical University of Crete.

The present work examines the chemical composition of the ore sample, its mineralogical composition and its macroscopic as well as the microscopic structure together with the intergrowth of the mineral phases present. Since the scope of the work is not only mineralogical but is mainly oriented to the production of a commercial concentrate from the raw material, several mineral processing procedures were also tried. These methods were chosen according to the mineralogical and structural characteristics of the ore. Macroscopically it appears that the ore consists of parallel zones, a few millimeters thick that vary in their P_2O_5 content. Microscopically the minerals appear to be very finely intergrown and the liberation is not easy.

Initially the ore was tested in a centrifugal crusher to study its breakage energy requirements and to obtain the energy size relationship. Heavy liquids laboratory tests were curried out designed mainly for relative coarse grains above 1 mm in order to take advantage of the macroscopic zone structure of the ore. As the liberation of the minerals present in all zones is very bad the ore sample was ground further down in an effort to liberate the minerals. Grinding tests were performed to decide the products size to be used for mineral separation at a lower particle size than the one used for heavy liquids. The process most likely to succeed at a low particle size after grinding is froth flotation. Two types of anionic collectors were used namely the oleic acid and dialkyl-phosphate sodium salts of varying alkyl chain length.

The physical separation processes used did not provide a commercial grade concentrate and for this reason it was decided to proceed with a thermal decomposition process followed by hydrolysis one. Although the cost of such a process is very high for commercial application it was selected in order to investigate such a possibility for theoretical purposes only.

2. Description of the Various Experimental Procedures

Primary crushing of the initial -50 mm sample was performed in a laboratory scale jaw crusher to a -30 mm particle size. A centrifugal crusher was used for secondary crushing to finer sizes as well as a means to investigate the breakage energy for different size classes of the material and to establish the energy size relationship. This crusher is equipped with a rotating disc capable to run at preset frequencies and thus control the kinetic energy of the material before crushing. For the grinding of the material down to flotation size a laboratory rod mill (D=20 cm L= 28 cm) was used, running at 85% of its critical rotation frequency and equipped with 9 kg of steel rods.

The sizing of the material was achieved in a laboratory screen, using 20 cm diameter screens with sieve openings at a constant ratio of two. The shaking of the screen was mechanically performed on a vibrating shaker. For the fine size fractions the laser beam size analysis was also used.

The chemical analysis of the samples was performed using a XR Fluorescence analysis apparatus. The loss on ignition (LOI) tests were performed in the available electric furnace at 950 ^{o}C.

The minerals identification was achieved using an XR Difractometer followed by the investigation of thin and polished sections with a metallurgical microscope.

The heavy liquids used for separation were mixtures of tetrabromoethane (sg 2.96) and carbon tetrachloride (sg 1.6) in suitable analogies (proportions) to obtain the required densities.

For the flotation tests a 4 liter laboratory cell was used with controlled rotation frequency of its rotor.

3. Description of the Material

Macroscopic examination of the particles of the initial sample, about 50 -70 mm in size, shows that all rock particles present have two parallel sides that follow the direction of zones with alternating dark and light coloring of pale brown. A thin section of the sample presented in Figure 1, was prepared vertical to the direction of the colored zones. A careful inspection can distinguish a vertical light color zone surrounded by darker ones. The only mineral crystals that can be identified are bright crystals of calcite, while the rest is microcrystalline

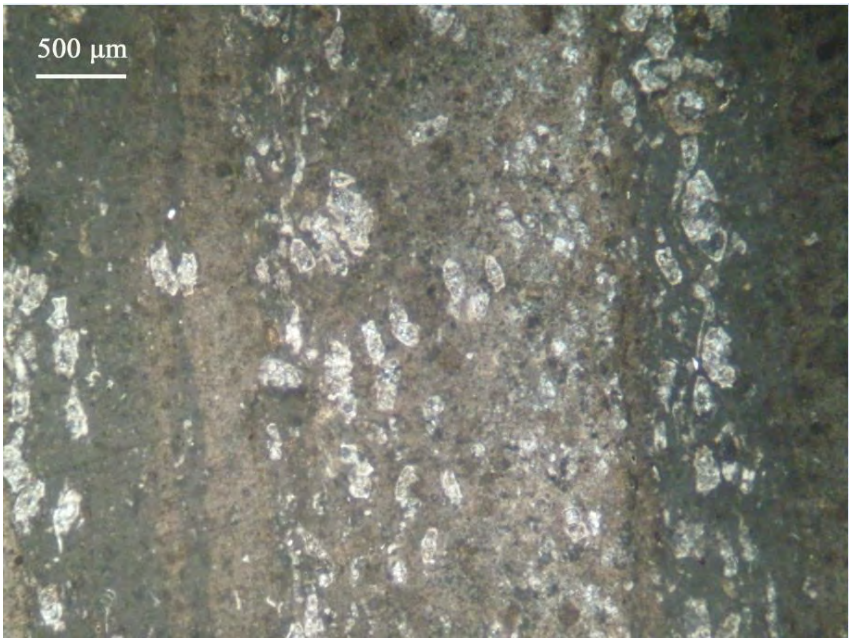

Figure 1 - Thin section, transmitted light //Nicols.

The initial sample after crushing to -4 mm was tested for its physical and chemical properties. Some grains of the material were used to prepare a polished section that appears in Figure 2. It is obvious that no crystals can be identified and all grains look the same

The mineralogical composition obtained by XRD appears in Table 1, which shows that the most abundant mineral is calcite followed by francolite, a carbonate rich fluoroapatite (Perdikatsis,1991). Quartz is a minority mineral.

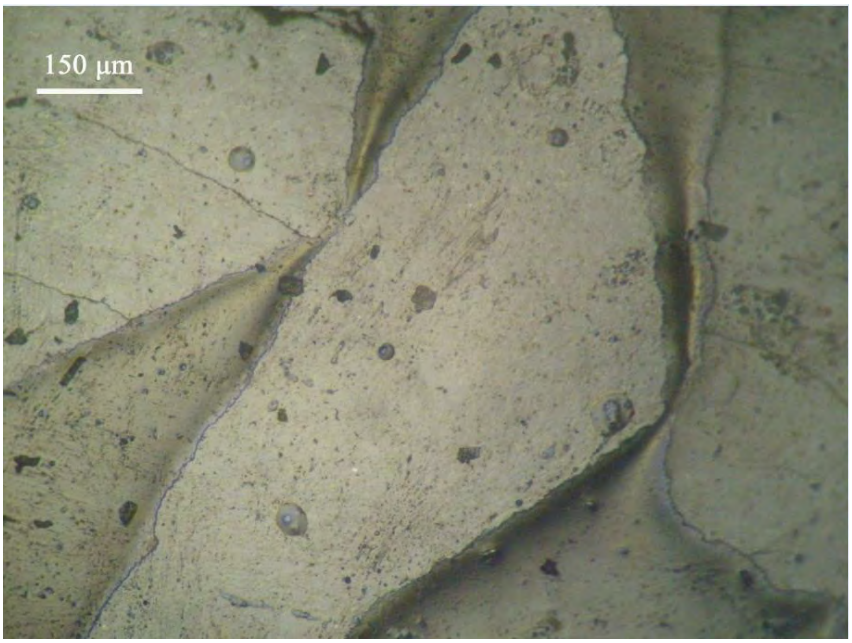

Figure 2 - Polished section, reflected light //Nicols.

Table 1 - Mineralogical composition of the initial sample.

Mineral	Chemical formula	Estimated weight %
Calcite	$CaCO_3$	61.2
Francolite	$Ca_5(PO_4.CO_3)_3(F.O)$	34.4
Quartz	SiO_2	4.4

The size analysis of the -4 mm crushed sample is presented in Table 2 together with the chemical analysis of each fraction (Bellis, 2013).

Table 2 - Size analysis and chemical analysis of the size fractions.

Screen size fractions mm	Weight %	P_2O_5 %	CaO %	Fe_2O_3 %	SiO_2 %	LOI %	N.D. %	Total
-4+2	7.24	12.12	40.44	0.27	3.03	29.55	14.59	100.00
-2+1	35.52	10.88	37.54	0.27	2.99	28.79	19.53	100.00
-1+0.5	30.00	10.97	40.21	0.29	2.89	29.26	16.38	100.00
-0.5+0.25	13.10	11.02	39.44	0.30	2.98	29.53	16.73	100.00
-0.25	14.14	13.35	46.31	0.45	3.43	29.09	7.37	100.00
Total	100.00	11.36	40.04	0.31	3.02	29.13	16.14	100.00

Table 2 shows that there is no significant difference of the chemical analysis of the different size fractions with a slight deviation of the very fine fraction. This is a clear index of the luck of liberation between the minerals and confirms what was also observed by the thin section of

Figure1. The majority constituents are CaO and LOI that according to the mineralogical analysis it represents the CO_2 of calcite and partially of francolite.

The non detected components are partially due to analytical error but also due to F, MgO, Na_2O, and SO_3 that according to (Perdikatsis, 1991) are constituents of francolite from Epirus which has the following exact formula.

$[(Ca)_{9.86}].[(Mg)_{0.08}].[(Na)_{0.38}].[(PO4)_{4.82}].[(CO3)_{0.95}].[(SO4)_{0.2}].[(F)_{2.34}]$

The F content was measured only in the total sample and is 2.3 %, within the specification of a commercial product. According to IGME, the phosphates of western Greece contain small quantities of uranium 15-300 ppm. Radiation measurements made by Professor (Pantinakis, 2013) at the laboratory of Physics of TUC, have shown that it is within acceptable limits and lower than soil samples around TUC.

It is obvious both from the mineralogical and the chemical analysis, as well as from the distribution of the minerals in the various size fractions that the liberation of the minerals is poor and the effort to obtain a P_2O_5 rich concentrate is also predetermined to give poor results.

4. Crushing Tests in a Centrifugal Crusher

Size reduction tests of the material were performed in a centrifugal crusher using the predetermined size fractions of the material (e.g. 16-22.4 mm, 4-5.6 mm and 1-1.4 mm). The crusher has a rotating disc that accelerates the particles due to its rotation.

Figure 3 - Inside view of the centrifugal crusher.

The particles leaving the rotating disc are drawn by centrifugal forces towards the periphery and obtain a specific kinetic energy given by Equation 1 (Stamboliadis, 2013).

Equation 1 - Specific Energy Formula

$$e = (\pi \cdot D \cdot N)^2 \qquad (1)$$

Table 3 presents the calculated specific energy at the frequencies used for the tests

Table 3 - Frequency – specific energy relationship

Rotation Frequency (rpm)	1000	1500	2000	2500
Specific energy (J/kg)	685	1541	2739	4279

Separate samples of each size fraction tested are fed to the crusher at the indicated frequencies and the product is screened at the lowest class size of the feed fraction. The mass percentage that passes through the screen is the mass broken below the specific size. The plot of broken mass at the different corresponding specific energies for the feed size-fraction tested is presented in Figure 4.

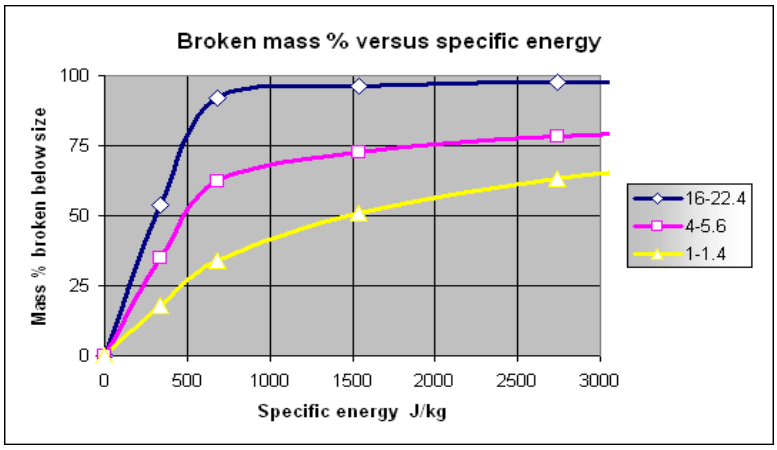

Figure 4 - Broken mass versus specific energy.

According to the model that describes the phenomenon, the breakage specific energy for a size fraction is defined as the one that if exerted on this fraction, half of its mass will be broken below its size class (Stamboliadis et al., 2012). After that, one can find from Figure 4 the corresponding energies ΔH for 50% broken mass for all the size fractions tested.

The corresponding plot of the breakage energy ΔH versus size is presented in Figure 5. The relationship is described by the Equation 2.

Equation 2 - Breakage Energy Formula

$$\Delta H = 1424 \cdot X^{-0.5564} \qquad (2)$$

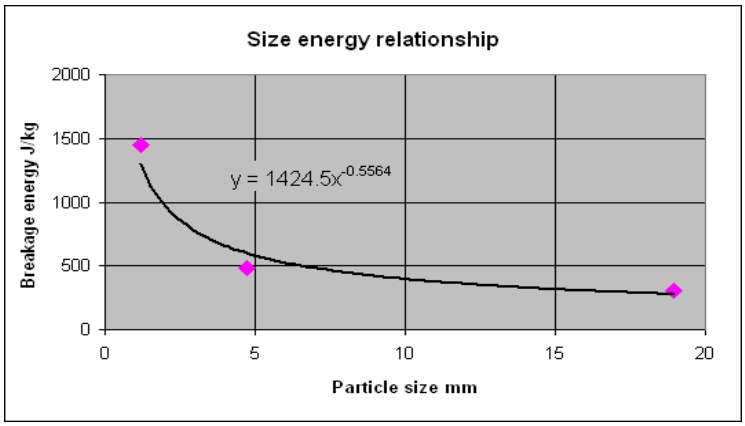

Figure 5 - Breakage energy versus particle size.

5. Heavy Liquid Tests

Heavy liquid tests were performed to the size fraction 0.5-4 mm at liquid densities 2.65 and 2.7 g/cm^3. The cumulative products obtained are presented in Figure 6 for the sinks and in Figure 7 for the floats.

From these two figures one can see that for the same density the sinks have a higher P_2O_5 content than the floats and a slightly lower CaO content. This means that there is an upgrading of the material in the sink products. The evaluation of the best density can be done by comparing the sink products in Figure 6. Obviously the wt % of the sinks drops at the higher density but the P_2O_5 content increases that best result in terms of product grade is obtained at the density of 2.7 g/cm^3. However this grade is only 15.7 % P_2O_5 and is not good enough.

The unsatisfactory results of the heavy liquids are obvious due to the insufficient liberation of the ore at the size fraction 0.5-4 mm tested and in order to overcome this problem it was decided to grind further the ore and try to achieve a better concentration using the froth flotation process.

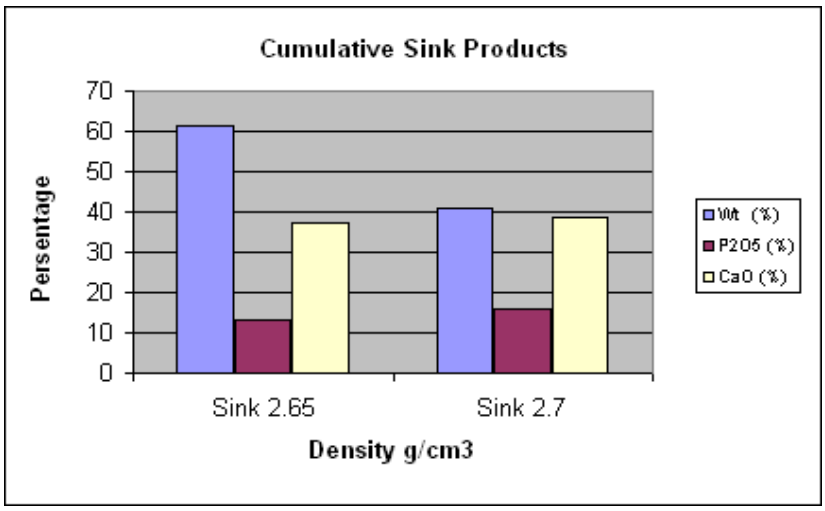

Figure 6 - Cumulative sink products.

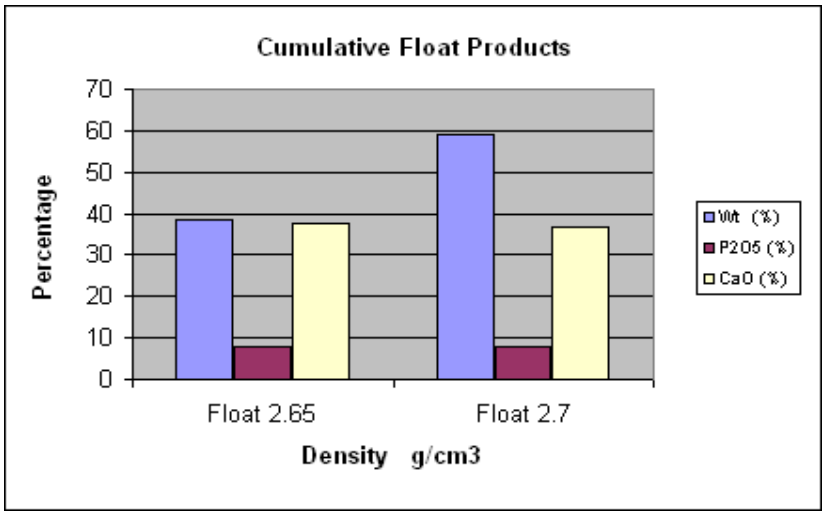

Figure 7 - Cumulative float products.

6. Flotation Tests

The size reduction of the ore, necessary for the flotation tests, was performed in the laboratory mill described earlier loaded with 500 g of feed and 350 ml water at various times. The time chosen to give a d80 size below 200 μm is 10 min. The ground product is transferred to the flotation cell adjusted to the right level with water. The reagent is added and the pulp is conditioned for 5 min. After conditioning the air is allowed to enter into the cell. The floating product is collected and the flotation time measured. At the following stage an additional quantity of the reagent is added, conditioned and floated. The process is continued until the floating product collected in minimum. The flotation products were collected and assayed. Two kinds of reagents were used, initially oleic acid and secondly sodium dialkyl phosphate salts of different alkyl lengths, namely propyl, butyl, exyl and octyl.

The results obtained for oleic acid are presented in Figure 8, where one can read the weight of the material remaining in the bottom of the flotation cell as a function of the reagent addition.

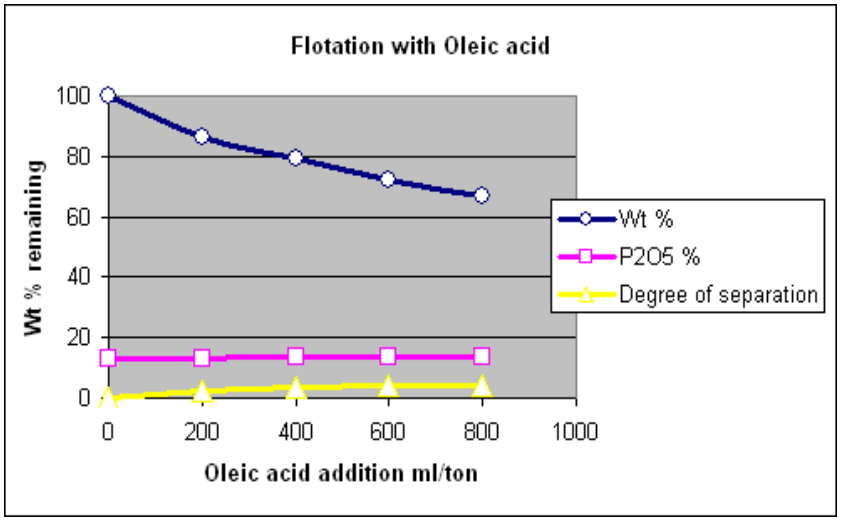

Figure 8 - Flotation with oleic acid.

In the same figure the P_2O_5 % content of the product and the degree of separation (Stamboliadis, 1984) achieved are also plotted. The weight of the product decreases with the addition of the collector but its P_2O_5 % content increases slightly. The degree of separation also increases but still it is not satisfactory. Obviously the floating product contains more CaO as the collector acts preferably on calcite. The selectivity is not good not only due to bad liberation but also in the fact that both francolite and calcite contain Ca that reacts with the reagent.

In an effort to investigate a different concentration procedure, a series of sodium dialkyl–phosphate salts were prepared that have the general formula NaR_2PO_4 where R is selected to be propyl, butyl, exyl and octyl. It was expected that these reagents could be more selective and that the length of their organic chain could play a role in the process.

The results are plotted in Figure 9 that shows the wt% of the product remaining in the flotation cell as a function of reagent addition. One can see that the remaining mass decreases as the number of carbons in the alkyl group increases from 3 to 8, or the same from propyl to octyl, How-ever the P_2O_5 % content of the floating and the remaining products is practically the same indicating no selectivity of all these reagents although the differ in the mass that they can drive with the froth.

Although for the flotation tests, the material is ground finer but the results obtained were even worse than those noted by the heavy liquids in a coarser size. Similar unsatisfactory results were obtained by Tsailas et al. (1980) and Anastassakis (1989).

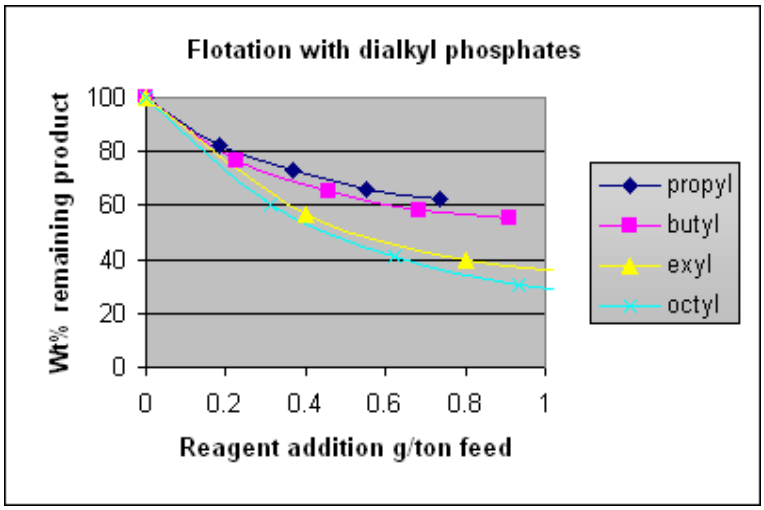

Figure 9 - Flotation with dialkyl-phosphates.

7. Calcinations and Hydrolysis Tests

Given the inability of the flotation process to produce a high grade concentrate, mainly due to the insufficient liberation, it was decided to abandon physicochemical separation methods and proceed with metallurgical and chemical methods. The aim was to separate francolite from calcite. The idea comes from the fact, that at high temperature, calcite decomposes to CaO and CO_2 that escapes to the atmosphere. The remaining CaO is easily hydrated with water to give $Ca(OH)_2$ that is diffused into the water in small molecular agglomerates that form a milky suspension. These fine $Ca(OH)_2$ agglomerates could be easily separated by size from the remaining francolite grains that hopefully would retain their initial size.

For this purpose, a quantity of the material, ground to -0.5 mm, was calcined at 950 ^oC that caused 29% loss of weight due to the evolution of CO_2. After calcination, 100 g of the calcined product are added into one liter of water with initial temperature 16 ^oC. The pulp temperature eventually increases to 22^oC and the pH of the suspension to 12.5. Both of these differences indicate that an exothermic reaction takes place that gives (OH^-) hydroxyl anions into the solution. The suspension is agitated very slightly and after one hour it is screened at 63 μm. The screen undersize and oversize are filtered, dried, weighted and assayed. The results are presented in Table 4.

Table 4 - Results after the hydration of the calcined sample.

Size	Wt %	P_2O_5 %	CaO %	SiO_2 %	LOI %
+63 μm	76,1	13.43	43.57	3.05	11.02
-63 μm	23,9	9.02	49.13	2.35	24.09

Table 4 shows that the P_2O_5 and SiO_2 contents are increased in the coarse fraction, while the CaO and LOI are increased in the fine fraction. It must be reminded that after calcination and hydration, there is no more $CaCO_3$ and the LOI is due to the decomposition of the $Ca(OH)_2$ that evolves H_2O. In any case there is a difference in the two products but still the result is not satisfactory.

8. Discussion and Conclusions

The sample of phosphate ore (11.4% P_2O_5) tested originates from the area of Epirus, Western Greece. Its main mineralogical constituents are francolite, the P_2O_5 bearing mineral, and calcite, the gangue one that is the most abundant and is responsible for the low quality of the ore. The two

minerals are very finely disseminated in the orebody and practically it is difficult, if not impossible, to liberate. The unique difference in the quality that appears is in the parallel zones, a few mm thick, of different calcite content that characterize the stromatography of the orebody obtained during different sedimentation events. This is the reason for which at relative coarse size 0.5-4 mm we were able to obtain the best possible product with 15.7 % P_2O_5 compared to flotation, where although the ore is finely ground the product assays 13.0 % P_2O_5 in the case of using oleic acid as collector.

The calcination and successive hydration tests have shown a tendency of separation that still is not efficient and needs further study. However the high cost of calcination, especially for such a low quality ore seems to be an opposing factor towards this direction.

It is recommended that further research in the processing of the ore should be combined with a parallel geological research to define places of higher ore grade and probably weathered material that perhaps could be easier to upgrade.

9. References

Anastassakis G. 1989. Contribution to the beneficiation of the unaltered phosphate rock of Epirous area (Greece), *PhD Thesis*, National Technical University, Greece, (in Greek).

Bellis G. 2013. A study for the upgrading of phosphate rock from Western Greece, *Undergraduate Thesis*, Technical University of Crete, Greece. (in Greek).

Pantinakis A. 2013. Professor of Physics, Technical University of Crete, Greece, Personal communication.

Perdikatsis B. 1991. X-Ray power diffraction study of Francolite by the Rietveld method, *Mat. Science Forum*, Vols. 79-82, pp 809-814.

Stamboliadis D. 2013. Design of a centrifugal crusher for minerals, based on the design of structures, *Undergraduate Thesis*, Technological Education Institute of Piraeus (TEI Piraeus) (in Greek).

Stamboliadis E. 1984. Measure of Separation, IMM, *Transactions Section C*, Vol 93, C16-C19.

Stamboliadis E., Stamboliadis D., Kiskira K. and Emejulu E., 2012. Crushing of mineral particles by control of their kinetic energy, Material Science and Applied Chemistry, *53rd International Scientific Conference*, Riga, Technical University.

Tsailas D., Grossou-Valta M. and Kalatzis G. 1980. Study on the possibilities of beneficiating Epirus unaltered phosphate rocks, *IGME Publications*, 016823. (in Greek).

Δελτίο της Ελληνικής Γεωλογικής Εταιρίας, τομ. XLVII , 2013
Πρακτικά 13ου Διεθνούς Συνεδρίου, Χανιά, Σεπτ. 2013

Bulletin of the Geological Society of Greece, vol. XLVII 2013
Proceedings of the 13th International Congress, Chania, Sept. 2013

"EXTRACTIVE INDUSTRIES TRANSPARENCY INITIATIVE-EITI" OUTLOOK ON THE EXPLOTATION OF ALBANIAN MINERAL RESOURCES

Shehu Ar.[1] and Shehu Ag.[2]

[1]*Aluizni-Drejtoria Qendrore, Rr. Skënder Kosturi, Tirana, Albania, arbishehu@gmail.com*

[2]*Sekretariati për Transparencë në Industrinë Nxjerrëse- AlbEITI, Blloku "Vasil Shanto", Tirana, Albania, shehu.agim@gmail.com*

Abstract

Albania is focusing its efforts in the achievement of medium and long-term development objectives, particularly so its goals for European integration and the processes to this end. Local and foreign investments and projects in the Extractive industry are growing in the last years. Statistical data and references show an increased level of production and payments made to the state. Income from hydrocarbon sector constitutes the most important part of these payments, followed by the mining sector for the production of construction materials.

The level of production and income recorded in these sectors is increasing. Proof of this are the payments made to the government by the extractive industry year after year, thus showing consistency of the economic sector and a moderate impact on the state budget and other macroeconomic indicators.

Joining this initiative comes as a continuation of reforms undertaken for this purpose, in order to increase the transparency for all payments made to the Albanian State by the Extractive Industry. It follows the path of a broad program of economic, financial and institutional reform where transparency and proper management of natural resources have a particular importance. These two factors are essential for sustainable development. The new Mining Law and other by-laws, in addition to other changes required by legal improvements and economic development of the country, reflect the requirements of this initiative.

Key words: *Natural Resources, EITI, Extractive Industries, Mining Economy, Mining Law.*

1. Introduction to EITI

1.1. What is EITI? Cumulative Data

In many countries money generated from the production of oil, gas and minerals is associated with poverty, conflict and corruption. Thus, we are dealing with what often comes as a result of the lack of transparency and accountability with respect to the payments that companies make to the governments. Extractive Industries Transparency Initiative (EITI) aims to ensure the transparency and accountability that is lacking. Undertaken on a voluntary basis and supported by a coalition of companies, governments, investors and civil society organizations, this initiative combines the efforts aimed at improving the transparency of state budget practice, by starting a process that will

provide opportunities to the citizens to urge their governments be accountable about the use of these incomes. (Mining Sector Reform, Restructuring and Future Prospects (June 2009).

Extractive Industries Transparency Initiative (EITI) supports the improvement of management in resource-rich countries through the verification and full publication of corporate payments and government income from oil, gas and mining.

Good governance is a precondition for converting large income from extractive industries into economic development and poverty reduction. When transparency and accountability are weak, extractive industries can promote poverty, corruption and conflict.

Extractive Industries Transparency Initiative (EITI) was launched by the British Prime Minister Tony Blair in Johannesburg in September 2002. The presentation was followed by the first EITI international conference, in Lancaster House, London, in June 2003, where participants from governments, extractive industries and civil society approved the following principles (www.eiti.org):

- Share a belief that the prudent use of natural resource wealth should be an important engine for sustainable economic growth that contributes to sustainable development and poverty reduction, but if not managed properly, can create negative economic and social impacts.
- Affirm that management of natural resource wealth for the benefit of a country's citizens is in the domain of sovereign governments to be exercised in the interests of their national development.
- Recognize that the benefits of resource extraction occur as revenue streams over many years and can be highly price dependent.
- Recognize that a public understanding of government revenues and expenditure over time could help public debate and inform choice of appropriate and realistic options for sustainable development.
- Underline the importance of transparency by governments and companies in the extractive industries and the need to enhance public financial management and accountability.
- Recognize that achievement of greater transparency must be set in the context of respect for contracts and laws.
- Recognize the enhanced environment for domestic and foreign direct investment that financial transparency may bring.
- Believe in the principle and practice of accountability by government to all citizens for the stewardship of revenue streams and public expenditure.
- Are committed to encouraging high standards of transparency and accountability in public life, government operations and in business,
- Believe that a broadly consistent and workable approach to the disclosure of payments and revenues is required, which is simple to undertake and to use.
- Believe that payments' disclosure in a given country should involve all extractive industry companies operating in that country.
- In seeking solutions, we believe that all stakeholders have important and relevant contributions to make – including governments and their agencies, extractive industry companies, service companies, multilateral organizations, financial organizations, investors, and non-governmental organizations.

Extractive Industries Transparency Initiative is now a global initiative supported by an International Secretariat based in Oslo, Norway, and the Council, which consists of representatives of countries, companies, civil society groups, investors and donors, who are committed to the implementation of EITI.

1.2. How does EITI Work?

The International Secretariat of the Extractive Industries Transparency Initiative works closely with the World Bank and the IMF and is responsible for daily activities related to the EITI, communication with stakeholders and organization of the Council's annual conferences by establishing important relationships through a global scale outreach and publicity program. Local EITI secretariats have been established in each implementing country. In addition to the implementing governments, EITI relies on the support from donors, many large oil companies in the world mining industry, as well as investors in those companies. They are also supported by civil society groups, many of which operate under the global Coalition "Publish what you pay".

1.3. What are the Advantages of EITI Implementation?

The entities that benefit the most from EITI are the governments and the citizens of resource-rich countries. Knowing how much companies pay and how much governments get is an essential first step in asking information from the decision-makers regarding the use of income. Resource-rich countries, which implement EITI, can benefit from the improved investment climate by to the investors and international financial institutions a clear signal that the government is committed to greater transparency and accountability. By supporting EITI in countries where they operate, companies and investors can contribute to mitigate investment risk. Civil society can benefit from the increased amount of information in the public sector for the incomes that governments manage on behalf of the citizens.

In brief, "implementing the EITI in the framework of the program for improving governance will serve to ensure that incomes from oil, gas and mining activities promote sustainable development and the poverty reduction."

Joining this initiative improves foreign business climate in the mining sector, increases investments in this sector, and creates the conditions for a broader participation of local business in mining activities. It provides new opportunities for finding donors for various funding, improvements to the legislation or other projects related to mining activities mainly related to the establishment of relations between government bodies and the public, etc.

1.4. EITI Criteria

During the EITI International Conference, held in London in March 2005, participants agreed on the EITI criteria. The Conference served to announce what countries should do to successfully implement EITI. Implementation of EITI must be consistent with the following Criteria (www.eiti.org):

- Regular publication of all the oil, gas and mining companies payments made by the companies to the government ("payments") and all revenues received by governments from oil, gas and mining companies ("revenues") to a wide audience in a publicly accessible, comprehensive manner.
- Where such audits do not already exist, payments and revenues are the subject of a credible, independent audit, applying international auditing standards.
- Payments and revenues are reconciled by a credible, independent administrator, applying international auditing standards and by the publication of the administrator's opinion regarding the matter.
- This approach is extended to all companies including state-owned enterprises.
- Civil society is actively engaged as a participant in the design, monitoring and evaluation of this process and contributes towards public debate.

- A public, financially sustainable work plan for all the above mentioned is developed by the host government, with assistance of the international financial institutions where required, including measurable targets, a timetable for implementation, and an assessment of potential capacity constraints.

1.5. How is EITI Implementation Financed?

Extractive Industries Transparency Initiative is supported by the legislation in force in the implementing countries. It is financed from implementing countries resources and partly through a Multi Donor Trust Fund (MDTF) managed from the World Bank. Furthermore, other donors provide some special funds for EITI implementation as per each country.

2. Community Profit Distribution Mechanism

2.1. Sustainable Communities

Sustainable communities are the outcome of good policies and laws that are planned and implemented at local level from the responsible institutions/organizations, with the active participation of community members. Some of the key instruments to ensure that local communities benefit from extractive industries are:

- community consultation framework, to assess and determine the roles and responsibilities of government(s), company(ies), non-governmental organizations, donors and the affected local communities on the measures to address the environmental and social impacts;
- community development plan, which is coordinated by the Government, both at central and local level, in consultation with stakeholders, including the active participation of communities, aiming the mainstreaming of mining operations and planning the closure of mines in broader economic plans at regional level.

The ultimate goal should be the transformation of the community from a mere beneficiary to a reliable partner.

2.2. Local Communities

Local communities affected by mining activities may be offered a wide range of benefits. These include: the provision of infrastructure in rural areas, the establishment of small and medium enterprises, building human resources through trainings that support companies, thus providing professional skills either to work directly in the mines, or in supporting secondary industries.

In principle, the full package of benefits for the community should include:

- **Employment and income related benefits**
- **Benefits aimed at building local human resources and institutional capacities**
- **Community benefits resulting from the establishment of infrastructure** - providing access to: (i) education (schools); (ii) markets, where local communities sell their products (roads); (iii) health care (medical facilities); and (iv) potable water etc., which, ideally, should be supported by the investor and the government and managed by the community. The distribution of benefits will be effective if the accumulation of human and social capital is promoted, by improving health care and education standards for the local population, as well as its collective ability to organize, prioritize, represent and negotiate effectively its interests towards third parties, such as the Government.

2. 3. Trust Funds

These funds are effective mechanisms to support the accumulation of human and social capital that are either:

- Set up to finance local development initiatives and be managed by the community, according to its needs;
- Or set up to provide funds for future generations.

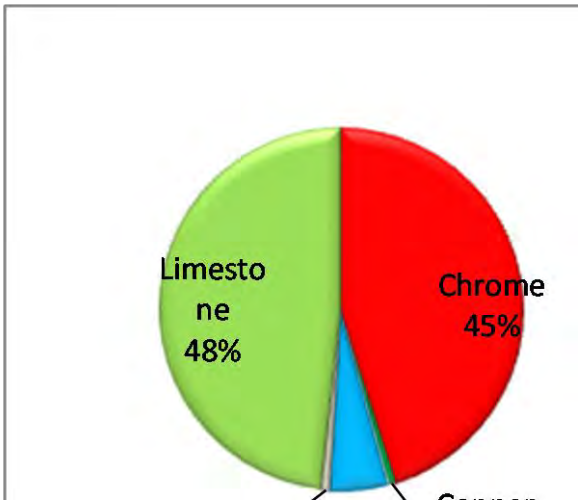

Chart 1 - Albanian Companies Operating in the Mining Sector.

2.4. Measures for the Distribution of Benefits from the Mining Sector

2.4.1. Mineral Property Royalties

The mining Law clearly stipulates that 25% of the mineral property royalties shall be paid to the local communities in the areas where mines for which exploitation permits are issued are located, while the rest shall be paid to the central government.

It would have been fairer if mineral property royalties were paid directly to the local government from the beneficiary company, and then reconciled with the central government payments for co-ordination and audit.

2.4.2. Model of the Community Development Forum

The forum has two main functions. The first function is to serve as a place for the exchange of information on the project between the user and the central and local government and landowners regarding the nature, scope and impact of the project. The second function is to determine how the various stakeholders will allocate the benefits of the project, which will then be reflected in the number of agreements for the project, or MoUs.

These agreements define the roles and responsibilities of all involved parties (government, mining companies and community), and include services and benefits that will be provided to the affected project area. To be mentioned among them is the provision of community infrastructure and sharing of financial benefits of the project. In exchange for the benefits, the community and landowners are committed not to interrupt the implementation of the project, and to cooperate with the government and the company. These agreements bind the parties to an ongoing process of consultations, where issues related to the development can be discussed and resolved during the process. This initial consultation process and drafting of various agreements should be finalized before the endorsement of the Development/Concession Agreement between the government and the mining companies.

This broad participation approach, which emphasizes cooperation and mutual obligations, has a number of key advantages.

- First, it provides a flexible model that can adapt to diverse issues and needs of different communities.
- Second, it is a comprehensive approach, and all relevant stakeholders are part of the management and decision-making based on communication, consultation and negotiation.
- Third, the approach has essentially a democratic and participatory character. People in the mining area play an active role in decision-making.
- Finally, the Development Forum should have strong legal grounds and it represents applicable contracts. Therefore, it constitutes reliable and legally binding commitments, which create the trus conomic activity.

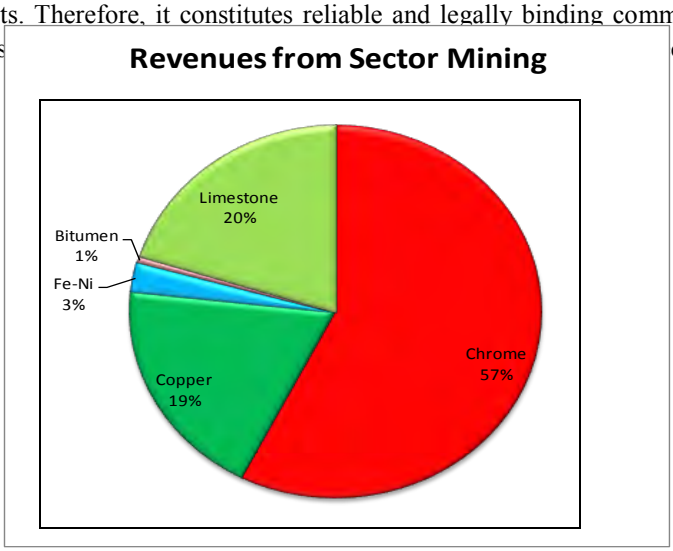

Chart 2 - Revenues from Mining Sector.

3. Interpretations and Conclusions

3.1. What do EITI Reported Data Show?

With income amounting to USD 3,950 per capita and a GDP of USD 12.168 million, Albania's extractive industry is based mainly on the hydrocarbon and mining sector.

The first EITI report on Albania was published in May 2011 with 2009 data. Data and statistical references show a payment level of USD 33.962 million made by these sectors of extractive industry, representing a moderate contribution to state income balance-sheet by about 1% and in the country's GDP by 0.3%. The mining sector accounts for 6% of payments made to the state in the extractive industry, as compared to the hydrocarbon sector, accounting for 94%.

According to the EITI report, incomes in 2009 amount to USD 10.6/capita only from the extractive industry. The data were evaluated and reviewed by the independent administrator, a foreign company "Fair Links" Srl, France, for 2009; the company is compiling the report for 2010, as part of the assessment work that is being done for Albania's participation in EITI's international structure.

Based on the respective reports and data it results that the majority of liabilities and payments made by manufacturing companies in favor of the state are:

- Signature bonuses
- Mineral royalties
- Corporate profit tax

- Surface fees
- Other important payments made to the state

The analysis for companies and the criteria for their inclusion in EITI report 2009 are mainly based on:

- Productivity (production) accounting for a considerable share in their activity;
- Revenue to state;
- Surface areas.

Table 1 - EITI declarations on the oil sector.

Ref	In K USD	Private Oil Companies (1)	Alb Petrol (2)	State (3)	(1) -(2)-(3)
A	Signature bonuses (exploration phase)	160	-	160	0
B	Royalties	8828	-	8175	653
C	Corporate profit tax (Private Oil Companies)	0	-	0	0
D	Signature bonuses (production phase)	0	50	-	(50)
E	Share of Production allocated to Alb-Petrol	22915	22915	-	0
F	Corporate profit tax (Alb Petrol)	-	0	0	0
G	Dividends (Alb Petrol)	-	0	0	0
Total		**31903**	**22965**	**8335**	

To this end, companies that occupy a significant share in the production and income generated in the mining production and hydrocarbons were assessed, i.e. those providing higher payments to the state.

Therefore, the sectors and companies that have exploitation permits, while assessing their activity in 2009 and 2010 were analyzed.

In the EITI report on the reconciliation of payments from the extractive industry sector in Albania in 2009, the independent administrator "Fair Links" Srl, France declared that, for the oil sector, payments of companies to the state amount to USD 31.903 million, of which 27.7% or USD 8.828 million in the form of mineral royalties, whereas in the mining sector payments amount to USD 2.059 million, of which 48.6% or USD 1 million in the form of mineral royalties. The analysis shows that the relevant amounts were reconciled based on EITI criteria and that they are evidence of state budget support and the opportunity for funding of projects in extractive industries.

In the 2010 report it was proposed to increase the level and number of indicators that will be analyzed as compared to the 2009 report, to include:

- a larger number of companies, for example from 48 in 2009 to 118 in 2010 (109 from mines and 9 from hydrocarbons),
- companies that produce construction materials,
- companies that produce bitumen and tar sands,
- all oil companies in Albania.

The proposals related to the limit of income generated and consequently the payments to be deposited to the state from the companies included in the 2010 EITI report are as follows:

- increase the number from about 60% to minimum 70% for the mining industry companies
- reach a percentage of 100% for companies in the hydrocarbons sector.

Table 2 - EITI declarations on the mining sector.

In M USD	Companies (1)	State (2)	(1) – (2)
Signature bonuses	0.2	0.1	0.1
Surface fees	12.2	12.1	0.1
Royalties	93.1	92.5	0.6
Corporate profit tax	86.2	81.4	4.8
TOTAL	**191.7**	**186.1**	**5.6**

Improvements to the extractive industry legislation, regulations and updated guidelines for highlighting the development and growth of investments, income, payments to the state, growth and structural improvements to the local budget of areas where extractive industries operate- are very favorable factors for the positive assessment done for Albania's participation in the EITI.

The activity and level of implementation of granted permits for use, along with the analysis of the results achieved on the level of implementation of the exploration permits, which were granted to private local and foreign companies, have to be analyzed, reconciled and described fully and clearly in the analytical statements of EITI reconciliation report in Albania based on the information, publication and broad public discussion, by referring to 2009, 2010 onwards.

The experience gained and the results obtained from the implementation of the first 2009 EITI Report, with 2009 being the baseline year (www.albeiti.org), the recommendations given by the EITI International Secretariat regarding the assessment of the work and achievements of Albania so far, are encouraging. The assessment conducted at the meeting of the Board of the EITI International Secretariat in October 2011 states that "The Board congratulates the government, the companies and civil society in Albania for the meaningful progress in implementing EITI". This requires the work and follow up process to be in accordance with the principles and criteria set out in the EITI rules.

In this regard, the main goal of this work is to achieve full compliance of the tasks, criteria and support the communities in the areas of extractive industry in order to implement EITI as part of a program for improving governance in order to serve and guarantee that the income from oil, gas and mining activities in the country promote sustainable development and poverty reduction.

3.2 EITI Implementation Results

The implementation of programs for Albania’s membership in the EITI, according to the principles, criteria and rules of EITI is an on-going process. The legislation on the mining sector has improved, reflecting the requirements and the economic development of the country. The application of international auditing regulations in the extractive industry companies in the country has improved as well.

EITI process is public and widely discussed, by having collaboration between government, stakeholders and civil society in order to promote sustainable development and poverty reduction.

EITI reports for 2009 and 2010 and the guarantee for the submission of reports for the coming years are a positive example for Albania, wishing to become a member with full rights in the EITI.

Central and local governments collaborate in programs and projects applicable to the extractive industry areas but this must be accompanied by an increase in the level of consultation with stakeholders and communities in these areas.

Community consultation framework is important in order to evaluate and assign roles and responsibilities of government, civil society, non-governmental organizations, donors, and local communities on measures to address the environmental and social impacts.

The establishment and operation of development forums in the communities of extractive industry areas is proposed. The final objective should to be turning the community from a mere beneficiary to a reliable partner (EITI Business Guide, How companies can support implementation).

4. Acknowledgements

We would like to express our gratitude to all those who gave us the possibility to complete this article. We want to thank METE, the National Agency for Natural Resources of Albania (AKBN), AlbEITI Secretariat and the World Bank Mission in Albania.

5. References

Albania-National Strategy for Development and Integration 2007 to 2013 – Government of Albania, Council of Ministers (March 2008). Available at web site: http://mie.gov.al/skedaret/1226905647-NSDI.pdf

Albania-Mining Sector Reform, Restructuring and Future Prospects (June 2009) – World Bank. Available at web site: http://www-wds.worldbank.org/external/default/WDSContentServer/WDSP/IB/2009/07/21/000333037_20090721002237/Rendered/PDF/475390ESW0P1101C0Disclosed071171091.pdf

Albania-Business and Investment Development Strategy 2007 to 2013 – METE (February 2007). Available at web site: http://www.mete.gov.al/doc/20071218084802_business_and_investment_development_strategy.pdf

Albania-World Bank, Report Nr. 47539-AL " Albanian mining sector reform, restructuring and future prospects", June 2009.

AlbEITI Secretariat, Work Plan for 2011-2013, Tirana 2011 Available at web site: www.albeiti.org

EITI Board Meeting, Board Paper Nr. 18-5-A, Validation: Albania, 25-26 October 2011, Jakarta

EITI Secretariat, Extracting Data - Overview of the EITI Reports published 2005-2011,Oslo, 2011. Available at web site: www.eiti.org

EITI Secretariat, EITI Rules including validation guide, 2011 Edition, Oslo, April 2011 Available at web site: www.eiti.org

EITI Secretariat, EITI Business Guide, How companies can support implementation, Oslo, 2008

Fair Links srl, France, Republic of Albania- EITI report for the year 2009, April 2011

Kalaja D. Communication Strategy and Action Plan for AlbEITI, June 2011, Tirana

Legislation in force, Law Nr.10304, dated 15.07.2010 "On the mining sector in the Republic of Albania ", other legal acts in force.

Mati S. - Mining policy for a sustainable development of mining activities- Workshop, Tirana 2010.

METE, JICA, Progress Report " The study for the master plan for promoting the mining industry of Albania", Tirana, November 2009.

Δελτίο της Ελληνικής Γεωλογικής Εταιρίας, τομ. XLVII , 2013
Πρακτικά 13ου Διεθνούς Συνεδρίου, Χανιά, Σεπτ. 2013

Bulletin of the Geological Society of Greece, vol. XLVII 2013
Proceedings of the 13th International Congress, Chania, Sept. 2013

SPECTROSCOPIC AND THERMAL STUDY OF BENTONITES FROM MILOS ISLAND, GREECE

Bourliva A.[1], Michailidis K.[1], Sikalidis C.[2] and Filippidis A.[1]

[1] *Department of Mineralogy-Petrology-Economic Geology, School of Geology, Aristotle University of Thessaloniki, 54124 Thessaloniki, Greece, annab@geo.auth.gr*

[2] *Department of Chemical Engineering, Aristotle University of Thessaloniki, 54124 Thessaloniki Greece*

Abstract

Bentonitic clays, currently in use in over hundred areas, are among the most important industrial raw materials. In most of the cases, bentonites predominantly consist of montmorillonite which is a 2:1 layer clay mineral formed by one alumina octahedral sheet placed between two silica tetrahedral sheets. Three bentonite composite samples (BN1, BN2, BN3) with some differences in mineralogical and chemical composition from Milos island ("Miloan"), Greece were investigated by X-ray diffraction (XRD), atomic absorption spectrometry (AAS), differential thermal analysis (DTA), thermogravimetric analysis (TG), Fourier transform infrared (FTIR) and surface area (BET) measurements techniques. Mineralogically, bentonite samples were characterized by high concentrations of smectite (>85%) and minor amounts of other clay minerals (illite and kaolinite). Nonclay minerals such as quartz, calcite and pyrite were also identified. The infrared spectrum of the bentonites also revealed the presence of dioctahedral smectite as the major component and quartz as the main impurity in all the samples. The stretching vibration at 3698cm^{-1} in the sample BN3 could be ascribed to kaolinite. DTA-TG curves of all samples were measured in the temperature range 75-1000^{o}C. The total weight losses for the bentonite samples BN1, BN2 and BN3 were determined as 16.25, 12.32 and 13.35% respectively.

Key words: *smectite, Milos, FTIR, DTA/TG.*

Περίληψη

Ο μπεντονίτης, με πληθώρα εφαρμογών και χρήσεων, αποτελεί μια από τις σημαντικότερες βιομηχανικές πρώτες ύλες. Στις περισσότερες περιπτώσεις, ο μπεντονίτης αποτελείται κυρίως από μοντμοριλλονίτη, ένα 2:1 αργιλικό ορυκτό με δομή που αποτελείται από ένα οκτάεδρο αργιλίου που τοποθετείται μεταξύ δύο τετραέδρων πυριτίου. Τρία σύνθετα δείγματα μπεντονίτη (BN1, BN2, BN3) με διαφορές τόσο στην ορυκτολογική όσο και στην χημική σύσταση από το νησί της Μήλου, μελετήθηκαν με την μέθοδο της περιθλασιμετρίας ακτίνων-Χ (XRD), με την μέθοδο της φασματοσκοπίας ατομικής απορρόφησης (Α.Α.S.), με διαφορική θερμική (DTA) και θερμοσταθμική ανάλυση (TG), με φασματοσκοπία υπέρυθρης ακτινοβολίας με μετασχηματισμούς Fourier (FTIR) και με μετρήσεις της ειδικής επιφάνειας (BET). Ορυκτολογικά τα δείγματα χαρακτηρίζονται από υψηλό ποσοστό σμεκτίτη (>85%) και μικρά ποσοστά άλλων αργιλικών ορυκτών (ιλλίτης και καολινίτης). Προσδιορίστηκαν,

επίσης, χαμηλά ποσοστά μη αργιλικών ορυκτών όπως χαλαζίας, ασβεστίτης και σιδηροπυρίτης. Το υπέρυθρο φάσμα των δειγμάτων επιβεβαίωσε την παρουσία του διοκταεδρικού σμεκτίτη ως κύριου συστατικού και του χαλαζία ως κύριας πρόσμιξης σε όλα τα δείγματα. Η δόνηση στα 3698cm^{-1} στο δείγμα BN3 αποδόθηκε στην παρουσία καολινίτη. Οι καμπύλες DTA/TG όλων των δειγμάτων μετρήθηκαν στο θερμοκρασιακό εύρος 75-1000^{o}C. Οι συνολικές απώλειες βάρους προσδιορίστηκαν σε 16.25, 12.32 και 13.35% για τα δείγματα BN1, BN2 και BN3, αντίστοιχα.
Λέξεις κλειδιά: *μοντμοριλλονίτης, Μήλος, FTIR, DTA/TG.*

1. Introduction

Bentonite, currently in use in over a hundred areas, is among the most important industrial raw materials (Grim and Goven, 1978; Murray, 2000). The dominant mineral in bentonite is montmorillonite which belongs to the smectite group (Grim and Goven, 1978). Smectite is a 2:1 layer clay mineral and has two silica tetrahedral sheets bonded to a central alumina octahedral sheet. Smectites are described either as dioctahedral or as trioctahedral depending upon whether the octahedral cations are predominantly trivalent or divalent, respectively. The net negative electric charge of the 2:1 layers arising from the natural isomorphic substitution of Fe^{2+} and Mg^{2+} for Al^{3+} in the octahedral sites and Al^{3+} for Si^{4+} in tetrahedral sites is balanced by the presence of exchangeable cations such as Na^{+} and Ca^{2+} located between the layers and surrounding the edges (Murray, 2000).

Bentonites are among the most important industrial raw materials and have wide range of uses in many industrial applications like oil, petroleum, cosmetics, ceramics and paintings (Murray, 1991). The application areas of bentonites depend on the quality and quantity of their smectites and other clay and non-clay mineral constituents (Grim, 1968). Some physico-chemical properties of bentonites as well as their mineralogy are greatly affected by thermal treatment. Due to these effects, the investigation of thermal behavior of bentonite samples is of great importance. Additionally, spectroscopic (FTIR) investigation in clay mineral speciation was recently regarded as a useful tool with a multipurpose application, since some physical details of clay lattices and experimental qualitative correlation between the samples were made possible (Davarcioğlu and Çiftçi, 2009).

Greek bentonite is mainly quarried in the north-eastern part of the island, where some of the economically most important bentonite deposits in Europe are concentrated (Kogel et al., 2006). The deposits have been formed by the alteration of Lower Pleistocene volcanoclastic rocks (Christidis et al., 1995). The bentonite reserves are estimated to exceed 20Mt and along with United States, Greece is one of the largest exporters of bentonites. Previous studies on the Miloan bentonites performed at different stages of quarry development, referred on their mineralogy, mode of formation and on their physical properties (Christidis et al., 1995; Christidis and Markopoulos, 1995; Christidis and Scott, 1996; Perraki and Orphanoudaki, 1997). Since information on the evolution of the smectite characteristics in space is very important, representative samples of the Miloan bentonites were used in this investigation. Thus, the aim of this study was to present new data concerning the mineralogical, structural and thermal properties of bentonites from Milos island.

2. Materials and Methods

2.1. Bentonite Samples

Three natural bentonite samples from W.Ankeria, N.Aspro Horio and S.Aspro Horio deposits of Milos island, coded as BN1, BN2 and BN3 respectively, were used in the present study. The samples were provided by the S&B Industrial Minerals S.A. The samples, were ground, sieved to

obtain the <63μm particle size fraction, washed with distilled water to remove the soluble salts possibly present and air dried before the experiments.

2.2. Analytical Methods and Instrumentation

Chemical analyses of the rock samples were performed by AAS using a Perkin Elmer 5000 apparatus. Sample was crushed in an agate mill till a size <20 μm. Then dried for a whole night at 105°C. 200 mg of powdered bentonite, weighed with a precision of ±0.03 was placed in Teflon autoclaves. Sample dissolution was achieved with the addition of 10 mL HF, 2 mL H_2SO_4 and 1 mL $HClO_3$. The autoclaves were heated at 110°C for 60 min. After being cooled in tap water for about 30 min, 5 g of H_3BO_3 were quickly added along with 30 mL of warm distilled water. The solution was stirred for 5–15 min on a magnetic plate. After this stage the solution was absolutely clear owing to complete dissolution. It was then transferred to a 250 mL volumetric flask, adjusted to volume and stored in a polyethylene container. From this solution Si, Al and Mn were determined with flame atomic absorption spectroscopy. 10 mL from the first solution was condensed in an open Teflon vessel until it was completely dry. Then 4 mL HCl 1:9 were added and left to evaporate (this procedure is done twice). Finally, after all the liquid has evaporated, 10 mL HCl 1:9 are added to the solid residue along with 1 mL dense HCl. The solution was transferred to a 100 mL volumetric flask along with 10 mL of 50 mg mL^{-1} $LaCl_3$ solution. The solution was adjusted to 100 mL volume and was used to determine K, Na, Ca, Mg and Fe with flame atomic absorption spectroscopy. P and Ti were determined with a Spekol, Carl Zeiss simple beam spectrophotometer. Loss of ignition (LOI) was determined by heating 0.5–1 g of rock powder for 2 h at 1050°C. Detection limits in solution were: Si 1.8 μg mL^{-1}, Al 1.0 μg mL^{-1}, Fe 0.12 μg mL^{-1}, Mn 0.055 μg mL^{-1}, Mg 0.007 μg mL^{-1}, Ca 0.08 μg mL^{-1}, Na 0.015 μg mL^{-1}, K 0.04 μg mL^{-1}.

Mineralogical characterization of the bentonites as well as semi-quantitative mineral determination was performed by X-Ray powder diffraction (XRPD) using a Philips PW1710 diffractometer. Ni-filtered copper Kα radiation was used energized to 35kV and 25mA, in the range 3-63^{o}2θ at a scan speed of 1.2^o/min. The characterization of the mineral phases was performed semi-quantitatively on the basis of the intensity (counts) of specific reflections, density, and mass absorption coefficient (CuKα) of the identified mineral phases.

Infrared spectra of the bentonite samples were recorded (4000–400cm^{-1}) with Perkin-Elmer FTIR Spectrum 1000 spectrometer at a resolution of 4cm^{-1} using KBr pellet technique. BET surface areas were calculated from the first part of the N_2 adsorption isotherm (P/Po<0.5) obtained at liquid nitrogen temperature with N_2 in Autosorb (Quantachrome Corporation) equipment. High-purity (99.99%) nitrogen was used in adsorption measurements. Simultaneous DTA/TG experiments were carried out using a TA Instrument SD 2960 thermal analyzer. Approximately 15±2 mg of sample was used in each run. The samples were placed in an alumina crucible and an empty alumina crucible was used as a reference standard. All experiments were performed at a linear heating rate of 10^{o}C min^{-1} over the temperature range of 75–1000^{o}C.

3. Results and Discussion

3.1. Chemical Analysis

The results of chemical analyses of bentonite samples are presented in Table 1. SiO_2 and Al_2O_3 constitute the main oxides in the bentonites composition with contents ranging 52.92-60.24% and 16.97-18.33% respectively, whereas TiO_2, MnO, K_2O and P_2O_5 are present only in small quantities. As shown in Table 1, the weight percent of calcium contained in the bentonite samples (1.39-3.05%) is higher than that of sodium (0.70-1.13%). The MgO content ranges between 1.78 and 4.30%. In both cases, the Fe_2O_3 content is high (about 5–10%).

Table 1 – Chemical analyses (wt %) of the bentonite samples.

Chemical analysis	BN1	BN2	BN3
SiO_2	56.83	60.24	52.92
Al_2O_3	16.97	18.33	18.04
TiO_2	0.67	0.72	0.63
MnO	0.07	0.01	0.01
Fe_2O_3	5.72	5.17	10.62
MgO	4.30	3.30	1.78
CaO	3.05	2.02	1.39
Na_2O	1.13	0.92	0.70
K_2O	0.57	0.68	1.13
P_2O_5	0.08	0.04	0.13
L.O.I. (Loss Of Ignition)	10.63	8.60	12.40
Total	**100.02**	**100.03**	**99.75**

3.2. Mineralogical Analysis

The X-ray diffraction patterns of the bentonite samples are illustrated in Figure 1.

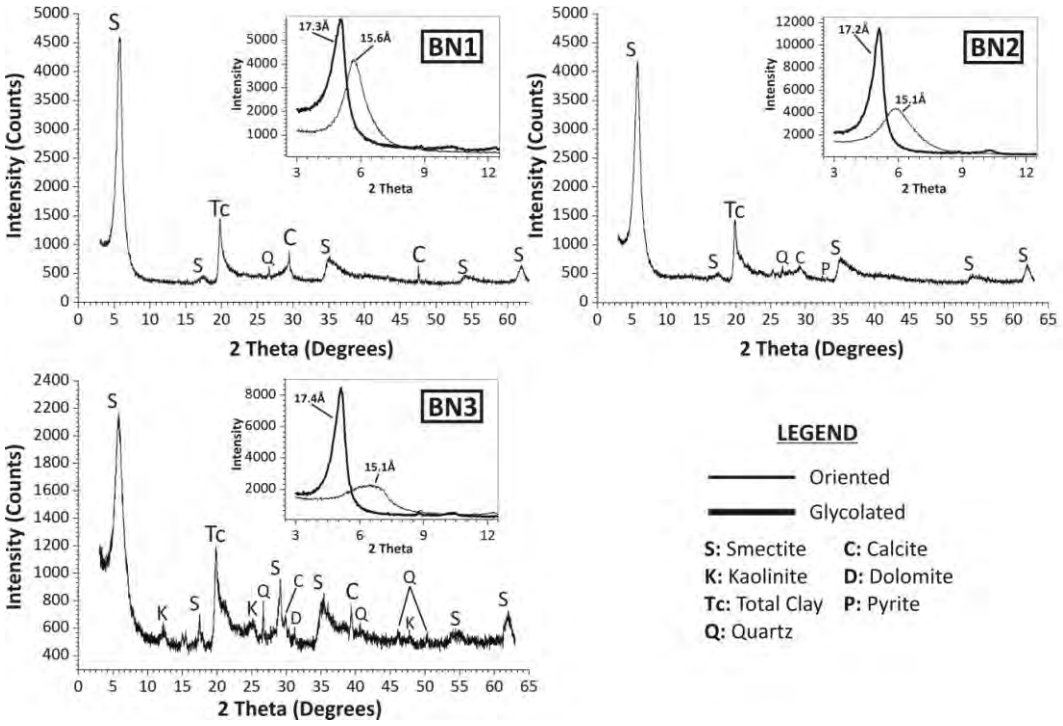

Figure 1 – X-ray diffraction patterns of the bentonite samples (bulk samples). In the detail there are the patterns of the oriented and glycolated samples.

Bentonites are mainly composed of dioctahedral smectite and specifically Ca-montmorillonite with the d_{001} basal reflection exhibited at about 15Å (Figure 1). The estimated smectite contents of the samples were found 94%, 97% and 88% for the samples BN1, BN2 and BN3, respectively. The BN3 sample additionally contains kaolinite (d_{001}=7.12Å, d_{002}=3.57 Å). Accessory minerals such as quartz (d_{101}= 3.34 Å, d_{100}=4.26Å) and calcite (d_{104}= 3.03Å) were detected in all samples. Minor amounts of pyrite (d_{200}=2.71Å) were present in BN2 bentonite, and traces of dolomite (d_{104}=2.88Å) in BN3 bentonite. Thus, bentonite samples are characterized by high concentration of smectite and low levels of impurities. Similar observations were reported by other authors (Christidis et al., 1995; Perraki and Orphanoudaki, 1997). According to Christidis et al. (1995) dioctahedral smectite is the main phase present in Ankeria and Aspro Horio deposits, while plagioclase is abundant, kaolinite, calcite and zeolites are secondary phases and sulphides are accessory minerals. Perraki and Orphanoudaki (1997) reported that Ankeria bentonite consists mainly of Ca-montmorillonite with minor amounts of calcite, feldspars, quartz, illite and iron sulphides (e.g. pyrite).

3.3. Specific Surface Area

The specific surface areas of bentonite samples were determined from the nitrogen adsorption isotherms given in Figure 2. The BET surface areas (obtained by N_2 adsorption isotherms at 77 K) were 87, 67 and 80 m^2/g for BN1, BN2 and BN3, respectively. BET surface areas of these samples were similar to those found for natural bentonites reported in previous workers (Volzone and Ortiga, 2000; Sakizci et al., 2010).

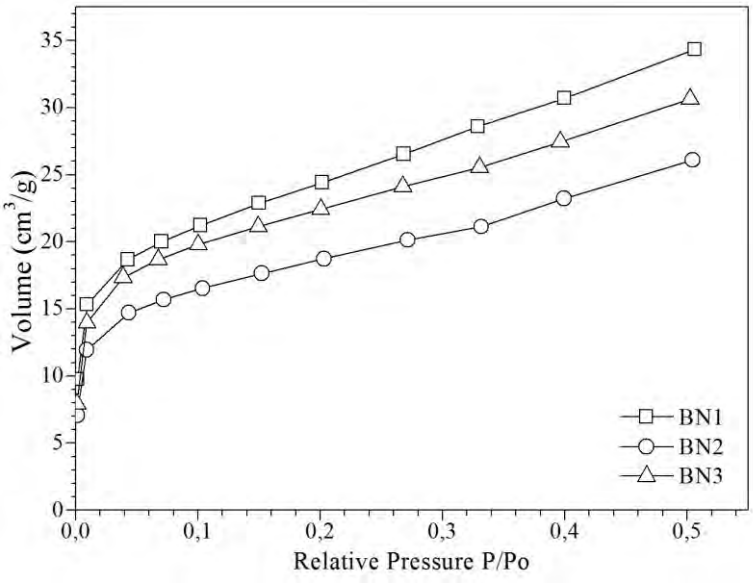

Figure 2 – The isotherms of the adsorption of nitrogen (N_2) on the bentonite samples.

3.4. Spectroscopic Study

FTIR spectra of bentonite samples are shown in Figure 3 and the vibrational modes are summarized in Table 2 together with FTIR data of the Miloan bentonites from previous studies (Christidis et al., 1995; Orphanoudaki and Perraki, 1997) and Wyoming (Tabak et al., 2007) and Ünye, Turkey (Sakizci et al., 2010) bentonites for comparison. Position and shape of the OH stretching band in the IR spectra of smectites is influenced mainly by the nature of the octahedral atoms to which the hydroxyl groups are coordinated (Madejova, 2003).

The absorption band at 3628, 3630 and 3622 cm^{-1} found in the spectra of BN1, BN2 and BN3 sample respectively, are typical for dioctahedral smectites and is due to stretching vibrations of

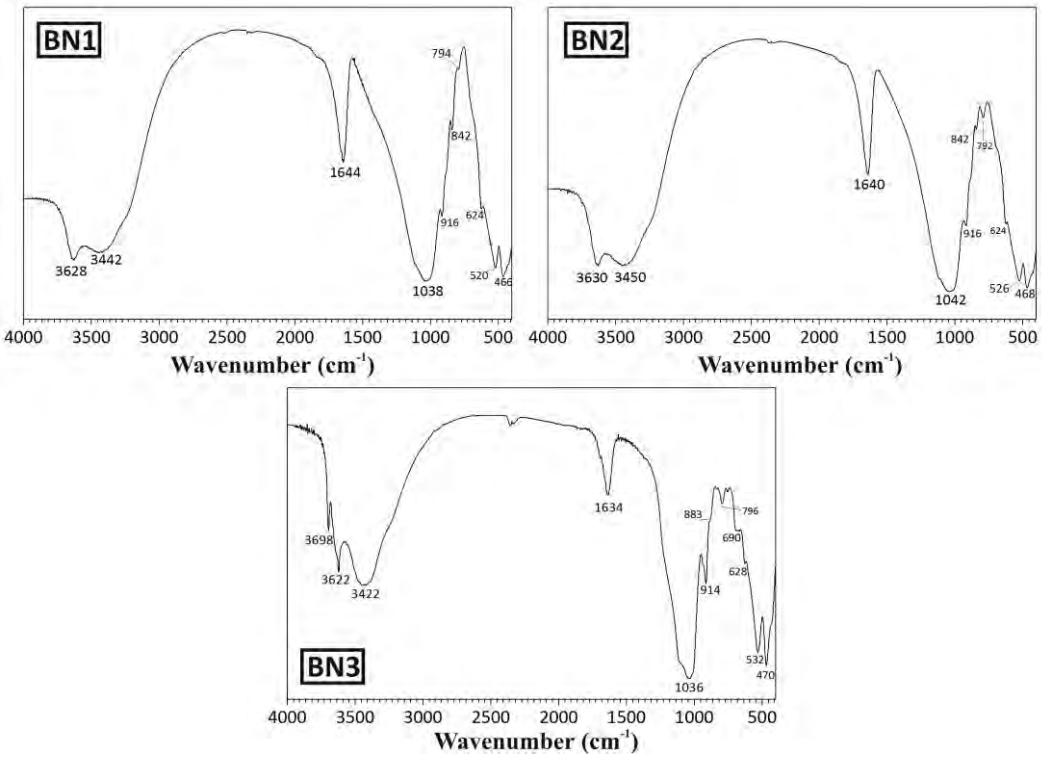

Figure 3 – FTIR spectra of the bentonite samples.

Table 2 – FTIR spectral data of the bentonite samples.

	Data from previous studies					Bentonite Samples (cm^{-1})		
Assignment	**1[a]**	**2[b]**	**3[c]**	**4[c]**	**5[d]**	**BN1**	**BN2**	**BN3**
u (X-O-H) of kaolinite impurity	-	-	-	-	-	-	-	3698
u (X-O-H), X=Al, Mg	3631	3630	3630	3631	3620	3628	3630	3622
u (H-O-H)	3432	3450	3425	3421	3400	3442	3450	3422
δ (H-O-H)	1640	1640	1635	1632	1640	1644	1640	1634
$CaCO_3$ impurity	-	-	-	1426	-	-	-	-
u (Si-O)	1090	1087	1118	1108	-	-	-	-
u (Si-O-Si)	1045	1041	1043	1054	-	1038	1042	1036
δ (Al-Al-OH)	919	916	920	919	918	916	916	914
δ (Al-Fe-OH)	-	-	883	878	875	-	-	883
δ (Al-Mg-OH)	843	843	848	-	845	842	842	-
u (Si-O) of SiO_2 impurity	798	795	796	796	-	794	792	796
Al-O, Si-O out of plane vibrations	-	624	-	623	-	624	624	628
δ (Si-O-Al^{VI})	524	521	528	525	516	520	526	532
δ (Si-O-Si)	465	471	467	468	467	466	468	470

u: stretchnig vibration, δ: bending vibration

1: Wyoming bentonite, 2: Ünye bentonite (Turkey), 3,5: Ankeria bentonite (Milos, Greece), 4: Aspro Horio bentonite (Milos, Greece)

[a] Tabak et al., 2007, [b] Sakizci et al., 2010, [c] Christidis et al., 1995, [d] Perraki and Orphanoudaki, 1997

structural OH groups of bentonites (Madejova, 2003; Eren and Afsin, 2008; Caglar et al., 2009; Alabarse et al., 2011; Holtzer et al., 2011). The band at 3698cm^{-1} observed in sample BN3 is characteristic for kaolinite which is present as impurity in the sample and is frequently used for identification of kaolinites in raw materials. This band is well separated from absorption bands of most other minerals, which allows identification of very low amounts of kaolinites (Joussein et al., 2001; Madejová et al., 2002). The broad band near 3420 cm^{-1}, observed in the spectra of all samples is due to O-H stretching vibrations of adsorbed water, while the bending vibration of water observed at 1644, 1640 and 1634cm^{-1}, respectively (Xu et al., 2000; Madejova, 2003).

The IR spectra of dioctahedral smectites show only one broad band in the 1040-1020cm^{-1} region due to Si-O stretching vibrations. The bands at 916 and 914cm^{-1} are attributed to Al-Al-OH bending vibration, while the band at 842cm^{-1} observed in the BN1 and BN2 samples corresponds to Al–Mg–OH bending vibration (Madejova, 2003; Eren and Afsin, 2008; Caglar et al., 2009). The peak at 883cm^{-1} observed in bentonite BN3 could be ascribed to Al-Fe-OH bending vibration (Madejova, 2003). The appearance of two peaks at about 915cm^{-1} (δAlAlOH) and about 843cm^{-1} (δAlMgOH) reflect partial substitution of octahedral Al by Mg in the samples BN1 and BN2. Si–O stretching of quartz (SiO_2) impurity appears at 794, 792 and 794cm^{-1}, respectively (Caglar et al., 2009; Davarcioğlu and Çiftçi, 2009). The bands at 520, 526 and 532cm^{-1} are due to the Si-O-Al^{VI} bending band (Al^{VI} is Al in octahedral positions), while the 466, 468 and 470cm^{-1} bands to the Si-O-Si bending vibration which is characteristic for smectites (Madejova, 2003). When compared to FTIR data of Miloan bentonites from previous studies (Christidis et al., 1995; Orphanoudaki and Perraki, 1997) and bentonites which have formed in different geological environments like Wyoming and Ünye bentonites, almost identical data were obtained in the present study. Changes in the vibrational frequencies and intensities of Si–O peaks must be ascribed to changes in the silicate structure such as Si–O bond length, Si–O–Si, angle and the angle through which the silica tetrahedra have rotated and the distance between next-nearest oxygens in the basal plane (Sakizci et al., 2010). Weight percentages of chemical compositions and amount of water of the bentonites under study show some differences compared to bentonites from previous studies. Due to these alterations it is not surprising to see some small shifts in the compared data in Table 2.

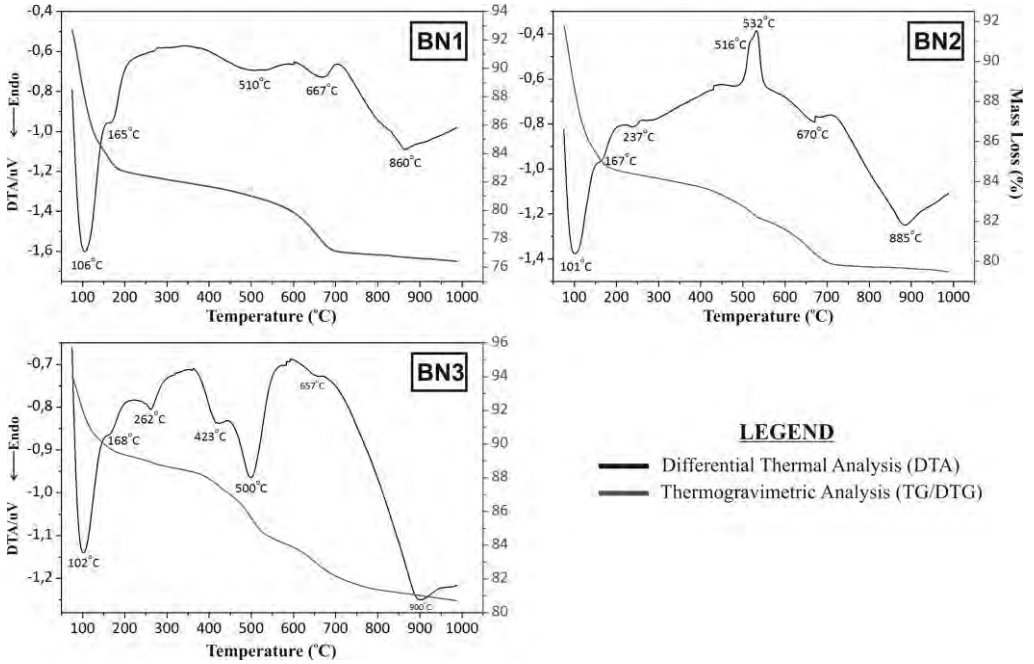

Figure 4 – Differential thermal analysis (DTA) and thermogravimetric analysis (TG) curves for the bentonite samples.

3.5. Thermal Properties

Physical, physicochemical and/or chemical transformation taking place with the application of a thermal effect, are displayed as endo-/exothermic peaks in relation to temperature. Thus, the respective endo- or exothermic peaks shown in DTA curves are very useful ways to establish transformations with or without mass loss and have been used as one of the major tools for qualitative clay characterization (Sakizci et al., 2009). DTA/TG curves of the bentonites are given in Figure 4 for temperature range of 75–1000^{o}C and the related mass losses are given in Table 3.

The DTA curves, shown in Figure 4, exhibit a low-temperature strong endothermic peak at 106^{o}C for the B1 sample, corresponding to the desorption of physically adsorbed water (Greene-Kelly, 1957; Köster, 1993). There is another very weak endothermic peak, around 165^{o}C, related to the water molecules bound to Ca^{2+} cations (Sakizci et al., 2009; Bayram et al., 2010). The endothermic peaks at 510 and 667^{o}C represent the dehydroxylation of structural OH groups (Caglar et al., 2009). The weak endothermic peak at 860^{o}C could be ascribed to structure decomposition. Christidis and Markopoulos (1995) reported complete destruction of the smectite structure between 900^{o}C and 940^{o}C. The DTA–TG curve related to the B1 exhibited a total of four mass losses up to 1000^{o}C is 16.25% for the B1 sample.

Table 3 – Thermal analysis (DTA/TG) data of the bentonite samples.

Sample	Temperature Range (^{o}C)	Peak Temperature (^{o}C)	Mass Loss (%)
BN1	75-140	106	8.02
	140-225	165	2.11
	350-540	510	1.26
	540-725	667	3.64
BN2	75-130	101	5.59
	130-225	167	1.80
	350-540	516, 532 (exo)	1.78
	540-725	670	2.34
BN3	75-125	102	3.38
	125-325	168, 262	2.14
	340-450	423	1.55
	450-540	500	2.45
	540-750	657	2.87

B2 bentonite sample exhibits four mass loss events on heating in simultaneous DTA/TG (Figure 4 and Table 3). Two dehydration stages with a total mass loss of 7.39% over the temperature range of 75–225^{o}C are noticeable on the TG curve of B2 sample. The removal of adsorbed water with a mass loss of 5.59% in the first stage 75–130^{o}C gives rise to an endothermic DTA peak centered at101^{o}C and the endothermic peak at 167^{o}C in the range of 130–225^{o}C which is accompanied by a mass loss of 1.80% corresponds to the elimination of the water species coordinated to the interlayer cations. The endothermic peak at 670^{o}C represents the dehydroxylation of structural OH groups. The endothermic peak at 670^{o}C is associated with 2.34% mass loss in the range of 540–725^{o}C. According to Christidis and Markopoulos (1995) the temperature of the major dehydroxylation for bentonite sample from Aspro Horio quarry was found to be between 685^{o}C

and 690°C. The two superimposing exothermal reactions at 516 and 532°C could be ascribed to the presence of pyrite in this sample (Bonamartini Corradi et al., 1996).

The evolution of adsorbed and cation-coordinated water species in B3 bentonite (Figure 4 and Table 3) is represented by three endothermic peaks at 102, 180 and 262°C, in the range of 75–325°C with a 5.52% mass loss (Figure 4 and Table 3). In DTA plot, a characteristic douplet of endotherms of dioctahedral smectite that appears at 423 and 657°C and are accompanied by a total mass loss of 6.87% in the range of 340–750°C denotes dehydroxylation of B3 bentonite. The strong endothermal reaction at 500°C is attributed to the dehydroxylation of kaolinite detected in this sample (Smykatz-Kloss, 1974).

4. Conclusions

In the present work, characterization of bentonite samples was performed using XRD, AAS, DTA, TG, FT-IR and surface area measurement methods. The XRD results of this investigation show that the clay deposits from Milos island, mainly consist of smectite and specifically Ca-montmorillonite with minor amounts of other clay minerals such as illite and kaolinite and quartz and calcite as impurities. The infrared spectrum of these samples confirmed the presence of dioctahedral smectite as the major mineral and quartz as the main impurity. Additionally, kaolinite was detected in the BN3 bentonite sample. The DTA/TG curves of the bentonite samples exhibit intensive endothermal dehydration peaks with one or two shoulders on the side of the peak that faces higher temperatures which characterize smectites with divalent interlayer cations. This comes in agreement with the chemical and mineralogical analysis which proved that the studied bentonites are mainly consisted of Ca-montmorillonites. The dehydroxylation peak doublet between 500 and 700 °C observed in BN1 and BN3 bentonites characterizes smectites with a mixture of both cis- and trans-vacancies in the octahedral sites in contrast to BN2 bentonite which is a smectite with mainly cis-vacant octahedral sheets. The total mass losses up to 1000°C for BN1, BN2 and BN3 were determined as 16.25%, 12.32%, and 13.35%, respectively.

5. Acknowledgments

The authors would like to express their appreciation to the European Social Fund of the European Union and to the Ministry of Education, Lifelong Learning and Religious Affairs of Greece for financing this research in the framework of HERACLITUS II. Additionally, we would like to thank the S&B Industrial Minerals S.A. company for providing the bentonite samples. Finally, two anonymous referees are fully acknowledged for their valuable comments to the manuscript and their constructive suggestions.

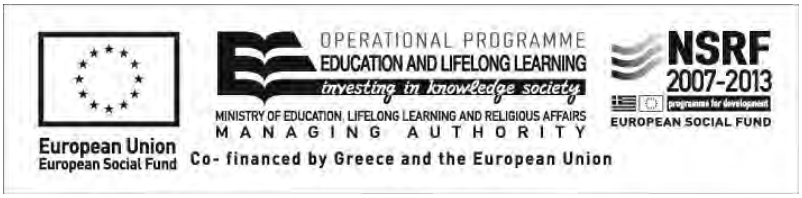

6. References

Alabarse F.G., Conceição R.V., Balzaretti N.M., Schemato F. and Xavier A.M. 2011. In-situ FTIR analyses of bentonite under high pressure, *Applied Clay Science,* 51, 202-208.

Bayram H., Önal M., Yilmaz H. and Sarikaya Y. 2010. Thermal analysis of a white calcium bentonite, *Journal of Thermal Analysis and Calorimetry*, 101(3), 873-879.

Bonamartini Corradi A., Leonelli C., Manfredini T., Pennisi L. and Romagnoli M. 1996. Quantitative determination of pyrite in ceramic clay raw materials by DTA, *Thermochimica Acta*, 287, 101-109.

Caglar B., Afsin B., Tabak A. and Eren E. 2009. Characterization of the cation-exchanged bentonites by XRPD, ATR, DTA/TG analyses and BET measurement, *Chemical Engineering Journal*, 149, 242-248.

Christidis, G.E. and Markopoulos T. (1995). Mechanisms of formation of kaolinite and halloysite in the bentonite deposits of Milos island, Greece, *Chemie Der Erde*, 55, 315-329.

Christidis G.E., Scott P.W. and Marcopoulos T. 1995. Origin of the bentonite deposits of eastern Milos, Aegean, Greece: geological, mineralogical and geochemical evidence, *Clays and Clay Minerals*, 43, 63-77.

Christidis G.E. and Scott P.W. (1996). Physical and chemical properties of bentonite deposits of Milos island, Greece, *Transactions Of The Institute Of Mining And Metallurgy, Section B, Applied Earth Science,* 105, B165-B174.

Davarcioğlu B. and Çiftçi E. 2009. Investigation of Central Anatolian clays by FTIR spectroscopy (Arapli-Yesilhisar-Kayseri, Turkey, *International Journal of Natural and Engineering Sciences*, 3, 154-161.

Eren E. and Afsin B. 2008. An investigation of Cu(II) adsorption by raw and acid-activated bentonite: A combined potentiometric, thermodynamic, XRD, IR, DTA study, *Journal of Hazardous Materials*, 151, 682-691.

Greene-Kelly R. 1957. The Montmorillonite Minerals (Smectites). In: Mackenzie R. C. (Ed.), The Differential Thermal Investigation of Clays. Mineralogical Society, London.

Grim R.E. 1968. *Clay Mineralogy*, 2nd Ed., McGraw Hill, New York.

Grim R.E. and Góven N. 1978. Bentonites, Geology, Mineralogy, Properties and Uses: *Development in Sedimentology*, Elsevier, Amsterdam.

Holtzer M., Bobrowski A. and Zymankowska-Kumon S. 2011. Temperature influence on structural changes of foundry bentonites, *Journal of Molecular Structure,* 1004, 102-108.

Joussein E., Petit S. and Decarreau A. 2001. Une nouvelle méthode de dosage des minéraux argileux en mélange par spectroscopie IR, *Comptes Rendus de l'Académie des Sciences,* 332, 83-89.

Kogel J.E., Trivedi N.C., Barker J.M. and Krukowski S.T. 2006. Industrial minerals and rocks: commodities, markets, and uses, *Society for Mining, Metallurgy, and Exploration*, INC. (SME), USA.

Köster H. M. 1993. Dreischichtminerale oder 2:1 Schichtsilikate. In: Jasmund K. & Lagaly G. (Eds.), Tonminerale und Tone. Darmstadt: Steinkopff Verlag.

Madejova J. 2003. FTIR techniques in clay mineral studies, *Vibrational Spectroscopy*, 31, 1–10.

Madejová J., Kečkéš J., Pálková H. and Komadel P. 2002. Identification of components in smectite-kaolinite mixtures, *Clay Minerals*, 37, 377-388.

Murray H.H. 1991. Overview-clay mineral applications, *Applied Clay Science*, 5, 379.

Murray H.H. 2000. Traditional and new applications for kaolin, smectite and palygorskite: a general overview, *Applied Clay Science*, 17, 207.

Perraki T. and Orphanoudaki A. (1997). Etude de la composition mineralogique et de proprietes phisiques des bentonites de l'ile de Milos (Grece), *Mineral Wealth*, 104, 35-42.

Sakizci M., Alver B.E., Alver O. and Yörükoğullari E. 2010. Spectroscopic and thermal studies of bentonites from Ünye, Turkey, *Journal of Molecular Structure*, 969, 187-191.

Sakizci M., Alver B.E. and Yörükoğullari E. 2009. Thermal behaviour and immersion heats of selected clays from Turkey, *Journal of Thermal Analysis and Calorimetry*, 98, 429-436.

Smykatz-Kloss W. 1974. Differential Thermal Analysis, Springer-Verlag, Berlin, 185 pp.

Tabak A., Afsin B., Caglar B. and Koksal E. 2007. Characterization and pillaring of a Turkish bentonite (Resadiye), *Journal of Colloid and Interface Science*, 313, 5-11.

Volzone C. and Ortiga J. 2000. O_2, CH_4 and CO_2 gas retentions by acid smectites before and after thermal treatment, *Journal of Materials Science*, 35(21), 5291.

Xu W., Johnston C.T., Parker P. and Agnew S.F. 2000. Infrared study of water sorption on Na-, Li-, Ca-, and Mg-exchanged (SWy-1 and SAz-1) montmorillonite, *Clays and Clay Minerals*, 48, 120–131.

Δελτίο της Ελληνικής Γεωλογικής Εταιρίας, τομ. XLVII , 2013
Πρακτικά 13ου Διεθνούς Συνεδρίου, Χανιά, Σεπτ. 2013

Bulletin of the Geological Society of Greece, vol. XLVII 2013
Proceedings of the 13th International Congress, Chania, Sept. 2013

AGGREGATE PRODUCTION ON THE ISLAND OF CRETE, GREECE: CURRENT PRODUCTION CONDITIONS AND FUTURE PERSPECTIVE

Galetakis M.[1], Zourbakis V.[2], Koinakis I.[2], Leventakis K.[1] and Alevizos G.[1]

[1]Technical University of Crete, Department of Mineral Resources Engineering, Chania, Greece
[2] NCSD/IGME Department of Crete

Abstract

Aggregate production is proven crucial for any infrastructure development, including construction work, for the island of Crete (Southern Greece), due to its individual geographical characteristics. Furthermore, since construction has traditionally been a dynamic sector of national economy, aggregate production is playing a major role in the economy of the island.
The aim of this study is to evaluate the current state of aggregate production in the island of Crete based on past and present production data and predict future demand under current state legal framework. Aggregate production and quality data, proven reserves within the state-defined "quarrying zones", as well as their spatial distribution are analyzed for every prefecture of the island. Prediction scenarios of future aggregate demand within the next 20 years are conducted, assuming different economic development rates. In each scenario the annual aggregate production as well as the remaining reserves per prefecture was predicted.
Key words: *Aggregate, production, demand, quality characteristics, forecast, Crete.*

Περίληψη

Λόγω των ιδιαίτερων γεωγραφικών χαρακτηριστικών της Κρήτης, η παραγωγή και διάθεση αδρανών υλικών αναδεικνύεται σε ιδιαίτερα κρίσιμο παράγοντα αφού σχετίζεται άμεσα με σημαντικές οικονομικές δραστηριότητες του νησιού, όπως η ανάπτυξη των υποδομών και οι κατασκευές.
Η εργασία αυτή έχει ως στόχο να αναλύσει την υπάρχουσα κατάσταση όσον αφορά την παραγωγή των αδρανών υλικών, τα ποιοτικά χαρακτηριστικά τους, τα υπάρχοντα αποθέματα εντός των νομοθετημένων λατομικών ζωνών και να εκτιμήσει τη μελλοντική ζήτηση. Η ανάλυση βασίζεται στα υπάρχοντα στοιχεία παραγωγής για κάθε νομό της Κρήτης. Οι προβλέψεις για την μελλοντική ζήτηση για τα επόμενα 20 χρόνια διενεργήθηκαν λαμβάνοντας υπόψη 3 διαφορετικά σενάρια οικονομικής ανάπτυξης. Για κάθε περίπτωση εκτιμήθηκε ανά νομό τόσο η αναμενόμενη ετήσια παραγωγή όσο και η επάρκεια των αποθεμάτων εντός των υφισταμένων λατομικών ζωνών.
Λέξεις κλειδιά: *Αδρανή υλικά, παραγωγή, ζήτηση, ποιοτικά χαρακτηριστικά, πρόβλεψη, Κρήτη.*

1. Introduction

Aggregate materials are extensively used for all kinds of construction applications and infrastructure development and are essential for every modern economy. The most common natural aggregates of mineral origin are sand, gravel and crushed rock. Their main uses are: ready-mixed and precast concrete production, road paving, asphalt production, railroad ballast, mortar production, harbour construction and maintenance, cement and lime production.

The European aggregates production is about 3 billion tons/year, representing an annual turnover of approximately €20 billion. The production of aggregates is the largest extractive activity in Europe (excluding the mineral fuels sector) while demand is around to 5.5 tonnes per capita per year. The aggregates industry comprises some 14,000 companies (mostly SMEs), producing at approximately 24,000 sites with 250,000 people employed (including contractors) Within the European Union (EU-27), total aggregate production for 2010 was 2.78 billion tons according to 2011-2012 annual review of the European Aggregates Association (UEPG) (abbreviation UEPG stands for "Union Européenne des Producteurs de Granulats").

In certain countries of the European Community, natural sand and gravel, extracted from river beds or conglomerate formations, are dominating the market of aggregate material. These are mainly countries, whose geological conditions and/or terrain morphology make the production of crushed aggregates unprofitable or even illegal. On the other hand, in countries like Greece and Spain, among others, abundance and variety of easily extracted suitable rock formations, makes the choice of crushed aggregates far more advantageous for local construction works. Furthermore, in countries of Northern Europe, recycled aggregates originated mainly from construction and demolition wastes and in minor quantities from other industrial processes, have gradually risen to notable percentages, during the last decades. The origin (main sources) of the produced aggregate in Europe is shown in Figure 1 (UEPG, 2012).

Figure 1 - Contribution of the different sources in total aggregate production in the European Union during 2005 (Source: www.uepg.eu).

In Greece approximately 90% of the produced aggregates are extracted via quarrying operations from calciferous rock formations (limestone), which are abundant and widespread all over the country. Quarrying is allowed within certain areas defined as quarrying zones. The percentage of each region's production (in comparison to the total production) for 2006 is shown in Table 1, while the percentage of produced aggregates size fractions is shown in Figure 2 (IGME, 2009).

Since concrete production and road paving are by far the most aggregate consuming construction activities in Greece, the common measured quality characteristics, related to such uses, are: Los Angeles value, sand equivalent value, water absorption, fines percentage and compressive strength of the source rock.

The basic statistical parameters of the aforementioned quality characteristics estimated by a large number of laboratory tests conducted according to European and ASTM standards (Los Angeles test: EN 1097-2:1998, sand equivalent test: EN 933-8, water absorption test: EN 1097-6, fines

percentage: EN 933-1, compressive strength: ASTM C109) are shown in Table 2 (IGME, 2009). As can be seen from Table 2, as well as from frequency histograms depicted in Figure 3, water absorption and fines percentage indicates considerably higher variability, compared to the rest quality characteristics.

Table 1 – Regional distribution of quarry production for 2006 (IGME, 2009).

Region	% of total production
Attica (prefecture hosting the capital)	19
Sterea Ellada	7
Thessaly	12
Central Macedonia	13
East Macedonia and Thrace	5
West Macedonia	4
West Greece	5
Epirus	5
Peloponnese	11
Crete	11
South Aegean Sea	4
Ionian Islands	2
North Aegean Sea	2
Total	**100**

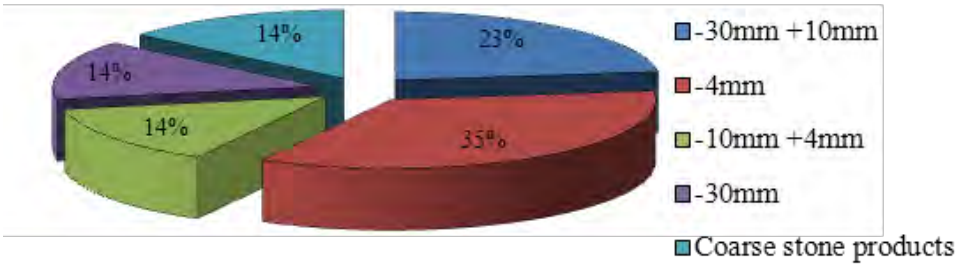

Figure 2 - Percentages of crushed aggregates sizes produced in Greece in 2006 (IGME, 2009).

Table 2 - Statistical data of quality characteristics of aggregates produced in Greece (IGME, 2009).

	Los Angeles value %	Sand equivalent %	Water absorption %	Fines percentage %	Compressive strength MPa
Number of samples	113	71	67	45	110
Average (m)	26.4	71.1	0.5	13.5	71.1
Standard deviation	4.3	5.6	0.3	7.0	5.6
Coefficient of variation %	16.4	7.9	55.0	51.7	7.9

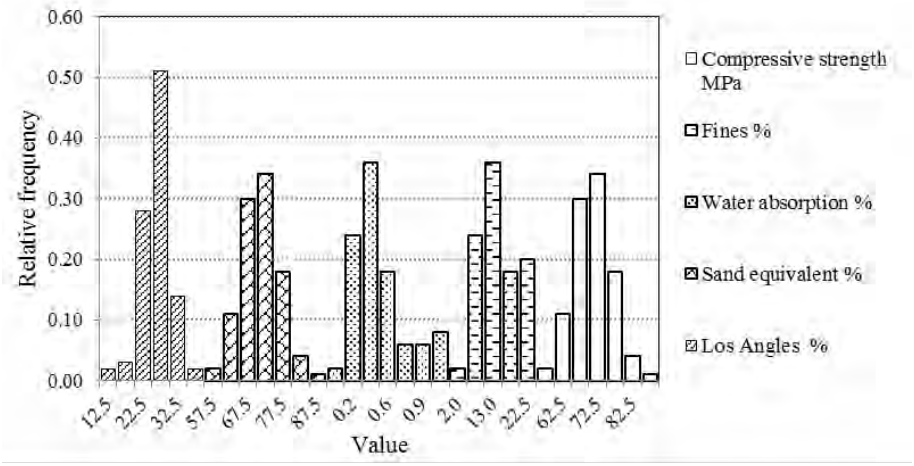

Figure 3 – Histograms of main aggregate quality parameters (Data source: IGME, 2009).

As far as state regulatory authority quarrying permits are concerned, definition of the zones of legitimate quarrying operation is a process that usually has to overcome numerous obstacles. Environmental and other restrictions set by state laws, in combination with local communities' reactions, are the main obstacles in defining new quarrying zones. Despite the aforementioned drawbacks, aggregate demand is met by production for almost all aggregate products, throughout the country, whilst shortages are restricted in the vicinity of the larger cities. The spatial distribution of aggregate quarries throughout Greece is quite uniform as can be seen in Figure 4.

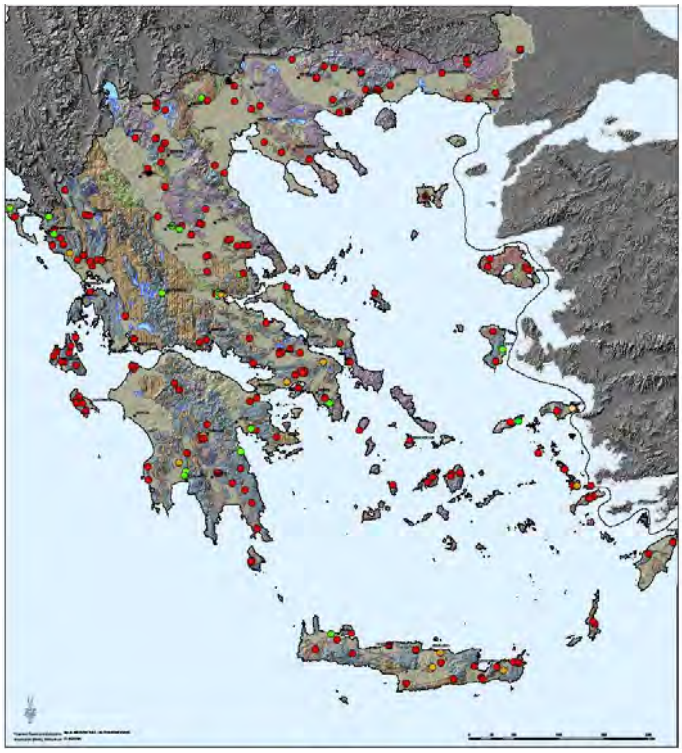

Figure 4 - Quarry distribution throughout Greece and operational status in 2011 (red dot: operating quarry, yellow dot: quarry under environmental reclamation (expended), green dot: currently non-operating quarry (Mines & Quarries Inspectorate of Greece, 2013).

In the following sections of this study the current state of aggregate production on the island of Crete, their quality characteristics and spatial distribution of production sites (quarries) are presented. Prediction scenarios of future market demand regarding the forthcoming two decades are examined and the geological availability, in terms of remaining reserves, is investigated.

2. Quarry Production on the Island of Crete

2.1. Spatial Distribution of Quarries in Crete

On the island of Crete, much like the rest of the country, a lot of diverse obstacles are met when quarry zones are to be defined. Hence, sites chosen for quarry zone delineation by the state bureau in charge (South Greece Mines & Quarries Inspectorate), often meet strong opposition from local communities.

Quarrying sites, as shown in Figure 5, are evenly spread throughout the island. Their locations are mainly controlled by their distances to prefectures' capital cities (Chania, Rethymnon, Heraklion, Agios Nikolaos), which are the main marketplaces. They are operated mostly by small-size enterprises, with the exception of few medium-size, usually well organised and modernised companies. The number and the operational status of the quarries in the island of Crete are depicted in Table 3.

Figure 5 – Locations of quarrying zones on the island of Crete.

Table 3 – Operational status of quarries in Crete.

Operational status	Operational	Currently non-operational	In the process of proper permit obtainment	Special use
Number	7	4	1	4
Operational status	Currently operating outside the quarry zones	Depleted, under environmental reclamation	Depleted/Closed	
Number	1	4	6	
Total number of quarries = 27				

2.2. Production Data of Aggregate Quarries in Crete

The island of Crete is geographically and administratively divided in four prefectures, named from west to east: Chania, Rethymnon, Heraklion and Lasithi. The four major cities of the island are the capitals of each prefecture. Annual aggregate demand and production during 2000-2012 is divided among the four prefectures as shown in Figure 6. During 2000-2008 the total annual production level was relatively constant at ~6.5 Mt. From 2009 to 2012 a significant decrease is observed, as a result of the economic recession (particularly in the construction sector). This decrease is higher for the prefecture of Heraklion, while the overall average decrease for the four prefectures, from 2008 to 2012, was ~70%.

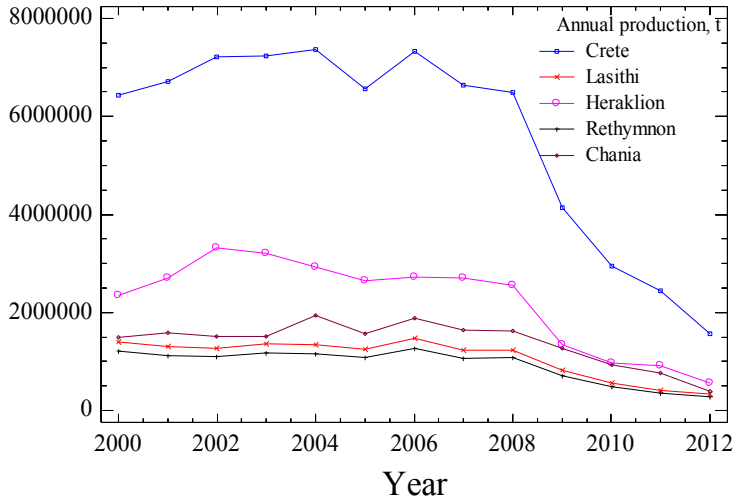

Figure 6 - Annual production of aggregates during 2000-2012 in Crete.

2.3. Quality Characteristics of Aggregates Produced in Crete

The basic parameters of aggregates quality data (Los Angeles, water absorption and compressive strength of the source rock) are given in Table 4. As far as compressive strength is concerned, measured values indicated that all operational quarries meet quality standard requirements for construction uses (EN 12620). Similarly Los Angeles and water absorption values satisfy quality requirements of construction works. In certain quarries (e.g. Viannos, Damasta) the source rock exhibits exceptional strength (over 100MPa). Aggregates extracted from such rocks, when also exhibiting low Los Angeles value, could be used in certain demanding applications.

3. Estimation of Future Demand

This section evaluates aggregate supply and demand scenarios within the island of Crete. It is assumed that equilibrium exists between supply and demand, while inventory levels are not considered significant therefore producers adjust to market needs.

The examined scenarios take into account the latest construction forecasts of the European Aggregates Association (UEPG). UEPG estimates that due to the European sovereign debt crisis there will be no overall growth in aggregates' production until 2014. Furthermore, based on the annual European average construction output increase (1.5%) during 1992-2007, UEPG suggests that activity will not return to 2008's level until around 2023 (UEPG, 2012).

The model used for the estimation of aggregate demand is based on forecasts of construction activity, as well as, on forecasts of other economic factors, such as the Gross Domestic Product (GDP) (Poulin and Bilodeau, 1993). A multiple linear regression model, based on previous years'

data, was developed. Initially the overall demand for the island of Crete is predicted by using the GDP and construction indices. The values of indices were taken from the Hellenic Statistical Authority's (ELSTAT) records and cover a period of 13 years, from 2000 to 2012.

Table 4 - Quality characteristics of aggregates produced in Crete

Quarrying zone	Source rock description	Number of samples	Los Angeles %		Water absorption %		Compressive strength MPa	
			Mean	St. dev.	Mean	St. dev.	Mean	St. dev.
Hordaki	Tripolis limestone	3	32.6	0.9	0.8	0.1	74.7	7.5
Kandanos	Ionian limestone	3	34.5	1.8	1.0	0.1	59.7	5.5
Akmi	Tripolis limestone	3	28.5	1.9	1.1	0.1	64.0	7.9
Latsimas	Tripolis limestone	6	28.2	2.1	0.8	0.1	85.0	7.5
Lambini	Tripolis limestone	3	26.2	0.8	0.9	0.1	97.0	2.6
Damasta	Ionian limestone	3	28.7	3.1	1.0	0.1	101.3	10.5
Zofori	Tripolis limestone	3	30.0	1.0	1.0	0.1	98.0	4.2
Pompia	Pindos limestone	3	31.0	0.5	1.0	0.1	75.3	20.6
Viannos	Pindos and Tripolis limestones	6	26.0	1.2	0.8	0.1	116.7	11.7
Tapes	Tripolis limestone	3	28.5	2.9	0.9	0.1	78.3	8.1
Total		*36*	*28.8*	*2.9*	*0.9*	*0.1*	*84.3*	*18.6*

According to ELSTAT methodology, indices are calculated by using constant values with base year 2005. For 2005 the GDP of Greece was 193050 M€ (2005 GDP index=100), while the turnover from construction activities was 14018 M€ (2005 Construction index=100). The aggregates production data of Crete were collected from the statistical records of the Greek Mines & Quarries Inspectorate. The developed model for the prediction of aggregates demand in Crete is given in equation 1.

$$demand = 16780*GDP_i + 33390*C_i \quad (R=0.96) \qquad (1)$$

Where *demand* is the overall aggregate consumption in tons in Crete, GDP_i is the Gross Domestic Product index and C_i is the Construction index. GDP_i and C_i for Crete were considered equal to relevant national indices.

The examined scenarios, S1, S2 and S3, shown in Figure 7, represent different forecasts for the evolution of GDP and construction indices during 2013-2033. S1 is considered as the optimistic, S2 the most probable, while S3 is the conservative. All scenarios consider negative rates for GDP and construction indices for 2013, zero change for 2014 and positive rates from 2015 to 2033. The assumed higher increase rate of construction index, in comparison to the increase rate of GDP, can be justified by previous years' data. According to this data, construction index has always exhibited a steeper change than GDP.

In a first step the annual aggregates production in the island of Crete, during 2013-2033, according to scenarios S1, S2 and S3 was estimated by using equation 1. Results, shown in Figure 8, indicate that the mean annual production of the period 2000-2008 (~6.5 Mt) could be achieved in 2028 according to S1 and in 2033 according to S2. In the case of S3 the mean annual production of 2000-2008 cannot be reached within the examined period.

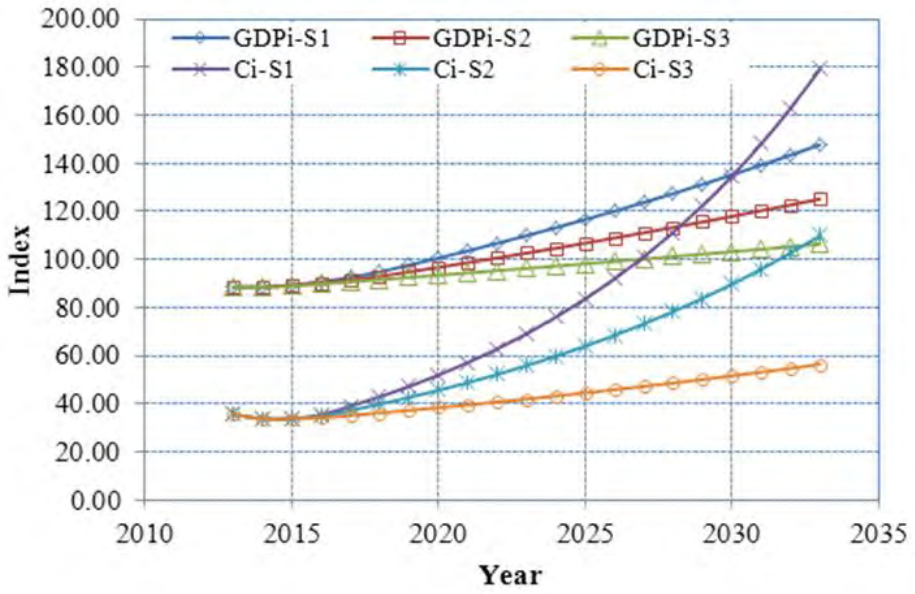

Figure 7 - Evolution of GDP and Construction indices for the examined scenarios (S1, S2 and S3) during 2013-2033 (GDPi-S1 denotes the evolution of GDP index according to scenario S1 and respectively for the other cases).

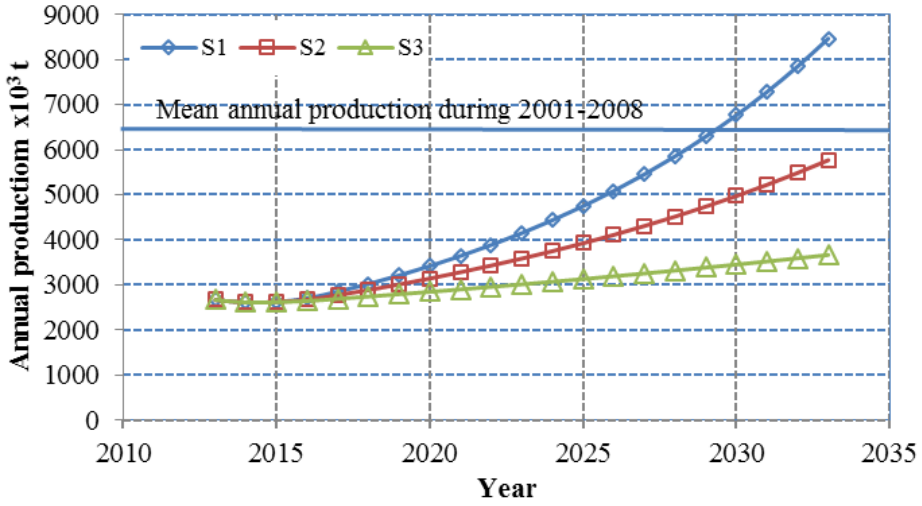

Figure 8 - Forecasts of annual aggregates production in the island of Crete, during 2013-2033, according to scenarios S1, S2 and S3.

In a second step the annual aggregates production for the prefecture of Crete was predicted. The percentage of each prefecture was estimated from its contribution to total aggregate production during 2000-2012. Furthermore the remaining exploitable reserves within the examined period were estimated (for the definition of a quarrying zone a feasibility study involving the estimation of the exploitable reserves is required). Initial reserves were considered the remaining exploitable reserves within the quarrying zones in 2012. These reserves were estimated as: 92Mt for Lasithi, 90Mt for Heraklion, 31Mt for Rethymnon and 28Mt for Chania.

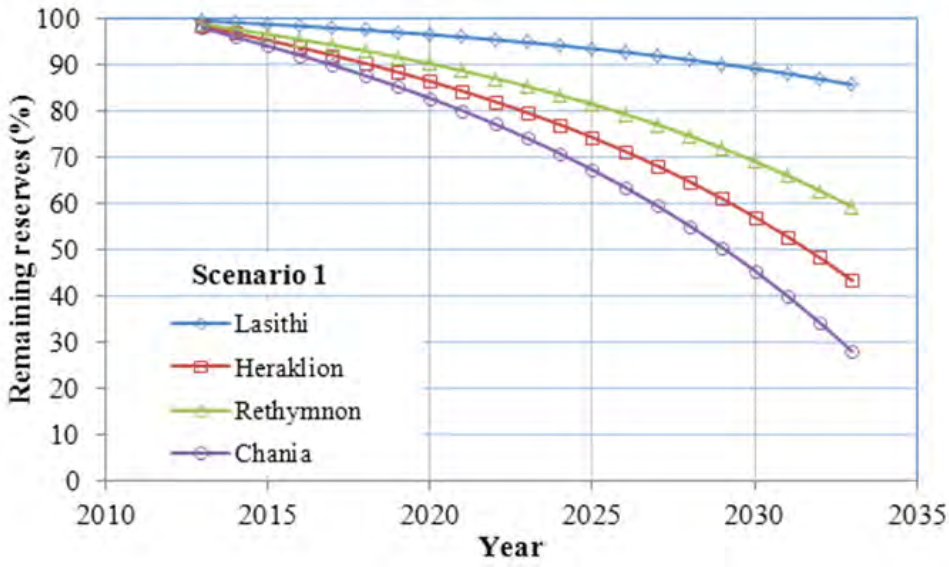

Figure 9 - Decrease of the remaining reserves (expressed as percentage of the initial reserves) in the municipalities of Crete according to the first scenario (S1).

The decrease of reserves for the first scenario S1 (represents the highest annual production) is shown in Figure 9. The largest remaining reserves (87%) at the end of the examined period (2033)

are those located in the prefecture of Lasithi, following by those of Rethymnon (59%). In contrast the remaining reserves in Heraklion (43%) and particularly in Chania (26%) are low.

4. Conclusions – Suggestions

Aggregate production is an important economic activity for Crete as it is closely related to infrastructure development and to residential and other construction activities. However the annual production level has significantly decreased during the last four years as result of the economic recession and particularly in the construction sector. The laboratory tests indicated that the quality of produced aggregates meets the requirements for construction uses (EN 12620).

The existing resources within the quarrying zones in 2012 are considered sufficient. The examined aggregate supply and demand scenarios for the next twenty years (2013-2033) revealed that the remaining reserves for the prefectures of Lasithi and Rethymnon are still sufficient. For the prefecture of Heraklion and particularly for the prefecture of Chania, the remaining reserves will be insufficient by 2033, if the recovery in construction sector is as fast as considered in the optimistic scenario. For the remaining two, less optimistic scenarios, depletion will come after that date.

Since the present study does not consider constrains imposed by transportation cost, it is suggested to enhance current analysis by incorporating more complicated models for the prediction of aggregate production and demand. Such models should not only rely on the economic indices but also take into consideration the spatial distribution of quarries and market places.

5. Acknowledgement

Part of this study was carried out within the framework of DURECOBEL project. The authors affiliated with Technical University of Crete, would like to thank the General Secretary of Research and Technology of Greece for the financial support of the aforementioned project.

6. References

European Aggregates Association (UEPG). 2012. A Sustainable Industry for a Sustainable Europe, Annual Review 2011 – 2012. Available online at: www.uepg.eu.

Greek Mines & Quarries Inspectorate 2013. Mining and Quarrying activities of Greece: Statistic Yearbook. Available online at: www.latomet.gr

Hellenic Statistical Authority (ELSTAT). Available online at: www.statistics.gr/portal/page/portal/ESYE/

IGME 2009. Atlas of crushed aggregates of Greece, Athens, p.118.

Poulin R. and Bilodeau M.L. 1993. A model of a mineral aggregate market, *Resources Policy,* June 1993, pp. 131-144.

Δελτίο της Ελληνικής Γεωλογικής Εταιρίας, τομ. XLVII , 2013
Πρακτικά 13ου Διεθνούς Συνεδρίου, Χανιά, Σεπτ. 2013

Bulletin of the Geological Society of Greece, vol. XLVII 2013
Proceedings of the 13th International Congress, Chania, Sept. 2013

ASSESSMENT OF THE QUALITY OF CALCINATION OF MARBLES FROM THASSOS ISLAND USING RAMAN SPECTROSCOPY AND X – RAY DIFFRACTION

Leontakianakos G.[1], Baziotis I.[2,3], Profitis E.[4], Chatzitheodoridis E.[4] and Tsimas S.[1]

[1]School of Chemical Engineering, Laboratory of Inorganic and Analytical Chemistry, National Technical University of Athens, Heroon Polytechniou 9 Street, 15773, Zografou, Athens, Greece, gleontakianakos@yahoo.gr

[2]Department of Mineralogy, Petrology and Economic Geology, School of Geology, Aristotle University of Thessaloniki, 54124, Thessaloniki, Greece, baziotis@metal.ntua.gr; ibazioti@utk.edu

[3]Department of Earth Sciences, University of Perugia, 06100 Perugia, Italy

[4]National Technical University of Athens, School of Mining and Metallurgical Engineering, Department of Geological Sciences, Athens, Greece

Abstract

The degree of calcination of a dolomitic and a calcitic marble from Thassos Island, was investigated, by combining both Raman spectroscopy (RS) and X-Ray diffraction (XRD) techniques. The samples were prepared in isometric 2 cm cubes and calcined at three different temperatures, 900, 1050 and 1200 ^{0}C for 2 hours in order to produce quick lime. RS was applied at the lime sample's surface and inner (near core) part after gently crushing. XRD was applied on the bulk rock specimens in order to verify the transformation process during heating of the raw material. Quality control of the applied calcination procedure is provided through the hydration of quick lime. The rise in solution temperature suggests the chemical "reactivity" of the produced slaked lime. Raman and XRD results revealed the presence of unburned quantities of calcite and dolomite on samples that were calcined at 900 ^{0}C. Furthermore, temperatures of 1050 and 1200 ^{0}C have shown comparable mineralogical features signifying evenly the conversion of carbonate minerals to their oxide equivalents, proving the completion of the calcination process. Finally, reactivity tests showed that the highest reactivity value of the produced quicklime, for both marbles is observed at the temperature of 1050 ^{0}C.

Key words: *Quicklime, Raman, XRD, Calcination temperature, Reactivity.*

Περίληψη

Στην παρούσα εργασία χρησιμοποιώντας τις τεχνικές της φασματοσκοπίας Raman και της περίθλασης ακτίνων Χ μελετήσαμε την εξέλιξη της ασβεστοποίησης δύο ανθρακικών πετρωμάτων (δολομιτικό κι ασβεστιτικό μάρμαρο) που προέρχονται από το νησί της Θάσου. Τα δείγματα κόπηκαν σε κύβους μέσης ακμής 2 cm και ασβεστοποιήθηκαν για 2 h σε τρείς διαφορετικές θερμοκρασίες έψησης (900, 1050 και 1200 ^{0}C). Η φασματοσκοπία Raman εφαρμόστηκε στα ασβεστοποιημένα δοκίμια

τόσο στην εξωτερική επιφάνεια όσο και στο εσωτερικό τους μετά από θραύση, με σκοπό την παρατήρηση της εξέλιξης της ασβεστοποίησης από το εξωτερικό προς τον εσωτερικό πυρήνα. Η περίθλαση ακτίνων-Χ σκοπό είχε να επιβεβαιώσει τις παρατηρήσεις της φασματοσκοπίας Raman στο σύνολο του ασβεστοποιημένου υλικού. Υπολογίσαμε τη δραστικότητα των ασβεστοποιημένων δοκιμίων με σκοπό να έχουμε ένα μέτρο της ποιότητας των ψημένων υλικών. Τα αποτελέσματα των φασματοσκοπικών τεχνικών δείχνουν την παρουσία άψητου υλικού (ασβεστίτη και δολομίτη) σε δείγματα που προέρχονται από τη χαμηλότερη θερμοκρασία έψησης των 900 ^{0}C. Στις θερμοκρασίες των 1050 και 1200 ^{0}C διαπιστώθηκε η παρουσία μόνο οξειδίων γεγονός που υποδηλώνει πως η διαδικασία της ασβεστοποίησης έχει ολοκληρωθεί. Από τα αποτελέσματα της δραστικότητας προκύπτει πως οι υψηλότερες τιμές παρουσιάζονται στην θερμοκρασία έψησης των 1050 ^{0}C, που σημαίνει οτι σε αυτή τη θερμοκρασία παράγεται ο ποιοτικότερος ασβέστης.
Λέξεις κλειδιά: *Άσβηστος ασβέστης, Φασματοσκοπία Raman, Περίθλαση ακτίνων Χ, Θερμοκρασία έψησης, Δραστικότητα.*

1. Introduction

Lime is the most frequently used material in construction application, ever since prehistorical times. Lime refers to calcareous rocks derivatives after calcination, such as quick lime (CaO) and slaked lime ($Ca(OH)_2$). Both forms have several uses and are used in many industries to neutralize acid waste, and as causticisers in the pulp and paper industry, as flux in the steel industry, in road stabilization, in gold recovery and in environmental applications (Triantafyllou & Manoutsoglou, 2004). The most abundant type of calcareous rocks is limestone, marble, travertine, chalk, coquina, tufa, stalactites and stalagmites. Marble is the most common metamorphic rock formed under high pressure and temperature of sedimentary carbonate rocks, most commonly of limestone or of dolomitic rock and is composed of recrystallized carbonate minerals, most commonly calcite and dolomite. Its principal uses are in construction, in interior decoration and in sculpture.

Quicklime production is based on carbonate calcination and of subsequent hydration of quicklime (slaking) through the following reactions:

$CaCO_3$ (s) + heat → CaO (s) + CO_2 (1)

CaO (s) + H_2O (l) → $Ca(OH)_2$ (2)

In case of dolomite the following reaction is considered:

$CaMg(CO_3)_2$ (s) + heat → CaO (s) + MgO (s) + CO_2 (3)

In this study we compared two quicklimes, a calcium lime and a dolomitic lime, derived from the calcination of carbonate rocks with different composition, a Ca-rich and a Mg-rich marble, respectively. In particular, the studied samples were calcined at 900, 1050 and 1200 ^{0}C and the products were hydrated in order to produce slaked lime (reactivity test). We studied the produced quicklime's in terms of Raman Spectroscopy (RS) and X-ray diffraction (XRD) analyses. The goal of the current study is to use RS and XRD in order to quantify the quality of calcination in terms of conversion of the carbonate minerals (calcite, dolomite) to their calcined equivalents (lime, periclase).

2. Geology of Thassos Marbles

Thassos Island (Figure 1) belongs to the Rhodope Massif, which is located in Northern Greece, between Strimona and Evros rivers. The lithology of Thassos is mainly composed of marble

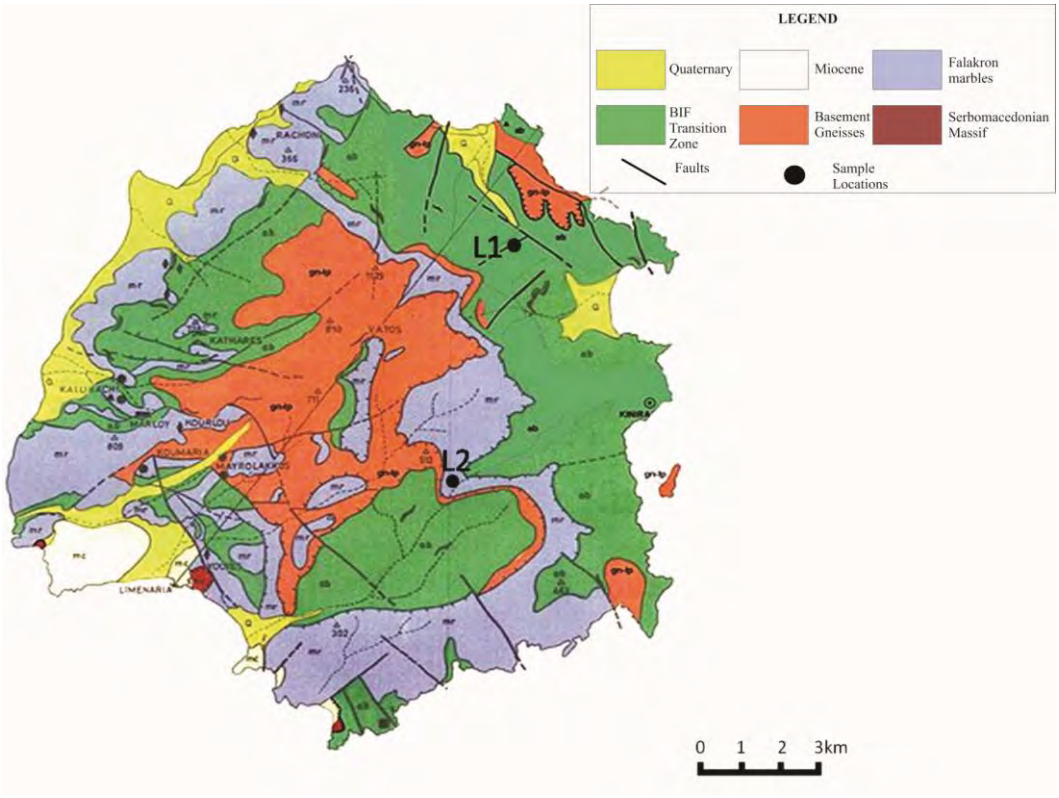

Figure 1 - Modified Geological map of Thassos Island and sampling locations (Source: http://www.geocaching.com).

complexes, ortho- and paragneisses, as well as amphibolites (Bestmann et al. 2000). These marble complexes are known as the Falakron Marbles. They are composed almost purely of calcite, with rare quartz and dolomite crystals (De Wall et al. 2000). They are up to 500 m thick and are separated from the underlying gneisses by a transition zone of about 300 m thick consisting of alternating dolomitic and calcitic marbles, intercalated by schists and gneisses.

3. Analytical Methods

3.1. Raman Spectroscopy

Raman spectroscopy is a technique used to observe vibrational, rotational, and other low-frequency modes in a system. It relies on inelastic scattering (the Raman scattering) of monochromatic light, usually from a laser in the visible, near infrared, or near ultraviolet range. It offers several advantages for microscopic analysis. For example, it does not require sample preparation, therefore specimens do not need to be fixed or sectioned, although flattened surfaces give better-resolved Raman spectra. It is also a non-destructive technique that produces characteristically distinct spectra, easing the identification of mineral phases, even mineral polytypes.

We used the RM1000 Ramascope microRaman system from Renishaw. This is based on optical microscope from Leica attached to a spectrometer with a grating of 1800lines/mm and an entrance slit of 50μm. The laser system used is a HeAr laser at 632.8 nm with the energy at the focus point on the sample not exceeding 7 mW, when the ×50 objective lens is used. With this lens, the spot size is about 4μm. Spectra acquisition is performed on a peltier-cooled CCD camera. During the analyses, the spot size was deliberately varied by changing the focus on the sample in order to

sample more area, therefore more mineral phases. A combination of the WiRE software from Renishaw and the Grams spectroscopy software from Thermo Scientific was used to store and manipulate the spectra.

3.2. X-Ray Diffraction

X-Ray Diffraction is a destructive technique, which is used to characterize and identify the crystallographic structure of natural and manufactured materials. It is one of the most powerful and well-established techniques for qualitative and quantitative analysis of crystalline compounds (Zussman, 1967).

The preparation of the specimen requires powdering in sizes between 0.1 μm and 40 μm. The XRD system used is the D8 from Brucker. X-rays are produced from a copper lamp operated at 40kV and 40mA, and the slit sizes used are of 1 mm. Both the Raman system and the XRD instrument are property of the National Technical University of Athens, School of Mining and Metallurgical Engineering.

4. Sampling Areas - Petrography of Samples

For the purposes of the current study, we used two different marbles (Laskaridis et al. 2000): a dolomite-rich (L1), and a calcite-rich (L2), both from the area of Thassos island. Sample L1 was taken from Tsipoptsi Limenas location. Its commercial name is Thassos Lienas White- Prinos. The second sample (L2) was taken from Stavrolagkada Theologou location. Its commercial name is Crystallina Theologou Thassou. Both marbles are coarse-grained with granoblastic texture. Sample L1 has a grain size ranging from 0.1-2.0 mm whereas sample L2 has a grain size varying from 0.1-3.0 mm. The predominant mineral phase in L1 is dolomite (94 %) and in L2 calcite (95 %).

5. Experimental Work - Methodology

Isometric 2 cm cubic-shaped samples from each marble were calcined in a furnace at three different temperatures, 900, 1050 and 1200^{o}C for 2 hours in order to produce quick lime on a laboratory scale. Similar procedure has been followed by Kantiranis et al., (1999) and Kantiranis (2001). After calcination, the quicklime cubes were stored in a dryer for 24h in order to cool evenly down to atmospheric conditions**.**

We applied Raman spectroscopy, analysing the exterior (at the surface) and interior (near core) part of the cubic samples. X-ray diffraction was applied on the bulk rock specimens in order to verify the mineral transformation process during heating of the initial material.

For reactivity measurement we used the suitably modulated arrangement that is shown in Figure 2. The quick-lime sieved for 5 min in a mechanical mortar down to a size of ~90 μm.

This arrangement is based on the European standard examination method of structural lime EN – 459:2 (2010), which is typically a calorimeter setup. It requires a Dewar vessel that is enclosed in a container with adiabatic walls so that heat loss is minimum. A high-accuracy thermometer is firmly immersed into the Dewar vessel. The device also includes a mechanical stirring system. Temperature readings are acquired from the digital thermometer connected to a computer through acquisition hardware and software.

Quality control of the applied methodology is provided by the reactivity tests. A lime/water = ¼ ratio was used at ambient temperature (~20 ^{0}C) to produce hydrated lime through the highly exothermic reaction #2. The chemical "reactivity" of the produced slaked lime and, ultimately, the quality of the calcination process, is inferred by the rise in temperature of hydration reaction. Acquired data where used to produce slaking curves for the three temperatures of the experiment

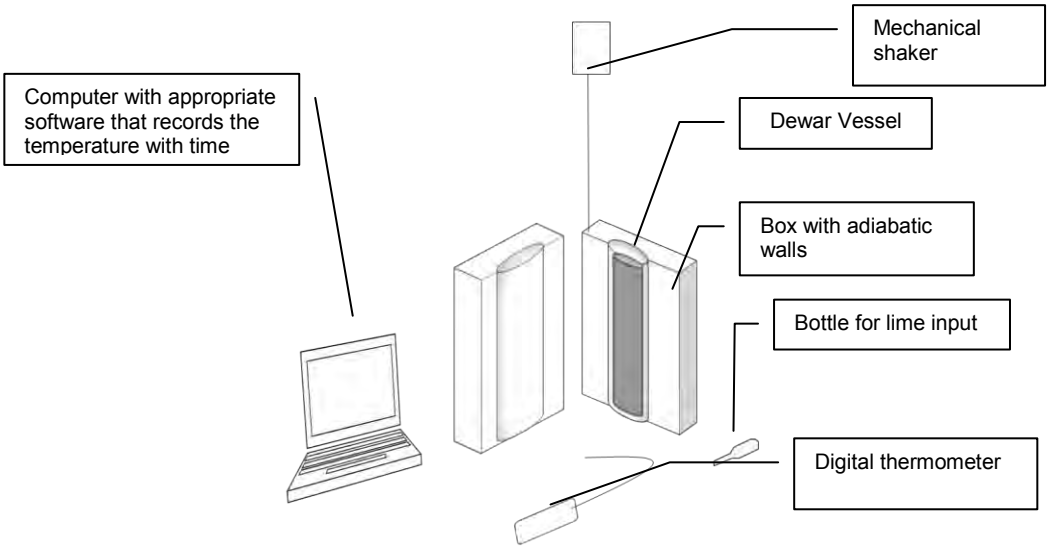

Figure 2 - Experimental arrangement for reactivity lime measurement (before CaO setting).

for each calcined sample. Three methodologies were used for the quantitative definition of the reactivity. These are:

Methodology 1: According to the EN459-2:2001 standard, the reactivity requires the definition of the maximum temperature of the reaction reached by the water-lime system. Then, the reactivity is equal to the temperature given by the formula $80\%*T_{max}+20\%*T_{in}$, where T_{max} is the maximum measured temperature and T_{in} is the initial temperature of the water (before the reaction starts).

Methodology 2: The simplest methodology of the quantitative definition of the reactivity is described in Baziotis et al. (2011). More specifically, the reactivity is computed as the difference between the maximum temperature that has been measured inside the water from the initial temperature of the water before the reaction.

Methodology 3: In this model, the reactivity parameter R_{DIN} is considered which results from the division of 2400 ($40^oC \times 60$ sec/min) by the time (in sec) required so that the temperature reaches 60^oC (Potgieter et al. 2002). The reactivity of lime, based on the R_{DIN} parameter, is divided into three categories: highly reactive lime $R_{DIN}>30$, reactive lime $10<R_{DIN}<30$, and unreactive lime $R_{DIN}<10$. Actually, this model reflects the kinetics of the reaction, and how fast the material will react with the water so that it modulates the respective value of reactivity (R_{DIN}).

6. Results and Discussion

6.1. Raman Analysis

Raman spectroscopy applied in order to study possible variations of the degree of calcination in the external and the internal volume of the samples. Thus, RS evaluates the quality of the calcination process using the modal of calcite, dolomite, lime and periclase in the sample. Figures 3 and 4 show spectra from the outer and inner volume of the cubic samples. Representative spectra are selected from a large number of analyses in order to better demonstrate the full range of transition/final products.

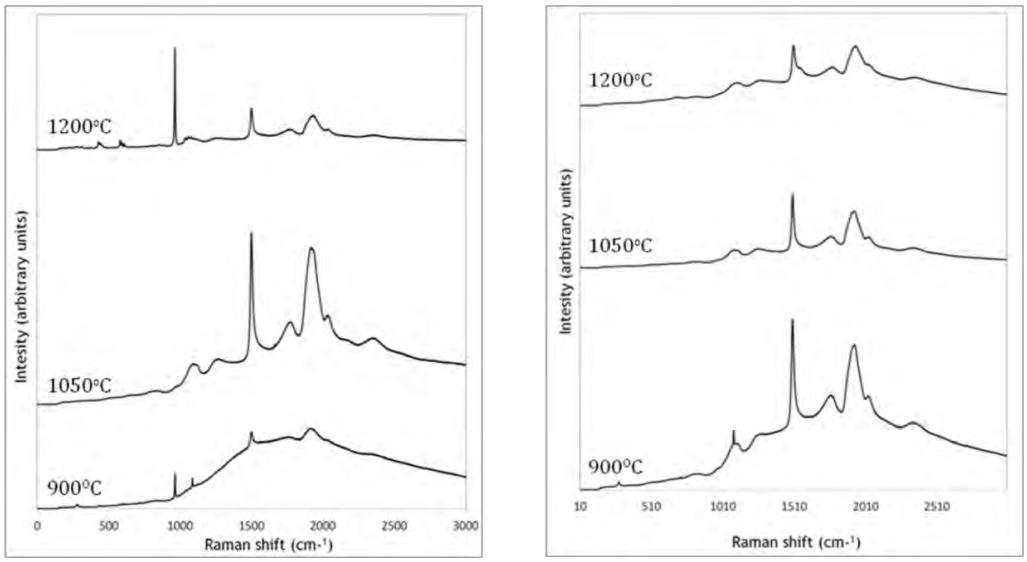

Figure 3 - Raman analyses for sample Q1 (dolomite-rich), showing acquired spectra from its interior (left) and its surface (right).

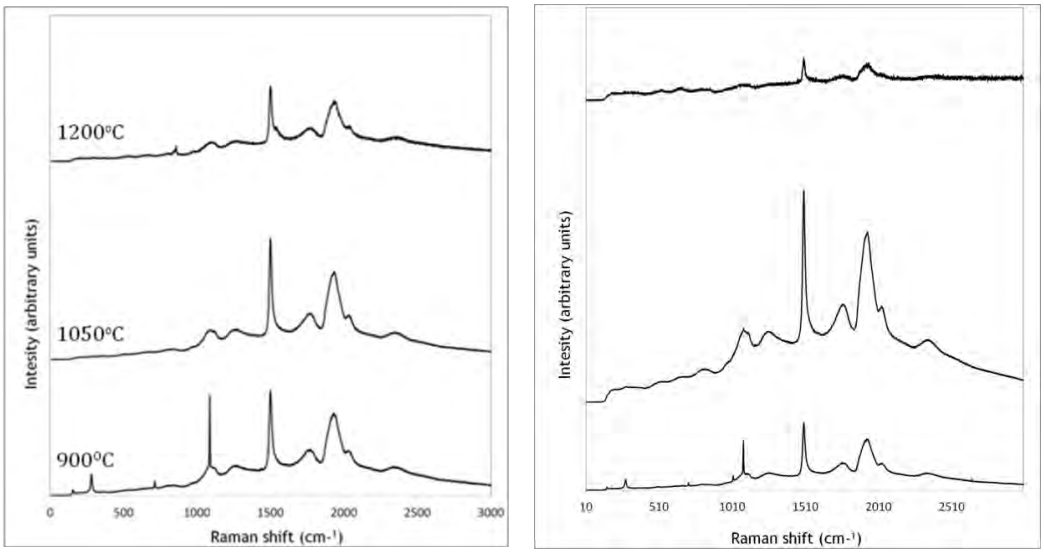

Figure 4 - Raman analyses for sample Q2 (calcite-rich), showing acquired spectra from its interior (left) and its surface (right).

Periclase (MgO) and Lime (CaO) crystallize both in the cubic system, with a the crystal lattice similar to the cubic arrangement of Sodium Chloride's (NaCl) structure (Boynton 1980); the latter forbids first-order Raman spectrum as it possesses inversion symmetry (Schlecht and Böckelmann 1973). It is therefore, not possible to detect MgO (or CaO) from the Raman spectrum (Sharma et al. 1991). Thus remain controversial in the literature the assignment of the observed Raman bands. Following Walzak et al. (2001), indeed Raman spectrum is due to second-order scattering but the defects in the micro-crystals could make them occasionally available as first-order bands. Further, the authors identify slight shifting of the peaks using different exciting sources (green to red laser

excitation source) due to fluorescence; the latter has vibrational structure with a characteristic spectrum for both defects in the microcrystals and crystalline lattice itself.

The broad peak at ~1085 cm^{-1} is assigned to the presence of un-burned material. This is indicated by the presence of calcite and dolomite that remained in large quantities from the initial carbonate precursors. The non-conversion process is strongly influenced from the location of the Raman spot and the calcined temperature. It is reasonable as soon as, the mineral dissociation is evolved from the outer to the inner through certain heat paths.

At 900 ^{0}C the conversion from carbonate to lime is incomplete. However, at temperatures of 1050 and 1200 ^{0}C, Raman spectroscopy shows similar to each other mineralogical features, signifying the complete conversion of carbonate minerals to their oxide equivalents. In particular, the principal bands at ~1500 (narrow peak) and 1930-1940 cm^1, assigned to alkaline-earth oxides (CaO and MgO), but due to aforementioned reasons (fluorescence vibrational structure, similar Raman spectra from both Ca- and Mg-rich quicklime) we are unable to assign the peaks either to CaO or MgO.

6.2. XRD Analysis

Results similar to the Raman analysis, are obtained from the bulk analysis of the XRD analysis (Figure 5). In particular, at 900 ^{0}C the un-burned carbonate minerals (calcite and dolomite) varies from 35 to 65 %, for the dolomitic and calcitic marble, respectively. At 1050 and 1200 ^{0}C after 2 hours of firing, the oxide calcium and magnesium minerals (CaO and MgO for the dolomitic, and CaO for the calcitic marble respectively) dominate in the calcined samples, approaching values of 100 %.

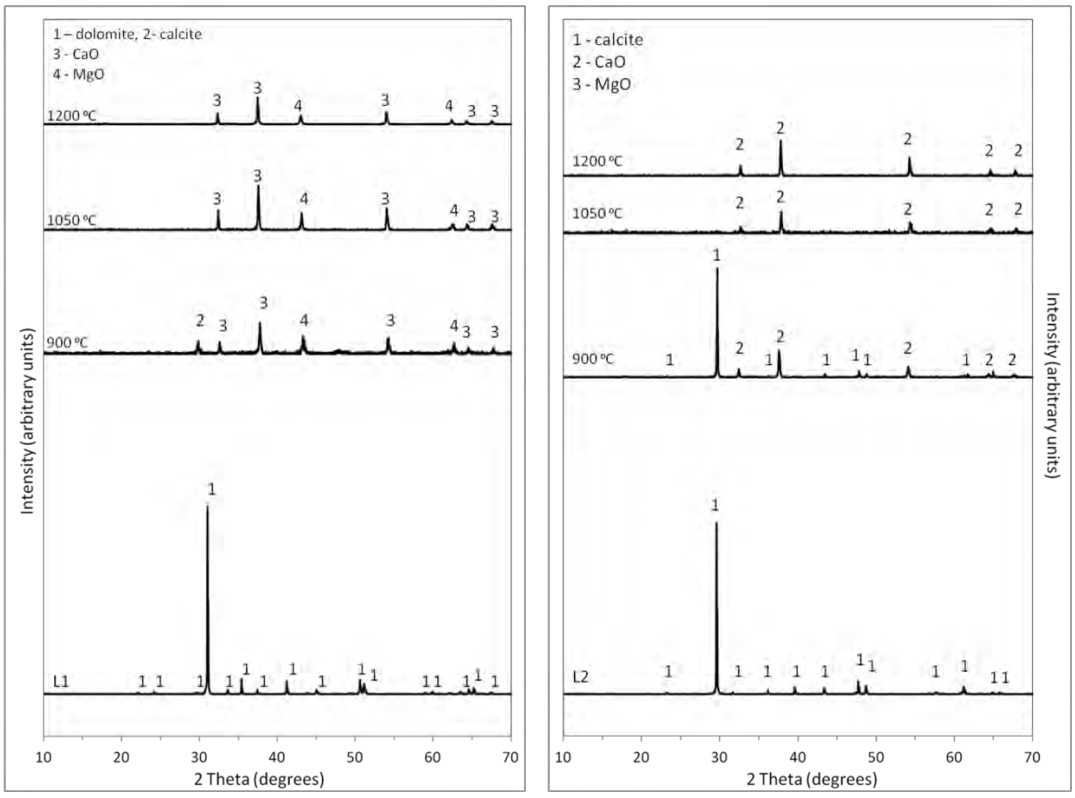

Figure 5 - XRD analyses of Q1 (left figure) and Q2 (right figure) samples for different calcination temperatures (900, 1050 and 1200^0 C).

6.3. Reactivity Test Analysis

From the above results we applied the reactivity test method. The hydration reaction shows that the optimum reactivity value is observed at the temperature of 1050°C (Table 1).

Table 1 - Reactivity values of Q1 and Q2 samples at temperatures 900, 1050 and 1200 0C

Sample	900°C	1050°C	1200°C	Qualitative definition
Q1	22.78* 39.66 ** -***	58.67 67.4 3.37	51,90 61,33 2.41	+Inactive lime
Q2	24.15 41.07 -	58.49 66.47 48	44,96 55,86 1.78	+Highly reactive lime

*: Reactivity computed according to Baziotis et al. (2011)
**: Reactivity computed according to EN459-2 standard
***: Reactivity computed according to 12485 standard of 1996 (European Norm En 12485)
+: Characterization of lime for 1050°C temperature that is based on following breadths: >30 very effective lime, 10-30 effective lime, <10 inactive lime according to 12485 standard of 1996 (European Norm En 12485)

Also, Figures 6 and 7 provide identification of the various regimes (e.g., Commandrè et al., 2007) of the hydration process over time. Furthermore it is clearly shown that the optimum temperature for both dolomitic (Q1) and calcitic (Q2) marbles is that of 1050 ^{0}C. Furthermore, the presence of magnesium plays an important role in the hard-burnt development (at 1200 ^{0}C) showing a "delaying" slaking curve due to late hydration (Figure 7).

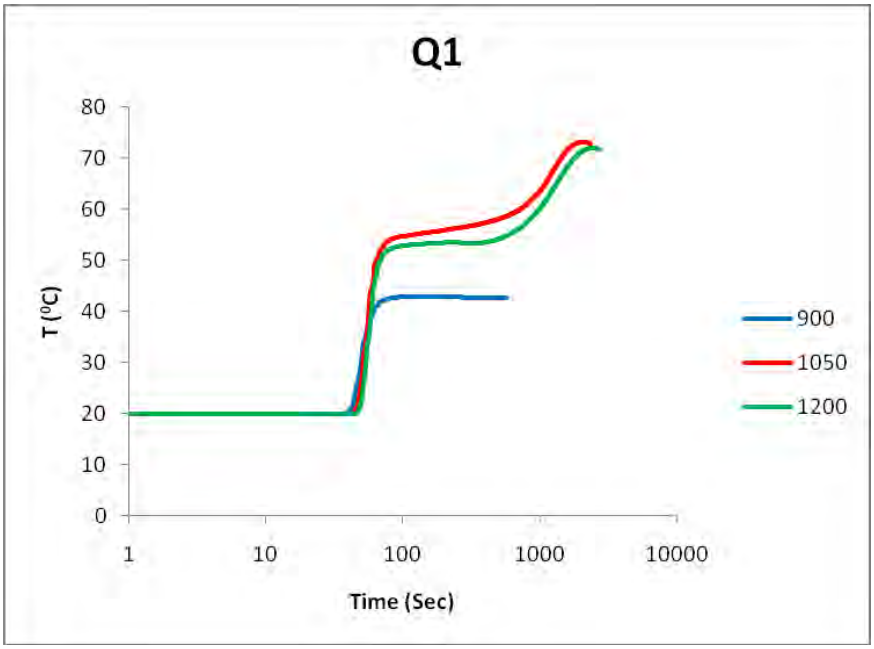

Figure 6 - Slaking curves in lognormal scale for magnesium-rich marble that came from three heating temperatures at 900, 1050 and 1200 ^{0}C.

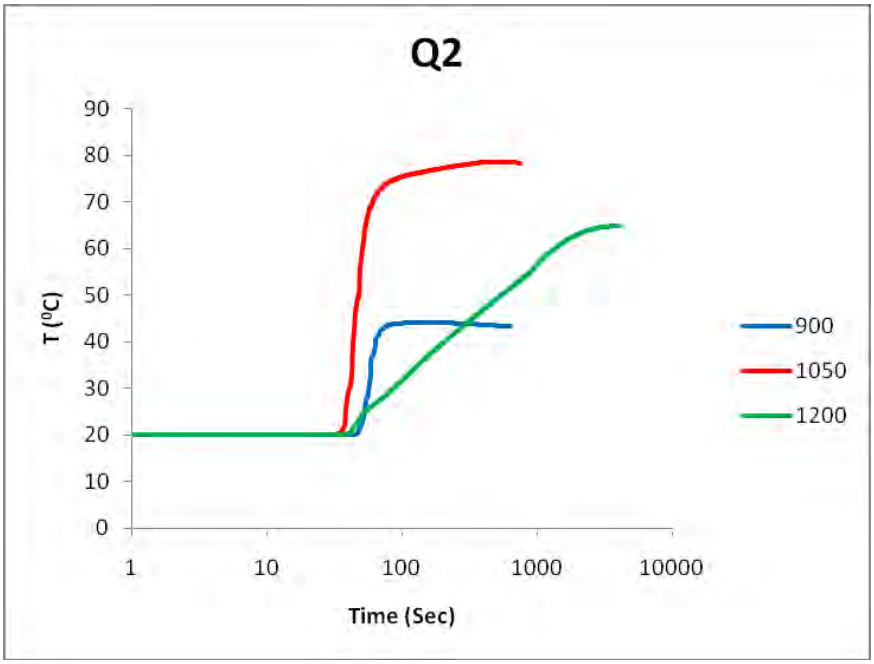

Figure 7 - Slaking curves in lognormal scale for calcium-rich marble that came from three heating temperatures at 900, 1050 and 1200 ^{0}C.

7. Conclusions

Raman and XRD results show unburned material (presence of residual calcite and dolomite) at the lowest measured temperature (900 ^{0}C). The above, combined with the low reactivity values, suggest that the conditions of 900 ^{0}C/2 h are not enough to complete the dissociation of carbonates. After that, we conclude using the current methodology the worst calcination temperature was that of 900 ^{0}C. Raman spectra from both the surface and core of the lime suggest that the carbonate minerals were almost fully converted to newly formed oxides (mainly CaO) at the temperature of 1050 ^{0}C. The above, combined with the results from the reactivity tests (highest reactivity value) suggest that 1050 ^{0}C is the optimum temperature for the studied system. The combination of the spectroscopic methods alone should be applied with caution, however, is able to provide the necessary information on the transformation of the initial material during progressive heating.

8. Acknowledgements

We gratefully acknowledge the helpful remarks by reviewers, G. Triantafyllou and an anonymous one. Also Prof. Manoutsoglou is thanked for his excellent editorial handling. Sincere thanks to Onassis Foundation for the financial support to G. Leontakianakos. G.L. is grateful to Dr K. Laskaridis who provide the samples of the current study.

9. References

Baziotis I., Leontakianakos G., Proyer A., Lee H. and Tsimas S. 2011. Physico-chemical Properties of Different Carbonate Rocks: Are They Highly Enough to Control Lime Reactivity?, *International Journal of Chemistry*, 3(2), 187-197.

Bestmann M., Kunze K. and Matthews A. 2000. Evolution of a calcite marble shear zone complex on Thassos Island, Greece: microstructural and textural fabrics and their kinematic significance, *Journal of Structural Geology*, 22, 1789-1807.

Boynton R.S. 1980. The Chemistry and Technology of Lime and Limestone. 2nd ed., Wiley, New York, 1980.

Commandrè J.M., Salvador S. and Nzihou A. 2007. Reactivity of laboratory and industrial limes, *Trans IChemE Part A Chemical Engineering Research and Design*, 85(A4), 473-480.

De Wall H., Bestmann M. and Ullemeyer K. 2000. Anisotropy of diamagnetic susceptibility in Thassos marble: A comparison between measured and modeled data, *Journal of Structural Geology*, 22, 1761-1771.

European Committee for standardization, 2010. EN 459-2, Building Lime, Test Methods.

European Norm En 12486, 1996. Chemicals used for the treatment of water intended for human consumption-Calcium carbonate, high-calcium lime and half-burnt dolomite. Test Methods.

Geological map of Thassos Island (http://www.geocaching.com).

Laskaridis K., Papaioannou N., Papatreha H., Kousseri I. and Christou G.. 2000. Marbles of Thassos Island. IGME, 1-67. (In Greek).

Kantiranis N., Tsirambides A., Filippidis A. and Christaras B. 1999. Technological characteristics of the calcined limestone from Agios Panteleimonas, Macedonia, Greece, *Materials and Structures*, 32, 546-551.

Kantiranis N. 2001. Calcination study of the crystalline limestone from Agios Panteleimonas, Florina, Greece, *PhD Thesis*, School of Geology, Aristotle University of Thessaloniki, 196 p. (in Greek with extensive English summary).

Potgieter J.H., Potgieter S.S., Moja S.J. and Mulaba-Bafubiandi A. 2002. An empirical study of factors influencing lime slaking. Part I: production and storage conditions, *Minerals Engineering*, 15, 201-203.

Schlecht R.G. and Böckelmann H.K. 1973. Raman scattering from microcrystals of MgO, *Physical Review Letters*, 31, 930-932.

Sharma S.K., Misra A.K. and Singh U.N., 1991. Remote Raman Spectroscopy of minerals at elevated temperature relevant to Venus exploration, *Proceedings of SPIE*, 7153, 715307.

Triantafyllou G. and Manoutsoglou E. 2004. The Use of Lime in the Treatment of Environmental Problems, *Bulletin of the Geological Society of Greece*, XXXVI, 246-253.

Walzak M.J., Davidson R.D. and McIntyre N.S. 2001. Interfacial reactions between SF_6 and molten magnesium. In: Hryn J. (ed) *Magnesium Technology. The minerals. Metals & Materials Society*, 37 - 41.

Zussman J. 1967. Physical methods in determinative mineralogy, in Zussman, J. (ed) *Physical methods in determinative mineralogy*, 514 pp.

Δελτίο της Ελληνικής Γεωλογικής Εταιρίας, τομ. XLVII , 2013
Πρακτικά 13ου Διεθνούς Συνεδρίου, Χανιά, Σεπτ. 2013

Bulletin of the Geological Society of Greece, vol. XLVII 2013
Proceedings of the 13th International Congress, Chania, Sept. 2013

CHARACTERIZATION OF A NEW LABORATORY CERAMIC PRODUCT FROM INDUSTRIAL BY-PRODUCTS AS RAW MATERIALS AND CAUSTIC MAGNESIA AS ADDITIVE

Skliros V.[1], Lampropoulou P.G.[1], Tsikouras B.[1,2], Hatzipanagiotou K.[1], Christogerou A.[3] and Angelopoulos G.N.[3]

[1]*University of Patras, Department of Geology, Section of Earth Materials, 265 00, Patras, Greece*
sklirosbill@gmail.com, p.lampropoulou@upatras.gr, v.tsikouras@upatras.gr, k.hatzipanagiotou@upatras.gr

[2]*University of Brunei Darussalam, Department of Petroleum Geoscience, Jalan Tungku Link, Gadong BE1410, Bandar Seri Begawan, Brunei Darussalam*

[3]*University of Patras, Department of Chemical Engineering, Laboratory of Materials and Metallurgy, 265 00 Patras, Greece, angiechristo@chemeng.upatras.gr, angel@chemeng.upatras.gr*

Abstract

A new ceramic product is introduced by mixing caustic magnesia, produced in the laboratory from pure, high quality magnesite, and natural silt. Bottom ash and red mud, two well known environmentally hazardous industrial by-products, were also added in the mixture. After testing various recipes we concluded that addition of 5% caustic magnesia in the ceramic product greatly enhances its performance. Increase bonding of the ceramic microstructure is attributed to the formation of periclase necks, the concurrent formation of small quantities of amorphous material and the homogeneously distributed pores during the experimental firing of the mixture. Combined X-ray Diffractometry and Scanning Electron Microscopy of the ceramic product revealed the occurrence of unreactive phases, inherited by the raw materials, as well as newly-formed albite and magnesioferrite. Our results show that utilization of by-products may be important and environmental friendly materials in producing low cost ceramic building materials.
Keywords: *ceramics, caustic magnesia, by-products, red mud, bottom ash.*

Περίληψη

Στην εργασία αυτή παρουσιάζεται ένα νέο κεραμικό προϊόν που παράχθηκε από μίξη καυστικής μαγνησίας, που παρασκευάστηκε εργαστηριακά από υψηλής καθαρότητας μαγνησίτη, φυσικού πηλού καθώς και τέφρας πυθμένα και ερυθράς ιλύος, προϊόντα γνωστά για τις δυσμενείς περιβαλλοντικές επιπτώσεις τους. Έπειτα από δοκιμή ποικίλων συνταγών, συμπεράναμε ότι προσθήκη 5% καυστικής μαγνησίας στο κεραμικό προϊόν βελτιώνει τις μηχανικές επιδόσεις του. Αυτό αποδίδεται στο γεγονός ότι το περίκλαστο της καυστικής μαγνησίας σχηματίζει «λαιμούς», οι οποίοι ισχυροποιούν τους δεσμούς στη μικροδομή του κεραμικού, σε συνδυασμό με τον ταυτόχρονο σχηματισμό μικρών ποσοτήτων άμορφου υλικού και την ομοιογενή κατανομή των πόρων, που δημιουργούνται κατά την όπτηση. Με συνδυαστική μελέτη Περιθλασιμετρίας Ακτίνων Χ και Σαρωτικού Ηλεκτρονικού Μικροσκοπίου του

κεραμικού υποδείχτηκε η παρουσία αναλλοίωτων φάσεων, προερχόμενων από τις πρώτες ύλες, καθώς και νεοσχηματισμένων κρυστάλλων αλβίτη και μαγνησιοφερρίτη. Τα αποτελέσματα της παρούσας μελέτης δείχνουν ότι η χρήση παραπροϊόντων μπορεί να είναι σημαντική και περιβαλλοντικά φιλική στην παραγωγή φτηνών δομικών κεραμικών.
Λέξεις κλειδιά: *κεραμικά, καυστική μαγνησία, παραπροϊόντα, ερυθρά ιλύς, τέφρα πυθμένα.*

1. Introduction

Pure magnesite has restricted industrial applications, mainly used as fertilizer, filler in rubber materials or plastics, paints and colour industries, comprising also a cheap source of MgO (Harben, 2002; Sikalidis *et al.*, 2003). Its basic features are its white colour and its relatively low hardness. Caustic magnesia and dead burned magnesia are produced from pure magnesite after heating at 1000^{o}C and 1800 – 2000^{o}C, respectively. Caustic magnesia has plenty of industrial applications, such as catalyst and pharmaceutical products (Harben, 2002) whereas dead burned magnesia is used as raw material in the production of basic refractories.

This study aims in synthesizing and characterizing a new, low-cost, ceramic material, using natural silt, bottom ash and red mud, as well as caustic magnesia, produced from pure Greek magnesite, as additive. Adopting usage of such materials will contribute to reduction of waste products, as they can be used in environmental-friendly, large-scale production of ceramic products.

2. Materials and Methods

2.1. Analytical Methods

Whole-rock geochemical analyses of magnesite were performed at Acme Analytical Laboratories LTD., Vancouver, Canada, by ICP-emission spectrometry following a Lithium metaborate/tetraborate fusion and dilute nitric digestion. Loss on ignition (LOI) was calculated by weight difference after ignition at 1000°C. The detection limit for major elements was 0.01%. The analytical precision calculated from replicate analyses was better than 5% for most elements. Scanning Electron Microscopy (SEM) was carried out at the Laboratory of Electron Microscopy and Microanalysis, University of Patras, using a JEOL JSM-6300 SEM equipped with EDS and WDS. Operating conditions were accelerating voltage 15 kV and beam current 3.3 nA with 4 μm diameter beam. EDS and WDS spectrum information with the ZAF correction software information was used. X-ray diffractometry (XRD), performed at the Research Laboratory of Minerals and Rocks, Department of Geology, University of Patras, using a BRUKER D8 ADVANCE diffractometer. Diffraction patterns were measured in 2θ range of 2 – 70^{o}, using CuKα radiation of 40 kV and 40 mA, with 0.3 s step time/0.015^{o} step. Qualitative analysis was performed by the DIFFRACplus EVA® software (Bruker-AXS) based on the ICDD Powder Diffraction File. Differential Scanning Calorimetry (Netzsch STA 449 F3) was employed in order to obtain the transition temperature of magnesite to periclase. DSC was performed at the Department of Chemical Engineering, University of Patras, using a Du Pond 910 calorimeter equipped with a 99 thermal analyzer. The instrument was calibrated with a sapphire (Al_2O_3) standard. The sample was heated up to 1400^{o}C, at a heating range of 10°C/min.

2.2. Raw Materials

2.2.1. Magnesite

Magnesite samples were collected from a mining industry quarry in the Gerakini area, Chalkidiki peninsula, north Greece. The magnesite has a cryptocrystalline structure (crystal size below 10 μm), hence no particles are discernible even under a microscope. Whole-rock geochemical

analysis revealed that the samples are highly pure magnesites, containing only low amounts of SiO_2 and CaO impurities (Table 1). The predominance of magnesite in the collected samples is also indicated in XRD patterns (Figure 1).

Table 1 - Chemical composition of the magnesite used in the laboratory production of caustic magnesia and of raw materials used as additives in the production of ceramic tiles (-: below detection limit; nd: not determined).

	Magnesite	*Natural silt*	*Bottom ash*	*Red mud*
Major oxides wt.%				
SiO_2	1.64	48.29	44.60	7.79
TiO_2	-	-	-	5.17
Al_2O_3		13.61	19.93	17.04
Fe_2O_3		5.30	6.28	44.34
MnO	-	-	-	-
MgO	43.13	3.11	1.43	0.57
CaO	0.46	12.72	7.51	11.64
Na_2O	-	0.59	-	3.17
K_2O	-	2.49	0.75	0.07
Cr_2O_3	-	-	-	-
SO_3	nd	nd	1.22	nd
C	nd	nd	10.10	nd
L.O.I	50.80	13.64	nd	9.77
Total	96.03	99.75	91.82	99.56

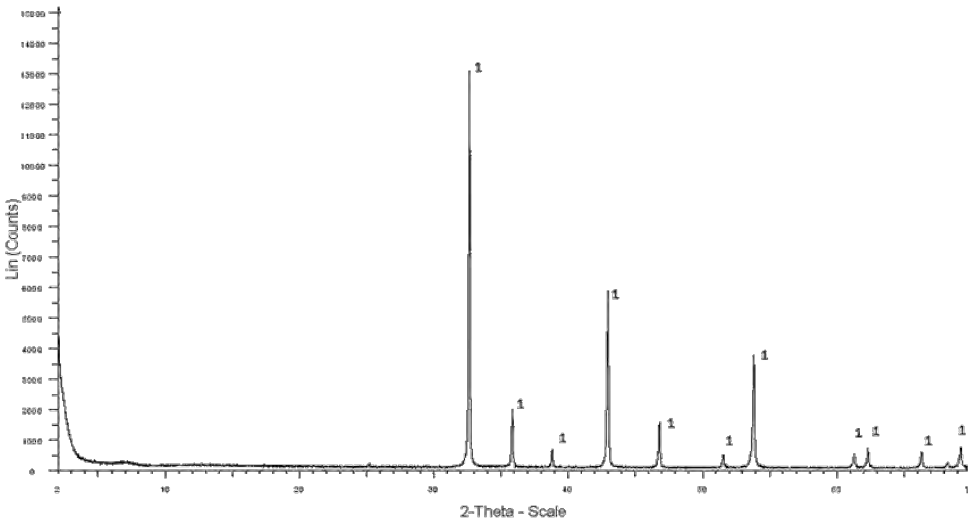

Figure 1 - XRD pattern of a highly pure cryptocrystalline magnesite (1) sample.

2.2.2. Production of Caustic Magnesia

Experimental thermal treatment of magnesite revealed that its decomposition to periclase and CO_2 starts at around 500°C and completes at 700°C, as it is indicated in a DSC thermogram (Figure 2).

There is a considerable mass loss of about 52%, plausibly due to escape of CO_2, and the decomposition of magnesite is a strongly endothermic event, which may be described by the reaction: $MgCO_3 \rightarrow MgO + CO_{2(g)}$. During this experiment, the sample was heated up to 1400°C but no other alteration was observed beyond 700°C.

The production of the caustic magnesia took place in the laboratory, after heating treatment of the magnesite at 1000°C for 4 hours, in an electric furnace. Crystalline periclase has been detected in the produced caustic magnesia by X-ray diffraction analysis (Figure 3). Magnesite was fully decomposed to periclase and CO_2, as it is suggested from the geochemical analysis of the caustic magnesia product that yielded MgO content above 94% wt. % (not shown). Traces of forsterite appear as a new phase in the caustic magnesia, as it is indicated by a small peak in the XRD pattern (Figure 3). It is interpreted that the forsterite was formed, during thermal treatment, from the reaction of magnesite or/and of magnesia with the impurities of silica.

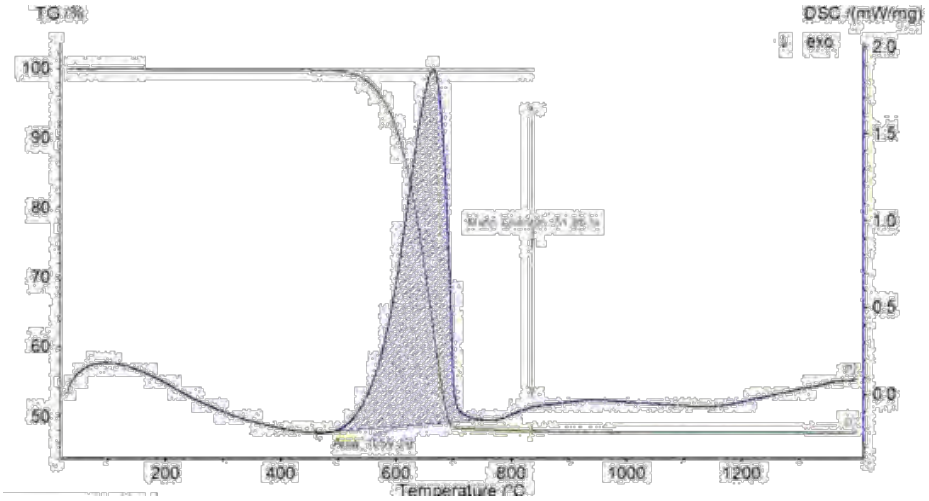

Figure 2 - DSC thermogram of the decomposition of natural magnesite from Gerakini to periclase and CO_2; the green line indicates mass change whereas the blue line shows the endothermic breakdown of magnesite at a temperature range between 500 and 700°C.

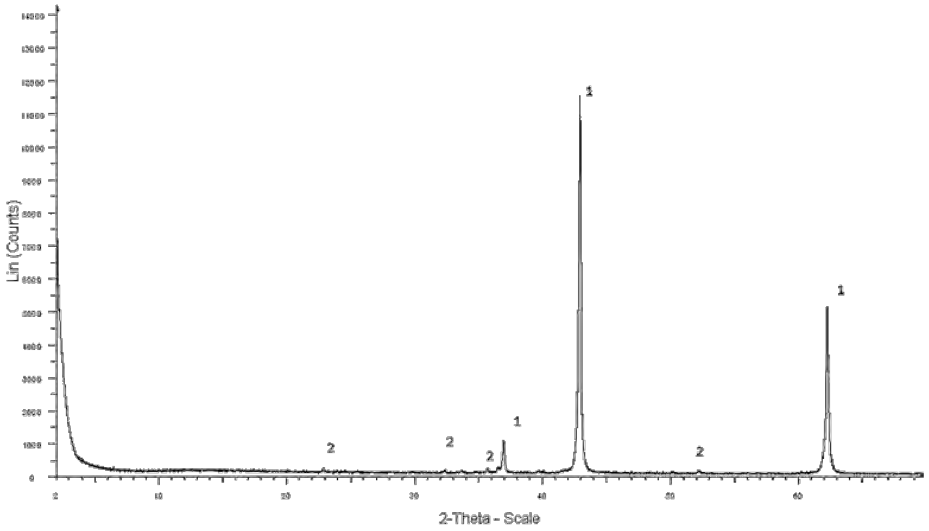

Figure 3 - XRD pattern of caustic magnesia produced after thermal treatment (1000 °C) of pure natural magnesite (1: periclase, 2: forsterite).

2.2.3. Other Raw Materials

Raw materials that were additionally used in order to synthesize various ceramic tiles include natural silt, used for industrial purposes, bottom ash by-product, derived from a lignite Power Plant, Megalopolis, N. Greece, as well as red mud, derived from waste deposits of aluminium production in central Greece. Chemical analyses of these materials were performed by Pontikes (2007) and Anagnostopoulos (2009) and their average compositions are listed in Table 1. Both bottom ash and red mud are generally thought to cause severe environmental problems (Georgakopoulos *et al.*, 1992, 2002; Varnavas and Achilleopoulos, 1995; Liu *et al.*, 2007, 2011; Izquierdo *et al.*, 2011).

2.2.4. Synthesis of the Ceramic Material

After testing several mixtures of the aforementioned raw materials, we found that the best performance was obtained by the ceramic recipe which included 70% silt (grain diameter < 30μm), 20% bottom ash (grain diameter < 30μm), 5% red mud (grain diameter < 40μm) and 5% caustic magnesia (grain diameter < 30μm). All materials were pulverized in a laboratory mill and subsequently the various mixtures were shaped under a load of 220 MPa. The pressed samples were dried initially at room temperature for 24 h and then in a drying oven at 110°C till constant weight. Sintering was performed in a laboratory muffle furnace at 1000°C following the industrial thermal cycle of ceramic products. The whole heating and cooling procedure lasted 36 h and conducted in the Department of Chemical Engineering, University of Patras.

3. Chemical Characterization of the new Ceramic Material

The geochemical composition of the ceramic product was calculated according to the percentage of its constituent raw materials. Plot of the calculated composition on a SiO_2-Al_2O_3-(TiO_2+Fe_2O_3+MgO+CaO+Na_2O+K_2O) diagram shows that this new product can be classified, according to its chemical affinities, as a high porosity ceramic material similar to majolica or cottoforte type (Figure 4).

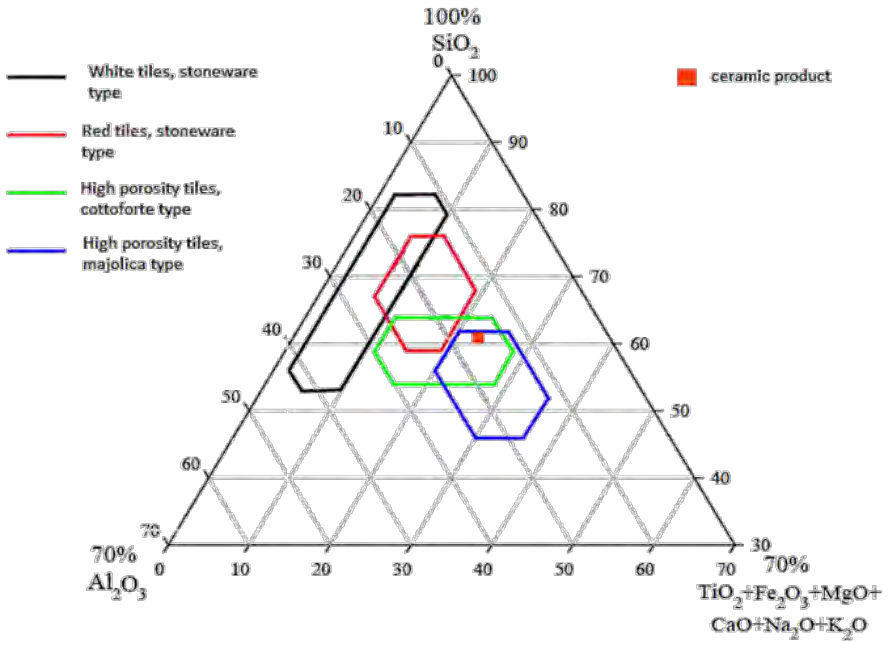

Figure 4 - Ternary SiO_2-Al_2O_3-(TiO_2+Fe_2O_3+MgO+CaO+Na_2O+K_2O) diagram for high porosity ceramics based on industrial uses (fields after Sandrolini and Palmonari, 1974).

4. Mineral Composition and Microstructure of the New Ceramic Product

The mineralogical composition of the new ceramic product was obtained using combined XRD and SEM/EDS analyses. Microstructure observations, with particular emphasis on the impact of the caustic magnesia as additive, were also undertaken by means of SEM. The observed mineral phases in the ceramic matrix include quartz, hematite, gypsum, periclase, albite and magnesioferrite surrounded mostly by a pelitic matrix (Figure 5, 6a). In places, amorphous (glassy) material of Ca-Al-Si, Fe-Al-Si and Ca-Si compositions surrounds the grains filling their interstices (Figure 6b, c). Numerous pores, up to 0.5 mm, are rather homogeneously distributed both in the pelitic groundmass, as intergranular porosity, and in the glassy matrix (Figure 6d, e). Notably, periclase crystals show characteristic "neck" formations around its rims (Figure 6f).

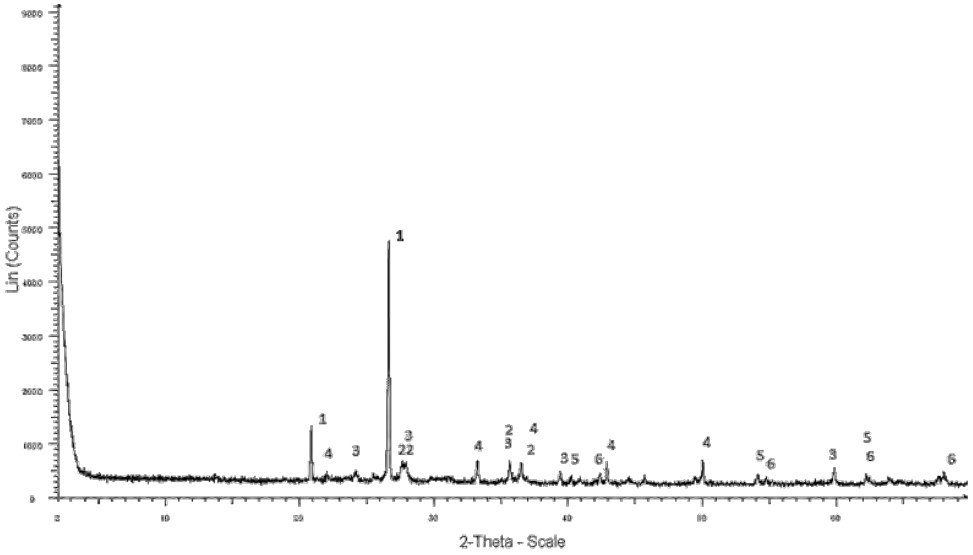

Figure 5 - XRD pattern of the new ceramic sample (1: quartz, 2: albite, 3: periclase, 4: hematite, 5: gypsum, 6: magnesioferrite).

5. Physicomechanical Properties

Psysicomechanical properties of the ceramic product were conducted according to ASTM C373-88 directions. Shrinkage and mass loss during firing, as well as density, open porosity, water absorption and bending strength of the ceramic were measured for its characterization (Table 2). The obtained values are in the range of similar products, which have been created in laboratory or in industry (e.g. Anagnostopoulos, 2009).

Table 2 - Physicomechanical properties of the new ceramic product.

Shrinkage (%)	*Mass loss (%)*	*Density (g/cm^3)*	*Water absorption (%)*	*Open porosity (%)*	*Bending strength MPa*
7.20	9.12	1.83	16.20	30.64	8.01

6. Discussion

He *et al*. (2012) and Zhao *et al*. (2010) have suggested the usage of red mud for high porosity ceramics due to the fact that it results in the increase of density of the ceramic products. Additionally, bottom ash is considered as a perfect raw material for ceramics due to its high carbon content (Porreca *et al*., 2007, Hu *et al*., 2008), and because it increases the bending strength between the particles (Schabbach *et al*., 2012).

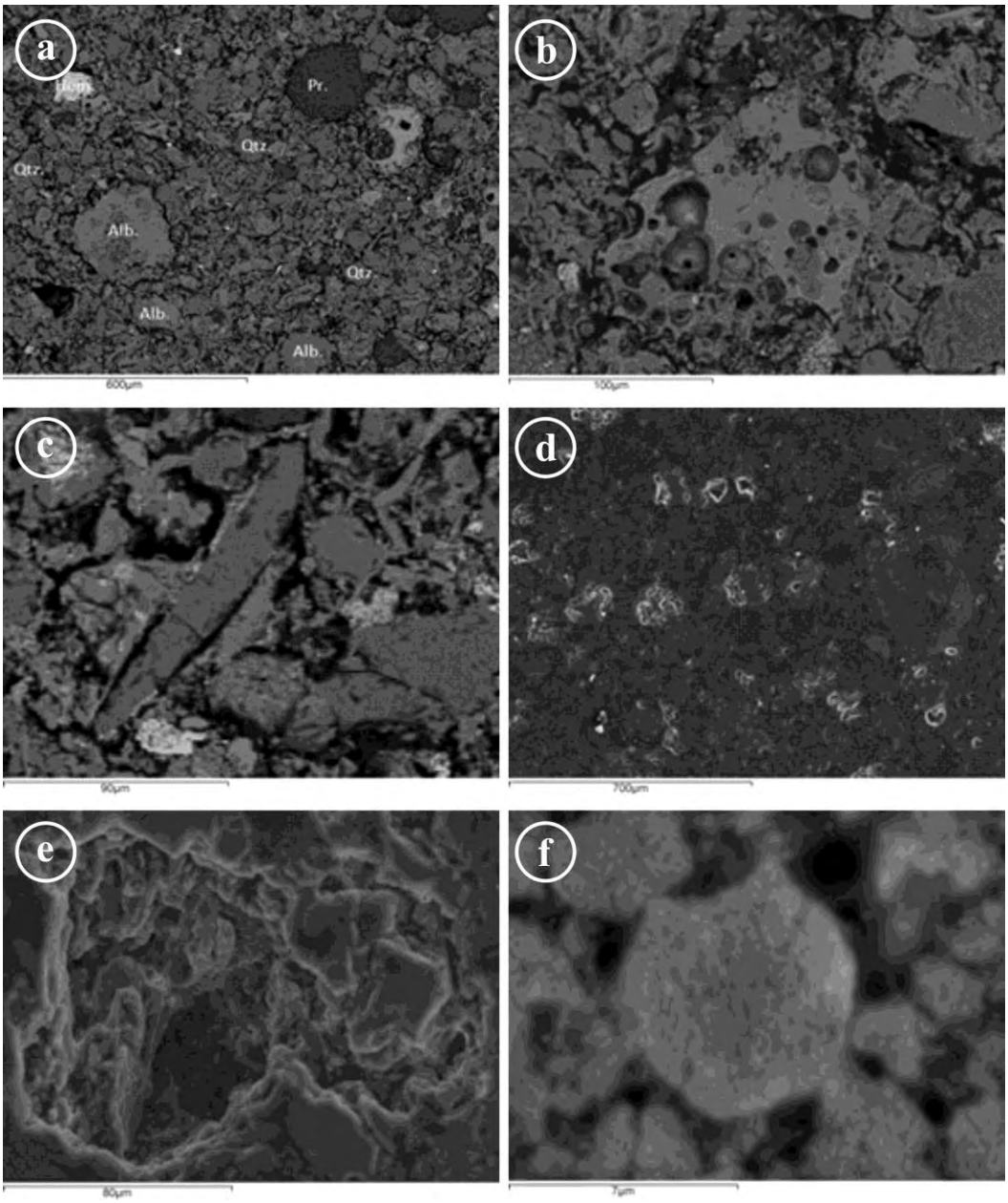

Figure 6 - Backscattered (BSE) and secondary electron (SE) images illustrating the main textural characteristics of the produced ceramic material: (a) coexisting unreactive and new phases (BSE); (b) development of Ca-Al-Si-rich amorphous phase (centre of the image) due to melting and vesicles formation possibly due to gas escape (BSE); (c) elongated quartz grain surrounded by a Ca-Al-Si-rich amorphous phase (BSE); (d) open porosity of the ceramic product (SE); (e) pore walls details (SE); (f) neck development among periclase crystals after firing of the ceramic (BSE) (Qtz.: quartz, Pr.: periclase, Alb.: Albite, Hem.: Hematite).

The desirable cohesiveness of the new ceramic product was achieved using as eutectic phases the red mud, bottom ash and natural silt. The research of the new ceramic took place among several mixtures and as a result we observed that 5% of caustic magnesia in the initial mixture improved

the properties of the ceramics, while adding more than 10% resulted in failure of the final product. The quality of the magnesite is crucial in producing high quality caustic magnesia, free of impurities. The Gerakini magnesite is an excellent raw material for this purpose.

The mineral chemistry of the new ceramic product includes unreactive phases that have been retained in the new product from the raw materials, as well as newly formed phases (Figures 5 and 6a). Albite and magnesioferrite comprise the newly-formed minerals, whereas very fine-grained quartz, hematite and gyspum are dispersed throughout the ceramic matrix or form aggregates in it and are considered as unaltered phases that were contained in the bottom ash and the red mud; periclase derived from the caustic magnesia additive. The improvement of the ceramic performance by addition of small amounts of caustic magnesia is attributed to the formation of "necks" around the rims of the unreactive periclase after further thermal treatment. This textural formation results in an interconnecting crystal framework, likely enhancing the cohesiveness of the product (Figure 6f). In addition to this, the occurrence of the amorphous phases contributed to bonding and partial cementation of the ceramic matrix (Figure 6b, c). Their chemical composition strongly suggests their derivation from partial melting of the eutectic phases occurring in the raw materials (silt, red mud and bottom ash).

Overall the obtained values of the physicomechanical properties of the ceramic that produced in our Laboratory indicate its good mechanical performance, suggesting also its effective in-service behaviour. Its high open porosity value (Table 2) is attributed to gas volatilization and to incomplete solid reactions and melting during the heating treatment. The observed homogeneous pore distribution, rather than an irregular segregation of pores that would result in localized areas of weakness, is another factor for the enhancement of the ceramic properties (Figure 6d, e). This, along with its rather high water absorption value do not negatively affect the mechanical properties of the material as it also yielded high bending strength value.

7. Conclusions

A new, low-cost, in-house, high porosity ceramic material was produced by mixing pure caustic magnesia and natural silt with bottom ash and red mud, which are commonly considered as environmentally hazardous industrial by-products. Caustic magnesia of high purity was synthesized after thermal treatment of a Greek magnesite. Testing various mixtures with caustic magnesia, we found that addition of 5% caustic magnesia positively affected the physicomechanical properties of the final product, while other mixtures gave products of inferior quality or unsuccessful. Necks developed on periclase during its formation after thermal treatment for producing caustic magnesia seem to promote significantly bonding of the ceramic microstructure. The mechanical performance of the final product is further enhanced by the sporadic presence of amorphous material and the homogeneous distribution of pores, developed during thermal treatment. Quartz, hematite and periclase remained as unreactive minerals inside the new ceramic microstructure, while albite and magnesioferite are formed during firing.

Utilization of environmental hazardous by-products and limitation of energy consumption during production of the final product are suggested for ceramics production. The recommended recipe for the ceramic produced in this study, at a laboratory scale, is suggested to be tested in an industrial scale production, in order its benefits to the environment, as well as to the building materials industry to be evaluated.

8. Acknowledgements

Critical reviews by Dr. I. Iliopoulos and Dr. P. Voudouris have improved the manuscript and are gratefully appreciated. Thanks are due to Vasilis Kotsopoulos for his support in the use of Scanning Electron Microscope.

9. References

Anagnostopoulos I.P. 2009. Utilization of lignite solid byproducts in the production of lightweight aggregates and lightweight aggregate concrete, *PhD Thesis*, Department of Chemical Engineering, University of Patras, 168pp.

ASTM C373–88. 2006. Standard Test Method for Water Absorption, Bulk Density, Apparent Porosity, and Apparent Specific Gravity of Fired Whiteware Products.

Georgakopoulos A., Kassoli-Fournaraki A. and Filippidis A. 1992. Morphology, mineralogy and chemistry of the fly ash form the Ptolemais lignite basin (Greece) in relation to some problems in human health, *Trends in Mineralogy*, 1, 301-305.

Georgakopoulos A., Filippidis A., Kassoli-Fournaraki A., Iordanidis A., Fernández-Turiel J.-L., Llorens J.-F. and Gimeno D. 2002. Environmentally important elements in fly ashes and their leachates of the power stations of Greece, *Energy Sources*, 24, 83-91.

Harben P.W. 2002. *The Industrial Minerals HandyBook - A Guide to Markets, Specifications, & Price*s, Fourth Edition, Industrial Minerals Information Services, UK, 412 pp.

He H., Yue Q., Qi Y., Gao B., Zhao Y., Yu H., Li J., Li. Q. and Wang Y. 2012. The effect of incorporation of red mud on the properties of clay ceramic bodies, *Applied Clay Science*, 70, 67-73.

Hu Y., Chen G. and di Maio F. 2008. Physical and chemical characterizations of MSWI bottom ash, *Taiyangneng Xuebao/Acta Energiae Solaris Sinica*, 29, 1187-1191.

Izquierdo M., Koukouzas N., Touliou S., Panopoulos K.D., Querol X. and Itskos G. 2011. Geochemical controls on leaching of lignite-fired combustion by-products from Greece, *Applied Geochemistry*, 26, 1599-1606.

Liu Y., Lin C. and Wu Y. 2007. Characterization of red mud derived from a combined Bayer Process and bauxite calcination method, *Journal of Hazardous Materials*, 146, 255-261

Liu Y., Naidu R. and Ming H. 2011. Red mud as an amendment for pollutants in solid and liquid phases, *Geoderma*, 163, 1-12.

Pontikes Y. 2007. Utilization of red mud in the heavy clay industry, *PhD Thesis*, Department of Chemical Engineering, University of Patras, 172pp.

Porreca P., Furlani E., Fedrizzi L., Brückner S., Minichelli D., Tubaro F., Bachiorrini A., Andreatta F. and Maschio S. 2007. Sintered ceramics from special waste incinerator ashes and steel making slag, *Industrial Ceramics*, 27, 197-203.

Sandrolini F. and Palmonari C. 1974. Variazioni strutturali e dimensionali durante la cottura di argille Italiane per materiali da costruzione, *La Ceramica*, 17, 6-12

Schabbach L.M., Andreola F., Barbieri L., Lancellotti I., Karamanova E., Ranguelov B. and Karamanov A. 2012. Post-treated incinerator bottom ash as alternative raw material for ceramic manufacturing, *Journal of the European Ceramic Society*, 32, 2843-2852.

Sikalidis C.A., Zampetakis Th. and Dagilas C. 2003. The effect of magnesite addition on the properties and production process of low porosity porcelain type ceramics, *L' Industrie Céramique*, 988, 22-27.

Varnavas S.P. and Achilleopoulos P.P. 1995. Factors controlling the vertical and spatial transport of metal-rich particulate matter in seawater at the outfall of bauxitic red mud toxic waste, *Science of the Total Environment*, 175, 199–205

Zhao S., Liang Y., Wu J. and Yang H. 2010. Experimental research of Bayer red mud preparation of porous ceramic filter balls, *Shenyang Jianzhu Daxue Xuebao (Ziran Kexue Ban)/Journal of Shenyang Jianzhu University (Natural Science)*, 26, 306-310.

Δελτίο της Ελληνικής Γεωλογικής Εταιρίας, τομ. XLVII , 2013
Πρακτικά 13ου Διεθνούς Συνεδρίου, Χανιά, Σεπτ. 2013

Bulletin of the Geological Society of Greece, vol. XLVII 2013
Proceedings of the 13th International Congress, Chania, Sept. 2013

SUITABILITY ASSESSMENT OF CARBONATE ROCKS FROM THE KATARAKTIS PASSAGE MEMBER OF THE OLONOS – PINDOS ZONE (ILEIA PREFECTURE, WESTERN GREECE) FOR INDUSTRIAL APPLICATIONS

Tseni X.[1], Tsikouras B.[1,2] and Hatzipanagiotou K.[1]

[1]*University of Patras, Department of Geology, Section of Earth Materials, 265 00 Patras, Greece, tseni@upatras.gr, v.tsikouras@upatras.gr, k.hatzipanagiotou@upatras.gr*
[2]*University of Brunei Darussalam, Department of Petroleum Geosciences, Jalan Tungku Link, Gadong BE1410, Bandar Seri Begawan, Brunei Darussalam*

Abstract

The potential industrial uses of Maastrictian-Paleocene carbonate rocks from the Kataraktis Passage Member of Olonos-Pindos Zone from Ileia Prefecture are evaluated based on their petrographic and geochemical characteristics, as well as their physical properties. Moreover, inter-relationships of the physical properties and geochemical composition were detrmined using simple linear regression analysis, in order to establish their mutual interactions. Investigation of the petrographic and geochemical characteristics of carbonate rocks may contribute to their quality assessment for their use in industrial applications.
Key Words: *Limestone, Physical properties, Peloponnesus.*

Περίληψη

Στην εργασία αυτή εκτιμώνται οι πιθανές βιομηχανικές χρήσεις των ανθρακικών πετρωμάτων των Στρωμάτων Μετάβασης του Καταρράκτη, ηλικίας Μαιστρίχτιου-Παλαιόκαινου, της ζώνης Πίνδου του Ν. Ηλείας, με βάση τα πετρογραφικά και γεωχημικά τους χαρακτηριστικά καθώς και τις φυσικές τους ιδιότητες. Επιπλέον καθορίστηκαν οι αμοιβαίες σχέσεις των φυσικών ιδιοτήτων και της γεωχημικής σύστασης με τη χρήση γραμμικής ανάλυσης παλινδρόμησης με σκοπό να καθοριστούν και οι αλληλεπιδράσεις των ιδιοτήτων αυτών. Η διερεύνηση των πετρογραφικών και γεωχημικών χαρακτηριστικών των ανθρακικών πετρωμάτων μπορεί να συμβάλλει σημαντικά στην εκτίμηση της ποιότητας τους για χρήση τους σε βιομηχανικές εφαρμογές.
Λέξεις Κλειδιά : *Ασβεστόλιθοι, Φυσικές ιδιότητες, Πελοπόννησος.*

1. Introduction

Limestones are industrial rocks mainly used as construction, concrete and road aggregates, as well as dimension stones and fillers. Ground limestone is widely used to raise the pH of acid soils and as additive in fertilizers. Large amounts of limestone are used in blast furnaces as slag conditioners and in the steel production to form slag. Physical and geotechnical properties of Cretaceous and Maastrictian-Paleocene limestones from different localities have been studied by several authors (Spyropoulos, 2007; Sabatakakis *et al.*, 2008; Mpalatsas *et al.*, 2010; Koulouris, 2011; Tseni *et al.*,

2012). Mineral and geochemical composition, grain size microstructure, grain packing and porosity are the most important parameters that influence their petrophysical properties.

This paper aims at investigating the physical properties of Maastrictian-Paleocene carbonate samples from the Pindos Zone of Ileia Prefecture, in order to establish their inter-relationships, to study the relationships of physical properties with their petrographic and diagenetic characteristics and to evaluate their suitability as industrial rocks in various applications.

2. Geological Setting

The geological setting of the Ileia Prefecture, west Peloponnesus, is characterized by the presence of the Ionian, the Gavrovo-Tripolitza and the Olonos-Pindos geotectonic Zones. The sedimentary rocks of the Pindos Zone (Figure 1) originate from an elongated, remnant ocean basin that formed during mid-Triassic, consisting typically of deep-water carbonate, siliciclastic and siliceous rocks, ranging in age from Late Triassic to Eocene, covered by thick detrital, late Paleocene to Oligocene flysch sediments (Fleury, 1980; Robertson *et al.*, 1991; Robertson, 1994; Degnan and Robertson, 1998, 2006).

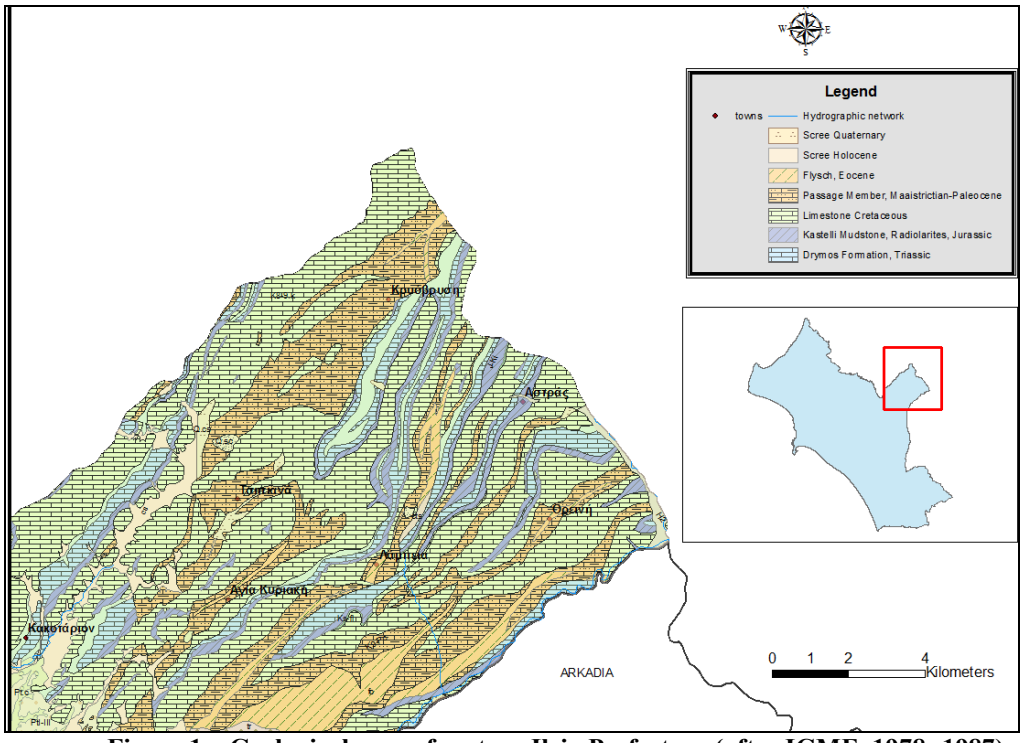

Figure 1 – Geological map of eastern Ileia Prefecture (after IGME, 1978; 1987).

The lower stratigraphic unit in the Pindos Zone is the Priolithos formation of Karnian age comprising medium-grained sandstone with mudstone intercalations (Figure 2). Overlying to the Priolithos formation is the Drimos formation composed of turbiditic and hemipelagic limestone. The Lestenna formation overlies the Drimos formation comprising, from bottom to top, the Kastelli mudstone member, mainly composed of multicolored mudstone, the Aroania member, consisting of Jurassic radiolarites and the first flysch, which includes pelites, limestone, sandstone and red mudstone. Subsequently, Lower Cretaceous to Maastrichtian, redeposited limestone and pelagic limestone were formed. The Kataraktis Passage member of Maastrichtian to Paleocene age overlies this formation, comprising the transition from carbonate to detrital sedimentation. It is

preserved as thrust imbricated slices (Degnan and Robertson, 1998) and includes pure limestone deposition at its base, comprising the investigated rocks, with increasing clastic input towards the top. The increased input of terrigenous clastic sediments to the basin during Late Cretaceous-Paleocene suggests that relative sea-level fell because of the erosion to the continental basement to the west and north. The member is dated as Maastrichtian-Paleocene and is marked by the disappearance of *Globotruncana sp.* and *Globorotalia sp.* (Degnan, 1998). Finally, the Late Palaeocene-Early Eocene Pindos flysch lies at the top of the pile, likely extending also to Mid-Eocene age in the SE Peloponnesus (Piper, 2006).

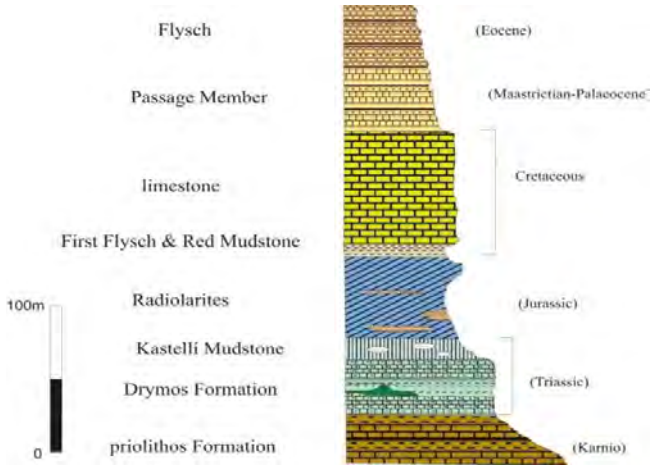

Figure 2 – Simplified stratigraphic section of the Pindos zone at Ileia Prefecture.

3. Analytical Methods

Determination of physical properties of the limestones was conducted in the Research Laboratory of Minerals and Rocks, Department of Geology, University of Patras. The insoluble residue was determined after digestion in 25 vol.% acetic acid (Hirst and Nicholls, 1958). The organic carbon content was determined with titration according to Walkley and Black (1934).

A Hunter color measuring system (Hunter Color Diff. Meter, Miniscan XE plus, Hunter Associates Laboratory Inc., Reston, VA) was used to measure the color. Individual corms were cut transversely and each sample was measured twice for color values. The information given by L*, a*, and b* is generally expressed as the total color, with L* representing the brightness or dullness, a* for redness to greenness, and b* for yellowness to blueness. The color properties of the carbonate powder were measured according to the CIELAB system using a Diffusion Systems. The source UV content is nominal match to D65 with port diameters 45/0.

The physical properties investigated included moisture content (ASTM D2216), water absorption (ASTM C97-47), bulk specific gravity (AASHTO TIOO-T85) and apparent specific gravity (AASHTO T147). Three tests were performed for each property and the mean values were recorded. Porosity values (n %) were calculated on rock powders using a pycnometer, according to the ISRM (1981) specification. The total volume of pores is calculated as the difference between the volume of the specimen and that of the powdered particles. Whole rock chemical analyses were performed at Activation Laboratories LTD, Ancaster, Ontario, by fusion ICP-OES for major elements and combined ICP-MS and INAA for trace elements. Detection limit for major elements is 0.01%, except for TiO_2 which is 0.005%. Replicate analyses suggest precision better than 5% for major elements and most trace elements. The determination of CO_2 was carried out by coulometry.

4. Results

4.1. Petrographic Characteristics

Petrographic study was perfomed on twenty thin sections, which were classified according to the schemes of Dunham (1962) and Folk (1959, 1962). Allochems are represented by fossil remains, intraclasts and lithoclasts.

Mudstones with bioclasts or *fossiliferous micrites* contain micritic calcite with few skeletal grains (5-15%) represented principally by pelagic foraminifera. *Wackestones* with pelagic foraminifers or *packed biomicrites* are also composed predominately of micritic matrix that supports packed distributed bioclasts (Figure 3a). The petrographic investigation reveals different types of porosity (after Choquette and Pray, 1970; Scholle and Ulmer-Scholle, 2003), which are represented by vug and intraparticle porosity (Figure 3b) along with irregular microchannels of stylolites, which are often associated with insoluble residue (mainly clay minerals), accumulated as a consequence of pressure-induced dissolution. Laminated *wackestone-packstone* include pelagic foraminifera, ranging in size from 50-250μm. The lamination comprises skeletal grains such as pelagic foraminifera (Figure 3c) and bioclast in size of fine sand and some lithoclast such as detrital grains of quartz, chlorite and muscovite (Figure 3c, d). Calcite veins and stylolites occur, too.

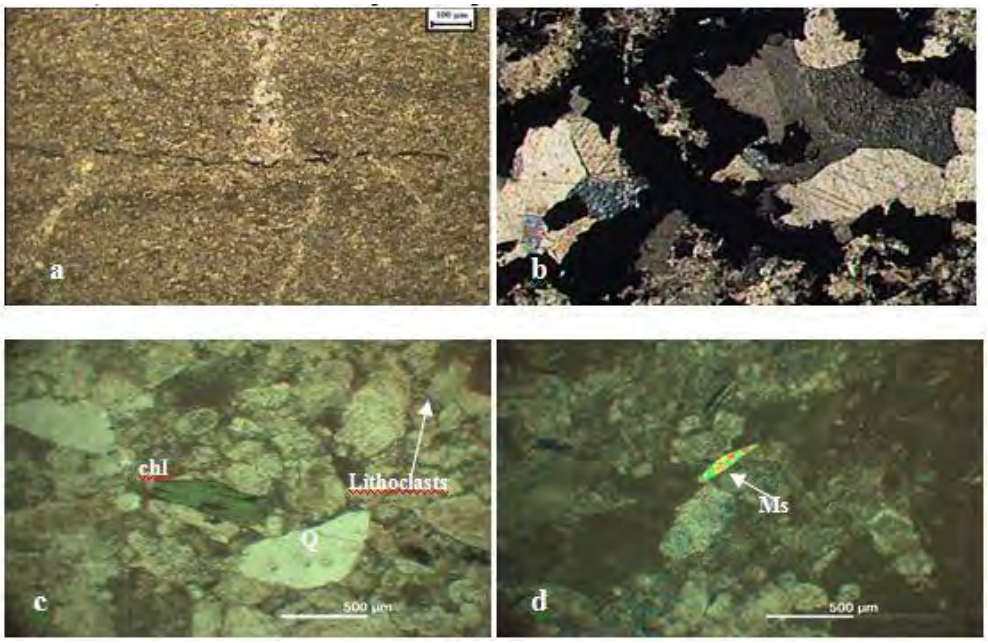

Figure 3 – Photomicrographs of representative carbonate samples from the Kataraktis Passage Member: (a) wackestone with packed bioclasts; calcite veins and a stylolite filled with clay minerals are also present (sample DHL7G, plane polarized light); (b) vug porosity filled with sparry calcite (sample DHL7A, crossed polarized light); (c, d) laminated wackestone-packstone with pelagic foraminifers and detrital grains of quartz (Q) and chlorite (chl) and muscovite (Ms) (sample DHL16B, crossed polarized light).

4.2. Physical Properties

The results of physical and physicochemical properties of the studied samples were determined from the mean values of three measurements and are listed in Table 1. Moisture contents of the Maastrictian-Paleocene carbonates are rather low (0.06-0.07%), whereas their water absorption values range between 0.05-0.57. These values are lower than the underlying Cretaceous limestone from the Pindos Zone in the Ileia Prefecture (Tseni *et al.*, 2012). Density is one of the most

Table 1 – Mean values, range and standard deviation (sd) of physical and physicochemical properties of the Maastrictian-Paleocene carbonate samples from the Ileia Prefecture.

Sample	**DHL7A**			**DHL7G**			**DHL16A**			**DHL16B**			**PK1A**		
Rock-type (after Dunham, 1962)	Wackestone			wackestone			laminated wackestone-packstone			laminated wackestone-packstone			wackestone		
	mean	*range*	*sd*	*mean*	*range*	*sd*	*mean*	*range*	*sd*	*mean*	*range*	*sd*	*mean*	*range*	*sd*
moisture content (%), n=3	0.07	0.06-0.09	0.015	0.06	0.05-0.07	0.010	0.070	0.06-0.09	0.016	0.060	0.489-0.493	0.002	0.070	0.065-0.074	0.005
water absorption (%), n=3	0.25	0.23-0.27	0.021	0.050	0.03-0.09	0.031	0.570	0.47-0.65	0.096	0.490	0.45-0.53	0.040	0.160	0.14-0.185	0.023
void ratio (%)	1.11	1.08-1.15	0.035	1.100	1.09-1.13	0.021	2.330	2.24-2.42	0.091	2.350	2.34-2.41	0.038	1.870	1.78-1.94	0.080
Apparent specific gravity (g/cm^3), n=3	2.70	2.69-2.72	0.015	2.730	2.69-2.77	0.042	2.580	2.54-2.65	0.059	2.550	2.51-2.63	0.064	2.680	2.65-2.72	0.035
bulk specific gravity (g/cm^3), n=3	2.73	2.73-2.76	0.015	2.760	2.73-2.78	0.025	2.640	2.61-2.66	0.026	2.610	2.59-2.65	0.035	2.730	2.69-2.77	0.040
total porosity (%)	0.53	0.5-0.58	0.040	0.520	0.49-0.55	0.031	0.700	0.703-0.706	0.002	0.700	0.61-0.79	0.090	0.650	2.68-2.76	0.042
L	92.42	92.33-92.55	0.111	90.100	89.65-90.25	0.317	89.460	89.458-89.463	0.003	78.160	77.23-79.52	1.165	94.980	94.33-95.35	0.572
a*	0.35	0.31-0.38	0.035	0.300	0.24-0.35	0.056	0.350	0.347-0.351	0.002	1.410	1.33-1.47	0.071	0.400	0.38-0.44	0.032
b*	3.54	3.51-3.56	0.025	6.260	6.15-6.34	0.097	5.690	5.688-5.692	0.002	5.080	4.85-5.39	0.279	3.970	3.97-3.985	0.010
insoluble residue (%)	0.05	0.03-0.09	0.031	0.010	0.08-0.12	0.025	2.010	2.007-2.012	0.003	3.260	3.16-3.97	0.407	0.010	0.07-0.11	0.020
TOC (%), n=3	0.08	0.04- 0 11	0.035	0.080	0.06-0.11	0.026	0.200	0.199-0.202	0.002	0.250	0.21-0.29	0.040	0.040	0.038-0.046	0.004

XLVII, 3, 2063 - 2063

important properties of rocks, mainly controlled by their texture and mineral composition. The bulk density depends on petrographic and structural features of the diagenetic processes and geotectonic conditions (Trafimov and Karalov, 1993; Rashed and Sediek, 1997). Bulk specific gravity ranges from 2.61 to 2.76 g/cm^3, in the investigated lithologies. Total porosity, which is an important factor in rock strength since a small change in pore volume can produce appreciable mechanical effect (ISRM, 1981), ranges between 0.52 and 0.70%. Laminated wackestone packstone samples of the formation have higher porosities. The total organic carbon is low ranging from 0.04 to 0.25%, while the insoluble residue shows a wider range of 0.05-3.26%. Samples DHL16A and DHL16B (laminated wackestone-packestone) with the highest total organic carbon and insoluble residue values are found towards upper members, unlike the rest samples that lie at the base of the Kataraktis Passage Member. Moisture content and bulk density are inversely correlated to the insoluble residue (Figure 4a, b), suggesting that clay minerals are not the prevalent water absorbents. The TOC is inversely correlated to the color index L with the following the empirical equation TOC = - 0.0122L + 1.2179 with a correlation coefficient R^2=0.75 (Figure 4c). From Figure 4d it is clear that the bulk density of the Kataraktis member limestones decreases with increasing porosity.

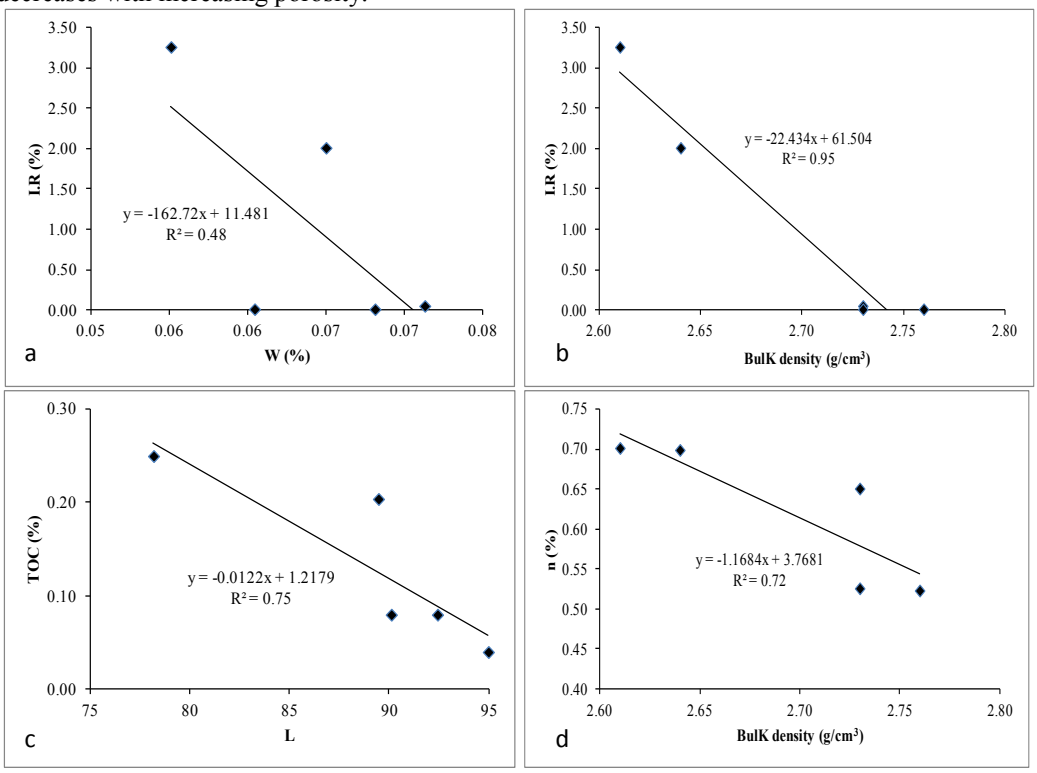

Figure 4 – Correlation diagrams of: a) moisture content (W) with insoluble residue (I.R.); b) bulk density with insoluble residue (I.R.); c) color index L with total organic carbon; d) bulk density with total porosity (n).

4.3. Geochemical Affinities

Whole-rock geochemical analyses from representative carbonate rocks are listed in Table 2. The CaO contents of the analyzed samples vary between 38.40 and 55.67 wt. %. According to the chemical classification based on $CaCO_3$ content (Oates, 1998), samples DHL7G and PK1A (wackestone with bioclasts) are calcium limestone of high purity ($CaCO_3$ = 97-98.5%) whereas samples DHL7A (mudstone with bioclasts) and DHL16A (laminated wackestone with bioclasts) are median purity limestones ($CaCO_3$=93.5-97.0%); sample DHL16B is a poor purity limestone

containing abundant siliciclastic material. The total amount of impurities (sum of all oxides excluding CaO and CO_2) for the four samples except DHL16B, is rather low to moderate (Table 2). The concentrations of MgO, Fe_2O_3, MnO and Na_2O are low in the analyzed samples. The low concentration of phosphorus reflects the absence of apatite in the samples (Parekh *et al.*, 1977;

Table 2 – Whole-rock geochemical analyses of representative samples of Cretaceous and Maastrictian-Paleocene limestones from Ileia Perfecture ($Fe_2O_3^t$: total Fe as Fe_2O_3; -: below detection limit).

Sample	**DHL7A**	**DHL7C**	**DHL16A**	**DHL16B**	**PK1A**
Major elements (wt. %)					
SiO_2	1.93	1.73	1.43	20.32	0.92
Al_2O_3	0.32	0.21	0.33	2.95	0.18
$Fe_2O_3^t$	0.23	0.19	0.25	1.10	0.15
MnO	0.05	0.05	0.13	0.10	0.04
MgO	0.37	0.42	0.64	1.02	0.31
CaO	54.64	55.09	54.17	38.40	55.67
Na_2O	0.08	0.06	0.22	0.73	0.03
K_2O	0.13	0.07	0.08	0.47	0.06
TiO_2	0.01	0.01	0.01	0.19	0.00
P_2O_5	0.01	0.01	0.09	0.06	0.02
LOI	43.20	43.13	42.74	34.72	43.14
Total	101.00	101.00	100.10	100.10	100.50
$CaCO_3$	96.87	97.25	96.81	73.05	98.32
Trace elements (ppm)					
Ag	0.7	-	-	-	0.6
As	-	-	-	2	-
Ba	12	7	-	495	6
Co	6	4	9	19	4
Cr	5	5	12	124	3
Cs	-	-	-	0.7	-
Cu	13	6	6	7	4
Hf	-	-	-	1.5	-
Ni	7	2	9	40	3
Pb	-	-	9	10	-
S	110	150	590	1010	90
Sb	-	-	-	0.2	-
Sc	0.4	0.4	0.6	2.9	0.4
Sr	600	508	513	372	671
Th	-	-	-	1.3	-
U	-	-	1.2	1.2	-
V	-	-	12	23	-
W	10	21	88	186	25
Y	5	4	11	10	2
Zn	4	5	5	20	4
Zr	21	12	4	62	15

Cullers, 2002). Chemical analyses for the amount of trace elements show that only one sample (DHL16B) present higher concentrations of Cr and Ni compared to the other samples. Sulfur content is fairly coherent displaying inconsiderable variations between 90 and 150 ppm (apart from sample DHL16A with S = 1010 ppm). Sr was detected in all samples, however the amount of Sr in the wackestone with bioclast (PK1A) is higher than the rest samples. Sr is easily mobilized during weathering, especially in oxidizing, acid environments, thus it is incorporated in clay minerals (Kabata-Pendias 2011). Sample DHL16B displays high Ba contents. Ba is also strongly adsorbed by clay minerals and it commonly substitutes for K in feldspars (Kabata-Pendias 2011). Sample DHL7A demonstrates the highest Cu values compared to the remaining samples

5. Discussion-Conclusions

The Maastrictian-Paleocene carbonate rocks of the Kataraktis Passage Member are divided into 3 microfacies: (i) mudstones with bioclast, (ii) wackestones with bioclast, and (iii) laminated wackestone-packstone. The color index L is negatively correlated with TOC, suggesting that increasing organic components in carbonate rocks have a negative affection on their whiteness, high values of which are commonly desirable in most applications. Organic matter, in carbonate rocks, may shows variable compositions and amounts and may affect their properties. A considerable amount of some impurities may be acceptable in carbonate rocks for some uses, if they are finely disseminated throughout the rocks. On the other hand, if the impurities are concentrated in distinct laminas, they may form planes of weakness that seriously affect the performance of the rocks (Boynton, 1980; Harben, 1992; Carr *et al.*, 1994; Oates, 1998; Christidis *et al.*, 2004).

The $CaCO_3$ content in all analyzed samples exceeds 96.5%, except sample DHL16B with $CaCO_3$ = 76% (Table 2). The high SiO_2 and Al_2O_3 contents in sample DHL16B are consistent with the presence of quartz and clay minerals in its insoluble residue. Ba content is low in all samples, except DHL16B with rather high Ba contents (Table 2), likely related to its significant amounts of clay minerals (Kabata-Pendias 2011).

The $CaCO_3$ content in the Maastrictian-Paleocene carbonates from the Kataraktis Passage Member exceeds the limit of 65%. Furthermore their MgO content is small indicating that these carbonate rocks could be suitable as calciferous raw material for cement production. Also, the insoluble residue, the total organic carbon and the color index, which affect the rock properties, suggest that all samples are suitable for cement production, apart from and the laminated wackestone-packstone of the Maastrictian-Paleocene limestone (sample DHL16B).

All the studied limestones are suitable as pH regulators in acid soils as well as additives in fertilizers since $CaCO_3$ content exceeds 60% and their MgO contents are below 5%. Finally all examined samples (except the laminated wackestone-packstone sample DHL16B) are suitable for desulphurization of exhaust gases since their $CaCO_3$ contents exceed 95% while their concentrations in Al_2O_3 (< 1%), SiO_2 (<2%) and MgO (<2%) are low.

From this study, it is evident that petrographic investigation coupled with mineralogical and geochemical analysis is useful for preliminary assessment of limestones' quality.

6. Acknowledgments

The senior author wishes to thank the Greek State Scholarship Foundation (I.K.Y.) for the financial support of this study. Critical review by an anonymous reviewer is gratefully appreciated.

7. References

AASHATO T147. The Field Determination of Density of Soil In-Place (1954-70).
AASHATO TT85. Specific gravity and absorption of coarse aggregates.

AMERICAN SOCIETY FOR TESTING AND MATERIALS C97-47. Standard Test methods for Laboratory determination of water absorption.

AMERICAN SOCIETY FOR TESTING AND MATERIALS D2216-10. Standard Test Methods for Laboratory Determination of Water (Moisture) Content of Soil and Rock by Mass.

Boynton S.R. 1980. *Chemistry and Technology of Limestone*, 2nd edition, New York, Wiley & Sons, 577 pp.

Carr D.D. Rooney L.F. and Freas R.C. 1994. Limestone and dolostone, in: Carr, D.D. (eds), Industrial minerals and rocks*: Society for Mining, Metallurgy and Exploration, Littleton, Colorado, 6th Edition,* 605-629.

Choquette P.W. and Pray L.C. 1970. Geological nomenclature and classification of porosity in sedimentary carbonates, *Bulletin American Association of Petroleum Geologists 54*, 207-250.

Christidis G.E., Sakellariou N., Repouskou E. and Markopoulos Th. 2004. Influence of organic matter and iron oxides of the color properties of a micritic limestone from Kefalonia, *Bull. Geol. Soc. Greece,* 72-79.

Cullers R.L. 2002. Implications of elemental concentrations for provenance, redox conditions and metamorphic studies of shales and limestones near, *Chemical Geology 191*, 305-327.

Degnan P.J. and Robertson A.H.F. 1998. Mesozoic-early Tertiary passive margin evolution of the Pindos ocean (NW Peloponnese, Greece), *Sedimentary Geology 117*, 33-70.

Degnan P. J. and Robertson A.H.F. 2006. Synthesis of the tectonic-sedimentary evolution of the Mesozoic-Early Cenozoic Pindos ocean: Evidence from the NW Peloponnese, Greece., in: Robertson, A.H.F., Mountrakis, D., eds.,Tectonic development of the Eastern Mediterranean region, *Geological Society London, Special Publications 260*, 467-491.

Dunham R.J. 1962. Classification of carbonate rocks according to their depositional texture. In: Ham, W. E., eds., Classification of carbonate rocks: *American Association of Petroleum Geologists Memoir 1*, 108-121.

Fleury J.J. 1980. Les zones de Gavrovo-Tripolitza et du Pinde-Olonos (Grèce Continental), et Péloponesse du Nord. Evolution d'une plate-forme et d'un bassin dans leur cadre Alpin. *Societé de la Géologie de Nord, Lille Publication* 4, 1–651.

Folk R.L. 1959. Practical petrographic classification of limestones, *Bulletin of American Association of Petroleum Geologists 43*, 1-38.

Folk R.L. 1962. Spectral subdivision of limestone types. In: Ham, W. E., eds, Classification of carbonate rocks: *American Association of Petroleum Geologists Memoir 1*, 62-84.

Harben P.W. 1992. The industrial minerals handybook - A Guide to Markets, Specifications, and Prices, Industrial Minerals Division, *Metal Bulletin PLC*, United Kingdom 148p.

Hirst D.M. and Nicholls G.D.1958. Techniques in sediment geochemistry-I. Separation of the detrital and non-detrital fractions of limestones. *Journal of Sedimentary Petrology 28*, 461-481.

IGME. 1979. Geological map of Greece, Kertezi sheet, Institute of Geological and Mineral Exploration, Athens

IGME. 1987. Geological map of Greece, Kertezi sheet, Institute of Geological and Mineral Exploration, Athens

ISRM 1981. Rock characterization, testing and monitoring, in: Brown E.T. (eds), ISRM Suggested Methods: International Society for Rock Mechanics, *Pergamon Press, London* 211p

Kabata-Pendias A., 2011. Trace elements in soils and plants, 4th edition. CRS Press, New York.

Koulouris S., 2011. Strength parameters and rock mechanics of hard soils - soft rocks, Sector of Applied Geology & Geophysics. *Ph.D Thesis*, University of Patras, Patras 512 p.

Mpalatsas I., Rigopoulos I., Tsikouras B. and Hatzipanagiotou K. 2010. Suitability assessment of cretaceous limestones from Thermo (Aitolokarnania, western Greece) for their use as base and sub-base aggregates. *Bulletin of the Geological Society of Greece*, *Proceedings of the 12th International Congress Patras*, 2010, pp. 2501-2509.

Oates, J.A.H., 1998. Lime and limestone. Chemistry and technology, production and uses, Wiley-VCH Weinheim, 455 pp.

Parekh P.P., Moler P., Dulski P. and Basch W.M.1977. Distribution of trace elements between carbonate and non carbonate phases of limestone, *Earth and Planetary Science Letters 34*, 39-50.

Piper D.J.W. 2006. Sedimentology and tectonic setting of the Pindos Flysch of the Peloponnese, Greece, in: Robertson, A.H.F., Mountrakis, D., eds., Tectonic Development of the Eastern Mediterranean Region: *Geological Society, London, Special Publications 260*, 493-505.

Robertson A.H.F. 1994. Role of the tectonic facies concept in orogenic analysis and its application to Tethys in the Eastern Mediterranean region, *Earth-Science Reviews 37*, 139-213.

Robertson A.H.F., Clift P.D., Degnan P.J. and Jones G. 1991. Palaeographic and palaeotectonic evolution of the eastern Mediterranean Neotethys, *Palaeogeography, Palaeoclimatology, Palaeoecology 87*, 289-343.

Rashed M A. and Sediek K. 1997. Petrography, diagenesis and geotechnical properties of the El-Rufuf formation (Thebes Group), El-Kharga Oasis, Egypt, *Journal of African Earth Sciences, 25,*-407–423.

Sabatakakis N., Koukis G., Tsiambaos G. and Papanakli S. 2008. Index properties and strength variation controlled by microstructure for sedimentary rocks*, Engineering Geology, 97*, 80–90.

Scholle P.A. and Ulmer-Scholle Dana S. 2003. A color Guide to the Petrography of Carbonate Rocks: Grains, textures, porosity, diagenesis. AAPG Memoir No. 77, AAPG Publications, Tulsa, OK, 459pp

Spyropoulos A. 2007. Research of the engineering geological conditions of Achaia prefecture in order to find materials suitable for aggregates, Sector of Applied Geology & Geophysics, *Ph.D Thesis*, University of Patras, Patras 512 p.

Trafimov V.T. and Karalov B.A. 1993. Practical Soil Sciences in Russian, Moscow State University Publisher, Moscow, 390 pp.

Tseni X., Koutsopoulou E., Tsikouras B. and Hatzipanagiotou K. 2012. Investigation of the mineralogical petrographic, geochemical and physical properties from Ileia Prefecture and assesmnet for industrial applications, *Bull. Geol. Soc. Greece, XXXXVI*, 105-104

Walkley A. and Black I.A. 1934. An examination of the Degtjareff method for determining organic carbon in soils: Effect of variations in digestion conditions and of inorganic soil constituents, *Soil Science 63*, 251-263.

Δελτίο της Ελληνικής Γεωλογικής Εταιρίας, τομ. XLVII , 2013
Πρακτικά 13ου Διεθνούς Συνεδρίου, Χανιά, Σεπτ. 2013

Bulletin of the Geological Society of Greece, vol. XLVII 2013
Proceedings of the 13th International Congress, Chania, Sept. 2013

CORRELATIONS BETWEEN MECHANICAL AND GEOMETRICAL PARAMETERS IN AGGREGATES: A TOOL FOR QUALITY ASSESSMENT AND CONTROL

Xirouchakis D.

GeoTerra Ltd, Geomechanics & Quality Control Laboratory, 12 Anthrakorichon Street, 142 35 Nea Ionia, dxirouch@gmail.com

Abstract

Correlations between mechanical and geometrical parameters in aggregates can be used as quality and performance prediction tools. I evaluated the following paramet er pairs: dry and wet resistance to wear (MD_E & MD_S), and resistance to fragmenta tion (LA); polishing resistance and abrasion (PSV–AAV); and flakiness and shape in dex (FI–SI). The data set comprises slags, sedimentary, igneous, and metamorphic r ocks tested according to EN standard test methods. FI and SI are positively correlat ed (r = 0.83) and can be well described by the 1:1 line. Wet and dry resistance to we ar are strongly correlated (r = 0.98) with $MD_E \approx 2 \cdot MD_S$. Dry resistance to fragment ation (LA) and wet resistance to wear (MD_E) are well correlated (r = 0.81), and can be described with the equation $LA = 4.95 \times MD_E^{0,61}$ ($R^2 = 0.69$). According to the PS V–AAV correlation, aggregates are divided into two groups with contrasting behavi or. Limestones and slags (r = −0.49 to −0.69) exhibit high polishing for high abrasi on resistance (high PSV–low AAV), whereas sandstones and mafic to intermediate v olcanics (r = 0.44 to 0.39) exhibit high polishing for low abrasion resistance (high PSV–high AAV). Peridotites belong to either PSV–AAV group depending on the soft minerals.

Key words: *aggregates, shape, wear, polishing, abrasion.*

Περίληψη

Η συσχέτιση των μηχανικών και γεωμετρικών χαρακτηριστικών των αδρανών μπορεί να χρησιμοποιηθεί ως εργαλείο ελέγχου και πρόβλεψης. Εξετάστηκαν τα ακόλουθα ζεύγη: υγρή & ξηρή αντοχή σε φθορά (MD_E & MD_S) και αντίσταση σε θρυμματισμό (LA), δείκτης στίλβωσης (PSV) και απότριψης (AAV) και ο δείκτης πλακοειδούς (FI) και μορφής (SI). Οι δοκιμές έγιναν σύμφωνα με τα ευρωπαικά πρότυπα και αφορούν σκωρίες, ιζηματογενή, πυριγενή και μεταμορφωμένα πετρώματα.. Η συσχέτιση FI & S I είναι θετική (r = 0,83) και γραμμική (1:1). Η συσχέτιση υγρού και ξηρού MD είναι υ ψηλή (r = 0,98) με $MD_E \approx 2 \bullet MD_S$. Η αντίσταση σε θρυμματισμό (LA) και υγρή αντοχή σε φθορά (MD_E) συσχετίζονται θετικά (r = 0,81) και περιγράφονται με την εξίσωση $LA = 4,95 \times MD_E^{0,61}$ ($R^2 = 0,69$). Η συσχέτιση μεταξύ PSV & AAV διακρίνει τα αδρανή σε δύο ομάδες με αντίθετη συμπεριφορά. Ασβεστόλιθοι και σκωρίες(r = −0,49 & −0,69) παρουσιάζουν υψηλή αντίσταση σε στίλβωση με υψηλή αντίσταση σε απότριψη (υψηλό PSV–χαμηλό AAV), ενώ ψαμμίτες και βασικά έως ενδιάμεσα ηφαιστειακά (r = 0,44 & 0,39) παρουσιάζουν υψηλή αντίσταση σε στίλβωση με χαμηλή αντίσταση σε απότριψη (υψηλό PSV–υψηλό AAV). Ανάλογα με

την περιεκτικότητα σε μαλακά ορυκτά, οι περιδοτίτες κατατάσσονται στην μία ή άλλη ομάδα.
Λέξεις κλειδιά: *αδρανή, σχήμα, φθορά, στίλβωση, απότριψη.*

1. Introduction

According to the European Aggregates Association, approximately 90% of all aggregates produced in EU are from quarries (49%) and pits (41%). The rest are recycled aggregates, and marine and manufactured aggregates. The aggregates sector is the largest amongst the nonenergy extractive industries, directly and indirectly employing 250,000 people and representing a turnover of around €20 billion. Aggregates are a granular material typically used in construction (concrete and asphalt plants, new construction, and repairs), and the most common natural aggregates of mineral origin are sand, gravel and crushed rock. Market demand dictates production quantity and quality. The latter strongly depends on materials properties and processing technology.

Producers of aggregates face more than one set of materials performance requirements (e.g., grading, particle shape, surface texture, durability, abrasion resistance). Therefore, aggregate testing is critical to evaluate production quality and anticipated performance. In this study, I concentrated on pairs of parameters. Specifically, I looked at the correlation between parameters for particle shape, resistance to wear and fragmentation under dry and wet conditions, and resistance to polishing and abrasion. The goal was to critically evaluate the apparent or suspected correlations between them, and their potential as a quality control and prediction tool. I have not attempted to correlate materials properties and processing technology because of lack of relevant data. Nonetheless, this something that industry has been exploring (e.g., Magerowski, 2000).

2. Materials and Methods

For self-consistency, only data from tests performed according to EN standard methods by GeoTerra personnel or reported by others were considered. The data set comprises slags, igneous, metamorphic, and sedimentary rocks. The GeoTerra data base includes coarse aggregates (4/31.5) from sites either sampled once or multiple times between 2007 and 2012. Sampling was commonly performed by the same quarry employee at each site according to EN 932-1, and the same pool of laboratory technicians has performed the testing. Part of the GeoTerra data base in Tables 1, 2, and 3 was previously reported as ranges and averages along with mineralogy data (Xirouchakis and Theodoropoulos, 2009; Xirouchakis and Manolakou, 2011). The sources for the rest of data, which are not included in the tables, are: Reis Ferreira et al. (2010) and Sofilić et al. (2007) for EAF slags; Prapidis et al. (2005) for Fe and Pb slags; Thompson et al. (2004) for EAF & BOF slags, sandstones, and mafic to intermediate crystalline volcanics (basalt–andesite, s.l.); Kalofotias et al. (2011) for limestones; Rigopoulos et al. (2006, 2008) and Pomonis et al. (2007) for mafic rocks; and Kossiari (2007), and Rigopoulos et al. (2012) for peridotites; and Lucieri et al. (2005) for limestones and mafic to intermediate crystalline volcanics (basalt–andesite, s.l.) from Tuscany, Italy.

Construction Materials Testing (CMT) laboratories rely on the Flakiness Index (FI) and Shape Index (SI) for evaluating particle shape. The FI (EN 933-3) and SI (EN 933-4) values represent mass percentages of flaky and elongate grains. Resistance to wear under wet and dry conditions is assessed by the Micro-Deval method (EN 1097-1) and expressed as MD_E and MD_S, respectively. Resistance to fragmentation (EN 1097-2) is performed under dry conditions and is reported as the LA value. The resistance of coarse aggregates to polishing and abrasion prior to use in road surfaces is assessed through the Polishing Stone and Abrasion method (EN 1097-8 & Appendix A). Test procedures as well as precision statements are given in the standard test methods. The relative expanded uncertainty %U (95% confidence level) for all non-GeoTerra data was estimated from the precision and accuracy statements in the standard test methods. For the GeoTerra data set, the

relative expanded uncertainty is 5.1%, 2.0%, 5.1%, 8.0%, 6.7%, 0.6%, and 5.7% for FI, SI, MD_E, MD_S, LA, PSV, and AAV, respectively. The relative expanded uncertainty is used to construct the error bars in Figures 1, 2, and 3. To evaluate data variability for sites that were sampled over a period of years, which applies to many cases in the GeoTerra data base, I opted to look at the ratio of single-year to multiple-year standard deviation ($s_{single\text{-}year}/s_{multiple\text{-}year}$) or average ($\mu_{single\text{-}year}/\mu_{multiple\text{-}year}$) as proxy for within-group to between-group variability. For low-variability data, the abovementioned ratios will be unity or close to unity. Considering that sampling and testing procedures are executed according to standard test methods and thus contribute little to variability, mineral and rock properties are the likely source for the data variability and correlations for same-source, low-variability data.

3. Results and Discussion

3.1. FI versus SI

Particle shape affects packing and mechanical stability of mixtures with and without binder as well as road surface properties (e.g., Janoo 1998; Janoo and Korhonen 1999; Naidu and Adisheshu 2011). Generally, a grain is classified as flaky if the width–thickness ratio is >2.0, elongated if the length–thickness ratio is >2.5, and cubic if the width–thickness ratio is <2.0 and the length–thickness ratio is <2.5.

According to the SI test, the grains are divided into cubical and noncubical, where the noncubical grains have a length–thickness ratio greater than 3, and SI represents the ratio of the mass of noncubical grains to the total mass of grains. FI distinguishes particles to flaky and nonflaky and is the ratio of the mass of flaky grains to the total mass of grains. Uthus et al. (2005) estimated that cubic and cubic rounded grains correspond to SI values of 0.083 and 0.056 and FI values of 10.99 and 8.08, whereas flaky and flaky rounded grains have SI values of 55.5 and 63.3 and FI values of 12.42 and 20.34, respectively. Hann (2009) experimentally determined the relation between SI and shape factor F, on the basis of which, it appears that spherical and cubical grains with F between 1 and 0.785 correspond to SI between 4 and 20.

The FI and SI values for EAF slags, limestones, and igneous rocks are listed in Table 1 and shown in Figure 1. Both indices are positively correlated regardless of rock type, site, or region with a correlation coefficient of 0.83. The average $s_{single\text{-}year}/s_{multiple\text{-}year}$ for FI and SI is 1.0 ± 0.1 and 0.9 ± 0.1, respectively. For comparison, the average $\mu_{single\text{-}year}/\mu_{multiple\text{-}year}$ for FI and SI is 1.0 ± 0.1 and 1.0 ± 0.1, correspondingly.

Table 1 - Flakiness Index (FI) and Shape Index (SI) for slags & volcanics.

FI	*SI*	*Comments*	*FI*	*SI*	*Comments*
4	5	*EAF slag*	4	3	*EAF slag*
5	6	"	5	8	"
7	8	"	4	4	"
10	9	"	4	2	"
6	7	"	5	3	"
5	7	"	5	3	"
7	8	"	6	3	"
4	4	"	3	5	"
2	1	"	2	3	"
5	4	"	5	2	*EAF slag*
3	7	"	4	1	"

FI	*SI*	*Comments*	*FI*	*SI*	*Comments*
3	4	"	1	2	"
6	6	"	6	9	*Trachyte*
4	5	"	5	9	"
2	2	"	11	10	"
3	5	"	9	9	"
3	2	"	7	7	"

Table 1 continued - Flakiness Index (FI) and Shape Index (SI) for limestone aggregates.

FI	*SI*	*FI*	*SI*	*FI*	*SI*	*FI*	*SI*
9	10	12	12	7	6	8	11
9	7	8	5	7	1	5	8
8	12	5	8	10	6	10	16
8	10	11	10	11	8	10	12
8	13	9	11	8	6	4	13
8	10	12	13	12	9	11	14
13	13	12	3	11	10	6	14
24	30	9	7	8	7	15	14
24	22	9	7	13	10	10	9
13	11	9	22	15	13	16	18
15	11	11	14	19	11	12	13
15	22	6	6	5	6	21	25
19	21	11	22	19	15	13	11
13	20	12	12	33	26	14	10
21	16	14	20	8	6	7	8
6	6	13	8	10	10	22	26
9	10	6	4	6	10	23	31
14	20	9	7	10	18	40	47
22	29	5	9	12	16	12	9
8	10	22	15	14	24	10	14
10	10	5	4	17	15	11	13

The data in Figure 1 can be equally well described by the 1:1 line or the equation FI = 1.01 × SI (R^2 = 0.63). The dashed line in Figure 1 represents the equation SI = 1.13 × FI + 1.04 that Péturrson et al. (2000) used to describe the FI and SI correlation in Icelandic basaltic aggregates. Bulevicius et al. (2011) reported strong correlation between FI and SI for dolomitic and granitic aggregates (r = 0.7) and fitted the data with the equation SI = 2.714 + 0.595 × FI (dot-dashed line in Figure 1). Xirouchakis and Theodoropoulos (2009) reported an *r* of 0.62 between FI and SI for limestone aggregates and little to weak positive correlation between FI and LA (r = 0.10), FI and MD_E (r = 0.09), SI and LA (r = 0.15), and SI and MD_E (r = 0.36). Bulevicius et al. (2011) found a positive, albeit strong, correlation between LA and FI (r = 0.64–0.73) and LA and SI (0.62–0.76).

In contrast, the data in Ioannou et al. (2010) suggest a moderate negative correlation between LA and FI (r = −0.55). However, this is opposite to what is intuitively expected and the data in Figure 1, which strongly suggest that hard materials will have low SIs and FIs and, therefore, higher mass percentages of nonflaky and cubical grains.

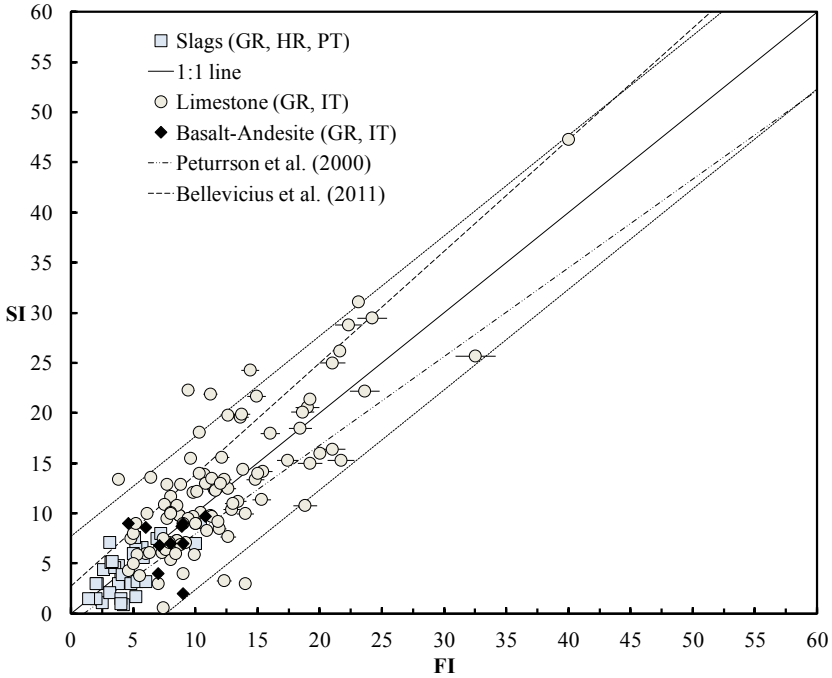

Figure 1 - FI vs SI values. GR: Greece; HR: Croatia; IT: Italy; and PT: Portugal. Dashed lines are 95% confidence limits for the 1:1 line.

3.2. MD_S versus MD_E and MD_E versus LA

Resistance to wear and fragmentation are used to evaluate materials suitability for construction and predict long-term performance; low MD_S, MD_E, and LA values typically characterize hard, mechanically strong materials. The data for resistance to wear under wet (MD_E) and dry conditions (MD_S), and resistance to fragmentation (LA) are given in Table 2. The MD_S data set is less comprehensive than the rest but nonetheless useful. MD_S and MD_E are, unsurprisingly, strongly correlated (r = 0.98) with MD_S approximately half the corresponding MD_E values regardless of rock type and d_i/D_i fraction. Clearly, water enhances sample attrition. The MD_E and LA data are listed in Table 2 and shown in Figure 2. Dry resistance to fragmentation (LA) and wet resistance to wear (MD_E) are positively correlated (r = 0.81). In the GeoTerra data set and for the same sampling sites, the $s_{single\text{-}year}/s_{multiple\text{-}year}$ ($\mu_{single\text{-}year}/\mu_{multiple\text{-}year}$) ratio for LA is 0.9 ± 0.1 (1.5 ± 0.2) and for MD_E is 0.8 ± 0.03 (1.0 ± 0.0).

Table 2 - Resistance to wear (MD) and fragmentation (LA).

d_i/D_i	MD_E	MD_S	LA	Comments	MD_E	LA	Comments
10/14	7		18	*EAF slag*	8	14	*Basalt–Andesite*
10/14	7	4	15	"	10	13	"
6.3/10	7	4	15	"	12	12	"
6.3/10	8		18	"	8	13	"

d_i/D_i	MD_E	MD_S	LA	*Comments*	MD_E	LA	*Comments*
11.2/16	7		16	"	8	12	"
6.3/10	8		21	"	12	13	"
10/14	8		19	"	31	61	*Phyllite–Quartzite*
11.2/16	8		15	"			
6.3/10	7		17	"			
11.2/16	7		16	"			
11.2/16	9		17	"			
8/11.2	8		15	"			
11.2/16	7		14	"			

Table 2 continued - Resistance to wear (MD_E) and fragmentation (LA) for limestones.

MD_E	LA	MD_E	LA	MD_E	LA
17	27	14	30	14	28
25	26	16	31	15	25
16	27	25	38	20	31
24	26	25	31	15	25
15	26	21	32	21	26
15	26	20	35	15	28
28	29	15	28	17	32
27	29	10	26	17	31
41	46	11	23	20	30
33	42	10	27	17	37
11	26	14	24	26	32
11	25	15	30	26	32
15	26	26	31	24	33
10	25	28	36	30	38
10	26	30	39	32	46
9	21	34	43	25	46
16	29	15	25	28	38
18	30	15	24	31	43
24	32	29	39	32	40
12	29	26	36		

Table 2 continued - Resistance to wear (MD) and fragmentation (LA) as a function of d_i/D_i.

d_i/D_i	MD_E	MD_S	LA	d_i/D_i	MD_E	LA	d_i/D_i	MD_E	LA
4/6.3	10	6	22	11.2/16	13	24	31.5/50	18	35
10/14	9		26	31.5/50	12	30	11.2/16	20	27

d_i/D_i	MD_E	MD_S	LA	d_i/D_i	MD_E	LA	d_i/D_i	MD_E	LA
8/11.2	11		26	31.5/50	16	36	11.2/16	16	26
11.2/16	28	12	31	10/14	22	35	11.2/16	21	26
6.3/10	30	16	34	8/11.2	17	26	11.2/16	24	21
11.2/16	30	14	35	8/11.2	17	32	10/14	16	29
11.2/16	30	15	35	11.2/16	15	24	10/14	16	30
11.2/16	31	14	38	11.2/16	17	25	10/14	16	26
10/14	32		38	31.5/50	19	31	31.5/50	13	33
11.2/16	35	17	40	31.5/50	14	27	31.5/50	15	33
11.2/16	32		42	31.5/50	16	26	31.5/50	16	36
10/14	29		44	8/11.2	22	30	31.5/50	17	34
10/14	31		38	4/6.3	19	31	31/5/50	18	35
31.5/50	26		40	11.2/16	22	34	11.2/16	18	26
31.5/50	22		45	11.2/16	17	29	11.2/16	20	28
31.5/50	24		42	8/11.2	22	32	31.5/50	17	38
31.5/50	27		44	8/11.2	20	30	31.5/50	14	37
6.3/10	15		17	31.5/50	18	33	31.5/50	15	38
11.2/16	15		28	31.5/50	15	28			
11.2/16	17		35	31.5/50	18	29			
11.2/16	20		28	31.5/50	18	30			

Dashed lines separate sampling sites. Test results at each site span a period of 3–4 years and represent limestone aggregates.

The LA–MD_E relation can be described with the equation $LA = 4.95 \times MD_E^{0.61}$ ($R^2 = 0.69$), which affords slightly better fitting than linear-type equations and better models the subtle nonlinearity in the LA–MD_E relation at low values for hard aggregates. The correlation of MD_E and LA to the d_i/D_i fraction is weak (MD_E–d_i/D_i, r = 0.18) to moderate (LA–d_i/D_i r = 0.40). Rigopoulos et al. (2006, 2008) and Pomonis et al. (2007) also found a positive correlation between MD_E and LA and used linear and nonlinear equations to model the LA–MD_E relation. However, the proposed equations fail to describe the full extent of the data and only reproduce part of them within the 95% envelope in Figure 2.

In general, there is neither much research in EU for the micro-Deval vs. LA correlation nor the limits associated with good long-term performance; probably because of the past lack of universal tests across EU. In contrast, Departments of Transportation (DOTs) and Research Centers (e.g., ICAR) in North America (CA & USA) have adapted faster, even to a new test such a wet micro-Deval. Despite the differences between the EN and ASTM, or CAS, standard test methods, MD_E and LA exhibit moderate to strong, positive correlation (r = 0.45–0.89, Cooley et al., 2002; r = 0.80, Cuelho et al., 2007; r = 0.89, Richardson, 2009). Cuelho et al. (2008), after reviewing the US literature, also concluded that aggregates with good long-term performance have ASTM LA less than 40 and ASTM MD_E less than 18. Despite the lack of similar research in Europe, using the limiting LA value of 30 for high-specification aggregates (Thompson et al. 2004) and the proposed equation, the corresponding limiting MD_E value is 20. The LA value of 30 and MD_E value of 20 encompass hard materials such as slags and mafic to intermediate crystalline volcanics.

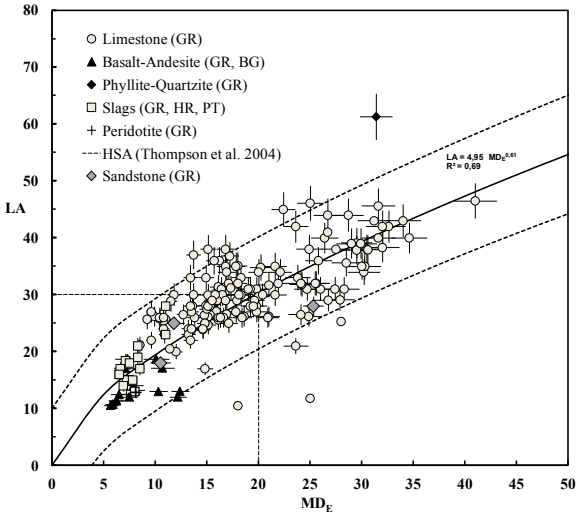

Figure 2 - MD_E vs. LA. BG: Bulgaria; GR: Greece; HR: Croatia; PT: Portugal; HSA: High-specification aggregates.

3.3. AAV versus PSV

Resistance to polishing is required for skid-resistant road surfaces. Aggregates with a rough micro texture, maintained by differential wear or continuous plucking, or by the presence of intergranular voids, have high resistance to polishing (high PSV). Abrasion resistance is also an important parameter that characterizes road-surfacing materials; it is affected by mineral hardness, grain size and orientation, and mineral weathering. The PSV and AAV data are listed in Table 3 and shown in Figure 3. The data were grouped according to material type and examined as such. The boundaries for high-specification aggregates (HSA, Thompson et al. 2004) are also given for comparison. The control stone (EN 1097-8) data in Table 3 (CS) are from the definitive study of West and Sibbick (1988) and the GeoTerra stock. Control stone is a fine- to medium-grained aphyric equigranular microgabbro, and the PSV and AAV are listed to aid the reader in the evaluation of the GeoTerra data reproducibility and bias.

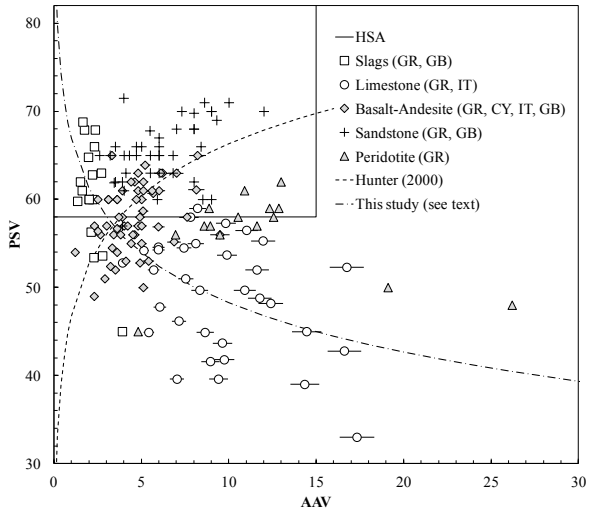

Figure 3 - AAV vs PSV. Aggregate sources are CY: Cyprus; GR: Greece; GB: Great Britain IT: Italy. HSA: High-specification aggregates.

Two groups of aggregates and correlations are apparent in Figure 3. First, aggregates with moderately negative correlation such as limestones (r = −0.49) and slags (r = −0.63). Within this group, subgroups may exhibit stronger negative correlation than as a group; for example, Greek limestones with r = −0.63 and Italian limestones with r = −0.68. The second group comprises aggregates with variably moderate positive correlation such as basalt–andesite (r = 0.39), sandstones (r = 0.44), and serpentine-poor peridotites (r = 0.79). The basalt–andesite group consists of crystalline rocks, and the sandstones are hard graywackes and gritstones. When serpentine-rich peridotites are included in the peridotites, the group as a whole exhibits weak negative correlation between PSV and AAV (r = −0.26). Rigopoulos et al. (2012) noted the decrease in PSV and increase in AAV with increasing content of serpentine in peridotite samples. The dashed line in Figure 3 represents the equation PSV = 8.5 × ln AAV + 46.8 (R^2 = 0.76) of Hunter (2000) for igneous rocks and sandstones that exhibit positive PSV–AAV correlation—the data in Hunter (2000) are not shown or included in the analysis. A similar trend is produced by the equation(s) of Thompson et al. (2004) for such aggregates. The antithetic equation PSV = -8.1 × ln AAV + 60.9 (R^2 = 0.56) (dot-dashed line in Figure 3) of this study is for aggregates with negative PSV–AAV correlation. Apparently, such aggregates may not rejuvenate during service as mafic–intermediate volcanics and sandstones may do—polishing by traffic during the dry months and restoration by weathering during the rainy months. Therefore, in such cases, aggregates with high PSV and low AAV need to be selected as they will resist polishing and abrasion, e.g., steel slags.

Table 3 - Polishing Stone (PS) and Aggregate Abrasion (AA) values.

PSV	***AAV***	***Comments***
67.9	2.35	*EAF slag*
64.8	1.96	″
56.3	2.11	″
53.4	2.27	″
53.6	2.77	″
59.8	1.34	″
62.8	2.19	*EAF slag*
67.9	1.73	″
68.8	1.64	″
49.7	8.3	*Limestone (GR)*
43.7	9.6	“
45.0	14.4	“
41.8	9.7	“
46.2	7.1	“
39.6	7.0	“
39.0	14.3	“
39.6	9.4	“
42.8	16.6	“
44.9	8.6	“
47.8	6.0	“
33.0	17.3	“
54.2	5.1	“
52.8	3.9	“
49.7	10.9	“
55.0	8.1	“
58.0	7.8	“
59.0	8.2	“
57.3	9.8	“

PSV	*AAV*	*Comments*
52.0	5.7	*Siliceous limestone (GR)*
54.3	6.0	"
53.7	9.9	*Limestone (CY)*
52	3.5	*CS (West & Sibbick, 1988)*
51	2.9	*CS (GeoTerra)*
63.9	5.2	*Trachyte (GR)*
60.0	5.0	*Gabbro (GR)*
57.0	2.3	*Basalt (GR)*
56.0	4.6	*Andesite (GR)*
52.8	4.9	*Basalt (CY)*
49.0	2.3	"
61.0	6.0	*Spillite (GR)*
57.0	3.0	"

CS: Control Stone. GR: Greece. CY: Cyprus. IT: Italy.

4. Conclusions

The FI–SI, MD_S–MD_E, MD_E–LA, and PSV–AAV correlations were evaluated considering a large number of samples and different rock types. The FI–SI correlation is strongly positive and is well described by the 1:1 line; furthermore, the data suggest that hard materials with low FI and SI will contain a larger number of cubical and nonflaky grains. Strong positive correlation is also seen between MD_S and MD_E, and MD_E and LA that can be well fitted with the equation $LA = 4.95 \times MD_E^{0.61}$ ($R^2 = 0.69$). As anticipated, hard aggregates have low MD and LA values. The PSV–AAV correlation divides aggregates into aggregates that exhibit high polishing for high abrasion resistance (high PSV–low AAV), such as limestone and slags, and into aggregates exhibiting high polishing for low abrasion resistance (high PSV–high AAV) that apparently characterizes sandstones and mafic–intermediate crystalline volcanics; peridotites belong to either PSV–AAV group depending on the content of low-hardness minerals.

5. Acknowledgments

I wish to thank the GeoTerra laboratory personnel for performing most of the tests reported here.

6. References

Bulevicius M., Petkevicius K., Cirba S., Zilioniene D., Oginskas R. and Bertuliene L. 2011. The influence of geometrical parameters on the strength of crushed stone used for the manufacture of asphalt mixtures, *Environmental Engineering, Proc. 8th International Conference*, 1051–1056.

CEN (European Committee for Standardization) 2012. *EN 933-3. Tests for geometrical properties of aggregates. Determination of particle shape. Flakiness index*. Brussels.

CEN (European Committee for Standardization) 2008. *EN 933-4. Tests for geometrical properties of aggregates. Determination of particle shape. Shape index*. Brussels.

CEN (European Committee for Standardization) 2011. *EN 1097-1. Tests for mechanical and physical properties of aggregates. Determination of the resistance to wear (micro-Deval)*. Brussels.

CEN (European Committee for Standardization) 2010. *EN 1097-2. Tests for mechanical and physical properties of aggregates. Methods for the determination of resistance to fragmentation*. Brussels.

CEN (European Committee for Standardization) 2009. *EN 1097-8. Tests for mechanical and physical properties of aggregates. Determination of the polished stone value*. Brussels.

Cooley A.L., Huner M.S. and James R.H. 2002. Micro-Deval testing of aggregates in the South-East. *National Center for Asphalt Technology*. Report 02-09.

Cuelho E., Mokwa R. and Obert K. 2007. Comparative Analysis of Coarse Surfacing Aggregate Using Micro-Deval, L.A. Abrasion and Sodium Sulfate Soundness Tests, *Report No. FHWA/MT-06-016/8117-27*.

Cuelho E., Mokwa R., Obert K. and Miller A. 2008. Comparative analysis of micro-Deval, L.A. abrasion, and sulfate soundness tests. *TRB 87th Annual Meeting: Conference Recordings*, Washington D.C.

Hann D. 2009. Applicability of two different methods for determining particle shape, *RMZ – Materials and Geoenvironment*, Vol. 56, No. 1, 88–96.

Hunter R.N. 2000. Assessing aggregates, in Hunter and Edgar eds., *Asphalts in Road Construction*. London, UK: Thomas Telford. 568 pp.

Ioannou I., Petrou M.F., Fournari R., Andreou A. Hadjigeorgiou C., Tsikouras B., and Hatzipanagiotou K. 2010. Crushed limestone as an aggregate in concrete production: the Cyprus case in Limestone, in Smith, B.J., Gomez-Hera, M., Viles, H.A., and Cassar, J., eds., *Limestone in the Built Environment: Present-Day Challenges for the Preservation of the Past: Geological Society, London, Special Publications, 331*, 127–135.

Janoo V.C. 1998. Quantification of Shape, Angularity, and Surface Texture of Base Course Materials, *US Army Corps of Engineers, Cold Regions Research & Engineering Laboratory*, Special Report 98-1, 29 pp.

Janoo V.C. and Korhonen C. 1999. Performance Testing of Hot-Mix Asphalt Aggregates, *US Army Corps of Engineers, Cold Regions Research & Engineering Laboratory*, Special Report 99-20, 29 pp.

Kosiari S. 2007. Study of Northern Evia's Ultramafic Rocks as Skid-resistant Aggregates in Pavement Construction, *Proc. 11th Congress Geol. Soc. Greece*, XXXVII, Athens.

Lancieri F., Losa M., and Marradi A. 2005. Resistance to polishing and mechanical properties of aggregates for asphalt concrete wearing courses. *Proc. 3rd International SIIV Congress*, Vol. 4, 162–178, Bari, Italy.

Magerowski A., 2000. Controlling Crushing Costs And Particle Shape. International Center for Aggregates Research (ICAR), *8th Annual Symposium Research Papers*, B1-1.

Naidu G. and Adisheshu P.S. 2011. Influence of Coarse Aggregate Shape Factors on Bituminous Mixtures. *International Journal of Engineering Research and Applications*, Vol. 1, Issue 4, 2013–2024

Péturrson P., Bjarnasson G., and Torfason H. 2000. Testing of the aggregate bank with two CEN methods, MD_E and FI. *BUSL Report E-38*, 17 pp.

Prapidis A., Doulis G. and Zotiadis V. 2005. Use of Slag in skid resistant asphalt mixes based on mechanical and environmental criteria, *HELECO 05*, Athens.

Pomonis P., Rigopoulos I., Tsikouras B. and Hatzipanagiotou K. 2007. Relationships between petrographic and physicomechanical properties of basic igneous rocks from the Pindos ophiolitic complex, NW Greece, *Proc. 11th Congress Geol. Soc. Greece*, XXXVII, Athens, 947–958.

Reis Ferreira S.M., Correia A.G., Rogue A. and Cavalheiro A.M. 2010. Mechanical and environmental behavior of granular materials. Application to National Steel Slag, *Semana de Engenharia*. Guimaraes.

Rigopoulos I., Pomonis P., Tsikouras B. and Hatzipanagiotou K. 2006. Comparative study of dolerites from Pindos and Vourinos ophiolites for use as aggregates, *Tech. Chron. Sci. J. TCG*, I, No 3.

Rigopoulos I., Pomonis P., Tsikouras B., Hatzipanagiotou K. and Stournaras K. 2008. A comparative study of the physicomechanical properties of mafic and ultramafic rocks from the Vourinos Ophiolite Complex (NW Greece), *1st Greek Conference on Structural Materials and Elements, TGG*. Athens

Rigopoulos I., Tsikouras B., Pomonis P. and. Hatzipanagiotou K. 2012. The impact of petrographic characteristics on the engineering properties of ultrabasic rocks from northern and

central Greece, *Quarterly Journal of Engineering Geology and Hydrogeology*, 45, 423–433.

Richardson D.N. 2009. Quick Test for Percent of Deleterious Material, *Missouri University of Science and Technology*. RI07-052, 169 pp.

Sofilić T., Rastovčan-Mioč A., Cosić M., Merle V., Mioč B. and Sofilić U. 2007. EAF steel slag application possibilities in Croatian Asphalt mixture production, *4th International Conference on Molten Slags and Fluxes*, Sendai, Japan, 481–486.

Thompson A., Burrows A., Flavin, D. and Walsh I. 2004. The Sustainable Use of High Specification Aggregates for Skid-Resistant Road Surfacing in England, *Report to the Office of the Deputy Prime Minister and the Mineral Industry Research Organization*. Published by Capita Symonds Ltd, East Grinstead.

Xirouchakis D. and Theodoropoulos A. 2009. Crushed limestone aggregates for concrete and masonry: Results from tests according to EN 12620, EN 13043, EN 13242, and EN 13139 standards, *Proc. 16th Concrete Conference*, Cyprus.

Xirouchakis D. and Manolakou V. 2011. Properties of an EAF slag produced in Greece, a construction material for sustainable growth, *Proc. 5th International Conference for Bituminous Mixtures and Pavements*. Thessaloniki, Greece.

Kalofotias A., Mavridou S. and Oikonomou N. 2011. Report on characteristics of natural aggregates, *EU-LIFE+ Environment Policy and Governance LIFE 09 ENV/ GR/304"ROADTIRE,"* "Integration of end-of-life tires in the life cycle of road construction," ROADTIRE, Deliverable 4.1.1.

Uthus L., Hoff I. and Horvli I. 2005. Evaluation of grain shape characterization methods for unbound aggregates, *Proc. 7th International Conference on the Bearing Capacity of Roads, Railways and Airfields*, Trondheim, Norway.

West G. and Sibbick R.G. 1988. Petrographical comparison of old and new control stones for the accelerated polishing test, *Quarterly Journal of Engineering Geology*, London, Vol. 21, 375–378.

Δελτίο της Ελληνικής Γεωλογικής Εταιρίας, τομ. XLVII , 2013
Πρακτικά 13ου Διεθνούς Συνεδρίου, Χανιά, Σεπτ. 2013

Bulletin of the Geological Society of Greece, vol. XLVII 2013
Proceedings of the 13th International Congress, Chania, Sept. 2013

GEOLOGICAL MATERIALS TESTING AND UNCERTAINTY CALCULATIONS: A SIMPLE GUM-BASED ALGORITHM

Xirouchakis D.[1] and Bouzinos A.[2]

[1] GeoTerra Ltd, Geomechanics & Quality Control Laboratory, 12 Anthrakorichon Street, 142 35 Nea Ionia, Athens, Greece, dxirouch@gmail.com

[2] Energy Resources Consulting Pty Ltd, 3/55 Clarence St PO Box 54 Coorparoo, Qld 4151 Australia, antonis.bouzinos@energyrc.com.au

Abstract

We have applied a simple GUM-based procedure to estimate the uncertainties of physical and mechanical properties in geological materials. First, we define the quantity to measure and decide whether we want to work with units or relative quantities. Subsequently, we calculate the repeatability standard deviation (s_r) and the standard uncertainty. If we have proficiency test data or use certified reference materials, we use them to estimate the laboratory bias, the reproducibility standard deviation (s_R) and the reproducibility standard uncertainty. We also make sure that we know or have estimated the standard uncertainty of the instruments that we use in the measurements. The latter is typically taken from the instrument calibration or precision statement. We estimate the standard uncertainty of the reference materials and the standard uncertainty of the laboratory bias. The final two steps include the calculation of (1) the laboratory standard uncertainty uncorrected for bias and corrected for bias, and (2) the laboratory expanded uncertainty at the 95% confidence limit.

Keywords: *uncertainty, repeatability, reproducibility, vitrinite reflectance, specific gravity.*

Περίληψη

Εφαρμόσαμε μια απλή διαδικασία υπολογισμού αβεβαιοτήτων φυσικών και μηχανικών παραμέτρων γεωλογικών υλικών με βάση τον οδηγό υπολογισμού αβεβαιοτήτων του Διεθνούς Γραφείου Μέτρων & Σταθμών. Αρχικά, ορίζουμε την ποσότητα προς μέτρηση και αποφασίζουμε αν θέλουμε να χρησιμοποιήσουμε μονάδες ή σχετικά μεγέθη. Ακολούθως, υπολογίζουμε την τυπική απόκλιση της επαναληψιμότητας (s_r) και την τυπική αβεβαιότητα. Επίσης, χρησιμοποιούμε δεδομένα δοκιμών από διεργαστηριακά ή υλικά αναφοράς ώστε εκτιμηθεί η συστηματική απόκλιση του εργαστηρίου, η τυπική απόκλιση της αναπαραγωγιμότητας (s_R) και η τυπική αβεβαιότητα της αναπαραγωγιμότητας. Εκτιμούμε ή υπολογίζουμε την τυπική αβεβαιότητα των οργάνων που χρησιμοποιούμε στις μετρήσεις, την τυπική αβεβαιότητα του υλικού αναφοράς και την τυπική αβεβαιότητα της συστηματικής απόκλισης του εργαστηρίου. Τα τελευταία βήματα περιλαμβάνουν τον υπολογισμό (1) της συνολικής τυπικής αβεβαιότητας του εργαστηρίου με ή χωρίς διόρθωση για την συστηματική απόκλιση και (2) την διευρυμένη αβεβαιότητα του εργαστηρίου σε επίπεδο εμπιστοσύνης 95%.

Λέξεις κλειδιά: *αβεβαιότητα, επαναληψιμότητα, αναπαραγωγιμότητα, ανακλαστικότητα βιτρινίτη, ειδικό βάρος.*

1. Introduction

Understanding and evaluating measurement uncertainty is important to fully exploit laboratory results. The basic step involves the estimation of uncertainty either for a single operator or within a laboratory, or among laboratories. A measurement technique should (1) distinguish between error and uncertainty; (2) recognize that all measurements have uncertainty; (3) identify types of error, sources of error, and how to detect or minimize errors; and (4) estimate, describe, and express uncertainty in measurements and calculations.

The Guide to the Expression of Uncertainty (GUM) published by the Joint Committees for Guides in Metrology establishes the general rules for evaluating and expressing uncertainty in measurements (BIPM, 2008). For further explanation or clarifications to definitions and detailed procedures the reader may refer to the excellent publications by NIST, EURACHEM, NordTest, UKAS, and ASTM. The GUM defines uncertainty as the parameter that is associated with the result of a measurement and characterizes the dispersion of the values that could be attributed to the measurand. In addition, the GUM recognizes two types of uncertainty components: (1) type A that are evaluated using statistical analysis of measurement series, and (2) type B that are evaluated using other than statistical analysis of measurement series.

For type A uncertainty components, the standard uncertainty is

$$u = \frac{s}{\sqrt{n}}, \tag{1}$$

where s is the standard deviation and n the number of measurements used to calculate the standard deviation. Examples of type B components are the resolution of a thermometer and the tolerance of an instrument. Type B components are commonly described by rectangular-, trigonal-, and U-type distributions. To estimate the total uncertainty associated with the quantity $Y = f(X_i)$, the GUM combines the type A and B components of the uncertainty of the measurand $y = f(x_i)$, which is designated as $u_c(y)$ (BIPM, 2008).

Assuming normal (Gaussian) probability distribution for y and its combined standard uncertainty $u_c(y)$, the quantity Y is greater than or equal to $y - u_c(y)$ and is less than or equal to $y + u_c(y)$ at an approximate level of confidence of 68%, which is expresses as $Y = y \pm u_c(y)$. The combined standard uncertainty u_c is used to express the uncertainty of many measurement results. Nonetheless, it is often required to express the uncertainty at the 95% or 99% confidence level. This is called the expanded uncertainty U and is obtained by multiplying $u_c(y)$ by a coverage factor k ($k = 2$ for 95% confidence and $k = 3$ for 99% confidence), thus $U = k \cdot u_c(y)$ and $Y = y \pm U$.

2. Materials and Methods

We have used the GUM (BIPM, 2008) and the NordTest TR 537 report (Magnusson et al., 2003) to formulate a simple algorithm for calculating the uncertainties of physical and mechanical parameters that are commonly determined in testing laboratories of geological materials by using standard test methods. We introduce the relevant parameters and basic equations that we have used under the assumption of normally distributed data and, subsequently, we give two examples of our adopted approach.

The agreement between results obtained with the same method on identical test or reference material under the same conditions (job done by one person, in the same laboratory, with the same equipment, at the same time or with only a short time interval) is the best precision a laboratory can obtain. This is called the within-batch precision or single-operator repeatability. The repeatability standard deviation is estimated by

$$s_r = \sqrt{\frac{\sum_i (x_i - \mu)^2}{n-1}} \quad \text{and} \tag{2}$$

$$\mu = \frac{\sum_i x_i}{n}, \tag{3}$$

where n represents the number of measurements x_i (e.g., Mandel, 1964). In the case of combining several (k) series of measurements performed under similar conditions, which is also common in testing laboratories, the repeatability standard deviation is estimated with Eq. (4)

$$s_r = s_P = \sqrt{\frac{(n_1-1)s_1^2 + (n_2-1)s_2^2 + (n_3-1)s_3^2 + ... + (n_k-1)s_k^2}{(n_1-1)+(n_2-1)+(n_3-1)+...+(n_k-1)}}. \tag{4}$$

The repeatability limit r is calculated by using $r = (1.96 \times \sqrt{2}) \times s_r = 2.8 \times s_r$. This means that the difference between two measurements made under repeatability conditions is unlikely to exceed the repeatability limit r (with 95% confidence).

The within-laboratory repeatability is a measure of the agreement between results obtained with the same method on identical test material under different conditions (execution by different persons, with the same or different equipment, in the same laboratory, at different times) is a more realistic type of precision for a method over a longer span of time when conditions are more variable than defined for repeatability. The measure is the standard deviation of these results s_L, which is also called the between-batch precision. The within-laboratory repeatability limit R_L is calculated by $R_L = 2.8 \times s_L$; that is, two measurements of the same material from the same laboratory should not exceed R_L. The within-laboratory repeatability standard deviation is estimated as above.

Reproducibility is the agreement between results obtained with the same method on identical test or reference material under different conditions (execution by different persons, in different laboratories, with different equipment and at different times). The measure of reproducibility R is the standard deviation of these results s_R and is defined by $R = 2.8 \times s_R$; that is, the difference between the measurements of two different laboratories under reproducibility conditions should not exceed R (with 95% confidence). The reproducibility standard deviation is typically derived from interlaboratory (*IL*) measurements and proficiency tests (*PT*), and is given by the agency that is responsible for these tests. Nonetheless, it can be readily calculated providing that all the measurements from all the laboratories are known. From the above it is anticipated that $s_R > s_L \geq s_r$.

To calculate the laboratory uncertainty, we first assume uncorrelated uncertainties, then define the quantity y to measure, and finally decide whether we want to work with units or relative quantities (e.g., s or $\%s = 100 \times s/\mu$). The latter is preferred. Furthermore, in the case a laboratory uses reference materials (RF), or participates in proficiency tests, the bias, which is a measure of nonrandom error, is estimated. Second, we calculate the single-operator (s_r) or the within-laboratory repeatability standard deviation (s_L), and the repeatability standard uncertainty

$$u_r = \frac{s_r}{\sqrt{n}}, \text{ or}$$

$$u_r = \frac{s_L}{\sqrt{n}}. \tag{5}$$

Third, we estimate the standard uncertainty associated with all the laboratory apparatus that we use in the measurements

$$u_{instruments} = \sqrt{\sum_i u_{instrument}^2} \,. \tag{6}$$

Fourth, from proficiency tests, or reference materials, we estimate the standard uncertainty of the reference material(s)

$$u_{RF} = \frac{s_R}{\sqrt{n}} \tag{7}$$

and the standard uncertainty of the laboratory bias

$$u_{bias} = \sqrt{RMS_{bias}^2 + u_{RF}^2} \,, \tag{8}$$

where $RMS_{bias} = \sqrt{\frac{\sum_i (Y_i - Y_{ref})^2}{n}}$,

or the percent relative RMS_{bias}

$$pRRMS_{bias} = 100 \cdot \sqrt{\frac{\sum_i (\frac{Y_i - Y_{ref}}{Y_{ref}})^2}{n}} \,. \tag{9}$$

The fifth step is the calculation of the bias-uncorrected laboratory standard uncertainty

$$u_{Lab,\,bias-uncorrected} = \sqrt{(u_r^2 + u_{instruments}^2)} \,, \tag{10}$$

or bias-corrected laboratory standard uncertainty

$$u_{Lab,\,bias-corrected} = \sqrt{(u_r^2 + u_{instruments}^2 + u_{bias}^2)} \,. \tag{11}$$

Finally, we calculate the expanded laboratory uncertainty, either bias-uncorrected or bias-corrected,

$$U_{Lab} = k \times u_{Lab} \tag{12}$$

at the 95% confidence limit. The factor k depends on the degrees of freedom ($v = n - 1$), (Mandel, 1964).

3. Examples

3.1. Vitrinite Reflectance

In this example, the laboratory (Energy Resources Consulting) estimates the single-operator and within-laboratory uncertainty using a reference material (ICCP Single Coal Accreditation

Program). The test involves the determination of the vitrinite reflectance according to ISO 7404-5. Six different samples are measured by three laboratory scientists, and the data are listed in Table 1.

Table 1 – Vitrinite reflectance data measured on coal samples.

Sample	User	N	μ	s	%s	s_p	%s_p	μ_{RF}	s_{RF}	%s_{RF}
#1	A	100	0.64	0.047	7.3	0.04	6.3	0.64	0.04	6.6
	B	100	0.63	0.050	7.9					
	C	100	0.63	0.005	0.8					
#2	A	100	0.67	0.042	6.2	0.05	7.0	0.67	0.04	5.9
	B	100	0.67	0.045	6.7					
	C	100	0.67	0.053	7.9					
#3	A	100	0.89	0.054	6.1	0.05	5.8	0.88	0.06	7.3
	B	100	0.91	0.045	4.9					
	C	100	0.90	0.058	6.4					
#4	A	100	1.17	0.050	4.2	0.05	4.1	1.15	0.10	9.0
	B	100	1.20	0.033	2.8					
	C	100	1.18	0.058	4.9					
#5	A	100	0.98	0.043	4.4	0.04	4.1	0.95	0.05	5.1
	B	100	0.97	0.032	3.3					
	C	100	0.98	0.045	4.6					
#6	A	100	0.91	0.055	6.0	0.06	6.2	0.88	0.06	6.3
	B	100	0.90	0.047	5.2					
	C	100	0.91	0.066	7.2					

The within-laboratory standard deviation and standard uncertainty are calculated as follows:

number of group measurements $N = 6$;
number of measurements per group $n = 100$;
repeatability standard deviation (pooled) $s_L = 5.7\%$;
repeatability limit $r = 2.8 \cdot s_L = 15.9\%$;
standard uncertainty $u_L = \frac{S_L}{\sqrt{N}} = 2.3\%$.

The microscope standard uncertainty is estimated from the daily calibration log and the nominal reflectance of Y–Al garnet. Thus, the instrument standard uncertainty is

$$u_{instrument} = \frac{s_{instrument}}{\sqrt{N}} = 0.3\%.$$

The reference material standard uncertainty is

number of samples $N = 6$;

standard uncertainty $u_{RF} = \frac{s_{RF}}{\sqrt{N}} = 2.7\%$.

The standard uncertainty of the laboratory bias is the square root of the sum of the squares of *pRRMS* and u_{RF},

pRRMS = 2.5%;

standard uncertainty of reference material (global average) $u_{RF} = 2.7\%$;

standard uncertainty of bias $u_{bias} = 2.9\%$.

Finally, the expanded laboratory uncertainty U at the 95% confidence level is

bias-uncorrected standard uncertainty $u_{Lab,\,bias-uncorrected} = 2.3\%$;

bias-corrected standard uncertainty $u_{Lab,\,bias-corrected} = 3.4\%$;

degrees of freedom $v = N - 1 = 5$;

coverage factor $k = 2.571$;

expanded uncertainty $U_{Lab} = k \cdot u_{Lab,\,bias-corrected} = 9.5\%$.

3.2. Soil Specific Gravity

In this example, the laboratory (GeoTerra) participates in proficiency tests (AASHTO Materials Reference Laboratory) that involves the determination of soil specific gravity according to ASTM D 854 and the results are from a period of six years. The details are given in Table 2. Each test comprises two soil samples that are analyzed by different members of the laboratory staff and the results are sent to the PT provider for evaluation. Several hundred laboratories around the globe take part in the test and the large number of the participating laboratories (N > 800) ensures that the global average for each A–B pair can be safely considered as the reference value.

Table 2 – Laboratory and proficiency test data for soil specific gravity.

Sample	Laboratory			Global			
	G_s	s_r	$\%s_r$	G_s	S_R	$\%S_R$	N
A	2.694	0.004	0.1	2.683	0.0318	1.2	803
B	2.696			2.680	0.0336	1.3	
A	2.703	0.004	0.1	2.658	0.0380	1.4	809
B	2.696			2.657	0.0367	1.4	
A	2.685	0.002	0.1	2.704	0.0349	1.3	849
B	2.682			2.699	0.0336	1.2	
A	2.726	0.0002	0.01	2.733	0.0417	1.5	829
B	2.687			2.694	0.0341	1.3	
A	2.664	0.016	0.6	2.681	0.0350	1.3	862
B	2.627			2.667	0.0333	1.2	
A	2.636	0.004	0.2	2.654	0.0326	1.2	881
B	2.629			2.653	0.0338	1.3	

The within-laboratory standard deviation and standard uncertainty are calculated as follows:

number of group measurements $N = 6$;
number of measurements per group $n = 2$;
repeatability standard deviation (pooled) $s_L = 0.3\%$;
repeatability limit $r = 2.8 \cdot s_L = 0.8\%$;
standard uncertainty $u_L = \frac{s_L}{\sqrt{N}} = 0.1\%$.

The standard uncertainty of the instruments, in this case balance(s) and pycnometer(s) that conform to the requirements of the standard test method, is the combined uncertainties of the balance(s) and the pycnometer(s). For reasons that have to do with the daily use of the laboratory equipment, we prefer to estimate the uncertainty of instruments from tolerances than calibration records even if this results in higher standard uncertainty. The balance(s) for soil specific gravity according to ASTM D 854 should have a readability of 0.01 g and a basic tolerance α equal to 0.1% (Class GP5, ASTM D 4753). The Class A 250 ml and 500 ml pycnometers have a specified tolerance of 0.15 ml and 0.25 ml, respectively, and the corresponding relative tolerance values are 0.06% and 0.05%. Consequently, the instrument standard uncertainty is calculated, assuming rectangular distribution,

standard uncertainty of balance $u_{balance} = \frac{a_{balance}}{\sqrt{3}} = 0.06\%$;

standard uncertainty of pycnometer $u_{pycnometer} = \frac{\sqrt{a_{250ml}^2 + a_{500ml}^2}}{\sqrt{3}} = 0.05\%$.

The test method reproducibility standard deviation and uncertainty are similarly calculated
the number of proficiency tests $N = 6$;
the number of measurements per proficiency test (average) $n = 839$;
the reproducibility standard deviation (pooled) $S_R = 1.8\%$;
the reproducibility limit $R = 2.8 \cdot S_R = 5.2\%$;
the standard uncertainty $u_R = \frac{S_R}{\sqrt{N}} = 0.8\%$.

The laboratory bias standard uncertainty is then estimated

root mean square $RMS = 0.05\%$;
standard uncertainty of reference material (global average) $u_{RF} = u_R = 0.06\%$;
standard uncertainty of bias $u_{bias} = 0.08\%$.

Finally, the expanded laboratory uncertainty U at the 95% confidence level is

bias-uncorrected standard uncertainty $u_{Lab,\,bias\text{–}uncorrected} = 0.1\%$;
bias-corrected standard uncertainty $u_{Lab,\,bias\text{–}corrected} = = 0.2\%$;
degrees of freedom $v = N - 1 = 5$;
coverage factor $k = 2.571$;
expanded uncertainty $U_{Lab} = k \cdot u_{Lab,\,bias\text{–}corrected} = 0.4\%$.

4. Conclusion

We have shown the use of a simple but sound procedure to calculate the standard and expanded uncertainty for typical tests of geological materials considering repeatability measurements, reference materials, and proficiency tests. In the future, we plan to expand the above described procedure to mineral chemistry and thermochemistry data.

5. Acknowledgments

We would like to thank all laboratory staff members who performed the tests.

6. References

ASTM International.2010. Standard Test Methods for Specific Gravity of Soil Solids by Water Pycnometer, ASTM D 854, West Conshohocken, PA, 2007, DOI: 10.1520/D0854-10, 7 pp., www.astm.org.

ASTM International.2007. Standard Guide for Evaluating , Selecting, and Specifying Balances and Standard Masses for use in Soil, Rock, and Construction Materials Testing, ASTM D 4753, West Conshohocken, PA, 2007, DOI: 10.1520/D4753-07, 5pp., www.astm.org.

BIPM. 2008. Evaluation of measurement data—Guide to the expression of uncertainty in measurement, JCGM 100, 82 pp.

Mandel J. 1964. The statistical analysis of experimental data, Dover Publications, Inc., New York, 410pp.

Magnusson B., Näykki T., Hovind H., and Krysell M. 2011. Handbook for Calculation of Measurement Uncertainty in Environmental Laboratories, NT TECHN REPORT 537, 54pp. www.nordtest.info.

ISO 7404-5 1994. Methods for the Petrographic Analysis of Bituminous Coal and Anthracite–Part 5: Method of Determining Microscopically the Reflectance of Vitrinite, *International Organization for Standardization*, Geneva, Switzerland, 12pp.

Δελτίο της Ελληνικής Γεωλογικής Εταιρίας, τομ. XLVII , 2013
Πρακτικά 13ου Διεθνούς Συνεδρίου, Χανιά, Σεπτ. 2013

Bulletin of the Geological Society of Greece, vol. XLVII 2013
Proceedings of the 13th International Congress, Chania, Sept. 2013

SIMULATION OF UNDERGROUND COAL GASIFICATION PROCESS IN A BULGARIAN COAL FIELD

Koukouzas N.[1], Katsimpardi I.[1] and Merachev D.[2]

[1] *Chemical Processes and Energy Resources Institute /The Centre for Research and Technology Hellas, koukouzas@certh.gr, katsimpardi@certh.gr*

[2] *Overgas, 5 Philip Kutev st. 1407 Sofia, Bulgaria*

Abstract

The sustainable and environmentally friendly energy production has been a major issue of the world energy sector in recent years. Coal is a major fossil fuel that provides approximately 25% of the total energy demand worldwide; coal reserves still remain significant, although in several cases its exploitation trends to be economically marginal. Underground Coal Gasification (UCG) has been identified as a technology which can bridge the gap between energy production and environmental and financial sustainability. Several UCG trials have taken place, although, there are still questions relative to their safety, performance and applicability. To that direction, modelling can prove to be a very effective and practical tool for the prediction of the project performance and the reduction of the risk involved. UCG is a complex process which incorporates mechanical and chemical processes thus modelling is complex since it demands coupling the aforementioned processes. The current study aims at investigating the applicability of the UCG process in a Bulgarian coal site through 2D modelling. The proposed approach uses FLAC software as a modelling tool and attempts to combine thermal and mechanical effects during the gasification process. Several simulation runs have taken place in an attempt to quantify the effect of the different mechanical and thermal properties of the surrounding rocks to the UCG process, the environmental effects and the stability of the geological formations.

Key words: *UCG, Underground Coal Gasification, Geomechanical modelling.*

Περίληψη

Η βιώσιμη και φιλική προς το περιβάλλον παραγωγή ενέργειας αποτελεί σημαντικό ζήτημα του ενεργειακού τομέα τα τελευταία χρόνια. Ο γαιάνθρακας είναι ένα κύριο ορυκτό καύσιμο που παρέχει περίπου το 25% των συνολικών ενεργειακών αναγκών παγκοσμίως. . Η Υπόγεια Αεριοποίηση Άνθρακα (UCG) έχει χαρακτηριστεί ως μια τεχνολογία που μπορεί να γεφυρώσει το χάσμα μεταξύ της παραγωγής ενέργειας και περιβαλλοντικών επιπτώσεων. Σημαντικός αριθμός δοκιμών εφαρμογής έχει λάβει χώρα σε όλο τον κόσμο, όμως, εξακολουθούν να υπάρχουν τεχνικές δυσκολίες και ασάφειες σχετικά με την ασφάλεια, την απόδοση και τη δυνατότητα εφαρμογής. Η μοντελοποίηση της διαδικασίας μπορεί να αποδειχθεί ένα πολύ χρήσιμο εργαλείο για την πρόβλεψη της απόδοσης του έργου και τη μείωση του κινδύνου. Η συγκεκριμένη τεχνολογία είναι μια σύνθετη διαδικασία, η οποία ενσωματώνει μηχανικές και χημικές διεργασίες και έτσι καθιστά τη μοντελοποίηση αρκετά πολύπλοκη. Η παρούσα μελέτη

στοχεύει στη διερεύνηση της δυνατότητας εφαρμογής της διαδικασίας σε κοιτάσματα άνθρακα στη Βουλγαρία μέσω 2D μοντέλων. Η μελέτη χρησιμοποιεί το λογισμικό FLAC ως εργαλείο μοντελοποίησης και προσπαθεί να συνδυάσει θερμικές και μηχανικές επιδράσεις κατά τη διάρκεια της διαδικασίας αεριοποίησης. Κατάλληλος αριθμός προσομοιώσεων έχει λάβει χώρα σε μια προσπάθεια να ποσοτικοποιηθεί η επίδραση των διαφόρων μηχανικών και θερμικών ιδιοτήτων στην απόδοση της μεθόδου, και τη γεωτεχνική συμπεριφορά της περιοχής.
Λέξεις κλειδιά: *Υπόγεια Αεριοποίηση Γαιάνθρακα, Λιγνίτης, Γεωτεχνικό Μοντέλο.*

1. Introduction

Coal is one of the most important sources of energy worldwide. It is used to produce coke for steel production plants, it can be burned directly as a fuel to generate heat or electricity, and finally it can be gasified (World Coal Institute, 2011). Normally the gasification process takes place in large reaction vessels on surface, but an alternative and more environmentally friendly method is Underground Coal Gasification (UCG), during which coal is being converted into gaseous products in-situ. UCG presents a number of advantages such as no ash production, no need of coal handling on surface, no need for transportation of coal, minimum need for mining and land reclamation processes. The overall surface disruption due to the UCG process is minimal, as the process takes place in depth, CO_2 gas produced can be captured and sequestrated thus reducing the amount of CO_2 emission up to 0.4 tonnes/MWh which is half of the amount released in surface gasification process (Burton, 2006).

During the UCG process, initially, two wells, injection and production, are drilled vertically from the surface to the coal seam at a certain distance, and a permeable channel link is created between them. To gasify the coal, a mixture of air/oxygen and steam is introduced into the coal seam through the injection well. The product gas travels through the cavity and elutes from the production well through the cavity (Chappell et all, 1983). The generated product gas is collected at the surface and sent for end use after being cleaned. The quality of the product gas is influenced by several parameters such as the pressure inside the coal seam, coal properties, feed conditions, kinetics, and heat and mass transport within the coal seam. As gasification proceeds, an underground cavity is formed. The volume of the cavity increases progressively with coal consumption and thermo mechanical spalling, from the roof. Numerical modelling has been used in the past to investigate a variety of problems in underground mining and tunnelling thus making UCG and cavity formation a process which can be investigated through geomechanical modelling (Harloff, 1983). The finite difference analysis software FLAC has been utilised for this purpose. The model includes the detailed lithologic structure of a section of the Dobrudzha Coal Deposit (DCD) site. A vertical geological fault is also incorporated in the geometry of the model. The gasification process is simulated using small increments of heat flux to represent its duration.

2. The Dobrudzha Coal Deposit

The Dobrudzha Coal Deposit is situated in a geologically complex area with several geological layers and numerous faults. Figure 1 presents the geological West-East cross section at Gurkovo local area at DCD site. The specific area in the blue box has been selected as it includes the majority of geological formations in the DCD area, a fault crossing; and various layers of coal seams which are located in the carboniferous layer. Coal seam P3 has been selected for the purposes of modelling. The coal seam P3 is approximately 5m thick. The ignition point and the production well has been set at a distance of 300m and the 100m from the right hand section accordingly. The model includes the detailed lithologic information and material properties to account for gasification cavity growth as well as the reaction of the geologic fault.

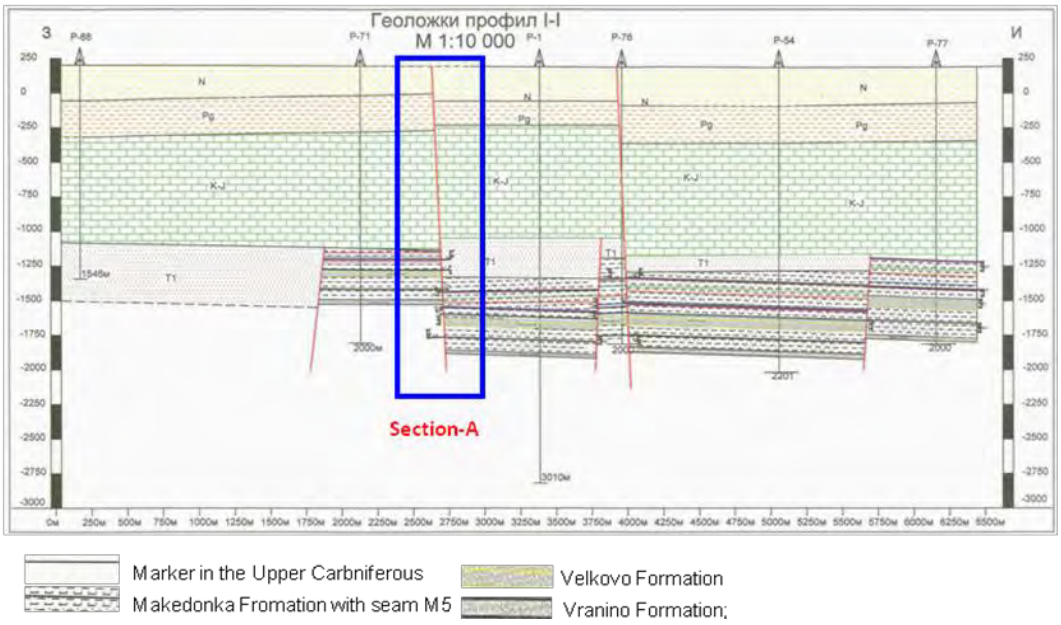

Figure 1 - Geological west-east cross section, Gurkovo local area at DCD (Overgas, 2011).

3. Basic FLAC Model of the DCD Area

In this initial stage of the modelling process, the construction of a simplified model that simulates the thermal and mechanical processes of Underground Coal Gasification was attempted. The main objective of this modelling stage is to achieve the thermal- mechanical coupling, and investigate the effect of temperature to the cavity formation.

Taking into consideration, the fact that the geology of the specific area is extremely complex, a simplified model was first constructed in order to get a preliminary idea of how the software works and check the thermal mechanical coupling feature. In the next stage a more enhanced model with additional geological features incorporated will be used, aiming at giving more precise results in what concerns the determination of ground deformation and cavity development.

3.1. Model Construction

A simple geometry (Figure 2) has been used for this model which consists of a 10-meter coal layer in a depth of 100 meter (depth of roof). The gasification takes place in the middle of the coal seam to a length of 30 meters and is surrounded by rock layers on both sides. The model expands 30 meters to both side directions and 45 meters below the coal seam so that localization effect is avoided. The UCG process has been divided in three stages for monitoring purposes. In that way the cavity development and thermal distribution into the rock during the UCG process can be monitored in a precise way.

- Boundary conditions

Prescribed-displacement boundaries have been used in this model, and are applied by prescribing the boundary's velocity. So, in this case, 151 roller supports have been used to fix x-direction displacement of models right and left edge and 101 rollers to fix y-direction displacement of the bottom of model.

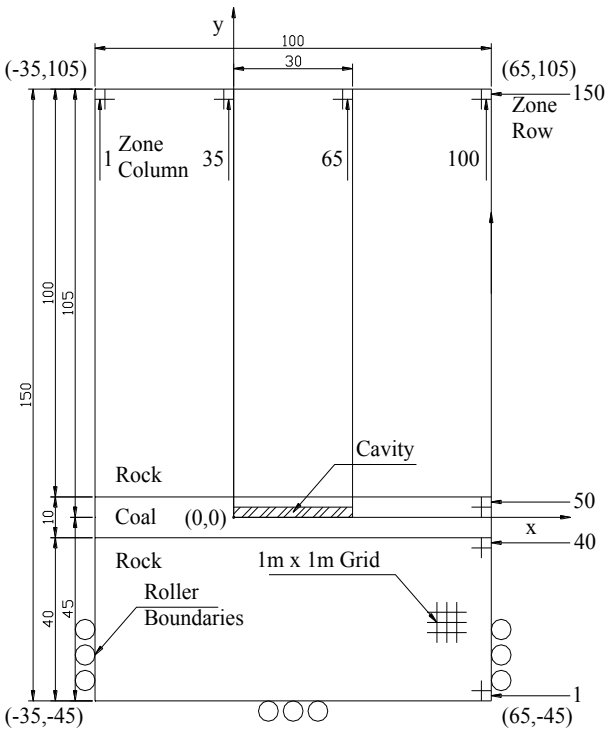

Figure 2 - Model geometry in FLAC.

- Surface load and initial stresses

As previously stated, the specific site of interest is free of any particularly heavy infrastructure on the surface. Only pipe networks are assumed to be located on the surface. If a 200 kg/m^2 surface load is assumed, approximately a 2000 Pa vertical stress is applied on surface, which due to the depth of process its effect is small and it has been ignored to reduce the calculation time (FLAC, 2008).

On the other hand, rock layers exist in stressed state prior any excavation. By setting initial conditions in the FLAC grid this in-situ state is reproduced. And thus, gravity and in-situ horizontal stresses are incorporated into the model.

Gravitational loading is specified by setting the magnitude of gravitational acceleration to 9.81 m/sec^2. The model is allowed to undergo deformations, and this is being done by activating the Large-Strain option. The equilibrium state in model is achieved when the maximum ratio of the unbalanced mechanical force to the applied mechanical force for all grid points drops below 0.001 by default, in order to reduce the running time this ratio has been increased to 0.01. This will also reduce the number of steps taken in thermal calculation to reach equilibrium.

- Material properties

The Mohr-Coulomb model is the conventional model used to represent shear failure in soils and rocks. The failure envelope for this model corresponds to a Mohr-Coulomb criterion (shear yield function or f_s) with tension cutoff (tensile yield function or f_t), where f_s is friction angle, c cohesion, t tensile strength and σ_1, σ_2 and σ_3 are the principle stresses (Equation 1 and 2):

Equation 1 - Formula for Friction Angle

$$fs = \sigma 1 - \sigma 3 N\varphi + 2c\sqrt{N\varphi} \qquad N\varphi = \frac{1+\sin\varphi}{1-\sin\varphi}$$

Equation 2 - Formula for Tensile Strength

$$t = \sigma 1\text{-}\sigma 3 \qquad \sigma 1 \leq \sigma 2 \leq \sigma 3$$

In Figure 1 it is evident that there are several types of rock formation in each age layer at the DCD site. The thermal properties of these formations were calculated on the basis of their thickness and material properties. For thermal options, isotropic conductivity has been assumed for the model, in order to verify the functionality of thermal-mechanical coupling. In what concerns the mechanical properties of the geologic formations, the properties used have been obtained through experimental testing carried out by Overgas. The respective values are presented in Tables 1 and 2 respectively. In this model, the initial rock and coal temperature has been assumed to be 10 ^{o}C and the temperature at the burn front is assumed to be 1000 ^{o}C.

3.1.1. Simulation

The process includes 3 runs. In the first run, the geology of the model is allowed to reach equilibrium under gravity, which due to initial stresses defined this would happen instantaneously (after 2 steps). Two series of codes are defined in this model, the first one models excavation by a loop, which sets the constitutive model for excavated zones to null. The second code incorporates the burn with excavation, by moving a 1000^{o}C temperature front along the excavation (Yang, 2004). The initial temperature of strata is 10^{o}C and the heat is allowed to conduct through strata. The burn speed assumed for this model is 1 meter/day. Excavation and Burn runs have been saved at every 5 meters of excavation in order to study the developments of failed zones, temperature contour distributions, surface and cavity's roof displacements.

Table 1 - Mechanical properties of Geologic Formations.

Geologic age	Density ρ (Kg/m^3)		Elastic modulus E (GPa)		Poisson's ratio v	
Neogene (N)	0 °C	2440	0 °C	55.28	0 °C	0.274
	1000 °C	2404	700 °C	18.74	700 °C	0.274
			1000 °C	14.27	1000 °C	0.274
Paleogene (Pg)	0 °C	2471	0 °C	40.1	0 °C	0.265
	1000 °C	2467	700 °C	11.5	1000 °C	0.265
			1000 °C	10.2		
K - J (Lower Cretacerous-Upper Jurassic)	0 °C	2350	0 °C	80	0 °C	0.31
	1000 °C	2256	700 °C	35.2	1000 °C	0.31
			1000 °C	24		
Triassic (T1)	0 °C	2350	0 °C	80	0 °C	0.31
	1000 °C	2256	700 °C	35.2	1000 °C	0.31
			1000 °C	24		
Carboniferous (C)	0 °C	2465	0 °C	29.9	0 °C	0.225
	1000 °C	2465	700 °C	11.88	1000°C	0.225
			1000 °C	10.90		
Devonian(D)	0 °C	2350	0 °C	80	0 °C	0.31
	1000 °C	2256	700 °C	35.2	1000 °C	0.31
			1000 °C	24		

Table 2 - Thermal Properties of Geologic Formations.

Age	Specific heat c (J/(Kg.^{o}C)		Thermal conductivity k (W/(m.^{o}C)		Thermal expansion α (/^{o}C) (1e^{-6})	
Neogene (N)	0 °C	1152	0 °C	1.84	0 °C	8.4
	1000 °C	1664	600 °C	0.368	100 °C	8.4
			1000 °C	0.368	500 °C	1.68
					1000 °C	1.15
Paleogene (Pg)	0 °C	1007	0 °C	1.96	0 °C	9.18
	1000 °C	1343.5	600 °C	0.483	100 °C	9.18
			1000 °C	0.418	500 °C	1.2
					1000 °C	0.87
K - J (Lower Cretacerous-Upper Jurassic)	0 °C	1530	0 °C	1.6	0 °C	6
	1000 °C	2540	600 °C	0.32	100 °C	6
			1000 °C	0.32	500 °C	3.6
					1000 °C	2.28
Triassic (T1)	0 °C	1530	0 °C	1.6	0 °C	6
	1000 °C	2540	600 °C	0.32	100 °C	6
			1000 °C	0.32	500 °C	3.6
					1000 °C	2.28
Carboniferous (C)	0 °C	1070	0 °C	2	0 °C	8.4
	1000 °C	1532	600 °C	0.9	100 °C	8.4
			1000 °C	0.5	500 °C	2.24
					1000 °C	1.49
Devonian(D)	0 °C	1530	0 °C	1.6	0 °C	6
	1000 °C	2540	600 °C	0.32	100 °C	6
					500 °C	3.6
			1000 °C	0.32	1000 °C	2.28

4. Enhanced FLAC Model of the DCD Area

For the enhanced model, a 135×275 mesh has been used, thus resulting in a model consisting of 37125 grids. A finer mesh structure has been used for the area around the coal seam, where the gasification takes place so that more accurate results can be obtained. The mechanical and thermal properties of the different geological layers, has been assigned in accordance with the relative results of experimental studies on Dobrudzha coal samples (Table 1). The grid has the left- and right-hand sides fixed to the horizontal direction, and the bottom boundary fixed in the vertical direction. The temperature of the model is assumed to be initially 10^{o}C and reaches a maximum value of 800^{o}C. The thermal model used to simulate the heat transfer along the different geologic materials is the "Isotropic Heat Conduction" model.

4.1. Sensitivity Analysis

Underground Coal Gasification process is believed to be directly linked to hazards due to the surface subsidence. In the case of the DCD though, due to the large depth of the coal seam, the properties of the overburden rock and the lack of surface infrastructure, the main potential hazards will be developed due to the complex geology of the area and more specifically the presence of numerous faults which are intersecting the whole DCD area. Faults and the area around can potentially be source of instabilities as well as a path of possible leakage of the product gas,

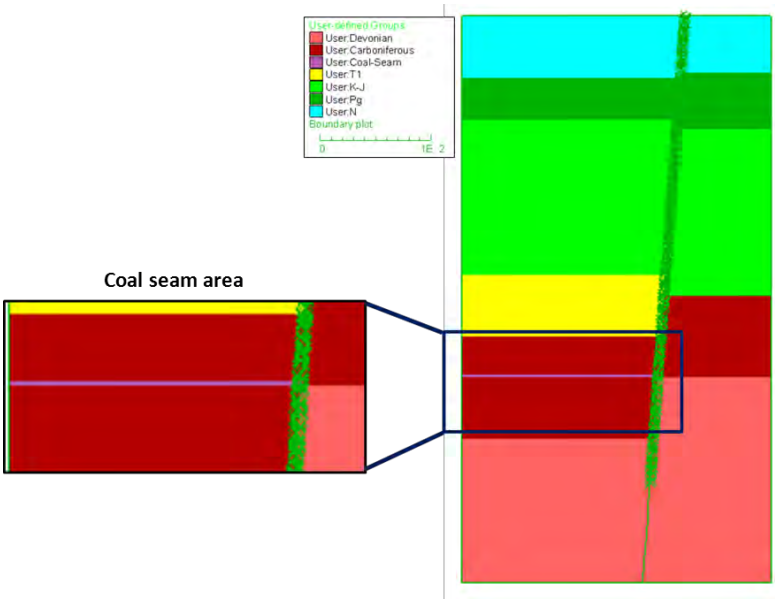

Figure 3 - Enhanced FLAC model.

especially in the case of their reactivation. As such, the following simulation process is a Sensitivity Analysis, in an attempt to decide the degree of UCG impact to the nearby faults and thus the minimum allowed distance between the UCG tunnel and the faults. More specifically, several runs have been carried out simulating the UCG process, maintaining the majority of the model properties constant and varying the normal stiffness and shear stiffness values assigned to the fault.

The gasification process is assumed to begin 100m away from the left model boundary-in order to avoid any boundary effects-and extends laterally for 400m to the direction of the fault. The tunnel developed due to the coal gasification finishes 100m away from the fault zone.

In order to acquire a better understanding of the simulation process, how this proceeds and how the several mechanical and thermal effects develop during the gasification process, several measurements have been acquired during the gasification process within equal timesteps, in order to gain a good understanding of the model state throughout the gasification process. More specifically, the gasification process has been divided into 8 steps, during which equal seam lengths have been gasified, and the model state has been saved at the end of each step.

Figure 4 - Excavation Steps.

In the basecase run the fault included in the model has been characterized as glued i.e. no slip or opening is allowed between the two interfaces, but elastic displacement still occurs. The normal and shear stiffness are 0.4 and 1.0 respectively. In the first set of runs the shear stiffness has been kept constant and the value of normal stiffness varies between 0.3 and 0.6. In the second set of runs the normal stiffness has been kept constant at 0.4 and the shear stiffness varies between 0.6 and 0.9.

Table 3 - Simulation and Fault Properties.

	Normal stiffness (N/m)	Shear stiffness (N/m)
Basecase	0.4	1.0
1St set of Runs		
Case_1	0.3	1.0
Case_2	0.2	1.0
Case_3	0.5	1.0
Case_4	0.6	1.0
2nd set of Runs		
Case_a	0.4	0.9
Case_b	0.4	0.8
Case_c	0.4	0.7
Case_d	0.4	0.6

4.1.1. Mechanical Effects- Stress Distribution

In the first set of runs, the shear stiffness has been kept constant and the normal stiffness varies according to the values indicated in the aforementioned table. During the first steps of the gasification process one can see the stresses and fault zones developing around the cavity to an extent of approximately 100m above and below the seam. The stress zones develop approximately in the same way for all the cases of this set of runs, although, one can observe little difference in the timing of the stress development. More specifically the lower the value of the normal stiffness the quicker the stress zones begin to develop around the cavity and to the vertical direction. This difference in the timing though is so small, that cannot be easily depicted

The same applies for the two cases in which the normal stiffness has been assumed 0.5 and 0.6 N/m respectively. Again, the stress distribution presents a slight delay in the development, though finally the overall area influenced by the process remains more or less the same. In Figure 5, the stress distribution and failed zones are presented during the 4th and the 6th step of the excavation process.

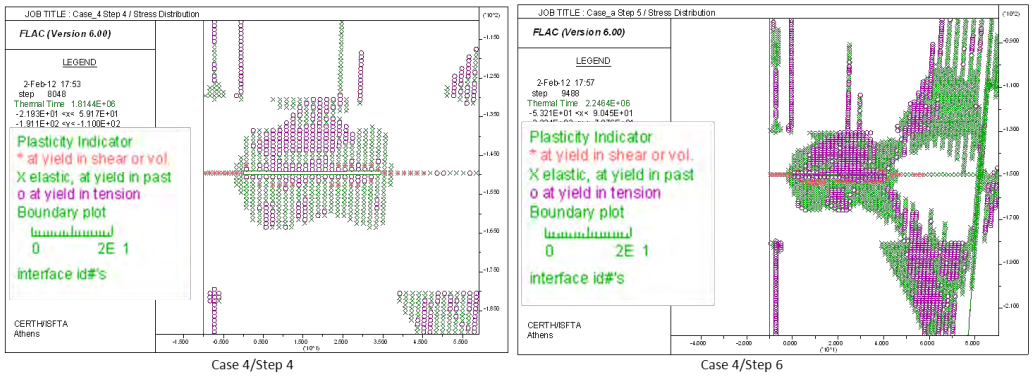

Case 4/Step 4 Case 4/Step 6

Figure 5 - Stress Distribution.

In the 2nd set of runs, it is observed that the different values of shear and normal stiffness have little effect at the timing of the stress distribution expansion towards the fault, as well as the shape of the failed zones and the fault zone behavior.

Initially the fault zones develop to an extent of approximately 100m above and below the seam length excavated. As the gasification proceeds towards the fault, the stress distribution expands further towards the fault and the interfaces between the other geological layers present in the mod-

el. What can be concluded from the simulation runs is that the end of the gasification tunnel should be placed at least 400m away from the fault zone. As it is obvious in Figure 5 after step 5 i.e. 350m of gasification tunnel, there is a major failed zone expansion towards the fault.

The temperature effects extend to a distance of approximately 50m above and below the gasification channel (Figure 6). It is also worth noting that the lateral temperature effect is even smaller due to the low thermal conductivity of the coal, and so the temperature effects extend laterally approximately 20m, As such the presence of the fault is not affected at all by the temperature changes around the gasification channel. A safe distance of approximately 80m even after the last step of the gasification process is maintained, which has already been excluded from the process due to the intense mechanical influence of the gasification channel to the fault.

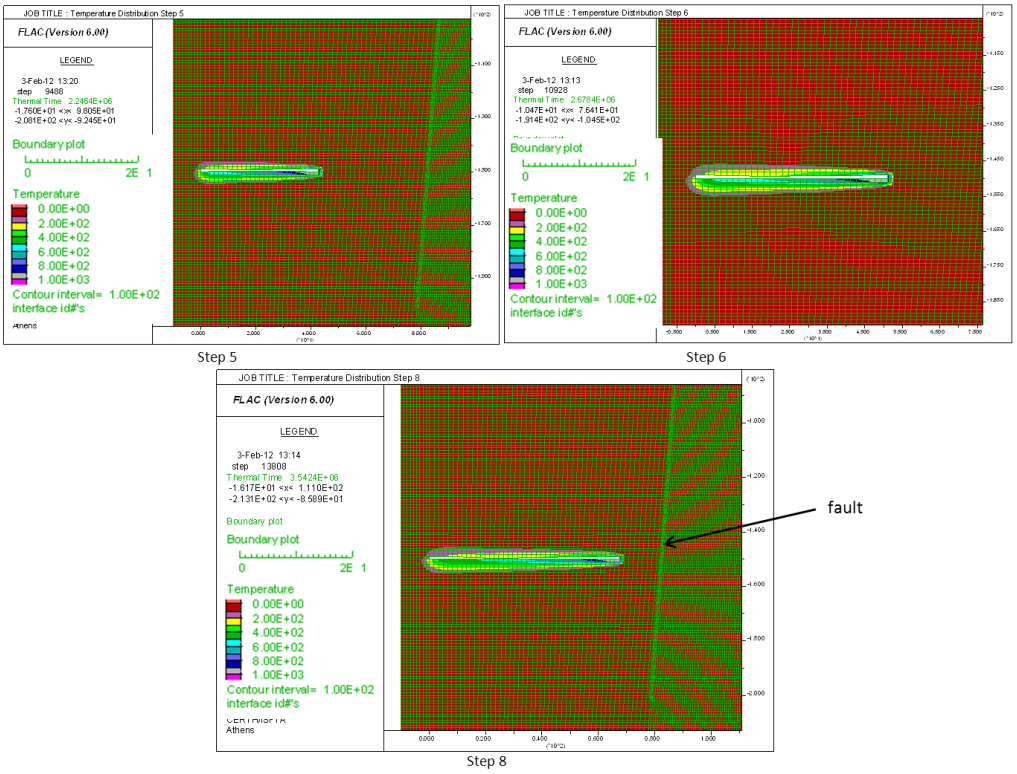

Figure 6 - Temperature Distribution.

Moreover and since the thermal properties of the geological layers have not been altered throughout these two sets of simulation runs, the temperature distribution remains the same throughout the two sets of runs and so further results of the rest of the cases are not presented within this paper.

5. Discussions

In order to acquire a clear and well-rounded understanding of the process, the development of the gasification has been divided in three distinct stages. The first one represents the state of cavity and the surrounding rock at the beginning of the gasification/excavation process. The second stage presents the process status mid-ways the gasification/excavation process and the third and final stage presents the geomechanical status of the area at the end of the gasification/excavation process. Under this scheme the results of the process simulation will be presented.

Figure 6 presents the temperature distribution around the cavity, during the gasification process. Although accurate quantitative conclusions cannot be drawn in this case, these profiles can provide

a qualitative approach of the temperature distribution during the gasification process. With respect to the thermal time passed, the maximum temperature reached during the gasification process is 1000 ºC, which by the end of this process has dropped to 600 ºC at the end of excavation length, temperature contours are redistributed more evenly and the distance between contours has increased. Another point observed at different stages is that, the heat has only penetrated a depth of 2 meter into cavity's vicinity.

New cavity shape is formed by fall of roof elements that fail in tension, which are next to the existing cavity's perimeter. The cavity shape changes by inclusion of burn as well as the overall area of failed zones especially on the two ends of the excavation length. Different snapshots clearly illustrate the development of a vertical crack in the beginning of excavation length, which propagates upwards as the excavation proceeds in the burn model. The effect of temperature is a vital parameter for calculation of both displacements and stresses developed.

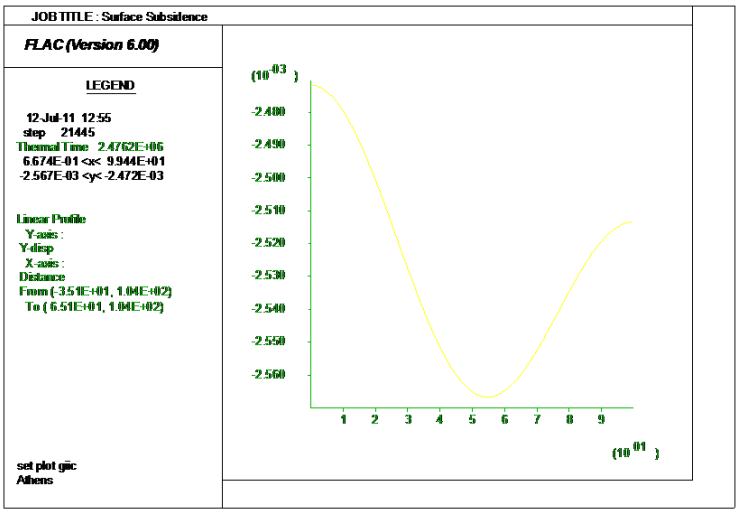

Figure 7 - Surface Subsidence.

The surface subsidence profile (Figure 7) has an inverted bell shape thus, indicating that the maximum subsidence occurs in the middle of excavation length. There is also a slight asymmetry in the surface subsidence, which is possibly the effect of the asymmetric cavity development. It is noted that cohesion and tension are measured in pascals (Pa) and friction and dilation angles in degrees (°).

6. Conclusions

After the analysis of the aforementioned results, it can be concluded that

- The stress zones present the same pattern, and extend approximately 100m above and below the fault, regardless of the fault properties. Moreover, it is worth noting that the pattern of the failed zones is the same regardless of changes in the fault properties, though there are changes at the rate at which the failure begins and proceeds.
- The lower the value of the normal stiffness, the quicker the stress development
- It is concluded that the presence of the fault in the area were the gasification process takes place is of critical importance. The fault itself along with the surrounding area which is already mechanically disrupted. Moreover, once the first zones fail, the failure pattern extend to the direction of the fault, thus making it clear the presence of the fault influences the geomechanical behaviour of the area. The gasification channel should be placed at least 400m away from the fault in order to avoid any instability issues

- The temperature effects extend to a distance of approximately 50m above and below the gasification channel. As such the effect of mechanical failure due to high temperature is dominating a relatively limited area. This is mainly attributed to the low thermal conductivity of coal and the surrounding rocks.

7. Acknowledgements

We acknowledge the "UCG-CO_2 Storage" project funded under the RFCS Framework Programme and the partners.

8. References

Burton E., Friedmann J. and Upadhye R. 2006. Best Practices in Underground Coal Gasification. *Contract W-7405-Eng-48; Lawrence Livermore National Laboratory: Livermore, CA.*

Chappell R. S. and Wilks I.H.C. 1983. A theory for the underground gasification of deep coal by the linked vertical well method, Stanhope Bretby-*Mining Research and Development Establishment*.

Coal Statistics 2012. *World Coal Association*. Available online at: http://www.worldcoal.org/resources/coal-statistics/

FLAC 6.0 Theory and Background 2008. *Itasca Consulting Group*, Minneapolis, Minnesota, USA.

FLAC 6.0 User's Guide, 2008. *Itasca Consulting Group*, Minneapolis, Minnesota, USA.

Harloff G. J., 1983. Underground Coal Gasification Cavity Growth Model, *J. Energy*, *7*, 410–415.

Overgas Inc, 2011. Geological and Geomechanical data for the Dobrudzha coal field area.

Yang L. 2004. Study on the Model Experiment and Numerical Simulation for Underground Coal Gasification, *Fuel*, *83*, 573–584.

Δελτίο της Ελληνικής Γεωλογικής Εταιρίας, τομ. XLVII , 2013
Πρακτικά 13ου Διεθνούς Συνεδρίου, Χανιά, Σεπτ. 2013

Bulletin of the Geological Society of Greece, vol. XLVII 2013
Proceedings of the 13th International Congress, Chania, Sept. 2013

DEPOSITIONAL ENVIRONMENTS AND HYDROCARBONPOTENTIAL OF THE MIOCENE DEPOSITS OFZAKYNTHOS ISLAND

Mpotziolis Ch.[1], Kostopoulou S.[2], Triantaphyllou M.[2], Maravelis A.[3] and Zelilidis A.[1]

[1]*University of Patras, Department of Geology, Laboratory of Sedimentology, 26504 Patras,Greece, A.Zelilidis@upatras.gr*

[2]*Faculty of Geology and Geoenvironment, University of Athens, Panepistimioupolis 15784,Athens, Greece,*

[3]*School of Environmental and Life Sciences, University of Newcastle, Callaghan 2308 NSW, Australia, Angelos.Maravelis@newcastle.edu.au*

Abstract

Structure, sedimentary features, and biostratigraphy were taken into account to provide additional knowledge into the depositional conditions that influenced the sedimentary sequence along the southern coast of Zakynthos. This succession is exposed from Keri village to Ag. Sostis peninsula and appears to have been influenced by intense tectonic activity. The active tectonics resulted in the formation of at least four coarsening upward cycles. The co-occurrence of Bouma sequence subdivisions and slump horizons within the studied sediments suggest a deep-sea depositional environment. Grain size analysis indicates a regional swallowing upward trend. TOC and $CaCO_3$ contents are presented with both positive and negative correlations while the TOC values indicate that the study area contain samples with source rock potential.

Key words: *Sedimentology, source rocks, Bouma sequence, grain-size analysis.*

Περίληψη

Λαμβάνοντας υπόψητις ιζηματογενείς δομές,τα τεκτονικά χαρακτηριστικά και την βιοστρωματογραφία μπορούμε να αντλήσουμε γνώσεις για τις συνθήκες απόθεσης που επηρέασαν την ιζηματογενή ακολουθία κατά μήκος της νότιας ακτής της Ζακύνθου. Η ιζηματογενής ακολουθία από το χωριό Κερί μέχρι και τη χερσόνησο του Άγιου Σώστη φαίνεται να έχει επηρεαστεί από έντονη τεκτονική δραστηριότητα, παράγοντας τουλάχιστον τέσσερις κύκλους με αυξανόμενο κοκκομετρικό μέγεθος προς τα πάνω. Η παρουσία των υποδιαιρέσεων της ακολουθίας Bouma και των οριζόντων ολίσθησης εντός των υπό μελέτη ιζημάτων προτείνουν ένα βαθύ θαλάσσιο περιβάλλον απόθεσης. Η κοκκομετρική ανάλυση έδειξε μια σταδιακή πλήρωση του κάθε κύκλου ιζηματογένεσης, αλλά και ολόκληρης της περιοχής. Επιπροσθέτως, η ανάλυση του TOC και του $CaCO_3$ έδειξε ότι υπάρχει μια σχέση του ποσοστού τους με το περιβάλλον απόθεσης, ενώ οι τιμές TOC δείχνουν ότι η περιοχή μελέτης περιλαμβάνει δείγματα με *δυνατότητα γένεσης υδρογονανθράκων.*

Λέξεις κλειδιά: *Ζάκυνθος, ιζηματολογία, μητρικά πετρώματα, ακολουθία Bouma.*

1. Introduction

Marine depositional environments with low depositional rate are typified by increasing carbonate content towards the coarse fractions (Saadellah & Kukal, 1969). The organic material is intimately related to sedimentary environments (Folk, 1968). The accumulation of organic matter requires: (1) high organic productivity, (2) high subsidence rates and (3) anoxic conditions. Such conditions occur either because of overproduction and deposition of organic material, or because of limited water circulations resulting in non-oxygen recycle.

In contrast, erosion results to the oxidation of the organic material of the rock and to the dissolution and precipitation of minerals in both sandstones and limestones. The dissolution of calcium carbonate ($CaCO_3$) is affected by the temperature, pressure and the partial pressure of carbon dioxide (CO_2). The dissolution of calcium carbonate ($CaCO_3$) is controlled by the dissolution of carbon dioxide (CO_2). In particular, the more carbon dioxide (CO_2) dissolved in water, the more the calcium carbonate ($CaCO_3$) will be dissolved. The CO_2 is dissolved rapidly at high pressures and low temperatures and thus, the $CaCO_3$ is dissolved more in the deep ocean waters of the, compared to shallow, surface water. The saturation of CaCO3 is also related to the pH. The higher the pH of the water is, the greater is the concentration of CO_2. Since more CO_2 is incorporated to the deep ocean waters because of the respiration of organisms, the more easily the water erodes the calcareous shells. The organic matter and amount of oxygen are also affected by the level of sea level (Reolid et al. (2010)).

The decomposition of marine sediments from the oxygen and the oxidation of organic material, results in the release of CO_2 into the water. Such process reduces the pH of the water and leads to a subsaturation of the $CaCO_3$. Through this procedure, the $CaCO_3$ may be subjected to post-consequential dissolution (Martin & Sayles, 2004). The dissolution of $CaCO_3$ by organisms can be independent of the saturation of water environments (Milliman et al., 1999). On the other hand, $CaCO_3$ in pelagic sediments is controlled by several factors described by (Khim et al., 2011). The extent of carbon provided in the seabed at a constant volume of dilution factor (productivity), variations in the content of carbon in carbon feed rate constant (factor of dissolution), change in the proportions of calcareous/silicate particles in the flow and dilution of non biogenic material such as wind and volcanic suspensions are the principles factors that affect the $CaCO_3$ content.

When there is an inverse correlation between $CaCO_3$ and Corg in sediments, then the CO_2 that is produced by the decomposition of Corg in the subsurface layer of water (where we have no circulations and O_2 recycling) and sediments, resulted in a decrease in the pH of water, thus expediting the dissolution of $CaCO_3$ produced in the surface layer of water. This happens when the sediment's Corg percentage is above 12% or there are seasonal anoxic bottoms (Dean, 1999; 2002). On the other hand, when there is a positive correlation between the two percentages, occurs due to removal of CO_2. At high temperatures, where the solubility of $CaCO_3$ and the pH in the surface layer of water is reduced, thus accelerating the production of $CaCO_3$ (Hodell et al., 1998). The interruption of this relation in stratigraphic column shows that the $CaCO_3$ in sediments is mainly controlled by dissolution of the subsurface layer of water and sediment due to the decomposition of organic material.

For this purpose, five sections have been selected from Keri to Kalamaki area, where fifty samples have been selected in order to determine grain-size; total organic carbon (wt. % ToC) and $CaCO_3$ contents (Figure 1).

2. Geological Setting

The study area is situated at the western part of Greece. Western Greece represents the southern edge of the Dinarides-Albanides-Hellenides active margin and has been the focus of oil/gas exploration over the last decade (e.g. Zelilidis et al., 2003; Karakitsios and Rigakis, 2007; Maravelis et al., 2012). It has been influenced by both a compressional and an extensional tectonic

regime, because of the motion of the Adriatic and the Apulia plates. Zakynthos Island is part of theparautochthonus Apulian lithospheric plate of Hellenic mountain belt and containsrocks of two different geotectonic zones, the western Pre-Apulian zone and the eastern Ionian zone (Underhill, 1985).

The region under study was influenced by the Ionian thrust during the early Pliocene (Zelilidis et al., 1998). As a result, the area was fragmented and separated into two discrete sedimentary basins, the westward Alikanas foreland basin and the eastward Gerakas piggy-back basin (Zelilidis et al., 1998). The Foreland basin hosts the oldest rocks seen in the area (Kontopoulos et al., 1997). The study area was served as a continental shelf during Tortonian and thus, mudstones that contain rare sandstone beds were accumulated (Keri area, Figure 1).The upward coarsening upward trend suggests a progressive regional swallowing upward. A large-scale NNW directed normal fault brings in contact the Tortonian shelf with the underlyingLate-Cretaceus limestones(Figure 1). Messinian evaporites have been also identified (Agios Sostis area, Figure 1). Such salts evolve into a depositional sequence that contains evaporitic beds of turbiditic origin and further upslope, early Pliocene deep-sea sands. The sedimentation develops with the deposition of shelf deposits with hummocky cross-stratification. This depositional environment is represented by “trubi” marly limestone.

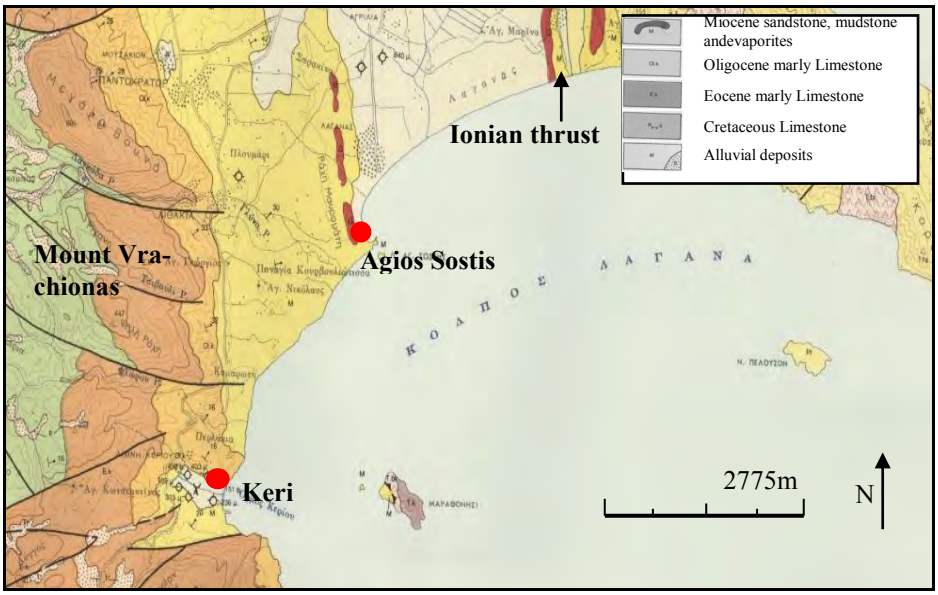

Figure 1 - Geological map of the study area (IGME, 1980, Zakynthos).

3. Tectonostratigraphy

The activity of the Ionian thrust during the early Pliocene is the most important tectonic event that affected the study area. This orogenic event separated the main basin into two discrete sub-basins, a westward foreland and an eastward piggy-back basin (Zelilidis et al., 1998). The foreland basin is typified by major NNW – SSE anticline, which is crossed-cut by both eastward and westwarddirected faults. Vrachionas anticline was developed during the Pliocene as part of the foreland-propagating fold and thrust system within Pre-Apulian zone (Underhill, 1989). The Pre-Apoulian zone is characterized by a compression regime, after Miocene time (Sorel, 1976; Underhill, 1989), followed by a Pliocene extension regime (Underhill, 1989). Nowadays, there is a shift in the tectonic regime and the study area is typified by a NNE – SSW directed regime. Finally, palaeomagnetic measurements indicate a late Pleistocene 25^{o} clockwise rotation (Duermeijer et al., 1999).

4. Materials and Methods

A suite of fifty samples were selected from five different sections (Figure. 2). The base of the depositional sequence is exposed at section one while, the younger sediments are exposed at sections four and five(Figure 2).

Section one: This section is cited at the southern end of Keri gulf. It is eight meters in total thickness and is composed of at least eight coarsening upward sedimentary cycles. Each cycle is up to 1m in total thickness and is represented by a basal mudstone that evolves upslope into coaly beds. Coals are with 30 cm in total thickness.

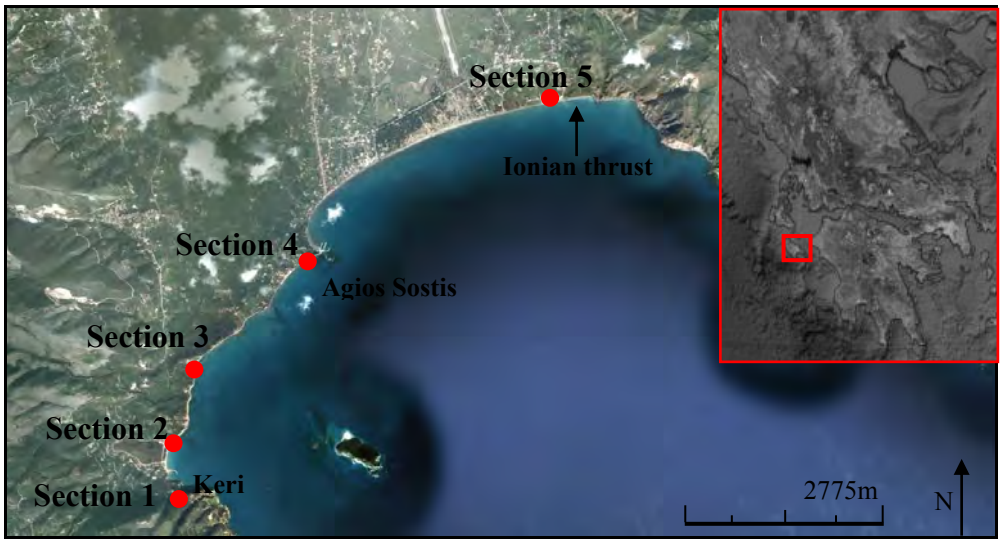

Figure 2 - Map showing the study area and the sections of where the samples were taken. (Photo from Google Earth).

Section two: This section corresponds to the laterally equivalent of section one, is located at Keri gulf and is presented with up to 6 meters total thickness. This outcrop consists of a basal gray/brown mudstone up to 25cm thick interbedded with thin-bedded sandstones. There is an upward increase in mudstone-sandstone ratio.

Section three: This section is located northeast of the section two between the Keri gulf and Agios Sostis peninsula. In this area a sedimentary succession with up to 65 meters in total thickness is exposed (Figure 3).This sequence is characterized by a thick slump horizon, placed at the top and with 25 meters in total thickness (figure 4). This slump horizon overlies sandstone beds, one meter thick with no evidence of deformation. The deformation unit underlies undisturbed mudstone strata. Throughout the sedimentary sequence Bouma subdivision are the dominant sedimentary features (Figure 5).

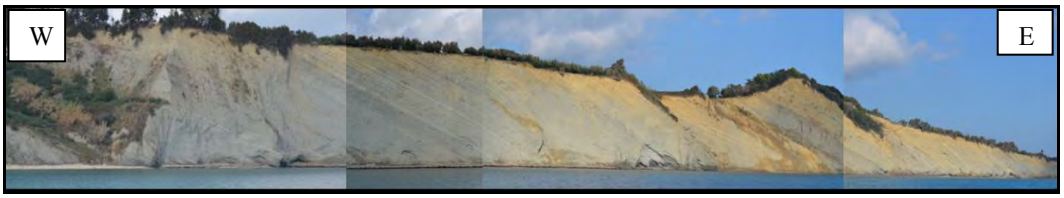

Figure 3 - Panoramic view of Section three.

Figure 4 - Slump horizon within section three.

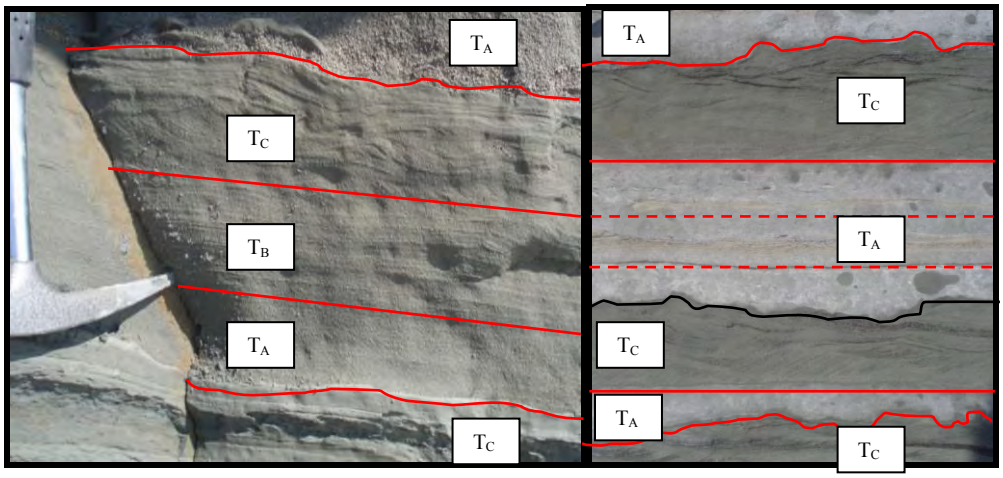

Figure 5 - Bouma sequence within section three.

Section four: This section represents the upper parts of the studied stratigraphy (Kontopoulos et al., 1997). In the current research samples were collected at the base of the section. The upper parts of both sections four and five are represented by carbonates. The “Trubi” marly limestones are considered as the typical early Pliocene sedimentary facies of the Mediterranean. Such facies are overlain the turbiditic sequence, which contains sandstone and re-sedimented evaporitic turbidites (Kontopoulos et al., 1997). Both the upper part of the studied section four (overlying the stratigraphic column of this work), and the upper part of the Kalamaki cross-section (Section five) consist of the typical for the Mediterranean environment during the Early Pliocene, "trubi" marly limestone (Figures 6 and 7), formed over Pliocene turbiditic sequence, with sandstone and resedimented evaporitic clasts turbidites (Kontopoulos et al., 1997).

Figure 6 - The "trubi" marly limestone on the upper part of section four, at Agios Sostis.

Figure 7 - The "trubi" marly limestone on the upper part of section five at Kalamaki.

According to the above description a synthetic stratigraphic column was produced (Figure 8). From the whole sequence a detailed calcareous nannofossil biostratigraphy showed that the age ofsection one and twosediments is Tortonian, and only from slumps we found many resedimented mostly Oligocene and Aquitanian to Burdigalian sediments (Figure 8). Samples of section three and section five (e.g. samples 30, 45, 52) display rare to common small *Gephyrocapsa* spp. coccoliths (2.5-3.0 μm), within a rich but redeposited from Eocene, Late Oligocene, Aquitanian-Burdigalian, Messinian, assemblage. *Gephyrocapsa* spp. presence along with the absence of *Discoaster* species (*D. tamalis, D. pentaradiatus, D. surculus*); only *Discoaster* cf. *brouweri* has been documented, enables tentative age assignment in Early Pliocene (subbottom of *Gephyrocapsa* spp. at 4.33 Ma, Lourens et al., 2004). Sample 36 from section three yields nannofossil flora (*Reticulofenestra pseudoumbilicus, Pseudoemiliania lacunosa*, small *Gephyrocapsa* spp.) of Early Pliocene (NN14-15 biozone).

As depicted on Figure 8, a synthetic stratigraphic column was constructed based on sedimentologic evidence. The detailed calcareous nannofossil biostratigraphy indicates a Late Miocene (Tortonian) age for the sections one and two. Samples from the slump horizon determined as Oligocene-early Miocene in age (Figure 8).Sections three and five (e.g. samples 30, 45, 52) display rare to common small Gephyrocapsa spp. coccoliths (2.5-3.0 μm), within a rich but re-deposited fossils from Eocene, Late Oligocene, Miocene (Aquitanian-Burdigalian, Messinian) sedimentary sequence. The occurrence of Gephyrocapsa spp. in association with the absence of Discoaster species (only Discoaster cf. brouweri has been documented), suggests an Early Pliocene age (subbottom of Gephyrocapsa spp. at 4.33 Ma, Lourens et al., 2004). Sample 36 from section three yields nannofossil flora (Reticulofenestra pseu-doumbilicus, Pseudoemiliania lacunosa, and small Gephyrocapsa spp.) of Early Pliocene (NN14-15 biozone).

One cycle of section fourat Agios Sostis and fourteen cycles of section fivein Kalamaki display the influence of the Ionian thrust during the depositional evolution. The section five is intimately related to the activity of the Ionian thrust because of its proximity to the thrust front whereas; the remotely positioned section four is little influenced by the thrust activity.

5. Methodology - Materials and Methods

Sieve analysis for sediments sandstone (>63mm) and pipette analysis for mudstones (<63mm) were used in order to determine grain size and their parameters. The determination of organic carbon content was based on the method of titration (Gaudette et al., 1974). The content of calcium carbonate was measured with the complete dissolution of calcium carbonate ($CaCO_3$) with acetic acid (CH_3COOH) (Varnavas, 1979).

6. Results

The grain size analysis aims to determine the lithology and grain size parameters in order to describe the particle size distribution of sediments. The data exported from the grain size analysis were used for the construction of cumulative grading curve and the determination of the lithologic character of the sediments. The statistical parameters were calculated based on the Folk & Ward (1957) method.

The grain size analysis suggests that silt is the main lithology with minor presence of clay. Coarser material is totally absent. As portrayed on Figure 9, the depositional depth of the studied samples is variable. In Figure 11, it is depicted that the selected samples display a random scatter in terms of the stagnant water.

Generally, the main lithology is siltstone. The analysis of the statistical parameters suggests that studied sediments were mostly deposited in a deep basin depth, but a considerable number of samples were deposited in low depth too. Additional evidence for the deep basin depth is provided by the common presence of Bouma subdivisions in section three.

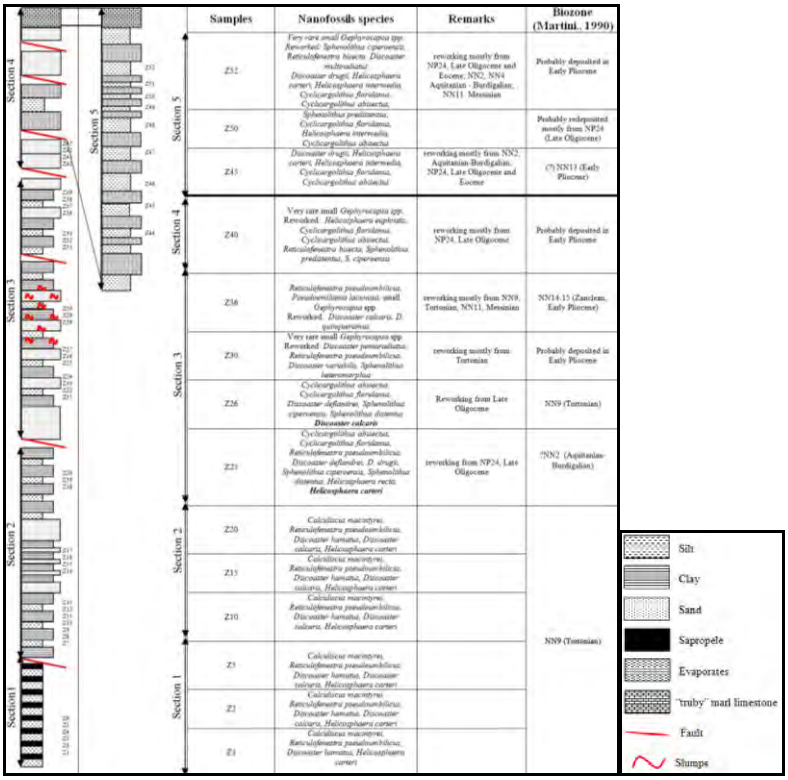

Figure 8 - Synthetic stratigraphic column of the studied area (age determination was according to Martini, 1971).

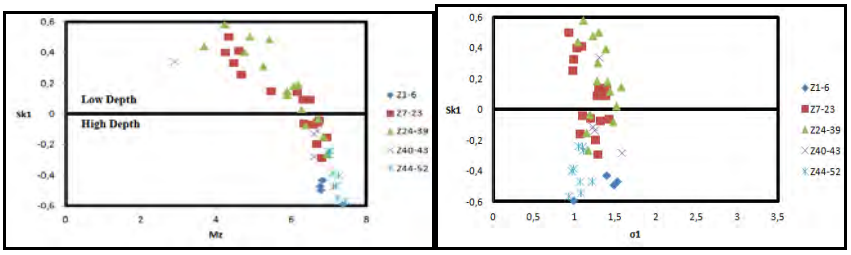

Figure 9 - Diagram of Valia and Cameron (1979), showing the depositional depth (Sk1=asymmetry, Mz=mean and σ1= deviation).

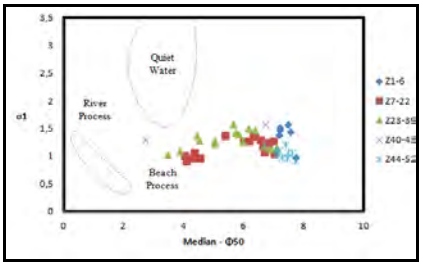

Figure 10 - Diagram of Steward (1958) for the determination of the depositional environment.

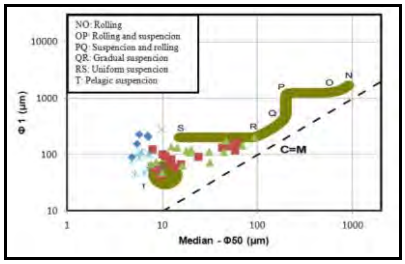

Figure 11 - Diagram of Passega (1957) 1964) for the determination of the depositional environment.

The amount of organic matter in sedimentary rocks is usually measured as the total organic carbon content (TOC) and expressed as a percentage of the dry rock. TOC is not a clear indicator of petroleum potential. as thick, organic-rich potential source rocks cannot become effective source rocks without sufficient burial and thermal maturation (Kenneth et al., (2007)).

Organic carbon content of the studied sediments exhibits variable contents, ranging from 0 to 3.19 wt. % (Figure 12).

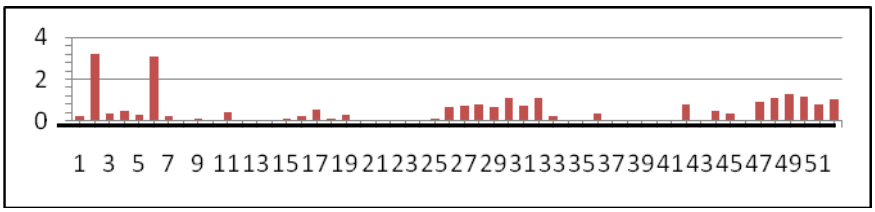

Figure 12 - The content of TOC in studied deposits, where the line depict the lower limit of 0,5% that differentiate the potential source rocks with those that have no potential.

Studies of numerous global samples of different ages have led to the conclusion that the minimum TOC value required for the designation as an immature source rock is 0.5 wt. % (Hunt, 1979; Hedberg & Moody, 1979; Tissot & Welte, 1984). Thus, these values suggest that the studied sedimentary sequence contains samples with poor to good source rock potential.

The calcium carbonate of the studied samples ranges between 1.76 to 61.29 (Figure 13).

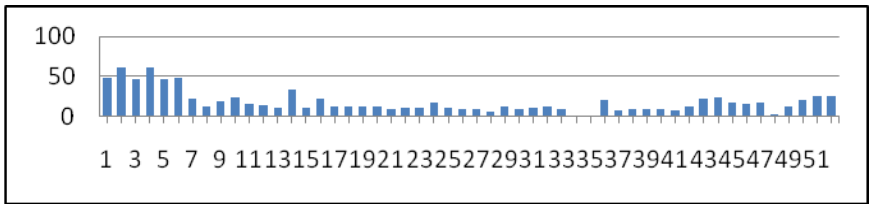

Figure 13 - The content of $CaCO_3$ in studied deposits.

In the study area the content of calcium carbonate is high among the fine material, suggesting high sedimentation rates. The combination of total organic carbon (TOC) content and calcium carbonate contents in sedimentary rocks can be employed to add knowledge into the depositional conditions during sedimentation (Figure 14).There is not a constant trend between these two parameters throughout the studied sedimentary succession. The contents of the total organic carbon and calcium carbonate display both positive and negative correlation. This fact indicates that that the CaCO3 content is mainly controlled by dissolution in the subsurface layer of water and sediment due to the decomposition of organic material.

The first stratigraphic cycle is typified by a positive correlation between the two parameters. The high percentage of CaCO3 indicate high sedimentation rates while the variable TOC content can be explained by the existence of seasonal anoxic bottom (no circulation and recycling of O_2) (Dean, 1999; 2002). Additionally, low organic productivity and high rate of burial of the organic matter resulted in no oxidization.In the other cycles, however, the lower content of $CaCO_3$ indicates lower sedimentation rates and so the TOC content is not influenced by the depositional environment.

The reduction in the content of $CaCO_3$ from cycle one to four indicates a gradual swallowing of the basin. Cold climatic conditions are also suggested and are in agreement with the Miocene regional icehouse conditions (Bertolani - Marchetti, (1985). Such conditions may potentially have resulted into an increase in solubility of $CaCO_3$. However, the third cycle is characterized by the

presence of slump horizon and thus, the low rates of $CaCO_3$ cannot be connected to low sedimentation rates. The slumps led to scarification of the subsurface layer and the production of suspensions, which probably concluded to the low content of $CaCO_3$ caused by the dilution due to non-biogenic material (Khim et al., 2011). The high rates of TOC observed in a group of samples of this cycle possible can be related to quick of burial rate, where the organic matter does not have time to be oxidized.

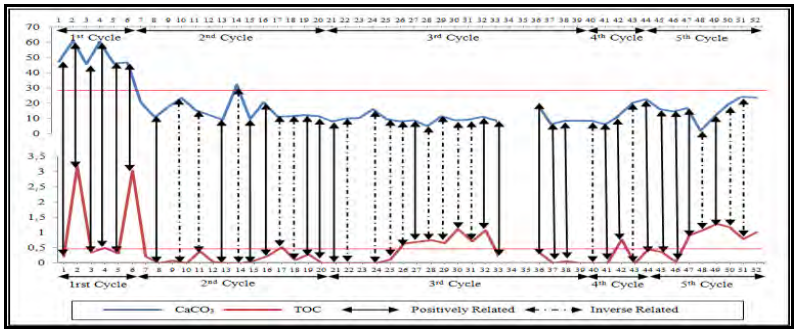

Figure 14 - Correlation of $CaCO_3$ and TOC contents within studied deposits.

7. Conclusions

Grain size analysis suggests a regional upward swallowing upward trend. Sedimentation took place in a deep basin with steep western margins during Tortonian to early Pliocene.
The $CaCO_3$ content indicates high deposition rates, while TOC contents indicate potential source rocks for hydrocarbon generation. The comparison of TOC and $CaCO_3$ indicates that these two parameters are presented with both positive and negative correlation. This character is intimately related to the dissolution of the $CaCO_3$ at the subsurface layer of water and sediment because of the decomposition of organic material, in oxic conditions.

8. References

Bertolani–Marchetti D. 1985. Pollen palaeoclimatology in the Mediterranean since Messinian ti me, in: D. J. Stanley and F. C. Wezel (Editors), *Geological Evolution of the Mediterranean bas in*. Springer, New York, pp. 525.

Dean W.E. 1999. The carbon cycle and biogeochemical dynamics in lake sediments, *Journal of Paleolimnology*, v. 21, p. 375–393.

Dean W.E. 2002. A 1500-year record of climatic and environmental change in Elk Lake, Minne sota II: Geochemistry, mineralogy, and stable isotopes, J*ournal of Paleolimnology* v.27

Duermeijer C. E., Krijgsman W., Langereis C. G., Meulenkamp J. E., Triantafyllou M.V. and Zachariasse W.J. 1999. A late Pleistocene clockwise rotation phase of Zakynthos (Greece) and implications for the evolution of the western Aegian arc, *Earth and Planetary Science Let ters* 173 (1999), p. 315-331.

Folk R.L. 1968. Petrology of Sedimentary Rocks, *Hemphill Publishing Co*, Austin, Texas, 170p

Folk R. L. and Ward W. S. 1957. Brazos river bar. A study in the significance of grain size parameters. *Jour. Sed. Petr.*, 27, Nol, 3-26.

Gaudette H.E., Flight W.R., Toner L. and Folger D.W. 1974. An inexpensive titration method for the determination of organic carbon in recent sediments, *Jour. Sed. Petr.*, 44, 249-253.

Hedberg R.M. and Moody J.D. 1979. Petroleum prospects of the deep offshore, *Am. Assoc. Pe t. Geol. Bull*. 63:p. 286-300.

Hodell D.A. and Schelske C.L. 1998. Production, sedimentation, and isotopic composition of or ganic matter in Lake Ontario, *American Society of Limnology and Oceanography*. 43(2), p 2 00-214.

Hunt J.M. 1979. Petroleum Geochemistry and Geology, Freeman, San Francisco ISBN 0-7167-1005-6.

Karakitsios V. and Rigakis N. 2007. Evolution and petroleum potential of Western Greece, *Journal of Petroleum Geology* 30 (3):197-218.

Kenneth, E.P., Leslie B.M., Zenon C.V. and Paul G.L., 2007. Source-Rock Geochemistry of the San Joaquin Basin Province, California, Chapter 11, *Petroleum Systems and Geologic Assessment of Oil and Gas in the San Joaquin Basin Province*, California

Khim B.K., Kim H.J., Cho Y.S., Chi S.B., Yoo C. M. 2011. Orbital Variations of Biogenic $CaCO_3$ and Opal Abundance in the Western and Central Equatorial Pacific Ocean During the Late Quaternary, *Terr. Atmos. Ocean. Sci*. 23 -1, 107-117.

Kontopoulos N., Zelilidis A., Piper D. and Mudie P. 1997. Messinian evaporates in Zakynthos, Greece. Palaeo, 129, 361-367.

Maravelis A., Makrodimitras G. and Zelilidis A. 2012. Hydrocarbon prospectivity in Western Greece, *Oil and Gas European Journal* 38 (2), 84-89.

Martin W. and Sayles F. 2004. The recycling of biogenic material of the seafloor, in: Holland, H.D. and Turekian, K.K. (eds.), *Treatise on Geochemistry*, Vol. 7, Sediments, Diagenesis and Sedimentary Rocks (ed. F.T. Mackenzie), Elsevier. Amsterdam, 37-66 pp.

Martini E. 1971. Standard Tertiary and Quaternary Calcareous Nannoplankton Zonation, *Proceedings of the II Planktonic Conference*, Roma , 1970, A. Farinacci, ed., Ed. Tecnoscienza, p. 739 - 785, Rome.

Milliman J.D., Troy P.J., Balch W.M., Adams A.K., Li Y.H. and Mackenzie F.T. 1999. Biologically mediated dissolution of calcium carbonate above the chemical lysocline, *Deep Se a-Res.* I, 46, 1653–1669.

Moila R.J. and Visher D. 1968. Textural parameters: an evaluation, *Jour. Sed. Petr.*, V260, p. 45-63.

Passega R. 1957. Texture as characteristic of clastics deposition: Am. Soc. Asoc. Petrol. *Geol. Bull. Tulsa,* Okland, 41, 1952-1984.

Passega R. 1964. Grain size representation by CM patterns as a geologic tool, *Jour. Sed. Petrol. Tulsa Ok*., 34, No. 4, 830-847.

Reolid M., Nagy J., Rodríguez-Tovar F.J. 2010. Ecostratigraphic trends of Jurassic agglutin ated foraminiferal assemblages as a response to sea-level changes in shelf deposits of Svalb ard (Norway), *Palaeogeography, Palaeoclimatology, Palaeoecology,* 293: 184–196.

Saadellah A. and Kukal Z. 1969. Grain size and carbonate content in costal sediment of Iraq, Jo *ur. Iraq G. Soc*, 2, 3-10.

Sorel D. 1976. Etude neotectonique dans l'arc egeen externe occidental: les iles ioniennes de Ke fallinia et Zakinthos et l'Elide*, These 3me cycle*, Universite de Paris Sud, Orsay.

Stewart H.B. 1958. Sedimentary reflections of depositional environments in San Miguel Lagoo n, Baja California, Mexico, *Am. Assoc. Petr. Geol. Bull*., V42, p. 2567-2618.

Tissot B. and Welte D.H. 1984. Petroleum Formation and Occurrence, Springer Verlag.

Underhill J. R. 1985. Neogene and Quartenary tectonics and sedimentation in Western Greece, *PhD thesis* Cardif, Wales, University College, University of Wales.

Underhill J.R. 1989. Late Cenozoic deformation of the Hellenides foreland, western Greece, *Bulletin of the Geological Society of America,* 101, p 613-634.

Valia H.S. and Cameron B. 1977. Skewness as a Paleoenviromental indicator, *Jour. Sed. Petr*., 4 7, No2, 784-793.

Varnavas S.P. 1979. Geochemistry of sediments from the eastern Pacific, *PhD Thesis* Univer sity London pp. 431.

Zelilidis A., Piper D.J.W., Vakalas I., Avramidis P. and Getsos K.. 2003. Oil and gas plays in Albania: Do equivalent plays exist in Greece? *Journal of Petroleum Geology* 26 (1):29-48.

Zelilidis A., Kontopoulos N., Avramidis P. and Piper D. 1998. Tectonic and sedimentological evolution of the Pliocene-Quaternary basins of Zakynthos Island, Greece: case study of the transitions from compressional to extensional tectonics, *Basin Research,* 10, 393-408.

Δελτίο της Ελληνικής Γεωλογικής Εταιρίας, τομ. XLVII , 2013
Πρακτικά 13ου Διεθνούς Συνεδρίου, Χανιά, Σεπτ. 2013

Bulletin of the Geological Society of Greece, vol. XLVII 2013
Proceedings of the 13th International Congress, Chania, Sept. 2013

COAL DEPOSITS OF TURKEY: PROPERTIES AND IMPORTANCE ON ENERGY DEMAND

Oskay R.G.[1], Inaner H.[2], Karayigit A.I.[3] and Christanis K.[1]

[1] *University of Patras, Department of Geology, Rio-Patras, Greece, oskay@upatras.gr, christan@upatras.gr*

[2] *Dokuz Eylül University, Department of Geological Engineering, İzmir, Turkey*

[3] *Hacettepe University, Department of Geological Engineering, Ankara, Turkey*

Abstract

In the last two decades electricity generation and consumption in Turkey was increasing steadily. Around 80% of the electricity generated is derived from fossil fuels such as imported natural gas and oil, and domestic coal. As the energy policy now is focusing on reducing the dependency on imported fuels, coal, particularly this of low-rank, is becoming important for the country. Latest explorations showed that total coal reserves of Turkey reach to 13 Gt with low-rank coals (i.e. lignite and sub-bituminous) being dominant. Coal deposits, formed under various conditions and in various geological times, are widely spread over the territory. The most significant deposits are of Tertiary, especially Neogene age. Neogene coals are most appropriate for combustion in the thermal power plants due to the high total reserves despite the high ash yields and the low calorific values. We imply that applying reasonable exploitation planning and appropriate washing techniques, coal will play a key role in future energy supply of the country.
Key words: *Low-rank coal, Neogene, coal-bearing basin, thermal power plants*

Περίληψη

Κατά τις τελευταίες δυο δεκαετίες η παραγωγή και η κατανάλωση ηλεκτρικής ενέργειας στην Τουρκία αυξήθηκε με γρήγορους ρυθμούς. Περίπου 80% της παραγόμενης ηλεκτρικής ενέργειας προέρχεται από συμβατικά καύσιμα, όπως εισαγόμενο φυσικό αέριο και πετρέλαιο, αλλά και εγχώριους γαιάνθρακες. Καθώς όμως η σύγχρονη ενεργειακή πολιτική προσανατολίζεται σε μείωση της εξάρτησης από εισαγωγές καυσίμων, ο εγχώριος γαιάνθρακας, ιδιαίτερα ο χαμηλού βαθμού ενανθράκωσης, αποκτά σημασία για τη χώρα. Οι τελευταίες έρευνες ανεβάζουν τα αποθέματα σε ~13 Gt, με τον λιγνίτη και τον υποβιτουμενιούχο γαιάνθρακα να κυριαρχούν. Κοιτάσματα γαιανθράκων, που σχηματίστηκαν κάτω από διάφορες συνθήκες και σε διάφορες γεωλογικές περιόδους, υπάρχουν σε όλη τη χώρα. Τα σημαντικότερα είναι Τριτογενούς ηλικίας, με αυτά του Νεογενούς να είναι τα καταλληλότερα για ηλεκτροπαραγωγή εξαιτίας των μεγάλων αποθεμάτων παρά την υψηλή τέφρα και τη χαμηλή θερμαντική ικανότητα. Με την εφαρμογή ορθολογικής εκμετάλλευσης και καταλλήλων μεθόδων εμπλουτισμού ο γαιάνθρακας θα διαδραματίσει στο μέλλον σημαντικό ρόλο στην ενεργειακή τροφοδοσία της Τουρκίας.

Λέξεις κλειδιά: *γαιάνθρακας χαμηλού βαθμού ενανθράκωσης, Νεογενές, ανθρακοφόρα λεκάνη, σταθμός ηλεκτροπαραγωγής*

1. Introduction

In the last two decades electricity demand in Turkey was increasing steadily from 128 TWh in 2000 to 209 TWh in 2010, with an 8% increase per year, on average, due to industrial development and economic growth (Lynch, 2003; EÜAŞ, 2004, 2011). Around 80% of the electricity generated is derived from fossil fuels such as imported natural gas and oil, and domestic coal. To support the increasing demand, several natural gas-fired power plants were constructed as electricity generation from natural gas used to be cheaper and cleaner than from the domestic coals (EÜAŞ, 2004; Yilmaz and Uslu, 2007; Biresselioğlu et al., 2012). However, the rapid increase of oil price and some problems in natural gas supply (Biresselioğlu et al., 2012; Ekşi et al., 2012), led the Turkish energy policy to focus on domestic energy sources such as coal, as well as on renewable sources (wind, geothermal and solar energy) (MENR, 2004; Melikoğlu, 2013).

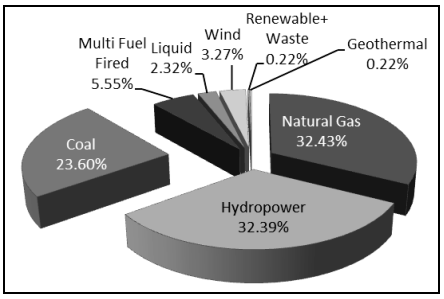

Figure 1 - Share of the sources of Turkey's installed capacity for power generation (from EÜAŞ, 2011)

Even though Turkey does not own enough natural gas reserves to support demand, about 33% of the installed capacity is based on power plants mostly supplied by imported natural gas (Figure 1, Tables 1, 2). Domestic oil and gas reserves are located in SE Turkey and on Thrace Peninsula, whereas some gas reserves are recently discovered off-shore in western Black Sea (TPAO, 2011).

Table 1 - Installed capacity of Turkey's Electricity Generation System by Primary Source (simplified from EÜAŞ, 2011); *: not available data

Source	Installed Capacity*		Power Generation	
	(MW)	(%)	(TWh)	(%)
Natural Gas	17,159	32.43	104.04	45.36
Hydropower	17,137	32.39	52.34	22.82
Coal (lignite + subbit. & bit. coal + asphaltite)	12,491	23.60	66.22	28.87
Multi Fuels (diesel and natural gas)	2,936	5.55	*	*
Wind	1,729	3.27	4.72	2.06
Liquid Fuels (e.g. diesel oil etc.)	1,229	2.32	0.90	0.39
Renewable + Waste	115	0.22	0.46	0.20
Geothermal	114	0.22	0.69	0.30
Total	**52,911**	**100.00**	**229.40**	**100.00**

Table 2 - Installed capacity and power generation based on coal (simplified from EÜAŞ, 2011)

Resources	Installed capacity (MW)	Generation (TWh)
Lignite + subbituminous coal	8,140	38.87
Bituminous coal	300	2.00
Imported coal + asphaltite	4,051	25.34

Recent studies indicate that Turkey has a great potential of renewable energy resources like solar, wind and geothermal energy (MENR, 2004; Demirbaş, 2006; EÜAŞ, 2011; Melikoğlu, 2013); on the other hand, the exploitation of the coal resources seems to be more advantageous than this of the renewable ones. The main reason is that several economic coal deposits suitable for electricity generation are, in general, located close to the capital city and some industrial cities (e.g. Çayırhan/Ankara; Orhaneli/Bursa; Karapınar/Konya; Figure 2). The average power generation cost from lignite is also low (c. US$ 0.014 per kWh; Kıncay and Öztürk, 2003; Kocaoğlu, 2009). Recent coal explorations imply that low rank coals will be the most important domestic energy source for the next decades in Turkey (MTA, 2010; EÜAŞ, 2011).

There are also other alternative hydrocarbon resources in Turkey (Figure 2), which are of minor utilisation capacity such as asphaltite (Karayiğit and Querol, 2002) and bituminous shale (Kok, 2010), whereas non-economic oil sand outcrops also occur (Taşman, 1950). Peatlands are not exploited for energy purposes, but for using peat in horticulture and agriculture only (İnaner and Nakoman, 2004).

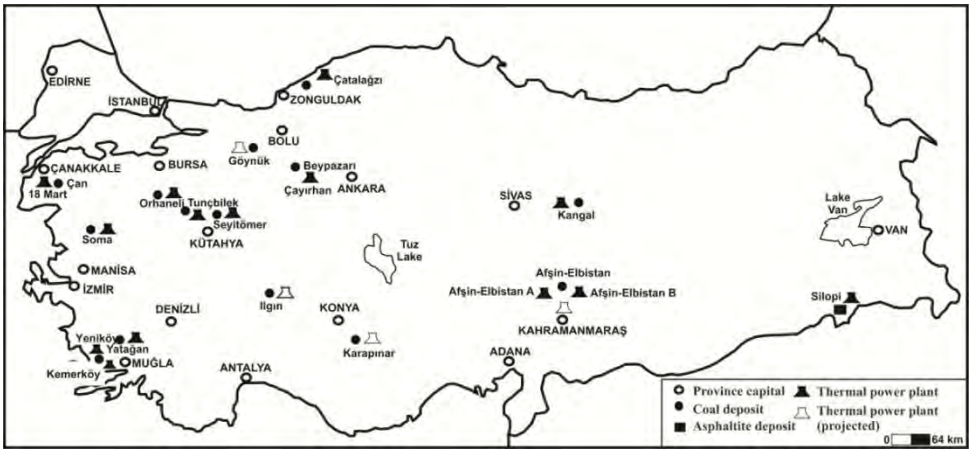

Figure 2 – Coal-fired thermal power plants and supporting coal deposits in Turkey (modified from İnaner and Nakoman, 2004; MTA, 2010; Şengüler, 2010; EÜAŞ, 2011; Parkmaden, 2012)

The coal deposits, especially the lignite ones, have been studied by several researchers with various aims and scopes (Ünalan, 2010); however, there is no comparable study till now. The aim of this paper is to review the distribution, quality and reserves of Turkish coal deposits by compiling results of previous studies.

2. Coal-bearing basins

Coal-bearing basins are widely distributed throughout the country (Figure 3); they formed under variable tectonic regimes during geological times, and thus the basins show various features (arc-related, epirogenic, rift, '*ova'* basin, etc.). Several researchers categorize the coal deposits according to the coal age, features, rank, utilization etc. Age categorization seems to be the most suitable due to structural differences of the basins within the same geographic region and hence, genetic and quality variations of the hosted coal deposits.

The coal-bearing basins formed mainly during Palaeozoic and Cenozoic eras (İnaner and Nakoman, 1997; Tuncali et al., 2002; Palmer et al., 2004; Besbelli, 2009; Toprak, 2009), whereas during Mesozoic the palaeoenvironmental conditions favoured carbonate-platform deposition with terrestrial regime being limited; a few Mesozoic coal deposits were locally formed in eastern Pontides (NE Turkey) and eastern Taurides (Mann et al., 1998; Ünalan, 2003; Korkmaz and Kara-Gülbay, 2007).

2.1. Palaeozoic Coals

The Zonguldak coal deposits (Figure 3) of Namurian to Westphalian D age were formed in a progradational delta and flood plain environment (Akgün and Akyol, 1992; Karayiğit et al., 1998). The deposits were affected by palaeotectonic events (Hercynian orogenic movements) resulting in overlapped seams in the basin (Okay et al., 1994; Karayiğit et al., 1998, 2000). The calorific values of Zonguldak coal are on average 6600 kcal/kg (on air-dry basis); coal displays low sulphur (avg. 0.77%, on air-dry basis) and volatile matter contents (avg. 42.49%, on dry, ash-free basis), and low ash yield (8.27%, on dry basis) (Karayiğit et al., 1998; 2000). Other Palaeozoic coal deposits (Figure 3), were locally formed around Kemer (Pamucak and Çukurboy)/S Turkey and Hazro/SE Turkey; they have no economic importance (Ünalan, 2003; İnaner and Nakoman, 2004).

2.2. Mesozoic Coals

As already mentioned, the Mesozoic was not suitable for coal formation in Turkey. The Mesozoic (mainly Jurassic) coal deposits at Feke and Kozan/Adana, Norsun and Gödül-Alansa/Gümüşhane have no economic significance. They are of sub-bituminous (Feke, Alansa) to bituminous rank (Kozan, Norsun, Gödül) and display low moisture (avg. 4.70%, as-received basis) and high ash yields (avg. 38.70%, dry basis). All Jurassic coals are deposited under marine-influenced telmatic conditions (Mann et al., 1998; Korkmaz and Kara-Gülbay, 2007).

2.3. Cenozoic Coals

During Cenozoic, especially in Southern and Western Turkey, several sedimentary basins (e.g. rift or foreland basins) were formed in a range of tectonic (compressional, extensional and strike-slip) settings, hosting coal-bearing sequences with large reserves (Şengör and Yılmaz, 1981; Görür et al., 1997; Kelling et al., 2005; Toprak, 2009). The Cenozoic coal deposits formed in paralic and/or limnic environments, and consist mostly of lignite and sub-bituminous coals (Gökmen et al., 1993; İnaner and Nakoman, 1997; Tuncali et al., 2002; Palmer et al., 2004). Shallow marine-influenced coal deposits generally formed during Palaeogene, while terrestrial conditions (limnic, continental with volcanic intercalations, fluvial, deltaic) were common during Neogene times (Palmer et al., 2004).

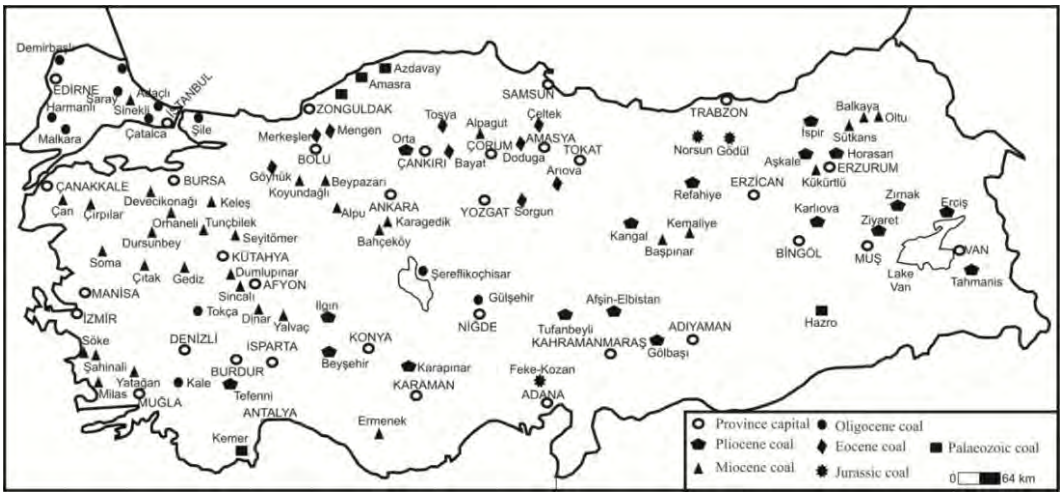

Figure 3 - Important coal deposits of Turkey (modified from İnaner and Nakoman, 2004; MTA, 2010)

2.3.1. Palaeogene Coals

Palaeogene coal-bearing basins formed in foreland basins between Upper Eocene and Oligocene (Görür et al., 1997). Eocene coal-bearing basins are mostly located in central part of the western

Black Sea region (Mengen and Merkeşler/Bolu; Dodurga and Alpagut/Çorum); whereas Sorgun/Yozgat is located in north-eastern Central Turkey (Gökmen et al., 1993; İnaner and Nakoman, 1997; Toprak, 2009). The sedimentary fillings of these basins consist of terrestrial and/or shallow marine sediments. The coal-bearing sequences are intercalated with marl, cross-bedded conglomerate, and sandstone. The basement consists generally of Mesozoic crystalline rocks such as marble, schist, gneiss (Erdoğan et al., 1996; Görür et al., 1997; İnaner and Nakoman, 1997; Palmer et al., 2004; Akkiraz et al., 2008). All Eocene coals are of subbituminous rank, and display (on average, as-received basis) low moisture (11.19%), moderate ash yield (28.18%), high total sulphur content (5.13%), high calorific values (4050 kcal/kg) and fixed carbon content (avg. 55%, dry, ash-free basis) (İnaner and Nakoman, 1997; Karayiğit and Whateley, 1997; Tuncali et al., 2002, Besbelli, 2009; Toprak, 2009). Although the all the Eocene geological reserves are low (629 Mt), the rank is higher and the quality better than these of other Tertiary low-rank coals in the country (Gökmen et al., 1993; İnaner and Nakoman, 1997).

Oligocene and Oligocene/Miocene coal-bearing basins are mainly located on Thrace Peninsula such as Uzunköprü, Harmanlı and Vize/Edirne, Saray and Malkara/Tekirdağ, Şile/İstanbul and also in Southwestern (Kale/Denizli; Çardak and Tokça/Burdur) and Central Turkey (Şereflikoçhisar/Ankara). They generally formed in paralic (fluvial-delta) environments (İnaner and Nakoman, 1997; Tuncali et al., 2002; Besbelli, 2009). During Early-Middle Oligocene coal-bearing deposits on Thrace Peninsula formed in limnic-fluvial and paralic environments. Furthermore, lacustrine-fluvial and molasse facies are typical for SW Turkey during Late Oligocene and coal-bearing sediments are generally hosted within molasse facies (Akgün and Sözbilir, 2001; Palmer et al., 2004; Akgün and Akkiraz, 2005; Sözbilir, 2005). The Oligocene geological reserves amount to around 1 Gt (Besbelli, 2009) but the quality is poorer than this of the Eocene coals. They are of subbituminous rank with high ash yield and moisture (on avg. 25% and 32%, respectively). The net calorific value is 2500 kcal/kg (on avg., as-received basis) (İnaner and Nakoman, 1997; Karayiğit and Whateley, 1997; Tuncali et al., 2002; Besbelli, 2009; Toprak, 2009).

2.3.2 Neogene Coals

Significant coal formation took place during Neogene times (between Middle Miocene to Pliocene). Within the onset of Miocene terrestrial conditions dominated over the greatest part of the territory. The formation of the major coal-bearing basins and the activation of volcanoes in Western Turkey such as in Çan/Çanakkale, Soma/Manisa, Bigadiç/Balıkesir, Orhaneli/Bursa, Seyitömer/Kütahya and Yatağan/Muğla, took generally place due to extensional tectonics (Ediger, 1990; Ercan et al., 1996; Görür et al., 1997; Akgün and Akyol, 1999; Bozkurt and Sözbilir, 2004; Akkiraz et al., 2011). In Eastern Turkey the coal-bearing basins are strike slip-related (Gölbaşı/Adıyaman; Karlıova/Bingöl), intermontane (Muş and Adilceviz/Bitlis; Pasinler/ Erzurum); in Central Turkey they are '*ova*' (Afşin-Elbistan/Kahramanmaraş; Kangal/Sivas; Ulukışla/Niğde; Ilgın/Konya) or epirogenic (Alpagut/Çorum; Şarkışla/Sivas; Refahiye/Erzincan) (Şengör et al., 1984; Görür et al., 1997; Karayiğit and Whateley, 1997; Kayseri and Akgün, 2008; Besbelli, 2009; Toprak, 2009).

The basement of the Miocene coal-bearing basins generally consists of Palaeozoic and/or Mesozoic metamorphic and carbonates rocks. The coal-bearing sequences consist of conglomerate, sandstone, silty claystone and are overlain by marl, lacustrine limestone, tuff and/or basaltic lava and andesite. They usually contain one or two seams with variable thicknesses ranging from 1 to 25 m (Görür et al., 1997; İnaner and Nakoman, 1997). Miocene coals such as at Seyitömer/Kütahya,Yatağan/Muğla and Beypazarı/Ankara, are of lignite rank, and at Tunçbilek/Kütahya, Soma/Manisa, Ermenek/Karaman and Çan/Çanakkale, of subbituminous rank. There are additionally two Miocene coal deposits namely these of Gökler/Gediz and Aşkale/Erzurum, which were heat affected by nearby volcanic activity and reached the rank of bituminous coal; this effect caused also enrichment in Sb, (Karayiğit and Whateley, 1997; Toprak,

2009). The total Miocene lignite reserves amount to approximately 4 Gt (Besbelli, 2009) of variable quality and calorific values (from 1300 kcal/kg to 4500 kcal/kg, on as-received basis).

During Pliocene limnic-fluvial and volcanic-limnic deposits widely formed in Central Anatolia (around Konya, Sivas), SE parts of South Anatolia (Adana, Kahramanmaraş-Afşin-Elbistan) and Eastern Anatolia (Erzurum, Bingöl, Adıyaman) (İnaner and Nakoman, 1997; Palmer et al., 2004; Toprak, 2009). The basement consists of Palaeozoic or Mesozoic rocks and the coal-bearing sequences include pebblestone, sandstone, sandy-silty claystone and marl. These series are generally overlain by marl and/or volcanic rocks (andesite, basalt, and tuff). They host one or two coal seams with variable thickness, up to 100 m (Gökmen et al., 1993; İnaner and Nakoman, 1997; MTA, 2010). The total Pliocene reserves are large (7 Gt); two important coal deposits belong to this group, namely these of Afşin-Elbistan Basin (4 Gt) in Kahramanmaraş, Southern Turkey, and of Karapınar-Ayrancı Basin (1.8 Gt) in Konya, Central Turkey. The latter is recently discovered and explored (MTA, 2010; Salman, 2010). Other important Pliocene coal deposits are located in Beyşehir-Seydişehir/Konya (422 Mt), Tufanbeyli/Adana (400 Mt), Kangal/Sivas (220 Mt), Orta/Çankırı (123 Mt), Karlıova/Bingöl (105 Mt); small deposits are these at Gölbaşı/Adiyaman, Ilgın/Konya and Ispir, Erciş, Horasan/Erzurum (İnaner and Nakoman, 1997; Besbelli, 2009; Toprak, 2009; MTA, 2010). The Pliocene coals are of lignite rank and display (on as-received basis) high moisture (25.31-53.42%) and ash yield (11.38-36.37%), and low calorific values ranging from 1100 to 2200 kcal/kg (Gökmen et al., 1993; İnaner and Nakoman, 1997; Palmer et al., 2004; MTA, 2010).

3. Coal Reserves

The coal exploration in Turkey begun in late 19th century; the first discovery in Zonguldak is dated back to 1848 (Can et al., 2012). The main exploration was carried out between 1950s and 1970s (Lüttig, 1968; Gold and Lüttig, 1972; Yilmaz and Uslu, 2007). Based on the 1990s studies the total coal reserves in Turkey were estimated to around 9.4 Gt (Tuncali et al., 2002; Ünalan, 2003), placing Turkey at the seventh place worldwide (Tuncali et al., 2002). Most of the reserves correspond mainly to low-rank (lignite and sub-bituminous) coals. The total reserves of bituminous coal amount to 1.4 Gt (TKK, 2009). Lignite displays low calorific values (< 2000 kcal/kg) and only 6% of the reserves have > 3000 kcal/kg (Figure 4; İnaner and Nakoman, 1995; Ersoy, 2003; EÜAŞ, 2011). The Pliocene basins host the highest share (60%) of the total lignite reserves (Figure 4); Afşin-Elbistan and Karapınar-Ayrancı deposits with 4 Gt and 1.8 Gt, respectively, are the biggest ones. In 2005 the Turkish General Directorate of Mineral Research and Exploration (MTA) began a new coal exploration campaign in several basins. Within this context MTA explored several Neogene basins and discovered few new coal deposits. As a result, the total lignite reserves increased up to 12 Gt (Besbelli, 2009; MTA, 2010).

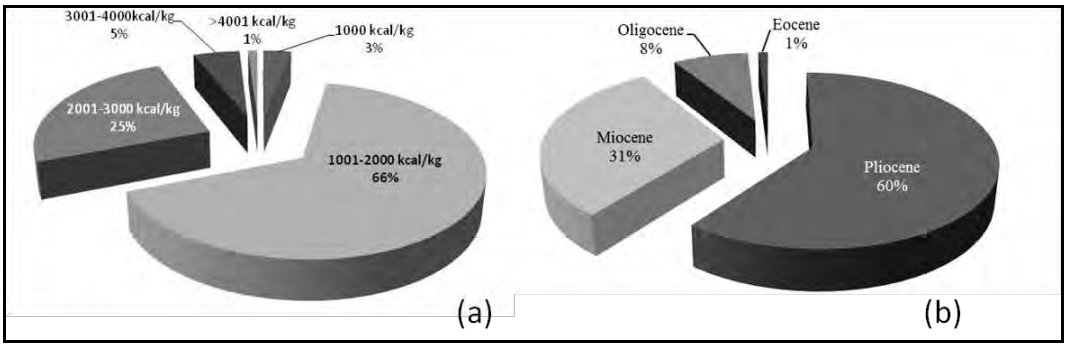

Figure 4 – (a) Distribution of Turkish lignite by calorific value (from EÜAŞ, 2011) and (b) Distribution of Cenozoic coal reserves by age (from Besbelli, 2009)

4. Coal Production and Consumption

The annual total coal production in Turkey is around 78 Mt (TKK, 2009; TKI, 2010; EÜAŞ, 2011). The coal-fired thermal power plants (11,900 MW installed capacity) contribute to 24% in Turkey's installed capacity (total of 52,911 MW) and the electricity generation (66 TWh) amounts to 29% of the total 229.4 TWh (Tables 1, 2; EÜAŞ, 2011).

Bituminous coals are only mined at Zonguldak coalfield, NW Turkey. The annual production is around 2.9 Mt (Ersoy, 2003; TKK, 2009), 80% of which are generally directed to the iron and steel industry. Despite the low reserves, Zonguldak field mainly contains high quality and low-sulphur coking coal (Karayiğit et al., 1998). The Çatalağzı Power Plant in Zonguldak consumes bituminous coal generating 2004 GWh per year (Table 3; EÜAŞ, 2011). In addition, the Middle Miocene Gökler-Gediz deposits include coking coal with very high sulphur contents, being suitable for the cement industry (Karayiğit and Whateley, 1997). Bituminous coal utilisation for domestic heating is very low (Ersoy, 2003).

The lignite and subbituminous coal reserves contribute to 90% of the total reserves; however, they display low calorific values (<2500 kcal/kg), high moisture, ash yield and total sulphur content (İnaner and Nakoman, 1997; Karayiğit et al., 2000; Tuncali et al., 2002; Palmer et al., 2004; Anaç, 2009). These properties make lignite suitable for power generation only. The annual low-rank coal production is around 67 Mt (TKI, 2010) mainly combusted in power plants (76% of total lignite production; Anaç, 2009). Lignite-fired power plants generate 38.87 TWh per year (Table 3; EÜAŞ, 2011). Domestic heating is a secondary application of lignite (14% of annual production) mainly exploited from the Soma/Manisa and Tunçbilek/Kütahya and some other small deposits such as these of Ispir, Erciş/Erzurum and Refahiye/Erzican (İnaner and Nakoman, 1997; Anaç, 2009). Domestic heating is also supported by imported lignite, whereas c. 3 Mt of domestic lignite is consumed by cement, ceramic and food industry (TKI, 2010).

Table 3 - Installed capacity and generation of the major coal-fired thermal power plants in Turkey and the feeding deposits (modified from Karayiğit et al., 2000; EÜAŞ, 2011)

Thermal power-plant	Fuel Type	Installed Capacity (MW)	Power Generation (GWh)	Feeding Deposit/Age
Çatalağzı	Bitumimous coal	300	2,004	Zonguldak/Carboniferous
Afşin-Elbistan A	Lignite	1,335	3,251	Afşin-Elbistan/Pliocene
Afşin-Elbistan B	Lignite	1,440	5,733	Afşin-Elbistan/Pliocene
Canakkale 18 Mart	Subbitum. coal	320	2,127	Çan/Miocene
Orhaneli	Lignite	210	1,300	Orhaneli/Miocene
Seyitömer	Lignite	600	3,896	Seyitömer/Miocene
Tunçbilek	Subbitum. coal	365	1,791	Tunçbilek/Miocene
Kangal	Lignite	457	2,491	Kangal/Pliocene
Soma A+B	Subbitum. coal	1,034	5,020	Soma/Miocene
Kemerköy	Lignite	630	2,503	Hüsamlar/Miocene
Yeniköy	Lignite	420	2,611	Yeniköy/Miocene
Yatağan	Lignite	630	3,274	Yatağan/Miocene
Çayırhan	Lignite	620	5,000	Beypazarı/Miocene
Total		**8,361**	**41,001**	

Of course, the environmental impacts from coal mining (dust, water-table lowering and contamination, landslides, acid drainage, etc.), washing (acid leaching, contamination) and combustion (emissions of trace elements and gasses such as CO_2, NO_x and SO_x; the latter due to the generally high sulphur contents of the Turkish coals) constitute severe disadvantages, which can be reduced by applying proper exploitation techniques.

5. Conclusion

Tectonics is the most important factor controlling the formation of coal-bearing basins in Turkey. Cenozoic era was favourable for coal formation. Eocene coal deposits display low reserves but better quality than the younger Miocence-Pliocene ones. The latter deposits include larger reserves but their calorific values are lower than these of the Eocene coals. Mesozoic era did not favoured coal formation, whereas most Palaeozoic coal deposits (besides this of Zonguldak) are not mineable.

Recent estimations reveal an increasing trend in the energy demand of Turkey. Electricity generation is mainly based on hydropower and fossil fuels. Although the share of imported energy resources is currently higher than this of domestic ones, domestic coal will decrease dependence on imported fuels. Total coal reserves of Turkey amount to around 12 Gt in total; they mostly consist of lignite with low calorific value. Low-rank coal (lignite and sub-bituminous) mining is higher than this of bituminous coal that derives from one coal deposit only, and goes to thermal power plants; household and industrial utilisation is limited.

Low-rank coals are of great importance and their exploration and exploitation are more advanced than these of other domestic energy sources. Turkey hosts large coal reserves mineable at low cost. Thus coal, along with renewable energy sources, might gain more importance in the future supporting the increasing energy demand of the country.

6. References

Akgün F. and Akyol E. 1992. Palynology and paleoecology of the coals in Amasra–Bartin Carboniferous basin, *Turkish Journal of Earth Science*, 1(1), 49-56 (in Turkish with English abstract).

Akgün F. and Akyol E. 1999. Palynostratigraphy of the coal-bearing Neogene deposits graben in Büyük Menderes Western Anatolia, *Geobios*, 32(3), 367-383.

Akgün F. and Sözbilir H. 2001. A palynostratigraphic approach to the SW Anatolian molasse basin: Kale-Tavas molasse and Denizli molasse, *Geodinamica Acta*, 14(1-3), 71-93.

Akgün F. and Akkiraz M.S. 2005. Palynology and age of the Early Oligocene units in Çardak-Tokça Basin, Southwest Anatolia: Paleoecological implications, *Geobios*, 38(3), 283-299.

Akkiraz M.S., Kayseri M.S. and Akgün F. 2008. Palaeoecology of coal-bearing Eocene sediments in Central Anatolia (Turkey) based on quantitative palynological data, *Turkish Journal of Earth Sciences*, 17(2), 317-360.

Akkiraz M.S., Akgün F., Utescher T., Bruch A.A. and Mosbrugger V. 2011. Precipitation gradients during the Miocene in Western and Central Turkey as quantified from pollen data, *Palaeogeography, Palaeoclimatology, Palaeoecology*, 304(3-4), 276-290.

Anaç S. 2009. Present situation of coal in energy policy of Turkey and Turkish coal industry, *Proc. of 26th Annual International Pittsburgh Coal Conference*, Pittsburgh, 20-23 Sept.

Besbelli B. 2009. Coal Potential of Turkey and the Importance of Coal in Electricity Supply, *Proc. of the 62th Geological Congress of Turkey*, Ankara, 16-22April.

Biresselioğlu M.E., Demir M.H. and Kandemir C. 2012. Modelling Turkey's future LNG supply security strategy, *Energy Policy*, 46, 144-152.

Bozkurt E. and Sözbilir H. 2004. Tectonic evolution of the Gediz Graben: Field evidence for an episodic, two-stage extension in western Turkey, *Geological Magazine*, 141(1), 63-79.

Can E., Kuşçu Ş., and Mekik Ç. 2012. Determination of underground mining induced displacements using GPS observations in Zonguldak-Kozlu Hard Coal Basin, *International Journal of Coal Geology*, 89, 62-69.

Demirbaş A. 2006. Turkey's Renewable Energy Policy, *Energy Sources*, Part A, 28, 657-665.

Ediger V.S. 1990. Paleopalynology of coal-bearing Miocene sedimentary rocks associate with volcanics of the Biga Peninsula (NW Turkey) and effect of volcanism on vegetation, *Neues Jahrbuch für Geologie, Abh.*, 180, 259-277.

Ekşi I.H., Şentürk M. and Yıldırım H.S. 2012. Sensitivity of Stock Market Indices to Oil Prices: Evidence from Manufacturing Sub-Sectors in Turkey, *Panoeconomicus*, 59(4), 463-474.

Electricity Generation Co. Inc. (EÜAŞ) 2004. Annual Report of 2004.

Electricity Generation Co. Inc. (EÜAŞ) 2011. Annual Report of 2011.

Ercan T., Satır M., Sevin D. and Türkercan A. 1996. Interpretation of the new radiometric age determinations from the tertiary and quaternary volcanic rocks in Western Anatolia, *Mineral Res. Expl. Bull. Turkey*, 119, 103-112 (in Turkish with English abstract).

Erdoğan B., Akay E. and Uğur M.S. 1996. Geology of the Yozgat region and evolution of the collisional Çankırı Basin, *International Geology Review*, 38(9), 788-806.

Ersoy M. 2003. Current status of Turkish lignite sector. *UNECE Ad Hoc Meeting of Experts on Coal in Sustainable Development*, Geneva, Switzerland.

Gold O. and Lüttig G. 1972. Elbistan: Erfolg einer Untersuchung der Türkei auf Braunkohle mit Mitteln der Deutschen Technischen Hilfe (Känozoikum und Braunkohle der Türkei 7), *Braunkohle*, 24(8), 253-268.

Gökmen V., Memikoğlu O., Dağlı M., Öz D. and Tuncalı E. 1993. *Inventory of Turkish lignites*. MTA Publication, Ankara, 356 pp. (in Turkish).

Görür N., Akkök R., Sakınç M., Ünalan G. and Yaltırak C. 1997, Tertiary basin Turkey and their coal potentials. In Önal, G., Kurşun, İ. and Yazıcı, H. (eds), *Defining Targets and Methods on Turkish Coal Explorations*, 8-37 (in Turkish).

İnaner H. and Nakoman E. 1997. Turkish lignite deposits. In Gayer, R., Pesek, J. (eds), European Coal Geology and Technology, *Geol. Soc. Spec. Pub.*, 125, 77-99.

İnaner H. and Nakoman E. 2004. Resources, quality and economic importance of solıd fossil fuels in Turkey, *Geologica Belgica*, 7(3-4), 245-250.

Karayiğit A.İ. and Whateley M.K.G. 1997. Chemical characteristics, mineralogical composition and rank of high sulphur coking coals of Middle Miocene age in the Gökler coalfield, Gediz, Turkey. In Gayer, R., Pesek, J. (eds), European Coal Geology and Technology, *Geol. Soc. Spec. Pub.*, 125, 115-130.

Karayiğit A.İ., Gayer R.A. and Demirel I.H. 1998. Coal rank and petrography of Upper Carboniferous seams in the Amasra coalfield, Turkey, *International Journal of Coal Geology*, 36, 277-294.

Karayiğit A.İ., Gayer R.A., Querol X. and Onacak T. 2000. Contents of major and trace elements in feed coals from Turkish coal-fired power plants, *International Journal of Coal Geology*, 44, 169-184.

Karayiğit A.İ. and Querol X. 2002. Mineralogy and elemental contents of the Şırnak Asphaltite, Southeast Turkey, *Energy Sources*, 24, 703-713.

Kayseri M.S. and Akgün F. 2008. Palynostratigraphic, palaeovegetational and palaeoclimatic investigations on the Miocene deposits in Central Anatolia (Çorum region and Sivas Basin), *Turkish Journal of Earth Sciences*, 17(2), 361-403.

Kelling G., Robertson A. and van Buchem F. 2005. Cenozoic sedimentary basins of southern Turkey: an introduction, *Sedimentary Geology*, 173, 1-13.

Kıncay O. and Öztürk R. 2003. Thermal Power Plants in Turkey, *Energy Sources*, 25, 135-151.

Kocaoğlu Y. 2009. Study on the electricity generation cost. *Proc. of the TMMOB Energy Symposium*, Ankara, 17-19December (in Turkish).

Kok M.V. 2010. Geological considerations for the economic evaluation of Turkish oil shale deposits and their combustion-pyrolysis behaviour, *Energy Sources,* Part A, 32, 32-335.

Korkmaz S. and Kara-Gülbay R. 2007. Organic geochemical characteristics and depositional environments of the Jurassic coals in the eastern Taurus of Southern Turkey, *International Journal of Coal Geology*, 70, 292-304.

Lüttig G. 1968. Stand und Möglichkeiten der Braunkohlen-Prospektion in der Türkei, *Geologisches Jahrbuch*, 85, 585-604 (in German with English abstract).

Lynch R. 2003. An energy overview of the Republic of Turkey. U.S. Department of Energy. Available online at: http://www.fe.doe.gov/international/turkover.html.

Maden Tetkik ve Arama Genel Müdürlüğü (MTA) 2010. Inventory of Turkish lignites. MTA Publication, Ankara, 202 pp. (in Turkish).

Mann U., Korkmaz S., Boreham C.J., Hertle M., Radke M. and Wilkes H. 1998. Regional geology, depositional environment and maturity of organic matter of Early to Middle Jurassic coals, coaly shales, shales and claystones from the Eastern Pontides, NE Turkey, *International Journal of Coal Geology*, 37, 257-268.

Melikoğlu M. 2013. Vision 2023: Feasibility analysis of Turkey's renewable energy projection, *Renewable Energy*, 50, 570-575.

Ministry of Energy and Natural Resources (MENR) 2004. Energy Report of Turkey, Ankara.

Okay A. I., Şengör A.M.C. and Görür N. 1994. Kinematics history of the opening of the Black Sea and its effect on the surrounding regions, *Geology*, 22, 267-270.

Palmer C.A., Tuncali E., Denen K.O., Coburun T.C. and Finkelman R.B. 2009. Characterization of Turkish coals: a nationwide perspective, *International Journal of Coal Geology*, 60, 85-115.

Parkmaden 2012. Konya-Ilgın project. Available online at: http://www.cinergroup.com.tr/energy.

Salman M. 2010. Lignite possibilities of Ereğli-Ayrancı-Karapınar (Konya) region and determination of its economic value. *MSc. Thesis*, Çukurova University (unpublished).

Sözbilir H. 2005. Oligo-Miocene extension in the Lycian orogen: Evidence from the Lycian molasse basin, SW Turkey, *Geodinamica Acta*, 18(3-4), 255-282.

Şengör A.M.C. and Yilmaz Y. 1981. Tethyan evolution of Turkey: A plate tectonic approach, *Tectonophysics*, 75, 181-241.

Şengör A.M.C., Görür N. and Şaroğlu F. 1984. Strike-slip faulting and related basin formation in zones of tectonic escape: Turkey as a case study, In Biddle K.T., Christie-Blick N. (eds.), Strike-slip Faulting and Basin Formation, *Soc. Econ. Paleontol. Mineral. Sp. Pub.,* 37, 227-264.

Şengüler İ. 2010. Lignite explorations in Turkey: New projects and new reserves. *Proc. of the 27th Annual International Pittsburgh Coal Conference*, October 11-14, 2010, İstanbul.

Taşman, C.E., 1950. Stratigraphic distribution of bituminous appearing in Turkey, *Mineral Res. Expl. Bull. Turkey*, 40, 41-49 (in Turkish with English abstract).

Toprak S. 2009. Petrographic properties of major coal seams in Turkey and their formation, *International Journal of Coal Geology*, 78, 263-275.

Tuncalı E., Çiftci B., Yavuz N., Toprak S., Köker A., Gencer Z., Ayçık H. and Pahin N. 2002. *Chemical and Technological Properties of Turkish Tertiary Coals*, MTA Publication, Ankara, 401 pp.

Turkish Coal Enterprise (TKI) 2010. *Annual Report of 2010*, Ankara, 53 pp.

Turkish Hard-Coal Enterprise (TKK) 2009. *Annual Report of 2008*, Zonguldak, 103 pp.

Turkish Petroleum Corporation (TPAO) 2011. *Annual Report of Turkish Petroleum and Natural Gas Sector of Turkey in 2011*, Ankara, 23 pp.

Ünalan G. 2003. General evaluation of energy resources of Turkey, *Geological Engineering Journal*, 27 (1), 17-44 (in Turkish with English abstract).

Ünalan G. 2010. *Coal Geology*, MTA Publication, 41, Ankara, 556 pp.

Yilmaz A.O. and Uslu T. 2007. Energy policies of Turkey during the period 1923-2003, *Energy Policy*, 35, 258-264.

Δελτίο της Ελληνικής Γεωλογικής Εταιρίας, τομ. XLVII , 2013
Πρακτικά 13ου Διεθνούς Συνεδρίου, Χανιά, Σεπτ. 2013

Bulletin of the Geological Society of Greece, vol. XLVII 2013
Proceedings of the 13th International Congress, Chania, Sept. 2013

THE PROSPECT OF USING GREEK LIGNITE IN AN ENERGY PORTFOLIO RELATED TO POWER GENERATION

Papanicolaou C.[1], Typou J.[2], Ioakeim J.[2], Kotis Th.[1] and Foscolos A.[3]

[1] Institute of Geology & Mineral Exploration, 1st Spirou Louis St., Olympic Vilage, Acharnae, P.C. 13677,Athens, cassipapani@igme.gr, thkotis@gmail.com

[2] Public Power Corporation SA/West Macedonia Lignite Center,

i.typou@dei.com.gr, i.ioakeim@dei.com.gr

[3] Technical University of Crete / Department of Mineral Resources Engineering,Chania, Crete, foscolos@mred.tuc.gr

Abstract

The lignite-based power generation contributes 38% towards Greece's energy independence. Reducing the lignite use while simultaneously importing more expensive natural gas both government deficit and the cost of energy will increase. This surcharge is passed to consumers. Switching to renewable resources invokes an even greater fiscal imbalance, since the costs from the use of wind turbines and solar photovoltaic panels are 87 €/MWh, and 180–284 €/MWh respectively, while natural gas stands at 95 €/MWh and lignite-derived energy is 45 €/MWh.

In case of replacing a 300 MW lignite fed power unit with a 300 MW natural gas fed power unit, the loss in income will be 66,540,000 €/year. Coupled with the increased cost of natural gas (31,800,000 €/year) the total is 98,340,000 €/year in addition to the loss of 1235 jobs.

Greek authorities intends to replace lignite-fired plants having a total installed capacity of 2531 MW with equivalent natural gas-fired plants resulting in annual total deficit in excess of 787 M€. The targets set by the Greek Ministry of Energy and Climatic Changes to reduce emissions include halving Greek lignite-derived power output from 4800 MW to 2300 MW (>-52%). This move simultaneously increases Greek energy dependence on expensive foreign energy sources and will potentially provoke social unrest at the loss of 12500 jobs with loss of annual income on the order of 670 M€. However, if the existing power output from lignite-fed power plants is maintained, the penalty that PPC (Public Power Corporation) has to pay for the resultant CO_2 emissions is significantly smaller (300 M€ at 7.5 €/t of emitted CO_2/GWh.

Proceeding with the immediate reduction in lignite-fired energy results in economic and social catastrophe (annual income loss:-670 million € + annual CO_2 emissions penalty: 348 M€= -322 M€). Lignite-fired plants will become obsolete only when the CO_2 emissions penalty exceeds 63.5 €/t of emitted CO_2/GWh from a purely economic perspective.

Key words: Power units, CO_2, Natural gas.

Περίληψη

Ο λιγνίτης συμβάλλει στη μείωση της ενεργειακής εξάρτησης της Ελλάδας κατά 38%. Η μείωση της συμμετοχής του λιγνίτη στο ενεργειακό ισοζύγιο της χώρας προκαλεί αύξηση του κρατικού ελλείμματος λόγω εισαγωγής πανάκριβων ενεργειακών πρώτων υλών και βέβαια αύξηση του κόστους της κιλοβατώρας με μεγάλες επιβαρύνσεις στους καταναλωτές και στις επιχειρήσεις. Στο ίδιο αποτέλεσμα οδηγεί και η χρήση των ΑΠΕ διότι σήμερα το κόστος της παραγόμενης ενέργειας από τους αιολικούς σταθμούς είναι 87 €/MWh και από τους ηλιακούς 180-284 €/MWh έναντι των 95 €/MWh από αυτούς του φυσικού αερίου και 45 €/MWh από τους λιγνιτικούς.

Υπολογίζοντας τις απώλειες από την αντικατάσταση μιας λιγνιτικής μονάδας των 300 MW με μία μονάδα της ίδιας ισχύος, που θα λειτουργεί με φυσικό αέριο, θα υπάρξει απώλεια εισοδήματος 66.540.000 €/έτος στην οποία αν προστεθεί το κόστος αγοράς φυσικού αερίου, που είναι 31.800.000 €/έτος, θα ανέλθει σε 98.340.000 €/έτος και απώλεια 1235 θέσεων εργασίας.

Η προβλεπόμενη, όμως από το σενάριο επίτευξης στόχων αντιμετώπισης κλιματικής αλλαγής, μείωση της εγκατεστημένης ισχύος των λιγνιτικών μονάδων της τάξης του 52% (από 4800 MW σε 2300 MW) οδηγεί σε αύξηση της ενεργειακής εξάρτησης της χώρας, που σήμερα είναι στο 62%. Επίσης δημιουργείται κοινωνική αναταραχή με την απώλεια 12500 θέσεων εργασίας και απώλεια εισοδήματος, κυρίως στη Δυτική Μακεδονία, της τάξης των 670 Μ€/έτος.

Αν διατηρηθεί η σημερινή ισχύς των λιγνιτικών μονάδων το κόστος/πρόστιμο των εκπομπών του CO_2 που επιβαρύνει την ΔΕΗ (7,5 €/t εκπεμπόμενου CO_2), δεν υπερβαίνει τα 300 Μ€//έτος, δεδομένο που καθιστά την αντικατάσταση των λιγνιτικών μονάδων από αυτές του φυσικού αερίου ή των ανεμογεννητριών εντελώς ασύμφορη οικονομικά (ετήσια απώλεια εισοδήματος:-670 Μ€/+ετήσιο κόστος ρύπων:348 Μ€/= -322 Μ€/έτος) και κοινωνικά μη αποδεκτή λύση. Η ηλεκτροπαραγωγή από τις λιγνιτικές μονάδες θα γίνει αντιοικονομική και θα μπορεί να αντικατασταθεί από μονάδες ηλεκτροπαραγωγής με φυσικό αέριο εφ' όσον το πρόστιμο για τις εκπομπές υπερβεί τα 63,5 €/t εκπεμπόμενου CO_2.

Λέξεις κλειδιά: *Μονάδες ηλεκτροπαραγωγής, CO_2, Φυσικό αέριο.*

1. Introduction

The use of lignite for power generation in Greecebegan in 1953 following the construction of the 125 MW power plants at Aliveri, Evia. To day there are 19 power units throughout Greece with a total installed capacity of 4826 MW. These units are fed with 58 Mt of lignite/year from the surrounding coal mines. The Lignite Center of Western Macedonia in Greece directly employs 7780 workers, while each job creates a further 3.28 (Technical Chamber of Greece, 2012) indirect jobs in the region for a total of 25,518 jobs.

Lignite contributes 38% to Greece's energy independence (Figure 1). Decreasing its relative importance in the energy portfolio will increase the budget deficit due to reliance on imported energy raw materials which will increase the cost of generated kWh.

Lignite feedstock represents the cheapest cost per MWh (45 €), followed by wind turbines (87 €/MWh), natural gas **(**95 €/MWh) and solar photovoltaic (180-284 €/MWh) (Operator of Electricity Market, 2012; Regulatory Authority for Energy, 2012). Currently, renewable resources remain a very expensive option.

Greece's lignite reserves are presented in Table 1 while the distribution of the mineable ones is shown in Figure 2.

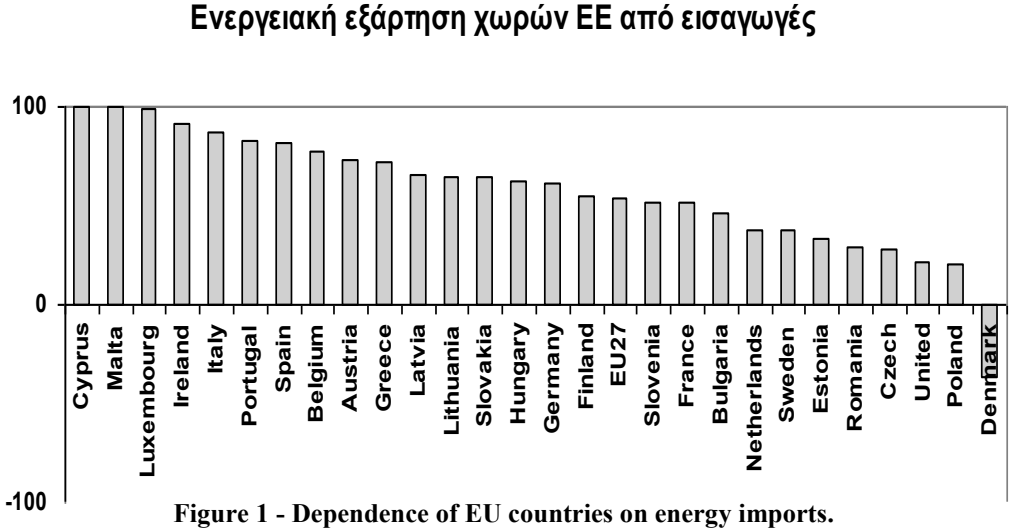

Figure 1 - Dependence of EU countries on energy imports.

Table 1 - Lignite reserves in million tonnes.

A.	PROVEN	9300
	• MINEABLE	3320
	• NON MINEABLE	2850
	• PHILIPPI PEAT	1700[(1)]
	CONSUMED SINCE 1953	1350
B.	INDICATED	1600
C.	INFERRED	2300

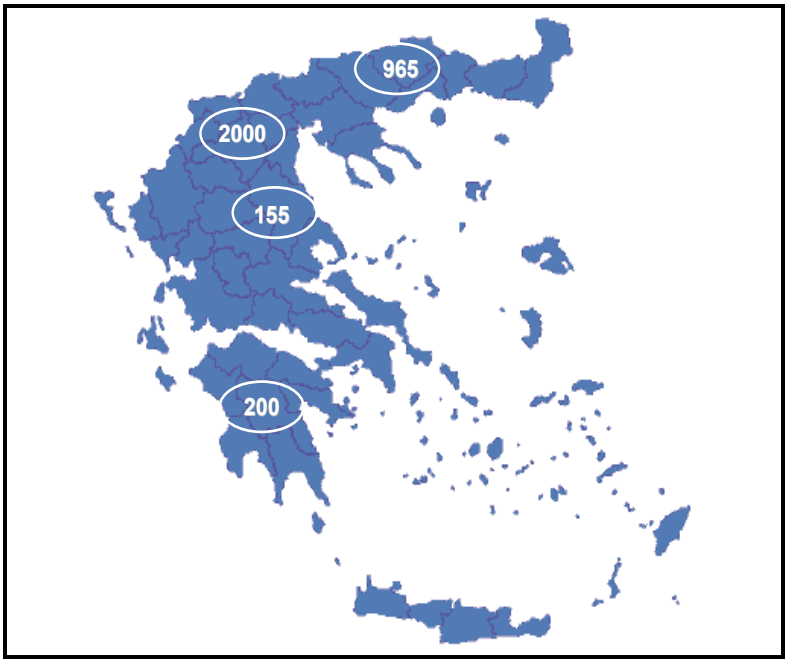

Figure 2 – The lignite deposits throughout Greece (in Mt) throughout Greece (Papanicolaou, 2001).

[(1)] 4300 Mt of peat having, equivalent calorific value to Ptolemais lignites, 1350 kcal/kg

Annual lignite production from the Lignite Center of Western Macedonia (LCWM) and the Lignite Center of Megalopolis, Peloponnese (LCMP) as well as their contribution to power generation in TWh are given in Tables 2 and 3.

The contribution of domestic lignite to the national economy should not be underestimated. Since 1960 a single area (Western Macedonia) has produced the energy equivalent of 1.15 billion barrels of oil, generating 562,000 GWh thus contributing $49.7 billion (inflation-adjusted) to the Greek economy. It is considered that further exploitation of the remaining lignite reserves until 2054 will add to the economy $26 billion not including the lignite reserves of Drama Basin (Philippi peatland) and those encountered in Elassona, Thessaly.

Table 2 - Lignite production (in kt) from the Lignite Center of Western Macedonia (LCWM) and the Lignite Center of Megalopolis, Peloponnese (LCMP) from 2006 to 2011 (Public Power Corporation of Greece S.A., 2011).

	2006	2007	2008	2009	2010	2011	2012
LCWM	49,000	49,300	40,250	50,300	43,200	47,400	52,100
LCMP	13,500	14,100	13,200	11,500	10,400	9,350	9,600
TOTAL	**62,500**	**63,400**	**53,450**	**61,800**	**53,600**	**56,750**	**61,700**

Table 3 - Electricity generation (in TWh) and percent contribution of each source to the energy grid in Greece (European Union, 2012).

Type/year	Units	2004	2005	2006	2007	2008	2009	2010	2011
Lignite	TWh	35.38	35.54	32.26	34.68	33.36	34.19	30.8	27.57
	%	59.6	59.2	53.1	54.6	52.35	55.7	53.66	49.5
Natural Gas	TWh	9	8.2	10.61	13.77	13.8	11.02	9.8	14.85
	%	15.20	13.60	17.45	21.70	21.65	18.00	17.07	26.70
Oil	TWh	8.4	9.2	9.6	9.6	10	7.7	6.1	4.77
	%	14.10	15.30	15.79	15.20	15.70	12.50	10.60	8.60
Hydro	TWh	5.2	5.6	6.48	3.4	4.15	5.65	7.5	3.68
	%	8.80	9.40	10.66	5.30	6.50	9.20	13.07	6.60
Renewable	TWh	1.4	1.5	1.84	2.03	2.45	2.8	3.2	4.79
	%	2.30	2.50	3.00	3.20	3.80	4.60	5.60	8.60
TOTAL	**TWh**	**59.4**	**60**	**60.8**	**63.5**	**63.7**	**61.4**	**57.4**	**55.66**
	%	**100**	**100**	**100**	**100**	**100**	**100**	**100**	**100**

2. The Future of Greek Lignites in an Energy Portfolio Related to Power Generation as Perceived by the Scenario to Meet Climate Change

2.1. Financial and Social Impact

The Greek government is currently attempting to respond to binding EU requirements to confront Climate Change. To this end, the Ministry of Environment, Energy and Climate Change Committee 20-20-20 on June 21, 2010 has proposed phased changes to the energy resource portfolio for the period until 2030 (Ministry of Environment, Energy and Climate Change, 2010).This initiative results from EU "Energy 2020" guidelines aimed at promoting competitive, viable and secure energy while at the same time reducing greenhouse gas emissions. The guidelines stipulate

- 20% reduction in greenhouse gas emissions below 1990 levels
- 20% reduction of the energy needs to be produced from renewable energy sources
- 20% reduction in primary energy use to be achieved by improving energy efficiency

The measures should be implemented in such a way that economic and social impacts are minimized (Ministry of Environment, Energy and Climate Change, 2010). Hence, the scenario proposed by the Greek Committee from the Ministry of Environment, Energy and Climate Change (Table 4) shows the following shortcomings.

Table 4 - Scenario for meeting the CO_2 emission targets set by the EU by 2030 (Ministry of Environment, Energy and Climate Change, 2010). Installed capacity in MW from various energy sources.

ENERGY SOURCE	2010	2015	2020	2025	2030
LIGNITE	4,826	3,992	3,363	2,295	2,295
NATURAL GAS	3,456	5,909	7,312	8,412	9,259
OIL	2,146	1,381	1,378	1,378	1,325
BIOGAS	60	120	250	370	500
HYDROELECTRIC	3,237	3,615	4,531	4,531	4,531
WIND POWER	1,327	4,303	7,500	8,750	10,000
PHOTOVOLTAIC	184	1,270	2,200	3,167	3,833
GEOTHERMAL	0	20	120	340	400
SOLAR COMB. SYSTEMS	0	30	250	380	510
TOTAL	**15,236**	**20,640**	**26,903**	**29,623**	**32,653**

First, instead of implementing a reduction of energy consumption by 20% between the years 2010 to 2030 the proposal aims to double the installed power capacity from 15,236 MW in 2010 to 32,653 MW by 2030. This is hard to justify in the face of far more modest increases in projected population growth and industrial output within the next 20 years. On the contrary, the last 3 years have seen the trend for increased energy demand reversed in the face of economic crisis, high unemployment, decrease in industrial output, and overseas migration of the working force. Doubling the installed power capacity is moreover contrary to EU directives for future energy management.

Secondly, the EU directive 20-20-20 proposes that from the total power capacity to be installed by 2030 over 59% (Table 4) should be derived from the renewable resources. About 30.6% will come from wind turbines, 12% from solar panels and the remaining 17.4% from hydro, geothermal and others. This not only renders the electrical grid unstable (Regulatory Authority for Energy, 2011) but also introduces energy sources which produce very expensive electricity. This high cost will be passed on to consumers

Third, using as an excuse the reduction of CO_2 emissions in order to minimize the greenhouse effect, introduces overwhelmingly the consumption of imported natural gas, 28.4%, at a delivery price of 16 $/GJ or 12.31 €/GJ[(2)] (National Natural Gas System Operator S.A., 2012) when the price of locally produced lignite is 3.5 $/GJ or 2.7 €/GJ (Kolovos, 2010) thus creating immense social and economic problems not only in western Greek Macedonia but in the whole country.

The EU guidelines did not specify what measures should be taken to reduce the CO_2 emissions from the power plants but to reduce it in any way that Greek authorities considers appropriate. However in order to reduce CO_2 emissions by 20%, the so-called 20-20-20 Greek Committee has decided to reduce coal fired power by 50%, creating a "vital space" for the introduction of very expensive energy sources thus neglecting the colossal social and economic impact without study-

[(2)] 1 € = 1.30 $

ing alternative and less painful ways of achieving the directives set by EU. Specifically by substituting one 300MW coal fired power unit with an energy efficiency of 34% with an equivalent power unit which burns natural gas:

- Public Power Corporation S.A. of Greece (PPC) loses 31,820,000 € (annual cost of natural gas 93,170,000 € [(3)] - annual cost of 4,090,000 t of lignite X 15 €/t = 61,350,000 €) (Kolovos, 2010; National Natural Gas System Operator S.A, 2012; Technical Chamber of Greece, 2012).
- 1235 jobs are lost (each 300 MW coal fired power unit creates 1559 jobs while each 300 MW power unit which uses natural gas creates 324 jobs) (Technical Chamber of Greece, 2012).
- An annual income of 66.54 M€ is lost (Loss of 1559 jobs leads to an annual income loss of 84 M€ (Technical Chamber of Greece, 2012) while the creation of 324 jobs from the equivalent natural gas power plant yields an annual income of 17.46 M€).

Consequently, the net loss is 66.54 M€/year. Hence by decreasing the installed power of the coal fed power plants from 4828 MW, to 2295 MW (Table 4), and counterbalancing this with power plants which are fed by natural gas (equivalent of eight 300MW coal fired power units) the net financial losses incurred by the Public Power Corporation S.A. of Greece will be 254,560,000 €. This is attributed to the price difference of the feedstock being $3.5/GJ or 2.7 €/GJ for the indigenous lignite and 16 $/GJ or 12.31 €/GJ, for the imported natural gas. On top of it, there is a net annual income loss of 532,320,000 € (loss of Income of 66.54 €/unit of 300MW unit X 8 units = 532 M€). This means a grand total annual loss of 787 M€.

If the new natural gas fed power plants are not going to be located in Greek Western Macedonia, 12500 jobs will be lost along with an annual income loss of 670 M€.

The Committee however goes one step further by proposing the power plants fed with natural gas to reach 9259 MW, which means that, besides the existing ones of 3456 MW and the substitution of another 2531 MW lignite fired power plants by natural gas, 3272 MW natural gas fired power plants are going to be added. This means that besides the horrendous construction cost, Public Power Corporation S.A should pay for feeding the additional new 5803 MW with natural gas the exuberant price of 1.8 billion € (5803 MW X 93,170,000 € [(3)] /300 MW). One wonders from where the money will come for such an undertaking when Public Power Corporation S.A (PPC) tries to reduce its dependence from natural gas. PPC used 2,400,000 kNm^3, 1,700,000 kNm^3 and 1,000,000 kNm^3 of natural gas in 2007, 2009 and in 2011 respectively (Public Power Corporation, 2012). So the Greek Committee proposes the installation of more natural gas power plants that is complete dependence on the imported and very expensive natural gas.

Taking into account that the mean average CO_2 emissions in the last 5 years from the lignite fired plants are 40 Mt (mean price of the last five years) (United Nations Framework Convention on Climate Change, 2012) and that the penalty for it is 7.5 €/t of emitted CO_2 (September 2012), the total annual sum to be paid by the Public Power Corporation S.A. for CO_2 emissions, reaches 300 M€ (The price of allowances is 3.5 €/t CO_2 in March 2013). As a result, it is more preferable for Public Power Corporation S.A. of Greece to pay the annual penalty of 300 M€ for CO_2 emissions than assume an annual loss of 787 M€. And pay the same amount of penalty than lose 12500 jobs in Western Greek Macedonia leading to an annual income loss of income of 670 M€.

2.2. CO_2 Emissions

Based upon the guidelines of the European Committee 20-20-20 CO_2 emissions from all power plants which are 46 Mt (mean price of the last five years) (United Nations Framework Convention

[(3)] Each 300 MW power unit using natural gas as feedstock and with an energy efficiency of 39% requires 7,568,640 GJ/year. Hence 7,568,640 GJ/year × € 12.31/GJ = 93,170,000 € the cost of feedstock

on Climate Change, 2012) should be reduced by 20% taking as a baseline the CO_2 emissions in 1990 which were 40 million tonnes. This implies that by 2030 CO_2 emissions should not be more than 32 Mt.

By following the scenario which is presented in Table 4, CO_2 emissions instead of being reduced to 32 Mt increase to 48.72 Mt (14800 GWh from the 2295 lignite fired power plants X 1100 t of CO_2/GWh = 16.28 Mt of CO_2 (Figure 3). Plus, 64887 GWh(4) from the 9259 MW natural gas power plants X 500 t of CO_2/GWh = 32.443 Mt. So by following the scenario indicated in Table 4, instead of having reduction of the CO_2 emissions an increase is got by 52% from the Directive's target. Furthermore, the operation of lignite fired power plants will become uneconomical when the penalty for CO_2 emissions will reach the tag of 63.5 €/t of emitted CO_2 (Technical Chamber of Greece, 2012). Since this price may never be reached the guidelines set up by the Greek Committee 20-20-20 of the Ministry of Energy and Climatic Changes (Table 4) should be radically revised.

2.3. Amount and Cost of Imported Natural Gas

The amount of imported natural gas for the 9259 MW power plants is huge. Each 300 MW power plants need 7500000 GJ. Therefore the 9259 MW power plants require 231,475 X 10^6 GJ. Since 1GJ is equal to 1000 cubic feet of natural gas then the amount of natural gas equals 231,475 X 10^9 ft^3 or 6.55 Gm^3. Today Greece imports something in the order of 3.5 Gm^3. From where are we going to get the required amount of natural gas, 4.11 Gm^3, for the new 5803 MW power plants (145,075 X 10^6 GJ = 145,075 X 10^9 cubic feet of natural gas /35.315 cubic feet of natural gas/m^3 = 4.11 Gm^3 of natural gas). The annual cost of importing 231,475 X 10^6 GJ is calculated on the basis of $ 16/GJ. This totals 3.7 billion $ or 2.85 billion €. And the annual penalty for the CO_2 emissions will increase from the to days 348 M€ (46,400,500 t of emitted CO_2 X 7.5 €/t of emitted CO_2/GWh = 348 M€) to 366 M€.

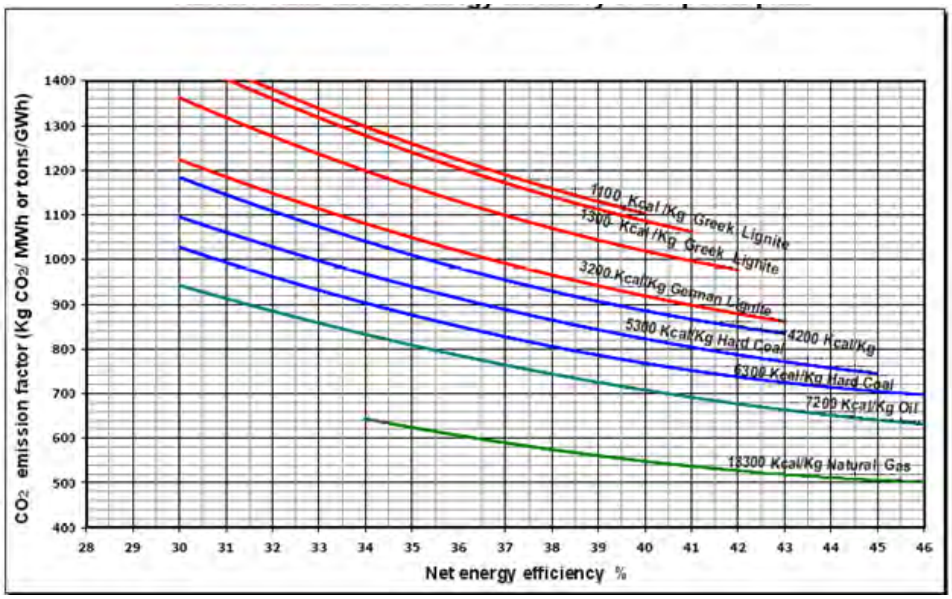

Figure 3 - Correlation of CO_2 emissions (kg CO_2/MWh or t/GWh) with the type of coal and hydrocarbon burnt its lower calorific value and the energy efficiency of the power plant (Technical Chamber of Greece, 2012).

(4) Each 300MW unit which is fed with natural gas and with an energy efficiency of 39% produces, annually, 2,102.4 GWh. Hence the 9259 MW power stations will produce 9259 MW X 2,102.4 GWh /300MW = 64,887.072 GWh

Hence, the efforts of the Greek government to respond to the binding requirements to confront the Climatic Changes, Ministry of Environment, Energy and Climate Change Committee 20-20-20 in June 21, 2010 by advancing the energy portfolio which appears on Table 4 should be radically revised otherwise we will be facing a social unrest, especially in Western Macedonia, Greece will totally lose its energy independence since the country will rely exclusively on imported energy sources, Public Power Corporation of Greece S.A. will go bankrupt, the power grid will become totally unstable due to the excessive introduction of wind turbines while the price of electricity will skyrocket.

In order to conform to the European 20-20-20 guidelines the following are proposed:

- Reduction of energy consumption from 60340 GWh which is the mean average of the last 5 years (Table 3) to 48272 GWh.
- 55% of the 48272 GWh will be derived from newly constructed lignite fed power plants having an energy efficiency of 40%. The amount of CO2 emitted will be 29.21 Mt/year (26550 GWh X 1100 t CO2/GWh).
- 30% of the 48272 GWh, which is 14483 GWh will be derived from renewable resources. Particularly, 15% will be the contribution from wind turbines having an installed power of 4000 MW and 15% from the hydroelectric power with an installed capacity of 2600 MW while CO2 emissions will be zero.
- 15% of the 48272 GWh that is 7241 GWh will be derived from natural gas power plants with an installed capacity of 3000 MW and energy efficiency of 43% to 44% thus emitting 3.69 Mt of CO2/year (7241GWh X 510 t CO2/GWh).

3. Conclusions

In the present work a detailed study of the future energy portfolio, which is related to power generation as perceived by the Greek Committee 20-20-20, set up by the Ministry of Energy and Climatic Changes, for meeting the climatic changes, is examined in relation to the European 20-20-20 guidelines which stipulates reduction of power consumption by 20%, reduction of CO_2 emissions from power plants by 20% and power production by renewable resources 20%. Unfortunately the goals suggested by the European guidelines were not implemented and the necessity of revision is imperative. Specifically,

- It doubles, unjustifiably, the installed capacity for power generation from 15236 MW to 32653 MW contrary to the EU recommendations which stipulates 20% reduction.
- Introduces into the power system more than 60% the renewable resources. Over 42 % is the contribution from wind turbines and photovoltaic systems and the remaining 17.4% from hydro and geothermal that renders the electrical grid unstable and introduces energy sources for power generation which produce very expensive electricity, >87 €/MWh for wind turbines and 180 €/MWh to 284 €/MWh for solar panels versus 45 €/MWh from lignites
- Presupposes the import of additional 4.11 Gm^3 of natural gas to feed the new 5803 MW power plants at an annual cost of 2.32 billion $ or 1.78 billion €. Today Greece imports 3.5 Gm^3 of natural gas.
- Imposes on Public Power Corporation of Greece S.A. to buy expensive natural gas at a price of 16 $/GJ (12.31 €/GJ) thus spending annually 3.7 billion $ or 2.85 billion €.
- Increases CO2 emissions to 48.72 Mt/year instead of reducing it to 32 Mt as required by the EU guidelines. Thus promoting a 52% increase of CO2 emissions.
- Promotes an annual income loss of 670 M€ derived from the laying off of 12500 jobs in western Greek Macedonia thus creating a social unrest something that the European guidelines do not stipulate.

In order to conform to the European 20-20-20 guidelines the following are proposed:

- Reduction of energy consumption from 60340 GWh which is the mean average of the last 5 years to 48272 GWh.
- 55% of the 48272 GWh will be derived from newly constructed lignite fed power plants having an energy efficiency of 40%. The amount of CO2 emitted will be 29.21 Mt/year (26550 GWh X 1100 t CO2/GWh.
- 30% of the 48272 GWh that is 14483 GWh will be derived from renewable resources. 15% will be the contribution from wind turbines having an installed power of 4000 MW and 15% from the hydroelectric power with an installed capacity of 2600 MW. CO2 emissions will be zero.
- 15% of the 48272 GWh that is 7241 GWh will be derived from natural gas power plants with an installed capacity of 3000 MW and energy efficiency of 43% to 44% thus emitting 3.69 Mt of CO2/year (7241 GWh X 510 t CO2/GWh)

Thus following to a large extend the guidelines 20-20-20 of the European Union, energy consumption is reduced by 20%, renewable resources have a share in power generation of over 20% and CO_2 emissions are reduced almost by 20%.

The net result is minimal social and economic impact in Western Greek Macedonia, stable power grid, large energy independence from imported energy sources such as natural gas and huge annual financial savings for Public Power Corporation of Greece S.A. in the order of 3 billion €.

4. Acknowledgments

Authors would like to thank Dr. Andy Mort, geochemist, of the Geological Survey of Canada-Calgary for editing this paper.

5. References

European Union, 2012. Available online at: http://ec.europa.eu/energy/observatory/countries/countries_en.htm

Kolovos Ch. 2010. « Η θέση του Ελληνικού λιγνίτη στο ενεργειακό ισοζύγιο της χώρας» Διημερίδα Σωματείου " ΕΝΩΣΗ", 29-30 Οκτωβρίου, 2010, Κοζάνη, Πτολεμαίδα, Ελλάς, σελ. 53.

Ministry of Environment, Energy and Climate Change, 2010. «Ανάλυση Ενεργειακών Σεναρίων διείσδυσης των τεχνολογιών ΑΠΕ στο Ενεργειακό Σύστημα και Επίτευξης των Εθνικών Στόχων του 2020 με χρήση των μοντέλων MARKAL, ENPEP, WASP, COST, ΥΠΕΚΑ, Επιτροπή 20-20-20, Ιούλιος 2010», Πίνακας 2.3.6 σελ. 18.

National Natural Gas System Operator (DESFA) S.A, December 2012. Tariff Regulation of the Basic Activities of the National Natural Gas System, Available online at: http://www.desfa.gr/default.asp?pid=535&la=2

Operator of Electricity Market December, 2012. Available online at: http://www.lagie.gr/systima-eggyimenon-timon/ape-sithya/adeiodotiki-diadikasia-kodikopoiisi-nomothesias-ape/periechomena/times-energeias-apo-ape-sithya-plin-fb/

Operator of Electricity Market S.A., December, 2012. Available online at: http://www.lagie.gr/systima-eggyimenon-timon/ape-sithya/adeiodotiki-diadikasia-kodikopoiisi-nomothesias-ape/periechomena/times-energeias-apo-ape-sithya-plin-fb/times-energeias-apo-fb-ektos-eidikon-programmaton/

Papanicolaou, C., 2001. Atlas of Greek coals. Coal petrographic parameters. Quality-Biomarkers (in Greek), Institute of Geology and Minelal Exploration, Athens, Greece 418 p. ISBN 960-87453-1-4

Public Power Corporation, 2012. Available online at: www.dei.gr

Public Power Corporation of Greece S.A. Division of Mines, 2011.

Regulatory Authority for Energy, 2012. «Τελικές Προτάσεις της Ρυθμιστικής Αρχής Ενέργειας για την αναδιοργάνωση της εγχώριας αγοράς ηλεκτρικής ενέργειας», Νοέμβριος 2012.

Regulatory Authority for Energy, 2011. «Μελέτη επιπτώσεων στη λειτουργία του Ελληνικού Συστήματος από αιολική διείσδυση 5 έως 8 GW μέχρι το έτος 2025: προϋποθέσεις και εκτίμηση του κόστους ένταξης» (Μελέτη που έχει ανατεθεί από τη ΡΑΕ, Φεβρουαριος 2011). Available online at: http://www.rae.gr/site/categories_new/renewable_power/ape_penetration.csp

Technical Chamber of Greece, West Macedonia Branch, 2012. «Εκτίμηση του κόστους μετάβασης της Δυτικής Μακεδονίας σε Καθεστώς χαμηλής λιγνιτικής παραγωγής». ΤΕΕ Τμήμα Δυτικής Μακεδονίας, Ιούλιος 2012.

United Nations Framework Convention on Climate Change, 2012. Available online at: http://unfccc.int/national_reports/annex_i_ghg_inventories/national_inventories_submissions/items/6598.php

Δελτίο της Ελληνικής Γεωλογικής Εταιρίας, τομ. XLVII , 2013
Πρακτικά 13ου Διεθνούς Συνεδρίου, Χανιά, Σεπτ. 2013

Bulletin of the Geological Society of Greece, vol. XLVII 2013
Proceedings of the 13th International Congress, Chania, Sept. 2013

GEOLOGICAL SOLUTIONS CONCLUDED BY PETROLEUM GEOCHEMICAL DATA IN WESTERN GREECE

Rigakis N.[1], Karakitsios V.[2], Marnelis F.[1] and Sotiropoulos Sp.[1]

[1]Hellenic Petroleum S.A. Exploration and Production of Hydrocarbons, 8A, Chimaras Str., 15125, Maroussi, Athens, nrigakis@helpe.gr, fmarnelis@helpe.gr, ssotiropoulos@helpe.gr

[2]National and Kapodistrian University of Athens, Faculty of Geology and Geoenvironment, Department of Hist. Geology - Paleontology, vkarak@geol.uoa.gr

Abstract

A detailed petroleum geochemical study has been performed in the previous years in the Western Greece. Several source rock horizons have been identified, the oil window has been calculated for the most significant sub-basins and the oil correlation study has distinguished the different oil groups of the area, generated from different hydrocarbon sources. These results are very significant and useful for the oil exploration. But, further to these, some more geochemical observations can also be very important on solving some geological problems of the area.

- *A major problem is the deposition and preservation of the organic matter in the Western Greece.*
- *The dolomitization in relation with the oil generation is also an issue.*
- *Another issue is the calculation of the eroded overburden formations thickness.*
- *The Paleogeothermal gradient determination is also very important.*

The last two parameters are absolutely necessary for organic matter maturity calculations.

The study of all the above parameters completes the geochemical study of the Western Greece, and in relation with other geological studies can provide solutions in the petroleum exploration of the area.

Key words: *organic matter, paleogeothermal gradient, dolomitization, hydrocarbon exploration.*

Περίληψη

Τα προηγούμενα χρόνια έχει πραγματοποιηθεί μια λεπτομερής γεωχημική μελέτη πετρελαίου στη Δυτική Ελλάδα. Εντοπίστηκαν αρκετοί ορίζοντες πιθανών μητρικών πετρωμάτων πετρελαίου, προσδιορίστηκε το παράθυρο πετρελαίου στις πιο σημαντικές υπολεκάνες, ενώ από τη μελέτη συσχετισμού πετρελαίων προσδιορίστηκαν οι διαφορετικές ομάδες πετρελαίου της περιοχής, που έχουν παραχθεί από τα διαφορετικά μητρικά πετρώματα υδρογονανθράκων. Τα αποτελέσματα αυτά είναι πολύ σημαντικά και απαραίτητα για την έρευνα πετρελαίου στην περιοχή. Όμως, εκτός από αυτά τα δεδομένα, κάποιες επιπλέον γεωχημικές παρατηρήσεις μπορεί να

αποβούν εξίσου σημαντικές στην επίλυση ορισμένων γεωλογικών προβλημάτων της Δυτικής Ελλάδας.

- *Ένα πολύ σημαντικό πρόβλημα είναι η απόθεση και διατήρηση του οργανικού υλικού στις λεκάνες της Δυτικής Ελλάδας.*
- *Η δολομιτίωση σε συνάρτηση με τη γένεση πετρελαίου είναι ένα πρόβλημα.*
- *Ένα άλλο θέμα είναι ο υπολογισμός του πάχους που διαβρώθηκε από τους υπερκείμενους σχηματισμούς.*
- *Ο προσδιορισμός της παλαιογεωθερμικής βαθμίδας είναι επίσης πολύ σημαντικός.*

Οι δύο τελευταίοι παράμετροι είναι απόλυτα απαραίτητοι για τον προσδιορισμό της ωριμότητας του οργανικού υλικού.

Η μελέτη όλων των παραπάνω παραμέτρων συμπληρώνει τη γεωχημική μελέτη της Δυτικής Ελλάδας, και σε συνδυασμό με άλλες γεωλογικές μελέτες μπορεί να δώσει λύσεις σε προβλήματα που σχετίζονται με την έρευνα υδρογονανθράκων στην περιοχή.

Λέξεις κλειδιά: *οργανικό υλικό, παλαιογεωθερμική βαθμίδα, δολομιτίωση, έρευνα υδρογονανθράκων.*

1. Introduction

Geological provinces of Greece are subdivided in to geotectonic zones, based on their paleogeographic position and the evolution of their formations. The Gavrovo, Ionian and Paxi (or Pre-Apulian) are the most External (western) zones of Greece (Figure 1). They are mainly consisted from sedimentary rocks, and for this reason their petroleum generation potential had been studied in details; their organic matter quantity, quality and maturity had been studied, as well as the timing of oil generation and the origin of the surface oil seeps and drilled oil shows (Rigakis, 1999; Rigakis & Karakitsios, 1998; Karakitsios & Rigakis, 2007; Rigakis et al., 2007). The results are helpful for the identification of the petroleum potential of Western Greece.

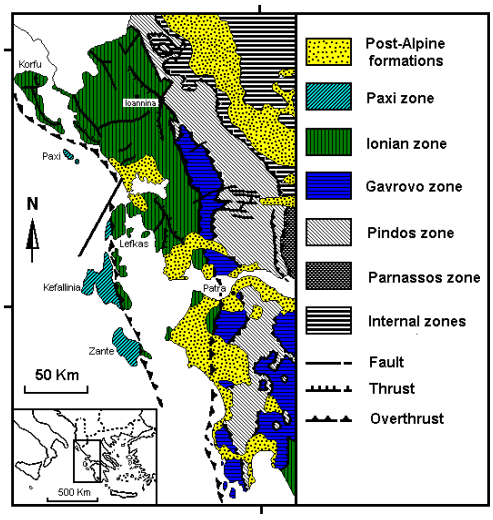

Figure 1 – Geotectonic map of Western Greece.

The Gavrovo zone consists of platform carbonates, deposited in a high-energy intertidal environment. The outcropping sequence comprises Lower Cretaceous to Eocene limestones followed by the Oligocene flysch (BP, 1971). The Ionian zone is a basin which was formed during the Middle Lias between Apulian and Gavrovo platforms. It can be divided into the Internal (eastern), Central and External (western) Ionian (IGRS-IFP, 1966). The Ionian zone is made up of three distinct stratigraphic sequences (Karakitsios, 1995): The pre-rift sequence is represented by

Triassic evaporites, and overlain Foustapidima and Pantokrator limestones (Middle Triassic-Early Liassic). The syn-rift sequence is characterized by unconformities and great thickness and facies variations. The complete sequence includes the Siniais and Louros limestones (Pliensbachian), the Ammonitico Rosso or Lower Posidonia Beds (Toarcian-Aalenian), the "Limestones with Filaments" (Bathonian-Callovian) and the Upper Posidonia Beds (Oxfordian-Tithonian). The post-rift sequence comprises the Vigla limestones (Lower Cretaceous), the Senonian and the Paleocene-Eocene limestones followed by Oligocene flysch. Clastic sediments of Aquitanian and Burdigalian overly unconformably the flysch, in the central and western areas of the Ionian zone (IGRS-IFP, 1966). In Paxi zone the older formations are Upper Triassic dolomites, followed by Lower Jurassic evaporites and limestones, Middle-Upper Jurassic limestones, anhydrites and shales, Lower Cretaceous carbonates, Upper Cretaceous limestones, Paleocene-Eocene limestones, Oligocene limestones and Miocene-Pliocene marly limestones and marls (Bornovas, 1964; Dermitzakis, 1978; Rigakis, 1999). In Figure 2, the simplified stratigraphic columns of the External zones are presented, and the stratigraphic position of the hydrocarbon source rocks is indicated.

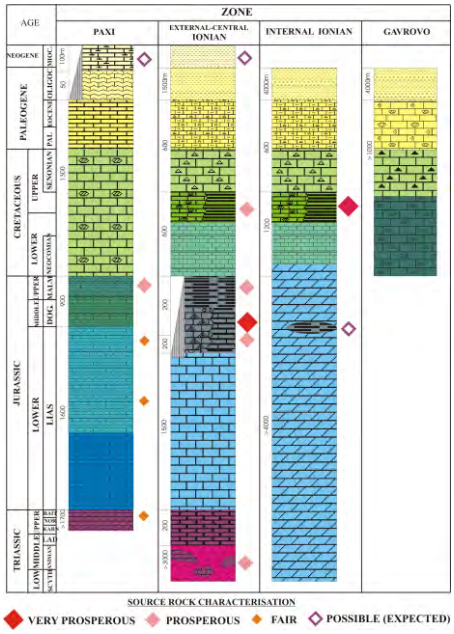

Figure 2 – Stratigraphy and hydrocarbon source rocks in Western Greece.

2. Hydrocarbon Source Rocks Presence and Maturity

The main hydrocarbon source rocks in the Western Greece are the Vigla shales, the Posidonia Beds and the Triassic shale fragments in Ionian zone and the Upper Jurassic shales in Paxi zone (Rigakis, 1999; Rigakis & Karakitsios, 1998; Karakitsios & Rigakis, 2007).

Especially in the Internal Ionian zone the main source is the Vigla shales, member of Vigla formation, dated in the interval Albian-Cenomanian, which are rich to very rich in organic matter. The most promising horizons are found in two intervals. Zone A': 3120-3270m, with total organic carbon (TOC) up to 11.7% and petroleum potential (PP) up to 60.9 mg/g. Zone B': 3375-3580m, with TOC up to 4.8% and PP up to 23.5 mg/g. The very high hydrogen indexes in relation to the very low oxygen indexes and also their maceral content indicate a type I to II organic matter, capable for oil generation. The differences in the results between the two intervals and the increased maturity show that, these horizons are indeed two different ones (Rigakis, 1999).

The Vigla source rocks are mature in the location of Agios Georgios-3 well, drilled in Arta syncline, since the onset of oil generation is identified at 2950m depth, as concluded from vitrinite reflectance (Ro%) measurements and confirmed by Rock Eval data (Tmax and PI), and biomarker maturity ratios. The oil window in the deeper parts of the sub-basin is calculated by maturity models to be in the interval 3450-5600m depth (Rigakis, 1999).

In the Central and External Ionian the most prosperous hydrocarbon source rock is the Lower Posidonia Beds (Rigakis, 1999, Rigakis & Karakitsios, 1998), which contain high quantities of organic matter in many outcrops and in all the wells where they were drilled. The higher values are measured in the thin-bedded marls of Dragopsa-1 well; TOC up to 19.1%, PP up to 125.8 mg/g. Their organic matter type is I to II capable for generation of high quantities of oil.

Secondary but quite significant source rocks are the Vigla shales, which are rich in organic matter in outcrops and drilled wells. Another quite prosperous source rock is the Upper Posidonia Beds which also contain high petroleum potential. Finally the shale fragments incorporated in the Triassic breccias and gypsum, which are the surface expression of Triassic evaporites (Karakitsios & Pomoni-Papaioannou, 1998), are very rich in TOC (up to 16.1%) and in PP (up to 98.8mg/g), with a type I organic matter, capable for oil generation in the interval 1250-1270m of Ioannina-1 well (Karakitsios & Rigakis, 1996).

Several parameters have been examined for estimating the thermal maturity of the potential source rocks. The maturity of the outcrop samples is generally low since these horizons have been emerged prior to the maturation of their organic matter. More reliable measurements have resulted from wells' samples. According to that the oil window in the deeper parts of Botsara syncline is estimated to be in the interval 3750-5800m. Based on this observation, Posidonia Beds are mature in terms of oil generation. The degree of organic matter maturation is generally low, but it favors the generation and preservation of oil in deep areas from possible source rocks under the Triassic evaporites. In areas where extensive Triassic formations are outcropping, the oil window is found in shallow depths, between 1000-3600m (Rigakis, 1999; Rigakis & Karakitsios, 1998).

In the Paxi (Pre-Apulian zone) the most prosperous source rock is the Aptici shales of the Middle-Upper Jurassic carbonates, as concluded from Paxi-Gaios-1X well. There have been identified horizons very rich in organic matter, with a TOC up to 5.5%, PP up to 41.5 mg/g and a type II organic matter capable for oil generation. Secondary source rocks have been identified inside the Lower Jurassic and Triassic formations, but their organic matter has been decreased due to their high maturity (Rigakis, 1999; Karakitsios & Rigakis, 2007).

Their organic matter maturity had been calculated by Vitrinite reflectance (Ro%) measurements; the oil window is found in the interval 1850-3260m depth. This depth is also confirmed by biomarker maturity ratios. In the deeper parts of Paxi basin the oil window is estimated to be in the interval 5600-7250m (Rigakis, 1999; Karakitsios & Rigakis, 2007).

3. Geological Observations Based on Geochemical Data

3.1 Deposition and Preservation of High Organic Matter Amount

The deposition and preservation of high organic matter quantities in Vigla shales is characteristic for this formation in the Internal Ionian zone. According to the published data and based on our observations, this procedure can be attributed:

1. To the anoxic events of Cenomanian/Turonian OAE2, early Albian Paquier OAE1b and Aptian-Albian Selli OAE1a (Farrimond et al., 1990; Kuhnt et al., 1990; Bralower et al., 1994; Herrle, 2002) that were recorded in the Cretaceous black shales of the Vigla limestones formation (Karakitsios et al., 2010; Karakitsios et al., 2007; Tsikos et al., 2004; Danelian et al., 2004 respectively). The alternations of oxic-anoxic sedimentary conditions

resulted in the deposition and preservation of organic matter in thin-bedded horizons. These are cyclic phenomena which are related to the climatic conditions (Ebukanson & Kinghorn, 1985; Huang et al., 1996). The duration of the cycle is low for the upper stratigraphic layers, while for the deeper horizons the duration is quite long.

2. To the high organic matter supply, due to the significant deposition rates, as concluded by the great formation thickness. So the organic matter passed quickly, without any alteration, through the oxygenated layers and was preserved in low oxygen areas, formed by the oxygen deficiency due to high oxygen demand (Habib, 1982; Farrimond et al., 1990). We believe that this process favored the high organic matter preservation into the two rich Vigla intervals (A' and B'), the main petroleum source rocks of the whole area. Another possibility is that anoxia in the photic zone was the main factor for organic matter preservation during the Vigla shales deposition.

In the Central and External Ionian zone remarkable organic matter quantities have been deposited during Lower Cretaceous in Vigla shales horizons, during Jurassic in horizons of Upper and Lower Posidonia Beds and finally during Triassic in shaly horizons (Karakitsios & Rigakis, 1996; Rigakis & Karakitsios, 1998; Rigakis, 1999). The conditions of deposition and preservation of the above horizons are more or less the same for Cretaceous and Jurassic formations, but they are different for the Triassic formations (Rigakis & Karakitsios, 1998).

The organic matter accumulation in the syn-rift formations of Early Toarcian through Tithonian is a result of upwelling (Jenkyns, 1985). Organic matter preservation is directly related to the geometry of the syn-rift period of the Ionian basin. The geometry of the restricted sub-basins favored water stagnation and consequently the development of locally anoxic conditions in the bottom waters (Karakitsios, 1995). Anoxic conditions occurred locally even during the post-rift period in the areas where the Vigla shales (Albian-Cenomanian), lithological member of Vigla formation, is well developed; these areas probably represent sub-basins that were preserved due to the continuation of halokinetic movements during the post-rift period. The well-documented early Toarcian OAE, Aptian-Albian Selli OAE1a, early Albian Paquier OAE1b and Cenomanian/Turonian OAE2 oceanic anoxic events that affected the entire Tethys Ocean, reinforced the anoxia for smaller time intervals as these are recorded in the thin but most organically rich black shale horizons of the corresponding stratigraphic levels. These horizons although cannot by themselves be considered as source rocks (because of their small thickness) they contribute to the oil potential of the whole source rocks (Karakitsios et al., 2007; Karakitsios et al., 2010). So, the local sub-basins geometry during the syn-rift and post-rift period of Ionian zone together with OAEs favored the preservation of the significant organic matter quantities, which are identified in the Lower Posidonia Beds of Toarcian age and in the Vigla shales of Albian-Cenomanian age (Rigakis & Karakitsios, 1998; Rigakis, 1999).

The dimension of the source rock horizons corresponding to the Lower Posidonia Beds is a significant problem, because it directly affects the quantities of generated hydrocarbons. Questions are raised first because this formation presents great thickness variations and second because in many outcrops the formation is eroded and altered with low organic matter. Two acceptances can be set:

1. The lower organic matter content is because of secondary alteration of these horizons due to external factors, which in some cases left intact the most resistant horizons. Alteration mainly affected the sediments in the surface till some meters in depth, where can act the climatic conditions; for this reason this formation whenever has been drilled contains horizons rich in organic matter (Rigakis & Karakitsios, 1998; Rigakis, 1999).
2. The organic matter decrease is due to the low quantities of organic matter deposition. According to the tectonic model of the syn-rift period that led to the deposition of prismatic syn-sedimentary wedges (Karakitsios, 1995), high amounts of organic matter were deposited and preserved in the deeper areas (depocenters) of the half grabens, while this

amount was reduced towards the shallower areas. This aspect is strengthened by the fact that in some outcrops, like the Paliogrimbiani section (Rigakis, 1999), only the deepest shale horizon contains significant amounts of organic matter, while the overlying horizons present low TOC content. Obviously this deeper horizon was deposited in an anoxic environment that changed to more oxic (with the progressive filling of the graben) in the upper horizons of the formation. After the exposition of these horizons to the surface conditions, their organic matter was further reduced due to secondary alterations. Evidently the Ioannina-1 and Dragopsa-1 wells were drilled in areas corresponding to the deepest parts of the half-grabens; that account for the high thickness of the sedimentary strata and for the source rock richness found in these wells.

The second interpretation which is directly associated with the depositional model of the area, is considered as more possible, but in some areas the first acceptance works too, which means that the complementary action of both cases can not excluded. According to the second model, the expected hydrocarbon quantities, in the total Ionian basin, are reduced. But, in areas where the Posidonia Beds were deposited in deep and extensive sub-basins, like the Botsara syncline, N. Kerkyra etc., their extensive depocenter accepted very large quantities of organic matter which were preserved, due to the anoxic conditions imposed by the geometry of the sub-basins. So, in these areas, high quantities of hydrocarbons are expected to be generated.

The Triassic breccias of the Ionian zone correspond to typical evaporite dissolution collapse breccias (Karakitsios & Pomoni-Papaioannou, 1998). It is suggested that, the shale fragments, with significant content in organic matter, incorporated into the Triassic breccias were initially deposited as stratigraphic layers in relatively shallow restricted sub-basins inside the evaporitic basin. The lack of detailed stratigraphy of the evaporitic sequence in Ionian zone does not allow any possible correlation of the shale layers' deposition with any geological event of Triassic age. However, it is known that organic rich sediments are usually deposited in the base of the evaporitic basins (Busson, 1988). In any case it can be accepted that, initially the organic matter preservation was due to eustatic sea level changes (Christiansen et al., 1993; Herbin et al., 1995). After that, the establishment of the evaporitic sedimentation in the entire basin favored the preservation of the organic matter (Powell, 1986, Busson, 1988, Miller, 1990). Consequently, the formation process of the evaporite dissolution collapse breccias also caused the fragmentation of the initially organic rich shale layers, which now appear as organic rich shale fragments incorporated into the Triassic breccias (Karakitsios & Rigakis, 1996; Rigakis & Karakitsios, 1998). This process took place in an anoxic environment, so the organic matter did not altered, but it preserved in significant quantities. Obviously, according to the stratigraphic position of this source rock, most of the oil generated by these horizons is expected to be found under the Triassic evaporites, charging laterally possible structures beneath this excellent cap rock.

In Paxi zone finally, the organic matter deposition and preservation are due to upwelling (Farrimond et al., 1990; Rigakis, 1999).

3.2 Calculation of the Eroded Formation Thickness

The eroded flysch thickness was calculated by the vitrinite reflectance (Ro) and sonic methods, by using the indigenous flysch horizons (Figure 3).

According to the vitrinite reflectance method (Dow, 1977), the eroded formation thickness can be calculated by the extrapolation of the Ro vs. depth curve till the depth corresponding to the value Ro=0.25%. This value corresponds to the maturity degree of the recent-immature sediments. In our case, in order to proceed to the extrapolation of the curve, we have first of all to choose the proper vitrinite measurements. In most cases the analytical results indicate the presence of two vitrinite populations. In the case of carbonates, the population with the low value was coming from caved material, while the population with the higher value was coming from the indigenous formation and was considered as the representative value of this formation. In the case of the

overlying flysch strata, the opposite thing happens. The population with the high vitrinite reflectance values is coming from reworked-oxidized material, while the population with the lower value was coming from the indigenous formation and was considered as the representative value of flysch (Rigakis, 1999). Based only on the representative values, the maturity vs. depth curve was drawn in a semi logarithmic plot (Figure 3). By this curve is concluded that the upper limit of petroleum generation is located at 2950m depth. Analogous depth for the onset of petroleum generation is concluded by other maturity methods (pyrolysis methods and biomarker maturity ratios). The accordance of all these methods supports the accuracy of each one of the used methods and furthermore reinforces the above selection of the proper vitrinite populations.

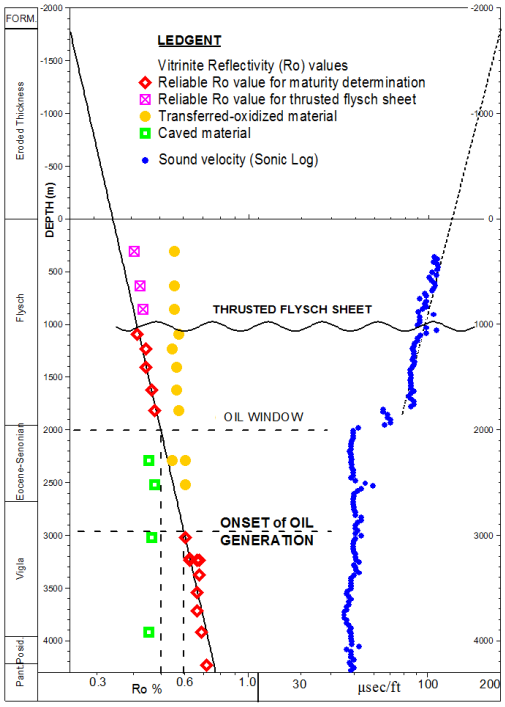

Figure 3 – Vitrinite reflectance (Ro%) vs. depth and Sonic vs. depth diagram for calculation of the eroded formation thickness.

After choosing the proper vitrinite values and drawing the correct maturity-depth curve, the next step was the extrapolation of this curve till the depth which corresponds to the value Ro=0.25%, the maturity degree of the recent-immature sediments. The depth found was -1780m. As a result, **the eroded formation thickness must be 1780m**. Furthermore, by studying the maturity-depth curve, the presence of a thrust block of flysch was observed at 1050m depth (Figure 3). The ascertainment was based on the fact that newer sediments of 856m depth appear higher maturity degree (Ro=0.44%) than older sediments at 1092m depth (Ro=0.42%). Based on the maturity that should hold these sediments, we proceeded to the calculation of the thrust out sediments thickness; this thickness reaches the 500m. Obviously, in the maturity calculations, the values of the in situ flysch sediments were used and not those of the thrust block (Figure 3).

The sonic method (Magara, 1978) is similar to the vitrinite one for calculation of the eroded formation thickness. It is considered as a fact that in the recent-unconsolidated sediments the sound velocity is almost 1520 m/sec (like the water), which corresponds to 200 µsec/ft in the sonic log measurements. The sonic log values of Agios Georgios-3 well, were plotted in the semi logarithmic plot of the Figure 3 (the "opposite" diagram of the vitrinite one). For the plotting was selected one point every 25m, which was the average value of the 25m interval; measurements

were taken only from the shale intervals. Looking at this plot, the grate difference between the carbonate units at the bottom of the section and the upper flysch horizons is found at the beginning, as well as a transitional layer of about 170m thick. Studying the flysch interval, the presence of the thrust flysch sheet at 1050m was confirmed. Like in the vitrinite diagram, the lower lied sediments appear to be less consolidated than the upper ones. So, in order to calculate the formation thickness removed by the erosion, only the in situ-lower flysch sediments were used. A sonic vs. depth curve was created, and afterward this curve was extrapolated till the value of 200 μsec/ft. The depth which corresponds to this value is -1780m. That means that **the eroded formation thickness is 1780m**, which is exactly the same with the depth calculated by the vitrinite method.

The accordance of the results of these two methods supports the accuracy of both of them and of the resulted data. This calculated thickness of 1780m is the one that was used for the maturity calculations, through maturity models. Furthermore the presence of the flysch thrust sheet, which was observed at 1050m depth, helped to a better understanding and a more accurate interpretation of the seismic lines in the surrounding area.

3.3 Dolomitization

Another problem of great importance in the Internal Ionian zone is the extensive dolomitization, which has reduced the oil generation capability of some source rocks. It is known (Beales & Hardy, 1980) that dolomitization can oxidize the organic matter which had deposited and preserved to the sediments. This phenomenon is strong in the case of Agios Georgios-3 well, where the reduction of the organic matter quantity by depth is directly related with the increase of the percentage of the Magnesium Carbonate ($MgCO_3$) in the well samples. From Figure 4 which indicates a combination between the percentage of the Total Organic Carbon (TOC) and the percentage of the $MgCO_3$ by depth, it is concluded that:

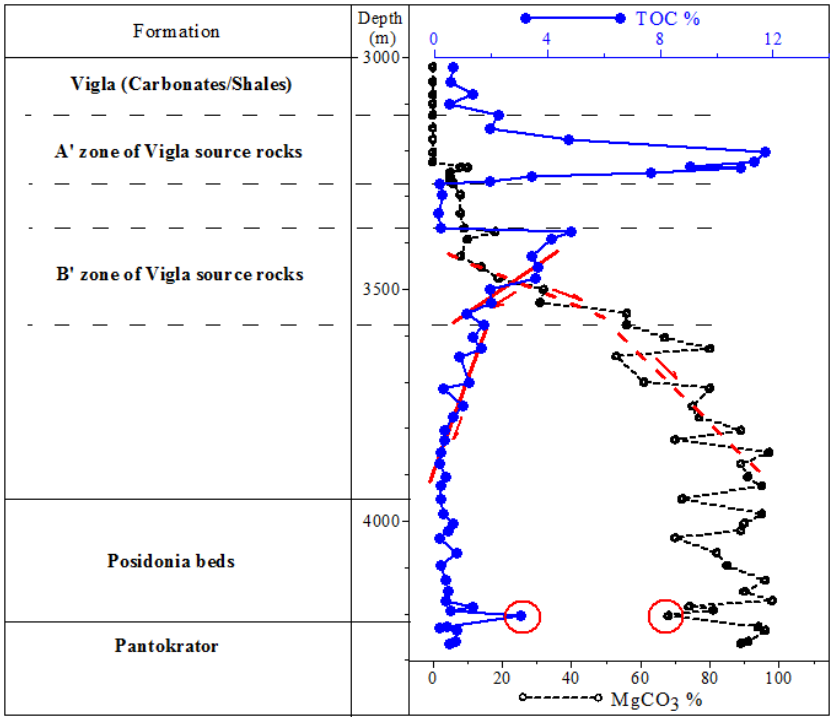

Figure 4 – Dolomitization effects to the organic matter in the formations drilled by Agios Georgios-3 well, Arta syncline.

1. In the A' zone of Vigla source rocks where the percentage of $MgCO_3$ is almost zero, the source rocks are much more rich in TOC than the source rocks of zone B', where the $MgCO_3$ ranges between 8 and 56%.
2. In the interval between 3476 and 3576m of zone B', where the percentage of $MgCO_3$ appears significant increase from 19 to 56%, it is observed a corresponding significant decrease in the TOC content from 4.84 to 1.13%.
3. In the deeper horizons where the $MgCO_3$ increase shows a lower rate (from 67 to 94%), the rate of the TOC content decrease is also lower.
4. Posidonia Beds appear low TOC content, obviously due to the dolomitization. But, whenever some Posidonia horizons appear high TOC content, the corresponding $MgCO_3$ percentage is low.

All the above observations indicate that dolomitization has strongly affected the presence of organic matter in the source rock horizons. Further to the results concluded by the diagram, it is also observed in the deeper shale horizons some samples with high TOC content without analogous high petroleum potential values (Rigakis, 1999). This fact is also assigned to the oxidation of the organic matter during dolomitization. This oxidation didn't affect the residual carbon and for this reason the TOC appears high values, while the oxidation reduced the pyrolyzable carbon and the petroleum potential, which are reduced. Furthermore the dolomitization didn't affect the free hydrocarbons (S1). The S1 values remain high, while on the other hand the kerogen values (S2) appear significant reduction. As a result the values of the production index (PI=S1/S1+S2) are high; obviously these high PI values are not only a result of maturation and/or migration, but they have also been affected from the different influence of dolomitization to the S1 and S2 peaks (Rigakis, 1999).

The presence and the extension of dolomitization is a problem for the whole surrounding area. Dolomitization probably extend to a great area since the organic matter of the sediments favors the dolomitization processes, by the contribution of Magnesium ions (Beales & Hardy, 1980; Zenger & Dunham, 1980). Furthermore dolomitization is stronger in the deeper layers, where the source rocks expected to be more mature, and as a result to generate higher quantities of hydrocarbons. So, if a big part of their organic matter content has been destroyed, the anticipated hydrocarbon quantities significantly reduced. Of course, these can happen only if dolomitization has affected the source rocks prior to the oil generation process.

The timing of dolomitization is a very critical point, which must be studied very carefully. If dolomitization has started prior to the oil generation, then the anticipated quantities of generated hydrocarbons will be reduced. On the other hand, if the oil generation had already started prior to the dolomitization, then the source rocks would already have generated some quantities of hydrocarbons. About the timing of dolomitization two acceptances can be set:

1. Dolomitization starts during orogenesis and continues after it, because of fracturing and solution circulation, like meteoric waters or hydrothermal liquids (Nichols & Silberling, 1980). That is the favor case, since the dolomitization takes place after oil generation in most areas, and as a result its influence in the oil-generated quantities is generally low, especially in the basin center, where the oil generation process had started long before orogenesis.
2. Dolomitization has started earlier, after deposition and before or during diagenesis (Dunham & Olson, 1980). In this case the kerogen was strongly affected and the expected quantities of oil have been reduced, limited mainly to the oil potential of the source rocks located at the sub-basin margins.

All the above mentioned referred especially to the lower-deeper source horizons. Especially the Posidonia Beds, which are strongly dolomitized even in the periphery of the basin, are not anticipated to be potential source rocks. These horizons may have contributed to the oil potential

of the basin only in the case that dolomitization has taken place after orogenesis that means after the oil generation. Taking into consideration that the oil generation from the Posidonia Beds started during Lower Oligocene and continued till Burdigalian (Rigakis, 1999), these source rocks would had generated their whole petroleum potential before the oxidation of their organic matter. Of course part of this oil may have been lost during orogenesis processes. In any other case it is not anticipated oil from this formation. On the other hand, high quantities of oil in the Internal Ionian zone are expected from the **Vigla shales**, which were not so much affected by dolomitization, and consequently can be considered as **the main source rocks** of this sub-basin.

3.4 Paleogeothermal Gradient Estimation

A very important application of the maturity calculation through maturity models is the paleotemperature determination; it is achieved by combining the time-temperature index (TTI) calculated by maturity models (Waples, 1980), with the vitrinite reflectivity (Ro) data, which is a very reliable paleo-thermometer (Dow, 1977; Tissot & Welte, 1984; Katz et al., 1988).

The initial maturity models for the Paxi-Gaios-1X well, indicated that the calculated maturity curve (TTI vs. depth) does not agree at all with the real maturity curve of the sediments, as it is expressed by the Ro vs. depth curve. These modeling attempts used only the present day low geothermal gradients and accepted that the same temperatures had also affected the older formations. The negative correlation of the maturity curves however clearly show that such an assumption does not suffice to describe the paleotemperatures; the difference should be assigned to the increased values of the paleogeothermal gradients, which could be associated with the periods of earth crust thinning (McKenzie, 1981).

After this ascertainment some arbitrary higher paleogeothermal gradients was used, which brought a closure to the curves' "opening". But, the best abridgement of the two curves was achieved after the application of the paleogeothermal gradient values suggested by Professor Pieri (personal communication). The suggestion is that during Triassic times the gradient was 2.5°C/100m and started increasing reached its higher value of 3.5°C/100m during Upper Cretaceous, before the Tethys closure. This high value decrease to 2.5°C/100m during Oligocene times with the flysch deposition and by further decrease reached the today low values (Flores et al., 1991).

By using these paleogeothermal gradients, a very well coincidence of TTI versus depth curve with Ro versus depth curve is obtained (Figure 5). After that, the suggested paleotemperature data are accepted as correct, and were applied for maturity determinations through maturity models in the whole area. These high paleotemperature values mainly affected the older formations, exposed for log period under high temperatures. On the other hand, the newer formations have been less affected by these paleogeothermal gradients.

4. Conclusions

The paleogeographic conditions during deposition and preservation of the organic matter in the Western Greece are not always the same. In the Triassic shales, the preservation of the organic matter was probably a result of eustatic sea level changes, in combination with the evaporite sedimentation. The source rocks of the Jurassic syn-rift formations were deposited in restricted subbasins, whose geometry favored water stagnation, development of local anoxic conditions in the bottom water and organic matter preservation. In the eastern areas of the Ionian basin accumulation and preservation of very high quantities of organic matter in Vigla shales was a result of the high deposition rates. In both the Jurassic and Cretaceous Ionian zone formations, the prevalence of anoxic conditions, during the corresponding oceanic anoxic events, reinforced organic matter preservation. In the Paxi zone deposition and preservation of the organic matter was a result of upwelling movement of seawater.

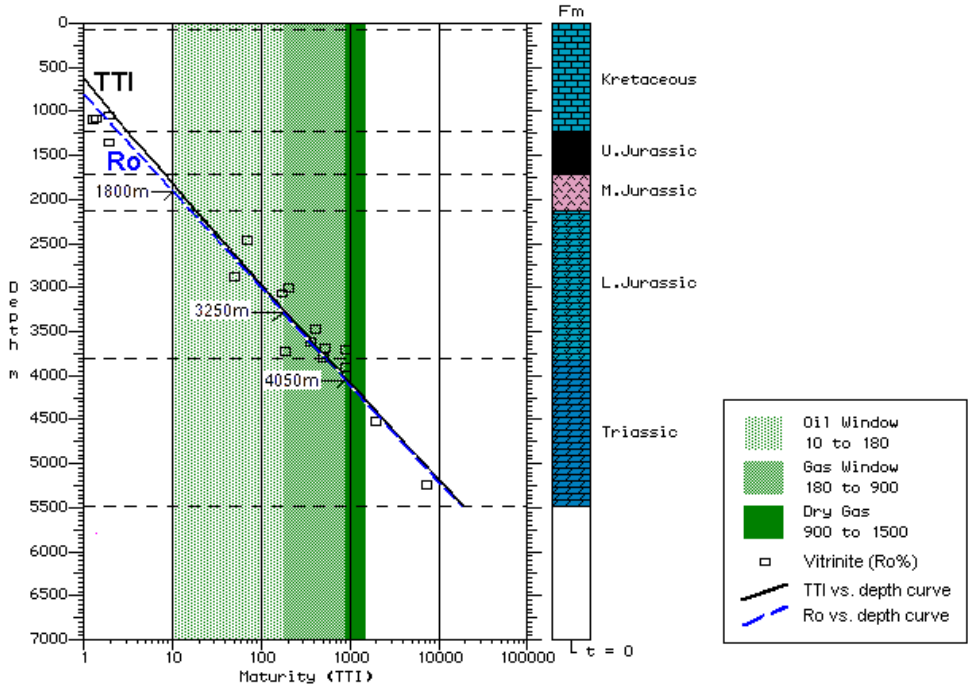

Figure 5 – Paleogeothermal gradient estimation by comparing TTI vs. depth with Ro vs. depth curves in Paxi-Gaios-1X well.

The eroded formation thickness in Internal Ionian zone, calculated by both vitrinite reflectance (Ro) and sonic methods is 1780m. This thickness was used for maturity calculations through maturity models.

One factor, that affects negatively the oil generation, is the dolomitization in the Internal Ionian zone. In this area, oil can be generated either from the upper horizons-Vigla shales, which are not affected by dolomitization, or from the older horizons-Posidonia Beds, which could have generated oil prior to dolomitization.

The paleogeothermal gradient in the Western Greece was estimated by using vitrinite reflectance (Ro%) data from the deep well Paxi-Gaios-1X in combination with maturity models. This gradient starts from 2.5°C/100m in Triassic, increase to 3.5°C/100m in Upper Cretaceous and decrease to 2.5°C/100m in Oligocene. These data are absolutely necessary for maturity estimations through maturity models.

5. References

Beales F. W. and Hardy J. W. 1980. Criteria for the recognition of diverse dolomite types with an emphasis on studies of host rocks for Mississippi valley-type ore deposits, In Zenger D. H., Dunham J. B. and Ethington R. L. (eds.), Concepts and models of dolomitisation, *SEPM Special Publication No 28*, 197-213.

BP - British Petroleum Corporation Limited 1971. The geological results of petroleum exploration in Western Greece, *Institute of Geology and Subsurfuce Research*, 10, 73 pp.

Bornovas I. 1964. Geology of Lefkada Island, *Institute of Geology and Subsurfuce Research*, X/1, 142 pp.

Busson G. 1988. Relations entre les types de depots evaporitiques et la presence de couches riches en matiere organique (roches-meres potentielles), *Revue de l' Institut Francais du Petrole*, 43/2, 181-215.

Christiansen F. G., Piasecki S., Stemmerik L. and Telnaes N. 1993. Depositional environment and organic geochemistry of the Upper Permian Ravnefield formation source rock in East Greenland, *AAPG Bulletin*, 77, 1519-1537.

Danelian T., Tsikos H., Gardin S., Baudin F., Bellier J. P. and Emmanuel L. 2004. Global and regional palaeoceanographic changes as recorded in the mid-Cretaceous (Aptian–Albian) sequence of the Ionian Zone (northwestern Greece), *Journal of the Geological Society of London,* 161/4, 703-709.

Dermitzakis M. 1978. Stratigraphy and sedimentology history of the Miocene of Zakynthos (Ionian Islands, Greece), *Annales Geologiues des Pays Helleniques*, series 1, XXIX/1, 47-186.

Dow W. G. 1977. Kerogen studies and geological interpretations, *Journal of Geochemical Exploration*, 7, 79-99.

Dunham J. B. and Olsom E. R. 1980. Shallow subsurface dolomitization of subtidally deposited carbonate sediments in the Hanson Greek formation (Ordovician-Silurian) of Central Nevada, In Zenger D. H., Dunham J. B. and Ethington R. L. (eds.), Concepts and models of dolomitisation, *SEPM Special Publication,* No 28, 139-161.

Ebukanson E. J. and Kinghorn R. R. F. 1985. Kerogen facies in the major Jurassic Mudrock formations of Southern England and the implication on the depositional environments of their precursors, *Journal of Petroleum Geology*, 8/4, 435-462.

Farrimond P., Eglinton G., Brassell S. C. and Jenkyns H. C. 1989. Toarcian anoxic event in Europe: An organic geochemical study, *Marine and Petroleum Geology*, 6, 136-147.

Farrimond P., Eglinton G., Brassell S. C. and Jenkyns H. C. 1990. The Cenomanian/Turonian anoxic event in Europe: An organic geochemical study, *Marine and Petroleum Geology*, 7, 75-89.

Flores G., Pieri M. and Sestini G. 1991. Geodynamic history and petroleum habitats of the South-East Adriatic region. In: Spencer A. M. (ed.), Generation, accumulation, and production of Europe's hydrocarbons, *EAPG Special Publication* 1, 389-398, *Oxford University Press*.

Habib A. 1982. Sedimentary supply origin of Cretaceous black shales. In Schlanger S. O. and Cita M. B. (eds.), *Nature and Origin of Cretaceous Carbon-rich Facies*, *Academic Press,* 113-127.

Herbin J. P., Fernandez-Martinez J. L., Geyssant J. R., Albani A. El., Deconinck J. F., Proust J. N., Colbeaux J. P. and Vidier J. P. 1995. Sequence stratigraphy of source rocks applied to the study of the Kimmeridgian/Tithonian in the North-west European shelf (Dosret/UK, Yorkshire/UK and Boulonnais/France), *Marine and Petroleum Geology*, 12, 177-194.

Herrle J. O. 2002. Paleoceanographic and paleoclimatic implications on Mid-Cretaceous black shale formation in the Vocontian Basin and the Atlantic: evidence from calcareous nannofossils and stable isotopes, *Tuebinger Mikropalaeontologische Mitteilungen,* 27, 114 pp.

Huang Z., Williamson M. A., Bateman J., McAlpine K. D. and Fowler M. G. 1996. Cyclicity in the Egret member (Kimmeridgian) oil source rock, Jeanne d' Arc basin, offshore Eastern Canada, *Marine and Petroleum Geology*, 13/1, 91-105.

IGRS-IFP - Institut de Geologie et Recherches du Sous-sol-Institut Francais du Petrole 1966. Etude geologique de l' Epire (Grece Nord-occidentale), *Editions Technip,* 306 pp.

Jenkyns H. C. 1985. The Early Toarcian and Cenomanian-Turonian anoxic events in Europe: Comparisons and contrasts, *Geologische Rundschau*, 74/3, 505-518.

Jenkyns H. C. 1988. The Early Toarcian (Jurassic) anoxic event: Stratigraphic, Sedimentary, and geochemical evidence, *American Journal of Science*, 288, 101-151.

Karakitsios V. 1995. The influence of preexisting structure and halokinesis on organic matter preservation and thrust system evolution in the Ionian basin, Northwestern Greece, *AAPG Bulletin*, 79, 960-980.

Karakitsios V. and Rigakis N. 1996. New oil source rocks cut in Greek Ionian basin, *Oil & Gas Journal*, 94/7, 56-59.

Karakitsios V. and Pomoni-Papaioannou F. 1998. Sedimentological study of the Triassic solution-collapse breccias of the Ionian zone (NW Greece), *Carbonates & Evaporites*, 13/2, 207-218.

Karakitsios V. and Rigakis N. 2007. Evolution and petroleum potential of Western Greece, *Journal of Petroleum Geology,* 30/3, 197-218.

Karakitsios V., Tsikos H., Van Breugel Y., Koletti L., Sinninghe Damste J. S. and Jenkyns H. C. 2007. First evidence for the Cenomanian – Turonian Oceanic Anoxic Event (OAE2 or "Bonarelli" Event) from the Ionian Zone, Western Continental Greece, *International Journal of Earth Sciences*, 96, 343-352.

Karakitsios V., Kafousia N. and Tsikos H. 2010. Oceanic Anoxic Events as recorded in the Mesozoic sedimentary record of mainland Greece, *Hellenic Journal of Geosciences*, 45, 123-131.

Katz B. J., Pheifer R. N. and Schunk D. J. 1988. Interpretation of discontinuous vitrinite reflectance profiles, *AAPG Bulletin*, 72, 926-931.

Kuhnt W., Herbin J. P., Thurow J. and Wiedmann J. 1990. Distribution of Cenomanian-Turonian organic facies in the Western Mediterranean and along the adjacent Atlantic margin. In Huc A. Y. (ed.), Deposition of Organic Facies, *AAPG studies in geology,* 30, 133-160.

Magara K. 1978. Geological models of petroleum entrapment, *Elsevier, Applied Science Publishers* (eds.), 328 pp.

McKenzie D. 1981. The variation of temperature with time and hydrocarbon maturation in sedimentary basins formed by extension. *Earth and Planetary Science Letters*, 55, 87-98.

Miller R. G. 1990. A paleoceanographic approach to the Kimmeridge clay formation. In Huc A. Y. (ed.), Deposition of Organic Facies, *AAPG studies in geology,* 30, 13-26.

Nichols K. M. and Silberling N. J. 1980. Eogenetic dolomitization in the Pre-Tertiary of the Great basin. In Zenger D. H., Dunham J. B. and Ethington R. L. (eds.), Concepts and models of dolomitisation, *SEPM Special Publication No 28*, 237-246.

Powell T. G. 1986. Petroleum geochemistry and depositional setting of lacustrine source rocks, *Marine and Petroleum Geology*, 3, 200-219.

Rigakis N. 1999. Contribution to stratigraphic research on wells and outcrops of the Alpine formations in Western Greece, in relation to the petroleum generation efficiency of their organic matter, *Ph.D. Thesis*, Athens University, 255 pp.

Rigakis N. and Karakitsios V. 1998. The source rock horizons of the Ionian basin (NW Greece), *Marine and Petroleum geology*, 15, 593-617.

Rigakis N., Nikolaou K., Marnelis F. and Pakos Th. 2007. The utility of oil shows in the hydrocarbon exploration of Western Greece, *Bulletin of the Geological Society of Greece XXXX, 2007, Proceedings of the 11th International Congress*, 959-971.

Tissot B. P. and Welte D. H. 1984. Petroleum formation and occurrence, *Springer-Verlag,* 699 pp..

Tsikos H., Karakitsios V., Breugel Y., Walswarth-Bell B., Bombardiere L., Petrizzo M. R., Sinninghe Damste J. S., Schouten S., Erba E., Premoli Silva I., Farrimond P., Tyson R. V., and Jenkyns H. C. 2004. Organic-carbon deposition in the Cretaceous of the Ionian Basin, NW Greece: the Paquier Event (OAE1b) revisited, *Geological Magazine*, 141/4, 401-416.

Waples D. W. 1980. Time and temperature in petroleum formation: Application of Lopatin's method to petroleum exploration, *AAPG Bulletin*, 64, 916-926.

Zenger D. H. and Dunham J. B. 1980. Consepts and models of dolomitization - An indroduction. In Zenger D. H., Dunham J. B. and Ethington R. L. (eds.), Concepts and models of dolomitisation, *SEPM Special Publication,* No 28, 1-9.

ΕΥΡΕΤΗΡΙΟ ΣΥΓΓΡΑΦΕΩΝ/AUTHOR INDEX